

PROCEEDINGS OF SPIE



SPIE—The International Society for Optical Engineering

Optoelectronic Materials and Devices II

Yan-Kuin Su
Pallab Bhattacharya
Chairs/Editors

26-28 July 2000
Taipei, Taiwan

Sponsored by
SPIE—The International Society for Optical Engineering
National Science Council (Taiwan)
PIDA—Photonics Industry Development Association

DISTRIBUTION STATEMENT A
Approved for Public Release
Distribution Unlimited

20010122 146



Volume 4078



The papers appearing in this book compose the proceedings of the technical conference cited on the cover and title page of this volume. They reflect the authors' opinions and are published as presented, in the interests of timely dissemination. Their inclusion in this publication does not necessarily constitute endorsement by the editors or by SPIE. Papers were selected by the conference program committee to be presented in oral or poster format, and were subject to review by volume editors or program committees.

Please use the following format to cite material from this book:

Author(s), "Title of paper," in *Optoelectronic Materials and Devices II*, Yan-Kuin Su, Pallab Bhattacharya, Editors, Proceedings of SPIE Vol. 4078, page numbers (2000).

ISSN 0277-786X
ISBN 0-8194-3717-4

Published by
SPIE—The International Society for Optical Engineering
P.O. Box 10, Bellingham, Washington 98227-0010 USA
Telephone 1 360/676-3290 (Pacific Time) • Fax 1 360/647-1445
<http://www.spie.org/>

Copyright ©2000, The Society of Photo-Optical Instrumentation Engineers.

Copying of material in this book for internal or personal use, or for the internal or personal use of specific clients, beyond the fair use provisions granted by the U.S. Copyright Law is authorized by SPIE subject to payment of copying fees. The Transactional Reporting Service base fee for this volume is \$15.00 per article (or portion thereof), which should be paid directly to the Copyright Clearance Center (CCC), 222 Rosewood Drive, Danvers, MA 01923 USA. Payment may also be made electronically through CCC Online at <http://www.directory.net/copyright/>. Other copying for republication, resale, advertising or promotion, or any form of systematic or multiple reproduction of any material in this book is prohibited except with permission in writing from the publisher. The CCC fee code is 0277-786X/00/\$15.00.

Printed in the United States of America.

Contents

xiii Conference Committee

PLENARY PAPER

-
- 2 **Photonic technologies in the 21st century: creation of new industries [4078-201]**
T. Hiruma, Hamamatsu Photonics K.K. (Japan)

SESSION 1 GaN LED AND MATERIALS I

-
- 8 **Radiative recombination mechanisms in InGaN/AlGaIn single-quantum-well LED revealed by time-resolved photoluminescence spectra under external electric fields [4078-02]**
H. Kudo, T. Tanabe, H. Ishibashi, R. Zheng, Y. Yamada, T. Taguchi, Yamaguchi Univ. (Japan)

SESSION 2 GaN LED AND MATERIALS II

-
- 18 **Optical quality of InGaAsN/GaAs [4078-03]**
B. J. Robinson, L. Yuan, D. A. Thompson, S. A. McMaster, McMaster Univ. (Canada);
R. W. Streater, Nortel Networks (Canada)
- 28 **Optical pumping spectra for In_xGa_{1-x}N/GaN multiple-quantum-well structures with indium content $x > 0.35$ [4078-06]**
C.-C. Chen, H.-W. Chuang, G.-C. Chi, C.-C. Chuo, J.-I. Chyi, National Central Univ. (Taiwan)
- 35 **Dielectric function of GaN: model calculations [4078-07]**
A. B. Djurišić, Technische Univ. Dresden (Germany); E. H. Li, Univ. of Hong Kong

SESSION 3 GaN LED AND MATERIALS III

-
- 44 **Effect of indium surfactant on the optical and structural properties of MBE-grown GaN (Invited Paper) [4078-08]**
W. K. Fong, C. F. Zhu, C. Surya, B. H. Leung, C. C. Cheng, Hong Kong Polytechnic Univ.;
B. Sundaravel, E. Z. Luo, J. B. Xu, I. H. Wilson, Chinese Univ. of Hong Kong
- 58 **Effect of pre-treatment of GaN substrate for homoepitaxial growth by rf MBE [4078-11]**
S. Kubo, T. Okazaki, S. Manabe, S. Kurai, T. Taguchi, Yamaguchi Univ. (Japan)
- 66 **Effects of gamma-ray irradiation on the microstructural and luminescent properties of radio-frequency magnetron-sputtered GaN thin films [4078-12]**
C.-W. Wang, B.-S. Soong, C.-T. Tzeng, J.-Y. Chen, C.-L. Chen, I-Shou Univ. (Taiwan)
- 74 **Etch of gallium nitride and other III-IV materials using a novel high-density plasma configuration [4078-13]**
T.-N. Kuo, J.-H. Yeh, H.-J. Lee, C.-A. Chen, G.-K. Jeng, C.-P. Lin, Nano-Architect Research Corp. (Taiwan)

SESSION 4 QUANTUM DOTS: GROWTH, DEVICES, AND APPLICATIONS

- 84 **Quantum dot carrier dynamics and far-infrared devices (Invited Paper) [4078-14]**
P. Bhattacharya, S. Krishna, J. D. Phillips, D. Klotzkin, Univ. of Michigan (USA); P. J. McCann, Univ. of Oklahoma (USA)
- 90 **Temperature dependence of quantum dot lasers (Invited Paper) [4078-15]**
D. G. Deppe, G. Park, O. B. Shchekin, Univ. of Texas at Austin (USA)
- 100 **Quantum dot devices (Invited Paper) [4078-16]**
S. Fafard, H. C. Liu, Z. R. Wasilewski, J. P. McCaffrey, M. Spanner, S. Raymond, C. N. Allen, K. Hinzer, J. M. Lapointe, C. Struby, M. Gao, P. Hawrylak, C. Gould, A. Sachrajda, P. Zawadzki, National Research Council Canada
- 115 **Observation of self-assembled InAs/GaAs quantum dot structure with temperature-dependent photoluminescence and measurement of electrical characteristics [4078-17]**
S.-F. Tang, S.-Y. Lin, Y.-C. Liao, S.-C. Lee, National Taiwan Univ.; Y.-T. Cherng, Chung Shan Institute of Science and Technology (Taiwan)
- 124 **One-dimensional arrays of self-assembled InAs/InP quantum dots [4078-18]**
J. Lefebvre, P. J. Poole, J. P. McCaffrey, B. Lamontagne, G. C. Aers, National Research Council Canada; C.-P. Lee, National Chiao Tung Univ. (Taiwan); S.-F. Hu, National Nano Device Labs. (Taiwan); R. L. Williams, National Research Council Canada

SESSION 5 QUANTUM WELL INTERMIXING AND LASERS

- 130 **Material growth investigation and high performance of InGaAs/InGaAsP/AlGaAs quantum well diode lasers ($\lambda=0.98\ \mu\text{m}$) [4078-20]**
R. J. Hwu, G. W. Yang, Univ. of Utah (USA)
- 137 **Low-threshold current densities of 1.5- μm wavelength (110) GaInAs(P) QW lasers along [001] direction [4078-21]**
K. Oe, Kyoto Institute of Technology (Japan); R. J. Bhat, Corning Inc. (USA); M. Ueki, NTT Electronics (Japan); M. Mitsuhashi, NTT Photonics Labs. (Japan)

SESSION 6 SEMICONDUCTOR LEDs AND LASERS

- 148 **New methods of defect-enhanced quantum well intermixing and demonstrated integrated distributed-feedback laser modulator (Invited Paper) [4078-22]**
D. A. Thompson, J. F. Hazell, A. S. W. Lee, T. Yin, G. J. Letal, B. J. Robinson, N. Bertsch, J. G. Simmons, McMaster Univ. (Canada)
- 162 **Characteristics of oxide-confined AlGaAs/GaAs resonant-cavity light-emitting diodes [4078-24]**
H.-P. D. Yang, C.-Z. Wu, M.-L. Wang, W.-C. Jiang, S.-J. Yu, C.-P. Sung, Industrial Technology Research Institute (Taiwan)
- 170 **High-efficiency tunneling-regenerated multi-active-region light-emitting diodes [4078-25]**
X. Guo, G. Shen, G. Wang, J. Du, W. Guo, G. Gao, W. Zhu, D. Zou, Beijing Polytechnic Univ. (China)

SESSION 7 EPITAXIAL GROWTH

- 182 **Phase calculation of (100) oriented InGaAsP grown with liquid phase epitaxy [4078-27]**
J. Zhu, X. Mao, Y.-C. Chan, Y.-L. Lam, Nanyang Technological Univ. (Singapore)
- 191 **New concept technology: pressure-variation liquid phase epitaxy [4078-28]**
X. Mao, Y.-C. Chan, Y.-L. Lam, J. Zhu, Y. Shi, Nanyang Technological Univ. (Singapore)
- 203 **Infrared reflectance study of chemical-vapor-deposition-grown 3C-silicon carbide on silicon substrate [4078-29]**
W. Y. Chang, National Univ. of Singapore; Z. C. Feng, Institute of Materials Research and Engineering (Singapore); S. J. Chua, Institute of Materials Research and Engineering (Singapore) and National Univ. of Singapore; J. Lin, National Univ. of Singapore
- 211 **Optical characterization of low-temperature GaAs [4078-30]**
G. Chen, H. E. Ruda, Univ. of Toronto (Canada); Q. Liu, Filtronic Solid State (USA); L. Z. Jedral, Delphax Inc. (Canada); C. H. Edirisinghe, SDL, Inc. (USA); B. G. Yacobi, Univ. of Toronto (Canada); P. W. E. Smith, S. D. Benjamin, Univ. of Toronto (Canada)

SESSION 8 INTEGRATED OPTICAL COMPONENTS AND DEVICES

- 220 **Semiconductor photonic integration: a regrowth free approach (Invited Paper) [4078-31]**
J. H. Marsh, Univ. of Glasgow (UK)
- 232 **Design of wideband dispersion compensating optical fiber device based on higher-order LP₁₁ mode [4078-33]**
A. Goel, J. L. Rana, Maulana Azad College of Technology (India)
- 239 **Integrated magneto-optic waveguide material structures and devices [4078-34]**
C. S. Tsai, Ctr. for Applied Science and Engineering (Taiwan) and Univ. of California/Irvine (USA)
- 247 **Light propagation characteristics of microsphere array [4078-35]**
F. Huang, H. Ebihara, S. Morita, Nagoya Univ. (Japan)
- 254 **Preferential input and output coupling of oval-shaped optical microcavities: fluorescence emission from oval-shaped dye-doped glass fibers [4078-36]**
A. W. Poon, S. L. Kan, Yale Univ. (USA); P. A. Tick, D. A. Nolan, Corning Inc. (USA); R. K. Chang, Yale Univ. (USA)
- 263 **Novel three-branch optical power divider by Ti diffusion on lithium niobate [4078-38]**
T.-J. Wang, National Taipei Univ. of Technology (Taiwan); W.-S. Wang, National Taiwan Univ.

SESSION 9 ORGANIC LIGHT-EMITTING DEVICES

- 272 **Temperature- and field-dependent quantum efficiency in tris-(8-hydroxy) quinoline aluminum light-emitting diode [4078-39]**
S. K. Saha, Y. K. Su, National Cheng Kung Univ. (Taiwan); F. S. Juang, National Huwei Institute of Technology (Taiwan)

- 279 **Origin of the blue emission from poly(1-phenyl-2-alkynes) and poly(phenylacetylenes)** [4078-41]
W. Ge, Y. M. Huang, J. W. Y. Lam, B. Z. Tang, Hong Kong Univ. of Science and Technology
- 289 **New multichamber evaporator for organic devices** [4078-42]
Q. Wang, Shenyang Institute of UHV Technology and Applications (China); W. Guo, Univ. of Hong Kong; M. C. Y. Chan, Hong Kong Polytechnic Univ; S. Liu, Shenyang Institute of UHV Technology and Applications (China); E. H. Li, Univ. of Hong Kong, C. Surya, Hong Kong Polytechnic Univ.
- 292 **Novel material for blue organic light-emitting diode** [4078-43]
W. Guo, E. Li, C. Che, Univ. of Hong Kong; Y. Zhao, S. Liu, Jilin Univ. (China)

SESSION 10 ADVANCED OPTICAL DEVICES

- 298 **Picosecond imaging of hot electron emission from CMOS circuitry** [4078-45]
K. Ramanujachar, D. Landheer, S. Raymond, N. S. Charbonneau, P. T. Coleridge, National Research Council Canada; T. Wang, National Chiao Tung Univ. (Taiwan)
- 304 **Photonic components fabricated using ion implantation** [4078-46]
N. S. Charbonneau, P. J. Poole, G. C. Aers, J. E. Haysom, S. Raymond, P. G. Piva, National Research Council Canada; I. V. Mitchell, T. Simpson, Univ. of Western Ontario (Canada)
- 313 **Integration of waveguide-type wavelength demultiplexing photodetectors by selective intermixing of InGaAs/InGaAsP quantum well structure** [4078-47]
D. H. Yeo, K. H. Yoon, H. R. Kim, S. J. Kim, Seoul National Univ. (Korea)
- 321 **Concentration effect of spectroscopic properties of Yb³⁺-doped borate glasses** [4078-50]
C. Jiang, Q. Zeng, Shanghai Jiaotong Univ. (China); F. Gan, Shanghai Institute of Optics and Fine Mechanics (China)

POSTER SESSION

- 330 **Theoretical study on coupling effects of modulation depth between two photorefractive phase gratings with an external applied field** [4078-51]
B. Yuan, Z. Zhou, C. Hou, X. Sun, Harbin Institute of Technology (China)
- 345 **Performance improvement in XGM wavelength conversion exploiting SLAOLM** [4078-52]
X. Zhang, D. Huang, J. Sun, D. Liu, Huazhong Univ. of Science and Technology (China); H. Yi, Wuhan Research Institute of Posts and Telecommunications (China)
- 353 **SPICE circuit models for semiconductor lasers with effects of carrier and lattice heating** [4078-53]
C.-Y. Tsai, C.-H. Chen, T.-L. Sung, De Montfort Univ. (UK); C.-Y. Tsai, National Cheng Kung Univ. (Taiwan); C. C. Yang, National Taiwan Univ.
- 365 **HF signal measurement device for DVD disk** [4078-54]
S.-T. Lu, K.-Y. Wang, K.-Y. Chuang, C.-P. Kuei, D.-R. Huang, Industrial Technology Research Institute (Taiwan)
- 373 **Design of two-dimensional 1×16 and 1×32 array waveguide optical power splitters** [4078-55]
S.-L. Tsao, P.-C. Peng, Yuan Ze Univ. (Taiwan)

- 383 **Shrinkage of spacing in fabricating sol-gel optical elements [4078-56]**
L. Pang, D. Yi, Y. Yan, G. Jin, M. Wu, Tsinghua Univ. (China)
- 389 **Design of wavelength-selective directional coupler made of W-index waveguide for WDM [4078-57]**
J.-H. Yun, K. T. Ra, P.-J. Kim, Chosun Univ. (Korea); S.-D. Kim, DongA-InJae College (Korea); J.-G. Lee, J.-B. Kim, Chosun Univ. (Korea)
- 397 **Analysis of MMI characteristics with periodic air pads on SOI waveguide-based optical interconnects [4078-58]**
S.-L. Tsao, H.-C. Guo, Yuan Ze Univ. (Taiwan)
- 406 **Analysis of the optimal light launching position of SOI tapered waveguides [4078-59]**
S.-L. Tsao, M.-C. Chen, Yuan Ze Univ. (Taiwan)
- 414 **Experimental study of the temperature effect on the polarization state of MQW semiconductor optical amplifier [4078-60]**
S.-L. Tsao, Y.-L. Shen, Yuan-Ze Univ. (Taiwan)
- 422 **Fermi-level pinning of GaAs at room temperature directly determined by the amplitude of photoreflectance spectra [4078-61]**
Y. H. Chen, R. M. Chen, National Taipei Univ. of Technology (Taiwan)
- 429 **Analysis of novel polarization analyzer [4078-62]**
R.-C. Twu, W.-S. Wang, National Taiwan Univ.
- 437 **Characterizations of Zn-diffused lithium niobate directional coupler by post thermal treatment [4078-63]**
R.-C. Twu, W.-S. Wang, National Taiwan Univ.
- 445 **Improved interferometric method for determination of the mechanical properties of metal oxide films [4078-65]**
C.-L. Tien, Chung Shan Institute of Science and Technology (Taiwan) and National Central Univ. (Taiwan); C.-C. Lee, K.-P. Chuang, National Central Univ. (Taiwan)
- 456 **Fabrications and characterizations of micromachined Fabry-Perot interferometers [4078-66]**
R.-J. Lin, Industrial Technology Research Institute (Taiwan)
- 467 **256 × 256 InSb focal plane arrays [4078-67]**
Y.-T. Gau, L.-K. Dai, S.-P. Yang, P.-K. Weng, K.-S. Huang, Y.-N. Liu, C.-D. Chiang, F.-W. Jih, Y.-T. Cherng, H. Chang, Chung Shan Institute of Science and Technology (Taiwan)
- 480 **Cosputtering effect in titanium oxides by ion-beam sputtering deposition [4078-68]**
J.-C. Hsu, C.-C. Lee, National Central Univ. (Taiwan); L.-G. Hwa, Fu Jen Catholic Univ. (Taiwan)
- 489 **Raman and hot electron-neutral acceptor luminescence studies of electron-optical phonon interactions in GaAs/Al_xGa_{1-x}As quantum wells [4078-69]**
C. M. Wang, H. Y. Chang, K. W. Sun, Feng Chia Univ. (Taiwan); S. Y. Wang, C.-P. Lee, National Chiao Tung Univ. (Taiwan)

- 500 **High-growth-rate epitaxy of InN film by a novel-design MOCVD [4078-70]**
F.-H. Yang, Y.-J. Yang, National Taiwan Univ.; J.-H. Hwang, C.-H. Lee, K.-H. Chen, Institute of Atomic and Molecular Sciences (Taiwan); C.-Y. Lin, National Taiwan Univ.
- 507 **Performance and reliability of wafer-bonded AlGaInP/mirror/Si light-emitting diodes [4078-71]**
R. H. Horng, National Chung Hsing Univ. (Taiwan); D. S. Wu, W. C. Peng, Da-Yeh Univ. (Taiwan); M. F. Huang, P. H. Liu, C. H. Seieh, K. C. Lin, Visual Photonics Epitaxy Co. (Taiwan)
- 514 **Built-in electric field investigation on InAs and InGaAs nanostructures by photoreflectance [4078-72]**
C.-M. Lai, J.-H. Huang, G.-J. Jan, National Taiwan Univ.
- 521 **Metastable photoluminescence in heavily Mg-doped GaN grown by metalorganic chemical vapor phase epitaxy [4078-75]**
C.-K. Shu, W.-H. Lee, Y.-C. Pan, H.-Y. Huang, H.-H. Chen, W.-H. Chen, W.-K. Chen, M.-C. Lee, National Chiao Tung Univ. (Taiwan)
- 527 **ZnSe/Si growth by liquid phase deposition [4078-76]**
M. Y. Yeh, H. M. Yen, Yung-Ta Institute of Technology and Commerce (Taiwan)
- 535 **Gallium K-edge EXAFS study of GaN:Mg films [4078-78]**
Y.-C. Pan, S.-F. Wang, W.-H. Lee, W.-C. Lin, C.-K. Shu, National Chiao Tung Univ. (Taiwan); C.-I Chiang, C.-W. Lin, H. Chang, Chung Shan Institute of Science and Technology (Taiwan); J.-F. Lee, L.-Y. Jang, Synchrotron Radiation Research Ctr. (Taiwan); D.-S. Lin, M.-C. Lee, W.-H. Chen, W.-K. Chen, National Chiao Tung Univ. (Taiwan)
- 544 **New methodology to predict energy bandgaps in $Ga_xIn_{1-x}As_yP_{1-y}$ compounds by ANFIS theories [4078-79]**
S.-L. Chen, D.-A. Fann, Da-Yeh Univ. (Taiwan)
- 551 **GaAs-based long-wavelength traveling-wave photodetector [4078-80]**
J.-W. Shi, C.-K. Sun, Y.-J. Yang, National Taiwan Univ.; Y.-J. Chiu, J. E. Bowers, Univ. of California/Santa Barbara (USA)
- 559 **Novel electrically tunable FBG laser [4078-82]**
L. Ding, Y. Xu, D. Feng, G. Kai, X. Dong, Nankai Univ. (China)
- 562 **Rapid thermal annealing effects on radio-frequency magnetron-sputtered P-type GaN thin films and Al/P-type GaN Schottky diodes [4078-83]**
C.-W. Wang, B.-S. Soong, J.-Y. Chen, C.-T. Tseng, C.-L. Chen, I-Shou Univ. (Taiwan)
- 570 **II-VI light-emitting diode with low operation voltage [4078-85]**
W.-H. Lan, Y. T. Cheng, A. C. H. Lin, Y. T. Cheng, H. Chang, Chung Shan Institute of Science and Technology (Taiwan); W.-R. Chen, Y.-K. Su, S.-J. Chang, National Cheng Kung Univ. (Taiwan); W. C. Chou, C. S. Yang, Chung Yuan Christian Univ. (Taiwan)
- 579 **Temperature-dependent optical properties of InGaN semiconductor materials: experimental and numerical studies [4078-89]**
Y.-K. Kuo, J.-Y. Chang, K.-K. Horng, Y.-L. Huang, Y. Chang, H.-C. Huang, National Changhua Univ. of Education (Taiwan)

- 587 **Broadband Cr:YSO solid state saturable absorber for ruby, alexandrite, and Cr:LiCAF lasers: numerical study on passive Q-switching performance [4078-90]**
Y.-K. Kuo, J.-Y. Chang, H.-M. Chen, National Changhua Univ. of Education (Taiwan)
- 595 **Experimental and numerical study on the optical properties of yellow-green AlGaInP light-emitting diodes [4078-91]**
M.-F. Huang, P.-H. Liu, J. S. Liu, Visual Photonics Epitaxy Co. Ltd. (Taiwan); Y.-K. Kuo, Y.-L. Huang, Y. Chang, H.-C. Huang, K.-K. Horng, J.-Y. Chang, National Changhua Univ. of Education (Taiwan)
- 603 **Nearly single-mode high-density two-dimensional vertical-cavity surface-emitting laser arrays for optical communications [4078-92]**
H.-P. D. Yang, M.-L. Wang, W.-C. Jiang, Y.-S. Su, C.-P. Sung, Industrial Technology Research Institute (Taiwan)
- 611 **DC and AC characteristics of 850-nm broad-area vertical-cavity surface-emitting lasers [4078-93]**
H.-P. D. Yang, Y.-S. Su, W.-C. Jiang, M.-L. Wang, S.-J. Yu, C.-P. Sung, Industrial Technology Research Institute (Taiwan)
- 620 **Fabrication of a micromachined optical modulator using the CMOS process [4078-94]**
H. Chen, K. Yen, H. Huang, J. Chio, Industrial Technology Research Institute (Taiwan); C. Dai, Oriental Institute of Technology (Taiwan); C. Chang, P. Chang, National Taiwan Univ.
- 627 **Fabrication of diffractive optical elements using the CMOS process [4078-95]**
H. Chen, H. Huang, K. Yen, J. Chio, Industrial Technology Research Institute (Taiwan); C. Dai, Oriental Institute of Technology (Taiwan); C. Chang, P. Chang, National Taiwan Univ.
- 637 **Integrated eyeball-tracking device [4078-96]**
H. Chen, K. Yen, J. Chio, H. Huang, Industrial Technology Research Institute (Taiwan); C. Dai, Oriental Institute of Technology (Taiwan); C. Chang, P. Chang, National Taiwan Univ.
- 646 **Finite-element analysis of solder joint strength in laser diode packaging [4078-97]**
C.-H. Chang, M.-T. Sheen, J.-H. Kuang, C.-C. Chen, G.-L. Wang, W.-H. Cheng, National Sun Yat-sen Univ. (Taiwan); H.-L. Chang, S.-C. Wang, C. Wang, C.-M. Wang, Chunghwa Telecom Labs. (Taiwan)
- 652 **Finite-element analysis of fiber shifts in fiber-solder-ferrule joints using AuSn solder [4078-98]**
M.-T. Sheen, P.-C. Chen, J.-H. Kuang, G.-L. Wang, W.-H. Cheng, National Sun Yat-sen Univ. (Taiwan); H.-L. Chang, S.-C. Wang, C. Wang, C.-M. Wang, Chunghwa Telecom Labs. (Taiwan)
- 659 **Stress distributions in patterned-substrate InGaAs/InP [4078-99]**
J. Lefebvre, G. C. Aers, P. J. Poole, R. L. Williams, National Research Council Canada
- 664 **Optical and transport properties of MOCVD-grown InSb thin films [4078-101]**
T. R. Yang, G. Kuri, M. R. Kim, National Taiwan Normal Univ.; Z. C. Feng, S. J. Chua, Institute of Materials Research and Engineering (Singapore)
- 672 **Radiation damage and surface modification of InSb(111) by MeV C⁺ and C₂⁺ ions [4078-102]**
G. Kuri, T. R. Yang, National Taiwan Normal Univ.
- 680 **Conduction mechanisms in undoped polycrystalline diamond films [4078-103]**
H.-T. Chou, C.-C. Lee, C.-H. Sun, National Yunlin Univ. of Science and Technology (Taiwan)

- 689 **Sensing characteristics of ISFET based on AlN thin film [4078-104]**
J.-L. Chiang, S.-S. Jan, Y.-C. Chen, National Sun Yat-sen Univ. (Taiwan); J.-C. Chou, National Yunlin Univ. of Science and Technology (Taiwan)
- 697 **Initial growth effects on the properties of GaN buffer layer and subsequent GaN overlayer by MOCVD [4078-105]**
D.-S. Wu, W.-H. Tseng, W.-T. Lin, Da-Yeh Univ. (Taiwan); R.-H. Horng, National Chung Hsing Univ. (Taiwan)
- 704 **Exchange interaction of 3D transition metal impurity with band electrons in diluted magnetic semiconductors [4078-107]**
T.-R. Yang, M.-R. Kim, National Taiwan Normal Univ.
- 712 **Optoelectronic frequency discriminated phase tuning technology and its applications [4078-110]**
G.-R. Lin, Y.-C. Chang, Tatung Univ. (Taiwan)
- 724 **High performances of InGaP/GaAs MSM photodetectors using Cu/Au Schottky contact [4078-112]**
C.-D. Tsai, Y.-J. Lin, D.-S. Liu, C.-T. Lee, National Central Univ. (Taiwan)
- 732 **ED-Litho color filter process and its application [4078-113]**
C.-H. Wen, S.-H. Cheng, Y.-T. Wu, H.-D. Liu, C.-H. Chao, Industrial Technology Research Institute (Taiwan); J.-I. Yasukawa, Sumitomo Chemical Co., Ltd. (Japan)
- 739 **Low-dielectric-constant photoresists for insulation on TFT array [4078-115]**
R.-J. Lee, Y.-C. Wu, S.-L. Chen, S.-S. Lin, H.-W. Chien, Industrial Technology Research Institute (Taiwan)
- 745 **Novel grating-frustrated wavelength division multiplexer using polymer waveguides with inverted-ridge structure [4078-118]**
W.-C. Chuang, National Institute of Technology (Taiwan); Y.-T. Hsueh, W.-C. Chang, Southern Taiwan Univ. of Technology; W.-S. Wang, National Taiwan Univ.
- 754 **Polymer waveguide polarizers fabricated by electric poling [4078-121]**
S.-J. Hwang, H. H. Yu, National Huwei Institute of Technology (Taiwan)
- 765 **Percolation and ripening in $\text{Si}_{1-x}\text{Ge}_x/\text{Si}(001)$ islands: effect of misfit strain [4078-122]**
R. A. Budiman, H. E. Ruda, D. D. Perović, B. Bahierathan, Univ. of Toronto (Canada)
- 773 **Novel semiconductor/superlattice distributed Bragg reflector (DBR) grown by molecular beam epitaxy (MBE) and its characteristics [4078-127]**
C. Yan, J. Zhong, Y. Zhao, R. Li, Changchun Institute of Optics and Fine Mechanics (China)
- 779 **Basic element for integrated electro-optical devices based on liquid crystal waveguides [4078-128]**
P. Mormile, L. Petti, Istituto di Cibernetica (Italy); G. C. Righini, Istituto di Ricerca sulle Onde Elettromagnetiche (Italy); G. Abbate, INFN (Italy) and Univ. degli Studi di Napoli Federico II (Italy)
- 786 **Estimation of shallow-energy-level location in BaTiO_3 [4078-129]**
S.-Y. Chiang, M.-T. Chen, Y.-J. Huang, S. C. Donn, Chung Yuan Univ. (Taiwan); J.-Y. Chang, National Central Univ. (Taiwan)

- 793 **Hysteresis effect of pH-ISFET based on Beckman Φ 110 (Si_3N_4 gate pH-ISFET) [4078-132]**
J.-C. Chou, Y.-N. Tseng, National Yunlin Univ. of Science and Technology (Taiwan)
- 801 **Sensitivity and hysteresis behavior of the commercial Sentron 1090 Al_2O_3 gate pH-ISFET [4078-133]**
J.-C. Chou, C. Y. Weng, National Yunlin Univ. of Science and Technology (Taiwan)
- 809 **Temperature dependence of the hysteresis for the a-Si:H gate pH-ISFET [4078-134]**
J. C. Chou, H.-M. Tsai, Y.-F. Wang, National Yunlin Univ. of Science and Technology (Taiwan)
- 817 **Compact laser sources for photorefractive research [4078-135]**
J. Chen, Chung Shan Institute of Science and Technology (Taiwan) and National Central Univ. (Taiwan); T.-C. Chen, H.-C. Kung, H.-F. Yau, C.-C. Cheng, H.-S. Tsai, H.-P. Liu, National Central Univ. (Taiwan)
- 825 *Author Index*

Conference Committee

Conference Chairs

Yan-Kuin Su, National Cheng Kung University (Taiwan)
Pallab Bhattacharya, University of Michigan (USA)

Program Committee

Frank Mau-Chung Chang, University of California/Los Angeles (USA)
Tao Yuan Chang, Lucent Technologies/Bell Laboratories (USA)
N. Sylvain Charbonneau, National Research Council Canada
Richard M. De La Rue, University of Glasgow (UK)
Jin-Kuo Ho, Industrial Technology Research Institute (Taiwan)
R. Jennifer Hwu, University of Utah (USA)
Kenichi Iga, Tokyo Institute of Technology (Japan)
Thomas Jackman, National Research Council Canada
Ching-Ting Lee, National Central University (Taiwan)
Yong Hee Lee, Korea Advanced Institute of Science and Technology
E. Herbert Li, University of Hong Kong
Ming Fu Li, National University of Singapore
Sheng S. Li, University of Florida (USA)
Coe-Yen Nee, Highlight Optoelectronics Inc. (Taiwan)
Stephen J. Pearton, University of Florida (USA)
Manfred H. Pilkuhn, Universität Stuttgart (Germany)
Harry E. Ruda, University of Toronto (Canada)
Kunio Tada, Yokohama National University (Japan)
Tsunemasa Taguchi, Yamaguchi University (Japan)
Chen S. Tsai, Center for Applied Science and Engineering (Taiwan)
and University of California/Irvine (USA)
Chih-Chung Yang, National Taiwan University

Session Chairs

- 1 GaN LED and Materials I
Pallab Bhattacharya, University of Michigan (USA)
- 2 GaN LED and Materials II
Yasuhiko Arakawa, University of Tokyo (Japan)
Yan-Kuin Su, National Cheng Kung University (Taiwan)
- 3 GaN LED and Materials III
E. Herbert Li, University of Hong Kong
Ching-Ting Lee, National Central University (Taiwan)

- 4 Quantum Dots: Growth, Devices, and Applications
 John H. Marsh, University of Glasgow (UK)
 Chen S. Tsai, Center for Applied Science and Engineering (Taiwan)
 and University of California/Irvine (USA)
- 5 Quantum Well Intermixing and Lasers
 Simon Fafard, National Research Council Canada
- 6 Semiconductor LEDs and Lasers
 Dennis G. Deppe, University of Texas at Austin
 Chih-Chung Yang, National Taiwan University
- 7 Epitaxial Growth
 Hoe H. Tan, Australian National University
 Gou-Chung Chi, National Central University (Taiwan)
- 8 Integrated Optical Components and Devices
 David A. Thompson, McMaster University (Canada)
 Wen How Lan, Chung Shan Institute of Science and Technology (Taiwan)
- 9 Organic Light-Emitting Devices
 Way-Seen Wang, National Taiwan University
 Shymal K. Saha, National Cheng Kung University (Taiwan)
- 10 Advanced Optical Devices
 Jin-Kuo Ho, Industrial Technology Research Institute (Taiwan)

Plenary Paper

Photonic Technologies in the 21st Century : Creation of New Industries

Teruo Hiruma
Hamamatsu Photonics KK
Hamamatsu, Japan

ABSTRACT

As we approach the new millennium, the ongoing aim of human society is not only for promoting scientific technology but also creating new industries. To achieve this goal, each person in industry must recognize anew that the real meaning of science is to explore the absolute truth. It is also important that people recognize that there are unlimited matters which we humans do now yet know.

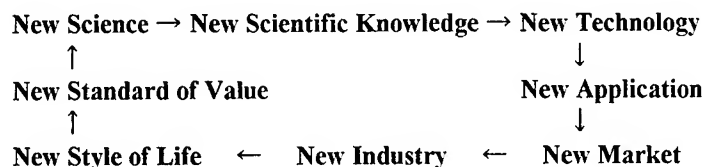
1. INTRODUCTION

The 20th century was one that witnessed many great discoveries and our knowledge increased many times during the last one hundred years. Yet even with such an explosion of knowledge and information there is much more that we do not yet understand. Our present knowledge represents only a fraction of what there is to know. For example, there have been major breakthroughs in understanding cell structure by studying individual components or systems such as the role of calcium ions in signal transduction. However very little is known about how all of these components work in concert. It is very much like trying to understand an orchestra by studying the individual instruments. In the future we will develop methods to study the function of the entire cell not just individual systems. On the molecular level we are just beginning to study the details of molecular dynamics during a chemical reaction. The work of this year's Nobel Prize winner in chemistry, Dr Zewail shows how it is possible to use photonics to study the intimate detail of a chemical reaction. Once we gain such detailed information about more complex systems it will be possible to more efficiently produce the chemicals we need and to destroy those that we no longer require.

At Hamamatsu Photonics it is our corporate mission to provide photonics technology that will help us to gain new knowledge of the world we live in. Photonic technologies are very unique in that they let us observe the parts of the world that are very far away (thousands of light years), very small (nanometers) or happen very quickly (in femtoseconds). The roots of our company can be found in the pioneering spirit of Professor Kenjiro Takayanagi who independently developed the technology of television despite the fact those around believed it could not be done because it had never been done. Professor Takayanagi hoped to develop a new way for people to experience the world. We inherited his spirit and continue this idea by using photonics to gain knowledge as well as improve the quality of life for all people.

In the twenty first century it will be possible that we could make all of mankind healthy. Not just in a physical sense but in the definition of the World Health Organization where "Health is a state of complete physical, mental and social well-being and not merely the absence of disease or infirmity." Photonics has the potential for creating the knowledge and industry that could make this possible. It is our hope that this new century sees the beginning of a new economic cycle shown in Figure 1. While industry is designed to generate profit, the purpose of industrialization is for all of mankind to share a common understanding of the New Life Style and to benefit from the New Standard of value, namely Health as defined above.

Figure 1:



Through the application of photonics we are now beginning to develop the New Science that will lead to the cycle illustrated in Figure 1. In this cycle, mankind is constantly improving its status by using new technologies to discover new knowledge. The application of this new knowledge leads first to new industries and then to a change in the social fabric of society. We understand that this is a very long-term goal. But mankind needs to dream in order to progress. Only by trying to see over the horizon can we discover something that will radically improve all of our lives. Thus while Hamamatsu Photonics' short-term goal is to generate profits, these profits are to be used in the quest for new knowledge which is our long-term target.

2. TECHNOLOGIES

This paper will discuss several technologies that are key to the development of new knowledge which will eventually produce new industries. Application of these technologies will be also discussed.

A. The Ultimate Laser Photon (Photon Factory)

The light emitted by a laser is unique in that it is monochromatic, coherent and directional. These properties have made laser-generated photons vital to all types of research ranging from biology to high-energy physics. We need to obtain a better understanding of exactly what is a photon and how it interacts with the world. By better understanding the photon on a fundamental level we will be able to use it more effectively. Phenomena such as the particle wave duality and teleportation must be better understood through a study of the photon.

The development of very small terawatt and pedawatt laser systems give many researchers access to inexpensive ultra high power. New physical phenomena are being discovered when such intense laser beams interact with matter because these lasers create electric fields much greater than those seen in any other experiment do.

B. Ultra Fast Measurement Technology

By continuing to push the speed at which we make measurements we will discover greater detail of how our world operates. We now have lasers that are capable of measuring the individual motion of atoms in molecules. Newer and faster methods will help get even greater detail of how molecules react. Even faster methods will allow us to follow the motion of electrons during important chemical reactions such as photosynthesis or vision.

C. Optical Correlation Technology

Even though we have discovered only a small fraction of our knowledge, we are severely limited in using it because even this limited amount of knowledge is too great to process with conventional computer systems. We must learn how to process information in parallel with optical processors such as spatial light modulators. Ultimately our goal is to process information in 3 or more dimensions using technology that must still be invented.

D. Forecast Simulators

With time not only has our information become too complex, but also the questions we need to answer become more difficult. As our planet's population increases and our technology becomes more complex, the risk of answering a question incorrectly grows exponentially. For example, the consequences of incorrectly predicting the outcome of global warming will be severe if we either under estimate or over estimate the significance of burning fossil fuels. Premature curtailing of fossil fuels will severely curtail the growth of developing countries leading to unnecessary pain and suffering. Failure to prevent global

warming will have even worse consequences. We need better methods to simulate events or conditions so we can better guide environmental, economic, technical, political, and military decisions.

Ultimately nations will never again fight a war on the battlefield but instead will use simulations to replace them. The simulations will simultaneously decide the output as well as convince the parties that physical conflict is too costly.

E. High Power Lasers

Photons are capable of doing many important things such as curing cancer, printing this manuscript or repairing an integrated circuit. At very high photon densities there are many new things that photons can do. At present, it is expensive to generate a lot of photons because the photon sources are expensive. Semiconductor laser diodes hold the promise of being able to reliably and inexpensively generate photons for many new and exciting applications. Just like the replacement of the vacuum tube with the transistor and then to the integrated circuit, so too will the semiconductor laser evolve and result in important technologies and new industries that we cannot even imagine today.

F. New Photochemistry

Much of our planet's energy is wasted in creating chemicals that we need to live or to improve our lives. Lasers are capable of creating specific excited states. Finding ways to selectively excite molecules so that they can be moved along specific reaction pathways will lead to huge savings in cost, energy and pollution. New knowledge on how to perform pathway specific photochemistry is vital to the goal of making everyone healthy according to the World Health Organization's definition of health.

3. APPLICATIONS

We can only speculate on what the full effect of such new photonic technologies will have in the long term. However over a short period of time we can easily imagine some of the benefits we might enjoy from these as well as other photonic technologies. Some of these benefits are discussed below.

A. Measurement of Physiological Functions

The pulse oximeter has already found an important role in guaranteeing that the oxygen concentration of the blood is maintained at as close to optimum as possible. Countless lives have been saved and others have had severe injury prevented by this simple optical device. Not very far away are devices that will permit rapid and painless screening for diabetes. Noninvasive cancer diagnosis is already being tested in clinical trials.

Ultimately a device will be available that checks your body's functions on a daily basis. It screens for potential problems before they cause disease. Adjustments to exercise, diet or even administration of drugs can be performed before the individual is aware of a problem. Such an advanced detection system would save costs, pain and anxiety. It would go as long way to attaining the goal of making people truly healthy.

B. Optical Medicine

In the past few years, photodynamic therapy has been shown to be a valuable treatment for some forms of cancer. In some cases it is far more useful than other techniques such as surgery because it leaves the effected organ in tact. Therefore for young women, cancer of the cervix no longer means that it is the end of their dream to have a family. For older people suffering from the wet form of macula degeneration, photodynamic therapy will soon be used to prevent the blindness caused by this disease.

New chemicals are being developed that are absorbed faster by the cancer cells and discharged more rapidly by the body. This will make treatment simpler and more effective. Patients may not even need to stay overnight in a hospital. Presently PDT can only be used on cancers that are found on a surface. Techniques are being developed that will be used in the treatment of cancers that are deep inside an organ.

Cosmetic uses of photons for hair removal, port wine stain removal or tattoo removal make it easier for a person to be accepted by society. These applications are far from superficial since they greatly improve the quality of life for those that need them.

Other applications of photonics to medical practice will certainly emerge in the near future for things such as the treatment of stroke, heart disease, healing of wounds and reducing or relieving pain.

C. Early Detection of Disease

Cancer screening using Positron Emission Tomography (PET) holds the promise of early detection and cure of this terrible affliction. Injection of fluorodeoxyglucose into the blood stream is current used to uncover cells that are metabolizing at rates faster than those of their neighbors. These cells are then analyzed to determine if they are malignant. Such a screening method could in the near future make an entire city cancer death free.

Light CT uses nonionizing infrared photons to take a three dimensional image of the body. Work is under way in many places around the world to use light CT as a method for detecting breast cancer. This technique could be less expensive than x-ray methods and used safely on all individuals including pregnant women. Other uses of the light CT would be to quickly determine if a stroke is caused by ischemia or a hematoma. Such information is vital in determining the correct treatment. Rapid treatment of stroke can greatly reduce the damage to the brain resulting in a patient that can lead a normal life even after such a severe trauma.

In the future we hope to quantify the health of a person, not just the presence of disease.

D. Fiberless Optical Communication

Information is the most important commodity in our society. We are constructing very large and expensive infrastructures to move information from one location to the other. Fiber optics is one of the key technologies for information transport because of the very high capacity available due to wavelength division multiplexing. This technique suffers from the fact that fibers must be placed between locations. At Hamamatsu Photonics we have developed a series of fiberless optical communications systems. These operate by transmitting the optical signals through air. They have the capability to send data, or video without the need for government licenses or owning a right of way. One such a fiberless system is used at sporting events such as golf tournaments to transmit the video camera output to the broadcaster's trailer or even back to a studio. Such a system was used at the Atlanta Olympics and is now being tested in Hamamatsu City. In our hometown it is being used to connect elementary schools with the city hall. It could also be used to connect remote clinics with the medical school for telemedicine.

E. Health Industry for Successful Aging

Many countries will soon suffer from an increase in their average age. In the past such an increase in age would greatly burden society in terms of medical expenses and the cost of financially supporting an aging population. We believe that it is possible to completely eliminate the impact of a graying population by finding ways to reduce the pace and effect of the aging process. At Hamamatsu Photonics we are using photonic technology to understand how locomotion is effected as a person ages. We hope to develop exercises that will prevent the loss of mobility and greatly reduce the probability of an older person falling. While just a small step, it will have a big impact on the quality of life of our seniors.

F. Disposal of Industrial Waste

High power lasers and controlled photochemistry hold the promise of being able to safely dispose of dangerous waste products. It will do this by selective destruction of the dangerous ingredients into less danger or even harmless smaller molecules. These smaller molecules can then be recycled into new products.

G. Search for New Energy Sources

Perhaps the biggest impact that photonics can have on mankind is the development of clean and inexpensive energy. For once this is available; the quality of life of the entire world can be improved without damaging the planet. We must continue our search for a way to harness laser fusion and solar energy for they are needed to make the world a better place to live for all of us.

Photonics holds the promise of creating New Science and New Technology which will lead to New Industrial and of course to a world population that is truly healthy.

SESSION 1

GaN LED and Materials I

Radiative recombination mechanisms in InGaN/AlGaN single-quantum well LED revealed by time-resolved photoluminescence spectra under external-electric fields

Hiromitsu Kudo*, Tomoyuki Tanabe, Hiroki Ishibashi, Ruisheng Zheng, Yoichi Yamada,
and Tsunemasa Taguchi

Faculty of Engineering, Yamaguchi University, 2-16-1 Tokiwadai, Ube, Yamaguchi 755-8611, Japan

ABSTRACT

The radiative recombination mechanism in InGaN single-quantum-well (SQW) blue light-emitting diodes (LEDs) and InGaN double heterostructure (DH) ultraviolet (UV) LEDs has extensively been investigated by means of the dependence of photoluminescence (PL) and time-resolved PL (TRPL) spectra on an external-electric field. Two emission components are found in the luminescence spectra from each LED on the condition of reverse-bias at 77 K. It is also found that the luminescence intensity of the LEDs decreases dramatically with increasing reverse-bias voltage at room temperature (RT). The model based on field ionization of excitons cannot explain the present experimental phenomena. It is therefore suggested that the free-carrier recombination process is dominant at RT. We have also suggested that these experimental results on the blue and UV LEDs can be explained by the same recombination model. Finally, on the basis of both the experimental evidence in $\text{In}_{0.08}\text{Ga}_{0.92}\text{N}$ epitaxial layers and strong electron-phonon interaction, the radiative recombination mechanism on $\text{In}_x\text{Ga}_{1-x}\text{N}$ ternary alloys has been discussed.

Keywords: InGaN, Reverse bias, Time-resolved luminescence, Recombination, Electron-phonon interaction

1. INTRODUCTION

Recent progresses on high-brightness blue and green light-emitting diodes (LEDs) have realized a full-color displays and full-color indicators with the characteristics of high efficiency and high reliability.¹ However, the radiative recombination mechanism in $\text{In}_x\text{Ga}_{1-x}\text{N}$ ternary alloys used as the active light-emitting medium is not fully understood in spite of a considerable amount of researches.²⁻⁷ Furthermore, it has been pointed out that an internal piezoelectric field plays a major role in strained InGaN/GaN single quantum wells (SQWs).^{8,9} On the other hand, Mukai et al. have observed a higher efficiency of LEDs with increasing In content in the InGaN well layers from ultraviolet (UV) to green LEDs.¹⁰ This result directly indicates that the internal piezoelectric field induced by a large lattice mismatch between InGaN well layer and GaN barrier layer plays a minor role in InGaN UV to green LEDs. At present, InGaN-based laser diodes (LDs) have been realized only the purplish blue region,¹¹ because the efficiency is strongly dependent on In composition. It is therefore very important to clarify the radiative recombination mechanism in $\text{In}_x\text{Ga}_{1-x}\text{N}$ ternary alloys for realizing the InGaN-based violet to red LDs.

Recently, InGaN double-heterostructure (DH) and SQW UV LEDs have been developed by Mukai et al.^{12,13} It has been pointed out that the effect of a little amount of In involved in an active layer of an InGaN ternary alloy is very important for obtaining an efficient UV power.^{12,14}

It has been well known that electric fields applied perpendicularly to the layers of quantum wells change the optical absorption, reflection, and photoluminescence (PL) properties. A low-energy shift of the two-dimensional exciton emission line and a corresponding increase of the recombination lifetime have been explained by the field-induced charge separation and the corresponding decrease in electron-hole wave function overlap.¹⁵ In the case of InGaN quantum wells, there have been few reports on the applied-voltage dependence of PL properties,^{3,16,17} and no report on the applied-voltage dependence of time-resolved PL (TRPL) properties.

In this paper, we have investigated the radiative recombination properties of InGaN SQW blue LEDs and InGaN DH UV LEDs by means of an external-electric field dependent PL and TRPL spectral measurements.

*Electronic mail: c2426@stu.cc.yamaguchi-u.ac.jp

2. EXPERIMENTAL PROCEDURES

An InGaN SQW blue LED and an InGaN DH UV LED on a (0001) sapphire substrate were used in this study. The structure of blue LEDs (UV LEDs) consists of 100-nm thick p-Al_{0.2}Ga_{0.8}N (60-nm thick p-Al_{0.15}Ga_{0.85}N), active In_{0.2}Ga_{0.8}N (active InGaN), and 4-μm thick n-GaN (30-nm thick n-Al_{0.1}Ga_{0.9}N). An In composition in the active layer of UV LEDs was estimated to be nearly zero. For measuring PL spectra, a cw He-Cd laser (325 nm) was used as an excitation source. TRPL measurements were performed using a synchroscan streak camera in conjunction with a 25-cm single grating monochromator. The excitation source was the third-harmonic light (267 nm) of amplified titanium sapphire laser pulses. The repetition rate and the pulse width were 250 kHz and 200 fs, respectively.

3. EXPERIMENTAL RESULTS

3.1 Applied-voltage dependence of photoluminescence spectra

Figures 1 show the reverse-bias-voltage dependence of PL spectra obtained at 77 K from an InGaN active layer of (a) InGaN SQW blue LEDs and (b) InGaN DH UV LEDs, respectively. The excitation-power density of both LEDs is 0.76 mW/cm². Two dashed curves of each figure were drawn by fitting the experimental curve using the Gaussian function. The open-circuit voltage of blue LEDs and UV LEDs are 2.7 and 2.68 V, respectively. As shown in Fig. 1 (a), there appears a single emission band at 2.59 eV with a linewidth of about 80 meV at an open-circuit configuration. The PL spectrum at -0.2 V is almost the same as the PL spectrum at an open-circuit configuration. The luminescence intensity is dramatically decreased with increasing applied reverse-bias voltage. We have also clearly observed for the first time two emission components with an energy separation of about 40 meV by applying reverse-bias voltage.

Reverse-bias voltage dependence of PL spectra from an InGaN DH UV LED is also shown in Fig. 1 (b). There appears a single emission band at 3.395 eV with a linewidth of about 30 meV at an open-circuit configuration.¹⁸ The luminescence

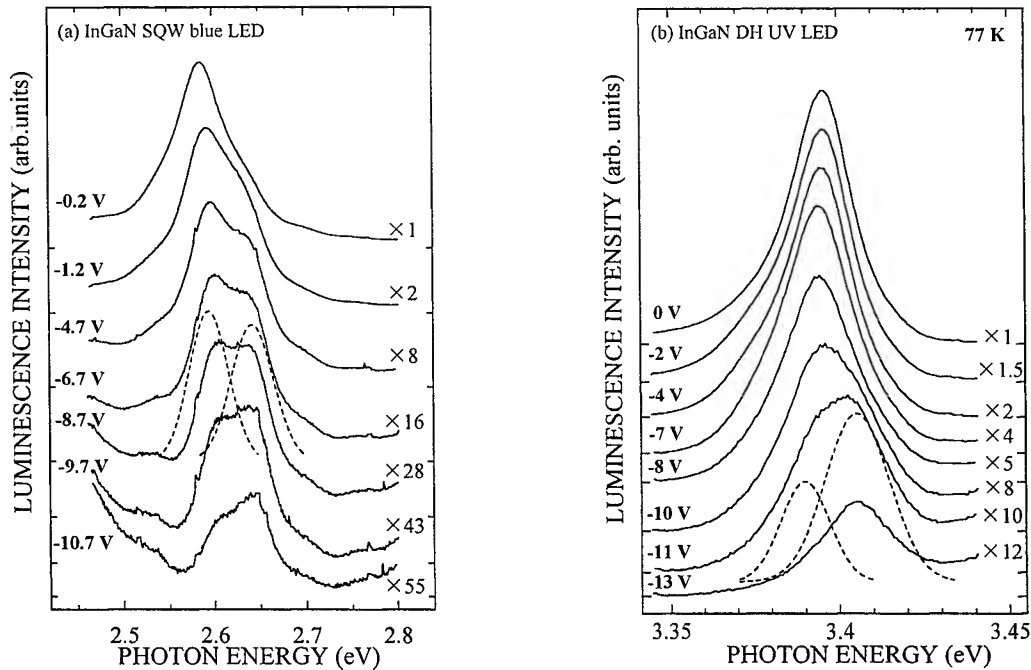


Fig. 1. Dependence of reverse-biased voltage on two emission components of (a) InGaN SQW blue LEDs and (b) InGaN DH UV LEDs, respectively. Two dashed curves of each figure were drawn by fitting the experimental curve using the Gaussian function.

intensity is dramatically decreased with increasing applied voltage. As a result, two emission components with an energy separation of about 20 meV are found.¹⁹ From 0 to -7 V, the PL peak position shifts slightly to lower energy side. With further increasing reverse-bias voltage (from -8 to -13 V), the PL peak position shifts apparently to higher energy side owing to the field-induced quenching of the lower-energy component.

We have also clearly observed two emission components from the temperature-dependent PL measurements in $\text{In}_{0.08}\text{Ga}_{0.92}\text{N}$ epitaxial layers,²⁰ and an abnormal temperature dependence of PL spectra²¹ can be fully understood by considering the existence of two emission components. It is therefore suggested that the two emission components are related to intrinsic characteristics in $\text{In}_x\text{Ga}_{1-x}\text{N}$ ternary alloys.

Figures 2 show the applied-voltage dependence of luminescence intensities at 77 K and RT of (a) InGaN SQW blue LEDs and (b) InGaN DH UV LEDs, respectively. Excitation-power densities of the both LEDs at 77 K and RT were 0.76 and 25 mW/cm^2 , respectively. The luminescence intensities of two emission components were obtained by fitting the experimental curve using the Gaussian function (See Fig. 1). As shown in Fig. 2 (a), at 77 K, the luminescence intensity is decreased by two orders of magnitude with increasing applied voltage. It is therefore suggested that the decrease of PL intensity might be due to spatial separation of the electrons and holes under the influence of the electric field.^{22,23} Since a field ionization of excitons occurs at the value of E_i ($E_i = E_x/ea_x$, where E_x is the exciton binding energy and a_x is the exciton Bohr radius),²² the field strength to dissociate excitons in bulk GaN is estimated to be 7.6×10^4 V/cm using the values of the binding energy (26 meV) and the Bohr radius (3.4 nm) of the excitons.^{3,18} In the present experiment, at 77 K, the electric field applied to the InGaN SQW blue LED corresponds to the order of 10^4 V/cm. On the other hand, at RT, the dramatically decrease in luminescence intensity is observed at the order of 10^3 V/cm. It is therefore clear that this decrease in luminescence intensity at RT can not be explained by the model of a field ionization of excitons. It is also noted that the leakage current of the LED at RT is almost constant for different reverse-bias voltages, and is below 0.1 μA under the condition of -25 V. Therefore, the effect of reverse leakage current on the decrease of luminescence intensities is significantly small, and can not be applicable to explain the experimental data shown in Fig. 2 (a). Since the luminescence intensity depends strongly on the reverse-bias voltage, we have suggested that the free-carrier recombination process is dominant at RT.²⁴

Applied-voltage dependence of luminescence intensities from an InGaN DH UV LED is also shown in Fig. 2 (b). With increasing applied voltage at 77 K, the luminescence intensity of the lower-energy component is decreased by two orders of magnitude. This result suggests that the degree of localization of the lower-energy component is weak. Therefore, the decrease of luminescence intensity might be due to spatial separation of the electrons and holes under the influence of the

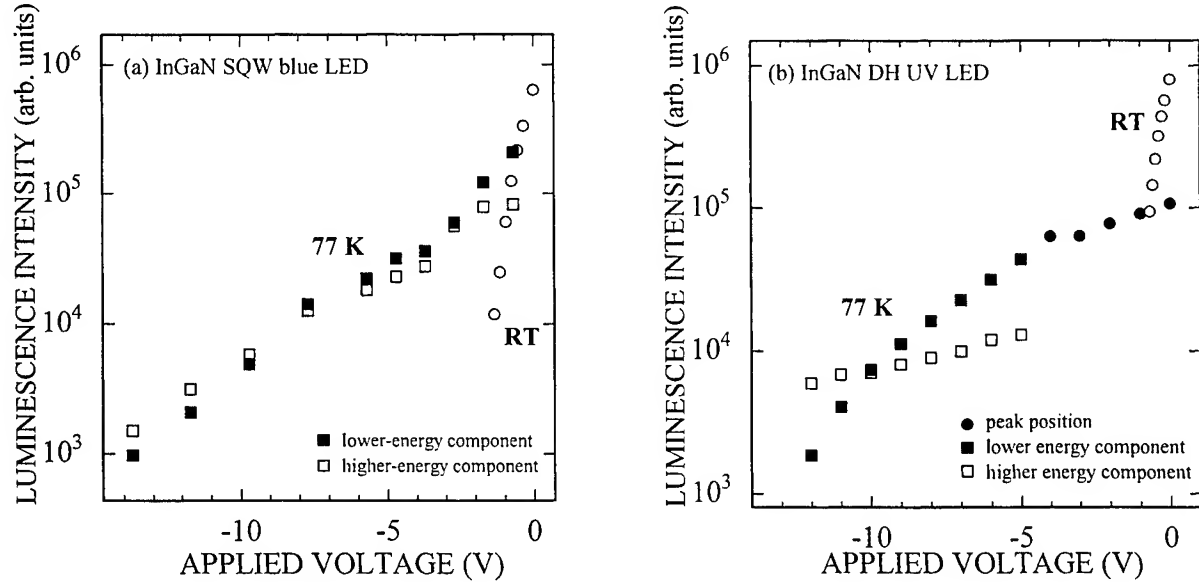


Fig. 2. Applied-voltage dependence of luminescence intensities at 77 K and RT of (a) InGaN SQW blue LEDs and (b) InGaN DH UV LEDs, respectively. The excitation-power densities of each LED at 77 K and RT were 0.76 and 25 mW/cm^2 , respectively.

electric field. On the other hand, with increasing applied voltage, the luminescence intensity of the higher-energy component is gradually decreased, which indicates that the carrier localization of the higher-energy component is relatively stronger than that of the lower-energy component. As shown in Fig. 2 (b), at RT, the luminescence intensity dramatically decreases compared to that obtained at 77 K. In this case, the electric field applied to the InGaN DH UV LED corresponds to the order of 10^3 V/cm. It is therefore suggested that the free-carrier recombination process is dominant at RT. Figures 3 show the applied voltage dependence of peak photon energies at 77 K of an InGaN DH UV LED. The peak photon energies of two emission components were obtained by fitting the experimental curve using the Gaussian function (See Fig. 1). With increasing reverse-bias voltage, the PL peak energy of the lower-energy component shifts slightly towards lower energy side. Takeuchi et al. have found that the piezoelectric field induced in InGaN QWs is set against the built-in bias field.¹⁶ They have also suggested that the PL peak energy shifts towards higher energy side with increasing reverse-bias voltage, and that the reverse-bias voltage cancels the internal piezoelectric field.¹⁶ Our experimental data, on the contrary, shows the PL peak energy shifts towards lower energy side with increasing reverse-bias voltage, which can not be interpreted by a cancellation of the piezoelectric field.¹⁹ The PL peak energy of the higher-energy component is almost independent of reverse-bias voltage. Anomalous PL peak shifts, which appear in Fig.1, can be well explained by considering two emission components. From the reverse-bias voltage dependence of both the luminescence intensity and peak photon energy mentioned above, it is concluded that carriers, which are trapped in the recombination center, are not so strongly localized. The present results will support our previous emission model of the UV LED which is based on the free-carrier recombination.¹⁸

3.2 Applied-voltage dependence of time-resolved photoluminescence spectra

Figures 4 show the TRPL spectra at 77 K from an InGaN active layer of an InGaN SQW blue LED under the applied voltage of (a) 0 and (b) -6 V. The excitation-energy density is estimated to be $107 \mu\text{J}/\text{cm}^2$. When the zero-bias condition, there appears a single emission band located at about 2.62 eV after a delay time of 0.8 ns. When the delay time changes from 0.8 to 83 ns, there appears the lower-energy component from lower-energy shoulder of the main emission band. This behavior indicates that the lifetime of the lower-energy component is longer than that of the higher-energy component at the condition of zero bias. On the other hand, as shown in Fig. 4(b), two emission components are clearly observed after a delay time of 2.5 ns.²⁴ An energy separation between two components is estimated to be about 50 meV. It is found that both the higher- and lower-energy components do not indicate a simple exponential decay profile. As shown in Fig. 4 (b), the peak energy of the higher-energy component gradually shifts to lower-energy side with delay time. On the contrary to the zero-biased condition, the lower-energy component indicates a fast decay profile compared to the higher-energy component. Usually, with increasing applied reverse-bias voltage, an increase of the recombination lifetime should be observed as a consequence of the decreased electron-hole overlap.¹⁵ However, the decay times of the higher- and lower-emission components are decreased with applied reverse-bias voltage from 13 to 1.7 ns, and from 19 to 2.1 ns, respectively. It is therefore speculated that this decrease of the decay times is owing to the increased transport of carriers, which is separated by applied reverse-bias voltage, to nonradiative recombination centers which are formed by a large number of dislocations above 10^7 cm^{-2} .

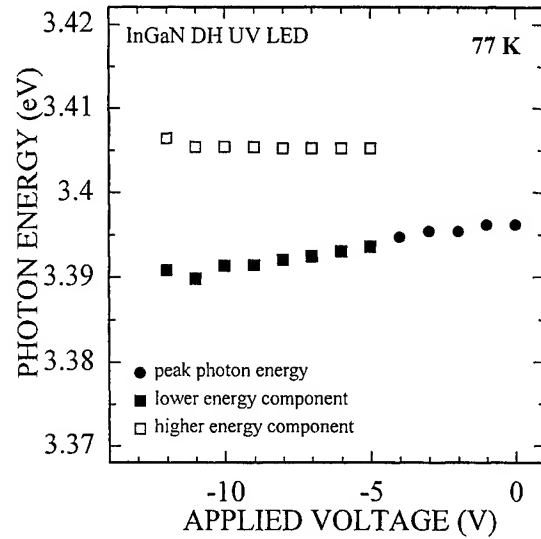


Fig. 3. Applied-voltage dependence of peak photon energies of an InGaN DH UV LED. The excitation-power density was $0.76 \text{ mW}/\text{cm}^2$.

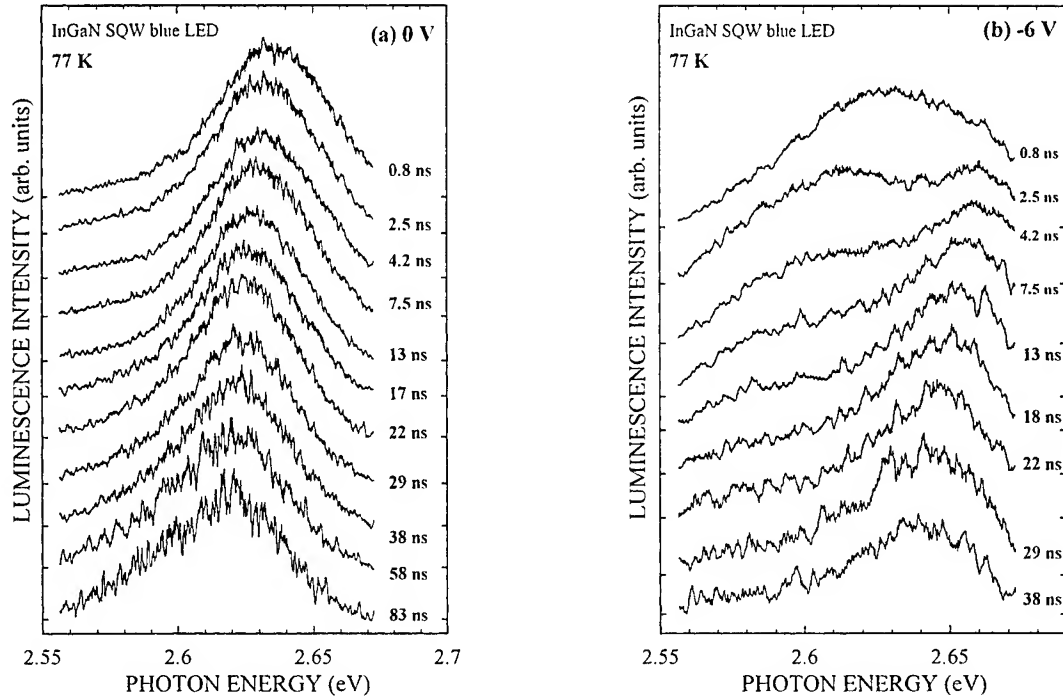


Fig. 4. TRPL spectra at 77 K of an InGaN SQW blue LED under the applied voltage of (a) 0 and (b) -6 V. The excitation-energy density was estimated to be $107 \mu\text{J}/\text{cm}^2$.

4. DISCUSSION

Comparing to other III-V materials, InGaN ternary alloys have a strong electron-phonon interaction characterized by a large LO-phonon energy ($\hbar \omega_{\text{LO}} \approx 90 \text{ meV}$). However, concerning the localization of carriers, there has been nothing reports on the effect of electron-phonon interaction. We have, so far, extensively investigated the radiative recombination mechanism in $\text{In}_{0.08}\text{Ga}_{0.92}\text{N}$ epitaxial layers by means of temperature dependence, magnetic-field dependence, and TRPL measurements.^{20,25,26}

Figures 5 (a) show the temperature-dependent PL spectra of an $\text{In}_{0.08}\text{Ga}_{0.92}\text{N}$ epitaxial layer obtained from 4 K to RT under an excitation-power density of $25 \text{ mW}/\text{cm}^2$. There appears a single emission band at about 3.23 eV having a band width of about 47 meV at 4 K. With increasing temperature, the 3.23 eV band becomes two distinct emission bands with an energy separation of about 40 meV. For instance, at 100 K, two peaks at higher- and lower-photon energies are located at about 3.24 and 3.20 eV, respectively, after the deconvolution of the two peaks using the Gaussian function.²⁰ Cho et al. have reported that the temperature dependence of PL spectrum in $\text{In}_x\text{Ga}_{1-x}\text{N}/\text{GaN}$ multiple quantum well (MQW) structures indicates an abnormal peak shift like S-shaped character as if this band was a single emission band.²¹ However, from our observations mentioned above, this behavior does not originate from the abnormal temperature dependence because two emission components must be involved in the recombination center. From the magnetic-field dependent PL measurements, the higher-energy component shows a linear energy shift with increasing external magnetic field. The shift is about 2.5 meV at 8 T, which can be derived from the Landau energy shift of electrons.²⁵ It is therefore clear from our finding that this large energy shift can not be interpreted by a diamagnetic energy shift of usual localized excitons or excitons confined in the quantum dots.

Furthermore, we have investigated the TRPL measurements. Figures 5 (b) show the time-resolved luminescence spectra obtained at 8 K under an excitation-energy density of $0.4 \mu\text{J}/\text{cm}^2$. Two spectra shown by (A) and (B) were obtained at 10 and 30 ps after the excitation, respectively. As shown in Fig. 5 (b), when the delay time changes from 10 to 30 ps, the

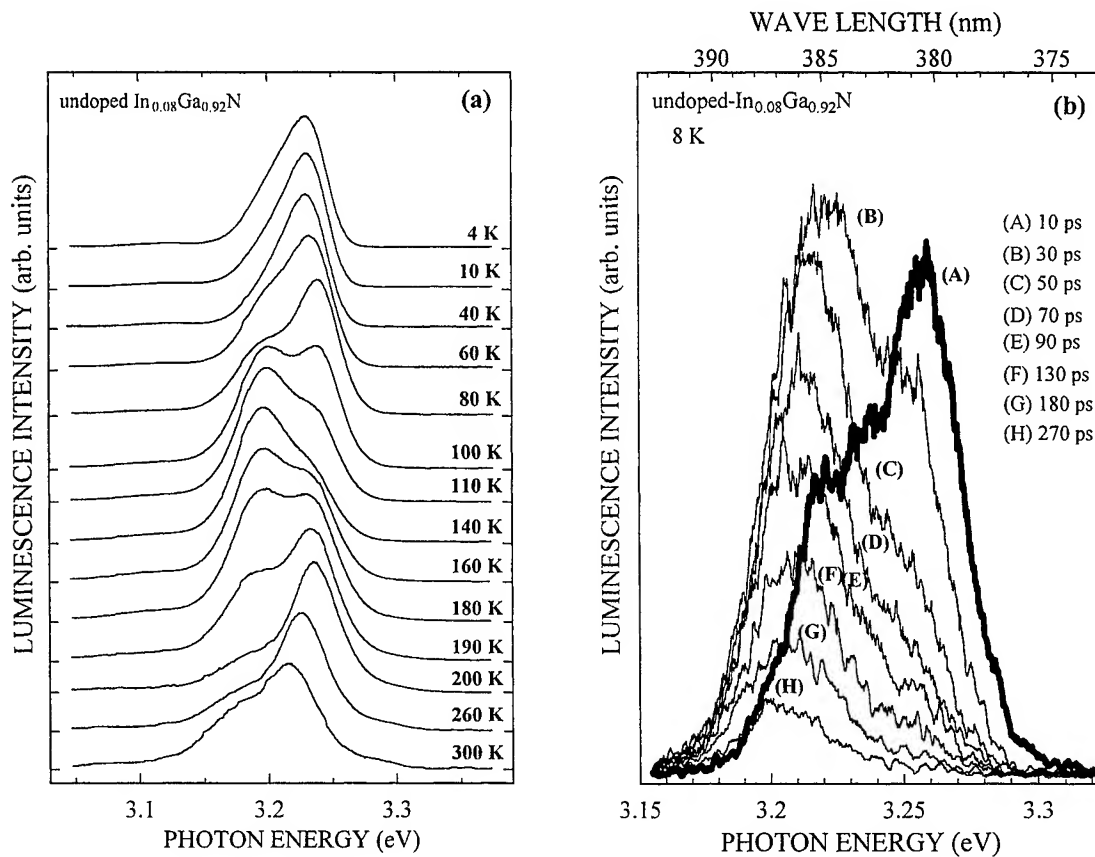


Fig. 5. (a) Temperature dependent and (b) time-resolved PL spectra in $\text{In}_{0.08}\text{Ga}_{0.92}\text{N}$ epitaxial layers. For measuring time-resolved PL spectra, temperature and the excitation energy density were 8 K and $0.4 \mu\text{J}/\text{cm}^2$, respectively.

luminescence intensity of the higher-energy component decreases rapidly with a decay-time constant of about 30 ps, whilst the luminescence intensity of the lower-energy component increases. After 30 ps, it decreases gradually with a decay-time constant of about 540 ps. This dynamical behavior indicates that the energy transfer of carriers between the two levels takes place. It is found that the peak energy of the lower-energy component slightly shifts to the lower-energy side as the delay time proceeds. With increasing temperature, the decay-time constant of the higher-energy component was almost constant of about 30 ps, whilst that of the lower-energy component dramatically decreased from 540 to 20 ps.²⁶ Such behavior of the lower-energy component can be interpreted in terms of a non-radiative decay process. The decay time of the lower-energy component is shortened owing to both the thermal depopulation and the non-radiative process of carriers with increasing temperature. On the other hand, the decay time of the higher-energy component is found to be about 40 ps at RT, which is equal to the estimated intrinsic lifetime of the carriers.²⁷ On the basis of both the experimental evidence and strong electron-phonon interaction,²⁸ we have proposed that a polaron state of electrons is dominant at the higher-energy component.²⁶ This proposal well explains the observed large Stokes shift and the fast decay time of the higher-energy component.

In order to clarify the radiative recombination mechanism in InGaN SQW blue LEDs and InGaN DH UV LEDs, we have investigated the external electric-field dependent PL spectral measurements. With increasing applied voltage, at 77 K, two emission components are clearly observed from each LED. It is therefore suggested that the two emission components are originated from intrinsic characteristics in $\text{In}_x\text{Ga}_{1-x}\text{N}$ ternary alloys. Applied voltage dependence of luminescence intensities on each LED can be well explained by the free-carrier recombination model at RT. These experimental results will support our previously proposed recombination model on the basis of the strong electron-phonon interactions. We have also investigated the external electric field dependent TRPL spectral measurements in InGaN SQW blue LEDs. Two emission components are clearly observed at a delay time of 2.5 ns under the applied voltage of -6 V. A lifetime of the lower-energy

component is strongly dependent on applied electric field compared to that of the higher-energy component. This decrease of lifetime with applied reverse-bias voltage cannot be explained by the decrease of electron-hole overlap.

From these results, common characteristics to all samples (InGaN SQW blue LEDs, InGaN DH UV LEDs, and $\text{In}_{0.08}\text{Ga}_{0.92}\text{N}$ epitaxial layers) are summarized as follows.

(1) It is suggested that the free-carrier recombination process is dominant at RT.

(2) Two emission components are clearly observed at low temperature.

In addition to (1) and (2), it is tentatively suggested that the radiative recombination mechanism of $\text{In}_x\text{Ga}_{1-x}\text{N}$ ternary alloys with the different In compositions could be explained by the same recombination model.

5. CONCLUSIONS

In order to clarify the radiative recombination mechanisms in InGaN SQW blue LEDs and InGaN DH UV LEDs, the effects of an external-electric field on PL and TRPL spectra have been investigated. With increasing reverse-bias voltage, at 77 K, we have clearly observed two emission components in the luminescence spectra from each LED. In addition to the experimental results of $\text{In}_{0.08}\text{Ga}_{0.92}\text{N}$ ternary alloys, we have suggested that the two emission components are originated from intrinsic characteristics in $\text{In}_x\text{Ga}_{1-x}\text{N}$ ternary alloys. It was also found that the luminescence intensity of each LED decreased dramatically with increasing reverse-bias voltage at RT. The model of field ionization of excitons was difficult to explain the present experimental phenomena. It was therefore suggested that the free-carrier recombination process was dominant at RT. These experimental results will support our previously proposed recombination model on the basis of the strong electron-phonon interactions.

ACKNOWLEDGEMENTS

We acknowledge a financial support of "The light for the 21st century" National project from MITI/NEDO/JRCM, Japan. The samples used in this study were provided from Nichia Chemical Industries.

REFERENCES

1. S. Nakamura, and G. Fasol, *The blue laser diode*, Springer, Berlin, 1997.
2. T. Taguchi, T. Maeda, Y. Yamada, S. Nakamura, and G. Shinomiya, *Proceedings of International Symposium on Blue Laser and Light Emitting Diodes*, pp. 372, Ohmsha, Tokyo, 1996.
3. S. Chichibu, T. Azuhata, T. Sota, and S. Nakamura, "Spontaneous emission of localized excitons in InGaN single and multiquantum well structures," *Appl. Phys. Lett.* **70**, pp. 4188-4190, 1996.
4. Y. Narukawa, Y. Kawakami, M. Funato, Sz. Fujita, Sg. Fujita, and S. Nakamura, "Role of self-formed InGaN quantum dots for exciton localization in the purple laser diode emitting at 420 nm," *Appl. Phys. Lett.* **70**, pp. 981-983, 1997.
5. C. -K. Sun, S. Keller, G. Wang, M. S. Minsky, J. E. Bowers, and S. P. DenBaars, "Radiative recombination lifetime measurements of InGaN single quantum well," *Appl. Phys. Lett.* **69**, pp. 1936-1938, 1996.
6. W. Shan, B. D. Little, J. J. Song, Z. C. Feng, M. Schurman, and R. A. Stall, "Optical transitions in $\text{In}_x\text{Ga}_{1-x}\text{N}$ alloys grown by metalorganic chemical vapor deposition," *Appl. Phys. Lett.* **69**, pp. 3315-3317, 1996.
7. K. P. O'Donnell, R. W. Martin, and P. G. Middleton, "Origin of Luminescence from InGaN Diodes," *Phys. Rev. Lett.* **82**, pp. 237-240, 1999.
8. H. Kollmer, Jin Seo Im, S. Heppel, J. Off, F. Scholz, and A. Hangleiter, "Intra- and interwell transitions in GaInN/GaN multiple quantum wells with built-in piezoelectric fields," *Appl. Phys. Lett.* **74**, pp. 82-84, 1999.
9. L. -H. Peng, C. -W. Chuang, and L. -H. Lou, "Piezoelectric effects in the optical properties of strained InGaN quantum wells," *Appl. Phys. Lett.* **74**, pp. 795-797, 1999.
10. T. Mukai, M. Yamada, and S. Nakamura, "Characteristics of InGaN-Based UV/Blue/Green/Amber/Red Light-Emitting Diodes," *Jpn. J. Appl. Phys.* **38**, pp. 3976-3981, 1999.
11. S. Nakamura, M. Senoh, S. Nagahama, N. Iwasa, T. Yamada, T. Matsushita, H. Kiyoku, Y. Sugimoto, T. Kozaki, H. Umemoto, M. Sano, and K. Chocho, "InGaN/GaN/AlGaIn-Based Laser Diodes with Modulation-Doped Strained-Layer Superlattices," *Jpn. J. Appl. Phys.* **36**, pp. 1568-1571, 1997.
12. T. Mukai, D. Morita, and S. Nakamura, "High-power UV InGaN/AlGaIn double-heterostructure LEDs," *J. Crystal Growth* **189/190**, pp. 778-781, 1998.

13. T. Mukai, M. Yamada, and S. Nakamura, "Current and Temperature Dependences of Electroluminescence of InGaN-Based UV/Blue/Green Light-Emitting Diodes," *Jpn. J. Appl. Phys.* **37**, pp. L1358-L1361, 1998.
14. Y. Narukawa, S. Saijou, Y. Kawakami, S. Fujita, T. Mukai, and S. Nakamura, "Radiative and nonradiative recombination processes in ultraviolet light-emitting diode composed of an $\text{In}_{0.02}\text{Ga}_{0.98}\text{N}$ active layer," *Appl. Phys. Lett.* **74**, pp. 558-560, 1999.
15. H. -J. Polland, L. Schultheis, J. Kuhl, E. O. Göbel, and C. W. Tu, "Lifetime Enhancement of Two-Dimensional Excitons by the Quantum-Confined Stark Effect," *Phys. Rev. Lett.* **55**, pp. 2610-2613, 1985.
16. T. Takeuchi, C. Wetzel, S. Yamaguchi, H. Sakai, H. Amano, I. Akasaki, Y. Kaneko, S. Nakagawa, Y. Yamaoka, and N. Yamada, "Determination of piezoelectric fields in strained GaInN quantum wells using the quantum-confined Stark effect," *Appl. Phys. Lett.* **73**, pp. 1691-1693, 1998.
17. P. Mierry, S. Dalmaso, B. Beaumont, and P. Gibart, "Effect of an Electric Field on the Electroluminescence and the Photocurrent in InGaN Single Quantum Well Light Emitting Diodes," *Phys. Status Solidi B* **216**, pp. 321-324, 1999.
18. T. Taguchi, H. Kudo, C. Onodera, Y. Yamada, and T. Mukai, "Magneto-optical properties of the 3.34 eV emission band in InGaN UV LEDs," *Institute of Physics Conference Series*, **162**, pp. 43-48, 1999.
19. H. Kudo, Y. Yamada, and T. Taguchi, "Effects of electric field on photoluminescence spectra in InGaN ultraviolet light-emitting diodes," *Physica E* (in press).
20. H. Kudo, H. Ishibashi, R. Zheng, Y. Yamada, and T. Taguchi, "Efficient UV Emission Encompassing Two Recombination Centers in $\text{In}_x\text{Ga}_{1-x}\text{N}$ Epilayers," *Phys. Status Solidi B* **216**, pp. 163-166, 1999.
21. Yong-Hoon Cho, G. H. Gainer, A. J. Fischer, J. J. Song, S. Keller, U. K. Mishra, and S. P. DenBaars, "S-shaped temperature-dependent emission shift and carrier dynamics in InGaN/GaN multiple quantum wells," *Appl. Phys. Lett.* **73**, pp. 1370-1372, 1998.
22. D. S. Chemla, T. C. Damen, D. A. B. Miller, A. C. Gossard, and W. Wiegmann, "Electroabsorption by Stark effect on room-temperature excitons in GaAs/GaAlAs multiple quantum well structures," *Appl. Phys. Lett.* **42**, pp. 864-866, 1983.
23. J. A. Kash, E. E. Mendez, and H. Morkoc, "Electric field induced decrease of photoluminescence lifetime in GaAs quantum wells," *Appl. Phys. Lett.* **46**, pp. 173-175, 1985.
24. H. Kudo, H. Ishibashi, R. Zheng, Y. Yamada, and T. Taguchi, "Recombination dynamics of carriers in an InGaN/AlGaIn single-quantum-well light-emitting diode under reverse-bias voltages," *Appl. Phys. Lett.* **76**, pp. 1546-1548, 2000.
25. H. Kudo, H. Ishibashi, R. Zheng, Y. Yamada, and T. Taguchi, "Ultraviolet emission properties in $\text{In}_x\text{Ga}_{1-x}\text{N}$ epitaxial layer revealed by magnetoluminescence and time-resolved luminescence studies," *J. Lumin.* **87-89**, pp. 1199-1201, 2000.
26. H. Kudo, T. Tanabe, H. Ishibashi, R. Zheng, Y. Yamada, and T. Taguchi, "Radiative recombination dynamics of carriers in $\text{In}_x\text{Ga}_{1-x}\text{N}$ epitaxial layers revealed by temperature dependence of time-resolved photoluminescence spectra," *Phys. Status Solidi* (in press).
27. E. Berlcowicz, D. Gershoni, G. Bahir, A. C. Abare, S. P. DenBaars, and L. A. Coldren, *Proceedings of the 24th International Conference on the Physics of Semiconductors*, pp. 251, World Scientific, Singapore, 1998.
28. R. Zheng, T. Taguchi, and M. Matsuura, "Properties of $\text{Ga}_{1-x}\text{In}_x\text{N}$ mixed crystals and $\text{Ga}_{1-x}\text{In}_x\text{N}/\text{GaN}$ quantum wells," *J. Appl. Phys.* **87**, pp. 2526-2532, 2000.

SESSION 2

GaN LED and Materials II

The Optical Quality of InGaAsN/GaAs

Brad J. Robinson^a, Lixiang Yuan^a, David A. Thompson^a, Scott A. McMaster^a,
Richard W. Streater^b

^aCentre for Electrophotonic Materials and Devices, McMaster University
Hamilton, ON L8S 4L7, Canada

^bNortel Networks, PO Box 3511, Station C, Ottawa ON K1Y 4H7, Canada

ABSTRACT

Bulk Layers of GaAsN and InGaAsN on GaAs and GaAs/InGaAsN/GaAs quantum wells with nitrogen concentration of about 1% have been grown by gas source molecular beam epitaxy with a radio frequency discharge N source. The material has been characterized by X-ray diffraction, secondary ion mass spectrometry, photoluminescence (PL) and Hall effect with the intention of understanding and overcoming the mechanism responsible for the diminished optical quality of the nitride material relative to the material without nitrogen. The PL yield of the InGaAsN quantum wells can be significantly improved by optimized annealing treatment, although the quality is currently still inferior to the nitrogen-free material. Hall effect measurements on the nitride material indicate the presence of states in the bandgap acting as hole traps and electron traps; it is expected that these states act as the non-radiative recombination centres responsible for the reduced optical quality.

Keywords: InGaAsN, GaInAsN, quantum wells, photoluminescence, Hall effect, molecular beam epitaxy, defects

1. INTRODUCTION

It has been approximately six years since the first reports of epitaxial growth of InGaAsN on GaAs with the intention of obtaining improved temperature characteristics of laser diodes operating at 1.3 μm wavelength¹. Since then considerable progress has been made towards achieving this goal, with recent reports of improvements in the threshold current density² and characteristic temperature³ of InGaAsN/GaAs quantum well laser diodes emitting at 1.3 μm .

The obstacle preventing the use of simply InGaAs/GaAs quantum wells to achieve 1.3 μm emission is that the required indium content results in a compressive strain that is incompatible with the constraint that the well thickness not be greater than the critical thickness for coherent epitaxy. For example, a 7nm thick quantum well requires an In content of about 54%, which implies a lattice mismatch of 0.039 and a critical thickness of 1.5nm. The addition of small amounts of nitrogen (~ 1 to 2 %) to InGaAs quantum wells relieves the bandgap-strain constraint by two mechanisms. One mechanism is "bandgap bowing" in which the addition of nitrogen reduces the bandgap due to the relatively small atomic size of nitrogen compared to arsenic. This phenomenon has been experimentally studied and modelled⁴ in terms of an interaction between the InGaAs conduction band and a resonant band of states due to the nitrogen that results in a reduction of the bandgap at a rate of approximately 150 meV / %N. Besides this reduction in bandgap, the addition of nitrogen reduces the compressive strain inherent in the InGaAs/GaAs system at a rate such that roughly 1% N compensates the strain due to 3% In. Thus, 1.3 μm emission has been obtained from $\text{In}_{0.3}\text{Ga}_{0.7}\text{N}_{0.02}\text{As}_{0.98}$ quantum wells with a practically convenient thickness of 6 nm, which is well below the calculated critical thickness of 10 nm⁵. A further consequence of the addition of nitrogen is that since the bandgap bowing occurs in the conduction band, the conduction band offset between InGaAsN and GaAs increases and therefore the electron confinement in quantum wells is increased. The rate of increase of conduction band offset has been estimated from photoluminescence measurements⁶ to be ~ 100 meV / % N, and has been reported to result in a high characteristic temperature ($T_0 = 150$ K) and higher slope efficiencies at elevated temperatures in diode lasers³.

In spite of the promising material properties of InGaAsN, virtually every experimental report on the subject has either directly or indirectly alluded to a reduction in the optical quality of InGaAsN/GaAs material with increasing N concentration. Consequently, a variety of growth techniques, conditions and post growth annealing treatments have been employed to "improve crystallinity" and "reduce non-radiative recombination centres". In this paper we report on our efforts to grow and understand the properties of InGaAsN, and in particular the nature of the reduction in optical quality associated with the N incorporation.

2. EXPERIMENT

2.1. Calibration and growth techniques

The growth technique in this work is gas source molecular beam epitaxy (MBE) : the As₂ flux is derived from pyrolysis of AsH₃ on a Ta filament at 1000 °C; In and Ga fluxes are derived from conventional effusion cells; the atomic N flux is produced by a radio frequency (RF) discharge source manufactured by EPI⁷. The discharge chamber in this source is constructed of BN. Two aperture configurations for the N source were tested with the following observations.

One aperture configuration consisted of a 1 mm thick BN plate drilled with 253 holes, each 200 µm in diameter. With this high conductance aperture it was found to be virtually impossible to achieve significant (i.e. > 0.3 %) N incorporation in the sample, in spite of the fact that the "correct" discharge glow was observed visually and confirmed by optical emission spectroscopy. The lack of N incorporation is attributed to a low discharge chamber pressure which is a consequence of both the high conductance aperture and an upstream flow element in the source delivery line which is included by the manufacturer to reduce the discharge chamber pressure to levels which support a discharge. Evidently, an inadequate discharge chamber pressure was obtained with the gas delivery pressures (maximum 15 mbar) available in this work, and the observed glow was likely a result of N-N recombination on the walls of the discharge chamber which in turn resulted in effectively no N flux from the source. Although no significant N content was obtained in the samples, the adjacent Si doping cell, idling at 1000 °C, suffered a severe reduction in flux, likely due to the formation of a Si-N compound on the surface of the charge. This could have been formed by the reflection of nitrogen, or more likely ammonia produced from the backflow of H₂ into the N-source, from the N-source shutter into the Si cell. The correct Si flux calibration was recovered with several hours of degas at 1300 °C. Also, a reduction in the Ga flux by several percent was observed, but the correct calibration could be recovered with the normal pregrowth degas. Neither of these flux calibration problems was encountered with the second aperture configuration tested.

The second aperture configuration consisting of 25 holes, each 200 µm in diameter, produced a significant N incorporation in the samples. Indeed, with our gas delivery system it is difficult to achieve fluxes sufficiently low to yield less than 0.5% N at 1 µm per hour growth rate, yet the gas flow is sufficiently low that the N-flux is effectively interrupted by a mechanical shutter that is better than 98 % effective. This means that the N source can be turned on and stabilized prior to use, and the N flux turned on simply by removing the shutter as for In and Ga fluxes. It is with this aperture that the material discussed in this work was grown.

N incorporation in GaAs grown at 1 µm/hr on (100) substrates was calibrated by fixing the N₂ delivery pressure (at ~ 1 mbar) and performing several growths for various RF input powers to the source. The thickness of a layer was typically not greater than twice the calculated critical thickness so that any relaxation effects were negligible. The substrate growth temperature of the GaAsN was 515 °C, a temperature which we have found to result in high quality InGaAs/GaAs quantum wells. Analysis of the layers was performed with a conventional double crystal rocking X-ray diffractometer and the N content calculated from the peak splitting such that 1% N gives 520 arcseconds splitting (this follows from the lattice parameters given in reference 8 and the elastic constants of GaAs). The results are shown in Fig. 1 for an AsH₃ flow of 2.8 sccm. The N incorporation was found to decrease with increasing AsH₃ flow, indicating a competitive incorporation process. Lowering the growth temperature to 480 °C did not change the N fraction. Subsequent growths were performed at 515 °C and 2.8 sccm AsH₃ flow unless otherwise stated.

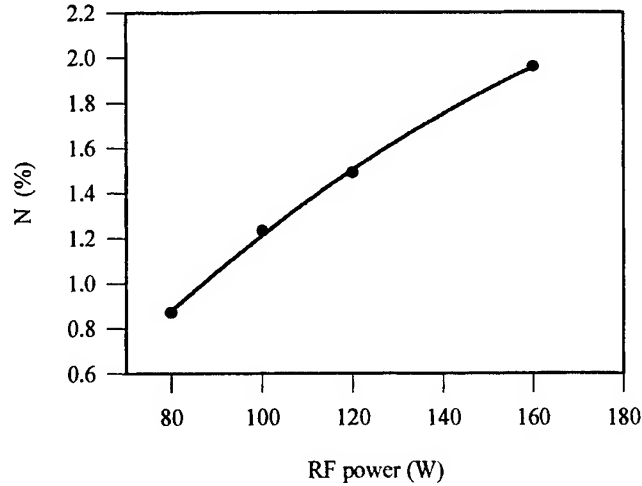


FIG.1 N concentration in GaAsN versus RF power with input N_2 flow fixed

GaAs	300nm
$In_{0.045}Ga_{0.955}As_{0.985}N_{0.015}$	200nm
$In_{0.045}Ga_{0.955}As$	50nm (N shutter closed)
$In_{0.045}Ga_{0.955}As_{0.985}N_{0.015}$	200nm
GaAs	300nm
n-type GaAs substrate	

FIG.2 Schematic diagram of growth structure of SIMS sample

2.2. Compositional analysis of InGaAsN

Based on the calibration of Fig. 1, a bulk structure containing nominally $In_{0.045}Ga_{0.955}As_{0.985}N_{0.015}$ was grown as shown in Fig. 2. X-ray analysis of the 50 nm N-shuttered InGaAs layer indicated that the In content was 0.047, essentially consistent with the nominal target value. The N and In fractions in this sample were measured by secondary ion mass spectrometry (SIMS) as shown in Fig. 3. The SIMS technique for In yield was calibrated against InGaAs lattice matched to InP, and therefore at much higher In levels than contained in this sample. The N yield was calibrated against an implanted sample, and therefore at much lower levels than contained in this sample. Nevertheless, in spite of the extrapolations involved, the In and N fraction agree well with nominal target values derived from the calibration procedures based on the X-ray characterization described above. Analysis of the N-shuttered layer indicates the N shutter is at least 98% effective. The constancy of the In signal through the InGaAsN/InGaAs/InGaAsN structure indicates the independence of the In incorporation on the presence of N.

This sample was also analyzed with SIMS for the presence of H, O, B, C, and Si. The results are shown in Fig. 4. The remarkable signal for B indicates that the plasma discharge within the BN chamber liberates B that, ultimately

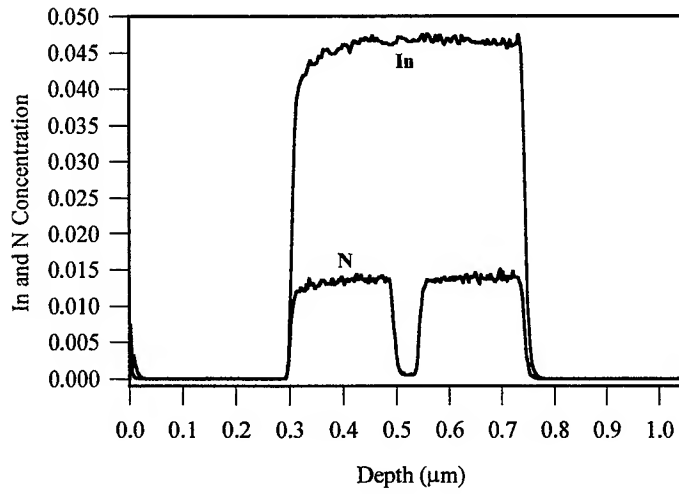


FIG.3 SIMS of N and In concentration distribution in InGaAsN for structure of Fig.2

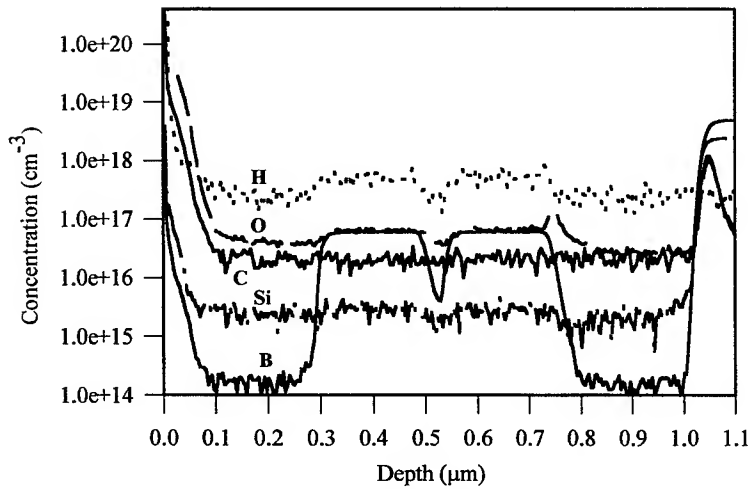


FIG.4 SIMS results for impurities in as-grown InGaAsN for the structure of Fig.2

incorporates in the sample at levels of $\sim 5 \times 10^{16} \text{ cm}^{-3}$. It is noted that however that the B levels are even higher in the GaAs substrate, a characteristic of LEC grown GaAs⁹. Fig. 4 also shows slightly elevated levels, relative to background, of H and O in the InGaAsN. As for the ubiquitous dopants, C and Si, only Si shows a very slight increase above background for the nitride layer. These SIMS observations on trace constituents will come under further consideration in the discussion of the properties of InGaAsN below.

2.3. Photoluminescence and annealing

The structure shown in Fig. 5 was used for photoluminescence and annealing studies of InGaAsN quantum wells. The InGaP layers create a specific electron-hole pair "collection basin" removing variable substrate and surface effects resulting in better consistency in PL yield from growth to growth. The 20 nm GaAs cap layer is provided for rapid thermal annealing with a proximity cap. The reference InGaAs quantum wells emitted at a wavelength of ~ 980 nm. The nitrogen content of the InGaAsN quantum wells was assigned based on the red shift relative to the reference wells according to a rate of $150 \text{ meV} / \% \text{ N}^{4,10}$. Thus, the N concentration in the quantum wells has not been directly measured. However, this method of assigning a concentration to each well is adequate for this comparative PL study; in addition, the assignment is consistent with the calibrations based on bulk layers discussed above.

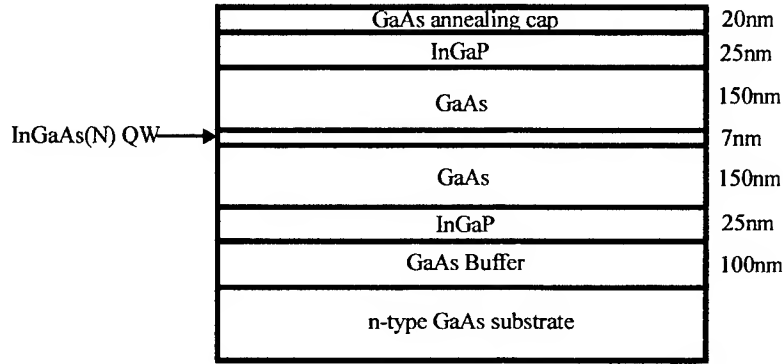


FIG.5 Schematic diagram of InGaAs(N) QW samples for PL and annealing studies

The results for PL yield (peak intensity) from as-grown and annealed samples are shown in Fig. 6 for four samples with N concentrations: (1) 0.87%, (2) 0.78%, (3) 1.05%, and (4) 1.25%. The N variation for (1) and (4) was obtained by varying the RF power, while the variation for (2) and (3) was obtained by a change in the AsH_3 flow. For comparison, the yield for as-grown InGaAs wells is ~ 450 times greater (a yield of 180 in Fig. 6) than the wells designated as (1) and (2). In general the PL yield decreases with increasing N content for both as-grown and annealed samples. The essentially equivalent quality of (1) and (2), even though (2) has lower N concentration, is due to the fact that AsH_3 flow was higher for (2) than (1), and higher AsH_3 flow results in material of slightly poorer optical quality.

In Fig. 6a,b,c the impact of annealing on PL yield is shown as a function of anneal time at temperatures of 700°C , 750°C and 800°C . The measure of PL yield, although in arbitrary units (a.u.), is the same across all three graphs. Thus, although annealing generally results in an increased yield, the magnitude of the increase depends on the details of the annealing schedule. For 700°C and 750°C anneals the yield saturates at sufficiently long times; in particular, the saturated or maximum yield for 700°C is greater than the maximum yield for 750°C , although the maximum is reached only after > 1 hour at 700°C compared to ~ 1 minute at 750°C . Annealing at 650°C did not show any enhancement in PL yield. For the 800°C anneal, the decrease in yield for times > 10 seconds is due to surface damage caused by excessive As loss at the surface. In comparison, the yield from nitrogen-free InGaAs wells is essentially constant, independent of anneal time and temperature, except for a decrease at 800°C for times > 10 seconds due to surface damage.

The annealing behavior is summarized in Fig. 6d where the maximum yield is plotted versus the annealing temperature. Thus an anneal temperature of about 700°C is optimum, but requires long times to achieve the maximum (optimized anneal temperatures have been reported, but for fixed times¹¹). The unusual annealing behavior suggests that one mechanism is activated at about 700°C that results in increased PL yield, however the yield increase saturates due to a competing mechanism, with a slightly higher activation temperature, that limits the yield improvement. Some insight to

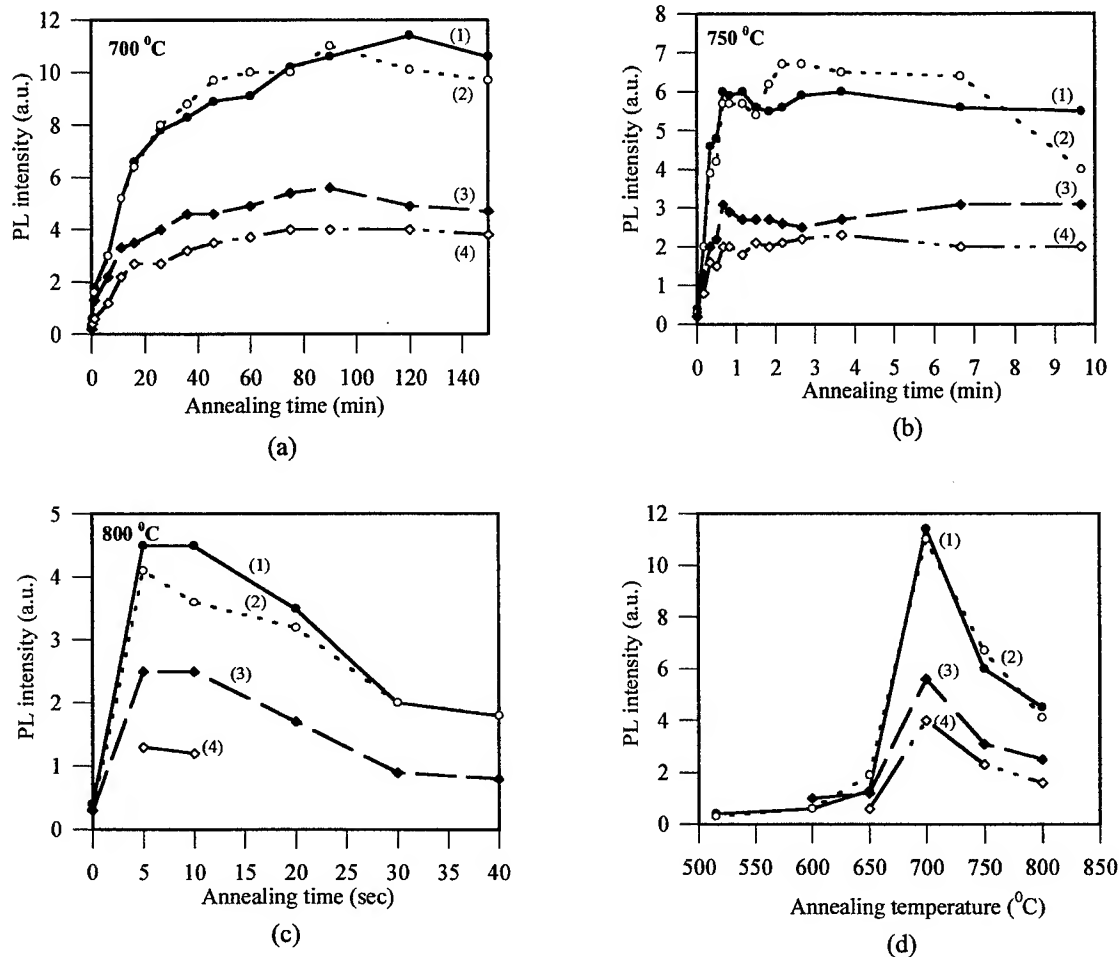


FIG.6 PL intensities versus annealing time at (a) 700 °C, (b) 750 °C, (c) 800 °C; and (d) the maximum PL signal intensity after annealing at given temperature. N concentration are (1) 0.87%, (2) 0.78%, (3) 1.05% and (4) 1.25%

the annealing process is provided by Fig. 7 where the PL emission wavelength is plotted against the annealing temperature. These wavelengths are obtained after long anneal times, that is, when the maxima of Fig. 6d have been reached. Thus, Fig. 7 demonstrates that between 650 °C and 700 °C a mechanism is activated that causes a blue shift in the emission wavelength, but saturates so that annealing at 750 °C produces little additional blue shift. The cause of the redshift at 800 °C for sample (3) and (4) is not known, but may be due to the development of clusters of N rich material which shift the PL peaks to the red. Associated with the blue shift is the increase in the PL yield discussed above. Since no significant blue shift or change in PL yield is observed in nitrogen-free InGaAs wells, it is presumed that the InGaAsN material contains defects, responsible for the poor PL yield, some of which become mobile at 650 to 700 °C, and result in quantum well intermixing which is observed as a blue shift. The diffusion of defects away from the wells, or their annihilation, improves the PL yield. However, a second mechanism limits the process of increasing PL yield and associated blue shifting /intermixing. This second mechanism, presumably another type of defect, actually becomes "stronger" as the annealing temperature increases above 700 °C, so that the higher temperature anneals are not as effective in improving the PL. Thus, the annealing behavior of InGaAsN quantum wells suggests the presence of at least two mechanisms responsible for poor optical quality: one mechanism involving a mobile defect which is "annealable" at

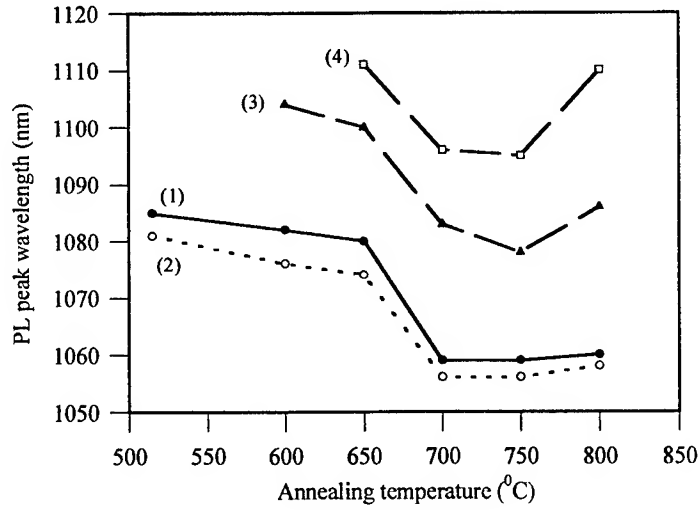


FIG.7 Blue shift of PL peak wavelength versus annealing temperature

700 °C, the other due to an immobile or "un-annealable" defect which becomes a more effective, or more plentiful, non-radiative recombination centre due to higher anneal temperatures.

Hall measurements on doped and undoped InGaAsN provide further insight into the characteristics of the defects present in the nitride material.

2.4. Hall Measurements

Bulk Layers of $\text{In}_{0.45}\text{Ga}_{0.955}\text{As}_{0.985}\text{N}_{0.015}$ and GaAs reference layers were grown undoped, Si doped (nominally $n = 4 \times 10^{17} \text{ cm}^{-3}$), and Be doped (nominally $p = 4 \times 10^{17} \text{ cm}^{-3}$) on semi-insulating GaAs substrates at 515 °C. Hall measurements were performed with the van der Pauw configuration on as-grown samples and after annealing at 725 °C for 30 minutes. The results are given in Table 1. The range of values for the background carrier concentration of undoped GaAs depend on the correction for depletion at the surface and substrate. The lower value is uncorrected for depletion and is therefore a lower limit on the carrier concentration. The calculation for depletion correction is sensitive to the depletion model at this concentration and thickness, and therefore the larger value in the table is an estimated upper limit on the carrier concentration corrected for depletion. For the undoped InGaAsN, the measured values for the carrier concentration are so low that no attempt can be made to correct for depletion; that is, the entire epilayer is depleted. For all the other doped layers, the concentrations have been corrected for depletion effects based on the depletion model for GaAs.

Consider first the as-grown undoped p-type GaAs and undoped n-type InGaAsN. The reduction in carrier concentration in InGaAsN by more than a factor of 1000 compared to GaAs is consistent with the introduction in the nitride material of defects acting as donors that result in (weakly) n-type material. The low mobility for n-type material suggests that a large number of such defects acting as scattering centers are present, but the donor level is sufficiently deep in the bandgap to produce only weakly n-type material. An estimate of the number of deep donor defects (i.e. hole traps) is provided by the Be-doped material. The reference GaAs growth confirms $p = 3.8 \times 10^{17} \text{ cm}^{-3}$, but the InGaAsN shows only $2.7 \times 10^{16} \text{ cm}^{-3}$. Thus, the number of defects acting as hole traps is at least $3.5 \times 10^{17} \text{ cm}^{-3}$, the actual value depending on the energy level of the trap in the energy gap. In addition, the measurements on Si-doped material indicate the presence of defects acting as electron traps (deep acceptors). The GaAs growth confirms $n = 4.0 \times 10^{17} \text{ cm}^{-3}$ (and a high mobility of $3600 \text{ cm}^2/\text{Vs}$), but the InGaAsN has only $n = 2.7 \times 10^{16} \text{ cm}^{-3}$ and a low mobility of $260 \text{ cm}^2/\text{Vs}$. Thus, there are at least $3.7 \times 10^{17} \text{ cm}^{-3}$ electron traps, the actual number depending on their energy level in the energy gap. The lower mobility compared to the undoped case reflects both the high density of defects plus the additional scattering due to the Si dopant.

Hall measurements were repeated after annealing with the results as shown in Table 1. The GaAs remains essentially unchanged, but the InGaAsN properties show a considerable improvement, as indicated by the increase in mobility of the n-type material, both doped and undoped, and the increase in carrier concentration to values closer to the nominal values obtained for the reference GaAs. However, they still remain at least $1.9 \times 10^{17} \text{ cm}^{-3}$ defects acting as hole traps, and $2.1 \times 10^{17} \text{ cm}^{-3}$ defects acting as electron traps. The apparent equality between the number of hole traps and electron traps, and

	Material	Doping	Thickness (μm)	Type	Carrier conc. (cm^{-3})	Mobility ($\text{cm}^2/\text{v.s}$)
As-grown	GaAs	undoped	2	p	5.9×10^{14} $\sim 2.0 \times 10^{15}$	450
	InGaAsN	undoped	2	n	3.6×10^{11}	480
	GaAs	Be	1	p	3.8×10^{17}	200
	InGaAsN	Be	1	p	2.7×10^{16}	150
	GaAs	Si	1	n	4.0×10^{17}	3600
	InGaAsN	Si	1	n	2.7×10^{16}	260
Annealed	GaAs	undoped	2	p	6.7×10^{14} $\sim 2.0 \times 10^{15}$	460
	InGaAsN	undoped	2	n	5.7×10^{12}	1680
	GaAs	Be	1	p	3.7×10^{17}	250
	InGaAsN	Be	1	p	1.8×10^{17}	170
	GaAs	Si	1	n	3.9×10^{17}	3700
	InGaAsN	Si	1	n	1.8×10^{17}	470

Table 1: Hall measurement results of undoped, Be-, Si-doped InGaAsN and GaAs

the number (each $1.5 \times 10^{17} \text{ cm}^{-3}$) removed by annealing, may be coincidental, but may also reflect a common mechanism responsible for the charge compensation produced by the defects in the InGaAsN. Further measurements at different doping levels would confirm or deny this apparent "commonality".

The properties of InGaAsN are now discussed with joint reference to the SIMS, PL and Hall measurements.

3. DISCUSSION

The observations indicate that the as-grown InGaAsN contains defects responsible for significant degradation of the optical quality compared to InGaAs, and significant free carrier charge compensation and reduction in electron and hole mobility compared to GaAs.

One possible source of defects could be material impurities deriving from the operation of the N source. For example, high O levels (10^{18} cm^{-3}) have been reported in InGaAsN, with the suggestion that O might act as a non-radiative recombination center¹². However, it is felt that the SIMS measurements in this work (Fig.4) discount the possibility of a significant role for material impurities in the degradation of the properties of InGaAsN that we have observed. In particular, the levels of O in this work are less than 10^{17} cm^{-3} , and in the InGaAsN material only marginally above ($\sim 3 \times 10^{16} \text{ cm}^{-3}$) the background levels in InGaAs and GaAs. These O levels are an order of magnitude lower than the defect concentrations indicated by Hall measurements. Also, SIMS levels of the other significant contaminant, B, are below 10^{17} cm^{-3} , and as a group III element, B is expected to be electrically inactive. Similarly, the levels of Si and C, which could be electrically active, are far too low to account for the observed charge compensation effects. Thus, other than H to be discussed, it is felt that the observed properties of InGaAsN cannot be attributed to the usual material impurity suspects Si, C, O, B.

SIMS measurements in this work indicate concentrations of H of $\sim 2.5 \times 10^{17} \text{ cm}^{-3}$ in InGaAsN above the background level. Interestingly, after anneal at 725°C for 30 minutes the excess H is no longer present. Although perhaps coincidental, it is plausible that the excess H is associated with the "annealable" defects responsible for the increase in PL and reduced carrier compensation after annealing. The concentrations involved are mutually consistent and, although the mechanism is not known, the H might be the "commonality" link between the quantitatively similar changes in defect concentration in the n-type and p-type InGaAsN. Others^{12,13}, using organometallic chemical vapor deposition growth, have suggested that N-H_2 complexes could be the defects responsible for the poor optical quality of InGaAsN.

Another possible source of defects in this work is related to the energetics of the RF discharge. Our group has studied the impact of a flux of energetic He atoms derived from an ECR plasma on the material properties of InGaAsP/InP¹⁴. It has been found that energetic He (25 eV) impinging on the growing surface introduces both electron traps and hole traps, much like the observations in this study. Thus, it is possible that energetic N atoms produced by the RF discharge might act in a similar fashion and introduce defects. Although such a mechanism might explain some of the defects in this work, it could not entirely account for the generality of the degradation of the optical quality of InGaAsN grown by other non-plasma chemical vapour deposition techniques. To investigate the possible role of energetics, a single growth of an InGaAs well, similar to the structures in the PL study, has been performed with the RF source operating with He gas. Although the energetics would be quantitatively different with N_2 , it is expected that at least qualitatively this growth would indicate if energetics play a role. The results indicate that there is no difference between the InGaAs reference wells and the well grown with the source operating with He. Therefore the energetics of the source is not responsible for the optical and electrical properties of InGaAsN.

Thus, it appears that the defect structure of InGaAsN is derived from the N incorporation process. Although the miscibility gap arising from the lattice mismatch of the binary constituents leads to spatial fluctuations in the material composition that can degrade optical quality¹⁵, the observations in this work indicate that there are also significant concentrations of point defects that act as non-radiative recombination centers and traps for electrons and holes. The overall concentration of defects is at least $8 \times 10^{17} \text{ cm}^{-3}$ before annealing. Although the mechanism by which they are produced is unknown, it is plausible that it is related to the concentration of adjacent pairs of N atoms on the growth surface. The probability that a group V surface site is occupied by N is just the N concentration, C_N ; the probability of two particular adjacent sites (say, in a particular dimer row) being occupied by N is C_N^2 , assuming uniform material composition. If the surface lattice distortion produced by such a N-N pair leads to a point defect when the group III layer grows on this surface, then the concentration of defects would be $\sim 5 \times 10^{18} \text{ cm}^{-3}$ for an N concentration of 1.5 %, a value which is larger than but not inconsistent with the lower limit encountered in this work. If such a growth related mechanism is operating to produce the defects, then it may be possible to reduce the defect concentration by changing growth conditions; one promising approach to this end employs Sb as a surfactant².

4. SUMMARY

InGaAsN grown by gas source MBE with an RF plasma N source has been characterized by X-ray diffraction, SIMS, PL and Hall measurements. For bulk layers of $\text{In}_{0.045}\text{Ga}_{0.955}\text{As}_{0.985}\text{N}_{0.015}$ lattice matched to GaAs, Hall measurements on doped as-grown material indicate the presence of at least $\sim 4 \times 10^{17} \text{ cm}^{-3}$ electron traps in n-type material and at least $\sim 4 \times 10^{17} \text{ cm}^{-3}$ hole traps in p-type material. Annealing at 725°C for 30 minutes eliminates $\sim 1.5 \times 10^{17} \text{ cm}^{-3}$ electron traps and a

similar number of hole traps. Perhaps coincidentally, an approximately similar concentration $\sim 2.5 \times 10^{17} \text{ cm}^{-3}$ of H is removed from the material by this anneal. The optical quality of $\text{In}_{0.18}\text{Ga}_{0.82}\text{As}_{0.99}\text{N}_{0.01}$ quantum wells is significantly improved by an optimum annealing treatment at 700°C for long times (> 1 hour). The improvement in quality is presumed to be due to the decrease in defect concentration observed in the Hall study; however, the optical quality remains inferior to the InGaAs reference, again presumably due to the defects which survive the annealing as indicated by the Hall results.

ACKNOWLEDGMENTS

This work was supported by the Ontario Research and Development Challenge Fund (ORDCF).

REFERENCES

1. M. Kondow, K. Uomi, A. Niwa, T. Kitatani, S. Watahiki, and Y. Yazawa, "GaInNAs: A novel material for long-wavelength-range laser diodes with excellent high-temperature performance", *Jpn. J. Appl. Phys.* **35**, pp. 1273-1275, 1996.
2. X. Yang, J.B. Heroux, M.J. Jurkovic, and W.I. Wang, "Low-threshold 1.3- μm InGaAsN:Sb-GaAs single-quantum-well lasers grown by molecular beam epitaxy", *IEEE Photon. Technol. Lett.* **12**, pp. 128-130, 2000.
3. M.R. Gokhale, P.V. Studentkov, J. Wei, and S.R. Forrest, "Low-threshold current, high-efficiency 1.3- μm wavelength aluminum-free InGaAsN-based quantum-well lasers", *IEEE Photon. Technol. Lett.* **12**, pp. 131-133, 2000.
4. W. Shan, W. Walukiewicz, J.W. Ager III, E.E. Haller, J.F. Geisz, D.J. Friedman, J.M. Olson, and S.R. Kurtz, "Band anticrossing in GaInNAs alloys", *Phys. Rev. Lett.* **82**, pp. 1221-1224, 1999.
5. H.P. Xin, K.L. Kavanaugh, C.W. Tu, "Gas-source molecular beam epitaxial growth and thermal annealing of GaInNAs/GaAs quantum wells", *J. Crystal Growth* **208**, pp. 145-152, 2000.
6. H.P. Xin and C.W. Tu, "GaInNAs/GaAs multiple quantum wells grown by gas-source molecular beam epitaxy", *Appl. Phys. Lett.* **72**, pp. 2442-2444, 1998.
7. EPI, MBE Products Group, 1290 Hammond Road, Saint Paul MN 55110.
8. S. Sakai, Y. Ueta, and Y. Terauchi, "Band gap energy and band lineup of III-V alloy semiconductors incorporating nitrogen and boron", *Jpn. J. Appl. Phys.* **32**, pp. 4413-4417, 1993.
9. I.C. Bassignana, D.A. Macquistan, G.C. Hiller, R. Streeter, D. Beckett, A. Majeed, C. Miner, "Variation in the lattice parameter and crystal quality of commercially available Si-doped GaAs substrates", *J. Crystal Growth*, **178**, pp. 445-458, 1997.
10. M. Kondow, T. Kitatani, s. Nakatsuka, M.C. Larson, K. Nakahara, Y. Yazawa, M. Okai, and K. Uomi, "GaInNAs: A novel material for long-wavelength semiconductor lasers", *IEEE J. Select. Topics Quantum Electron.* **3**, pp. 719-730, 1997.
11. L.H. Li, Z. Pan, W. Zhang, Y.W. Lin, Z.Q. Zhou, and R.H. Wu, "Effects of rapid thermal annealing on the properties of $\text{GaN}_x\text{As}_{1-x}/\text{GaAs}$ single quantum well structure grown by molecular beam epitaxy", *J. Appl. Phys.* **87**, pp. 245-248, 2000.
12. R. Bhat, C. Caneau, L. Salamanca-Riba, W. Bi and C. Tu, "Growth of GaAsN/GaAs, GaInAsN/GaAs and GaInAsN quantum wells by low-pressure organometallic chemical vapor deposition", *J. Crystal Growth* **195**, pp. 427-437, 1998.
13. E.V.K. Rao, A. Ougazzaden, Y. LeBellego, M. Juhel, "Optical properties of low band gap $\text{GaAs}_{(1-x)}\text{N}_x$ layers: Influence of post-growth treatments", *Appl. Phys. Lett.* **72**, pp. 1409-1411, 1998.
14. H. Pinkney, D.A. Thompson, B.J. Robinson, L. Qian, S.D. Benjamin and P.W.E. Smith, "Growth of novel InP-based materials by He-plasma-assisted epitaxy", *J. Crystal Growth* **209**, pp. 237-241, 2000.
15. R.R. LaPierre, T. Okada, B.J. Robinson, D.A. Thompson and G.C. Weatherly, "Lateral composition modulation in InGaAsP strained layers and quantum wells grown on (100) InP by gas source molecular beam epitaxy", *J. Crystal Growth*, **158**, pp. 6-14, 1996.

Optical-pumping spectra for $\text{In}_x\text{Ga}_{1-x}\text{N}/\text{GaN}$ multiple quantum well structures with indium content $x>0.35$

Chii-Chang Chen^a, Hui-Wen Chuang^a, Gou-Chung Chi^a, Chang-Cheng Chuo^b, Jen-Inn Chyi^b

^aDepartment of Physics, National Central University, 32054 Chung-Li, Taiwan

^bDepartment of Electrical Engineering, National Central University, 32054 Chung-Li, Taiwan

ABSTRACT

Photoluminescence (PL) measurement and optical pumping at 25K were studied for high-indium-composition InGaN/GaN multiple quantum well (MQW) structures grown by low-pressure metalorganic chemical vapor deposition. The result show that thermal annealing can reduce the compositional fluctuation of indium content. The optical pumping spectra show 5 stimulated emission (SE) peaks. This phenomenon might be attributed to intersubband transition. The transition between quantized levels for each peak was precisely identified by solving the time-independent Schrödinger equation and finite-difference method. The ratio of conduction-band discontinuities to valence-band discontinuities of InGaN/GaN QW, $\Delta E_c:\Delta E_v=38:62$, can be obtained.

Keywords: GaN, InGaN , multiple quantum well, annealing, optical pumping, photoluminescence, stimulated emission, X-ray, band offset parameter.

1.INTRODUCTION

GaN is a promising wide-bandgap material for light emitting devices in the violet-blue-green region. Most reported optical properties studies were on low-indium-content $\text{In}_x\text{Ga}_{1-x}\text{N}/\text{GaN}$ MQW structures ($x \leq 25\%$). The compositional fluctuations of indium content were often observed because of alloy disorder, interface irregularities, and/or self-formed “quantum dots” in quantum well (QW) active region¹. The degree of indium-content fluctuations plays an important role in the optical gain of MQW laser which has been investigated experimentally^{2,3} and theoretically⁴. To achieve longer-wavelength laser, high indium content in QW layers is necessary. However an increase in indium composition augments the chemical inhomogeneity of InGaN alloy due to the poor miscibility of InN and GaN ⁵. This influences significantly their optical properties⁶.

In this work, we study an InGaN/GaN multiple quantum well structure with higher indium composition ($x>35$). The optical pumping spectra showed several SE peaks. The origin of the peaks was discussed. The intersubband transition might be the most probable explanation for the observed SE peaks. The intersubband transition between quantized levels in QW can be calculated by solving the time-independent Schrödinger equation for each SE peak. Up to now, the important parameter for MQW structure, the ratio of conduction-band discontinuities to valence-band discontinuities (band offset parameter) is only roughly measured by X-ray photoemission spectroscopy⁷. In this paper, we report the band offset parameter measured by optical pumping. The influence of thermal annealing to optical properties of MQW will be discussed.

2.EXPERIMENT

The samples studied in this work were grown by LP-MOCVD on (0001)-oriented sapphire substrate. The InGaN/GaN MQW structures were made up of 5 periods of silicon doped InGaN well with 3 nm in thickness and 7-nm-thick GaN barrier layers. The QW layers were sandwiched with 1.5- μm -thick GaN buffer layer and 30-nm-thick GaN capping layer. Some samples were annealed at 900°C for 10 min by rapid thermal annealing.

* Correspondence: Email: chx@joule.phy.ncu.edu.tw

X-ray diffraction measurement was used to analyze the structure of MQW in an X-ray diffractometer using Cu K α radiation. A Ge (1 1 1) monochromator was used to filter the Cu K α_2 . Only K α_1 line ($\lambda=1.54\text{\AA}$) was used.

The samples having a size of $4\times 4\text{ mm}^2$ were attached to a copper holder inside a cryostat. The optical excitation source was a N $_2$ laser (wavelength at 337nm) with a pulse width of 0.5ns and a repetition rate of 30Hz. Since the absorption depth at 337nm is around 90nm for GaN 8 ($\alpha \cong 11\times 10^4\text{cm}^{-1}$), MQW layers can be excited by N $_2$ laser. In a surface-emitting geometry, PL measurement was performed at 25K by the 0.55-m monochromator with PMT. In an edge-emitting geometry, by focusing laser beam on the sample surface using a cylindrical lens to form a rectangular excitation spot, optical pumping spectra were also analyzed at 25K by the 0.55-m monochromator with PMT. The excitation length was equal to 4mm, the width of the samples.

3.RESULTS AND DISCUSSION

The PL spectra of these samples using He-Cd laser (3.8eV) at 40mW/cm 2 and Ar $^+$ laser (2.5eV) at 40mW/cm 2 and the analysis of cross-sectional transmission electron micrograph (TEM) were reported recently 9 . The results implied that the compositional fluctuations of high indium content were reduced after thermal annealing. Fig. 1 shows the PL spectra for the as-grown and the annealed samples reported in ref. 9 and the PL spectra measured in this work with N $_2$ laser (3.69eV) at 440kW/cm 2 . All spectra were measured at 25K. The intensity of the spectra in Fig. 1 was normalized. The peaks at 366nm were attributed to the emission from GaN layers. The broad spontaneous emission peaks originated from the emission of the InGaN/GaN MQW layers show a large composition fluctuation in QW. The significant difference in peak position of the spectra for different excitation lasers should be due to the different excitation power densities and the different photon energies of the lasers. Under excitation of low power density (He-Cd laser and Ar $^+$ laser), carriers drop into the lowest energy gap in QW before recombination. Since the photon energy of He-Cd laser is higher than the photon energy of Ar $^+$ laser, during the lifetime of carriers, the carriers excited by Ar $^+$ laser can drop into the lower band gap of well than the carriers excited by He-Cd laser. This leads to a longer wavelength of PL spectrum for Ar $^+$ laser than He-Cd laser. The peak position of the PL spectra for the annealed samples excited by Ar $^+$ laser (dashed line in Fig. 1b) shows that the highest indium composition in the QW of the samples was about 73%. Under the high excitation power density with N $_2$ laser (solid line in Fig. 1b), carriers fill the QW and the peak position shifts to 470nm indicating that the principal indium composition of QW should be around 35%. These results showed a large inhomogeneity of indium content in QW. It is noted that the broad spontaneous emissions were modulated by the modes of the 1.6- μm Fabry-Pérot microcavity formed by the GaN/sapphire interface and the surface of the samples. The calculated separation of modes was about 22nm, which corresponds to the difference of wavelength of the peaks a, b and c in Fig. 1b.

Fig. 2 shows the XRD measurement for the as-grown and the annealed samples. Two spectra are almost identical. There is no significant difference between the spectra for the as-grown sample and for the annealed sample. However, there is a noticeable difference between the PL spectra for the as-grown and annealed sample (Figs. 1). This indicates that PL measurement is more sensitive to the variation of indium composition than XRD measurement.

With the zeroth-order peak at 34.127° , the average indium composition in a period of superlattice is 10.6% which can be calculated by assuming that the QW's and barriers are fully relaxed and that Vegard's law holds. According to the growth condition, the ratio of thickness of well and barrier is about 3:7. The principal indium composition in QW layers which is determined to be 35% can be determined. This result corresponds to the peak position of PL spectra of the annealed sample excited by N $_2$ laser.

Fig. 3 shows the optical pumping spectra in edge-emission geometry for the annealed samples (solid lines) and the as-grown samples (dotted line) at different excitation power density in the TE- and TM-mode. Several SE peaks were observed in the spectra of our samples. The appearance of the several SE peaks might be due to interference or intersubband transition in QW. If this phenomenon is due to interference, according to the wavelength of each SE peaks in Fig. 3a, the mode separation of the peaks is about 33nm. The corresponding length of the Fabry-Pérot microcavity is calculated to be about 1.5 μm . However no periodic quantum dots or 1.5 μm -long microcavity can be found in the TEM image of the ref. 9. The ratio of the peak intensity to the background spontaneous emission in Fig. 3 (solid lines) is much greater than the Fabry-Pérot interference effect mentioned above in Fig. 1b. This implies that the quality of two interfaces of Fabry-Pérot microcavity for the Fig. 3a is better than for the Fig. 1b. However, periodic 1.5 μm -long interfaces with better quality in transversal direction of QW layers might not exist. Therefore, the interference can not be responsible for the appearance of the SE peaks. Fig. 3b showed that SE peaks can be also observed in the optical pumping spectra in the TM-mode. However, the intensity of the peaks in the TM mode was obviously weaker than the TE mode. This implies that the TE mode

dominates the mechanism of the emission of the SE peaks. This should be attributed to the fact that the light emission of compressive-strain layer is dominated by the heavy holes which contribute principally the emission of the TE mode. In Fig. 3a, the saturation of output intensity in order of peak A, peak B, peak C and peak D can be observed in the spectra of the annealed sample (solid lines) as pumping power density increases. This implies the subband filling from the lowest quantized level of QW to the higher quantized levels as carrier supply increases. To identify the transition between quantized levels in QW for the SE peaks in the optical pumping spectra of the as-grown samples in the TE mode (dotted line in Fig. 3a), the time-independent Schrödinger equation was solved using the finite-difference method¹⁰. The value of the effective mass of electron, the effective mass of light hole and the effective mass of heavy hole are $m_e^* = 0.11m_0$ (m_0 is the mass of electron.), $m_{lh}^* = 1.56m_0$ and $m_{hh}^* = 1.56m_0$, respectively¹¹. Four parameters (wellwidth, conduction/valence band discontinuity and electric field in QW) were varied to find the eigenenergies for each probable transition. The range of the 4 parameters is as follows:

$2\text{nm} \leq \text{wellwidth} \leq 3\text{nm}$, $0.2\text{eV} \leq \text{conduction-band discontinuity} \leq 0.6\text{eV}$, $0.5\text{eV} \leq \text{valence-band discontinuity} \leq 1\text{eV}$ and $0 \leq \text{electric field in QW} \leq 5.5 \times 10^8 \text{ V/m}$, respectively.

We assume that peak A in Fig. 3a corresponds to intersubband transition from the 1st quantized level of conduction band to that of valence band. We can deduce that peak B and peak D correspond to the intersubband transition energies from the 1st quantized level of conduction band to the 3rd and the 5th quantized levels of valence band, respectively. By assuming the peak C corresponds to the intersubband transition from the 2nd quantized level of conduction band to that of valence band, we can deduce that peak E corresponds the intersubband transition of the 2nd quantized level of conduction band to the 4th quantized level of valence band. The solution that corresponds to the SE peaks in optical pumping spectra at 25K of the as-grown sample can be obtained only when 4 parameters are chosen as:

wellwidth=2.6nm, conduction-band discontinuity=0.48eV, valence-band discontinuity=0.8eV and electric field in QW= $3.75 \times 10^8 \text{ V/m}$.

These calculated intersubband transitions which have a good agreement with the experimental results are summarized in Table 1. The difference between the calculated and the experimental value for the peak E might be due to insufficiency of carrier to fill the highest energy levels in QW leading to an uncertainty of peak position. According to the result of the calculation, the band gap of the well is 2.1eV. This value corresponds to the peak position of the PL spectrum for the sample excited by Ar⁺ laser. According to this result of calculation, the band offset parameter, $\Delta E_c / (\Delta E_c + \Delta E_v) = 0.38$ was obtained.

Fig. 1 shows that the distribution of the indium composition is between 20% and 73%. The half width at full maximum (FWHM) of broad spontaneous emission was narrowed after annealing. The PL peak shows a blue shift after annealing. The same phenomena can also be observed in Fig. 3. This implies that high indium phase in QW diminished after annealing and that the indium composition fluctuation was also reduced. Fig. 3 shows that the ratio of the intensity of SE peaks to the spontaneous emission gets greater after the samples were annealed. This reveals that indium composition might get more uniform after annealing leading to a more effective stimulated emission.

The optical pumping spectra showed that the longest wavelength of the SE peaks was near the lowest band gap which corresponds to an 73% indium composition. The results might imply that during the lifetime of excited carriers, carriers can drop into the lowest band gap in QW and that the population inversion of the excited carriers for SE might takes place in high indium phase of QW.

A red shift of the SE peaks was observed in Fig. 3a after the samples were annealed. This might be attributed to the inhomogeneity reduction of indium content after annealing. This phenomenon can be proved by calculating the different quantized energies for two QW's with different composition fluctuations using the Schrödinger equation and the finite-difference method. When the composition fluctuation is reduced, the quantized energy also decreases. Fig. 4 show a schematic diagrams of potential fluctuation for the conduction band of QW induced by compositional inhomogeneity (a) for the as-grown samples and (b) for the annealed samples. This induces the red shift of the SE peaks after thermal annealing.

4.CONCLUSION

PL measurement, optical pumping in edge emitting geometry and XRD measurement were performed to analyze the high indium composition InGa_N/Ga_N MQW structure. To our best knowledge, several SE peaks were observed in the optical

pumping spectra of InGa_N/Ga_N MQW structure for the first time. The SE peaks might be originated from the intersubband transition instead of interference. By calculating the quantized energies of each quantized level using the Schrödinger equation, the intersubband transition for each SE peak can be identified. The band offset parameter which is 38:62 can be obtained.

The indium composition fluctuation was reduced after the samples were annealed leading to a more effective emission. PL measurement showed a higher sensitivity to the change of indium composition fluctuation than XRD measurement. The principal indium composition of the samples was 35% confirmed by PL and XRD measurement. However, according to the PL spectra of the samples, the distribution of indium composition in QW was between 20% and 73%. During the lifetime of excited carriers, carriers can drop into the lowest band gap in QW and that the population inversion of the excited carriers for SE might takes place in high indium phase of QW.

The red shift of the SE peaks should be attributed to the change of composition fluctuation. This phenomenon was proved by calculating the quantized energies of two QW's with different degree of composition fluctuation. The reduction of inhomogeneity of indium content induces the decrease of quantized energy leading to a red shift of the SE peaks.

ACKNOWLEDGEMENT

The work was supported by the grants NSC89-2218-E008-014 from National Science Council, Taiwan.

REFERENCES

1. T. J. Schmidt, Y.-H. Cho, G. H. Gainer, J. J. Song, S. Keller, U. K. Mishra, and S. P. DenBaars, "Energy selective optically pumped stimulated emission from InGa_N/Ga_N multiple quantum wells," *Appl. Phys. Lett.* **73**, pp. 560-562, 1998.
2. K. Domen, A. Kuramata, and T. Tanahashi, "Lasing mechanism of InGa_N/Ga_N/AlGa_N multiquantum well laser diode," *Appl. Phys. Lett.* **72**, pp. 1359-1361, 1998.
3. T. Deguchi, T. Azuhata, T. Sota, S. Chichibu, and S. Nakamura, "Gain spectra in cw InGa_N/Ga_N MQW laser diodes," *Mater. Sci. Eng. B*, **B50**, pp. 251-255, 1997.
4. T. Uenoyama, "Optical Gain Spectra in GaN/InGa_N Quantum Wells with the Compositional Fluctuations," *MRS Internet J. Nitride Semicond. Res.* **4S1**, G2.9, 1999.
5. D. Doppalapudi, S. N. Basu, K. F. Ludwig Jr., and T. D. Moustakas, "Phase separation and ordering in InGa_N alloys grown by molecular beam epitaxy," *J. Appl. Phys.* **84**, pp. 1389-1395, 1998.
6. C. A. Tran, R. F. Karlicek Jr., M. Schurman, A. Osinsky, V. Merai, Y. Li, Eliashevich, M. G. Brown, J. Nering, I. Ferguson, and R. Stall, "Phase separation in InGa_N/Ga_N multiple quantum wells and its relation to brightness of blue and green LEDs," *J. Cryst. Growth* **195**, pp. 397-400, 1998.
7. G. Martin, A. Botchkarev, A. Rockett, and H. Morkoç, "Valence-band discontinuities of wurtzite Ga_N, Al_N, and In_N heterojunctions measured by x-ray photoemission spectroscopy," *Appl. Phys. Lett.* **68**, pp. 2541-2543, 1996.
8. J. F. Muth, J. D. Brown, M. A. L. Johnson, Zhonghai Y., R. M. Kolbas, J. W. Cook, JR. and J. F. Schetzina, "Absorption Coefficient and Refractive Index of Ga_N, Al_N, and AlGa_N Alloys," *MRS Internet J. Nitride Semicond. Res.* **4S1**, G5.2, 1999.
9. C. C. Chou, C. M. Lee, T. E. Nee and J. I. Chyi, "Effects of thermal annealing on the luminescence and structural properties of high indium-content InGa_N/Ga_N quantum wells," *Proc. of Electronics Devices and Materials Symposia 99*, pp. 81-84, Chung-Li, Taiwan, 1999.
10. S. L. Chung, *Physics of Optoelectronic Devices*, Chap. 3, Wiley, New York, 1995.
11. Y. C. Yeo, T. C. Chong, and M.F. Li, "Electronic band structures and effective-mass parameters of wurtzite Ga_N and In_N," *J. Appl. Phys.* **83**, pp. 1429-1436, 1998.

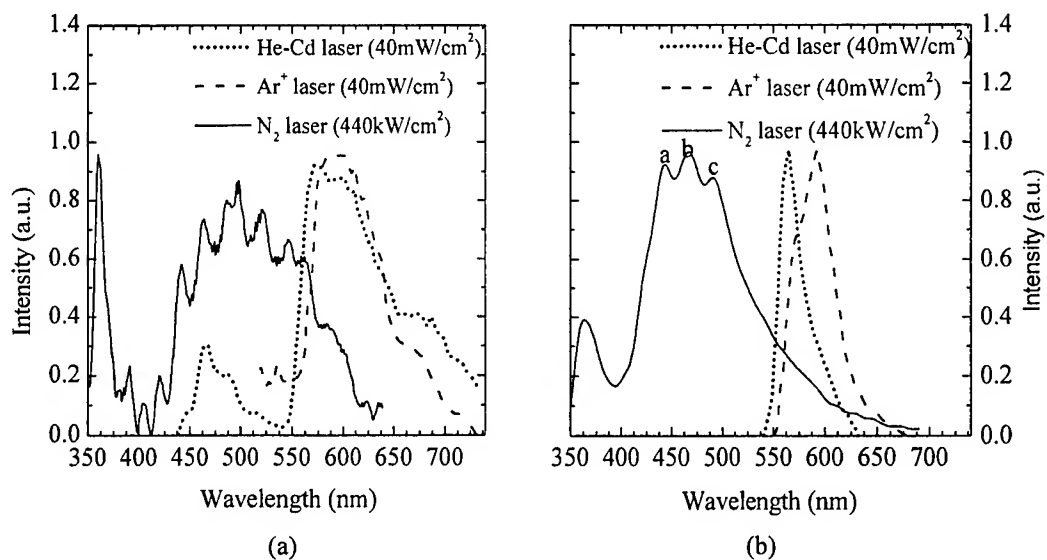


Figure 1 PL Spectra (a) for as-grown samples and (b) for annealed samples excited by N_2 laser, He-Cd laser and Ar^+ laser at 25K.

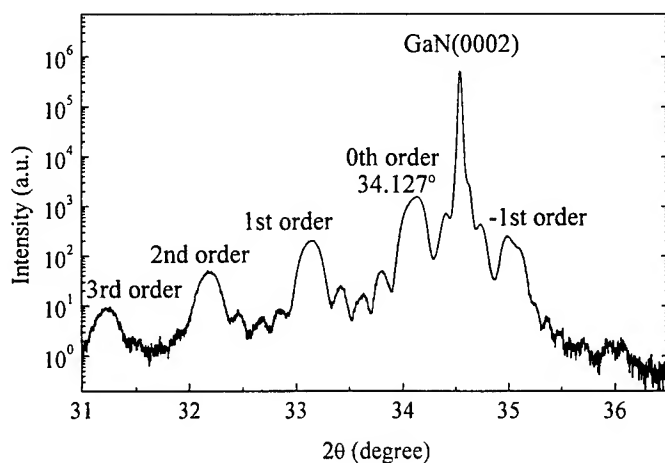


Figure 2 XRD measurement for the as-grown sample and the annealed sample. Two spectra are superimposed.

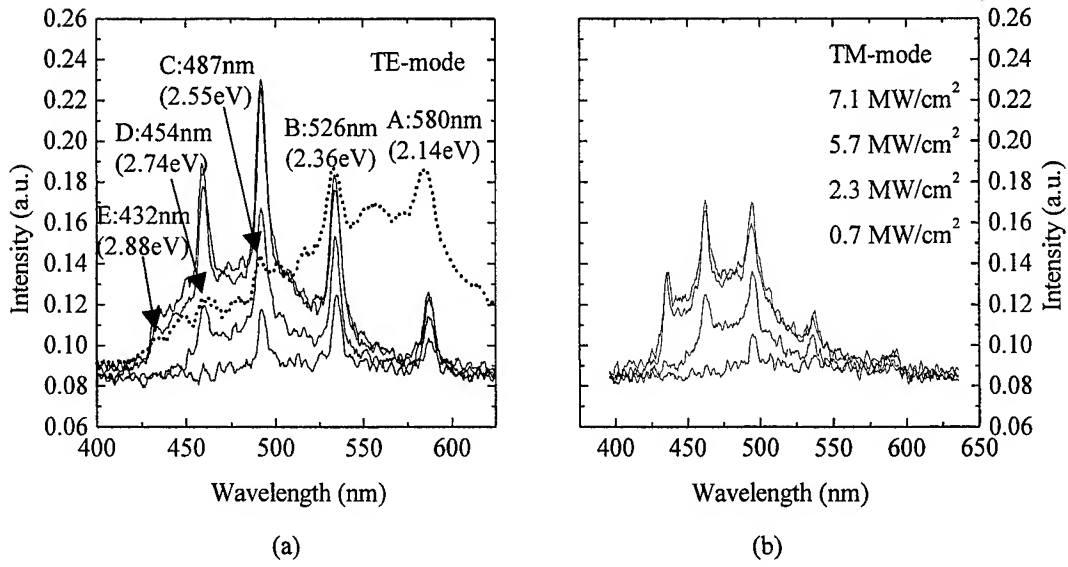


Figure 3 Optical pumping spectra at 25K of (a) the as-grown sample (dotted line) at 11.4MW/cm² and the annealed sample at 0.7MW/cm²-7.1MW/cm² in the TE mode (solid lines) and (b) the annealed sample in the TM mode at 0.7MW/cm²-7.1MW/cm².

Intersubband transition energy $E_{\text{conduction band-valence band}}$	Calculated intersubband transition energy	Peak position in optical pumping spectra in Fig. 3a
E_{2C-4V}	2.85eV	2.88eV (peak E)
E_{1C-5V}	2.74eV	2.74eV (peak D)
E_{2C-2V}	2.55eV	2.55eV (peak C)
E_{1C-3V}	2.36eV	2.36eV (peak B)
E_{1C-1V}	2.14eV	2.14eV (peak A)

Table 1 Comparison of calculation and optical pumping measurement.

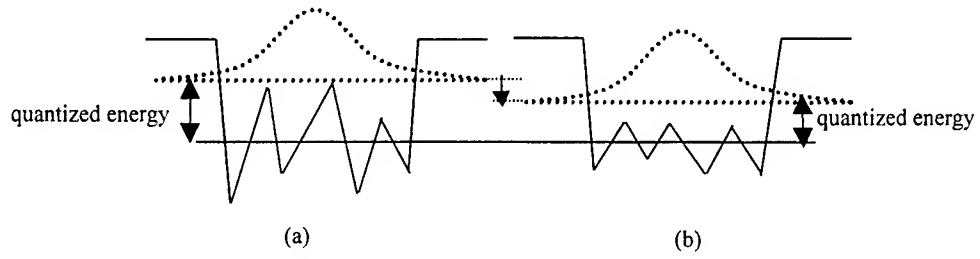


Figure 4 Schematic diagrams of potential fluctuation for the conduction band of QW induced by compositional inhomogeneity (a) for the as-grown samples and (b) for the annealed samples. Reduction of quantized energy is resulted from the decrease of composition fluctuation.

Dielectric function of GaN: model calculations

Aleksandra B. Djurišić,^a E. Herbert Li^{**b}

^aInstitut fuer Angewandte Photophysik, TU Dresden, Mommsenstr. 13, D-01062 Dresden, Germany

^bDepartment of Electrical & Electronic Engineering, University of Hong Kong,
Pokfulam Road, Hong Kong

ABSTRACT

In this work we have modeled the optical functions of hexagonal GaN (corresponding to E_{1c}) in the range from 1 eV to 10 eV using a modified critical points model. The difference between the model employed and the standard critical points model is that the exponent m is an adjustable parameter, and does not have fixed value depending on the type of critical point. Excellent agreement with the experimental data has been achieved over the entire investigated spectral range. Obtained relative rms errors equal 0.6% for the real part, and 2.0% for the imaginary part of the index of refraction.

Keywords: optical properties, gallium nitride

1. INTRODUCTION

Group-III nitride materials are particularly interesting for optoelectronic device applications.^{1,2} Bandgaps of nitride ternary alloys cover the spectral region from orange to ultraviolet. GaN represents the most frequently studied group-III nitride material. Band gap of wurtzite GaN is about 3.42 eV.³ The band structure of GaN has been studied, and the imaginary part of the dielectric function has been calculated using a strict quantum mechanical approach, while the real part can be obtained via Kramers-Kronig (KK) transformation.⁴⁻⁷ However, such an approach is useful only for comparing the position of the peaks in the calculated dielectric function with the experimental data, while there are significant differences in magnitude and the shape of peaks between the calculated and experimental data. In general, quantum mechanical calculations produce peaks in the dielectric function which are sharper and more pronounced than the corresponding structures in the experimental dielectric function spectra. Therefore, for the purpose of more accurate calculations of the dielectric function, or the index of refraction, which is needed in the optoelectronic device design, a semi-empirical model of the dielectric function would be more useful.

Parameters of a semi-empirical model are determined by minimizing the discrepancies between the experimental data and the data calculated from the model equations. Therefore, the obtained parameters strongly depend on the experimental data employed in model parameter estimation. The optical functions of GaN reported in the literature widely differ among themselves. This is illustrated in Fig. 1, where dashed line denotes spectroscopic ellipsometry (SE) data by Whetkamp *et al.*,⁸ solid line represents Whetkamp *et al.*'s data corrected for the surface roughness,⁹ circles denote Goldhahn's data,⁹ triangles are the SE data measured by Logothetidis *et al.*,¹⁰ squares are the data of Kawashima *et al.*¹¹ who performed the surface correction over the data of Logothetidis *et al.*,¹⁰ dotted line denotes the reflectance data of Lambrecht *et al.*,⁶ and dash-dot line are the data for the real part of the dielectric function calculated from the expression given by Brunner *et al.*³ In general, the optical functions obtained by SE are more accurate than the data obtained by KK transformation of normal incidence reflectance data. From the criterion of Aspnes and Studna¹² it is clear that the reflectance data by Lambrecht *et al.*,⁶ are clearly inferior to SE data. However, reflectivity studies can yield accurate estimates of the optical functions of GaN, as demonstrated by Shokhovets *et al.*¹³ and Goldhahn *et al.*¹⁴ Also, better quality of nitride films, leading to more accurate optical functions data, can be obtained if a low temperature buffer layer is deposited first.^{15,16} The surface abruptness of nitride films can be further improved by wet chemical treatments.¹⁷ Taking into consideration the method employed for the determination of the optical functions and the criterion of Aspnes and Studna,¹² we have chosen to determine the model parameters from the data consisting from the data of Goldhahn⁹ in the range from 1 eV to 4.5 eV and the data of Whetkamp *et al.*'s⁹ corrected for the surface roughness in the range 5.8-10 eV. We have decided to disregard

* Correspondence: ehli@eee.hku.hk; Telephone: +852 2859 7091; Fax: +852 2559 8738

Whetkamp *et al.*'s^{8,9} data below 5.8 eV since the data do not join smoothly with the data of Goldhahn⁹ and accuracy of Whetkamp *et al.*'s⁸ data below 6 eV may be lower. For detailed review of SE in the 6-35 eV range see Ref. 18.

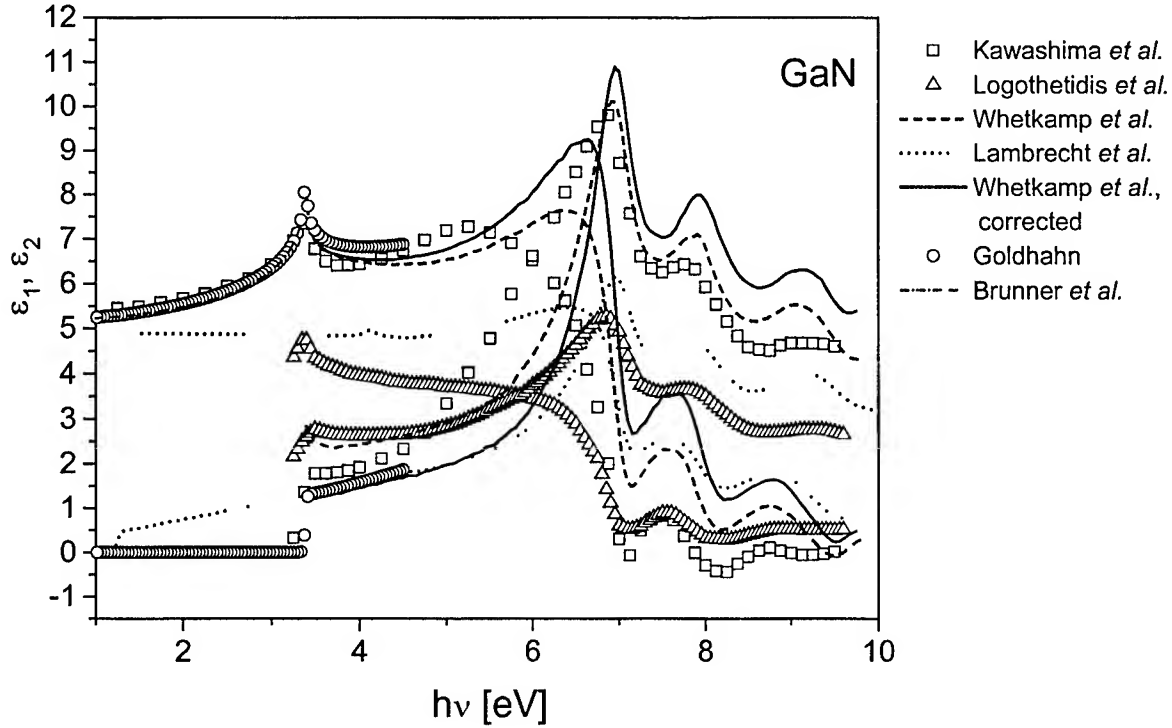


Figure 1. Dielectric function of wurtzite GaN (E.L.c) vs. energy. The dashed line denotes spectroscopic ellipsometry (SE) data by Whetkamp *et al.*,⁸ solid line represents Whetkamp *et al.*'s data corrected for the surface roughness,⁹ circles denote Goldhahn's data,⁹ triangles are the SE data measured by Logothetidis *et al.*,¹⁰ squares are the data of Kawashima *et al.*¹¹ who performed the surface correction over the data of Logothetidis *et al.*,¹⁰ dotted line denotes the reflectance data of Lambrecht *et al.*,⁶ and dash-dot line are the data for the real part of the dielectric function calculated from the expression given by Brunner *et al.*³

The paper is organized as follows. In the following section, description of the model is given. In the section 3, obtained results are compared with experimental data and discussion is given. Finally, conclusions are drawn.

2. DESCRIPTION OF THE MODEL

Standard critical points (CPs) model^{19,20} describes contributions of each critical point with the following expression

$$\varepsilon(\omega) = C - A \exp(i\phi) (\hbar\omega - E + i\Gamma)^m, \quad (1)$$

where A is the amplitude, $\hbar\omega$ is the energy, E is the energy of a CP, Γ is the broadening constant, and ϕ is the excitonic phase angle. The exponent n has different values for different types of CPs. For one dimensional (1D) CPs $m=-1/2$, for two dimensional (2D) CPs $\ln(\hbar\omega - E + i\Gamma)$ is considered, and $m=1/2$ for three-dimensional (3D) CPs. Discrete excitons with Lorentzian lineshape are represented by $m = -1$. This model provides an excellent fit to the second and third derivatives of the dielectric function.²¹ Ability for describing the derivatives of the dielectric function is necessary for modeling the electoreflectance and photoreflectance data. Also, critical point energies can be more accurately determined from fitting the derivative spectra. The standard CPs model has been frequently applied for the determination of positions of the critical points and their temperature dependence for several materials, including both cubic and hexagonal GaN.^{10,22} Brunner *et al.*³ have used standard CPs model for describing the refractive index of $\text{Al}_x\text{Ga}_{1-x}\text{N}$ below the fundamental absorption edge, by taking into account only transitions at the band gap E_0 in the form:

$$n^2(\hbar\omega, x) = \varepsilon(\hbar\omega, x) = C(x) + A(x)y^{-2} \left[2 - (1+y)^{1/2} - (1-y)^{1/2} \right], \quad (2)$$

where $C(x) = -(2.2 \pm 0.2)x + (2.66 \pm 0.12)$, $A(x) = (3.17 \pm 0.39)\sqrt{x} + (9.98 \pm 0.27)$, $y = \hbar\omega / E_g(x)$, and $E_g(x) = (6.13 \text{ eV} - 3.42 \text{ eV})x + 3.42 \text{ eV} - b x (1-x)$, where $b=1.3 \text{ eV}$. This expression is valid only below the bandgap, where $y \leq 1$. However, it can still be used for the values above the band gap, if we take into account that $\varepsilon = \varepsilon_1 + i\varepsilon_2$ is a complex value, so that

$$\varepsilon_1(\hbar\omega, x) = C(x) + A(x)y^{-2} \left[2 - (1+y)^{1/2} - (1-y)^{1/2} \Theta(1-y) \right], \quad (3)$$

and

$$\varepsilon_2(\hbar\omega, x) = A(x)y^{-2} (y-1)^{1/2} \Theta(y-1), \quad (4)$$

where

$$\Theta(x) = \begin{cases} 1, & x \geq 0 \\ 0, & x < 0 \end{cases}. \quad (5)$$

The real and imaginary parts of the index or refraction can then be calculated from the formulae:

$$n(E) = \left[0.5 \left(\varepsilon_1(E) + (\varepsilon_1^2(E) + \varepsilon_2^2(E))^{1/2} \right) \right]^{1/2}, \quad (6)$$

and

$$k(E) = \left[0.5 \left(-\varepsilon_1(E) + (\varepsilon_1^2(E) + \varepsilon_2^2(E))^{1/2} \right) \right]^{1/2}. \quad (7)$$

However, standard CPs model assumes Lorentzian broadening of the transitions. Simple Lorentzian broadening, which is frequently used, does not represent accurate approximation of the lifetime broadening effect.^{21,23-27} The Lorentzian function has wide wings, which give rise to the excessive absorption below the bandgap. It has been shown that the Gaussian lineshape yields better fits to the experimental data than the Lorentzian one in case of direct bandgap binary semiconductors.²⁵ However, if a Gaussian broadening is assumed, the dielectric function cannot be expressed in a closed analytical form. In order to overcome this problem, Kim *et al.*²¹ have replaced the damping constant Γ_i in their model with frequency dependent expression $\Gamma_i(\omega)$:

$$\Gamma_i(\omega) = \Gamma_i \exp \left[-\alpha_i \left(\frac{\hbar\omega - E_i}{\Gamma_i} \right)^2 \right], \quad (8)$$

where E_i is the critical point energy, and α_i and Γ_i are model parameters. For the model of Kim *et al.*²¹ $\alpha \approx 0.2$ approximates well the Gaussian broadening. They have investigated only two cases $\alpha = 0$ (Lorentzian broadening) and $\alpha \approx 0.2$ (Gaussian-like broadening). Better agreement with the experimental data for all the investigated materials has been achieved in the latter case. It has been shown that the room temperature dielectric function of binary compounds is approximately a linear combination of 75% Gaussian and 25% Lorentzian representations.²⁵ Since broadening is neither pure Gaussian nor pure Lorentzian, adjustable broadening concept is necessary to deal with this problem. Similar changes in the shape of the dielectric function achieved by varying α/Γ ratio²⁴ can be obtained by a convolution of Lorentzian and Gaussian lines, which can be determined analytically in a closed form²⁷ or calculated numerically.²⁶ The type of broadening is usually not known a priori. Fourier approach to the determination of the critical points energies and broadening parameters has been proposed.^{28,29} It has been found that the broadening of E_1 , $E_1 + \Delta_1$ transitions in CdTe is purely Lorentzian.²⁹ E_0 transition where inadequacy of the Lorentzian approximation in the form of extended absorption tail is

most notable was not analyzed with this method. However, the dependence of the logarithm of Fourier coefficients $\log_{10} C_n$ on the order n is not independent on the false data (or the choice of boundaries outside which false data are used) and baseline correction. Furthermore, results are dependent on the number of data points and the width of the spectral region considered. It has been shown that the accuracy of the broadening parameter Γ obtained by this method depends on how close the data are spaced in energy, and poor values can be obtained if the data spacing is larger than 0.4Γ .³⁰ Therefore, Fourier analysis method proposed by Aspnes^{28,29} can be useful for the determination of the energies of the critical points but caution is needed in deriving any conclusions about the broadening.

Another alternative to achieve adjustable broadening is to treat exponents in the standard CPs model as adjustable model parameters. The dielectric function within the parabolic approximation and for the Lorentzian representation²⁵ can be described with

$$\varepsilon(E) = \varepsilon_{\infty} + \sum_{i=1}^N C_i (E - E_i + i\Gamma_i)^{-m_i}, \quad (9)$$

where C_i is a constant, E_i is the critical point energy, Γ_i is the damping constant, ε_{∞} is the contribution of higher-lying transitions, and $m_i = 1 - d/2$ where d is the dimension of the critical point (for $d=2$, $\ln(E - E_i + i\Gamma_i)$ is considered in the standard critical points model). A modification where m_i , $i = 1, N$ are treated as adjustable parameters achieves the similar effect as introducing Gaussian lineshape.²⁵ The modified critical points (MCP) model is simple, does not require large number of parameters and can achieve excellent agreement with the experimental data. However, as in the case of adjustable broadening given with Eq. (8), parameters Γ_i cannot be directly compared with the damping constant Γ of a purely Lorentzian representation.

3. RESULTS AND DISCUSSION

Model parameters are determined using acceptance-probability-controlled simulated annealing algorithm,³¹ by minimizing the following objective function

$$F = \sum_{i=1}^N \left[\left| \frac{n(\omega_i) - n^{\text{exp}t}(\omega_i)}{n^{\text{exp}t}(\omega_i)} \right| + \left| \frac{k(\omega_i) - k^{\text{exp}t}(\omega_i)}{k^{\text{exp}t}(\omega_i)} \right| \right], \quad (10)$$

where $n(\omega_i)$, $n^{\text{exp}t}(\omega_i)$, respectively, are the calculated and the experimental values of the real part, and $k(\omega_i)$, $k^{\text{exp}t}(\omega_i)$ are the calculated and the experimental values of the imaginary part of the index of refraction at frequency ω_i .

We have compared the results of MCP model with the modified Adachi's model dielectric function with adjustable broadening (MMDF). For a detailed description of MMDF, see Ref. 24. Figure 2 shows the real and imaginary parts of the index of refraction of GaN. The inset shows the enlarged region around the absorption edge. Figure 3 shows the real and imaginary parts of the dielectric function of GaN vs. energy. The solid line represents the experimental data,⁹ dotted line denotes MMDF, dashed line denotes MCP model. The obtained relative rms errors for the real and imaginary part of the index of refraction, ρ_n and ρ_k , are: $\rho_n = 1.0\%$ and $\rho_k = 7.4\%$ for MMDF, $\rho_n = 0.6\%$ and $\rho_k = 2.0\%$ for MCP model. Obtained model parameters for MCP model are given in Table 1. It can be clearly observed that MCP model achieves better agreement with the experimental data than MMDF. However, MCP does not include directly excitonic effects, which are taken into account via change of m_i . Therefore, this model cannot be used for estimation of the exciton related parameters from the optical data. MMDF includes excitonic effects, but the estimates of exciton related parameters usually cannot be considered very reliable due to low sensitivity of the objective function to those parameters, especially over a wide spectral region.

KK consistency of the obtained results has been checked numerically, and satisfactory results have been obtained. It is advisable to check KK consistency numerically when using adjustable broadening modification.³² Also, it can be recommended to artificially set ε_2 to zero in MCP below the fundamental absorption edge E_0 after it reaches 0.001 value to avoid small oscillations which can be present. Both MMDF and MCP can also be employed for describing the first derivative of the dielectric function. In this case also MCP exhibits better agreement with the experimental data than

MMDF. This is illustrated in Figure 4, depicting the first derivative of the imaginary part of the dielectric function vs. energy. The solid line denotes experimental data, dotted line denotes MMDF, while dashed line represents MCP. For derivatives of the higher order, discrepancies between the experimental and calculated data get larger for both models. However, this does not imply that those models are not suitable for description of dielectric function derivatives. It is a logical consequence of the fact that model parameters were determined by minimizing discrepancies with the experimental dielectric function only, and not its derivatives. If one is interested in describing the derivatives of the dielectric function, both MCP and MMDF could be employed, but with different parameters obtained by minimizing an appropriate objective function.

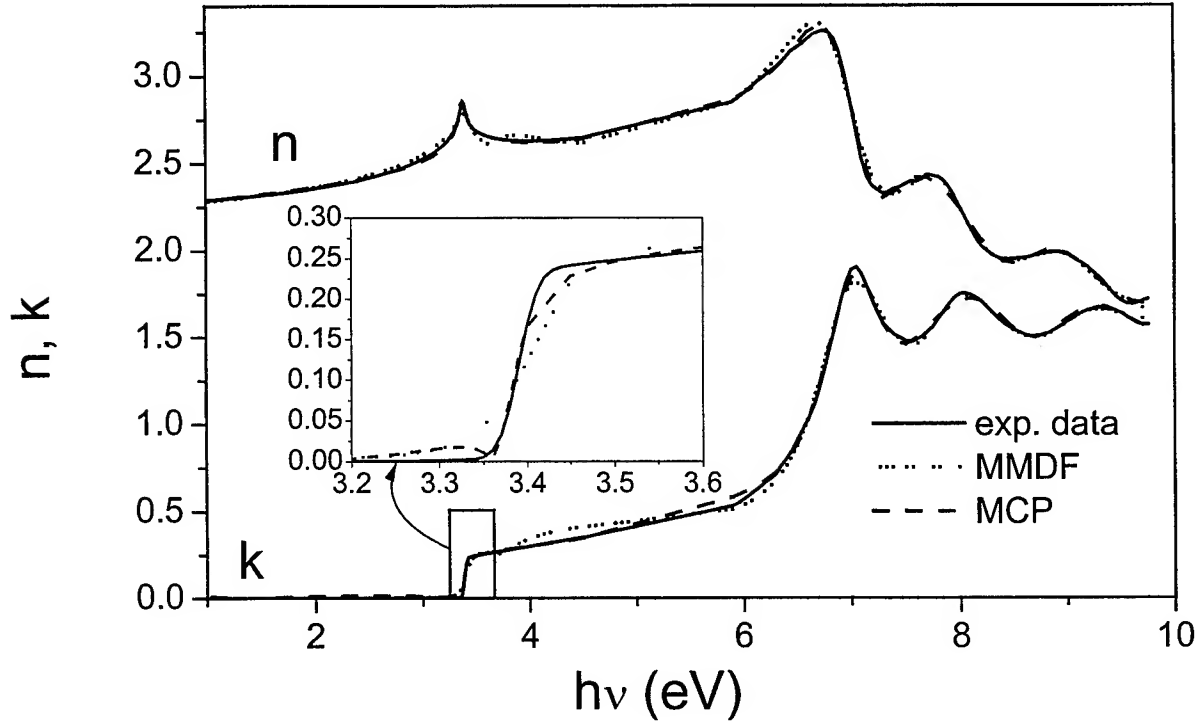


Figure 2. The real and imaginary parts of the index of refraction of GaN as a function of energy. The solid line represents the experimental data,⁹ dotted line denotes MMDF, dashed line denotes MCP model. The inset shows the enlarged region around the absorption edge.

Table 1. Obtained model parameters for MCP model. $\epsilon_{1\infty}=2.148$.

i	0	1	2	3	4
C_i	2.533	0.907	4.023	52.474	212.48
E_i (eV)	3.379	7.010	8.661	8.213	14.694
Γ_i (eV)	0.020	0.567	1.273	2.593	4.023
m_i	0.141	2.650	4.497	2.553	1.878

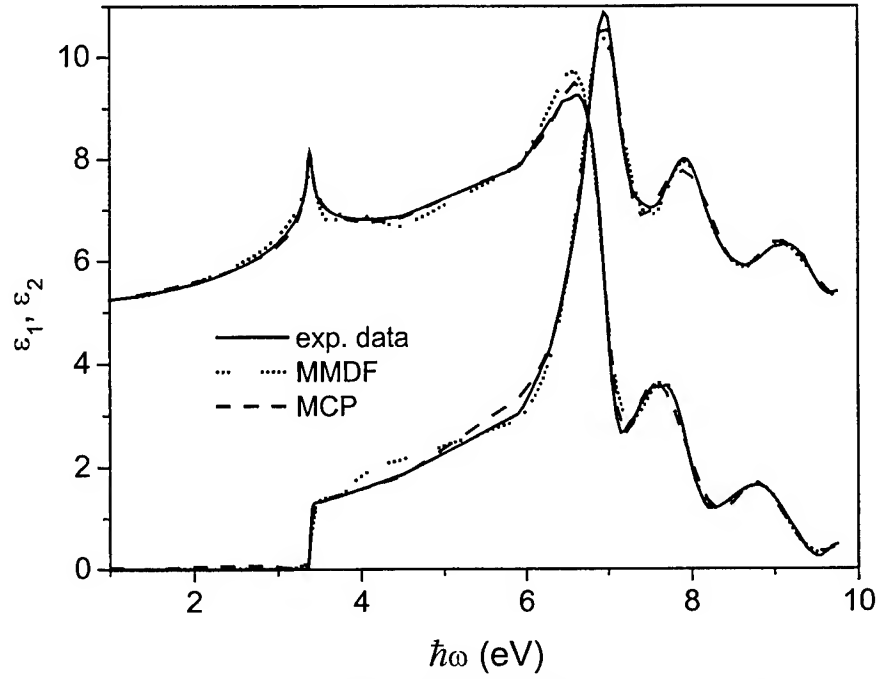


Figure 3. The real and imaginary parts of the dielectric function of GaN as a function of energy. The solid line represents the experimental data,⁹ dotted line denotes MMDF, dashed line denotes MCP model.

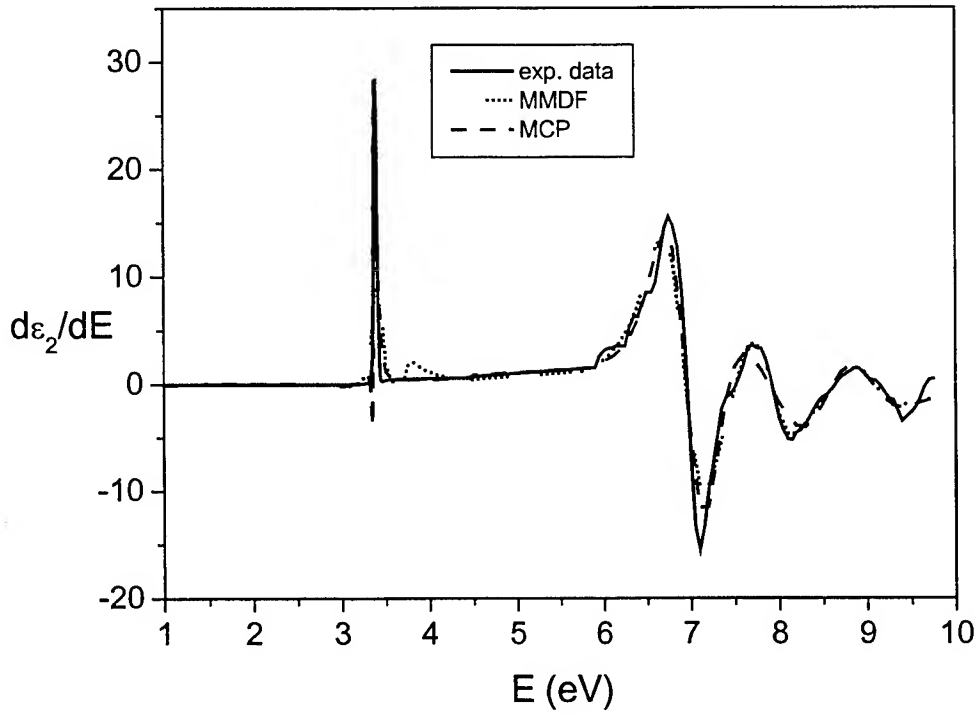


Figure 4. The first derivative of the imaginary part of the dielectric function of GaN as a function of energy. The solid line represents the experimental data,⁹ dotted line denotes MMDF, dashed line denotes MCP model.

4. CONCLUSION

We have modeled the optical functions of hexagonal GaN ($E_{\perp c}$) in the 1 - 10 eV spectral range using a modified critical points model. In the modified critical points model, exponent m in the expressions describing contributions of each critical point to the dielectric function does not have a fixed value. This enables accomplishing effects similar to those caused by changing the shape of the broadening function. Excellent agreement with the experimental data has been achieved over the entire investigated spectral range, with relative rms error equal 0.6% for the real part, and 2.0% for the imaginary part of the index of refraction. The results of the modified critical points model have also been compared to the results obtained with modified Adachi's model with adjustable broadening. It has been found that modified critical points model achieves better agreement with the experimental data, especially for the imaginary part of the index of refraction.

ACKNOWLEDGEMENTS

The authors would like to thank the RGC earmarked grant of Hong Kong and the University of Hong Kong CRCG research grant for financial support. The authors would like to thank Dr. R. Goldhahn, T. Whetkamp and Dr. N. Esser for supplying the data in electronic form.

REFERENCES

1. I. Akasaki and H. Amano, "Widegap column-III nitride semiconductors for UV/blue light emitting devices", *J. Electrochem. Soc.*, **141**, pp. 2266-2271, 1994.
2. S. Nakamura and G. Fasol, *The blue laser diode: GaN based light emitters and lasers*, Springer, Berlin, 1997.
3. D. Brunner, H. Angerer, E. Bustarret, F. Freudenberg, R. Höpler, R. Dimitrov, O. Ambacher, and M. Stutzmann, "Optical constants of epitaxial AlGaIn films and their temperature dependence", *J. Appl. Phys.*, **82**, pp. 5090-5096, 1997.
4. Z. Yang and Z. Xu, "A theoretical study of electronic and optical properties of wurtzite GaN", *J. Phys. C: Condensed Matter*, **8**, pp. 8303-8308, 1996.
5. Z. Yang and Z. Xu, "Electronic and optical properties of unstrained and strained wurtzite GaN", *Phys. Rev. B*, **54**, pp. 17577-17584, 1996.
6. W. R. L. Lambrecht, B. Segall, J. Rife, W. R. Hunter and D. K. Wickenden, "UV reflectivity of GaN: theory and experiment", *Phys. Rev. B*, **51**, pp. 13516-13532, 1995.
7. J. L. P. Hughes, J. Wang, and J. Sipe, "Calculation of linear and second-order optical response in wurtzite GaN and AlN", *Phys. Rev. B*, **55**, pp. 13630-13640, 1997.
8. T. Whetkamp, K. Wilmers, N. Esser, W. Richter, O. Ambacher, H. Angerer, G. Jungk, R. L. Johnson and M. Cardona, "Spectroscopic ellipsometry measurements of $\text{Al}_x\text{Ga}_{1-x}\text{N}$ in the energy range 3-25 eV", *Thin Solid Films* **313-314**, pp. 745-750, 1998.
9. R. Goldhahn, private communication.
10. S. Logothetidis, J. Petalas, M. Cardona and T. D. Moustakas, "Optical properties and temperature dependence of the interband transitions of cubic and hexagonal GaN", *Phys. Rev. B*, **50**, pp. 18017-18029, 1994.
11. T. Kawashima, H. Yoshikawa, S. Adachi, S. Fuke and H. Ohtsuka, "Optical properties of hexagonal GaN", *J. Appl. Phys.*, **82**, pp. 3528-3535, 1997.
12. D. E. Aspnes and A. A. Studna, "Dielectric function and optical parameters of Si, Ge, GaP, GaAs, GaSb, InP, InAs, and InSb from 1.5 to 6.0 eV", *Phys. Rev. B*, **27**, pp. 985-1009, 1983.
13. S. Shokhovets, R. Goldhahn, G. Gobsch, T. S. Cheng, C. T. Foxon, G. D. Kipshidze, and W. Richter, "Reflectivity investigations as a method for characterizing group III nitride films", *J. Appl. Phys.*, **86**, pp. 2602-2610, 1999.
14. R. Goldhahn, S. Shokhovets, J. Scheiner, G. Gobsch, T. S. Cheng, C. T. Foxon, U. Kaiser, G. D. Kipshidze, and W. Richter, "Determination of group III nitride film properties by reflectance and spectroscopic ellipsometry studies", to be published.
15. T. Takeuchi, H. Takeuchi, S. Sota, H. Sakai, H. Amano, and I. Akasaki, "Optical properties of strained AlGaIn and GaInN on GaN", *Jpn. J. Appl. Phys. Part 2*, **36**, pp. L177-L179, 1997.
16. J. N. Kuznia, M. Asif Khan, D. T. Olson, R. Kaplan, and J. Freitas, "Influence of buffer layers on the deposition of high quality single crystal GaN over sapphire substrates", *J. Appl. Phys.*, **73**, pp. 4700-4702, 1993.

17. N. V. Edwards, M. D. Bremser, T. W. Weeks, Jr., R. S. Kern, R. F. Davis, and D. E. Aspnes, "Real-time assessment of overlayer removal on GaN, AlN, and AlGaIn surfaces using spectroscopic ellipsometry", *Appl. Phys. Lett.*, **69**, pp. 2065-2067, 1996.
18. J. Barth, R. L. Johnson and M. Cardona, "Spectroscopic ellipsometry in 6-35 eV region", *Handbook of Optical Constants of Solids II*, pp. 213-246, Academic Press Inc., San Diego, 1991.
19. M. Cardona, *Modulation spectroscopy*, pp. 15-23, Academic Press, New York, 1969.
20. P. Y. Yu and M. Cardona, *Fundamentals of semiconductors*, Springer, Berlin, 1998.
21. C. C. Kim, J. W. Garland, and P. M. Raccach, "Modeling the optical dielectric function of semiconductors: extension of the critical-point parabolic-band approximation", *Phys. Rev. B*, **45**, pp. 11749-11767, 1992.
22. J. Petalas, S. Logothetidis, S. Bouladakis, M. Alouani, and J. M. Wills, "Optical and electronic-structure study of cubic and hexagonal GaN thin films", *Phys. Rev. B*, **52**, pp. 8082-8091, 1995.
23. A. D. Rakić and M.L. Majewski, "Modeling the optical dielectric function of GaAs and AlAs: extension of Adachi's model", *J. Appl. Phys.*, **80**, pp. 5909-5914, 1996.
24. A. B. Djurišić and E. H. Li, "Modeling the optical constants of hexagonal GaN, InN and AlN", *J. Appl. Phys.*, **85**, pp. 2848-2853, 1999.
25. J. W. Garland, H. Abad, M. Viccaro, and P. M. Raccach, "Lineshape of optical dielectric function", *Appl. Phys. Lett.*, **52**, 1176-1178, 1988.
26. A. Franke, A. Stendal, O. Stenzel and C. Von Borczyskowski, "Gaussian quadrature approach to the calculation of the optical constants in the vicinity of inhomogeneously broadened absorption lines", *Pure Appl. Opt.*, **5**, pp. 845-853, 1996.
27. R. Brandel and D. Boreman, "An infrared dielectric function model for amorphous solids", *J. Appl. Phys.*, **71**, pp. 1-6, 1992.
28. D. E. Aspnes, "The analysis of optical spectra by Fourier methods", *Surface Science*, **135**, pp. 284-306, 1983.
29. D. E. Aspnes, "Fourier critical point analysis: extension to Gaussian lineshapes", *Solar Energy Materials and Solar Cells*, **32**, pp. 413-419, (1994).
30. J. W. Garland, C. Kim, H. Abad, and P. M. Raccach, "Determination of accurate critical point energies and linewidths from optical data", *Phys. Rev. B*, **41**, pp. 7602-7610, 1990.
31. A. B. Djurišić, A. D. Rakić, and J.M. Elazar, "Modeling the optical constants of solids using acceptance-probability-controlled simulated annealing with adaptive move generation procedure", *Phys. Rev. E*, **55**, pp. 4797-4803, 1997.
32. M. Schubert, J. A. Woollam, G. Leibiger, B. Rheinländer, I. Pietzonka, T. Saß, and V. Gottschalch, "Isotropic dielectric functions of highly disordered $\text{Al}_x\text{Ga}_{1-x}\text{InP}$ ($0 \leq x \leq 1$) lattice matched to GaAs", *J. Appl. Phys.*, **86**, pp. 2025-2033, 1999.

SESSION 3

GaN LED and Materials III

Effects of indium surfactant on optical and structural properties of MBE grown GaN

W.K. Fong, C.F. Zhu, C. Surya, B.H. Leung, and C.C. Cheng
Department of Electronic and Information Engineering
The Hong Kong Polytechnic University
Hong Kong

B. Sundaravel, E.Z. Luo, J.B. Xu and I.H. Wilson
Department of Electronic Engineering and
Materials Technology Research Center
The Chinese University of Hong Kong
Hong Kong

ABSTRACT

A small indium flux was used as a surfactant during the growth of gallium nitride films by rf-plasma assisted molecular beam epitaxy. The effects of the indium surfactant on the optical and structural properties of undoped GaN were studied by photoluminescence spectroscopy, high-resolution X-ray diffraction, atomic force microscopy, Rutherford backscattering spectroscopy, and low-frequency noise. Photoluminescence spectra show that GaN thin films grown in the presence of In surfactant exhibit suppressed yellow luminescence compared to films grown under the same experimental conditions but without In surfactant. The X-ray rocking curves demonstrate a 20% decrease in the full width at half maximum value for the films grown with In surfactant. AFM studies show that the root mean squared roughness for films grown with and without In surfactant are 5.86 and 6.99 nm respectively, indicating significant improvement in surface morphology. RBS and ion channeling shows the presence of stacking faults and dislocations in GaN grown with In surfactant and stacking faults in GaN grown without In. For the characterization of defect properties in the films we conducted detailed studies of $1/f$ and Generation-Recombination (G-R) noise on our samples. About 65% reduction in the Hooge parameter was observed in the film grown with In surfactant, indicative of a corresponding reduction in defect states within the material. For $f > 500$ Hz, G-R noise was the dominating fluctuation process. Detailed characterization of the G-R noise over a wide range of temperatures enabled the determination of the energy levels of the traps responsible for the G-R noise. Three different trap levels were observed using noise measurement technique. For films grown without In surfactant, traps with activation energies 806 meV, 241 meV and 100 meV were observed, whereas for samples grown with In surfactant traps were observed at 666 meV, 208 meV and 90 meV. Such systematic reduction in the energy levels of the traps may arise from the relaxation of strains in the material when grown under the application of In surfactant.

1. INTRODUCTION

Recently, III-V nitrides have been under intense research because of their important applications in optoelectronic and electronic devices such as blue light emitting diodes[1], blue laser diodes, UV photodetectors and high temperature and high power devices. The lack of GaN substrates remains to be the biggest technological hurdle for the growth of high quality GaN epitaxial layers. Presently, sapphire is the most frequently used substrate for GaN epitaxial growth due to its low price, availability of large-area wafers with good crystallinity and stability at high temperatures. The lattice mismatch between GaN and sapphire is about 14%. Such huge mismatch in the lattice constants results in poor crystal quality if GaN films were to be grown directly on the sapphire. Typically, GaN thin films exhibit wide X-ray rocking curve, rough surface morphology, high intrinsic electron concentration and significant yellow luminescence. A buffer layer is typically used for improving the crystal quality of the epitaxial films. The role of the buffer layer has been studied extensively. It was found that the AlN or GaN buffer layer serves to enhance two-dimensional growth and the density of nucleation for the epitaxial films. This is because the interfacial energy for the GaN/buffer system is found to be significantly lower than the GaN/sapphire system.

It is known for a long time that the structural quality of the epitaxial films plays a crucial role in determining the optoelectronic properties of the material. One of the most undesirable characteristics in the luminescence of GaN films is the yellow luminescence peaking at around 2.2 – 2.3 eV. This is a universal feature in both doped and undoped GaN epilayers grown by various techniques such as molecular beam epitaxy (MBE)[2], and metalorganic chemical vapor phase epitaxy (MOVPE)[3]. A number of possible origins have been postulated to account for the observed yellow luminescence, including Ga vacancy (V_{Ga}), or complexes involving V_{Ga} and a carbon impurity occupying the nitrogen site, or extended defects like dislocations and grain boundaries. In general, V_{Ga} is commonly accepted as the candidate for such deep-levels. However, the physical processes underlying the phenomenon remain unknown. The presence of mixed cubic and wurtzite phases, due to stacking faults, is also one of the major factors affecting the crystal quality. Lin *et al.* has shown that the mixed cubic and wurtzite phases may partly be responsible for the yellow luminescence[4]. It has long been known that growth conditions such as buffer layer quality, nitridation time, growth temperature, and III/V ratio have significant effects on the structural and optical properties. Previous studies also showed that yellow luminescence intensity is quite inhomogeneous over the entire film. Cathodoluminescence performed on undoped GaN hexagonal crystallites showed that while the band edge emission originates in the bulk of the GaN hexagonal crystallites, the yellow luminescence, on the other hand, is associated with the crystalline boundary and appeared to correlate with the presence of defects in the material[5]. Since the yellow luminescence significantly affects the operation of the device in the visible regime, it is important to determine the growth conditions to minimize the phenomenon.

It has been shown that the III/V ratio plays a critical role in governing the defect density as well as the electronic and optical properties of the film. Recent studies on the application of arsenic surfactant during the growth of GaN thin films resulted in improvements of the structural and optical properties in cubic GaN[6]. Theoretical calculations showed that the surface energy of (001) GaN surface is lowered when covered by As dimers. It is suggested that the surfactant lowers the energy barrier for the horizontal motion of Ga atoms, resulting in improved two-dimensional growth of the films. However, calculations showed that the lowering in the surface energy resulting from the application of As surfactant for wurtzite phase is expected to be small. The use of In as a surfactant in place of As has been investigated by Widmann *et al.*[7] It is an attractive alternative because In has low solubility in GaN at typical growth temperatures for GaN thin films, due to the low sticking coefficient for In at such temperatures. As discussed in later sections, all our experimental results on photoluminescence and high resolution X-ray diffraction pattern show that there is no incorporation of In in our material. In addition, In is an important component for the growth of blue LEDs and lasers. Thus, no foreign material needs to be added to the growth chamber. Experiment by Widmann *et al.*[7] showed that In surfactant led to improvements in the surface morphology of GaN thin films grown by MBE as indicated by the observed oscillations in the reflective high electron energy diffraction (RHEED) intensity. When In surfactant was used, the RHEED oscillation was found to be more intense, indicative of improved surface morphology under the presence of In surfactant during film growth. It was also shown that in the absence of In surfactant, films grown under the N-rich condition resulted in the formation of dislocations. However, in the presence of In surfactant, films grown under N-rich condition did not exhibit the formation of dislocations and showed resemblance of those grown under Ga-rich condition. The results indicated that the technique improves two-dimensional growth of GaN. Moreover, transmission electron microscopy analysis performed in different regions of the samples grown with and without In surfactant revealed significant differences in the structural properties depending on the N/Ga ratio as well as on the presence of In during the growth. It was demonstrated by Widmann *et al.*[7] that growth of GaN films under N-rich condition results in dislocations that are tilted with respect to the growth direction. However, samples grown with the application of In surfactant do not demonstrate the presence of inclined dislocations and the material, as a whole, is quite similar to typical samples grown under the Ga-rich condition. In this paper, we report a systematic study on the effects of indium surfactant on the optical and structural properties of undoped GaN epilayer grown by plasma-assisted MBE. The films were examined by photoluminescence (PL) spectroscopy, high-resolution X-ray diffraction (HRXRD), atomic force microscopy (AFM), Rutherford backscattering spectrometry (RBS) and low-frequency noise. In particular, detailed characterization of the low-frequency noise properties was performed to determine the exact energy levels of the traps present in the material. The work provides a basis for further elucidation of the effects of indium surfactant on the optical and structural properties of GaN films.

2. EXPERIMENT AND RESULTS

The undoped GaN epilayers were grown on single side polished (0001) sapphire substrates by an SVTA BLT-N35 MBE system. The backsides of the substrates were coated with molybdenum to improve the effectiveness of radiation heating. The substrates were cleaned by organic solvents, followed by etching in hot $H_2SO_4:H_3PO_4 = 3:1$ solution and rinsing in

deionized water. The sapphire substrates were then placed in the preparation chamber for outgassing at 850°C for 30 minutes. The substrates were then transferred to the growth chamber and were maintained at 550°C while being exposed to plasma activated nitrogen for the nitridation. It was shown that this process changes the surface layer of the sapphire substrate to AlN. Subsequently, 200 Å of a low-temperature GaN buffer layer was deposited at around 450°C. The substrate temperature was then raised to 770°C for the growth of the epilayer. High purity metallic Ga and In were evaporated by EPI SUMO cells and N₂ gas was excited by an EPI UNI-Bulb nitrogen plasma source. The In flux was kept at about 1/10 that of the Ga flux. Sample A was grown with a small In flux while sample B was grown in exactly the same experimental conditions except that no In surfactant was used. The typical growth rate was 0.9 µm/hr and the final thickness of the epilayers were about 2 - 3 µm.

Room temperature PL measurements were done using a 10 mW HeCd laser as the excitation source. The luminescence was dispersed in a 1/8 m spectrometer and detected by a photomultiplier tube. The results of the PL are shown in Fig. 1. Both samples exhibit strong band edge emission at 3.40 eV with a 57.5 meV full width at half maximum (FWHM). Yellow luminescence is observed in both samples. However, sample A exhibits significant reduction in yellow luminescence compared to sample B.

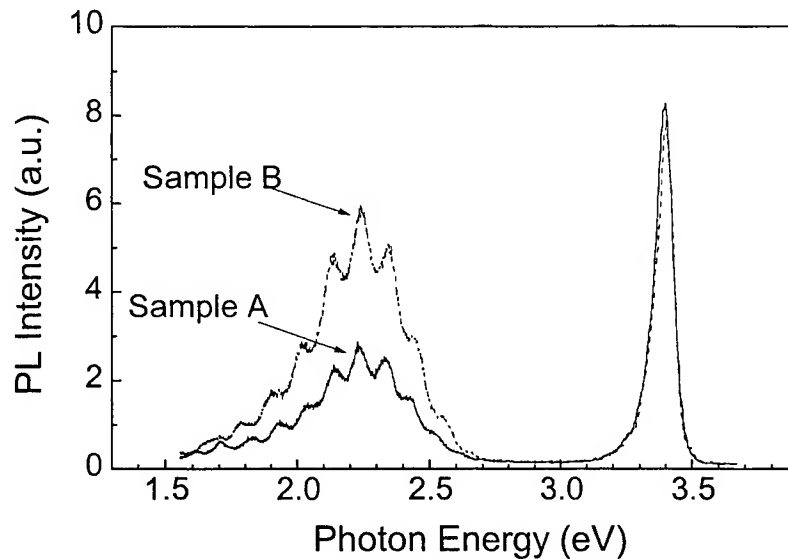


Fig. 1: Photoluminescence of samples A and B, which are grown with and without indium surfactant respectively.

Atomic force microscopy observations were made in air at room temperature using a Digital Instruments Nanoscope III. Large field 125 µm × 125µm piezo heads were used with standard Si₃N₄ cantilevers. The images were acquired using constant force mode with the force set at 10 nN. The root mean squared roughness for films grown with and without In surfactant are 5.86 and 6.99 nm respectively, indicating significant improvement in the surface morphology.

The crystallinity of the films was studied by examining the high-resolution X-ray diffraction pattern and RBS. The HRXRD experiment was carried out with CuK_{α1} line radiation (1.54056 Å), monochromated by a four-crystal Bartels monochromator. The results of the GaN (0002) X-ray rocking curve are shown in Fig. 2, which showed a FWHM of 24.06 and 26.64 arcmin for samples A and B respectively. RBS and ion channeling studies were conducted to evaluate the crystallinity and to study the presence of mixed cubic and hexagonal phases in GaN thin films. The RBS and ion channeling measurements were performed with 2 to 4.2 MeV He⁺⁺ beam from a 2 MV tandem accelerator at the Chinese University of Hong Kong. The ion beam size was 1 mm in diameter with a divergence of 0.05°. A surface barrier detector with a resolution of 15 keV was used at a scattering angle of 170°. The results for RBS experiment are shown in Fig. 3, which

indicate a χ_{\min} of 2.06% and 2.16% for samples A and B respectively. Ion channeling experiments were done at tilt angles 35.26° and 43.22°. The results are shown in Fig. 4a and 4b respectively for samples A and B.

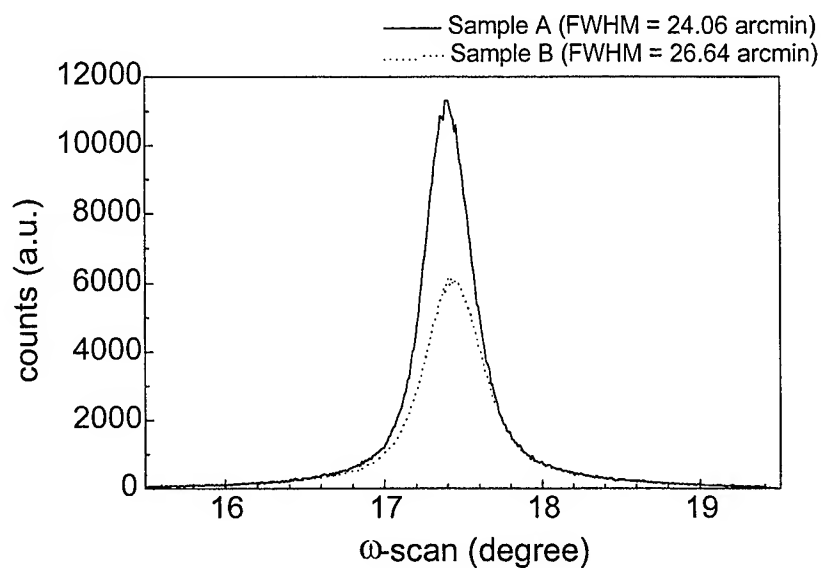


Fig. 2: Rocking curves of GaN (0002) for samples A and B.

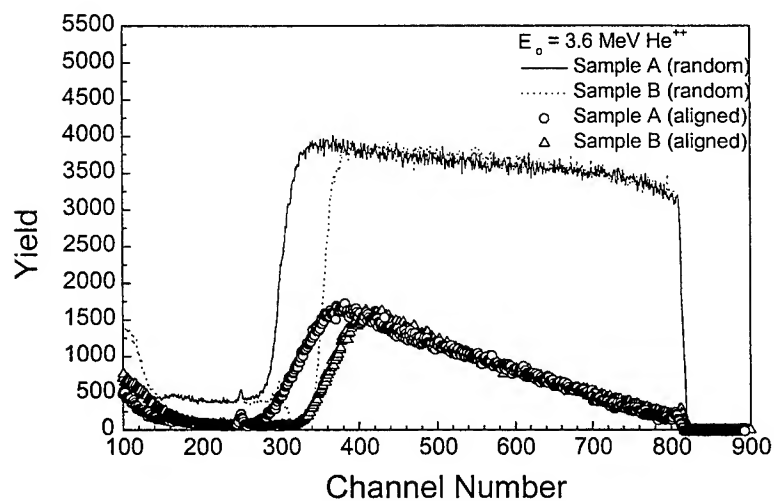


Fig. 3: RBS and ion channeling spectra of GaN taken with 3.6 MeV He^{++} beam incident along [0001] direction and at a random direction.

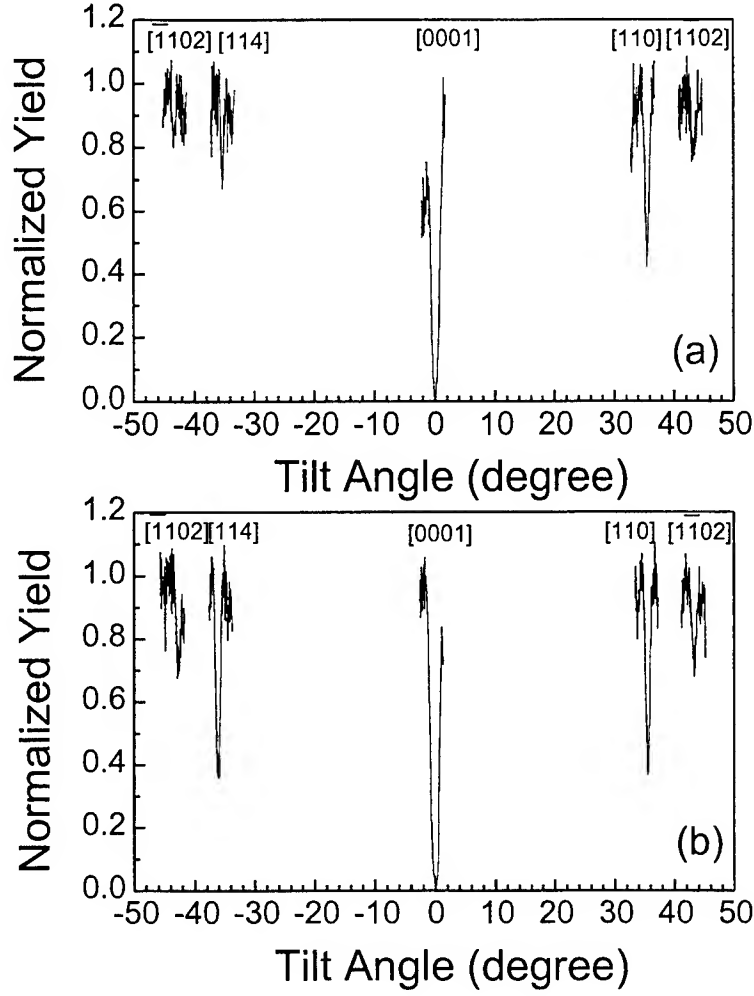


Fig. 4: Tilt angular scans of GaN with 2 MeV He^{++} beam in the $\{11\bar{2}0\}$ plane of GaN grown (a) with In surfactant and (b) without In surfactant.

Defects in the crystal can be identified from RBS and ion channeling measurements[8]. If the defect density is small, the probability of dechanneling per unit depth dP/dz is equal to $d\chi_D/dz$ where χ_D is the χ_{\min} of the crystal with defects[9]. By measuring the energy dependence of dP/dz , we can identify the type of defects[8]. The experimental data are shown in Fig. 5 below. The results show that for sample A, dP/dz varies as $E^{0.2689}$, whereas for sample B, dP/dz varies as E^0 indicating the application of In surfactant has led to significant difference in the microstructure of the films.

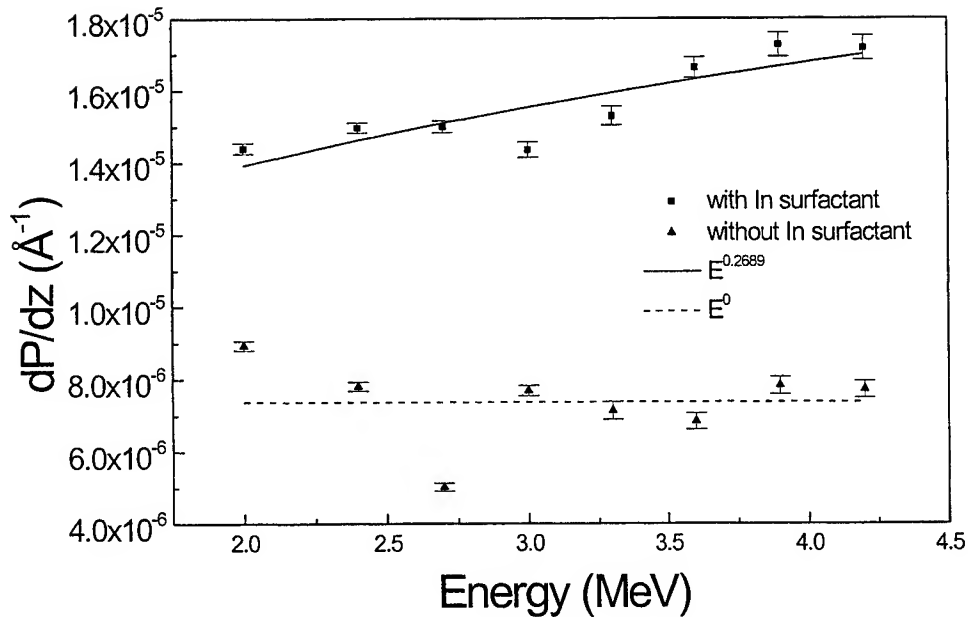


Fig.5: Energy dependence of dechanneling probability (dP/dz) in the depth interval of 100 to 500 nm in GaN grown with and without In surfactants.

Low-frequency noise was investigated over a wide range of temperatures. The experimental setup is shown in Fig. 6 below. First the device under test (DUT) was placed inside a continuous flow cryostat, which can be cooled down to 77 K using liquid nitrogen as cryogen. The temperature of the device was controlled by a Lakeshore 91C temperature controller, which used battery powered current sources for the biasing of the silicon diode temperature sensors to eliminate the 50-cycle ripples associated with the dc biasing current source from the 91C temperature controller. Also, an all-passive RLC filter was used to filter the Lakeshore 91C current supply to the heater. The temperature controller is capable of stabilizing the device temperature to within 15 mK. To further minimize the extraneous noise, the cryostat, the all-passive biasing circuit, and the battery powered PAR 113 low-noise preamplifier were all placed inside a shielded room. The biasing current supplied to the device can be adjusted using a ten-turn potentiometer. To attain the ac open-circuit condition of a current source, the potentiometer is connected to the sample through a large metal-film resistor, of value typically at least 30 times or more larger than the ac conductance of the sample. In this way, the finite output resistance of the non-ideal current source contributes no more than 0.1% error to the measured voltage noise spectral density. The amplified voltage noise is then coupled to an HP3561A dynamic signal analyzer for the measurement of noise power spectral density.

To examine the low-frequency noise of GaN thin films, cross-bridge resistive structures were fabricated by reactive ion etching. This structure facilitates the characterization of I-V properties of the sample, accurate characterization of the Hall mobility and four-probe measurement of low-frequency noise over the entire temperature range of our experiment. Ohmic contact was achieved by sputter deposition of a Ti/Al bilayer. The contact resistance was characterized by a linear configuration of rectangular pads utilizing the transmission line model and was found to be less than $10^{-4} \Omega\text{cm}^2$. The I-V characteristics of the samples were done over the entire temperature range from 80K to 400K. The experimental results exhibit well behaved I-V properties for the samples over the entire range of temperature at which the noise was investigated indicative of high quality contacts with relatively low potential barriers.

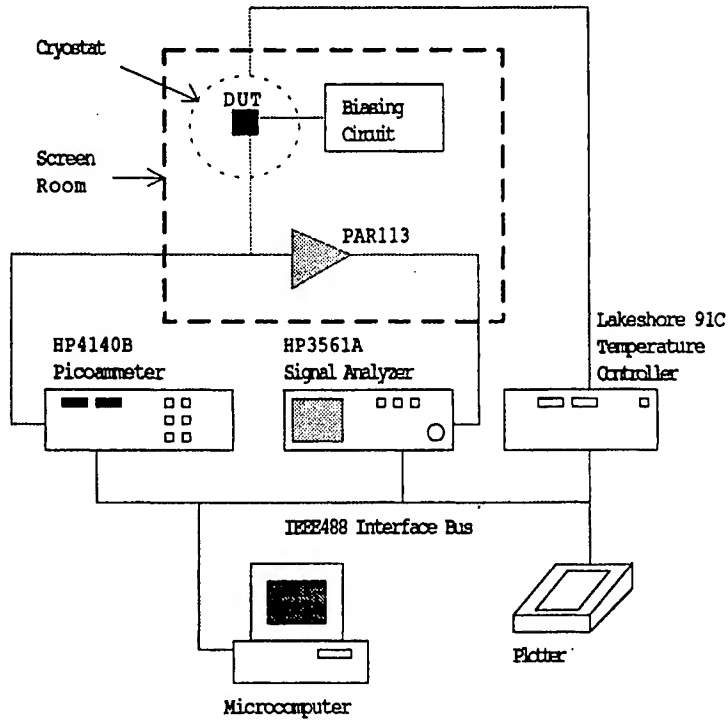


Fig. 6: Experimental setup for low-frequency noise measurement

To examine the effects of In surfactant on the defect properties of GaN films, we systematically measured the low-frequency noise spectra of the samples from 80K to 450K over the frequency range from 30 Hz to 100 kHz. At high frequencies, the noise is dominated by Generation-Recombination (G-R) processes. Typical results are shown in Fig. 7(a) and (b).

From the data we observed that as the device temperature increased from 80 K to 400 K, the voltage noise power spectra indicated the presence of a superposition of $1/f$ noise and three distinct G-R noise processes characterized by Lorentzians. The cut-off frequencies, f_0 , of the associated Lorentzians are found to be strongly temperature dependent, and decrease with decreasing temperature. For frequencies below 500 Hz, the noise is dominated by $1/f$ fluctuations. We measured the voltage noise power spectra from both samples A and B. The results are shown in Fig. 8, from which we observe that flicker noise measured from sample A is substantially lower than that measured from sample B.

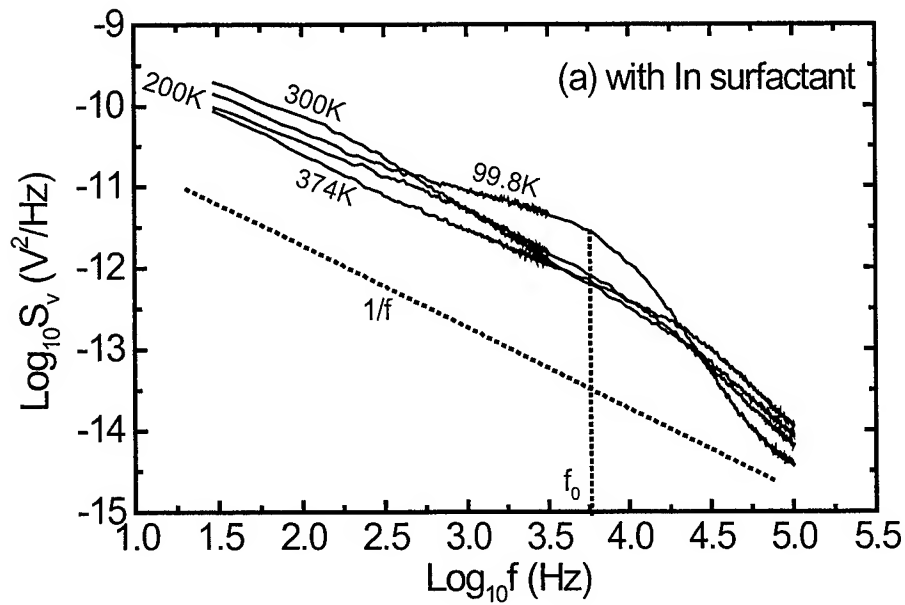


Fig. 7(a): Low-frequency voltage noise power spectra measured from a sample grown with the application of In surfactant

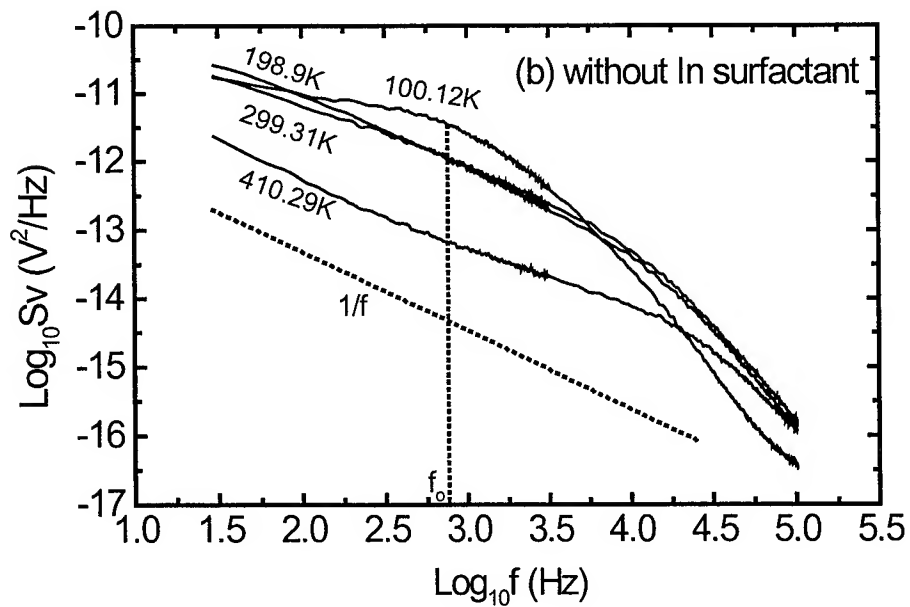


Fig. 7(b): Low-frequency voltage noise power spectra measured from a sample grown without the application of In surfactant.

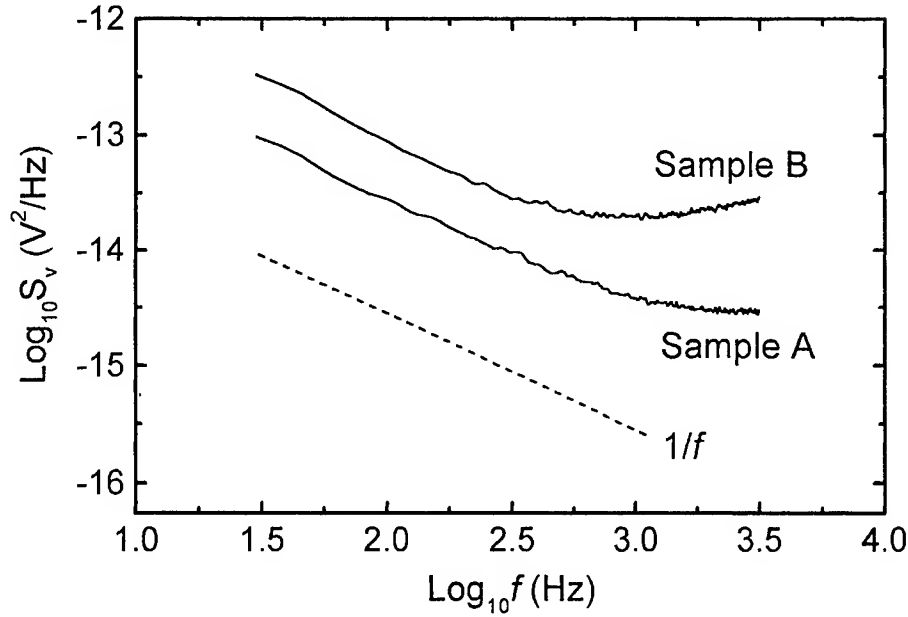


Fig. 8: Comparison of the level of flicker noise for a sample grown with the application of In surfactant (sample A) and one grown without the application of In surfactant (sample B).

3. DISCUSSIONS

Previous studies of yellow luminescence suggest that it may originate either from defects or impurities. A number of defects have been studied in detail for their roles in the observed yellow luminescence including gallium vacancy (V_{Ga}) and its related complexes[10], nitrogen antisite (N_{Ga})[11] and native point defects that nucleate at the dislocation sites[12]. Gallium vacancy is widely accepted as the source of yellow luminescence in undoped and n-doped GaN, for the reason that yellow luminescence is rarely observed in Mg-doped GaN because Mg may occupy the Ga vacancies and reduce the formation of nitrogen antisites[13]. Cathodoluminescence studies have shown that the yellow luminescence intensity is enhanced when increasing the probing depth towards the film-substrate interface[14]. The enhanced yellow luminescence intensity can be attributed to the high density of native defects near the interface rather than impurities. Similar observation is found by PL with the excitation source illuminated from the sapphire substrate side[15]. These results provide strong support for defect origin of yellow luminescence.

Our PL results demonstrate that the use of In surfactant during growth can reduce the formation of deep-level defects in undoped GaN responsible for the observed yellow luminescence. Typical room temperature PL spectra of GaN grown with (solid curve, sample A) and without (dotted curve, sample B) In surfactant are shown in Fig. 1. Sample A exhibits a small improvement in band edge transitions, at 3.40 eV, over sample B. A broad yellow luminescence centering at ~2.2 eV is observed for both samples. The yellow luminescence is modulated by the Fabry-Pérot interference fringes. This microcavity effect is formed by GaN-air interface and GaN-substrate interface[16], which shows that the samples have smooth surface. AFM studies showed that the root mean squared surface roughness for samples A and B are 5.86 and 6.99 nm respectively indicating significant improvement in the surface morphology due to the use of an In surfactant. This is attributed to the enhanced two-dimensional growth when an In surfactant is used during growth. The studies of the effects of As surfactant on the growth of cubic GaN have provided much light on the physical processes that underly the growth of GaN[17]. It is well known that in N-terminated surface, the high concentration of N dangling bonds can reduce Ga atom surface lifetime, as the Ga atoms are captured before they can go to the proper lattice sites leading to crystalline defects. The surface energy of the cubic phase GaN surface is lowered when covered by a monolayer of As atoms. The lowering in the surface energy can promote two-dimensional diffusion of Ga atoms especially in a nitrogen-terminated surface[18]. Our results show that In is a suitable candidate as a surfactant in MBE growth of wurtzite GaN and is beneficial to the lowering of yellow luminescence related defects, the enhancement of 2-D growth and the improvement of surface morphology of GaN.

To further investigate the improvement in crystallinity due to the use of In surfactant, high resolution X-ray diffraction measurement and RBS spectra have been done. Figure 2 shows the X-ray rocking curves of GaN (0002). The full width at half maximum (FWHM) values of sample A and sample B are 21.06 and 26.64 arcmin, respectively. The reduction in the FWHM of the rocking curve in sample A is indicative of the improvement in the crystallinity due to the application of In surfactant. It is noteworthy that InGa₂N is not seen in the θ - 2θ scan showing that In is not incorporated in the film. Figure 3 shows the RBS spectra of samples A and B with 3.6 MeV He⁺⁺ beam incident in a random direction and aligned along [0001] direction of GaN. The thickness of films measured from the Ga signals in the random spectra are 2.34 μ m for sample A and 2.12 μ m for sample B, which is quite consistent with our measurements using an Alpha-step 500 profilometer. The backscattering signal from In is expected around the channel number 905 and its absence in the spectra clearly shows that no In incorporation is found in the films. The ratio of the yield near the film surface in an aligned spectrum to the yield in the random direction spectrum is defined as χ_{\min} which is a measure of crystal quality in that particular aligned direction. The $\chi_{\min}^{(0001)}$ values along [0001] direction calculated from spectra taken at 2 MeV (not shown) for samples A and B are 2.06% and 2.16%, respectively. This shows excellent crystallinity with no significant difference between samples A and B in the [0001] direction.

Off-normal ion channeling was done at tilt angles of 35.26° and 43.22° in the $\{1\bar{1}20\}$ plane of GaN, which correspond to the [110] or [114] axis of the cubic phase of GaN and the $[1\bar{1}02]$ axis of the hexagonal phase, respectively. In a previous publication[19], we have identified the presence of mixed cubic and hexagonal phase of GaN by off-normal ion channeling. It was reported that the cubic structure existed in twins of ABCABC and CBACBA packing sequences due to the presence of stacking faults. Figure 4 shows the tilted angular scans in the $\{1\bar{1}20\}$ plane of GaN. The $\chi_{\min}^{[1\bar{1}02]}$ for the $[1\bar{1}02]$ axis is 0.8 and 0.7 respectively for samples A and B. These values are larger than previously reported value of 0.3. This can be attributed to the presence of mixed cubic and wurtzite phases as the dips are observed at 35.26° with respect to the [0001] direction axis. But in the photoluminescence we observed only one peak at 3.4 eV corresponding to hcp phase. The off normal axial channeling dips around 35.26° could be due to stacking faults present in the samples. Albrecht *et al.*[20] has recently observed the GaN samples that contain a high concentration of stacking faults exhibit a luminescence line at 364 nm (3.4 eV). Stampfl *et al.*[21] has also shown theoretically that stacking faults can give rise to quantum-well-like regions of zincblende material embedded in the wurtzite lattice that can bind excitons and give rise to luminescence. As the band edge emission of wurtzite phase at room temperature is also at 3.4 eV, the contribution by the presence of stacking faults cannot be resolved in PL spectrum at room temperature.

The study of the energy dependence of dP/dz can be used to identify the type of defects in the material. $E^{1/2}$ dependence corresponds to dislocations, E^0 dependence corresponds to stacking faults and $E^{-1/2}$ dependence corresponds to interstitials present in the sample[8]. Figure 5 shows the variation of dP/dz in the depth interval 100 to 500 nm in GaN grown with and without In surfactant for the incident He⁺⁺ beam energies from 2 to 4.2 MeV aligned along GaN[0001]. In sample A, there is an energy dependence of $E^{0.27}$, which corresponds to the presence of dislocations and stacking faults. In sample B, there is no obvious energy dependence and it shows the presence of stacking faults.

In figure 4, we can see that dips around 35.26° are asymmetric in sample A and symmetric for sample B. Symmetric dips stipulates the presence of stacking faults with two equivalent stacking sequences ABCBCB... or ABACAC... in equal proportions with the lowest stacking fault energy which are growth related. If inverse domains are present in the GaN layer then the presence of only one of the above stacking sequences can give rise to symmetric dips. The asymmetric dips in sample A can be due to the absence of inverse domains. The number density of stacking faults in sample A must be smaller than sample B. For the same defect density, $\chi_{\min}^{[110]}$ along [110] direction is expected to be smaller in sample A than that of sample B. The $\chi_{\min}^{[1\bar{1}02]}$ of sample A along $[1\bar{1}02]$ should be lower than that of sample B. The observed value is comparable to sample B and this could be due to dechanneling by dislocations, which is confirmed from Fig.5. The energy dependence of dechanneling probability along the normal axial direction and the dips around 35.26° in the off-normal axial scans show that there are defects in the GaN film grown with In surfactant. However, the use of In surfactant gives rise to a smooth surface during nucleation and the GaN epilayer should have low density of defects. This implies that there is a critical thickness beyond which epilayers grown in the presence of In surfactant will exhibit substantial increase in defect density and the film thickness of 2.34 μ m is larger than the critical thickness.

Low-frequency noise is an important figure-of-merit for electronic and optoelectronic devices. It represents the smallest signal a device can manipulate. Thus, reduction of the intrinsic noise of devices is a particularly important issue especially for devices utilized for the amplification or reception of small signals. In general, there are different types of noise classified by their physical origin such as Johnson noise (or thermal noise) which arises from the thermal agitation of carriers. Shot noise arises from random transit of carriers, each carrying a discrete quantity of charge. In the low-frequency regime, the noise is dominated by $1/f$ or flicker noise and generation-recombination (G-R) noise. In addition to being an important figure-of-merit for devices, low-frequency noise is also a sensitive probe to the material quality. Our systematic study of low-frequency noise facilitates the characterization of defects in the material.

The experimental data above showed that for $f > 500$ Hz the voltage noise power spectral density is dominated by Lorentzians, indicative of the presence of G-R noise. It has been shown that the G-R noise is caused by the capture and emission of carriers by single-energy traps in the material. The parameters of the traps can be calculated from the Arrhenius plots of the time constant, τ . From the frequency dependence of voltage noise power spectra density at different temperatures, the time constant, associated with the return to equilibrium of the occupation of the trap level can be determined by $\tau = 1/2\pi f_0$. This time constant is expressed in terms of the capture τ_c and emission τ_e time constants $1/\tau = 1/\tau_c + 1/\tau_e$. Figure 9(a) and (b) show the Arrhenius plots of τ for samples A and B, respectively. It is observed that there are three distinct G-R processes existing in samples A and B at different temperature range. The thermal activation energies of the different trap levels are 666 meV, 208 meV and 90 meV for sample A, and 808 meV, 241 meV and 100 meV for sample B. It is obvious that the thermal activation energy of each trap level is smaller for the sample grown with In-surfactant. Such noise arises from the random filling and emptying of traps in the material. Thus, G-R noise is, in general, a multi-variable stochastic process, involving random transition of carriers between the conduction band, valence band and various trap levels in the material. By assuming that each trap level interacts independently with either the conduction or valence band, the dynamics of the carriers is described by separate independent, trapping and emission processes. The resulting noise spectrum is then the linear superposition of the noise spectra of the individual processes. Van Rhee *et al.*[22] showed that for this approximation to be valid, the Fermi levels must be at least several $k_B T$ away from the trap level and that the carrier density was much larger than the density of each trap level. The noise power spectral density for the occupancy of traps at one single energy level is given by

$$S_{\Delta N}(f) = 4 < \Delta N^2 > \frac{\tau}{1 + 4\pi^2 f^2 \tau^2}, \quad (1)$$

where the fluctuation time constant, τ , is given by

$$\tau = \tau_0 \exp\left(\frac{E}{k_B T}\right), \quad (2)$$

where τ_0 is given by the inverse phonon frequency and E is the activation energy of the trap, which is the difference between the Fermi energy and the trap level. The current noise power spectral density is then given by

$$\begin{aligned} S_I(f) &= 4(\Delta I_0)^2 \frac{\tau_e \tau_c}{(\tau_e + \tau_c)^2} \frac{\tau}{1 + 4\pi^2 f^2 \tau^2}, \\ &= 4(\Delta I_0)^2 f_T (1 - f_T) \frac{\tau}{1 + 4\pi^2 f^2 \tau^2}, \end{aligned} \quad (3)$$

where (ΔI_0) is the fluctuation in the current level due to the capture of one single electron by the traps, and f_T is the Fermi level. The fluctuation time constant for the traps responsible for G-R noise can be obtained from the corner-frequency, f_c , of the noise power spectral density as given by $f_c = 1/(2\pi\tau)$. The Arrhenius plot of the fluctuation time constant gives the activation of the trap.

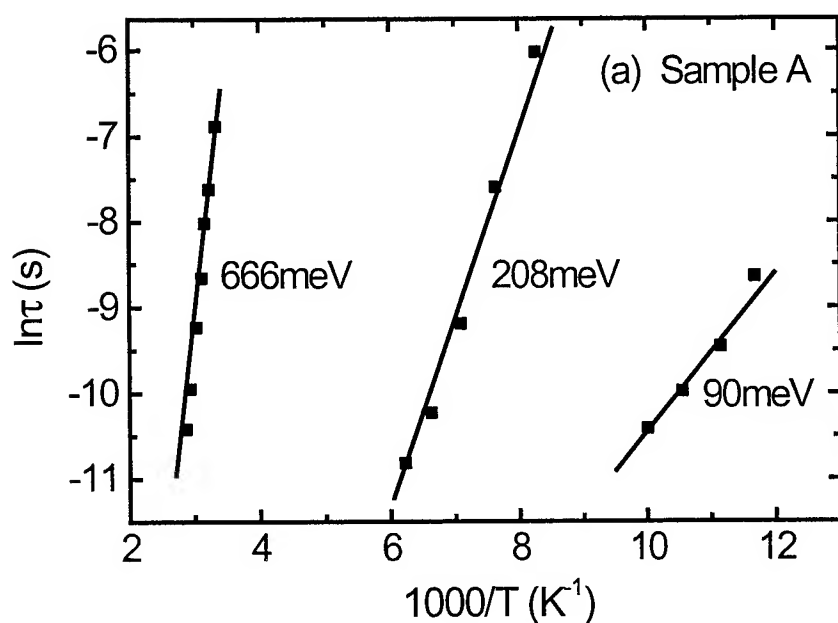


Fig. 9(a): Arrhenius plots of the fluctuation time constants for the G-R processes observed in samples grown with the application of In surfactant.

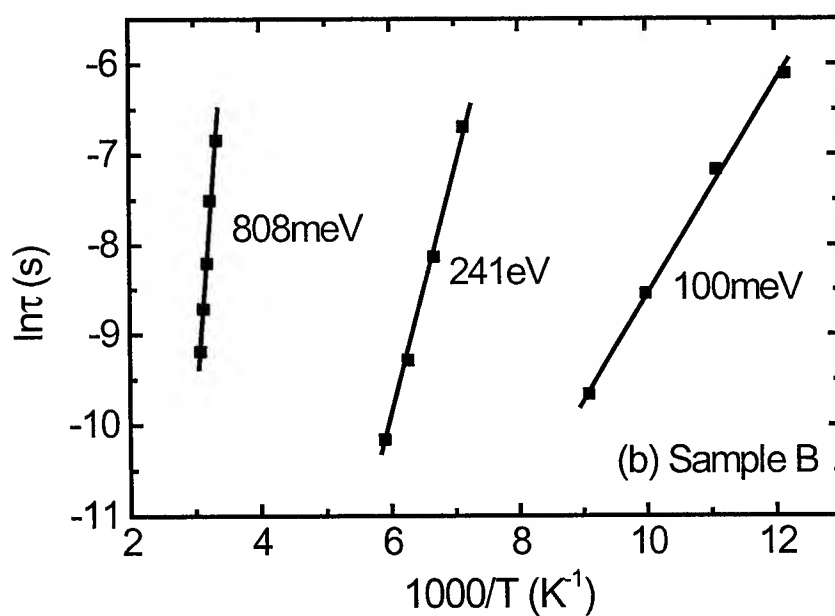


Fig. 9(b): Arrhenius plots of the fluctuation time constants for the G-R processes observed in samples grown without the application of In surfactant.

Flicker noise is characterized by a power-law spectrum, in which the noise power spectral density is proportional to $1/f^\gamma$, with γ approximately equals 1 and remains constant over the entire observable frequency range. The physical origin of $1/f$ noise has been controversial. Hooge *et al.*[23] proposed that flicker noise can be described by a phenomenological equation

$$\frac{S_I(f)}{I^2} = \frac{\alpha_H}{N_C f}, \quad (4)$$

where $S_I(f)$ is the current noise power spectral density, I is the dc current applied to the device, N_C is the total number of carriers in the device and α_H is known as the Hooge parameter. Originally the Hooge parameter, α_H , is believed to be a universal dimensionless constant of value 2×10^{-3} for all types of devices and materials. This suggests a universal mechanism for $1/f$ noise. Also, Eq. 4 stipulates that $S_I(f)$ is directly proportional to N_C , which implies that the noise is caused by independent fluctuations associated with each free carrier, and thus a bulk effect. It was proposed by Vandamme and Hooge[24] that flicker noise arises from lattice scattering of the electrons. Thus, Hooge parameter is proportional to the square of the mobility due to lattice scattering as given by the following equation

$$\alpha_H = \left(\frac{\mu_{Latt}^2}{\mu^2} \right). \quad (5)$$

However, later studies showed that α_H varies significantly from device to device and for high quality devices the Hooge parameter may be as small as 10^{-9} . In addition, flicker noise typically maintain a $1/f^\gamma$ down to frequencies below 1 Hz. This stipulates that the fluctuation process is correlated over a time duration of at least 1 second. The typical mean free time for electrons in a typical device is of the order of a picosecond. The transit time for carriers in a typical semiconductor device is of the order of a millisecond. It is not clear how noise arising from lattice scattering would give rise to such long correlation times. Also, Eq. 4 stipulates that γ is identically equal to 1 for all frequencies and temperatures. This contradicts with known experimental facts obtained by the authors on flicker noise measured from GaN based heterostructures, which indicated that γ is between 0.8 and 1.4 and varies with temperature[25]. The data also indicate significant changes in γ after electrical stressing. Moreover, the experiment also shows that the magnitude of the flicker noise increase This shows that $1/f$ noise arises from defect in the material.

It has been shown by Surya *et al.*[26-27] that the temperature dependence of $1/f^\gamma$ noise can be successfully accounted for by a thermal activation model, which was first proposed by Dutta and Horn[28]. In this model, flicker noise is attributed to the capture and emission of carriers by traps within the material. Each independent capture and emission process is characterized by a time constant τ , which is a function of the energy level of the particular trap. Traps with different energy levels give rise to different values of τ . The total noise power spectrum for a fluctuation process originated from the independent capture and emission of carriers by traps distributed over a wide range of energies is then obtained by the linear superposition of the individual Lorentzians for each trap as given by the equation below

$$S_I(f) = \int_{E_1}^{E_2} dE \ D(E) \frac{C\tau(E)}{1 + 4\pi^2 f^2 \tau^2(E)} \quad (6)$$

where $D(E)$ is the density of traps as a function of energy and E_1 and E_2 are the lower and upper limits of the energy range where $D(E)$ is found to be active in contribution to the overall noise level. This is shown to give rise to a noise power spectral density of the form $1/f^\gamma$. A careful examination of the Lorentzian shows that for a fixed frequency, f , and temperature, T , the magnitude of the Lorentzian increases exponentially with E for $E < E_p$ and decreases exponentially with E for $E > E_p$, where $E_p = -k_B T \ln(2\pi f \tau_0)$. For trap density, $D(E)$, that varies smoothly in energy over a range of $k_B T$, it can be shown that $S_I(f)$ can be approximated by

$$S_I(f) \approx \frac{CD(E_p)}{4f}. \quad (7)$$

Equation 7 clearly shows that flicker noise is a sensitive probe for the traps located at energy level E_p . Our experimental results indicated that films grown with In surfactant resulted in 65% reduction in the flicker noise power spectral density indicating a corresponding reduction in the trap density.

4. CONCLUSION

In conclusion, we have conducted detailed experiments on the study of the effects of indium surfactants on the structural and optical properties of MBE grown GaN epitaxial layers. To characterize the properties of the films, we have studied the Photoluminescence, X-ray diffraction, Rutherford backscattering spectroscopy and low-frequency noise of GaN films grown with and without the application of indium surfactant. Our results clearly show that application of indium surfactant result in the reduction of defect density, reduction of yellow luminescence and substantial improvements in the low-frequency noise properties of the films indicative of the corresponding substantial reduction in the defect density of the films.

5. ACKNOWLEDGE

This work is funded by an RGC grant under the CRC scheme, additional support is provided by The Hong Kong Polytechnic University URG grant.

6. REFERENCE

1. S. Nakamura, T. Mukai, and M. Senoh, *Jpn. J. Appl. Phys.* **30**, L1998 (1991).
2. H. Liu, J.G. Kim, M.H. Ludwig, and R.M. Park, *Appl. Phys. Lett.* **71**, 347 (1997).
3. E.F. Schubert, I.D. Goepfert, and J.M. Redwing, *Appl. Phys. Lett.* **71**, 3224 (1997).
4. H.C. Lin, J. Ou, W.K. Chen, W.H. Chen, and M.C. Lee, *Jpn. J. Appl. Phys. Part 2* **36**, L598 (1997).
5. F.A. Ponce, D.P. Bour, W. Gotz, and P.J. Wright, *Appl. Phys. Lett.* **68**, 57 (1966).
6. H. Okumura, H. Amaguchi, G. Feuillet, Y. Ishida, and S. Yoshida, *Appl. Phys. Lett.* **72**, 3056 (1998).
7. F. Widmann, B. Daudin, G. Feuillet, N. Pelekanos, and J.L. Rouvière, *Appl. Phys. Lett.* **73**, 2642 (1998).
8. L.C. Feldman, J.W. Mayer, and S.T. Picraux, *Materials analysis by ion channeling* (Academic Press, New York, 1982).
9. G.A. Smith, K.H. Park, G.C. Wang, T.M. Lu, and W.M. Gibson, *Surf. Sci.* **233**, 115 (1990).
10. J. Neugebauer and C.G. Van de Walle, *Appl. Phys. Lett.* **69**, 503 (1996).
11. W. Shan, T.J. Schmidt, R.J. Hauenstein, J.J. Song, and B. Goldenberg, *Appl. Phys. Lett.* **66**, 3492 (1995).
12. T.L. Tansley and R.J. Egan, *Phys. Rev. B* **45**, 40942 (1992); *Physica B* **185**, 190 (1993).
13. H.M. Chen, Y.F. Chen, M.C. Lee, and M.S. Feng, *Phys. Rev. B* **56**, 6942 (1997).
14. C. Trager-Cowan, K.P. O'Donnell, S.E. Hoopes, and C.T. Foxon, *Appl. Phys. Lett.* **68**, 355 (1996).
15. E. Calleja, F.J. Sánchez, D. Basak, M.A. Sánchez-García, E. Muñoz, I. Izpura, F. Calle, J.M.G. Tijero, J.L. Sánchez-Rojas, B. Beaumont, P. Lorenzini, and P. Gibart, *Phys. Rev. B* **55**, 4689 (1997).
16. A. Billeb, W. Grieshaber, D. Stocker, E.F. Schubert, and R.F. Karlicek Jr., *Appl. Phys. Lett.* **70**, 2790 (1997).
17. H. Okumura, H. Hamaguchi, G. Feuillet, Y. Ishida, and S. Yoshida, *Appl. Phys. Lett.* **72**, 3056 (1998).
18. G. Feuiller, H. Hamaguchi, K. Ohta, P. Hacke, H. Okumura, and S. Yoshida, *Appl. Phys. Lett.* **70**, 1025 (1997).
19. B. Sundaravel, E.Z. Luo, J.B. Xu, I.H. Wilson, W.K. Fong, L.S. Wang, and C. Surya, *J. Appl. Phys.* **87**, 955 (2000).
20. M. Albrecht, S. Christiansen, G. Salviati, C. Zanolli-Fregonara, Y.T. Rebane, Y.G. Shreter, M. Mayer, A. Pelzmann, M. Kamp, K.J. Ebeling, M.D. Bremser, R.F. Davis, and H.P. Strunk, in *Gallium Nitride and Related Materials II*, edited by C.R. Abernathy, H. Amano, and J.C. Zolper, MRS Symposia Proceedings No. **468** (Materials Research Society, Pittsburgh, 1997), p.293.
21. C. Stampfl and C.G. Van de Walle, *Phys. Rev. B* **57**, R15052 (1998).
22. A.D. van Rheenan, G. Bosman, and R.J.J. Zijlstra, *Solid-State Electron.* **30**, 259 (1987).
23. F.N. Hooge, *Physica B* **83**, 14 (1976).
24. F.N. Hooge and L.K.J. Vandamme, *Phys. Lett. A* **66**, 315 (1978).
25. W.Y. Ho, C. Surya, K.Y. Tong, L.W. Lu, and W.K. Ge, to be published in *IEEE Trans. On Electron Devices*, July 2000.
26. C. Surya and T.Y. Hsiang, *Solid-State Electron.* **31**, 959 (1988).
27. C. Surya, S.H. Ng, E.R. Brown, and P.A. Maki, *IEEE Trans. Electron Devices*, ED-41, 2016 (1994).
28. P. Dutta and P.M. Horn, *Rev. Mod. Phys.* **53**, 497 (1981).

Effect of pre-treatment of GaN substrate for homoepitaxial growth by RF-MBE

Shuichi Kubo*, Tomokazu Okazaki, Shigeki Manabe, Satoshi Kurai and Tsunemasa Taguchi

Faculty of Engineering, Yamaguchi University, 2-16-1, Tokiwadai, Ube, Yamaguchi 755-8611 Japan

ABSTRACT

We have attempted the growth of GaN by RF-MBE which crystalline quality is a match for that by MOCVD, performing homoepitaxial growth using MOCVD-GaN as a substrate. We confirmed that homoepitaxial GaN had Ga polarity by (1 x 1) RHEED streaky pattern after cooling down. 10 min-BHF-etching was the most effective for cleaning the surface of GaN substrate, and as the result crystalline quality of homoepitaxial GaN was improved. Thermal annealing of GaN substrate was also affect for the improvement of crystalline quality of homoepitaxial GaN. From XRD measurement, FWHM of diffraction spectrum from homoepitaxial GaN almost equaled to that from GaN substrate. So, the crystalline quality of homoepitaxial GaN was not inferior to that of GaN substrate. Large compressive strain in c plane of homoepitaxial GaN indicated that homoepitaxy prevented 3D growth and/or formation of defects. From PL measurement, we observed radiative recombination of free excitons clearly from homoepitaxial GaN.

Keywords: RF-MBE, GaN, homoepitaxial growth, surface pre-treatment, BHF etching, free exciton luminescence

1. INTRODUCTION

The development of GaN (gallium nitride) based luminescence devices is remarkable, and so far candela class blue/green light-emitting diodes (LEDs)¹ and violet laser diodes (LDs) were commercialized. These devices were fabricated by metalorganic chemical vapor deposition (MOCVD) using sapphire as a substrate.² Considering the further development of GaN based devices, molecular beam epitaxy (MBE) will become important, because MBE has large advantages compared with MOCVD, for example controllability of the film thickness of the order of atomic scale, *in-situ* observation of the surface microstructure of a growing film by reflection high energy electron diffraction (RHEED), use of high-purity source, and so on. However, the crystalline quality of MBE-grown GaN using sapphire substrate is inferior to that of MOCVD-grown GaN. It is thought that this result is due to the difference of lattice polarity between MBE-grown and MOCVD-grown GaN. N polarity is predominant in MBE-grown GaN, and Ga polarity is predominant in MOCVD-grown GaN.³ GaN with flat surface can be grown with Ga polarity.^{4,5} High-crystalline quality GaN epilayer will be grown by control of the Ga polar surface even in MBE growth.

In this paper, we have performed the growth of homoepitaxial GaN layer by MBE using MOCVD-grown GaN with Ga polarity as a substrate. The problem concerning with large lattice mismatch and difference of thermal expansion coefficient between GaN and sapphire, which is widely used as a substrate for GaN growth, will also be improved by homoepitaxy. When we use a GaN substrate, we need to clean the surface of GaN substrate. We have therefore studied the effect of etching and thermal annealing for GaN substrate.

2. EXPERIMENT

2.1. MOLECULAR BEAM EPITAXY EQUIPMENT

Fig.1 shows schematic illustration of our MBE equipment. The MBE equipment can be evacuated up to about 5×10^{-11} Torr. Growth chamber was cooled by liquid nitrogen to make high-evacuated condition and to concentrate Ga molecular beam. 8N-purity gallium metal as the group III source was thermally evaporated by a conventional Knudsen cell (K-cell), and 6N-purity nitrogen gas as the group V source was cracked to active nitrogen species by radio frequency (RF) nitrogen plasma cell.⁶ The substrate was mechanically mounted on molybdenum (Mo) block, and was loaded into growth chamber. The substrate temperature can be elevated up to 900°C. The surface microstructures can be monitored *in-situ* by RHEED system.

*Correspondence: Email: b4520@stu.cc.yamaguchi-u.ac.jp; Telephone: 81 836 85 9407; FAX: 81 836 85 9401

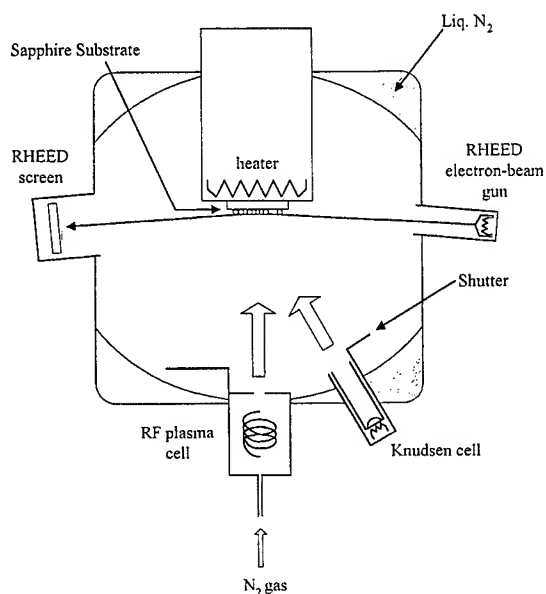
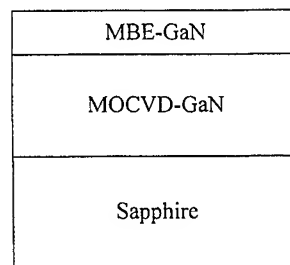
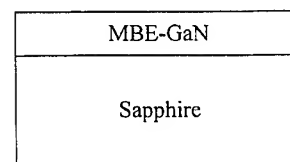


Fig.1 Schematic illustration of our RF-MBE growth chamber. The chamber is cooled by liquid nitrogen, to make high-evacuated condition and concentrate Ga molecular beam.



(a)



(b)

Fig.2 The cross-sectional structure of (a) homoepitaxial and (b) heteroepitaxial GaN in this work.

2.2. GAN SUBSTRATE

A 3 μm -thick MOCVD-grown GaN on sapphire was used as a substrate for the growth of homoepitaxial GaN by RF-MBE. (Hereafter, we call the MOCVD-GaN as "GaN substrate".) Fig.2 shows the cross-sectional structure of homoepitaxial and heteroepitaxial GaN in this work. Heteroepitaxial GaN was grown under its optimum conditions, where growth temperature of epilayer was the same as that of homoepitaxial GaN. The root mean square (RMS) of the surface roughness of GaN substrate was ~ 4 Å by atomic force microscopy (AFM) observation. Carrier density of GaN substrate was estimated to be $2.8 \times 10^{16} \text{ cm}^{-3}$ by Van der Pauw Hall measurement.

2.3. PRE-TREATMENT OF GAN SUBSTRATE

For the purpose of cleaning the surface of GaN substrate, we have investigated the etching and thermal annealing. We selected buffer hydrogen fluoride (BHF), ammonia water and phosphoric acid as the etchant.

Generally, thermal annealing of a substrate is thought to be an important pre-growth treatment to clean up the surface of the substrate. However, thermal annealing is also in danger of the decomposition for the materials, which are unstable against heat. The melting point of GaN is about 2500°C ,⁷ but the vapor pressure of nitrogen is extremely high. As the result, thermal annealing may cause the evaporation of nitrogen from the surface of GaN. We have studied the influence of thermal annealing on GaN substrate. Procedures of the experiment were as follows; GaN substrate was etched by BHF for 10 min, and after that it was loaded into the growth chamber and annealed at 775°C for 60 min under high vacuum ($\sim 10^{-9}$ Torr), non-excited nitrogen atmosphere (2.7×10^{-4} Torr) and nitrogen plasma irradiation (4.5×10^{-5} Torr). Then MBE growth of GaN layer was performed on this GaN substrate with pre-treatment. The growth temperature was 775°C . A Ga cell temperature was set to 970°C , which corresponds to Ga flux of 5.3×10^{-7} Torr, and RF nitrogen plasma cell was operated at a power of 250 W and nitrogen gas flow ratio of 2.0 sccm corresponding to 4.5×10^{-5} Torr.

2.4. THE EVALUATION OF THE CRYSTALLINE QUALITY OF GAN

To evaluate the crystalline quality of GaN, surface AFM, X-ray diffraction (XRD) and photoluminescence (PL) and photoreflectance (PR) measurements were performed. XRD patterns were measured by four-circle X-ray diffractometer with four-crystal monochromator and Cu-K α_1 radiation. For PL measurement, the 325 nm line of a cw He-Cd laser was used as the excitation source. For PR measurement, light from a Xe lamp was used. All spectra were calibrated with the emission lines of a mercury lamp.

3. RESULTS AND DISCUSSIONS

3.1. THE EFFECT OF ETCHING FOR GAN SUBSTRATE

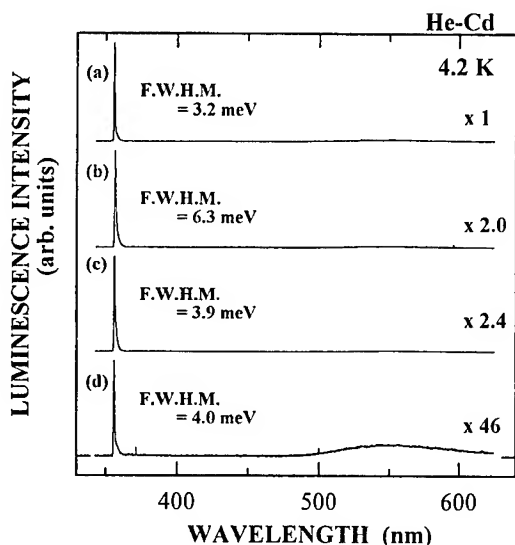


Fig.3 PL spectra at 4.2 K taken from homoepitaxial GaN layer with (a) BHF etching, (b) ammonia water etching at RT, (c) ammonia etching at 50°C and (d) cleaning by organic solvents (acetone and trichloroethylene) before the growth.

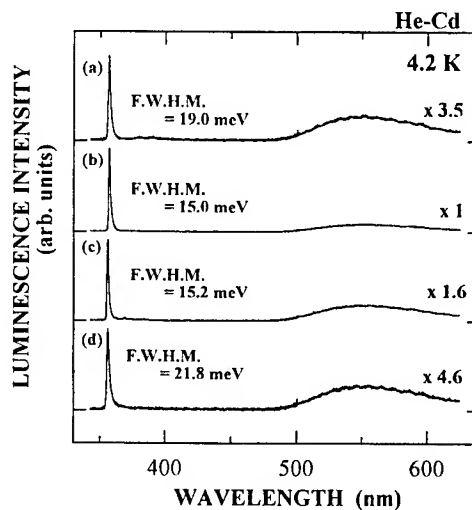


Fig.4 PL spectra at 4.2 K taken from homoepitaxial GaN with BHF etching for (a) 0, (b) 10, (c) 20 (d) 30 min before the growth.

Fig.3 shows PL spectra at 4.2 K from homoepitaxial GaN layer with pre-growth etching by BHF, ammonia water, and with cleaning by organic solvents (acetone and trichloroethylene) before the homoepitaxial growth. The full-width at half maximum (FWHM) of neutral donor bound exciton (I_2) emission line at around 357 nm was the narrowest in the GaN layer with BHF etching. In addition, the PL intensity from GaN layer with BHF etching was much larger than that without etching (with only cleaning). This is related to the reduction of contamination on the surface of GaN substrate. Ammonia is not suitable for the pre-growth etching of GaN in this condition. We hereafter used BHF as the suitable etchant for GaN. Fig.4 shows PL spectra at 4.2 K from homoepitaxial GaN layer with BHF etching for 0 ~ 30 min before the growth. The line width of excitonic emission from GaN layer with 10 min-BHF-etching was the narrowest, and PL intensity showed also the largest value at the same condition. From these results, the optimal BHF-etching-time is decided around 10 min. Less BHF etching time was insufficient for removal of contaminant, and excess BHF etching roughen the surface of GaN substrate. We observed the surface morphology of GaN substrate with BHF etching for 30 min by AFM. Fig.5 shows the AFM images of surface morphology of GaN substrate with BHF etching for 30 min. From these images, it was clearly indicated that the surface of GaN with BHF etching for 30 min is rougher than that of GaN without any treatment.

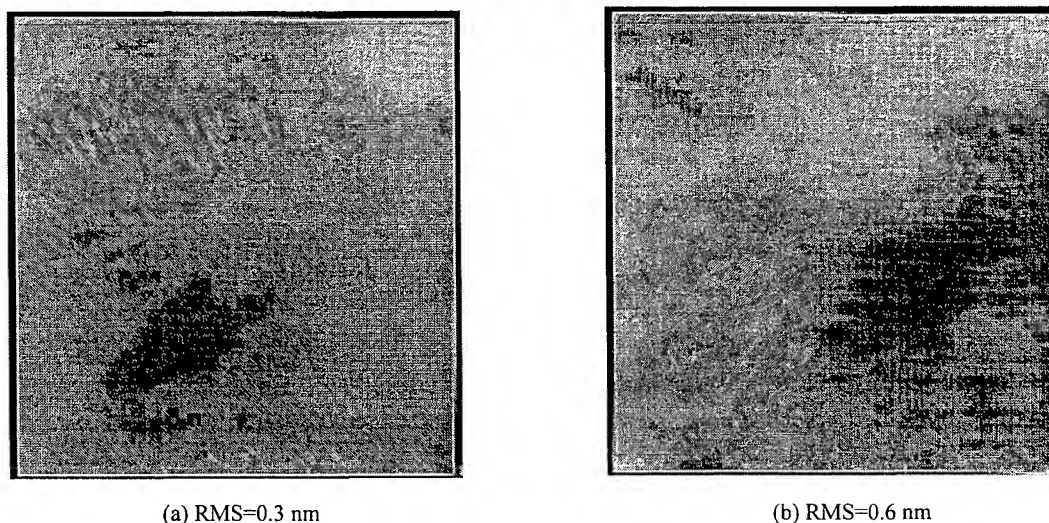


Fig.5 The AFM images of the surface morphologies of GaN substrate (a) without any treatments, (b) with BHF etching for 30 min.

3.2. THE EFFECT OF THERMAL ANNEALING OF GAN SUBSTRATE

The GaN substrate was annealed under high vacuum ($\sim 10^{-9}$ Torr) at 800°C, which was higher than the growth temperature (775°C), for 60 min. Quadrupole mass spectroscopy (QMS) showed no clear evidence of nitrogen evaporation during this process.

Fig.6 shows PL spectrum taken from thermal-annealed GaN substrate at 4.2 K. It was understood that I_2 -line width from GaN substrate decreased, radiative recombination of free excitons at shorter wavelength side of I_2 -line became clear and each peak shifted toward the higher-energy side. These results were explained by re-arrangement of GaN crystalline during thermal annealing and generation of compressive strain in c-plane during cooling procedure.

Fig.7 shows PL spectra at 4.2 K taken from homoepitaxially-grown GaN layer with thermal annealing before the growth. PL spectra of homoepitaxial GaN layer with thermal annealing showed narrower I_2 -line width and larger PL intensity than that of GaN layer without thermal annealing. It was considered that the thermal cleaning of GaN substrate prevented taking in contaminant to epilayer. On the other hand, since the thermal annealing caused re-arrangement of GaN crystalline as mentioned above, it was also considered that the crystalline quality of GaN layer took over the improved crystalline quality of the GaN substrate. The I_2 -line from the homoepitaxial GaN layer with thermal annealing also shifted toward the higher-energy side compared with that from homoepitaxial GaN layer without thermal annealing because of the compressive strain containing in annealed GaN substrate.

Next, we will mention the effect of the atmosphere during thermal annealing. The thermal annealing under non-excited nitrogen atmosphere and nitrogen plasma irradiation was carried out for the purpose of suppressing the evaporation of nitrogen from GaN substrate. The PL intensity of I_2 -line in homoepitaxial GaN layer annealed under non-excited nitrogen atmosphere was decreased in comparison compared with that under high vacuum; in contrast, the I_2 -line width was increased. Therefore, it is thought that the removal of contamination on the surface of GaN substrate was insufficient due to higher pressure, which prevents decomposition of oxide on GaN substrate. PL spectrum from homoepitaxial GaN layer with thermally annealed under nitrogen plasma irradiation showed almost same I_2 -line width and weaker intensity compared with homoepitaxial GaN layer with thermal annealing under high vacuum. Under nitrogen plasma irradiation, it is thought that higher pressure prevented the removal of contamination on the surface of GaN substrate similar to that under non-excited nitrogen atmosphere. However, the effect of nitrogen plasma is not clear at present.

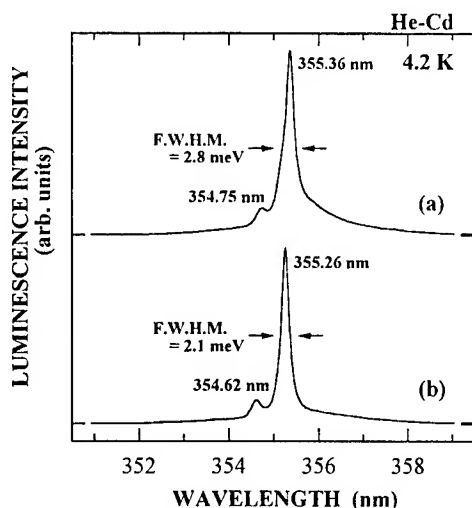


Fig.6 PL spectra at 4.2 K taken from GaN substrate (a) without any treatments, (b) with thermal annealing.

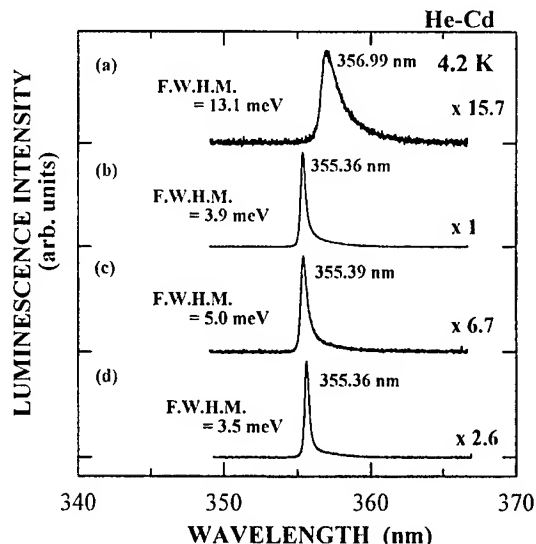


Fig.7 PL spectra at 4.2 K taken from homoepitaxial GaN (a) without any treatments, with thermal annealing (b) under high vacuum, (c) non-excited nitrogen atmosphere and (d) nitrogen plasma irradiation.

3.3. THE CRYSTALLINE QUALITY OF HOMOEPITAXIAL GAN

Fig.8 shows the RHEED pattern from homoepitaxial GaN at RT. This (1×1) pattern indicates that homoepitaxial GaN has Ga polarity. Fig.9 shows X-ray diffraction spectra from homoepitaxial GaN, heteroepitaxial GaN and GaN substrate. The FWHM of (0002) diffraction peak from homoepitaxial GaN was almost same as that of GaN substrate. The FWHM of diffraction peak from heteroepitaxial GaN was the broadest (173 arcsec). The diffraction angle of GaN substrate showed the lowest value, and the diffraction angle of homoepitaxial GaN was lower than that of heteroepitaxial GaN. Each diffraction angle was lower than that of bulk GaN. Therefore, each sample contains tensile strain toward c-axis, or biaxial compressive strain in c-plane. Table 1 shows 2θ diffraction angles, constant c , tensile strain toward c-axis, compressive strain to a-axis and magnitude of compressive strain toward a-axis. Compressive strain in c-plane and magnitude of compressive strain to a-axis were calculated using Poisson's ratio of 0.38⁸ for GaN and Young's modulus of 150 GPa for GaN, respectively. Compressive strain in c-plane was caused by large lattice mismatch and difference of thermal expansion coefficient between GaN and sapphire. It was expected that the strain in heteroepitaxial GaN is larger than that in homoepitaxial GaN, however, Fig.9 showed smaller strain in heteroepitaxial GaN. It was explained by 3D growth and/or formation of defects; the strain must be relaxed in such sample. It is supposed that growth mode or grain size between homoepitaxial GaN and heteroepitaxial GaN was different due to the difference of polarity at the beginning of the growth.⁹

Fig.10 shows PL spectra from homoepitaxial GaN, heteroepitaxial GaN and GaN substrate. A sharp I_2 -line was obtained for each sample. The I_2 peak energy is highest in GaN substrate, second in homoepitaxial GaN, and lowest in heteroepitaxial GaN. This is also due to the strain effect, and biaxial compressive strain in c-plane enlarges band-gap energy. This is consistent with the shift of X-ray diffraction angles due to the strain. Fig.11 shows the relationship between the strain and the I_2 peak energy. This result is consistent with that in other papers.^{10, 11.}

Fig.12 shows an enlarged PL and photoreflectance (PR) spectrum from homoepitaxial GaN. The PL spectrum showed a dip around 355.57 nm, where the origin of the shoulder was attributed to radiative recombination of A-free excitons (X_A).

Fig.13 shows the temperature-dependent PL spectrum from homoepitaxial GaN ranged from 4.1 to 220 K. As increasing the temperature, X_A -line was clearly observed due to thermal dissociation of excitons from a neutral donor. The first observation of the X_A -line from GaN in our system was achieved by homoepitaxial growth on typical MOCVD-GaN/sapphire. These results show that the crystalline quality of MBE-grown GaN can be greatly improved by homoepitaxy.

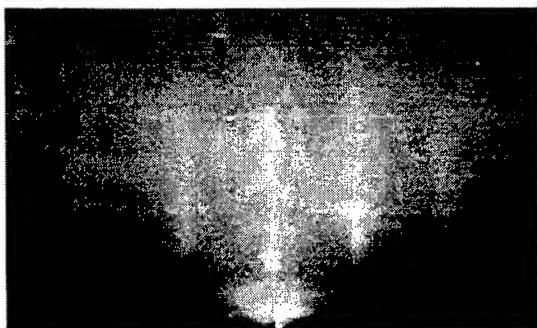


Fig.8 RHEED pattern from homoepitaxial GaN at RT.

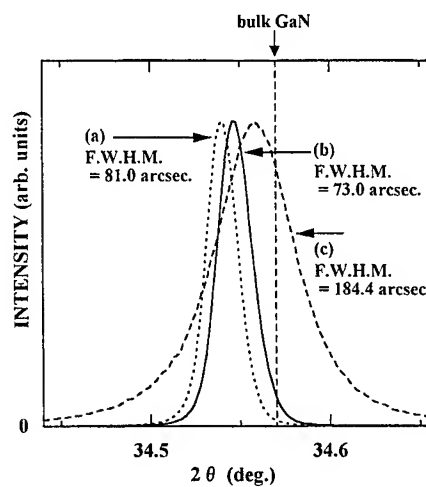


Fig.9 X-ray diffraction spectra taken from (a) GaN substrate, (b) homoepitaxial and (c) heteroepitaxial GaN.

Table.1 Magnitude of compressive strain in GaN

	GaN substrate	homoepitaxial GaN	heteroepitaxial GaN
2 θ diffraction peak [$^{\circ}$]	34.540	34.547	34.559
constant c [\AA]	5.1893	5.1882	5.1865
tensile strain toward c-axis [%]	0.082	0.063	0.029
compressive strain toward a-axis [%]	0.22	0.16	0.076
constant a [\AA]	3.1821	3.1838	3.1866
magnitude of compressive stress toward a-axis [GPa]	0.32	0.25	0.11

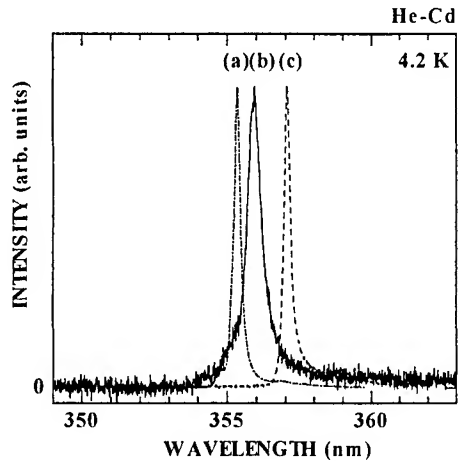


Fig.10 PL spectra at 4.2 K taken from (a) GaN substrate, (b) homoepitaxial and (c) heteroepitaxial GaN.

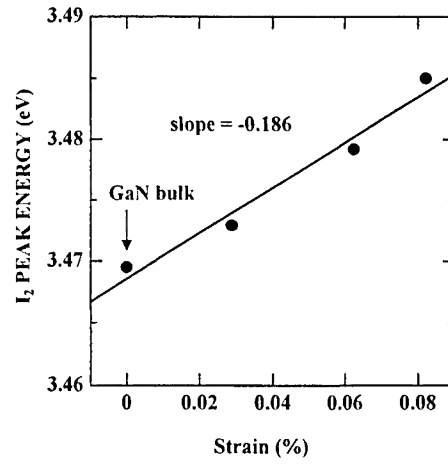


Fig.11 The relationship between strain and I_2 peak energy.

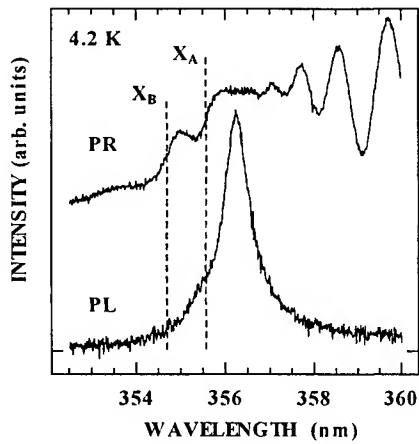


Fig.12 PL and PR spectra at 4.2 K of homoepitaxial GaN.

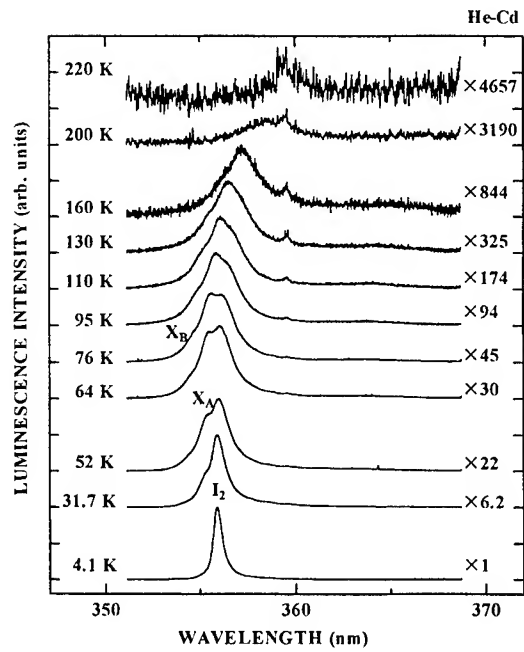


Fig.13 Temperature dependence of PL spectra taken from homoepitaxial GaN.

4. CONCLUTIONS

We have performed the homoepitaxial growth of GaN using MOCVD-grown GaN as a substrate. The effect of treatment of GaN substrate before the growth has been investigated in detail. A 10 min BHF etching was the most effective for cleaning of GaN substrate. Thermal annealing was also effective to clean up and to improve the crystalline-quality of GaN substrate. The homoepitaxial GaN has good structural and optical properties, although homoepitaxially-grown GaN layers include larger strain to c-axis than that in heteroepitaxial GaN by RF-MBE. It was supposed that growth mode or grain size between homoepitaxial GaN and heteroepitaxial GaN by RF-MBE was different due to the difference of polarity at the beginning of the growth. Our results will support that the problems in MBE growth, which are derived from the heterointerface between GaN layer and sapphire substrate, can be improved by homoepitaxial growth. Our proposal is that the MBE-grown GaN is not inferior to MOCVD-grown GaN essentially.

ACKNOWLEDGEMENTS

This work was supported by the Japanese National Project "The Light for the 21st century" (MITI/NEDO/JRCM).

REFERENCES

1. S. Nakamura, M. Senoh, N. Iwasa, S. Nagahama, T. Yamada and T. Mukai, "Superbright Green InGaN Single-Quantum-Well-Structure Light-Emitting Diodes," *Jpn. J. Appl. Phys.* **34**, pp. L1332-L1335, 1995.
2. S. Nakamura, "GaN Growth Using GaN Buffer Layer," *Jpn. J. Appl. Phys.* **30**, pp. L1705-L1707, 1991.
3. A. R. Smith, R. M. Feenstra, D. W. Greve, M.-S. Shin, M. Skowronski, J. Neugebauer and J. E. Northrup, "Determination of wurtzite GaN lattice polarity based on surface reconstruction," *Appl. Phys. Lett.* **72**, pp. 2114-2116, 1998.
4. F. A. Ponce, D. P. Bour, W. T. Young, M. Saunders and J. W. Steed, "Determination of lattice polarity for growth of GaN bulk single crystals and epitaxial layers," *Appl. Phys. Lett.* **69**, pp. 337-339, 1996.
5. P. Daudin, J. L. Rouviere and M. Ariery, "Polarity determination of GaN films by ion channeling and convergent beam electron diffraction," *Appl. Phys. Lett.* **69**, pp. 2480-2482, 1996.
6. S. Kubo, S. Kurai and T. Taguchi, "Homoepitaxial Growth of GaN Thin Layer by Molecular Beam Epitaxy with an RF Nitrogen Plasma," *The Second International Symposium on Applied Plasma Science*, Osaka, Japan, pp. 331-336, 1999.
7. J. A. Van Vechten, "Quantum Dielectric Theory of Electronegativity in Covalent Systems. III. Pressure-Temperature Phase Diagrams, Heats of Mixing, and Distribution Coefficients," *Phys. Rev. B* **7**, pp. 1479-1507, 1973.
8. T. Detchprohm, K. Hiramatsu, K. Itoh, and I. Akasaki, "Relaxation Process of the Thermal Strain in the GaN/Al₂O₃ Heterostructure and Determination of the Intrinsic Lattice Constants of GaN Free from the Strain," *Jpn. J. Appl. Phys.* **31** pp. L1454-L1456, 1992.
9. S. Kurai, S. Kubo, T. Okazaki, S. Manabe, T. Sugita, A. Kawabe, Y. Yamada and T. Taguchi, "Homoepitaxial Growth and Luminescence Characterization of GaN Epilayer by RF-MBE on MOCVD-Grown GaN Substrate," *The Third International Conference on Nitride Semiconductors*, Montpellier, France, pp. 459-463, 1999.
10. H. Amano, K. Hiramatsu and I. Akasaki, "Heteroepitaxial Growth and the Effect of Strain on the Luminescent Properties of GaN Films on (11-20) and (0001) Sapphire Substrates," *Jpn. J. Appl. Phys.* **27** pp. L1384-L1386, 1988.
11. A. A. Yamaguchi, K. Kobayashi, A. Sakai, Y. Mochizuki and H. Sunakawa, "Valence Band splitting of GaN Assessed by Peculiar Strain Distribution in HVPE-ELO Films," *2nd Intern. Symp. on Blue Laser and Light Emitting Diodes*, Chiba, Japan, pp. 692-695, 1998.

Effects of Gamma-Ray Irradiation on the Microstructural and Luminescent Properties of Radio-Frequency-Magnetron-Sputtered GaN Thin Films

Ching-Wu Wang, Bo-Shao Soong, Chung-Tung Tseng,
Jing-Yu Chen, and Chih-Liang Chen
Dert. of Electronic, I-Shou University
Ta-Hsu Hsiang, Kaohsiung County,
Taiwan, ROC.

ABSTRACT

The microstructural and luminescent properties of sputtered GaN thin films pre-irradiated and γ -ray irradiated were systematically investigated. Analytical results revealed that the increasing dose of γ -rays could enhance the more occurrence of nitrogen vacancies which not only created a prominent deep level luminescence but also destroyed the crystallinity of GaN thin films. For low dose of γ -ray irradiation (4 Mrad (GaN)), evidence showed that by raising the irradiation dose, more associated Ga-H complexes will be effectively promoted, yielding an enhanced yellow band emission. However, for high dose of γ -ray irradiation (4 Mrad (GaN)), further higher dose of γ -rays could lead the dissociation of Ga-H complexes in GaN samples, resulting in a repressed yellow band emission.

Keywords: microstructural, luminescent, GaN, γ -ray, nitrogen vacancies, crystallinity, Ga-H complexes, yellow band emission, dissociation

1. INTRODUCTION

Gallium nitride (GaN) exhibits some unique properties, such as a large direct band gap, strong interatomic bonds, and a high thermal conductivity, which make it an ideal material for optoelectronic and high-temperature/high-power devices. Recently, very efficient GaN-based blue/green light-emitting diodes and blue lasers have been fabricated¹⁻². Despite the impressive progress in GaN-made devices, the role of various defects in the material and their effect on device performance are not yet understood and therefore cause intense interest in studying the behavior of deep defects which affects the microstructural and luminescent properties of GaN thin film.

Among the defect-induced transitions, the ubiquitous yellow luminescence (YL)³⁻⁵ observed from photoluminescence (PL) at around 2.2 ~ 2.3 eV, is detected independently of the substrate and the epitaxial technique used, with its intensity being more pronounced at room temperature. Although the YL measurements reveal a distinct optical signature of the defect, the microstructure and chemical nature of the defects has not been identified.

On the other hand, there is also a growing interest in the effect of gamma and other ionizing radiation on GaN devices because of the increasing concerns related to the stability of devices in radiation environments⁶. Many papers have reported radiation-induced defects in silicon⁷, GaAs⁸⁻⁹, and ZnSe¹⁰ materials, but up to now little work has been done to connect irradiation effects on the microstructural and luminescent properties.

In this article, the effects of γ -ray irradiation on the defect status of radio-frequency-sputtered GaN thin films are systematically investigated. Moreover, in addition to the variation of γ -ray-irradiated defects, the results of microstructural and luminescent characteristics of GaN thin films in relation to the dose of γ -ray irradiation are also understood.

2. EXPERIMENT

GaN thin films were prepared by a two-stage-growth¹¹ of radio-frequency (rf) magnetron sputtering method. The source material, made by Superconductive Components, Inc. (USA), was GaN target (3 inch diam.) with 99.999 % purity. Prior to loading the p⁺-Si (111) substrates into the sputter chamber, the wafers were rinsed in 10:1 HF acid to remove thenative oxide layer and blown dry. During the growth process, the rf power was controlled at 50W and a mixed

* Correspondence: E-mail: cwwang@isu.edu.tw; Telephone: 886-7-6577711 ext. 6668; Fax: 886-7-6577056

sputtering gas of N_2 and Ar was utilized to keep the sputtered pressure at 5×10^{-3} Torr. For the first stage, a thin GaN buffer layer (500 Å) was deposited on Si substrate at 400°C. Then, the substrate temperature was elevated to 500°C for annealing the GaN buffer under a purified N_2 atmosphere for 30 min. Next, a 3500 Å thickness of GaN epilayer was grown on top of GaN buffer at 700°C. After deposition, rapid thermal annealing (RTA) treatment at 900 °C on the sputtered GaN thin films were carried out in 0.5 Torr purified N_2 ambient for 1 min. Subsequently, some RTA-treated GaN thin films were arranged to expose to the γ -ray irradiation of Co^{60} with various doses (1 ~ 12 Mrad (GaN)) under a dosing rate of 100 rads/sec.

The crystallinity of GaN thin films was examined using a x-ray diffraction (XRD) with a Cu-K α radiation source. Luminescent analysis of different doses of γ -ray-irradiated samples were carried out employing PL measurements excited by a 325 nm He-Cd laser at room temperature. Compositional analyses of different doses of γ -ray-irradiated samples and their comparisons with pre-irradiated ones were performed employing secondary ion mass spectrometry (SIMS). The accuracy of the SIMS data in depth of film thickness and in concentration of tested elements are within 5% and with 3% relative error, respectively. Fourier Transform Infrared Spectroscopy (FTIR) measurements were carried out using a MAGNA-IR 750 SPECTROMETER. The resolution of the spectrometer was 4 cm^{-1} , and all spectra given are expressed in absorbance. For the deep level transient spectroscopy (DLTS) measurement¹², Schottky diodes were made by evaporating gold (Au) and aluminum (Al) on top of GaN thin film which provide, respectively, a Schottky contact at Au/GaN and an Ohmic contact at Al/GaN junctions.

3. RESULTS AND DISCUSSION

The GaN thin films pre-irradiated and γ -ray irradiated were all found to be *n*-type from room temperature Hall-effect measurements, as is usual case for undoped GaN. Typical XRD profiles of GaN thin films pre-irradiated and γ -ray irradiated at various doses are shown in Fig. 1, indicating that the crystallinity was strongly influenced by the γ -ray irradiation. As illustrated in Fig. 1, the intensity of dominant peak in pre-irradiated GaN located at $2\theta = 32.4^\circ$, originating from (10 $\bar{1}0$) wurtzite (α)-GaN, evidently decreases with the increasing doses of γ -ray irradiation. It implies that most of irradiation energy might take on the destructive role deteriorating the crystallinity of GaN film.

In general, it is expected that for thin films with superior crystallized property, a well-performing band-to-band transition in photoluminescence should result. Such an expectation was realized by our photoluminescence of different doses of γ -ray-irradiated GaN thin films. As illustrated in Fig. 2, the strong near-band-edge emission at 3.3 eV for pre-irradiated sample was observed to decrease with the increasing dose. This band emission has been assigned to excitons bound to neutral donors¹³ and is considered a PL fingerprint of *N*-type GaN. It is worth noting that a significant phenomenon illustrating the intensity of a weak deep level luminescence at 2.8 eV for pre-irradiated specimen contrarily increased with increasing irradiation dose. Such a result implies that the deep level luminescence not only affects near-band-edge emission but also plays the destructive role in determining the crystallinity of GaN thin film. Another interesting observance showing the intensity of a broad yellow band around 2.2 eV for pre-irradiated sample increases with the increase of irradiation dose for low dose of γ -ray irradiation (< 4 Mrad (GaN)). However, for high dose of γ -ray irradiation (> 4 Mrad (GaN)), the intensity of yellow band emission contrarily decreases with the increasing irradiation dose. It implies that low dose (< 4 Mrad (GaN)) and high dose (> 4 Mrad (GaN)) of γ -ray irradiation play the promotive and repressive roles, respectively, in yellow band emission of GaN samples.

To investigate the physical origins for the variation of PL which occurred in our samples, DLTS measurements were employed to examine the deep defects existing within these GaN thin films. The DLTS results are shown in Fig. 3. As can be seen, two deep electron traps (designated as E_{t1} and E_{t2} , respectively) were consistently detected in all the samples. Moreover, the Arrhenius plots yielding the activation energies of E_{t1} and E_{t2} below the conduction band-edge minimum are $E_c - E_{t1} \cong 0.59$ eV (± 0.02 eV) and $E_c - E_{t2} \cong 0.82$ eV (± 0.02 eV). First, we suspect that E_{t1} is a nitrogen-vacancy-related deep trap. This inference is based on the SIMS observation that the higher dose of γ -ray-irradiated sample the more nitrogen deficiency detected inside the GaN bulk, as illustrated in Fig. 4. Moreover, the measured E_{t1} level at 0.59 eV below the conduction band in this experiment is quite in agreement with the nitrogen-vacancy-related deep level at 0.62 eV which was observed by thermally stimulated current (TSC) method¹⁴. Significantly, the observance of the DLTS signal intensity of E_{t1} in pre-irradiated sample enhanced by raising the dose of γ -ray irradiation provides a reliable deduction that E_{t1} not only is the causality of deep level luminescence at 2.8 eV but also behaves the main factor in destroying the crystallinity of GaN film. Next, the origin of E_{t2} is suggested to be a hydrogen-related deep electron trap since the FTIR results revealed such an assertion. In addition, the measured E_{t2} level at 0.82 eV below the conduction band in this work is also coincident with report by Pearton et al.¹⁵, that a hydrogen-induced electron trap at around $E_c - 0.8$ eV was found for implantation of hydrogen into GaN. Typical FTIR absorption spectra from the GaN samples are shown in Fig. 5, in which

the spectral region is $1500 \sim 2000 \text{ cm}^{-1}$. There is no observable absorption band except background from the pre-irradiated GaN samples, as shown by the curve (a) in Fig. 5. After the samples were irradiated by low dose of γ -rays ($\sim 4 \text{ Mrad}$ (GaN)), one absorption band around 1730 cm^{-1} was observed to be enhanced and reached a maximum by raising the dose of γ -rays until 4 Mrad (GaN) (see curves (b) and (c) of Fig. 5). Contrarily, for the case of high dose of γ -rays ($> 4 \text{ Mrad}$ (GaN)), increasing the irradiation dose of γ -rays significantly causes the intensities of the above absorption bands to decrease as shown by curves (d) and (e) of Fig. 5. The origin of FTIR band at around 1730 cm^{-1} has been ascribed as the local vibrational modes of Ga-H complexes in the vicinity of N vacancies¹⁶.

Based on the above results, we have the following deduction. Before the γ -ray irradiation, hydrogen could be situated in either IR inactivated states or very weak IR activated states. For the low dose of γ -ray irradiation ($\sim 4 \text{ Mrad}$ (GaN)), γ -ray irradiation can sufficiently dissociate hydrogen-related complexes in IR inactivated states and result in atomic hydrogen. Atomic hydrogen is very active and can combine with Ga dangling bonds beside the N vacancies to form Ga-H complex. However, as in the high dose of γ -ray irradiation ($\sim 4 \text{ Mrad}$ (GaN)), further higher dose of γ -rays not only introduces more defects but also lead to the dissociation of H complexes containing Ga-H complexes in GaN samples.

4. CONCLUSIONS

We have performed different doses of γ -ray irradiation treatment on undoped GaN samples. Two deep electron traps, E_{t1} and E_{t2} ($E_c - E_{t1} = 0.59 \text{ eV}$ and $E_c - E_{t2} = 0.82 \text{ eV}$), corresponding V_N -related defect and Ga-H complex, respectively, were demonstrated to be strongly influenced by different doses of γ -ray irradiation. The E_{t1} trap was observed to be enhanced by raising the irradiation dose and was deduced to be the main causality yielding the poor crystallinity as well as a deteriorated near-band-edge emission of GaN thin film. Interestingly, the E_{t2} trap increasing with the increases of γ -rays at low dose of irradiation ($\sim 4 \text{ Mrad}$ (GaN)) and decreasing with the increases of γ -rays at high dose of irradiation ($\sim 4 \text{ Mrad}$ (GaN)) was suggested to play the prominent role in influencing the YB luminescent behavior.

ACKNOWLEDGMENTS

One of the authors (Ching-Wu Wang) gratefully acknowledges the financial support from the National Science Council (NSC) in Taiwan under contract number: NSC89-2215-E-214-004.

REFERENCES

1. S. Nakamura, T. Mukai, and M. Senoh, *Appl. Phys. Lett.* **64**, p.1687 (1994).
2. S. Nakamura, M. Senoh, S. Nagahama, N. Iwasa, T. Tamada, T. Matsushita, H. Kiyoku, and Y. Sugimoto, *Jpn. J. Appl. Phys.* **35**, L74 (1996).
3. T. Ogino, and M. Aoki, *Jap. J. Appl. Phys.* **19**, p.2395 (1980).
4. E. R. Glaser, T. A. Kennedy, K. Doverspike, L. B. Rowland, D. K. Gaskill, J. A. Freitas, Jr., M. A. Khan, D. T. Olson, J. N. Kuznia, and D. K. Wickenden, *Physical Review B* **51**, p. 13326 (1995).
5. E. Calleja, F. J. Sanchez, D. Bassak, M. A. Sanchez-Garica, E. Munoz, I. Izpura, F. Calle, J. M. G. Tijero, J. L. Sanchez-Rojas, B. Beaumont, P. Lorenzini, and P. Gibart, *Physical Review B* **55**, p. 4689 (1997).
6. V. V. Emtsev, V. Yu. Davydov, I. N. Goncharuk, E. V. Kalinina, V. V. Kozlovskii, D. S. Poloskin, A. V. Sakharov, N. M. Shmidt, A. N. Smirnov, and A. S. Usikov, *Materials Science Forum*, **258-263**, p. 1143 (1997).
7. P. F. Lugakov, and T. A. Lukashevich, *Phys. Stat. Sol. (a)* **110**, p. 403 (1988).
8. B. Ziebro, J. W. Hensky, and D. C. Look, *J. Appl. Phys.* **72**, P. 78 (1992).
9. D. C. Look, Z-Q. Fang, J. W. Hensky, and P. Kengkan, *Phys. Rev. B*, **55**, p. 2214, (1997).
10. W. A. Barry and G. D. Watkins, *Phys. Rev. B*, **54**, p. 7789, (1996).
11. T. Sasaki, and T. Matsuoka, *J. Appl. Phys.* **77**, p. 192 (1995).
12. D. V. Lang, *J. Appl. Phys.* **45**, p. 3023 (1974).
13. R. Dingle, D. D. Sell, S. E. Stokowski, and M. Ilegems, *Phys. Rev. B* **4**, p. 1211 (1971).
14. Z. C. Huang, J. C. Chen, and D. Wickenden, *J. Cryst. Growth*, **170**, p. 362 (1997).
15. S. J. Pearton, C. R. Abernathy, R. C. Wilson, J. M. Zarada, C. Y. Song, M. G. Weinstein, M. Stavola, J. Han, and R. J. Shul, *Nuclear Instruments and Methods in Physics Research B*, **147**, p. 171 (1999).
16. J. Q. Duan, B. R. Zhang, Y. X. Zhang, L. P. Wang, G. G. Qin, G.Y. Zhang, Y. Z. Tong, S. X. Jin, Z. J. Yang, X. Zhang, and Z. H. Xu, *J. Appl. Phys.* **82(11)**, p. 5745 (1997).

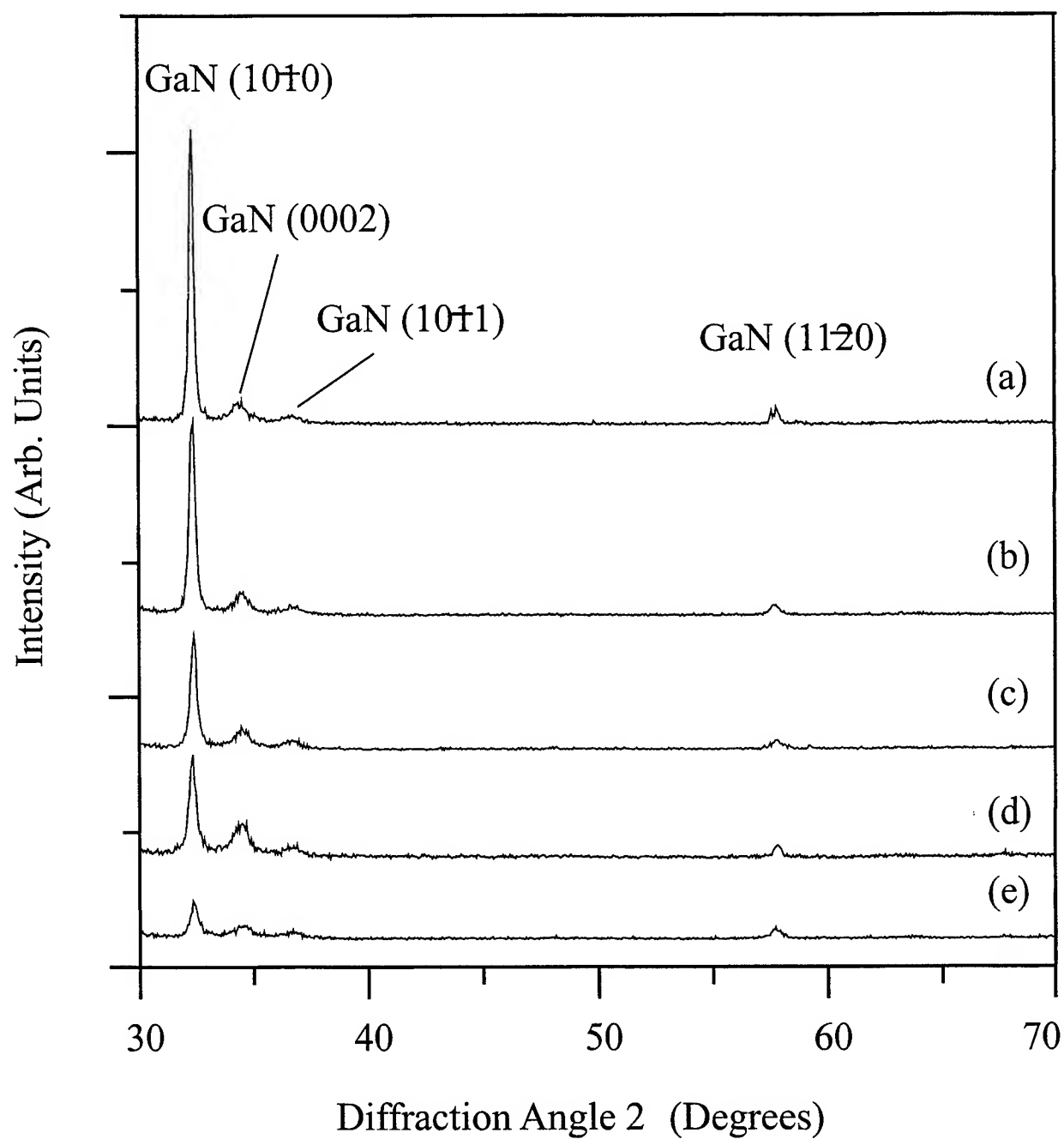


Fig. 1. X-ray diffraction spectra for sputtered-GaN thin films with different doses of γ -ray irradiation. Curve (a) represents the pre-irradiated sample. Curves (b) ~ (e) correspond samples treated by 1, 4, 8, and 12 Mrad (GaN) of γ -ray irradiation.

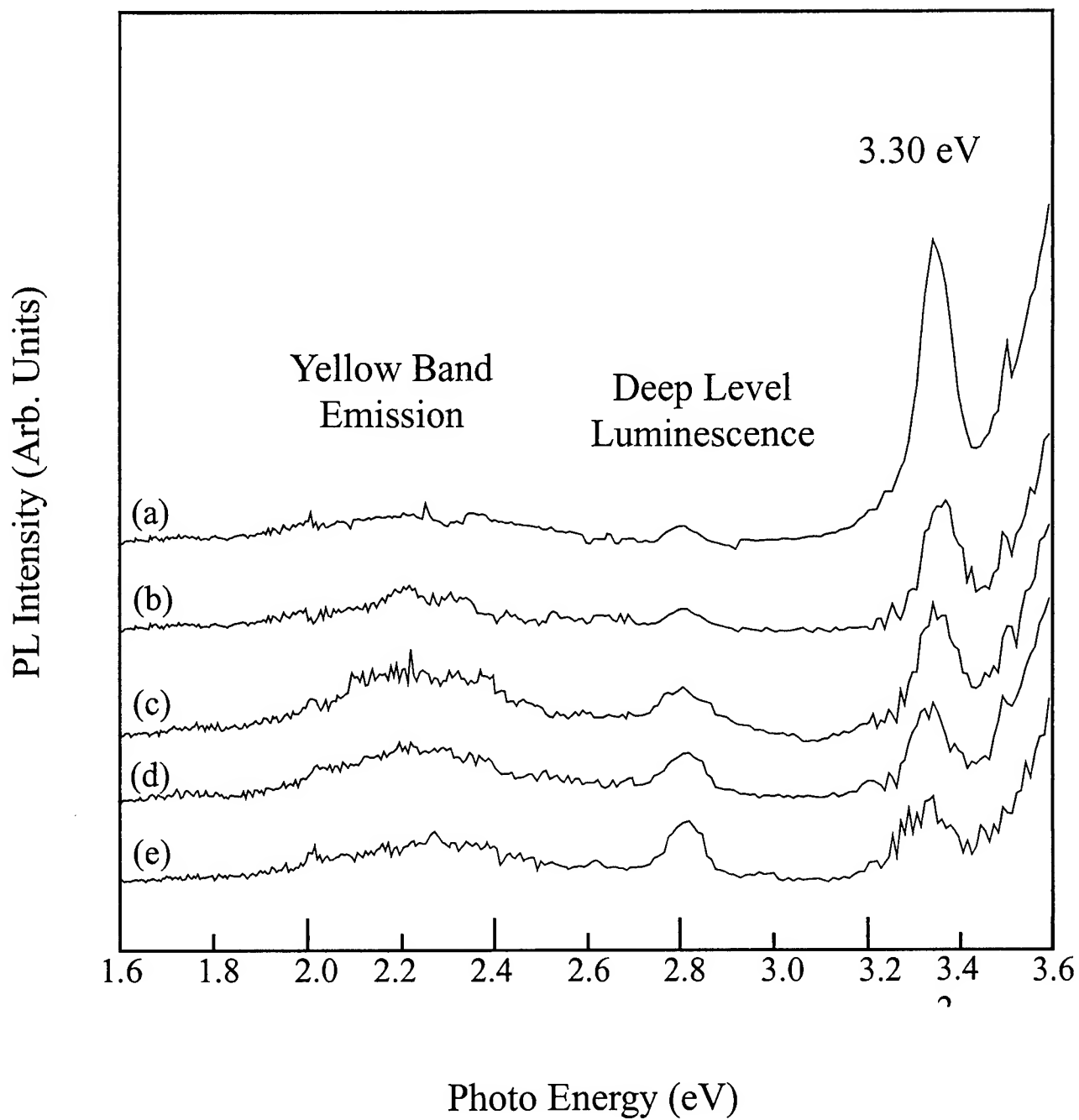


Fig. 2. Room-temperature photoluminescence spectra for sputtered GaN thin films treated by different doses of γ -ray irradiation. Curve (a) represents the pre-irradiated sample. Curves (b) ~ (e) correspond samples treated by 1, 4, 8, and 12 Mrad (GaN) of γ -ray irradiation

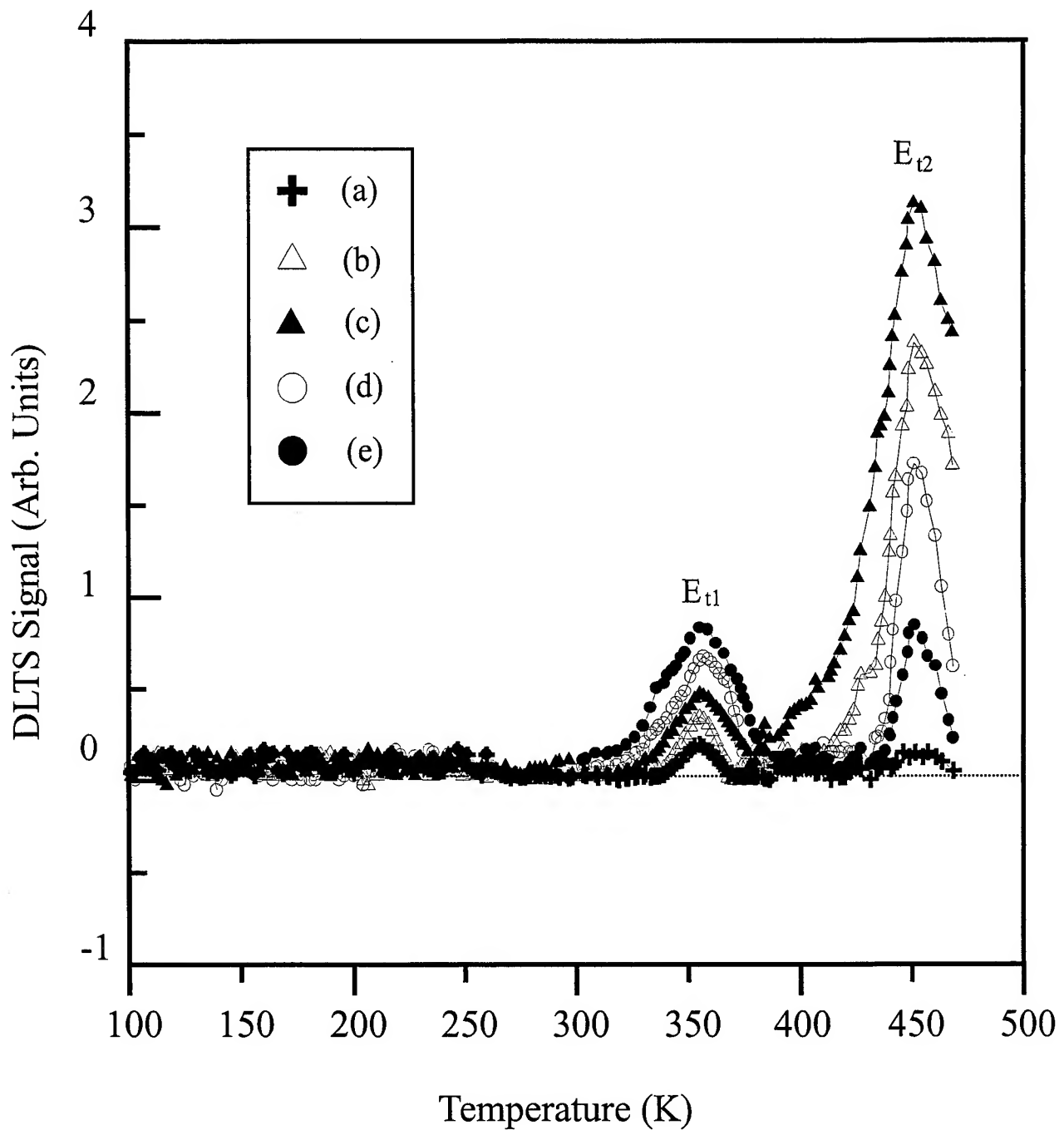


Fig. 3. DLTS signals of different doses of γ -ray-irradiated Au/GaN Schottky diodes. Curve (a) represents the pre-irradiated sample. Curves (b) ~ (e) correspond samples treated by 1, 4, 8, and 12 Mrad (GaN) of γ -ray irradiation.

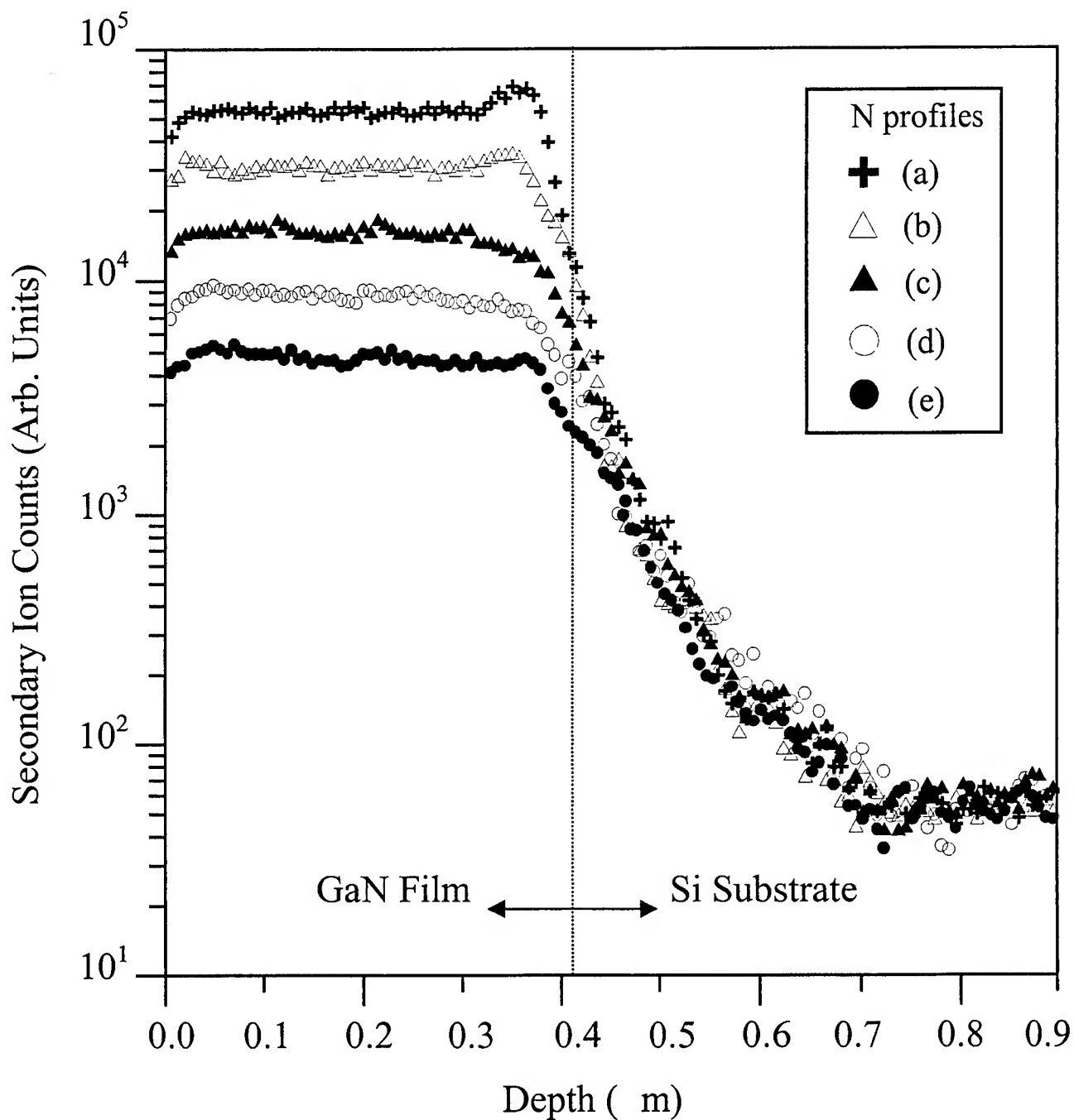


Fig. 4. SIMS depth profiles of N on GaN (epilayer)/GaN (buffer)/p⁺-Si devices with different doses of γ -ray irradiation. Curve (a) represents the pre-irradiated sample. Curves (b) ~ (e) correspond samples treated by 1, 4, 8, and 12 Mrad (GaN) of γ -ray irradiation.

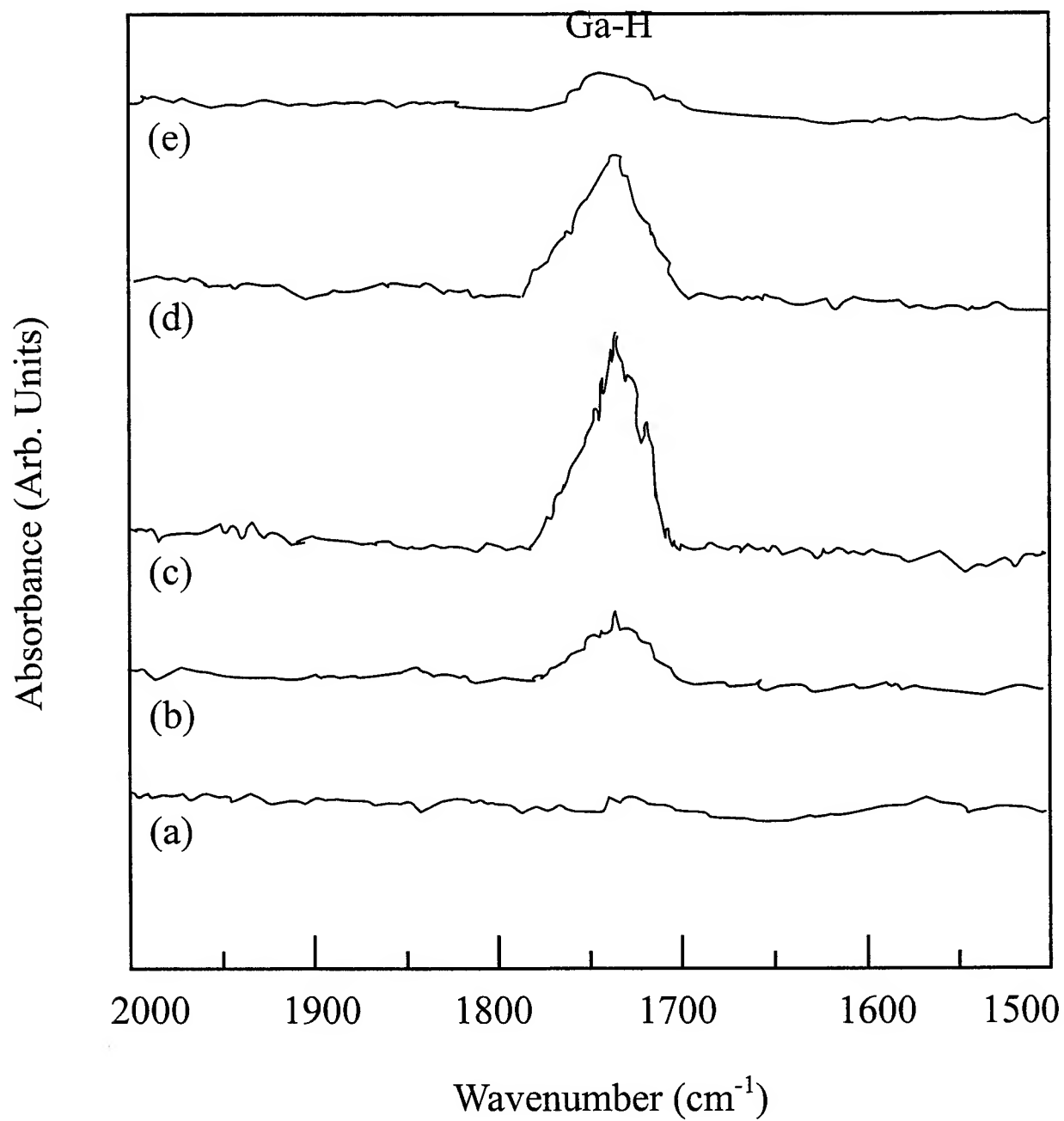


Fig. 5. FTIR spectra for sputtered-GaN thin films with different doses of γ -ray irradiation. Curve (a) represents the pre-irradiated sample. Curves (b) ~ (e) correspond samples treated by 1, 4, 8, and 12 Mrad (GaN) of γ -ray irradiation.

Etch of gallium nitride and other III-V materials using a novel high-density plasma configuration

Tsung-Nane Kuo, Jui-Hung Yeh, Hong-Ji Lee, Ching-An Chen,
Guang-Kai Jeng*, and Ching-Piao Lin

Nano-Architect Research Corporation,
1F, No.5-2, Industry E. Rd. IX,
Science-Based Industrial Park, Hsinchu, Taiwan

ABSTRACT

Implementation of a novel high-density plasma configuration has led to high etch rates of various opto-electronic device structures. The etch rate for multiple quantum well GaN/GaN structures exceeds 7500Å/min, and that for AlGaInP/GaInP structure is over 4.5 micron/min with near-vertical profile. Discussion will cover the analysis of the etch-rate, micro-morphology, etch-profile and selectivity with respect to the influence by various process parameters. Deep-etch for over 20 microns with photoresist as the protection layer has been achieved, which resulted in nearly 90-degree profile.

Keywords: high density plasma(HDP), inductively coupled plasma(ICP), dry etch, deep-etch, GaN/GaN, AlGaInP/GaInP, III-V semiconductor, HBT, VCSEL, LED/LD

1. INTRODUCTION

In the past two decades, III-V compound semiconductor materials have long been pursued and playing key roles in the field for optical-electronics. These include, but not limited to, laser in long-distance fiber communications, high-speed photo-detectors and displays.¹⁻³⁸ Successful development of gallium nitride (GaN) materials together with its related hetero-junction structures operating in the blue and UV region made it possible for laser and light emitting diodes devices of the same spectral range.¹⁻⁵ Applications include full-spectral range display and high-density optical disks. Processing for III-V and III-nitride materials and related device reaches a new frontier and encountered new challenges. This is attributed primarily to very rapid growth and unprecedented high demands in wide-band optical and wireless communications. Etch for III-V and III-nitride materials plays a key part in advanced device processing and related technologies. Structural complication in electronic communication devices, such as those in hetero-junction bipolar transistor (HBT) and high electron mobility transistors (HEMT); highly chemically inert bonds, such as those in gallium nitrides (GaN); highly differential lateral etching characteristic, such as those in vertical cavity surface emitting laser (VCSEL) all represent new challenges towards the new millennium. Etch of III-V and III-nitride compound materials using high-density plasma will be discussed in this paper.

2. EQUIPMENT SETUP AND EXPERIMENTS

Design of high-density plasma source, as well as related applications for etch and chemical vapor deposition (CVD) has been great efforts in Nano-Architect Research Corporation (or NARC to be used in the following context) in Hsinchu Science Industrial Park, Taiwan. An innovative plasma source categorized as inductively coupled plasma (ICP), which subsequently led to various transformations, has been used for research works to be discussed in this paper. The current version of source design can support high-density plasma in a 12" chamber with good uniformity. An automatic controlled load-lock (L/L), with a shuttle-robotic transporting mechanism, is annexed to the process chamber, which handles the transportation of the substrate, or a tray that carries a multiplicity of substrates back and forth between the L/L and the process chamber. A slit valve is used for vacuum isolation between the chamber and the L/L. A custom-designed ICP chamber contains a VAT series-64 medium-size throttle valve with its PM-5 controller, linked with one set of MKS-628 manometer capacitor gauge to form the downstream control loop. The upstream process contains 8 sets of MKS mass flow controller, gauges and regulators. The process chamber has a pumping package consisting of one medium-size turbomolecular pump backed up with one rotary pump or dry pump. The L/L has one dedicated rotary pump, this is to

* Electronic mail: narc@dressler.com

avoid cross contamination otherwise by the process chamber. A unique design of the process chamber makes very high pumping throughput capability possible. Thus the chamber is capable of processing at 1 mTorr at 25-30 standard cubic centimeter per minute (sccm) of gas injection. It is important for this high-pumping throughput capability for a number of certain etch applications. The inductively coupled high-density plasma, or ICP-HDP, is powered by one set of CESAR 1312 RF generator by Dressler, which is capable of delivering 1,200 watt of continuous power at 13.56 MHz. The wafer, on the bias platen, is biased by one set of Dressler CESAR 136, which is capable of delivering 600 watt of RF power at 13.56 MHz. Both RF generators are typically tuned to zero reflection level and are free of interference. Power level for the ICP-HDP used for processes to be discussed in this paper ranges between 600 watts to 850 watts. A bias mode was selected and used for platen bias application, which reads bias voltage rather than bias power. The DC bias voltage used in this research work fell between 100 volts and 250 volts. Various gas combinations were used for different groups of materials. Chlorine-based gases were used for etch of all materials to be discussed including those contains GaAs, GaN/GaN_{0.9}In_{0.1}N, and InP. Additives such as BCl₃, nitrogen and argon were added for observations of certain phenomena. Operating pressure through out these experiments was kept between 1 mTorr and 25 mTorr. HDP power was coupled into the process chamber through a ceramic window sealed at the top of the 12" chamber. Lanmuir probe confirms the plasma density ranges between high-10¹⁰ ion/cm³ to high-10¹¹ ion/cm³ between the operating conditions.

3. RESULTS AND DISCUSSION

ETCHED SURFACE MORPHOLOGY ON GALLIUM-NITRIDE

Gallium nitride has been widely used for blue LED/LD devices. Material stability, direct wide-band-gap nature are the most precious assets among all materials against harsh chemical and radiation environment, that make it suitable for high power applications with good figure of merits. Unfortunately, chemical inertness of this material makes etching process a challenge.

Etch of III-nitride materials has been pursued and discussed by many groups.¹⁻²¹ Most of these discussions were focused on the binary alloys – mostly on gallium nitride (GaN) and some on indium nitride (InN). Etch of ternary structured, GaInN, are scarcely discussed. It is understood that the GaInN ternary structure plays a very important role in devices applications. For device applications, such ternary alloy is not only necessary but a must. Etch of the ternary system becomes a very important process for devices development. Although past discussions have covered etch rates and the comparison thereof between various binary systems. The authors would like to point out that in the GaInN ternary system, complication problems arise when it is etched by plasma. Sharp needle-shaped or thorn-like textured surfaces have been frequently observed. The shape and density of the texture depend on the etching parameters. These needle-shaped or thorn-like textured arrays are attributed as the result of incomplete removal of compositional atoms left behind the etched surface, or due to non-optimized etching processes. Insufficient removal of the surface layer become micro-mask that can inhibit the underneath layers from being etched. Surface morphology depends strongly on the initial micro-mask shape and size as well as how the etching chemical species react with species within the underneath layers to be etched.

In general, chlorine-based chemistry is used for the etching of gallium nitride, and methane-based chemistry is used for the etching of indium nitride. Up so far, discussion on plasma etching for indium gallium nitride (InGa_{0.9}N) ternary material has been limited. Although general discussions, such as etch rates or Auger Electron Spectroscopy (AES) have been analyzed and discussed. Details in surface morphology have not been reported and related mechanism has not been discussed. In this section, we would like to demonstrate some etched phenomenon that were observed in our laboratory, based on these, we would like to further propose some hypothesis to share with the readers.

It is generally known that etching indium(In)-based materials with chlorine-based chemistry results in the formation of InCl_x, where x = 2 or 3, both are chemical compounds with low volatility. Faster etch rates have been reported and widely accepted by using modified chemistries. Taking the following structure as an example; it is a typical device structure known for blue LED. It consists of a top p-type GaN clad-layer of approximately 0.4-0.5 micron, followed by an InGa_{0.9}N layer of approx. 0.1 micron which contains 20-30% of indium, followed by a multiple GaN quantum wells followed by the lower layers, etc. Our observation showed that when chlorine chemistry is used for etch of this device, the first layer, GaN, is etched with no difficulty. The second layer that contains InGa_{0.9}N, where indium composition is 0.2-0.3 (or 20-30%), is possibly preferentially etched only for its GaN component. This leaves behind the 20-30% of indium, or a fraction of this element, to react with chlorine and forms low-volatile InCl_x compound and reside on the surface, resulting a masking effect and avoid the following layers from being etched.

Assuming that the indium atoms are homogeneously distributed among the InGa_N layer (this is reasonable hypothesis for a qualified epitaxially grown material), the distribution of InCl_x compound left on the surface is uniformly distributed accordingly. Each such tiny mask is surrounded by gallium and nitrogen atoms and mostly of which are theoretically removable in a chlorine-based chemistry.

We conducted a number of such experiments to find the clues of consistency between the hypothesis we made and the experiment results. Figure 1 shows the sample morphology etched with chlorine-based chemistry, which resulted in long-needle cross-section surface. It is interesting to find that the needle starts to form at approximately 0.4 micron below the initial surface. This phenomenon shows that it is highly possible that the InCl_x compound plays the role of nano-size mask, which prohibits the masked areas underneath from being etched.



Figure 1. Cross section of GaN/GaN_N after etching with chlorine-based chemistry, resulted in long-needle texture surface.

Figure 2 shows the obviously improved surface morphology, which was etched with a modified chemistry developed by NARC research group. Long-needle texture disappears and is replaced by short thorn-shaped texture surface, where the lengths of thorns as shown in Figure 3 are substantially reduced from that of the needles. Figure 4 shows the sample surface etched with recipe maturely developed in our laboratory, surface morphology is further and greatly improved and results in a smooth surface. With the recipe fine tuned, a near-polished surface can be consistently obtained. Since a protection of intellectual property is being pursued for these etching techniques, detailed process and data are not disclosed at this stage.



Figure 2. SEM micrograph of GaN/GaN with thorn-shaped texture



Figure 3. Thorn-shaped surface morphology of GaN/GaN after etching process.

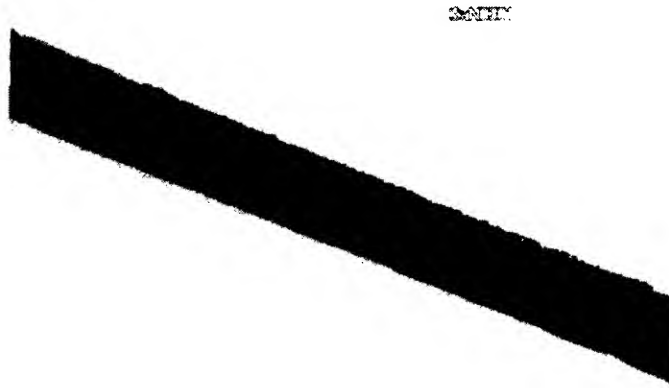


Figure 4. Smooth surface morphology of GaN/GaN_N after etching process.

PREFERENTIAL LATERAL ETCH ON III-V COMPOUND MATERIALS

Deep-etch using high-density plasma has potentially important applications. Among others, Vertical Cavity Surface Emitting Laser (VCSEL) is one, and optical sensor is another. Most devices, optical or electronic, are composed of hetero-junction structures, i.e., by controlling the contents of elemental components, viz. that of the group III or group VI elements.²²⁻³⁸ By using this technique, precise lattice match can be achieved and accurate band-gap requirement can be tuned simultaneously. Control of band-gap is important for the design of optical devices, since it is the key parameter on which the emission of the optical wavelength can be controlled. The same technique is also important for the design of communication chips, most of which are based on the hetero-junction structures. Carrier confinement efficiency can greatly influence the device performance. Some simple structures consists of three to five of such hetero-junction layers; while complicated ones can consist up to tens or even hundreds of such layers. Plasma etch has been used extensively for device patterning, and VCSEL is one of such applications. More recently, the same technique has been implemented to create mirror facets on edge-emitting lasers; this is to replace the existing facet-cleaving technique. Such applications, once successful, has great impacts on optical communications, since wafer cleaving will be no longer needed, and multiple-chip on a single wafer can be processed towards the final products stage. This can greatly simplify optical /electronic devices combination and integration.

Unequal lateral etch rate is commonly encountered in the hetero-junction structures, which is undesirable for some applications and unacceptable for many high-end devices applications. Multiple pairs of GaAs/GaAlAs have been used in VCSEL structures, and differential etch rate between GaAs and AlGaAs layers were commonly seen due to inherit nature of materials. This preferential etch rate causes saw-tooth edge profile on the etched wall, which can lead to device defects, poor performances and laser efficiency. It is clear that to make high quality devices, preferential lateral etch as this must be avoided and eliminated.

Research works conducted at NARC has led to the success for etching of 20-40 pairs of alternating layers consisting of GaAs/AlGaAs hetero-junction structures to make a cylindrical cavity with nearly 90 degree vertical wall angle. Preferential lateral etch-rate between GaAs and AlGaAs has been reduced to an unnoticeable level by the use of techniques developed in our laboratory.

DEEP ETCH FOR III-V COMPOUND MATERIALS

Deep-etch has been widely used for silicon-based materials for Micro Electrical Mechanical System (MEMS) applications. Unlike silicon-based materials, where the deep-etch is conducted mostly on silicon substrates where there is no concern

about the complication of junction structure need to be taken care of, late advances in communications technologies for wide-band, optical and wireless applications have led to very rapid growth in the demands of complicated chip processing techniques using III-V compound materials; this is in contrast to that of silicon. Demands for deep-etch for III-V compound materials see a number of important new applications; yet challenges arise in that the etched materials contain certain complicated epitaxial layers such that preferential lateral etch effect must be avoided. One of such examples, to be demonstrated in the following section, shows the possibility of extending this technique for various futuristic processing techniques.

AlInGaP/GaInP with multiple layers of quantum-well structure has been widely used for laser and high-efficiency LED. One of the difficulties is in the brittleness of the epitaxial layers that can cause serious chipping or completely peeled-off when the devices are being diced using conventional dicing saw. To avoid this difficulty, approaches have been pursued -- to cut the epitaxy layers by implementing high-density plasma. As the devices are composed of large number and complicated epitaxial layers, each varies in combination of parameters and composition of contents -- aluminum (Al), indium (In), gallium (Ga) and phosphorous (P). Cutting through these layers requires very good control of the plasma with high stability and reliability, and above all, requires the control of preferential lateral etch. These layers, as shown in Figure 5, are composed of 25-micron-deep epitaxial layers, which need to be cut completely through at high etch rates, and preferably at near 90-degree angle with nearly no preferential lateral etch rate. More important of all, excellent optical and electrical performances must be secured after the completion of the etch process.

At NARC, the authors have successfully developed an etching technique, which is capable of cutting through the epitaxial layers of 25 micron deep at an etch rate of 4.5 micron/min at nearly 90-degree angle. Figure 5 is an SEM photo showing a 10-micron-deep trench etched from a large number of hetero-junction epitaxy layers. This is a preliminary demonstration of the ICP-HDP for high-rate etch application of the III-V compound materials among many others.

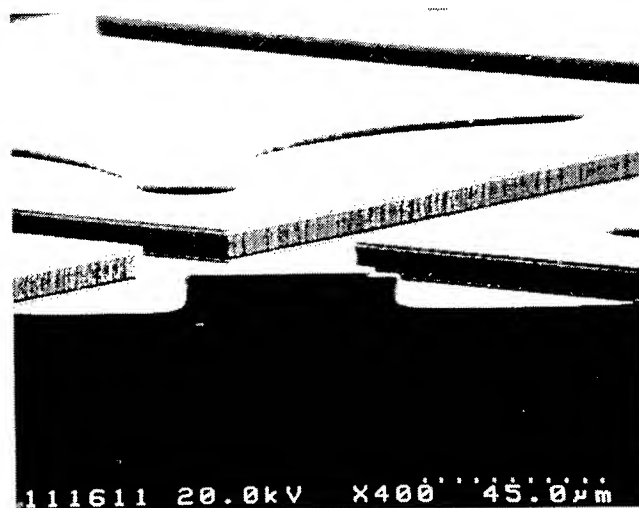


Figure 5. SEM micrograph of AlInGaP/GaInP multiple hetero-layer structure after deep-etch.

4. CONCLUSIONS

High-density plasma equipment will become a very important tool for the process of III-V and III-nitride compound semiconductor materials and devices in the future. Its applications cover from devices patterning to the replacement of chip dicing. HDP etch to replace conventional chemical etch processes is greatly beneficial to environmental protection, and cost consideration in the long run. HDP etch is superior to conventional plasma and conventional chemical etch in many

aspects such as the anisotropy, the etch rates, chemical consumption, especially in the control of preferential lateral etch rates, etch of inert materials such as III-nitride materials.

In this paper, we present several examples conducted at NARC showing interesting and important applications that can bring up with potentially high added values, or applications that are otherwise impossible if conventional methods are used. We would like to point out that etch with HDP is not only a replacement of conventional techniques, but rather a new technique that is used to conquer the new frontiers yet to arrive where conventional technique can never reach. These are a few such examples demonstrated by the authors to show new applications of HDP for the processing of III-V and III-nitride compound materials. HDP also differs from conventional plasma techniques in many aspects; it is important that with advantages of the HDP, it must be properly designed to meet with the right applications in order that the highest added values can be reached.

5. ACKNOWLEDGMENTS

The authors would like to thank Ms. Y.C.Twu, Mr. C.P.Chaung and Prof. S.L.Yang of Electrophysics Dept., National Chiao Tung University, for their kind assistance in the scanning electron microscopy (SEM) of the samples.

6. REFERENCES

1. R. F. Davis, *Proc. IEEE* 79, p. 702, 1991.
2. B. Goldenberg, J. D. Zook, and R. J. Ulmer, *Appl. Phys. Lett.* 62, p. 381, 1993.
3. J. S. Foresi and T. D. Moustakas, *Appl. Phys. Lett.* 62, p. 2859, 1993.
4. M. A. Khan, J. N. Kuznia, A. R. Bhattacharai, and D. T. Olson, *Appl. Phys. Lett.* 63, p. 1214, 1993.
5. T. L. Tansley and R. J. Egan, *Physica B* 85, p. 190, 1993.
6. G. F. McLane, L. Casas, S. J. Pearton, and C. R. Abernathy, *Appl. Phys. Lett.* 66, p. 3328, 1995.
7. R. J. Shul, S. P. Kilcoyne, M. Hagerott Crawford, J. E. Parmeter, C.B. Vartuli, C. R. Abernathy, and S. J. Pearton, *Appl. Phys. Lett.* 66, p. 1761, 1995.
8. L. Zhang, J. Ramer, J. Brown, K. Zheng, L. F. Lester, and S. D. Hersee, *Appl. Phys. Lett.* 68, p. 367, 1996.
9. A. Tempez, N. Medelci, N. Badi, I. Berishev, D. Starikov, and A. Bensaoula, *J. Vac. Sci. Technol. A* 17, p. 2209, 1999.
10. Y. H. Lee, H. S. Kim, G. Y. Yeom, J. W. Lee, M. C. Yoo and T. I. Kim, *J. Vac. Sci. Technol. A* 16, p. 1478, 1998.
11. S. J. Pearton, C. R. Abernathy, and F. Ren, *Appl. Phys. Lett.* 64, p. 2294, 1994.
12. R. J. Shul, C. G. Willison, M. M. Bridges, J. Han, J. W. Lee, S.J. Pearton, C.R. Abernathy, J.D. MacKenzie, S.M. Donovan, L. Zhang, and L.F. Lester, *J. Vac. Sci. Technol. A* 16, p. 1621, 1998.
13. S. J. Pearton, C. R. Abernathy, J. D. MacKenize, S. M. Donovan, L. Zhang, and L. F. Lester, *J. Vac. Sci. Technol. A* 16, p. 1621, 1998.
14. H. Lee, D.B. Oberman, and J.S. Harris Jr., *Appl. Phys. Lett.* 67, p. 1754, 1995.
15. G. Franz and F. Rinner, *J. Vac. Sci. Technol. A* 17, p. 56, 1999.
16. C.B. Vartuli, S.J. Pearton, C.R. Abernathy, R. J. Shul, A.J. Howard, S.P. Kilcoyne, J.E. Parmeter, and M. Hagerott-Crawford, *J. Vac. Sci. Technol. A* 14, p. 1011, 1996.
17. C.B. Vartuli, S.J. Pearton, J. W. Lee, J. Hong, J. D. MacKenize, C. R. Abernathy, and R. J. Shul, *Appl. Phys. Lett.* 69, p. 1426, 1996.
18. S.J. Pearton, C.B. Vartuli, R.J. Shul, and J.C. Zolper, *Materials Sci. & Eng. B* 31, p. 309, 1995.
19. C. Youtsey, I. Adesida, and G. Bulman, *Electron. Lett.*, 33, p. 245, 1997.
20. A.T. Ping, I. Adesida, and M. A. Khan, *Appl. Phys. Lett.* 67(9), p. 28, 1995.
21. M. Jalonen, M. Toivonen, J. Kongas, A. Salokatve and M. Pessa, *Electron. Lett.*, 33, p. 1985, 1997.
22. J. Hong, J.W. Lee, E.S. Lambers, C.R. Abernathy, C.J. Santana, S.J. Pearton, W.S. Hobson, and F. Ren, *J. Electron Materials*, 25(9), p. 1428, 1996.
23. G.J. Van Gorp and J.M. Jacobs, *Philips J. Res.* 44, p.211, 1989.
24. F. Ren, J.R. Lothian, J.M. Kuo, W.S. Hobson, J. Lopata, J.A. Caballero, S.J. Pearton, and M.W. Cole, *J. Vac. Sci. Technol., B* 14, p. 1758, 1996.
25. S.J. Pearton, *J. Vac. Sci. Technol., A* 12, p. 1966, 1994.

26. R.J. Shul, R.P. Schneider, Jr., and C. Constantine, *Electron. Lett.*, **30**, p. 817, 1994.
27. S. Miyakuni, R. Hattori, K. Sato, H. Takano, and O. Ishihara, *J. Appl. Phys.*, **78**(9), p. 5734, 1995.
28. J.W. Lee, J. Hong, and S.J. Pearton, *Appl. Phys. Lett.*, **68**(6), p. 847, 1996.
29. J.W. Lee, S.J. Pearton, C.J. Santana, J.R. Mileham, E.S. Lambers, C.R. Abernathy, F. Ren, and W.S. Hobson, *J. Electrochem. Soc.* **143**, p. 1093, 1996.
30. J.W. Lee, J. Hong, E.S. Lambers, C.R. Abernathy, S.J. Pearton, W.S. Hobson, and F. Ren, *J. Electrochem. Soc.* **143**, p. 2010, 1996.
31. Y.T. Kim, and C.W. Lee, *J. Appl. Phys.* **76**, p. 542, 1994.
32. I. G. Thayne, K. Elgaid, M. R. S. Taylor, M. C. Holland, S. Fairbairn, N. I. Cameron, S. P. Beaumont and G. Belle, *Electro. Lett.* **31**, p. 324, 1995.
33. J. W. Lee, J. Hong, E. S. Lambers, C. R. Abernathy, S. J. Pearton, W. S. Hobson and F. Ren, *J. Electrochem. Soc.* **143**, p. 2010, 1996.
34. R. J. Shul, G. B. McClellan, R.D. Briggs, D. J. Rieger, S. J. Pearton, C. R. Abernathy, J. W. Lee, C. Constantine and C. Barratt, *J. Vac. Sci. Technol. A* **15**, p. 633, 1997.
35. D. C. Hays, H. Cho, K. B. Hahn, C. R. Abernathy, S. J. Pearton, F. Ren and W. S. Hobson, *Appl. Surf. Sci.* **147**, p. 126, 1999.
36. S. Agarwala, O. King, S. Horst, R. Wilson, D. Stone, M. Dagenais, and Y. J. Chen, *J. Vac. Sci. Technol. A* **17**, p. 52, 1999.
37. F. Ren, J. R. Lothian, J. M. Kuo, W. S. Hobson, J. Lopata, J. A. Caballero S. J. Pearton, and M.W. Cole, *J. Vac. Sci. Technol. B* **14**, p. 1758, 1996.
38. N. Vojdani, and P. Parrens, *J. Vac. Sci. Technol. B* **5**, p. 1591, 1987.

SESSION 4

Quantum Dots: Growth, Devices, and Applications

Quantum dot carrier dynamics and far-infrared devices

Pallab Bhattacharya^a, Sanjay Krishna^a, Jamie D. Phillips^a, David Klotzkin^a and Patrick J. McCann^b

^a Solid State Electronics Laboratory, Dept. of Electrical Engineering and Computer Science,
University Of Michigan, Ann Arbor, MI -48109

^b School of Electrical and Computer Engineering, Laboratory for Electronic Properties of Materials,
University of Oklahoma, Norman, OK 73019-1023

ABSTRACT

Carrier dynamics in self-assembled quantum dots, grown by molecular beam epitaxy, have been studied. The temperature dependence of the relaxation times, measured by room temperature high frequency impedance response of quantum dot lasers and by low temperature ($T=4K$) differential transmission spectroscopy, strongly suggests that electron-hole scattering is the dominant scattering mechanism in quantum dots. The favorable relaxation times can be exploited to realize far infrared emission and detection based on intersubband transitions in the dots.

1. INTRODUCTION

Optoelectronic devices, with quantum dots (QD) in the active region, have been investigated in great detail in the past decade^{1,2,3}. Even though it has been known for a long time that zero dimensional systems would yield enormous advantages due to their singular atomic like density of states function⁴, there have always been practical limitations to the fabrication of such small structures in the laboratory. To observe quantum confined effects, the carriers need to be spatially confined to less than the De-Broglie wavelength of electrons ($\sim 200\text{-}250 \text{ \AA}$ in most semiconductors) along all three directions. Recently, formation of these quasi-zero dimensional systems has been enabled by self-organized or self-assembled epitaxy using molecular beam epitaxy (MBE) and metal organic chemical vapor deposition (MOCVD)⁵. It has been shown⁶ that if the lattice mismatch between the substrate layer and the epitaxial layer exceeds 1.8 %, then the growth proceeds by the initial formation of a strain relieving two dimensional wetting layer followed by a three dimensional island formation (Stranski-Krastonov growth mode). The equilibrium adatom kinetics energetically favors the formation of these self assembled quantum dots instead of the two dimensional layer by layer growth that is preferred in unstrained systems. These islands are typically lens shaped with a base dimension of $\sim 200\text{\AA}$ and a height of $\sim 70\text{\AA}$. A high-resolution cross-sectional transmission electron microscopy (XTEM) image of a single dot grown by solid source MBE is shown in Figure 1.

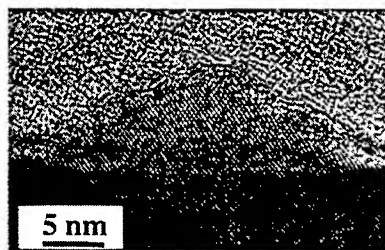


Fig. 1: (a) High resolution TEM image of a single self organized quantum dot grown by deposition of 16 periods of 0.25 ML InAs/0.25 ML GaAs, separated by 5s pauses.

High performance optoelectronic devices as lasers¹, modulators² and detectors³ have already been demonstrated using self-assembled quantum dots. The emission wavelength from these dots has been tuned from $\sim 0.6 \mu\text{m}$ to the technologically important wavelengths of $1.3 \mu\text{m}$ ⁷ and $1.55 \mu\text{m}$ ⁸ by alteration of the growth procedure and the in-situ modification of the cap layer used for covering the dots⁹. Recently, an ultralow room temperature continuous wave threshold current of 19 A/cm^2 has been reported for a $1.3\mu\text{m}$ edge emitting QD laser¹⁰. This is already a factor of two lesser than the lowest threshold currents reported in QW lasers. Far infrared detectors, based on intersubband and bound to continuum transitions in quantum dots, have also been demonstrated^{11,12}. Unlike quantum wells, quantum dot detectors are sensitive to

* Correspondence: Email: pkb@eecs.umich.edu, Telephone: 734 763 6678 Fax: 734 763 9324

normal incidence radiation and this makes them highly suitable for focal plane array applications. We have also recently reported far infrared emission, which we believe, is based on intersubband transitions in quantum dots¹³.

To realize the entire potential of these dots, their carrier dynamics needs to be understood in great detail. It has been found that the measured carrier relaxation times and the plausible scattering mechanisms involved in quantum dots are very different from the conventional optical phonon dominated scattering in quantum wells. A manifest indication of this difference lies in the vast increase in the modulation bandwidth of QD lasers at cryogenic temperatures, hitherto unobserved in QW lasers. This paper seeks to understand the carrier dynamics in self assembled quantum dots and exploit the favorable relaxation times to obtain far infrared intersubband sources and detectors.

2. ENERGY LEVELS AND RELAXATION TIMES IN SELF-ASSEMBLED QUANTUM DOTS

All the samples mentioned in this work comprise of In(Ga)As/GaAs dots that were grown in the Stranski-Krastonov growth mode using a solid source MBE system. A typical heterostructure of a multiple layer quantum dot laser is shown in Figure 2. The GaAs and the AlGaAs are grown at 620°C and 660°C respectively whereas the dots are grown at 530°C. The details of the growth procedure have been discussed elsewhere¹⁴.

0.1 μm GaAs	$p = 1 \times 10^{19} \text{ cm}^{-3}$
0.3 μm GaAs	$p = 5 \times 10^{18} \text{ cm}^{-3}$
1.0 μm $\text{Al}_{0.3}\text{Ga}_{0.7}\text{As}$	$p = 5 \times 10^{17} \text{ cm}^{-3}$
0.1 μm GaAs	
3.5 ML $\text{In}_{0.4}\text{Ga}_{0.6}\text{As}$	
15 \AA GaAs	
7 ML $\text{In}_{0.4}\text{Ga}_{0.6}\text{As}$	
0.1 μm GaAs	
1.0 μm $\text{Al}_{0.3}\text{Ga}_{0.7}\text{As}$	$n = 5 \times 10^{17} \text{ cm}^{-3}$
0.5 μm GaAs	$n = 5 \times 10^{18} \text{ cm}^{-3}$
N+ GaAs Substrate	

Figure 2: Schematic of a five layer $\text{In}_{0.4}\text{Ga}_{0.6}\text{As}/\text{GaAs}$ quantum dot laser heterostructure grown by solid source molecular beam epitaxy (MBE)

Due to the three dimensional confinement, bound states are formed both for the electrons in the conduction band and for holes in the valence band. The strain distribution in the dots has been calculated using a valence force field model proposed by Martin and Keating and the electronic energy levels have been calculated using a 8 band k.p model¹⁵, which takes into account even the effect of the remote bands on the bandstructure. The electronic energy levels calculated for a pyramidal shaped InAs/GaAs quantum dot, with base dimensions of 181 \AA and height of 45 \AA is shown in Figure 3(a). The calculated band gap is ~ 1.2 -1.3 eV as compared to the bulk band gap of 0.35 eV for InAs. This shows the large effect of strain on the bandstructure. The energy spacing between the ground state and the first excited state in the conduction band and valence band is ~ 60 meV and ~ 20 meV respectively. Photoluminescence and electroluminescence measurements on these dots show distinct evidence of excited state in the dots (Figure 3(b)) and the intersubband spacing obtained from these experiments agree very well with the results obtained from the 8 band k.p theory.

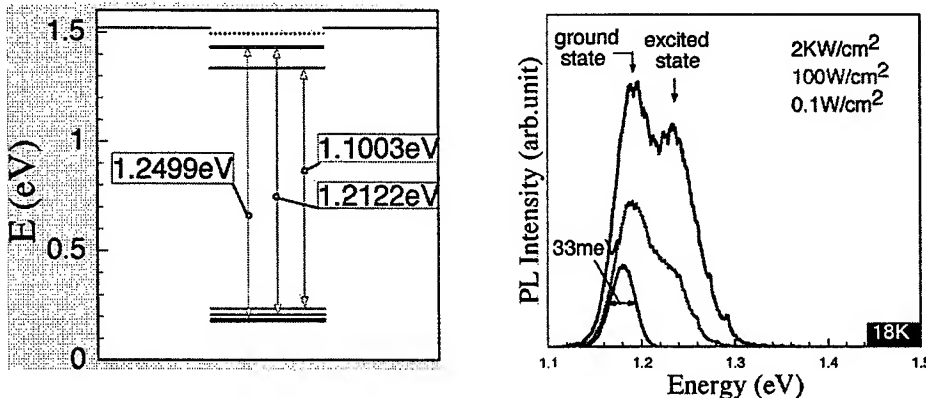


Figure 3: (a) Calculated electronic energy spectrum of InAs/GaAs quantum dot with base dimension of 181 \AA and height of 45 \AA using 8 band k.p model, (b) low temperature photoluminescence from a self assembled InGaAs/GaAs quantum dot

The carrier dynamics in the quantum dots is very different from the dynamics in quantum wells. Theoretical studies suggest the existence of a "phonon bottleneck" in quantum dots. Since the intersubband spacing in the dots is greater than the

LO phonon energy, the excited state and the ground state are phonon decoupled. This prevents their relaxation by a single phonon emission, a process that dominates scattering in quantum wells. Since multiphonon events require the satisfaction of a stringent resonant condition, they are very slow (>1 ns). Thus due to suppressed phonon scattering in quantum dots, the intersubband relaxation time in quantum dots is expected to be much longer in quantum dots. However, there have been other mechanisms that have been suggested in quantum dots like an auger-like scattering, in which a relaxing electron transfers energy to another electron that is promoted to the continuum or an electron-hole scattering, in which an excited state electron transfer energy to a ground state hole.

Direct measurement of the carrier relaxation times in self-assembled quantum dots was done using differential transmission spectroscopy (DTS) measurements at cryogenic temperatures¹⁶. In this measurement, carriers were created in the barrier using a pump beam and the carrier populations of the first excited state and the ground state of the dot was measured using a probe beam. The capture time from the barrier to the first excited state was measured to be 1-3 ps whereas the relaxation time from the excited state to the ground state was found to be 5.6 ps. This is much smaller than the relaxation times predicted solely on the basis of phonon scattering. This suggests that alternative scattering mechanisms exist that enable the excited state carriers to relax to the ground state.

Since the carrier densities in these measurements were very low (0.2 electron-hole pairs per dot), Auger-like scattering can be ruled out. The most likely mechanism is electron-hole scattering. A relaxation time of 10 ps was calculated from the barrier to the ground state of the dot based on an electron hole scattering and this agrees very well with the measured value of 8 ps from the DTS measurements. The mechanism for electron hole scattering is depicted in Figure 4. An excited state electron scatters off a ground state hole promoting the hole to an excited state. Since the hole mass is heavier and the hole states are phonon coupled, the excited hole quickly relaxes back to the ground state. A hole relaxation time of 0.6 ps has been estimated in the DTS measurement. The rate of electron-hole scattering depends greatly on the excited hole population and a larger relaxation time is expected at higher temperatures, due to the lesser number of empty excited hole states to scatter into. We have measured a capture time of 30 ps at room temperatures by analyzing the high frequency impedance response of a quantum dot laser¹⁷. This agrees with the increase in the relaxation time at high temperatures as predicted by the electron hole scattering. The increased modulation response of a quantum dot laser is shown in Figure 4. In contrast, the relaxation times in quantum well lasers do not display such strong temperature dependence of the modulation bandwidth.

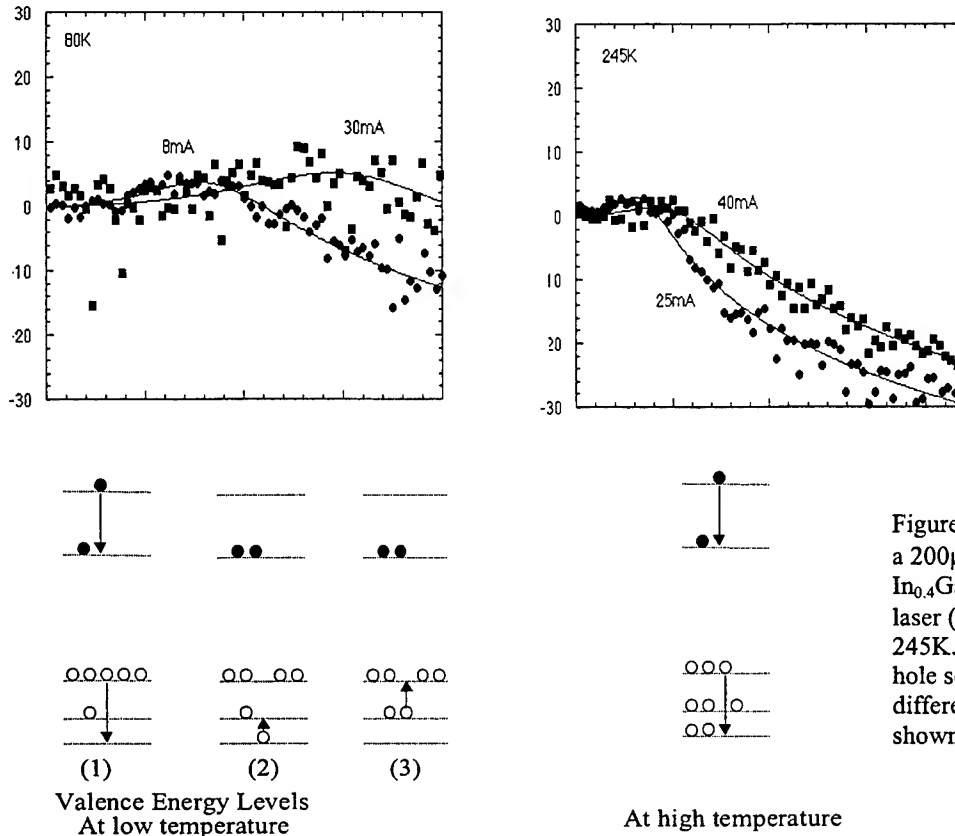


Figure 4: Modulation response of a 200 μ m long single-mode $\text{In}_{0.4}\text{Ga}_{0.6}\text{As}/\text{GaAs}$ 4-dot layer laser ($\lambda=1\mu\text{m}$) at (a) 80K, (b) 245K. The proposed electron hole scattering mechanism at different temperatures is also shown.

3. APPLICATION TO FAR INFRARED DEVICES

The large intersubband relaxation time poses a fundamental limit to the modulation bandwidth of quantum dot lasers. The largest modulation bandwidth in QD lasers has been measured to be about 7-8 GHz in contrast to the 30-40 GHz bandwidth obtained from GaAs based quantum well lasers. Alternative injection mechanisms like resonant tunneling into the ground state of the dots have been proposed. But the intersubband relaxation times in quantum dots can be favorably altered for applications in devices that are based on the intersubband transitions in the dots, such as far infrared sources and detectors. The lifetime of the excited state in the dot can be made even longer (\sim ns) using a unipolar device, in which there is essentially no electron-hole scattering. This can be very useful in intersubband detectors which require a very long lived excited state that does not allow the rapid relaxation of photogenerated carriers thereby enabling their efficient contribution to the photocurrent. In quantum well infrared photodetectors (QWIPs), the excited state carriers relax rapidly to the ground state (\sim 2-5 ps) and many of the photogenerated carriers do not contribute to the photocurrent. The performance characteristics of an intersubband detector based on quantum dots are discussed in the next section.

3.1 Far infrared detection using quantum dots

The advantage of a large intersubband relaxation time in QDs is most favorably utilized in a quantum dot infrared photodetector (QDIP). In a QDIP, the absorption of light raises electrons from the ground to the excited states and no holes are produced. Under these conditions, the relaxation time for the excited electrons to relax to the ground state is very long, of the order of several nanoseconds, since electron-hole scattering cannot take place. The longer relaxation times enable the photogenerated electrons to be collected more efficiently. If the intersubband relaxation time is small, as in the case of quantum wells, then the photogenerated carriers relax to the ground state before contributing to the photocurrent. Moreover, since the relaxation time in QDs increases with increase in temperature, quantum dots are attractive for high temperature detectors. It is to be noted that presently there are no room temperature photonic detectors in the range of 8-12 μ m, although these detectors are greatly required in atmospheric applications, night vision cameras and thermal imaging. Another major advantage of the quantum dot detector is its intrinsic sensitiveness to normal incidence radiation that is absent in quantum well detectors because of the polarization selection rule that requires a component of the incident electric field vector to lie along the growth direction. This makes quantum dots an ideal candidate for large area focal plane arrays.

Normal incidence QDIPs, with a 10 layer InAs/GaAs quantum dots as the absorption region, have demonstrated broad band detection around 8 μ m and 17 μ m, which we believe is based on the intersubband and subband to continuum transition respectively (Figure 5)¹¹. They have also demonstrated high detectivity and responsivity ($D^*=9-10 \times 10^9$ cmHz^{1/2}/W, $R=100$ mA/W, $T=40$ K) along with a large photoconductive gain ($g=12$). The performance characteristics of the detectors are summarized in Figure 5.

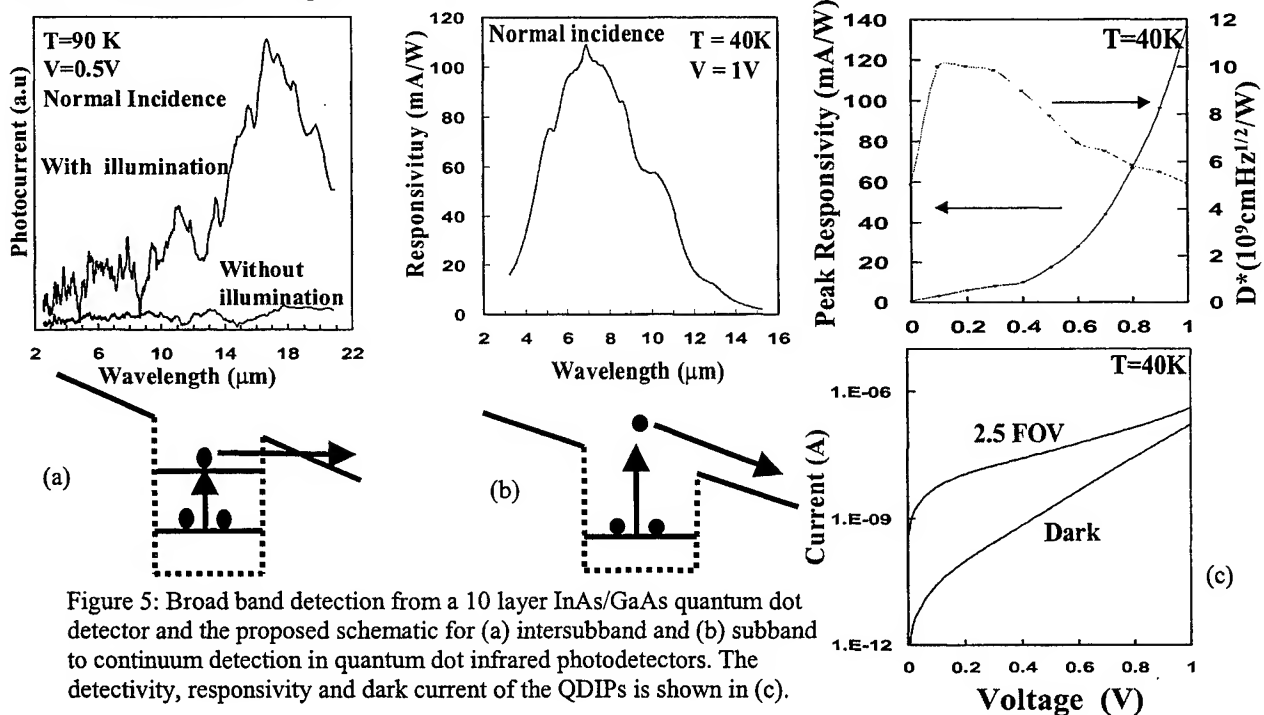


Figure 5: Broad band detection from a 10 layer InAs/GaAs quantum dot detector and the proposed schematic for (a) intersubband and (b) subband to continuum detection in quantum dot infrared photodetectors. The detectivity, responsivity and dark current of the QDIPs is shown in (c).

3.2 Far infrared emission from quantum dots

The relaxation times in the dots can also be altered to obtain far infrared emission based on intersubband and continuum to bound transitions. To observe intersubband transitions in the dot, favorable intersubband relaxation times are required. The relaxation times in self organized $\text{In}_{0.4}\text{Ga}_{0.6}\text{As}/\text{GaAs}$ dots are shown in Figure 6(a). We have measured long (30-50 ps) electron relaxation times from the continuum to the ground state at room temperature. Since the capture time from the continuum to the confined states is only a few picoseconds,¹⁸ the intersubband relaxation time can be estimated to be about 30-50 ps. This is supported by direct spectroscopic measurements. These large relaxation times invoke the possibility of intersubband lasing in quantum dots¹⁹. To achieve a population inversion between the ground state and the excited state in the dot, we need to have (a) a large intersubband relaxation time and (b) a very short lifetime for the ground state. The lifetime of the ground state of the dot in a quantum dot laser is inversely proportional to the number of modal photons present in the cavity ($\tau = \tau_r/n_{ph}$). Since switching from spontaneous emission to stimulated emission can increase the number of photons in the mode, the ground state lifetime can be reduced and the intersubband emission can be enhanced.

Far infrared measurements were performed on an interband ($\sim 1\mu\text{m}$) quantum dot laser at room temperature and 80K, and the emission was spectrally characterized using a Fourier transform infrared spectrometer. No FIR emission was observed when the laser was biased below threshold. However, as the threshold bias was reached, a broad peak, centered around $12\mu\text{m}$, was observed at $T=300\text{K}$ (Figure 6). We believe this peak is due to radiative transitions between the excited and the ground states in the dots. When the laser is biased above threshold, there is a build up of interband photons in the cavity. The electrons in the ground state of the dots are depleted at the stimulated emission rate ($\tau_{stim} \sim 5-10\text{ps}$) by the interband photons, leading to a more non-equilibrium intersubband population. Similar emission centered at $12\mu\text{m}$ was also observed at $T=80\text{K}$. However, at this temperature, the laser had to be biased well above interband threshold to observe the FIR emission. This could be due to the fact that the intersubband electron relaxation rate is much faster ($\tau \sim 5-6\text{ps}$) at lower temperatures. Therefore, a non-equilibrium population between the states is harder to achieve and maintain when the ground state population is depleted at approximately the same rate by interband lasing.

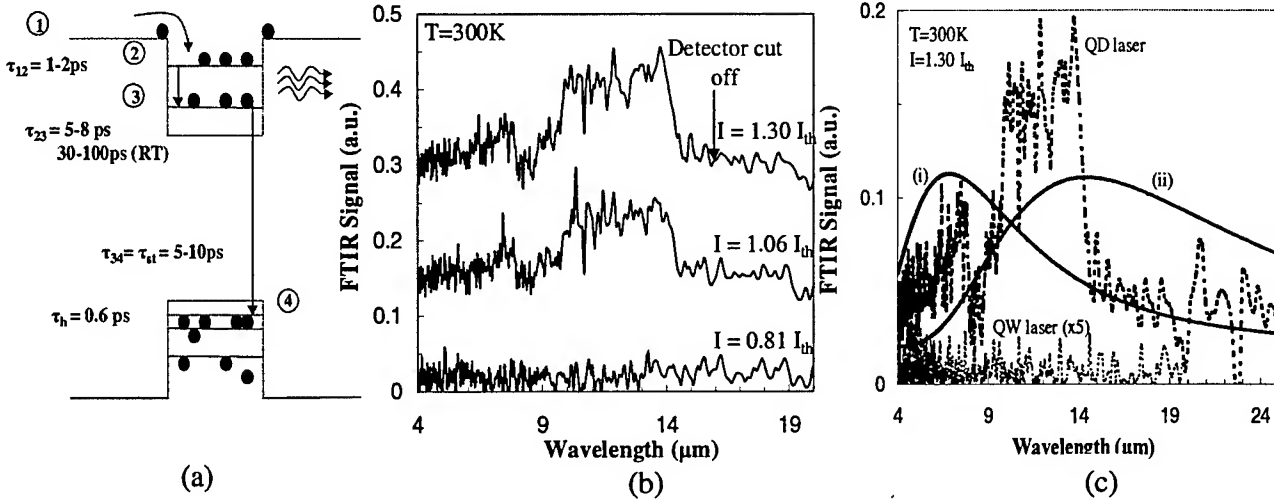


Fig.6: (a) Relaxation times measured in self organized $\text{In}_{0.4}\text{Ga}_{0.6}\text{As}/\text{GaAs}$ quantum dots, (b) enhanced spontaneous emission from self organized $\text{In}_{0.4}\text{Ga}_{0.6}\text{As}/\text{GaAs}$ quantum dot laser at $T=300\text{K}$ using a FTIR spectrometer, (c) radiation from a blackbody source at (i) $T=420\text{K}$ and (ii) $T=200\text{K}$, corresponding to heat sink temperatures of 300K and 80K , respectively. The dotted lines represent the room temperature FIR emission from the interband quantum dot laser. Also shown is the FIR response from a similar interband laser containing multiple quantum well layers.

To ensure that the observed peaks were not due to device heating, the data was analyzed by considering emission from a blackbody source. Using a value of $\Delta T=120^\circ\text{C}$, estimated by micro-Raman spectroscopy, the temperature in the laser mirrors is estimated to be about 420K and 200K when the heat sink is at 300K and 80K , respectively. The blackbody curve corresponding to these two temperatures is shown in Fig. 6 (c) along with the observed room temperature spontaneous emission from the interband QD laser. There is a large difference in the blackbody response between the two curves around $12\mu\text{m}$, where the FIR emission is observed. This suggests that the emission is not due to blackbody radiation from the

device. Furthermore, similar measurements performed on multi-quantum well lasers exhibited no FIR emission, as shown in Fig. 6 (c).

SUMMARY AND CONCLUSIONS

The unique carrier dynamics in self-assembled quantum dots has been discussed with emphasis on the intrinsic differences in the scattering mechanism and temperature dependence of relaxation times with respect to quantum well. Measurement of carrier relaxation times in self assembled dots, by differential transmission spectroscopy and high frequency impedance response of quantum dot lasers, suggest that electron-hole scattering is the most probable scattering mechanism in quantum dots. The use of the favorable intersubband relaxation time in far infrared sources and detectors was discussed.

ACKNOWLEDGEMENTS

The authors would like to thank W.Zhou, O. Qasaimeh, H-T. Jiang and J. Singh for their contribution. This work was supported by NSF/ARO Grant No.

REFERENCES

1. R. Mirin, A. Gossard and J. Bowers, *Electronic Lett.*, **32**, 1372-73 (1996).
2. O. Qasaimeh, K. Kamath, P. Bhattacharya and J. Phillips, *Appl. Phys. Lett.*, **72**, 1275-77 (1998).
3. D. Pan, E. Towe, and S. Kennerly, *Appl. Phys. Lett.*, **73**, 1937-39 (1998).
4. M. Asada, Y. Miyamoto and Y. Suematsu, *IEEE J. of Quantum Electron.*, **9**, 1915-21, (1986).
5. D. Leonard, M. Krishnamurthy, C. M. Reaves, S. P. Denbaars and P. M. Petroff, *Appl. Phys. Lett.*, **63**, 3202-04, (1993).
6. P. R. Berger, K. Chang, P. Bhattacharya, J. Singh and K. K. Bajaj, *Appl. Phys. Lett.*, **53**, 684-86, 1988.
7. S. Krishna, D. Zhu, J. Xu, K. K. Linder, O. Qasaimeh, P. Bhattacharya and D. L. Huffaker, *J. Appl. Phys.*, **86**, 6135-38 (1999).
8. M. Sopanen, H. P. Xin, and C.W. Tu, *Appl. Phys. Lett.*, **76**, 994-96 (2000).
9. K. Nishi, H. Saito, S. Sugou and J-S. Lee, *Appl. Phys. Lett.*, **74**, 1111-13 (1999).
10. G. Park, O. B. Shchekin, D. L. Huffaker, and D. G. Deppe, *IEEE Photon. Technol. Lett.*, **12**, 230-32, 2000.
11. J. Phillips, P. Bhattacharya, S.W. Kennerly, D.W. Beekman, and M. Dutta, *IEEE J. Of Quant. Electron.*, **35**, 936-43 (1999).
12. S. Maimon, E. Finkman, G. Bahir, S.E. Schacham, J.M. Garcia and P.M. Petroff, *Appl. Phys. Lett.*, **73**, 2003-05 (1998).
13. S. Krishna, O.Qasaimeh, P. Bhattacharya, P.J. McCann and K.Namjou, *Appl. Phys. Lett.*, (in press).
14. K. Kamath, P. Bhattacharya and J. Phillips, *J. of Crystal Growth*, **175/176**, 720-724, 1997.
15. H. Jiang and J. Singh, *IEEE J. of Quant. Elect.*, **34**, 1188-96 (1999).
16. T. Sosnowski T. Norris, H. Jiang, J. Singh, K. Kamath and P. Bhattacharya, *Phys. Rev. B*, **57**, R9423-26 (1998).
17. D. Klotzkin, K. Kamath, and P. Bhattacharya, *IEEE Photon. Technol. Lett.*, **9**, 1301-03 (1997).
18. R. Heitz, M. Veit, N.N. Ledestov, A. Hoffmann, D. Bimberg, V.M. Ustinov, P.S. Ko'pev, and Zh.I. Alfred, *Phys. Rev. B*, **56**, p. 10435-45, (1997).
19. J. Singh, *IEEE Photon. Technol. Lett.*, **8**, 488-90, (1996).

Temperature Dependence of Quantum Dot Lasers

D.G. Deppe, G. Park, and O.B. Shchekin

Microelectronics Research Center
Department of Electrical and Computer Engineering
The University of Texas at Austin, Austin, Texas 78712-1084

ABSTRACT

Quantum dots (QDs) generate zero-dimensional quantum states that form the active material of semiconductor lasers and light emitters. Because of their discrete energy levels, the QDs offer numerous advantages to fabricate improved lasers and low power light sources. However, their low optical gain and complex material structure also create design challenges. Below we discuss important device principles that are emerging for use of QDs in both semiconductor lasers that influence the temperature dependence of their lasing threshold. In particular, we describe the temperature dependence due to the quantum confinement.

1. INTRODUCTION

Since the 1994 demonstration of a quantum dot (QD) semiconductor laser,¹ the research progress in developing lasers based on QDs has been impressive. Because of their fundamentally different physics that stem from zero-dimensional electronic states, QD lasers now surpass advanced planar quantum well laser technology in several respects. These include their minimum threshold current density, the threshold dependence on temperature, and range of wavelengths obtainable in given strained layer material systems. However, these achievements also come at other prices in the QD laser performance. Low threshold current density is obtained with decreased slope efficiency, and the long wavelength QDs for which stacking is more difficult suffer low optical gain. In addition, the temperature dependence of the lasing threshold becomes dramatically stronger near room temperature, and QD lasers have not clearly yet shown a benefit in their characteristic temperature, T_0 . The T_0 of the QD laser can be extremely high due to its inhomogeneously broadened linewidth, reaching 700 K and above for temperatures above 200 K. However, near and above room temperature all QD lasers reported to date, to our knowledge, show that the T_0 rapidly drops into 30 K to 60 K range. This also makes comparisons between different groups tricky, unless the same temperature range is specified. It is mainly the temperature dependence of the QD optical response that sets the temperature dependence of the QD laser.

Self-organized QDs are formed from strained-layer epitaxy when the thin film thickness exceeds a critical value for formation of dislocations in planar epitaxy. Upon reaching such conditions, the growth front spontaneously reorganizes to form the crystalline coherent three-dimensional islands. The greater strain relief provided by the three-dimensionally structured crystal surface prevents the formation of dislocations. When covered with additional epitaxy, the coherently strained islands form the QDs that trap and isolate individual electron-hole pairs to create efficient light emitters.

Optimizing the QD characteristics for use as practical, commercial light sources is based on controlling their density, shape, and uniformity during epitaxy. In particular, the QD's shape helps establish its dynamic response through control of the energy level spacings. As we show below, engineering the QD shape to widely separate its energy levels is a key design path to temperature insensitive lasing. The QDs density, shape, and uniformity also establish the optical gain of a QD ensemble. All three physical characteristics can be engineered through the precise deposition conditions in which temperature, growth rate, and material composition are carefully controlled. The variety of heterostructures possible with the increased variety of material choices is being explored in many university laboratories. In great part through experimental trial and error, understanding is being gained as to how strain in both the QD material and adjoining semiconductor heterostructures influence formation and the electronic structure of self-organized QDs. In general, density can now be controlled to over two orders of magnitude, from 10^9 cm^{-2} and below up to $>10^{11} \text{ cm}^{-2}$. At the highest densities tunnel coupling and miniband formation become observable in the QD ensembles.² To a lesser degree uniformity can also be controlled in many laboratories, but all reported QD ensembles reported to date exhibit inhomogeneous broadening even at room temperature.

Several means exist to control QD density. A slow growth generally forms larger QDs with lower density. The same is true for higher temperatures. Both provide atoms more time to migrate on the crystal surface, and indicate that the QD formation is kinetically controlled. An atomic force microscope (AFM) image is shown in Fig. 1 that illustrates how a strained buffer layer can be used to control the density of InGaAs QDs.^{3,4} In Fig. 1 (a) the InGaAs QDs are deposited directly on GaAs, and alternating depositions of In, Ga, and As are used to achieve high surface atom mobility and slow growth rates to form the efficient 1.3 μm QD emitters. Their density is $\sim 10^{10} \text{ cm}^{-2}$. In Fig. 1 (b) the same strained-layer deposition is performed on a thin, strained InGaAs buffer layer of less In content, and the QD density increases to $\sim 2 \times 10^{10} \text{ cm}^{-2}$. The increase in the QD density significantly improves laser performance.⁴ Because of the novel physics associated with the QD ensemble, the active material shown in Fig. 1 (b) has resulted in the lowest threshold current density yet reported (19 A/cm^2) for any semiconductor material system for continuous-wave (CW) room temperature operation.⁴ Even lower threshold current densities could be possible in the future. At a slightly lower temperature of $\sim 200 \text{ K}$ the threshold current density of the InGaAs QD material of Fig. 1 (b) reduces to 5 A/cm^2 , and generates lasers with threshold currents of $\sim 400 \mu\text{A}$. The application of selective oxidation to fabricate QD lasers is discussed below.

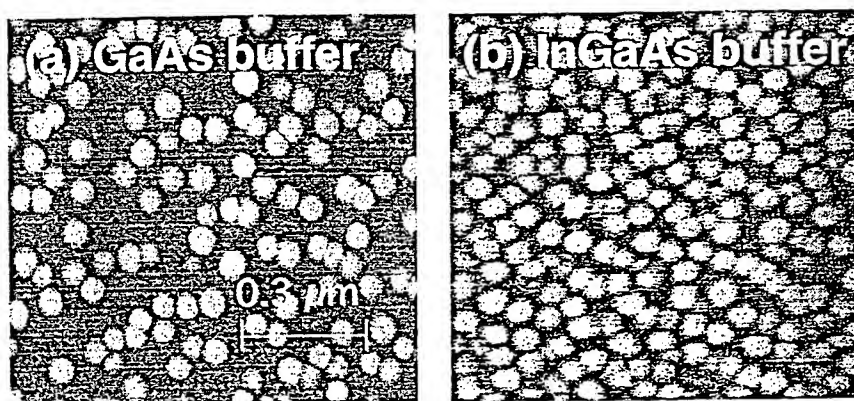


Fig. 1 Atomic force microscope images showing the control of the QD density using a strained buffer layer. (a) shows InGaAs QDs grown directly on GaAs, and the QD density is $\sim 10^{10} \text{ cm}^{-2}$. (b) shows similar InGaAs QDs grown with a strained layer buffer, which increases the QD density to $\sim 2 \times 10^{10} \text{ cm}^{-2}$.

2. QUANTUM DOT ELECTRONIC STRUCTURE TEMPERATURE CHARACTERISTICS OF QD LASERS

The InGaAs QD size can be controlled through the deposition conditions of the different constituent atom species. Slow growth rates set by alternately pausing delivery of column III and V species lead to large InGaAs QDs.³⁻⁸ Whereas InAs QDs are generally grown with less than 3 monolayers of deposited strained material thickness, $\text{In}_{0.5}\text{Ga}_{0.5}\text{As}$ QDs may be grown dislocation free with a deposition of 10 monolayers or more. The InGaAs QDs are measured by transmission electron microscopy to be $\sim 300 \text{ \AA}$ in diameter and $\sim 110 \text{ \AA}$ in height after covering. It has also been shown that in such QDs the In concentration that is higher in the QD center.⁸

The In grading and large size apparently give rise to approximately parabolic electron and hole confinement potentials, characterized by nearly uniform energy separations between discrete radiative transitions. Different rungs of the discrete energy levels have degeneracies set by the QD aspect ratio (height-to-base). For the case of the height being much less than the base, the first two radiative transitions exhibit level degeneracies due to cylindrical symmetry, in this case of nearly Gaussian waves. The 300 K luminescence spectra of QDs grown as those shown in Fig. 1 further covered with a GaAs/AlGaAs heterostructure exhibit well resolved emission peaks due to their

discrete levels, with energy separations of ~ 66 meV the ground and first excited radiative transitions. A schematic diagram of the InGaAs QD electronic structure is shown in Fig. 2. Four radiative transitions can be identified due to discrete energy levels in the QDs, and these are labeled by "m".

Previous works have treated the quasi-equilibrium approximation of QD lasers with single electron and hole levels, so that the wetting layer is mainly responsible for setting the temperature dependence of the lasing threshold.⁹ Here we use a model appropriate to the multi-level QDs used in the 1.3 μm laser.¹⁰ The quantum numbers and degeneracies used in the calculations below for the QD discrete levels are based on 3-dimensional parabolic confinement that gives the Hamiltonian for electrons as

$$\hat{H}_{\text{Electron}} = -\frac{\hbar^2}{2m_e} \nabla_e^2 + \frac{1}{2} m_e [\omega_{\perp,e}^2 (x_e^2 + y_e^2) + \omega_{z,e}^2 z_e^2] \quad (1)$$

where m_e is the effective electron mass, $\hbar\omega_{\perp,e}$ is the electron energy separation due to the lateral QD size, and $\hbar\omega_{z,e}$ is the energy separation due to the QD height. Therefore, the energy levels take on the nature of a three-dimensional harmonic oscillator. For energy levels near the wetting layer, the approximation of the parabolic confinement potential breaks down. For the discrete levels of interest below, however, the harmonic oscillator (parabolic confinement potential) energy levels that are inhomogeneously broadened serve as a good model for the experimental density of levels in the QD ensemble.¹⁴ Similar assumptions are made for discrete hole levels, except for different energy separations between the levels.

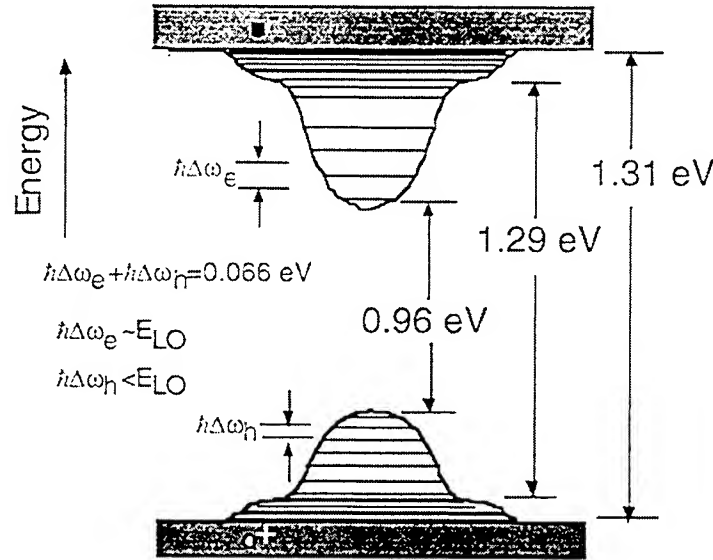


Fig. 2 Schematic diagram of the approximate QD electronic potential for the large InGaAs QDs.

The discrete energy levels are labeled by $\mathbf{m} = m_x, m_y, m_z$ where m_x, m_y, m_z are integers ≥ 0 . The corresponding energy level diagram is shown in Fig. 3. With the lowest energy transition given by $\hbar\omega_0$, the electron spectrum is described by

$$\hbar\omega_{\mathbf{m},e} = \hbar\omega_0 + \hbar[\omega_{\perp,e}(m_x + m_y + 1) + \omega_{z,e}(m_z + 1/2)], \quad (2)$$

so that, for example, the level labeled $\mathbf{m} = 0$ in Fig. 2 is made up of the quantum state (0,0,0), while $\mathbf{m} = 1$ is made up of quantum states (1,0,0) and (0,1,0), etc. We also assume a factor of 2 degeneracy for each level due to spin. The QD's height-to-diameter aspect ratio, h/D , sets the relative size of ω_{\perp} and ω_z for electrons or holes according to $\omega_{\perp}/\omega_z = h/D$. Since the transmission electron measurements give $h \approx 110$ Å and $D \approx 350$ Å, we approximately have $\omega_{\perp}/\omega_z = 0.3$ for the 1.3 μm QDs. Based on the quantum states of a harmonic

oscillator, one can readily show that the electron wavefunctions corresponding to the estimated energy separations fit the QD size.¹⁰ Letting s_m represent the degeneracy of a level given from (2), the lower level degeneracies are given by $s_0 = 2$, $s_1 = 4$, $s_2 = 8$, $s_3 = 12$, and $s_4 = 18$. In our modeling, it is the electronic spectra of these lowest energy levels that are most important in establishing the $m = 0$ transition gain characteristics. The reduced density of states of this QD ensemble is given by¹⁰

$$\rho_{red}(E) = 2 \sqrt{\frac{\ln 2}{\pi}} \frac{n_{QD}}{\hbar \Delta \omega_l} \sum_{m=0}^M s_m e^{-\ln 2 \frac{[\hbar \omega_0 + m\hbar(\omega_{\perp,e} + \omega_{\perp,h}) - E]^2}{(\hbar \Delta \omega_l)^2}} \quad (3)$$

including the degeneracy and Gaussian linewidth broadening, where $n_{QD} (\approx 1.5 \times 10^{10} \text{ cm}^{-2})$ is quantum dot number density, $\hbar \Delta \omega_l \approx 40 \text{ meV}$ is the full width at half maximum (FWHM) of each state, $\hbar \omega_0$ is the ground state energy, and $\hbar(\omega_{\perp,e} + \omega_{\perp,h}) \approx 66 \text{ meV}$ is the energy separation between radiation levels.

Rate equations provide the accurate means to account for equilibration, quasi-equilibration, or highly nonequilibrium carrier distributions. However, rate equations that are not derived from a quantum mechanical Hamiltonian cannot account for the correct reservoir physics. The reservoir approach derived from the quantum mechanical Hamiltonian always includes spontaneous emission, stimulated emission, and absorption rates that agree with the Einstein relations for these three processes. Because of the high scattering rates between QD electronic levels relative to the spontaneous emission rate, electrons and holes equilibrate in individual QDs. Whether or not the QD ground state equilibrates with the wetting layer depends on the thermalization rate to the wetting layer from the ground state relative to the spontaneous emission rate from the ground state. The lack of thermal equilibration between the QD ground state and wetting layer in steady-state operation is readily observed as the inhomogeneously broadened spontaneous linewidth at low temperature. Despite the fact that at room temperature the QDs due to equilibrate through the wetting layer, the inhomogeneously broadened gain spectrum is still approximately satisfied. As shown in the experimental data below, the thermalization between the wetting layer and QD ground state is readily measured as a slight reduction in the spontaneous linewidth, with the thermalization occurring at and above $\sim 200 \text{ K}$. This corresponds to the temperature at which the thermal escape of electrons out of the QDs becomes comparable to the spontaneous emission rate. Shallower energy QDs (shorter wavelength) then lose their carriers more rapidly than deeper energy QDs. This favors stronger emission from long wavelength QDs, which causes the thermal line narrowing of the ensembles spontaneous spectra.

At low temperatures, the QDs capture as if independently, because the spontaneous emission rate exceeds the thermal escape rate. However, electrons and holes still thermalize within the QDs, and on average each QD will be neutral with equal probabilities for electron and hole occupancy. The radiative current consumed by each QD will be the same (in the absence of lasing). Reference [10] shows that the carriers in the individual QDs are approximately in equilibrium among the lowest energy zero-dimensional levels. Under the assumption of quasi-equilibrium for electrons and holes, the numbers of electrons and holes in a QD is given by

$$n_{e,h} = \sum_{m=0}^M n_{m,e,h} = \sum_{m=0}^M \frac{s_m}{\exp\left(\frac{m\hbar\omega_{\perp,e,h} - F_{e,h}}{kT}\right) + 1} \quad (4)$$

where $n_{m,e}$ is the number of electrons and $n_{m,h}$ the number of holes in the QD's m -th energy level, and F_e and F_h are the quasi-Fermi levels for electrons and holes referenced to their $m=0$ levels, respectively. These conditions set the quasi-Fermi levels for electrons and holes for a given number of carriers in a QD.

The modal gain at the peak of the m -th level for a given number of carriers $n_{m,e}$ and $n_{m,h}$ in that level is given by¹⁰

$$\begin{aligned} g_m &= \sqrt{\frac{\ln 2}{\pi}} \frac{c \lambda_m^2 n_{QD} \Gamma_m}{2 v_g n^3 \Delta \omega \Delta z \tau_0} [n_{m,e} - (1 - n_{m,h})] \\ &= \sqrt{\frac{\ln 2}{\pi}} \frac{c \lambda_m^2 n_{QD} \Gamma_m}{2 v_g n^3 \Delta \omega \Delta z \tau_0} s_m (f_{m,e} - f_{m,h}) \end{aligned} \quad (5)$$

where c is the speed of light in free space, λ_m is the free space wavelength of the m -th level, $\frac{\Gamma_m}{\Delta z}$ is the optical confinement factor of the waveguide normalized by the active layer thickness, $n = 3.3$ is the refractive index, $v_g = 6.7 \times 10^7$ m/sec is the optical group velocity, $\tau_0 = 450$ psec is the spontaneous lifetime (with full electron and hole occupation), and $f_{m,e}$ and $f_{m,h}$ are the Fermi functions for electrons and holes, respectively [also used in (4)]. The modal gain given in (5) includes the inhomogeneous spontaneous linewidth, which is included in the density of energy levels given in (3). Using (4) in (5) gives the low temperature case in which the gain spectrum is inhomogeneously broadened, and the electrons and holes are quasi-equilibrated within each QD. The separations of electron levels are assumed to be 56 meV and for hole levels to be 10 meV for the best fit to the experimental data presented below for InGaAs QD lasers. These energy separations control the temperature dependence of the QD's optical gain. The relative values of the discrete level energy separations for electrons and holes are in approximate agreement with various calculations of electron and hole energy levels in self-organized InAs QDs.¹¹

Figures 3 the calculated modal gain versus the total number of electrons (or holes) in a QD for levels with $m = 0, 1$, and 2 for four different temperatures. Figure 4 shows a similar calculation versus current density. At 4 K, the maximum modal gain is 16.9 cm^{-1} for the $m = 0$ level, 31.7 cm^{-1} for the $m = 1$ level, and 57.3 cm^{-1} for $m = 2$

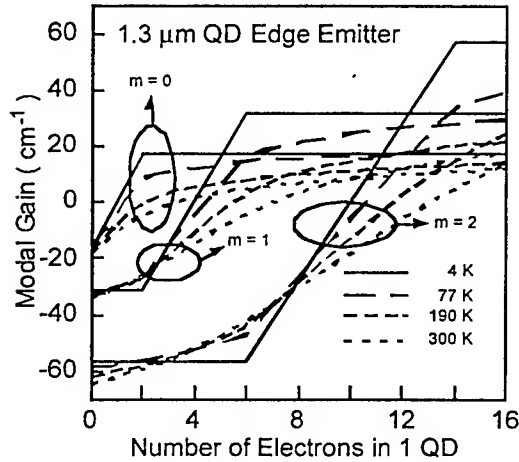


Fig. 3 Calculated modal gain of the ground ($m = 0$), the first excited ($m = 1$), and the second excited ($m = 2$) levels versus number of electrons in 1 QD. At 4 K, the gain of a higher level remains close to its minimum value until the gain of lower level reaches nearly its maximum. As the temperature increases however, the gain of a higher level can easily exceed that of a lower level well before the lower level reaches its maximum.

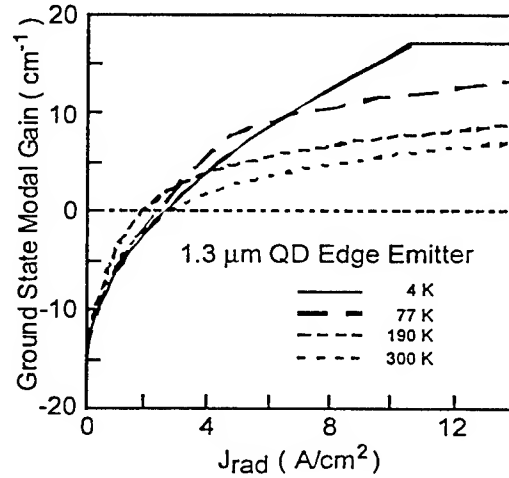


Fig. 4 Calculated modal gain for ground level versus radiative current density at various temperatures.

level. Note that the maximum gain of each level shows a strong temperature dependence due to thermal population of the higher energy levels. At 4 K, the carrier populations for higher energy levels remain negligible until the lower energy levels are completely filled. Therefore, the modal gain of $m = 1$ level remains at its minimum value until that of the $m = 0$ level reaches its maximum, and so forth. As the temperature increases, the carrier population of higher energy levels become increasingly important for a given number of carriers in a QD. The crossing points of maximum gain also significantly change. For example, the modal gain of the $m = 1$ level exceeds that of $m = 0$ level at the gain value of 16.9 cm^{-1} at 4 K, 14.1 cm^{-1} at 77 K, 9.0 cm^{-1} at 190 K, and 7.8 cm^{-1} at 300 K. The

gain of the $m = 2$ level exceeds that of the $m = 1$ level at the gain value of 31.7 cm^{-1} at 4 K, 27.6 cm^{-1} at 77 K, 20.6 cm^{-1} at 190 K, and 18.7 cm^{-1} at 300 K. The temperature dependence of the maximum gain is therefore quite strong. It becomes easy to see that if a laser requires a threshold gain of say 10 cm^{-1} , it can lase on the ground state for lower temperatures but will switch to lasing at the $m = 1$ level for temperatures greater than $\sim 150 \text{ K}$. We examine this effect specifically in the experimentally measured QD lasers described below.

In order to calculate the gain versus current, we determine the total spontaneous emission rate as a function of the carrier distribution in the discrete QD energy levels. The total spontaneous emission rate is set by the occupation probabilities of electron and hole levels, and sets the injected current needed to balance the total spontaneous emission rate.¹⁰ The expression is given by

$$J_{\text{rad}} = qn_{\text{QD}} \sum_{m=0}^M \gamma_0 s_m \frac{1}{\exp(\frac{m\hbar\omega_{\perp,e} - F_e}{kT}) + 1} \frac{1}{\exp(\frac{m\hbar\omega_{\perp,h} - F_h}{kT}) + 1} \quad (6)$$

where $\gamma_0 = 1/\tau_0$ ($\approx 2.2 \times 10^9 \text{ sec}^{-1}$) is the emission rate at full inversion. As the temperature goes up the spontaneous lifetime per electron becomes longer for a fixed number of carriers in the QD when selection rules are applied for the electrons and holes to recombine radiatively. Since each electron (and hole) are thermally distributed over more electron (and hole) levels, the probability of simultaneous occupation of radiatively coupled electron-hole levels is reduced. Figure 4 shows the modal gain at the peak of the ground level ($m = 0$) as a function of the total spontaneous radiative current density. The modal gain at a current density greater than $\sim 5 \text{ A/cm}^2$ significantly decreases as the temperature increases due to the increase of the higher level populations. However, from 4 K to 190 K the transparency radiative current density gets smaller as the temperature gets higher. This can be explained by the fact that the spontaneous lifetime becomes longer as the temperature increases for a fixed number of carriers in a QD. At 300 K the effect of higher level population is dominant, and the transparency current then increases with increasing temperature.

3. TEMPERATURE DEPENDENCE OF SELECTIVELY OXIDIZED InAs AND InGaAs QD LASERS WITH 1.3 μm OPERATION

A schematic illustration of the oxide-confined QD laser structure is shown in Fig. 5. The selective oxidation approach can result in low threshold operation when combined with the QD active region. The QD heterostructures are grown on n-type GaAs substrates using molecular beam epitaxy. The substrate temperature during growth is 610°C for all layers except the QD regions which are grown between 510°C and 515°C . The heterostructure consists of lightly doped p- and n-type $\text{Al}_{0.85}\text{Ga}_{0.15}\text{As}$ cladding layers that also contain oxidation layers and surround an undoped $0.19 \mu\text{m}$ thick waveguide of $\text{Al}_{0.05}\text{Ga}_{0.95}\text{As}$. The oxidation layers consist of 300 \AA thick $\text{Al}_{0.98}\text{Ga}_{0.02}\text{As}$ grown $0.25 \mu\text{m}$ above and below the short period superlattices. 200 \AA of short period superlattices are grown between each of the waveguide and cladding layer interfaces. A p^+ GaAs contact layer for electrical contacting is grown in the final epitaxy step.

Different active regions are investigated to study how the temperature dependence of the lasing threshold is influenced by the QD electronic structure. In one type, the active region at the waveguide center consists of 150 \AA of GaAs followed by 15 monolayers of $\text{In}_{0.09}\text{Ga}_{0.91}\text{As}$, a single layer QD deposition of 10 monolayers of average $\text{In}_{0.5}\text{Ga}_{0.5}\text{As}$, and another 150 \AA of GaAs. The QDs are formed using the sub-monolayer epitaxy sequence described elsewhere for growth on GaAs buffer layers.⁵ These are the large InGaAs QDs shown above in Fig. 1 (b).

For the second type of QD the temperature of the growth is again 610°C except for the growth of the QD layers, which are deposited at 515°C . A 2-stack QD active region is formed by depositions of 2.7 monolayers of bulk InAs separated by 300 \AA of GaAs, with 150 \AA regions of GaAs below and above the 2 QD layers. The 2-stack QD active region is also grown at the center of an undoped $0.19 \mu\text{m}$ thick $\text{Al}_{0.05}\text{Ga}_{0.95}\text{As}$ waveguide clad by p and n $\text{Al}_{0.85}\text{Ga}_{0.15}\text{As}$ layers of $2 \mu\text{m}$ thickness. The growth of the InAs QDs directly on GaAs increases the confinement potential and helps to generate a large energy separation between the ground and first excited radiative transitions. The QD density in each stack is $\sim 3 \times 10^{10} \text{ cm}^{-2}$. Their average diameter is $\sim 250 \text{ \AA}$ with a height of $\sim 30 \text{ \AA}$. In order

to form the oxide waveguide, stripes ranging from 33 μm to 45 μm are fabricated by wet etching a ridge structure through the upper cladding layer, waveguide layer, and most of the lower cladding layer. Wet oxidation at 470 $^{\circ}\text{C}$ for ~ 4 minutes is then used to convert the $\text{Al}_{0.98}\text{Ga}_{0.02}\text{As}$ layers to Al_xO_y , forming apertures of 5 to 17 μm in width. Laser cavities with lengths of 870 μm and 1130 μm are formed by cleaving and applying high reflectivity ZnSe/MgF_2 quarter-wave stacks to the end facets. The lasers are mounted with the p-side up and tested CW at room temperature.

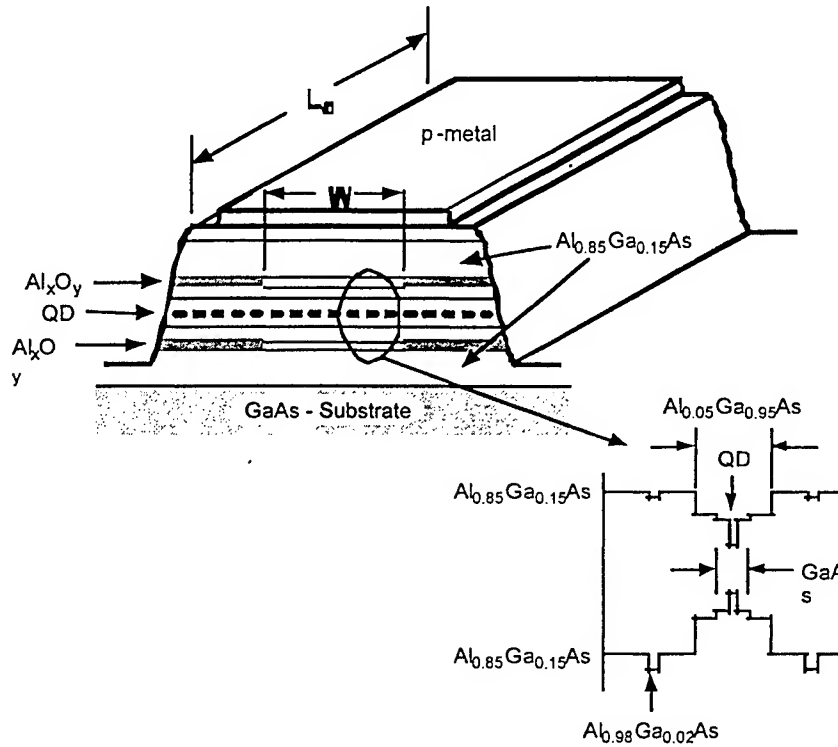


Fig. 5 Schematic illustration of the oxide apertured, QD laser. Two oxide layers have been place 0.25 μm above and below the waveguide layer.

Figures 6 shows the room temperature lasing characteristics of an oxide-confined QD laser with the large InGaAs QDs. Figure 6 is for an InGaAs QD laser that has an 870 μm long cavity and a 5 μm wide oxide aperture. The output facet is coated with 5 ZnSe/MgF_2 pairs and the back facet is coated with 6 ZnSe/MgF_2 pairs. The dielectric coatings have reflectivities that exceed 99% for plane wave modes, but diffraction in the mirrors will decrease the reflectivity for the laser waveguide mode. The CW threshold current is 1.2 mA, and to the best of our knowledge, is the lowest value yet reported for CW room-temperature operation of a QD laser. The threshold current density is also low, and $\sim 28 \text{ A/cm}^2$ for the device results shown in Fig. 6. The smallest CW threshold current density we have measured is 19 A/cm^2 on an oxide-confined laser with a slightly larger stripe width. The inset shows the ground state lasing with the wavelength of 1.33 μm just above the threshold. Low output power remains a problem, partly due to the high reflectivity facet coatings and relatively long cavity, and partly due to heating and nonradiative recombination. The external differential quantum efficiency just above the threshold is $\sim 2\%$, and decreases for increasing drive current. The decrease of the slope efficiency suggests that the device performance is limited by the heating which results in the increase of upper level population and non-radiative recombination. The maximum output power of 290 μW is obtained at 24 mA.

Quite similar low threshold results are obtained on an InAs QD laser has a higher QD density per layer of $3 \times 10^{10} \text{ cm}^{-2}$, and uses two QD layers. The InGaAs QD laser uses a single layer with a density of $2 \times 10^{10} \text{ cm}^{-2}$. The spontaneous lifetimes from the two different QD sizes, either the InGaAs QDs or InAs QDs, are also expected to be different. However, when the cavity loss is low as it is for these HR coated oxide-stripe lasers, these are not the main parameters that control the temperature dependence of the lasing threshold. Instead it is controlled through thermal excitation of electrons and holes to higher discrete energy levels, as shown in Figs. 3 and 4 above. The modeling shows that to improve the temperature dependence of the lasing threshold the first excited radiative transition should be separated in energy from the ground state as widely as possible. As we show below, widely separating these energy levels does, in fact, greatly reduce their temperature sensitivity.

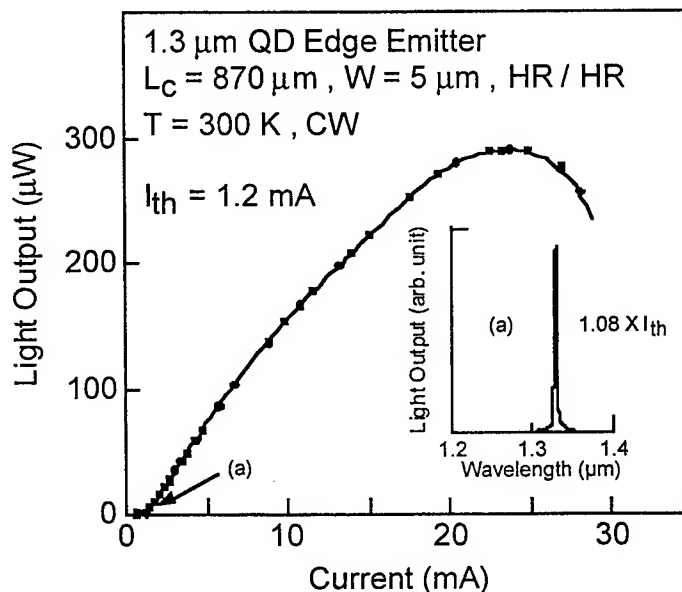


Fig. 6 Continuous-wave lasing characteristics of the low threshold, oxide-confined InGaAs QD laser. The lasing wavelength is $1.34 \mu\text{m}$.

The energy separations between the discrete levels is most easily determined from the spontaneous spectra. This measurement gives the energy separation of the radiative transitions, which is then due to separations of both electron and hole levels. Figure 7 show the spontaneous spectra for the InAs QD laser. In Fig. 7 it is shown that the first excited radiative transitions of the InAs QDs are separated from their ground states by $\sim 104 \text{ meV}$ using the smaller InAs QDs. In comparison, the $1.3 \mu\text{m}$ InGaAs QD laser has energy level separations of $\sim 65 \text{ meV}$. The energy separation of 104 meV is, to our knowledge, among the widest yet reported for InAs or InGaAs QD lasers. Therefore, we expect the temperature dependence of the lasing threshold to be greatly improved.

Figure 8 shows the measurement of the lasing threshold versus temperature for the InGaAs QD laser and the InAs QD laser. The measurement conditions are comparable, with both lasers mounted p-side up on copper heat sinks. Below room temperature both lasers show fairly flat temperature dependencies as might be expected for nearly ideal QD lasers. The InGaAs QD laser in fact shows remarkably low threshold current density of less than 10 A/cm^2 due to the small QD number in the single active layer. However, close to room temperature the thermal effects become important. Here the benefit of the InAs QDs with the wider separated energy levels becomes apparent. The typical parameter used to characterize the temperature sensitivity of a laser's threshold is the T_0 that comes from the empirical formula $J_{th}(T) = J_{th}(0)\exp(T/T_0)$. This formula breaks down for QD lasers, and gives a T_0 that depends strongly on temperature itself. Therefore, the T_0 is only meaningful for comparison of QD lasers around room temperature if precisely the same small temperature range is used.

At the highest measurement temperatures that range from 300 K to 325 K, the InGaAs QD laser with the 65 meV energy separation between the ground and first excited transitions exhibits a T_0 of ~45 K. This value is increased to over 90 K for the InAs QD laser. This difference is mainly due to the wider energy separations shown in Fig. 7 between the ground and first excited radiative transitions in the InAs QDs. Recognizing this, we believe that even better temperature sensitivity may be achieved in the future by engineering the QDs to have even wider energy separations between their two lowest discrete transitions.

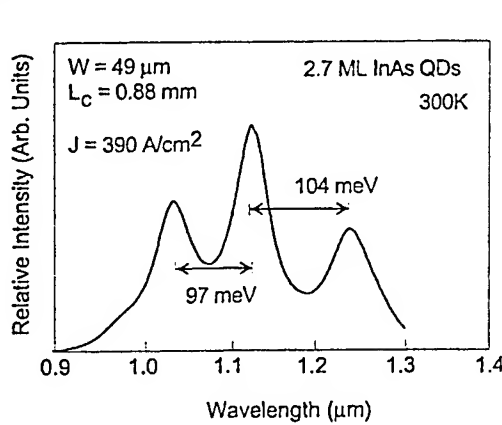


Fig. 7 Spontaneous emission spectra from the InAs QDs showing the ~104 meV energy separation between the ground and first excited radiative transitions.

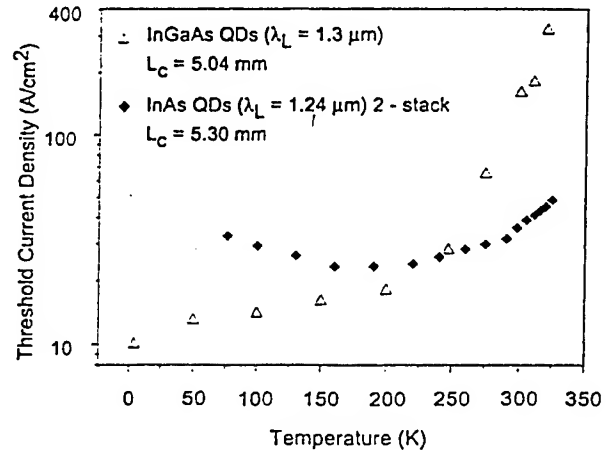


Fig. 8 Threshold versus temperature measured for the InGaAs QD laser with ~65 meV energy separation between radiative transitions, and the InAs QD laser with 102 meV energy separation. A rapid increase in threshold current density is measured near room temperature that depends on the energy separations.

6. SUMMARY

Quantum dot lasers are rapidly advancing and show many novel features. These include extremely low threshold current density, extended lasing wavelength for a given material system, and temperature insensitive threshold, at least at low temperatures. Although the low threshold current density and extended lasing wavelength has been achieved at room temperature for GaAs-based QD lasers, the temperature insensitive threshold has not. While the characteristic temperature, or T_0 , can reach several hundred Kelvin for temperatures up to ~250 K, it decreases rapidly at room temperature and above. Here we have shown that a limiting mechanism in this temperature dependence is excitation of electrons and holes to higher energy levels, which robs the ground state of its population and gain for the same total carrier density. This effect is surprisingly strong, easily limiting the maximum room temperature gain to less than 50% of what it may be for cryogenic temperatures. This effect can be controlled by engineering the QDs to give wide energy separations between the ground and first radiative transitions.

ACKNOWLEDGMENTS

This work has been supported by the National Science Foundation under grant ECS-9734829, the Army Research Office MURI program on the Adaptive Optoelectronic Eye, and by the DARPA OptoCenter led by the University of New Mexico.

REFERENCES

1. N. Kirstaedter, N. N. Ledentsov, M. Grundmann, D. Bimberg, V. M. Ustinov, S. S. Ruvimov, M. V. Maximov, P. S. Kop'ev, Zh. I. Alferov, U. Richter, P. Werner, U. Gosele, and J. Heydenreich, "Low threshold, large T_0 injection laser emission from InGaAs quantum dots," *Electron Lett.*, vol. 30, pp 1416-1417, 1994.
2. D.L. Huffaker, L.A. Graham, and D.G. Deppe, "Ultrasharp electroluminescence spectrum from the ground state of an ensemble of self-organized quantum dots," *Appl. Phys. Lett.*, vol. 72, pp. 214-216, 1998.

3. L.F. Lester, A. Stintz, H. Li, T.C. Newell, E.A. Pease, B.A. Fuchs, and K.J. Malloy, "Optical characteristics of 1.24 μm InAs quantum dot laser diodes," *IEEE Phot. Tech. Lett.*, vol. 11, pp. 931-933, 1999.
4. G. Park, O.B. Shchekin, D.L. Huffaker, and D.G. Deppe, "Low threshold oxide-confined 1.3 μm quantum dot laser," *IEEE Phot. Tech. Lett.*, vol. 12, pp. 230-232, 2000.
5. D. L. Huffaker and D. G. Deppe, "Electroluminescence efficiency of 1.3 μm wavelength InGaAs/GaAs quantum dots," *Appl. Phys. Lett.*, vol. 73, pp. 520-522, 1998.
6. K. Mukai, N. Ohtsuka, M. Sugawara, and S. Yamazaki, "Self-formed $\text{In}_{0.5}\text{Ga}_{0.5}\text{As}$ quantum dots on GaAs substrate emitting at 1.3 μm ," *Jpn. J. Appl. Phys.*, vol. 33, pp. 1710-1712, 1994.
7. R. Mirin, J. Ibbetson, K. Nishi, A. Gossard, and J. Bowers, "1.3 μm photoluminescence from InGaAs quantum dots on GaAs," *Appl. Phys. Lett.*, vol. 67, pp. 3795-3797, 1995.
8. S. Krishna, D. Zhu, J. Xu, K. Linder, O. Qasaimeh, P. Bhattacharya, and D. L. Huffaker, "Structural and luminescence characteristics of cycled submonolayer InAs/GaAs quantum dots with room-temperature emission at 1.3 μm ," *J. Appl. Phys.*, vol. 86, pp. 6135-6138, 1999.
9. L.V. Asryan and R.A. Suris, "Inhomogeneous line broadening and the threshold current density of a semiconductor quantum dot laser," *Semicond. Sci. Tech.*, vol. 11, pp. 554-567, 1996.
10. D. G. Deppe, D.L. Huffaker, S. Csutak, Z. Zou, G. Park, and O.B. Shchekin, "Spontaneous emission and threshold characteristics of 1.3 μm InGaAs-GaAs quantum dot GaAs-based lasers," *IEEE J. Quant. Electron.*, vol. 35, pp. 1502-1508, 1999.
11. H. Jiang and J. Singh, "Strain distribution and electronic spectra of InAs/GaAs self-assembled dots: An eight-band study," *Phys. Rev. B*, vol. 56, pp. 4696-4701, 1997.

Quantum dot devices

S. Fafard*, H.C. Liu, Z.R. Wasilewski, J. McCaffrey, M. Spanner, S. Raymond, C. Ni. Allen, K. Hinzer, J. Lapointe, C. Struby, M. Gao, P. Hawrylak, C. Gould, A. Sachrajda, P. Zawadzki.

Institute for Microstructural Sciences, National Research Council,
Ottawa, Ontario, Canada, K1A 0R6.

ABSTRACT

From a recent study of the growth and the optical properties of quantum dots (QDs), we demonstrated that artificial atoms with sharp electronic shells can be fabricated with good control, using self-assembled QDs grown by molecular beam epitaxy. Size and shape engineering of the QDs during growth permits the tailoring of their intersublevel energy spacings. We demonstrate a much improved uniformity of the macroscopic ensembles of QDs, with well-resolved electronic shells. In addition to size and shape engineering of the QDs in the case of single-layer samples, we demonstrate significant improvements in the uniformity of the vertically self-aligned stacked QDs. State-filling spectroscopy of the zero-dimensional transitions between confined electrons and holes demonstrates that the energy levels are readily tunable. One to five confined levels, with an inter-level energy spacing between 25 and 90 meV, are obtained by adjusting the growth temperature or with post-growth annealings. Such QDs having well-defined excited-states have been grown in the active region of devices and results will be presented for lasers, detectors, or for structures displaying optical memory effects. For example, QD laser diodes with well-defined electronic shells are fabricated, and shape-engineered stacks of self-aligned QDs are used to increase the gain in the active region. Lasing is observed in the upper QD shells for small gain media, and progresses towards the QD ground states for longer cavity lengths. We obtained at 77K thresholds of $J_{th} = 15 \text{ A/cm}^2$ for a 2 mm cavity lasing in the first excited state (p-shell), and at 300K for a 5 mm cavity, J_{th} is $\sim 430 \text{ A/cm}^2$ with lasing in the d-shell. For an increased QD density, J_{th} is smaller than 100 A/cm^2 at room temperature. For inter-sublevel transitions, we demonstrated broadband normal incidence detection with responsivity approaching 1 A/W at a detection wavelength of 5 microns. For interband detection, the photoluminescence decay time of a p-i-n diode can be changed from $\sim 3 \text{ nsec}$ to $\sim 0.3 \text{ nsec}$ (3Ghz) with a reverse bias. For QDs capped with less than $\sim 10 \text{ nm}$, remarkable charge transfers between the QD and surface states lead to optical memory effects lasting over time-scales of several minutes.

Keywords: Quantum dot, nanostructure, self-assembled, InAs/GaAs, QD intermixing, laser diode, infrared photodetector, QDIP, optical memory, zero-dimensional.

1. INTRODUCTION

Ideal zero-dimensional (0D) quantum systems are made of a deep confining potential yielding several discrete levels. The observation of a number of well-resolved excited-states is therefore the principal figure of merit for semiconductor heterostructures based on QDs. Studies of self-assembled QDs of high quality have revealed a number of resolved electronic shells in state-filling spectroscopy.¹⁻⁹ Recently, it has been demonstrated that self-assembled growth can be controlled to systematically and reproducibly fabricate QD structures which have well-defined excited-state transitions, like an artificial atom, and to manipulate their energy levels to tailor the number of confined states and their intersublevel energy-spacing.¹⁰⁻¹¹ Moreover, the structural quality of the self-assembled QDs and their compatibility with conventional III-V technology has permitted the demonstration of high performance prototype devices such as semiconductor QD lasers.¹²⁻²⁷ These developments are very promising for quantum dot devices which should yield novel nanostructures with unique properties due to their atomic-like shell configurations. For example, QD infrared detectors (QDIP) are sensitive in normal incidence detection due to the geometry of the QDs. Also, optical memories based on coupling of QDs can have large storage density. For most application, it is often desirable to have multiple layers of QDs. Uniformity in the QD ensemble can sometimes be a problem, and especially when multiple stacked-layers²⁵ are used for the purpose of trying to increase the gain in the active

* Correspondence: Email: simon.fafard@nrc.ca.

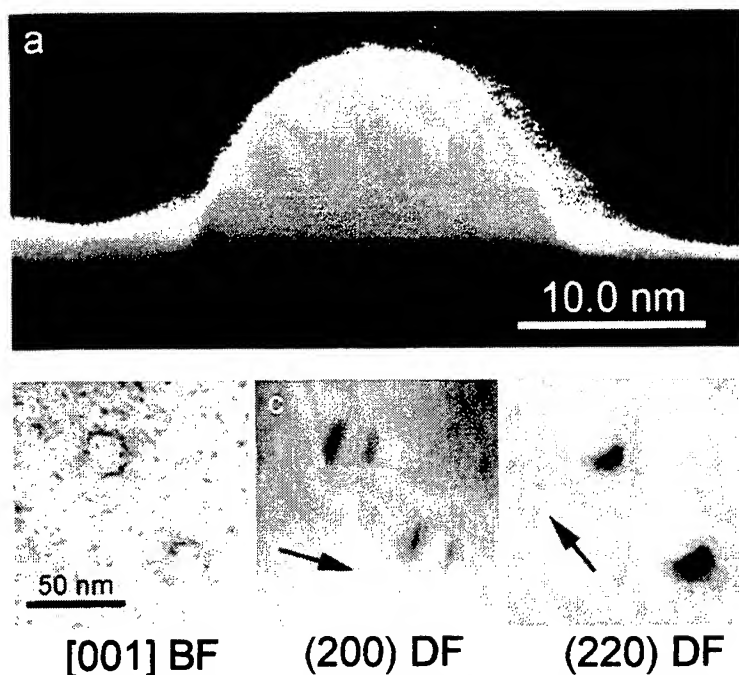


Fig. 1: Transmission Electron Microscope (TEM) images of InAs/GaAs self-assembled QDs. Cross-section [011] view of an uncapped QD in a), and plan view of 2 capped QDs from different bright field (BF) and dark field (DF) diffraction conditions.

spacers of $\sim 10\text{nm}$, for $x=0.7$ and $y=0.35$. The active region is followed by the symmetric step-graded cladding and p-doped contact layers, and terminated with a p^+ GaAs cap. For samples designed specifically for optical and structural studies, a $0.8\mu\text{m}$ GaAs buffer was grown below the QDs and they were covered with a thin GaAs cap of 35nm or 100nm .

Transmission Electron Microscopy (TEM) is a useful tool to assess the structural aspect of the QDs. For example, Fig. 1a shows a cross-section view of an InAs/GaAs which was grown without a cap layer. The sample was grown on (100) GaAs, at a substrate temperature of $\sim 515^\circ\text{C}$, with a deposition of the equivalent of 0.54nm of InAs at a growth rate of 0.02 nm/s , and followed with a growth interruption of 60s . For the uncapped QDs this was followed by a rapid cool down. The TEM give a nice illustration of the island growth and it might be useful for evaluating the diameter of the QDs, but is not representative of the height of the QDs since the latter can be adjusted by doing some size and shape engineering during the growth of the cap layer.^{13,28,32-34} To properly evaluate the shape and the size of the QDs, plane view TEM can be used on capped layers. Such imaging is complicated by the fact that contrast is mainly originating from the strain profile and it changes with the diffraction condition used for the imaging as seen in Fig. 1b to 1d. To interpret the apparent shape, accurate modeling is required,³⁵⁻³⁷ and it was found that the (220) DF condition gives very little differentiation in the shape, but the [001] BF condition can give useful information about the QD perimeter³⁵. The structural information can be useful to model the energy levels of the QDs. For example, fig. 2 depicts a QD having the shape of an hemispherical cap on top of the wetting layer (WL).³⁸ Such a QD would give a round perimeter in a plan-view TEM under the [001] bright field condition of fig. 1b.

region, or to increase the photoresponse. Here we review how size and shape engineered stacks^{13,28} of uniform QDs can be used to obtain QD lasers with sharp adjustable 0D shells, and to unambiguously identify which 0D-levels are involved for the gain, the stimulated emission, or the detection.

2. GROWTH AND ELECTRONIC SHELLS

The layers are grown in a modified V80H MBE system using a nominal As_2 molecular flux.²⁸ The self-assembled QDs were obtained using the spontaneous island formation in the initial stages of the Stranski-Krastanow growth mode during the epitaxy of highly strained InAs on (Al,Ga)As layers on (100) GaAs substrates.²⁹⁻³¹ The laser structures typically consist of a thick ($\sim 2\mu\text{m}$) n^+ $\text{Al}_x\text{Ga}_{1-x}\text{As}$ contact layer, followed by an $\text{Al}_y\text{Ga}_{1-y}\text{As}$ bottom cladding layer with a lower doping and with $y < x$ to form a 2-step separate confinement cladding region, followed by the active region. The active region is usually made of a 15-nm undoped GaAs on each sides of a stack of self-aligned InAs QDs. This study will review here the results for lasers obtained with stacks of 7 or 14 layers with GaAs

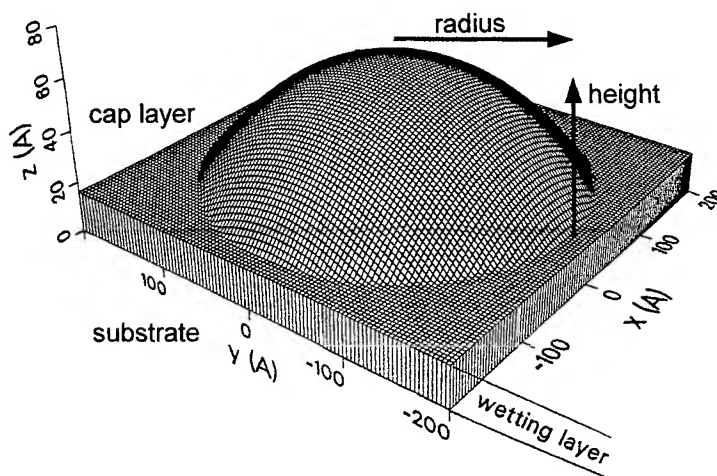


Fig. 2: Modeling of the self-assembled QD potential using an hemispherical cap of InAs on top of an InAs wetting embedded in a GaAs substrate and cap layer.

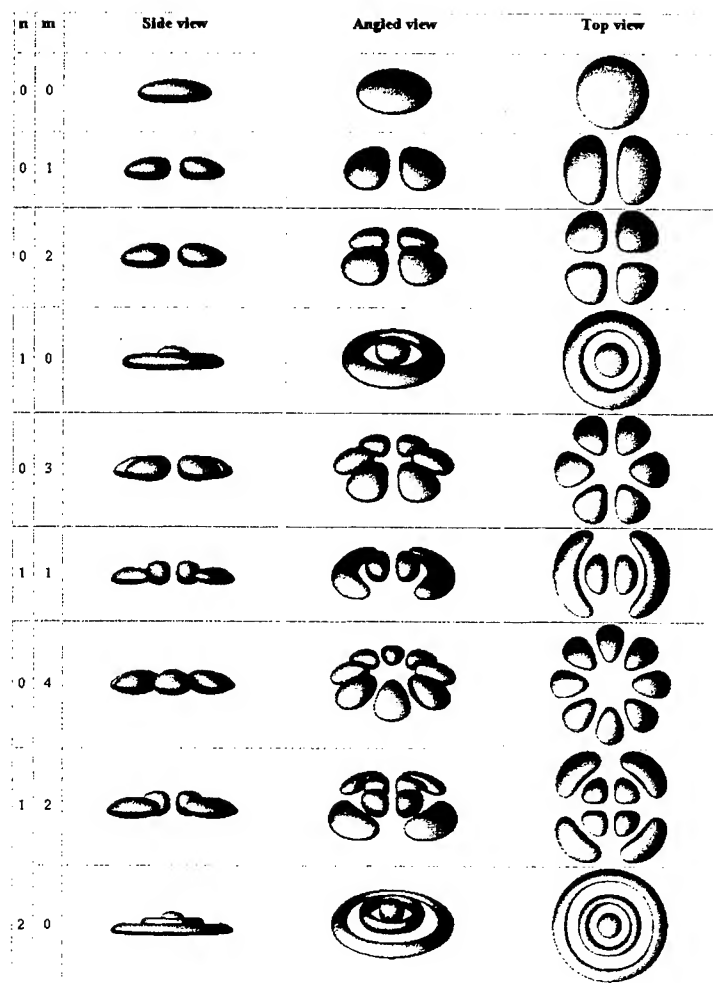


Fig. 3: Orbitals in a lens shape QD. The probability density of the electron wavefunction are displayed for the various radial (n) and angular (m) quantum numbers as viewed from different perspective. In similarity to the real atoms, the orbitals can be classified into s , p , d , f , g , etc, shells according to their quantum numbers $l = m + n$, for example single-degenerate $l = 0$ for the s -shell, double-degenerate $l = 1$ for p -shell, triple-degenerate $l = 2$ for d -shell, etc. Each level is double-degenerate for the spin.

picture presented above for the single particle energy levels.^{39,4} These electronic shells can be observed for QD ensembles for which the inhomogenous broadening leads to energy fluctuation smaller than the lateral quantization energy: i.e. an emission linewidth with full-width at half-maximum (FWHM) smaller than the intersublevel energy spacing. For example, we found that there is four main parameters to controlled during the growth to obtain good quality QDs with well-resolved excited-state emission: 1) the substrate temperature is selected to control the size of the QDs and thus to obtain the desired intersublevel energy-spacing;^{10,11,42} 2) the amount of strained material deposited (here InAs) has to be precisely determined for the chosen growth temperature to control the density of QDs and thus obtain well-resolved excited-states.^{10,43,44} For an optimized density, in addition to a number of QD states, the wetting layer photoluminescence (PL) is typically observed in state-filling spectroscopy; 3) depending on the growth rate chosen for the strain material, a growth interrupt (anneal) must be used to let the QDs evolve to their equilibrium shape and obtain good ensemble uniformity;¹⁰ 4) an *indium-flush* technique can be used during the capping of the QDs for additional size and shape engineering.^{10,13,28} Such shape-engineered stacks of self-aligned QDs with improved uniformity can be used to increase the gain in the active region of QD lasers having well-defined excited-states, as will be shown below.

Using a QD potential as in fig. 2, the wavefunctions and the QD energy levels can be calculated.³⁸⁻³⁹ For example, fig. 3 depicts the electron orbitals in such a lens shape QD.⁴⁰ In similarity to the real atoms, the orbitals can be classified into s , p , d , f , g , etc, shells according to their quantum numbers $l = m + n$, where n and m would be the radial and angular quantum numbers respectively. For example, for an effective harmonic oscillator potential, there is a single-degenerate $l = 0$ for the s -shell, double-degenerate $l = 1$ for p -shell, triple-degenerate $l = 2$ for d -shell, etc. The schematic of the energy levels in such an InAs/GaAs self-assembled QD having 5 electron and hole shells ($v = s, p, d, f, g$) are illustrated in fig. 4. There is a quasi-constant energy separation between the shells. This is reminiscent of the effective parabolic-potential, and it leads to a degeneracy $g_v = 2(l+1)$ where $l = 0$ for s , $l = 1$ for p , etc, and the factor 2 is for the spin. The resulting interband transition will be mainly between excitons formed from electrons and holes in the shells with the same quantum numbers, yielding S , P , D , etc transitions in photoluminescence experiments. Fig. 4 also shows that the dynamics of the state-filling involves the interband recombination time for the various shells (τ_v), the intersublevel relaxation rates (γ_{isl}) which will depend on the filling of the lower shells because of the Pauli exclusion principle, and also the carrier diffusion (τ_D) and capture (τ_c).⁸ This is a simplified single particle picture which neglects the effects of multiexciton complexes as the number of excitons in the QD is changed. The latter can lead to variation in the emission energy over tens of meV.^{39,41} Nevertheless, condensation of the electron holes into coherent many exciton states due to hidden symmetries yield emission spectra with electronic shells which can be associated with s , p , d , etc, electronic shells similar to the simple

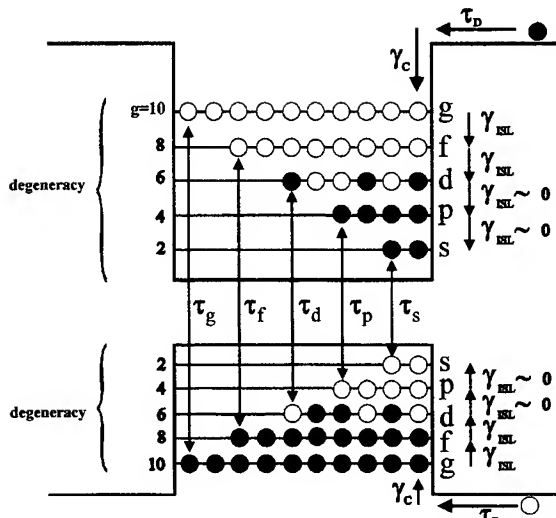


Fig. 4: Schematic of the energy levels in an InAs/GaAs self-assembled QD having 5 electron and hole shells ($v = s, p, d, f, g$) with a quasi-constant energy separation between the shells reminiscent of an effective parabolic-potential, and with a degeneracy $g_v = 2(l+1)$ where $l = 0$ for s , $l = 1$ for p , etc. The dynamic of the state-filling involves the interband recombination time for the various shells is τ_v , the intersublevel relaxation rates γ_{ISL} , the carrier diffusion (τ_D) and capture (τ_c).

W/cm^2) a $1/N$ dependence of the relaxation time was observed. These results clearly established the regime where the relaxation is governed by Auger processes. The relaxation which involves phonon and its dependence on the intersublevel energy can be further investigated by probing QDs with different shell spacing in the low intensity regime.

The excited state radiative lifetimes can be deduced from the state-filling spectroscopy of fig. 5.⁵² As the excitation intensity is increased, the lower shells are filled as depicted in fig. 4, and excited-state emission starts to appear, and may eventually show stronger emission than the ground state depending on the shell degeneracy and the radiative lifetime (τ_v) of the upper shells. However, for accurate state-filling spectroscopy, the excitation profile of the probe beam must be uniform. For example, for a typical Gaussian profile of excitation, a continuous range of excitation are effectively used because the QDs situated in the center of the focused spot will be highly excited but the QDs in the wings of the Gaussian beam will receive a lower excitation intensity. For non-uniform excitation profiles, the s -shell emission is favored over that of the upper shells because a large area is probed with low intensities, and also the s -shell emission will not saturate because the number of QDs effectively probed increases as the low intensity wings of the Gaussian beam are expanding. In fig. 5, a probe beam with a uniform intensity was used and an absolute saturation of the s , p , and d shells is observed for the intensity used. For such steady-state uniform excitation in the high-excitation limit, the ratio of the radiative lifetimes of any two shells is proportional to the ratio of their saturation intensities and inversely proportional to the ratio of the degeneracy of these shells.

Fig. 5 shows an example of state-filling spectroscopy. Photoluminescence spectra are obtained at different excitation intensity. For low excitation, only a low energy peak is observed, indicating a fast carrier relaxation toward the lowest states of the QDs (s -shell). Indeed the intersublevel relaxation rates are very fast compare to the interband radiative lifetime for the exciton recombination for the various shells. The carrier energy relaxation in quasi-zero-dimensional structures has been widely studied in recent years⁴⁵⁻⁴⁸ due to their important physical implications in the improvement performance of quantum-dot lasers. The discrete atomic-like energy spectrum of the QDs imposes constraints on the allowed inelastic relaxation mechanisms. In particular, single longitudinal-optical phonon emission is forbidden unless the energy levels of the dots are separated by exactly the fixed LO-phonon energy. The blocking of this normally important relaxation channel was expected to cause a strong reduction in the carrier relaxation scattering rate.⁴⁹ The observed good carrier relaxation efficiency can be explained by mechanisms such as Auger-type processes⁵⁰⁻⁵² and multiphonon processes.^{1,46,53} For example, recently, the nature of the relaxation mechanism in self-assembled QDs was investigated by studying the excitation density and the excitation wavelength dependencies of the PL rise times in time-resolved experiments.^{48,54} The measured QD rise times were smaller than 40 ps at low excitation, and at intermediate excitation densities (from ~ 3 to 300

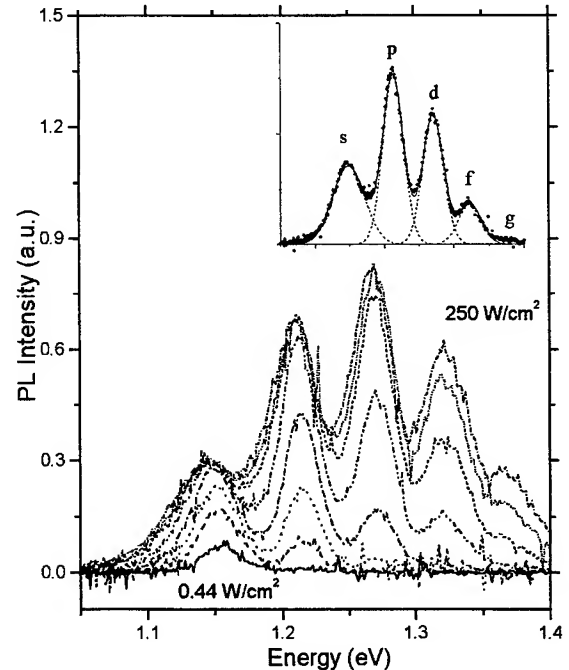


Fig. 5: State-filling of the QD shells with increasing excitation intensity between 0.44 W/cm^2 and 250 W/cm^2 in low temperature photoluminescence (PL) spectroscopy. Absolute saturation of the lower shells is observed when a the excitation beam has a constant intensity profile. The inset show a Gaussian fit used to deconvolute the contribution from the various shells.

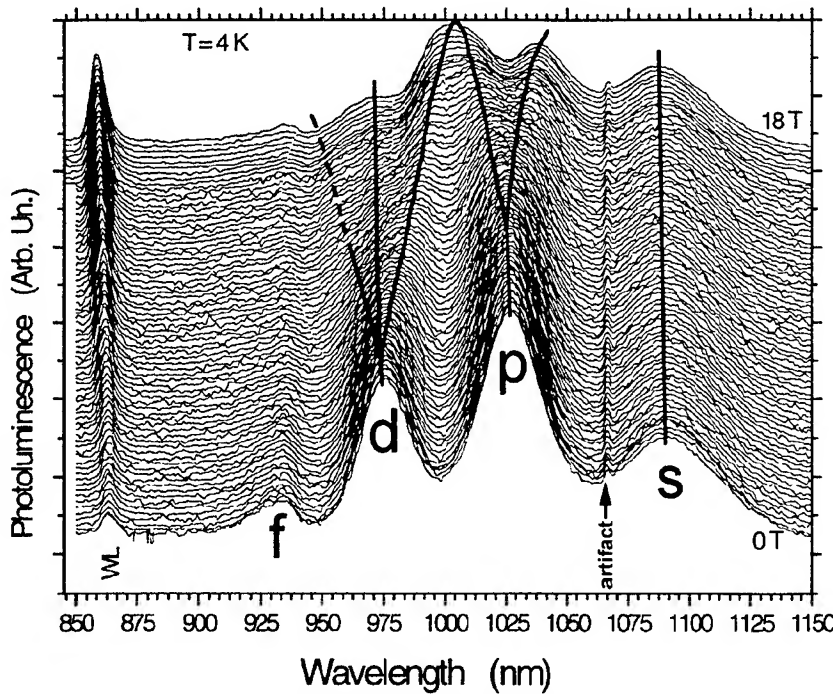


Fig. 6: State-filling spectra of a QD ensemble having well-resolved electronic shells in a magnetic field between 0T and 18T. The magnetic field lifts the degeneracy of the upper shells and leads to shell reconstruction.

It allows to quantitatively compare the relative importance of multi-phonon and Auger processes.

Probing the QDs with a magnetic field can further provide information about the symmetry of the QDs and also about the carrier capture. For example, fig. 6 shows the state-filling spectroscopy at 4K, for fields between 0T and 18T, on a QD ensemble displaying sharp electronic shells. Only the *s*, *p*, and part of *d* shells are observed in fig. 6 due to the somewhat lower excitation density used here because a fiber with a large diameter was used to deliver the excitation in this magneto-PL experiment. Nevertheless, the spectra clearly show a splitting into 2 of the *p*-shell and suggest a splitting into 3 of the *d*-shell with a shell reconstruction at higher magnetic field according to the various angular momenta. The recombination can be understood in terms of a gas of weakly interacting excitons. Such spectra of exciton droplets in zero-dimensional systems can be compared with modeling of coherent many-exciton states and the destruction of hidden symmetry by the magnetic field.^{4, 38}

It is also clear in the magneto-PL spectra that the diffusion and the capture of the photocarriers transferred from the wetting layer to the QDs is affected by their cyclotron orbit in the magnetic field. All the spectra in fig. 6 are obtained at a constant excitation intensity and displayed on the same scale (with an offset for clarity), and clearly the amplitude of the wetting layer

Depending on the QD density and on the photocarrier diffusion length, the wetting layer emission can also be observed. For example, time-resolved studies of the wetting layer PL can be combined with the state-filling spectroscopy of the QD and of the wetting layer emission to obtain carrier transfer rates from the wetting layer to the QDs. This provides a method to measure the capture rates and to experimentally determine the Auger capture coefficient in self-assembled QDs.⁵² The results show that the capture efficiency increases with the carrier concentration in the wetting layer, indicating the important role of the Auger processes in the capture dynamics. Such studies combining state-filling spectroscopy of the QDs and time-resolved PL of the wetting layer provide a unique method for studying the carrier dynamics with a regime of constant carrier concentration instead of with probe pulses in which case the number of carriers is varying with time.

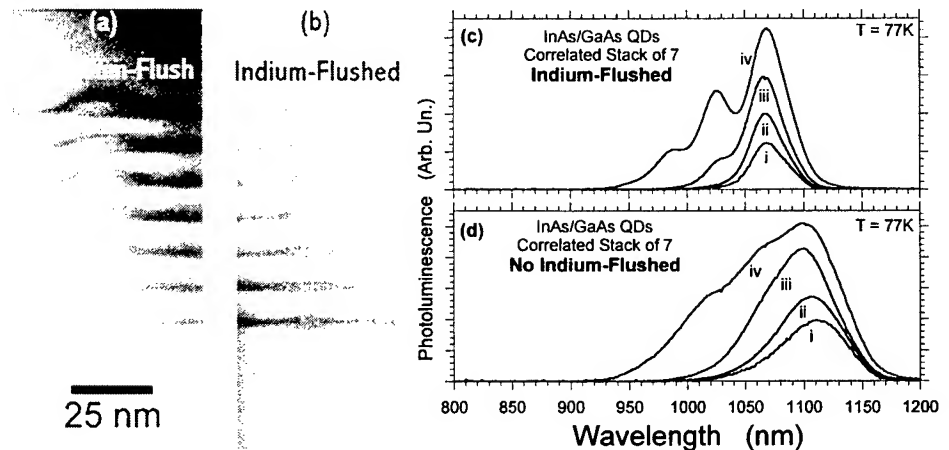


Fig. 7. Using the Indium-Flush technique to make InAs/GaAs QD stacks more uniform: (a) and (b) are cross-section Transmission Electron Microscope (TEM) images of shape-engineered InAs/GaAs QDs grown at 515°C, and the corresponding state-filling spectroscopy are in (c) and (d). For stacks Indium-Flushed at 5.0nm (b) and (c) showing better uniformity, and for stacks with no Indium-Flush (a) and (d). The GaAs spacers are 10nm, the PL is excited with various intensities up to a few kW/cm^2 (iv).

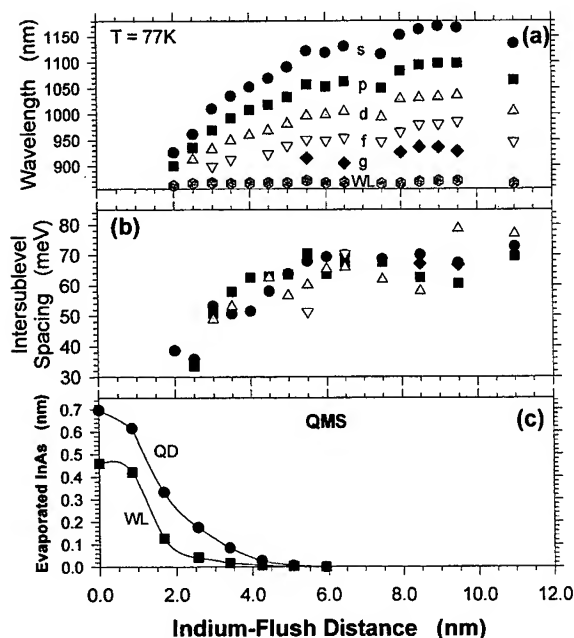


Fig. 8. Tuning of the energy levels (a), and of the intersublevel energy-spacing (b) with the position of the Indium-Flush during the capping of the InAs/GaAs QDs. Single layer of QDs, 1.9 monolayers of InAs grown in 27s at 515 °C, growth interruption of 60s, and the total GaAs cap thickness is 100nm. The InAs removal can be monitored with in-situ QMS measurements (c) for QD layers (circles) or wetting layers (square). The QD shells are labeled with the atomic notation: s, p, d, etc.

be used to do some size and shape engineering in the case of single layer samples, and to tailor the QD shell structure. This is demonstrated in fig. 8 which shows for that for an indium-flush executed after between 2.5 nm and ~5.5 nm, the QDs can be continuously adjusted from having a more disk-like shape to the more standard lens-shape (e.g. see fig. 7a and 7b). The total number of bound 0D states changes from three for the sample indium-flushed at 2.5 nm to five for the sample indium-flushed at more than ~5.5nm, as seen in fig. 8a. For the present growth temperature, the intersublevel energy-spacing is tuned from ~35 to ~65 meV (see fig. 8b). For the samples indium-flushed after a GaAs thickness larger than ~5.5nm, little InAs is removed and the intersublevel spacing remains about the same, but the energy level positions shift slightly due to changes in the confinement potential caused by the combined effects of QD intermixing and indium segregation in the barrier. The InAs removal can be monitored with in-situ quadrupole mass spectrometer (QMS) measurements and is shown in fig. 8c. It demonstrates that below ~2nm, most of the indium is evaporated (flushed), and that more InAs is removed in the case of the QDs compared to the WL.

Fig. 9 shows the active region of a QD laser grown with 14 layers where the QDs are quite uniform from one layer to the next. This is interesting for improving the gain saturation of QD lasers, but it is also of great interest for coupled QD structures.⁶⁹ Indeed, a prerequisite for observing the level splitting caused by quantum

peak (WL) increases as the field increases. At higher fields, the photocarriers are forced to orbit on a diameter which becomes smaller relative to the mean QD separation and diffusion length.

3. SIZE AND SHAPE ENGINEERING

Strain-induced vertical self-alignment has been observed for several years in the Stranski-Krastanow epitaxy.^{55-58,25} For devices, it can be desirable to have multiple layers of QDs, and also the electronic coupling between nanostructures is of great interest.^{59-68,44} However, it is only recently that it has been possible to observe well-resolved electronic shells in an ensemble of QDs having a number of correlated layers by using an indium-flush technique.¹³ For example, this is demonstrated in fig. 7 for correlated stacks of 7 layers separated with 10 nm spacers of GaAs, grown with and without the indium-flush. In fig. 7d for no indium-flush, no sharp electronic shell can be observed because of the change in the QD size from one layer to the next, as observed from the TEM images (fig. 7a). The uniformity problem with correlated stacks can be circumvented with the indium-flush, as illustrated in fig. 7b and 7c which is for a sample grown under the same conditions but with an indium-flush executed at 5.0 nm in the middle of the GaAs barrier. The number of stacked layers can be further increased while preserving the well-resolved electronic shell structure (see below). The indium-flush technique can also

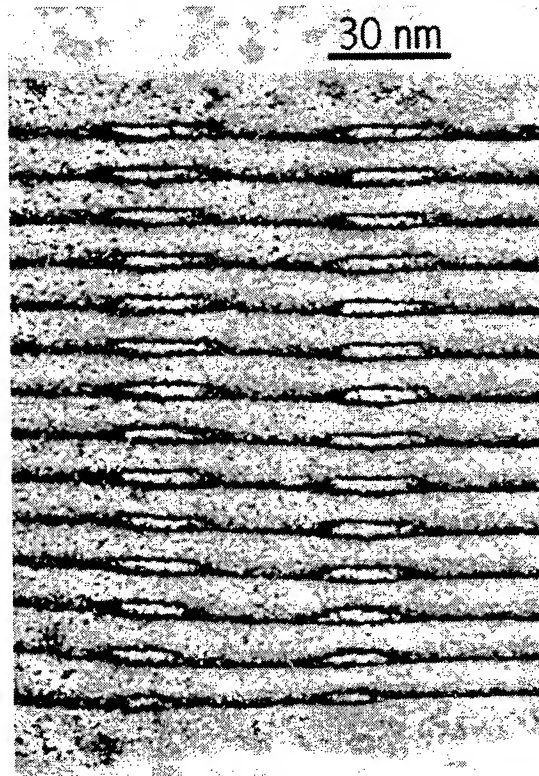


Fig. 9: Laser diode with shape-engineered self-aligned QDs. Cross-section TEM of a the active region of the laser diode containing a stack of 14 layers of InAs QDs indium-flushed at 5.0nm and separated by 10.0 nm GaAs spacers.

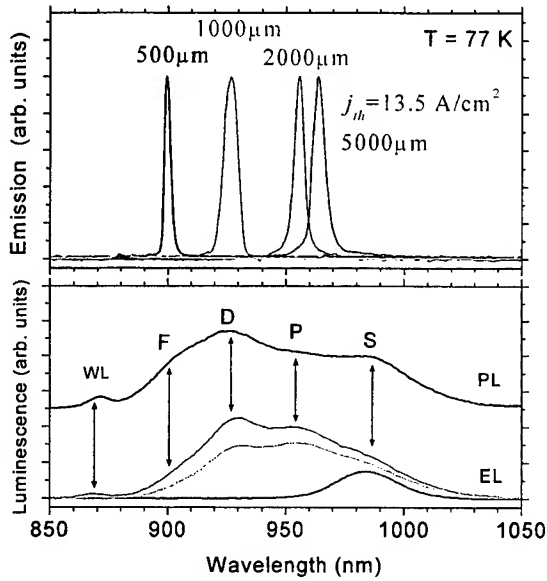


Fig. 10. Lasing at 77K in broad area lasers having shape-engineered QD stacks with well-resolved excited-states: The electroluminescence (EL) and PL are shown (bottom) to identify which of the electronic shell (s to f and wetting layer) are lasing for the various cavity lengths (top). Stacks of 7 InAs/GaAs QDs with indium-flush at 2.8nm and 10.4nm GaAs spacers

layers separated by 4 nm. Further studies could be done

mechanical coupling between overlapping states is that the levels of the uncoupled QDs would be close in energy. Size, composition, and strain changes in the stacks can often cause energy level variations in the adjacent QDs. This leads to larger inhomogeneous broadening in ensembles of uncoupled QD stacks as seen in fig. 7, and to charge transfer between asymmetric QDs instead of level splitting for the closely stacked QDs. The self-aligned uniform QDs obtained with the indium-flush technique as seen in fig. 9 opened up an opportunity for producing coupled QDs by reducing the spacer thickness further to grow in close proximity 2 or more layers of QDs which are as nearly identical as possible.⁶⁹ We recently demonstrated that artificial molecules can be obtained using such coupled quantum dot (CQD) ensembles with well-defined electronic shells. The coupling strength between the zero-dimensional states was varied by changing the distance between 2 layers of stacked self-assembled InAs/GaAs QDs. For strongly coupled QDs grown with a 4-nm spacer, state-filling spectroscopy reveals a shift of the QD symmetric state to lower energies by ~23 meV. The wetting layer states are also strongly coupled because of the shallow confinement, resulting in a red-shift of its symmetric state by ~26 meV. Single QD spectroscopy^{41,70} was also performed on double CQD with different spacer thickness to further study the entangling of the low-dimensional quantum states in the vertically self-aligned QDs. The entanglement was followed as a function of the coupling strength, and the coupling was measured as a splitting of the emission line from a single pair of entangled QDs. An energy splitting exceeding 30 meV was observed for the QD to tune the coupling with an applied electric field.

4. QUANTUM DOT LASERS

We used the indium-flush technique to engineer QD lasers and detectors with improved uniformity similar to the one seen by TEM in fig. 9. For example using the indium-flush study of fig. 8, a QD laser diode was design with an indium-flush performed at 3.0nm to provide a ground state emission at $\lambda \sim 980\text{nm}$, with uniform self-aligned QD stacks having 7 layers separated by 10.0nm, and which would yield sharp excited-state emission. The results are shown in fig. 10 for 77K, and in fig. 11 for 300K. The 0D shells involved in the stimulated emission can unambiguously be assigned when the injection current is increased above threshold. The lasing is observed in the upper QD shells for short laser cavities, and progresses towards the QD ground states when the cavity length is increased (larger gain medium). At 77K, we obtained very low current density thresholds of $J_{th} = 15 \text{ A/cm}^2$ for a 2 mm cavity lasing in the first excited state (p-shell), and of $J_{th} = 125 \text{ A/cm}^2$ for a 1 mm cavity lasing in the d-shell. At 300K for a 5 mm cavity, the threshold is increased to 430 A/cm^2 with lasing d-shell, whereas a shorter cavity of 1 mm gives lasing at 490 A/cm^2 in the f-shell.¹³

The top cladding layers of the QD laser structure were grown at lower temperatures (~540°C) to avoid additional in-situ QD intermixing. Indeed, it is also important to control the alloy intermixing between the QD and barrier materials during the growth, particularly for laser diodes which typically require long growth times after the deposition of the QDs. For laser structures grown with

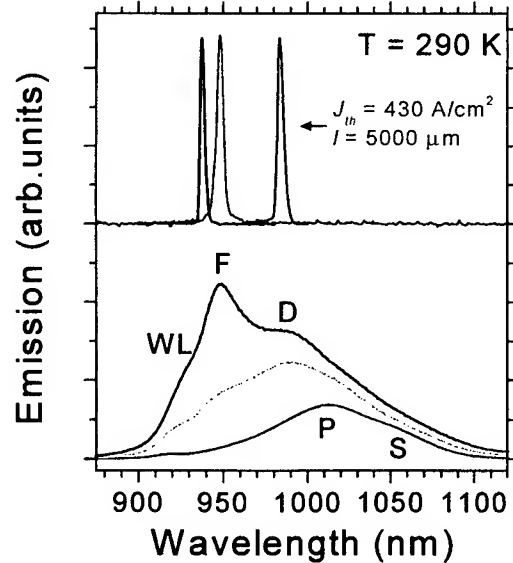


Fig. 11. Lasing at 300K in broad area lasers having shape-engineered QD stacks with well-resolved excited-states: The EL spectra below threshold are shown (bottom) to identify which of the electronic shell is lasing (top). Same sample as fig. 10, cavity lengths are 0.5mm, 1 mm, and 5mm from left to right.

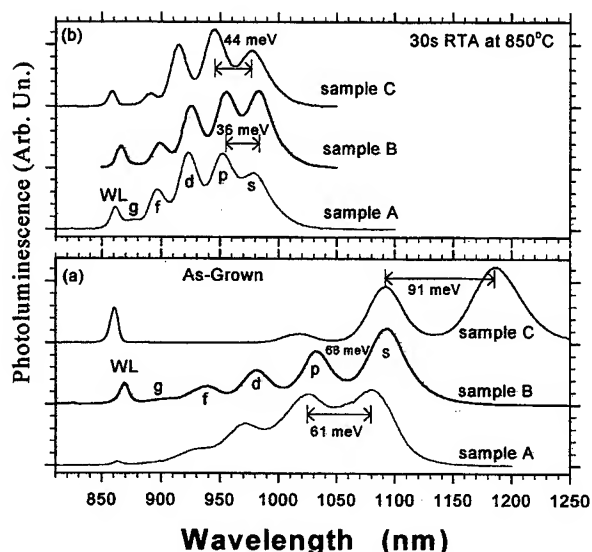


Fig. 12. Thermal intermixing of QDs having different intersublevel energy spacings. PL in (a), showing the state-filling spectra of the As-grown samples A, B, and C obtained at a substrate temperature of 530°C, 515°C, and ~480°C respectively. Same samples intermixed with a RTA of 30s at 850°C in (b).

obtained by adjusting the substrate temperature during the QD formation to change their equilibrium size.^{10,11,42} Fig. 12(b) shows the effects of QD intermixing using a 30s RTA at 850°C to interdiffuse the InAs QDs with the GaAs barriers. It is clear that the energy levels of the intermixed QDs from the different samples are more alike after intermixing: for example the energy difference between ground states (s-shell) of the various samples went from over 100meV for the As-grown samples to just a few meV after intermixing. Nevertheless, sample C originally with the largest intersublevel energy spacing is still the one with the largest lateral quantization energy after intermixing. The intense and sharp shell structures observed in the photoluminescence of the intermixed samples indicates unambiguously that the QDs retained their zero-dimensional density of states after the diffusion of the potential. No pronounced changes were observed in the intensity of the PL for the intermixed QDs. This is in contrast with what some groups have reported^{76,79} for their intermixed QDs where quantum well like behaviors were observed for the higher intermixing conditions, and/or a reduction in the PL were observed and attributed to the formation of dislocations. Such detrimental effects are not present here most likely because of the high quality and the low in-plane density of the initial QD ensemble.^{10,43,44}

5. QD INFRARED PHOTODETECTOR (QDIP)

The schematic of a quantum dot infrared photodetector (QDIP) structure is shown in fig. 13 on the left. Similar to a quantum well infrared detector (QWIP), the QDIP structure comprise multiple layers between a collector and an emitter. The emitter and collector are doped to act as a reservoir of charged carriers and to conduct the current during detection and for operation under applied bias. The charged carriers are introduced in the quantum dot layer by either doping the barrier and/or the dot layers, and after redistribution of the charged carriers and adjustment of the Fermi level.

the upper clad at a temperature around 540°C, the spontaneous emission of the diode matches well the targeted values deduced from the indium-flush study shown in fig. 8. However, it has been demonstrated that QD intermixing^{3,71-79} can have a pronounced effects on the optical properties of the nanostructure. For example a test QD structure grown with an in-situ anneal at a substrate temperature of 620°C for 30 minutes was used to simulate the growth of cladding layers at temperatures often used for GaAs growth by MBE. The QD structure grown with the in-situ anneal had its s-shell shifted by 94 meV compare to a control structure grown without the anneal (see ref. 13). Also the intersublevel energy spacing shifted from 68meV to 40meV.

More detailed studies on QD intermixing have revealed that there is 3 main effects for the intermixing of the InAs/GaAs self-assembled QDs:^{80,3} using rapid thermal annealing (RTA) to induce alloy intermixing on as-grown samples, 1) their intersublevel can be tuned between ~90meV and 25meV, 2) strong blueshifts (up to ~200meV) can be obtained, and 3) a pronounced narrowing of the inhomogeneously broadened emission (down to ~12meV) is observed. For example, fig. 12(a) presents results for different as-grown InAs/GaAs QD samples having intersublevel spacings of 61meV (sample A), 68meV (sample B), and 91meV (sample C). The various intersublevel energy spacings of the as-grown samples were

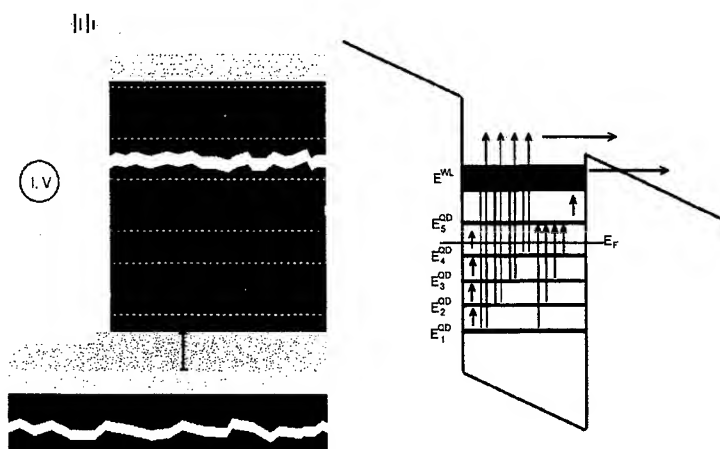


Fig. 13. Schematic of a QDIP structure (left) and its energy diagram (right). The self-assembled QDs are separated with barriers which are modulation-doped to populate the lower shells of the QDs. Transitions from the occupied QD states to the WL or to the continuum result in infrared detection with normal incidence response because of the zero-dimensional geometry.

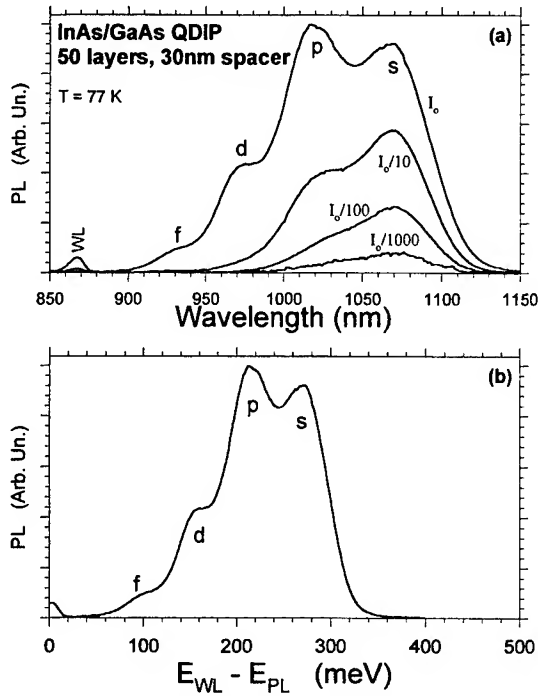


Fig. 14. State-filling spectroscopy of an InAs/GaAs QDIP sample displaying the zero-dimensional states. In (a), the photoluminescence is obtained at 77K excited with $\lambda_{ex} = 532$ nm and I_0 is a few kW/cm^2 . The position of the electronic shells relative to the WL position are plotted in (b) for the spectrum obtained at the highest intensity.

quite uniform from one layer to the next even for a stack of 50 layers having a total thickness of ~ 1.5 microns. For the spacer thickness used here however, the layers are not vertically self-aligned as in fig. 9, and are essentially 50 independent layers.

This was verified with cross-section TEM imaging of the QDIP structure which confirmed that the QDs are not correlated in the stack for the spacer thickness of 30 nm.

Fig. 14b displays the highest excitation PL spectrum with its energy axis relative to the wetting layer energy and can be compared with the response measured with a similar InAs/GaAs QDIP device shown in fig. 15. As can be seen in fig. 14b, for those QDs, the highest energy difference for transitions of carriers confined in the s-shell excited in the wetting layer by an infrared photon would be smaller than ~ 300 meV ($\lambda \sim 4.1$ microns). The QDIP response in fig. 15 is maximum between the energy range of ~ 140 meV to ~ 300 meV. From fig. 14b, that would correspond mainly to transitions from the s and p shell to the wetting layer which would cover a energy range between ~ 170 to ~ 310 meV. The sharp dips in the QDIP response corresponds to atmospheric absorption lines. The high energy tail which extends up to ~ 500 meV would correspond to transition from the QD states directly into continuum states above the GaAs barriers as illustrated in the energy diagram of fig. 13. The low energy cutoff is determined by the level of doping which rises the Fermi level closer to the wetting layer energy.

The level of doping in the various region of the device and the scheme of doping is adjusted to set the Fermi level such that the desired number of energy levels in the quantum dots are occupied with charged carriers to achieve the targeted range of detection wavelengths. For example, the right of fig. 13 shows the energy band diagram for a QD with 5 bound shells below the 2-dimensional wetting layer states. The self-assembled QDs are separated with barriers which are modulation-doped to populate the lower shells of the QDs. The size and the number of quantum dots per unit area is adjusted from the growth parameters in conjunction with the doping to achieve the desired detection range and while optimizing the detection efficiency for the wavelengths of interest. Transitions from the occupied QD states to the WL or to the continuum result in infrared detection with normal incidence response because of the zero-dimensional geometry. Indeed, a major limitation of the QWIPs is that due to the transition selection rules they are not sensitive to normally incident light, and only have narrow response range in the IR. Consequently, normal incidence detection over a broad range in the IR can only be achieved with complicate light coupling devices or schemes, and by combining layers with different sets of quantum wells each having its own narrow response range. Similarly, the choice of the barrier material, height, and thickness is adjusted in conjunction with the quantum dot size to set the detection range.

Fig. 14 shows the results of low temperature state-filling spectroscopy for a QDIP structure made with 50 InAs QDs layers with GaAs spacers 30nm thick. We observed a well-resolved s, p, d, f shell structure with intersublevel energy spacing of about 58 meV, as well as the wetting layer emission. The observation of the well-resolved excited-state structure clearly indicate that the QD are

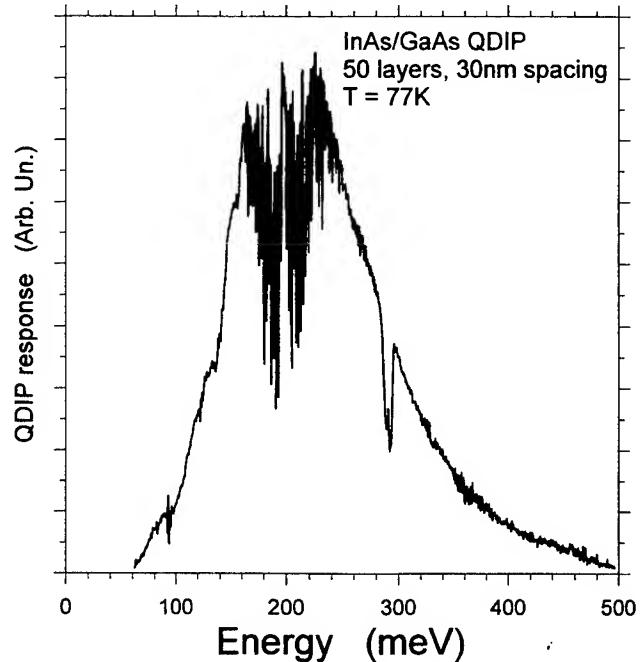


Fig. 15. Normal incidence detection in a InAs/GaAs QDIP at 77K.

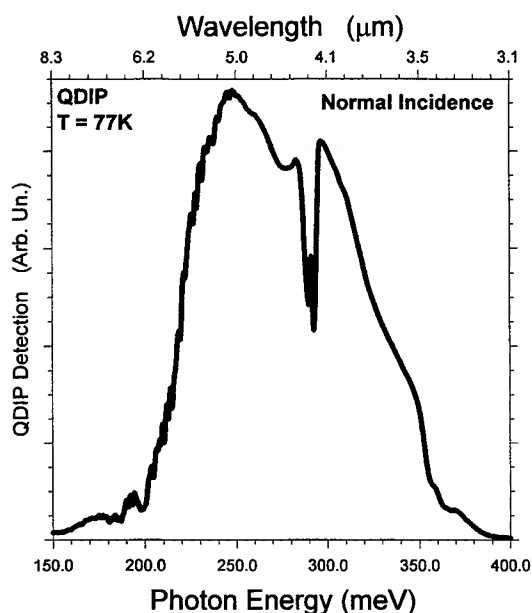


Fig. 16. Normal incidence detection in a InAs/AlGaAs QDIP at 77K.

have broad response ranges, they are promising for applications and are becoming a field of interest for several research groups.⁸²⁻⁸⁴

6. INTERBAND DETECTION

For detection in the visible and in the near infrared, QDs can be grown into a suitable p-i-n or n-i-n structure which would exploit the excitonic interband absorption in zero-dimensional nanostructures. In addition to unique properties which are interesting for device purposes such as the enhanced degradation resistance of QDs compare to quantum wells,^{85,86} these studies can also reveal interesting physics. For example, we demonstrated that self-assembled QDs exhibit an asymmetric Stark shift in an electric field applied along the growth direction because one polarity forces the electron towards the tip of the QDs whereas the holes are driven towards the wetting layer.⁸⁷

Fig. 17 shows the low temperature (curve i) and room temperature (curve ii) open circuit photovoltage measured on the QD laser diode shown by TEM in fig. 9. Well-resolved shell structures are observed and can be compared with the results obtained in PL or in electroluminescence (EL). The photovoltage gives a measure of the absorption when the zero-dimensional density of state is empty of carriers. The photovoltage therefore gives results about the shell structure when it is empty. This should be closer to the single particle picture (as discussed in fig. 3 and fig. 4), and the photovoltage spectra can be contrasted with the state filling spectroscopy and the lasing spectra

As mentioned above, the barrier material can be chosen to change the energy range for the detection of the QDIP. For example, fig. 16 shows another example of QDIP with normal incidence detection. Here the InAs QDs were embedded in $\text{Al}_{0.3}\text{Ga}_{0.7}\text{As}$ barriers. The spectral response is shifted to higher energies, peaking at ~ 250 meV (5.0 microns). The spectrum also contain a dip due to atmospheric absorption, but also appears to have 3 distinct broad features separated by about 40-50 meV which might be associated with the intersublevel energy spacing for the electrons. The responsivity was measured at 80K, and values above 0.1 A/W were obtained for voltages of ~ 3 V at a detection wavelength of 5 microns.⁸¹ The QDIP photodetectors will have a much broader response range in the infrared compared to typical QWIP designs because the self-assembled QDs naturally grow (or can purposely be grown) with an inhomogeneous broadening in the size, and/or composition and/or strain. In addition to the inhomogeneous broadening, the QDIP provides with a larger response because the reduced density of states yields a variety of transitions which depending on the occupancy of the QD states can participate in the detection and which effectively leads to a much larger homogeneous broadening. For many applications, the overall responsivity would actually be proportional to the wavelength-integrated response which would be higher by a factor directly proportional to the bandwidth of the response. Therefore, because the QDIPs are sensitive at normal incidence and

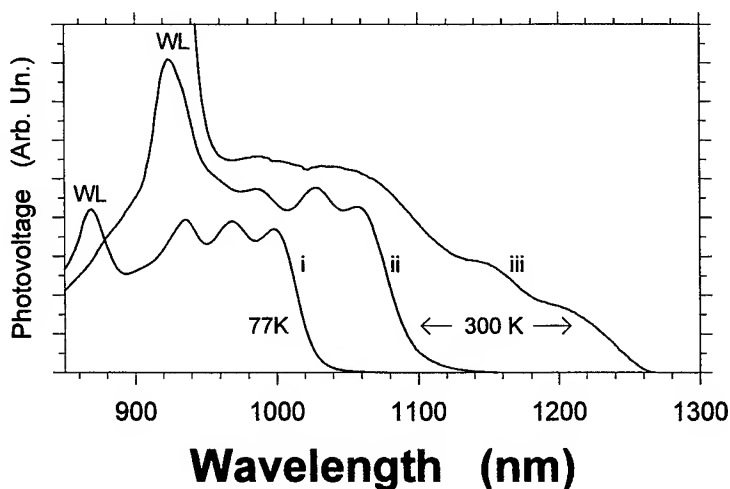


Fig. 17. Interband zero-dimensional transitions measured with open circuit photovoltage across QD laser diodes: curve i) is at 77K for a stack of 14 indium-flushed at 5.0nm (the laser shown in TEM in fig. 9), curve ii) is the same laser at 300K, and curve iii) is for a laser diode with a single layer indium-flushed at 8.5nm with a QD ground state at close to 1.3 μm at 300K.

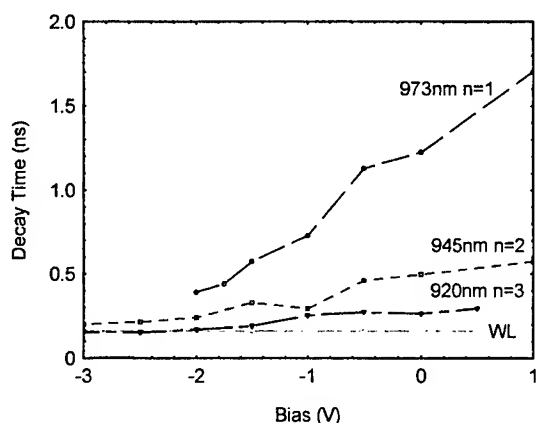


Fig. 18. Recombination dynamics of a QD laser under reverse bias probed with time-resolved photoluminescence (TRPL) at $T=100\text{K}$. The decay time for the various QD states, s-shell ($n=1$), p-shell ($n=2$), d-shell ($n=3$), and for the wetting layer (WL), are plotted as a function of reverse bias. Same QD laser as fig. 10 and 11.

to better understand multi-exciton interactions. Photovoltage is a useful tool to characterize the zero-dimensional states in the laser diodes, and for example curve iii) of fig. 17 shows for a laser diode with a single layer indium-flushed at 8.5nm (e.g. see fig. 8) with a QD ground state at close to $1.3\text{ }\mu\text{m}$ at 300K , and QD excited-states below the wetting layer (WL) peak at $\lambda \sim 920\text{ nm}$.

To study the dynamics of carriers in interband detectors, time-resolved PL was used to characterize the carrier relaxation processes and the carrier escape mechanisms in self-assembled QDs.⁸⁸ Fig. 18 shows the recombination dynamics of the QD laser of fig. 10 and fig. 11 under different reverse bias, probed with time-resolved photoluminescence (TRPL). The decay time for the various QD states, s-shell ($n=1$), p-shell ($n=2$), d-shell ($n=3$), and for the wetting layer (WL), are plotted as a function of reverse bias at 100K . The study performed at various temperature showed that the escape can occur by direct tunneling out of the excited states, by thermally assisted tunneling of ground state carriers through the upper QD states, or with thermionic emission to the wetting layer. The result shows that the QD lasers placed under reverse bias can make fast photodetectors with decay times down to $\sim 0.3\text{ ns}$.

7. MEMORY EFFECTS

Semiconductor self-assembled QDs efficiently capture photo-carriers into spatially localized zero-dimensional states. Likewise, most semiconductor surfaces have states localized to their surface. However, the carriers trapped at the surface typically recombine non-radiatively, wasting photo-carriers generated near the surface in the absence of passivation.⁸⁹ The surface is also effectively a high potential which can perturb the energy levels of a near-surface quantum heterostructure.⁹⁰⁻⁹³ For those reasons, near-surface quantum wells have been studied in the past to observe shifts of the quantized energy levels and study the properties of devices having finite cap thicknesses.⁹⁴⁻⁹⁸

It is interesting to study how the surface will influence the optical properties of QDs⁹⁹⁻¹⁰¹ for which case the in-plane motion of the carriers is eliminated. For that purpose samples with strained InAs/GaAs QDs exhibiting sharp shell structures have been grown with thin GaAs cap layers. Furthermore, such studies also provides useful information for the related case when small mesas are used to delineate the number of self-assembled QDs probed in single QD studies.^{1,41} For example, the QD states are found to initially red-shift when getting in closer proximity to the surface, because the thin cap allows partial relaxation of the QD strain. Competition between the capture of the photo-carriers in the QDs and the surface states leads to a pronounced decrease in the QD emission for cap thinner than $\sim 10\text{ nm}$. Also the transfer of carriers between the QDs and the surface gives rise to interesting optical memory effects lasting over time-scales of several minutes.

The energy levels of the near-surface QDs are revealed by observing the electronic shells of the QD ensemble using state-filling spectroscopy.^{1-9,39,102} For example, fig. 19 shows the low temperature photoluminescence (PL) spectra, obtained at an excitation intensity of a few kW/cm^2 , for QDs indium-flushed at 5.0nm with a cap thickness between 100 nm and 5.0 nm . The spectra reveal 5 well-resolved shells (s, p, d, f, g), as can be typically observed for a QD ensemble having a good homogeneity,^{1-9,102} together with the emission from the wetting layer (WL). The self-assembled QDs with the thick cap have an

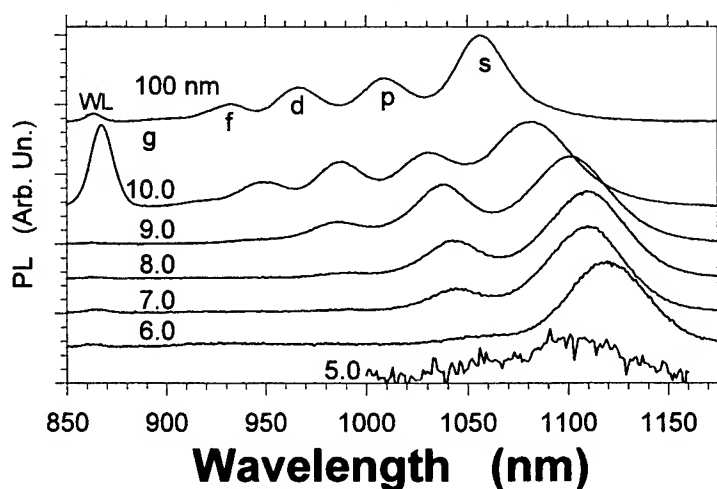


Fig. 19. State-filling spectroscopy of near-surface InAs/GaAs QDs covered with the indicated cap thickness. The 77K PL spectra are excited with a few kW/cm^2 and vertical offsets have been used for clarity.

constant intensity of a few kW/cm². For a cap thickness of 10.0 nm or larger (100 nm), the PL intensity does not vary with time. In contrast, for the samples with a cap 9.0 nm or smaller, a remarkable decrease of the steady-state PL with time is observed, with optical memory effects lasting over several minutes. The quenching of the photo-generated carriers is faster for smaller cap thicknesses or for higher temperatures. The memory effect remains for several minutes (e.g. “off” in fig. 21), but the intensity of the PL gradually recovers completely when the QDs are not photo-excited for tens of minutes. Very low excitations can also be used to monitor or to “read” the recovery of a “written” QD region. This effect is the opposite of a photo-carrier screening.¹⁰⁴ Here, for the near-surface QDs, the photo-carriers contribute to the formation of a build-in electric field. The field arises from the charge separation after the carriers transfer between the QD and surface states.

CONCLUSIONS

Quantum dot devices with genuine zero-dimensional properties, with good uniformity, and with strong carrier confinement can be realized by having a good control of the growth parameters during the epitaxy of self-assembled nanostructures. The observation of a number of well-resolved excited-states is the main figure of merit for semiconductor heterostructures based on quantum dots. Here results were presented for such quantum dot lasers having a sharp electronic shell structure and with low lasing thresholds in forward bias and with possibility for fast detection in reverse bias, for quantum dot infrared photodetectors (QDIPs) with broad normal incidence response, and for interesting memory effects in near-surface quantum dots which could be applied to coupled quantum dot structures. Alloy intermixing can be used to produce extensive changes in the electronic properties of quantum dots, including a pronounced blue-shift, and a narrowing of the inhomogeneous broadening and of the intersublevel energy spacing for the InAs/GaAs material system.

REFERENCES

1. S. Fafard, R. Leon, D. Leonard, J.L. Merz, and P.M. Petroff, Phys. Rev. B 52, 5752 (1995); *Ibidem*, Phys. Rev. B 50, 8086 (1994); *Ibidem*, Superlattices and Microstructures, 16, 303 (1994); S. Fafard, D. Leonard, J.M. Merz, and P.M. Petroff, Appl. Phys. Lett. 65, 1388 (1994); S. Fafard, S. Raymond, G. Wang, R. Leon, D. Leonard, S. Charbonneau, J.L. Merz, P.M. Petroff, and J.E. Bowers, Surface Science 361, 778, (1996).
2. K. Mukai, N. Ohtsuka, H. Shoji, M. Sugawara, Appl. Phys. Lett. 68, 3013 (1996).
3. R. Leon, S. Fafard, P. G. Piva, S. Ruvimov, Z. Liliental-Weber, Phys. Rev. B58, R4262 (1998).
4. S. Raymond, P. Hawrylak, C. Gould, S. Fafard, A. Sachrajda, M. Potemski, A. Wojs, S. Charbonneau, D. Leonard, P.M. Petroff and J.L. Merz, Solid State Communications 101, 883 (1997).
5. G. Park, O. B. Shchekin, D. L. Huffaker, D. G. Deppe, Appl. Phys. Lett. 73, 3351 (1998).
6. Y. Sugiyama, Y. Nakata, T. Futatsugi, M. Sugawara, Y. Awano, N. Yokoyama, Jpn. J. Appl. Phys. 36, L158 (1997).
7. M. Grundmann, N.N. Ledentsov, O. Stier, D. Bimberg, V.M. Ustinov, P.S. Kopev, and Zh. I. Alferov, Appl. Phys. Lett. 68, 979 (1996).
8. S. Raymond, X. Guo, J. L. Merz, and S. Fafard, Phys. Rev. B 59, 7624 (1999).
9. H. Lipsanen, M. Sopanen, J. Ahopelto, Phys. Rev. B 51, 13868 (1995).
10. S. Fafard, Z. R. Wasilewski, C. Ni. Allen, D. Picard, M. Spanner, J.P. McCaffrey, P.G. Piva, Phys. Rev. B 59, 15368 (1999).
11. S. Fafard, Z. R. Wasilewski, C. Ni Allen, D. Picard, P. G. Piva, J. P. McCaffrey, Superlat. and Microst. 25, 87 (1999).
12. S. Fafard, K. Hinzer, S. Raymond, M. Dion, J. McCaffrey, Y. Feng, and S. Charbonneau, Science 274, 1350 (1996)
13. S. Fafard, Z.R. Wasilewski, C. Ni. Allen, K. Hinzer, J.P. McCaffrey, Y. Feng, Appl. Phys. Lett. 75, 986 (1999).
14. S. Fafard, Photonics Spectra 31, 160 (1997).
15. R. Mirin, A. Gossard, and J. Bowers, Electronics Lett. 32, 1732 (1996).
16. Q. Xie, A. Kalburge, P. Chen, and A. Madhukar, IEEE Photonics Technology Letters, 8, 965 (1996).
17. H. Shoji, K. Mukai, N. Ohtsuka, M. Sugawara, et al., IEEE Photonics Technology Lett. 12, 1385 (1995).
18. H. Shoji, Y. Nakata, K. Mukai, Y. Sugiyama, M. Sugawara, N. Yokoyama, and H. Ishikawa, Jap. J. Appl. Phys. II, Lett., 35, L903 (1996); *Ibidem*, Electronics Lett. 32, 2023 (1996).
19. H. Saito, K. Nishi, I. Ogura, S. Sugou, and Y. Sugimoto, Appl. Phys. Lett. 69, 3140 (1996).
20. K. Kamath, P. Bhattacharya, T. Sosnowski, T. Norris, J. Phillips, Electronics Lett. 32, 1374 (1996).
21. D. G. Deppe and H. Huang, Appl. Phys. Lett. 75, 3455 (1999).
22. G. Park, O. B. Shchekin, S. Csutak, D. Huffaker, and D.G. Deppe, Appl. Phys. Lett. 75, 3267 (1999).

23. N.N. Ledentsov, V.M. Ustinov, V.A. Shchukin, P.S. Kop'ev, Zh.I. Alferov, D. Bimberg, *Semicond.* 32, 343 (1998).
24. K. Hinzer, J. Lapointe, Y. Feng, A. Delage, and S. Fafard, A. J. SpringThorpe and E. M. Griswold, *J. Appl. Phys.* 87, 1496 (2000).
25. S. Fafard, K. Hinzer, A. J. SpringThorpe, Y. Feng, J. McCaffrey, S. Charbonneau, and E. M. Griswold, *Material Science and Engineering* 51, 114 (1998).
26. S. Fafard, J. McCaffrey, Y. Feng, C.Ni Allen, H. Marchand, L.Isnard, P. Desjardins, S. Guillon, and R.A. Masut, *Proc. SPIE* 3491, 272 (1998).
27. M. Sugawara, K. Mukai, Y. Nakata, H. Ishikawa, and A. Sakamoto, *Phys. Rev. B* 61, 7595 (2000).
28. Z. R. Wasilewski, S. Fafard, and J.P. McCaffrey, *J. Crystal Gr.* 201, 1131 (1999).
29. D. Leonard, M. Krishnamurthy, C.M. Reaves, S.P. Denbars, P.M. Petroff, *Appl. Phys. Lett.* 63, 3203 (1993).
30. D. Leonard, S. Fafard, K. Pond, Y.H. Zhang, J.M. Merz, and P.M. Petroff, *J. Vac. Sci. Technol. B* 12, 2516 (1994).
31. D. Leonard, M. Krishnamurthy, S. Fafard, J.M. Merz, and P.M. Petroff, *J. Vac. Sci. & Technol. B* 12, 1063 (1994).
32. J.M. Garcia, T. Mankad, P.O. Holtz, P.J. Wellman, P.M. Petroff, *Appl. Phys. Lett.* 72, 3172 (1998).
33. G.D. Lian, J. Yuan, L.M. Brown, G.H. Kim, and D.A. Ritchie, *Appl. Phys. Lett.* 73, 49 (1998).
34. H. Saito, K. Nishi, S. Sugou, *Appl. Phys. Lett.* 73, 2742 (1998); *ibidem*, vol 74, 1224 (1999).
35. J.P. McCaffrey, M.D. Robertson, et al, to be published.
36. J.P. McCaffrey, M.D. Robertson, Z. R. Wasilewski, S. Fafard, and L.D. Madsen. *Inst. Phys. Conf. Ser.* 164, 107 (1999).
37. X. Z. Liao, J. Zou, D.J.H. Cockayne, R. Leon, and C. Lobo, *Phys. Rev. Lett.* 82, 5148 (1999).
38. A. Wojs, P. Hawrylak, S. Fafard, and L. Jacak, *Phys. Rev. B* 54, 5604, (1996); A. Wojs, P. Hawrylak, *Solid State Comm.* 100, 487 (1996).
39. P. Hawrylak, *Phys. Rev. B* 60, 5597 (1999); A. Wojs, P. Hawrylak, S. Fafard, L. Jacak, *Physica E* 2, 603 (1998).
40. M. Spanner et al, unpublished.
41. M. Bayer, O. Stern, P. Hawrylak, S. Fafard, A. Forchel, *Nature*, *in press* (2000).
42. R. Leon, C. Lobo, A. Clark, R. Bozek, A. Wysmolek, A. Kurpiewski, M. Kaminska, *J. Appl. Phys.* 84, 248 (1998).
43. R. Leon and S. Fafard, *Phys. Rev. B* 58, R1726, (1998).
44. S. Fafard, Z. R. Wasilewski, and M. Spanner, *Appl. Phys. Lett.* 75, 1866 (1999).
45. G. Wang, S. Fafard, D. Leonard, J.E. Bowers, J.M. Merz and P.M. Petroff, *Appl. Phys. Lett.* 64, 2815 (1994).
46. S. Raymond, S. Fafard, S. Charbonneau, R. Leon, D. Leonard, P.M. Petroff and J.L. Merz, *Phys. Rev. B* 52, 17238 (1995); J. Arlett, F. Yang, K. Hinzer, S. Fafard, Y. Feng, S. Charbonneau, R. Leon, *J. Vac. Sc. Techn.* B16, 578 (1998).
47. S. Raymond, S. Fafard, A. Wojs, P. Hawrylak, S. Charbonneau, D. Leonard, R. Leon, P.M. Petroff and J.L. Merz, *Phys. Rev. B* 54, 11548 (1996).
48. D. Morris, N. Perret, and S. Fafard, *Appl. Phys. Lett.* 75, 3593 (1999).
49. H. Benisty, C. M. Sotomayor-Torres, and C. Weisbuch, *Phys. Rev. B* 44, 10945 (1991).
50. A. V. Uskov, J. McInerney, F. Adler, H. Schweizer, and M. H. Pikuhn, *Appl. Phys. Lett.* 72, 58 (1998).
51. Al. L. Efros, V. A. Kharchenko, and M. Rosen, *Solid State Commun.* 93, 281 (1995).
52. S. Raymond, K. Hinzer, S. Fafard, J.L. Merz, *Phys. Rev. B* 61, 15 Jun. (2000).
53. T. Inoshita and H. Sakaki, *Phys. Rev. B* 46, 7260 (1992).
54. D. Morris, S. Fafard, to be published.
55. L. Goldstein, F. Glas, J. Y. Marzin, M. N. Charasse, and G. LeRoux, *Appl. Phys. Lett.* 47, 1099 (1985).
56. Q. Xie, A. Madhukar, P. Chen, and N. P. Kobayashi, *Phys. Rev. Lett.* 75, 2542 (1995).
57. G. S. Solomon, J. A. Trezza, A. F. Marshall, and J. J. S. Harris, *Phys. Rev. Lett.* 76, 952 (1996).
58. S. Rouvimov, Z. Liliental-Weber, W. Swider, J. Washburn, E.R. Weber, A. Sasaki, A. Wakahara, Y. Furukawa, T. Abe, S. Noda, *J. Elect. Mat.* 27, 427 (1998).
59. L.R.C. Fonseca, J.L. Jimenez, J.P. Leburton, *Phys. Rev. B* 58, 9955 (1998).
60. R. Provoost, M. Hayne, V.V. Moshchalkov, M.K. Zundel, K. Eberl, *Appl. Phys. Lett.* 75, 799 (1999).
61. R. Leon, S. Marcinkevicius, X.Z. Liao, J. Zou, D.J.H. Cockayne, S. Fafard, *Phys. Rev. B* 60, R8517 (1999).
62. R. Heitz, I. Mukhametzhanov, P. Chen, A. Madhukar, *Phys. Rev. B* 58, R10151 (1998); R. Heitz, A. Kalburge, Q. Xie, M. Grundmann, P. Chen, A. Hoffmann, A. Madhukar, D. Bimberg, *Phys. Rev. B* 57, 9050, (1998).
63. A. Endoh, Y. Nakata, Y. Sugiyama, M. Takatsu, N. Yokoyama, *Jap. J. Appl. Phys. B* 38, 1085 (1999); Y. Sugiyama, Y. Nakata, T. Futatsugi, M. Sugawara, Y. Awano, N. Yokoyama, *Jap. J. Appl. Phys.* 2, Lett. A36, L158 (1997); Y. Sugiyama, Y. Nakata, K. Imamura, S. Muto, N. Yokoyama, *Jap. J. Appl. Physics* 1, 35B, 1320 (1996).
64. W.V. Schoenfeld, T. Lundstrom, P.M. Petroff, D. Gershoni, *Appl. Phys. Lett.* 74, 2194 (1999).
65. S.S. Li, J.-B. Xia, Z.L. Yuan, Z. Y. Xu, W. Ge, X. R. Wang, Y. Wang, J. Wang, L.L. Chang, *Phys. Rev. B* 54, 11575 (1996).

66. L. Kouwenhoven, *Science* 268, 1440 (1995).
67. C. Pryor, *Phys. Rev. Lett.* 80, 3579 (1998).
68. J. Urayama, T.B. Norris, B. Kochman, J. Singh, P. Bhattacharya, *Appl. Phys. Lett.* 76, 2394 (2000).
69. S. Fafard, M. Spanner, J.P. McCaffrey, Z. R. Wasilewski, *Appl. Phys. Lett.* 76, 2268 (2000).
70. M. Bayer, S. Fafard, P. Hawrylak, O. Stern, K. Hinzer, M. Korkusinski, Z. R. Wasilewski, and A. Forchel, to be published.
71. R. Leon, D.R.M. Williams, J. Krueger, E.R. Weber, M.R. Melloch, *Phys. Rev. B* 56, R4336 (1997); R. Leon, et al, *Appl. Phys. Lett.* 69, 1888 (1996).
72. C. Lobo, R. Leon, S. Fafard, P.G. Piva, *Appl. Phys. Lett.* 72, 2850 (1998).
73. J.M. Garcia, G. Medeiros-Ribeiro, K. Schmidt, T. Ngo, J.L. Feng, A. Lorke, J. Kotthaus, P.M. Petroff, *Appl. Phys. Lett.* 71, 2014 (1997).
74. J.S. Lee, H.W. Ren, S. Sugou, Y. Masumoto, *J. Appl. Phys.* 84, 6686 (1998).
75. S. Malik, C. Roberts, R. Murray, and M. Pate, *Appl. Phys. Lett.* 71, 1987 (1997).
76. Q.W. Mo, T.W. Fan, Q. Gong, J. Wu, Z. G. Wang, and Y.Q. Bai, *Appl. Phys. Lett.* 73, 3518 (1998).
77. J. Johansson, W. Seifert, V. Zwiler, T. Junno, and L. Samuelson, *Appl. Surf. Sc.* 134, 47 (1998).
78. F. Heinrichsdorff, M. Grundmann, O. Stier, A. Krost, D. Bimberg, *J. Crystal Growth*, 195, 540 (1999).
79. S.J. Xu, X.C. Wang, S.J. Chua, C.H. Wang, W.J. Fan, J.Jiang, and X.G. Xie, *Appl. Phys. Lett.* 72, 3335 (1998).
80. S. Fafard and C. Ni. Allen, *Appl. Phys. Lett.* 75, 2374 (1999).
81. S. Fafard and H.C. Liu, unpublished.
82. S. Sauvage, P. Boucaud, F.H. Julien, J.M. Gérard, and V. Thierry-Mieg, *Appl. Phys. Lett.* 71, 2785 (1997).
83. D. Pan, E. Towe, S. Kennerly, *Appl. Phys. Lett.* 73, 1937 (1998).
84. L. Chu, A. Zrenner, G. Bohm, and G. Abstreiter, *Appl. Phys. Lett.* 75, 3599 (1999).
85. P.G. Piva, R.D. Goldberg, I.V. Mitchell, D. Labrie, R. Leon, S. Charbonneau, Z.R. Wasilewski, S. Fafard, to be published.
86. R. Leon, G. M. Swift, B. Magness, W. A. Taylor, Y. S. Tang, K. L. Wang, P. Dowd, and Y. H. Zhang, *Appl. Phys. Lett.* 76, 2074 (2000).
87. S. Raymond, J. P. Reynolds, and J. L. Merz, S. Fafard, Y. Feng, and S. Charbonneau, *Phys. Rev. B* 58, R13415 (1998).
88. F. Yang, K. Hinzer, C. Ni. Allen, S. Fafard, G. C. Aers, Yan Feng, J. McCaffrey, S. Charbonneau, *Superlattices and Microstructures* 25, 419 (1999).
89. Y.L. Chang, I.H. Tan, Y.H. Zhang, D. Bimberg, J.L. Merz, E. Hu, *J. Appl. Phys.* 74, 5144 (1993).
90. S. Fafard, *Phys. Rev. B* 50, 1961 (1994); S. Fafard, *Phys. Rev. B* 46, 4659 (1992).
91. J. Arriaga, *Appl. Surf. Sc.* 142, 619 (1999).
92. S.J. Vlaev, M.R. Muro-Ortega, D.A. Contreras-Solorio, V.R. Velasco, *Surface Science* 418, 536 (1999).
93. J.M. Sallese, J.F. Carlin, M. Gailhanou, M. Ilegems, *Appl. Phys. Lett.* 71, 2331 (1997).
94. S. Fafard, E. Fortin, A.P. Roth, *Phys. Rev. B* 47, 10588 (1993); *Ibidem*, *Phys. Rev B* 45, 13769 (1992).
95. Z. Sobiesierski, D.I. Westwood, D.A. Woolf, T. Fukui, H. Hasegawa, *J. Vac. Sc. Technol. B* 11, 1723 (1993).
96. J. Dreybrodt, F. Daiminger, J.P. Reithmaier, A. Forchel, *Phys. Rev. B* 51, 4657 (1995).
97. V. Emiliani, B. Bonanni, A. Frova, M. Capizzi, F. Martelli, S.-S. Stone, *J. Appl. Phys.* 77, 5712 (1995).
98. S.G. Tikhodeev, N.A. Gippius, A.L. Yablonskii, A.B. Dzyubenko, L.V. Kulik, V.D. Kulakovskii, A. Forchel, *Physica Status Solidi A* 164, 179 (1997).
99. I. Kamiya, I. Tanaka, H. Sakaki, *Physica E* 2, 637 (1998)
100. T.-E. Nee, N.-T. Yeh, J.-I. Chyi, C.-T. Lee, *Solid State Electronics* 42, 1331 (1998).
101. S. Fafard, *Appl. Phys. Lett.* 76, 2707 (2000).
102. R.P. Mirin, K.L. Siverman, D.H. Christensen, unpublished.
103. The sample with a 10.0nm cap must have been grown unintentionally with less InAs by a fraction of a tenth of a monolayer, which would result in a QD density ~7.8 times smaller (e.g. see ref. 43 and 44). The curve for the 10.0 nm sample in fig. 21 has thus been scaled accordingly.
104. S. Fafard, E. Fortin, J.L. Merz, *Phys. Rev. B* 48, 11062 (1993).

Observation of Self-Assembled InAs / GaAs Quantum Dot Structure with Temperature-dependent Photoluminescence and Measurement of Electrical Characteristics

Shiang-Feng Tang, Shih-Yen Lin, Yu-Cheng Liao, Si-Chen Lee^(a) and Ya-Tung Cherng^(b)

^(a) Department of Electrical Engineering, National Taiwan University, Taipei, Taiwan

^(b) Materials & Electro-Optics Division

Chung Shang Institute of Science and Technology

P.O.Box 90008-8-7, Lung Tan, Taoyuan 325, Taiwan

ABSTRACT

Self-assembled quantum dot has been realized in different optical-electric material systems and different growth techniques using Stranski-Krastanow growth mode [1]. The optical properties of quantum dots are of physical interest due to the experimental investigation. The theoretical predictions of quantum dot device have been well verified [2]. In the article, we studied the temperature dependent electrical and optical properties [2,3] of quantum dot under normal incidence. From the measurement results, we found the three-dimensional confinement of QD structure and the inter-confined state [4-6].

Keywords : Self-assembly quantum dot, Stranski-Krastanow (S.K), three-dimensional confinement.

1. INTRODUCTION

Self-organized growth of quantum dots has been successfully demonstrated using molecular beam epitaxy and metal organic chemical vapor deposition method [7]. The formation of self-assembled QDs was driven by strain in highly lattice-mismatched semiconductor materials with heteroepitaxy. The islands appeared beyond a critical thickness of the deposited layer when the growth mode switches from a two-dimensional wetting layer to three-dimensional growth. The process of the formation of the dots was controlled by reflection high-energy electron diffraction (RHEED) oscillations. In this article, we utilized Stranski-Krastanow growth mode to fabricate self-assembled quantum dot superlattice structure. The various n-doping in InAs/GaAs dots with Si was formed by using solid-source molecular beam epitaxy. The temperature dependent photoluminescence and current-voltage curve were measured and discussed.

2. EXPERIMENT

The InAs/GaAs QDs were grown in a solid-source MBE machine (Riber-32). The growth rate of nominal InAs was 0.25 ± 0.05 ML/s. The various n-doping in InAs/GaAs dot superlattice structures were grown as follows. After the growth of a 5000Å n-type GaAs buffer layer on (001) semi-insulating GaAs at 582°C, then the temperature was ramped up to 622°C to

grow the 300 Å-thick undoped $\text{Al}_{0.3}\text{Ga}_{0.7}\text{As}$ barrier layer. The next step was to ramp down to 492°C. The 20-period quantum dot structure of nominal 3ML InAs/ 300 Å GaAs was deposited on. The growth was paused in 6sec between InAs and GaAs layers, and kept the As_4 source opening. The QDs were formed at the condition. Then covered 300 Å-thick undoped $\text{Al}_{0.3}\text{Ga}_{0.7}\text{As}$ layer was again remained. Lastly, the capping layer was covered with 4000 Å-thick highly doping GaAs as the contact. The heterostructure was shown in Fig. 1.

The samples were cut by low speed diamond cutter to generate 1mm-thick slice and glued together using G-1 adhesive to crystal Si substrate. The sample was polished, burnished and central dimpled by precision ion polishing systems (PIPS) to form interfacial perforation. The high resolution JEM-4000FX microscopy was used to measure the cross section tunneling electron micrograph. The result was shown in Fig.2. We removed the top heavily doped GaAs capping layer for photoluminescence measurement. The InAs/GaAs quantum dot heterostructures photodetectors were also fabricated by standard photolithography. The I-V curves of dark and background photon-induced current verse bias voltage were measured by HP4156B precision semiconductor parameter analyzer under 10K and 300K, respectively.

3. RESULTS AND DISCUSSION

The temperature-dependent photoluminescences of n-doping $5 \times 10^{18}\text{cm}^{-3}$ and undoping InAs/GaAs dot heterostructures were shown in Fig. 3 (a) and 3 (b), respectively. The peak energy and full width at half maximum (FWHM) of photoluminescence spectra are depicted in Fig. 4 and Fig. 5. The results shown the PL peak energy of undoped and doped QD as a function of temperature with the same constituent structure. It was found when temperature increases between 10 and 50K, the peak energy of photoluminescence spectra both doped and undoped QD superlattice was invariable ($\sim 1.27\text{eV}$ and $\sim 1.21\text{eV}$). It can be explained that the exciton is localized in a certain potential minimum. When temperature greater than 50K, both peaks decrease more slowly as compared to the quantum well structure. This means that the PL energy of QD is less dependent on temperature variation. For the temperature range from 60 to 210K, a monotonous reduction ($\sim 100\text{meV}$) of the peak position was observed due to bandgap shrinkage effect with increasing temperature. A remarkable observation in the FWHM of photoluminescence spectra as a function of temperature was shown in Fig. 5. From 10 to 120 K, a Gaussian-shaped decrease ($\sim 50\text{meV}$) FWHM was been found. An interesting observation of PL is its full width at half maximum (FWHM) as a function of temperature as shown in Fig. 5. It was found that from 10 to 160 K the FWHM of PL slowly decreases. The phenomenon was different from the traditional semiconductor. The characteristics may be explained as optical recombination suppression in nonpredominant sized QD. Up to 210 K, FWHM increased smoothly due to gradual appearance of electron-phonon scattering but the suppression by the thermalized carriers. These carriers can easily be repopulated to nearby quantum dots and electronic coupling in vertically aligned InAs QD superlattice. From Fig. 2, the vertically aligned InAs QD superlattice was observed clearly. This property will benefit QD optoelectronic devices, such as laser diode.

From 210 up to 270K, the effect of electron-phonon scattering becomes a dominant contribution which increase FWHM. The PL peak energy for the undoped QD was lower than that of doped one by $\sim 65\text{ meV}$ between 10 and 250 K. It is believed that in the doped QD, the ground state in the conduction band is occupied. The photo-excitation and subsequent

electron-hole recombination emits photon at higher energy as compared to the undoped one.

The photoluminescence spectra of doped QD structure measured at room temperature shown in Fig. 6. The result indicates that QD is an efficient light emitter.

The I-V characteristics of dark and background photon-induced current versus bias voltage were measured under 10K and 300K. Fig. 7 and Fig. 8 shown the test results. Under 10K, the differences of current between dark and background photon-induced current in doped InAs/GaAs QD is larger than undoped one in the bias range between -0.5V and 0.5V . At 300K, the above phenomenon is more obvious. From the results, it is deduced that the influence of photo-induced current in doped InAs/GaAs QD is more sensitive than the undoped one and with lower dark current. From the photoluminescence data and I-V curve, the doped InAs/GaAs QD infrared photodetector (QDIP) might be operated at higher temperature.

4. CONCLUSION

Stacked 20 period InAs/GaAs quantum dot structure has been studied using variable temperature photoluminescence. The room temperature PL of doped quantum dot superlattice structure was observed. The PL FWHM of QD was found to decrease as temperature increases from 10 to 160 K which is contrary to traditional semiconductor. From the electric measurement results, it also gave us more information to understand of self-organized quantum dot.

REFERENCES

1. D. Leonard, M. Kishnamurthy, C. M. Reaves, S. P. Denbars, and P. M. Petroff, "Direct formation of quantum-sized dot from uniform coherent islands of InGaAs on GaAs surfaces," *Appl. Phys. Lett.*, vol. 63, no. 23, pp. 3203-3205, 1993.
2. M. Grundmann, N. N. Ledentsov, O. Stier, D. Bimberg, V. M. Ustinov, V. M. Ustinov, and Zh. I. Alferov, "Excited states in self-organized InAs/GaAs quantum dots: Theory and experiment," *Appl. Phys. Lett.*, vol. 68, no. 7, pp. 979-981, 1996.
3. J. Phillips, K. Kamath, X. Zhou, N. Chervela, and P. Bhattacharya, "Photoluminescence and far-infrared absorption in Si-doped self-organized InAs quantum dots," *Appl. Phys. Lett.*, vol. 71, no. 15, pp. 2079-2081, 1997.
4. R. P. Mirin, J. P. Lbbetson, K. Nishi, A. C. Gossard and J. E. Bowers, "1.3 μm photoluminescence from InGaAs quantum dots on GaAs," *Appl. Phys. Lett.*, vol. 67, no. 25, pp. 979-981, 1995.
5. B. Q. Sun, Z. D. Lu, D. S. Jiang, J. Q. Wu, Z. Y. Xu, Y. Q. Wang, J. N. Wang and W. K. Ge., "Photovoltage and photoluminescence spectroscopy of InAs/GaAs self-organized quantum dots," *Appl. Phys. Lett.*, vol. 73, no. 18, pp. 2657-2659, 1998.
6. Dong Pan, Y. P. Zeng, J. Wu, H. M. Wang, C. H. Chang, J. M. Li and M. Y. Kong, "Self-formed InGaAs/GaAs quantum dot superlattice and direct observation on strain distribution in the capped superlattice," *Appl. Phys. Lett.*, vol. 70, no. 18, pp. 2440-2442, 1997.
7. J. Oshinowo, M. Nishioka, S. Ishida, and Y. Arakawa, "High uniform InGaAs/GaAs quantum dots ($\sim 15\text{nm}$) by metal organic chemical vapor deposition," *Appl. Phys. Lett.*, vol. 65, no. 11, pp. 1421-1423, 1994.

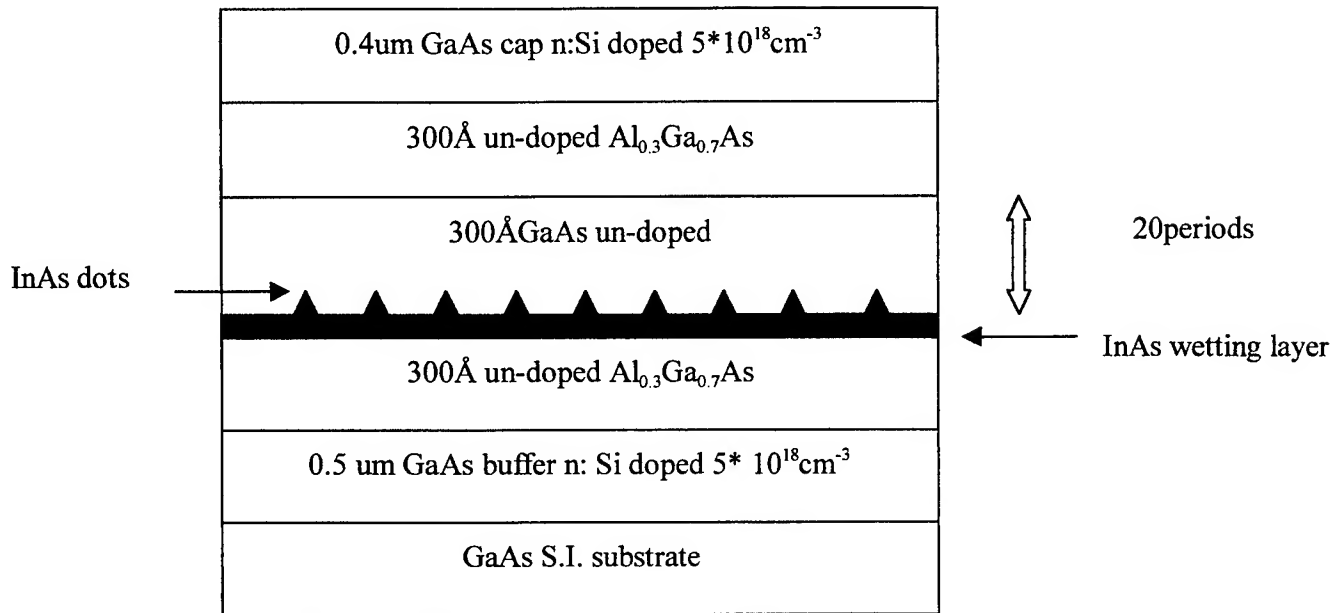


Fig. 1 The schematic of 20-periods InAs/GaAs quantum dot heterostructure.

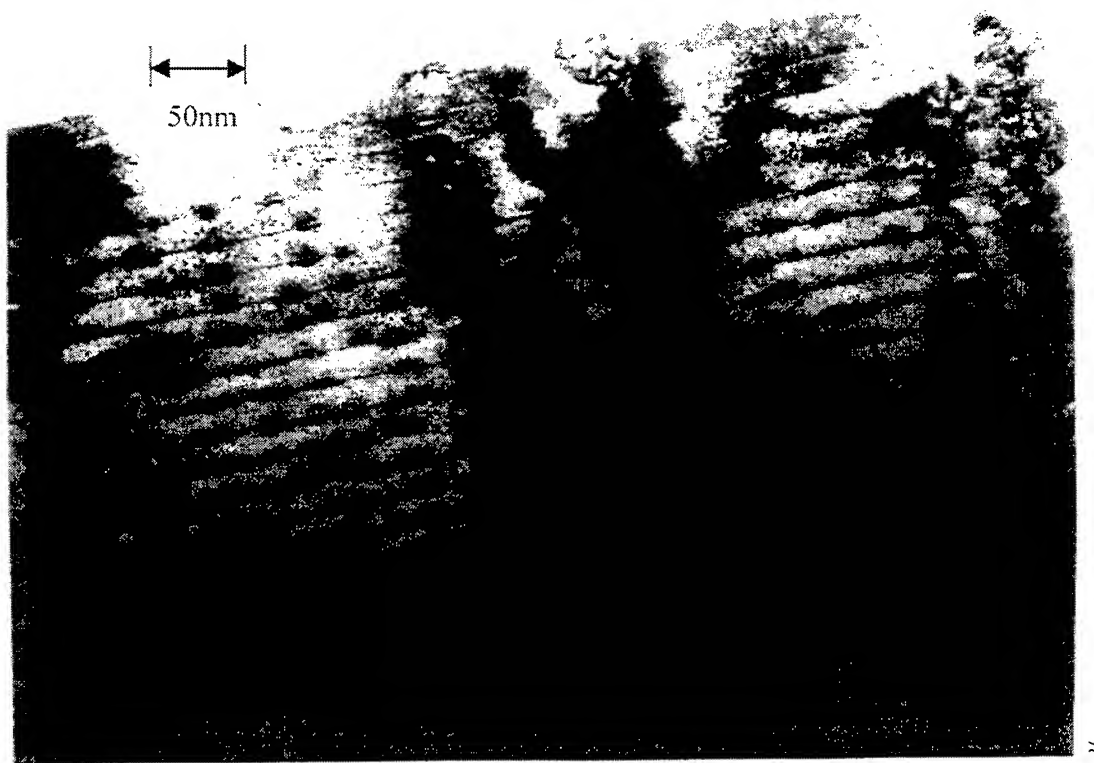


Fig.2 The micrograph of high resolution cross-section TEM

(a)

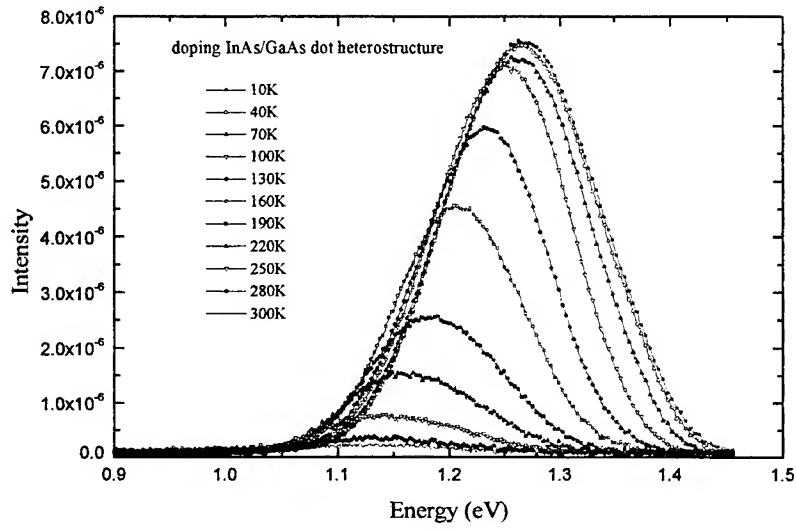
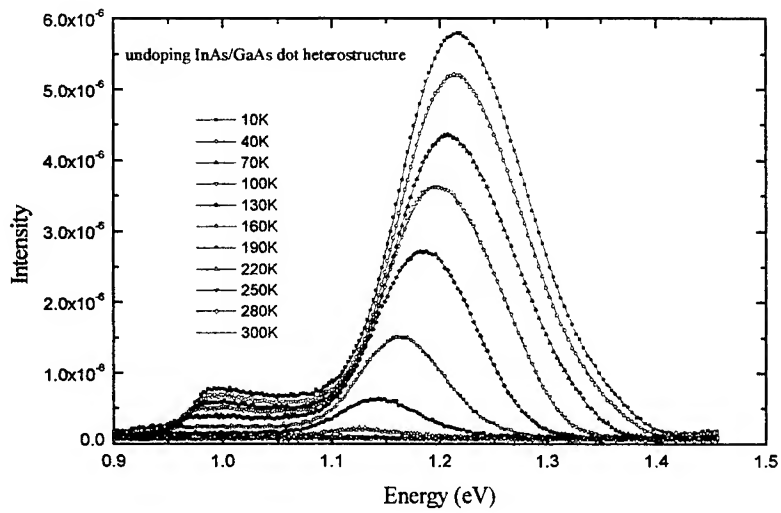


Fig 3. (a) and (b) The temperature-dependent photoluminescences with $5 \times 10^{18} \text{cm}^{-3}$ n-doped and undoped InAs/GaAs dot heterostructures

(b)



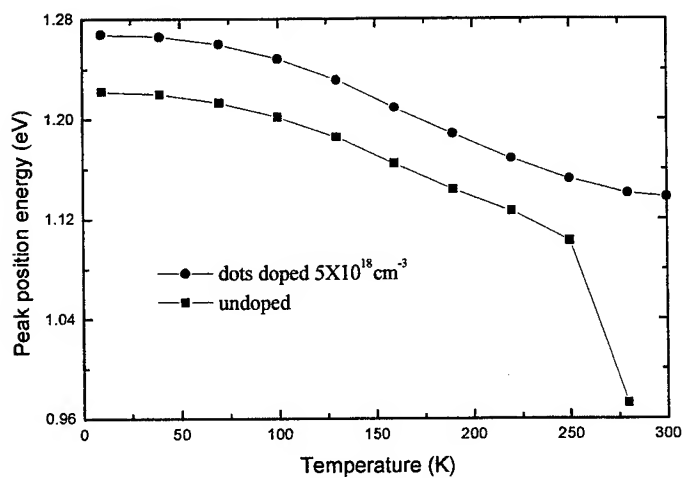


Fig. 4 The temperature-dependent peak energy of photoluminescence spectra with doped and undoped InAs/GaAs heterostructures

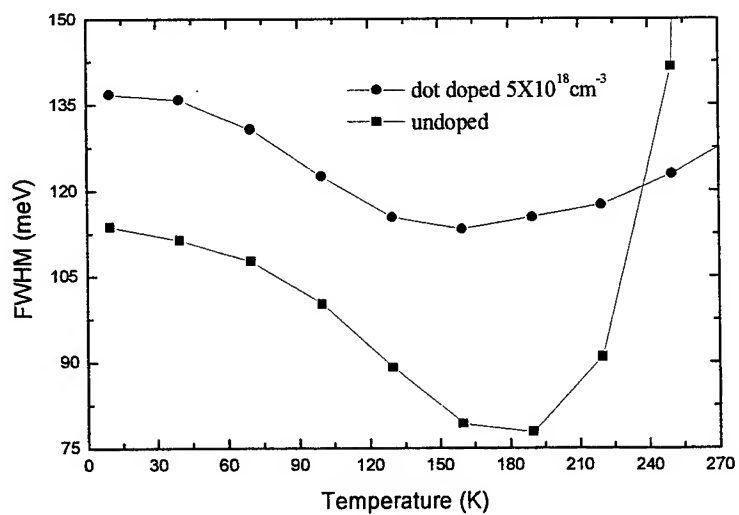


Fig. 5 The temperature-dependent FWHM of photoluminescence spectra for doped and undoped InAs/GaAs heterostructures

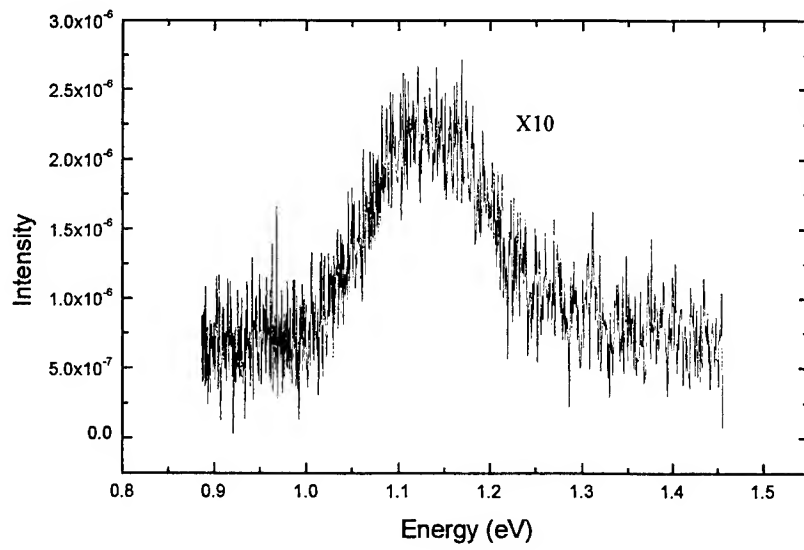


Fig.6 The room temperature photoluminescence spectra of doped QD structure

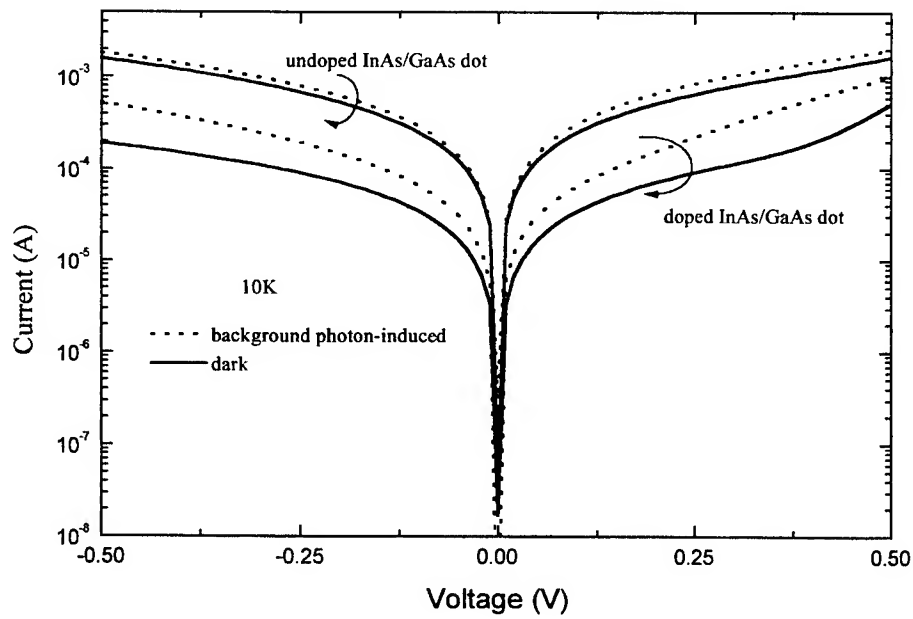


Fig.7 The 10K dark and background photon-induced current versus bias voltage curve

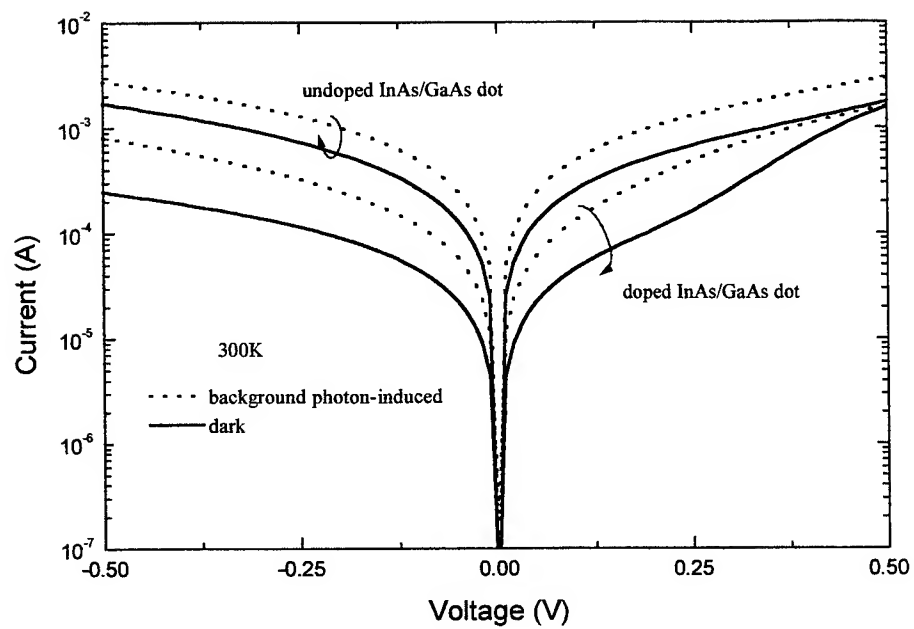


Fig.8 The 300K dark and background photon-induced current versus bias voltage curve

One-dimensional arrays of self-assembled InAs/InP quantum dots

Jacques Lefebvre^a, Philip J. Poole^a, John P. McCaffrey^a, Boris Lamontagne^a, Geof C. Aers^a, Chien-Ping Lee^b, Shu-Fen Hu^c, and Robin L. Williams^a

^aInstitute for Microstructural Sciences, National Research Council Canada, Ottawa, Ontario K1A 0R6, Canada

^bDepartment of Electronics Engineering and Institute of Electronics, National Chiao Tung University, Hsinchu, Taiwan.

^cNational Nano Device Laboratories, 1001-1, Ta-Hsueh Road, Hsinchu, Taiwan.

ABSTRACT

The Stranski-Krastanov (S-K) self-assembly process produces quantum dots with a large distribution of sizes. In the S-K growth mode, the in-plane spatial distribution of dots is quasi-random. Different strategies have been used to narrow the size distribution and increase the dot-dot spatial correlation. Here, we report a simple method to reduce the height of taller dots by using the P/As exchange exhibited during CBE growth. The fabrication of InAs/InP quantum dots self-assembled into linear arrays through growth on patterned substrates is described. Photoluminescence from one-dimensional arrays is compared with the non-correlated case of quantum dots grown on planar substrates. The interplay between size and spatial distributions is discussed.

Keywords: Quantum dots, InAs, InP, self-assembly, Stranski-Krastanov, photoluminescence

1. INTRODUCTION

Self-assembly methods already show great promises in fulfilling future requirements of going from micro- to nano-electronics/optics. In many cases, the self-assembly processes, inspired from biological systems, are based on the affinity of one chemical specie for another. In other cases, physical properties favor specific size, shape and configuration of clusters of atoms, molecules, etc. Chemical self-assembly produces virtually identical replica while physical self-assembly most often presents a significant spread around a required characteristic. This is the case of the Stranski-Krastanov growth method used to make self-assembled quantum dots (SADs) on crystalline substrates. In this process, the SAD formation results from an interplay between surface and strain energy, the latter building up as a consequence of an important difference in SAD and host lattice parameters. Optical and electrical measurements performed on individual SADs show a number of properties expected for a zero-dimensional (0D) system. However, as the measurements are performed on macroscopic scales, these features are washed out by the large spread in the SAD size distribution. Physically, this spread is due to the fact that the total energy obtained from strain and surface energy is a slowly varying function with a broad minimum as a function of SAD height/width.

0D systems such as SADs have unique properties that will only find good extensive applications if their size distribution can be narrowed significantly. So far, very few attempts have been made in such directions¹⁻⁸. In InAs SAD on GaAs, a process called indium flush has been used successfully to reduce the SAD height distribution¹. A similar process is presented here for InAs SADs on InP and relies on exchange between arsenic and phosphorus atoms when partially capped SADs are exposed to an arsenic overpressure at the growth temperature. A significant improvement in SAD uniformity was reported in germanium SADs on silicon². It was shown that ex-situ patterning of the Si substrate with sub-micron patterns decreases SAD size distribution and introduces strong spatial correlations. Similar spatial correlation has been obtained on InAs SADs on GaAs, but no mention was made of the size distribution³. In this paper, we address experimentally the issue of size distribution and location of InAs SAD on InP, and discuss the interrelation between the two. The method uses ex-situ sub-micron patterning of the InP substrates into stripes along the [110] direction. Contrary to previously reported work, we use photoluminescence (PL) to better characterize the SAD size distribution. In section 2., we present results on InAs SADs grown on planar InP substrates, and describe a method to shorten taller SADs. In section 3., we give a detailed description of the steps involved in substrate patterning and re-growth. Finally, section 4. deals with SADs grown on patterned substrates.

2.SELF-ASSEMBLED InAs QUANTUM DOTS ON PLANAR InP SUBSTRATES

The InAs/InP self assembled quantum dots reported here were grown by chemical beam epitaxy (CBE) using TMI, AsH₃ and PH₃. No carrier gas was used. The structures were grown on exactly oriented (001) InP substrates, and consisted of a 120 nm InP buffer, 3.1 monolayers (ML) of InAs, and a 40 nm InP cap. The substrate temperature was maintained at 500 °C using an infrared pyrometer. The buffer and InAs layers were grown at a growth rate of 0.51 ML/s, and all subsequent layers at 0.94 ML/s. Fig. 1 illustrates the gas switching sequence. The two interruption times allow formation of a smooth InP surface and completion of the self-assembly process (additional details are given elsewhere⁹). The structure is then capped with 40 nm of InP.

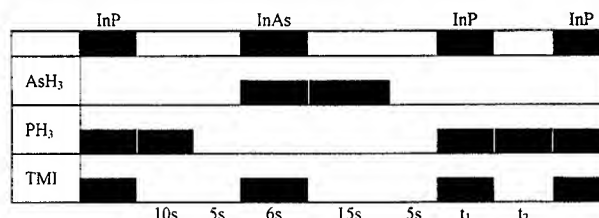


Fig. 1: Gas switching procedure. In the present work $t_1=0$, 6 and 10sec., and $t_2=0$, 15, 30 and 60sec. The growth proceeds from left to right.

Figure 2 shows plan view and cross-sectional view TEM (Phillips EM430) images after ion argon-milling of the samples. Care was taken in the preparation process to avoid artefacts associated with the formation of indium balls on the surface. Images were obtained using bright field [001] zone axis conditions to enhance the strain contrast. The plan view of Fig. 2a) reveals that SADs are faceted with a square base 30 to 40 nm wide oriented along the $\langle 100 \rangle$ crystal direction. The density is approximately $100 \mu\text{m}^{-2}$. Fig. 2(b) is a (200) darkfield TEM image of the same sample in cross section. Here, the InAs material is seen as a lighter contrast between the darker, strained regions above and below. Dots are flat topped with little or no evidence for rounding at the edges, and their height is significantly less than the lateral dimension. This suggests that the height and not the width of the dot will dominate electronic confinement energies within the dot. In terms of the PL emission spectrum, this implies that significant variations in lateral size can occur from dot to dot without broadening the PL linewidth.

Photoluminescence (PL) spectra of the samples, excited using an Ar⁺ laser, were taken at a temperature of 4.2K using a BOMEM FTIR spectrometer with InGaAs and InSb detectors. Fig. 3 ($t_2 = 0$ s) shows the PL spectra for a standard sample, i.e. with a continuous growth of the InP cap. Intense luminescence is observed over a broad energy range between 600 and 1100 meV. A series of sharper peaks (up to 11, 100 meV wide), superimposed on top of the broad spectrum, appear in almost all samples, with only small changes in their position. By performing PL experiments as a function of pumping intensity, we have excluded excited state emission as an explanation for these structures. We conclude that each peak is the result of emission from quantum dots with an average height around an integer number of monolayer steps. Since electrons and holes in thinner dots are more strongly confined, their PL is seen at higher energy. For each dot height, the width of the PL peak corresponds to the inhomogeneous broadening associated mainly with submonolayer fluctuations in the *effective* dot height. The effective dot height is obtained as an average over the lateral interface roughness in a given dot. The similarity of peak position from sample to sample is consistent with TEM images that reveal a large SAD width/height ratio and thus, a height-dominated quantum confinement.

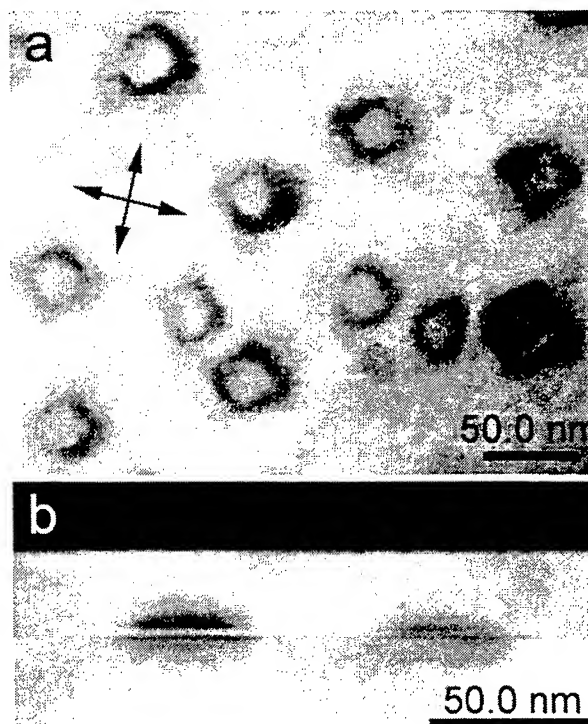


Fig. 2: TEM images of InAs quantum dots a.) plan view, the arrows indicate the $\langle 110 \rangle$ directions, b.) cross-section.

The first attempt to control the size distribution is called the trimming process in which taller dots have their height reduced. In the first of a two step process, the space between already formed SAD is partially filled with an InP layer (growth time t_1 in fig. 1). The top of the dots is not expected to be covered by InP since the elastic relaxation of the upper InAs layers of the dots makes this energetically unfavourable. In the second step, the growth is interrupted (time t_2 in fig. 1) while a phosphorus overpressure is maintained. The exposure of the bare InAs surface of a dot to phosphorus is expected to result in As/P exchange, forming InP on top of the dot. This InP then migrates off the dot as it does in the first step, thus reducing the dot height. The process, which affects more markedly taller dots, continues until the dot height approaches that of the InP layer grown during the first step. The final result is a reduction in the number of tall dots, and a subsequent increase in the number of short dots.

In Fig. 3, the PL spectra obtained with $t_1 = 3$ s and 5 s is compared with the standard sample ($t_1 = 0$ s). As expected for a sample where taller dots have been trimmed, the maximum PL intensity is shifted to higher energy. The shift is larger for $t_1 = 3$ s since a small value of t_1 corresponds to a smaller InP filling than for 5 s. As t_1 is decreased the spectra maintain the same broad envelope without any significant shift of the narrow peaks. This latter feature rules out intermixing as an alternative explanation for the overall blue shift in the PL. The growth rate during t_1 is 0.94 ML/s corresponding to 3 (5) monolayers of InP for $t_1 = 3$ s (5 s). Since the narrow PL peaks can be numbered in terms of monolayers, we expect the maximum PL intensity to shift by 3 (5) narrow peaks for $t_1 = 3$ s (5 s), in good agreement with Fig. 3. Since the trimming process should produce shorter SADs at the expense of taller ones (narrower SAD height distribution), one might expect a narrowing of the envelope. We believe the absence of clear narrowing is offset by a larger peak width for shorter SADs (emission energy of short SADs is more sensitive to monolayer fluctuations). Finally, the effect of t_2 has also been studied and we find no substantial PL shift for t_2 longer than 15 s. This phenomenon makes the trimming process easy to control since it is only sensitive to the amount of InP used to fill in-between the quantum dots.

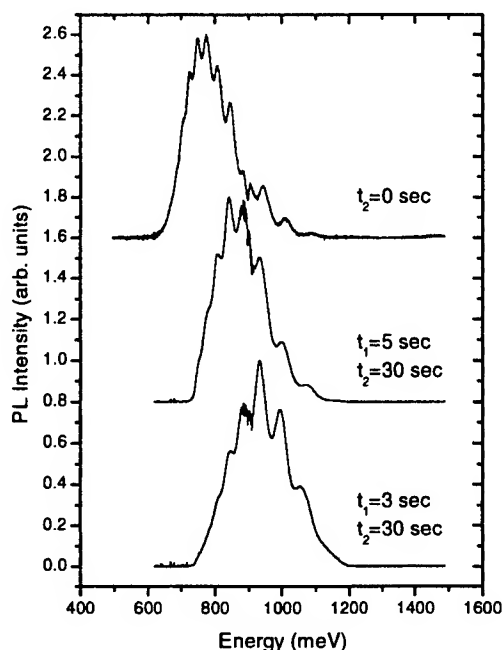


Fig. 3: 4.2K PL spectra for samples where time t_1 is varied from 3 to 5s, with $t_2=30$ s, and a standard sample where $t_2=0$ s (i.e. continuous growth of the InP cap).

3. Patterned substrates

As presented in the introduction, different methods have been reported to control SAD location. Here, we choose to pattern InP substrates ex-situ using conventional lithography and dry etching. Compared with selective growth obtained in windows etched in a SiO_2 layer, this method allows reproducible sub-micron resolution. It also allows extensive sample cleaning to be done prior to re-growth. The main steps of the process are illustrated in Fig. 4. After preparing the sample surface through BOE/UV ozone/HF cleaning, a 10 nm SiO_2 layer is deposited (step 1. in fig. 4). SiO_2 serves two purposes, as a masking material to define the pattern in the InP substrate, and as a protection layer to prevent surface contamination during processing. Optical lithography or electron-beam lithography, depending on the required resolution, is then performed to define regions where SiO_2 is removed. The pattern consists of stripes running along the $[110]$ direction for reasons discussed below. SiO_2 is etched using a reactive ion etcher with CHF_3 and O_2 as active gases (step 2.). In step 3., the InP substrate is etched using chemically assisted ion beam etching (CAIBE) that provides controllability of the etch profile. A 30 degree undercut is desirable to insure proper re-growth, and is obtained by tilting/rotating the sample stage. Prior to re-growth, the remaining SiO_2 mask is removed using BOE followed by a multiple-step cleaning of the sample in BOE/UV ozone/HF. In the absence of proper cleaning, re-growth is not predictable or will not occur at all. Fig. 5 shows a scanning electron microscopy (SEM) image of a 500 nm stripe etched in an InP substrate. Fig. 6 shows a cleaved edge view of a $[110]$ oriented 2 μm stripe after growing a series of InP and InGaAs layers. The 30 degree undercut obtained with CAIBE provides a good

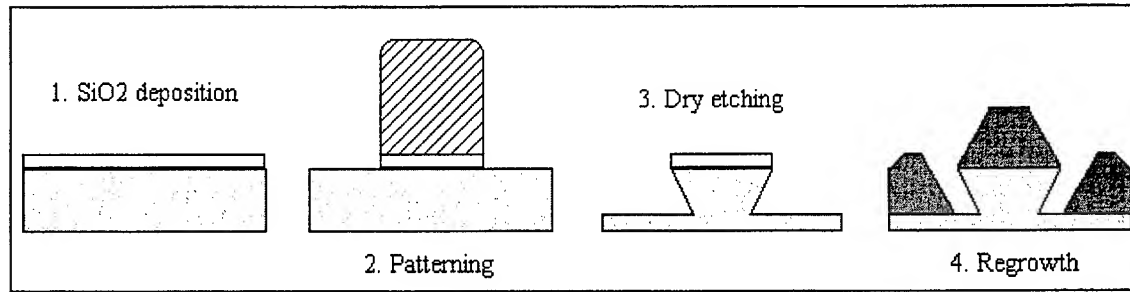


Fig.4: Re-growth on patterned substrates consists of four main steps. Extensive cleaning steps are necessary before SiO₂ deposition and re-growth. The undercut profile obtained with CAIBE (step 3.) is important in preventing the formation of bridges during re-growth between the planar substrate and the top of the stripes.

separation between material grown on the stripes and material grown on the flat substrate. The SEM micrograph reveals smooth [111]B facets along with a well defined ridge. When little or no undercut is used, bridges start to form between the flat surface and the stripes, preventing the formation of uniform ridges.

It is well-established that adatom diffusion is anisotropic in III-V materials and results in the formation of facets. On (001) InP, it has been shown that diffusion favors InP growth on (111)A and (001) planes compared with (111)B planes¹⁰. The result of Fig. 6, which shows formation of [111]B facets, is fully consistent with this picture. This type of re-growth is very appealing since it provides virtually defect free substrates onto which quantum well, quantum wires and SADs can be grown. However, the anisotropic growth presents some technical difficulties in terms of controllability. In anisotropic growth, the effective growth rate on top of the stripes (r_{eff}) increases more and more rapidly as the stripe gets closer to forming a ridge. It is straightforward to show that $r_{eff} = r_o \cdot W_i / W_f$ where r_o is the growth rate on a planar substrate, W_i is the starting stripe width, and W_f is the final target width. As the growth proceeds, it becomes increasingly difficult to control the top width of a stripe, an important parameter in the location of SADs on narrow mesas. As r_{eff} is directly proportional to W_i , the most direct way to increase the amount of control is to narrow the starting stripe width. 100-200 nm stripes have been fabricated using the method just described (not shown).

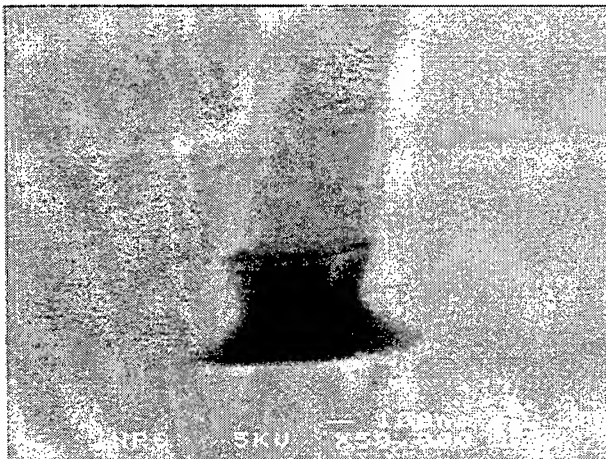


Fig. 5: SEM micrograph of a stripe etched in an InP substrate prior to SiO₂ removal and pre-growth cleaning. The stripes are aligned along the [110] direction .

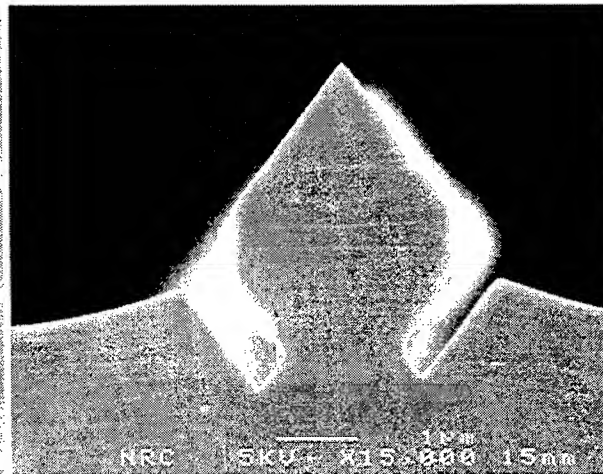


Fig. 6: SEM micrograph along the [110] direction of CBE-grown InGaAs/InP on patterned InP substrate. InGaAs markers appear as bright lines running along the surface.

4. Self-assembled InAs quantum dots on patterned InP substrates

Growing SADs on narrow stripes has been proven successful in two different SAD systems, InAs on GaAs³ and Ge on Si². In both cases, one-dimensional ordering is obtained and is attributed to a dimensional crossover in surface diffusion as the stripes are made narrower than the lateral diffusion length. In InAs on InP, micrometer-long diffusion lengths have been measured, making one-dimensional ordering in such a system a real possibility¹¹. Other methods including electron^{6,7} and ion⁸ beam induced surface damage have been used to tailor surface diffusion characteristics. These in-situ methods, although very appealing, are very involved and cannot be scaled for application purposes. Ex-situ patterning methods²⁻⁵ like the one presented in the previous section can be integrated in a multi-step process either as an initial, intermediate or final step.

If changes in surface diffusion characteristics affect SAD spatial ordering, we should expect SAD size distribution to be affected as well. In an ideal case where the distance between SADs is perfectly regular, the amount of material supplied to each SAD during the growth is necessarily uniform. We believe that an important step toward size distribution narrowing can thus be achieved by SAD spatial ordering. Spatial ordering is driven by the SADs capability to grasp supplied material, thus forming a depletion area around the SAD where no additional seeding can occur. In two dimensions, material diffuses in all directions toward SADs, and the depletion area might not be well defined. However, in one dimension the depletion area should better delimited since SADs feed mainly from two directions only. Consequently, a more regular spatial ordering would be favored in one dimension. The atomic force microscopy (AFM) of Ge SADs on Si by Kamins *et al.* reveals the close link between spatial ordering and good height uniformity². In order to fully characterize the size distribution, we believe that PL is more appropriate as it allows to probe both small and large scale uniformity.

The ability to control SAD parameters such as size and location opens up important avenues for both fundamental and applied physics. For example, since mesa stripes can be of virtually any sizes, it should be possible to fabricate ensembles consisting of only a small number of SADs.

5. Acknowledgements

J.L. would like to thank J. Lapointe, Y. Feng, J. Stapledon and M. Buchanan for their help in the clean room.

6. References

1. S. Fafard, Z. R. Wasilewski, C. Ni. Allen, D. Picard, M. Spanner, J. P. McCaffrey, and P. G. Piva, "Manipulating the energy levels of semiconductor quantum dots", *Phys. Rev. B* 59, pp. 15368-73, 1999
2. T. I. Kamins, and R. S. Williams, "Lithographic positioning of self-assembled Ge islands on Si(001)", *Appl. Phys. Lett.* 71, pp. 1201-1203 (1997)
3. R. Zhang, R. Tsui, K. Shiralagi, D. Convey, and H. Goronkin, "Selective formation and alignment of InAs quantum dots over mesa stripes along the [110] and [001] directions on GaAs (100) substrates", *Appl. Phys. Lett.* 73, pp. 505-507, 1998; K. Shiralagi, R. Zhang, and R. Tsui, "Controlled growth of quantum dots on mesa top", *J. Crys. Growth* 201/202, pp. 1209-1211 (1999)
4. D. S. L. Mui, D. Leonard, L. A. Coldren, and P. M. Petroff, "Surface migration induced self-aligned InAs islands grown by molecular beam epitaxy", *Appl. Phys. Lett.* 66, pp. 1620-1622, 1995
5. S. Jeppesen, M. S. Miller, D. Hessman, B. Kowalski, I. Maximov, and L. Samuelson, "Assembling strained InAs islands on patterned GaAs substrates with chemical beam epitaxy", *Appl. Phys. Lett.* 68, pp. 2228-2230, 1996
6. M. Lopez, N. Tanaka, I. Matsuyama, and T. Ishikawa, "AlGaAs/GaAs wire and box structures prepared by molecular beam epitaxial regrowth on in situ patterned GaAs substrates", *Appl. Phys. Lett.* 68, pp. 658-660, 1996
7. T. Ishikawa, T. Nishimura, S. Kohmoto, and K. Asakawa, "Site-controlled InAs single quantum-dot structures on GaAs surfaces patterned by in situ electron-beam lithography", *Appl. Phys. Lett.* 76, pp. 167-169, 2000
8. J. Ahopelto, M. Sopanen, H. Lipsanen, S. Lourdudoss, E. Höfling, J. P. Reithmaier, A. Forchel, E. R. Messmer, A. Petersson, and L. Samuelson, "Maskless selective growth of InGaAs/InP quantum wire on (100) GaAs", *Appl. Phys. Lett.* 70, pp. 2828-2830, 1997
9. P. J. Poole, R. L. Williams, J. Lefebvre, J. McCaffrey, C. Lacelle, G. C. Aers, submitted to *Appl. Phys. Lett.*
10. P. Finnie, S. Charbonneau, M. Buchanan, C. Lacelle, J. Fraser, and A. P. Roth, "Faceted GaInAs/InP nanostructures grown by selective area chemical beam epitaxy", *J. Appl. Phys.* 82, pp. 4883-4888, 1997
11. V. K. Gupta, Ph. D. Thesis, University of London (1998).

SESSION 5

Quantum Well Intermixing and Lasers

Material growth investigation and high performance of InGaAs/InGaAsP/AlGaAs quantum well diode lasers ($\lambda = 0.98 \mu\text{m}$)

R. Jennifer Hwu and G. W. Yang

Dept. of Electrical Engineering, Univ. of Utah/Salt Lake City

ABSTRACT

In this work, we conduct a theoretical analysis of the design, fabrication, and performance measurement of high power and high brightness strained quantum well lasers emitting at $0.98 \mu\text{m}$. The material system of interest consists of an Al-free InGaAs/InGaAsP active region and AlGaAs cladding layers. The laser material is grown by metal-organic chemical vapor deposition and demonstrates high quality with low threshold current density, high internal quantum efficiency, and extremely low internal loss. High performance broad-area multi-mode and ridge-waveguide single mode laser devices are fabricated. For $100 \mu\text{m}$ -wide stripe lasers having a cavity length of $800 \mu\text{m}$, a high slope efficiency of 1.08 W/A , a low vertical beam divergence of 340° , a high output power of over 4.45 W , and a very high characteristic temperature coefficient of 250 K were achieved. Lifetime tests performed at $1.2\text{--}1.3 \text{ W}$ ($12\text{--}13 \text{ mW}/\mu\text{m}$) demonstrates reliable performance. For $4 \mu\text{m}$ -wide ridge waveguide single mode laser devices, a maximum output power of 394 mW and fundamental mode power up to 200 mW with slope efficiency of $0.91 \text{ mW}/\mu\text{m}$ are obtained.

Index Terms: Semiconductor lasers, semiconductor epitaxial layers, quantum well lasers, semiconductor materials, semiconductor diodes.

1. INTRODUCTION

High optical power and high brightness semiconductor laser devices have gained increased attention based on their broad commercial applications, such as pumping sources of erbium-doped fiber amplifiers and solid-state lasers¹⁻³, generators of blue light via frequency doubling, free space optical communications sources, and focused energy sources for medical instruments. There are two conventional material systems for achieving $0.98 \mu\text{m}$ wavelength range lasers. One is the InGaAs/GaAs/AlGaAs system, which is a very mature material system but has a reliability problem especially for high-power operation because of the Al oxidation issue. Another one is the pure Al-free InGaAs/InGaAsP/InGaP system. It has the advantages of high-facet stability and low thermal and electrical resistance⁴⁻⁶, but it also has some drawbacks^{7,8}. Recently, a hybrid material system of InGaAs/InGaAsP/AlGaAs was proposed which has demonstrated many advantages over the pure Al-free system^{7,8}. These special features include: (1) Flexibility of structure design: AlGaAs is lattice matched to GaAs at all compositions so a broad bandgap range for the cladding can be used for optimal performance. (2) Improvement of surface morphology: the optical quality and surface morphology of InGaP and InGaAsP strongly depend on the substrate orientation with InGaP favoring the off-axis orientation and InGaAs and InGaAsP favoring the exact (100) orientation. Using AlGaAs as the cladding layer can overcome this contradiction. (3) Simple epitaxial growth: the precise requirement for the lattice constant controlling of thick InGaP cladding layers is avoided. (4) Low transverse beam divergence: the AlGaAs material with Al content from 0.35 ($E_g = 1.86 \text{ eV}$, $n = 3.33$) to 0.6 ($E_g = 2.0 \text{ eV}$, $n = 3.2$) can have both higher index and larger bandgap than those of InGaP ($E_g = 1.86 \text{ eV}$, $n = 3.2$), so smaller divergence (therefore, higher brightness) can be obtained without sacrificing the carrier confinement. (5) Reliable operation: by using the broad waveguide design, most of the optical intensity concentrates in the Al-free active region with only a few percent in the AlGaAs cladding layers. As a result, it can have high-facet stability and reduced defect propagation velocity than Al-free lasers and also an enhanced reliability due to the improvement of the material and interface quality. This material system is best suitable for the wavelength range of $0.9\text{--}1.1 \mu\text{m}$.

In this paper, we report on the performance of high power and high brightness $0.98 \mu\text{m}$ quantum well diode lasers employing InGaAs/InGaAsP/AlGaAs material system.

2. LASER STRUCTURE AND MATERIAL GROWTH

Two structures, one with 400 nm as the waveguide thickness (structure B1), and another one with 600 nm as the waveguide thickness (structure B2) were fabricated. Both of the structures use $\text{Al}_{0.42}\text{Ga}_{0.58}\text{As}$ as the cladding and InGaAsP as the waveguide. The corresponding theoretical beam divergences are 36° and 32° , respectively. Based on the theoretical analysis

results, the cladding thicknesses are chosen to be 0.9 and 0.75 μm , respectively, for these two structures.

Both structures were grown by low-pressure MOCVD on exact (100) $\text{n}^+\text{-GaAs}$ substrates. The source materials used were trimethylgallium (TMGa), trimethylindium (TMIn), trimethylaluminum (TMAI), 100% arsine (AsH_3) and phosphine (PH_3). Diethylzinc (DFZn) was used as the p-type dopant, and silane (SiH_4) diluted to 2% in hydrogen was used as the n-type dopant. Palladium-diffused hydrogen was used as the carrier gas. The n- and p- cladding layers were doped to $1 \times 10^{18} \text{ cm}^{-3}$, and the SCH active region is nominally undoped. The p-GaAs cap layer was doped from $5 \times 10^{18} \text{ cm}^{-3}$ to $1 \times 10^{20} \text{ cm}^{-3}$ to reduce the ohmic-contact resistance.

The as-grown InGaAs/InGaAsP/AlGaAs laser wafers have an excellent mirror smooth surface morphology with no evidence of crosshatch or any other textured patterns. Both photoluminescence and X-ray characterization demonstrated high material quality. To further assess the material performance, the wafer was processed into broad-area 100 μm -wide lasers. Chips with various cavity lengths and as-cleaved facets were tested at room temperature under pulsed condition, which deduced a high internal quantum efficiency, η_i , of 95-91% and a very low internal loss, α_i , of 1.2-0.7 cm^{-1} . The less than unity η_i is mainly due to the SCH structure having some free carriers to occupy the thick waveguide layers. Based on our theoretical analysis, the extremely low internal loss is due partly to the greatly reduced free-carrier absorption loss achieved by employing the thick waveguide structure. Reduced scattering loss through the improved material quality also contributes to the extreme low internal loss. The measured threshold current densities ($L = 800 \mu\text{m}$) are 210 and 340 A/cm^2 , respectively, for the two structures.

3. DEVICE FABRICATION

Broad stripe (100 μm) lasers are fabricated using epiwafers of structure B2. The broad contact stripe is formed by chemically etching through the $\text{p}^+\text{-GaAs}$ cap layer outside the 100 μm wide stripe to prevent current spreading. 120 nm SiN_x was used as the insulating layer deposited by plasma-enhanced chemical vapor deposition (PECVD). After the deposition of TiPtAu as the p-electrode, the wafer is then thinned to 100 μm and AuGeNi/Au was deposited as the n-electrode. Devices with a cavity length of 800 μm were coated (5%/95%) and mounted junction-side down on copper heatsinks.

Four μm -wide ridge waveguide (RW) structure lasers were fabricated using epiwafers of structure B1. The ridge shape was formed by standard photolithography and wet chemical etching. The top $\text{p}^+\text{-GaAs}$ and p-AlGaAs cladding layers were selectively etched off using a H_3PO_4 : Methanol: H_2O_2 chemical solution. The residual thickness from the top of the quantum well active layer was automatically controlled at 0.4 μm (the waveguide thickness). The effective refractive index step in the direction of the junction plane is 6×10^{-3} . This value provides a good condition for high-power fundamental mode operation. 200 nm SiN_x was deposited as the insulating film to define the metal contact window. After the deposition of TiPtAu as the p-electrode, the wafer was then thinned to $\sim 100 \mu\text{m}$ and AuGeNi/Au was deposited as the n-electrode. High reflective (HR $\sim 90\%$) and antireflective (AR $\sim 5\%$) optical films were applied to the rear and front laser facets. The fabricated devices (with a cavity length of 800 μm) were mounted junction-side up on copper heatsinks.

Fifty μm non-injection regions at both rear and front facets were used to improve the COD level. In the compressive-strained InGaAs QW lasers, the strain release at the laser facets can introduce bandgap shrinkage [9, 10], and, thus, induce an increase in the optical absorption and carrier leakage to the laser facets. As a result, heating of the laser facets easily occurs through the nonradiative recombination processes. Finally, COD occurs when the temperature reaches the critical (melting) point of the laser material. The use of non-injection regions near the laser facets greatly reduces the carrier leakage, and consequently, improves the COD level.

4. LASER PERFORMANCE

Broad Stripe Lasers

Figure 1(a) shows the light output power versus driving current characteristics of the InGaAs/InGaAsP/AlGaAs broad stripe laser over a temperature interval of 25-65°C. At 25°C, the slope efficiency is as high as 1.08 W/A (85%). The driving current is only 1.21 A at an output power of 1.0 W. From temperature dependence of the threshold current over the temperature interval of 25-65°C, a T_0 value of 250 K was achieved. The temperature coefficient of the external quantum efficiency, T_1 , was 400 K measured under CW condition and at the 1.0 W point.

Figure 1(b) shows light output power, forward voltage and power conversion efficiency versus driving current characteristics. Output power was as high as 4.45 W at a driving current of 5.0 A, which was limited by the driving current source. As can be seen from these results, through the optimization of the thickness and doping profile of AlGaAs cladding layers, the series

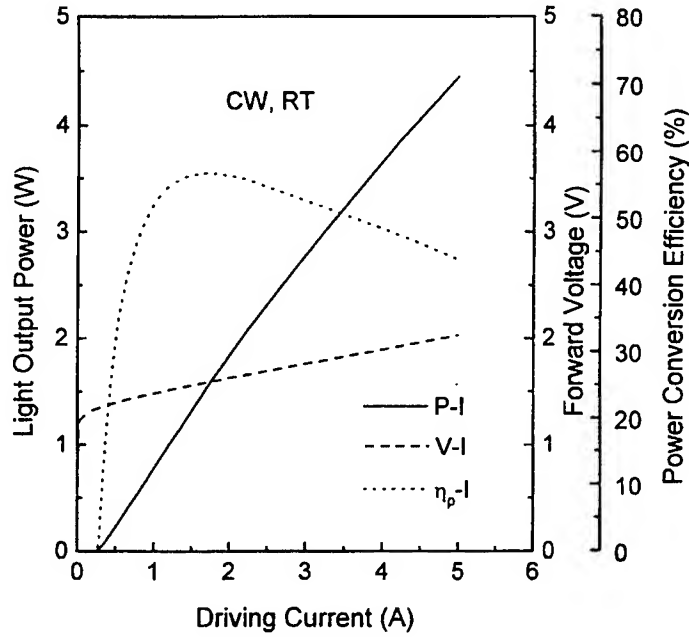
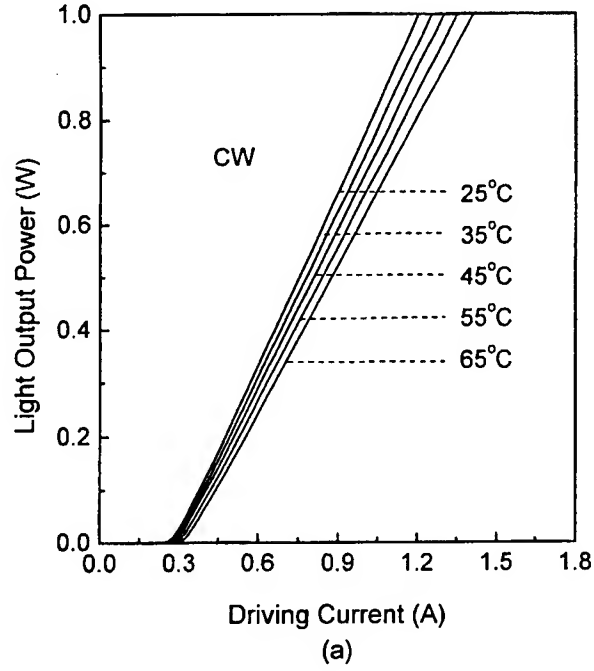


Fig. 1. (a) Light output power versus driving current characteristics for 800 μm -long, 100 μm broad stripe InGaAs/InGaAsP/AlGaAs laser diodes measured under CW condition at a temperature interval of 25-65°C. (b) Light output power, forward voltage and power conversion efficiency versus driving current characteristics at room temperature.

resistance and operating voltage are reduced. Power conversion efficiency reaches a maximum value of 56% at the 1.5 W point. Typical emitting wavelength at the output power of 1.0 W is 981 nm with spectral linewidth of 1.2 nm. Figure 2(a) shows the measured parallel and vertical far-field patterns under CW condition and at 1.0 W point. The beam angles are 7.8° and 34° , respectively. Note that the beam angles measured under pulse condition (300 Hz, 50 ms) are only 3° and 20° , respectively, as shown in Fig. 2(b). The small divergence is very useful for practical applications.

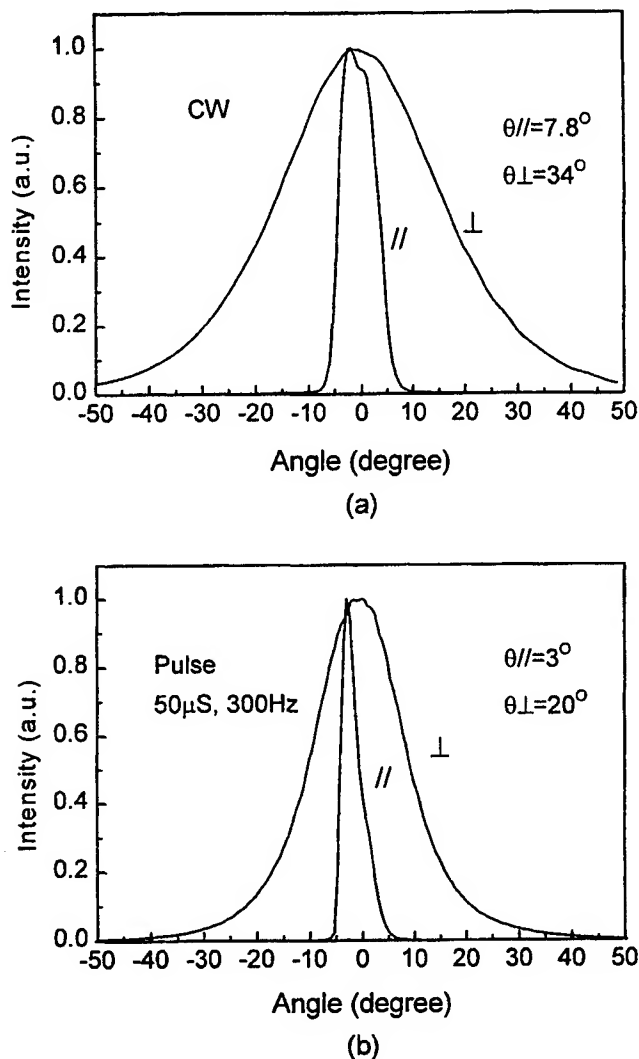


Fig. 2. Measured parallel and vertical far-field patterns for 100 μm broad stripe InGaAs/InGaAsP/AlGaAs laser diodes under (a) CW, and (b) pulse condition (300 Hz, 50 μs).

Figure 3 shows the results obtained from our reliability test, which was carried out on seven devices operating at a constant driving current of 1.5 A at room temperature. Light output power is about 1.2-1.3 W. Despite the high optical density at the laser facets (12-13 mW/μm), no obvious change was observed during 3000 hours of operation, which indicated very good reliability.

RW Lasers

For the 4 μm-wide ridge waveguide laser diode, Fig. 4 shows light output power versus driving current characteristic measured under CW condition and at room temperature. The threshold current is 38 mA. Output power reaches a

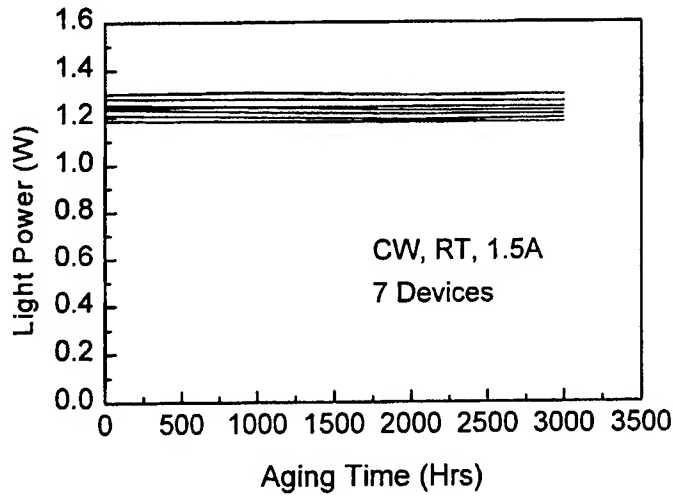


Fig. 3. Preliminary lifetime test results for 100 μm broad stripe InGaAs/InGaAsP/AlGaSd laser diodes.

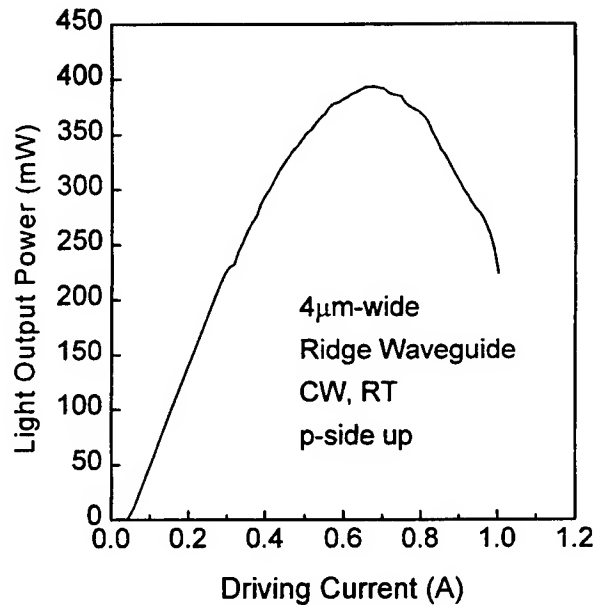


Fig. 4. Light output power versus driving current characteristic for the 4 μm RW InGaAs/InGaAsP/AlGaAs laser diodes.

maximum value of 394 mW and, then, decreases with driving current due to the thermal heating effect. COD is not observed at high powers and driving currents such that the device can be reversibly driven to over 1.0 A and back. The large equivalent spot size ($\sim 0.6 \mu\text{m}$) design, combined with the Al-free active region and non-injection regions near the laser facets, results in reduced optical density and lower facet overheating which are critical for improving COD. The kink-free fundamental mode output power is up to 200 mW with slope efficiency as high as 0.91 mW/mA. The high fundamental mode power results from the precise ridge size control and low confinement factor design that reduced spatial hole burning effects. Figure 5 shows the measured far-field patterns of the RW laser device. The parallel and vertical divergences are 8° and 38° , respectively. Preliminary life-test at 120 mW demonstrated good reliable operation over 3000 hours. Further reliability test for higher power operation is under study.

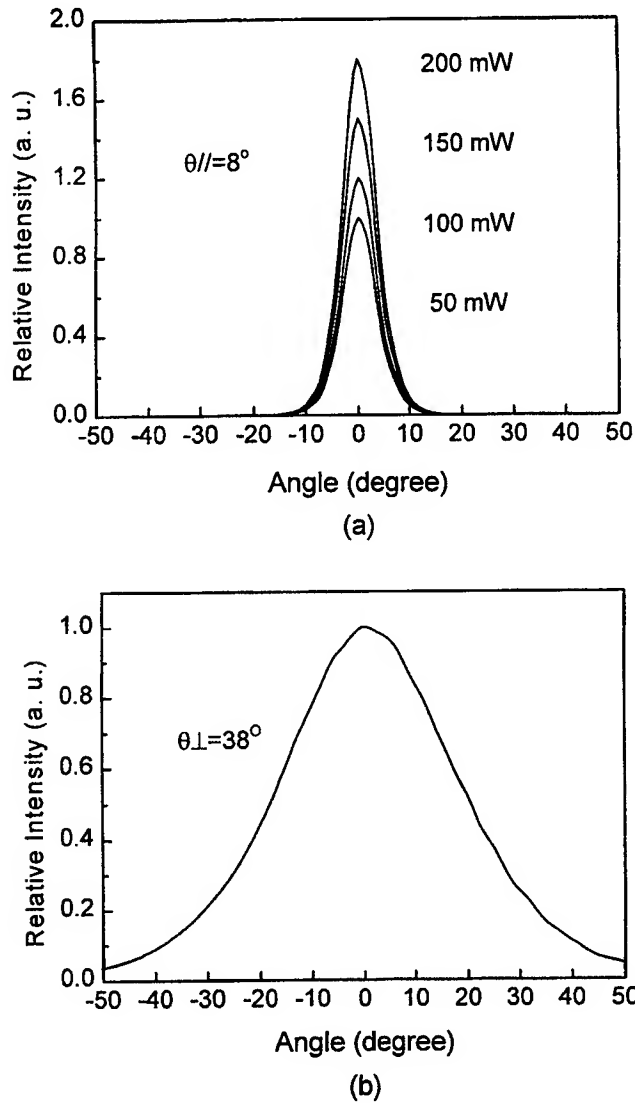


Fig. 5. Measured parallel and vertical far-field patterns for 4 μm RW InGaAs/InGaAsP/AlGaAs laser diodes.

5. CONCLUSIONS

In conclusion, we have analyzed the design of 0.98 μm InGaAs/InGaAsP/AlGaAs diode lasers. Optimization of key structure parameters lead to improvement of the laser performance. Specifically, the bandgap and thickness of the waveguide layer helps to improve carrier confinement, and consequently, quantum efficiency and the temperature coefficient of the laser. The broad waveguide design leads to very low internal loss and large spot size which are important properties for high power and high brightness laser devices. The Al-free active region enables high facet stability, and the use of AlGaAs cladding allows for high material quality and small beam divergence. The optimization of the cladding layer thickness is also useful in reducing the thermal and electrical resistances, and reducing the radiation loss.

InGaAs/InGaAsP(1.62 eV)/AlGaAs($x = 0.42$) laser structures with waveguide thicknesses of 400 and 600 nm were grown by MOCVD. The laser material exhibited high quality with low threshold current density, high internal quantum efficiency, and very low internal loss. 100- μm broad stripe multi-mode and 4- μm ridge waveguide single mode laser devices were both fabricated. For 100 μm -wide broad stripe lasers, a very high slope efficiency of 1.08 W/A, a low vertical beam divergence of 34° , and an extremely high T_0 value of 250 K are achieved. The maximum output power is over 4.45 W at the driving

current of 5.0 A. For the RW laser devices fabricated by selective etching, a threshold current of 38 mA, a high fundamental mode power of 200 mW with a slope efficiency as high as 0.91 mW/mA, and a maximum output power of 394 mW are demonstrated.

6. REFERENCES

1. B. Pederson, B. A. Thompson, S. Zemon, W. J. Miniscalco, and T. Wei, "Power Requirements for Erbium-Doped Fiber Amplifiers Pumped in the 800, 980, 1480 nm bands," *IEEE Photon. Technol. Lett.*, **4**, pp. 46-49, 1992.
2. S. Nikolov and L. Wetenkamp, "Single Frequency Diode-Pumped Erbium Lasers at 1.55 and 1.64 μm ," *Electron. Lett.*, **31**, pp. 731-733, 1995.
3. J. B. Roman, P. Camy, M. Hempstead, W.S. Brocklesby, S. Nouth, A. Beguin, C. Lermiaux, and J. S. Wilkinson, "Ion Exchange Er/Yb Waveguide laser at 1.5 μm Pumped by Laser Diode," *Electron. Lett.*, **31**, pp. 1345-1346, 1995.
4. J. Diaz, I. Eliashevich, K. Mobarhan, F. Kolev, L. J. Wabg, D. Z. Garbuzov, and M. Razeghi, "InGaP/InGaAsP/GaAs 0.808 μm Separate Confinement Laser Diodes Grown by Metalorganic Chemical Vapor Deposition," *IEEE Photon. Technol. Lett.*, **6**, pp. 132-134, 1994.
5. D. Z. Garbuzov, N.Y. Antonishkis, A. D. Bondarev, A. B. Gulakov, S. N. Zhigulin, N. I. Katsavets, A. V. Kocherin, and B. V. Rafailov, "High-power 0.8 μm InGaAsP/GaAs SCH SQW lasers," *IEEE J. Quantum Electron.*, **27**, pp. 1531-1536, 1991.
6. S. L. Yellen, A. H. Shepard, C. M. Harding, J. A. Baumarm, R. G. Waters, D. Z. Garbuzov, V. Pjataev, V. Kochergin, and P.S. Zory, "Dark-Line-Resistant, Aluminum-Free Diode Laser at 0.8 μm ," *IEEE Photon. Technol. Lett.*, **4**, pp. 1328-1330, 1992.
7. G. W. Yang, Z. T. Xu, X. Y. Ma, J. Y. Xu, J. M. Zhang, and L. H. Chen, "980 nm InGaAs/InGaAsP Quantum Well Lasers With AlGaAs Cladding Grown by Metal Organic Chemical Vapor Deposition," *Electron. Lett.*, **34**, pp. 1312-1313, 1998.
8. G. W. Yang, R. Jennifer Hwu, Z. T. Xu, and X. Y. Ma, "High Performance 980 nm Quantum Well Lasers Using a Hybrid Material System of an Al-free InGaAs-InGaAsP Active Region and AlGaAs Cladding Layers Grown by Metal-Organic Chemical Vapor Deposition," *IEEE J. Quantum Electron.*, **35**, pp. 1535-1541, 1999.
9. M. Okayasu, M. Fukuda, T. Takeshita, S. Uehara, and K. Kurumada, "Facet Oxidation of InGaAs/GaAs Strain Quantum-Well Lasers," *J. Appl. Phys.*, **69**, pp. 8346-8351, 1991.
10. M. Fukuda, M. Okayasu, J. Temmyo, and J. Nakano, "Degradation Behavior of 0.98 μm Strained Quantum Well InGaAs/AlGaAs Lasers Under High Power Operation," *IEEE J. Quantum Electron.*, **30**, pp. 471-476, 1994.

Low Threshold Current Densities of 1.5 μ m-Wavelength

(110) GaInAs(P) QW Lasers Along [001] Direction

Kunishige Oe^{*a}, Raj Bhat^b, Mineo Ueki^c, and Manabu Mitsuhashi^d

^aKyoto Institute of Technology, Matsugasaki, Sakyo-ku, Kyoto, 606-8585, Japan

^bCorning, Inc., SP PR 02-3, Sullivan Park, Corning, NY 14831, USA

^cNTT Electronics, Morinosato, Atsugi-shi, Kanagawa, 243-0198, Japan

^dNTT Photonics Laboratories, Morinosato, Atsugi-shi, Kanagawa, 243-0198, Japan

ABSTRACT

(110)-oriented GaInAs(P) quantum well lasers along [001] direction have been fabricated to investigate growth direction effects of the QW structure on laser performance. The structures were grown by two methods; MOVPE and MOMB. Threshold current densities of the QW lasers were investigated for wide stripes aligned in the [001] and [110] directions from the same wafer. As there is no cleaved facets for lasers along [001] direction, the mirror facets were formed parallel to the (001) face by reactive-ion-etching (RIE) using BBr₃ gas. Strong in-plane anisotropic lasing characteristics in the lasers made of the (110)-oriented QW structures were observed between the [001] and [110] cavity directions. This strong anisotropy in J_{th} is believed to come from the stronger oscillator strength in the [001] direction. Fairly low threshold current densities of less than 0.6 KA/cm² were obtained for the lasers with cavities along [001] direction in spite of the lower reflectivity of the RIE-etched mirror surface. The result in this research shows the expected advantage of the (110) lasers along [001] cavity direction and suggests an advantage of the (110) QW structure in the application for long wavelength surface emitting lasers.

Keywords: (110)-oriented Quantum Well Laser, GaInAsP, Low Threshold Current Density, Along [001] Cavity In-plane Anisotropy, Surface Emitting Laser, 1.5 μ m Wavelength

* Correspondence: Email: oeku@dj.kit.ac.jp; Telephone: +81-75-724-7412; Fax: +81-75-724-7400

1. INTRODUCTION

The performance of long wavelength semiconductor lasers has been upgraded by introducing quantum well (QW) structures. Up to now, most of the QW structures have been grown on (001)-oriented substrates as the substrates have two orthogonal cleaved facets which can be easily used for laser mirrors and device separation. On the other hand, the growth direction of the QW structure has significant effects on laser performance, and theoretical calculations on the optical gains in QW semiconductor lasers with non-(001) orientations have been much performed to clarify these points¹⁻⁴. These researches show that the oscillator strength for $[\bar{1}\bar{1}0]$ -polarized light in (110)-oriented QW structure is expected to be the strongest among many polarized light in various QW orientations and the (110) QW lasers whose cavity are formed along [001] direction are expected to give the best results for all QW lasers, due to the larger optical matrix element and the reduced in-plane hole mass. Also the oscillator strength for $[\bar{1}\bar{1}0]$ -polarized light is assumed to be much stronger than that for [001]-polarized light in (110)-oriented QW structures and in-plane anisotropic lasing characteristics are expected in the (110) QW lasers. Although there are a few reports on (110) QW lasers^{5,6}, the laser cavities are only formed along the $[\bar{1}\bar{1}0]$ direction except our recent report⁷, as cleaved facets can be used for mirrors in this direction. The lasers along the [001] direction is expected to give better results as they utilize the [110]-polarized light.

In this paper, lasing characteristics of the (110)-oriented GaInAs(P) QW lasers are reported. Threshold current densities of the QW lasers were investigated for wide stripes aligned both in the [001] and $[\bar{1}\bar{1}0]$ directions from the same wafer. The mirror facets for the lasers in the [001] direction were formed by reactive-ion-etching (RIE) using BBr_3 gas. Fairly low threshold current density of less than 0.6 KA/cm^2 was obtained in the (110)-oriented GaInAs(P) quantum well lasers in the [001] direction. Also strong in-plane anisotropic lasing characteristics of the (110) QW lasers have been confirmed for the first time. This research might be very useful for the development of long wavelength vertical cavity surface emitting lasers, as the lasers need more optical gain to compensate their low reflectance of the cavity mirrors and polarization control of the emitting light.

2. ADVANTAGES OF (110) QUANTUM WELL STRUCTURE

Theoretical calculations on the optical properties of (110)-oriented QW structures have been performed much as the QW properties will depend on the growth axis as a result of an anisotropy of the valence-band structure in bulk materials and QW lasers of better device performance are expected to be fabricated from the (110)-oriented QW structures. Houngh et al. have calculated valence-subband structures of GaAs/GaAlAs QWs grown on the (001), (111), and (110) substrates based on the bond-orbital model. They showed the subband structures of (110)-oriented QWs display large anisotropy with effective masses along two different in-plane directions ([001] and $[\bar{1}\bar{1}0])$ ¹. Kajikawa et al. studied optical matrix element at the Brillouin zone center in (110)-oriented QWs for linearly polarized light on the basis of an envelope-function approximation. They showed the optical matrix elements in the (110) QWs depend on the polarization direction in contrast

with polarization-independent character in (001)- or (111)-oriented QWs². Nojima also investigated the in-plane anisotropy of interband optical transitions for GaAs/AlGaAs (110)-oriented QWs in detail³. Yamaguchi et al. also investigated theoretically optical matrix elements and in-plane hole effective masses in GaAs QWs as functions of substrate orientation. They discussed the optimum substrate orientation for low-threshold QW lasers⁴. There are two factors involved in reducing the threshold current; enhancing the oscillator strength of the optical transition and reducing the in-plane hole mass. From the viewpoint of the oscillator strength, the (110) QW is superior to any other orientations. In terms of in-plane effective mass of heavy hole in GaAs QWs, the mass for a (111) QW takes the minimum value. However the mass for a (110) QW is also much smaller than that for a (001) QW and comparable to that for a (111) QW. Therefore (110) QW lasers are expected to give better performance than QW lasers of the other orientations from the viewpoint of the theoretical calculations. Although these calculations are performed on the GaAs QWs as physical parameters are well known in these materials, the calculated results might be true for GaInAs(P) QWs.

3. LASER STRUCTURE WAFERS

Two kinds of QW structure epitaxial wafer, grown on (110) InP substrates by Metalorganic Vapor Phase Epitaxy (MOVPE)⁵ or Metalorganic Molecular Beam Epitaxy (MOMBE)⁶ were used for laser fabrication. In MOVPE, the growth were carried out in a horizontal, low pressure (76 Torr) reactor using trimethylgallium (TMG) and trimethylindium (TMI), arsine, phosphine, and hydrogen as a carrier gas. The substrates for MOVPE growth had a orientation of 3° off (110) towards (111)B direction as it is almost impossible to grow the epitaxial layers on just (110) ones. The growth temperature was 575°C. The MOVPE wafer consists of n-InP cladding layer, 0.1 μ m-thick InGaAsP waveguide layer ($\lambda=1.3 \mu$ m), 3QW active layer {60Å InGaAsP well layers ($\lambda=1.64 \mu$ m) and 200Å InGaAsP barrier layers ($\lambda=1.3 \mu$ m)}, 0.1 μ m thick

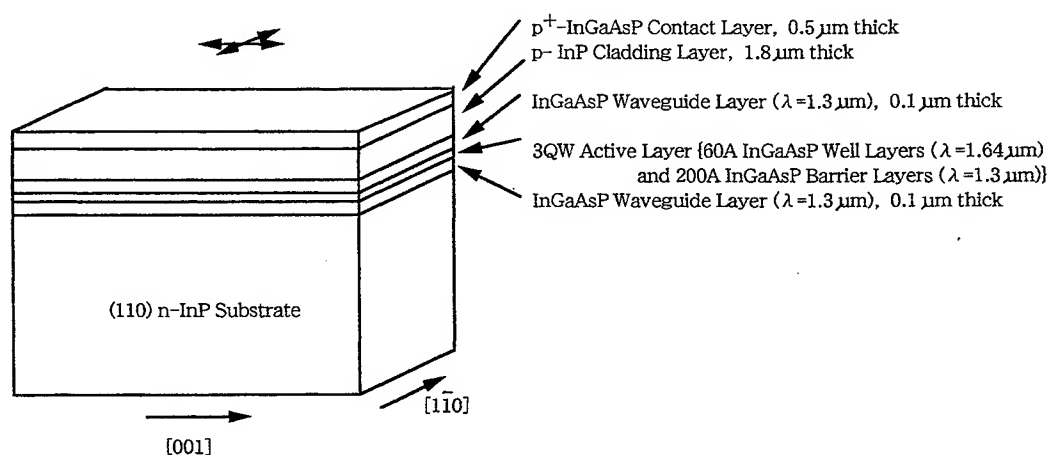


Fig. 1 (110) QW layer structure grown by MOVPE

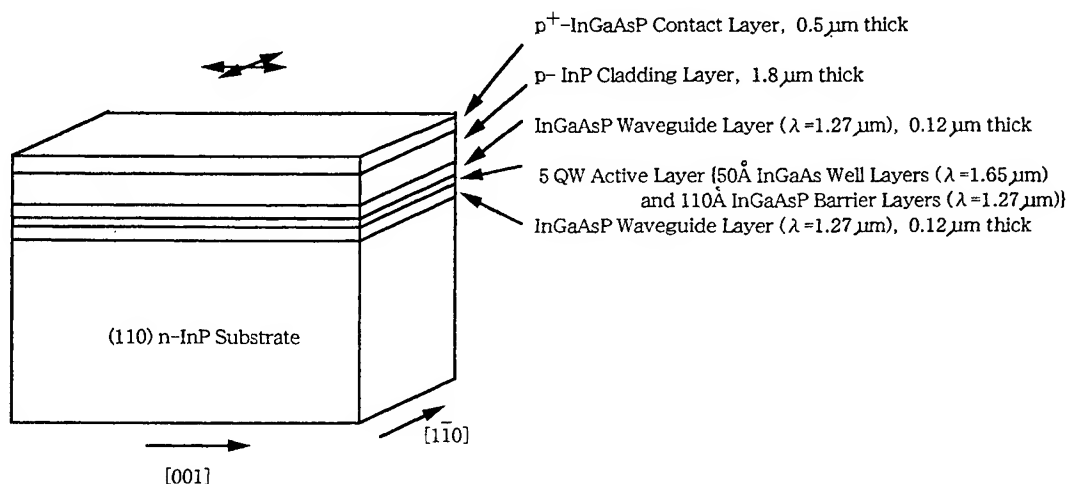


Fig. 2 (110) QW layer structure grown by MOMBE

InGaAsP waveguide layer ($\lambda = 1.3 \mu\text{m}$), $1.8 \mu\text{m}$ -thick p-InP cladding layer, and $0.5 \mu\text{m}$ -thick p^+ -InGaAsP contact layer, as shown in Fig. 1. It has been found that the growth of the lattice matched $\text{In}_{0.53}\text{Ga}_{0.47}\text{As}$ with specular surface on the tilted (110) InP surface is disturbed due to faceting; the InGaAs surface tends to break up into (110) treads and (111) risers. Adding an amount of P, however, has been found to greatly improve the surface regularity, resulting in smooth and planar interface. Therefore the well material was chosen to be InGaAsP with composition close to that of the lattice-matched $\text{In}_{0.53}\text{Ga}_{0.47}\text{As}$. Details concerning the growth procedure have been published elsewhere⁵. In MOMBE growth, group V hydrides (PH_3 , AsH_3) were thermally cracked in a low-pressure cell heated to 900°C . Group III metalorganics (TMI, TEG) were injected into the growth chamber without carrier gases. The typical growth temperature was 510°C , which is similar to the temperature used for the growth on (001) substrates.

The (110) InP substrates were oriented 5° off towards (111)A direction. The MOMBE wafer consists of n-InP cladding layer, $0.12 \mu\text{m}$ -thick InGaAsP waveguide layer ($\lambda = 1.27 \mu\text{m}$), 5QW active layer { 50 \AA InGaAs well layers and 110 \AA InGaAsP barrier layers ($\lambda = 1.27 \mu\text{m}$)}, $0.12 \mu\text{m}$ -thick InGaAsP waveguide layer, $1.8 \mu\text{m}$ p-InP cladding layer, and $0.5 \mu\text{m}$ p^+ -InGaAsP contact layer, as shown in Fig. 2. For InGaAs/InGaAsP QW structures grown on (110) substrates by MOMBE, the peak intensity of room temperature PL was comparable to the highest intensity of the QW structures grown on (001) substrate.

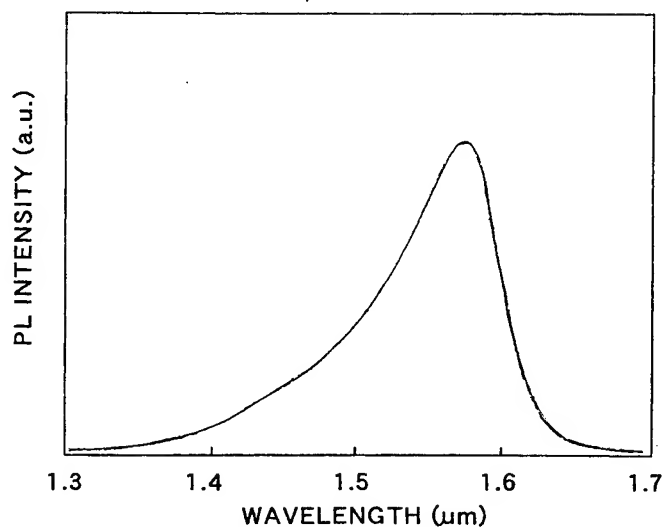


Fig. 3 PL spectrum of the (110) QW wafer measured at room temperatures.

4. OPTICAL PROPERTY OF THE (110) QW STRUCTURE

In order to investigate the advantageous optical properties of the (110) QW structure, a spectroscopic study of the (110)-oriented InGaAsP QW structure was performed on the MOVPE grown wafer. Figure 3 shows a photoluminescence (PL) spectrum of the QW wafer measured at room temperatures. As expected from the theoretical calculations, the PL intensity of the grown wafer is much stronger than that of the same structure grown on (001)-oriented substrates. This stronger PL intensity reflects the advantage of the (110) QW structure over (001) QW ones due to the larger optical matrix element and the reduced in-plane hole mass. PL and photoluminescence excitation (PLE) spectroscopies have been also undertaken on the structure at low temperatures (below 4K). For PL and PLE experiments, light from a 150-W tungsten halogen lamp dispersed by a 320-mm focal length monochromator was used as tunable excitation source. Figure 4 shows a PL and PLE spectra for the (110)-oriented InGaAsP QW structure. A sharp and intense PL line was observed despite a very low

excitation power density, typically of order of several $\mu\text{W}/\text{cm}^2$. The absolute PL intensity was found to be even higher by a factor of 2-4 than those from the usual QW structures grown on (100)-oriented substrates. Excellent luminescence efficiency of these (110)-oriented QW structure then allow us to observe the PLE spectra even under such a low excitation. The absorptions in the PLEs show a clear ground state exciton transition, i.e. the absorption via the first-heavy hole to first-electron exciton transition (11H). This transition peaks at higher energy than the PL. The anisotropy of the QW ground state transition is clear when comparing two PLE spectra recorded for $[1\bar{1}0]$ - and $[001]$ -polarized light. The absorptions in the PLEs show that the 11H absorption becomes maximum for $[110]$ - polarized light and minimum for $[001]$ -polarized light.

This result is consistent with the theoretical calculations on the optical anisotropy on (110)-oriented QW structures, and suggest the advantageous optical properties of (110)-oriented QW lasers with optical cavities in the $[001]$ direction.

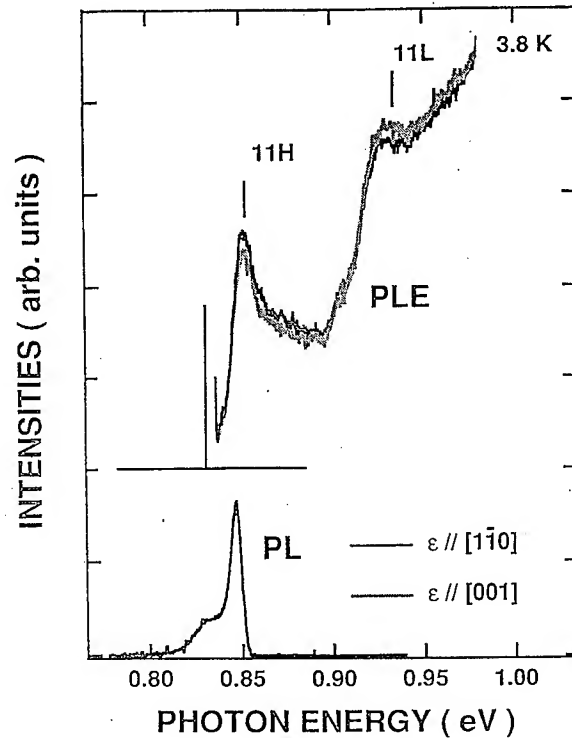


Fig. 4 PL and PLE spectra for an (110)-oriented QW structure. The PLE spectra are shown for the $[1\bar{1}0]$ -polarized light ($\epsilon//[1\bar{1}0]$) and $[001]$ -polarized light ($\epsilon//[001]$).

5. FABRICATION TECHNOLOGY OF THE LASERS

The wafers were processed for broad stripe laser structure to characterize laser threshold current densities. Broad stripe lasers in the $[1\bar{1}0]$ direction were fabricated by a usual processing technology with $[1\bar{1}0]$ cleaved facets. For lasers in the $[001]$ direction, special processing technology was required to fabricate the lasers as there is no cleaved facets perpendicular to the $[001]$ direction. Therefore processing technology as shown in Fig. 5 was developed to fabricate the lasers in the $[001]$ direction. At first Ohmic metal material (Au/Zn/Ni alloy) was deposited for the p-contact electrode on some portion of the InGaAsP cap layer by lift-off technique and sintered at 400°C . The p-electrode areas were designed to be a bit smaller than the mask areas of the broad stripe lasers. Then the laser regions of $40\text{ }\mu\text{m}$ -wide and 350, 500, 800, and 1100 μm long which include the p-electrode areas were covered by thick photo-resist layer and ion-milling were applied on the wafer to isolate the laser region islands. The widths of the laser region islands were reduced to $30\text{ }\mu\text{m}$ in this milling. The laser region islands are formed parallel to $[001]$ direction on the wafer. The depth was about $5\text{ }\mu\text{m}$. (Fig. 5(a)). After removing the photo-resist, SiO_2 film was sputtered on the surface and stripe windows were opened in the SiO_2 film on the p-electrode regions along the $[001]$ direction. Au/Pt/Ti metal were deposited on some part of the SiO_2 film for the pad electrode by lift-off technique. (Fig. 5(b)). Then

a thin film of SiO_2 was deposited on the surface in stripes of 150, 300, 600, and 900 μm width parallel to the $[110]$ direction by the usual rf sputtering and photoetching techniques using reactive-ion etching (RIE) based on a mixture gas of C_2F_6 and SF_6 . The stripe SiO_2 film were used as the etching mask for mirror formation by RIE using BrBr^3 gas. (Fig. 5(c)). As the RIE technique has been successfully applied to fabricate etched-faceted lasers on (001) -oriented QW lasers in the NTT laboratory and RIE is generally believed to be appropriate for making vertical walls in any direction, this RIE technique was applied to make etched-facets with (001) faces. Figure 6 shows a SEM photograph of the broad stripe lasers with RIE-etched mirror surfaces. The RIE etched facets seems to be smooth. Following the RIE with BrBr^3 gas, the wafer was RIE-etched using a mixture gas of C_2F_6 and SF_6 , which removes SiO_2 film on the wafer. After

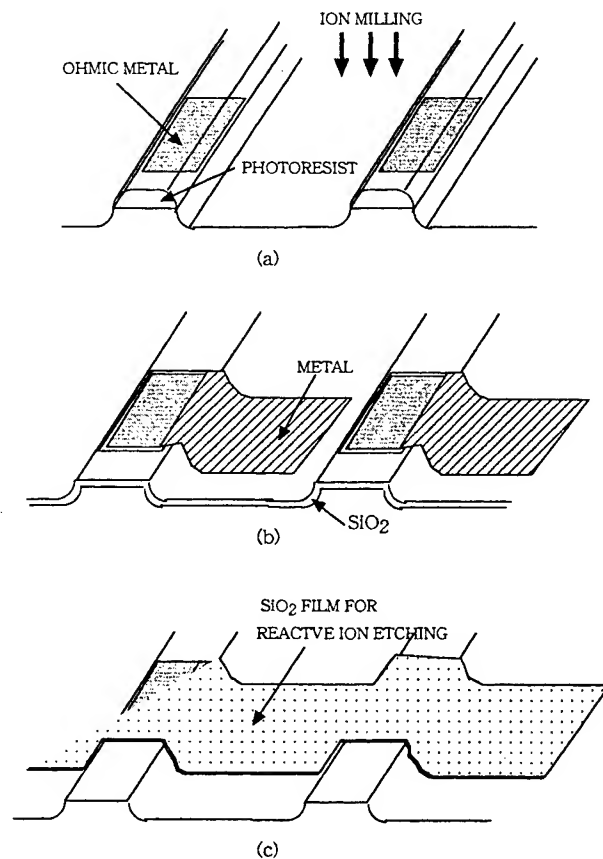


Fig. 5 Fabrication process of the (110) QW lasers along $[001]$ direction

thinning the substrate, Au/Ge/Ni were evaporated on the n type substrate, and subsequent sintering of the wafer at 430°C in a forming-gas ambient produced good Ohmic contacts. Four kinds of cavity length lasers with 150, 300, 600, and 900 μm length were formed on the same wafer. Device separation was easily performed for the direction along laser cavity as the direction has cleaved facets of (110). However the direction perpendicular to the laser cavity does not have cleaved facets. Therefore the lasers wafers were cleaved into bars with (110) facets at first and each laser chip was divided from the bars by appropriate technique.

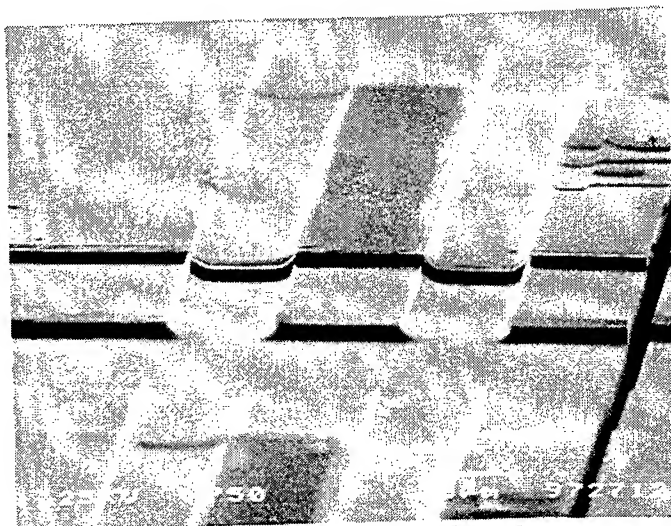


Fig. 6 SEM photograph of broad stripe lasers with RIE-etched mirror facets

6. LASING CHARACTERISTICS

Light output-current (L-I) characteristics has been measured on the broad stripe semiconductor lasers in pulse current condition. One of the results measured on 900 μm long cavity (110) QW lasers along [001] direction, is shown in Fig. 7. The output power which is shown in arbitrary unit in the figure means that not all the optical output power is received by the photodetector because some of the laser light is reflected by the wafer surface near the dry-etched mirror face. For comparison, L-I characteristic of (110) QW lasers along $[1\bar{1}0]$ direction with (110) cleaved facets from the same wafer is also shown in Fig. 7. The threshold current density (J_{th}) of the laser with the RIE-etched mirrors is about 0.6 KA/cm² and much lower than that of the laser in the $[1\bar{1}0]$ direction with cleaved facets from the same wafer. As the reflectivity of the RIE-etched mirror surface is lower than that of the cleaved facet, this result shows the expected advantage of the (110) lasers along [001] cavity direction. Figure 8 shows threshold current densities of the lasers fabricated with wide stripes aligned in the [001] and $[110]$ directions from the same wafer grown by MOVPE. The laser cavities in the $[110]$ direction were cleaved facets while those in the [001] directions were formed by the RIE-etching. It can be seen the threshold current densities of the lasers aligned in the [001] direction are much smaller than those aligned in the $[1\bar{1}0]$ direction for 300, 600, and 900 μm long cavity lasers. This strong anisotropy in J_{th} is believed to come from the stronger oscillator strength in the [001] direction and will be very useful to control polarization of laser output from surface emitting lasers (SELS) if the (110) QW structure is used for the SELs. QW lasers with 150 μm -long cavity showed no lasing or extremely high threshold current density. The reason might be small optical gain of the 3 QW laser structure. Remarkable points in the Fig. 8 are that the threshold current densities of the lasers decrease with the cavity length and the lowest threshold

density of less than 0.6 KA/cm^2 is obtained for the $900 \mu\text{m}$ long lasers in the $[001]$ direction. There is scattering in threshold current densities of the lasers with RIE-etched mirror facets along the $[001]$ direction and the scattering becomes larger when the laser cavity length becomes shorter. The reason can be assumed to be fluctuations of the reflectivity of the RIE-etched mirrors. Although the RIE-etched facets are seen to be smooth in most of the parts in the wafer, the flatness might be different from place to place with the present RIE technology. Lower threshold current density of the (110) QW lasers can be expected with a improved etching technique. In spite of the fact that the reflectivity of the RIE-etched mirror surface is lower than the cleaved facet, the lowest threshold current density of less than 0.6 KA/cm^2 is compatible with the lowest one for (001) QW lasers with cleaved facets. Results on the lasers made from MOMBE grown wafers were similar to those on lasers made from MOVPE grown wafers. These results in Fig. 8 show the expected advantage of the (110) lasers along $[001]$ cavity direction.

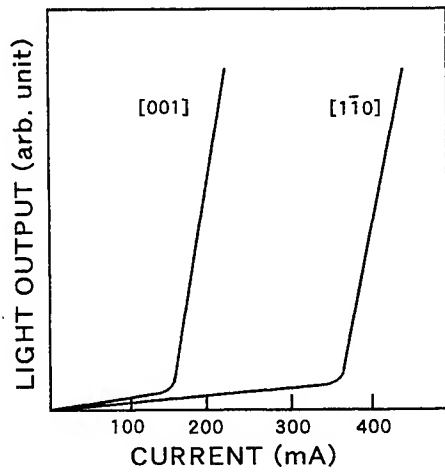


Fig. 7 L-I Characteristics of the $900 \mu\text{m}$ -long (110) QW laser

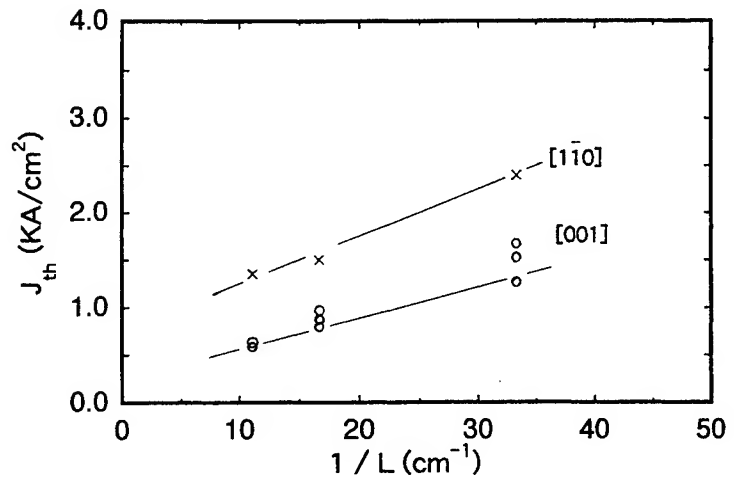


Fig. 8 Threshold current densities of the (110) QW lasers aligned in the $[001]$ and $[1\bar{1}0]$ directions

7. SUMMARY

(110) -oriented GaInAs(P) quantum well lasers along $[001]$ direction have been fabricated to investigate growth direction effects of the QW structure on laser performance. The structures were grown by two methods; MOVPE and MOMBE. Threshold current densities of the QW lasers were investigated for wide stripes aligned in the $[001]$ and $[110]$ directions from the same wafer. As there is no cleaved facets for lasers along $[001]$ direction, the mirror facets were formed parallel to the (001) face by reactive-ion-etching (RIE) using BBr_3 gas. Strong in-plane anisotropic lasing characteristics in the lasers made of the (110) -oriented QW structures were observed between the $[001]$ and $[1\bar{1}0]$ cavity directions.. This strong anisotropy in J_{th} is believed to come from the stronger oscillator strength in the $[001]$ direction. Fairly low threshold

current densities of less than 0.6 KA/cm^2 were obtained for the lasers with cavities along [001] direction in spite of the lower reflectivity of the RIE-etched mirror surface. The result in this research shows the expected advantage of the (110) lasers along [001] cavity direction and suggests an advantage of the (110) QW structure in the application for long wavelength surface emitting lasers.

ACKNOWLEDGMENTS

This research is partly supported by the Monbusho Grant-in-Aid (#11650346) and the Murata Science Foundation.

REFERENCES

- 1) M-P. Houn, Y-C. Chang, and W. I. Wang, "Orientation dependence of valence-subband structures in GaAs-GaAlAs quantum well structures," J. Appl. Phys., **64**, pp. 4609-4613, 1988
- 2) Y. Kajikawa, M. Hata, and T. Isu, "Optical matrix elements in (110)-oriented quantum wells," Jpn. J. Appl. Phys., **30** pp. 1944-1945, 1991
- 3) S. Nojima, "Anisotropy of optical transitions in (110)-oriented quantum wells," Phys. Rev. B **47**, pp. 13535-13539, 1993
- 4) A. A. Yamaguchi, K. Nishi, and A. Usui, "Anisotropic optical matrix elements in quantum wells with various substrate orientations," Jpn. J. Appl. Phys., **33**, pp. L912-L915, 1994
- 5) R. Bhat, M.A. Koza, D.M. Hwang, M.J.S.P. Brasil, R.E. Nahory, and K. Oe, "OMCVD growth of InP, InGaAs, and InGaAsP on (110) InP substrates," J. Crystal Growth, **124**, pp. 311-317, 1992
- 6) M. Mitsuhashi, M. Okamoto, R. Iga, T. Yamada, and H. Sugiura, "InP and related compounds grown on (110) InP substrates by metalorganic molecular beam epitaxy (chemical beam epitaxy)," J. Crystal Growth, **136**, pp. 195-199, 1994
- 7) K. Oe, R. Bhat, M. Ueki, and M. Mitsuhashi, "(110)-oriented InGaAs(P) quantum well lasers along [001] direction," Workshop on Contemporary Photonic Technologies, Tc-19, Tokyo, Jan. 2000

SESSION 6

Semiconductor LEDs and Lasers

New methods of defect-enhanced quantum well intermixing and demonstrated integrated distributed feedback laser –modulator

David A. Thompson, John F. Hazell, Alex S. W. Lee, Tao Yin, Gregory J. Letal, Brad J. Robinson,
Nicolas Bertsch and John G. Simmons
Centre for Electrophotonic Materials and Devices, McMaster University, Hamilton, ON. L8S 4L7,
CANADA

ABSTRACT

New methods of implementing quantum well intermixing (QWI) in InP-based materials using defect-enhanced diffusion are presented and compared to the widely reported technique employing dielectric (usually SiO₂) capping with subsequent rapid thermal anneal (RTA) treatments. The new methods discussed use InP layers grown either at low temperature by gas-source molecular beam epitaxy (GSMBE) or using He-plasma-assisted GSMBE where the growth surface is subjected to a continuous low energy He-plasma generated in an electron cyclotron resonance (ECR) source. The two new QWI processes, and the SiO₂ capping method, are applied to a 1.55µm InGaAsP multiple quantum well laser structure. For application of the QWI process the laser structure growths are interrupted in a manner and location appropriate to carrying out the QWI process and subsequent grating etch for the fabrication of a distributed feedback (DFB) laser. After implementing the QWI and grating etch, growth of the top cladding and contact layers completes the device structure. Finally, the fabrication of a DFB laser with an integrated electro-absorption (EA) modulator is described and the resultant characteristics given.

Keywords: quantum well intermixing, semiconductor lasers, distributed feedback, modulators, photonic integration

1. INTRODUCTION

Photonic integration involving lasers, detectors, modulators and passive wave-guides is an area of considerable interest for photonic integrated circuits (PICs). A requirement is the controlled change of the bandgap energy selectively across the wafer. While this can be achieved by selective area re-growths^{1,2}, this approach involves complex processing methods. Thus there has been considerable interest in developing post-growth techniques applicable to quantum well (QW) structures whereby local intermixing between the QWs and adjacent barrier regions is carried out using defect diffusion. Various approaches³⁻⁶ to quantum well intermixing (QWI) has been investigated for many years and several applications to actual device structures has been demonstrated⁷⁻⁹.

Quantum well intermixing occurs when a QW structure is subjected to a high temperature anneal treatment causing the constituent atoms in the well and barriers to inter-diffuse thus producing a blue-shift in the wavelength of light emitted by carrier recombination in the QWs. This inter-diffusion can be enhanced and made spatially selective through the controlled introduction and diffusion of defects^{3,6} or impurities^{10,11}. Since the introduction of impurities is generally undesirable, impurity-free processes using ion implantation or applying a dielectric cap, typically SiO₂¹², both followed by a subsequent RTA, have been used to produce local areas of bandgap increase. The SiO₂-cap + RTA process is of particular interest because such dielectric films are a standard process in most fabrication sequences. Much of the work on this process has been carried out with GaAs-based structures where it is demonstrated that group III vacancies are produced by Ga diffusing into the SiO₂ cap layer¹³. These vacancies then diffuse through the QW region during the RTA treatment causing the required QW/barrier inter-diffusion and bandgap increase. This process has been successfully applied to GaAs/AlGaAs QW structures¹⁴. There have also been substantial applications to InP-based structures^{15,16} and some work on actual laser structures^{7,9,14}.

In this paper we report on application of the QWI process on InGaAsP/InP 1.55µm laser structures using defect-enhanced QWI. Initially the thermal stability of the as-grown laser structure to the thermal anneal treatment will be discussed. This will be followed by a description and analysis of the enhanced QWI processes. Details of the response to the SiO₂-cap + RTA process on these structures will be given, suggesting that the mechanism of QWI for InP-based structures differs from GaAs-based materials. Other InP-based enhanced QWI processes using the low temperature grown InP (LT-InP) and the He-plasma-assisted GSMBE grown InP (He*-InP) will be described and their relative merits discussed in comparison to the

SiO₂-cap + RTA process. Finally, the fabrication of an integrated DFB laser with an electro-absorption (EA) modulator using the He*-InP QWI process will be described and its characteristics given.

2. EXPERIMENT.

The laser structure consists of a 3-QW all quaternary active layer grown by GSMBE on n-type, (001) InP substrates as shown in figure 1. The QWs are 5nm, 1% compressively strained undoped layers of composition In_{0.76}Ga_{0.24}As_{0.85}P_{0.15} separated by 10nm barriers of undoped, lattice-matched In_{0.76}Ga_{0.24}As_{0.52}P_{0.48} barriers. The growth temperature was 470°C. Note that the group III compositions are unchanged between the well and barrier layers. Above and below the active region are 70nm, 1.24Q and 80nm, 1.15Q wave-guiding layers, topped with 25nm InP. The structures are then terminated with additional layers depending on the specific QWI process being applied. After carrying out the QWI process, all samples are etched back to the 25nm InP layer for patterning and etching the DFB grating.

Typical terminating layers are shown in figure 1(a-c). Others were used depending on the experiment being conducted and will be described where relevant. Figure 1(a) corresponds to the structure used for the SiO₂-cap + RTA process. For this process, the sample growth is terminated with 100nm, lattice-matched InGaAs to allow for Ga out-diffusion into the SiO₂

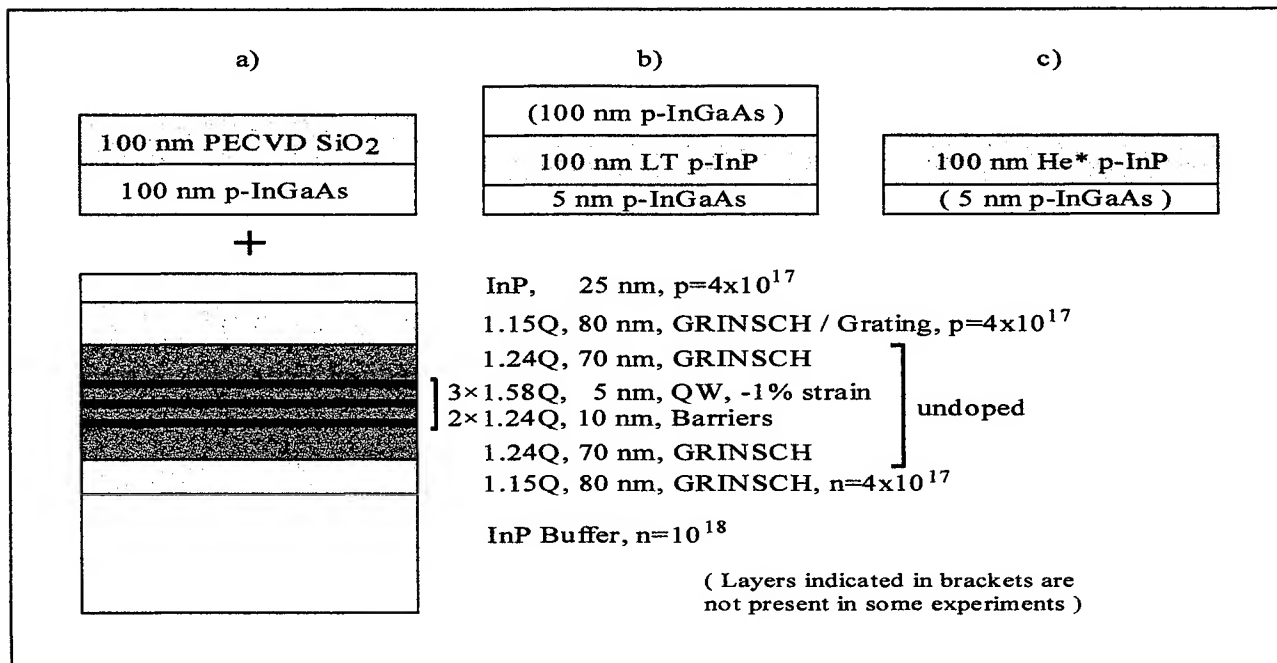


Figure 1. MBE grown structures for conducting the various QWI processes; (a) for the SiO₂-cap + RTA process, (b) for the LT-InP process, and (c) for the He*-InP process.

layer during the RTA treatment. The SiO₂ was deposited by plasma-enhanced chemical vapour deposition (PECVD). The structure termination shown in figure 1(b) was used for the LT-InP QWI process. The 5nm InGaAs layer was simply used as an etch-stop layer for etching back to the grating-etch layer. The 100nm LT-InP layer was grown 1x10¹⁸ cm⁻³ p-doped at 300°C and the structure capped with an InGaAs layer grown at 470°C. As will be shown later, this InGaAs layer has only a small effect on the QWI process in a limited temperature range (650 – 750°C). For the He*-InP QWI process a thin layer (100nm) of He*-InP was deposited (the details will be discussed in section 3.4) on the 25nm of normally grown InP as shown in figure 1(c). Some samples had a thin (5nm) InGaAs layer beneath the He*-InP layer.

The RTA treatments were carried out in an enclosed carbon boat and a flowing nitrogen atmosphere. The samples inside the boat were also covered with an InP proximity cap for surface protection. Anneals were carried out over the temperature range 600 – 800°C for times ranging from 2 – 1200s. Determination of the effectiveness of the QWI process was by room temperature photoluminescence (PL) through the change in emission wavelength and intensity.

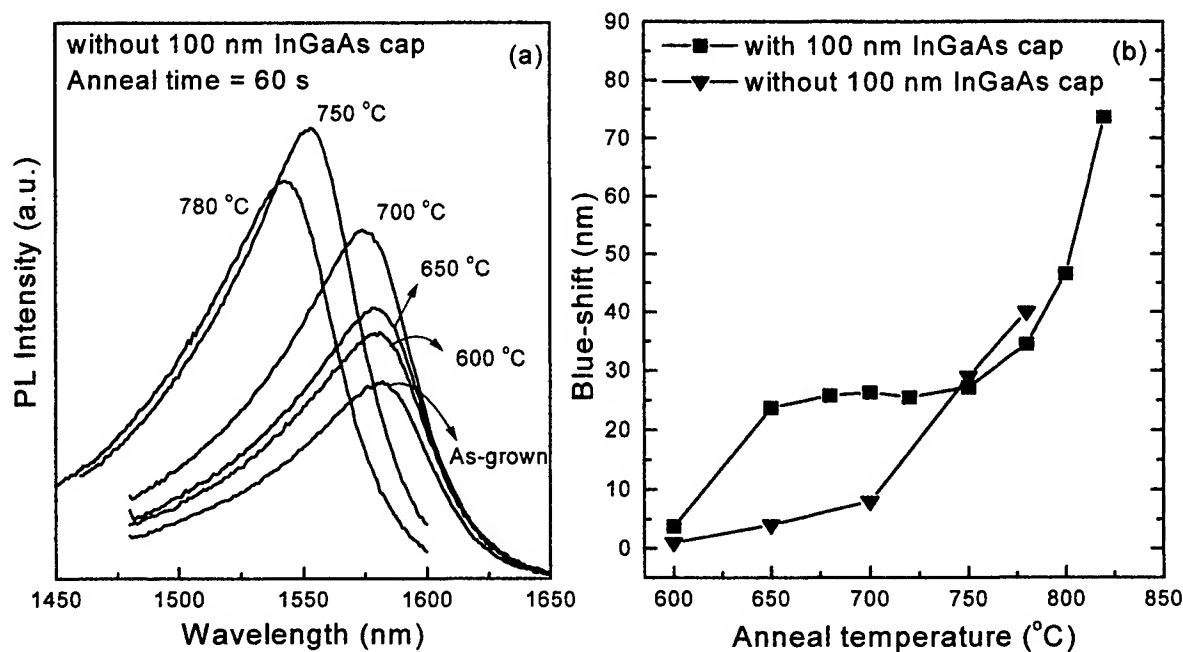


Figure 2. Photoluminescence data on samples, for thermal-only treatments, annealed at various temperatures; (a) PL emission spectra, (b) wavelength blue-shift.

3. RESULTS AND DISCUSSION

3.1. Thermal stability of laser structures.

Figure 2 shows the PL results for samples shown in figures 1(b), both with and without the InGaAs cap layer, and with the LT-InP layer replaced with an InP layer grown at normal temperature (NT-InP). Similar results were obtained with the structure of figure 1(a). Anneals were carried out for 30 and 60s at various temperatures above 600°C. In figure 2(a) it is seen that the PL intensity increases with anneal temperature and the line-width decreases. The change of the wavelength blue-shift with anneal temperature is shown in figure 2(b). For temperatures up to 600°C there is no observable change in the peak wavelength, between 600 – 700°C a small blue-shift is observed, but above 750°C the peak wavelength decreases rapidly with temperature. This wavelength blue-shift will be labeled as the “thermal blue-shift” and all measurements of the enhanced QWI blue-shift appearing in later sections will be denoted as the “net blue-shift”; i.e. with the thermal component subtracted. An interesting difference occurs between samples terminated with and without an InGaAs cap layer. Those terminated with InGaAs exhibit a larger blue-shift (by ~25nm) after anneal at 700°C than the otherwise identical structure without the InGaAs. For anneals above ~750°C the effect of the InGaAs cap layer is again negligible. Thus the effect of the InGaAs is to produce an early onset of blue-shift. However, that this blue-shift then remains constant between 700 – 750°C suggests that the concentration of defects that give rise to this phenomenon is limited.

In figure 3 the thermal blue-shift is shown versus anneal time (5 – 1200s) at various temperatures (>700°C). At short anneal times (~5s) the blue-shift appears to asymptote to ~25nm. This, and the reduction in the line-width (FWHM), indicates the initial changes occur over a very short time scale and could be the result of changes in the active region due to grown-in lateral composition modulation (or phase separation), and its associated interfacial defects¹⁷. For longer anneal times the structures become increasingly sensitive to the anneal temperature with, as expected, the higher temperatures showing the largest rate of change of blue-shift with time. In all cases there is a trend for the rate of change of blue-shift to decrease suggesting saturation of the blue-shift with the saturation level increasing with temperature.

3.2. SiO₂-cap + RTA QWI process.

The SiO₂ films were deposited by PECVD at 300°C using 5% SiH₄ in Ar and N₂O. The resultant dielectric constant of the

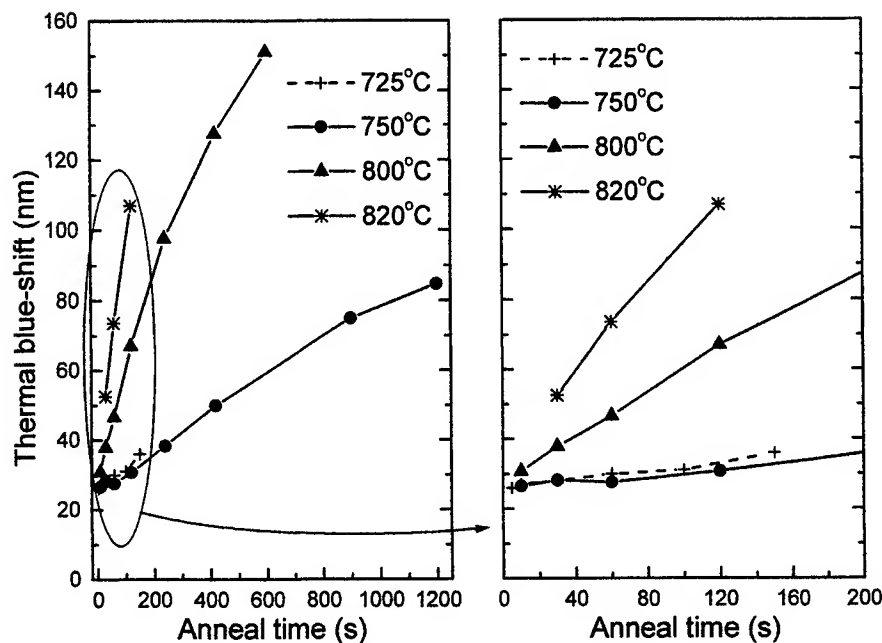


Figure 3. Thermal blue-shift versus anneal time for anneals at various temperatures.

film was 1.478. Auger electron spectroscopy shows the films to be near stoichiometric SiO_2 and Fourier transform infrared spectra indicates they contain ~5% hydrogen.

As shown in figure 1(a) the SiO_2 coatings are deposited on InGaAs terminated samples. These capped samples could be annealed at high temperatures (820°C) without decomposing and exhibited bandgap shifts well in excess of the thermal-only shifts for anneals above 720°C .

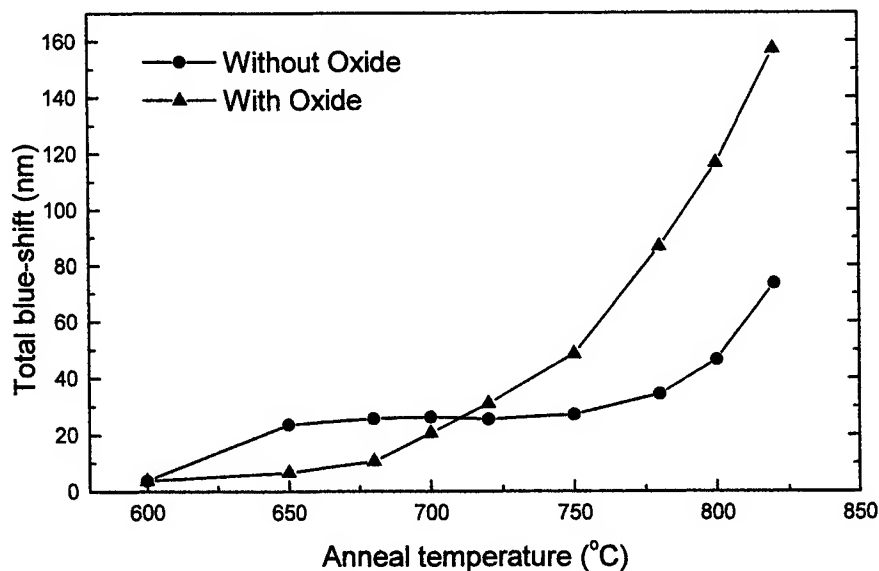


Figure 4. Comparison of thermal and SiO_2 -cap enhanced QWI annealed for 60s at different temperatures.

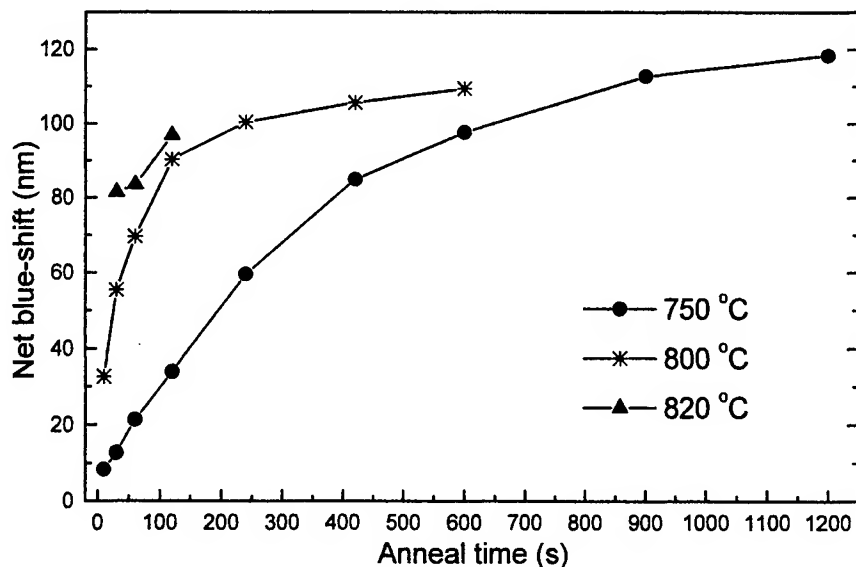


Figure 5. Net blue-shift for an SiO₂ capped structure versus anneal time at various temperatures

Figure 4 compares the total blue-shift for SiO₂-capped and un-capped (thermal-only) samples annealed for 60s at 600 – 820°C. In the low temperature range (600 – 700°C) the presence of the SiO₂ cap suppresses the thermal-only blue-shift, but above ~750°C a significant enhancement of the blue-shift is observed. The reasons for the suppression of the QWI are not currently understood.

Figure 5 shows the net blue-shifts after anneal at 750 – 820°C, demonstrating that the oxide capping process can easily produce net blue-shifts in excess of 100nm. Similar to the thermal-only annealed samples, a moderate increase in the PL intensity occurs until the anneal temperature exceeds 800°C, above which it drops sharply. The intensity also drops as the

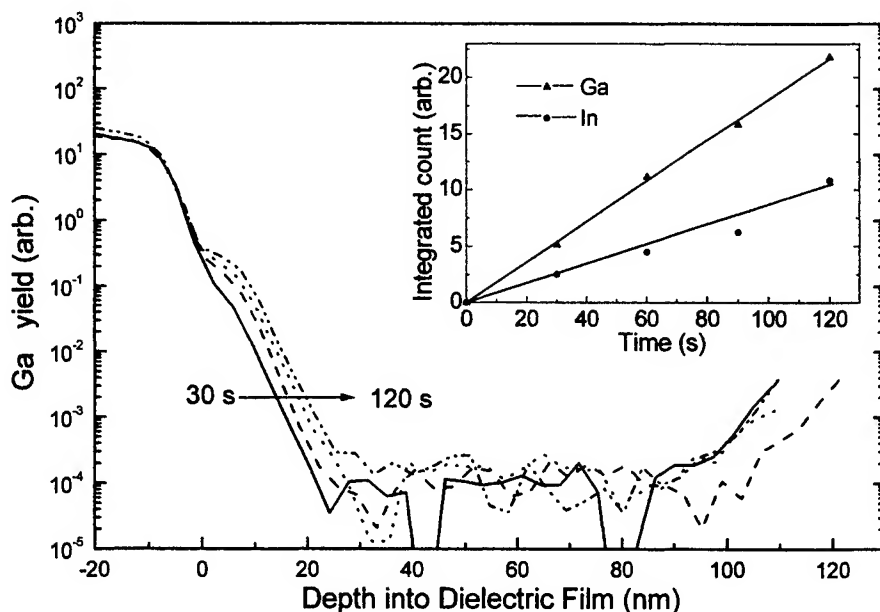


Figure 6. Secondary ion mass spectra showing the depth profiles of Ga incorporated into the dielectric film with anneal time. The inset shows the integrated amounts of Ga and In in the dielectric

anneal time increases, but not below that of the as-grown sample. The amount of net blue-shift appears to saturate in the neighborhood of 110-120nm, depending on anneal temperature. This would be expected to occur as the intermixing causes the QW and barrier layers to approach a uniform composition. It is estimated that when the QWs and barriers become fully intermixed, a saturated total blue-shift of approximately 250nm would be observed. This interpretation is consistent with the fact that the samples annealed at 750°C may ultimately exhibit a larger dielectric-enhanced shift than those annealed at 800°C; the reason being that the thermal-only component of blue-shift is less at the lower temperature, leaving the oxide enhanced process the opportunity to produce a larger shift in order to reach the saturation limit.

The PL line-width steadily increases with the amount of bandgap shift, most of this occurring on the short wavelength side of the spectra. This can be explained based on the large degree of intermixing that has occurred. As the wells become wider and shallower, additional levels are introduced that become more closely spaced and the hetero-barrier height becomes comparable to the thermal energy. This band filling contributes to the high energy tail.

Secondary ion mass spectroscopy (SIMS) measurements were carried out on dielectric-capped samples in order to better understand the mechanism of the SiO₂-cap + RTA process. The SIMS samples had an oxy-nitride cap (as opposed to the SiO₂ oxide film used in the blue-shift measurements) and were annealed at 800°C. The results show that both In and Ga migrate into the film, but As and P do not. Figure 6 presents SIMS data for various anneal times (30 – 120s) showing the progressive migration of Ga into the dielectric film. The zero depth corresponds to the dielectric/InGaAs interface. The integrated (total) amount of Ga and In incorporated into the dielectric film correlates with the anneal time and thus with the amount of bandgap shift that the sample experienced. This is shown in the inset to figure 6. A SIMS calibration sample, prepared by implanting Ga into a dielectric film, indicated that the amount of Ga out-diffused into the film during annealing was equivalent to approximately 0.4 monolayers. Another experiment (not shown here) indicated that the migration of Ga and In did not occur until temperatures where the dielectric-enhanced shift was manifest. These results demonstrate the linkage between the migration of semiconductor atoms into the dielectric film with the dielectric-enhanced process.

Because of the identical group III compositions between the QWs and adjacent barriers, it is expected that group III vacancy formation and diffusion is not the dominant process causing the intermixing and blue-shift. Thus we postulate that the out-diffusion of Ga and In into the dielectric is responsible for producing group V interstitials at the dielectric/semiconductor interface, and diffusion of these through the active region produces the observed blue-shift. We do have other evidence (not given here) that the intermixing is the result of fast diffusing defects; i.e. more consistent with interstitial diffusion.

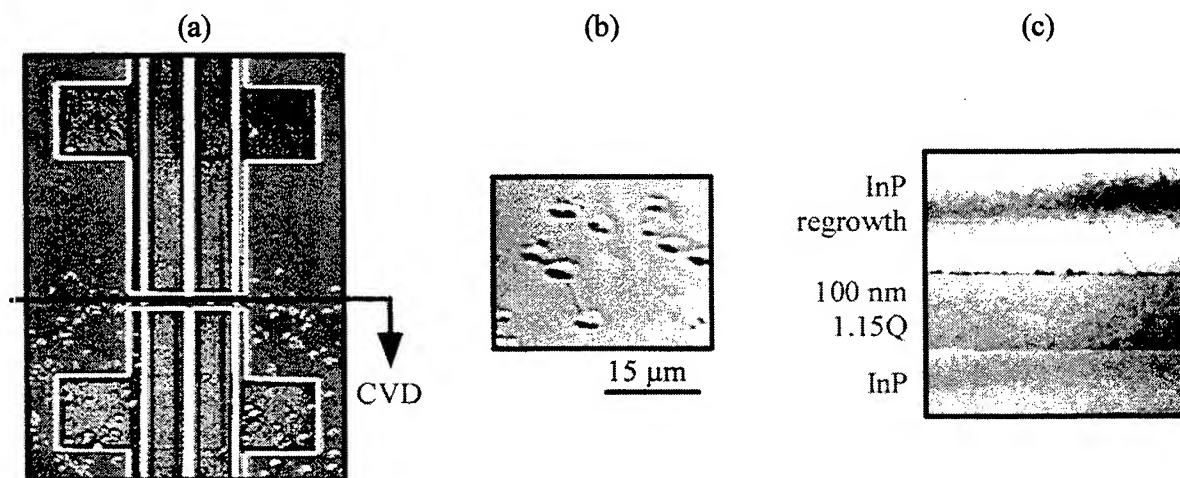


Figure 7: Re-growth of InP over samples patterned with SiO₂ and annealed. (a,b) show the resulting surface morphology as seen by Nomarski optical microscopy, (c) is a bright field TEM micrograph showing defects at re-growth interface in a SiO₂ capped and annealed sample.

The dielectric capped process appears to give good control over the spatial modification of the band-gap, however, the practical implementation has thus far proven troublesome. Difficulties have been experienced in obtaining high-quality GSMBE re-growth over areas that have been annealed with SiO₂ caps. Figure 7(a,b) shows the resulting surface morphology in plan view for a processed device.

Re-growth test structures (similar to figure 1(a) but without an active region) were prepared with a patterned SiO₂ film and annealed at 800°C for 60s. The top layers were then wet chemical etched to expose the 1.15Q top wave-guide layer. The sample was cleaned with repetitive UV ozone treatments followed by a BHF etch and DI water rinse. The re-growth consisted of ~0.75µm InP. Areas of the sample that were coated with SiO₂ during the RTA exhibited a high density of oval defects on the re-growth surface. Cross-sectional TEM samples were prepared from areas annealed both with and without the SiO₂. Figure 7(c) is a bright field image showing small high-contrast features at the InP re-growth interface. These features were absent in the sample prepared without SiO₂. High-resolution energy-dispersive X-ray measurements indicate that these features are Ga rich. A line defect is also apparent in the figure; these features may be the origin of the oval defects.

A second re-growth study consisted of a terraced sample with various thickness of semiconductor material between the SiO₂ and 1.15Q layer ranging from 0-725nm. After InP re-growth, areas where the SiO₂ was in direct contact with the subsequent re-growth surface exhibited very poor surface morphology. All other areas showed poor, but slightly improved re-growth, with no significant dependence on thickness removed. The effect causing this behavior has not yet been determined, nor have we been able to de-sensitize our re-growth procedures to this issue. Hence the motivation to find alternative processes to accomplish the QWI.

3.3. Low temperature grown InP enhanced QWI.

From earlier studies¹⁸⁻²⁰ it is known that InP grown at temperatures below ~400°C contains an increasing concentration of defects as the temperature is reduced. These defects make the material heavily doped n-type^{18,20,21}. Similar to the case of LT-GaAs²², it is possible that the defects in LT-InP could be used to produce enhanced QWI. The defects present in LT-InP have been postulated to be either P-antisite defects¹⁸ or In-vacancies²⁰. However, In-vacancies are generally considered to behave as acceptor-like defects²⁰. Thus it is likely that the defects are primarily P-antisites. Our objective was to establish whether the defects present in LT-InP could be used to enhance the QWI process since such an approach would remove some of the complexities in the SiO₂-cap + RTA approach that may be associated with film stress and interface non-reproducibilities.

The sample structure used to determine the QWI enhancement as a function of RTA temperature and time is shown in figure 1(b). Additional structures had different thickness LT-InP layers in order to determine how the QWI was influenced by the thickness.

Figures 8(a,b) show the PL spectra and peak wavelength, respectively, for samples annealed for 30s at 600 – 780°C. Similar to the thermal only and SiO₂-cap + RTA behaviour, the PL intensity initially increases, then decreases at the higher anneal temperatures; i.e. as the blue-shift increases. Also, the line-width increases, particularly on the high energy side of the peak, with increasing blue-shift.

The net blue-shift versus anneal temperature for 30s anneals is given in figure 8(b). Comparison with figure 4 indicates that the QWI process is considerably more sensitive to the LT-InP layer than the SiO₂ cap layer. As an example, for a 60s anneal at 780°C, the SiO₂-cap + RTA process yields a net blue-shift of only ~52nm, while the LT-InP sample annealed for only 30s at the same temperature produces a net blue-shift of 155nm. More important is the fact that blue-shifts necessary for making an integrated wave-guide or modulator structure sufficiently transparent can be achieved at considerably lower temperatures than required for the SiO₂-cap process. For example, using the LT-InP process it is possible to obtain a net blue-shift of 61nm following a 30s anneal at 700°C, and it is possible to produce adequate blue-shifts for anneals at temperatures below 700°C. The significance of this is that adjustments to the laser emission wavelength, produced in the non-QWI region, become small and possibly zero. Hence the laser structure can be grown for the specified emission wavelength and not red-shifted by tens of nanometers in order to compensate for the thermal shift.

In figure 9 the change in the net blue-shift with anneal time at an anneal temperature of 725°C is given. As can be seen, the net blue-shift tends towards a saturation for anneal times >150s. However, after the 150s anneal the total blue-shift is only 157nm (131nm net blue-shift plus a 26nm thermal blue-shift); this is less than the previously calculated blue-shift expected for total homogenization of the active region. This saturation may be due to a slowing down of the changes in energy of the electron and hole levels in the QWs as they approach the continuum levels or it could be related to annealing of the defects

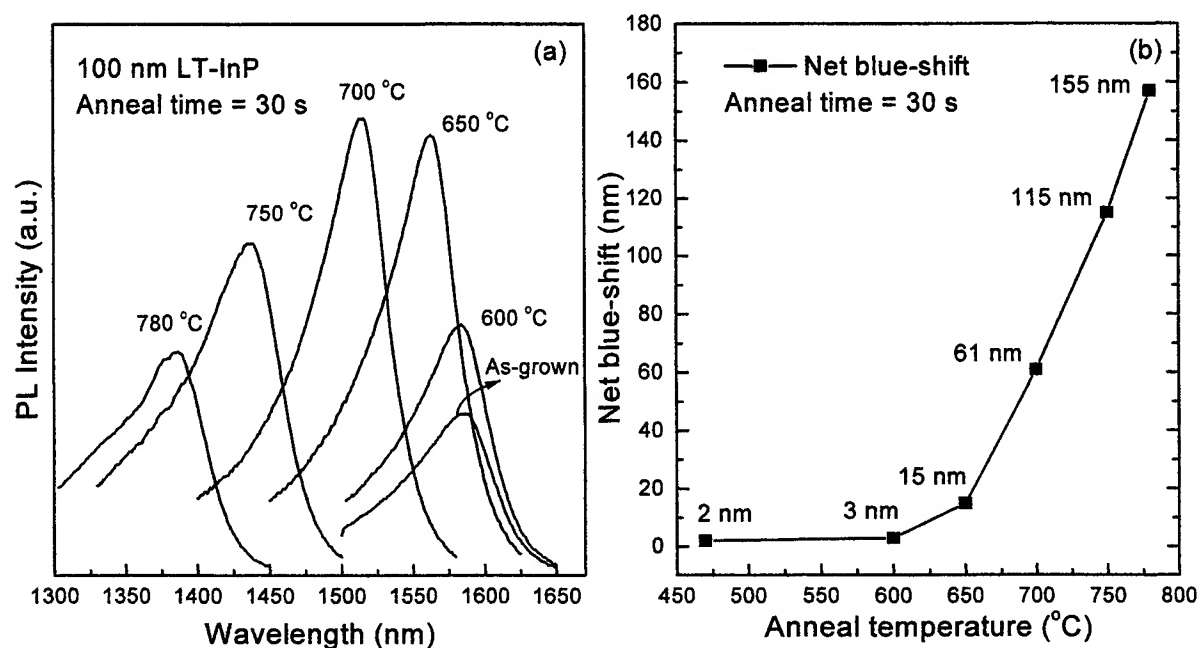


Figure 8. Photoluminescence data on samples annealed at various temperatures for 30s with a LT-InP layer (structure given in figure 1(b)); (a) PL emission intensity, (b) net blue-shift.

present in the LT-InP. It is known from earlier work²³ that InP grown at 300°C exhibits a significant reduction in the concentration of the donor-active defects upon anneal at 730°C for 10s. The carrier concentration decreases from $2 \times 10^{18} \text{ cm}^{-3}$ to $1 \times 10^{17} \text{ cm}^{-3}$ and the mobility increases from ~ 500 to $> 2000 \text{ cm}^2 \text{ V}^{-1} \text{ s}^{-1}$ during this anneal treatment. Thus, at temperatures where the LT-InP enhances the QWI, some of the defects present in the LT-grown layer are interacting in a way that improves the electrical properties. Thus the defects that enhance the QWI may be becoming exhausted leading to the saturation effect that does not correspond to active region homogenization.

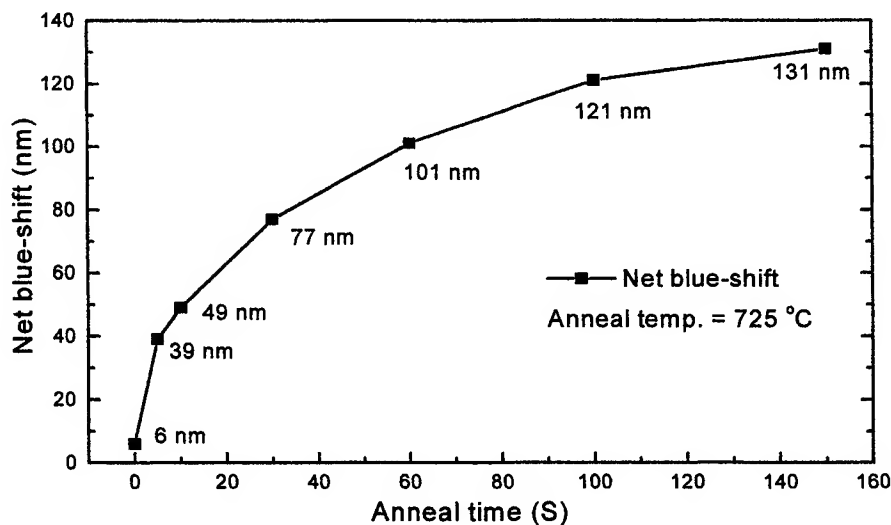


Figure 9. The amount of net blue-shift produced by anneal at 725°C for various anneal times.

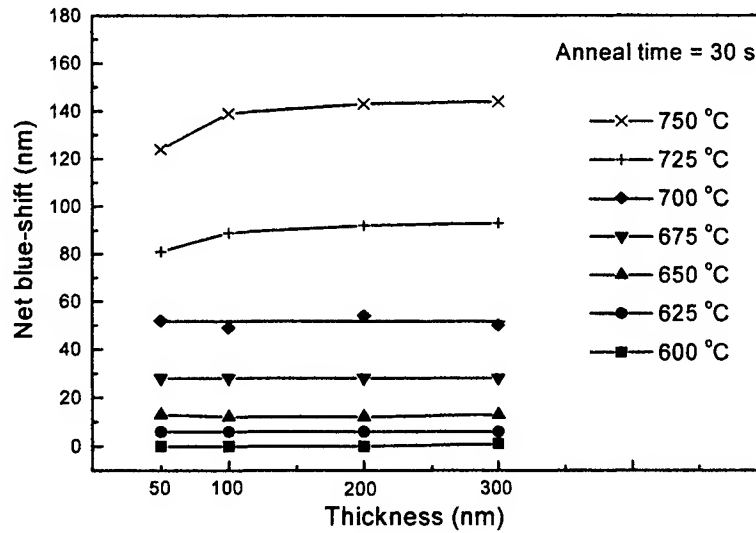


Figure 10. Blue-shift as a function of LT-grown InP layer thickness annealed for 30s at various temperatures.

The net blue-shift measured as a function of the thickness of the LT-InP layer is shown in figure 10 following anneals for 30s at temperatures of 600 – 750°C. For anneals at 700°C and below there is no dependence on the thickness of the LT-InP layer. At higher anneal temperatures (725 and 750°C) the blue-shift remains essentially unchanged for thickness greater than ~100nm but there is some reduction in blue-shift for the thinnest layer (50nm). Thus the defects that out-diffuse into the laser structure to cause the enhanced QWI originate essentially from the first 100nm of the LT-InP. This may mean that defects requiring a larger diffusion distance in order to migrate into the laser structure probably interact with other defects before reaching the LT-InP/laser structure interface and become immobile. This is consistent with the annealing behaviour leading to the blue-shift saturation.

3.4. Helium-plasma-assisted InP for QWI.

He-plasma assisted InP (He*-InP) material is grown by gas source molecular beam epitaxy (GSMBE), at 450°C, while simultaneously exposing the growth surface to a He plasma stream generated by electron cyclotron resonance (ECR)²⁴. The ECR is operated at a frequency of 2.45GHz and a power of 100-150W. From previous pump-probe measurements, it was found He*-InP and He*-InGaAsP have extremely low, even sub-picosecond, carrier lifetimes²⁵, which is very attractive for telecommunication applications. This lifetime response has been shown to result from several defect states lying in the bandgap, with one lying near mid-gap²⁶. These defect states are non-radiative and quench the PL. Thus, we argued that it may be possible to use these defects to produce enhanced QWI and that if they should produce deep states in the QWs then a fast response optical modulator could be fabricated.

From the earlier work²⁶ the predominant defects appeared to be P-vacancies. Since vacancies have a low diffusion coefficient the He*-InP layer was placed close to the 1.15Q layer. The structure is shown in figure 1(c). A similar sample was grown with a thin, 5nm, normally grown InGaAs layer separating the He*-InP layer from the laser structure. In another case the He*-InP layer was separated from the laser active and guiding regions with at least 500nm of normally grown InP. For the latter case the He*-InP had no effect on the properties of the QWs after anneal at 800°C. Since QWI effects were only observed in samples with He*-InP close to the laser active region, the above observation is evidence of slow diffusing defects.

The PL behaviour of samples annealed for 60s at 600 – 820°C, both with and without the thin InGaAs layer, are shown in figures 11(a) and 11(b), respectively. From figure 11(a) it is seen that the PL intensity and blue-shift behaviour are essentially identical to the thermal-only blue-shifts shown in figure 2. Thus the He*-InP layer has no effect when the InGaAs layer is present. However, when the thin InGaAs layer is not present, two types of changes are observed (see figure 11(b)). Firstly, the PL intensity decreases as the anneal temperature is increased, except after anneal at 820°C where the intensity starts to increase again. This is demonstrated more clearly in figure 12 using PL measurements at 15K. Secondly, a blue-shift of about 50nm can be achieved after anneal at 820°C. The intensity decrease suggests that the defects that cause the deep centres in

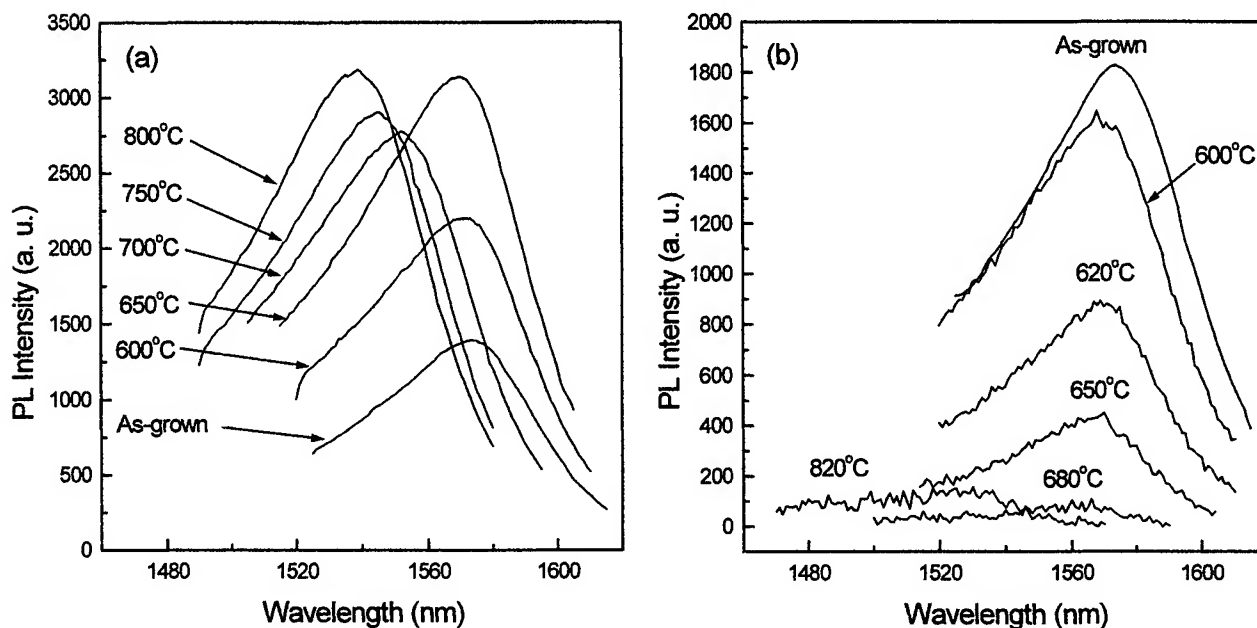


Figure 11. Photoluminescence spectra at room temperature for samples annealed at various temperatures for 60s with a He*-InP layer; (a) with a thin InGaAs layer beneath the He*-InP layer, (b) with no InGaAs layer.

in the He*-InP are diffusing into the QW causing non-radiative recombination centres and possibly the fast response seen in He-InP and He*-InGaAsP. The room temperature PL data is summarized in figures 13(a) and 13(b) which show the changes in PL intensity following anneals in the temperature range 600 – 820°C. The interesting feature is the effect of the thin (5nm) InGaAs layer separating the He*-InP from the laser structure. This layer acts as a barrier, stopping the defects from diffusing into the QW region. It appears that the InP-InGaAs heterostructure is trapping the defects from the He*-InP layer.

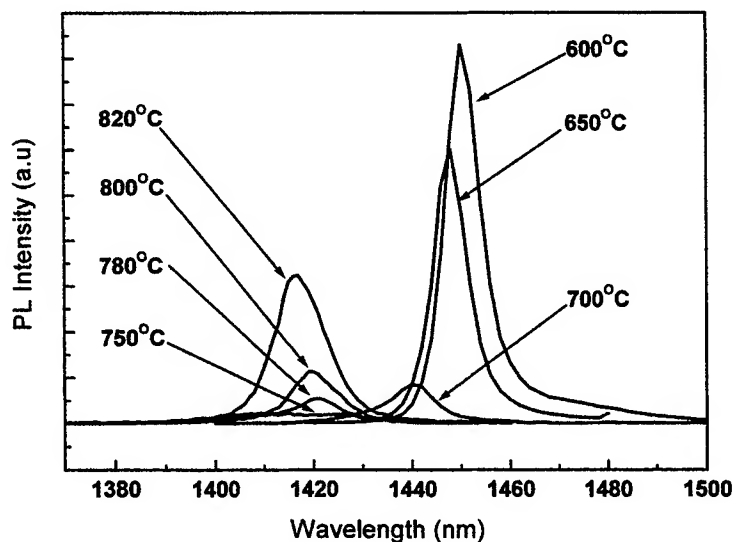


Figure 12. Low temperature photoluminescence spectra following 60s anneals at various temperatures.

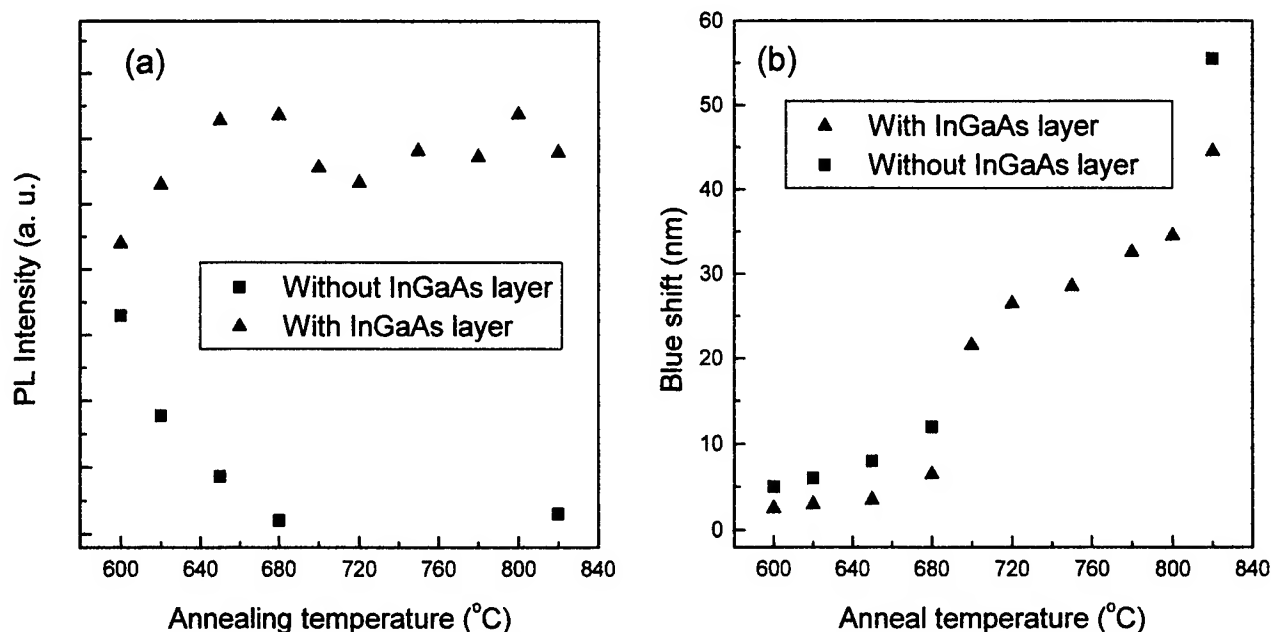


Figure 13. Photoluminescence data at room temperature for (a) intensity, and (b) blue-shift at various anneal temperatures for He*-InP layers both with and without the thin InGaAs separation layer.

Thus for employing this technique to produce a laser with a blue-shifted integrated electro-absorption modulator the laser section could either be protected by the InGaAs layer or the He*-InP should be removed above the laser section.

The main disadvantage attached to this process is the high anneal temperature (>800°C) required. However, it does have the possibility for producing a high speed modulator.

3.5. Integrated DFB laser with an electro-absorption (EA) modulator.

Integrated DFB lasers and EA modulators were fabricated using the QWI technique with a 70nm thick He*-InP layer over the modulator section. After anneal a 29nm relative blue-shift between the laser and modulator sections was obtained. The

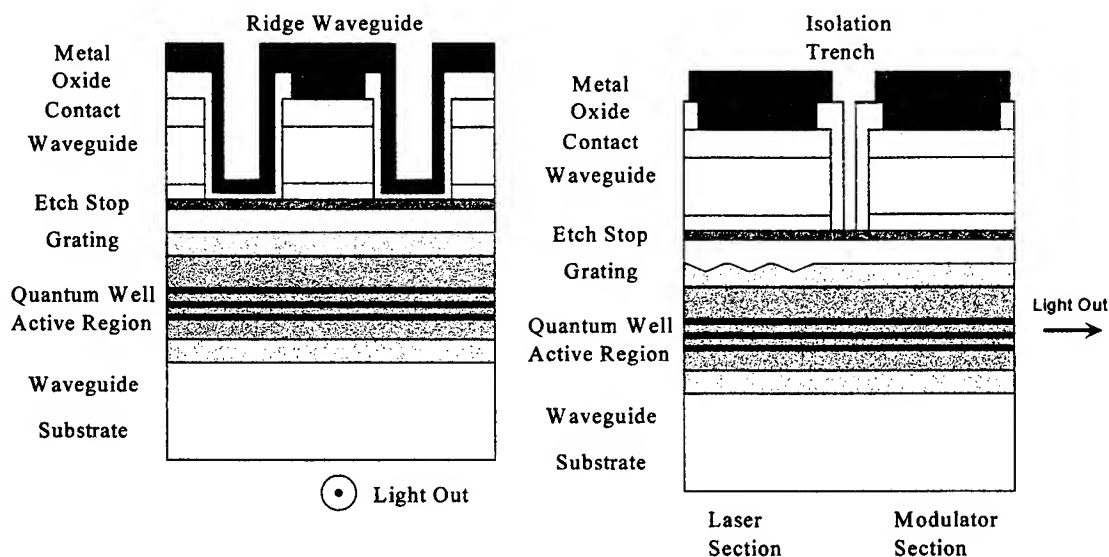


Figure 14. Schematic diagram of integrated DFB laser/EA modulator

devices were ridge wave-guide structures with 2 – 4 μ m ridges. A schematic diagram of the completed device structure is illustrated in figure 14. The isolation trench width was varied from 5 – 15 μ m resulting in a resistance between the top contacts of between 2 – 20k Ω depending on the trench width. Optical coupling is estimated at between 40 – 60% depending on the device geometry. Facet coatings were not used. The processing procedure is discussed in detail elsewhere²⁷, but a brief summary is provided here.

Device fabrication was complicated by the high anneal temperatures required to obtain a suitable blue-shift. Similar re-growth problems to those encountered with the SiO₂-cap + RTA process were initially encountered but this was overcome using 150nm of normally grown InP and InGaAs above the He*-InP layer. These sacrificial layers are used to protect the surface during anneal. The He*-InP layer was grown during growth of the laser structure then patterned to remove it over the laser section. The sacrificial layers were then grown. Thus two re-growths are required when fabricating the integrated device: one to grow the sacrificial layers used for the anneal and patterning the grating; and one to grow the top wave-guide and contact layers. Even though two re-growths were used only one additional mask step was necessary over that required for a simple DFB laser. The He*-InP layer was used for both inducing the QWI as well as an etch mask to inhibit grating formation in the modulator section.

The lasers had threshold currents of 18 – 35mA, depending on the ridge width. The L-I behaviour was linear and free of mode hopping up to a maximum input current of 100mA. The modulator showed no measurable electroluminescence up to a maximum forward bias current of 100mA confirming the presence of non-radiative recombination centres in the modulator section.

The change in absorption at the emission wavelength as a function of modulator bias (i.e. extinction coefficient) for a 400 μ m long modulator with a 2 μ m ridge wave-guide is given in figure 15. A 11.8dB reduction in intensity is measured at the modulator facet with the application of a 3V bias.

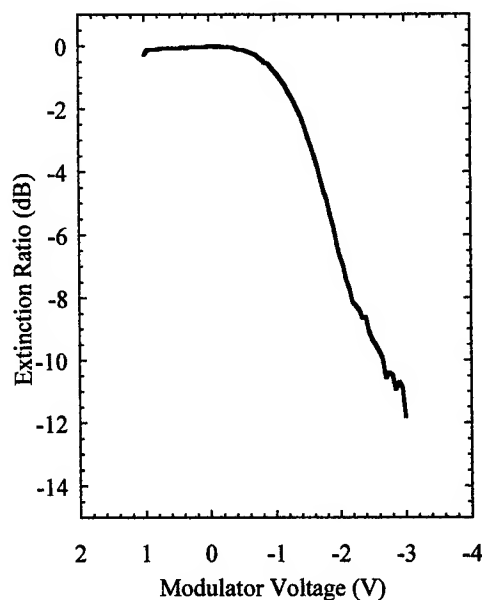


Figure 15. Modulator extinction ratio with applied bias.

4. SUMMARY

Defect-enhanced QWI methods have been discussed for application to InGaAsP quantum well laser structures designed for operation at 1.55 μ m. Two new methods using InP grown by GSMBE either at low temperature (300°C) or with a He-plasma bombardment of the growth surface have been described. These are compared to the method of SiO₂ capping plus an RTA treatment which has been widely reported in the literature. One problem associated with all the techniques discussed is that

they all involve high temperature anneals which cause the as-grown laser structures to exhibit QWI even in the absence of the QWI-enhancing layers. In other measurements, not discussed here, laser structures grown by MOCVD are less sensitive to QWI changes at all temperatures so the thermal blue-shift is reduced. However, the key to utilization of any QWI process in device manufacture is either to have the thermal response precisely calibrated and reproducible or to develop a process that can achieve enhanced QWI at a sufficiently low temperature that the thermal-only change in laser wavelength is negligible.

The thermal blue-shift has been found to be dependent upon whether the structure is terminated with an InGaAs top layer. With the InGaAs-cap the blue-shift is larger by up to 25nm than when the top layer is InP, i.e. the InGaAs is not present. For the case of no InGaAs, the blue-shift starts to increase rapidly for anneals above 700°C, so the ideal method for inducing enhanced QWI would be able to produce an adequate blue-shift below this temperature.

The presence of the SiO₂ capping layer on top of the InGaAs somehow suppresses the blue-shift due to InGaAs-only at 650 – 700°C. Blue-shift enhancement only becomes significant for anneals above ~750°C. In order to achieve a net blue-shift of ~50nm with short RTAs temperatures of ~800°C are required. Under such anneal conditions Ga-rich precipitates have been observed at the re-growth interface resulting in a poor re-growth surface morphology exhibiting a high concentration of oval defects.

For the process involving a layer of LT-InP, the change in blue-shift is much more sensitive to temperature than the SiO₂ capping method. Significant blue-shifts can be achieved for short anneals at <700°C where the thermal blue-shift is small, even for GSMBE grown structures. Also, no interface uncertainties exist since the LT-InP is grown as the last layer in the growth of the laser structure. By comparison, the SiO₂ layer is deposited in a separate vacuum system and the sample would normally be exposed to the atmospheric environment as it is transferred between deposition systems.

The most significant features in the use of the He*-InP layer for producing enhanced QWI are the elimination of interface uncertainties and the introduction of deep bandgap states into the laser active region that quench the luminescence. Although it remains to be confirmed, this may be used to increase the switching speed of the modulator consistent with the very fast carrier lifetimes seen in both InP and InGaAsP grown with the He-plasma. A disadvantage is the high temperature of the process, which affects the emission wavelength of the laser section. However, we have been able to produce good quality re-growths over the annealed surfaces and have demonstrated a DFB laser with an integrated EA modulator.

5. ACKNOWLEDGEMENTS.

Funding for this project was supplied by Materials and Manufacturing Ontario, a Government of Ontario Centre of Excellence, as well as by the Ministry of Energy, Science and Technology, Ontario. We wish to thank Irwin Sproule at the National Research Council of Canada for carrying out the SIMS and Auger Spectroscopy measurements.

6. REFERENCES.

1. K. Sato, I. Kotaka, K. Wakita, Y. Kondo and M. Yamamoto, "Strained-InGaAsP MQW Electroabsorption modulator integrated DFB Laser", *Electron. Letts.* **29**, 1087 (1993).
2. M. Aoki, H. Sano, M. Suzuki, M. Takahashi, K. Uomo and A. Takai, "Novel structure MQW Electroabsorption modulator/DFB-laser integrated device fabricated by selective area MOCVD growth", *Electron. Letts.* **27**, 2138 (1991).
3. Shu Yuan, Ying Kim, C. Jagadish, P. T. Burke, M. Gal, J. Zou, D. Q. Cai, D. J. H. Cockayne and R. M. Cohen, "Novel impurity-free inter-diffusion in GaAs/AlGaAs quantum wells by anodization and rapid thermal annealing", *Appl. Phys. Letts.* **70**, 1269 (1997).
4. B. S. Ooi, C. J. Hamilton, K. McIlvaney, A. C. Bryce, R. M. De La Rue, J. H. Marsh and J. S. Roberts, "Quantum-well intermixing in GaAs-AlGaAs structure using pulsed laser irradiation", *IEEE Photon. Technol. Letts.* **9**, 587 (1997).
5. Y. T. Oh, S. K. Kim, C. Y. Hong and T. W. Kim, "Carbon impurity effects in Al-Ga interdiffused GaAs/AlAs multiple quantum wells", *J. Appl. Phys.* **77**, 2415 (1995).
6. S. Charbonneau, P. J. Poole, P. G. Piva, G. C. Aers, E. S. Koteles, M. Fallahi, J. J. He, J. P. McCaffrey, M. Buchanan and M. Dion, "Quantum-well intermixing for optoelectronic integration using high energy ion implantation", *J. Appl. Phys.* **78**, 3697 (1995).

7. H. H. Yee, S. Ayling, R. M. De La Rue, B. Vogeles and Y. P. Song, "Fabrication of high-performance extended-cavity double-quantum-well lasers with integrated passive sections", *IEEE Proc. Optoelectron.* **143**, 94 (1996).
8. S. R. Andrew, J. H. Marsh, M. C. Holland and A. H. Kean, "Quantum-well laser with integrated passive waveguide fabricated by neutral impurity disordering", *Photon. Technol. Letts.* **4**, 426 (1992).
9. G. Lullo, A. McKee, C. J. McLean, A. C. Bryce, C. Button and J. H. Marsh, "Fabrication of electroabsorption optical modulators using laser disordered GaInAs/GaInAsP multiquantum well structures", *Electron. Letts.* **30**, 1623 (1994).
10. W. D. Laidig, N. Holonyak, M. D. Camras, K. Hess, J. J. Coleman, P. D. Dapkus and J. Bardeen, "Disorder of an AlAs-GaAs superlattice by silicon implantation", *Appl. Phys. Letts.* **38**, 776 (1981).
11. M. Razeghi, O. Archer and F. Launay, "Disorder of a $Ga_xIn_{1-x}As_yP_{1-y}$ quantum well by Zn diffusion", *Semicond. Sci. & Technol.* **2**, 793 (1987).
12. D. G. Deppe, L. J. Guido, N. Holonyak, Jr., K. C. Hsieh, R. D. Burnham, R. L. Thornton and T. L. Paoli, "Stripe-geometry quantum well heterostructure $Al_xGa_{1-x}As$ -GaAs lasers defined by defect diffusion", *Appl. Phys. Letts.* **49**, 510 (1986).
13. S. J. Lycett, A. J. Dewdney, M. Chisoni, C. E. Norman and R. Murray, "Uniform intermixing of quantum wells in p-i-n modulator structures by impurity free vacancy diffusion", *J. Electron. Mater.* **24**, 197 (1995).
14. A. C. Bryce, F. Camacho, P. Cusumano and J. H. Marsh, "CW and Mode-locked integrated extended cavity lasers fabricated using impurity from vacancy disordering", *IEEE Sel. Topics Quantum Electron.* **3**, 885 (1997).
15. J. H. Lee, S. K. Si, Y. B. Moon, E. J. Yoon and S. J. Kim, "Bandgap tuning of In_{0.53}Ga_{0.47}As/InP multiquantum well structures by impurity free vacancy diffusion using In_{0.53}Ga_{0.47}As cap layer and SiO₂ dielectric capping", *Electron. Letts.* **33**, 1179 (1997).
16. C. Francis, F. H. Julien, J.-Y. Emery, R. Simes and L. Goldstein, "Selective band-gap blueshifting of InGaAsP/InGaAs(P) quantum wells by thermal intermixing with phosphorus pressure and dielectric capping", *J. Appl. Phys.* **75**, 3607 (1994).
17. C. K. W. Wyllie and D. A. Thompson, "Compositional intermixing enhancement in InGaAs(P)/InP quantum well heterostructures related to lateral composition modulation", *Semicond. Sci. & Technol.* **13**, 750 (1998).
18. P. Dreszer, W. M. Chen, K. Seendripu, J. A. Wolk, W. Walukiewicz, B. W. Liang, C. W. Tu and E. R. Weber, "Phosphorus antisite defects in low-temperature InP", *Phys. Rev.* **B47**, 4111 (1993).
19. P. Hautajarvi, J. Makinen, S. Palko, K. Saarinen, C. Corbel and L. Liskay, "Point defects in III-V materials grown by molecular beam epitaxy at low temperature", *Matls. Sci. & Eng.* **B22**, 16 (1993).
20. B. W. Liang, Y. He and C. W. Tu, "Low-temperature growth and characterization of InP grown by gas-source molecular-beam epitaxy", *MRS Symp. Proc.* **241**, 283 (1992).
21. G. N. Maracas, K. T. Shiralagi, R. A. Puechner, F. Yu, K. T. Choi, J. S. Bow, R. Ramamurti, M. J. Kim and R. W. Carpenter, "Growth and characterization of low temperature InP by gas source MBE", *MRS Symp. Proc.* **241**, 271 (1992).
22. J. S. Tsang, C. P. Lee, S. H. Lee, K. L. Tsai and J. C. Fan, "Compositional disordering of InGaAs/GaAs heterostructures by low-temperature-grown GaAs layers", *J. Appl. Phys.* **79**, 664 (1996).
23. D. B. Mitchell, "Temperature-dependent growth of InP by plasma-enhanced GSMBE", PhD thesis, McMaster University, 1995.
24. D. B. Mitchell, B. J. Robinson, D. A. Thompson, L. Qian, S. D. Benjamin and P. W. E. Smith, "He-plasma assisted epitaxy for highly resistive, optically fast InP-based materials", *Appl. Phys. Letts.* **69**, 509 (1996).
25. L. Qian, S. D. Benjamin, P. W. E. Smith, B. J. Robinson and D. A. Thompson, "Subpicosecond carrier lifetime in beryllium-doped InGaAsP grown by He-plasma-assisted molecular beam epitaxy", *Appl. Phys. Letts.* **71**, 1513 (1997).
26. H. Pinkney, D. A. Thompson, B. J. Robinson, L. Qian, S. D. Benjamin and P. W. E. Smith, "Growth of novel InP-based materials by He-plasma-assisted epitaxy", *J. Cryst. Growth*, **209**, 237 (2000).
27. G. J. Letal, "Integrated distributed feedback lasers and electro-absorption modulators fabricated using helium-plasma-assisted InP defect induced quantum well intermixing", PhD thesis, McMaster University, 2000.

Characteristics of Oxide-Confined AlGaAs/GaAs Resonant-Cavity Light-Emitting Diodes

Hung-Pin D. Yang*, Cheng-Zu Wu, Mei-Li Wang, Wen-Chang Jiang, Sin-Jei Yu,
and Chia-Pin Sung

Division of Optoelectronic Materials and Devices
Opto-Electronics & Systems Laboratories
Industrial Technology Research Institute
Chutung 310, Hsinchu, Taiwan, R. O. C.

Abstract

Resonant-cavity light-emitting diodes (RCLEDs) are attractive light sources because of their applications in data communications, optical printing, display, and optical interconnects. Lower intensity LEDs with a modulation bandwidth of few hundred MHz are suitable for lower-speed optical fiber communications. In this work, we have made oxide-confined AlGaAs/GaAs RCLEDs for optical communication systems. The epitaxial layers of the RCLEDs were grown by a MBE system on the n^+ -GaAs substrates. The RCLED epitaxial layers mainly consisted of an n-type DBR (diffractive Bragg reflector), a p-type DBR, and an active region sandwiched between p- and n-type DBRs. The thickness of the optical cavity is 1λ . Reflectance measurement of the RCLED epitaxial wafers showed that the resonance of the RCLED cavity were about 850 nm. The wet oxidation process, which defined the current conducting aperture, was done at 425°C under nitrogen flow with steam. P-ohmic and n-ohmic contacts were then formed sequentially using electron beam evaporation and annealing. The optical power of the RCLED is measured as function of current and temperature. The beam pattern and the optical spectrum were also measured and analyzed.

KEY WORDS: resonant-cavity, light-emitting diode, distributed Bragg reflector (DBR), oxide-confined

1. INTRODUCTION

Resonant-cavity light-emitting diodes (RCLEDs) are attractive light sources because of their applications in data communications, display, optical printing, and optical interconnects. [1]-[10] For high-speed data communications, vertical-cavity surface-emitting lasers (VCSELs) are used because of their higher output optical power and high modulation bandwidth. The advantages of VCSELs include circular beam, lower threshold current, lower beam divergence, lower temperature sensitivity, one-dimensional and two-dimensional arrays, and on-wafer testability. Recently, oxide-confined VCSELs were also vastly investigated because of their very low threshold current and their capability of generating single-mode output. [11], [12] On other hand, lower intensity RCLEDs with a modulation bandwidth of a few hundred MHz are suitable for low cost, lower-speed, and eye-safe optical fiber applications. The basic structure of a RCLED includes an active region, sandwiched between

* Correspondence: e-mail : hpyang@itri.org.tw, Telephone : +886-3-5915126

top and bottom mirrors, and conducting electrodes. The bottom mirror is normally a n-type DBR (distributed Bragg reflector) grown on a semiconductor substrate. The top mirror can be a n-type DBR, a dielectric DBR, or a metal reflector. The thickness of the active region is the multiple of the emission wavelength. Spontaneous emitting light-wave resonates between top and bottom mirrors. For a top-emitting LED, the light output emit spontaneous light from the top side of the diode. The reflectance of the top mirror is higher than the reflectance of the bottom mirror. Compared to the conventional planar LEDs, RCLEDs have the advantages of higher quantum efficiency, smaller spectral widths, and smaller divergence angle. Circular beam of ring-type RCLEDs can have better coupling efficiency into the optical fiber. RCLEDs can be made by using proton implantation. [8] Here, proton implantation is used to define current conducting region of the device. Moreover, lateral oxidation process of the high Al-content $\text{Al}_x\text{Ga}_{1-x}\text{As}$ ($x \geq 0.95$) layers in the RCLED epitaxial layers has made oxide-confined VCLEDs possible. [4] The insulating oxide-layers (Al_xO_y) in the RCLED can provide confinement for current flow in the light-emitting region of the device. The optical divergence angle is smaller so that the coupling efficiency is higher. The spectral width of the light output is smaller because of the spontaneous emission resonance in the cavity. In this work, we have made ring-type oxide-confined AlGaAs/GaAs resonant-cavity light-emitting diodes in the 850-nm range. The optical power of the RCLEDs was measured as a function of injecting current. The spectral characteristics of the device were measured and analyzed.

2. DEVICE FABRICATION

The RCLED epitaxial layers were grown by a RIBER MBE system on two-inch (100) $\text{n}^+\text{-GaAs}$ substrates. The p-type distributed Bragg reflectors (DBRs) of the RCLEDs consist of 3 to 5 pairs of $\text{p}^+\text{-Al}_{0.12}\text{Ga}_{0.88}\text{As}/\text{p}^+\text{-Al}_{0.92}\text{Ga}_{0.08}\text{As}$ (Be-doped at $2 \times 10^{18} \text{ cm}^{-3}$) quarter-wave ($\lambda/4$) stacks, the n-type DBR consist 12 pairs of $\text{n}^+\text{-Al}_{0.12}\text{Ga}_{0.88}\text{As}/\text{n}^+\text{-Al}_{0.92}\text{Ga}_{0.08}\text{As}$ (Si-doped at $2 \times 10^{18} \text{ cm}^{-3}$) quarter-wave stacks. The number of pairs of $\text{p}^+\text{-Al}_{0.12}\text{Ga}_{0.88}\text{As}/\text{p}^+\text{-Al}_{0.92}\text{Ga}_{0.08}\text{As}$ is lower so that the series resistance is smaller and the optical output can transmit through p-DBR layers. Both p-type and n-type DBR layers were linearly graded at the $\text{Al}_{0.12}\text{Ga}_{0.88}\text{As}/\text{AlAs}$ interface to reduce the series resistance. The doping levels of the interface grading layers are the same as those of the $\text{Al}_{0.12}\text{Ga}_{0.88}\text{As}$ and AlAs layers. The GRINSCH (graded-index, separate-confinement heterostructure) active region of the RCLED mainly consists of three-quantum-well $\text{Al}_{0.3}\text{Ga}_{0.7}\text{As}/\text{GaAs}$ and grading layers, two $\text{Al}_{0.3}\text{Ga}_{0.7}\text{As}$ confinement layers, and $\text{Al}_x\text{Ga}_{1-x}\text{As}$ grading layers ($x = 0.3$ to 0.6 and $x = 0.6$ to 0.3). The thickness of the active region is about 1λ , where λ is the effective emission wavelength. Two undoped AlAs layers of 300 \AA are grown on top and below the active region. Reflectance measurements of grown layers (Fig. 1) showed the cavity resonance in the reflectance spectrum was near 850 nm . Other RCLED epi-wafers showed the cavity resonance in the 830 to 870 nm range.

The device fabrication is described as follows. Firstly, mesa isolation was done by a wet chemical etch of about 5400 \AA . Then, device isolation and current confinement were made by lateral wet oxidation of the AlAs layers in the p-DBR. The wet oxidation process was done in a oxidation furnace at 425°C under nitrogen flow with steam. The nitrogen gas bubble through water which was heated at 100°C . The p-type ohmic contacts, which defined the light-emitting aperture, were formed by evaporating Ti/Au and subsequent annealing. The light-emitting windows defined by p-ohmic metals have diameters of 20 to

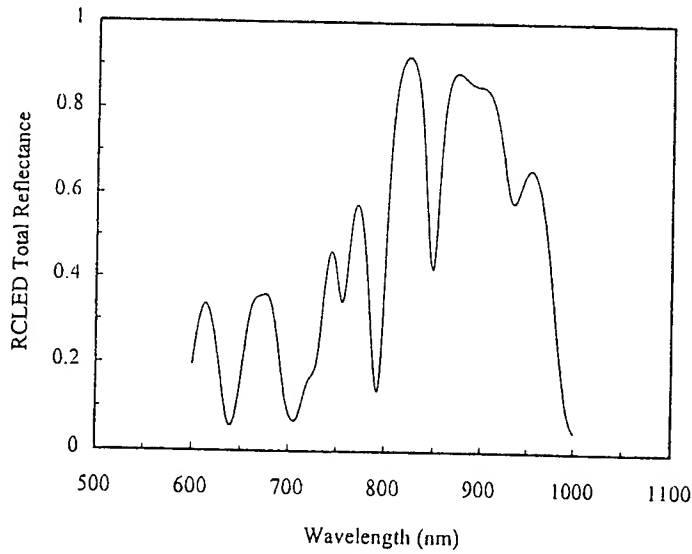


Fig. 1 Reflectance spectrum of a AlGaAs/GaAs RCLED epi-wafer.

50 μm . A SiN_x film was deposited by using PECVD for passivation and preventing current leakage. N-type ohmic contacts were formed by evaporating AuGe/Ni/Au. Pad metal was formed by using electron beam evaporation of Ti/Au and liftoff. The wafer was then diced into chips and packaged in TO-can for further tests. The oxidation processes were also made on $\text{Al}_{0.99}\text{Ga}_{0.01}\text{As}/\text{GaAs}$ layers with different oxidation time and temperatures with nitrogen flow of steam. The steam temperature was 100°C. The $\text{Al}_{0.99}\text{Ga}_{0.01}\text{As}$ thickness was 300 Å. The oxidation length versus oxidation time plot at 400, 425, and 450°C

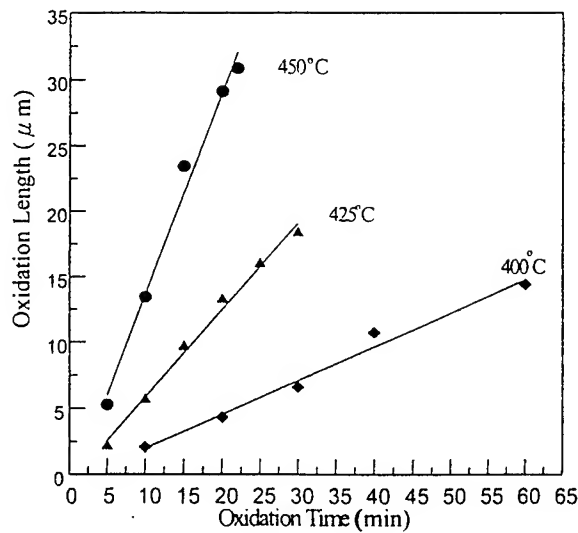


Fig. 2 Oxidation length vs. oxidation time of $\text{p-Al}_{0.99}\text{Ga}_{0.01}\text{As}$ in the $\text{p-Al}_{0.99}\text{Ga}_{0.01}\text{As}/\text{p-GaAs}$ layers.

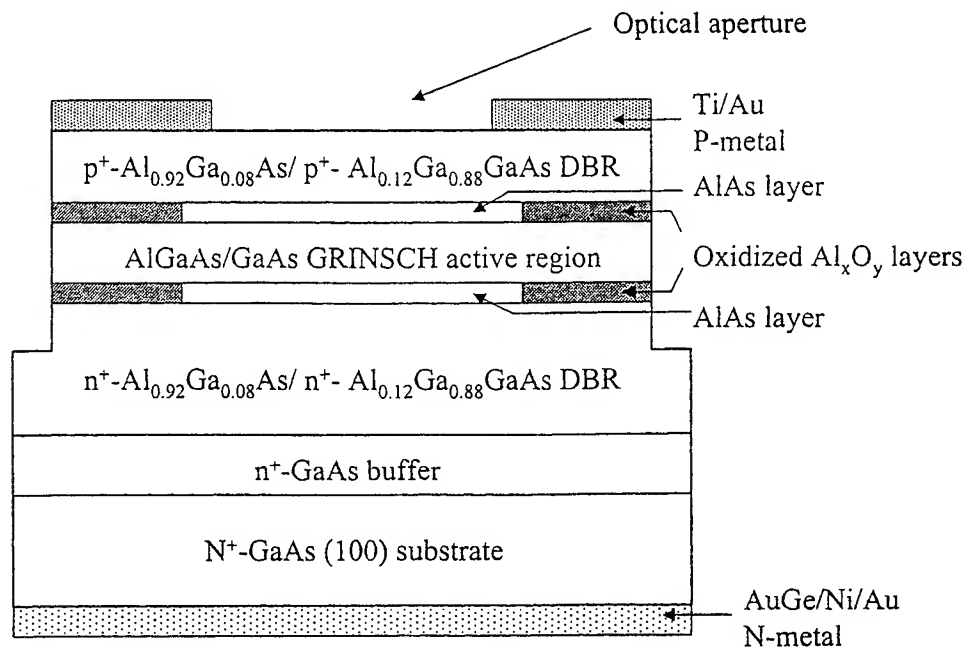


Fig. 3 Schematic device structure of an oxide-confined AlGaAs/GaAs RCLED.

is shown in Fig. 2. The oxidation rate results of our MBE-grown $\text{Al}_{0.99}\text{Ga}_{0.01}\text{As}$ layers is comparable to a previous report on the $\text{Al}_{0.98}\text{Ga}_{0.02}\text{As}$. [13] The schematic of the device structure of a RCLED is shown in Fig. 3. The optical power of the RCLED is measured as function of current and temperature. The beam pattern and the optical spectrum were also measured and analyzed.

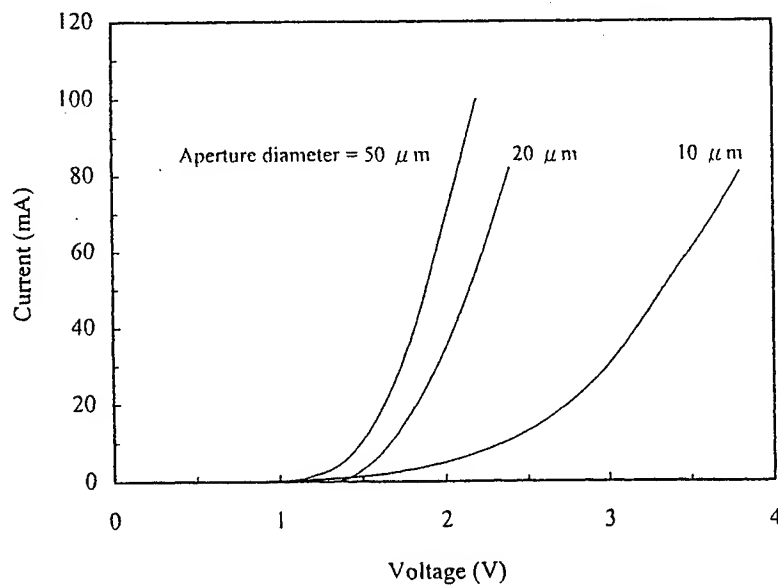


Fig. 4 I-V characteristics of oxide-confined AlGaAs/GaAs RCLED with diameters of 10, 20, and 50 μm .

3. RESULTS AND DISCUSSIONS

The current-voltage (I-V) characteristics of the oxide-confined AlGaAs/GaAs RCLEDs are shown in Fig. 4. The differential resistance are 108, 12, and 6.5Ω at 2 V for the 10, 20, and 50 μm aperture devices, respectively. The threshold voltage (V_{th}) are 2.06, 1.55, and 1.43 V for 10, 20, and 50 μm aperture devices, respectively. The differential resistance decreases with increasing device diameter. This because that the current-conducting areas are larger for the larger devices. The near-field beam patterns of the oxide-confined RCLEDs were measured using on-wafer probing and microscope. The optical output intensity of the devices increase with increasing current. The micrograph and output beam pattern of a 10- μm aperture RCLED (device A) is shown in Fig. 5. The output beam is measured at 0 and 20 mA. The beam spot is larger then than the light-emitting aperture because of the beam divergence of the RCLED output. The micrograph of another 10- μm aperture RCLED (device B) is shown in Fig. 6. The beam divergence of device B is larger so that its beam spot size is larger. This is mainly due to variations in the diameters of the current-conducting apertures of the 10- μm devices. The micrograph of a 20- μm aperture RCLED (device C) is shown in Fig. 7.

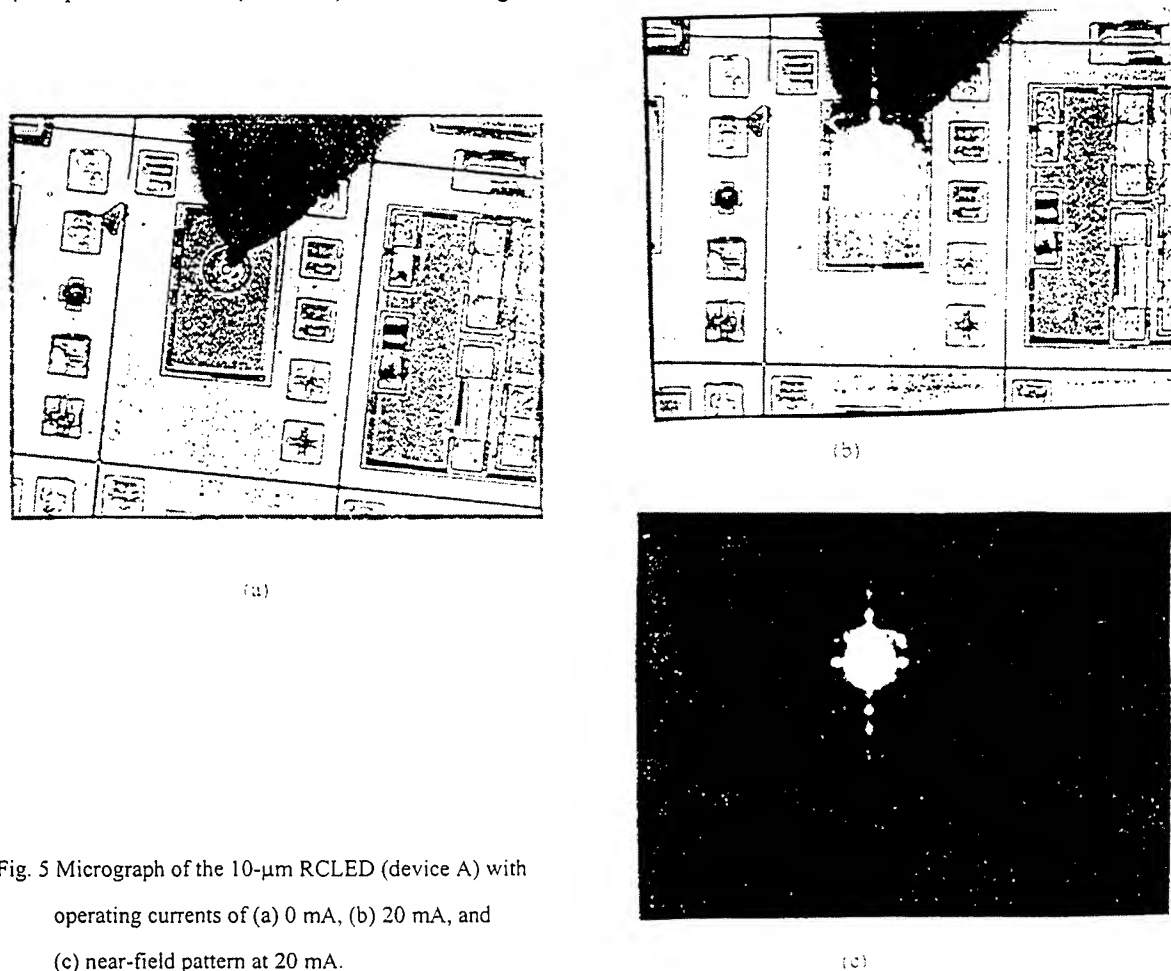
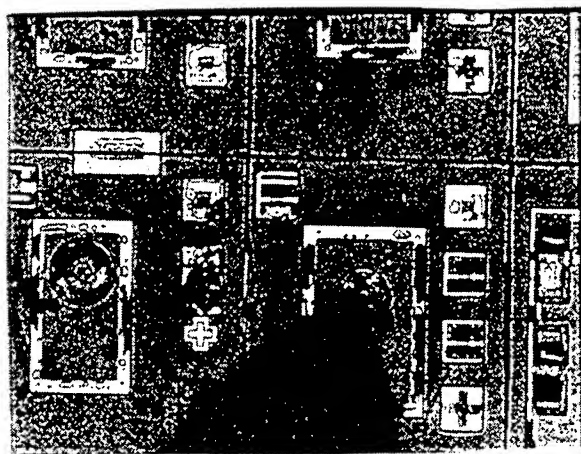
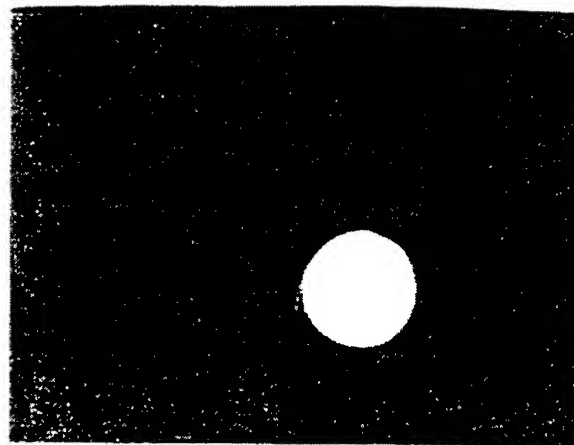


Fig. 5 Micrograph of the 10- μm RCLED (device A) with operating currents of (a) 0 mA, (b) 20 mA, and (c) near-field pattern at 20 mA.

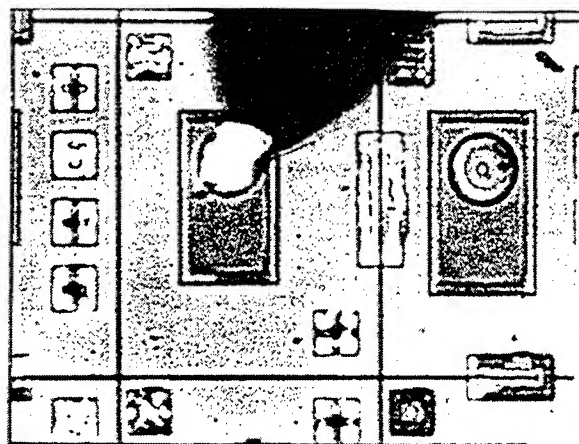


(a)

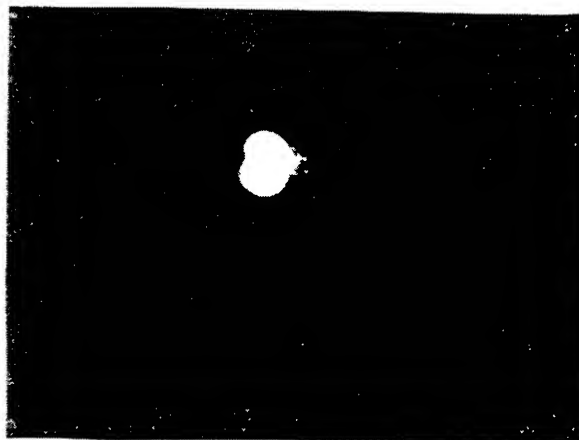


(b)

Fig. 6 Micrograph of a 10- μm aperture RCLED (device B) (a) at 0 mA and (b) near-field pattern at 20 mA.



(a)



(b)

Fig. 7 Micrograph of a 20- μm aperture RCLED (device C) (a) at 20 mA and (b) near-field pattern at 20 mA.

The photograph of the $20 \times 20 \mu\text{m}^2$ (device D) and $50 \mu\text{m}$ (device E) aperture RCLEDs are shown in Fig. 8 and 9, respectively. The optical output intensity is higher at the periphery of the light-emitting aperture for 50- μm device. This is because that the resistance is higher for current flow in the direction parallel to the epi-layer surface than the current flow in the direction perpendicular to the epi-layer surface. The current density is higher at periphery of near p-ohmic contact region. The photograph of a 8×8 ($5 \mu\text{m} \times 5 \mu\text{m}$) array (device F) is shown in Fig. 10. The width of the p-ohmic grid lines are $2 \mu\text{m}$. These

p-ohmic grid lines are used for current spreading. The current can therefore spread over the entire rectangular light-emitting aperture. The optical output of the device is rectangular in shape.

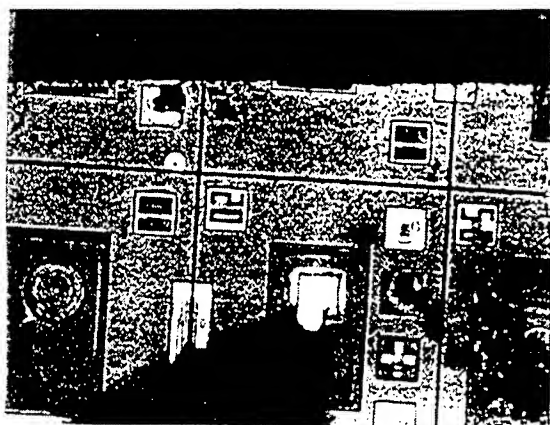


Fig. 8 Photograph of a $20\ \mu\text{m} \times 20\ \mu\text{m}$ aperture RCLED (device D) at 20 mA.

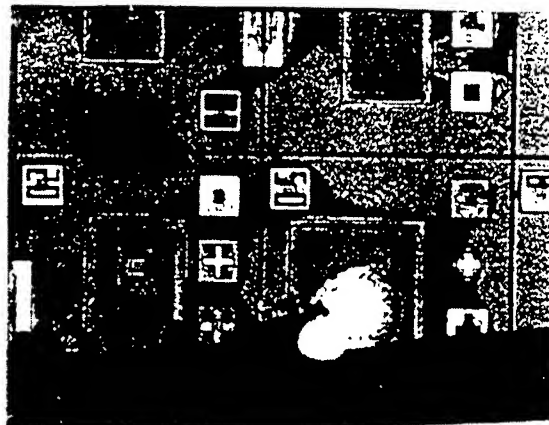
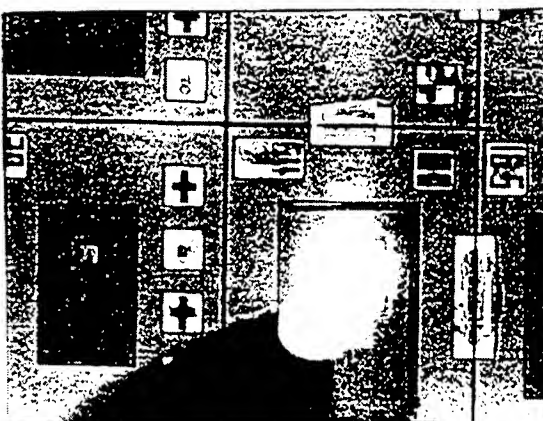


Fig. 9 Photograph of a $50\ \mu\text{m}$ aperture RCLED (device E) at 20 mA.



(a)



(b)

Fig. 10 Photograph of a 8×8 ($5\ \mu\text{m} \times 5\ \mu\text{m}$) aperture RCLED (device F) at (a) 0 and (b) 20 mA.

4. CONCLUSIONS

In conclusion, we have made oxide-confined AlGaAs/GaAs RCLEDs in the 850-nm range for optical communication applications. The devices are made with light-emitting apertures of 10 to $50\ \mu\text{m}$. Electrical and optical characteristics of the oxide-confined RCLEDs were measured. The output beam divergence is smaller for these RCLEDs, as compared to the conventional LEDs. These devices are suitable for optical communication applications.

ACKNOWLEDGEMENTS

The authors would like to thank Drs. C. A. Chang and J. Chi for useful discussions.

REFERENCES

1. R. Bockstaele, C. Sys, J. Blondelle, B. Dhoedt, I. Moerman, P. V. Daele, P. Demeester, and R. Boets, "Resonant Cavity LED's optimized for coupling to polymer optical fibers," *IEEE Photon. Technol. Lett.* vol. 11, no. 2, pp. 158-160, 1999.
2. E. F. Schubert, N. E. Hunt, R. J. Malik, M. Micovic, and D. L. Miller, "Temperature and modulation characteristics of resonant-cavity light-emitting diodes," *J. Lightwave Technol.* vol. 14, no. 7, pp. 1721-1728, 1996.
3. C. Wheeler, S. Daryanani, D. L. Mathine, G. N. Maracas, and D. R. Allee, "Monolithic integration of a GaAs MESFET with a resonant cavity LED using a buried oxide layer," *IEEE Photon. Technol. Lett.* vol. 9, no. 2, pp. 194-196, 1997.
4. D. L. Huffaker, C. C. Lin, J. Shin, and D. G. Deppe, "Resonant cavity light emitting diode with an $\text{Al}_x\text{O}_y/\text{GaAs}$ reflector," *Appl. Phys. Lett.* vol. 66, no. 23, pp. 3096-3099, 1995.
5. H. De Neve, J. Blondelle, P. Van Daele, P. Demeeter, R. Baets, and G. Borghs, "Recycling of guided mode light emission in planar microcavity light emitting diodes," *Appl. Phys. Lett.* vol. 70, no. 7, pp. 799-801, 1997.
6. H. De Neve, J. Blondelle, R. Baets, P. Demeeter, P. Van Daele, and G. Borghs, "High efficient planar microcavity LED's: comparison of design and experiment," *IEEE Photon. Technol. Lett.* vol. 7, no. 3, pp. 287-289, 1995.
7. G. Bjork, S. Machida, Y. Yamamoto, and K. Igeta, "Modulation of spontaneous emission rate in planar dielectric microcavity structures," *Phys. Rev. A*, vol. 44, no. 1, pp. 669-681, 1991.
8. J. A. Lott, R. P. Schneider, Jun., G. A. Vawter, J. C. Zolper, and K. J. Malloy, "Visible (660 nm) resonant cavity light-emitting diodes," *Electron. Lett.* vol. 29, no. 24, pp. 328-329, 1993.
9. E. F. Schubert, Y. -H. Wang, A. Y. Cho, L. -W. Tu, and G. J. Zydzik, "Resonant cavity light-emitting diodes," *Appl. Phys. Lett.* vol. 60, pp. 921-923, 1992.
10. N. E. J. Hunt, E. F. Schubert, R. A. Logan, and G. J. Zydzik, "Enhanced spectral power density and reduced linewidth at 1.3 μm in an InGaAsP quantum well resonant-cavity light-emitting diode," *Appl. Phys. Lett.* vol. 61, pp. 2287-2289, 1992.
11. K. L. Lear, K. D. Choquette, R. P. Schneider, S. P. Kilcoyne, and K. M. Geib, "Selectively oxidized vertical cavity surface emitting lasers with 50% power conversion efficiency," *Electron. Lett.* vol. 31, pp. 208-209, 1995.
12. M. Grabherr, R. Jager, R. Michalzik, B. Weigl, G. Reiner, and K. J. Reiner, "Efficient single-mode oxide-confined GaAs VCSEL's emitting in the 850-nm wavelength regime," *IEEE Photon. Technol. Lett.* vol. 9, no. 10, pp. 1304-1306, 1997.
13. K. D. Choquette, K. L. Lear, R. P. Schneider, Jr., K. M. Geib, J. J. Figiel, and R. Hull, "Fabrication and performance of selectively oxidized vertical-cavity lasers," *IEEE Photon. Technol. Lett.* vol. 7, no. 11, pp. 1237-1239, 1995.

High Efficiency Tunneling-regenerated Multi-active Region Light Emitting Diodes*

Xia Guo⁺, Guangdi Shen⁺, Guohong Wang, Jinyu Du, Weiling Guo,
Guo Gao, Wenjun Zhu, Deshu Zou

Department of Electronics Engineering, Beijing Polytechnic University
and Beijing Opto-electronic Technology Laboratory
Beijing 100022, China

ABSTRACT

A new mechanism of tunneling-regenerated multi-active region LEDs with high quantum efficiency and high brightness has been presented. The layer structure, MOCVD growth, device technology, a several of measured curves and their analysis of these new mechanism LEDs were shown in the paper. It was theoretically and experimentally resulted in that the efficiency of the electro-luminescence and the on-axis luminous intensity can linearly increase approximately with the number of the active regions.

Keywords: quantum efficiency, multi-active region, LED

1. INTRODUCTION

AlGaInP is direct band-gap light emitting quaternary material with high radiation recombination rate and wide spectrum which covers from red to greenish-blue, and the AlGaInP light emitting diodes (LEDs) now have been widely applied in the area of automotive lighting, traffic signal lighting, large-area displays, etc.¹ However, except the effect of the material quality, the brightness of traditional LED is limited by the two facts: 1. High density of light power and the over-heat induced by small light emitting region. 2. The low efficiency of light extraction. Many solutions are serves to enhance the brightness such as current spreading layer², transparent substrate³, complicated geometry figure chip⁴, etc. But they are both complicated art technology and high cost. The brightness is not obviously enhanced based on light emitting mechanism itself.

In this paper, we bring up a new mechanism of tunnel-regenerated multi-active region LEDs, with high quantum efficiency and high brightness, in which, after an electron-hole pair is recombined in the previous active region, the electrons in the

*This project is supported by National Nature science Foundation key program No. 69889601; National High Science and Technology Projects No. 863-307-15-5 and No. 863-307-22-16; Beijing High Science and technology key Project, No. 99270603.

⁺ Xia Guo, Guangdi Shen: Tel. and Fax: +86 10 6739 2390 Email: gdshen@bjpu.edu.cn

p-side valence band, under the action of high electrical field, will tunnel into n-side conduction band and can be radiantly recombined again in the next active region.⁵ In this way, the quantum efficiency and the brightness will linearly increase approximately with the number of the active regions. At the same time, highly doped GaAs tunneling junction region can effectively spreading the current, therefore the thickness of the current spreading layer can be reduced relatively.

2. THE LAYER STRUCTURE GROWTH AND THE DEVICE FABRICATION

The AlGaInP LED epitaxial layer structure was grown by low-pressure MOCVD on n-GaAs substrate. The (100) GaAs substrate was oriented at 15° off the <110> direction. The growth temperature was generally between 700°C-750°C. TMGa, TMAI, TMIIn were used as grouped V element precursors. The total hydrogen flow was 71 liter. The epitaxial layer structure is consisted of a wide band-gap n-AlGaInP confining layer doped with SiH₄, an i-type active layer 0.3-0.5 μm thick, and a p-type wide band-gap injection layer which was doped using DEZn and also serves as a window layer for the light emission. The active layer is lattice matched closely to the GaAs substrate. Between the two active regions there is the GaAs reverse-tunneling junction. Ti/Pt/Au and Au/Ge/Ni were used as p-type and n-type contact materials respectively. The wafer was cleaved into 300X300 μm² square slices bounded on the capsules for the measurements. Fig.1 shows the layer structure of the LED chip.

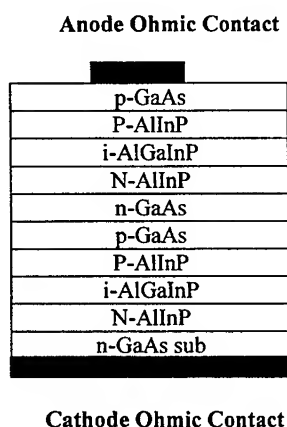


Fig.1 The layer structure of LED device epitaxial structure

3. EXPERIMENTS AND DISCUSSIONS

3.1 Four kinds of electrodes we used

In order to study mainly the physical mechanism, the current spreading layer has not been grown temporarily. Considering the high transverse resistance of p-type AlInP and the small current spreading, so we design several kinds of electrode figures to improve the light extraction efficiency, shown in Fig. 2. The measured results of the on-axis luminous intensity show that the brightness for the four-circle electrode figure with the same current ($I=20\text{mA}$) is the largest. It is almost two to three times than that of the crossed electrode figure or that of the two-circle electrode figure, and it is about 5/4 times than that of the six-circle electrode figure. Obviously, the extraction efficiency for the four-circle electrode figure is the highest.

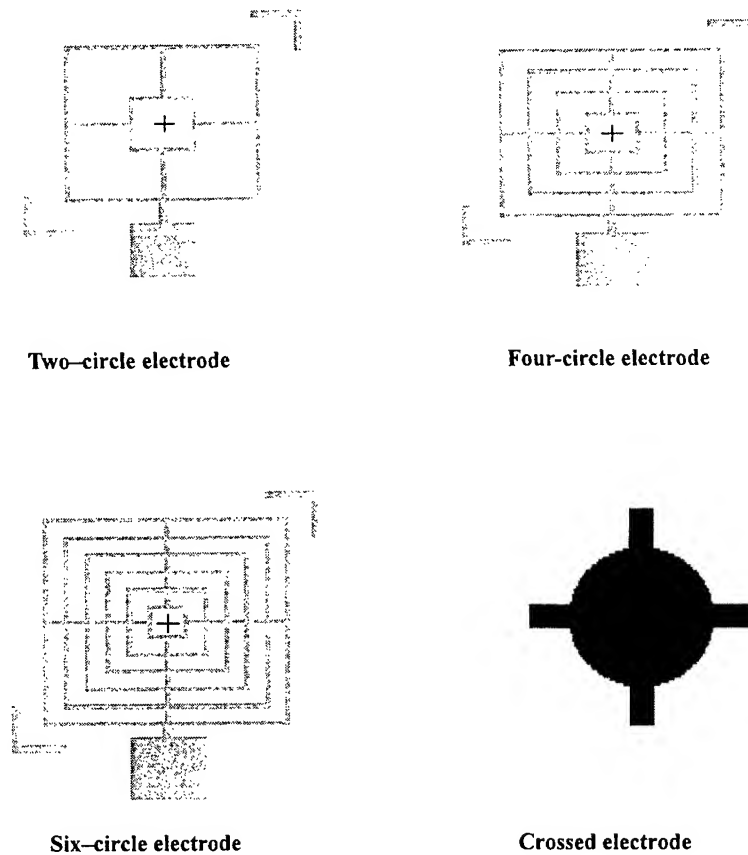


Fig.2 Four kinds of electrode figures

3.2 Absorption

In order to study the absorption of GaAs layer and its influence on the on-axis luminous intensity, we have measured the dependences of the on-axis luminous intensity with etching time of GaAs layer. The etching solution is H_3PO_4 , CH_3OH and H_2O , and the etch temperature is freezing point. It can be seen from Fig.3 that when GaAs layer is thicker, the more is GaAs layer etched, the higher is the on-axis luminous intensity, which could be dependence with the strong light (620nm) absorption of GaAs layer. However, during the process of experiment, we also find that when the GaAs layer is thinner, the on-axis luminous intensity is highest for a certain thickness GaAs layer, especially for the n-type GaAs, which may result from that the mobility of n-type GaAs is comparatively high and the transverse resistance of GaAs is relatively small, so that the current transverse spreading plays a major role and the absorption becomes a minor effect instead.

3.3 The new device structure of fabrication

In order to compare the on-axis luminous intensity of two active regions LEDs by experiments under the same preparation technology and test condition. We adopted the technological structure shown in Fig.4 using photolithography method,

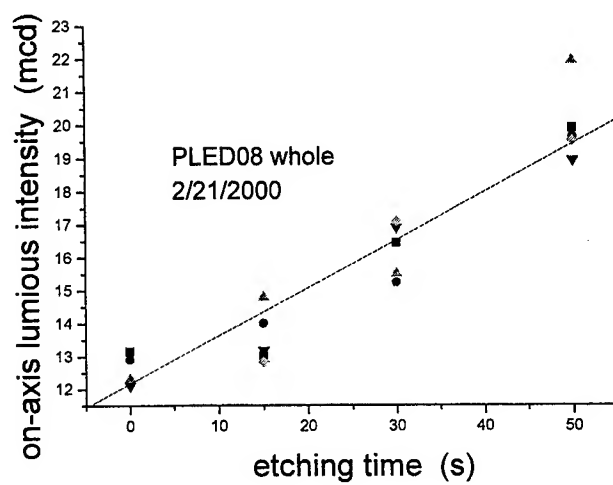


Fig.3 On-axis luminous intensity vs. etching time
The dots represent experimental results

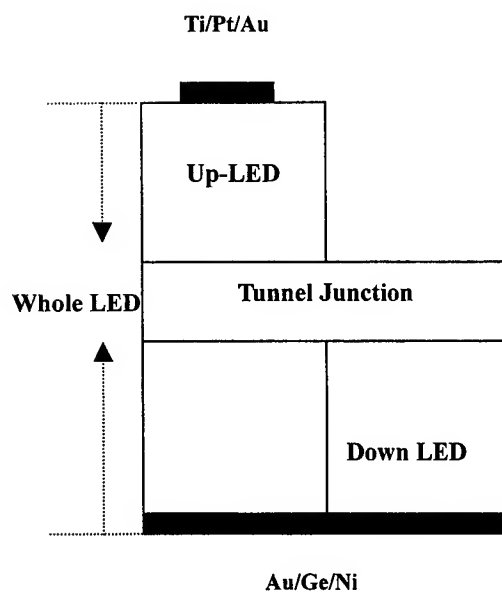
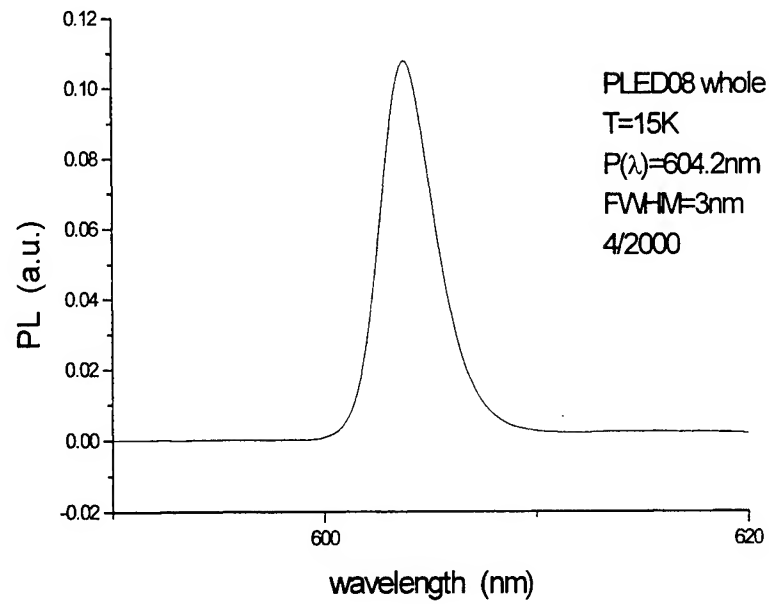
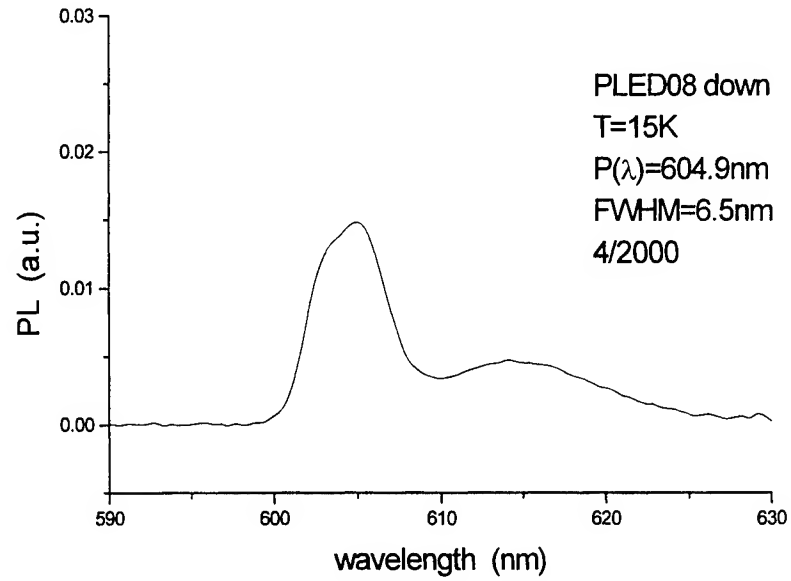


Fig.4 The schematic diagram of the device structure

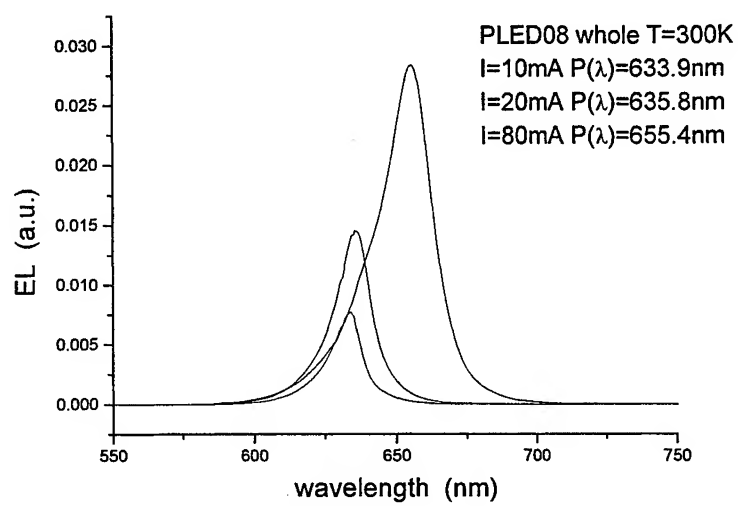


(a)

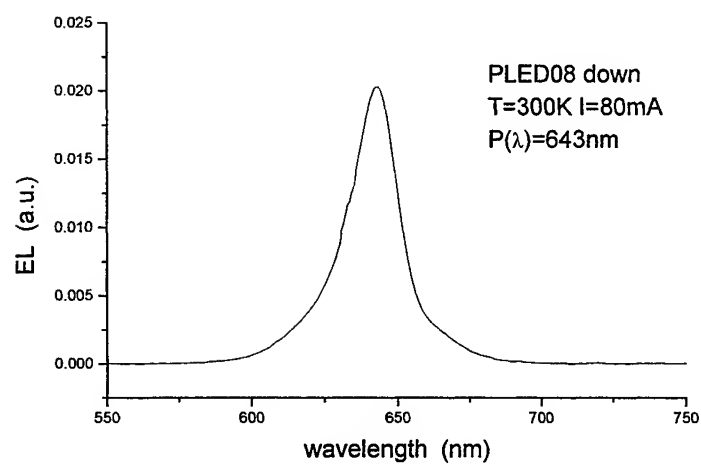


(b)

Fig.5 Low temperature (15K) PL spectrum result of i-AlGaInP active region of whole LED (a) and down LED (b)



(a)



(b)

Fig.6 Room temperature (300K) EL spectrum result of (a) the whole LED and (b) the down LED

considering that there is good selective etching between GaAs and AlInP. We made electrodes respectively on the surface of GaAs cap layer and GaAs tunnel junction layer. Now, we define Whole LED, Down LED and Up LED as show in the Fig.4.

3.4. Photo Luminescence (PL) spectrum measurement

Fig 5 is the PL spectrum measurement result of (a) the whole LED with two active regions and (b) the down LED with single active region at $T=15K$. The measurement system is IFS 120HR Fourier Transform Spectrometer of the BRUKER Corporation. The pumping light source is Ar iron laser with peak wavelength is 514.5nm. In the measurement process, we etched only GaAs cap layer to measure the Whole LEDs and etched the GaAs cap layer, Up LED and tunnel junction to measure PL spectrum of Down LEDs. The PL spectrum peak wavelength for the whole LED is 604.2nm and it is 604.9nm for the down LEDs, obviously, their difference is small, about 0.7nm. This small difference maybe results from the condition variation in the process of growth.

3.5 Electrical Luminescence (EL) spectrum measurement

Fig. 8 is the EL spectrum measurement result of (a) the whole LED and the (b) the down LED at $T=300K$. The EL spectrum peak wavelength of the whole LED is 633.9nm at $I=10mA$ and is 635.8nm with half width being 15nm at $I=20mA$, and is 655.4nm at $I=80mA$. With current increasing, the peak wavelength should move towards the blue light (short wavelength) direction due to the injection effect, but the thermal resistance of AlGaInP material is so large that the device severely heats, then the heat effect plays a major role, thus with the current increase, the wavelength moves towards the red light direction. The EL spectrum peak wavelength of the down LED is 643nm at room temperature with the half width being 20nm at $I=20mA$ and its heat effect is similar with that of the whole LED. From Fig.8, it also shows that the integrated increasing of EL spectrum is increases linearly with the current increasing approximately.

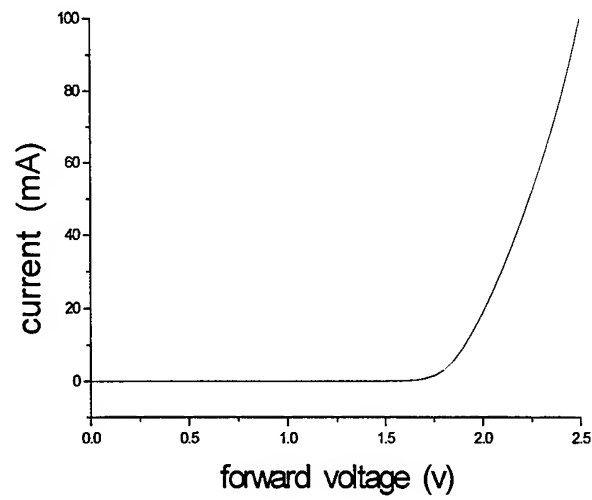
3.6 I-V characteristic

The voltage drop over the down LEDs is about 2.0v at $I=20mA$ and that over the whole LEDs is almost 4.0v. It is obviously that the electrical performance of the whole LEDs is still normal and does not become worse although a reverse tunnel junction is added. Besides, it can be seen that the voltage dropped in the reverse tunnel junction is so small to be almost negligible, thus it has almost no influence on the heating of the devices.

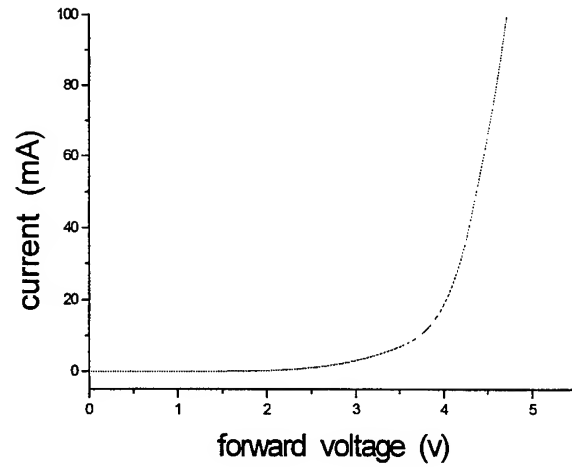
3.7 The on-axis luminous intensity

Fig.8 illuminates that the on-axis luminous intensity is about 13mcd for the down LEDs and is about 25mcd for the whole LEDs at $I=20mA$. We can see from Fig.9 that both the double DC resistance compared with traditional LEDs and the middle tunnel junction resistance do not influence the heat characteristic of the whole LEDs. With the current increase, the on-axis luminous intensity of the whole LEDs increase more quickly than that of the down LEDs. Of course, we can't rule out the influence of the high contact resistance of the down LEDs.

From these two figures, we can also get the result that the absorption of the GaAs tunnel junction is small, therefore, n-type current spreading layer can be used, which has higher mobility than that of p-type current spreading layer. For example, the mobility of n-type GaP is about $150cm^2/v*s$, while that of p-type GaP is only about $120cm^2/v*s$; the mobility of n-type GaAs is about $8000cm^2/v*s$, while that of p-type GaAs is only about $3000cm^2/v*s$, etc. Using n-type current spreading layer can dramatically reduce the transverse resistance and improve the current spreading, therefore the thickness of the total current spreading layer can be reduced relatively and the difficulty of high doped p-type material growth can be avoided.



(a)



(b)

Fig.7 The I-V characteristics of (a) the whole LED and (b) the down LED. While $I=20\text{mA}$, the voltage drop of the whole LED is 4.0V , and the voltage drop of the down LED is 2.0V

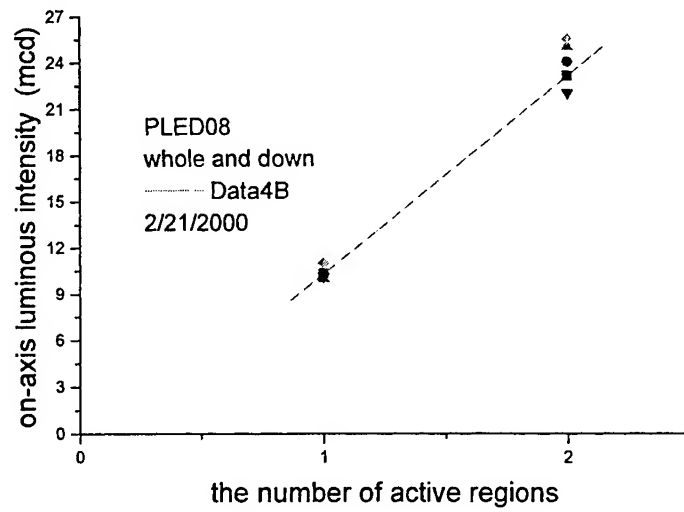


Fig.8 On-axis luminous intensity vs. the number of active region
The dots are the data of experiment, and the line is the linear fit of the data

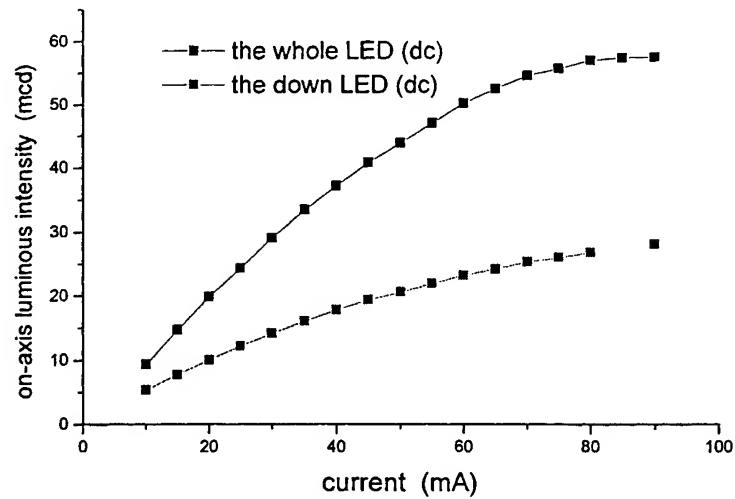


Fig.9 On-axis luminous intensity vs. forward current (dc)

4. CONCLUSION

A new mechanism of high efficiency tunnel-regenerated multi-active region LEDs has been presented theoretically and validated experimentally. The on-axis luminous intensity increases with the number of active region. The new LEDs would be easy fabrication, low cost and excellent optic-electronic performance.

5. ACKNOWLEDGMENTS

We thank Lisen Wang, Jiru Han, Ying Liu, Xin Dong and Shanna Liu for devices fabrication, Dr. Changhua Chen, Peng Lian, Jianjun Li, Bifeng Cui for helpful discussion, Xuezhong Wang, Jun Deng and Zechang Sun for technical support, Xiaoling Zhang, Lan Li, Pengcheng Lu for computation support. We also thank Professor Yonghai Chen for PL and EL measurements, and Professor Xiaoyu Ma and Professor Lianghui Chen of the Semiconductor Institute, Chinese Academy of Science for the guidance of structure growth.

6. REFERENCES

1. G.B.Stringfellow and M. George Craford, *High Brightness Light Emitting Diodes*, Academic Press, 1988.
2. G.C.Chi, Y.K.su, M.J.Jou, W.C.Hung, *Window Layer for Current Spreading in InGaAlP Light-Emitting Diode*, J.Appl.Phys. 76 (5) 1. 1994.
3. F.A.Kish, F.M.steranka, D.C.DeFever, et al, *Appl. Phys. Lett.* 64 (21) 1994.
4. M.R.Krames, M.Ochiai-Holcomb, et al, *Appl. Phys. Lett.* 75 (16) 1999
5. Guangdi Shen, et al, the Proceeding of the Fourth Two-side of Strait Chinese Photonics Symposium, Xinzhu, Taiwan, July 4-14, 1999

SESSION 7

Epitaxial Growth

Phase calculation of (100) oriented InGaAsP grown with liquid phase epitaxy

Jing-yi Zhu*, Xiang-jun Mao, Yuen-Chuen Chan and Yee-Loy Lam
Photonics Research Group, School of Electrical and Electronic Engineering
Nanyang Technological University, Block S1, Nanyang Ave., Singapore 639798

ABSTRACT

A comprehensive analysis of the phase of InGaAsP quaternary lattice-matched to the (100) oriented InP substrate was carried out. Here we used a very efficient computation method, the Levenberg-Marquardt least squares minimization method, to look into the $\text{In}_x\text{Ga}_{1-x}\text{As}_y\text{P}_{1-y}$ phase diagram in great detail. We obtained a novel result: Two solutions are available for each solid ingredient of InGaAsP. One of the solutions is new, while the other agrees well with the empirical expressions relating the solution and solid compositions in the temperature range of 570°C ~660 °C for the growth of $\text{In}_x\text{Ga}_{1-x}\text{As}_y\text{P}_{1-y}$ on (100) InP substrate.

Keywords: liquid phase epitaxy, InP, $\text{In}_x\text{Ga}_{1-x}\text{As}_y\text{P}_{1-y}$, phase diagram

1. INTRODUCTION

The GaInAsP/InP alloy systems have received considerable attention and have been studied extensively as materials for optical devices. This is because of the advantages relating to their growth and material properties, and interest in 0.9~1.6 μm wavelength emitters for optical fiber communication^[1-4]. The greatest advantage of this quaternary system is that single-phase solid solutions exist throughout the whole range of compositions and that the alloy can be epitaxially grown lattice-matched on InP substrates over a wide range of bandgaps from 0.74eV (1.68 μm)^[5, 6] to 1.34eV (0.92 μm)^[7] at room temperature. Therefore, compositional grading layers to relieve lattice-mismatch strain are unnecessary. LPE, VPE, MBE and MOCVD have been used to grow high quality quaternary materials, and the LPE technique has many advantages, such as simple apparatus and low running cost. Thus, it is extensively used in semiconductor epitaxial growth.

The thermodynamics basis of LPE growth is the phase diagram that provides information on the composition of the solution and the solid in equilibrium as a function of temperature. The existence of reasonably accurate liquid-solid phase data for the III-V alloy systems has played an important role in the development of LPE growth of III-V compounds, particularly in the ternary and quaternary systems. The basis of LPE is the control of this liquid-solid phase equilibrium. However, till now, few researchers have made a comprehensive analysis of the phase of InGaAsP quaternary lattice-matched to the (100) InP substrate in large range of temperatures. Beyond the conventional growth temperatures, there are several potential advantages. For example, the equilibrium concentrations of native defects are lower at reduced growth temperatures, while the pick up of impurities by the solution from the LPE boat should be reduced. The solubility of III-V solutes are reduced as the temperature falls, leading to lower growth rates which can be of advantage in the growth of thin layer structures such as quantum-well devices. The strain introduced during cool-down from the growth temperature to room temperature, due to differences in expansion coefficient between layer and substrate, can be reduced when epitaxy occurs nearer to room temperature. Based on these considerations, we calculated the InGaAsP on (100) InP phase diagram for a large range of temperatures, to extend our experimental limit.

* Correspondence: Email: ejyzhu@ntu.edu.sg; Telephone: 65 7905461; Fax: 65 7904161

2. PHASE DIAGRAM CALCULATION EQUATIONS AND METHODS

Jordan and Ilegems^[8, 9] have given a rigorous thermodynamic analysis of solid-liquid equilibria in quaternary systems by treating the quaternary solid as a regular mixture of binary compounds, subject to the restrictions imposed by the crystalline structure of the solid. According to this model, the solid-liquid equilibrium for the InGaAsP system is described by the following equations^[10]:

$$\begin{aligned}
 \Delta H_{\text{GaAs}}^F - T\Delta S_{\text{GaAs}}^F + RT \ln 4 X_{\text{Ga}}^I X_{\text{As}}^I \\
 = M_{\text{GaAs}}^I + RT \ln a_{\text{GaAs}} \\
 \\
 \Delta H_{\text{InAs}}^F - T\Delta S_{\text{InAs}}^F + RT \ln 4 X_{\text{In}}^I X_{\text{As}}^I \\
 = M_{\text{InAs}}^I + RT \ln a_{\text{InAs}} \\
 \\
 \Delta H_{\text{GaP}}^F - T\Delta S_{\text{GaP}}^F + RT \ln 4 X_{\text{Ga}}^I X_{\text{P}}^I \\
 = M_{\text{GaP}}^I + RT \ln a_{\text{GaP}} \\
 \\
 \Delta H_{\text{InP}}^F - T\Delta S_{\text{InP}}^F + RT \ln 4 X_{\text{In}}^I X_{\text{P}}^I \\
 = M_{\text{InP}}^I + RT \ln a_{\text{InP}}
 \end{aligned} \tag{1}$$

where

$$\begin{aligned}
 M_{ij}^I = & \alpha_{ij}^I [0.5 - X_i^I (1 - X_j^I) - X_j^I (1 - X_i^I)] \\
 & + (\alpha_{ik}^I X_k^I + \alpha_{im}^I X_m^I)(2X_i^I - 1) \\
 & + (\alpha_{jk}^I X_k^I + \alpha_{jm}^I X_m^I)(2X_j^I - 1) + 2\alpha_{km}^I X_k^I X_m^I
 \end{aligned} \tag{2}$$

and

i, j, k, m = Ga, In, As, P, respectively.

If the quaternary solid solution is treated as a regular solid solution then

$$\begin{aligned}
 RT \ln a_{\text{GaAs}} &= RT \ln x(1-y) + \alpha_{\text{Ga-In}}^s (1-x)^2 + \alpha_{\text{As-P}}^s y^2 + \alpha_c (1-x)y \\
 RT \ln a_{\text{GaP}} &= RT \ln xy + \alpha_{\text{Ga-In}}^s (1-x)^2 + \alpha_{\text{As-P}}^s (1-y)^2 - \alpha_c (1-x)(1-y) \\
 RT \ln a_{\text{InP}} &= RT \ln (1-x)y + \alpha_{\text{Ga-In}}^s x^2 + \alpha_{\text{As-P}}^s (1-y)^2 + \alpha_c (1-y)x \\
 RT \ln a_{\text{InAs}} &= RT \ln (1-x)(1-y) + \alpha_{\text{Ga-In}}^s x^2 + \alpha_{\text{As-P}}^s y^2 - \alpha_c xy
 \end{aligned} \tag{3}$$

where

$$\begin{aligned}
 \alpha_c = & \Delta H_{\text{GaAs}}^F - T\Delta S_{\text{GaAs}}^F + \Delta H_{\text{InP}}^F - T\Delta S_{\text{InP}}^F \\
 & - \Delta H_{\text{GaP}}^F + T\Delta S_{\text{GaP}}^F - \Delta H_{\text{InAs}}^F + T\Delta S_{\text{InAs}}^F \\
 & + 1/2 (\alpha_{\text{GaP}}^I + \alpha_{\text{InAs}}^I - \alpha_{\text{InP}}^I - \alpha_{\text{GaAs}}^I)
 \end{aligned} \tag{4}$$

and

$$\begin{aligned}
 \alpha_{\text{Ga-In}}^s &= 1/2 (\alpha_{\text{GaAs-InAs}}^s + \alpha_{\text{GaP-InP}}^s) \\
 \alpha_{\text{As-P}}^s &= 1/2 (\alpha_{\text{GaAs-GaP}}^s + \alpha_{\text{InAs-InP}}^s)
 \end{aligned} \tag{5}$$

To calculate the quaternary phase diagram equation group, we need the liquid and solid interaction parameters (α^I , α^s), entropies of fusion (ΔS^F), and melting temperatures. When improper data is used, the

calculated results deviate from the experimental data. One of the reasons for the disagreement is the unsuitability of the interaction parameters. To obtain reasonable agreement, with empirical results, we choose the thermodynamical parameters below ^[10, 11].

Table 1. Thermodynamical parameters

Parameter	Compound or system	Value
Melting point : T^F (K)	InAs	1215 ^[10]
	InP	1335 ^[10]
	GaAs	1511 ^[10]
	GaP	1740 ^[10]
Entropy of fusion ΔS^F (cal mol ⁻¹ K ⁻¹)	InAs	14.52 ^[10]
	InP	15.20 ^[10]
	GaAs	16.64 ^[10]
	GaP	17.30 ^[10]
Interaction parameters in solid phase: α^s (cal mol ⁻¹)	InAs-InP	400 ^[11]
	GaAs-GaP	400 ^[11]
	GaAs-InAs	2000 ^[11]
	GaP-InP	3500 ^[11]
Interaction parameters In liquid phase: α^l (cal mol ⁻¹)	In-As	3860-10.0T ^[10]
	In-P	3578-3.54T ^[10]
	Ga-As	5160-9.16T ^[10]
	Ga-P	2120-4.45T ^[10]
	Ga-In	1066 ^[11]
	As-P	1500 ^[11]

The above equation group is not easily solved by the normal method, but we can convert the equation problem to an optimization one. From the equation group, we can get an optimization function:

$$F(X_{In}^l, X_{Ga}^l, X_{As}^l) = (\Delta H_{InAs}^F - T\Delta S_{InAs}^F - RT \ln xy + RT \ln 4X_{In}^l X_{As}^l - (M_{InAs}^l + \alpha_{In-Ga}(1-x)^2 + \alpha_{As-P}(1-y)^2 - \alpha_c(1-x)(1-y)))^2 + (\Delta H_{InP}^F - T\Delta S_{InP}^F - RT \ln x(1-y) + RT \ln 4X_{In}^l X_P^l - (M_{InP}^l + \alpha_{In-Ga}(1-x)^2 + \alpha_{As-P}y^2 + \alpha_c(1-x)y))^2 + (\Delta H_{GaAs}^F - T\Delta S_{GaAs}^F - RT \ln (1-x)y + RT \ln 4X_{Ga}^l X_{As}^l - (M_{GaAs}^l + \alpha_{In-Ga}x^2 + \alpha_{As-P}(1-y)^2 + \alpha_c x(1-y)))^2$$

with $X_{In}^l + X_{Ga}^l + X_{As}^l + X_P^l = 1$ (6)

Now we focus on the solution optimizing, and the aim is how to get the smallest value of $F(X_{In}^l, X_{Ga}^l, X_{As}^l)$. Hence, this is a least squares minimization problem. There are mainly six methods to solve this problem, and they are:

- (1) Levenberg-Marquardt Method
- (2) Broyden-Fletcher-Goldfarb-Shanno Method
- (3) Davidon-Fletcher-Powell Method
- (4) Steepest Descent Method
- (5) Nelder-Mead Method
- (6) Gauss-Newton Method

Since the Levenberg-Marquardt Method is very efficient for solving the least squares minimization problem ^[12], we chose it in our paper, and we found that the Levenberg-Marquardt Method is the most efficient for the iteration in the course of calculation.

Up to now, the only problem left is to search for the initial value for the iterations. Considering the expression M_{ij}^1 in the equation group (1), it is obvious that the coefficient ΔH_{ij}^F is linear, that makes the problem simple. If we assume that X_i^1 is known and that ΔH_{ij}^F is unknown, we can work out it very easily because the new equations are linear. This merit brings forth a very good way to improve on optimization algorithms. Taking ΔH_{ij}^F and X_i^1 as unknown in turn, we can design a unique algorithm^[12, 13], and its ability of convergence is excellent. No matter what the initial values are, the optimization solution can be found easily.

3. CALCULATION RESULT AND DISCUSSIONS

Through the calculation, we obtain two solutions for the $\text{In}_x\text{Ga}_{1-x}\text{As}_y\text{P}_{1-y}$ phase diagram where the quaternary is lattice-matched to InP substrate. One is In-rich, and it agrees well with the empirical expression derived by Kuphal^[10]; and another one is P-rich. The P-rich solution is not of pragmatic significance in actual crystal growth, but it provides a more comprehensive phase diagram.

Figures 1 to 4 show the In-rich phase diagram of lattice matched $\text{In}_x\text{Ga}_{1-x}\text{As}_y\text{P}_{1-y}$ on the InP(100) substrate at 600°C. The phase diagram is similar at different temperatures. We found that InGaAsP can be grown from 385°C to 1060°C without considering P and As evaporation. Of the four elements In, Ga, As, and P, the temperature dependence of solubility is the strongest for As when growth is performed at low temperature of below 500°C, which is different from that at high temperature. This means that the As content in the solution essentially determines the liquidus temperature at low temperature growth. In addition, it was found that the solution composition of the melting ingredients In, Ga, As, P all changes monotonously with In-content in the solid phase at a fixed temperature.

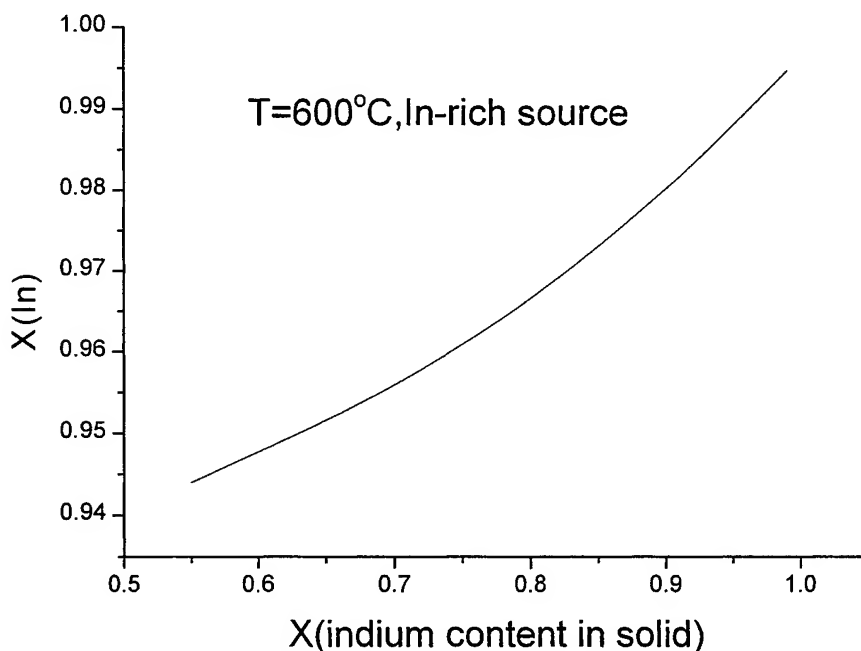


Figure 1: The atomic fraction $X(\text{In})$ in In-rich melt as a function of x (indium content in solid) for the growth of lattice matched $\text{In}_x\text{Ga}_{1-x}\text{As}_y\text{P}_{1-y}$ on the (100) InP substrate at 600°C.

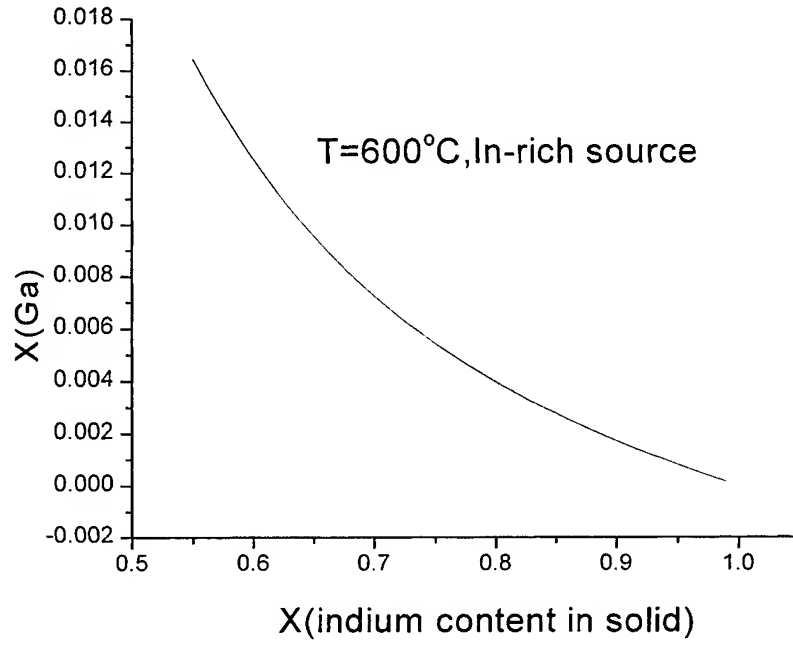


Figure 2: The atomic fraction $X(\text{Ga})$ in In-rich melt as a function of x (indium content in solid) for the growth of lattice matched $\text{In}_x\text{Ga}_{1-x}\text{As}_y\text{P}_{1-y}$ on the (100) InP substrate at 600°C .

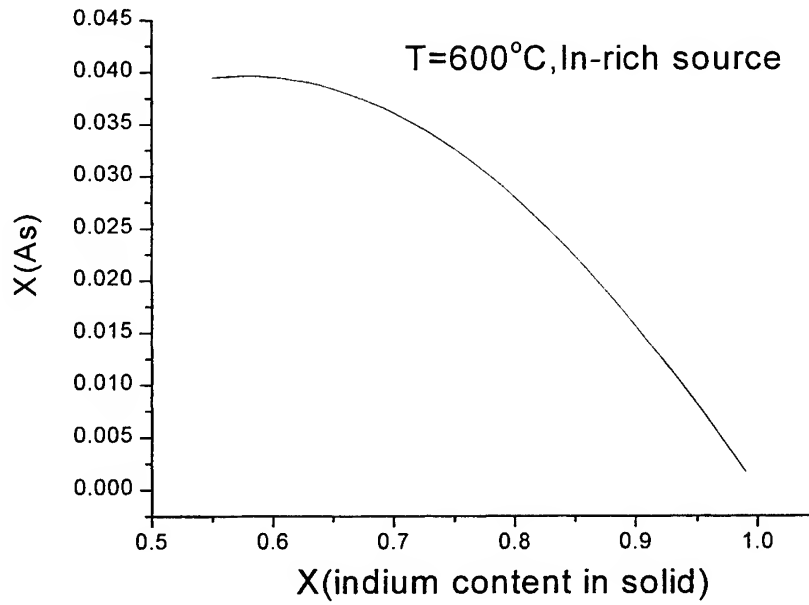


Figure 3: The atomic fraction $X(\text{As})$ in In-rich melt as a function of x (indium content in solid) for the growth of lattice matched $\text{In}_x\text{Ga}_{1-x}\text{As}_y\text{P}_{1-y}$ on the (100) InP substrate at 600°C .

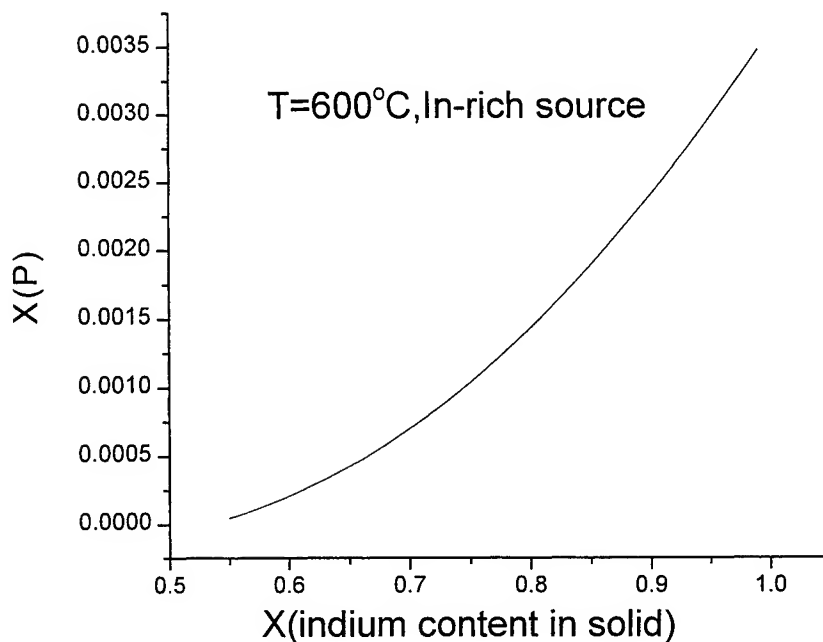


Figure 4: The atomic fraction $X(P)$ in In-rich melt as a function of x (indium content in solid) for the growth of lattice matched $\text{In}_x\text{Ga}_{1-x}\text{As}_y\text{P}_{1-y}$ on the (100) nip substrate at 600°C .

Figures 5 to 8 are the P-rich phase diagrams of lattice matched $\text{In}_x\text{Ga}_{1-x}\text{As}_y\text{P}_{1-y}$ on the (100) InP substrate in In-rich source at 600°C . In P-rich phase diagrams, P is the dominant component while In is the primary in the In-rich phase diagram. When indium content in solid increases, In and Ga fractions will decrease in the melt. On the contrary, the As and P content will increase with larger indium contents in the solid. All four curves are monotonous. Atomic fractions of In and Ga in the melt, both III group elements, take on the same performance, decreasing when the indium content increases. On the other hand, atomic fractions of group V elements As and P in the melt take on the same performance, increasing when the indium content increases. This can be explained as less III group ingredients dissolve in the V group solvent when indium content in solid increases. In growth experiments, it is not practical to use the P-rich source for $\text{In}_x\text{Ga}_{1-x}\text{As}_y\text{P}_{1-y}$ growth, but this analysis gives an important insight into the phase diagram of the quaternary.

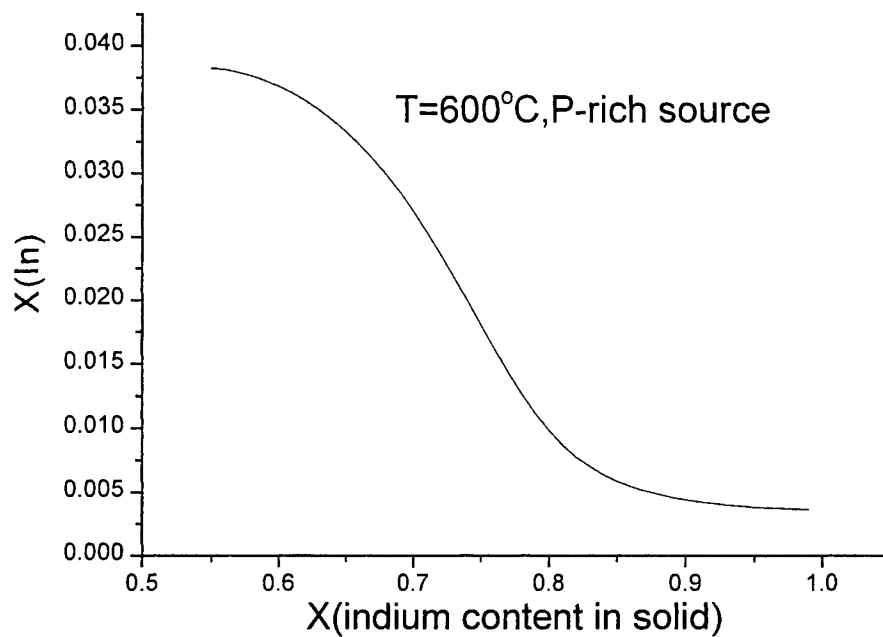


Figure 5: The atomic fraction $X(\text{In})$ in P-rich melt as a function of $x(\text{indium content in solid})$ for the growth of lattice matched $\text{In}_x\text{Ga}_{1-x}\text{As}_y\text{P}_{1-y}$ on the (100) InP substrate at 600°C.

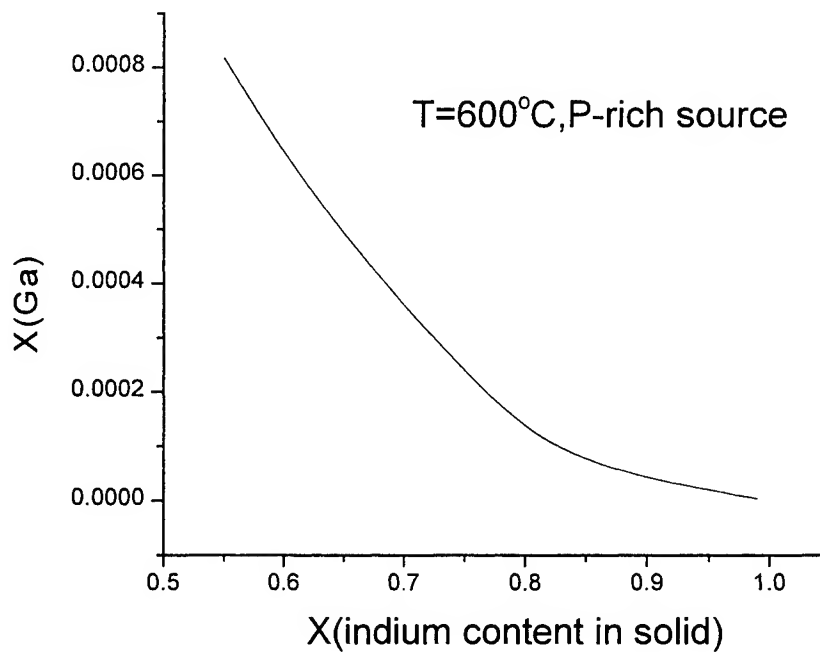


Figure 6: The atomic fraction $X(\text{Ga})$ in P-rich melt as a function of $x(\text{indium content in solid})$ for the growth of lattice matched $\text{In}_x\text{Ga}_{1-x}\text{As}_y\text{P}_{1-y}$ on the (100) InP substrate at 600°C.

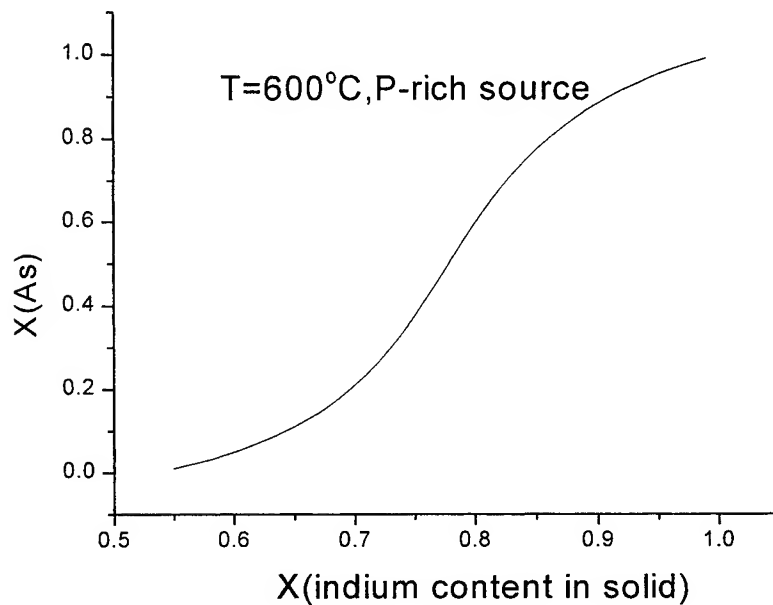


Figure 7: The atomic fraction $X(\text{As})$ in P-rich melt as a function of x (indium content in solid) for the growth of lattice matched $\text{In}_x\text{Ga}_{1-x}\text{As}_y\text{P}_{1-y}$ on the (100) InP substrate at 600°C .

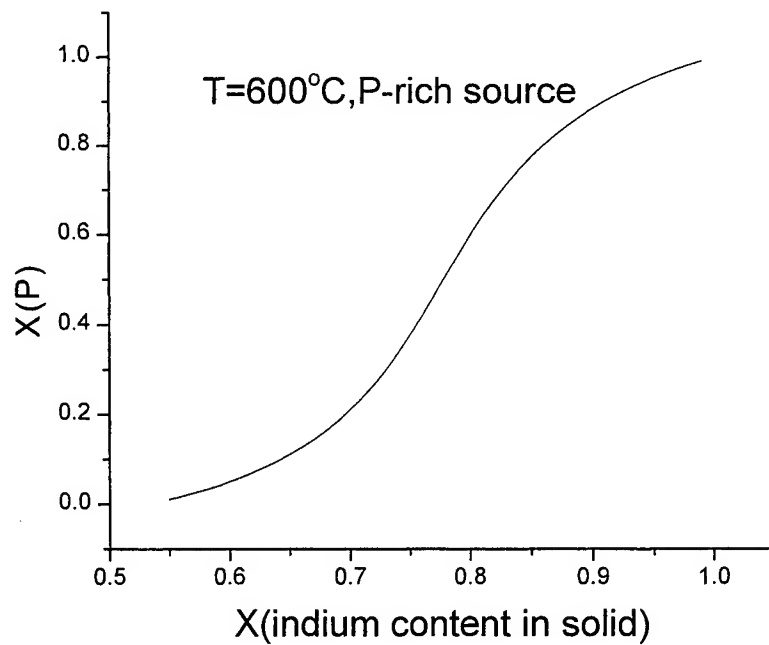


Figure 8: The atomic fraction $X(\text{P})$ in P-rich melt as a function of x (indium content in solid) for the growth of lattice matched $\text{In}_x\text{Ga}_{1-x}\text{As}_y\text{P}_{1-y}$ on the (100) InP substrate at 600°C .

4. CONCLUSION

We have calculated the $\text{In}_x\text{Ga}_{1-x}\text{As}_y\text{P}_{1-y}$ phase diagram in great detail, and made a comprehensive analysis of the phase of InGaAsP quaternary lattice-matched to the (100) oriented InP substrate. We obtained two solutions for each solid ingredient of $\text{In}_x\text{Ga}_{1-x}\text{As}_y\text{P}_{1-y}$ and found that $\text{In}_x\text{Ga}_{1-x}\text{As}_y\text{P}_{1-y}$ can be grown in a large range of temperatures. At low temperature growth, the As content in the solution essentially determines the liquidus temperature.

REFERENCES

1. J. J. Hsieh and C.C. Shen, "room-temperature CW operation of buried-stripe double heterostructure GaInAsP/InP diode lasers", *Appl. Phys. Lett.*, 30,709-710, 1979.
2. R. E. Nahory, M. A. Pollack, and J. DeWinter, "Growth and characterization of liquid-phase epitaxial $\text{In}_{1-x}\text{Ga}_x\text{As}$ ", *J. Appl. Phys.*, 46, 775-782, 1975.
3. T. Yamamoto, K. Sakai, S. Akiba, and Y. Suematsu, "500-h continuous CW operation of double-heterostructure GaInAsP/InP lasers", *Jpn. J. Appl. Phys.*, 16, 1699-1700, 1977.
4. M. A. Pollack, R. E. Nahory, J. C. Dewinter, and A. A. Ballman, "liquid phase epitaxial $\text{In}_x\text{Ga}_{1-x}\text{As}_y\text{P}_{1-y}$ lattice matched to (100) InP over the complete wavelength range $0.92 < \lambda < 1.65 \mu\text{m}$ ", *Appl. Phys. Lett.*, 33., 314-316, 1978.
5. R. Sankaran, R. L. Moon, and G. A. Antypas, "Liquid phase epitaxial growth of InGaAs on InP", *J. Cryst. Growth*, 33, 271-280, 1976.
6. K. Nakajima, T. Tanahashi, K. Akita, and T. Yamaoka, "determination of In-Ga-As phase diagram at 650°C and LPE growth of lattice-matched $\text{In}_{0.53}\text{Ga}_{0.47}$ ", *Appl. Phys.*, 4975-4981, 1979.
7. M. Cardona, K. L. Shaklee, and F. F. H. Pollack, "Electroreflectance at a semiconductor-electrolyte interface", *Phys. Rev. Rev.*, 154,696-720, 1967.
8. M.B. Panish and M. Ilegems, "Phase equilibria in ternary III-V system", *Progress in Solid State Chemistry*, Vol.7, ed. H. Reiss and J.O. McCaldin, Pergamon Press, New York, 1972, pp. 39-83.
9. A. S. Jordan and M. Ilegems, "Solid-liquid equilibria for quaternary solid solutions involving compound semiconductors in the regular solution approximation", *J. Phys. Chem. Solids* 36 (1975) 329.
10. V. Swanimathan and A. T. Macrander, 1991, "Materials Aspects of GaAs and InP Based Structures"
11. Stringfellow, G. B, "Calculation of ternary and quaternary III-V systems", *J. Cryst. Growth*, 27, p. 21 (1974).
12. X.J. Mao, Y.C.Chan, Y.L. Lam, "Phase calculation of (100) oriented InGaAsSb grown with liquid phase epitaxy", SPIE conference, 2000, Singapore.

NEW CONCEPT TECHNOLOGY — PRESSURE-VARIATION LIQUID PHASE EPITAXY

Xiang-jun Mao*, Yuen-Chuen Chan, Yee-Loy Lam, Jing-yi Zhu and Yun-xi Shi

Photonics Research Group, School of Electrical and Electronic Engineering
Nanyang Technological University, Block S1, Nanyang Ave., Singapore 639798

ABSTRACT

Liquid phase epitaxy (LPE) is an important technique to grow GaSb-based materials of good crystal quality. Normally, one has to lower the growth temperature below the liquid-phase liquidus temperature to realize supercooling of the liquid phase. Here we bring forth a new type of LPE, pressure-variation LPE (PV-LPE), where a varying pressure is used to realize supercooling of the liquid phase even though the growth temperature is kept constant. Calculations show that there exists a simple relationship between the liquid content and pressure, which theoretically illustrates that crystal growth could be easily controlled by changing the pressure.

Keywords: liquid phase epitaxy, GaSb, $\text{In}_x\text{Ga}_{1-x}\text{As}_y\text{Sb}_{1-y}$, mid-infrared, phase diagram

1. INTRODUCTION

GaSb-based material has a wide range of applications in high resolution gas spectroscopy, pollution monitor, industrial process control, space technology, medical diagnostics, free space communications, low loss fiber optic communication, and military counter measure systems¹⁻⁶.

It is well known that infrared detectors operating in the 3-5 and 8-12 μm wavelength ranges are very important for pollution monitoring. For such application, HgCdTe is the dominant material system used. However, some disadvantages, such as instability and nonuniformity, evidently exist for this material due to the high Hg vapor pressure that is noted during the growth. The toxic properties of the component materials Hg, Cd and Te, also pose problems in the production process. Therefore, it is anticipated that long wavelength materials from III-V compounds may offer an alternative to HgCdTe³. Theoretically, the cutoff wavelength for the $\text{InAs}_{0.39}\text{Sb}_{0.61}$ reaches 12 μm at room temperature.

In addition, GaSb-based materials are also important in optical fiber communication. Studies on ZrF_4 -based fluoride glass optical fibers predicted a attenuation around 0.01-0.03 dB/km at a wavelength of 2.55 μm . Such performances allow 1500km-repeater-less data links. These estimations have stimulated research in materials for 2.5 μm sources and detectors. Among the III-V materials, the InGaAsSb solid solution seems to be the most promising one.

There are several methods to grow the InGaAsSb quaternary alloy including liquid-phase epitaxy (LPE), metalorganic chemical vapor deposition (MOCVD), molecular beam epitaxy (MBE) and so on. In this paper the discussion will be focused on LPE¹⁻⁶.

The term 'liquid-phase epitaxy' is normally understood to mean the growth of epitaxial layers from solutions at elevated temperature. Here, we bring forth a new type of LPE, pressure-variation LPE (PV-LPE), with which a varying pressure is used to realize super-pressure of the liquid phase even though the growth temperature is kept constant. Super-pressure causes the deposition of solid material onto the substrate in pressure-variation LPE (PV-LPE), as super-cooling in normal LPE.

*Correspondence: Email: p145714704@ntu.edu.sg; Telephone: 65 790 5461;

2. NORMAL LPE GROWTH TECHNIQUES

The basis of normal LPE growth is the production of supersaturation in the growth solution by decreasing the growth temperature, such that the deposition of solid material occurs onto the substrate. Several LPE methods have been used to grow InGaAsSb material. They are step cooling, equilibrium cooling, supercooling, and the two-phase method. The kinetics of the LPE growth process have been studied extensively^{1,7,8}.

1. In the step-cooling technique, the substrate and the growth solution are cooled to a temperature ΔT_i below the saturation temperature of the solution. The substrate is slid under the solution and a constant temperature is maintained during the growth period. The growth rate is determined by the diffusion rate of layer constituents from the solution to the substrate surface. The thickness of the grown layer is related to ΔT_i and the growth time t by the relation

$$d = K \Delta T_i t^{1/2}$$

where K is a constant that depends on the diffusion of each solute and on the solute's mole fraction in the solution at the growth temperature.

2. In the equilibrium cooling technique, both substrate and solution are at the saturation temperature of the solution. Growth begins when the substrate is brought into contact with the solution and both are cooled at a uniform rate. The thickness of the grown layer is given by

$$D = 2/3 K R t^{3/2}$$

where t is the growth time and the cooling rate $R = dT/dt$.

3. The supercooling technique is a combination of step-cooling and equilibrium cooling. The substrate is brought into contact with the solution when both are at temperature ΔT_i below the saturation temperature of the solution. The growth solution and the substrate are further cooled during growth at a rate R . The thickness of the grown layer is given by the sum of the above two equations, i.e.,

$$D = K(\Delta T_i t^{1/2} + 2/3 R t^{3/2})$$

The value of ΔT_i used in the supercooling technique is generally smaller than that for the step-cooling technique.

4. In the two-phase technique, the cooling procedure is the same as in the equilibrium technique except that a piece of solid GaSb is added on top of the solution. The solid GaSb is in equilibrium with the solution during growth. The two-phase technique can in principle be used to grow very thin layers because the presence of the solid GaSb piece reduces the growth rate.
5. Ramp-cooled growth technique (RC) where the temperature of the solution is lowered at a rate R ($^{\circ}\text{Cmin}^{-1}$) from the liquidus temperature (T_L) to a temperature $T_L - \Delta T_R$ while in contact with the substrate.

3. PRESSURE-VARIATION LIQUID PHASE EPITAXY

According to thermodynamical model brought forth by Ilegems and M.B. Panish, thermodynamical parameters, such as melting point, entropy of fusion, interaction parameters in solid phase and interaction parameters in liquid phase, are major factors that influence the material compositions in the liquid phase. Most of these thermodynamical parameters are functions of pressure, which means that the thermodynamical parameters will vary when the growth pressure changes. Hence, parameters of the liquid ingredients for lattice-matching to some substrate will change according to pressure variation.

The principle of Pressure-Variation LPE (PV-LPE) is to realize supersaturation in the growth solution by changing the growth pressure. In all thermodynamical parameters related with phase diagram, melting points are very sensitive to pressure variation. According to Clapeyron equation,

$$\frac{dp}{dT} = \frac{\Delta H^{mol}}{T(V_{\beta}^{mol} - V_{\alpha}^{mol})},$$

when the pressure varies, the melting point will change, which consequently affects the supersturation of the liquid. PV-LPE is very suitable for the growth of GaSb and GaSb-based quaternary as the growth source does not evaporate easily. We

have carried out GaSb-based material growth with PV-LPE, and the result showed that pressure variation can realize supercooling of the liquid phase although the temperature is kept constant.

Supersturation is much easier to control with PV-LPE than normal LPE, because pressure is more easily controlled than temperature. With the temperature kept constant, the relationship between supercooling and pressure can be defined as $\Delta T = k\Delta P$, where k is a parameter. Since pressure is easy to control, the supercooling can be changed rapidly and precisely. Theoretically, devices with more complicated structures can be grown with PV-LPE.

4. PHASE DIAGRAM CALCULATION EQUATIONS AND METHODS

We use the thermodynamical model brought forth by Ilegems and M.B. Panish to calculate the phase diagram. For the solidus-liquidus phase diagram of (100) oriented $\text{In}_x\text{Ga}_{1-x}\text{As}_y\text{Sb}_{1-y}$ quaternary alloy, which is lattice-matched to GaSb substrate, the related equations are as follows^{7,8}:

$$\begin{aligned} \Delta H_F^{\text{InAs}} - T\Delta S_F^{\text{InAs}} - RT\ln xy + RT\ln 4X_L^{\text{In}}X_L^{\text{As}} \\ = M_L^{\text{InAs}} + \alpha_{\text{In-Ga}}(1-x)^2 + \alpha_{\text{As-Sb}}(1-y)^2 - \alpha_c(1-x)(1-y); \\ \Delta H_F^{\text{InSb}} - T\Delta S_F^{\text{InSb}} - RT\ln x(1-y) + RT\ln 4X_L^{\text{In}}X_L^{\text{Sb}} \\ = M_L^{\text{InSb}} + \alpha_{\text{In-Ga}}(1-x)^2 + \alpha_{\text{As-Sb}}y^2 + \alpha_c(1-x)y; \\ \Delta H_F^{\text{GaAs}} - T\Delta S_F^{\text{GaAs}} - RT\ln(1-x)y + RT\ln 4X_L^{\text{Ga}}X_L^{\text{As}} \\ = M_L^{\text{GaAs}} + \alpha_{\text{In-Ga}}x^2 + \alpha_{\text{As-Sb}}(1-y)^2 + \alpha_cx(1-y); \\ \Delta H_F^{\text{GaSb}} - T\Delta S_F^{\text{GaSb}} - RT\ln(1-x)(1-y) + RT\ln 4X_L^{\text{Ga}}X_L^{\text{Sb}} \\ = M_L^{\text{GaSb}} + \alpha_{\text{In-Ga}}x^2 + \alpha_{\text{As-Sb}}y^2 - \alpha_cxy; \end{aligned} \quad (1)$$

$$\begin{aligned} \alpha_c = \Delta H_F^{\text{InSb}} - T\Delta S_F^{\text{InSb}} + \Delta H_F^{\text{GaAs}} - T\Delta S_F^{\text{GaAs}} - \Delta H_F^{\text{InAs}} + T\Delta S_F^{\text{InAs}} - \\ \Delta H_F^{\text{GaSb}} + T\Delta S_F^{\text{GaSb}} + 0.5(\alpha_{\text{InAs}} + \alpha_{\text{GaSb}} - \alpha_{\text{GaAs}} - \alpha_{\text{InSb}}); \end{aligned} \quad (2)$$

According to the definition of the function M_L^{ij} , we can get:

$$\begin{aligned} M_L^{\text{InAs}} &= \alpha_{\text{InAs}}(1/2 - X_L^{\text{In}}(1 - X_L^{\text{As}}) - X_L^{\text{As}}(1 - X_L^{\text{In}})) + (\alpha_{\text{InGa}}X_L^{\text{Ga}} + \alpha_{\text{InSb}}X_L^{\text{Sb}})(2X_L^{\text{In}} - 1) + \\ &\quad (\alpha_{\text{GaAs}}X_L^{\text{Ga}} + \alpha_{\text{AsSb}}X_L^{\text{Sb}})(2X_L^{\text{As}} - 1) + 2\alpha_{\text{GaSb}}X_L^{\text{Ga}}X_L^{\text{Sb}}; \\ M_L^{\text{InSb}} &= \alpha_{\text{InSb}}(1/2 - X_L^{\text{In}}(1 - X_L^{\text{Sb}}) - X_L^{\text{Sb}}(1 - X_L^{\text{In}})) + (\alpha_{\text{InGa}}X_L^{\text{Ga}} + \alpha_{\text{InAs}}X_L^{\text{As}})(2X_L^{\text{In}} - 1) + \\ &\quad (\alpha_{\text{GaSb}}X_L^{\text{Ga}} + \alpha_{\text{AsSb}}X_L^{\text{As}})(2X_L^{\text{Sb}} - 1) + 2\alpha_{\text{GaAs}}X_L^{\text{Ga}}X_L^{\text{As}}; \\ M_L^{\text{GaAs}} &= \alpha_{\text{GaAs}}(1/2 - X_L^{\text{Ga}}(1 - X_L^{\text{As}}) - X_L^{\text{As}}(1 - X_L^{\text{Ga}})) + (\alpha_{\text{InGa}}X_L^{\text{In}} + \alpha_{\text{GaSb}}X_L^{\text{Sb}})(2X_L^{\text{Ga}} - 1) + \\ &\quad (\alpha_{\text{InAs}}X_L^{\text{In}} + \alpha_{\text{AsSb}}X_L^{\text{Sb}})(2X_L^{\text{As}} - 1) + 2\alpha_{\text{InSb}}X_L^{\text{In}}X_L^{\text{Sb}}; \\ M_L^{\text{GaSb}} &= \alpha_{\text{GaSb}}(1/2 - X_L^{\text{Ga}}(1 - X_L^{\text{Sb}}) - X_L^{\text{Sb}}(1 - X_L^{\text{Ga}})) + (\alpha_{\text{InGa}}X_L^{\text{In}} + \alpha_{\text{GaAs}}X_L^{\text{As}})(2X_L^{\text{Ga}} - 1) + \\ &\quad (\alpha_{\text{InSb}}X_L^{\text{In}} + \alpha_{\text{AsSb}}X_L^{\text{As}})(2X_L^{\text{Sb}} - 1) + 2\alpha_{\text{InAs}}X_L^{\text{In}}X_L^{\text{As}}; \end{aligned} \quad (3)$$

Accordingly, $\alpha_{\text{In-Ga}}$ and $\alpha_{\text{As-Sb}}$ in the quaternary solid solution are given by the linear relations⁹:

$$\begin{aligned} \alpha_{\text{In-Ga}} &= y\alpha_{\text{InAs-GaAs}} + (1-y)\alpha_{\text{InSb-GaSb}}; \\ \alpha_{\text{As-Sb}} &= x\alpha_{\text{InAs-InSb}} + (1-x)\alpha_{\text{GaAs-GaSb}}; \end{aligned} \quad (4)$$

In this work, the thermodynamical parameters of Dolginov¹⁰⁻¹² are used (Table 1). The equation group is not easily solved by the normal method. However, it is possible to convert the equation problem to an optimization problem. From the equation group, we can get an optimization function:

$$F(X_L^{\text{In}}, X_L^{\text{Ga}}, X_L^{\text{As}}) =$$

$$\begin{aligned}
& (\Delta H_F^{\text{InAs}} - T\Delta S_F^{\text{InAs}} - RT \ln x y + RT \ln 4 X_L^{\text{In}} X_L^{\text{As}} - (M_L^{\text{InAs}} + \alpha_{\text{In-Ga}}(1-x)^2 + \alpha_{\text{As-Sb}}(1-y)^2 - \alpha_c(1-x)(1-y)))^2 + \\
& (\Delta H_F^{\text{InSb}} - T\Delta S_F^{\text{InSb}} - RT \ln x(1-y) + RT \ln 4 X_L^{\text{In}} X_L^{\text{Sb}} - (M_L^{\text{InSb}} + \alpha_{\text{In-Ga}}(1-x)^2 + \alpha_{\text{As-Sb}}y^2 + \alpha_c(1-x)y))^2 + \\
& (\Delta H_F^{\text{GaAs}} - T\Delta S_F^{\text{GaAs}} - RT \ln(1-x)y + RT \ln 4 X_L^{\text{Ga}} X_L^{\text{As}} - (M_L^{\text{GaAs}} + \alpha_{\text{In-Ga}}x^2 + \alpha_{\text{As-Sb}}(1-y)^2 + \alpha_c x(1-y)))^2 \\
& \text{with } X_L^{\text{In}} + X_L^{\text{Ga}} + X_L^{\text{As}} + X_L^{\text{Sb}} = 1
\end{aligned} \tag{5}$$

The problem is to search for an optimization solution where the value of $F(X_L^{\text{In}}, X_L^{\text{Ga}}, X_L^{\text{As}})$ is smallest, which is a least squares minimization problem. There are mainly six methods to solve this problem, and they are:

- (1) Levenberg-Marquardt Method
- (2) Broyden-Fletcher-Goldfarb-Shanno Method
- (3) Davidon-Fletcher-Powell Method
- (4) Steepest Descent Method
- (5) Nelder-Mead Method
- (6) Gauss-Newton Method

In the course of our calculation, we find that the Levenberg-Marquardt Method is most efficient for the iteration. The reason is that the Levenberg-Marquardt Method is very efficient for solving the least squares minimization problem. Hence this method was chosen¹⁵.

Table 1. Thermodynamical parameters of Dolginov used in this work.

Parameter	Compound or system	Value
Melting point : T^F (K)	InAs	1215
	InSb	798
	GaAs	1511
	GaSb	983
Entropy of fusion ΔS^F (cal mol ⁻¹ K ⁻¹)	InAs	14.52
	InSb	14.32
	GaAs	16.64
	GaSb	15.80
Interaction parameters in solid phase: (cal mol ⁻¹)	InAs-InSb	1600
	GaAs-GaSb	4000
	GaAs-InAs	2000
	GaSb-InSb	1450
Interaction parameters in liquid phase: (cal mol ⁻¹)	In-As	1645-7.49T
	In-Sb	-4111+0.82T
	Ga-As	-2793-0.46T
	Ga-Sb	3154-4.02T
	Ga-In	1066
	As-Sb	750

So far, the remaining problem is how to search for the initial value for the iterations. Substituting the expression M_L^{ij} to the equation group(1), it is obvious that the coefficient ΔH_F^{ij} is linear, which means that if we assume that X_L^I is known and that ΔH_F^{ij} is unknown, we can work out it very easily because the new equations are linear. This merit brings forth a very good way to improve on optimization algorithms. Taking ΔH_F^{ij} and X_L^{In} as unknown in turn, we can design a unique algorithm, and its ability of convergence is excellent. No matter what the initial values are, the optimization solution can be found easily.

5. CALCULATION RESULT AND DISCUSSIONS

We obtained a series of phase diagrams of GaSb-based material lattice-matched to the GaSb substrate, from GaSb, ternary to quaternary. The phase plots of the melt content in the source as a function of pressure display one kind of monotone variation.

5.1 GaSb Growth Calculation

In order to calculate the phase diagram of GaSb as a function of pressure, we need to know the related parameters of following equation:

$$\frac{dp}{dT} = \frac{\Delta^{mol}}{T(V_{\beta}^{mol} - V_{\alpha}^{mol})}$$

To simplify the calculation, we assume that the relation between GaSb melting point and the pressure is

$$T(p) = T_0 - 30 \times p \quad (0 \text{ atm} \leq p \leq 1 \text{ atm})$$

where T_0 denotes the melting point at standard atmosphere pressure, $T(p)$ denotes the melting point at pressure of p (atm), parameter 30 is valued according growth experiments. Through this simplification, we get some phase diagrams for the Ga-rich source.

In Figure1 and Figure2, it is obvious that Sb content in the melt decreases when the pressure increases. The curve is flat at low temperature while it is steep at high temperature. Hence liquid supersturation can be easily realized by increasing the pressure at high temperature. It is difficult to form a GaSb film below 500°C with pressure-variation LPE (PV-LPE).

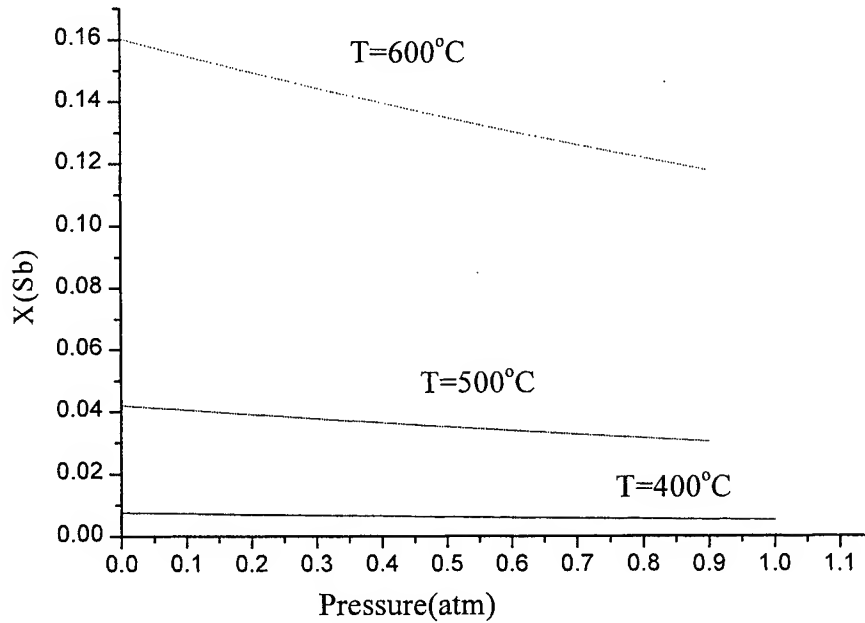


Figure 1. The atomic fraction $X(\text{Sb})$ in the melt for GaSb growth on the GaSb(100) substrate as a function of pressure.

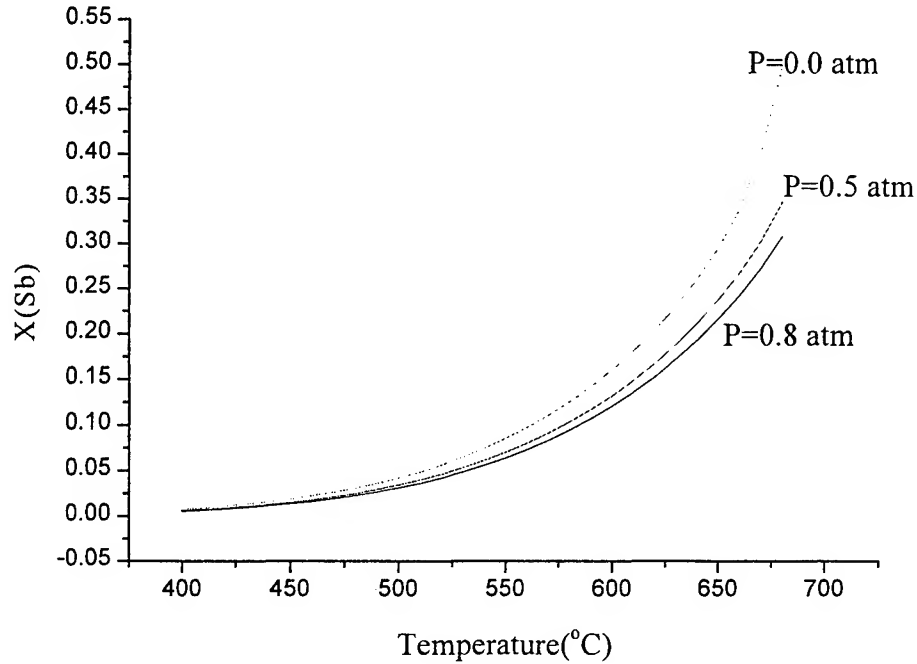


Figure2. The atomic fraction $X(\text{Sb})$ in the melt for GaSb growth on the GaSb(100) substrate at a series of pressure as a function of temperature.

5.2 InAsSb Growth Calculation

To determine precisely the functions of melting point, entropy of fusion, and interaction parameters as a function of pressure, we need a lot of thermodynamical parameters, in which most are unavailable. However melting point variation is most significant. To simplify the problem, we only take melting point variation into consideration by overlooking other factors. Furthermore, we regard all the relations between melting points and pressure as: $T(p) = T_0 - 30 \times p$ ($0 \text{ atm} \leq p \leq 1 \text{ atm}$).

We calculate the phase diagram of $\text{InAs}_{0.91}\text{Sb}_{0.09}$ lattice-matched to GaSb substrate at 600°C . The relation between melt content and the pressure is a monotonous function, which is showed in Figure 3,4 and 5. When the pressure increases, As and Sb content will decrease. On the contrary, the In content will increase with the growth pressure rising. The curves approximate to lines in the figures due to computation simplification. The calculation figures can show some trends although the relation between growth pressure and thermodynamical parameters is much simplified.

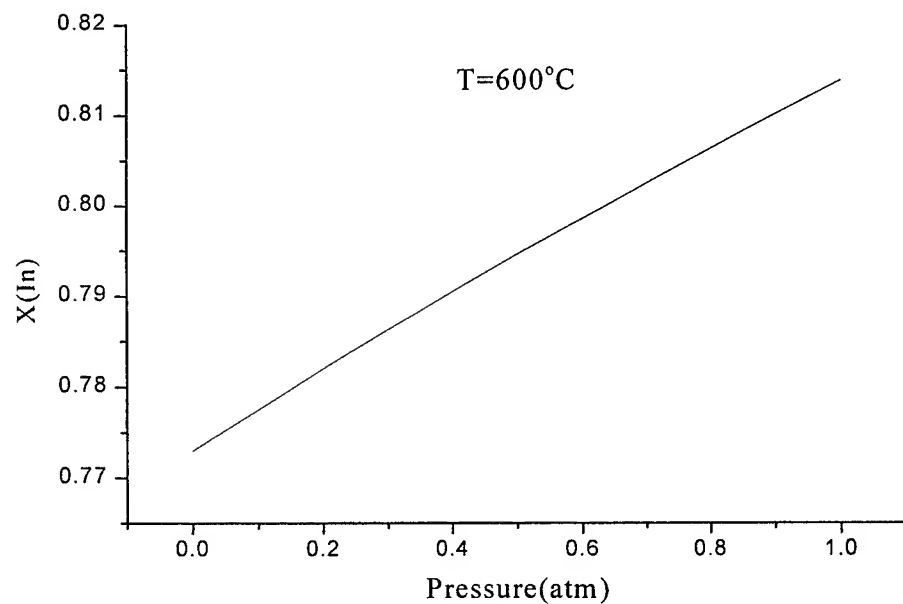


Figure 3. The atomic fraction $X(\text{In})$ in the melt for InAsSb growth on the GaSb(100) substrate at 600°C as a function of pressure.

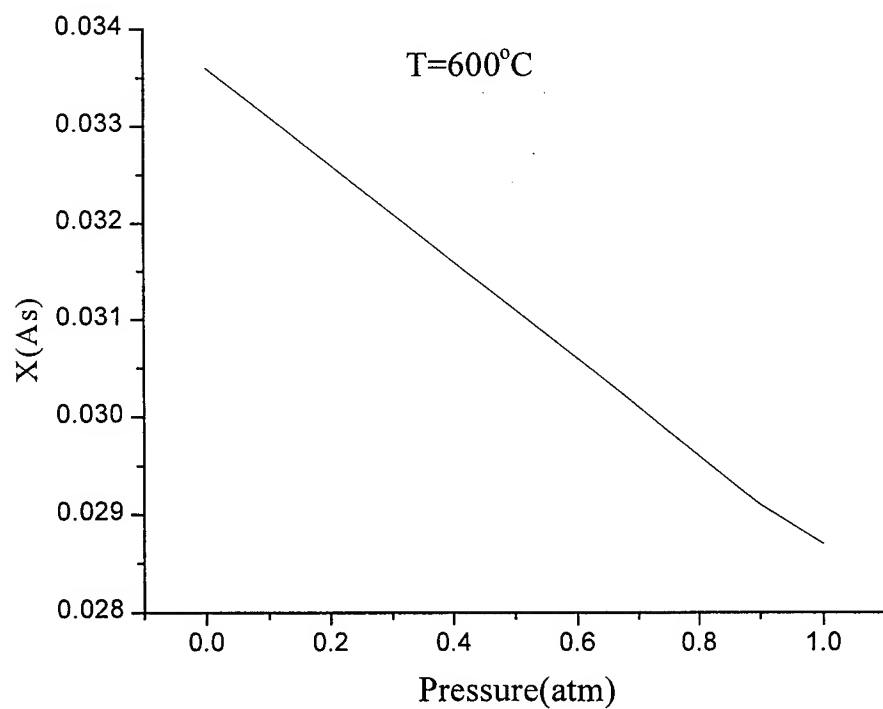


Figure 4. The atomic fraction $X(\text{As})$ in the melt for InAsSb growth on the GaSb(100) substrate at 600°C as a function of pressure.

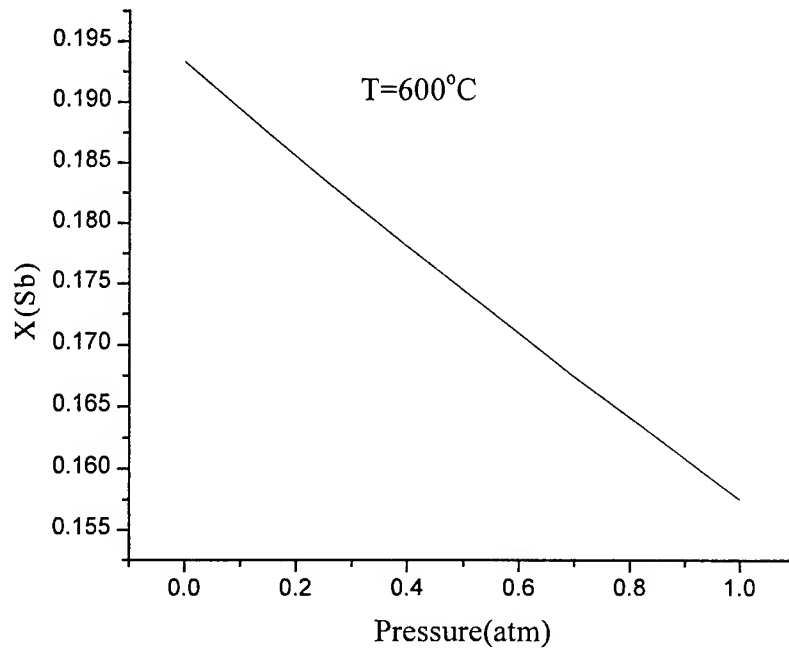


Figure 5. The atomic fraction $X(\text{Sb})$ in the melt for InAsSb growth on the GaSb(100) substrate at 600°C as a function of pressure.

5.3 InGaAsSb Growth Calculation

The phase diagram of InGaAsSb quaternary lattice-matched to GaSb can be dealt with the same as that of InAsSb ternary. Taking $\text{In}_{0.1}\text{Ga}_{0.9}\text{As}_{0.087}\text{Sb}_{0.913}$ as an example, we work out the phase diagram at 550°C as a function of growth pressure. The results are similar with those of InAsSb ternary, which are illustrated in Figure 6,7,8 and 9. When the pressure increases, As and Sb content will decrease. On the contrary, the In and Ga content will increase with the growth pressure rising. All four curves are monotonous. This can be explained as less V group ingredients dissolve in III group solvent when the pressure increases.

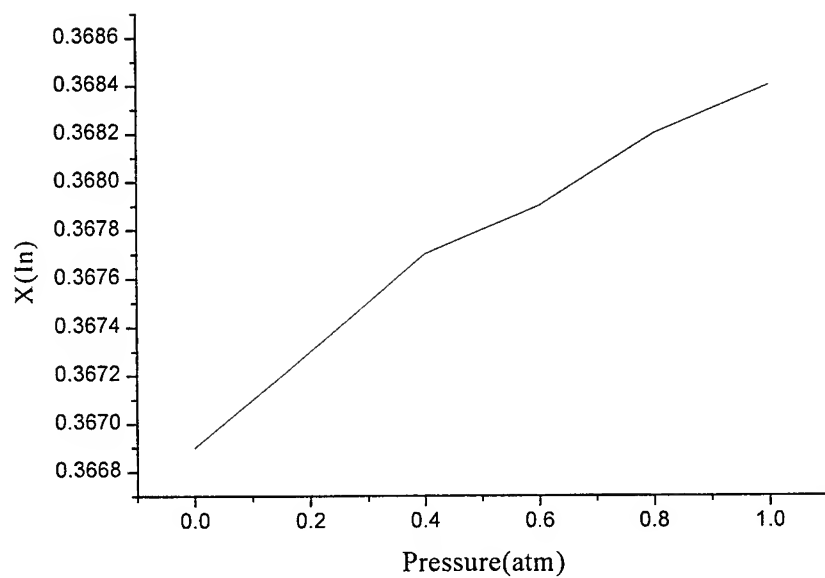


Figure 6. The atomic fraction $X(\text{In})$ in the melt for $\text{In}_{0.1}\text{Ga}_{0.9}\text{As}_{0.087}\text{Sb}_{0.913}$ growth on the GaSb(100) substrate at 550°C as a function of pressure.

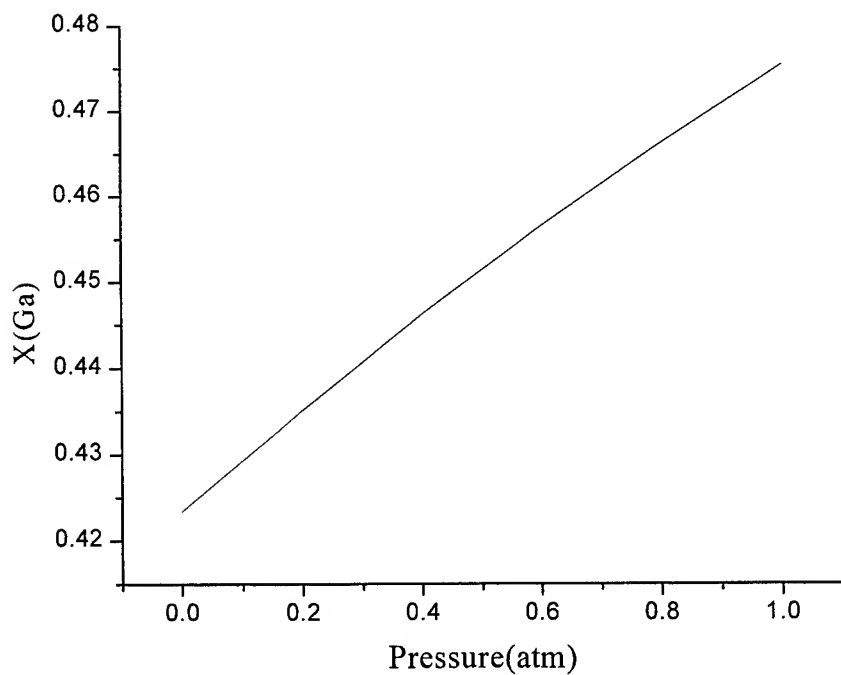


Figure 7. The atomic fraction $X(\text{Ga})$ in the melt for $\text{In}_{0.1}\text{Ga}_{0.9}\text{As}_{0.087}\text{Sb}_{0.913}$ growth on the GaSb(100) substrate at 550°C as a function of pressure.

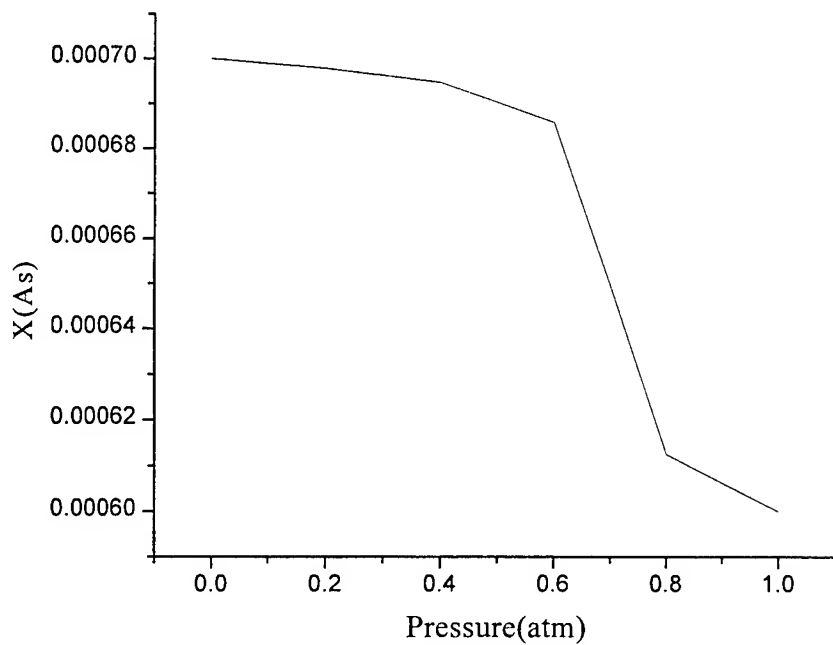


Figure 8. The atomic fraction X(As) in the melt for $\text{In}_{0.1}\text{Ga}_{0.9}\text{As}_{0.087}\text{Sb}_{0.913}$ growth on the GaSb(100) substrate at 550°C as a function of pressure.

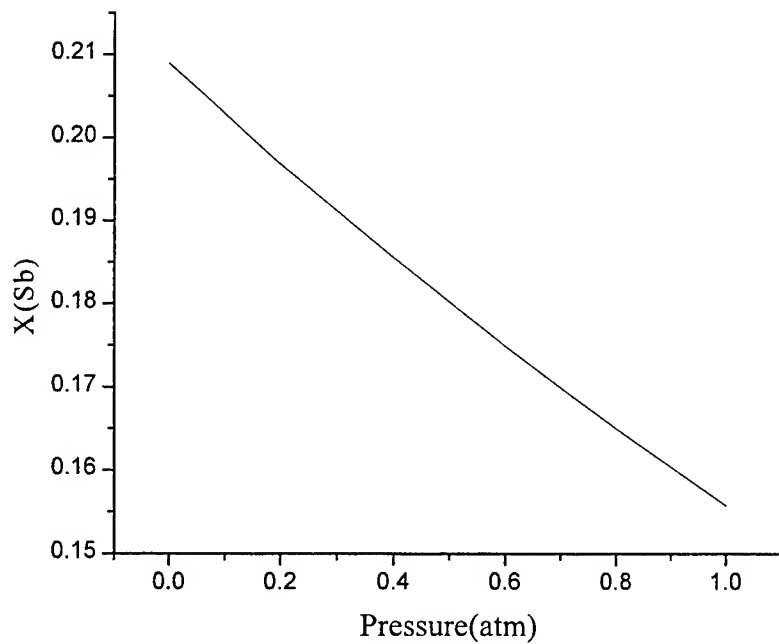


Figure 9. The atomic fraction X(Sb) in the melt for $\text{In}_{0.1}\text{Ga}_{0.9}\text{As}_{0.087}\text{Sb}_{0.913}$ growth on the GaSb(100) substrate at 550°C as a function of pressure.

5.4 Discussions.

Summarizing those calculation results, we compare between pressure variation LPE(PV-LPE) with normal LPE. PV-LPE has three advantages over normal LPE:

- 1) PV-LPE is easy to control super-saturation. The pressure is the main factor to control super-saturation in PV-LPE. Controlling pressure is a developed technique, and the pressure can be changed rapidly and accurately.
- 2) PV-LPE is easy to control the solid film ingredients. The phase diagram as a function of the pressure in PV-LPE is monotonous and quasi-linear, while the phase diagram as a function of the temperature in normal LPE is complicated and non-monotonous. Monotonous function relation in PV-LPE is beneficial to ingredient control in solid film¹⁴.
- 3) PV-LPE can implement iterative growth easily. In the course of growth process with normal LPE, the growth temperature can only decrease monotonously, and the temperature cannot be increased. However, the pressure can be controlled arbitrarily in the course of growth process with PV-LPE, which can bring about great flexibility to the growth process.

Normal LPE equipment can be used to implement PV-LPE growth. However, the normal LPE equipment need some improvement. The pressure cannot vary arbitrarily in normal LPE equipment, so some installation for pressure control should be added. The slider and boat is movable only when the pressure is standard atmosphere pressure in normal LPE equipment. However, the boat needs to be moved at low pressure in PV-LPE growth. Thus some improvement should be made in the normal LPE equipment so that the boat can be pulled at lower pressure than standard atmosphere pressure.

Obviously, there are some weaknesses in PV-LPE. PV-LPE is a completely new technique, and it is difficult to find all the necessary thermodynamical parameters to calculate the accurate phase diagram as a function of the pressure.

6. CONCLUSIONS

In this paper, we have brought forth a new mechanism for LPE growth, pressure-variation LPE(PV-LPE), with which a varying pressure is used to realize super-saturation of the liquid phase even though the growth temperature is kept constant. Furthermore, we calculated the phase diagrams of GaSb-based materials, which are lattice-matched to GaSb substrate. The plot of the phase diagram as a function of pressure shows quasi-linear and monotonous characteristic. PV-LPE is more flexible than normal LPE, and normal LPE equipments can be easily reorganized to implement PV-LPE growth.

REFERENCES

1. A.E.Drakin, Peter G. Eliseev, B. N. Sverdlov, A. E. Bochkarev, L.M. Dolginov and L.V. Duzhinina, "InGaSbAs injection lasers", *Journal of Quantum Electronics* 23, pp. 1089-1094, 1987.
2. H.K.Choi, G.W.Turner, M.K. Connors, S.Fox, C.Dauga and M.Dagenais, "High-power, high-temperature operation of GaInAsSb-AlGaAsSb ridge-waveguide lasers emitting at 1.9 μm ", *Photonics Technology Letters* 7, pp. 1041-1043, 1995.
3. Yu Zhu Gao, XY Gong, Hirofumi Kan, M. Aoyama and T. Yamaguchi, "InAs_{1-y}Sb_y single crystal with cutoff wavelength of 8-12 μm growth by a new method", *Jpn. J. Appl. Phys.* 38, pp. 1939-1940, 1999.
4. Xiu Ying Gong, Hirofumi Kan, Takamitsu Makino, Takefumi Iida, Yuzhu Gao, Mitsuru Aoyama, Masahi Kumagawa and Tomuo Yamaguchi, "Room-temperature Operation of InAsSb/InAsPSb photodetectors with a cut-off wavelength of 4.3 μm ", *Jpn.J.Appl.Phys.* 38, pp. 685-686, 1999.
5. T.H. Chiu, J.L.Zyskind and W.T. Tsang, "Molecular beam epitaxial growth of InGaAsSb on (100) GaSb with emission wavelength in the 2 to 2.5 μm range", *J.Electron. Matter* 16, pp. 57-61, 1987.
6. G.Gougnot, F.Delannoy, F.Pascal, F.Roumanille, A.Foucaran, P.Grosse, J.Bougnot, L.Gouskov, "Metal organic chemical vapor deposition (MOCVD) growth of GaInAsSb: first electrical and optical characterization of materials and devices", SPIE "Material and Technologies for Optical Communications", pp. 135-142, 1987.
7. M.B.Panish, M. Ilegems, "Phase equilibria in ternary III-V systems", *Progress in Solid State Chemistry* 7, pp. 39-83, Pergamon Press, Oxford, 1972.

8. A.S. Jordan and M. Ilegems, "Solid-liquid equilibria for quaternary solid solutions involving compound semiconductors in the regular solution approximation", *J. Phys. Chem. Solids* **36**, pp 329, 1975.
9. J. Lazzari, E. Tournie, F. Pitard and A. Joullie, "Growth limitations by the miscibility gap in liquid phase epitaxy of $\text{Ga}_{1-x}\text{In}_x\text{As}_y\text{Sb}_{1-y}$ on GaSb", *Materials Science and Engineering* **9**, pp. 125-128, 1991.
10. E. Tournie, F. Pitard and A. Joullie, "High temperature liquid phase epitaxy of (100) oriented GaInAsSb near the miscibility gap boundary", *Journal of Crystal Growth* **104**, pp. 683-694, 1990.
11. E. Tournie, J.L. Lazzari, H. Mani, F. Pitard, C. Alibert, A. Joullie, "Growth by liquid phase epitaxy and characterization of GaInAsSb and InAsSbP alloys for mid-infrared application (2-3 μm)", SPIE Vol. 1361 Physical Concepts of Materials for Novel Optoelectronic Device Applications, pp. 641, 1990.
12. G.B. Stringfellow and P.E. Greene "Calculation of III-V ternary phase diagram: In-Ga-As and In-As-Sb", *J. Phys. Chem. Solids* **30**, pp. 1779-1791, 1969.
13. K. Levenberg, "A Method for the Solution of Certain Problems in Least Squares", *Quart. Appl. Math.* **2**, pp. 164-168, 1944.
14. X. J. Mao, Y. C. Chan and Y. L. Lam, "Phase calculation of (100) oriented InGaAsSb grown with liquid phase epitaxy", International Symposium on Photonics and Applications, 29 Nov. - 3 Dec. 1999, Singapore.

Infrared reflectance study of chemical vapor deposition grown 3C - silicon carbide on silicon substrate

W. Y. Chang ^a, Z. C. Feng ^{b*}, S. J. Chua ^{b, c} and J. Lin ^a

^aDepartment of Physics, National Univ. of Singapore, Singapore 119260

^b Institute of Materials Research and Engineering, 3 Research Link, Singapore 117602

^cDepartment of Electrical Engineering, National Univ. of Singapore, Singapore 119260

ABSTRACT

Room Temperature (RT) Infrared (IR) Reflectance spectra are studied both theoretically and experimentally on 3C-SiC films grown on silicon (100) substrate by low pressure chemical vapor deposition (LPCVD). By the use of transfer matrix method, the spectral features influenced by film thickness, phonon-damping constant and free carrier concentration are systematically studied. Comparisons of reflectance spectra are made between experimental spectra and those of ideal samples. A modified effective medium model with consideration of the presence of interfacial layer is introduced to interpret some unusual features. Although some of our results are qualitative, careful analysis of reflectance spectra does provide valuable information about film quality.

Keywords: 3C-SiC, infrared reflectance, LPCVD, dielectric function, transverse and longitudinal optical mode, interfacial layer, effective medium model

1. INTRODUCTION

Silicon carbide has long been considered as a promising candidate material for semiconductor devices operating at high temperature, high power or high frequency, due to its wider band gap, greater electron saturation velocity, higher dielectric strength and greater thermal conductivity compared to some familiar semiconductors like silicon and gallium arsenide. Realization of these advantages has been limited by lack of large single-crystalline substrate suitable for conventional device processing. Single crystal growth of cubic silicon carbide was especially difficult for a long time because of large lattice mismatch (20%) and thermal expansion difference (8%) between SiC and Si. In order to measure and control the single crystal film growth, a quick and convenient characterization technique is needed. IR reflectance spectroscopy, a well-known simple and nondestructive diagnostics tool, can meet this requirement.

In this article, we first present a series of theoretical simulations of IR reflectance spectra for ideal SiC film on semi-infinite silicon substrate. Then some of the experimental spectra obtained from our SiC sample are compared with the ideal spectra. Some unusual features are interpreted using our modified effective medium model and possible origins are presented.

2. CALCULATED IR REFLECTANCE SPECTRA OF IDEAL SiC/Si SYSTEM

In this section, we present theoretically calculated spectra for ideal sample configurations. These calculated spectra provide a basis set to compare with experimental spectra. For frequency dependant complex dielectric constant of SiC, the lattice dielectric function $\epsilon(\omega)$ takes the form: ¹

$$\epsilon(\omega) = (n + ik)^2 = \epsilon_{\infty} \left[1 + \frac{\omega_{LO}^2 - \omega_{TO}^2}{\omega_{TO}^2 - \omega^2 - i\gamma_{TO}\omega} - \frac{\omega_p^2}{\omega(\omega + i\gamma_p)} \right], \quad (1)$$

*Correspondence: E-mail: zc-feng@imre.org.sg; Telephone: (65)-874-8366, Fax: (65)-872-0785

where n is the refractive index, k is the extinction coefficient, ω is the infrared frequency, ϵ_∞ is the high frequency dielectric constant, ω_{TO} and ω_{LO} are the transverse and longitudinal optic-phonon frequency, respectively, γ_{TO} is the phonon damping constant, $\omega_p^2 = 4\pi N e^2 / m^* \epsilon_\infty$ defines the plasma frequency due to free carrier of density N and effective mass m^* , and γ_p is the plasma damping constant. We express all frequencies in wave numbers (cm^{-1}). For cubic SiC we use $\omega_{TO} = 794 \text{ cm}^{-1}$ and $\omega_{LO} = 973 \text{ cm}^{-1}$. Other parameters are adjustable. We assume that $n_{\text{si}} = 3.43$ and $k_{\text{si}} = 0$ for the silicon substrate. Both are independent of the wavelength (frequency) of the incident light beam.

The reflectance of multilayer film system is calculated by the use of matrix method,³ in which an arbitrary number of layers can be included and structural parameters and experimental conditions determine the matrix elements. The substrates are considered as half-infinite bulk materials because their rough backsides scatter the radiation and negligible amount is reflected back.

2.1. IR reflectance spectra for different film thickness

Fig.1 shows the IR spectrum with different film thickness together with that for bulk SiC. For clarity, the ordinate zeros of spectra are shifted down by offset of 40%. For thin SiC film, IR only exhibits a peak near ω_{TO} . As film thickness increases, the peak rises and broadens. When films reach several micrometers, they present a well-developed reststrahlen band. The reflectance peaks close to that of bulk SiC but with skew edge at high frequency side. The Fabry-Perot interference fringes are observed in transparent region. The epitaxial film thickness determines the fringe spacing in the form: $d = 1 / 2n_f \Delta\omega$, where $\Delta\omega$ is the spacing between two adjacent maxima or minima in interference pattern. The accuracy of the film thickness depends on the value of ϵ_∞ , which also influences the reflectance top in reststrahlen band.

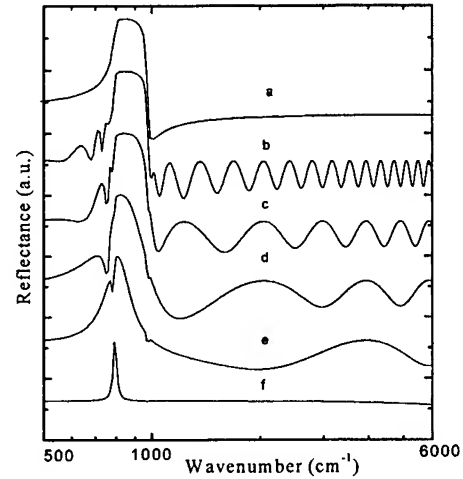
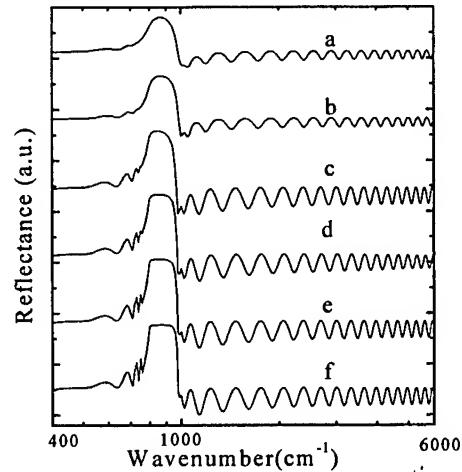


Fig.1. Calculated IR spectrum of 3C-SiC on Si with different film thickness of a) Bulk SiC, b) 5 μm , c) 2 μm , d) 1 μm , e) 0.5 μm and f) 0.05 μm

2.2. IR reflectance spectra for different phonon damping constants

From Fig.2, it can be clearly seen that phonon-damping factor has great influence on reflectance peak. Larger damping factor leads to lower reflectance. The interference fringes will smear out when γ_{TO} is large enough. The structural perfection of the SiC surface can be evaluated from the damping of the TO phonon. Because crystalline imperfections or defects are expected to introduce dissipative processes that increase the damping of the TO resonance.

Fig.2 Calculated IR spectrum of SiC on Si with different phonon damping factors γ_{TO} (cm^{-1}) of a) 50, b) 30, c) 15, d) 9, e) 5 and f) 3



2.3. IR Reflectance spectra for different carrier concentration

Fig.3 shows the changes of IR reflectance with plasma frequency ω_p (also free carrier concentration N) at $\gamma_p = 300 \text{ cm}^{-1}$. Two obviously changes are detected. First, for nominally undoped system, the first reflectance minimum appeared near ω_{LO} (973 cm^{-1}). With the increase of ω_p , the reflectance minimum shifts to high frequency side so reststrahlen band broadens. The variation of reflectivity minimum position indicates that the LO phonon mode coupled with an overdamped plasmon. The LO phonon-plasmon coupled modes have been studied in 6H-SiC⁴ and GaN.⁵ By definition, plasma frequency ω_p correlates with free carriers of density N in the form $\omega_p^2 = 4\pi Ne^2 / m^* \epsilon_\infty$, where m^* is the effective mass. Fig 4 displays the relationship between plasma frequency and carrier concentration. Table 1 lists the values of carrier concentration and corresponding plasma frequency involved in Fig.3. Through simulation in IR spectrum, the carrier concentration can be estimated by locating reflectance minimum position. In Fig.3, curve A is with $\omega_p = 2100 \text{ cm}^{-1}$, corresponding to $N = 1 \times 10^{20} \text{ cm}^{-3}$.

In addition, significant changes are observable at lower frequency side below ω_{TO} . The reflectance increases interference fringes even smear out when carrier concentration is high enough. So in highly doped SiC/Si system ($N > 10^{19}$), stronger reflectance exists for lower frequency side accompanied with the decrease of penetration depth of incident light beam.

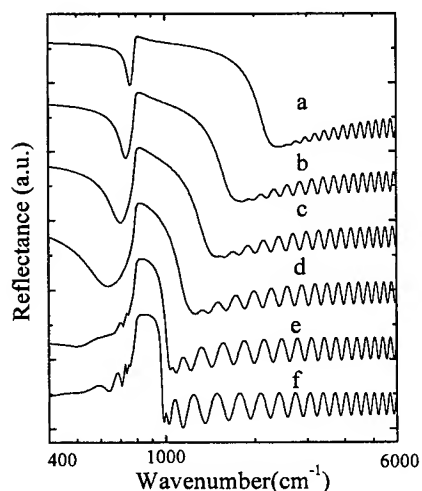


Fig.3 Calculated IR spectrum of SiC on Si with different ω_p at $\gamma_{TO} = 300 \text{ cm}^{-1}$
a) 2100 b) 1500 c) 1200 d) 900 e) 500 f) 100

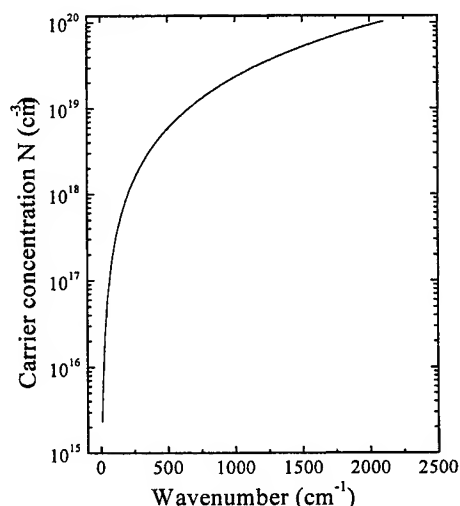


Fig.4 Relationship between carrier concentration N and plasma frequency ω_p , $\omega_p^2 = 4\pi Ne^2 / m^* \epsilon_\infty$.
($m^* = 0.31m_0$, $\epsilon_\infty = 6.7$)

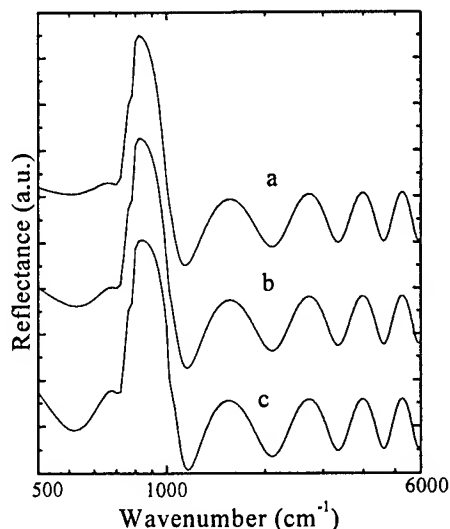
Table 1 Values of carrier concentration and corresponding plasma frequency.

$\omega_p \text{ (cm}^{-1}\text{)}$	2100 (a)	1500 (b)	1200 (c)	900 (d)	500 (e)	100 (f)
$N \text{ (cm}^{-3}\text{)}$	1.03×10^{20}	5.23×10^{19}	3.35×10^{19}	1.88×10^{19}	5.82×10^{18}	2.33×10^{18}

2.4. IR Reflectance spectra for different plasma damping factors

Plasma damping factor determines the carrier mobility in the form $\gamma_p = e / m^* \mu$. Fig.5 shows the influence of carrier mobility on reflectance. The decrease of mobility lowers the reflectivity at lower frequency. The band also narrows with the decrease of carrier mobility.

Fig.5 Calculated IR spectrum of SiC on Si with different γ_p (cm^{-1}) of a) 800 b) 400 c) 100, at $\omega_p = 500 \text{ cm}^{-1}$



2.5. Effect of film surface roughness

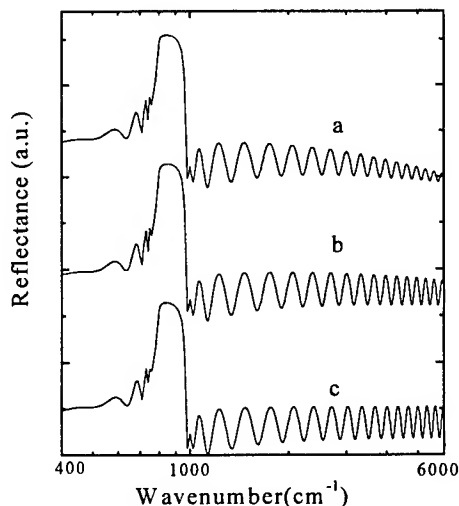
Surface roughness can lead to the loss of reflectance with the increase of incident light frequency and the contrast of interference fringes becomes smaller. It can be described as

$$R = R_0 \exp[-16(\pi\delta/\lambda)^2], \quad (2)$$

where R_0 is the ideal reflectance, δ is the film surface roughness in μm . Fig.6 displays the theoretical variation above reststrahlen band regarding surface roughness condition. Rough surface has significant influence on reflectance in high frequency side.

Fig.6 Calculated IR with different film surface condition. The film thickness is $6.0 \mu\text{m}$. δ is in μm .

a) $\delta = 0.15$ b) $\delta = 0.08$ c) $\delta = 0$



3. EXPERIMENTAL RELECTANCE OF SiC FILM ON Si SUBSTRATE

The epitaxial 3C-SiC films were grown by vertical chemical vapor deposition (V-CVD) at Auburn university. This system employed a vertical reactor configuration with a rotating susceptor. Details of growth procedure can be referred in.^{6,7}

An ideal sample structure consists of single crystalline SiC film on Si substrate. The epitaxial film is uniform and all the interfaces would be optically sharp and parallel. However, in any real samples, various imperfections may occur. The interfaces may be so rough that diffusely scattering is dominant. Also, the film thickness maybe non-uniform, the film may be unintentionally doped and additional layer may exist. So the ideal model cannot fully reproduce satisfactory fitting results to some unusual features in IR spectra.

3.1. Interfacial layer

In some of our measured spectra, decreasing interference fringes were observed above the reststrahlen band. But in ideal sample reflectance, the fringes contrast is only determined by the refractive index difference between the films and substrates. For $n_f < n_s$ (e.g., SiC on Si),⁸

$$R_{\max} = \left[\frac{(n_s - 1)}{(n_s + 1)} \right]^2, \quad R_{\min} = \left[\frac{(n_s - n_f^2)}{n_s + n_f^2} \right]^2. \quad (3)$$

Fringe contrast is defined by $(R_{\max} - R_{\min}) / (R_{\max} + R_{\min})$. Note that R_{\max} does not depend on n_f . In order to interpret this phenomenon, we first attempted to model this effect by varying the doping level in film and substrate, respectively. But simple differences in the free carrier concentration between the film and the substrate cannot account for the minimized phenomenon. We employed our modified model considering the presence of an "optical transition layer" between film and substrate. Fig.7 shows an excellent fitting result compared to measured spectrum. The insert is the configuration. The transition layer is about 2.4% of the thickness of the film.

In GaN on sapphire, an interfacial layer has been demonstrated, which is GaN with voids. Influence of the interfacial layer on IR reflectance was studied by Feng *et al.*^{9,10} For SiC on Si, A. Addamiano *et al.*¹¹ have found empty and pyramidal pits on and underneath the surface film of SiC buffer layer. Mogab *et al.*¹² also observed triangle voids extending from Si substrate to interfacial layer. They suspected that these voids were the result of diffusion of Si atoms to epilayer during the initial stage of epitaxial stage. In addition, because of the discrepancy in crystal lattice dimension and thermal expansion coefficient between SiC film and Si substrate, residual strain induced dislocations and considerable imperfections may occur. All of these largely reduced the reflectivity of incident light beam. The transition layer with spatial variation of refractive index may magnify its presence with decreasing fringes contrast.

Our model supported these observations. In sample a121, once the refractive index is larger than n_f with an average factor of 1.2, a decreasing contrast is observed. Otherwise, if $n_f > n_{\text{tran}}$, enhanced fringe contrast appeared above reststrahlen band. The thickness of this transition layer combined with refractive index determines the contrast decreasing speed. If the transition layer is very thin, its effect is neglected so fringe extreme remain almost constant. From this point, the film-substrate configuration is estimated thus film quality is evaluated.

Finally, one point should be made. Besides the effect of interfacial layer, rough surface scattering influences reflectance as well in sample a121. Roughness coefficient δ is 0.08 μm . Rough surface leads to the lower reflectivity at higher frequency and the contrast of interference fringes becomes smaller as photon frequency increases. We have mentioned this effect above.

3.2. Three-component effective medium model

Reststrahlen band, in the region from about ω_{TO} to ω_{LO} , is the result of resonance between incident light and lattice vibration. Theoretical peak reflectance reaches 95% for ideal 3C-SiC/Si system. The reststrahlen peak is sensitive to film surface condition. Holm *et al.* conducted a detailed investigation on the influence of surface roughness.⁶ They pointed out slight roughness on film surface brought out anomalous features on the peak reflectance. With the increase of surface roughness, a shallow dip became into deep notch near $\omega = 900 \text{ cm}^{-1}$. However, there is another possibility that the dip or notch is associated with the lack of periodicity in disordered SiC, which will weaken the selection rules and cause the phonon modes to become infrared active. Spitzer *et al.*¹³ also found a pronounced a dip at 885 cm^{-1} (11.3 μm) in α -II SiC. They proposed a two-resonance oscillator theory in which dispersion parameters were assumed to be the sum of two set of form. They ascribed the dip to the second oscillator, with a resonance strength approximately 0.3% of that of the fundamental resonance. In our sample a409 and a713, shallow dips are detected at 895 cm^{-1} (Fig.6) and 894 cm^{-1} (Fig.7) with different depth at reflectance peak. A modified "three-component effective medium model" was employed to model this feature in terms of this assumption. According to this model, three kind of effective mediums, namely, pores, crystalline grains and

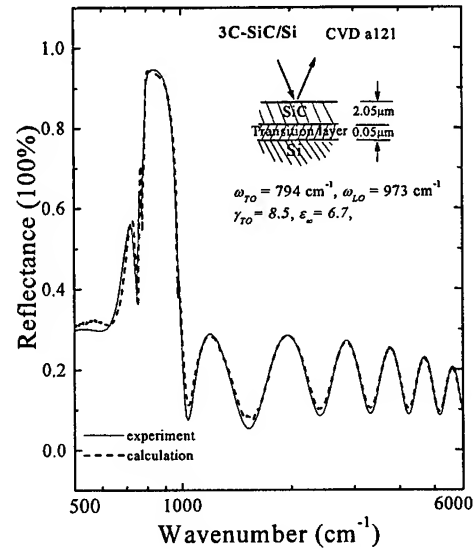


Fig.7 IR spectrum of 3C-SiC on Si (100)

intergranular materials, were assumed to co-exist in SiC sample. The effective dielectric function can be evaluated from the self-consistency condition: ¹⁴

$$\sum_{i=1}^3 \frac{f_i [\varepsilon_i(\omega) - \varepsilon(\omega)]}{\varepsilon_i(\omega) + 2\varepsilon(\omega)} = 0,$$

ε_i is the i th component dielectric function with volume fraction f_i ($i=1-3$) respectively.

Using ω_{TO} and ω_{LO} frequency of the intergranular materials and volume fractions f_1, f_2, f_3 as adjustable parameters, reproduced curves are showed in Fig. 6 and Fig.7. Higher TO frequencies, close to 940 cm^{-1} , are deduced from intergranular materials in sample a713 and a409, compared to the value of 794 cm^{-1} in crystalline SiC. The volume fraction f_2 of intergranular materials varies from 2.5% in a713 to 0.5% in a409, which determines the dip's depth. Effect of pores is considered but cannot produce better fitting results. Table 2 lists the fitted parameters of these two samples.

In order to get further information about the effect of intergranular and pores, three effective model was used to analysis the variation of reflectance as function of volume fraction of f_1 and f_2 . In fig. 10, curve *a* have a shallow indentation with $f_2=0.5\%$. A notch is very obvious when f_2 reaches 2%. From our simulation, it is evidenced that intergranular materials determine this unusual feature.

Finally, we must consider the case of rough surface diffusely scattering. The reflectance at the top of reststrahlen peak is sensitive to the film surface condition. The specula reflectance decreases over the entire spectrum with frequencies side due to surface roughness. However, we observed obvious interference fringes even at visible and UV frequency regions. It indicates that the interface scattering will play no important role for SiC/Si.

In spite of our successful fitting to measured spectrum, further effort should be focused on the understanding of the physical origin of this unexpected feature.

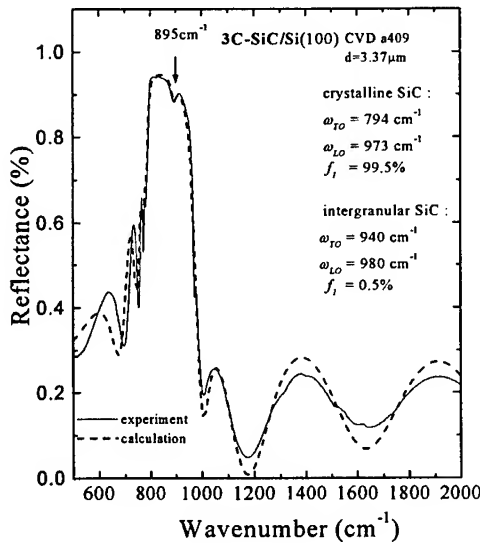


Fig.8 IR spectrum of 3C-SiC on Si (100), a409

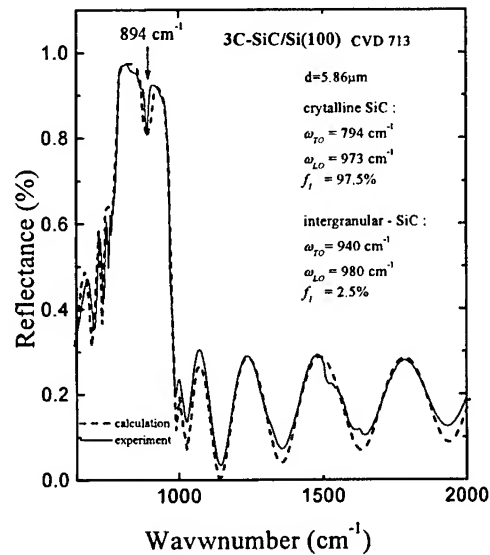
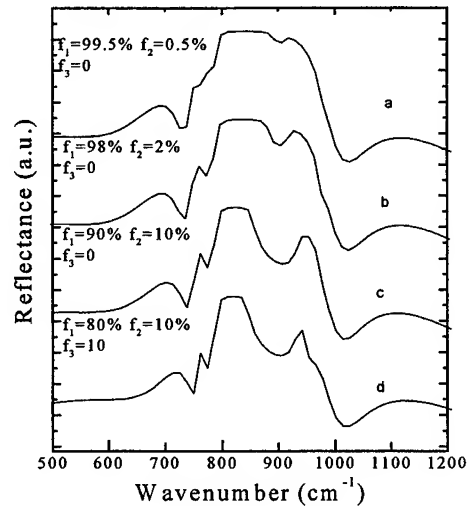


Fig.9 IR spectrum of 3C-SiC on Si (100), a713

Table 2. Fitted parameters of sample a409 and a713

		Volume fraction	ω_{TO} (cm ⁻¹)	ω_{LO} (cm ⁻¹)	ϵ_{∞}	γ_{TO} (cm ⁻¹)	Thickness (μm)
Sample 409	crystalline SiC	$f_1 = 99.5\%$	794	973	6.7	8.5	8.77
	intergranular SiC	$f_2 = 0.5\%$	943	973	6.0	25	
Sample 713	crystalline SiC	$f_1 = 97.5\%$	794	973	6.7	8.5	2.1
	intergranular-SiC	$f_2 = 2.5\%$	940	973	6.0	25	

Fig.10 Top reflectance change with different volume fractions of f_1 , f_2 , f_3 , when ω_{TO} of intergranular material (f_2) is 950cm⁻¹



4. CONCLUSION

In summery, infrared (IR) reflectance of 3C-SiC on Si (100) is studied both theoretically and experimentally. Influences of structural and electric properties on reflectance are investigated in details. Through simulation, film thickness, free carrier concentration and phonon damping constant are determined. Furthermore, based on proposed effective medium model that takes into account of the effect of intergranular and pores, together with the influence of interfacial layer, some unusual features are characterized. Information can be inferred about roughness at film surface and possible presence of interfacial layer at film-substrate interface. In addition to the contribution of surface roughness, intergranular materials and pores are the possible origins of anomalous features in peak reflectance of the reststrahlen band. It is demonstrated that careful analysis of the reflectance line-shape can provide quantitative evaluation about the microstructure and crystalline properties of 3C-SiC film on Si substrate.

5. ACKNOWLEDGEMENTS

The authors would like to thank C. C. Tin for his kind providing 3C-SiC samples in our experiments. Y.T. Hou is also gratefully acknowledged due to his help in fitting programs and many useful discussions.

REFERENCES

1. W. G. Spitzer, D. A. Kleinamn, and C. J. Frosch, "Infrared properties of cubic silicon carbide film," *Phys. Rev.* **113**, pp. 133-136, 1959.
2. D. Olego, M. Cardona, and P. Vogl, "Pressure dependence of the optical phonons and transverse effective charge in 3C-SiC," *Phys. Rev. B* **25**, pp. 3878-3888, 1982.
3. Pochi Yeh, *Optical waves in layered Media*, Joh Wiley-sons, New York, 1988.
4. M. V. Klein, B. N. Ganguly and P. J. Colwell, "Theoretical and experimental study of Raman scattering from couple LO-phonon-plasmon modes in silicon carbide," *Phys. Rev. B* **6**, pp. 2380-2388, 1972.
5. T. Kozawa, T. Kachi, H. Kamo, Y. Taga, M. Hashimoto, N.Koide and K. Manabe "Raman scattering from LO phonon-plasmon coupled modes in gallium nitride," *J. Appl. Phys.* **75**, pp. 1098-1101, 1994.
6. Z. C. Feng, C. C. Tin, K. T. Yue, R. Hu, J. Williams, S. C. Liew, Y. G. Foo, S. K. L. Choo, W. E. Ng and S. H.Tang, "Combined structural and optical assessment of CVD grown 3C-SiC/Si," *Mat. Res. Soc. Symp. Proc.* Vol. **339**, pp.417-422, 1994.
7. Z. C. Feng, C. C. Tin, R. Hu and J. Williams, " Raman and Rutherford backscattering analyses of cubic SiC thin fims grown on Si by vertical chemical vapor deposition," *Thin Solid film* **266**, pp. 1-7, 1995.
8. R. T. Holm, P. H. Klein and P. E. R. Nordquist, Jr., "Infrared reflectance studies of evaluation of chemically vapor deposited β -SiC films grown on Si substrate," *J. Appl. Phys.* **60**, pp.1479-1485, 1986.
9. Z. C. Feng, Y. H. Hou, S. J. Chua and M. F. Li "Infrared reflectance studies of GaN epitaxial film on sapphire substrate," *Surf. & Interface Anal.* **28**, pp. 166-169, 1999.
10. Y. T. Hou, Z. C.Feng, S. J. Chua, M. F, Li, N. Akutsu and K.Matsumoto, "Influence of Si-dopping on the characteristics of GaN on sapphire by infrared flectance," *Appl. Phys. Lett.* **75**, pp. 3117-3119, 1999.
11. A. Addamiano and J. A. Sprague, "'Buffer layer' technique for the frowth of single crystal SiC on Si," *Appl. Phys. Lett.* **44**, pp. 525-527, 1984.
12. C. J. Mogab and H. J. Leamy, "Conversion of Si to epitaxial Si by reaction with C_2H_2 ", *J. Appl. Phys.* **45**, pp.1075-1082, 1974.
13. W. G. Spitzer, D. A. Kleinman, and D. Walsh, "Infrared properties of hexagonal silicon carbide," *Phys. Rev.* **113**, pp. 127-133, 1959.
14. Y. Okamoto, C. V. Ordin, T. Kawahara, M. I. Fedorov, Y. Miida, and T. Miyakawa, "Semiconductor with the use of a four-component effective medium model" *J. Appl. Phys.* **85**. pp. 6728-6737, 1999.

Optical Characterization of Low Temperature GaAs

Genmao Chen^a, Harry E. Ruda^a, Qiang Liu^b, Lech Jedral^c, Champika H. Edirisinghe^d
and Ben G. Yacobi^a

*a. Energenius Centre for Advanced Nanotechnology
Department of Metallurgy & Materials Science, University of Toronto
Rm 204, Houtain Building, 170 College St., Toronto, On. Canada M5S 3E3*

b. Filtronic Solid State, 3251 Olcott St., Santa Clara, CA 95054-3095

c. Delphax Inc, 5030 Timberlea Blvd., Mississauga, On, Canada L4W 2S5

d. SDL Inc, 80 Rose Orchard Way, San Jose, CA 95134-1365

Peter W. E. Smith, and Seldon D. Benjamin

*Department of Electric & Computer Engineering, University of Toronto
10 King's College Rd., Toronto, On., Canada M5S 3G4*

ABSTRACT

Molecular beam epitaxial (MBE) grown GaAs at low substrate temperature (LT-GaAs) possesses a unique combination of properties (i.e., semi-insulating and short carrier lifetime) that has led to a variety of electronic and photonic device applications. In this paper, we report on the optical characterization of LT-GaAs, including carrier lifetime, photorefectance (PR), and surface photovoltage (SPV) measurements. The undoped LT-GaAs samples were grown using our custom designed MBE system at the following substrate temperatures: 200 °C, 250 °C and 300 °C. These samples were then annealed at 700-850 °C in a rapid thermal annealing (RTA) system. The PR spectra revealed that the PR amplitude depends strongly on the carrier lifetime, while the PR spectral broadening of the near bandgap peak depends strongly on the internal field non-uniformity caused by buried Schottky barriers around the As precipitates. Above bandgap SPV measurements revealed a unique SPV spectrum compared with that for bulk GaAs. Carrier lifetime was measured for LT-GaAs samples grown at 200, 250, and 300 °C, respectively, and annealed at 700 °C for 30 seconds, and the corresponding carrier lifetimes are 1.5, 2.2, and 12 ps.

Keywords: MBE, LT-GaAs, carrier lifetime, photorefectance, surface photovoltage, annealing, precipitate, point defect.

1. INTRODUCTION

High quality MBE GaAs is normally grown at temperature (T_g) of 580-600 °C. MBE grown GaAs at low substrate temperature ($T_g = 200-400$ °C), however, has attracted considerable attentions owing to its unique electronic, optical, and materials properties [1]. LT-GaAs is normally grown in substrate temperature range of 200-400 °C with beam equivalent pressure (BEP) ratio of As₄ or As₂ to Ga ~ 10-20:1 and growth rate of ~ 1 $\mu\text{m}/\text{hour}$. Under these growth conditions, the material shows a large non-stoichiometry, i.e., about 1-2 at. % arsenic rich (the value of excess arsenic depends on the growth temperature). These excess arsenic atoms in the lattice also cause the as-grown material to exhibit a large lattice strain of ~ 0.1%. Although the material is non-stoichiometric and strained, x-ray rocking curve measurements indicated that it is still single crystal [2]. However, defect analyses have demonstrated that the material contains a variety of native point defects including arsenic antisites (As_{Ga}), gallium vacancies (V_{Ga}), and arsenic interstitials (As_i). Table 1 shows the results of point defects analysis of LT-GaAs grown at $T_g = 200$ °C. As_{Ga} is a deep donor, while V_{Ga} is a deep acceptor. In practice, these deep level defects lead to a pinning of Fermi energy near mid-bandgap [3-5]. Due to defect charge compensation, the as grown LT-GaAs exhibits a firmly high resistivity of ~10 $\Omega\text{-cm}$ [6]. The high concentration of traps also lead to high infrared absorption [7] and short carrier lifetime (subpicosecond) for as-grown LT-GaAs [1].

Table 1. Defect analysis of as-grown LT-MBE GaAs at $T_g = 200\text{ }^\circ\text{C}$

Defect	Concentration (cm^{-3})	Analysis Method	References
$[\text{As}_{\text{Ga}}]^0$	1×10^{20}	Infrared Absorption	[7]
$[\text{As}_{\text{Ga}}]^+$	$\sim 5 \times 10^{18}$	Electron Paramagnetic Resonance (EPR)	[8]
V_{Ga}	$\sim 5 \times 10^{18}$	EPR or Photoluminescence	[9,10]
As_i	$\sim 2 \times 10^{20}$	Rutherford Backscattering Spectroscopy	[2]

Upon annealing at 500-900 $^\circ\text{C}$ for 10 seconds to 1 hour, the point defect concentrations are greatly reduced by two to three orders of magnitude, and the lattice strains are relaxed. Meanwhile, arsenic precipitates are formed in the material. The LT-GaAs layer, however, remains crystalline, and its stoichiometry shows no measurable change [1]. Transmission electron microscopy (TEM) analysis has revealed that the annealed LT-GaAs is actually a semiconductor/metal (GaAs:As) two-phase material. The size and the density of arsenic precipitates as well as their average inter-precipitate spacing depend on the annealing temperature and time. In general, higher annealing temperature and longer annealing time will induce larger arsenic precipitate size and larger inter-precipitate spacing, but lower precipitate densities. Table 2 shows typical TEM analysis results from LT-GaAs samples grown at 250 $^\circ\text{C}$ and annealed for 30 seconds at 700 $^\circ\text{C}$, 800 $^\circ\text{C}$, and 900 $^\circ\text{C}$, respectively [11].

Table 2. TEM analysis results from LT-GaAs grown at 250 $^\circ\text{C}$, and annealed for 30 s

Anneal temperature ($^\circ\text{C}$)	Average precipitate diameter (\AA)	Average inter-precipitate spacing (\AA)	Precipitate density (10^{16} cm^{-3})	Precipitate volume fraction
700	70	225	8.7	0.015
800	150	475	0.93	0.016
900	200	675	0.325	0.013

Annealing of LT-GaAs also results in a decrease of the infrared absorption [7], one to two orders of magnitude increase of the carrier lifetime [1], and a dramatic increase of resistivity up to $10^6\text{ }\Omega\text{-cm}$ [12]. The origin of the resistivity increasing upon annealing is still an open question, but many experimental results support the buried Schottky barrier model for annealing temperatures higher than 600 $^\circ\text{C}$ [1,5]. In this model, the arsenic precipitates are believed to deplete free carriers from the material around them; and the multiple overlapping depletion regions fully deplete the material, rendering a high resistivity [13]. Also, many experiments have demonstrated that the Fermi level is pinned close to mid-bandgap for annealed LT-GaAs [3-5].

In this article, we report on the results of carrier lifetime, PR and SPV measurements of both as-grown and annealed LT-GaAs. We also present qualitative explanation for these PR and SPV spectra.

2. SAMPLE PREPARATIONS

Liquid encapsulated Czochralski (LEC) semi-insulating (SI) GaAs (100) substrates were cleaned using standard procedures in a clean room. The substrates were then indium mounted onto molybdenum sample holders. During the indium mounting, the substrates were heated up $\sim 170\text{ }^\circ\text{C}$. At this temperature, a thin oxide layer formed on the surface of the cleaned substrates, and protects the substrates from further contaminations during sample transfer from clean room to MBE system. The substrates were then loaded into the analysis chamber of our MBE system, and outgassed at 200 $^\circ\text{C}$ for 1 hour under 2×10^{-9} Torr ultra-high vacuum (UHV) condition. Finally the substrates were introduced into the MBE growth chamber where the substrates were first outgassed by light irradiation for 30 minutes under 2×10^{-10} Torr UHV condition, then heated up to 620 $^\circ\text{C}$ by sample heater for about 10 minutes to desorb the surface oxide layer. During this surface oxide layer desorption, arsenic source beam was opened to prevent As loss from substrate surface. After the oxide layer desorption, reflection high energy electron diffraction (RHEED) analysis showed a clear 2×4 surface reconstructions.

Three LT-GaAs samples were grown in our custom designed five-chamber MBE system. The growth conditions and procedures were as follows: the vacuum background for the MBE growth is $\sim 2 \times 10^{-10}$ Torr; the growth rate for all layers was set to 0.8 $\mu\text{m/h}$; and the BEP ratio of Ga or Al over As_4 was set to 1: 15. First, 0.5 μm GaAs buffer layer was grown at 580°C for 38 minutes; then the substrate temperature was raised to 720 °C to grow the 20 nm AlAs lift-off layer for 90 seconds. After the growth of AlAs layer completed, the growth was interrupted by closing the Al source beam, but leaving the As_4 beam open to prevent arsenic loss from the sample surface during lowering the sample temperature. Within 5-10 minutes, when the sample temperature reaches the designed LT-GaAs growth temperature, the Ga source beam was opened and 2 μm of LT-GaAs was grown for 2.5 hours at $T_g = 200$ °C, 250 °C, and 300 °C corresponding to sample LT- GaAs #003, #004, and #005, respectively.

The three LT-GaAs samples were cleaved into 5x5 mm² pieces. For each growth temperature, three cleaved pieces were rapid thermal annealed at annealing temperature (T_a) of 700 °C, 800 °C, and 850 °C, respectively, for 30 seconds with hydrogen gas flowing, and surface covered with a piece of SI GaAs substrate to prevent contamination and arsenic loss during annealing.

3. CARRIER LIFETIME MEASUREMENTS

The samples of LT-GaAs #003 ($T_g = 200$ °C), LT-GaAs #004 ($T_g = 250$ °C) and LT-GaAs #005 ($T_g = 300$ °C) annealed at $T_a = 700$ °C for 30 seconds were selectively etched in 10% hydrofluoric (HF) acid for 12 hours. The HF acid preferentially etched the AlAs lift-off layer. After selective etching, the LT-GaAs layers were removed from their substrates, then bonded to glass slides by Van der Waals interaction, and prepared for carrier lifetime measurements.

The carrier lifetimes were measured using the transient absorption saturation method. The experimental set up is a pump-probe femtosecond time-resolved differential transmission spectroscopy arrangement as described elsewhere [14]. A titanium: sapphire ultra-fast pulse laser was used to produce 150 fs laser pulses. The laser wavelength was tuned to 870 nm to match the band edge transition wavelength of GaAs. The beam was split into a pump beam and a probe beam by a beam splitter. The pump beam had an average power of 25 mW, and was focused to ~ 7 μm on the sample. The probe beam had an average power of 1.2 mW. After being reflected from a micro stepping time-delay stage, it was focused onto the pump beam spot with a diameter of slightly smaller than the pumping beam spot. The pump pulses were used to generate free carriers in the material (or to excite electrons from valence band to conduction band). When a pump pulse is terminated, the free carrier

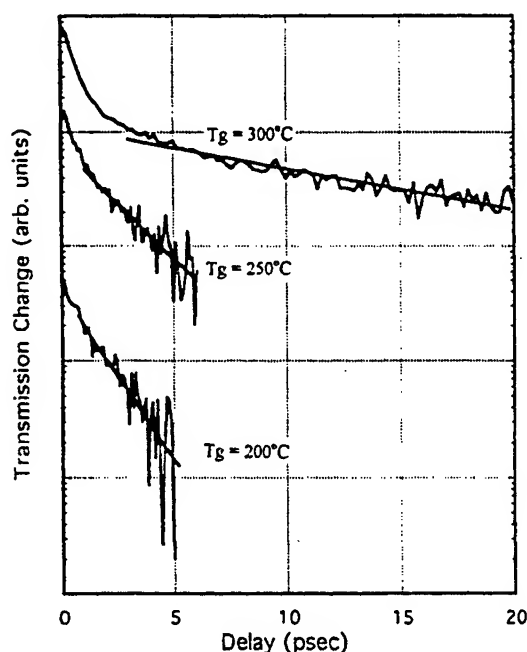


Fig. 1. The results of differential transmission measurements of LT-GaAs grown at $T_g = 200$ °C, 250 °C, and 300 °C, respectively, and annealed at 700 °C for 30 s; the corresponding carrier lifetime of 1.5 ps, 2.2 ps, and 12 ps were obtained..

concentration $N(t)$ will decay exponentially. The decay can be expressed by equation (1) [15]:

$$N(t) \propto \exp(-t / \tau) \quad (1)$$

where, t is time, τ is carrier lifetime of the material. When a probe pulse passes through the sample, the sample will absorb a fraction of its power. The absorption is inversely proportional to the free carrier concentration $N(t)$, but the transmission T is proportional to $N(t)$ [15], and can be expressed by equation (2)

$$T \propto \exp(-t / \tau) \quad (2)$$

$$\text{or} \quad \frac{d \ln T}{dt} = -\frac{1}{\tau} \quad (3)$$

Hence, by scanning the probe pulse delay time t , and measuring the transmission, the carrier lifetime τ can be deduced from the slope of the curve of $\ln T$ vs. t .

Fig. 1 shows the results of the carrier lifetime measurements from the LT-GaAs sample #003 ($T_g = 200^\circ\text{C}$), #004 ($T_g = 250^\circ\text{C}$), and #005 ($T_g = 300^\circ\text{C}$) and all annealed at 700°C for 30 seconds; after curve fitting, the corresponding carrier lifetime of 1.5 ps, 2.2 ps and 12 ps were obtained. These results demonstrate that under same annealing conditions, lower growth temperature renders shorter carrier lifetime for LT-GaAs. The lifetime measurements of the three as-grown LT-GaAs were not shown in fig. 1 because their lifetime is even shorter than the 150 fs ultrafast pumping laser pulse so that no accurate carrier lifetime for as-grown LT-GaAs can be obtained from the measurements. For the same growth temperature, but different annealing temperature or different annealing time, LT-GaAs also exhibited different carrier lifetime. It is believed that higher annealing temperature or longer annealing time will lead to longer carrier lifetime.

4. PHOTOREFLECTANCE MEASUREMENTS

Photoreflectance (PR) is used extensively in the study of semiconductor microstructures because this technique not only has high sensitivity and high spectral resolution, but also can provide non-destructive measurements [16]. Experimental apparatus for PR has been described elsewhere [14]. In the PR measurements, an argon ion laser beam with 3 mW incident power was used as the modulating light source; a notch filter was used to allow only the 488 nm laser line to pass through; then, the beam was focused onto the sample at 45° incident angle. A monochromator dispersed white light source was used as a probe light beam, and was focused on the sample at near normal incidence.

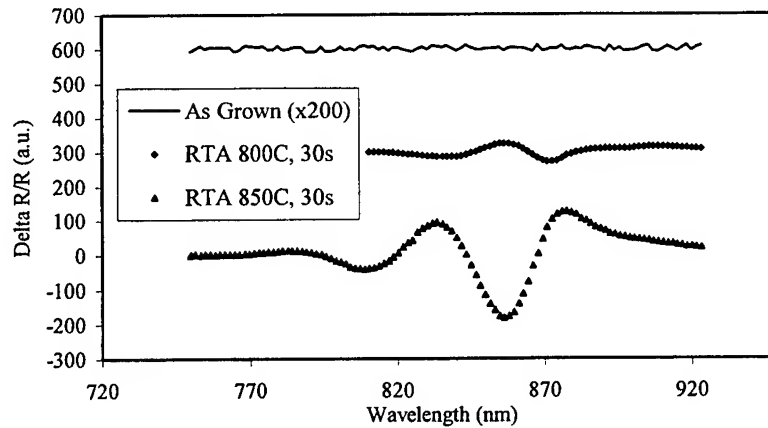


Fig. 2. Room temperature PR spectra of LT-GaAs ($T_g = 200^\circ\text{C}$)

Fig. 2 shows room temperature near bandgap PR spectra measured from LT-GaAs #003 ($T_g = 200^\circ\text{C}$); the triangles, diamonds, and solid line are corresponding to spectrum of the sample annealed at 850°C for 30 s, the sample annealed at 800°C for 30 s, and the as-grown sample, respectively. The top two spectra are offset for clarity. The as-grown sample shows no detectable PR response, i.e., $\Delta R/R$ is below the sensitivity of the PR system (10^{-6}). While, the annealed samples show clear PR responses. It is also clearly demonstrated that the higher annealing temperature enhanced the PR spectral peak, but increased the PR spectral broadening too. These PR spectra cannot be explained by the high and intermediate field PR theories, which are usually used to analysis bulk materials and normal MBE grown materials [16,17]. To understand the PR spectra of LT-GaAs, two characteristics of LT-GaAs have to be considered in the PR modelling. a) As-grown LT-GaAs has an extremely short carrier lifetime $\tau < 150$ fs; and carrier lifetime for annealed LT-GaAs is in the ps range. The extremely short carrier lifetime makes the lifetime broadening parameter ($\Gamma \sim \hbar/2\tau$) [16] very large, thus, low field PR model, i.e., $\Gamma > \hbar\Omega$ should be used to analysis PR Spectra of LT-GaAs; where $\hbar\Omega$ is the characteristic energy that measures the average energy gained from the uniform field by the optically excited carrier, and is given by [16,17]

$$(\hbar\Omega)^3 = e^2 F^2 \hbar^2 / 8\mu_{||} \quad (4)$$

where \hbar is Planck constant over 2π , F is the modulation light induced field, and $\mu_{||}$ is the reduced interband effective mass in the field direction. b) Annealed LT-GaAs is actually a two-phase (semiconductor/metal) material, GaAs:As. Around the As clusters, buried Schottky barriers create a localized field which makes the annealed LT-GaAs exhibit a high internal field non-uniformity (ΔF), and can strongly influence the PR spectral broadening. Thus, field non-uniformity broadening should be considered in the PR modelling for LT-GaAs, especially, for annealed LT-GaAs. As indicated by Aspnes, the theoretical PR modelling for the above case is rather complex. For simplicity, if we only consider the near bandgap PR features, the PR spectrum can be described as follows [17]:

$$\frac{\Delta R}{R} \sim \frac{1}{E^2(E-E_g)} \exp\left[-\frac{(E-E_g)^{1/2}\Gamma}{(\hbar\Omega)^2}\right] \cos\left[\theta + \frac{2}{3}\left(\frac{E-E_g}{\hbar\Omega}\right)^{3/2}\left[1 - \frac{3}{4}\left(\frac{\Delta F}{F}\right)^2\right]\right] \quad (5)$$

where E is the probe photon energy, E_g is sample bandgap energy, θ is a phase factor. From equation (5), we can see the carrier lifetime broadening parameter Γ and modulating field (in $\hbar\Omega$ term) strongly affect the amplitude of PR signal, while, the modulating field and the internal field non-uniformity ($\Delta F/F$) strongly affect PR spectral width.

As revealed by carrier lifetime measurements, as-grown LT-GaAs #003 has a the carrier lifetime shorter than 150 fs that is about 4 orders of magnitudes smaller than the carrier lifetime of normal MBE grown GaAs (\sim ns). This extremely short carrier lifetime leads to a very large lifetime broadening parameter Γ . As described by equation (5), the large Γ eventually makes the PR signal diminished for as-grown LT-GaAs #003. After annealing, however, the carrier lifetime enhanced at least one order of magnitude, thus, clear PR features recovered. Similarly, we can explain why the 850°C annealed sample has a PR signal ~ 10 times stronger than that for the 800°C annealed sample because of the sample annealed at higher temperature has longer carrier lifetime.

Fig. 2 also shows that the PR spectral width of 850°C annealed sample (36 meV or 21.8 nm) is much larger than the PR spectral width of 800°C annealed sample (23 meV or 14 nm), and both of them are larger than the PR spectral width of typical GaAs substrate (15 meV) [18]. As indicated by Melloch et. al. [1], the higher annealing temperature lead to bigger As precipitates size, and a large average inter-precipitate spacing, which, in turn, causes the a larger internal field non-uniformity. From equation (5), we know the larger internal field non-uniformity caused by higher annealing temperature is responsible for the larger PR spectral broadening. Our PR spectra of LT-GaAs and their explanations is probably the first exploring of considering the influence of carrier lifetime and internal field non-uniformity on PR spectra of LT-GaAs.

5. SURFACE PHOTOVOLTAGE MEASUREMENTS

Surface photovoltage technique is a well established non-destructive technique suitable for bulk minority carrier diffusion length and surface state characterization [19,20]. The experimental setup was described in previous paper [19]. We first report on the room temperature SPV phenomena of LT-GaAs for both as-grown and annealed samples. For comparing, we also measured SPV spectrum of a n-type GaAs substrate ($n = 2 \times 10^{18} \text{ cm}^{-3}$). It has been found that as-grown LT-GaAs exhibits a very strong SPV response compared with n-GaAs substrate. The SPV response, however, greatly suppressed on annealing. The unique of SPV spectra for LT-GaAs is that the slope of above bandgap SPV versus wavelength (λ) or absorption depth $1/\alpha$ (for above bandgap absorption, $1/\alpha \propto \lambda_e$) is positive for both as-grown and annealed samples; n-GaAs substrates, however, always show a negative slope of above bandgap SPV versus wavelength or absorption depth ($1/\alpha$).

Fig.3 shows the room temperature above bandgap SPV spectra of LT-GaAs #004 ($T_g = 250^\circ \text{C}$), the solid line, diamonds, and triangles are corresponding to the spectrum for as-grown LT-GaAs, LT-GaAs annealed at 850°C for 30 s, and n-GaAs substrate, respectively. From these spectra we can see, at just above bandgap energy, SPV response for as-grown LT-GaAs is ~ 6 times stronger than that for 850°C annealed LT-GaAs, and more than 200 times stronger than that for bulk n-GaAs. As explained in our previous studies [19-21], the weak SPV response for bulk n-GaAs, is mainly caused by its high conductivity (or high doping concentration N_D). While the difference of SPV amplitude between the as-grown and annealed LT-GaAs is believed to be mainly attributed to the difference of initial band bending (V_{bi}) (Chen et. al. have reported a initial band bending of $\sim 90 \text{ meV}$ for as-grown LT-GaAs ($T_g = 250^\circ \text{C}$) and a initial band bending of $\sim 5 \text{ meV}$ for 850°C annealed sample [5]).

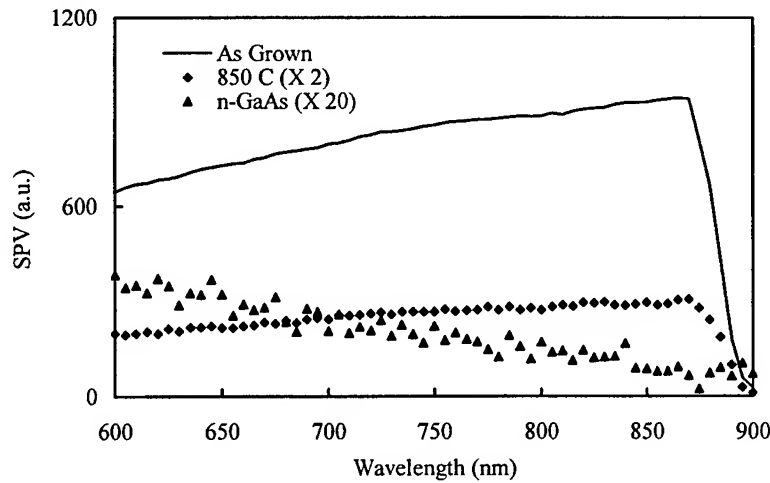


Fig. 3. Room temperature constant photon flux SPV spectra of as-grown LT-GaAs ($T_g = 250^\circ \text{C}$), LT-GaAs ($T_g = 250^\circ \text{C}$) annealed at 850°C for 30 s and n-GaAs ($n_o = 2 \times 10^{18} \text{ cm}^{-3}$)

Considering both as-grown and annealed LT-GaAs contain high concentration of surface (surface and space charge range) deep traps, which could lead to a high surface recombination velocity S_n (for electron) and S_p (for hole). According to our previous discussion [20], under this condition, the majority carrier back diffusion will have a considerable contribution to SPV, especially, for strong absorption (or small absorption depth) and small width of space charge range (W) like LT-GaAs. Fig. 4 recalls our pervious SPV simulation results for high surface recombination and weak initial band bending situations [20]. From these SPV plots, we can see SPV response of V_{oc}/V_t is approximately proportional to absorption depth $1/\alpha$, where V_{oc} is the measured open circuit voltage, V_t is the thermal voltage kT/q . Thus, the unique slope of SPV response vs. wavelength for LT-GaAs may attribute to the strong majority carrier back diffusion in LT-GaAs.

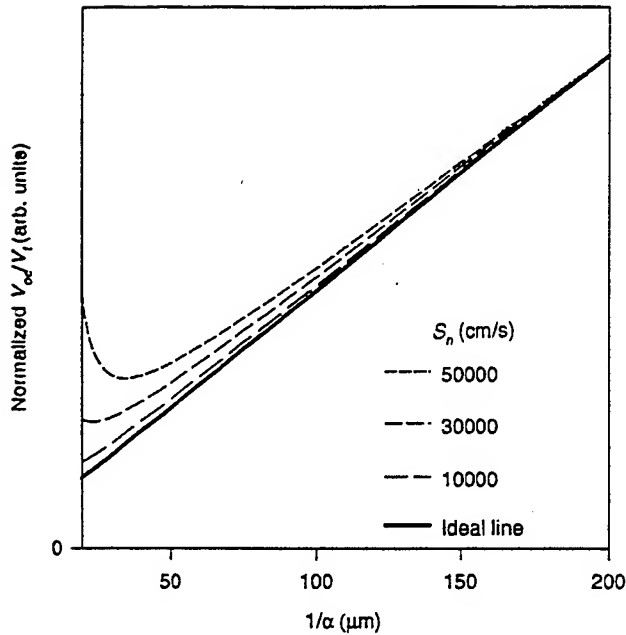


Fig. 4 SPV plot for high S_n and low V_{bi} :
 $V_{bi} = 100$ mV, $S_p = 10$ cm/s,
 $L_p = 10$ μ m $\Phi = 5 \times 10^{13}$ cm $^{-2}$ s $^{-1}$,
 $f = 0.1$, where f is the occupation
probability of trap.

On the other hand, compared with LT-GaAs, n-GaAs substrate is a weak surface recombination material. For high doping level of n-GaAs and low excitation level SPV measurement (i.e., our n-GaAs sample and SPV measurement conditions), $V_{bi} \gg V_t > V_{oc}$, and $\alpha W \ll 1$ are normally satisfied. As shown in previous work [20, 21], in this case, numerical calculations of SPV response have demonstrated that SPV response for materials with low surface recombination is approximately proportional to absorption coefficient α (or inversely proportional to wavelength λ). It is consistent with our results of SPV measurement of n-GaAs substrate.

4. CONCLUSION

In conclusion, we have reported on the carrier lifetime measurements for LT-GaAs grown at 200, 250, and 300 °C, respectively, and annealed at 700 °C for 30 s; the corresponding carrier lifetimes are 1.5, 2.2, and 12 ps. The carrier lifetime for the three as-grown LT-GaAs was found less than 150 fs. PR characterization of LT-GaAs has revealed that the extremely short carrier lifetime is responsible for the disappearing of PR features for as-grown LT-GaAs, while, the internal field non-uniformity caused by buried Schottky barrier around As precipitates responses for the PR spectral broadening of annealed LT-GaAs. We have first reported SPV spectra for both as-grown and annealed LT-GaAs, and presented qualitative explanation for the unique LT-GaAs SPV phenomena. We believe the unique SPV spectra of LT-GaAs may attribute to high surface recombination and weak initial band bending.

ACKNOWLEDGEMENT

The authors gratefully acknowledge a grant support from the Natural Science and Engineering Research Council of Canada (NSERC).

REFERENCES

1. M. R. Melloch, J. M. Woodall, E. S. Harmon, N. Otsuka, F. H. Pollak, D. D. Nolte, R. M. Feenstra, and M. A. Lutz, *Ann. Rev. Mat. Sci.* **25**, 547 (1995).
2. K. M. Yu, M. Kaminska, and Z. Liliental-Weber, *J. Appl. Phys.* **72**, 2850 (1992).
3. Y. H. Chen, Z. Yang, R. G. Li, Y. Q. Wang, and Z. G. Wang, *Phys. Rev. B* **55**, R7379 (1997).
4. H. Shen, F. C. Rong, R. Lux, J. Pamulapati, M. Taysing-Lara, M.utta, L. Calderon and Y. Lu, *Appl. Phys. Lett.* **61**, 1585, (1992).
5. Y. H. Chen, Z. G. Wang, and Z. Yang, *J. Appl. Phys.* **87**, 2923, (2000).
6. D. C. Look, D. C. Walters, M. O. Manasreh, J. R. Sizelove, C. E. Stutz, and K. R. Evans, *Phys. Rev. B* **42**, 3578 (1990).
7. M. O. Manasreh, D. C. Look, K. R. Evans, and C. E. Stutz, *Phys. Rev. B* **41**, 10272 (1990).
8. M. Kaminska, E. R. Weber, Z. Liliental-Weber, R. Leon, and Z. U. Rek, *J. Vac. Sci. Tech. B7*, 710 (1989).
9. D. C. Look, *Thin Solid Films* **231**, 61 (1993).
10. G. Witt, *Mat. Sci. and Engi. B* **22**, 9 (1993).
11. M. R. Melloch, N. Otsuka, K. Mahalingam, A. C. Warren, J. M. Woodall, and P. D. Kirchner, *Mat. Res. Symp. Proc.* **241**, 113 (1992).
12. F. W. Smith, *Mat. Res. Soc. Symp.* **241**, 3 (1992).
13. A. C. Warren, J. M. Woodall, J. Freeouf, D. Grischowsky, D. McInturff, M. R. Melloch, and N. Otsuka, *Appl. Phys. Lett.* **57**, 1331 (1990).
14. G. M. Chen, M. A. Sc. Thesis (1996).
15. Q. Svelto, and D. C. Hanna, *Principles of Laser*, Third Edition, Plenum Press, New York, P1-13 (1989).
16. D. E. Aspnes, *Surface Science* **37**, 418 (1973).
17. D. E. Aspnes, *Phys. Rev. B*, **10**, 4228 (1974).
18. G. M. Chen, H. E. Ruda, L. Jedral, Q. Liu, and C. Edirisinghe, OESC, Hamilton, (1995).
19. Q. Liu, H. E. Ruda, I. P. Koutzarov, L. Jedral, G. M. Chen, and M. Prasad, *Mat. Res. Soc. Symp. Proc.* **426**, 569 (1996).
20. Q. Liu, H. E. Ruda, and G. M. Chen, *J. Appl. Phys.* **79**, 7790 (1996).
21. Q. Liu, Ph. D. Thesis, (1996).

SESSION 8

Integrated Optical Components and Devices

Semiconductor Photonic Integration: A Regrowth Free Approach

John H. Marsh.

Dept. of Electronics & Electrical Engineering,
Rankine Building, Oakfield Avenue.
University of Glasgow, Glasgow, G12 8QQ, UK.

ABSTRACT

A robust impurity free quantum well intermixing process has been developed that allows complex photonic integrated circuits to be fabricated. Characteristics of the process are discussed and its attributes summarised. The use of the process in three widely differing fabricating applications is described: high-power high-brightness AlGaInP semiconductor laser diodes, nonlinear GaAs/AlGaAs waveguide devices and InGaAsP/InP crosspoint switches.

Keywords: Photonic integrated circuits, semiconductor laser, nonlinear optics, photonic switches, quantum well intermixing.

1. INTRODUCTION

An important goal for future optical communication systems is the development of photonic integrated circuits, in which high bit rate information is transmitted between active devices through low-loss waveguides. Such integration would provide considerable advantages in terms of device miniaturisation, resultant increases in component density and reductions in cost, improved reliability and robustness, simplified packaging and potential improvements in data handling rates. Quantum-well intermixing (QWI) techniques permit a postgrowth modification to the absorption edge of multiple-quantum-well (MQW) material, and therefore provide a flexible, reliable, simple and low-cost approach compared to competing integration schemes, such as selective area epitaxy, or selective etching and regrowth. QWI also allows novel devices to be created for applications other communications, and examples are given in this paper of high power lasers and nonlinear waveguide devices.

Since the initial demonstration of intermixing in the GaAs-AlGaAs system, a number of techniques have been developed including impurity induced disordering (IID)¹, impurity free vacancy disordering (IFVD)², various laser disordering processes^{3,4,5} and ion implantation induced disordering.⁶ IID techniques utilise surface dopant diffusion or ion implantation to introduce impurities within the crystal structure, the presence of which alters the Fermi level and changes the equilibrium concentration of certain point defects, resulting in an increased rate of atomic interdiffusion during a subsequent anneal stage⁷. The technique has been used to intermix GaAs-AlGaAs, InGaAs-InGaAsP, and InGaAs-InAlGaAs MQW structures with varying degrees of success. As the IID technique requires an annealing stage, particular problems are encountered for the InGaAs-InGaAsP MQW system, where the poor thermal stability of the material enables only limited differential shifts between intermixed and intermixing suppressed regions. IID can also have deleterious effects in terms of the electrical characteristics of integrated devices, and leads to increases in free carrier absorption due to the introduction of dopants within the active region, resulting in increased modal propagation losses.

IFVD is an extremely successful technique employed primarily in the GaAs-AlGaAs system, in which a high-temperature anneal induces the out-diffusion of Ga from the epilayer cap into a suitable dielectric cap (e.g., SiO₂). This leads to an increase in the Group III vacancy concentration at the surface and an enhanced Ga-Al interdiffusion rate². While certain caps enhance the out-diffusion, others suppress it. It is, therefore, possible to achieve spatially selective intermixing using photolithographic patterning of the appropriate capping layers. Both SrF₂⁸ and P:SiO₂⁹ have proved effective caps for suppressing the intermixing process, enabling the fabrication of extended cavity lasers with low passive section loss. The poor thermal stability of the InGaAs-InGaAsP system makes it difficult to suppress intermixing, leading to the generation of only small and unreliable differential shifts using IFVD. However this poor thermal stability has been used to great advantage in the photoabsorption-induced disordering (PAID) process, in which photons from a 1064 nm CW Nd:YAG laser are absorbed in the InGaAs-InGaAsP active region, with the subsequent carrier cooling and nonradiative recombination thermally intermixing the MQW layers⁵. The process allows large differential bandgap shifts to be achieved, with the processed material exhibiting extremely high optical and electrical characteristics. Spatial selectivity can be achieved by using a gold mask to reflect the incident photons and thereby prevent intermixing in regions in which it is not required. However, due to the thermal nature of the process, diffusion of heat beneath the gold mask leads to a poor spatial resolution for the process (100–200 μm), which limits its applications for monolithic integration. The use of ion

implantation to generate point defects through high-energy impact with the crystal matrix elements has been used widely in many III–V material systems (AlGaAs, InP, etc.). This involves the use of relatively high energy ion implants to considerable depths ($>1\text{ }\mu\text{m}$), usually with electrically inactive implant species e.g., P and As. Although successful, the requirement for specialised facilities for implantation makes this technique relatively complicated and expensive.

The intermixing technique used in the work described in this paper is related to IFVD, but makes use of sputtered SiO_2 films^{10,11}. The technique involves deposition of a thin film ($\sim 200\text{ nm}$) of sputtered SiO_2 , and subsequent annealing using a rapid thermal annealer (RTA). Point defect generation takes place at the surface of the semiconductor during the sputter deposition, and then, during a subsequent annealing step, the point defect diffuse through the underlying QWs, so giving rise to QWI. At the same time, SIMS studies show that group III elements (In and Ga) diffuse into the SiO_2 , as happens in conventional IFVD. However, QWI using sputtered SiO_2 take place at temperatures of 150 to 200 K lower than for conventional IFVD. The new technique has so far proved highly successful for all of the above mentioned material systems. In addition to its wide range of applicability, it is impurity free, low cost and involves relatively simple processing stages, with only photoresist required for inhibition of intermixing. In this paper, we present results for InGaAsP and GaAs/AlGaAs material systems as well as for the visible wavelength GaInP–AlGaInP MQW system for which no impurity free spatially selective intermixing technique has previously been demonstrated.

The content of the remainder of this paper is as follows: Section 2 describes the application of QWI to high power visible laser diodes; Section 3 describes the fabrication of photonic crosspoint switches in the GaInP–AlGaInP material system; Section 4 illustrates the applicability of the technique for the fabrication of quasi-phase matched nonlinear waveguide devices in the GaAs–AlGaAs system. In the final section, the results are summarised and some conclusions presented.

2. HIGH POWER VISIBLE LASER DIODES

GaInP/AlGaInP laser diodes have attracted considerable interest due to the widespread applications of visible laser radiation. Since the laser emission is at wavelengths within the red region of the visible spectrum, their potential in display applications is already being exploited, especially with regard to laser pointers. The high transmission of human tissue at these wavelengths has also led to GaInP/AlGaInP red laser diode devices being used for medical applications, most notably in cancer treatment using photodynamic therapy (PDT). The short wavelength also has advantages in optical storage applications such as CD-ROMs. There are other more specialised applications, for example the lasers can be used as pump sources for ultrafast tuneable lasers such as Cr:LiSAF and Cr:LiSCAF¹², which can provide the versatility of a tunable all solid state laser source as well as the unique characteristics of sub-picosecond pulses. All of these applications benefit from semiconductor laser sources that possess high powers and/or brightness.

Various schemes and geometries have been proposed to increase the brightness and power from semiconductor laser diodes. The majority of these solutions would benefit from effective facet passivation and/or a reliable monolithic integration technology. Approaches to facet passivation include sulphur treatment, cleaving in ultra high vacuum with the subsequent application of high band gap semiconductor, and etch and regrowth. These suffer from being difficult and costly to implement and, in the case of sulphur treatments, they are potentially hazardous. Furthermore, etching and regrowth is very undesirable for Al-containing alloys such as the GaInP/AlGaInP material system. The development of a QWI technology for this material system would enable the many problems associated with regrowth to be circumvented. Successful intermixing has previously been reported in the GaInP/AlGaInP system using impurity induced disordering (IID) by the surface diffusion of zinc¹³. However, while such IID techniques enable significant bandgap shifts to be realised, they degrade the electrical properties of intermixed material and, due to the presence of active dopants within the active region, free carrier absorption losses are increased¹⁴.

Because the sputtered SiO_2 QWI process uses vacancies, it preserves both the electrical and optical properties of intermixed material. In this Section, we describe the integration of low optical loss sections within laser diodes to give high power and high brightness operation.

2.1 ALGAINP MATERIAL

The structure used was a 670 nm double quantum well laser layer, grown on a (100) Si doped GaAs substrate misoriented 10° to the (111)A direction. The misoriented wafer ensured that ordering of the AlGaInP quaternary was minimised securing good laser performance. The layers starting from the substrate in growth sequence were a 500 nm Si doped ($3 \times 10^{18}\text{ cm}^{-3}$) GaAs layer, 1.0 μm Si ($6 \times 10^{17}\text{ cm}^{-3}$) doped $(\text{Al}_{0.7}\text{Ga}_{0.3})_{0.5}\text{In}_{0.5}\text{P}$ lower cladding layer, an undoped $(\text{Al}_{0.3}\text{Ga}_{0.7})_{0.5}\text{In}_{0.5}\text{P}$ waveguide layer, 1.0 μm Zn ($7 \times 10^{17}\text{ cm}^{-3}$) doped $(\text{Al}_{0.7}\text{Ga}_{0.3})_{0.5}\text{In}_{0.5}\text{P}$ upper cladding layer, a 20 nm Zn

($2 \times 10^{18} \text{ cm}^{-3}$) doped $\text{Ga}_{0.41}\text{In}_{0.59}\text{P}$ barrier reduction layer, and finally a 300 nm Zn ($1 \times 10^{19} \text{ cm}^{-3}$) GaAs capping layer. Within the waveguide region two strained 6.8 nm wide $\text{Ga}_{0.41}\text{In}_{0.59}\text{P}$ quantum wells were centrally placed separated by a $(\text{Al}_{0.3}\text{Ga}_{0.7})_{0.5}\text{In}_{0.5}\text{P}$ barrier. The lasing spectrum was centred on 676 nm with a turn-on voltage of 1.987 V. The threshold current density for infinite cavity length was 330 A cm^{-2} .

2.2 INTERMIXING

As described above, the intermixing process simply involves the deposition of a thin film of sputtered SiO_2 and a subsequent high temperature anneal. Samples were annealed in a Rapid Thermal Processor (RTP) and 77 K photoluminescence (PL) measurements were used to determine the resultant bandgap shifts. Fig. 1 shows typical shifts from intermixed and suppressed material. It can be seen that the shift obtained is of the order of 40 nm, (>100 meV). Moreover, the full-width at half maximum FWHM of the PL peak only increases from 5.5 nm for suppressed material to 6.5 nm for intermixed material.

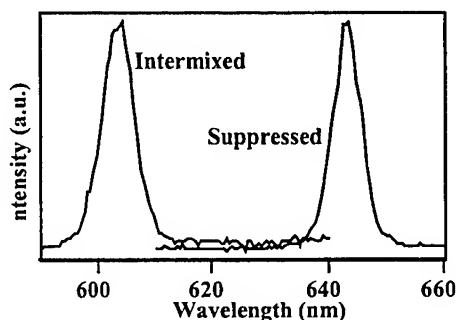


Fig. 1. Low temperature (77K) PL spectra from a sample possessing regions of both intermixed and suppressed material.

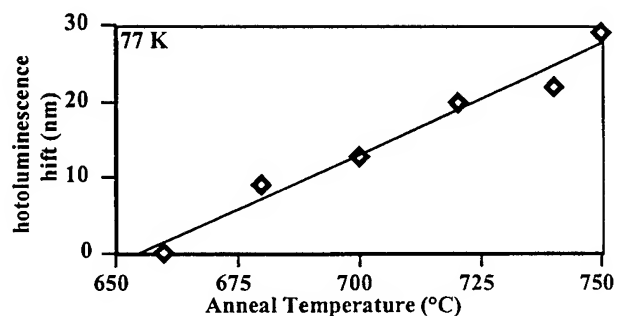


Fig. 2. Shift of PL wavelength against annealing temperature for anneal time of 60 s

Fig. 2 shows the PL shifts obtained for samples annealed at various temperatures, for a constant duration of 60 s. A near-linear relationship between the anneal temperature and PL shift is obtained. The maximum shift shown is 29 nm (equivalent to 91 meV). Control samples capped with SiO_2 deposited by electron beam evaporation or plasma enhanced chemical vapour deposition were annealed simultaneously and they exhibited no bandgap shift over the same temperature range.

2.3 NON-ABSORBING MIRRORS

One of the simplest but most effective uses of QWI is for the fabrication of non-absorbing mirrors (NAMs). The high power operation of semiconductor laser diode devices is limited by the occurrence of catastrophic optical damage (COD) at the laser facets. NAMs are bandgap-widened regions at the laser facet, which reduce optical absorption and so raise the COD threshold. Such bandgap widening can be achieved using QWI.

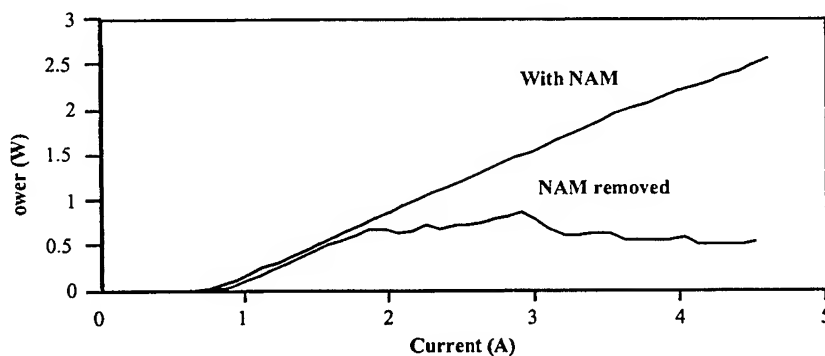


Fig. 3. OSLs with NAMs and after NAMs are removed

To demonstrate the viability of NAMs in the AlGaInP/GaInP material system, oxide stripe lasers (OSLs) were fabricated with NAMs using the material structure described above. The NAMs had a bandgap shift of over 100 meV. The lasers were 1500 μm long and 100 μm wide with no AR/HR coatings. The devices were tested in the pulse regime and then the NAMs were cleaved off and the devices re-tested. Fig. 3 shows the light-current curve for a laser with NAMs and the same device with the NAMs removed. The effect of the NAMs is clear since, before they were cleaved off, the device was capable of delivering over 2.5 W of light at 670 nm. When the NAMs are removed, each facet can only deliver ~ 300 mW before COD occurs.

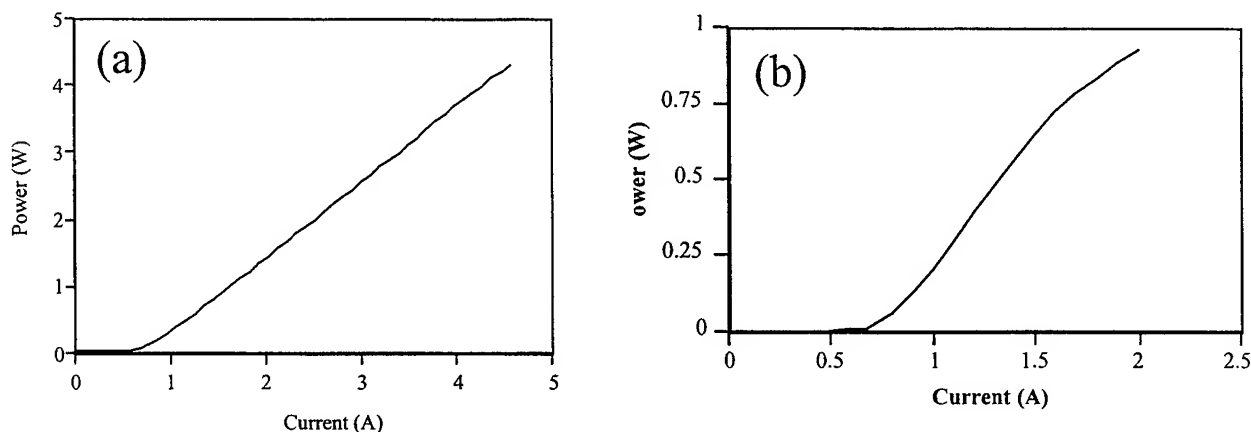


Fig. 4. (a) Pulsed and (b) CW operation of OSL with NAMs.

The OSLs were also evaluated to determine their CW performance. Fig. 4(a) shows the combined power delivered from both facets in pulsed mode from a typical uncoated NAM device, with the device producing more than 4 W of optical power. Fig. 4(b) shows the CW characteristics of the same device at room temperature bonded p-side down onto a copper heatsink: it produces a total of 1 W at 2 A before thermal effects start to impair the device performance. At present various schemes, including the use of diamond heatsinks, are being implemented to increase the CW power.

2.4 EXTENDED CAVITY LASERS

High-brightness single-lobed operation of OSLs is unlikely due to optical filamentation. The use of laser arrays is a potential route to obtaining high power and brightness, however such devices tend to operate with a double lobed far-field due to the nearest neighbour coupling forcing adjacent array elements to operate 180° out of phase. Another solution makes use of the fact that light from filaments experiences larger diffraction angles than that from the fundamental (Gaussian) mode of the device. If passive slab waveguide sections are placed between the gain section and the facets, the slab waveguide sections act as diffraction regions within the laser cavity and ensure the fundamental mode experiences the lowest cavity loss (Fig. 5). Single-lobed far-fields can then be produced.

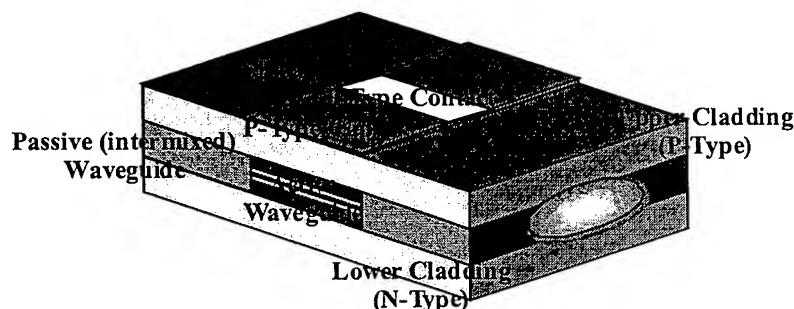


Fig. 5. Schematic diagram of the Extended Cavity Laser (ECL).

The light-current characteristics of such an extended cavity lasers (ECL) and a comparable OSL are shown in Fig. 6(a). The OSL has a stripe width of 75 μm and a cavity length of 750 μm giving a threshold current of ~ 400 mA. The gain section of the ECL is also 75 μm wide and 750 μm long, and its passive regions are 1000 and 500 μm long. Fig. 6(a) shows that the threshold current of the ECL is not significantly higher than that of the OSL and its efficiency is only lower by around 3-4%. The far-field behaviour of the lasers is shown in Fig. 6(b). At twice threshold, the OSL has an extremely divergent beam (8°) with many lobes due to filamentation within the gain section. Single lobed behaviour can be observed from the ECL laser with a FWHM of 2° .

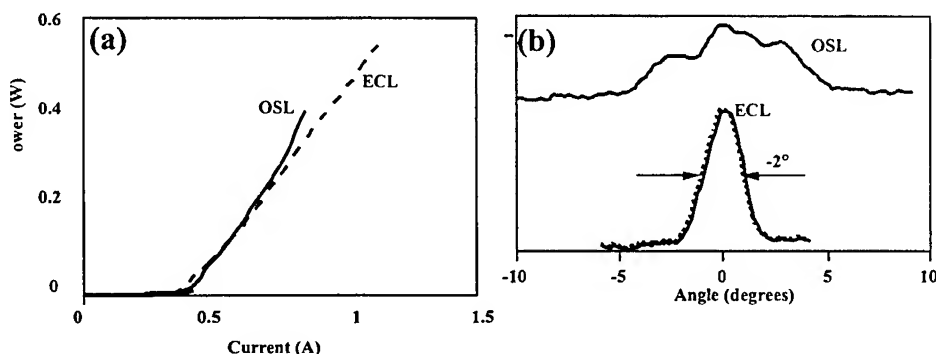


Fig. 6. (a) Light-current and (b) far-field characteristics of typical OSLs and ECLs.

3. PHOTONIC CROSSPOINT SWITCH

3.1 INTRODUCTION

In this Section we report the fabrication of a 2×2 crosspoint switch, which monolithically integrates passive waveguides and electro-absorption modulators on one chip, using the sputtered SiO_2 technique. Optical switching and routing are highly desirable functions in future optical communication networks, particularly in optical packet switching¹⁵. Monolithic integration of electro-absorption (EA) modulators, and passive components to form a 2×2 crosspoint switch is an ideal approach for such optical switches, giving both a high switching speed and low insertion loss. For many system purposes, the operation wavelength for the switches should be 1.55 μm , the wavelength of optical communication at which silica based optical fibre has minimum loss. The absorption edge for the passive components, e.g. multimode interference (MMI) couplers, is, therefore, required to be blue-shifted from the operation wavelength to such a degree that direct bandgap absorption is negligible. Due to the requirements of a high ON-OFF switching ratio and low insertion loss for the EA modulators, the band-edge for the modulator sections should also have a blue-shift of around 30-50 nm, compared to the operation wavelength. Although some 2×2 switches have been reported previously, the implementation of different bandgaps has relied on regrowth or selective growth¹⁶, which require either repeated use of metal-organic vapour phase epitaxy (MOVPE) or molecular beam epitaxy (MBE) facilities and are, therefore, inflexible and expensive.

Use of the sputtered SiO_2 technique for quantum well intermixing (QWI) makes it possible to integrate the passive and active components monolithically and opens a way to allow extensive photonic integration which is cost effective and flexible. Here we describe a 2×2 crosspoint switch based on EA modulators, using the QWI approach. Fig. 7 shows the schematic structure of the switch. Two MMI couplers and four EA modulators are linked by passive waveguides to form a 2×2 crosspoint structure. The entire structure was 3.2 mm long, with the modulators being 500 μm long.

3.2 PIC FABRICATION

The material used to fabricate the switches was a laser structure, with an emission wavelength of around 1.55 μm . It was grown on a (100)-oriented n-type InP substrate with an active region consisting of five 65 \AA InGaAs wells with 120 \AA InGaAsP ($\lambda_g = 1.26$ μm , where λ_g is the wavelength corresponding to the bandgap) barriers. The active region was bounded by a stepped graded index (GRIN) waveguide core consisting of InGaAsP confining layers. The thicknesses and compositions of these layers (from the QWs outward) were 500 \AA of InGaAsP with $\lambda_g = 1.18$ μm and 800 \AA of $\lambda_g = 1.08$ μm . The structure, which was lattice matched to InP throughout, was completed by a 1.4 μm thick InP cladding layer and an

InGaAs contact layer. The first 0.2 μm of the upper cladding layer was an undoped spacer layer and the remaining 1.2 μm was doped with Zn to a concentration of $7 \times 10^{17} \text{ cm}^{-3}$. The lower cladding layer was Si doped to a concentration of $5 \times 10^{18} \text{ cm}^{-3}$. The waveguide core was undoped, thus forming a *pin* structure with the intrinsic region restricted to the QWs and GRIN layers.

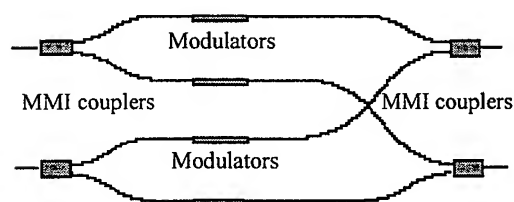


Fig. 7. Schematic illustration of a 2×2 crosspoint switch

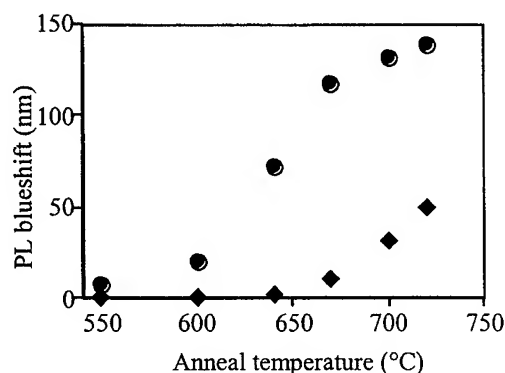


Fig. 8. Bandgap shifts as function of anneal temperature for samples coated with 200 nm sputtered SiO₂ (circle) and 500 nm PECVD SiO₂ (diamond).

Once again, QWI is the key to achieve photonic integration. Photoluminescence (PL) measurements were performed at 77 K to determine the bandgap shifts. Fig. 8 shows the blue-shift for the samples coated with 200 nm of sputtered SiO₂ and PECVD SiO₂ as function of annealing temperature. Samples with sputtered SiO₂ caps start to exhibit bandgap shifting at significantly lower temperatures than those required for thermally induced intermixing of the material, as illustrated by the shifts observed for samples capped with PECVD SiO₂, which are zero up to 650 °C. From Fig. 8, it can be seen that, for temperatures >650 °C, it is possible to obtain two different bandgap shifts in one annealing stage. For this application, the blue-shift in the modulator section should be ~30–50 nm compared to the bandgap of as-grown material, while a larger blue-shift is required for the passive waveguide components.

Future 2×2 switches will require three bandgaps, so that amplifiers can be included to compensate for the coupling, splitting and absorption losses in the device. For this reason, the bandgap of the as-grown wafer was specified to be suitable for the amplifier section, and the bandgaps of both the modulator and passive waveguides were tuned by quantum well intermixing. For the three-bandgap switches, the bandgap shift in the amplifier section of the devices must be completely suppressed, so a process is being developed that can precisely control the bandgap shift across a sample. However, the modulators in the three-bandgap switch will be tuned by the same amount as those reported here, and their performance should be similar.

To utilise the technique to realise two bandgaps, a sample was patterned using photolithography such that the modulator section of the sample was protected with 500 nm of PECVD SiO₂ only, while for the passive section no protection layer was deposited. After sputtering, the samples were cleaned to remove the photoresist on the top of the samples and annealed at a temperature of 720 °C for 60 s. Fig. 9 shows the resultant 77 K PL spectra. As can be seen, a blue-shift of 40 nm occurs for the modulator region, while the blue-shift in the passive region is around 102 nm, which together perfectly meet the requirements for the modulator and passive sections.

After intermixing, 4 μm wide ridge waveguides were formed using CH₄/H₂ reactive ion etching. The devices were completed by the deposition of a 200 nm PECVD silica film, the wet etching of a p-contact window, substrate thinning and contact evaporation. The p-side contact was restricted to only the modulator section of the waveguides and, to ensure electrical isolation between the active and passive sections, the InGaAs contact layer on the passive ridge waveguide was removed by wet-etching. The sample was annealed at 360 °C for 60 s using RTA, and then cleaved into individual devices. Finally, individual devices were mounted onto a copper block with silver epoxy and wire bonding was carried out.

3.3 TESTING AND RESULTS

A tunable semiconductor laser, 1480-1580 nm, was used to assess the device performance. Light from the laser was endfire coupled into the device. A polarisation controller was used to ensure that only the TE mode was excited in the waveguide. The output from the device was coupled into a fibre and then to an optical spectrum analyser to monitor the output power. A reverse DC bias, which could be adjusted from 0 to 2.5 V, was applied to the device. Fig. 10 shows the transmitted optical power as function of the reverse bias voltage for the bar states. Similar results were observed for the cross state.

An estimate of the loss in the switches was made by comparing the losses in a straight waveguide with those of the switches. The straight waveguides, which had same structure as that of the switches, were fabricated using an identical process. The propagation losses in the straight waveguides were then measured using the Fabry-Perot method. A loss of 11 ± 3 dB cm^{-1} has been obtained at a wavelength of 1.55 μm . From this result, it can be deduced that the insertion loss of the whole structure is around 10 dB, which includes the 3 dB losses due to the MMI couplers. Although the radiation loss from the curved waveguide is another factor to be considered, modelling has shown it is sufficiently low that it can be neglected when the radius of the curvature of the waveguides is >200 μm . In our design, a radius of 500 μm was employed.

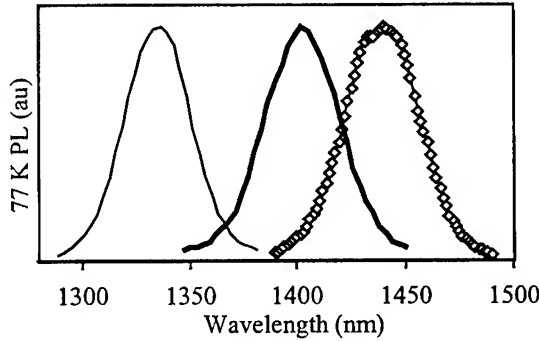


Fig. 9. 77 K PL spectra for modulator region (thick line), passive region (thin line), and as-grown material (diamonds).

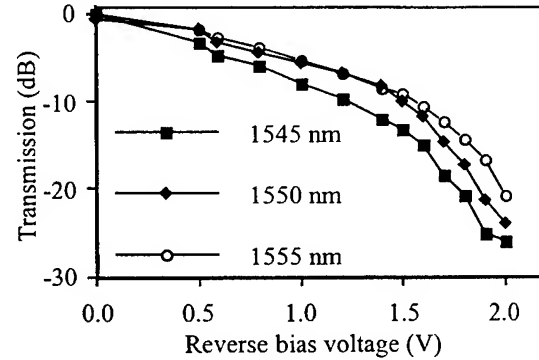


Fig. 10. Measured transmission power against reverse bias for different wavelengths

4. QUASI-PHASE MATCHING IN GALLIUM ARSENIDE SUPERLATTICE WAVEGUIDE

We finally report a novel application of QWI in the GaAs-AlGaAs system, in which second harmonic generation is observed by quasi-phase matching superlattice waveguide^{17,18}. Quasi-phase matching was achieved through the modulation of the nonlinear coefficient $\chi_{zy}^{(2)}$, which was realised by periodically tuning the superlattice bandgap.

The use of second-order nonlinearities in III-V semiconductors, which have intrinsically large $\chi^{(2)}$ coefficients, offers the possibility of efficient optical frequency conversion. The mature GaAs-based fabrication technology and the potential for direct integration with laser diodes could lead to the development of numerous functional devices,^{19,20} ranging from second harmonic generation structures, to integrated devices for difference frequency generation (with applications in WDM channel conversion²¹), parametric amplification and oscillation. Due to the lack of intrinsic birefringence in III-V semiconductor structures and the large dispersion, it is difficult to phase match the second-order nonlinear process. Recently a technique has been developed to induce an artificial birefringence by embedding native oxide layers in the waveguide, but work is still in progress to overcome the excessive optical losses incurred in these waveguides.²² Greater flexibility is possible using quasi-phase matching (QPM) with initial studies in semiconductors investigating domain inversion using growth on patterned substrates.^{23,24} Although promising, patterned substrate growth is still associated with high optical losses and low yield. An alternative technology, described here, is domain disordering (DD-QPM) which may not achieve

the same depth of modulation in the nonlinear coefficient, but can have dramatically lower losses and be more straightforward to implement.²⁵

The modulation of $\chi^{(2)}$ in semiconductor waveguides using DD-QPM can be achieved, for example, by implantation, which periodically destroys the lattice symmetry thus reducing $\chi^{(2)}$ (non-zero coefficients require the lack of inversion symmetry).²⁶ Here we realise DD-QPM through the modulation of the heterostructure bandgap, which subsequently provides a modulation in the bulk-like $\chi_{yz}^{(2)}$ and $\chi_{zy}^{(2)}$ coefficients when operating near a material resonance. Values for this modulation in GaAs/AlAs superlattices are predicted to be as large as those attained in periodically poled LiNbO₃ (PPLN).²⁷ Control over the bandgap can be achieved using QWI, by which lateral control over heterostructure bandgap can be obtained with no substantial increase in the optical losses.²⁸ In addition, DD-QPM using QWI is attractive since it is based on non-destructive, lithography-based semiconductor fabrication. An alternative method for using QWI to obtain DD-QPM is based on the growth of asymmetric heterostructures where additional $\chi^{(2)}$ tensor elements can be induced (xzx , zxx and zzz) which revert to zero upon quantum well intermixing.²⁹ However these induced coefficients tend to be relatively small (typically a few pmV⁻¹)²⁵ and hence the absolute modulation is rather limited.

In this work we present measurements of the second harmonic (SH) generation from third-order quasi-phase matched gratings achieved using QWI. The structure comprised 0.6 μm of a symmetric superlattice (SL) waveguide core made of 14:14 monolayers of GaAs:AlAs respectively. The lower and upper cladding were bulk Al_{0.6}Ga_{0.4}As of 1.5 μm and 1 μm width respectively. A 100 nm GaAs cap was used to cover the upper cladding. The structure was nominally undoped, and was grown by molecular beam epitaxy (MBE) on a semi-insulating GaAs substrate. The room temperature photoluminescence emission wavelength of the structure was 745 nm from the central portion of the wafer. This design allows the operating fundamental wavelength, ~ 1550 nm, at 30 meV below the half-bandgap to avoid two-photon absorption and use the modulation attained in the resonant component of $\chi^{(2)}$ as the bandgap of the structure is modulated (further details are given in reference 27). Domain disordering was achieved using sputtered silica defect induced intermixing. After annealing, the room temperature PL wavelength was observed to be 743 nm in the suppressed region and 688 nm in the disordered region.

The optical source used in the measurements was a synchronously-pumped, singly resonant femtosecond PPLN optical parametric oscillator (OPO) based on a semi-monolithic cavity design. The OPO was pumped by a Kerr-lens mode-locked Ti:sapphire laser at 820 nm providing pulses of ~ 100 fs duration at 80 MHz repetition rate. An average power of 80 mW was obtained from the OPO prior to chopping with a 50% duty cycle for lock-in detection. A 4 mm-long sample with third-order grating periods between 5.8 μm to 12.4 μm was mounted on an end-fire coupling rig. TE polarised light from the OPO was launched into the waveguide, while the output of the waveguides was aligned into a monochromator with a 0.1 nm resolution. A photomultiplier tube (PMT) was then used to detect the second harmonic at the output of the monochromator using an internal PMT amplifier, and a lock-in amplifier. The PMT has a spectral range between 185 nm and 900 nm and therefore no signal resulting from the fundamental could be detected. The power into the waveguide was plotted as a function of the detected fundamental power at the waveguide output to ensure the linearity of their relation confirming that there is no significant two-photon absorption of the fundamental.

The periodic modulation in the SL bandgap induces a modulation in $\chi^{(2)}$, as illustrated in Fig. 11, where intermixing occurs under the sputtered silica caps only. There are two possible phase-matching geometries: (1) type-I phase-matching exploiting the modulation in $\chi^{(2)}$, accessed by launching the fundamental TE polarised at the input and the SH expected with TM polarisation and (2) type-II phase-matching exploiting the modulation in $\chi_{yz}^{(2)}$, accessed with a mixed TE:TM polarisation for the fundamental and the SH expected with TE polarisation. These two cases will be phase-matched at different QPM periods due to the variation in propagation constant with polarisation mode. The superlattice breaks the degeneracy between $\chi_{yz}^{(2)}$ and $\chi_{zy}^{(2)}$ which exists in bulk semiconductors with a zinc-blende structure, but is restored upon QWI with the larger modulation predicted for $\chi_{yz}^{(2)}$.²⁷ However, for simplicity in this work we shall report on the type-I phase-matching where we launch the fundamental solely TE polarised and investigate the polarisation of the SH.

A typical measurement of the SH spectra is shown in Fig. 12, where there is a clear SH signal for TM polarisation and there is no signal for the TE. The measured bandwidth of the SH shows a FWHM of ~ 3 nm in comparison to the fundamental which had a FWHM of ~ 11 nm. The additional spectral narrowing is due to the fact that the bandwidth of the QPM grating is smaller than that of the input optical pulse. The SH signal only appears when the output spectrum of the OPO is tuned so that it contains the appropriate wavelength for the QPM grating under test. Fig. 13 shows a typical result for the dependence of the SH power on the fundamental power. The best fit to the slope on a log-log plot is 1.9 confirming the expected parabolic power dependence with no observed saturation. The wavelength of the SH generated as a function of the various grating periods available in the sample is plotted in Fig. 14. As the grating period is decreased the QPM wavelength also

decreases in this normally dispersive medium. The lower wavelength limit was reached when the SH photon energy approaches the material bandgap and it experiences excessive band-tail absorption.

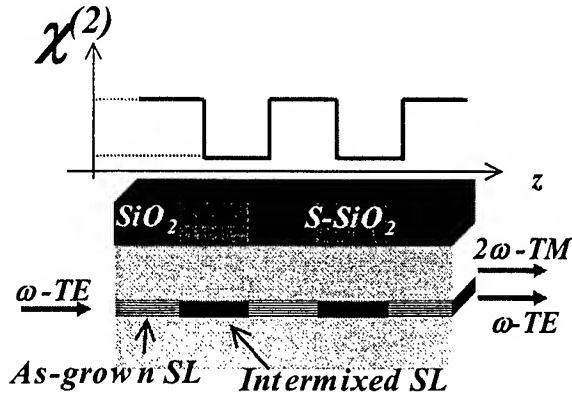


Fig. 11 Illustration of the second harmonic generation process used in this work, where the resonant part of the $\chi_{xy}^{(2)}$ bulk coefficient is modulated by selective area quantum well intermixing to achieve QPM.

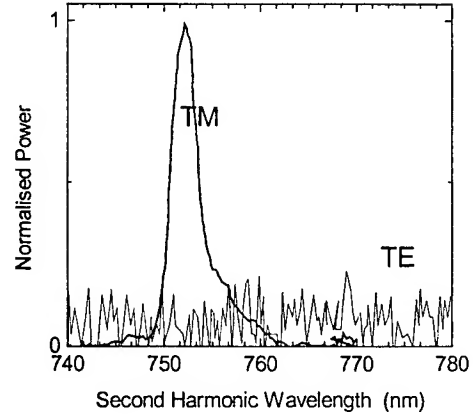


Fig. 12 Second harmonic spectra for both output polarisations. The waveguide used is with a QPM period of 12.4 μ m

At the PMT the largest average SH power measured was 25 nW for a wavelength of 758 nm. However the optical measurement system has a measured 5 dB loss between waveguide and PMT and, with a further 30% reflection loss at the rear facet of the waveguide, we can make a best estimate of the average SH power of \sim 110 nW in the waveguide. In this case we measure a transmitted fundamental average power of 250 μ W which, with a 30% loss at the rear facet and a measured optical loss of \sim 2 dB/cm in the waveguide, translates to an average pump power of \sim 450 μ W just after the front facet of the waveguide. We note that there is a reduction of approximately 2 orders of magnitude in fundamental power between the OPO output and the guided-mode, due principally to coupling losses.

Hence we obtain a maximum SH conversion of \sim 0.02% with the present setup for which there is considerable scope for improvement: (1) The coupling losses presently severely limit the fundamental power launched into a guided mode using the end-fire rig. (2) The femtosecond optical source has a bandwidth larger than the QPM grating and hence the majority of the guided fundamental power is not phase-matched. Furthermore dispersion will result in significant temporal broadening of the fundamental pulse as it propagates in the waveguide. A transform-limited picosecond source would avoid both of these restrictions. (3) In this sample we have used a third-order grating in order to ensure the resolution of the intermixing process is sufficient. However the period of the grating for phase matching is larger than our first estimates and first-order gratings should be acceptable with potentially an order-of-magnitude improvement in conversion efficiency. Indeed we were able to observe SHG by first-order QPM using our shortest grating period at the long-wavelength limit of our optical source.

5. CONCLUSIONS

Various devices using a robust impurity free QWI process have been fabricated and their operation outlined. Characteristics of the process have been discussed and shifts of well in excess of 100 meV are obtained. Bandgap shifted lasers have been fabricated to demonstrate the integrity of the material after thermal processing. NAMs are shown to increase the COD threshold of OSL devices. High brightness ECLs are shown to significantly improve the beam quality and the insignificant change in the threshold current and slight decrease of the external efficiency demonstrates that the process is low loss. In the GaInAsP system, a 2 \times 2 crosspoint switch has been fabricated using a single stage of epitaxy and QWI integration technology. A modulation depth of 25 dB was obtained for the operation wavelength of 1.55 μ m, indicating the sputtered

SiO₂ process did not produce any dramatic degradation in the performance of the MQW structure as an EA modulator. The insertion losses were estimated to be around 10 dB. The fabrication process can easily allow the inclusion of amplifiers to compensate for the losses in the switch, as well as the coupling loss between optical fibres and the switch. Finally, in the GaAs-AlAs system, second harmonic generation by quasi-phase matching in superlattice waveguides was demonstrated. Quasi-phase matching was achieved through the modulation of the bulk-like nonlinear coefficient $\chi_{20}^{(2)}$, which was realised by periodically tuning the superlattice bandgap with quantum well intermixing. Second harmonic generation was demonstrated for fundamental wavelengths between 1480 nm and 1520 nm, from third-order gratings with periods between 10.5 μm and 12.4 μm respectively. The second harmonic signal spectra were acquired and had a FWHM of ~ 3 nm determined by the QPM bandwidth. An average power of ~ 110 nW was obtained for the second harmonic using an average pump power of ~ 450 μW .

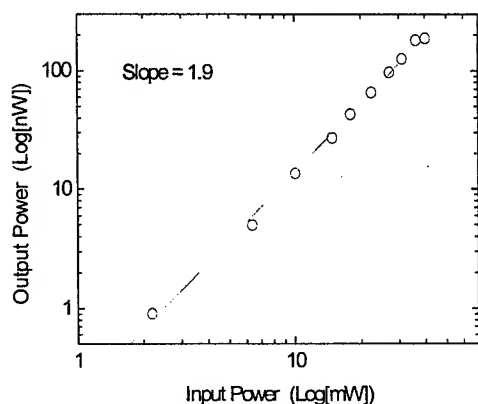


Fig. 13 Second harmonic output average power (measured at PMT) as function of fundamental input average power (measured after the chopper) on a log-log scale. The best fit to the slope is 1.9 confirming the expected parabolic power dependence.

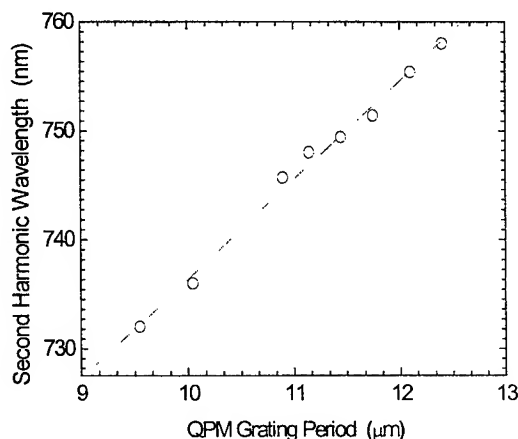


Fig. 14 Tuning curve indicating the second harmonic wavelength as function of the waveguide QPM period.

6. ACKNOWLEDGEMENTS

This work was funded by the EPSRC (UK) and the EU ESPRIT project OFCORSE II.. The author acknowledges the work of many individuals at the University of Glasgow, in particular A. Saher Helmy, C. J. Hamilton, O. P. Kowalski, B. C. Qiu, Y. H. Qian, R. M. De La Rue, D. C. Hutchings, J. S. Aitchison, A. C. Bryce, J. M. Arnold. In addition, much of the work was carried out in collaboration with other institutes, including the Universities of Cardiff (P. Blood, P. Smowton), Bristol (M. Owen, I. H. White, R. V. Penty), Strathclyde (A. Franzen, D. K. Hunter, I. Andonovic) and St Andrews (C. T. A. Brown, K. Moutzouris, M. Ebrahimzadeh).

REFERENCES

1. W. D. Laidig, N. Holonyak, Jr., M. D. Camras, K. Hess, J. J. Coleman, P. D. Dapkus, and J. Bardeen, "Disorder of an AlAs-GaAs superlattice by impurity diffusion," *Appl. Phys. Lett.*, vol. 38, pp. 776-778, 1981.
2. L. J. Guido, N. Holonyak Jr., K. C. Hsieh, R. W. Kaliski, W. E. Plano, R. D. Burnham, R. L. Thornton, J. E. Epler, and T. L. Paoli, "Effect of dielectric encapsulation and As overpressure on Al-Ga interdiffusion in Al_xGa_{1-x}As quantum well heterostructures," *J. Appl. Phys.*, vol. 55, pp. 540-542, 1989.

3. J. E. Epler, F. A. Ponce, F. K. J. Endicott, and T. L. Paoli, "Laser disordering of GaAs/AlGaAs by diffusion of laser incorporated Si," *J. Appl. Phys.*, vol. 64, pp. 3439–3444, 1988.
4. C. J. McLean, J. H. Marsh, R. M. De La Rue, A. C. Bryce, B. Garrett, and R. Glew, "Layer selective disordering by photo-absorption induced thermal diffusion in InGaAs/InP based multiple quantum well structures," *Electron. Lett.*, vol. 28, pp. 1117–1119, 1992.
5. A. McKee, C. J. McLean, G. Lullo, A. C. Bryce, R. M. De La Rue, J. H. Marsh, and C. C. Button, "Monolithic integration in InGaAs-InGaAsP multiple-quantum-well structures using laser intermixing," *IEEE J. Quantum Electron.*, vol. 33 pp. 45–55, 1997.
6. B. Tell, J. Shah, P. M. Thomas, J. W. Sulhoff, K. F. Brown-Goebler, A. D. Giovanni, B. I. Miller, and U. Koren, "Phosphorous ion implantation induced intermixing of InGaAs/InP quantum well structures," *Appl. Phys. Lett.*, vol. 54, pp. 1570–1572, 1989.
7. D. G. Deppe and N. Holonyak Jr., "Atom diffusion and impurity-induced layer disordering in quantum well III–V semiconductor heterostructures," *J. Appl. Phys.*, vol. 64, pp. 93–113, 1988.
8. B. S. Ooi, K. McIlvaney, M. W. Street, A. S. Helmy, S. G. Ayling, A. C. Bryce, J. H. Marsh, and J. S. Roberts, "Selective quantum well intermixing in GaAs-AlGaAs structures using impurity free vacancy diffusion," *IEEE J. Quantum Electron.*, vol. 33, pp. 1784–1793, 1997.
9. P. Cusamano, J. H. Marsh, M. J. Rose, and J. S. Roberts, "High-quality extended cavity ridge lasers fabricated by impurity free vacancy diffusion with a novel masking technique," *IEEE Photon. Technol. Lett.*, vol. 9, pp. 282–284, 1997.
10. O. P. Kowalski, C. J. Hamilton, S. McDougal, J. H. Marsh, A. C. Bryce, R. M. De La Rue, B. Vögele, C. R. Stanley, C. C. Button and J. S. Roberts: 'A Universal Technique For Quantum Well Intermixing', *Applied Physics. Letters*, Vol.72, No.5, pp.581-583.
11. S. D. McDougall, O.P. Kowalski, C. J. Hamilton, F. Camacho, B. C. Qiu, M.L. Ke, R. M. De La Rue, A. C. Bryce, J. H. Marsh, "Monolithic integration via a universal damage enhanced quantum-well intermixing technique", *IEEE J. Sel. Topics In Quantum Electronics*, 4, pp. 636-646, 1998
12. M. D. Perry, S. A. Payne, T. Ditmire, R. Beach, G. J. Quarles, W. Ignatuk, R. Olsen and J. Weston: 'Better Materials Trigger Cr:LiSAF Laser Development', *Laser Focus World*, September 1993, pp. 85
13. K. Itaya, M. Ishikawa, G. -I. Hatakoshi and Y. Uematsu, "New window-structure InGaAlP visible light laser diodes by self-selective Zn diffusion-induced disordering", *IEEE J. of Quantum Electron.*, Vol. 27, No. 6, 1991., pp 1496-1500
14. J. H. Marsh, "Quantum well intermixing", *Semiconductor Sci. Technol.* Vol. 8, 1993, pp. 1136-1155
15. D. K. Hunter, D. Cotter, R. B. Ahmad, W. D. Cornwell, T. H. Gilfedder, P. J. Legg, I. Andonovic, "2x2 buffered switch fabrics for traffic routing, merging, and shaping in photonic cell networks", *J. Lightwave Technol.*, 15, pp. 86-101, 1997
16. F. Dorgeuille, B. Mersali, M. Feuillade, S. Sainson, S. Slemphkes, M. Foucher, "Novel approach for simple fabrication of high-performance InP-switch matrix based on laser-amplifier gates", *IEEE Photon. Technol. Letters*, 8, pp. 1178-1180, 1996
17. A. Saher Helmy, D. C. Hutchings, T. C. Kleckner, J. H. Marsh, A. C. Bryce, J. M. Arnold, C. R. Stanley, J. S. Aitchison, C. T. A. Brown, K. Moutzouris and M. Ebrahimzadeh 'Quasi-Phase-Matching in GaAs-AlAs Superlattice Waveguides via Bandgap Tuning using Quantum Well Intermixing', *CLEO 2000 postdeadline paper*, San Francisco.

18. A. Saher Helmy, D. C. Hutchings, T. C. Kleckner, J. H. Marsh, A. C. Bryce, J. M. Arnold, C. R. Stanley, J. S. Aitchison, C. T. A. Brown, K. Moutzouris and M. Ebrahimzadeh 'Quasi-Phase-Matching in GaAs-AlAs Superlattice Waveguides via Bandgap Tuning using Quantum Well Intermixing' submitted to Optics Letters.
19. J. S. Aitchison, M. W. Street, N. D. Whitbread, D. C. Hutchings, J. H. Marsh, G. T. Kennedy and W. Sibbett, IEEE J. Sel. Topics Quantum Electron. 4, 695 (1998).
20. J. B. Khurgin, E. Rosencher, Y. J. Ding, J. Opt. Soc. Am. B 15, 1726 (1998).
21. S. B. Yoo, J. Lightwave Technol. 14, 955 (1996).
22. A. Fiore, S. Janz, L. Delobel, P. van der Meer, P. Bravetti, V. Berger, E. Rosencher, Appl. Phys. Lett. 72, 2942 (1998).
23. S. B. J. Yoo, R. Bhat, C. Caneau and M. A. Koza, Appl. Phys. Lett. 66, 3410 (1995).
24. C. B. Ebert, L. A. Eyres, M. M. Fejer, J. S. Harris, Jr., J. Cryst. Growth 202, 187 (1999).
25. D. C. Hutchings and J. M. Arnold, Phys. Rev. B 56, 4056 (1997).
26. S. Janz, M. Buchanan, F. Chatenoud, J. P. McCaffrey, R. Normandin, U. G. Akano, I. V. Mitchell, Appl. Phys. Lett. 65, 216 (1994).
27. D. C. Hutchings, Appl. Phys. Lett. 76, 1362 (2000).
28. C. J. Hamilton, J. H. Marsh, D. C. Hutchings, J. S. Aitchison, G. T. Kennedy, W. Sibbett, Appl. Phys. Lett. 68, 3078 (1996).
29. M. W. Street, N. D. Whitbread, C. J. Hamilton, B. Vögele, C. R. Stanley, D. C. Hutchings, J. H. Marsh, J. S. Aitchison G. T. Kennedy and W. Sibbett, Appl. Phys. Lett. 70, 2804 (1997).

Design Of Wideband Dispersion Compensating Optical Fiber Device : Based on Higher Order LP₁₁ Mode

Aditya Goel and J.L. Rana
Department of Electronics & Computer Sc. Engineering
Maulana Azad College Of Technology
Bhopal - 462007, India.

ABSTRACT

With the advent of erbium - doped fiber amplifiers (EDFA), the fiber loss in the 1550 nm window can be easily compensated and the transmission distance extended even to few thousands of kms without the use of electronic regenerators. However, in order to utilize the vast transmission capacity of the Single mode fiber, the positive chromatic dispersion exhibited by the existing standard single mode fibers remains to be the primary limitation. This development has motivated the researchers to find new techniques for compensating the positive dispersion of the existing single mode fiber network. It has been demonstrated that higher order modes exhibit large negative dispersion when operated close to their cutoff wavelength. This negative dispersion can be used to compensate the positive chromatic dispersion of the existing single mode fiber. In this paper we discuss the issues related to the design and optimization of a passive device, dispersion compensating fiber (DCF), which is capable of compensating the chromatic dispersion of the existing fiber over a wide wavelength span from 1500 nm to 1600 nm. This wavelength range encompasses both the bandwidth of EDFA and the low attenuation window of single mode optical fiber. A finite element method (FEM) is used to calculate the dispersion characteristics of a single mode optical fiber with arbitrary refractive index profile. Computer simulations show that an optimally designed dispersion compensating fiber can reduce the dispersion of standard fiber from 18.62 ps / km - nm to 0.45 ps / km - nm over the entire wavelength span, when it is added with the existing standard fiber in a ratio of 20.56 : 1.

Keywords : Erbium Doped Fiber Amplifier (EDFA), Finite Element Method, Wideband Dispersion Compensating Fiber (1500 to 1600 nm), Negative Dispersion, Generalized Multiple Index Profile, Higher Order LP₁₁ Mode, WDM system (1500 to 1600 nm).

1. INTRODUCTION

Optical fibers are now the medium of choice for long distance telecommunications systems. The widespread use of optical fibers is driven by the unique properties of fibers : very low attenuation (< 0.2 dB / km), large potential bandwidth (> 1 Tb/s in the 1550 nm band)¹. The practical implementation of erbium - doped fiber amplifiers (EDFA's) has made it possible to transmit light waves over thousands of kilometers of single - mode fiber without electronic regeneration and therefore , has reduced the importance of attenuation in the 1550 nm window as a key fiber-optic system design parameter. The full exploitation of fiber capacity is not easy, but tremendous progress has been made over the past 20 years, during which the capacity of long - haul terrestrial networks doubled every two years¹. The use of dispersion shifted and dispersion flattened fibers are some of the obvious solutions. However, these are not always cost effective, especially for conventional fiber networks that are already installed. Dispersion flattened fibers are excellent for the new network to be installed in future, but not for the existing network. A significant portion (Millions of kms) of the installed optical fiber in today's networks comprises of standard single mode step index fiber , exhibiting zero dispersion wavelength at 1310 nm but rather high dispersion at 1550 nm. The use of EDFA's to upgrade and simplify most existing fiber systems is therefore presently limited by chromatic dispersion of embedded networks. The span length that is possible without electronic regeneration is limited by the pulse spreading that occurs with EDFA operation in the 1550 nm window. As such, a variety of techniques have been explored in recent years , for upgradation of the existing optical fiber networks from 1310 nm to

1550 nm wavelength region. This development has created a need for dispersion compensation techniques and has motivated much recent work in this area. Periodic conversion of the signal to higher order modes has been proposed as one of the promising techniques for dispersion compensation. It has been demonstrated that higher order modes exhibit large negative dispersion when operated close to their cutoff wavelength². This negative dispersion can be used to compensate the positive chromatic dispersion of the existing single mode fiber. Because the dispersion can be quite large near cutoff, relatively small amount of fiber is needed to compensate a given amount of positive dispersion.

Large dispersion of opposite sign can be engineered at a single wavelength by designing a fiber so that the guided mode's propagation constant ' β ' varies rapidly with the wavelength. However, the advent of wavelength division multiplexing (WDM) means that dispersion should be compensated not just at one wavelength, but over as large wavelength range as possible. The wavelength range over which high dispersion can be sustained is fundamentally limited by the refraction index variation in the fiber, which determines the limits within which ' β ' is constrained³. If n_1 is the maximum index in the core of the fiber and n_2 is the index of the far cladding, then a guided mode's index β/k is bounded by :

$$n_1 \geq \beta/k \geq n_2 ; \text{ Where 'k' is the free space propagation constant.}$$

A larger index contrast between core and cladding therefore, permits a high dispersion over a greater wavelength range. However, in conventional fibers comprising region of glass with different composition, this index contrast is limited by material incompatibilities that cause loss. A standard transmission system would not tolerate the additional loss that results from propagating through the additional length of dispersion compensating fiber (DCF). In an amplified system however, the additional loss is compensated by EDFA's that are present in the system.

In this paper we explore the possibility of designing a wideband dispersion compensating fiber based on LP₁₁ mode using multiple index profile. This device can compensate the dispersion over a wide span of wavelength. The wavelength span over which dispersion compensation is to be achieved is selected from 1500 to 1600 nm. This wavelength span is centered around low attenuation window (near 1550 nm) and also encompasses the EDFA band. A generalized refractive multiple index profile is used⁴, which is capable of generating a variety of earlier proposed profiles. Quadratic FEM⁵ is used to solve the scalar wave equation for carrying out the dispersion calculations of an arbitrary index profile.

2. DISPERSION COMPENSATION BASED ON LP₁₁ MODE

The important features of the dispersion compensation technique² based on higher order LP₁₁ mode are : a compensating fiber that guides higher order LP₁₁ mode, an input mode converter to convert the LP₀₁ mode of the single mode fiber span into the higher order LP₁₁ mode of the compensating fiber, and an output mode converter to convert back to the fundamental LP₀₁ mode in the output single - mode fiber. The compensating fiber is inserted periodically in the existing fiber optic link. The mode converters also acts as the matching devices between the conventional fiber and the compensating fiber that might have different core radii. Mode converters can be accomplished through grating coupling² by introducing a periodic perturbation in the core region of the fiber that has period matched to the inter modal beat length $L_B = 2\pi / (|\beta_1 - \beta_2|)$ between the two modes to be coupled. Here β_1 and β_2 are propagation of the two modes to be coupled.

Excess losses for these devices are often less than 1 dB, with reported coupling efficiencies of better than 99 %^{2,6}. Grating based mode converters can be made broad band and coupling efficiencies better than 90% can be achieved over a wide spectral width of 74 nm². Fibers different from compensating fiber are used to make the mode converter because operation near cutoff provides less bandwidth for mode conversion.

2.1 Dispersion Compensating Fiber Design

Dispersion Compensation demonstrated by Craig D. Poole et al. ², using step index profile is effective only over a very narrow bandwidth (30 nm). However with the advent of WDM systems , it is highly desirable to obtain dispersion compensation over a wide range of wavelength. A dispersion compensating fiber based on LP₁₁ mode is designed here, which is capable of compensating the chromatic dispersion of the existing fiber over a wide span of wavelength, and thus making it suitable for WDM system. A generalized multiple index profile ⁴ is used here , which can generate a variety of multiple cladded profiles eg. Step Index, W - Profile, Triple - Clad, Quadruply - Clad etc. Dispersion calculations for arbitrary varying refractive index profile are carried out by using the Quadratic FEM approach ⁵. A simple addition of the two components (Material and Waveguide dispersion) to give total chromatic dispersion is justified here, as the negative waveguide dispersion of the DCF is going to be much larger compared to the material dispersion.

Let the total dispersion of the Dispersion Compensating fiber (DCF) at the wavelength λ be given by $D_{DCF}(\lambda)$ and that of the conventional step index fiber ⁷ by $D_{CMF}(\lambda)$. The compensated dispersion at a particular wavelength λ can now be calculated by the relation :

$$D_{comp}(\lambda) = \frac{D_{DCF}(\lambda) + (d) D_{CMF}(\lambda)}{d + 1} \quad (1)$$

Where 'd' is the length ratio in which the above two fibers are concatenated.

The whole problem is considered as an optimization problem with $D_{comp}(\lambda)$ as the optimization parameter for a particular wavelength. For the whole wavelength span over which compensation is to be achieved , the maximum absolute value of $D_{comp}(\lambda)$ is selected as the optimizing parameter. The $D_{comp, max}$ is therefore minimized with respect to various profile parameters (a : core radius, n_2 : refractive index of cladding , α : exponential factor , N : No. of crossings within the core radius) and the length ratio 'd' over the entire wavelength span. The profile solutions are thus iterated to an optimum using an optimization algorithm (Simplex technique). In our earlier work ⁴, Compensating fiber has been designed for the wavelength range from 1480 to 1580 nm, but the design gives poor dispersion compensation especially between the wavelength range from 1530 to 1570 nm (EDFA band). Moreover the wavelength range is not centered around 1550 nm (low attenuation window). This is not a desirable characteristic and hence the design of DCF has been subsequently modified here by selecting a new wavelength range, which is centered around 1550 nm .

2.2 Numerical Results and discussion

The dispersion compensating fiber is designed here for the wavelength range from 1500 to 1600 nm. This wavelength span is centered around 1550 nm, which is the low attenuation window of the silica based fiber. It also covers the band of EDFA (1530 - 1570 nm). The existing conventional single mode fiber ⁷ exhibits maximum dispersion of about 18.62 ps /km - nm over the wavelength range from 1500 to 1600 nm. The optimization algorithm converges with in the desired accuracy after 132th iteration. Computations shows that for $n_1 = 1.50$, the minimum value of $D_{comp, max} = 0.45$ ps / km -nm is obtained with the set of optimized parameters , $a = 5.9896 \mu m$, $n_2 = 1.4666$, $\alpha = 0.02218$, $N = 4$, $d = 20.56$. Fig. 1 shows the optimized profile(Quadruply Cladded) of the designed DCF for the above profile parameters. It is different from the conventional Step Index profile by the separate structure which has been added in the near cladding. This modification ultimately results in exhibiting large negative dispersion. Fig. 2 shows the transverse field distribution of the LP₁₁ mode as a function of axial distance 'r' at the longest wavelength of 1600 nm , which is closer to cutoff wavelength . The modal field which starts decaying near the first cladding region is again trapped due to the nearby additional structure and thus mode power further extends into the cladding, the group velocity necessarily increases. Thus, the group - delay time which is the reciprocal of the group velocity decreases further. Obviously the group - delay also decreases with respect to the increase in wavelength as more and more power travels with the cladding. This gives rise to the negative dispersion. The large

magnitude of the negative dispersion results from the rapid transition with wavelength of mode power from the core to the cladding especially near cutoff. The modal field thus seems to be further extended into the cladding and this may increase the fiber susceptibility towards the bending losses, as we are operating close to the cutoff wavelength (1645 nm). The cutoff wavelength for LP_{11} mode is found by searching for the maximum wavelength that yield solutions to the scalar wave equation, when propagation constant is at its minimum value. Though in this case the modal field even at the longer wavelength (1600 nm) is reasonably guided inside the proposed fiber. Moreover the band of EDFA is quite far from the longest wavelength of 1600 nm. Therefore it is expected that the bending losses will be negligible if the fiber is not bent over a radius smaller than 20 cm⁸. Fig. 3 shows the dispersion characteristics of the designed DCF carrying LP_{11} mode, over the spectral range of 1500 nm to 1600 nm. The designed profile exhibits large negative dispersion (-260 to -390 ps / km - nm) over the entire wavelength span. The average compensated dispersion characteristics carrying LP_{11} mode, as a function of wavelength for the above parameter values is shown in Fig. 4. The large negative dispersion of an optimally designed DCF can reduce the dispersion of standard fiber from 18.62 ps/ km - nm to 0.45 ps/ km - nm over the entire wavelength span of 1500 to 1600 nm, when it is added in a length ratio of 20.56 : 1. This dispersion characteristics has the interesting feature of confining the compensated dispersion within ± 0.1 ps / km -nm over the entire band of EDFA (1530 - 1570 nm), which makes it more suitable for future WDM system.

3. CONCLUSION

In this paper a novel design of wideband dispersion compensating fiber device based on higher order LP_{11} mode is proposed. The positive dispersion of the existing conventional single mode fiber can be compensated by the large negative dispersion exhibited by the higher order LP_{11} mode, when operated close to its cutoff region. Computation shows that the best dispersion compensation can be achieved and the dispersion of the existing fiber can be reduced from 18.62 to 0.45 ps / km -nm, when 20.56 parts of existing fiber are added with 1 part of DCF. The proposed DCF profile is a Quadruply cladded (QC) profile. From the field distribution of LP_{11} mode at 1600 nm, it seems that the field is better guided inside the proposed fiber. It has also been observed that the compensated dispersion can be confined within ± 0.1 ps / km - nm over the wavelength range from 1530 - 1570 nm (EDFA band). This means that the dispersion of the existing fiber can be reduced to ± 0.1 ps / km - nm over the wavelength range from 1530 to 1570 nm. The bending losses will also be negligible for the above wavelength span, as it is quite far away from the cutoff wavelength of LP_{11} mode. This interesting feature will enable the existing single - mode fiber networks to reap the maximum benefits of EDFA's.

4. REFERENCES

- [1] M.J. Yadlowsky, E.M. Deliso, and V.L. Silva, " Optical fibers and amplifiers for WDM systems," *Proc. of IEEE*, vol. 85, No. 11, pp 1765 - 1777, 1997.
- [2] C.D.Poole, Jay M. Wiesenfield, and Ashish M. Vengsarkar, "Optical fiber-based dispersion compensation using higher order modes near cutoff," *IEEE / OSA J. Lightwave Technol.*, vol. 12, No. 10, pp 1746-1758, 1994.
- [3] T.A. Birks, D. Mogilevtsev, J.C. Knight, and P.St.J. Russell, " Dispersion compensation using single - material fibers," *IEEE Photon. Technol.*, vol. 11, No. 6, pp. 674 - 679, 1999.
- [4] A. Goel et al., " Wide band dispersion compensating optical fiber," *IEEE Photon. Technol.*, vol.84, pp. 1668 - 1670, 1996.
- [5] Aditya Goel and J.L. Rana, " Wideband optical waveguides with arbitrary index profile : Propagation solution by finite element approach," *Proc. of S.P.I.E.*, (Part of S.P.I.E. Conference on Optical Fiber Communication Taiwan), vol. 3420, pp 346 - 354, Taipei, 1998.
- [6] H.G. Park and B.Y. Kim, " Intermodal Coupler using permanently photoinduced grating in two - mode optical fiber," *Electron. Lett.*, vol. 25, pp 797 - 798, 1989.

[7] L.Cohen and D.Kalish,"Single-mode fiber from research and development to manufacturing," *AT & T Tech. J.*, vol. 16, pp 19-32, 1987.

[8] A. M. Vengsarkar and W.A. Reed," Effect of refractive index profiles on two - mode optical fiber dispersion compensator," *Optics. Lett.*, vol. 2, pp 585 - 587, 1990.

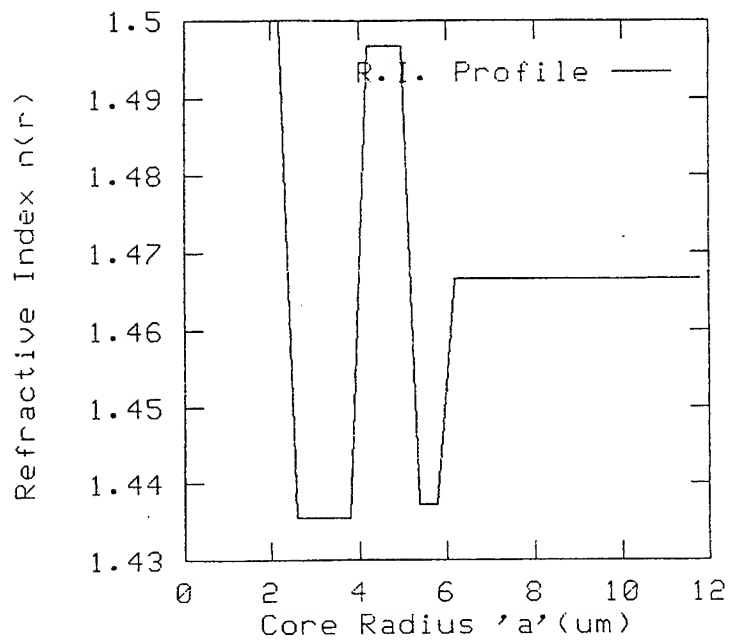


Fig. 1 Proposed Optimized Quadruply Cladded Profile for DCF (LP_{11} mode)

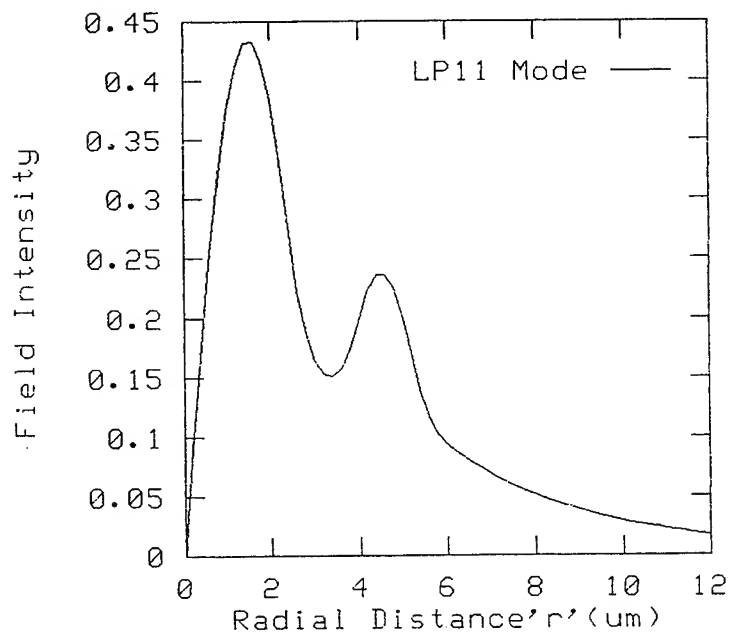


Fig. 2 Transverse Field Distribution of LP_{11} mode inside DCF at 1600 nm wavelength

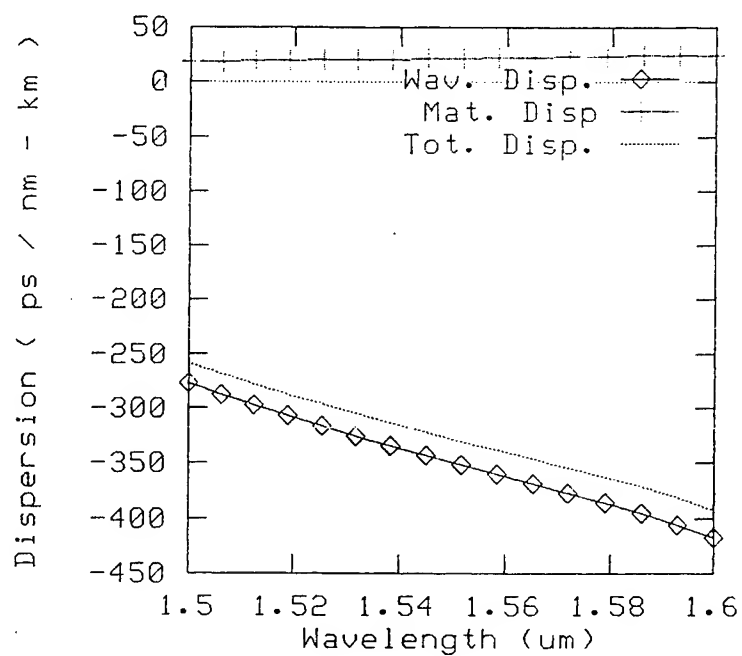


Fig. 3 Dispersion Characteristics of DCF based on LP₁₁ mode.

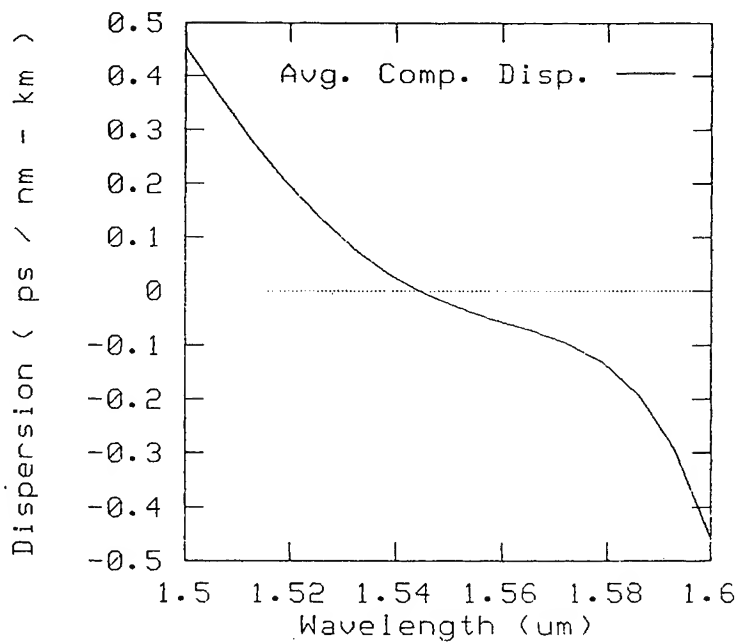


Fig. 4 Avg. Compensated Dispersion Characteristics using DCF (LP₁₁ mode).

Integrated Magneto optic Waveguide Material Structures and Devices^{*†}

Chen S. Tsai

Center for Applied Science and Engineering Research, Academia Sinica,
Taipei, Taiwan 11529

and

Department of Electrical and Computer Engineering, University of California,
Irvine, CA 92697, U.S.A.

ABSTRACT

Recent advances in the preparation of Bi- and Ce-substituted (doped) yttrium iron garnet (YIG) films on gadolinium gallium garnet (GGG) and semiconductor substrates such as gallium arsenide (GaAs), the design of hybrid material structures, and the construction of wideband integrated microwave and magneto optic (MO) devices, and their potential applications are presented.

Keywords: Magnetic Film, Yttrium Iron Garnet (YIG), Gadolinium Gallium Garnet (GGG), YIG-GaAs Hybrid Layer Structure, Integrated Magneto optic Devices, Integrated Microwave Devices, Magneto optic Bragg Cell Modulator, Magnetostatic Wave, Integrated Acousto optic Devices

1. INTRODUCTION

A variety of insulating, ferroelectric, and semiconducting materials and layered structures have been utilized for construction of integrated acousto optic (AO) devices [1]. In the meantime, integrated magneto optic (MO) devices are also being developed, and shown to possess a number of unique capabilities [2-4]. As to the materials for integrated MO devices, although yttrium iron garnet (YIG) film remains the only viable base material, a number of significant advances have been made recently in YIG-based material in terms of doping, substrate materials, layer structures, and devices. In this paper, such advances are presented and discussed.

2. WAVEGUIDE MATERIALS PREPARATION

Despite the lack of better alternative to the basic YIG films at present, significant advances in terms of the deposition techniques, doping (or substitution) in YIG films, and the substrate materials are being made. In this Section two relatively new deposition techniques are described.

2.1. Metalorganic Chemical Vapor Deposition (MOCVD) Technique

YIG films have been prepared using various techniques such as sputtering, liquid phase epitaxy (LPE), vapor phase epitaxy (VPE), and pulsed laser deposition (PLD) [4(a)]. The MOCVD technique was used for deposition of YIG films at a relatively low deposition temperature as a function of the composition. Note that a high deposition temperature is required in the conventional LPE, which is capable of producing high quality epitaxial single crystal YIG waveguide films. The samples with high Ce concentration (for substitutions of yttrium ions Y) have been grown on lattice-matched GGG substrate at a relatively low temperature (around 600°C) and have shown excellent magnetic and optical properties as well as

* Supported by the Academia Sinica, Taiwan and the ONR, U.S.A.

† To be presented at Photonics Taiwan, July 26-28, 2000

large MO (e.g. Faraday rotation) effects [5]. Furthermore, high quality YIG films have been grown on semiconducting substrates such as GaAs, InP and Si via MgO buffer layer at a low substrate temperature [5]. Note that the MgO buffer layer deters the decomposition and chemical reaction of the semiconducting substrates.

2.2. Pulsed Laser Deposition Technique

Bismuth-substituted YIG films were previously prepared by laser ablation [6]. Ce-substituted YIG films have also been grown on (111) GGG substrates at relatively low temperature (790°C) using pulsed laser ablation of the $\text{Ce}_1\text{Y}_2\text{Fe}_5\text{O}_{12}$ ceramic pellet target [7]. The thickness and quality of the films were controllable by the ablation time and the oxygen partial pressure. For example, the FMR absorption linewidth was found to be inversely proportional to the oxygen partial pressure.

3. HYBRID MATERIAL STRUCTURES

YIG/GGG-based MO waveguide devices are generally grouped into three types: isolators, sensors, and Bragg cell modulators. The first type of devices utilizes non-reciprocal properties of such MO waveguides, while the other two types of devices do not.

An optical isolator is a device which is used to keep reflected lights from returning to the light source that may cause instability. A commonly used material structure for channel waveguide isolators is shown in Fig. 1 [8]. The triple-film structure consists of two Bi-substituted YIG layers and one rare earth iron garnet (REIG) of high optical loss. With application of an external magnetic field for saturation of the film along the channel waveguide the triple-film serves to rotate the plane of polarization of an incident light by 45 degrees as is required. The external magnetic field required was subsequently replaced with sputter-deposited thin film SmCo permanent magnets directly over the MO waveguide [9]. Other versions of waveguide isolators and that using non-reciprocal phase shift and/or interferometric architectures [10-18] have also been constructed. Finally, various schemes for integrating MO garnet films with III-V semiconductor materials have also been reported [12-15].

An MO sensor utilizes Faraday effect to sense and measure magnetic fields or currents [19-21]. The same triple-film material structure of Fig. 1 can be used as the active part of fiber magnetometers [20]. The change in the magnetic domains of the magnetic material in response to an external magnetic field causes variation in the polarization of an incident light through the Faraday effect from a polarization maintaining fiber. By using an analyzer this variation in polarization will in turn cause a variation in the intensity and be detected at the far end of the fiber [20].

As to the third type of devices, YIG/GGG layer bonded on dielectric or metallic substrates has been the long-standing structure for construction of magnetostatic wave (MSW)-based thin-film microwave [22] and MO Bragg cell devices [2]. With the increasing needs and prospects toward realization of integrated microwave and MO devices composite structures of both hybrid and monolithic types that involve YIG or YIG/GGG and GaAs, InP or Si have been examined. Here we shall limit the discussion to those related to MSW-based microwave and MO devices that utilize YIG/GGG-alumina or YIG/GGG-GaAs hybrid material structures. Fig. 2 shows the basic delay-line configuration and architecture for the MSW-based devices using the hybrid material structure. A pair of microstrip lines at a separation L is incorporated on GaAs or alumina (or quartz) substrate. An YIG layer grown on GGG or GaAs is then brought into contact with the microstrip lines for excitation and reception of the MSW. Depending on the direction of the bias magnetic field three distinct modes of the MSWs, namely, magnetostatic surface waves (MSSW), magnetostatic forward volume waves (MSFVW) and magnetostatic backward volume waves (MSBVW) may be excited and propagated [2,3]. While the general

characteristics of the MSW-based devices using such basic delay-line configuration are similar to that of the SAW-based device counterparts [3], the magnetic field-dependent carrier frequency-wave number characteristics of the MSWs involved facilitates the unique and desirable electronic tunability of the resulting devices. Such electronic tunability is important in the resulting analog microwave devices such as phase shifters, delaylines, filters, couplers, and oscillators with applications to wideband real-time RF signal processing [22].

It is clear that utilization of the GaAs substrate enables the prevalent GaAs-based microwave technology be employed toward miniaturization and ultimate integration of the resulting microwave and MO devices. On-going work in this author's group on wideband microwave bandstop (notch) filters which utilize such GaAs-based microstrip lines together with the YIG/GGG films will be presented in Section V.

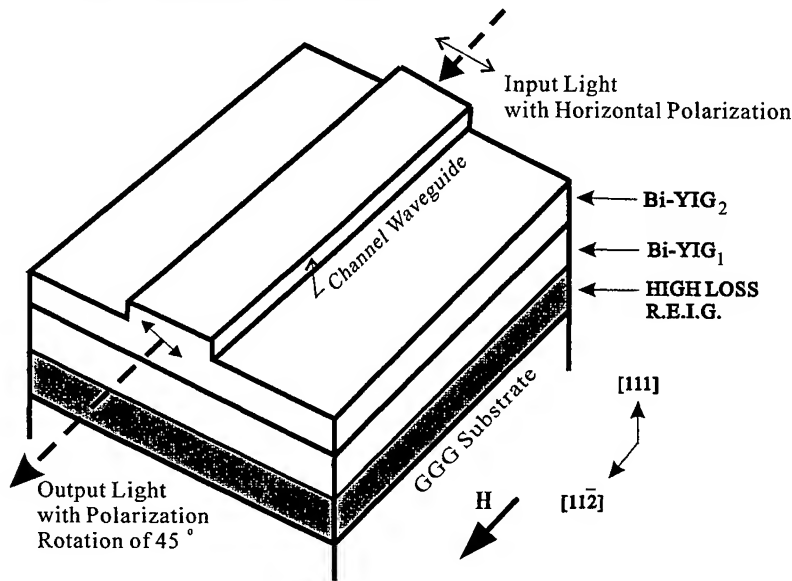


Fig. 1 Triple YIG/GGG Layer Structure for Magneto-optic Waveguide Isolator

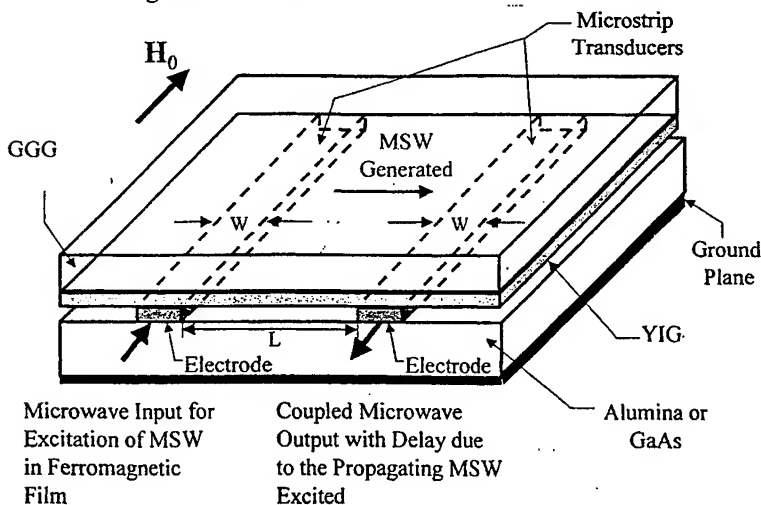


Fig. 2 Technique for Generation and Detection of Magnetostatic Waves

4. MAGNETOSTATIC WAVE-BASED INTEGRATED MAGNETOOPTIC DEVICES

4.1. Basic Magneto-optic Bragg Cell Modulator

A basic coplanar guided-wave MO Bragg interaction configuration with the MSWs in YIG/GGG waveguides [2] and the resulting Bragg cell modulator is shown in Fig. 3. MSWs result from propagation of electron spin precession around a bias magnetic field. MSWs can be readily and efficiently generated by applying a microwave signal to a microstrip line deposited directly on pure or substituted- YIG-GGG substrate or brought over it. The carrier frequency of the MSWs can be tuned, typically from 0.5 to around 35 GHz, by simply varying an external bias magnetic field in synchronism with the carrier frequency of the microwave signal. The corresponding range of wavelength for the MSW is as large as 1,000 to 0.5 μm . MO Bragg interactions between the guided-optical waves and the MSWs result from the moving diffraction gratings induced by the latter via Faraday and Cotton-Mouton effects [2].

The Bragg-diffracted light is scanned in the plane of the waveguide when the carrier frequency for the MSW is varied at a fixed bias magnetic field. The diffracted light can also be scanned at a fixed carrier frequency of the MSW by varying the bias magnetic field. This is based on the fact that the wave number of the MSW not only depends on the carrier frequency, but also the bias magnetic field H_0 . The latter is not possible with AO Bragg diffraction. The guided-wave MO Bragg diffraction has resulted in a miniaturized MO Bragg cell modulator and hybrid integrated MO Bragg-type devices. Since a very large range of velocity is associated with the MSW, e.g., one to three orders of magnitude higher than that of the SAW, the transit time of the MSW across the aperture of the incident light beam and thus the speed of the resulting MO space switches, scanners, and RF spectrum analyzers can be one to three orders of magnitude faster than their AO counterparts [1].

The diffraction efficiency of the MO Bragg cell modulators were greatly enhanced recently. First, we note that a maximum Bragg diffraction efficiency of 12% was previously measured in a modulator that utilized a 5.0 mm interaction length in a Bi-doped YIG/GGG waveguide and a uniform bias magnetic field [2]. The required RF drive power was 2.0 watts. Recently, the Bragg diffraction efficiency was increased by three-to six-fold using a non-uniform bias magnetic field [23]. Most recently, enhancement of Bragg diffraction efficiency by two-to four-fold was accomplished by inserting an electrical feedback loop to the MO Bragg cell modulator [24]. Further increase in Bragg diffraction efficiency together with a tilted bias magnetic field is also expected [25].

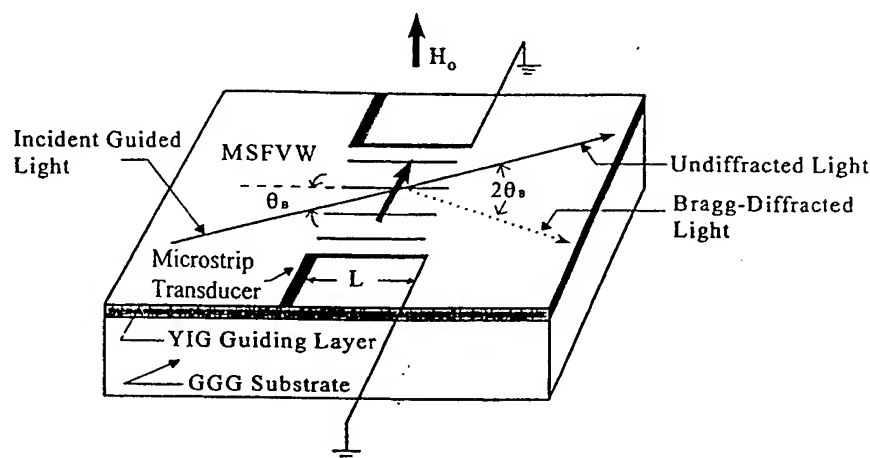


Fig. 3 A Basic Planar Waveguide Magneto-optic Bragg Cell Modulator

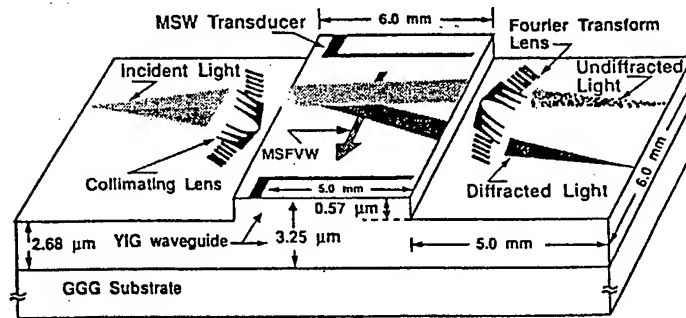


Fig. 4 Integrated Magneto-optic Bragg Cell Modulator in YIG-GGG Taper Waveguide Structure

4.2. Integrated MO Bragg Cell Modulator

As in the integrated AO device modules, a collimation-focusing waveguide lens pair is required in a variety of integrated MO device modules such as RF signal processors, optical space switches and scanners, and optical frequency shifters and modulators [1]. For this purpose, a *curved* hybrid ion-milled collimation-focusing lens pair of parabolic contour has been integrated with a MO Bragg cell modulator in a common YIG-GGG taper waveguide substrate as shown in Fig. 4 [26].

The tapered YIG-GGG waveguide structure served to accommodate simultaneously the requirements for large MO Bragg bandwidth and high lens throughput. The initial layer thickness of a Bi-doped YIG waveguide, 6.0 X 16.0 mm² in size, was 3.25 μm. The two end regions (each 5.0 mm in length) of the tapered waveguide were ion-milled down to 2.68 μm in several steps in order to produce a tapered transition, and thus ensure a high transmission for the light beam. The curved hybrid lenses with 4.0 mm focal length and 0.8 mm aperture were then fabricated onto the two end regions using the ion-milling technique. The measured focal spot profiles obtained at 1.3 μm wavelength from the curved hybrid lenses show sidelobe levels lower than 12.3 dB from the main lobe for the incident light angle up to +3.5° from the lens axis. The level of coma was also much lower than that of the flat hybrid lenses. The resulting integrated MO Bragg cell modulator [26] has provided performance figures such as a bandwidth of 260 MHz at the center carrier frequency of 10.0 GHz, a diffraction efficiency of 2.0% at 1 W RF drive power, and a dynamic range of 30 dB. Again, the device module was used to demonstrate light beam scanning and switching, and RF spectral analysis.

5. ULTRAHIGH CARRIER FREQUENCY INTEGRATED MICROWAVE AND MAGNETO-OPTIC DEVICES IN YIG/GGG-GAAS MATERIAL STRUCTURE

The integrated MO Bragg cell modulators have thus far utilized microstrip transmission lines fabricated on alumina or quartz substrates for generation of the MSW. We have recently succeeded in the design and fabrication of microstrip transmission lines on GaAs substrates that have shown flat frequency response approaching the carrier frequency of 50 GHz. These design/fabrication and testing capabilities have enabled us to utilize such ultrawide bandwidth GaAs-based microstrip transmission lines for construction of wideband bandstop filters in the

YIG/GGG-GaAs material structure.

Fig. 5 shows the hybrid material structure, the device configuration, and the detailed dimensions of the YIG/GGG-GaAs-based bandstop filter that was constructed recently [27]. A 50-ohm microstrip transmission line was first formed in a 350 μm -thick GaAs substrate. The transmission characteristic of the microstrip line for a quasi TEM mode extends to a frequency as high as 35 GHz. A YIG/GGG sample with 6.8 μm thick YIG layer at a length of 6.0 mm along the microstrip line was laid upon the GaAs-based microstrip line. An incident microwave propagating along the microstrip transmission line in the GaAs substrate is coupled into the YIG film and excite the MSW in the YIG film. Maximum coupling and, thus, the maximum absorption of the microwave power occur at the ferromagnetic resonance (FMR) frequency determined by the following relation:

$$f_{\text{res}} = \gamma [(H_0 + H_{\text{an}}) (H_0 + H_{\text{an}} + 4\pi M_s)]^{1/2}$$

where $4\pi M_s$ and H_{an} are the saturation magnetization and the anisotropy field of the YIG film, and H_0 is the applied magnetic field. As discussed earlier, absorption of the microwave power is due to the effective coupling of the input microwave to the MSW at the FMR frequency f_{res} . For YIG film, $H_{\text{an}} \approx 100$ Oe, and $4\pi M_s = 1,750$ Oe. Thus, $f_{\text{res}} = 14.0$ GHz at $H_0 = 4,150$ Oe.

In the experiment, the YIG/GGG sample and the GaAs-based microstrip line combination was inserted in a magnetic field H_0 that was tunable in both amplitude and direction. The magnetic field was applied in the plane of the YIG film (the Y-Z plane) and in directions adjustable from that of the microstrip line. Fig. 6 shows the measured transmission characteristics of the device versus the carrier frequency of the incident microwave, with the magnetic field as a parameter, and applied along the microstrip line. Note that for this special direction of the magnetic field the MSWs mode excited in the YIG film corresponds to the MSSW [3]. It is seen that a carrier frequency tuning range as large as 2.5 to 23.0 GHz with the corresponding magnetic field tuning range of 290 to 7,300 Oe has been achieved. A maximum absorption of 15 to 38 dB has also been measured with these particular sets of experiment. Finally, the same GaAs-based microstrip line has also been employed to facilitate ultrathin iron/GaAs -GaAs hybrid material structure and realize microwave bandstop filters at the carrier frequency as high as 35 GHz [28].

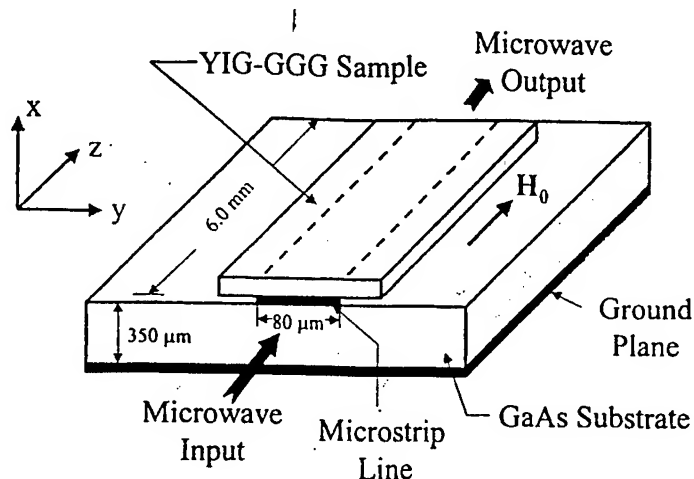


Fig. 5 Tunable Microwave Notch Filter Using YIG-GaAs Flip-Chip Configuration

The carrier frequency of the MSW generated can be readily tuned by a bias magnetic field. Accordingly, the resulting MSWs will facilitate MO Bragg diffraction experiment at such ultrahigh carrier frequency together with ultrawide bandwidth. Note that this high-end carrier frequency (50 GHz or higher) will represent a four-fold increase over that (12 GHz) used in prior MO Bragg diffraction experiments.

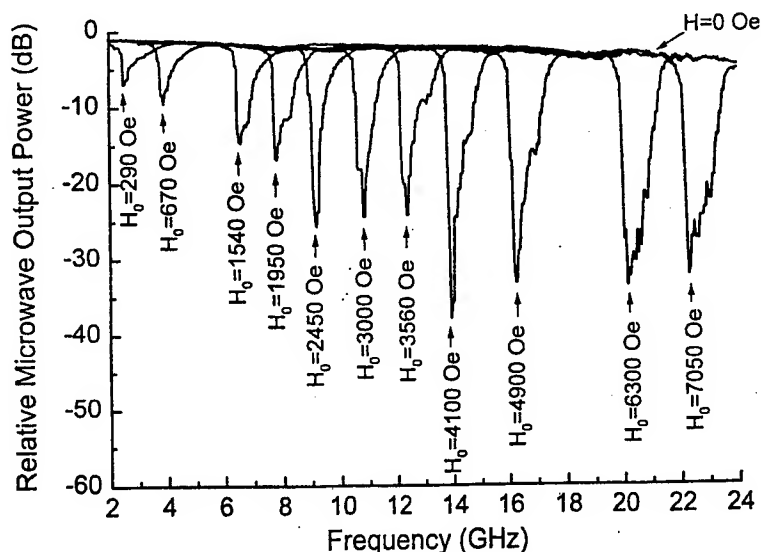


Fig. 6 Measured Transmission Characteristics of YIG/GaAs-Based Microwave Notch Filter with the Magnetic Field Applied along the Microstrip Line as a Parameter.

6. CONCLUSION

Increasing needs and prospects toward realization of electronically tunable wideband integrated microwave and MO devices justify further research and development efforts on hybrid and monolithic magnetic material structures involving substituted YIG such as those with Bi- and Ce-substitution and semiconductor substrates such as GaAs, InP and Si. Recent demonstration of large carrier frequency tunability with microwave bandstop filters using YIG/GGG-GaAs hybrid material structure and Fe-GaAs integrated material structure suggests its utilization for realization of ultrahigh carrier frequency and wide band integrated MO devices as well.

REFERENCES

1. See, for example, C. S. Tsai, IEEE Trans. UFFC, 39, 529 (1992).
2. See, for example, C.S. Tsai and D. Young, IEEE Trans. Microwave Theory and Techniques, 38, 560 (1990).
3. C.S. Tsai, Proc. IEEE, 84, 853 (1996).

4. (a) V.J. Fratello and R. Wolfe, to be published in *Magnetic Film Devices*, edited by M. Francombe and J.D. Adam, a volume of Handbook of Thin Film Devices, Academic Press.
 (b) J.P. Krumme, V. Doorman and R. Eckhart, IEEE Trans. Magn, **MAG-20**, 983 (1984).
 (c) H. Lenz, P. Hansen, and W. Tolksdorf, Appl. Phys. Lett, **54**, 2484 (1989).
5. Y.Q. Li, J.K. Huang, H. Jing, and Q.S. Chen in *Abstracts* (Materials Research Society Spring Meeting, Symposium M. Integrated Magneto-Optics-Materials and Devices, San Francisco, CA, 1998) pp. 233.
6. (a) H. Kidoh, A. Morimoto, and T. Shimizu, Appl. Phys. Lett., **59**, 237 (1991).
 (b) J.S. Horwitz et al., Mater. Res. Soc. Proc., **285**, 391 (1992).
 (c) T.M. Le, F. Huang, D.D. Stancil, and D.N. Lambeth, J. Appl. Phys., **77**, 2128 (1995).
7. H. Kim, A.M. Grishin, S.C. Yu, and K.V. Rao, (Digests of INTERMAG 99, Kyongju, Korea, 1999) pp. AR-06.
8. R. Wolfe, R. A. Lieberman, V. J. Fratello, R. E. Scotti and N. Kopylov, Appl. Phys. Lett. **56**, 426 (1990).
9. M. Levy, R. M. Osgood, H. Hegde, F. J. Cadieu, R. Wolfe and V. J. Fratello, IEEE Photonics Tech. Lett. **8**, 903 (1996).
10. J. -P. Castera and G. Hepner, IEEE Trans. Magn. **MAG-13**, 1583 (1977).
11. K. Ando, T. Okoshi and N. Koshizuka, IEEE Trans. Magn. **MAG-23**, 3485 (1987).
12. H. Yokoi, T. Mizumoto, K. Maru, N. Fuke and Y. Naito, Jpn. J. Appl. Phys. **35**, 4138 (1996).
13. H. Yokoi and T. Mizumoto, Electron. Lett. **33**, 1787 (1997). H. Yokoi and T. Mizumoto, Mat. Res. Soc. Symp. Proc. **517** (1998 Spring Meeting) to be published.
14. M. Levy, R. M. Osgood, Jr., A. Kumar and H. Bakhru, Appl. Phys. Lett. **71**, 2617 (1997); W. A. Johnson, J. C. North, and R. Wolfe, J. Appl. Phys. **44**, 4753 (1973).
15. M. Razeghi, P. -L. Meunier, and P. Maurel, J. Appl. Phys. **59**, 2261 (1986); J. Haisma, B. H. Koek, J. W. F. Maes, D. Mateika, J. A. Pistorius and P. J. Roksnoer, J. Cryst. Growth **83**, 466 (1987); J. Haisma, A. M. W. Cox, B. H. Koek, D. Mateika, J. A. Pistorius and E. T. J. M. Smeets, J. Cryst. Growth **87**, 180 (1988); B. J. H. Stadler, Y. -Q. Li, M. Cherif, K. Vaccaro and J. P. Lorenzo, Mat. Res. Soc. Symp. Proc. **446**, 389 (1997).
16. F. Auracher and H. H. Witte, Optics Commun. **13**, 435 (1975).
17. M. Wallenhorst, M. Niemler, H. Dersch, P. Hertel, R. Gerhardt, and B. Gather, J. Appl. Phys. **77**, 2902 (1995).
18. H. Yokoi, T. Mizumoto, K. Maru and Y. Naito, Jpn. J. Appl. Phys. **36**, 2784 (1997).
19. M. N. Deeter, A. H. Rose and G. W. day, *Fiber Optic and Laser Sensors VIII*, SPIE Vol. **1367**, 243 (1990).
20. R. Wolfe and R. A. Lieberman, Appl. Phys. Lett. **58**, 1733 (1991).
21. M. N. Deeter, G. W. Day, R. Wolfe and V. J. Fratello, IEEE Trans. Magn. **29**, 3402 (1993).
22. See, for example,
 (a) W.S. Ishak, Proc. IEEE, **76**, 159 (1988).
 (b) J.D. Adam, Proc. IEEE, **76**, 159 (1988).
23. C.S. Tsai, Y.S. Lin, J. Su, and S. Calciu, Appl. Phys. Lett., **70**, 3185 (1997).
24. J. Su and C.S. Tsai, Appl. Phys. Lett., **74**, 2878 (1999).
25. B.J. Wu, G.Q. Liu, and C.S. Tsai, J. of Magnetism and Magnetic Materials, **195**, 206 (1999).
26. C.L. Wang and C.S. Tsai, IEEE J. of Lightwave Technology, **15**, 1708 (1997).
27. C.S. Tsai and J. Su, Appl. Phys. Lett., **74**, 2079 (1999).
28. C.S. Tsai, J. Su, and C.C. Lee, IEEE Trans. on Magnetics, Vol. **35**, 3178 (1999).

Light propagation characteristics of micro-sphere array

Fujun Huang, Hiroyuki Ebihara, Shinzo Morita

Department of Electronics, Graduated School of Engineering, Nagoya University

Furo-cho, Chikusa-ku, Nagoya 464-8603, Nagoya, Japan

ABSTRACT

With using 5 glass spheres of 5mm diameter, a linear and a curvilinear array arrangement were realized and an image on a paper was transferred similarly for both arrangements. When the number of sphere was varied in the array, the transferred image was varied from normal to reversed and reversed to normal.

By using polystyrene micro-sphere of 10 μm diameter, a laser light was propagated in a linear and a curvilinear array. For a laser light at a wave length of 670nm, the attenuation coefficient was evaluated to be 0.051dB/sphere in the linear array. The attenuation coefficient was increased for the curvilinear array.

The image and the light transfer in the sphere array are attractive for new optical device application.

Keywords: linear array of sphere, curvilinear array of sphere, 10 μm polystyrene micro-sphere, 5mm glass sphere, light propagation, image transfer, 670nm laser, attenuation coefficient

1. INTRODUCTION

Sphere lens are utilizing variously in the industry. However the using is limited to collect the light like as a short focus lens. This is because the sphere has a large aberration. Therefore, it was expected that the multiplied sphere lenses arrangement is not profitable for the optical application. Recently it is known that micro-spheres are variously arranged for the optical experiments like as evanescent light transfer phenomena.^[1-8] However there are very few for the arrangement along a line. In this work, two kinds of transparent spheres were used. One is a glass sphere of 5mm diameter and the other is a polystyrene micro-sphere of 10 μm diameter. Their diameters of sphere in both groups are uniform. The spheres are arranged along a linear and curvilinear line. An image and a laser light transfer in the arrangement were studied.

2. EXPERIMENTALS

5 glass spheres of 5mm diameter were arranged linearly and curvilinearly, in which the spheres were contacted each other. The image of Chinese characters on a paper was connected on the sphere surface at the end of array. The transferred image was observed at the other end by a video camera connected to a computer.

An experimental setup for a measurement of light propagation characteristics on a polystyrene micro-sphere array is shown in Fig.1. where the micro-sphere array was arranged on a substrate which was covered by a spin coated film of

*Correspondence: Email: fj-huang@echo.nuee.nagoya-u.ac.jp ; Telephone: 052-789-4696

PMMA(polymethyl-methacrylate). Where the refractive index of polystyrene was 1.6. supplied from JSR Corp. and PMMA showed the refractive index to the 1.49 commercially supplied. A laser light at a weve length of 670nm was introduced into the quartz optical fiber through a lens and the light from the fiber was used as a light source in this experiment. The laser light was irradiated on one side of micro-sphere array and measured the output light intensity at the another side of micro-sphere array through an optical fiber-probe connected to a photo-multiplier. The photo-multiplier can detect the light in the wave length range from 300nm to 850nm.

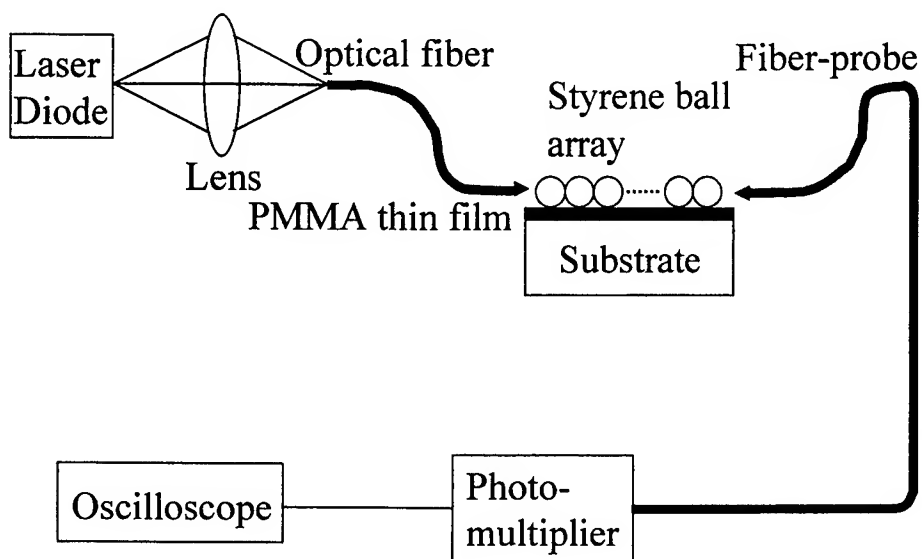


Fig. 1 Experimental setup



Fig. 2 A curvilinear array of 5mm diameter glass sphere at a curvature radius of 50mm

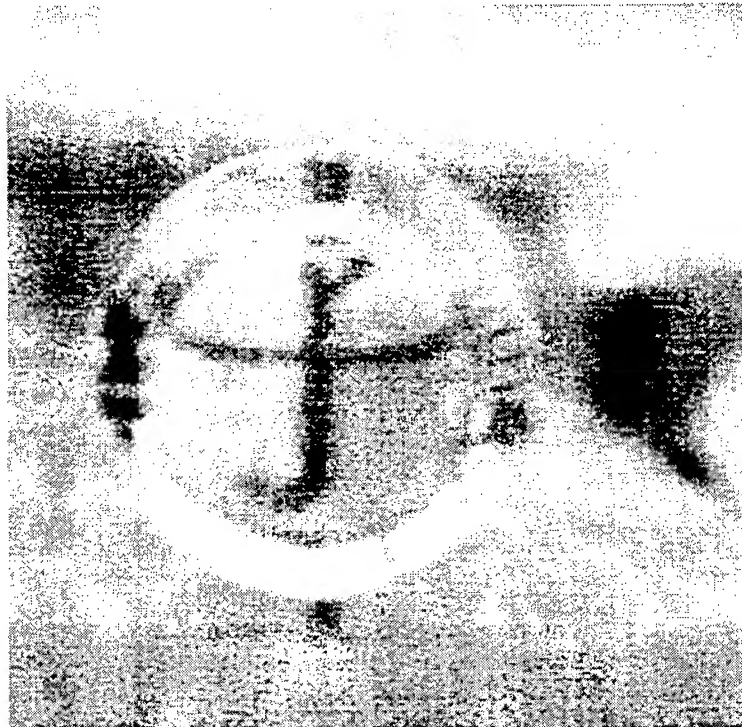


Fig. 3(a) Imaging transfer in 5 sphere linear array of diameter 5mm glass sphere



Fig. 3(b) Imaging transfer in 5 sphere curvilinear array of 5mm diameter glass sphere at a curvature radius of 50mm

3. EXPERIMENTAL RESULTS

a, Image transfer

The image on the paper set on the surface of top sphere in the arrangement were transferred successfully to the other side of arrangement. The curvilinear array of sphere at a curvature radius of 50mm is shown in Fig. 2. The transferred images in a linear and a curvilinear array are shown in Fig. 3(a) and Fig. 3(b) respectively. Transferred images are almost same for the arranges. When the number of sphere was varied from one to five the transferred image was varied from normal to reversed, reversed, normal, and normal, in order. as shown in Table 1.

Table 1. Transferred images

Number of sphere	Image
1	normal
2	reversed
3	reversed
4	normal
5	normal

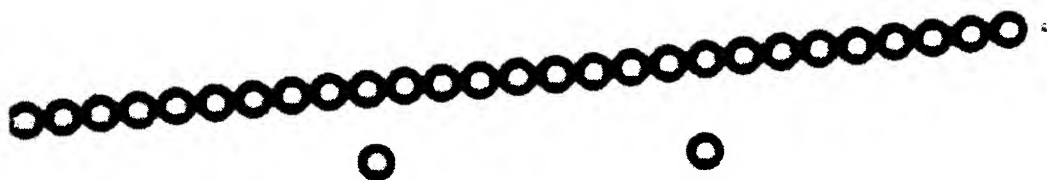


Fig. 4(a) A photograph of linearly arranged 10µmΦ polystyrene micro-sphere array

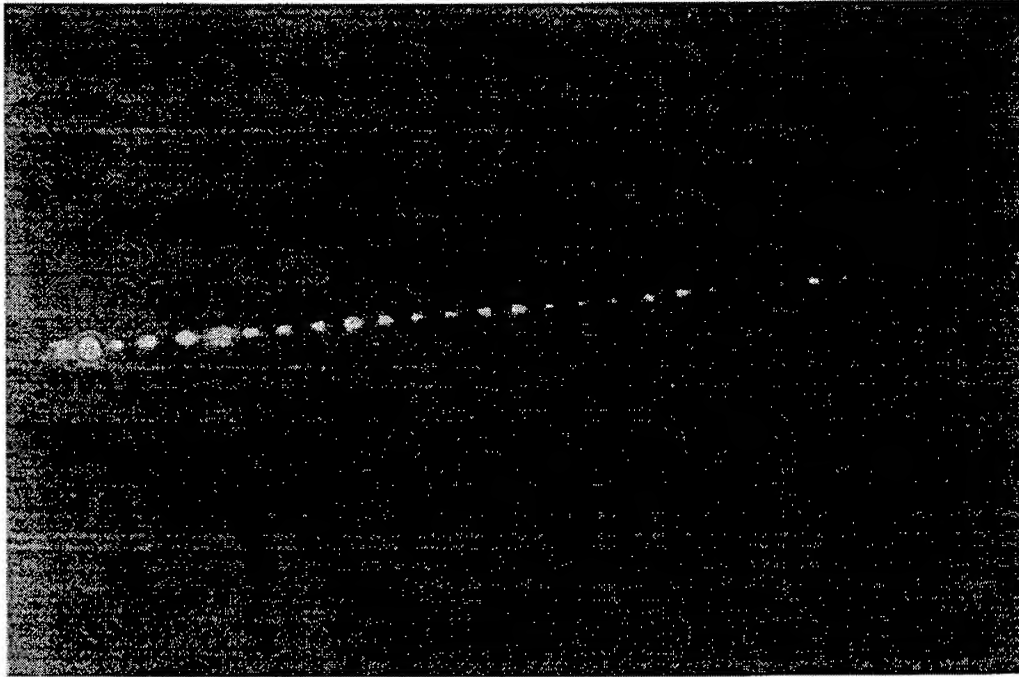


Fig. 4(b) An optical microscope photograph of scattered laser light along the linear array

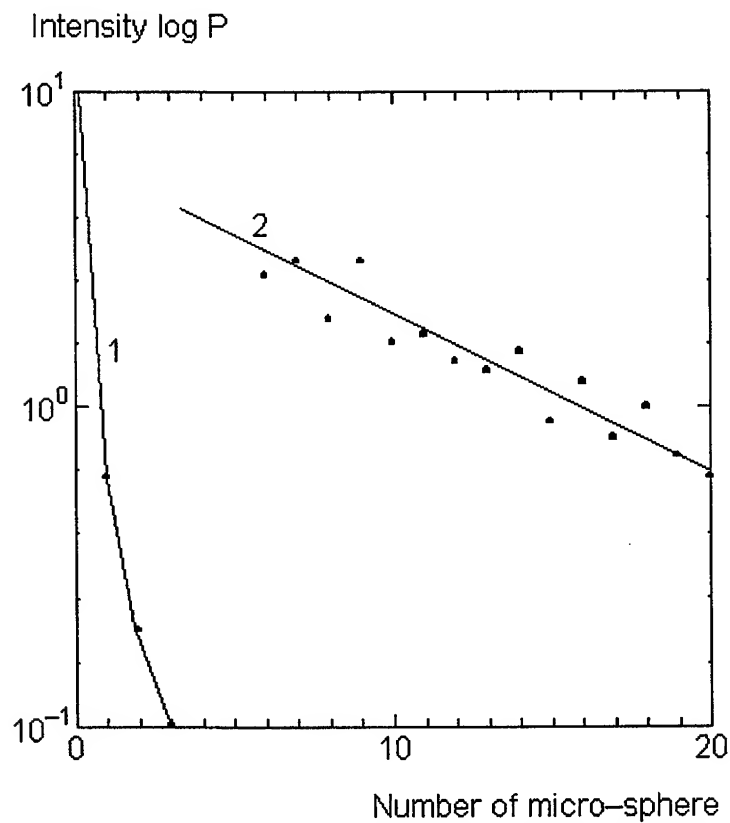


Fig. 5 Relations between the voltage and the number of micro-sphere, where curve 1 shows the measurement in the air and curve 2 shows the measurement in the line (P is a voltage of photomultiplier output)

b, Light propagation

The propagated light intensity was recorded for the maximum intensity selected by moving the probe near the end of array. the linear array of polystyrene micro-sphere of $10\text{ }\mu\text{m}$ diameter is shown in Fig.4(a). Under the laser light propagation, the linear array can be observed in the dark space as shown in Fig.4(b) caused on the scattered light. The propagated light intensities were measured as a paramant of number of sphere shown in Fig.5. The light propagation in the air without the sphere was also measured as shown in Fig. 5. The light in the air was attenuated with square of distance but the light attenuation on the sphere array was much more moderate. The attenuation coefficient was 0.051dB/sphere for the linear array. In Fig. 5 curve 1 is the loss in the air without micro-sphere array and curve 2 is in the micro-sphere array.

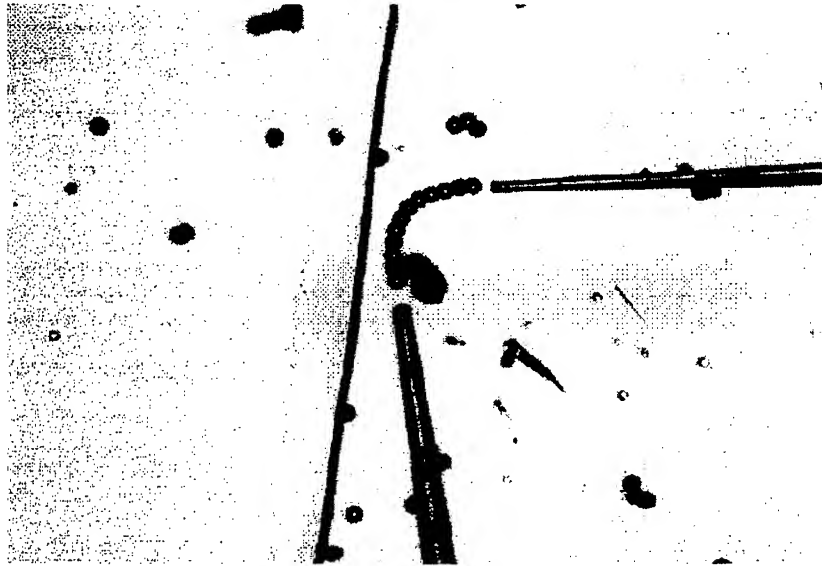


Fig. 6(a) An optical microscope photograph of polystyrene micro-sphere curvilinear array in curvature redias of $50\mu\text{m}$

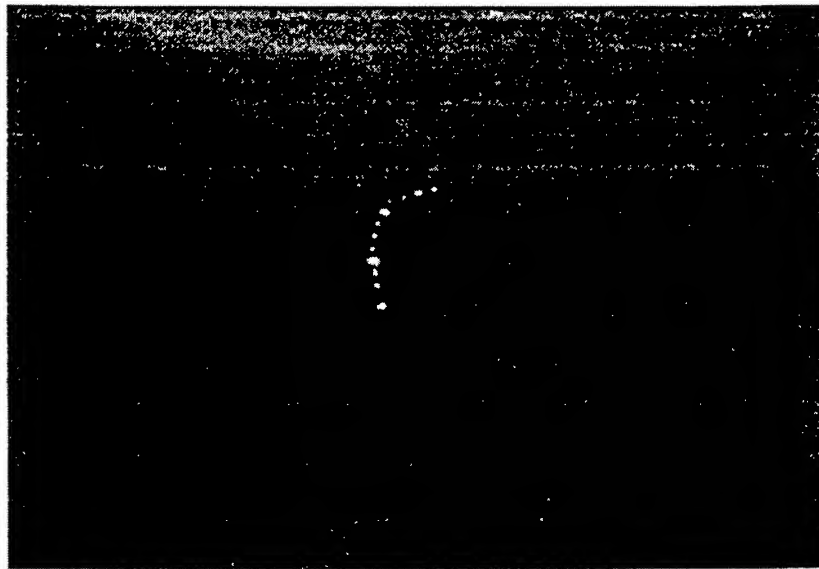


Fig. 6(b) An optical microscope photograph of scattered laser light along the curvilinear array

A curvilinear array of polystyrene sphere of 10 μm diameter is shown in Fig. 6(a). When the light was propagated in the curvilinear array, the scattered light was observed as shown in Fig. 6(b). The propagated light intensity was measured as a function of number of sphere in the curvilinear array. The attenuation constant was increased with decreasing the curvature radius. For the curvature radius of 50 μm the attenuation constant was evaluated to the 0.071dB/sphere, which is about 140% of that for the linear array as shown in Table 2.

Table 2. Attenuation coefficient in linear and curvilinear polystyrene micro-sphere array

Diameter of micro-sphere	A linear array of polystyrene micro-sphere	Curvilinear array (the curvature radius of 50 μm)
10 μm	0.051dB/sphere	0.071dB/sphere

4. CONCLUSIONS

The image transfer was successfully performed in the linear and curvilinear array of glass sphere of 5mm diameter. The laser light was also observed to propagate along the polystyrene sphere of 10 μm diameter linear and curvilinear array. These observation is a good evidence for the utilization of sphere array as optical elements.

ACKNOWLEDGEMENT

We express our thanks to JSR Co. for the polystyrene micro-sphere.

REFERENCES

- [1]Toshiro Kishikawa, *Introduction to Optics*,(in Japanese) Optronics Co. 1990
- [2]Yablonovitch, E.,Gmitter, T.J. and Leung, K.M.,*Phys. Rev. Lett.*,1991,2295
- [3]E.H.Synge, *Phil. Mag.* 6(1928)356
- [4]T. Fujimura, K. Edamatsu, T. Itoh, R. Shimada, A. Imada, T.Kota, N. Chiba, H. Muramatsu and T. Ataka, *Opt. Lett.* 22(1997)489
- [5]]T. Fujimura, T. Itoh, K. Hayashibe, K.Edamatsu, K.shimada, A. Imada, T. Kota, Y. Segawa, N. Chiba, H. Muramatsu and T. Ataka, *Mater. Sci. Eng. B* 48(1997)94
- [6]K. Nagayama, *Mater. Sci. and Eng. C* 1(1994)87
- [7]E. Yablonovitch, *J. Opt. Soc. Am. B* 10(1993)283
- [8]H. Imanishi and K. Hamanaka, Applied Patent, 175402(1989)Dec.5

Preferential input and output coupling of oval-shaped optical microcavities: fluorescent emission from oval-shaped dye-doped glass fibers

Andrew W. Poon^a, Steven L. Kan^a, Paul A. Tick^b, Daniel A Nolan^b, Richard K. Chang^a

^aDept. of Applied Physics, Yale University, New Haven, Connecticut 06520-8284, USA

^bCorning Inc., Corning, New York 14831, USA

ABSTRACT

We report an experimental study of the preferential input and output side coupling of oval-shaped optical microcavities. The cavity was in the cross-section of an oval-shaped dye-doped glass fiber, which was optically pumped perpendicular to the fiber axis. Fluorescent emission perpendicular to the fiber axis was imaged with a lens onto a CCD camera. The integrated intensity of the image profile at different angles provided the far-field angular pattern of the fluorescent emission peaked at $\sim 45^\circ$ relative to the cavity major axis. The near-field spatial profiles revealed refractive output coupling from an extended high-curvature region. A simple ray-path model was used to calculate the fluorescent near-field spatial profile. Preferential input side coupling was also observed in the direction $\sim 45^\circ$ relative to the cavity major axis. By focusing the pump beam at the high-curvature region in the preferred coupling direction, we observed \sim a factor of 8 enhancement in the integrated intensity at the preferred fluorescence output angle. By imaging from the fiber top surface, we demonstrated that the preferentially input coupled light could be guided along the cavity circumference.

Keywords: input/output coupling, optical microcavity, fluorescence, near-field imaging, glass fiber

1. INTRODUCTION

1.1. 2D Circular microcavities and non-directional coupling

Total internal reflection (TIR) is a simple and an approximate way to describe the confinement of light in micron-sized cavity that has relevance to photonics. Light of any wavelengths can be total internally reflected at the dielectric side interface without complications of multiple reflection layers or gratings. In order to select discrete wavelengths, the confined light wave can be guided to travel in round-trips in a 2D dielectric cavity. The light wave that is in-phase after travelling each cavity round-trip interferes with the input wave constructively. Discrete wavelengths at high-Q cavity modes can then be selected. 2D-microcavities with light confined by TIR therefore represent a class of wavelength-selective photonics components.

Circular microcavity disk and ring resonators are the most conventional design of 2D-microcavities demonstrated previously by various workers.^{1,2,3,4} Light wave is confined by TIR along the circular circumference in round trips, forming high-Q whispering-gallery cavity modes. The light ray incident angles at the circular boundary remain constant and the only output coupling mechanisms are diffraction or evanescent tunneling. By time-reversal argument, light wave outside the circular cavity could only input couple by diffraction or by evanescent tunneling. The problems are that, in circular microcavity lasers, the diffractive edge-emission is tangential to the cavity circumference and therefore the emission is non-directional.^{1,4} Moreover, in integrated microcavity-waveguides devices such as passive resonant-filters, the evanescent coupling between the circular microcavity and the side-coupled waveguides depends critically on a sub- μm gap separation.^{2,3} Hence, a novel microcavity design that allows the cavity to be side coupled at specific angles, and potentially with waveguides at a distance that is larger than the sub- μm evanescent-coupling limit will promise new opportunities for photonics devices.

1.2. Oval-shaped Asymmetric Resonant Cavities (ARCs) and directional refractive coupling

We found a class of resonators in 2D oval-shaped microcavities, so called Asymmetric Resonant Cavities (ARCs)⁵ which have the desirable properties of being able to couple the light in refractively. The oval-shaped boundary can be defined in cylindrical coordinates (r, ϕ) as a quadrupolar deformation from a circle as follow:

$$r(\phi) = R(1 + \varepsilon \cos(2\phi)), \quad (1)$$

where R is the circle radius and ε determines the amplitude of deformation from a unit circle. The cavity major axis has a length of $2R(1+\varepsilon)$ in the direction along the two highest-curvature poles at $\phi = 0^\circ$ and 180° .

Because of the oval-shaped boundary, light ray incident angles at the boundary are not constant. Hence, the light rays that are confined initially by TIR may eventually have the incident angles drop below the critical angle and escape by refraction. The refractive escape may preferentially occur at the cavity higher-curvature region, much like the fiber bending loss. The refractive output ray directions are determined according to Snell's law.

By time-reversal argument, light rays outside the oval cavity could couple into the cavity by refraction near the higher-curvature region in specific angles. The refractively input-coupled light ray could be trapped by TIR, and subsequently the angle of incidence falls below the critical angle and the light ray escape refractively at the higher-curvature region. Hence in oval cavities, we would gain the advantages of the refractive input and output coupling by trading off the constant angle of incidence requirement of a circular-shaped resonator.

1.3. Directional microlasers and passive filters

Although the light ray incident angles vary along the oval circumference, some trajectories remain relatively regular for many cavity round trips. Therefore, many photonics applications may exploit such refractively coupled quasi-regular light ray trajectories. For example, in directional-emission microlasers and in passive optical filters with non-evanescent coupling from waveguides. Indeed, directional emission in the mid-IR from ARCs in electrically pumped semiconductor Quantum Cascade (QC) lasers was demonstrated recently by Gmachl et al.⁶ Numerical studies employing a Surface-of-Section (SOS) technique suggested a "bow-tie" cavity orbit to emit refractively in the observed far-field directions. However, direct experimental evidence of the "bow-tie" near-field emission locations is yet to be achieved. By near-field imaging, one could reveal the emission locations along the sidewall that could not be extracted from the far-field angular pattern measured by a photodiode.

2. METHOD OF EXPERIMENT

2.1 Optical side-pumping and near-field imaging

In this paper, we report the first time to our knowledge, the angular dependence of the input and output refractive side-coupling to an oval-shaped microcavities formed from a dye-doped glass fiber. The microcavity was in the cross-section of the oval-shaped fluorescent dye-doped glass fiber, which was pumped optically perpendicular to the fiber-axis. Fluorescent emission in the visible wavelengths perpendicular to the fiber-axis was imaged with a lens onto a CCD camera. At a fixed input-pumping configuration, the fluorescent image measures the sidewall emission locations and the emission directions, when the aperture of the camera is kept small. By integrating the image-profile intensity within the aperture acceptance angle, we also measured an equivalent far-field intensity. By varying the camera angle, we can map out the sidewall emission distribution and the far-field angular profile.

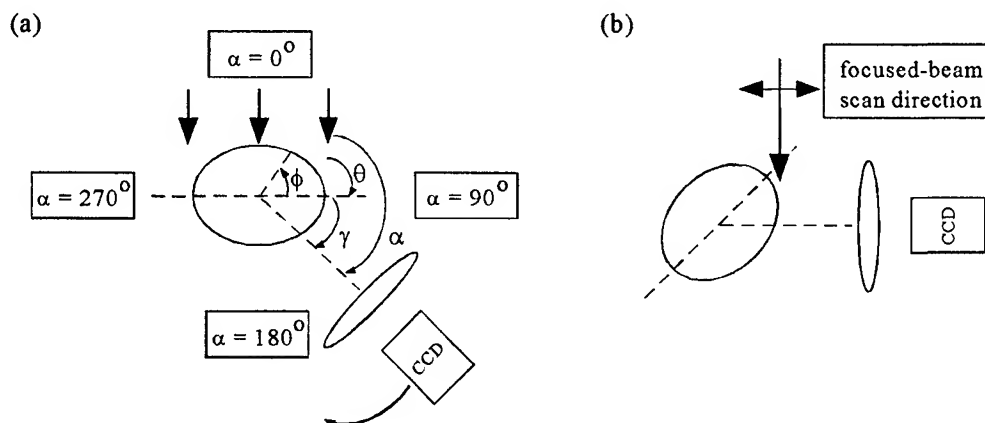


Figure 1 Schematic of the near-field imaging and the different optical side pumping (a) with broad beam at different input and output far-field angles, (b) with focused beam at different input positions.

In order to measure the effects of the side pumping on the fluorescent emission directionality, different optical side pumping configurations were used. In each configuration, the sidewall near-field spatial profiles and the integrated intensities were measured. Figure 1(a) shows the schematic of the broad-beam pumping, and the angle definitions of the cavity major axis, the laser beam pumping direction, and the far-field imaging angle. The three arrows pointing towards the cavity represent the broad-beam pumping. The far-field angle α is defined relative to the pump-beam direction. The angle θ defines the orientation of the cavity major axis relative to the input beam direction. The imaging axis angle γ is defined relative to the cavity major axis and $\gamma = \alpha - \theta$. In order to measure the preferred side-pumping angle, the cavity major axis angle θ was rotated while preserving the imaging angle γ at the preferred fluorescent emission angle. Figure 1(b) shows the schematic of the focused-beam scan experiment. In order to measure the effects of the side pumping at different input locations, the input beam (represented by one arrow) was focused onto different positions across the cavity. The sidewall fluorescent emission was imaged in the preferred far-field angle.

In order to measure the fluorescent trajectory of the focused input beam, the fluorescent emission was also imaged from above the fiber top surface. This provides us a "bird's-eyes" view of the input coupling dependence without the dependence on the output coupling. The top-view image serves much like an experimental ray tracing for visualizing the trajectories of the input beam.

2.2 Experimental setup

Figure 2 shows the experimental setup. The dye-doped glass fiber was pumped at 532 nm (SHG of ND:YAG) with a 70 ns pulse-width laser at 1 kHz repetition rate and a $\approx 2 \mu\text{J}$ pulse-energy. The fiber was mounted (with multiple degree of freedom) on a rotation stage, a x-y-z translation stage and on a goniometer. In the broad-beam pumping experiment, the laser beam was unfocused. In a focused-beam experiment, the laser was focused with a f/15 lens. The fluorescent emission was imaged with a f/11 camera lens (acceptance angle of $\approx 4^\circ$) onto a continuous-mode CCD camera. The camera lens and the CCD camera were mounted on a rotation stage to allow imaging at far-field angles from 90° to 270° far field in $\approx 11^\circ$ steps. The top-view experiment was imaged by a microscope objective lens onto a separate CCD camera. Orange color filters were placed in front of the CCD cameras to block the green pump light scattering.

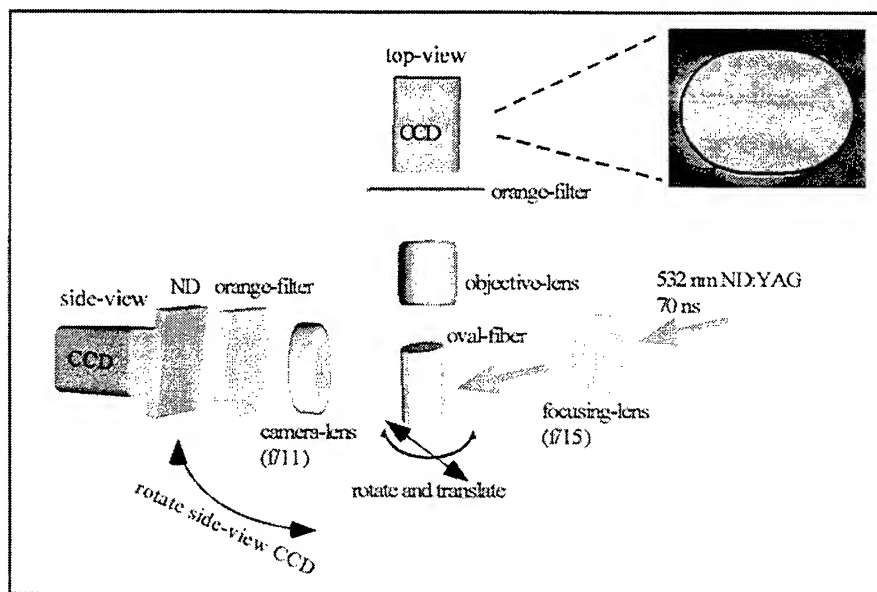


Figure 2. Schematic of the experimental setup. The dye-doped glass fiber was pumped perpendicularly at 532 nm (SHG of ND:YAG). The fluorescent emission from the sidewall was imaged with a $f/11$ camera lens onto a CCD camera. The fiber top-surface was imaged by a microscope objective lens onto a separate CCD camera. The inset shows a top-view image of a typical oval-shaped dye-doped glass fiber, with a solid-line quadrupolar boundary of $\epsilon = 0.18$.

2.3 Oval-shaped dye-doped glass fibers

The oval-shaped glass fibers with cavity major axis of a few hundred microns and a fiber length of a few centimeters allowed convenient handling of the microcavity. The fiber was made in a low melting-temperature Corning specialty glass (refractive index $\approx 1.6 - 1.7$).⁷ The low-melting temperature allowed rhodamine 6G fluorescent dye to be doped into the glass. The dye-concentration was ≈ 2 ppm by weight. The fiber was pulled to a size of a few hundred microns through a die with a designed oval-shape of deformation amplitude $\epsilon \approx 0.15$. The glass fiber sample had a measured deformation amplitude $\epsilon \approx 0.15 - 0.18$ (aspect ratio $\approx 1.35 - 1.44$). The inset of Fig. 2 shows a top-view optical microscope image of a typical oval-shaped dye-doped glass fiber, with the oval major axis $\approx 780 \mu\text{m}$ and the oval minor-axis $\approx 560 \mu\text{m}$. The cavity shape shows a good agreement with the overlaid quadrupolar boundary at $\epsilon = 0.18$.

3. BROAD-BEAM PUMPING

3.1 Fluorescent emission far-field directionality

In order to measure the fluorescent emission far-field directionality, we first illuminated the fiber by a broad unfocused beam at fixed cavity major-axis angle. Fluorescent emission was imaged at angles α from 90° to 270° in $\approx 11^\circ$ steps. The fluorescent intensity within the acceptance angle of $\approx 4^\circ$ was integrated. In Fig. 3(a), the solid line shows the integrated fluorescent intensity when the fiber was illuminated at $\theta \approx 90^\circ$. The angular pattern peaks at $\alpha \approx 135^\circ$ and $\approx 225^\circ$ far-field angles. The half-width of the α angular peak is $\approx 45^\circ$. The dashed line of Fig. 3(a) shows the integrated fluorescent intensity angular pattern when the fiber was illuminated at $\theta \approx 45^\circ$. The far-field maximum shifted from $\alpha \approx 225^\circ$ to $\alpha \approx 180^\circ$ with a small enhancement in the peak integrated intensity. Hence, in both broad-beam pumping conditions, the far-field fluorescent emission was anisotropic and the maximum integrated fluorescent intensity was observed at $\approx 45^\circ$ relative to the cavity major axis.

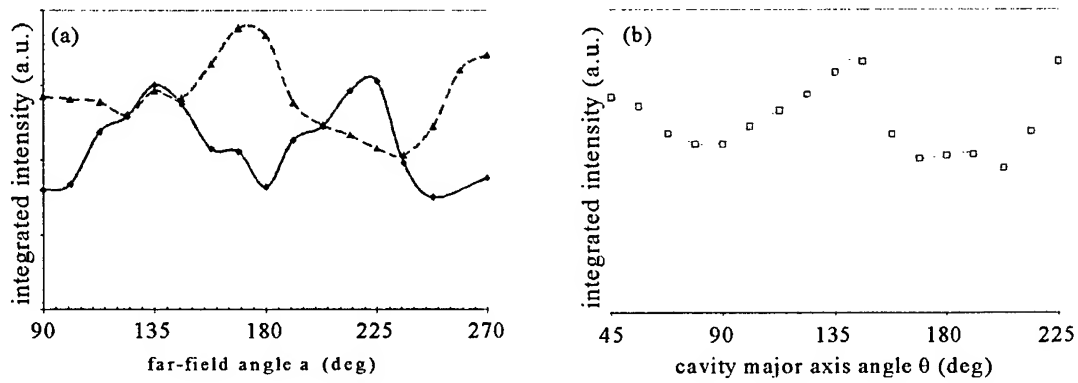


Figure 3(a). Fluorescent emission far-field angular pattern with broad-beam pumping at $\theta \approx 90^\circ$ (solid-line) and at $\theta \approx 45^\circ$ (dashed-line). (b) Broad-beam pumping angular dependence with imaging angle γ fixed at $\approx 45^\circ$.

3.2 Preferential broad-beam pump angle

The enhancement in the integrated fluorescent intensity when pumping at $\theta \approx 45^\circ$ (as shown in Fig. 3(a)) suggested that there exist a preferred broad-beam pump angle. In order to measure such enhancement of the fluorescent intensity with preferred pump angle, we rotated the cavity major-axis angle θ in $\approx 11^\circ$ steps, while keeping the imaging angle γ fixed at $\approx 45^\circ$. Figure 3(b) shows a maximum integrated fluorescent intensity with broad-beam pumping at $\theta \approx 135^\circ$ (imaged at $\alpha \approx 180^\circ$) with an angular width in $\theta \approx 45^\circ$. Notice that $\theta \approx 135^\circ$ is equivalent to $\theta \approx 45^\circ$ in a broad-beam pumping as far as the integrated fluorescent intensity is concerned. A minimum integrated fluorescent intensity was observed at $\theta \approx 90^\circ$ (imaged at $\alpha \approx 135^\circ$). The maximum-to-minimum contrast ratio is consistent with the enhancement shown in Fig. 3a. The preferential broad-beam pump angle is therefore consistent with the preferential fluorescent emission direction in the far field.

In the geometric approximation, the equivalence of the preferential input pump angle and the output fluorescent emission direction is expected from a time-reversal argument (neglecting dispersion of the index of refraction). If the external light ray can input couple into the cavity efficiently at particular region and angles, then by reversing the light ray k -vector, the cavity light ray can output couple with the same efficiency at the same region but in the opposite directions.

3.3 Fluorescent emission near-field spatial profile

In order to interpret the preferential fluorescent emission in the far field and the preferential broad-beam pumping, the light ray coupling locations is crucial. The near-field fluorescent images, rather than the integrated fluorescent intensity, are therefore more informative. Fig. 4(a) shows the near-field spatial profile imaged at $\alpha \approx 135^\circ$ with the broad-beam pumping at $\theta \approx 90^\circ$. The spatial profile shows preferred emission from the high-curvature region with a large angular range in ϕ . Since the image was taken with a small acceptance angle of the camera, the directional fluorescence rays radiating along the high-curvature region into the camera-lens indicates a refractive output coupling.

We could trace the cavity fluorescence ray-paths of the output fluorescence in a fixed far-field direction. Figure 4(a) shows the ray-trace for the output fluorescence ray in $\gamma \approx 45^\circ$ at the polar region. The cavity was assumed to be defined by eq. (1) with $\varepsilon = 0.18$. The external refractive angle at the pole is 45° , and the internal angle at the pole was calculated according to Snell's law using a refractive index of 1.65 (critical angle $\approx 37^\circ$). The internal ray was traced geometrically by first measuring the tangent and the normal vector (shown as the cross hair "+" in the ray-trace in Fig. 4(a) at each reflection location). The internal reflection angle at each reflection is shown in Fig. 4(a). Notice that the output ray as shown could be traced in the cavity for at least one round trip with all incident angles above the critical angle. Similar round-trip trajectories could be traced for the output rays coupling from the preferred high-curvature emission region. However, the output rays coupling from the lower-curvature region could only have a short path length before the internal incident angles reach below the critical angle.

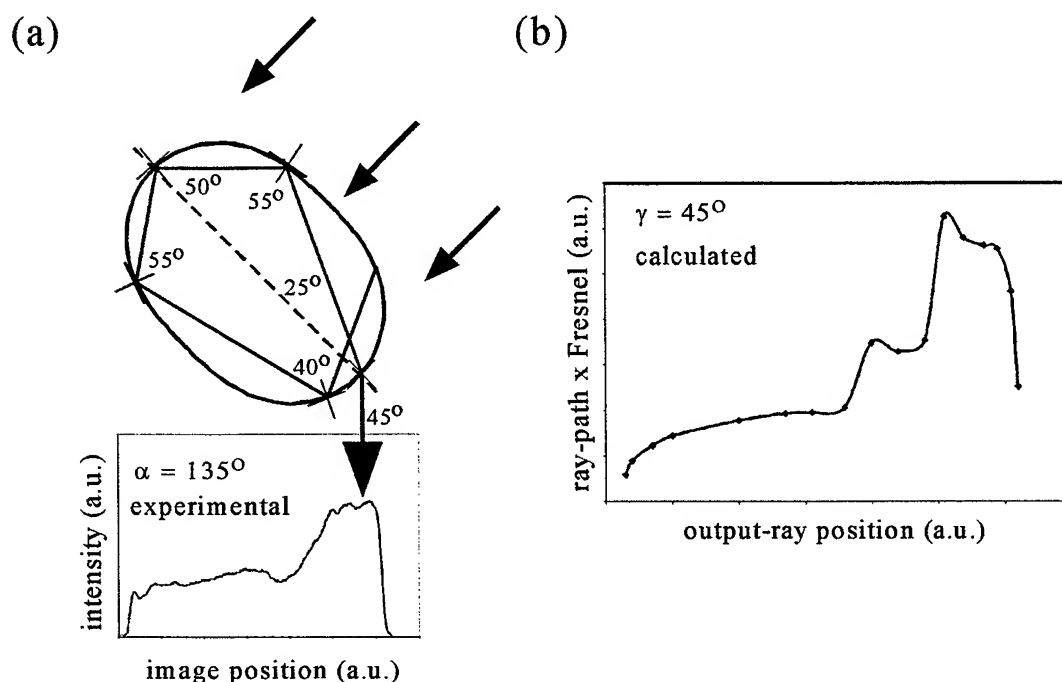


Fig. 4(a) The near-field spatial profile imaged at $\alpha \approx 135^\circ$ with broad-beam pumping at $\theta \approx 90^\circ$. A schematic of the broad-beam pumping is shown. The three arrows pointing towards the cavity represent the broad pump-beam. The output fluorescence ray from the highest curvature region is traced for one cavity round trip. The external refractive angle and the internal incident angles are shown. (b) The calculated spatial profile at $\gamma = 45^\circ$ using the simple ray-path model.

3.4 A simple ray-path model

Based on ray-tracing model, the near-field fluorescent emission spatial profile could be approximated by a simple model. Since the fluorescent emission is spontaneous, the relative intensity of the output fluorescent light ray at different output locations is proportional to the fluorescent ray-path length. The coupling efficiency at different output locations could be approximated by the Fresnel transmission. Therefore, the fluorescent light ray spatial profile could be approximated with the product of the ray-path length and the Fresnel transmission. Figure 4(b) shows the calculated spatial profile at $\gamma = 45^\circ$, which has good agreement with the imaged near-field spatial profile shown in Fig. 4(a). At each output locations, the cavity fluorescent ray-path was traced until the internal incident angle was smaller than the critical angle, or the fluorescent ray completed one cavity round trip. The calculated spatial profile with the assumed one-round-trip maximum path length agrees with observation implies that the fiber was relatively lossy. The loss may be dominated by the rough fiber surface.⁷ In future work, the far-field fluorescent emission directionality could also be predicted by similar calculations for a range of far-field angles.

4. FOCUSED-BEAM PUMPING

In order to measure the preferential side pumping at different coupling locations, the pump beam in the preferred input coupling angle ($\theta \approx 45^\circ$) was focused and scanned across the fiber. In the experiment, the fiber was translated across the focused beam in 50 - 100 μm steps. Fluorescent emission was imaged at $\gamma \approx 45^\circ$. Figure 5 shows the integrated fluorescent intensity depends on the focused beam positions. There exists a preferred input coupling at the high-curvature region. The profile contrast ratio is approximately a factor of 8. The inset of Fig. 5 shows the near-field spatial profile, with the focused beam coupling at the position corresponding to the peak of the input position-dependence profile. A ray-trace of one cavity round trip of the refractive coupled pump light ray is shown. We note that the near-field fluorescent spatial profile is similar to the input position-dependence profile.

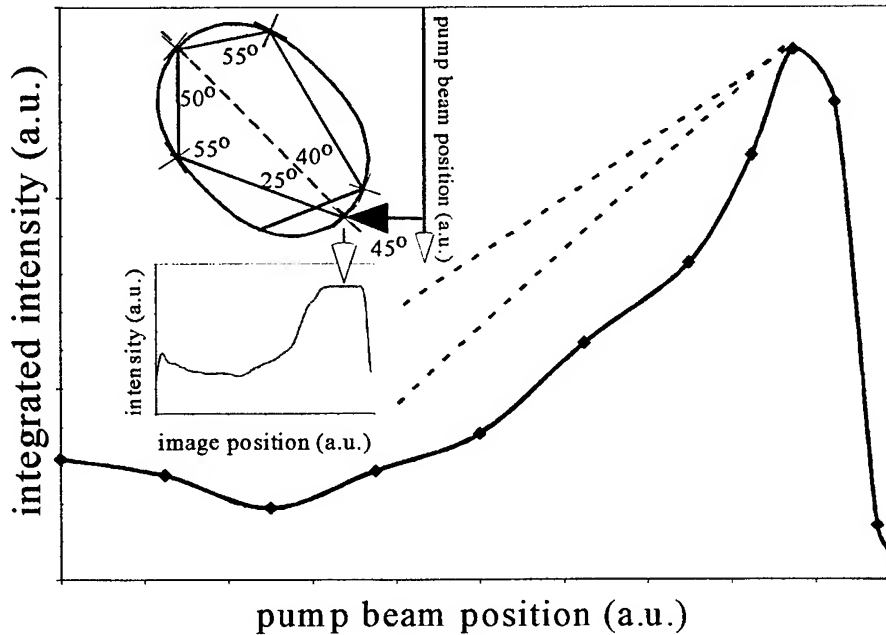


Figure 5. Focused pump beam input-position dependence in the preferred input coupling direction. The fluorescent emission was imaged at the preferred output coupling direction. There exists a preferred input coupling position at the high-curvature region. The inset shows the corresponding near-field spatial profile at the peak of the focused beam position-dependence profile. A ray-trace of the input pump (the arrow with a solid head) coupling at the highest curvature region indicates a geometric path length of one cavity round trip. The refractive input angle and the internal incident angles are shown. The preferential fluorescent output ray is also shown (the arrow with a hollow head).

We interpreted the focused beam position-dependence profile as follow. By focusing the pump beam at the high-curvature region in the preferred input direction, most of the pump light rays could couple into the cavity and make round trips, as suggested by the ray-trace (the inset of Fig. 5). The relative fluorescent intensity of pump-light rays input couple at different locations is proportional to the relative geometric pump ray-path length. We could use our ray-path model to approximate the input position-dependence profile. The calculated pump-light ray position-dependence profile at $\theta = 45^\circ$ is identical to the calculated output fluorescence spatial profile at $\gamma = 45^\circ$ shown in Fig. 4b. The dye-molecules absorption sets a limit to the maximum pump length. With a cavity size of a few hundred microns and a typical dye-absorption length of ~ 1 mm, our one-cavity-round-trip assumption is still reasonable. Therefore, it comes as no surprise that the refractive input coupled pump position-dependence profile is similar to the refractive output coupled near-field fluorescent emission spatial profile, and both could be approximated by our simple ray-path model. However, we conjecture that the input-position profile may also hint contributions from amplified spontaneous emission. Further studies with different input-pumping intensities with focused input beam are in progress.

5. TOP-VIEW IMAGING

5.1. Fluorescent cavity circumference

In order to have direct evidence of the input pump beam trajectory, we imaged the fluorescent trajectory from the fiber top surface onto a separate CCD camera. The laser pumping was reduced to a lower laser-pulse energy ($< 2 \mu\text{J}$) and to a repetition rate of 5 Hz. Figure 6 shows the top-view images (in false-color intensity scale) at the fluorescence wavelengths with the input pumping positions at $\theta \sim 40^\circ$. When pumping at the high-curvature edge region in the preferred input coupling direction, Fig. 6(a). shows a higher intensity fluorescent emission from the cavity circumference. The fluorescent circumference suggested that the input pump light were guided along the circumference, as suggested by the geometric ray-trace shown in Fig. 6(a). However, when the focused beam coupled into the low-curvature region, Fig. 6(b) shows that the

focused pump beam fluorescent trajectory was not cavity-guided, as also suggested by the geometric ray-trace shown in Fig. 6(b).

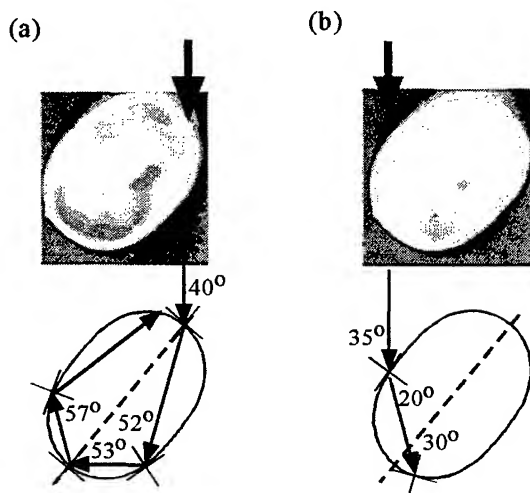


Figure 6. Top-view fluorescence images (in false-color intensity scale) and typical ray-trace with focused beam coupling at (a) the high-curvature region and (b) the low-curvature region.

6. DISCUSSION

6.1 Oval cavity modes

Because of the typically unstable trajectories in oval cavities, light ray dynamics of large number of cavity round trips could be chaotic.^{5,6} Thus far, the cavity modes of such quadrupolar cavities are mostly unknown theoretically. The numerical SOS method is essentially a geometric ray tracing and hence carries no phase information to construct wave interference. For these large size 2D microcavities of quadrupolar shape, it is possible in principle to solve Maxwell's equation, which is exceedingly computer intensive, and the solutions are not intuitive.

Our typical dye-doped fibers were too large for the multi-mode fluorescence cavity modes to be spectrally resolved. In order to investigate the cavity modes, a separate elastic-scattering experiment using a smaller sized oval-shaped un-doped glass fiber and with a tunable diode laser is in progress. Preliminary results suggest that the resonant spectra are highly sensitive to the input and the output coupling angles. At particular coupling conditions, we observed a high-contrast quasi-periodic filter spectrum. Future experiments on the light coupling directionality and cavity spectra could involve oval-shaped microcavities in dye-doped glass substrates. However, the side input coupling to the cavities via refractive coupling may involve further engineering design, such that light can be coupled from the end-face of a waveguide (or a laser beam) onto a typically few-micron height cylindrical pillar-cavity structure which is the microcavity.

7. CONCLUSION

In a variety of side-couple optical-pumping and near-field fluorescence imaging experiments of the oval-shaped fluorescent dye-doped glass fibers, we have shown that the input pumping and the output fluorescent emission have preferred refractive coupling at $\sim 45^\circ$ relative to the cavity major axis. The near-field imaging revealed directional fluorescent emission from the high-curvature region. Preferential focused pumping was also demonstrated at the high-curvature region. A geometric ray trace of the preferred input and output coupled rays indicated ray-paths with cavity round-trips. Based on ray-tracing model, the fluorescent emission near-field spatial profile and the input pump position-dependence profile could be approximated. By imaging from the fiber top surface, we demonstrated that the focused pump beam coupling at the high-curvature region could be guided along the cavity circumference.

ACKNOWLEDGEMENTS

We gratefully acknowledge the support of this work by the National Science Foundation (Grant No. PHY-9612200).

REFERENCES

1. Y. Yamamoto and R. E. Slusher, "Optical processes in microcavities," *Phys. Today* **46**, pp. 66-73, 1993.
2. D. Rafizadeh, J. P. Zhang, S. C. Hagness, A. Taflove, K. A. Stair, and S. T. Ho, "Waveguide-coupled AlGaAs/GaAs microcavity ring and disk resonators with high finesse and 21.6-nm free spectra range," *Opt. Lett.* **22**, pp. 1244-1246, 1997.
3. B. E. Little, J. S. Foresi, G. Steinmeyer, E. R. Thoen, S. T. Chu, H. A. Haus, E. Ippen, L. C. Kimerling, and W. Greene, "Ultra-compact Si/SiO₂ microring resonator optical channel dropping filters," *IEEE Photon. Technol. Lett.* **10**, pp. 549-551, 1998.
4. N. B. Rex, R. K. Chang, L. J. Guido, "Threshold Minimization and Directional Laser Emission from GaN Microdisks," *Proceedings of SPIE/Laser Resonators III Conference*, Vol. 3930, pp. 163-169, SPIE Bellingham, Washington, 2000.
5. J. U. Nockel, A. D. Stone, "Ray and wave chaos in asymmetric resonant optical cavities," *Nature* **385**, pp. 45-47, 1997.
6. C. Gmachl, F. Capasso, E. E. Narimanov, J. U. Nockel, A. D. Stone, J. Faist, D. L. Sivco, and A. Y. Cho, "High-Power Directional Emission from Microlasers with Chaotic Resonators," *Science* **280**, pp. 1556-1564, 1998.
7. However, the low-melting temperature glass is a relatively soft material and water absorbing, which results in a rough fiber surface. We believe that the fiber surface roughness degraded the cavity quality factor Q value and resulted in a high lasing threshold. By coating the fiber with a thin layer of mineral oil, we found that the contrast ratio in the far-field angular pattern and that in the near-field image profile can be improved. The low melting-temperature also sets a low temperature damage-threshold, which limits our maximum laser-pump power to reach the possibly high-lasing threshold. However, we believe that observing fluorescent emission is sufficient to further our understanding of the preference for the input and output coupling directionality.

*Correspondence: Email: wing.poon@yale.edu

Novel Three-Branch Optical Power Divider by Ti diffusion on Lithium Niobate

Tzyy-Jiann Wang^a, and Way-Seen Wang^b

^aInstitute of Opto-Electronics Engineering,
National Taipei University of Technology, 10647, Taipei, Taiwan

^bDepartment of Electrical Engineering,
National Taiwan University, 10617, Taipei, Taiwan

ABSTRACT

A novel three-branch optical power divider by Ti diffusion on lithium niobate is proposed and analyzed. For the conventional three-branch power divider, most of the optical power is transmitted to the central output waveguide and only little power is distributed to the two sideward output ones. Several designs have been proposed to increase the power in the two sideward output waveguides. Because they require extra regions of indices lower than that of substrate or higher than that of waveguide, it is difficult to find such indices for realizing their designs. In this work, we propose a novel three-branch optical power divider, which includes one substrate microprism and two waveguide expanders. Because of not requiring extra regions of indices different from that of substrate and waveguide, the realization of the proposed devices becomes very easy. Prior to the diffusion process, only one lithography step is required. For the proposed structure, the transmitted power in the two sideward output waveguides can be higher or lower than that in the central output one under a large branching angle. It is known that the index distribution in the Ti-diffused waveguide is varied with the diffusion process parameters. In order to understand the effect of waveguide fabrication parameters on power distribution in three output waveguides, the parameter variations are considered. Moreover, in comparison to the previous works, the proposed power divider has the advantages of low insertion loss, large branching angle, and easy fabrication.

Keywords: titanium diffusion, lithium niobate, and power divider

1. INTRODUCTION

Over the past decade, LiNbO₃ has attracted a lot of researchers' attention because of its excellent electro-optical and acousto-optical properties. The LiNbO₃ waveguide devices are widely studied and utilized in diversified applications. To have more complicated functions and become more compact, a variety of devices must be integrated on a single LiNbO₃ chip. In order to increase the packing density in the optical integrated circuit, large-branching-angle optical power dividers are required. Previously, almost all the related researches are made for the optical power dividers with step-index waveguide. However, on LiNbO₃, the most popular waveguide fabrication method, Ti diffusion, produces waveguide with a graded-index profile. Hence, the design of the large-branching-angle optical power divider on LiNbO₃ is desideratum.

For 1×3 optical power dividers, Belanger et al.¹ showed that almost all the input optical power is transmitted into the central output waveguide. In order to increase optical power in the two sideward output waveguides, several designs are proposed to improve the transmission characteristic of the 1×3 optical power dividers. Belanger et al.¹ proposed the concept of index modification to achieve equal-power division. Later, Haruna et al.² put a layer of dielectric cladding of higher index on the two sideward output waveguides to realize this concept. Hung et al.³ added two relatively-lower-index phase-front accelerators at two branching regions between the central and sideward output waveguides to aid the power transmission into the two sideward output waveguides. Banba et al.⁴ added a straight waveguide at the branch side of the Y-branch to form a 1×3 branching waveguide. Utilizing the triangular region formed by laterally shifting the straight waveguide from the center of the Y-branch, the optical power in the two output sideward waveguides increases. Lin et. al.⁵ put two high-index microprisms at the taper region of a 1×3 branching waveguide. By tuning the microprism index, the equal-power

division is achieved. In most of the previous works, extra regions of indices higher than that of waveguide or lower than that of substrate are needed. To realize such required index greatly increases the difficulties in device fabrication.

In this work, we proposed a novel three-branch optical power divider by Ti diffusion on LiNbO₃ using one substrate microprism and two waveguide expanders. Unlike the previous works, no extra regions of indices different from that of waveguide and that of substrate are needed. This greatly increases the possibility in the realization of the proposed optical power divider. It is shown that with appropriate phase-front tilt and field modification, equal-power division and low insertion loss can be attained for a large branching angle.

2. DESIGN

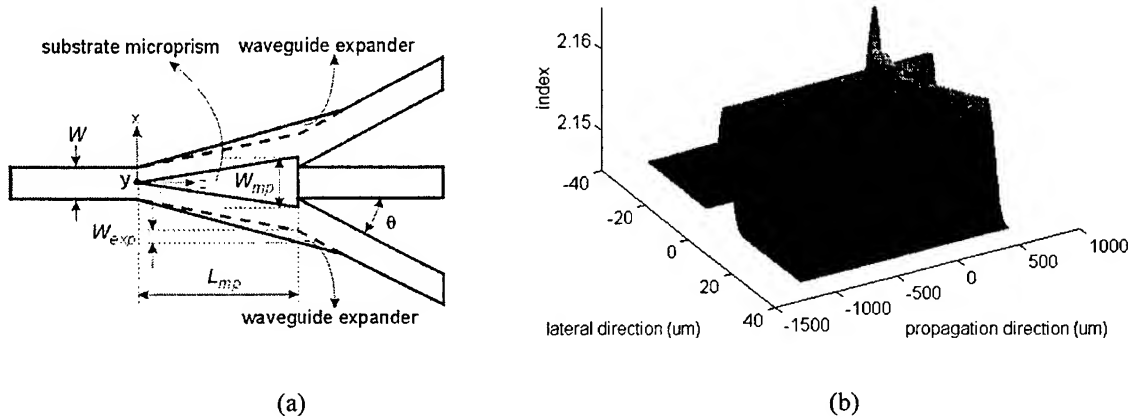


Fig. 1 The proposed three-branch optical power divider, (a) in the form of Ti-film geometry, (b) the index distribution on the substrate surface.

On LiNbO₃, Ti-diffused waveguide is formed by diffusing Ti film into LiNbO₃ substrate at the temperature about 1025°C. The produced index distribution is graded and depends on various waveguide fabrication parameters. On the substrate surface, its index distribution is mainly dependent on the Ti-film geometry. As to the depth direction, its index variation is related to the other waveguide fabrication parameters, such as Ti-film thickness τ , Ti-diffusion temperature T , and Ti-diffusion time t . In the proposed optical power divider, the required device region is formed by one-step Ti-diffusion and no other regions of indices different from that formed by Ti diffusion are required. For simplicity in elucidation, the device structure is shown in the form of the Ti film geometry.

The proposed three-branch optical power divider with the form of Ti-film geometry is shown in Fig. 1(a). The corresponding index distribution on the substrate surface with the following parameters: $\theta=3^\circ$, $W=6\mu\text{m}$, $\tau=700\text{\AA}$, $T=1025^\circ\text{C}$, $t=4\text{hr}$, $W_{mp}=6\mu\text{m}$, $L_{mp}=123.5\mu\text{m}$, $W_{exp}=0\mu\text{m}$, is displayed in Fig. 1(b). In a conventional optical power divider, because the phase-front in two sides of the input optical field is not appropriately tilted, only little input optical power can enter into the two sideward output waveguides and most of them is transmitted through the central output waveguide. To solve this problem, a microprism with index equal to that of the substrate, called substrate microprism, is placed at the transition region between the input and the output waveguides. The substrate microprism has a width W_{mp} and a length L_{mp} . Since the phase-front near the center of the microprism propagates a longer distance in the substrate microprism than the phase-front near two sides of the microprism, the former propagates faster than the latter. That results in a phase-front tilt and is in favor of the optical power transmission into the two sideward output waveguides.

The optical power transmitted into the two sideward output waveguides mainly comes from the power in two sides of the input optical field. However, for a single-mode waveguide, most of the optical power is concentrated in the center of the waveguide. In order to increase the optical power in two sides of the optical field, two waveguide expanders with width W_{exp} are appended at two sides of the taper region.

3. NUMERICAL MODELING AND SIMULATION METHODS

The proposed optical power divider is formed by diffusing Ti-film into LiNbO₃ substrate. In the simulation, the required refractive index profile of Ti-diffused region refers to the literature⁶. The substrate micropism placed at the transition between the input and the output waveguides is formed by removal of the Ti-film in this region. After Ti diffusion, some Ti ions enter the substrate micropism region and make the range of substrate micropism diminished. Besides, the index distribution on the boundary of three sides of the substrate micropism is gradually varied. This index variation is also considered in the refractive index model of the proposed optical power divider.

The 3D semi-vectorial finite-difference beam propagation method⁷ (3D-SVFDBPM) is employed to simulate the propagation characteristic of the optical field in the optical power divider. In order to use the largest electrooptic coefficient r_{33} on LiNbO₃, only the TM mode on a z-cut x-propagating LiNbO₃ substrate is considered in simulation. Its wavelength is $\lambda=1.3\mu\text{m}$. The transmitted power η in the output waveguide is calculated by the overlap integral.

4. SIMULATION RESULTS

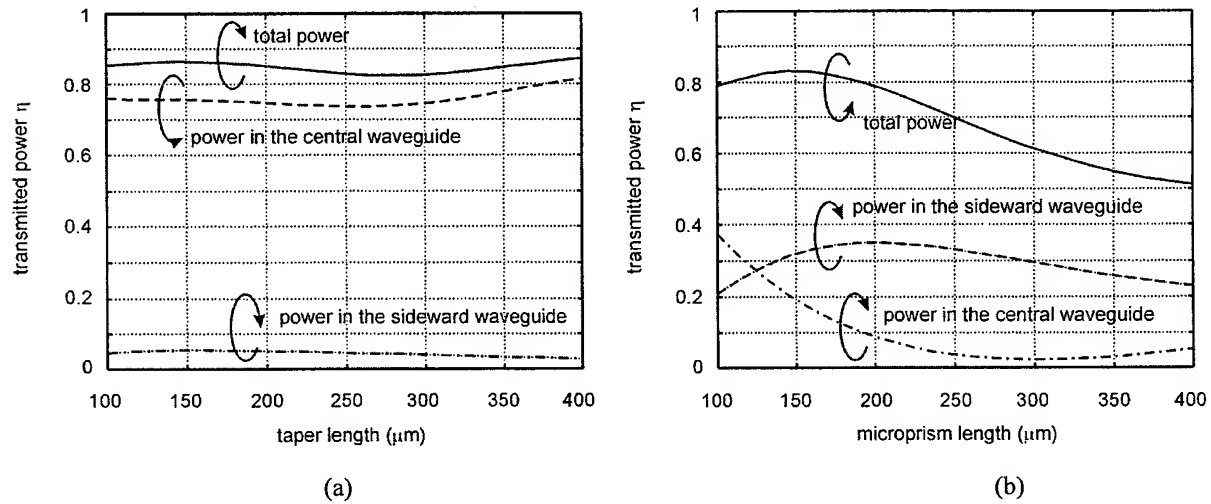


Fig. 2 The transmitted power versus the taper/micropism length for the optical power divider, (a) without the substrate micropism, (b) with the substrate micropism.

4.1 The Effect of the Substrate Micropism

To show the effect of the substrate micropism on the transmission of the input optical power into the two sideward output waveguides, the transmission characteristics for optical power dividers without and with the substrate micropism are displayed in Fig. 2(a) and (b). These optical power dividers with a branching angle $\theta=3^\circ$ are formed by diffusing a patterned Ti-film with $\tau=700\text{\AA}$ and $W=6\mu\text{m}$ at $T=1025^\circ\text{C}$ for $t=4\text{hr}$. For the optical power divider without the substrate micropism, most of the transmitted optical power is still concentrated in the central output waveguide as the taper length increases from $100\mu\text{m}$ to $400\mu\text{m}$. Thus, equal-power division can not be achieved for this structure. As the substrate micropism with $W_{mp}=6\mu\text{m}$ is appended, the transmitted power in the two sideward output waveguides can be effectively increased such that equal-power division can be obtained for $L_{mp}=123.5\mu\text{m}$, as shown in Fig. 2(b). It is demonstrated that the substrate micropism can appropriately tilt the phase-front of the input optical field and is in favor of the optical power transmission into the two sideward output waveguides.

The power splitting ratio γ is defined as the ratio of the power in the sideward output waveguide to that in the central output one. For a conventional optical power divider, it is always less than 1. Note that the proposed optical power divider can be designed such that $\gamma > 1$, $\gamma = 1$, or $\gamma < 1$, dependent on the value of L_{mp} . In this work, the power divider is designed

such that γ is as close to one as possible.

Fig.3 displays the field distributions in the proposed optical power divider with the following parameters: $\theta=3^\circ$, $W=6\mu\text{m}$, $\tau=700\text{\AA}$, $T=1025^\circ\text{C}$, $t=4\text{hr}$, $W_{mp}=6\mu\text{m}$, $L_{mp}=123.5\mu\text{m}$, $W_{exp}=0\mu\text{m}$ at different positions. It is found that the input optical fields in the proposed optical power divider can be smoothly split into three output waveguides. The optical powers in the central and the sideward output waveguides are as high as 27.65% and 27.11%, respectively, with a total transmission of 81.86%.

The index distribution of the optical power divider is altered by the fabrication parameters of Ti-diffused waveguide. To understand the effect of those parameters on the transmission characteristics of the proposed optical power divider, two situations with varying Ti-film thickness and with varying Ti-diffusion time are considered with the same $W=6\mu\text{m}$, $W_{mp}=6\mu\text{m}$, $W_{exp}=0\mu\text{m}$, and $T=1025^\circ\text{C}$.

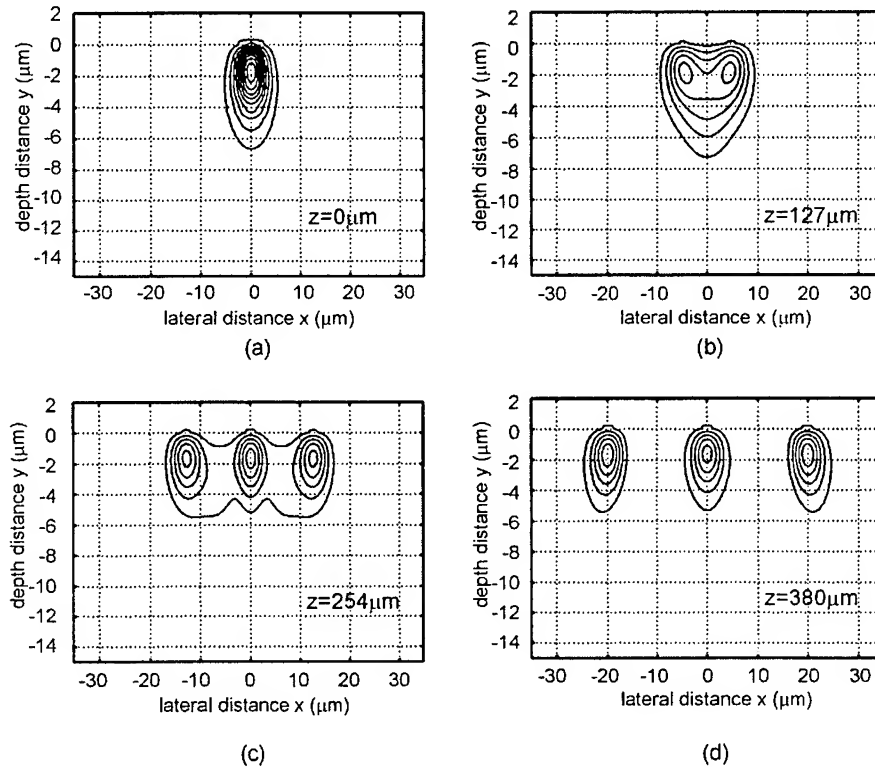


Fig. 3 The field distributions in the proposed optical power divider at (a) $z=0\mu\text{m}$, (b) $z=127\mu\text{m}$, (c) $z=254\mu\text{m}$, (d) $z=380\mu\text{m}$.

4.1.1. Varying Ti-film thickness τ

Consider three cases with different Ti-film thickness $\tau=500\text{\AA}$, 600\AA , and 700\AA . Their diffusion time is set as $t=4\text{hr}$. They have refractive index profiles with the same depth but different maximum index value. The microprism length L_{mp} versus the branching angle θ is shown in Fig. 4. Because more phase-front tilt is required for a larger θ , the microprism length increases with θ . For the curves corresponding to different τ , because the refractive index becomes larger as τ increases, the index difference between waveguide and substrate augments. More phase difference can be obtained from the field propagation in the substrate microprism. Hence, the required microprism length is reduced.

Fig. 5 shows the power splitting ratio γ versus the branching angle θ . Because the case for $\tau=700\text{\AA}$ can provide adequate phase-front tilt, the branching angle for equal-power division can be larger than 6° . As to the case for $\tau=500\text{\AA}$ and

600Å, the branching angles for the equal-power division are 3° and 4.5°, respectively. The total transmitted power, which is the sum of the powers in three output waveguides, varied with the branching angle is shown in Fig. 5. The branching angles with $\eta > 80\%$ are $\theta = 2.7^\circ, 3.2^\circ, 3.3^\circ$ for $\tau = 500\text{Å}, 600\text{Å}, 700\text{Å}$, respectively.

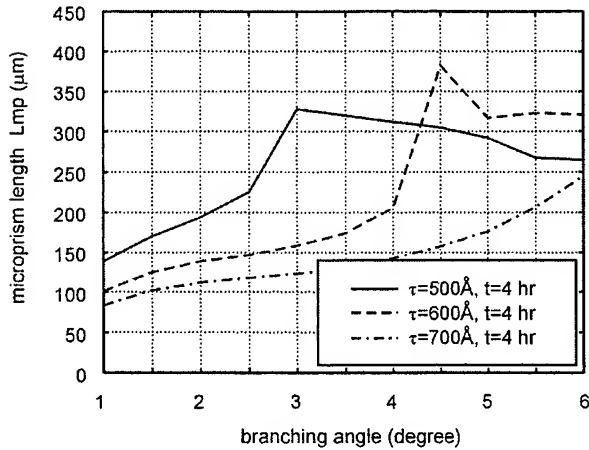


Fig. 4 The microprism length L_{mp} versus the branching angle θ in the situation of varying Ti-film thickness

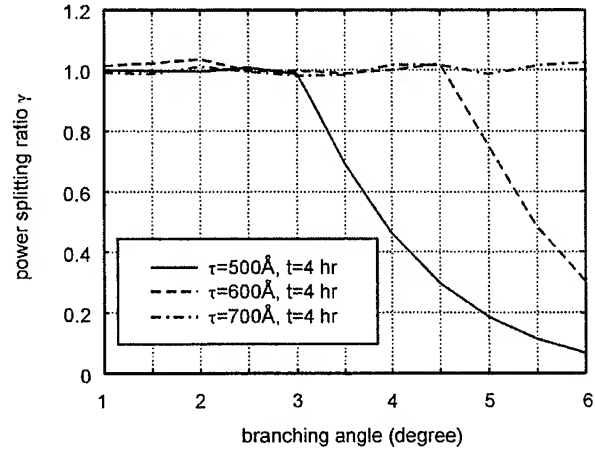


Fig. 5 The power splitting ratio γ versus the branching angle θ in the situation of varying Ti-film thickness

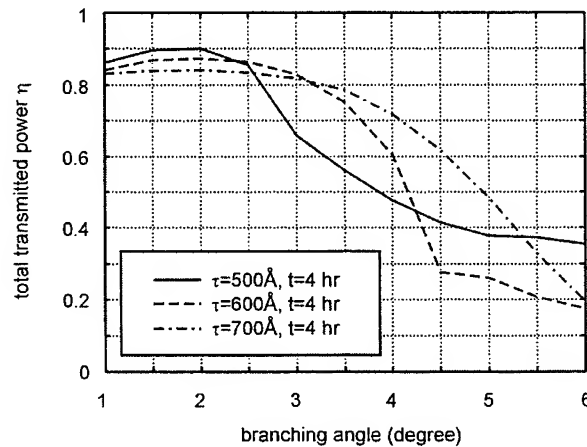


Fig. 6 The total transmitted power η versus the branching angle θ in the situation of varying Ti-film thickness.

4.1.2. Varying Ti-diffusion time t

Consider three cases with different Ti-diffusion time $t = 4\text{hr}, 5\text{hr},$ and 6hr . The Ti-film thickness is set as $\tau = 700\text{Å}$. Different Ti-diffusion time not only varies the depth of the index profile, but also change the maximum index value. Fig. 7 shows the required microprism length L_{mp} for different branching angle θ . Because the index becomes smaller as Ti-diffusion time increases, the similar variation of L_{mp} mentioned in the previous section is observed. Fig. 8 and Fig. 9 show the power splitting ratio γ and the total transmitted power η , respectively, versus the branching angle θ . It is shown that the

branching angles with the equal-power division are 3.5° , 4.5° , $> 6^\circ$, each for $t=4\text{hr}$, 5hr , 6hr . Besides, the branching angle with $\eta > 80\%$ is 2.6° , 3° , 3.3° , for $t=4\text{hr}$, 5hr , 6hr , respectively.

Since varying the Ti-diffusion time simultaneously changes the depth of the index profile and the maximum index value, it seems that the effect of varying Ti-diffusion time should be more obvious than that of varying Ti-film thickness. However, from the observation of the simulation results, it is not so. That is because in the simulation for the effect of varying Ti-diffusion time, a larger Ti-film thickness $\tau=700\text{\AA}$ is used. Because $\tau=700\text{\AA}$ can produce a waveguide with adequate index increment, even though the Ti-diffusion time is varied from 4hr to 6hr, the reduced index and the increased depth of the index profile do not seriously degrade the power transmission in the proposed optical power divider.

4.2 The Effect of Two Waveguide Expanders

As shown in the previous subsection, when the Ti-film thickness is reduced or the Ti-diffusion time is prolonged, the total transmitted power is somewhat degenerate. Though the equal-power division still can be remained by using a longer substrate micropism, more serious variation of the optical field results in a larger field mismatch loss and reduces the total transmitted power. In the following, the effect of two waveguide expanders with $W_{exp}=2\mu\text{m}$ for two situations of varying Ti-film thickness and varying Ti-diffusion time are considered. The other parameters of the proposed optical power dividers are set as: $W=W_{mp}=6\mu\text{m}$, $T=1025^\circ\text{C}$, and $\theta=3^\circ$.

The simulated results for the cases of varying Ti-film thickness are shown in Table 1. It is found that for the optical power dividers without two waveguide expanders ($W_{exp}=0\mu\text{m}$), as the Ti-film thickness decreases from 700\AA to 500\AA , the total transmitted power η is reduced about 15.87%. This power degradation can be avoided by appending two waveguide expanders with $W_{exp}=2\mu\text{m}$. The total transmitted power η for the optical power divider with two waveguide expanders can be as high as 87.45%, even higher than that for the case of $\tau=700\text{\AA}$ without two waveguide expanders. Besides, the required substrate micropism length can be reduced to $181.0\mu\text{m}$, which can greatly lessen the occupied area of the device in the LiNbO_3 chip.

For the cases of varying Ti-diffusion time, the simulated results are shown in Table 2. The total transmitted power η is reduced about 11.74% as the Ti-diffusion time increases from 4hr to 6hr. As mentioned above, it also can be improved by adding two waveguide expanders and has an additional advantage of shorter substrate micropism length.

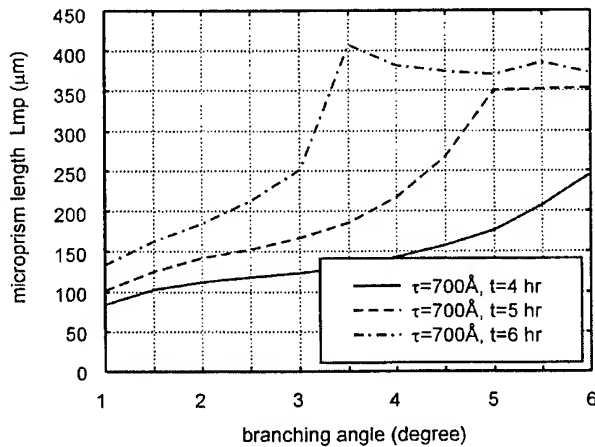


Fig.7 The microprism length L_{mp} versus the branching angle θ in the situation of varying Ti-diffusion time.

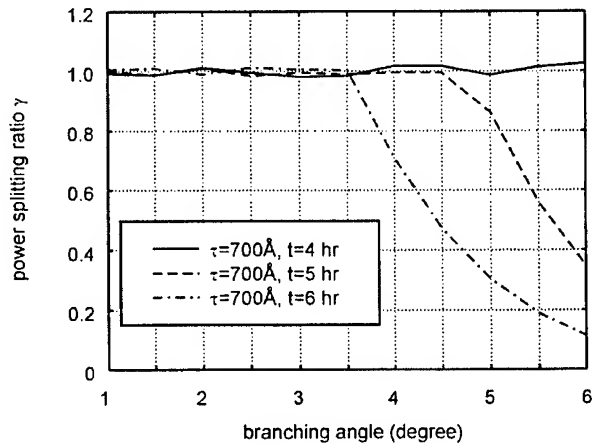


Fig. 8 The power splitting ratio γ versus the branching angle θ in the situation of varying Ti-diffusion time.

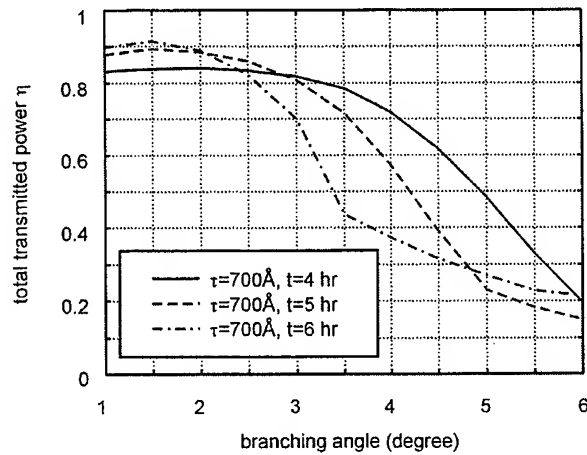


Fig.9 The total transmitted power η versus the branching angle θ in the situation of varying Ti-diffusion time.

Device parameters					Simulation results	
τ (Å)	T (°C)	W_{exp} (μm)	W_{mp} (μm)	L_{mp} (μm)	γ	η
700	4	0	6	123.5	0.98	81.86%
500	4	0	6	327.7	0.99	65.99%
500	4	2	6	181.0	1.00	87.45%

Table 1 The device parameters of the proposed optical power divider, and the corresponding simulation results for the cases of varying Ti-film thickness.

Device parameters					Simulation results	
τ (Å)	T (°C)	W_{exp} (μm)	W_{mp} (μm)	L_{mp} (μm)	γ	η
700	4	0	6	123.5	0.98	81.86%
700	6	0	6	250.5	1.01	70.12%
700	6	2	6	175.0	1.03	82.6%

Table 2 The device parameters of the proposed optical power divider, and the corresponding simulation results for the cases of varying Ti-diffusion time.

5. SUMMARY

A novel three-branch optical power divider by Ti diffusion on LiNbO₃ using one substrate microprism and two waveguide expanders is proposed. With the appropriate phase-front tilt and field modification, the power in the two sideward output waveguides can be greatly increased. The proposed optical power divider can be designed such that the power in the two sideward output waveguides can be larger or smaller than that in the central output waveguide, dependent on the substrate microprism length. When the equal-power division is desired, even the branching angle is larger than 6°, the purpose of the equal-power division still can be achieved.

The variations of device performance with waveguide fabrication parameters are also considered. For the optical power divider only with one substrate microprism, when the index of the fabricated waveguide decreases, caused by using either a smaller Ti-film thickness or a longer Ti-diffusion time, the total output power is dropped. This power degradation

can be avoided by appending two waveguide expanders to the proposed optical power divider. Simulation results show that the total output power can be as high as 87.45% even for a branching angle $\theta=3^\circ$. To our knowledge, for optical equal-power dividers by Ti diffusion on LiNbO₃ reported so far, it is the largest output power achieved for such a large branching angle $\theta=3^\circ$.

Since no extra regions of indices different from that of substrate and that of Ti-diffused region are required, the proposed three-branch optical power divider can be easily fabricated. It has the advantages of low insertion loss, large branching angle, and easy fabrication. The proposed optical power divider will be experimentally demonstrated in the near future.

ACKNOWLEDGEMENTS

This work was supported by National Science Council, Taipei, Taiwan, R.O.C. under Contract NSC89-2215-E-002-009.

REFERENCES

1. M. Belanger, G.L. Yip, and M. Haruna, "Passive planar multibranch optical power divider: some design considerations," *Appl. Opt.*, **22**, pp. 2283-2289, 1983.
2. M. Haruna, M. Belanger, and G.L. Yip, "Passive 3-branch optical power divider by K⁺-ion exchange in glass," *Electron. Lett.*, **21**, pp.535-536, 1985.
3. W.Y. Hung, H.P. Chan, and P.S. Chung, "Single-mode 1 3 integrated optical branching circuit design using phase-front accelerators," *Electron. Lett.*, **24**, pp.1365-1366, 1988.
4. S. Banba and H. Ogawa, "Novel symmetrical three-branch optical waveguide with equal power division," *IEEE Microwave & Guided Wave Lett.*, **2**, pp.188-190, 1992.
5. H.B. Lin, Y.H. Wang, and W.S. Wang, "Single-mode 1×3 integrated optical branching circuit design using microprism," *Electron. Lett.*, **30**, pp.408-409, 1994.
6. F.S. Chu and P.L. Liu, "Simulations of Ti:LiNbO₃ waveguide modulators – a comparison of simulation techniques," *J. Lightwave Technol.*, **8**, pp.1492-1496, 1990.
7. P.L. Liu and B.J. Li, "Study of form birefringence in waveguide devices using the semivectorial beam propagation method," *IEEE Photon. Technol. Lett.*, **3**, pp.913-915, 1991.

*Correspondence: Email: fl10939@ntut.edu.tw, wswang@cc.ee.ntu.edu.tw; Telephone: 886-2-2363-5251 ext.423

SESSION 9

Organic Light-Emitting Devices

Temperature- and field-dependent quantum efficiency in tris-(8-hydroxy) quinoline aluminum light emitting diode

S. K. Saha^{1*}, Y. K. Su¹, F. S. Juang²

¹Department of Electrical Engineering, National Cheng Kung University, Tainan, Taiwan 70101, R.O.C.

²Department of Electro-Optics Engineering, National Huwei Institute of Technology, Huwei, Yunlin 63208, Taiwan, R.O.C.

Abstract

Temperature- and field-dependent electroluminescence and quantum efficiency have been investigated in tris-(8-hydroxy) quinoline aluminum (Alq₃) light emitting diode over the temperature range from 10K to 300K. It has been observed that up to a certain temperature luminescence intensity decreases with decreasing temperature and then saturated in the low temperature region. The quantum efficiency increases with decreasing temperature and finally reaches to almost a constant value. At lower applied voltage, two peaks have been observed in the quantum efficiency with temperature. The two peaks are attributed due to deep trap levels (high temperature regime) and shallow trap levels (low temperature regime) in Alq₃.

Introduction

Organic electroluminescent (EL) devices are of great importance because of their potential application in large area flat panel displays¹⁻³. For many optoelectronic applications, an understanding of the processes limiting charge injection and conduction is critical for device optimization and hence high efficiency operation. However, there remains little detailed understanding of the charge transport mechanisms, and of the role played by organic interfaces in controlling the operation of such devices. It has recently been shown⁴ that the current voltage (I-V) and EL characteristics of OLED are consistent with the injection of charge carriers into a thin film with a large density of traps distributed in energy beneath the lowest unoccupied molecular orbital (LUMO). The physical nature of trap states in the materials is important to the carrier transport in the organic

* Correspondence

Email: sksaha@mail.ncku.edu.tw

Fax: 886-6-2351864

layers. It is believed that EL in OLED originates due to the recombination of these trap states. The study of temperature dependent luminescence is a very useful tool to understand the device physics especially, the band states and charge transport mechanisms. In this work we report the temperature dependence of electroluminescence and quantum efficiency to understand the effect of trap states on the efficiency of the OLED devices containing tris-(8-hydroxy) quinoline aluminum (Alq_3) as the electron transport layer as well as emissive layer and N,N'-diphenyl-N,N' bis (3-methylphenyl)-[1-1'-biphenyl]-4-4'-diamine (TPD) as the conventional hole transport layer.

Experimental

Figure 1 shows a typical structure of the device fabricated for this study. ITO glass with $20\ \Omega/\text{cm}^2$, was cut into $2 \times 2\ \text{cm}^2$ pieces and then cleaned in an ultrasonic bath of isopropyl alcohol, methanol and acetone respectively. A layer of about 100nm thickness of TPD has been spin coated on ITO substrate. Alq_3 obtained from Aldrich Co. has been purified by sublimation technique. Alq_3 layer of thickness $\sim 60\text{nm}$ was deposited at a rate of $1\ \text{\AA}/\text{sec}$, under pressure of 10^{-5} Torr. The cathode material (Aluminum) was evaporated on top of the Alq_3 layer by evaporation technique. The EL spectra have been measured using Acton Research Corporation Spectra pro 500 and I-V measurements have been carried out by HP 4145B semiconductor parameter analyzer over the temperature range from 10 to 300K. The power of the device has also been measured by power meter over the same temperature range.

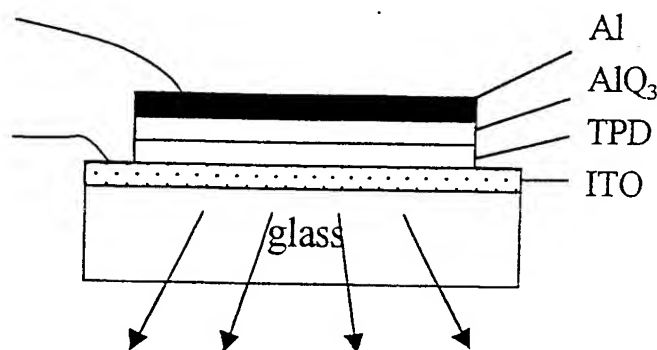


Fig. 1 Schematic device structure of the OLED.

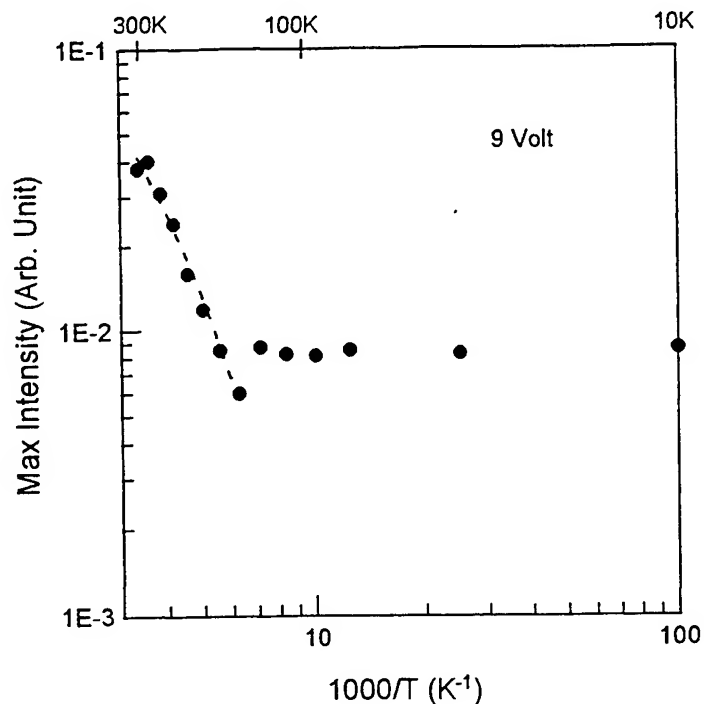


Fig. 2. Variation of EL intensity with temperature. The dashed line is the fitting of the exponential function.

Results and discussion

It has previously been shown that the optical properties of low-mobility organic solids are dominated by small radius Frenkel exciton⁴. Forrest et al⁵ assumed that the electroluminescence originates from the generation and subsequent radiative recombination of Frenkel excitons in the Alq₃ layer. These excitons are formed by electrons, localized in the traps and holes injected from the TPD layer. The EL flux, ϕ_{EL} , is then proportional to the rate of radiative recombination from these localized states, and hence to the rate of recombination of minority carrier holes in Alq₃.

Forrest et al⁵ have calculated the hole density, $p(x)$, using the steady state continuity equation where D_p is the hole diffusion constant, μ_p is the hole mobility and $F(x)$ is the mean life time of the

$$\frac{p(x)}{\tau_p(x)} = D_p \frac{d^2 p(x)}{dx^2} - \mu_p \frac{d}{dx} [p(x)F(x)] \dots (1)$$

holes at a distance x from the electron injecting electrode.

The expression for $p(x)$ valid near $x=d$ is given by, The expression for $p(\chi)$ is given by,

$$p(x) = p(d) \frac{d}{x} \exp \left[\frac{x-d}{\mu_p F(d) \tau_p(d)} \right] \dots \dots \dots (2)$$

where

$$p(d) = N_{HOMO} \exp \left[\frac{E_{HOMO} - E_p}{kT} \right] \dots \dots \dots (3)$$

is the hole density at the hetero interface, E_p is the hole quasi-Fermi level and N_{HOMO} is the density of states in the highest occupied molecular orbital (HOMO)

In Eq.3, $p(d)$ is the hole density at the heterointerface, E_p is the hole quasi-Fermi level and N_{HOMO} is the density of states in the HOMO.

The total recombination rate per unit area is then given by

$$R = \int_0^d p(x) / \tau_p(x) dx = p(d) \mu_p F(d) \dots \dots \dots (4)$$

The temperature dependent EL flux $\phi_{EL}(T)$ is then obtained by multiplying the temperature dependent photoluminescence (PL) efficiency which is the ratio of radiative to total recombination. The expression for $\phi_{EL}(T)$ is given by,

$$\phi_{EL}(T) = \alpha \eta_{PL}(T) p(d) \mu_p F(d) \dots \dots \dots (5)$$

where α is a constant.

Fig. 2 gives the maximum EL intensity with temperature. From this figure it is observed that initially the intensity decreases with decreasing temperature and finally saturates after a certain temperature. We have fitted our high temperature data by the exponential equation like $\exp(-\Delta E/kT)$ where ΔE is activation energy. But in the low temperature region there is a large deviation. To analyze our data over the whole temperature range we have splitted the temperature ranges into two regions. As the electroluminescence in Alq_3 occurs due to radiative recombination of the trapped electrons and the holes injected from the TPD layer, the luminance intensity depends on the distribution of hole density with temperature. From the energy band scheme it is seen that the

energy barrier between the LUMO levels of TPD and Alq₃ is very large compared to that of the HOMO levels. Therefore the device current is dominated by holes and light emission originates from the Alq₃ layer. The hole mobility in TPD ($\sim 7.0 \times 10^{-3} \text{ cm}^2/\text{Vs}$) is also much higher than the electron mobility ($5 \times 10^{-5} \text{ cm}^2/\text{Vs}$) in Alq₃. For this reason under some bias, holes can easily reach the Alq₃ layer than electrons and will be accumulated at the TPD/Alq₃ interface. At high temperature hole mobility in Alq₃ layer ($\mu_p \sim 1/T^2$ taken by other workers⁶) is very low. Therefore recombination takes place mainly very near to TPD/Alq₃ interface and intensity depends only on hole concentration at the interface. As the hole concentration decreases exponentially according to equation 3 intensity also decreases accordingly. At lower temperature, hole mobility in Alq₃ layer increases therefore more and more holes will be mobile and consequently charge accumulation decreases at the interface and recombination zone shifts toward the bulk of Alq₃. Below certain temperature, when accumulation of holes at the interface is low, the recombination takes place mainly in the bulk of Alq₃ and intensity will be constant due to constant supply of holes from TPD to Alq₃ at a fixed bias voltage.

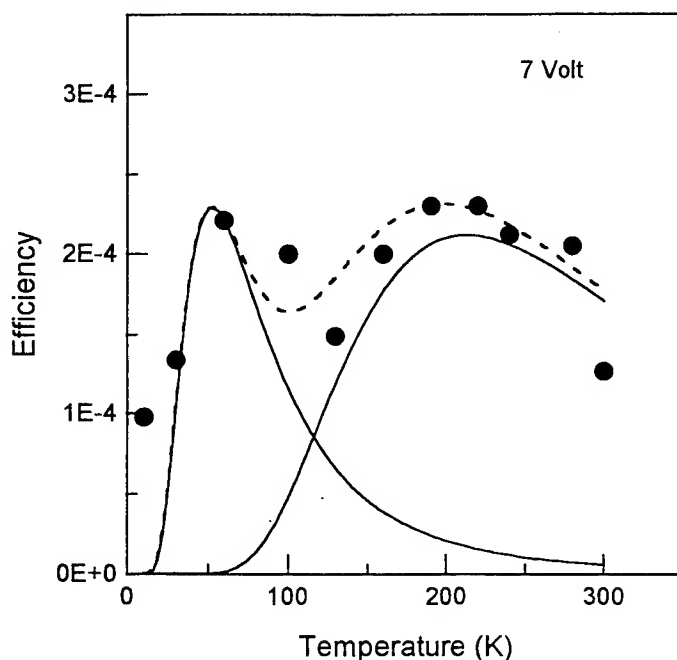


Fig. 3 Variation of quantum efficiency with temperature.

The solid lines represent the theoretical curves as obtained by equation 5.

The dashed line is the resultant curve of the two peaks.

In Fig. 3 we have fitted the experimental data by equation (5). The solid lines represent the theoretical curves as obtained by equation (5) and the points are the experimental data. We have used

the hole mobility (μ_p) as $1/T^2$ (taken by other workers⁶). From the fitting procedure it has been observed that the best fit curve (dotted line shown in Fig. 3) is the resultant of two peaks, one in the high temperature region and the other in the low temperature region.

The origin of two peaks at low voltage might be explained by considering the trap states distributed in two different energy region. From the thermally stimulated luminescence (TSL) spectra of Alq_3 , it has been observed that apart from deep trap states ($\sim 0.15\text{eV}$), there are also shallow trap states ($\sim 0.07\text{eV}$). The high-temperature peak in Fig. 3 is attributed to the deep trap states and the low-temperature peak is due to shallow trap states. The most interesting phenomenon is the origin of the low-temperature peak. To our knowledge, so far most of the results⁷ in the literature regarding quantum efficiency in alq_3 device show a saturation in the low temperature regime. This is because of the fact that the quantum efficiency have been measured with higher voltage. In the present work it has been observed that as voltage increases the high temperature peak shifts toward lower temperature and finally at voltage around 10 V the two peaks superpose and causes the apparent saturation as shown in fig. 4.

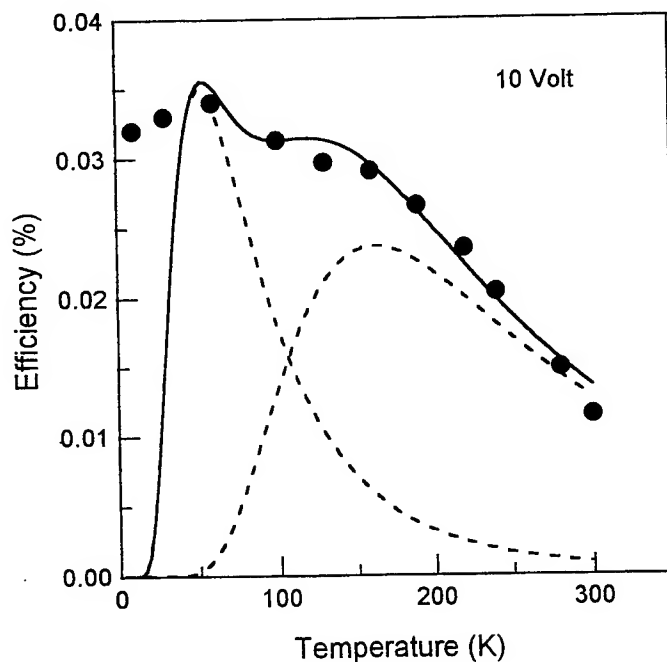


Fig. 4 The high-temperature quantum efficiency peak converges with the low-temperature peak at voltage 10V

In summary, the temperature-dependent quantum efficiency of the ITO/TPD/Alq₃/Al device have been studied over the temperature range from 10K to 300K on the basis of Frenkel exciton model. Two peaks have been observed one in the high temperature regime and the other in the low temperature regime. The high-temperature peak originates due to recombination of the trapped deep level electrons and the mobile holes and the low-temperature peak due to trapped (Shallow) holes with the mobile electrons.

References

1. C. W. Tang and S. A. Van Slyke, Appl. Phys. Lett. 51 913 (1987)
2. J. H. Burroughes, D. D. C Bradley, A. R. Brown, R. N. Marks, K. Macky, R. H. Friend, P. L. Burns and A. B. Holmes, Nature (London) 347 539 (1990)
3. D. Braun and A. J. Heeger, Appl. Phys. Lett. 58 1982 (1991)
4. E. A. Silinsh, "organic molecular crystals", (Springer verlag:Berlin) (1980).
5. S. R. Forrest, P. E. Burrows and M. E. Thomson, "Organic electroluminescent materials and devices", Edited by Seizo Miyata and Hari Singh Nalwa, P415 (1997).
6. L. Friedman, "Electron phonon interaction in organic molecular crystals", Phys. Rev. 140 P A1649 (1965).
7. S. R. Forrest, P. E. Burrows and M. E. Thomson, "Organic electroluminescent materials and devices, " Edited by Seizo Miyata and Hari Singh Nalwa 435 (1997)

Origin of the blue emission from poly(1-phenyl-2-alkynes) and poly(phenylacetylenes)

Weikun Ge^a, Yuan Ming Huang^a, Jacky W. Y. Lam^b, and Ben Zhong Tang^b

^aDepartment of Physics, Hong Kong University of Science and Technology, Clear Water Bay, Kowloon, Hong Kong, China

^bDepartment of Chemistry and Center for Display Research, Hong Kong University of Science and Technology, Clear Water Bay, Kowloon, Hong Kong, China

ABSTRACT

We have studied the electronic structure, absorption, and photoluminescence of poly(1-phenyl-2-alkynes) – $[(C_6H_5)C=C(C_mH_{2m+1})]_n$ ($m = 1, 2$), poly(phenylacetylene) $-[HC=C(C_6H_5)]_n$ and its derivatives $-[HC=C(C_6H_4-p-R)]_n$ with various non-liquid crystal ring substituents. For poly(1-phenyl-2-alkynes), the PL efficiency is very sensitive to the molecular structure of the alkyl pendant and can be enhanced up to 50 times as the alkyl side-chain increases in length. But for poly(phenylacetylenes), their luminescent efficiency can be improved several times only as the tail becomes bulky. Regardless of the types of the pendants, the emission color of the polymers is pinned at ~450 nm (2.7 eV). The band structure of the polymers, which has been calculated using extended Hückel tight-binding method, is essentially an ensemble of the backbone (extended states) and the pendants (localized states), and the processes of optical absorption and blue emission are confined in the directly attached aromatic ring. The interaction between the phenyl chromophore and its nearest neighbors is of vital importance in improving the emission efficiency. Although the band gap of the backbone can be enlarged by the pendant, its π - π^* interband transition is insignificant for the blue emission.

Keywords: substituted polyacetylene, poly(1-phenyl-2-alkynes), poly(phenylacetylenes), photoluminescence, density of states, electronic structure, localized states, extended states.

1. INTRODUCTION

The extensive research of polyacetylene (PA) in the last 30 years has contributed greatly to the understanding of the physics of conjugated polymers. PAs, however, are generally regarded as unsuitable candidates for electronic and optoelectronic applications because of its disappointing photoluminescence (PL) behavior.¹⁻⁴ Substitution of the hydrogen atoms of PA with other atoms or groups can perturb the electronic structure of the macromolecules. These substituted polyacetylenes have substantially different optical properties from those of PAs, and indeed a variety of PAs with two substituents [or disubstituted PAs; $-(RC=CR')_n$] have been found to be highly luminescent. Emission of intense blue or green light has been observed in a number of disubstituted PAs including poly(diphenylacetylene) derivatives $-(C_6H_5)C=C(C_6H_4-p-R)]_n$ { $R = OC_6H_5$, n - C_3F_7 , n - and t - C_4H_9 , $C_{10}H_{16}$ (adamantyl), $Si(CH_3)_3$, $Si[CH(CH_3)_2]_3$, and $Si(C_6H_5)_3$ }, poly(1-phenyl-2-alkynes) $-(C_6H_5)C=C(C_mH_{2m+1})]_n$ ($m = 1, 2, 6$), poly(1-chloro-2-arylacetylene) with the aryl groups being phenyl and naphthyl, and poly(1-methyl-2-naphthylacetylene).⁵⁻¹³ The PL behavior of monosubstituted PAs $-(HC=CR)_n$ has also been investigated, but (normally) only weak luminescence has been observed in such polymers, examples of which include poly(phenylacetylene) and its derivatives $-[HC=C(C_6H_4-R)]_n$ with ring substituents of CF_3 , $Si(CH_3)_3$, $Si(CH_3)_2C_6H_5$, i - C_3H_7 , and n - C_4H_9 at ortho and para positions, and poly(propargyl) derivatives $-[HC=C(CH_2-R)]_n$ with $R =$ diphenylamino and indolyl.^{7, 9, 10, 14} Monosubstituted PAs are thus often referred to as nonluminescent polymers and are generally regarded as unpromising candidates for light emitting materials.

In order to explain why disubstituted polyacetylenes are highly luminescent while monosubstituted polyacetylenes are poorly luminescent, the enlarged band gap of the backbone is widely adopted to explain the intense blue or green emission from some disubstituted polyacetylenes, while the generation of non-emissive solitons in the degenerate backbones of those monosubstituted polyacetylenes is exploited to account for their weak emission.¹⁻¹⁴ Although such interpretations can explain some results qualitatively, they lack of self-consistency because not all disubstituted polyacetylenes are highly luminescent. On the other hand, as a prediction of these interpretations, bulky side-chains should be able to tune the emission color of substituted polyacetylenes no matter they are classified as disubstituted polyacetylenes or monosubstituted ones. The emission energies of poly(1-phenyl-2-alkynes) $-(C_6H_5)C=C(C_mH_{2m+1})]_n$ ($m=1, 2, 6$) and poly(phenylacetylene) $-[HC=C(C_6H_5)]_n$, however, are all pinned at ~2.7 eV regardless of the types of alkyl side-chains. Moreover, the pinned emission energy does not change as a result of the change in the excitation energy.^{3, 6-8} Finally, the interpretations contradict to the recent experimental observations. For instance, we have synthesized a group of highly luminescent monosubstituted

polyacetylenes with liquid crystalline pendants.¹⁵⁻²² They can emit intense and electrically tunable deep-blue PL.¹⁸⁻²² The electronic structures are of crucial importance in the interpretation of their optical properties because they are closely related. A semi-quantitative calculation is proven to be very helpful in giving a physically reasonable interpretation because conjugated polymers can be considered as organic semiconductors, and the concepts of energy band theory can be used to characterize their electronic states and optical properties.^{23, 24} The calculated electronic structures for our highly luminescent monosubstituted PAs indicate that, instead of the distorted backbone, the side-chains with biphenyl chromophores are the origin of their deep-blue emissions.²⁰

In this paper, we studied the origin of the blue emissions from non-liquid crystalline substituted polyacetylenes. Disubstituted polyacetylenes poly(1-phenyl-2-alkyns) $-(C_6H_5)C=C(C_mH_{2m+1})_n$ ($m = 1, 2$) and monosubstituted polyacetylene and its derivatives $-[HC=C(C_6H_4-p-R)]_n-$ are used as typical examples to serve our purpose. Regardless of the types of the side-chains or the bulky tails, all of these polymers emit blue lights with their emission energy pinned at 2.7 eV. In Section 2, the experimental details are described. In Section 3, we have probed the roles of the alkyl pendant and the phenyl pendant in the blue emissions of poly(1-phenyl-2-alkyns). In Section 4, we have investigated the effect of the phenyl ring-substituent on the blue emissions of poly(phenylacetylenes). Theoretical calculations are outlined and compared to experimental results obtained by optical absorption and PL, and our study leads to the establishment of the origin of their blue emissions. A conclusion is given in Section 5.

2. EXPERIMENTAL DETAILS

In Section 3, Monosubstituted poly(phenylacetylene) (PPA), disubstituted poly(1-phenyl-2-propyl) (PPP) and poly(1-phenyl-2-butyne) (PPB) were used in our experiment. Their molecular structures are shown in Fig. 1. The first replacement, an *aromatic* ring, is directly attached to the polymer backbone while the second replacement is an alkyl such as CH_3 and C_2H_5 . The sample synthesis and characterization were reported elsewhere.²⁵ In Section 4, poly(phenylacetylene) and its derivatives were used in the study. The molecular structures of poly(phenylacetylenes) with various ring-substituents are shown in Table 1. Polymers 3-7 have more bulky and branched tails than 1 and 2.

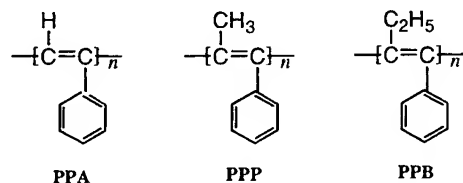


Figure 1 Molecular structures of poly(phenylacetylene) (PPA), poly(1-phenyl-2-propyl) (PPP) and poly(1-phenyl-2-butyne) (PPB).

The solutions for the PL measurements were prepared by dissolving the polymers in spectroscopic grade chloroform ($CHCl_3$). The concentrations (mM) of the solutions PPA, PPP and PPB were about 1.16, 0.125, and 0.064, respectively. The concentrations of solutions of 1-7 were about 10^{-3} mM. The molar concentrations of the polymer solutions were calculated on the basis of the molecular masses of their repeat units. Solutions were kept in a 1-mm-thick quartz cell. The absorption spectra of the polymer solutions were recorded on a Shimadzu UV-Vis spectrophotometer (UV-2401PC). The 325-nm line from an Omnicrome helium-cadmium laser was used as the excitation source. The PL spectra were measured at room temperature in the quartz cell on a Spex-500M spectrofluorometer. To compare their luminescent efficiency, we took PL data under similar measurement conditions. All the absorption and PL spectra were reproducible.

Table 1 Molecular structures of poly(phenylacetylene) and its derivatives. E_g : band gap of the backbone.

$-\text{[HC=C(C}_6\text{H}_4\text{)-}p\text{-R)]}_n\text{---}$	R	E_g (eV)
	H (1)	1.4
	$(CH_2)_4CH_3$ (2)	2.2
	$CONH(CHCH_3)CO_2CH_3$ (3)	2.4
	$CONH(CHC(CH_3)_3)CO_2CH_3$ (4)	1.4
	$CONH(CHCH_2CH(CH_3)_2)CO_2CH_3$ (5)	1.4
	CO_2 -glucose (6)	1.2
	CO_2 -galactose (7)	1.2

The calculations were performed with the extended Hückel tight binding method,^{26, 27, 28} which can give a good semi-qualitative description of the band structures of conjugated polymers. As a check on the accuracy of our calculations, the band structure of *trans*-PA was computed. Our computed band gap for *trans*-PA of an infinite conjugation length is ~1.2 eV, which agrees very well with experimental result.⁴ *Cis* backbone conformation was used in the calculations, molecular structure optimisation was implemented by minimizing its steric energy. Standard Slater parameters for hydrogen, carbon and oxygen atoms were selected from Ref. 28 and kept fixed in our computations.

3. THE ROLE OF ALKYL AND PHENYL PENDANTS IN THE BLUE EMISSIONS OF DISUBSTITUTED POLYACETYLENES

3.1 DENSITIES OF STATES OF DISUBSTITUTED POLYACETYLENES

The densities of states (DOSs) for PPA, PPP and PPB are shown in Fig. 2. The DOS of a *cis*-PA with infinite conjugation length is shown for comparison, its π - π^* transition yields an infrared PL because of its narrow band gap.⁴ When comparing the DOSs of PA, PPA, PPP, and PPB, one can see that the alkyl pendant can effectively engineer the electronic structures of the polymers. The modifications in DOSs include: (1) alkyl pendants can enlarge the band gap of the conjugated backbone to ~2 eV; (2) characteristic electronic states of the phenyl pendant are introduced into the widened π and π^* bands of the backbone; (3) the electronic states introduced by the phenyl pendant are sensitive to the molecular structures of the alkyl side-chains, and shift gradually towards the band edge of the backbone; and (4) the DOS of the conjugated backbone is comparably low in intensity and is hidden in the states generated by the phenyl. The change in the electronic states is responsible for the optical properties of these polymers. In Table 2, we list the band gaps of the backbones, the energy differences between the lowest unoccupied molecular orbital (LUMO) and the highest occupied molecular orbital (HOMO) of the phenyl pendants (Δ_1), and the energy differences between the π - π^* of the backbone (Δ_2).

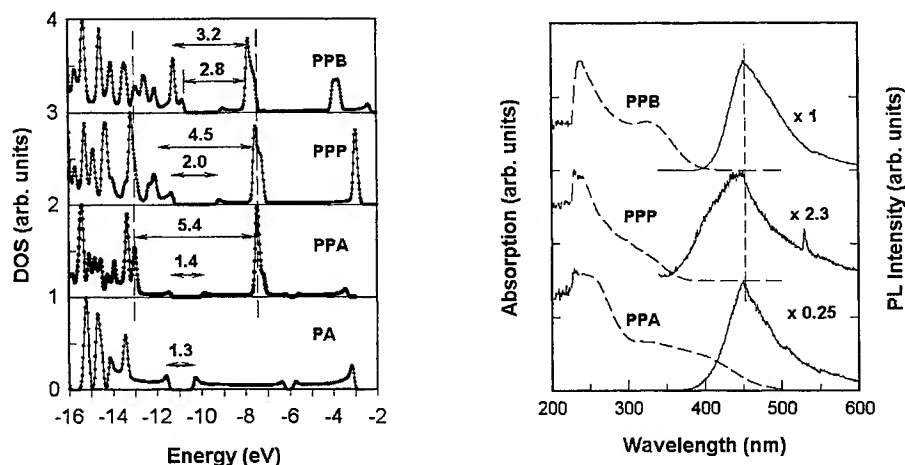


Figure 2 Electronic structures of PPA, PPP and PPB (left panel).

Figure 3 Normalized absorption (dashed line) and photoluminescence (solid line) spectra of PPA, PPP and PPB (right panel). Excitation wavelength: 325 nm; solvent: chloroform; concentration (mM)/power (mW): 1.61/14(PPA), 0.125/14(PPP), 0.064/1.78(PPB).

Due to the bond distortion induced by the alkyl and phenyl pendants, the band gap of the backbone becomes enlarged. This is well acknowledged that the alkyl side-chains can increase the band gap of substituted polyacetylenes.⁵⁻¹⁴ We, however, find that a limit of ~2.0 eV is quickly reached as the alkyl pendant increases in length. The widened band gap of the backbone can, at most, give off red emission. Therefore the π - π^* transition in the backbone is impossible to be the origin for the blue emissions for the disubstituted polyacetylenes.¹⁴

In the E-k diagram, the phenyl related energy levels are nearly horizontal, which suggests the electronic states of the phenyl pendant be localized. The electronic structure of pendant-group polymer is essentially that of an ensemble of molecular

subunits because the overlap of pendant groups is so small,^{20, 24} and the electronic properties of pendant-group polymers are determined by localized electronic states characteristic of the pendants. By inspection Fig. 2, one can see clearly that the electronic states generated by the phenyl pendant can be tailored efficiently by the alkyl side-chains. The localized states of the phenyl can be modulated by its polymeric environment, such as the molecular and geometrical structure of the alkyl substituent and the backbone. As shown in Table 2, the large-scale change in the numerical values of Δ_1 and Δ_2 reflects the effect of the alkyl side-chain on the electronic states of the polymers. The effective engineering of the electronic states possibly stems from the strong electron coupling between the phenyl pendant attached to backbone and its polymeric environment.

Table 2 Band gaps (E_g) of the backbones, the energy differences between the LUMO and the HOMO of the phenyl (Δ_1), and the energy differences between the π - π^* band of the backbone (Δ_2), energy “gap” obtained from absorption (E_{Abs}), and PL peak energy (E_{PL}) for PPA, PPP and PPB.

	in our work (eV)					data in literature (eV)		
	E_g	Δ_1	Δ_2	E_{Abs}	E_{PL}	$E_g(\text{exp})$	PL	Ref
PPA	1.4	5.4	3.1	2.8	2.75	3.0~3.42	~2.5	7, 8, 11, 30
PPP	2.0	4.5	3.8	3.6	2.75	3.2~3.35	~2.7	8, 11
PPB	1.8	3.3	2.2	3.3	2.75	3.2~3.35	2.7	8, 11

3.2. UV ABSORPTION AND PHOTOLUMINESCENCE OF DISUBSTITUTED POLYACETYLENES

Fig. 3 shows the normalized absorption and PL spectra of PPA, PPP and PPB. The absorption from 230 to 300 nm is associated with the phenyl side-chain, the absorption maximum at ~230 nm (5.4 eV) is phenyl-related. PPA starts its absorption at ~500 nm, PPP at ~350 nm, and PPB at ~400 nm. Interestingly, PPB exhibits an eminent absorption peak at ~325 nm. From the photon energy of maximum slope of optical absorption, which is commonly used to determine the energy gap for a conjugated polymer,²⁹ the energy “gaps” are estimated to be about 2.8, 3.6, and 3.3 eV for PPA, PPP and PPB, respectively. We list these “gap” values in Table 2 for comparison. The three polymers exhibit quite different absorption behaviours in the range of 300-500 nm. It is safe to conclude that such differences are the results of the interaction of the phenyl chromophore and its polymeric environment. Surprisingly, the PL peaks of PPA, PPP and PPB locate at the same position of ~450 nm (2.75 eV). In literature, the PL energies of PPA, PPP and PPB have also pinned at ~2.7 eV despite the excitation energies vary in a wide range from 3.2 to 3.8 eV.^{7, 8, 11, 30} Even for poly(1-phenyl-2-acetylenes) with excessively long alkyl pendants, such as poly(1-phenyl-2-hexyne), the PL energy is also reported to pin at the same value.¹⁰ Regardless of the different absorption behaviour and different excitation energy, the emission energy is still pinned at 2.7 eV, which suggests the blue emission of poly(1-phenyl-2-alkynes) is phenyl inherent.

Although the alkyl side chain cannot shift the emission colour of the polymers, it can increase their emission efficiency. When measured under similar measurement conditions, PPB emits strong blue emission while PPA and PPP exhibit only faint blue light. The ratio of integrated intensity per unit concentration per unit excitation power is about 1:2:50 for PPA:PPP:PPB. Compared to the PL efficiency of PPA, PPP doubles only, but PPB is about 50 times higher. Our data agree well with the published results.¹¹ In principle, PL efficiency is determined primarily by the product of carrier generation rate and recombination rate,³¹ while the high densities created by the phenyl pendant in the HOMO and LUMO contribute to high absorption rate and recombination rate, too. On the other hand, it has also reported that the bulky alkyl side-chain in PPB can lower its non-radiative process, which helps PPB to gain a high recombination rate for intense emission.³⁰ Therefore, the high DOS product for PPB is a key factor for its strong absorption at 2.8 eV and its intense PL emission.

3.3. EFFECT OF THE PHENYL ROTATION ON THE ELECTRONIC STRUCTURES OF POLY(1-PHENYL-2-BUTYLNE)

Bulky alkyl side-chain will inevitably cause the phenyl to rotate. In order to understand the origin of the blue emission, we now probe the effect of the phenyl rotation on the electronic structures of the polymers. An azimuthal angle, ϕ , is defined to be zero when the phenyl locates in its equilibrium plane. As phenyl rotates out of its equilibrium plane along the axis of the pendant, we keep the geometry of the backbone and the alkyl pendant untouched. PPB is used here as a representative. Fig. 4 illustrates the DOS evolution of PPB with the rotation of the phenyl ring. For small angle rotation, i.e., $0 \leq \phi \leq 5^\circ$, the localized states of the phenyl remains intact. For medium angle rotation, i.e., $5 \leq \phi \leq 15^\circ$, the localized states in HOMO shift

toward the π band edge of the backbone while its localized states in LUMO still keeps unchanged. For large angle rotation, i.e., $\phi \geq 15^\circ$, phenyl's localized states in HOMO continue to shift, but the localized states in LUMO begin to move to higher energy. As the phenyl rotates, its located states move into the band-gap of the backbone, looking like "gap states" but physically they are not. Although the localized energy levels of the phenyl pendant are independent of the extended energy levels of the backbone, the polymeric environment in the neighbourhood of the phenyl is changed. That is, the electron coupling between the phenyl and its neighbour atoms also change. That is why the electronic structure of the polymer changes as the phenyl rotates. On the other hand, we can check it with experiment because it is well known that gap states are the main energy loss mechanism of fast charged particles in polymers and may quench, partially or completely, the blue PL. For a highly luminescent substituted polyacetylene, its deep-blue PL undergoes progressive 1.2-eV-redshift when its solution gets concentrated and finally becomes squeezed powder. Instead of complete quenching, its luminescent intensity remains at a reasonable level. In concentrated solutions or in squeezed powder, the macromolecules are so close that they are entangled with each other. The most straightforward change in the configuration of the molecules is the rotation of the phenyl chromophore. If the blue PL originates from the transition between the localized states in the phenyl pendant, then its emission colour will undergo red shift when the phenyl rotates. That is just what we have observed.

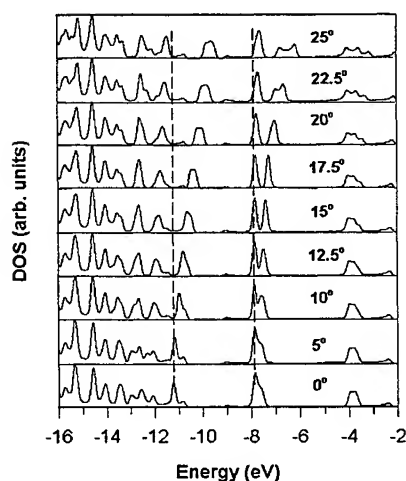


Figure 4 DOS evolution with the rotation of the phenyl in PPB.

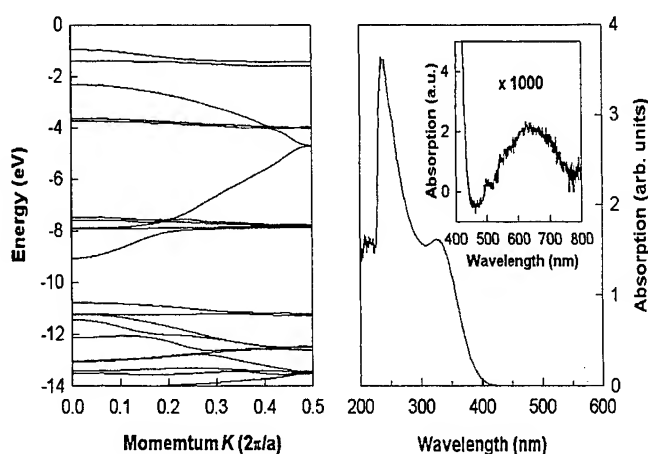


Figure 5 Band structure (left) and red absorption of PPB (right).

The colour of emission can also be tuned by attaching a bulky molecule to the ortho position of the phenyl chromophore. For example, poly[*o*-iso-propylphenyl]acetylene gives off red emission by attaching an *i*-C₃H₇ molecule at the ortho position of the phenyl chromophore.¹⁰ This bulky molecule at ortho position can induce phenyl rotation more easily than at para position. We will discuss that topic in Section 4.

3.4. THE ROLE OF THE PHENYL PENDANT IN THE BLUE EMISSIONS OF DISUBSTITUTED POLYACETYLENES

Our results suggest that the detected 2.7 eV emissions are phenyl inherent. We now need to clarify the nature of electronic states of the phenyl pendant—are they extended or localized? There is no doubt that the energy band picture of extended states can be applied to many polymers such as PA and the backbone of our polymers. Duke *et al* has described the nature of localization in these systems.^{32, 33, 24} For pendant-group polymer, its electronic structure is an ensemble of the backbone (extended states) and the pendants (localized states) due to the weak inter-pendant bonding. Because of the localization, the electronic and optical properties of pendant-group polymers are determined by localized electronic states characteristic of the pendants.²⁴ Fig. 5 shows the band structure of PPB (left panel). The localized states of the phenyl pendant are represented by the horizontal lines, and the extended states of the backbone are presented by curves. The interaction between the phenyl and its environment makes these "horizontal" lines not perfectly horizontal. The optical absorptions shown in Fig. 3 for the three pendant-group polymers are clearly related to those of the isolated pendant groups.²⁴

If our interpretation is correct, excited carriers should be also created in the backbone. Fig. 5 depicts the red absorption of PPB (right panel). In addition to its strong absorption in the UV region, a very weak absorption appears at about 620 nm (2.0 eV). For a same solution of PPB and in a same scan, the absorption of the backbone at its peak is about one thousandth of its phenyl chromophore at 325 nm. Moreover, infrared PL at ~740 nm has been detected in a class of highly luminescent substituted polyacetylenes.²⁰ These results indicate that the blue PL originates from the phenyl pendant while the infrared PL from the distorted backbone.

As stated above, the localized states and hence the PL emission can be tailored by the polymeric environment of the phenyl chromophores. Because of the electron coupling in the polymer, the localized states can be engineered by changing the polymeric environment of the phenyl chromophore. For example, faint orange (2.0 eV),¹⁰ intense green (2.4 eV),¹⁰ and intense deep-blue (3.1 eV)^{18,20} emissions have been obtained by changing the molecular structures of the other substituent in the neighbour of the phenyl pendant. Figs. 2 and 3 also show clearly that the characteristic low-lying excited states in these polymers are those of pendants, more or less disturbed by polymeric environment to which the side groups are chemically linked. Upon photoexcitation, majority of the carriers is generated in the localized states of the phenyl chromophore, and energy transfer takes place subsequently.³⁴ It is expected that the excited states migrate via energy transfer among various sites until it finds a trap. The pinned PL energy implies that the carrier recombination occurs in the phenyl chromophores and most probably via traps.³⁴

4. ORIGIN OF THE BLUE EMISSIONS FROM POLY(PHENYLACETYLENE) WITH DIFFERENT RING SUBSTITUENTS

4.1. ABSORPTION AND PHOTOLUMINESCENCE

Fig. 6 shows the normalized absorption and PL spectra of **1**, **3-7**. Many polymers composed of an aliphatic backbone and aromatic side groups absorb in the near UV region, for example, aromatic vinyl polymers. The absorption of our polymers in the range 250-300 nm is associated with the phenyl in the pendant. **1** and **3** start their absorption at ~500 nm, **4** and **5** at ~450 nm, while **6** and **7** at ~520 nm. Additional absorption bands appear at ~450 nm for **6** and **7**. The differences in the absorptions are produced by the bulky tails. The characteristic low-lying excited states (> 300 nm) in these polymers are those of the tails, more or less disturbed by polymeric environment to which the side groups are chemically linked.²⁴

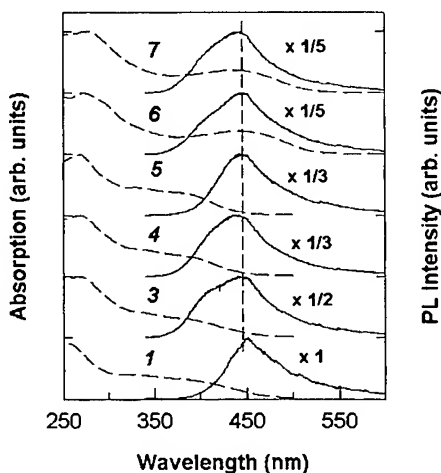


Figure 6 Normalized absorption and PL spectra of **1** and **3-7**.

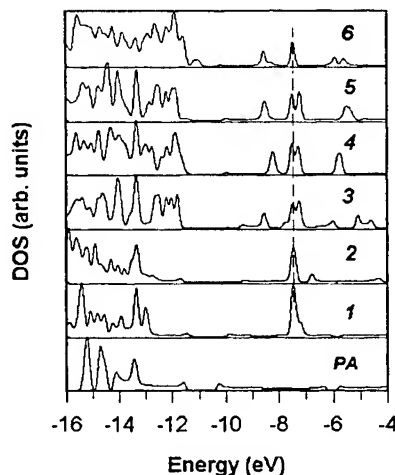


Figure 7. Density of states of cis-PA and **1-6**.

Fig. 6 shows that, no matter what types the tails are or how bulky they are, the emission energy of the polymers is always pinned at ~450 nm (2.7 eV). Very bulky tails (**6**, **7**) still fails in enhancing their luminescent efficiency. When measured under similar conditions, the PL intensity of **3-7** is only several times higher than **1**. As reported, bulky alkyl pendants in poly(1-phenyl-2-alkynes) can enhance their luminescent efficiency up to 50 times. However, the same alkyl tails or even more bulky ones (**2**) failed to achieve similar effect for poly(phenylacetylenes). The failure stems from the origin of the blue luminescence, which will be discussed later.

4.2. ELECTRONIC STRUCTURES OF POLY(PHENYLACETYLENES)

The features of absorption and PL of these polymers are related to their electronic structures. Fig. 7 shows the density of states (DOS) of 1-6. As a comparison, the DOS of cis-PA has also illustrated. A pendant, even though a single aromatic ring (1), can drastically disturb the electronic states of pristine PA: due to steric effect, the band gap of the conjugated backbone is enlarged up to 1.8 eV for 1. It is well acknowledged that pendants can distort the backbone and thus can widen the band gap of substituted PAs.¹⁻¹⁰ For 1-3, the increase in the band-gaps is shown clearly in Fig. 7. We have noted that a limit of ~2.3 eV is quickly reached even for short alkyl tails (1-3), and that excessively bulky tails (4-7) can cause shrinkage of the band gap. For a comparison, the band gaps (E_g) of the backbones of the polymers are listed in Table 1. Although the band gap can be enlarged, they can, at most, ensure red or infrared emissions. That is, the π - π^* interband transition of the backbone is impossible to be the origin for the observed blue emissions.

After comparing the DOS of 1 to that of pristine polyacetylene, the phenyl pendant can introduce its characteristic states into the widened π and π^* bands of the backbone. Similar characteristic states of other phenyl-containing pendant polymers (2-7) are easily discernable in Fig. 7. Other atoms such as oxygen and nitrogen in the tails also generate their characteristic states in the bands of the backbone, and the total DOS of the polymer becomes sensitive to the molecular structures of the tail. Now the information about the nature of electronic states—extended or localized—is important for our data interpretation. Organic polymers are molecular solids with weak intermolecular bonding. Their intramolecular covalent bonding, however, is strong and can be described by one-dimensional energy bands. For linear polymers without side groups, energy band picture of the extended states can be applied. In the top panel of Fig. 8, we illustrate the energy levels of cis-polyacetylene. Its clear-cut dispersion curves, which are consistent with those documented in literature, show that the electronic states of pristine polyacetylene are extended states. For pendant-group polymers, the electronic states characteristic of the pendant are localized because the overlap between the pendant groups is very small.¹⁷ Typical band structures of pendant polymers 5 and 6 are depicted in the middle and bottom panels of Fig. 5.8, respectively. The dispersion curves of the pendants are nearly horizontal, that is, $E(k)$ is independent of k . Such independence gives credit to our assignment of the localized states to the pendant. Fig. 8 indicates that the electronic structure of pendant-polymer is essentially an ensemble of the molecular subunits: the backbone and the phenyl-containing pendant.²⁴

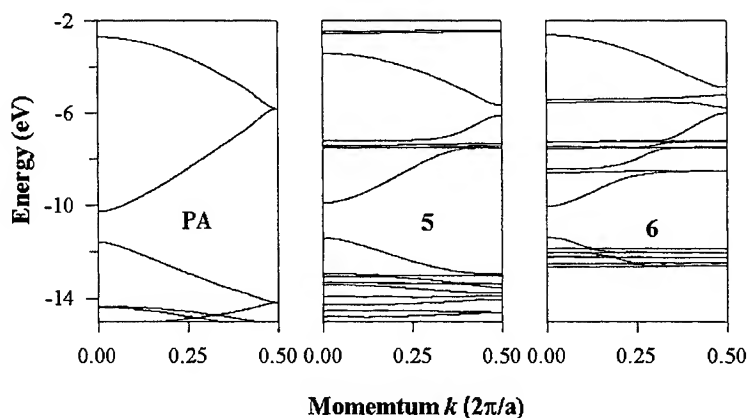


Figure 8 Typical electronic energy levels of 1, 5, and 6.

4.3. LOCALIZED STATES OF PENDANT-GROUP POLYMERS

For pendant-group polymers, Duke *et al.*^{22, 23} has described the nature of localization, later Baeriswyl²⁴ and Mort and Pfister reviewed it.³⁴ Generally speaking, the nature of the electronic localization is due to disorder in a fashion similar to that proposed by Anderson.³⁵ There are two kinds of disorder: “diagonal disorder” and “off-diagonal disorder”. Diagonal disorder is characterized by a distribution of on-site energies, $\Delta\alpha$. For most organic materials, $\Delta\alpha$ is ~0.5 eV. Similarly, off-diagonal disorder produces a distribution, β , in the transfer integrals. While the specific requirements for Anderson localization depend on dimensionality, localization occurs when $\Delta\alpha \gg \bar{\beta}$, where $\bar{\beta}$ is the average transfer integral.

Transfer integrals for intramolecular interaction are estimated as $\bar{\beta}_{\text{intra}} \leq 0.1$ eV, and for intermolecular interactions $\bar{\beta}_{\text{inter}} \leq 0.01$ eV. Therefore, the charged electronic states of pendant-group polymers consist of electrons (or holes) localized primarily on the pendant group.³⁴

As shown in Fig. 6, the intensity of the localized states is many times higher than that of the extended states. The electronic structures, and hence the absorption and photoemission spectrum, of the pendant-group polymers should be dominated by electrons bound in the molecular orbitals of the pendant group. As a result of photon excitations, majority of photogenerated carriers do not exist in extended energy band states (backbone) but rather are localized in the pendant. Our interpretation has been supported by numerous experimental results. For example, for pendant polymers such as poly(1-phenyl-2-butyne), we have detected a weak absorption at ~620 nm (2.0 eV) in addition to its strong ultraviolet absorption. Moreover, weak infrared emissions at ~740 nm are detected in a number of monosubstituted PAs in addition to their intense blue emissions.²⁰ Transient PL also yields additional evidence. If a luminescence originates from localized states, its luminescence decay should be a simple exponential, i.e., $I = I_0 \exp(-t/\tau)$.³⁶ Indeed, single decay time (~180 ps) has been reported for pendant polymer **1**.³⁰

Fig. 6 also shows that the emission energy of **1-7** does not change with the types of the tails, no matter how bulky they are. The blindness of the emission colour to the molecular structures of the tails strongly supports that the blue emission is phenyl inherent. Although the emission colour is determined by the localized states, the luminescent efficiency can be improved by a few times for the polymers with bulky tails. The limited improvement in the efficiency is possibly due to the limited change in the polymeric environment in the neighbourhood of the phenyl chromophore because the atoms near the phenyl chromophore affect the polymeric environment more effectively. The modulation of the polymeric environment can enhance the luminescent efficiency or even be able to tune its emission colour of a pendant-group polymer. For instance, the PL efficiency of **1** can be enhanced by more than 50 times as a butyl side-chain substitutes the other hydrogen atom in the repeat unit.³⁷ In another case, the emission colour of **1** shifts to ~330 nm as its backbone becomes saturated (polystyrene).³⁸ The eminent change in the emission efficiency and in the emission colour is believed to stem from the wavefunction overlap of the electrons in the aromatic ring and in its neighbour atoms. The nearer a group approaches to the phenyl chromophore, the larger the overlap is. That is one of the reasons why the bulky side-chains can effectively enhance the PL efficiency for poly(1-phenyl-2-acetylenes) but they fail to do so for poly(phenylacetylenes).

5. CONCLUSION

Contrary to the general belief that the blue PL of substituted polyacetylenes originates from the distorted backbones, we have shown that the distorted backbone can emit red PL at most while the blue emissions stem from the phenyl chromophores in the pendants. Our results show that the alkyl side-chain can dramatically improve the PL efficiency but fail to tune the emission color. For poly(phenylacetylenes) with numerous non-liquid crystal tails, all the polymers exhibit weak blue emissions with the PL peak energy pinned at ~450 nm (2.7 eV) in spite of their bulky tails.

Using Hückel tight binding method, we have calculated their electronic structures. The electronic structure of the pendant polymer is essentially an ensemble of the extended states characteristic of backbone and the localized states characteristic of the phenyl-containing pendant. The processes of optical absorption and blue emission are confined in the localized states of the pendant. Our results suggest that the origin of the blue emission is phenyl inherent, resulting from transitions between some localized states of the aromatic ring in the pendant polymer. Most of the observed blue emissions from mono- and di-substituted polymers belongs to this category. The localized states of the phenyl pendant and the optical properties of the substituted polyacetylenes are strongly correlated. We have also shown that the interaction between the phenyl chromophore and its neighbors is of vital importance for improving the emission efficiency and tuning the emission color of pendant polymers. Our calculations are quite successful in explaining the main features of the polymer photoemission spectra, they provide a physical ground for the molecular engineering endeavor in the design of new highly luminescent materials.

By intentionally incorporating chromophous aromatic rings and by carefully engineering their polymeric environment, highly efficient emissions with required emission color can be achieved. It is here that the concept of molecular design proves so extremely powerful because it allows one to choose, at will, the density and the kind of localized states since they are associated with pendant molecules. Hence by using this concept, it has been possible to explore on a molecule level the steps involved in the transfer of carrier generation and recombination. Various polyacetylene derivatives with novel optical properties can be obtained by careful macromolecular design and by delicate electronic states tailor.

REFERENCES

1. H. Shirakawa, T. Masuda, and K. Takeda, in *The chemistry of triple-bonded functional groups*, edited by S. Patai, Wiley, New York, 1994
2. L. Lauchlan, S. Etemad, T. -C. Chung, A. J. Heeger, and A. G. MacDiarmid, "Photoexcitations in polyacetylenes", *Phys. Rev. B* **24**, pp. 3701-3711, 1981
3. K. Yoshino, S. Hayashi, Y. Inuishi, K. Hattori, and Y. Watanabe, "Photo-luminescence of cis-polyacetylene and trans-polyacetylene", *Solid State Commun.* **46**, pp. 583-585, 1983
4. P. W. Carter and J. D. Porter, "Probing of p conjugation in transpolyacetylene using near-infrared photoluminescence spectroscopy", *Phys. Rev. B* **43**, pp. 14478-14487, 1991
5. K. Tada, H. Sawada, J. Kyokane, and K. Yoshino, "Optical-properties of perfluoroalkylated poly(diphenylacetylene)", *Jpn. J. Appl. Phys. Part 2* **34**, pp. L1083-1085, 1995
6. K. Tada, R. Hidayat, M. Hirohata, M. Teraguchi, T. Masuda, and K. Yoshino, "Optical properties and blue and green electroluminescence in soluble disubstituted acetylene polymers", *Jpn. J. Appl. Phys. Part 2* **35**, pp. L1138-1141, 1996
7. R. G. Sun, T. Masuda, and T. Kobayashi, "Green electroluminescence emission from substituted polyacetylenes", *Jpn. J. Appl. Phys. Part 2* **35**, pp. L1434-1437, 1996
8. R. G. Sun, T. Masuda, and T. Kobayashi, "Blue electroluminescence of substituted polyacetylenes", *Jpn. J. Appl. Phys. Part 2* **35**, pp. L1673-1676, 1996
9. K. Yoshino, M. Hirohata, R. Hidayat, K. Tada, T. Sada, M. Teraguchi, T. Masuda, S. V. Frolov, M. Shkunov, Z. V. Vardeny, and M. Hamaguchi, "Optical properties and electroluminescence characteristics of polyacetylene derivatives dependent on substituent and layer structure", *Synth. Met.* **91**, pp. 283-287, 1997
10. R. Sun, T. Masuda, and T. Kobayashi, "Visible electroluminescence of polyacetylene derivatives", *Synth. Met.* **91**, pp. 301-303, 1997
11. M. Hirohata, K. Tada, R. Hidayat, T. Masuda, and K. Yoshino, "Effect of alkyl and aromatic substituents on blue electroluminescence in polyacetylene derivatives", *Jpn. J. Appl. Phys. Part 2* **36**, pp. L302-305, 1997
12. S. V. Frolov, M. Shkunov, Z. V. Vardeny, K. Tada, R. Hidayat, M. Hirohata, M. Teraguchi, T. Masuda, and K. Yoshino, "Spectral narrowing of emission in di-substituted polyacetylene", *Jpn. J. Appl. Phys. Part 2* **36**, pp. L1268-1271, 1997
13. R. Hidayat, M. Hirohata, K. Tada, M. Teraguchi, T. Masuda, and K. Yoshino, "Photoluminescence and electroluminescence in polymer mixture of poly(alkylphenylacetylene) and poly(diphenylacetylene) derivatives", *Jpn. J. Appl. Phys. Part 2* **37**, pp. L180-183, 1998
14. K. Yoshino, H. Takahashi, S. Morita, T. Kawai, and R. Sugimoto, "Electrochemical characteristics of stable polyacetylene derivatives-poly(o-trimethylsilylphenylacetylene)", *Jpn. J. Appl. Phys. Part 2* **33**, pp. L254-257, 1994
15. X. Kong, W. T. Lam, and B. Z. Tang, *Polym. Mater. Sci. Eng.* **80**, pp. 151, 1999
16. X. Kong and B. Z. Tang, "Synthesis and novel mesomorphic properties of the side-chain liquid crystalline polyacetylenes containing phenyl benzoate mesogens with cyano and methoxy tails", *Chem. Mater.* **10**, pp. 3352-3363, 1998
17. B. Z. Tang, X. Kong, X. Wan, H. Peng, W. Y. Lam, X. Feng, and H. S. Kowk, "Liquid crystalline polyacetylenes: Synthesis and properties of poly{n-[(4'-cyano-4-biphenyl)oxy]carbonyl}-1-alkynes}", *Macromolecules* **31**, pp. 2419-2432, 1998
18. Y. M. Huang, J. W. Y. Lam, K. K. L. Cheuk, W. Ge, and B. Z. Tang, "Strong luminescence from poly(1-alkynes)", *Macromolecules* **32**, pp. 5976-5978, 1999
19. Y. M. Huang, J. W. Y. Lam, K. K. L. Cheuk, W. Ge, and B. Z. Tang, "Poly(1-alkyne): a new class of highly luminescent polyacetylenes", *Thin Solid Films* **363**, pp. 146-148, 2000
20. Y. M. Huang, W. Ge, J. W. Y. Lam, and B. Z. Tang, "Strong photoluminescence from monosubstituted polyacetylenes containing biphenyl chromophores", *Appl. Phys. Lett.* **75**, pp. 4094-4097, 1999
21. B. Z. Tang, J. W. Y. Lam, X. Kong, P. P. S. Lee, X. Wan, H. S. Kwok, Y. M. Huang, W. Ge, H. Chen, R. Xu, and M. Wang, "Liquid crystalline polyacetylenes: A new class of mesomorphic materials with novel optical and electronic properties", *Proc. SPIE* **3800**, pp. 62-67, 1999
22. Y. M. Huang, J. W. Y. Lam, K. K. L. Cheuk, W. Ge, and B. Z. Tang, *Macromolecules* (submitted, 2000).
23. F. Gutman and L. Lyons, *Organic Semiconductors*, Wiley, New York, 1967
24. D. Baeriswyl, Chap.2 in *Electronic Properties of Polymers*, edited by J. Mort and G. Pfister, Wiley, New York, pp. 13 (1982).
25. B. Z. Tang, W. H. Poon, S. M. Leung, W. H. Leung, and H. Peng, "Synthesis of stereoregular poly(phenylacetylene)s by organorhodium complexes in aqueous media", *Macromolecules* **30**, pp. 2209-2212, 1997
26. L. Salem, *Molecular Orbital Theory of Conjugated Polymer Systems*, Benjamin, London, 1966
27. D. Baeriswyl, in *Theoretical aspects of band structures and electronic properties of pseudo-one-dimensional solids*, edited by H. Kamimura, Reidel, Dordrecht, pp. 1-10 (1985).
28. M. Brändle and G. Calzaferri, "Molecular geometries by the extended-Huckel molecular-orbital method III-band

- structure calculations", *Helv. Chim. Acta* 76, pp. 2350-2355, 1993
29. R. H. Friend and N. C. Greenham, *Physical properties of polymer handbook*, edited by J. E. Mark (AIP, New York, 1996) p. 479.
 30. H. Wang and K. S. Wong, "Time resolved photoluminescence investigation of polyacetylene derivatives", *Appl. Phys. Lett.* 73, pp. 1637-1639, 1998
 31. C. M. Wolfe, N. Holonyak, Jr., and G. E. Stillman, *Physical properties of semiconductors* (Prentice Hall, New Jersey, 1989).
 32. C. B. Duke, W. R. Salaneck, T. J. Fabish, J. J. Ritsko, H. R. Thomas, and A. Paton, *Phys. Rev. B* 18, 5717 (1978).
 33. C. B. Duke, *Mol. Cryst. Liq. Cryst.* 50, 63 (1979).
 34. J. Mort and G. Pfister, Chap.6 in *Electronic Properties of Polymers*, edited by J. Mort and G. Pfister, Wiley, New York, p. 246 (1982)
 35. P. W. Anderson, *Phys. Rev.* 109, 1492 (1958).
 36. S. Shionoya, in *Luminescence of Solids*, edited by D. R. Vij, Plenum, New York, pp. 114 (1998).
 37. Y. M. Huang et al (to be published).
 38. L. J. Basile, *J. Chem. Phys.* 36, 2204 (1962).

A New Multichamber Evaporator for Organic Devices

Wang QiuLai^a, WeiLing Guo^{lb}, Michael C.Y.Chan^c, Liu ShiChuang^a, E. Herbert Li^b, and C. Surya^c

a-Shen yang institute of UHV Technology and Applications, shenyang 110015, China

b-Department of Electrical and Electronics Engineering, The University of Hong Kong, Hong Kong

c- Department of Electronic and Information Engineering, The Hong Kong Polytechnic University, Hung Hom, Kowloon, Hong Kong.

ABSTRACT

A new four vacuum chamber evaporator for organic devices was proposed and specially designed. The chamber one is for ITO/glass pretreatment, it's have ozone treatment and plasma treatment. The chamber two is used for organic thin film evaporating. There has six sources for organic material, and three power sources can work at the same time, there is a mask storage chamber in the organic evaporation chamber, so for some material research, you can get three kind of doping density or thickness OLED at the same fabrication. The chamber three is vacuum glove box. It's used for package. The chamber four is used for cathode evaporating, it can evaporates Mg, Ag, LiF, Ca and Al, Au.

Keywords: Organic Light emitting diodes, Evaporator, multi-chamber

1. INTRODUCTION

Organic Light-emitting diodes (OLEDs) have been widely investigated due to their potential application for high efficiency, low-drive voltage, large area and full color displays¹⁻³. Much progress has been made and the device performance has increased dramatically since Tang and co-workers first reported on high performance organic EL devices. During the past decade, enormous progress has been made in growing ultra-thin organic films and multilayer structures with a wide range of optoelectronics properties. The progress has been made by several important advances in the understanding of organic films and their modes of growth. The most important advance is the use of ultrahigh vacuum (UHV) as a mean to achieve monolayer control over the growth of organic thin films with extremely high chemical purity and structural precision⁴⁻⁵. Ultrahigh vacuum growth, sometimes referred to as organic molecular beam deposition (OMBD) or organic molecular beam epitaxy (OMBE), has the advantage of providing both layer thickness control and an atomically clean environment and substrate. OMBD have provided an entirely new prospect for understanding many of the fundamental structural and optoelectronics properties of thin organic film systems⁶.

In this paper, we design a new OMBD system, multi-chamber organic evaporator for organic devices. The system includes four vacuum chamber and six organic evaporation sources and four metal evaporation sources. All work can be done in vacuum condition, we send ITO/glass substrates in the evaporator, and then get the packaged Organic devices out.

2. MAIN BODY DESIGN

Fig.1 shows the main body structure of our multichamber organic evaporator. It's consist of four

¹ Correspondence: email: wlguo@eee.hku.hk, ehli@eee.hku.hk

chambers, e.g. evaporation chamber for small molecular organic materials and for metal, pretreatment chamber and vacuum glove box. The organic material and metal are separately evaporated in order to prevent from the contamination of different materials. There are six evaporation sources and UHV shutter plates in the organic material evaporation chamber, and four evaporation sources and UHV shutter plates in the metal evaporation chamber. The standard substrate size is 3inX4in, it can be transferred from chamber to chamber by mechanical arm. Substrates can be heated up to 200°C and can continuous rotary with adjustable speed (5-60r/min) during evaporation. There are three power sources ready for the organic material evaporation at the same time and two more thickness monitor can be connected to monitor the three kind of materials evaporation rate, the minimum rate can be controlled to 0.1nm/sec.

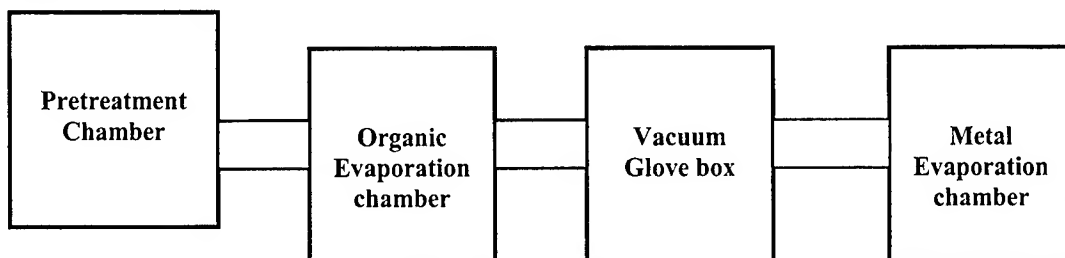


Fig1 sketch diagram of the multi-chamber organic evaporator.

All work can be done at vacuum condition. First the substrate is put into the pretreatment chamber, and cleaned by ozone treatment or plasma treatment. Then the sample is sent to organic material evaporation chamber by mechanical arm. All organic thin films and pattern will be finished there. And then the samples go through the vacuum glove box and arrive at the metal evaporation chamber. When the metal or other contact layers (LiF, Ca, Mg, Ag, Au or Al) is evaporated there, the sample was sent back to vacuum glove box. The samples can be packaged there or be storage here before parameter measurement.

3. MASK STORAGE CHAMBER

One special design of this system is there is a mask storage chamber in organic evaporation chamber and metal evaporation chamber, respectively. The mask can be changed during organic and metal evaporation by transfer arms. It makes material research easily done. For example, if we want to know how the organic light emitting diodes performance change as the different density of a new organic dye doping into a host. Fig.2 (a) and (b) show the different masks for material density and thickness research. From the Fig 2(a), We use the first mask for the first doping density, and then change the mask as second one, and also change density as second density, and so does for the third and fourth one. Finally in one cycle of fabrication, we can get the four kinds of density OLED. From the Fig2 (b), first we use mask one evaporate organic material, and then stop and change mask one as mask two and then continue to evaporate the same material, and then stop and change mask two as mask three, and so does for the mask four. Finally, we got four kinds of OLED with different organic material thickness in the same substrate; the thickness will decrease from I to IV on the sample. And then the sample is sent to metal evaporation chamber for contact evaporation. So we can study the OLED performance at different emitting layer thickness, hole transport layer thickness and electron-transport

layer thickness or buffer layer thickness.

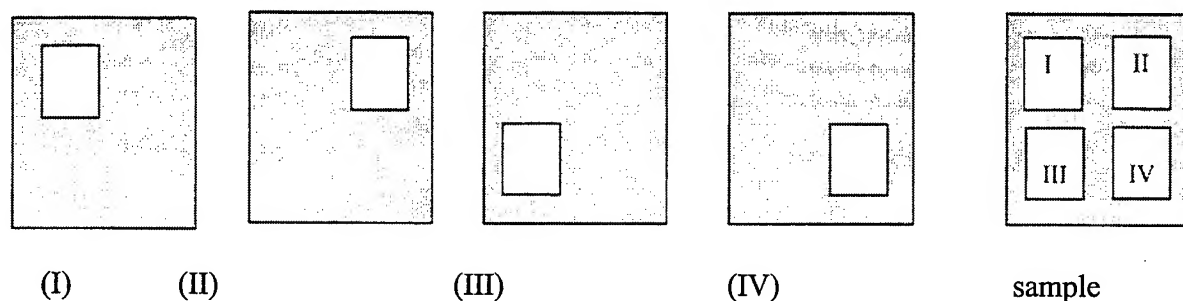


Fig.2 (a) masks for material density research.

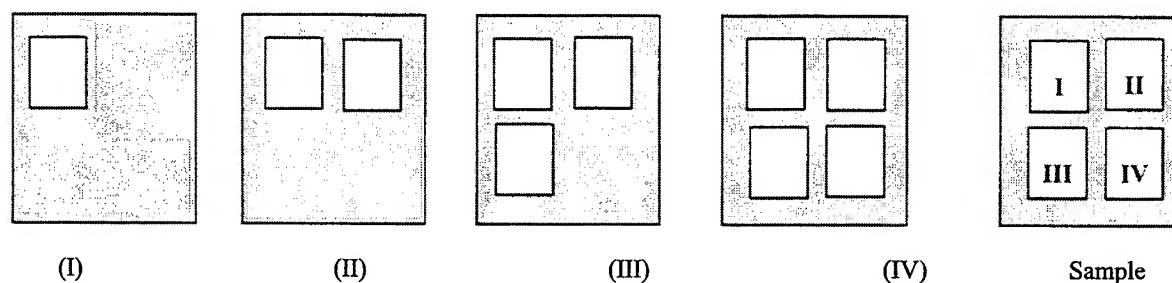


Fig.2 (b) masks for material thickness research.

4. CONCLUSION

A new multichamber organic evaporator was specially designed and made for organic devices. The chamber one is for substrate pretreatment by ways of ozone treatment or plasma treatment. The chamber two is used for organic thin film evaporation. There has six sources for organic material, and three power sources can work at the same time, there is a mask storage in this organic chamber, so for some material research, you can get four kinds of doping density or thickness OLED at the same fabrication. The chamber three is vacuum glove box. It's used for package. The chamber four is used for cathode or metal evaporation. All work can be done in vacuum condition.

ACKNOWLEDGMENTS

This work was done by the cooperation among Universities and company. The authors would like to thanks Prof. Liu shiyong and Dr. Li Chuannan and other members in Prof.liu's group for there fruitful suggestion and discussion for this evaporator.

REFERENCES

1. C.W.Tang and S.A.Van Slyke, Appl.Phys.Lett. 51, 913(1987).
2. J.Kido, M.Kohda, K.Okuyama, and K.Nagai, Appl.Phys.Lett. 61, 761(1992)
3. R. Dixon, Compound semiconductor 5(9), 43(1999)
4. S.R.Forrest, P.E.Burrows, E.I.Haskal, F.F.So, Phys.Rev.B, 49, 11309(1994)
5. M.Hara, H.Sasabe, A.Yamada, A.F. Garito, Jpn. J. Appl. Phys., 28, L306(1989)
6. Stephen R.Forrest, Chem.Rev. 97, 1793(1997)

Novel Material Blue Organic Light Emitting Diode

Weiling Guo^a, E. Herbert Li^{1a}, ChiMing Che^b, Yi Zhao^c and S.Y.Liu^c

a-Department of Electrical and Electronics Engineering, The University of Hong Kong

b-Department of Chemistry, The University of Hong Kong

c-State Lab of Integrated Optoelectronics, Jilin University, Changchun 130023, China.

ABSTRACT

A novel blue organic light emitting diode is fabricated base on a new organic material, Dipyrrole3, which can emit a pure blue light. The Dipyrrole3 is used as a dopant and is doped into an electron-transporting host. NPB is used as the hole transport layer. The device consists structure of ITO/NPB/Bepp2:Dipyrrole3 (100:5)/BePP2/LiF/Al. It shows a bright blue light emission at 451nm and 480nm, the full width at half maximum is 61nm. The maximum luminance is 2600cd/m² at a voltage of 20V. The peak power efficiency is 0.765lm/W at a voltage of 7V.

Keywords: Organic Light emitting diodes, Blue, Dipyrrole3, New materials

1. INTRODUCTION

Organic Light-emitting diodes (OLEDs) have been widely investigated due to their potential application for high efficiency, low-drive voltage, large area and full color displays¹⁻³. Much progress has been made and the device performance has increased dramatically since Tang and co-workers first reported on high performance organic EL devices. However, full color display needs the three basic colors: red, green and blue. Recently some green organic EL devices with high efficiency and superior stability have been reported by Kodak group⁴ and others⁵. In search of blue-light emitting devices, scientists have spent the last few years designing and modifying the architecture of some candidate organic materials, but till now blue light devices have not been as successful as green. In General, blue-emitting OLEDs have lower efficiencies than green or red devices due to the larger band-gap energy of the emission material, which inhibits the injection of carriers. Although a bright blue OLED was reported recently⁶, information and results about high efficient blue OLED are still limit. Therefore, high efficiency and stable blue OLED still need to investigate.

In this work, A new highly fluorescent and vacuum evaporable organic material Dipyrvole3 was synthesized. We fabricated OLEDs using it as an emitting layer and as a dye, the maximum luminance obtained from the devices was 2610cd/m².

2. EXPRIMENTS

A new fluorescent material Dipyrvole3 was synthesized, Fig.1 shows the chemical molecular structure and the Ultra-Violet absorption and Photo-Luminescence (PL) emission spectra of the materials. The peak wavelengths (448nm, 483nm) show it emit a blue light.

¹ Correspondence: email: ehli@eee.hku.hk

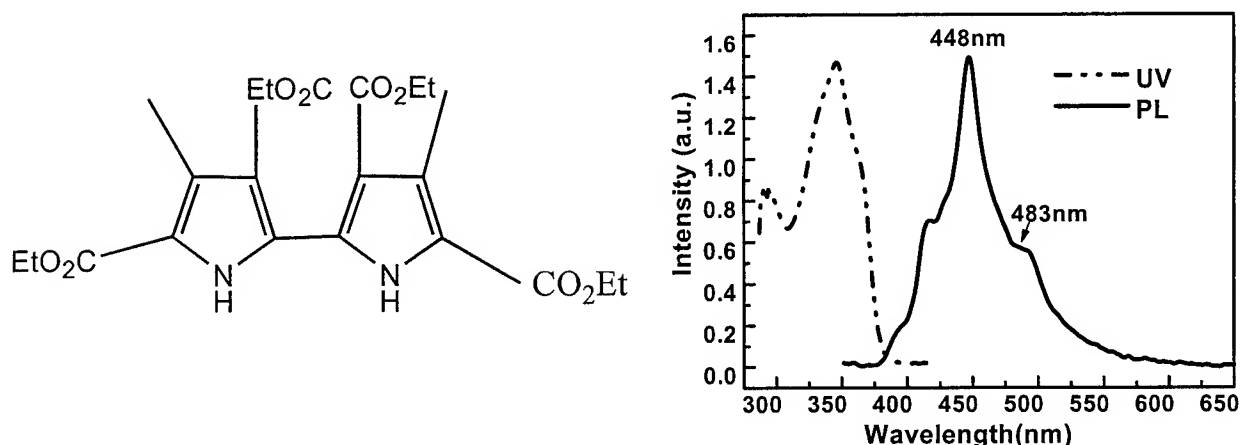


Fig1 molecular structure and Ultra-Violet absorption and photoluminescence spectrum of Dipyrrole3.

Organic light emitting diodes were fabricated on indium-tin-oxide (ITO) coated glass substrates with a nominal surface resistance of $30 \Omega/\square$. Substrates were cleaned in ultrasonic baths of isopropyl alcohol, Acetone and methanol, dried for 10 min in an oven of 100°C , and then treated with ozone plasma immediately prior to the organic film evaporation. N, N'-bis-(1-naphthyl)-N,N'-diphenyl-1,1'-biphenyl-r,r'-diamine (NPB) was used as a hole transport layer in our devices. The Organic materials were grown by organic molecular beam deposition system, the chamber pressure was maintained below $2 \times 10^{-4} \text{ Pa}$ and the thickness were determined by an oscillating quartz thickness monitor. Then samples were transfer to another evaporator in air, and Aluminum (Al) was thermal deposited as cathode. Current-voltage and luminance characteristics of devices were measured in forward bias. All measurement was done at room temperature.

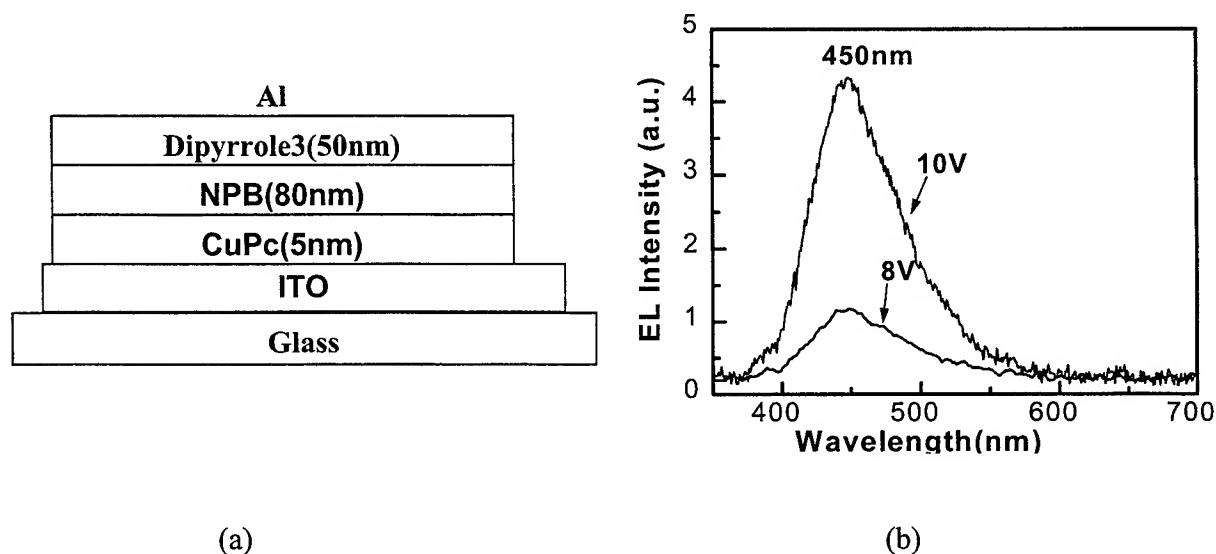


Fig.2 (a) The cell configuration and (b) EL emission spectrum of the OLED with Al/Dipyrrole3/NPB/CuPc/ITO structures.

3. RESULTS AND DISCUSSION

When Dipyrrole3 is used for emitting layer and the OLED emits a pure blue light. The Device structure was Al/Dipyrrole3/NPB/CuPc/ITO (shown as Fig.2a). Copper Phthalocyanine (CuPc) was used as a buffer layer between cathode and hole transport layer in order to increase the stability of devices. Figure 2b shows the Electro-luminescence (EL) spectrum of this device; the Dipyrrole3's emission peak is at 450nm, compared with the PL spectrum, there just the strong peaks emit light. The device is not very bright maybe due to the materials "self-quenching".

In order to get some high performance devices based on this new material, A Doped organic light emitting diode was fabricated where Dipyrrole3 was used as a blue luminescent dye. The device structure was shown in Fig 3(a). In the devices, material BePP2 was used as a host⁷, BePP2 doped with Dipyrrole3 was used as a emitting layer (EML), the ratio of BePP2:Dipyrrole3 is 100:5, and BePP2 also used as a electron transporting layer (ETL), LiF was used to enhance the electron injection. LiF/Al was used as a double layer cathode.

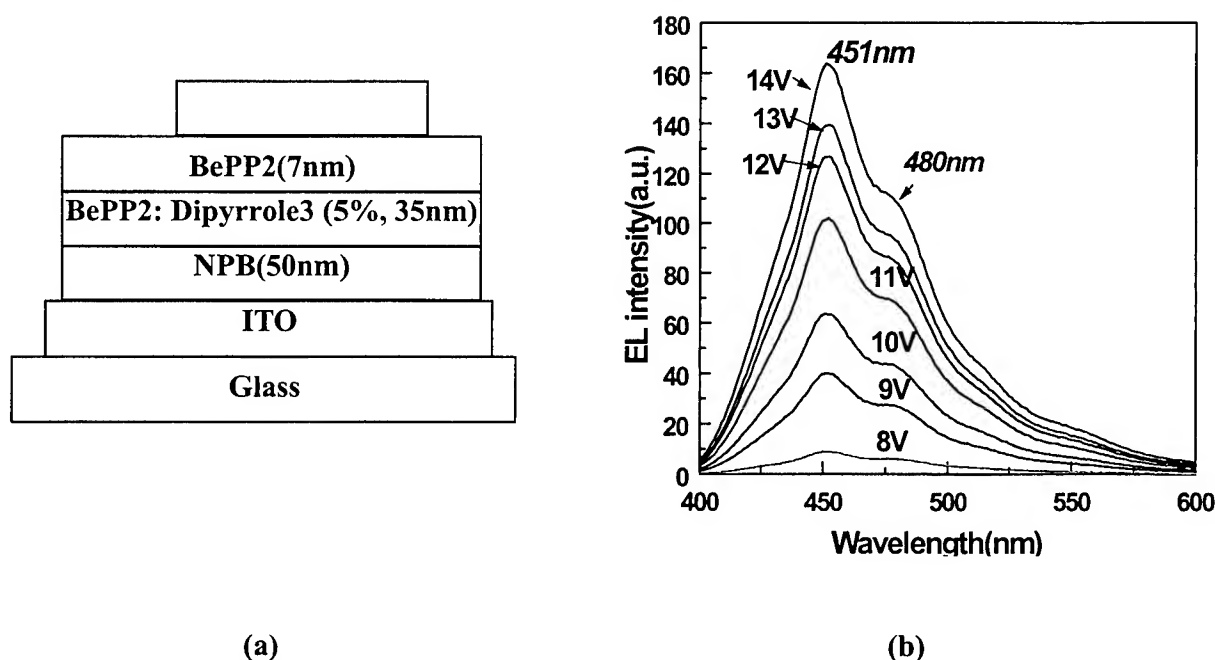


Fig.3 (a) Schematic cross-section of (b) Electroluminescent spectra at different applied voltages for OLED with structure ITO/CuPc/NPB/BePP2:Dipyrrole3(5%)/BePP2/Al.

The energy levels (HOMO: the highest occupied molecular orbital or ionization potential and LUMO: lowest unoccupied molecular orbital) of BePP2 and Dipyrrole3 were measured by circular volt-ampere. The HOMO and LUMO energy levels of Dipyrrole3 are 3.05eV and 6.11eV respectively. And that of BePP2 is 2.57 and 5.73eV respectively. So the energy transfer from the host BePP2 to guest Dipyrrole3 can readily occur via the Foster-type resonance energy transfer⁸. Figure 3(b) shows the EL emission spectrum of the doped device at different voltage. The peak wavelength of this device

is 451nm and 480nm. The EL spectrum results of OLED are consistent with the PL spectrum of Dipyrrole3. It means at least the peak wavelength of 480nm coming from the Dye Dipyrrole3's emission. As to the peak 450nm, anyway, it maybe emits from both the host BePP2 and the Dye Dipyrrole3 compared with the results from ZhiYuan Xie's paper⁹. Some other host will be used to confirm the emission of Dipyrrole3.

In fig.4, we plot luminance and current as functions of voltage. The peak luminous is 2600cd/m² at a voltage of 20V. The peak power efficiency for these devices is 0.75lm/W at a voltage of 7V. The device structure has the potential for further optimization. For example, the optimized doping densities that result in a reduction in operation voltage or increased quantum efficiency are also applicable to this work. So the blue emission from Dipyrrole3 has potential to fabricate some high performance OLED, the work will be continued.

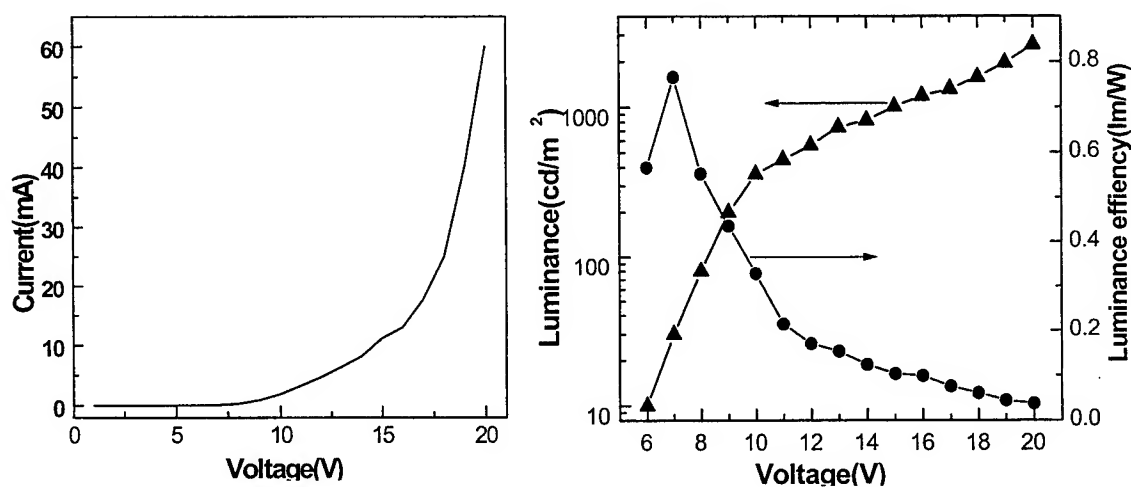


Fig.4 (a) I-V characteristics, (b) Luminance and efficiency vs. voltage of OLED with structure as: ITO/CuPc/NPB/BePP2:Dipyrrole3 (100:4)/BePP2/Al

4. CONCLUSION

A new organic luminescent material Dipyrrole3 was synthesized and used to fabricate organic light emitting diode. When this material was used as a single emitting layer, it's emitting a pure blue light (450nm). When it was used as a luminescent dye, there have two peak wavelength in the OLED's Electroluminescent spectrum (451nm, 480nm), it's almost the same as the photoluminescent spectrum of Dipyrrole3. The maximum brightness is 2600cd/m² at a voltage of 20V. The peak power efficiency is 0.765lm/W at a voltage of 7V.

ACKNOWLEDGMENTS

This work is supported by the HKU-CRCG grant and appreciates the support of the opening project scheme at the China State Lab of Jilin University. The authors would like to thanks Dr. WuFang and Dr. Tian Wenjing for the HOMO and LUMO measurement. Thanks also go to Prof. Niu Zhongguo

for his help in traveling and living in Changchun.

REFERENCES

1. C.W.Tang and S.A.Van Slyke, Appl.Phys.Lett. 51, 913(1987).
2. J.Kido, M.Kohda, K.Okuyama, and K.Nagai, Appl.Phys.Lett. 61, 761(1992)
3. RICHARD DIXON, Compound semiconductor 5(9), 43(1999)
4. J.Shi and C.W.Tang, Appl.Phys.Lett. 70, 1665(1997)
5. M.A.Baldo, S.Lamansky, P.E.Burrows, M.E.Thompson and S.R.Forrest, Appl.Phys.Lett. 75, 4(1999)
6. Zhiqiang Gao, C.S.Lee, I.Bello, and S.T.Lee, Appl.Phys.Lett. 74, 865(1999)
7. Z.Y.Xie, J.S.Huang, C.N.Li and S.Y.Liu, Appl. Phys.Lett. 74, 641(1999)
8. Takeshi Sano, Yuji Hamada and Kenichi Shibata, IEEE journal of selected topics in quantum electronics, 4, 34(1998)
9. Zhiyuan Xie, Yangqin Li, Jingsong Huang, Yue Wang, Chuannan Li, Shiyong Liu, Jiacong Shen, Synthetic Metals, 106, 71(1999)

SESSION 10

Advanced Optical Devices

Picosecond imaging of hot electron emission from CMOS circuitry

Kartik Ramanujachar^a, Dolf Landheer^a, Sylvain Raymond^a, Sylvain Charbonneau^{*a}, Peter Coleridge^a
and Tahui Wang^b

^aInstitute for Microstructural Sciences, National Research Council of Canada, Ottawa, Canada K1A 0R6

^bDepartment of Electronics Engineering, National Chiao-Tung University, Hsin-Chu, Taiwan, R.O.C.

ABSTRACT

This paper describes the spatially and temporally resolved images obtained from submicron NFETS and a CMOS ring-oscillator circuit. The spatial and temporal information is supplemented by spectral measurements obtained using a set of optical band-pass filters. The intensity of luminescence has been observed on individual transistors with gate-lengths down to 0.2 microns. The time-resolution of ~ 100 ps is sufficient to observe the response of individual invertors for gate lengths of 0.8 microns and even lower. Preliminary work on spectral distributions of emission from both the ring oscillator and NFET indicated a peak around 850 nm. This may be limited on the long-wavelength side by the response of the photomultiplier photocathode, indicating that better sensitivity could be achieved with extended infra-red sensitivity. The spectral distribution is explained with reference to current theories.

Keywords: CMOS circuits, hot-electrons, luminescence spectrum, imaging, failure analysis

1. INTRODUCTION

As silicon transistors shrink and their speed increases further, many traditional methods of circuit failure analysis and troubleshooting become less effective or impractical. Thus a recently demonstrated technique [1] for spatially and temporally resolving the luminescence from integrated circuits is becoming more valuable. It employs a cooled microchannel plate photomultiplier with a position-sensitive resistive anode to spatially resolve the luminescence and obtains temporal information by using the time-correlated photon-counting mode [2]. Although the mechanism responsible for the luminescence is still the subject of controversy, it is generally believed that the emission is generated by hot electrons. As a consequence of the shrinking geometries, electric fields within an individual NFET operated in saturation in integrated CMOS circuits can approach 10^5 volt/cm. Electrons which traverse the channel of such an NFET can be considerably heated and possess more than 2 eV of kinetic energy [3]. A fraction of such energetic carriers can give up their kinetic energy through the emission of photons. For CMOS circuits, emission emanates only from switching transistors, and no emission is obtained under steady state conditions.

In this paper we describe spatially, temporally, and wavelength-resolved measurements on the hot-electron luminescence from submicron NFETS and CMOS ring oscillators obtained using the gated photomultiplier with a set of optical band-pass filters. The paper is organized in the following manner. Section 2 describes the apparatus used for the luminescence measurements and Section 3 describes our experimental results on individual NFETs and a CMOS ring oscillator circuit. This is followed by a discussion in Section 4 and the paper ends with conclusions in Section 5.

* Correspondence: E-mail sylvain.charbonneau@nrc.ca; Telephone: (613) 993 9870

2. EXPERIMENTAL DETAILS

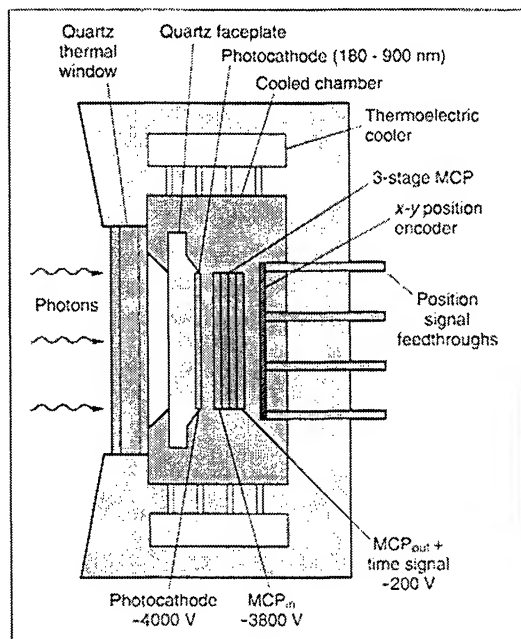


Figure 1. Construction of imaging PMT

counts/pixel/second. As a result of electron multiplication within the microchannel plates the original electron is multiplied into a cascade of about 10^7 electrons. This cascade of electrons is then incident upon a resistive anode encoder which is electrically equivalent to a diffusive RC transmission line a set of preamplifiers at its four corners. The fraction of charge that each preamplifier collects can be used to obtain the spatial position of each photon event. The system includes electronics

called ratio section circuitry to compute the ratios that are then output as voltages to both an oscilloscope for real time display of each arriving photon as well analog digital converters for digitization on a 1024 scale (10 bits). It is also possible to electronically gate out the spatial region of interest.

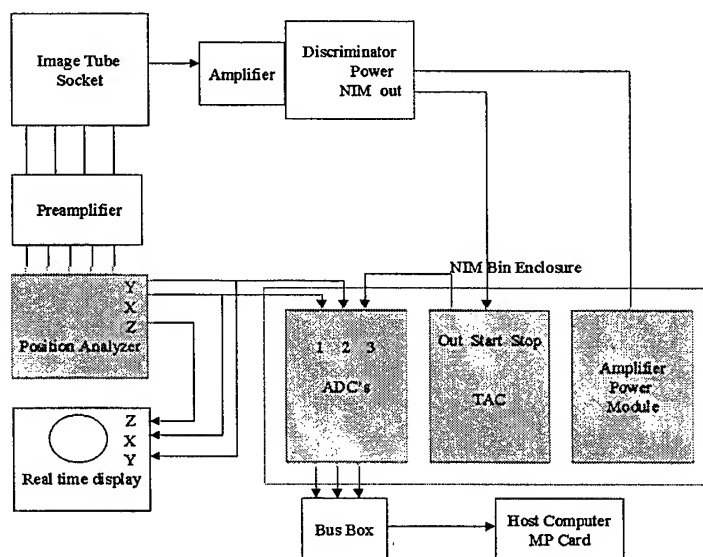


Figure 2. Time resolved system block diagram.

The second subsystem is the temporal subsystem. When the multiplied electron cascade passes through the microchannel plates of the PMT there is a momentary fluctuation in the high voltage bias that supplies the microchannel plates. This transient signal can be amplified and shaped to yield the start pulse for a time amplitude converter (TAC). The stop pulse for the time amplitude converter is usually derived from the device under test (DUT). The output from the TAC is a voltage whose amplitude is proportional to the time elapsed between the start and the stop pulses. The resulting analog voltage can be digitized with an ADC. The TAC also includes the ability to acquire data only in

specific temporal regions of interest. In summary, there are three outputs from the system of Fig. (2). The first two are the X and the Y outputs for the spatial co-ordinates of the photon event and the third output is the time of the photon event with respect to a stop pulse derived from the DUT. For every photon event this set can be written to the memory of the controlling computer. When the resulting binary file is decoded a matrix with three columns is obtained. The first column contains the X position, the second column contains the Y position and the third column contains the time of each photon incident on the photocathode face. When the third column is momentarily ignored and an image is constructed from the data in the X and Y columns a time integrated image results. When only specific time windows in the third column are considered and an image is constructed a time resolved image results. By concatenating a number of sequential time-resolved images a movie can be constructed. In the experimental results section we include work on both individual NFETs and a ring oscillator circuit.

3. RESULTS

Experimental results on individual NFETs and a ring oscillator circuit are described in this section. For the NFET time-integrated images of the luminescence and spectrum obtained using a series of band-pass filters is presented. For the ring oscillator circuit we present time-integrated images of luminescence from the individual stages, time resolved images from the various stages as well as the spectrum from the output driver of the circuit.

3.1 NFET with 0.2 Micron Gate

An NFET with a 0.2 micron gate length was used for the following experiments. The NFET was biased with the source at 0 volts, the drain was held at 2.5 volts, and the gate was biased at 1.2 volts. Under these conditions the NFET is in saturation and its emission centered in the gate region was imaged with the PMT. These acquisitions typically lasted only a few minutes as the FET emitted brightly (> 5000 counts/second). Band pass filters in the 750 nm to 1000 nm wavelength regime with a pass band of ~ 50 nm were used for coarse spectral analysis. Fig. (3) shows the emission observed from the gate region of the NFET. The emission is observed along the length of the gate.

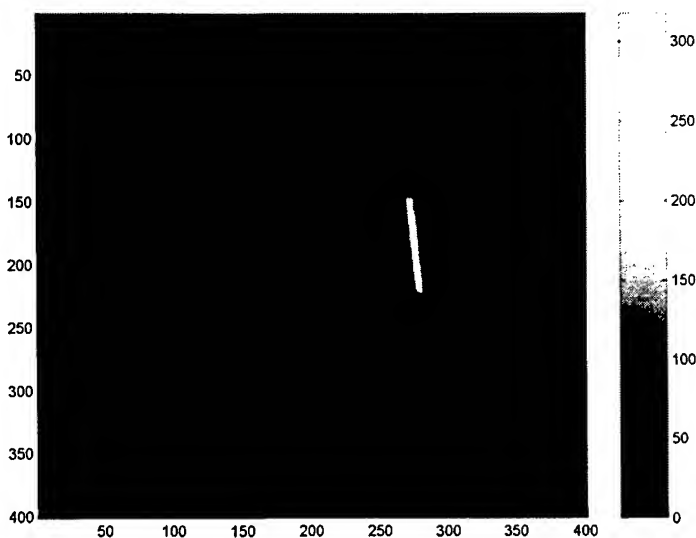


Figure 3. Streak of emission from the gate of NFET. 50 units on x and y scales equal 57.50 micron (50X mag.)

from the count down stages. The period of this output was ~ 0.9 microseconds. This divided down output was shaped into NIM trigger pulses utilizing a HP 8112 function generator and EG&G Ortec discriminator combination. This shaped pulse was then used as the stop pulse for the time amplitude convertor. Utilizing the time windowing capabilities of the TAC a temporal sequence of switching activity within the ring was obtained. Fig. (6) provides a time-integrated image of the luminescence seen from the NFET stages. Fig. (7) shows one such slice in which just one NFET of the ring switches. An entire temporal sequence showed every other NFET in the ring switch in a given cycle and that NFETs alternate between

Fig. (4) shows a spectrum observed after corrections for the quantum efficiency of the PMT as a function of the wavelength as well as the transmissivities of the band-pass filters. A spectral peak in the region of 875 nm was observed.

3.2 Ring Oscillator

The ring oscillator circuit consists of 19 inverter stages with individual NFET gate lengths of 0.8 microns, a divide by 64 count-down stage, and an output driver. Fig. (5) shows a CCD image of the ring oscillator stages. The circuit was run at a V_{dd} of 7 volts in order to maximize light output from the inverters. Since the inverters were generally dim (< 2000 counts/second) relatively long acquisitions of about an hour were necessary for acquiring data. Time resolved imaging of the ring oscillator circuitry was accomplished using divided down output

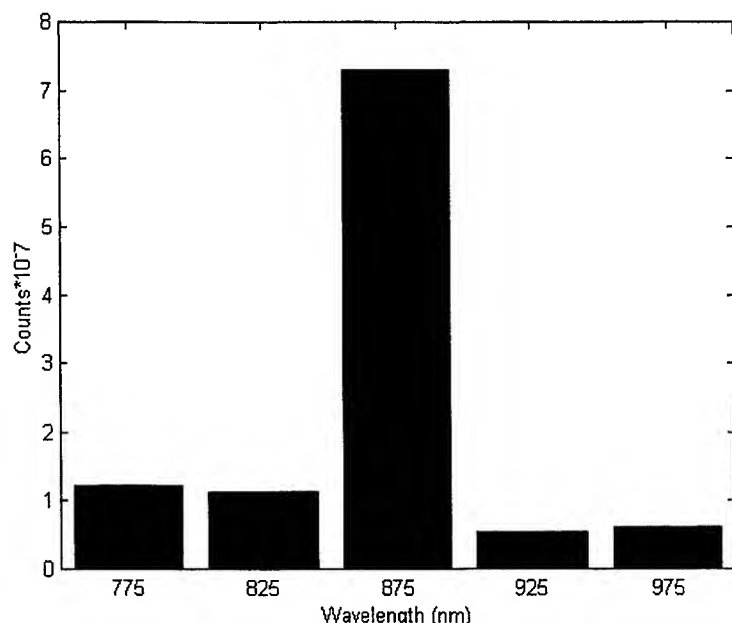


Figure 4. Spectrum of emission from NFET

a peak is seen in the spectrum in the vicinity of 875 nm (1.42 eV).

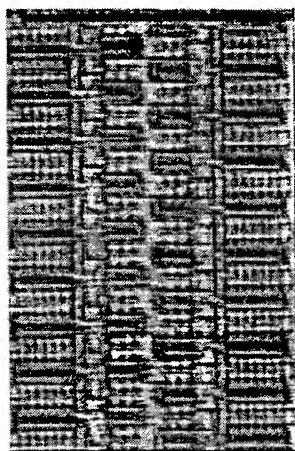


Figure 5. CCD image of ring oscillator at 200X.

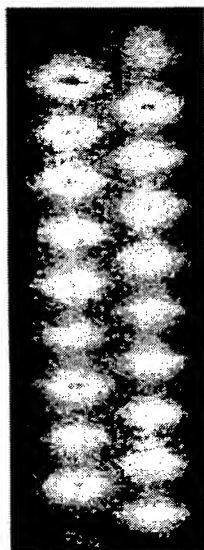


Figure 6. Time integrated PMT image showing 19 NFETs at 100X.



Figure 7. Time slice showing NFET of inverter 10 firing.

cycles. In the one time slice shown the magnification is 100X. Temporal sequences enable estimation of propagation delays. Fig. (8) provides an optical waveform of the ring oscillator computed from individual time resolved slices. The numbers above the curves indicate the various invertors for which the waveform was constructed. The scale of time is to be read backward with larger time channels indicating earlier times in the cycle of the ring. From such an optical waveform it was estimated that the propagation delay between alternate stages is 180 ± 10 ps. For this time plot each temporal channel corresponds to 65.1 ps. As for the NFET the spectrum of emission from the output driver stage was obtained. The spectrum corrected for both filter transmissivity and detector radiant quantum efficiency is provided by Fig. (9). As was observed for the case of the NFET,

4. DISCUSSION

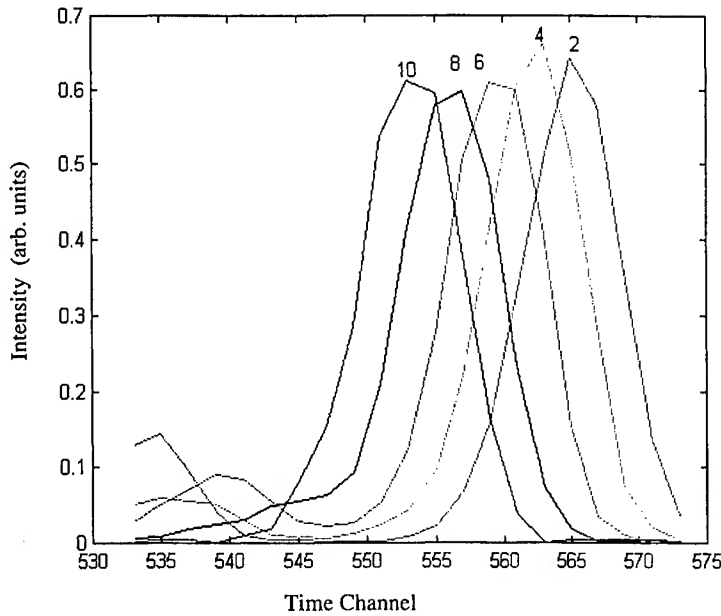


Figure 8. Optical waveform from ring oscillator.

PFET of the inverter, the capacitance of the routing and the gate capacitance of the following inverter stage) to ground and a transient current flows through the NFET of the inverter. For the case of the output going from the low state to the high state the PFET of the inverter attempts to pull the attached capacitive load to V_{dd} and a transient current flows through the PFET of the inverter. This is the major component of the transient current. Concomitant with the flow of these transient currents light emission is obtained from either the NFET or the PFET of the inverter. Given the higher mobility of the electrons, for a NFET or PFET of similar dimensions it is the NFET which will luminesce brighter. For the above reason it is

the NFET luminescence that we see in our experiments with the ring oscillator and not the PFET. In any given cycle around the ring the logic states of the inverter alternate and consequently we see luminescence only from every other inverter in the ring [4].

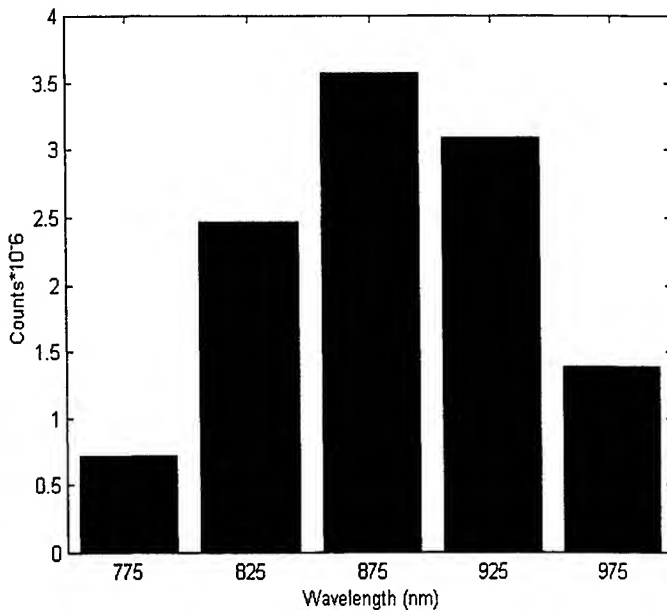


Figure 9. Spectrum of output driver of ring oscillator

We briefly dwell on the underlying physical mechanism that is responsible for emission from NFETs. Most studies of hot electron luminescence in Si devices are concerned with the relatively strong emission associated with avalanche breakdown in reverse biased p-n junctions but this discussion will focus previous more-relevant work on MOSFETs. Obeidat et al. [5] show a peak in reversed biased p-n junction at $\sim 2\text{eV}$ emission and attributed it to the model of Wolff [6] which was further elaborated by Yamada et al. [7] The model describes the emission as the result of indirect (phonon-mediated) recombination between conduction band electrons and valence band holes generated by impact ionization. Obeidat et al. report that the emission from CMOS devices was similar to that of their reverse-biased p-n junctions and they

attributed the emission from the NFETS to the reverse-biased junctions at the drain contact. Generally, this theory results in much broader peaks than observed in Figs. (4) and (9); however, the calculated peak energy Fig. (4) of Yamada and Kitao is at ~ 1.4 eV, whereas our peak is at 1.42 eV. Akil et al. [8] claim that the previous analysis leads to a monotonic, rather than peaked, emission and therefore evoked a multimechanism model for photon generation. This model results in broad peaks at photon energies near 2 eV, much higher energies than the peak we observed. None of the mechanisms described above can account for the sharp low-energy peak in the luminescence shown in Figs. (4) and (9).

Our devices are not deliberately operated to enhance impact ionization or avalanche break-down and our spectra most closely resemble the results reported by Das et al. [9] Their spectra obtained over a much wider spectral range than ours, were obtained in the sub-bandgap region with a PbS detector. Their emission peaked at ~ 1 eV. Due to the poor infrared response of the gated photomultiplier used for our time-resolved measurements it is possible that, in fact, our emission peak is at a lower energy than shown in Figs. (4) and (9). The presence of emission at energies below the silicon bandgap would rule out any mechanism that involves recombination between electrons and holes at the band-edges. It would require either static measurements using infra-red sensitive detectors to resolve this issue. Moreover, it appears that gated photomultipliers with improved infrared response would be a definite asset.

Recent simulations (10,11) and static luminescence measurements (10) show monotonically increasing luminescence with decreasing photon energy. The latter measurements, which produce excellent agreement with simulations, were performed on lateral n^+/n^+ structures designed to simulate the fields and hot electron distributions encountered in MOSFETs, while being free of the gate or extra dielectric layers that can confuse measurements. The simulations showed that impurity-assisted emission processes are of minor importance, while emission is dominated by direct and phonon-assisted conduction band to conduction band transitions. Our spectral measurements, though rudimentary, can be considered to be in agreement with these results since the peak emission shown in Figs. (4) and (9) is cut off on the low energy side by the tube responsivity. On the high energy side the rapid fall off is consistent with the calculated and observed exponential decays, as a function of photon energy, exhibited in Refs. (10) and (11).

5. CONCLUSIONS

An experimental system which is capable of spatially and temporally resolving hot electron emission from silicon CMOS circuitry has been developed. Luminescence from 0.2 micron NFETS and 0.8 micron ring oscillator circuits have been analysed with a temporal resolution of ~ 100 ps and a spatial resolution of ~ 0.5 microns. A spectral peak in the luminescence from both NFETS and CMOS gates has been observed at 875 nm (1.42 eV) near the cut-off of the photomultiplier's spectral response. An increase in sensitivity can thus be expected if gated PMTs with extended infra-red response can be developed.

REFERENCES

1. J.C. Tsang and J.A. Kash, Appl. Phys. Lett. **70**, 889 (1997).
2. Charbonneau .S. , Allard .L.B. Jeff F.Young, G. Dyck., B.J. Kyle Rev. Sci. Instrum **63** (11) 1992.
3. M.V. Fischetti, L.E. Laux, E.J. Crabbe., J. Appl. Phys. **78**, 1058 (1995).
4. N.H.E. Weste, E. Kamran, Principles of CMOS VLSI design , Second Edition , (Addison Wesley, Reading, Mass.,1993).
5. A.T. Obeidat, Z. Kalayjian, A.G. Andreou, and J.B. Khurgin Appl. Phys. Lett. **70**, 470, (1997).
6. P.A. Wolff J. Phys. Chem. Solids **16**, 184 (1960).
7. S. Yamada and M. Kitao Jpn. J. Appl. Phys. **32**, 4555 (1993).
8. N.Akil, S.E. Kerns, D.V. Kerns, Jr., A. Hoffman, and J.P.Charles, IEEE Trans Elec. Dev. **46**, 1022 (1999)
9. N.C. Das and B.M. Arora Appl. Phys. Lett. **56**, 1152 (1990).
10. L. Selmi, M. Mastrapasqua, D.M. Boulín, J.D. Bude, M. Pavesi, E. Sangiorgi, M.R. Pinto, IEEE Trans. Elec. Dev. **45**, 802, (1998).
11. J. Bude, Phys. Rev. B **45**, 5848 (1992).

Photonics Components Fabricated Using Ion Implantation

Sylvain Charbonneau^a, Philip Poole^a, Geof Aers^a, Joan Haysom^a, Sylvain Raymond^a, Paul Piva^b,
Ian Mitchell^b and Todd Simpson^b

^aInstitute for Microstructural Sciences, National Research Council of Canada,
Montreal Road, Ottawa, Ontario, Canada K1A 0R6

^bDepartment of Physics, University of Western Ontario,
London, Ontario, Canada N6A 3K7

ABSTRACT

A technique, based on quantum well (QW) intermixing, has been developed for the post growth, spatially selective tuning of the QW bandgap in a semiconductor laser structure. High energy (MeV) ion implantation is used to create a large number of vacancies and interstitials in the device. During high temperature processing (rapid thermal annealing), these defects simultaneously enhance the intermixing of the QW and the barrier materials, producing a blue shift of the quantum well bandgap, and are annealed out. Increases in the bandgap energy of greater than 100 nm at 1.55 μm in InGaAs/InGaAsP/InP structures can be achieved, while absorption losses are unaffected or reduced. Absorption spectroscopy in the waveguide geometry is used to quantify any excess loss in the structure. Using a simple masking scheme to spatially modify the defect concentration, different regions of a wafer can be blue shifted by different amounts. This allows the integration of many different devices such as lasers, detectors, modulators, amplifiers and waveguides on a single wafer using only a single, post-growth processing step. The performance of both passive (waveguide) and active (laser and amplifier) devices produced using this technique will be described, as well as the practicality of this technique in the production of photonic integrated circuits.

Keywords: Photonic integrated circuits, Wavelength division multiplexing, waveguide optics

1. INTRODUCTION

Rapid developments in optoelectronics (OE) are crucial for the development of advanced land-based telecommunications systems. For example, the development of semiconductor laser diodes and photodiodes was essential for the realisation of cost effective optical fibre communications networks. These optical fibre systems are in wide use today for both long and short haul networks. The next step in the development of these systems is to combine optical and electronic components into optoelectronic integrated circuits (OEIC).

The primary objectives of optoelectronic integration are similar to those of electronic integration: enhancing the performance, reliability and increasing the functionality while lowering the manufacturing cost. The cost and reliability improvements achieved through very large scale integration (VLSI) have been largely responsible for enabling all the advancements in electronic information transmission and processing. Like electronic integrated circuits, which involve the replication of huge numbers of components of various functionalities (transistors, diodes resistors, capacitors etc.), optoelectronic integration requires the integration of fundamentally different types of components. These include light emitters, waveguides, modulators and detectors. Each of these different components may require different material structures to achieve optimised performance.

Photonic integrated circuits (PICs) are a subset of OEICs utilising a single substrate for the monolithic integration of optically interconnected guided-wave optoelectronic devices. As optical communications systems advance the number of individual optical devices that need to be connected together to make photonic circuits increases. A large portion of the cost of such architectures is due to the difficulty of achieving single-mode optical connections between the guided wave components. Such devices often require tightly confining waveguides for optimised performance, resulting in difficult submicron alignment tolerances when such structures are coupled to single-mode optical fibres. By replacing individually aligned connections with lithographically produced waveguides, PICs offer the promise of cost reduction, dramatically reduced size, and increased packaging robustness.

This paper will describe a technique that allows the integration of multiple function devices onto a single substrate. The criteria needed for the practical integration of OE devices will be reviewed and the various approaches for monolithic photonic integration based on QW active layers will be given. The use of ion-implantation-induced QW intermixing (QWI) as an integration technique will be described, and its influence on device performance discussed. Details of the intermixing process at a microscopic level will be given and its effect on the optical properties of devices.

2. TECHNIQUES FOR MONOLITHIC INTEGRATION

We will concern ourselves here only with waveguiding PICs, in which the signal carrying optical beam is confined within a waveguide near the surface of a wafer. All signal processing takes place in this plane. This is believed to be the most likely form for monolithic PICs, as waveguide optical modes are the most compatible with optical fibers and on-chip optical signal processing.

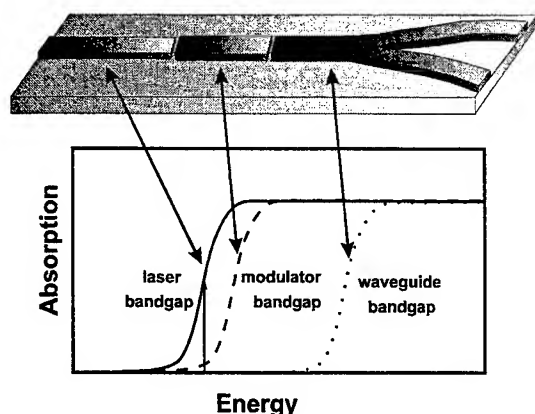


Figure 1. Schematic diagram of a "generic" PIC containing a laser diode whose output is directed into a transparent waveguide 3-dB splitter through an external electroabsorption modulator. The optimum operation of this PIC requires that the bandgap energies of these three components possess the specific relationship illustrated in the figure.

The primary requirement for waveguiding PICs is bandgap compatibility among the various optoelectronic devices, as illustrated schematically in Figure 1 for a "generic" PIC. In such PICs, the signal carrying light beam is directed by passive, transparent, optical waveguides to various active optoelectronic devices in the plane of the wafer. Optimum performance demands that the bandgap energies of the various components be related to each other in a specific fashion. For example, in Figure 1, it is essential that the passive waveguide collecting and distributing the light from the laser diode be as transparent as possible to the laser wavelength (i.e., have a larger bandgap energy than that of the laser structure) so that a minimum amount of optical power is lost to absorption during transit. On the other hand, the external electro-absorptive modulator (a quantum confined Stark effect (QCSE) modulator - essentially a reverse biased laser structure) should have a slightly larger bandgap than the laser to achieve optimum operating parameters (low loss and good contrast). The advantage of even such a simple PIC lies in the increased operational bandwidth, reduced chirp, and possibly reduced demands on the drive circuits that external

modulation provides.

The realisation of PICs requires spatially selective control over the optical and electrical characteristics of the multiple quantum well material. Several approaches to integration based on QW active layers are emerging, and we will

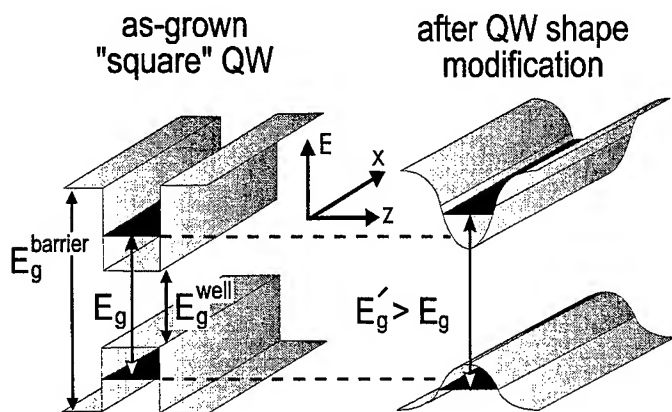


Figure 2. Schematic diagram illustrating the effect of QW shape modification on QW bandgap energies.

concentrate on the use of quantum well intermixing¹. In this technique the bandgap of a QW structure is modified selectively, after growth, by intermixing the well and barrier materials to form an alloy. This mechanism is based on the fact that a QW is an inherently metastable system due to the large concentration gradient of atomic species across the QW/barrier interface. For example, in InGaAs/InGaAsP QWs, the phosphorus concentration changes from 43% to 0% (for layers lattice-matched to InP) in a distance of less than 1 nm. At temperatures above ~750°C significant diffusion of atomic species will occur resulting in an interdiffusion of the QW and barrier materials, as shown schematically in Figure 2.

This process causes a rounding of the initially square QW bandgap profile and, in

general, results in an increase of the bandgap energy. This provides a route to fabricating low-loss optical waveguides, and bandgap-shifted QCSE modulators, lasers and detectors, using only one epitaxial step. In addition, because the bandgap is increased, the refractive index is modified enough to provide optical confinement, allowing for the fabrication of gratings and laser reflectors.

This intermixing process can be greatly enhanced by the presence of impurities or defects in the vicinity of the interfaces of the QW, allowing intermixing to occur at temperatures that are substantially lower than that normally required. A number of intermixing techniques such as impurity induced disordering²⁻⁴, laser beam induced disordering,⁵ impurity free vacancy diffusion⁶⁻⁸ and ion-implantation-enhanced interdiffusion⁹⁻¹¹ have been utilized to enhance the thermally-driven interdiffusion. All these techniques are spatially selective, permitting intermixing enhancement only in the regions requiring a larger bandgap, leaving other regions unmodified. In addition, they use standard QW structures and require no special growth processes

To be practical, any monolithic photonic integration technique must fulfill several requirements:

- 1) there must be large, controllable bandgap energy differences between the various devices in the PIC,
- 2) loss in the integrated waveguide devices must be comparable to or lower than that present in the as-grown (i.e., unmodified) structure,
- 3) the electrical properties of the various devices must suffer insignificant deterioration due to the processing technique,
- 4) there should be no substantial adverse effects on the operating lifetimes of the various devices in the PIC, after processing,

We have demonstrated that for many cases spatially selective QW bandgap energy shifting due to QW shape modification using ion implantation fulfills these requirements.

3. EXPERIMENTAL DETAILS

All of the work discussed in this paper concerns the InGaAsP/InGaAs/InP based material system where the devices are grown on InP substrates using either MOCVD or CBE. Ion implantation of the samples was performed using a 1.7MV Tandem accelerator, using phosphorus as the implantation species. Phosphorus was chosen since it is one of the lattice constituents, and so would not result in any doping of the structure. The introduction of dopants could modify the electrical properties of the devices and add extra optical losses, which could degrade performance. The ions were implanted at 7° off-normal to minimise channelling effects. To determine the distribution of implanted ions in the structures the simulation package TRIM¹² (TRansport of Ions in Matter) was used, this also gave information on the number and location of displacements created. Typical conditions used were a dose of 10^{14} P/cm² at a substrate temperature of 200°C and energy of 1 MeV. Following the implantation the samples were annealed using a rapid thermal annealer (RTA). During the anneal,

defects created by the implantation process diffused through the active region of the devices (containing the QWs) enhancing the intermixing process. Typical annealing conditions for the InP based materials are rapid heating to ~700°C for 0.5 to 3 min. To protect the sample surface during the RTA a GaAs proximity cap was used, as well as surrounding it by GaAs.

Following intermixing the structures are characterised using a number of different techniques, 300 and 4.2K photoluminescence (PL), waveguide absorption, double crystal x-ray diffraction (DCXRD), electrical performance and device performance (e.g. lasing characteristics). From these measurements the effectiveness of the ion implantation induced QWI for device integration can be determined.

The structure used in this study was an InP based 1.5μm laser structure, shown in Figure 3. This consisted of five In_{0.53}Ga_{0.47}As QWs with In_{0.74}Ga_{0.26}As_{0.57}P_{0.43} barriers and doped InP cladding, capped with InGaAs. The QWs were 1.75 μm beneath the surface.

Following results from earlier studies on the laser material¹⁰ it was decided only to use ion implantation energies for the phosphorus that left all of the implantation damage well above the QW region. This was because as soon as implantation damage was directly created within the QW region the optical properties of the material was dramatically degraded, low PL intensity and large PL linewidths, even

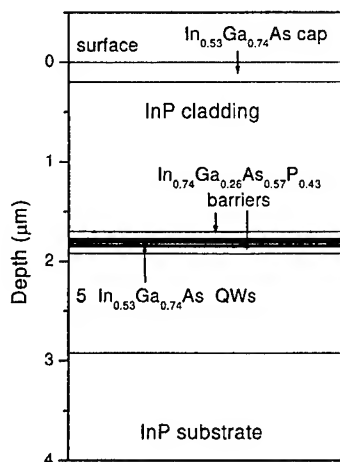


Figure 3. Schematic diagrams of the laser structure used for the intermixing studies.

after annealing. Since we want to be able to make high quality active devices from material that had been intermixed we avoided this regime.

4. WAVEGUIDES

To determine the effect of the intermixing process on the waveguide transmission properties the laser sample was implanted with a dose of 2.5×10^{13} P/cm² at an energy of 2 MeV, giving an expected mean range of 1.5 μ m. The implant was performed at a temperature of 200°C with a flux of 6.6 nA/cm². The sample was then annealed at 700°C for 120 s.

Waveguide loss measurements using the Fabry-Perot fringe technique were performed. Four micron wide ridge waveguides were fabricated from both intermixed and non-mixed material on the same sample. The sample was then cleaved

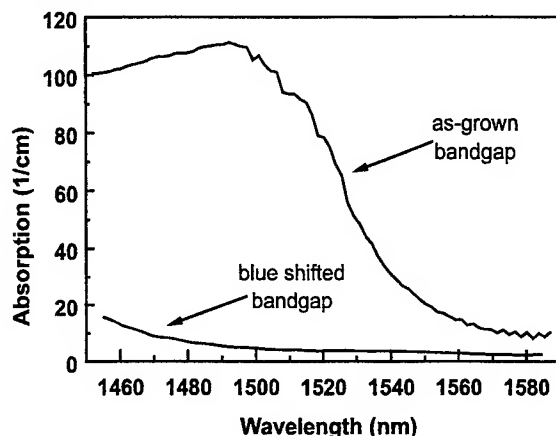


Figure 4. Absorption constants derived from measured transmission spectra for as-grown and quantum well intermixed waveguides.

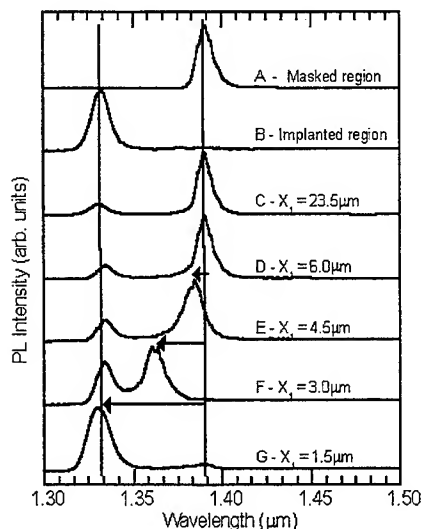


Figure 5. Normalised low temperature PL from a large masked region (spectrum A), a large uniformly implanted region (spectrum B), and from arrays with varying mask stripe widths, as noted by the value of X_1 (spectra c through G).

to form 1 mm-long Fabry-Perot cavities. A tuneable (1.45-1.59 μ m) laser diode was used for the absorption experiments. The light was modulated at 10 kHz and coupled into the TE mode of the waveguide through a tapered polarisation preserving fibre. The transmitted light was then captured by a similar fibre coupled to a Ge-detector, followed by a lock-in amplifier. Fabry-Perot interference fringes were formed due to multiple reflections at the cleaved facets. From the contrast of these fringes the waveguide loss can be determined. A change in the refractive index, between the unimplanted and implanted waveguides, can also be extracted from the spacing of the fringes and yields a value of $\Delta n_{\text{group}} = 0.08$ (~2.5%) at 1550 nm with $\Delta n_{\text{phase}} = 0.2\%$. It should be noted that, for photon energies larger than the bandgap, the Fabry-Perot fringes disappear due to the high absorption, and therefore another method based on the relative transmitted intensity was used.

Figure 4 presents the absorption as a function of wavelength derived from the measured transmission spectra using both methods for the implanted and the unimplanted waveguides. As observed from the spectra, the bandgap of the implanted QWs was blue-shifted 90 nm with respect to the as-grown QWs. The actual bandgap cannot be observed since it is beyond the range of the tuneable source. At the absorption edge of the unimplanted waveguide (~1.54 μ m), the absorption coefficient is reduced from 110 cm⁻¹ to only 4 cm⁻¹. Note that this absorption value also includes excess losses such as scattering losses resulting from imperfections of the ridge waveguide. It should be noted that the loss in the implanted waveguide appears to be lower than the unimplanted one, even after considering the 90 nm difference in bandgap. For example, the absorption of the unimplanted waveguide is ~8 cm⁻¹ at 1580 nm, while it is 5 cm⁻¹ at 1490 nm for the implanted sample. This indicates that no excess loss results from the damage created by the implantation. This decrease could be due to a reduction in Auger effects and inter-valence band absorption, as the bandgap wavelength becomes shorter. In addition, the free carrier absorption coefficient is, to a first approximation, proportional to the square of the wavelength and so would be reduced by about 12% over the range of wavelength studied. Another contributing factor is that the guided mode will be more strongly confined within the active region as the wavelength is reduced, decreasing the interaction of the mode with doped regions in the cladding layers.

5. LATERAL SELECTIVITY

Another important aspect of a process for device integration is the spatial resolution that can be obtained, which has to be small enough to allow realistic circuits to be fabricated. To address this

issue, PL in combination with a specially designed mask to monitor the intermixing of QWs under masked regions was employed. The implantation conditions were dose= $1.0 \times 10^{14} \text{ cm}^{-2}$, energy=1.0 MeV, Flux= 7 nA/cm^2 , $T_{\text{substrate}}=200^\circ\text{C}$. Prior to implantation, a $2.0 \mu\text{m}$ silicon dioxide layer was deposited on the surface and patterned to act as a selective area mask (the mask pattern is described in more detail below). Where it covered the surface, the thick oxide completely blocked any ions from reaching the sample. After implantation, the silicon dioxide was removed and the samples were rapid thermal annealed at 675°C for 180 s in flowing nitrogen.

The implantation mask had thirteen distinct arrays, each containing parallel stripes of oxide of width and spacing X_1 and X_2 respectively. From one array to the next, the mask stripe width, X_1 , varied from $1.5 \mu\text{m}$ to $23.5 \mu\text{m}$, while the spacing between masked stripes, X_2 , also increased proportionately from $6.5 \mu\text{m}$ to $32.5 \mu\text{m}$ (the regions between masked stripes will be referred to as implanted stripes). Each array was approximately 1.2 mm square, and thus contained twenty or more masked stripes. During low temperature PL, the excitation laser was directed at the centre of an array, with a spot size of approximately $100 \mu\text{m}$. Due to this spot size, the PL spectra from an array exhibited luminescence peaks from both the implanted and the masked regions. The excitation laser was a Ti:Sapphire tuned to 880 nm with an excitation power of a few milliwatts.

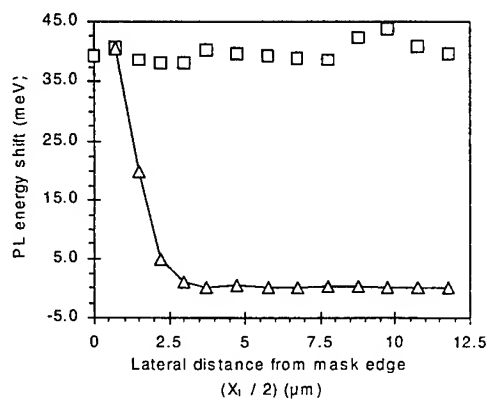


Figure 6. Energy shifts of PL peaks from QWs in implanted stripes (squares) and masked stripes (triangles). The shift is obtained by comparison to PL peaks in fully masked regions surrounding each array.

linewidths of unaltered QWs were $8 \pm 1 \text{ nm}$ ($6 \pm 1 \text{ meV}$), and those of intermixed QWs were slightly larger at $10 \pm 1 \text{ nm}$ ($8 \pm 1 \text{ meV}$). Linewidths of partially intermixed “masked” stripes (of spectra F and G) were comparable to those of the implanted stripes.

If the positions of PL peaks from both implanted and masked stripes are compared with the peak position of masked regions from surrounding material, an energy shift can be obtained. The mask stripe width, X_1 , is divided by 2 to give a value for the lateral distance from a mask edge. In Figure 6, a plot showing the energy shift as a function of $X_1/2$ clearly indicates that QWs within the first $2.5 \mu\text{m}$ of a mask edge undergo some degree of intermixing. From these observations, the lateral selectivity of QWI on these structures with this implantation energy is determined to be $2.5 \mu\text{m}$. This resolution is high enough to allow the integration of complex devices.

6. MULTIPLE SHIFTS WITH A SINGLE IMPLANT

For maximum flexibility in design, and the minimum number of processing steps it would be advantageous to be able to blue shift different regions of a wafer by different amounts with a single implantation step. As was discussed in ref. 13, for InGaAs/InGaAsP QWs embedded in InP cladding layers, a strong correlation exists between the PL energy shift after implantation and annealing and the calculated *total* vacancy creation in the sample per implanted ion. This observation suggests that defects are extremely mobile in InP and that, wherever they are created in the structure, they can diffuse through the QW region and promote intermixing. Therefore, an increase in either dose or energy of the implanted ions will lead to an increase in intermixing. For simplicity, we decided to keep the dose and energy of the ions fixed and vary the damage generated in the semiconductor structure by masking different parts of the sample with different thicknesses of SiO_2 , obtained

Low temperature PL spectra of these samples are shown in Figure 5. Spectra A and B are reference spectra taken from relatively large regions of the same material which were completely masked and implanted, respectively, while spectra C through G were taken from arrays with masked stripes of varying widths (X_1). Spectra from arrays which are not shown (those from arrays with X_1 between $6.0 \mu\text{m}$ and $23.5 \mu\text{m}$) were nominally identical to spectra C and D. For spectra C through G, the longer wavelength peak at $1.39 \mu\text{m}$ originates from the QWs underneath masked stripes (i.e., unaltered), while the shorter wavelength peak at $1.33 \mu\text{m}$ originates from intermixed QWs (i.e., in the implanted regions). For $X_1 \geq 6.0 \mu\text{m}$, the PL peak from masked stripes is in the same position as peaks from the reference spectra A, but as masked stripes become narrower (spectra E and F) these peaks are blue shifted due to partial intermixing of the QWs. The degree of intermixing increases until this peak merges with $1.33 \mu\text{m}$ peak of the neighbouring implanted stripes (spectra G). In contrast, implanted stripes from all arrays were blue shifted by approximately the same amount, 57 nm (40 meV), equal to the shift of uniformly implanted material (spectra B). PL

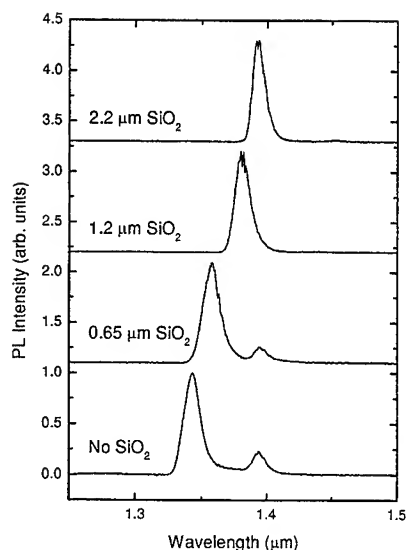


Figure 7. Low temperature PL spectra following implantation through different thicknesses of SiO₂ and then annealing.

through standard UV lithography and SiO₂ PECVD evaporation. Three different SiO₂ layer thicknesses, 0.65 μm, 1.2 μm, 2.2 μm and an unmasked region, i.e. 0 μm, were deposited on a single piece of laser material. The maximum SiO₂ thickness was chosen so that the 1 MeV P⁺ ions would be completely stopped in the SiO₂, leaving unimplanted material beneath. The SiO₂ layers were again removed before thermal treatment (RTA). Low temperature (5K) PL measurements were made using weak (1mW) titanium-sapphire excitation tuned below the InP bandgap. The diameter of the exciting beam was 100 μm.

The low temperature PL spectra obtained from the four implanted and annealed regions of the laser structure are shown in Figure 7. As expected, the magnitude of the blue shift in the PL emission correlates with the total number of defects generated in the laser structure¹⁰. Where the SiO₂ mask was the thickest, no disordering took place and the peak of the PL emission is at 1.396 μm (1.56 μm at room temperature). In the case where no SiO₂ mask was used, maximum interdiffusion was achieved and the PL emission was blue shifted by 52 nm. The weaker emission band observed at 1.396 μm from implanted regions which have 0.65 μm SiO₂ and no SiO₂ can be attributed to the laser spot size extending over non-intermixed areas of the sample. The PL linewidth does not increase significantly (FWHM increases from 10 nm to 13 nm) as the intermixing increases. This small change could be due to variation in the degree of intermixing across the probed area.

Using this technique an arbitrary shift can be obtained at any location on the wafer.

7. LONG TERM DEVICE PERFORMANCE

Although it is clear from the studies discussed above that QW shape modification produces no short term deleterious effects on the optical and electrical properties of active device structures, residual damage may produce cumulative effects and eventually reveal itself during the operation of these devices by, for example, reducing lifetimes. In order to study this possibility, accelerated lifetime tests were performed on a series of QW intermixed laser diodes. These were stressed by operating them with large forward currents and at elevated temperatures.

High energy phosphorus ion implantation was used to selectively control the bandgap energy of InGaAsP/InP QW laser structures operating at 1.31 μm. The p-i-n laser structure used for this study was grown using metal-organic chemical vapour deposition. The active region consists of twelve 3.5 nm InGaAsP QW (emitting at 1.3 μm) sandwiched between 10 nm InGaAsP barriers. An implant energy of 1 MeV was chosen to centre the peak of the implantation induced damage at least 1 μm away from the active QW region with a dose of $1 \times 10^{14} \text{ cm}^{-2}$ at a constant flux of 120 nA/cm². Different blue shifts were achieved by ion implanting through a SiO₂ mask of varying thicknesses as described earlier. A total of four different wavelength regions were created, varying from 0 to 65 nm blueshifts from the as-grown material.

Ridge waveguide laser diodes from each of the four regions of the centre portion of the wafer were cleaved and tested. Approximately 30 device chips were cleaved from each bar and measured for light and voltage dependencies on drive current (L-I and V-I), then mounted p-side down on diamond/copper blocks. Mounted chips were remeasured for L-I and I-V curves, then measured individually for spectral intensity vs. wavelength. No significant difference in threshold current (20-25 mA) or differential quantum efficiency (0.25-0.30 W/A) was observed from the four different implanted regions. These are the same values obtained from laser structures fabricated from the as-grown wafer which had not undergone any implantation or rapid thermal annealing. This indicates that the shifted laser material is of high quality, as any damage left in the active region of the device after implantation/anneal would add to the loss in the cavity and increase the threshold current. This observation suggest that factors contributing to changes in the threshold current such as alteration of the well shape, barrier height, and dopant diffusion in the active region and changes in the number of nonradiative recombination centres within the material are not significant.

The reliability of intermixed InGaAsP/InP QW lasers, which is of primary importance for any practical application, was tested in this study. Accelerated lifetime testing of devices obtained from the four intermixed regions was carried out at a temperature of 100 °C with a driving current of 150 mA for a period of 500 hours. For devices from shifted by 0 and 29 nm,

the predicted device lifetime (based on 50% increase in current) for operation at 25 °C is in excess of 25 years (using 0.4 eV activation energy). This is currently used as a benchmark for standard (non-implanted) devices. Devices shifted by 46 and 65 nm exhibit higher and more random degradation rates and were deemed to be less reliable. Hence, for the present implantation and anneal conditions, active devices fabricated from material that is wavelength shifted up to ~ 30 nm were observed to be reliable. Further optimization of implantation temperature and annealing time (presently 200°C and 90 sec. respectively), may result in wavelength shifts greater than 30 nm while retaining 25 years predicted reliability of active devices.

8. INTEGRATED AND NOVEL DEVICE APPLICATIONS

Since the technique of ion-induced QW intermixing is simple to implement, and results in material of very high optical quality, many novel PICs can be envisioned. An elementary example, a very simple two-wavelength demultiplexer, is shown in Figure 8. It consists of two regions of a standard waveguide laser structure, one of which has been intermixed and one that has not. Light is coupled into the waveguide and passes through the intermixed into the non-intermixed region.

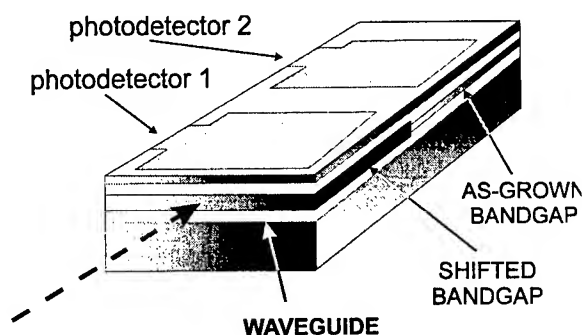


Figure 8. Schematic diagram illustrating the principle of operation of a two wavelength WDM DEMUX fabricated using QW intermixing.

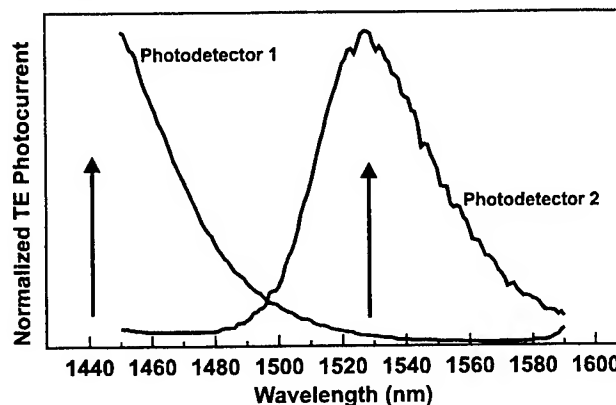


Figure 9. Normalized room temperature TE photocurrent spectra of as grown and intermixed regions of the two wavelength WDM demultiplexer shown schematically in figure 8.

Photons with a wavelength shorter than the bandgap of the first, blue-shifted, section will be absorbed in that region, generating a photocurrent. Longer wavelength light that is not absorbed in the first section will pass through to the as-grown region which has a smaller bandgap energy, and will be absorbed and detected there.

Figure 9 presents the photocurrent spectra observed in each of the two regions as the wavelength of TE light from a tunable laser is scanned from 1.45 μm to 1.59 μm . Clearly each photodetector is sensitive to a different region of the optical spectra and so this device is able to distinguish between low (arrow at 1.53 μm) and high (arrow at 1.40 μm) energy photons. This device is extremely simple to fabricate and provides an elementary form of demultiplexing.

Other PICs which could be fabricated using QWI would include laser-external modulators (as in Figure 1), laser-rear-facet monitors, optical drops, and add&drops. However, more complex PICs, such as optical switches, optical routers, multiple wavelength MUXes (which multiplex, or combine, optical signals of differing wavelengths) and DEMUXes (which demultiplex multiplexed optical signals) would be equally feasible.

9. COMPOSITIONAL CHANGES AT THE QW

The microscopic details of the intermixing process at the QW can be quite complex for the InP based materials system in comparison to GaAs/AlGaAs. For GaAs/AlGaAs only the group III species are in motion (the group V sublattice consists solely of As) and the structure is always lattice matched. In the InP/InGaAs materials system both group III and V species can move, and strain variations can develop. The way in which the different species move can have a significant impact on the optical properties of the intermixed structure. For example, intermixing only on the group III sublattice will result in a red shift with intermixing, whilst motion only on the group V sublattice will result in blue shifts. The development of strain can also significantly modify the optical properties of devices. Therefore it is important to understand the microscopic details of the intermixing process.

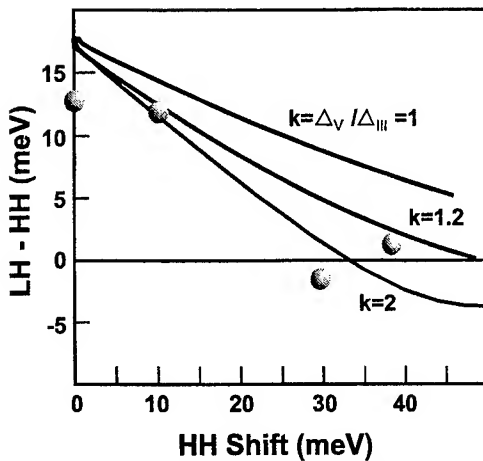


Figure 10. Comparison of experimental HH-LH bandgap splitting as a function of heavy hole shift after implantation and annealing with theory for different diffusion length ratios, k .

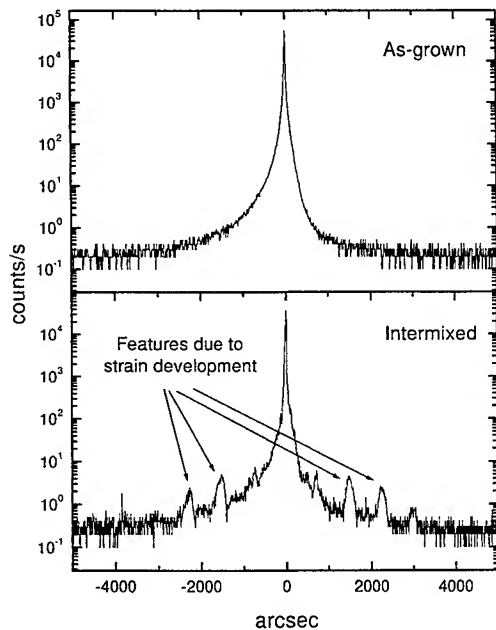


Figure 11. (004) x-ray diffraction spectra for the laser structure before and after intermixing. Satellite peaks develop indicating the generation of local strain within the structure due to different diffusion behaviour on the group III and V sublattices.

The intermixing process was studied with the use of a theoretical model for the diffusion of the different species. The interdiffusion process was modeled assuming independent Fickian behaviour for the group III and V sublattices¹³ where Δ_{III} and Δ_V are the group III and V diffusion lengths respectively. We then define the ratio of the group V to group III diffusion lengths, Δ_V/Δ_{III} as k ; local strain develops when k is not equal to 1. The effect of interdiffusion on the energy band profile (including strain effects) and confined states for valence and conduction bands has been modeled.

For a given QW structure, the light hole (LH)-heavy hole (HH) energy splitting as a function of HH energy can be calculated for various values of k and compared with experimental values obtained near flat band conditions. Experimentally, polarisation dependent waveguide absorption measurements were made on the intermixed laser structure for different degrees of intermixing. The comparison of the experimental data and theory are shown in figure 10. From this analysis, it is clear that, within this model, our experimental data can only be explained by assuming $k > 1$ (group V motion is significantly greater than group III). Scatter in the data and a decreasing sensitivity of LH-HH splitting on increasing k values preclude a more accurate determination of the ratio. For such values of k , a tensile strain develops at the quantum well centre with compressive regions either side of the QWs.

Since the strain variations generated by this process are quite large and the starting material was lattice matched it should be possible to observe the intermixing process using x-ray techniques. Figure 11 shows the (004) double crystal x-ray diffraction (DCXRD) spectra for a lattice matched laser structure before and after intermixing. The featureless spectrum for the starting material indicates the high degree of lattice matching for this structure. After intermixing, satellite peaks are observed associated with the five QWs in the laser core. To be able to observe this effect, areas of different strain must have been generated in the QW region, consistent with a value of k that was significantly different from 1. This has further been confirmed in cross section scanning tunneling microscopy studies of intermixed material¹⁴, where a k value of 1.7 was determined.

The increased motion on the group V relative to the group III sublattice has an impact on a number of the optical properties of devices created using QWI. The most obvious is the ability to make the HH and LH transitions degenerate (see figure 10), resulting in the polarization independent operation of devices such as optical amplifiers. The knowledge of this behaviour is important to allow the future design of structures utilizing QWI.

10. CONCLUSIONS

In this paper we have shown that QWI using ion implantation is a viable technique for creating photonic integrated circuits in which all of the devices can consist of the same basic layer structure. Control of the bandgap shift and its spatial

resolution has been demonstrated. Under appropriate conditions the process results in no degradation in device performance, and can even add to the device capabilities such as providing polarization insensitivity.

11. REFERENCES

1. J.H. Marsh, "*Quantum well intermixing*", Semiconductor Sci. Technol. **8**, 1136-1155 (1993).
2. S. R. Andrew, J. H. Marsh, M. C. Holland, A. H. Kean, "*Quantum well laser with integrated passive waveguide fabricated by neutral impurity disordering*", IEEE Photon. Tech. Lett. **4**, 426-428 (1992).
3. W. D. Laidig, N. Holonyak, M. D. Camras, K. Hess, J. J. Coleman, P. D. Dapkus, J. Bardeen, Appl. Phys. Lett. **38**, 776 (1981).
4. E. V. K. Rao, M. Juhel, Ph. Krauz, Y. Gao, H. Thibierge, "*Long range disordering of GaAs-AlGaAs multiple quantum wells by isoelectronic antimony implants*", Appl. Phys. Lett. **62**, 2096-2098 (1993).
5. J.J. Dubowski, S. Charbonneau, A.P. Roth, P.J. Poole, C. Lacelle, M. Buchanan, I.V. Mitchell and R.D. Goldberg, "*A comparative study of laser- and ion implantation-induced quantum well intermixing in InGaAsP/InP microstructures*", SPIE Proceeding **2991**, 113-118 (1997).
6. D. G. Deppe, L. J. Guido, N. Holonyak, K. C. Hsieh, R. D. Burnham, R. L. Thornton, T. L. Paoli, "*Stripe-geometry quantum well heterostructure AlGaAs-GaAs lasers defined by defect diffusion*", Appl. Phys. Lett. **49**, 510-512 (1986).
7. J. D. Ralston, W.J. Schaff, D.P. Bour and L. F. Eastman, "*Room temperature exciton electroabsorption in partially intermixed GaAs/AlGaAs quantum well waveguides*", Appl. Phys. Lett. **54**, 534-536 (1989).
8. Emil S. Koteles, B. Elman, R. P. Holmstrom, P. Melman, S. Charbonneau and M.L.W. Thewalt, "*Modification of the shape of GaAs/AlGaAs quantum wells using rapid thermal annealing*", J. Superlatt. Microstruct. **5**, 321-325 (1989).
9. S. Charbonneau, P. J. Poole, P. G. Piva, G. C. Aers, Emil S. Koteles, M. Fallahi, J. J. He, J. P. McCaffrey, M. Buchanan, M. Dion, R. D. Goldberg, I. V. Mitchell, "*Quantum well intermixing for optoelectronic integration using high energy ion implantation*", J. Appl. Phys. **78**, 3697-3704 (1995).
10. P. J. Poole, S. Charbonneau, G. C. Aers, T. E. Jackman, M. Buchanan, M. Dion, R. D. Goldberg, I. V. Mitchell, "*Defect diffusion in ion implanted AlGaAs and InP: Consequence for quantum well intermixing*", J. Appl. Phys. **78**, 2367-2371 (1995).
11. P. Gavrilovic, D. G. Deppe, K. Meehan, N. Holonyak, J. J. Coleman, Intern. J. Superlatt. Microstruct. **47**, 130 (1985).
12. J.F. Ziegler, The Transport of Ion in Matter, TRIM-90, New York: IBM Corporation (1990).
13. Wai-Chee Shiu, Joseph Micallef, Isaac Ng, and E. Herbert Li, "*Effect of different cation and anion interdiffusion rates in disordered InGaAs/InP single quantum well*", Jpn. J. Appl. Phys., **34**, 1778 (1995).
14. Huajie Chen, R. M. Feenstra, P. G. Piva, R. D. Goldberg, I. V. Mitchell, G. C. Aers, P. J. Poole, and S. Charbonneau, "*Enhanced group-V intermixing in InGaAs/InP quantum wells studied by cross-sectional scanning tunneling microscopy*", Appl. Phys. Lett. **75**(1), 79-81 (1999).

Integration of waveguide type wavelength demultiplexing photodetectors by selective intermixing of InGaAs/InGaAsP quantum well structure

Deok Ho Yeo*, Kyung Hun Yoon, Hang Ro Kim, Sung June Kim

School of electrical engineering, Seoul national university, Seoul, Korea,

ABSTRACT

Wavelength demultiplexing photodetectors was fabricated using selective intermixing of InGaAs/InGaAsP multi-quantum well (MQW) structure. An InGaAs/InGaAsP MQW with u-InP cladding layer and u-InGaAs cap layer grown by metal organic chemical vapor deposition (MOCVD) was used for this experiment. Intermixing of InGaAs/InGaAsP MQW structure was done by a rapid thermal annealing after depositing SiO₂ dielectric layer on the InGaAs cap layer by plasma-enhanced chemical vapor deposition (PECVD). Three sections of shorter-wavelength PD, absorber region and longer-wavelength PD lined up linearly and the front two regions were intermixed. Output current ratios of fabricated photodetectors at wavelengths of 1550 and 1480 nm were about 20 dB and thus the photodetectors were proven to demultiplex both wavelengths.

Keywords: Quantum well intermixing, InGaAs/InGaAsP multi-quantum wells, dielectric cap annealing, dual wavelength photodetector, wavelength demultiplexing, waveguide type photodetector, integrated optics

1. INTRODUCTION

Photodetectors with a wavelength demultiplexing function is predicted to play an important role in future fiber optic communication system utilizing wavelength division multiplexing (WDM). To have such operation, hybrid integration of devices on planar lightwave circuit (PLC) technique¹ or monolithic integration of devices is possible²⁻⁵. PLC can utilize well made devices and can have good quality, but the system becomes bulky as compared to monolithic integration. Monolithic integration of devices is expected to bring about cost reduction and packaging robustness associated with replacing individual alignment, single-mode optical connections between discrete optoelectronic devices with lithographically produced integrated waveguides. There have been several reports on integration of wavelength demultiplexing detectors. A demultiplexing photodetector fabricated using Ar laser-assisted metal organic molecular beam epitaxy (MOMBE) has been reported³. In the Ar laser-assisted MOMBE growth, there are changes in growth rate and composition in laser focused area thus it has different bandgap energies. Tunable superlattice pin photodetector using the quantum confined Stark effect (QCSE) has been reported⁴. By varying applied voltages to the photodetector that has quantum well structure inside, changes in band-to-band transition energy can be obtained. Selective intermixing of quantum well structure can also be applied to demultiplexing photodetectors. Waveguide type InGaAs/GaAs metal-semiconductor-metal (MSM) demultiplexing photodetector using selective bandgap tuning has been reported⁵.

Among the above techniques, quantum well intermixing can change confined bandgap energy of the quantum well easily and can produce large bandgap shift. This technique can be applied to fabrication of optical waveguides, wavelength shifted laser diode, and monolithic optoelectronic ICs. The intermixing technique renders the fabrication process easier than the epitaxial regrowth technique when different bandgap material is needed on the wafer. Various techniques such as ion implantation, Zn diffusion, pulsed laser irradiation, and impurity free vacancy diffusion using dielectric cap annealing have been developed for GaAs- or InP-based MQW structures. Intermixing of InP-based MQWs is particularly important because of their potential application at high capacity, and in long haul fiber optic communication systems. We have, recently, used a SiO₂ dielectric film on an InGaAs cap layer to promote the intermixing of an InGaAs/InP MQW system. MQWs annealed with a SiO₂ dielectric film on an InGaAs cap layer showed large blue shifts in photoluminescence spectrum and compositional mixing at the MQW region⁶⁻⁷. Applying this methods to an InGaAsP/InP MQW system, the spatial resolution of the IFVD process was found to be less than 3 μ m. In our previous study, group III and V elements of MQW interdiffused at a similar rate after quantum well intermixing and this can reduce the separation between electron-heavy hole and electron-light hole transition energy in the MQW. Ridge-type waveguides were fabricated and showed large propagation loss reduction at the original bandgap after quantum well intermixing. In accordance with our previous results, we report, in

* E-mail: ydh@helios.snu.ac.kr; WWW:<http://helios.snu.ac.kr>; Telephone: 82-2-880-5451(ext.236); Fax: 82-2-887-6575

this paper, the integration of wavelength demultiplexing photodetectors using selective intermixing of InGaAs/InGaAsP MQW structure.

2.EXPERIMENTAL METHODS AND DEVICE FABRICATION

An InGaAs/InGaAsP MQW grown by metal organic chemical vapor deposition (MOCVD) was used for this experiment. The epitaxial layer structure was grown on an n-InP (Sn-doped; $1 \times 10^{18} \text{cm}^{-3}$) substrate and had included a $1 \mu\text{m}$ S-doped n-InP buffer, a $0.15 \mu\text{m}$ u-In_{0.85}Ga_{0.15}As_{0.3}P_{0.7}, a $0.05 \mu\text{m}$ u-In_{0.81}Ga_{0.19}As_{0.43}P_{0.57} confinement layer on both sides of the MQW, a $0.5 \mu\text{m}$ u-InP cladding layer and a $0.1 \mu\text{m}$ u-In_{0.53}Ga_{0.47}As cap layer. The MQW structure consists of five layers of 84 \AA In_{0.53}Ga_{0.47}As and four layers of 100 \AA In_{0.77}Ga_{0.23}As_{0.47}P_{0.53}. The epitaxial layers were intentionally undoped to avoid impurity induced disordering by Zn diffusion during the intermixing process and electrical isolation between devices. For the as-grown epitaxial layer, the PL peak wavelength of the MQW was found to be 1480 nm at 10 K and 1588 nm at room temperature. A 1700 \AA SiO₂ dielectric layer was deposited on the InGaAs cap layer by plasma-enhanced chemical vapor deposition (PECVD) to enhance the intermixing of the MQW. To observe SiO₂ dielectric layer on InGaAs cap layer and annealing effect, bandgap energy shifts as a function of annealing time at a temperature of 750°C was measured as shown in Fig. 1. Samples with and without SiO₂ dielectric layer on InGaAs cap layer were mounted on a rapid thermal annealer (RTA) and heated in N₂ environment. Bandgap shifts as large as 82 meV can be found upon annealing for 60 sec with SiO₂ dielectric layer. However, small shifts due to self-diffusion of MQW at high temperature were found for the samples without SiO₂ dielectric layer. Thus using the deposition and patterning of SiO₂ dielectric layer on InGaAs cap layer, different bandgap energies on one chip can be made.

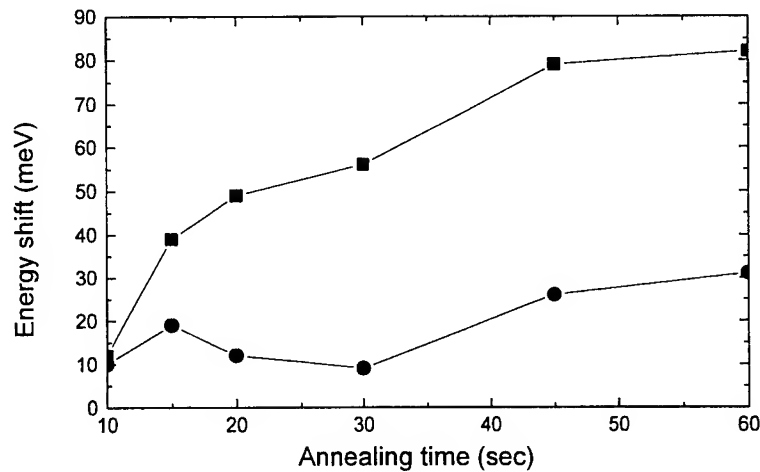


Fig. 1. Bandgap energy shifts of a MQW structure as a function of annealing time at a temperature of 750°C . Squares and circles denote bandgap energy shifts with and without SiO₂ dielectric layer on InGaAs cap layer, respectively.

From the above bandgap shift data, annealing at 750°C for 45 s was adopted for the device fabrication because of the relatively large bandgap difference for the samples with and without SiO₂ dielectric on InGaAs cap layer. SiO₂ dielectric layer was selectively patterned using photolithography and wet chemical etch and the sample was mounted carefully on a rapid thermal annealer (RTA) and heated for 45 s in N₂ environment at 750°C . Figure 2 shows normalized

photoluminescence (PL) spectrums at 10 K for the MQWs, as-grown and annealed with and without SiO₂ dielectric layer. The full-width at half maximum (FWHM) of the PL spectrum remains nearly constant for the intermixed MQW demonstrating that the quality of the epitaxial layer was not significantly degraded after the intermixing process. MQW annealed without SiO₂ dielectric layer show a slight increase in bandgap in comparison with that annealed without SiO₂ dielectric layer. This is due to self-diffusion of well and barrier materials at high annealing temperature. Regions with and without SiO₂ dielectric layer had bandgap shifts of 26 and 79 meV and the bandgap difference between the two regions was 53 meV.

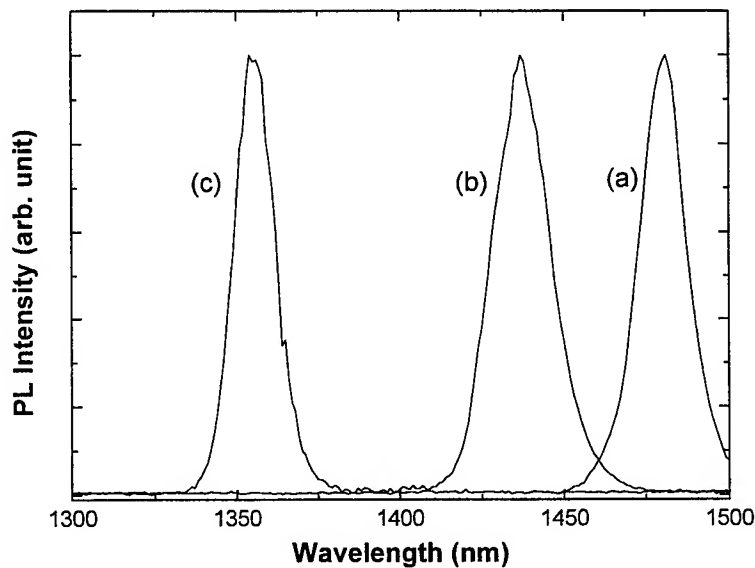


Fig. 2. Normalized PL spectrum of (a) as-grown , (b) annealed without SiO₂ and (c) with SiO₂ dielectric on InGaAs cap layer.

Figure 3 shows the device structure used in this work. Regions for shorter wavelength detection, dummy waveguide and longer wavelength are linearly lined up and coupled light propagates each region through 20 μ m wide rib waveguide. The width of waveguide is 20 μ m and the length of each detector is 250 μ m. 1700 Å SiO₂ dielectric layer was deposited on the wafer by PECVD and patterned using photolithography and wet chemical etch. Regions for shorter wavelength detection and waveguide are annealed with SiO₂ dielectric layer and that for longer wavelength was annealed without it. After annealing, SiO₂ dielectric layer was removed by wet chemical etching. InGaAs cap layer between two detectors was wet chemically removed to reduce propagation loss. P-ohmic layer was formed at the contact region by Zn₃P₂ evaporation and annealing so that two photodetectors can be isolated electrically. Rib waveguide was formed by wet etch and SiO₂ dielectric layer was deposited by PECVD for the passivation layer. Au/AuZn/Cr/Au and AuGe/Ni/Au multi-level systems were used for P- and N-type contact metal.

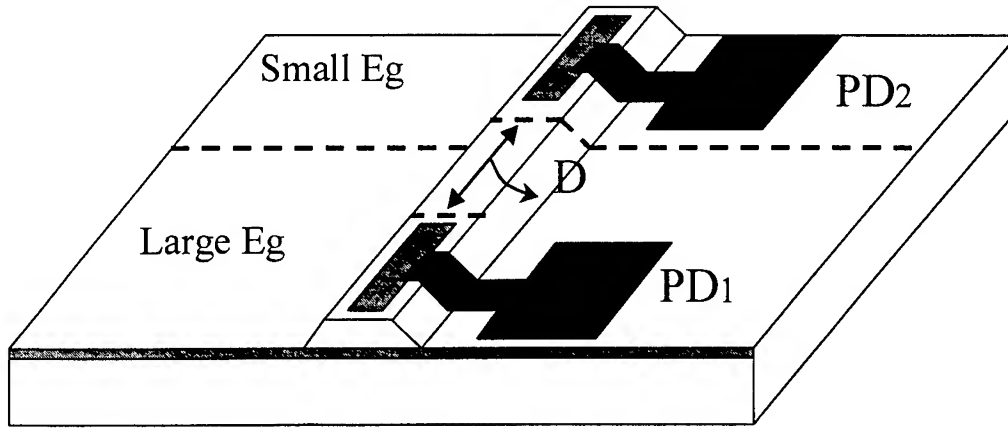


Fig. 3. Schematic diagram of integrated waveguide type photodetectors. Large bandgap area was annealed with SiO₂ dielectric layer on InGaAs cap layer.

3. MEASUREMENTS OF SPECTRAL RESPONSE

The detector response was characterized using tunable laser. We used two tunable lasers to obtain wide spectral range and as a result we could have wavelength range from 1480 to 1625 nm. Light was end-fiber coupled into the photodetector and the input polarization was set to TE or TM mode by polarization controller and the detector was zero biased. Figure 4 shows measured photocurrent spectrum of each detector for the polarization of TE/TM mode, respectively. Photocurrent was slightly reduced near 1480 nm due to instability of tunable laser light source. Photocurrent spectrum of PD₁ with larger bandgap energy shows blue shift with respect to that of PD₂ with smaller bandgap energy as is expected from PL measurements. For the photocurrent of TE mode, weak exciton peaks related to electron-heavy hole transition is seen at 1560 and 1490 nm for PD₁ and PD₂ respectively. Exciton peaks related to electron-light hole can not be seen because calculated transition occurs at a shorter wavelength than 1480 nm.

For a multi-segment waveguide photodetector, the photocurrent generated in segment i of length L_i can be expressed as⁸

$$I_i = \left(\frac{e\lambda}{hc}\right) P_0 \gamma (1-R) \eta \frac{\Gamma \alpha_i^{\text{int}}(\lambda)}{\alpha_i(\lambda)} e^{-\sum_{k=1}^{i-1} \alpha_k(\lambda) L_k} (1 - e^{-\alpha_i(\lambda) L_i}) \quad (1)$$

where $e\lambda/hc$ is the conversion factor from optical power to photocurrent, P_0 is the input optical, γ is the coupling efficiency, R is the reflectance at the waveguide facet, η is the internal quantum efficiency, Γ is the optical confinement factor of the active layer, $\alpha_i^{\text{int}}(\lambda)$ is the interband absorption coefficient in the segment i , and $\alpha_i(\lambda) = \Gamma \alpha_i^{\text{int}}(\lambda) + \alpha_0$ is the total attenuation coefficient in the segment i , where α_0 is the scattering loss coefficient of the waveguide. For the waveguide photodetector, α_0 is a negligible effect. From eq. 1, light coupled to PD₁ propagates through waveguide and its intensity decreases due to absorption and propagation loss in the MQW. Non-absorbed light from PD₁ and absorber region propagates to PD₂.

Figures 5 and 6 shows normalized photocurrent spectrum of integrated wavelength demultiplexing photodetectors for the TE and TM mode, respectively. Generated photocurrent spectrum of PD₁ will be same as figure 4 but that of PD₂ will be deformed. As can be seen in eq. 1, the amount of photons that reaches PD₂ region will be reduced as that absorbed and scattered in previous region. So the photocurrent of PD₂ at short wavelength decreases and that of long wavelength is unchanged. Photocurrent of PD₁ reduced to almost zero wavelength over 1570 nm and peak of photocurrent in spectral response of PD₂ is near 1570 nm.

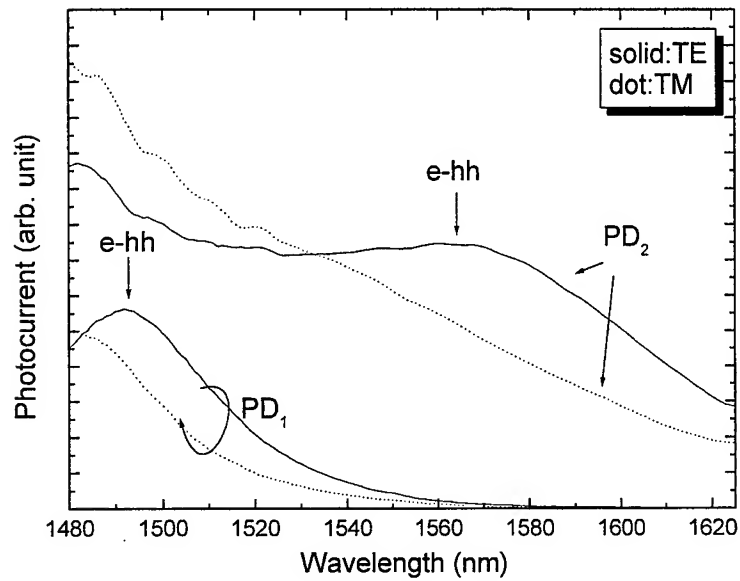


Fig. 4. Photocurrent spectra of fabricated photodetectors. Solid and dot line shows photocurrent spectrum for TE and TM mode, respectively.

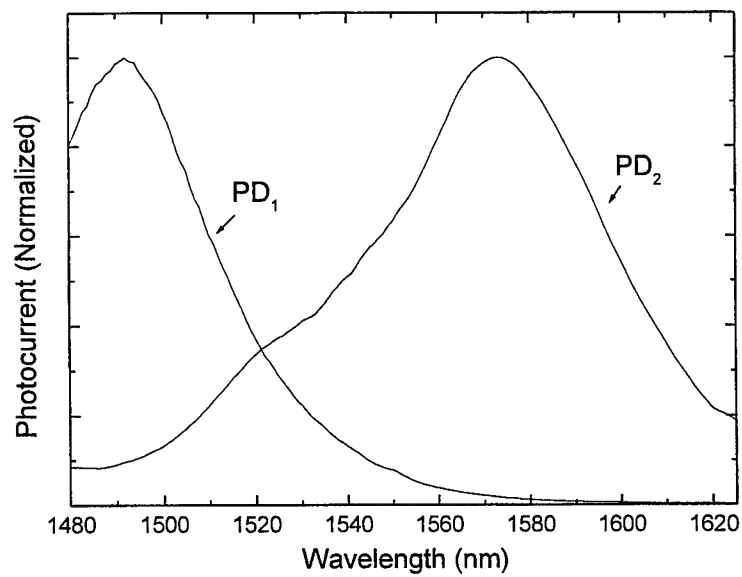


Fig. 5. Photocurrent spectra of integrated waveguide photodetectors for TE mode.

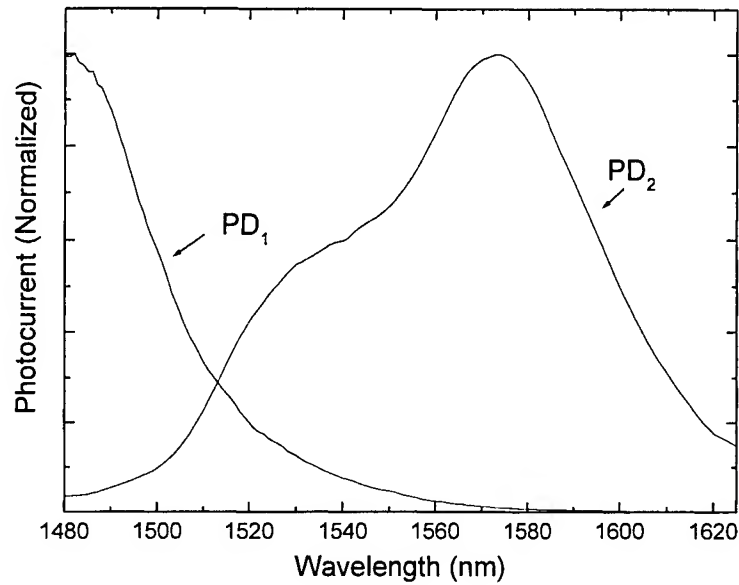


Fig. 6. Photocurrent spectra of integrated waveguide photodetectors for TM mode.

The crosstalk for the TE and TM mode light at short wavelength is due to incomplete absorption at PD₁. This results also from the scattered and unguided light that can reach PD₂ and generate photocurrent. For 100 μm dummy waveguide, photocurrent ratio of PD₁ and PD₂ was 4 to 1 at a wavelength of 1480 nm. Increasing the spacing between two photodetectors will reduce this crosstalk. Figure 7 shows the photocurrent ratio at 1477 nm changes as a function of the spacing between photodetectors. Light from DFB laser diode was coupled to the wavelength demultiplexing photodetectors and the light is attenuated at the waveguide. As can be expected from eq. 1, the photocurrent of the PD₂ will be decreased exponentially and the ratio of PD₁ to PD₂. Solid line in the Fig. 7 Shows fitted line as an exponent function. For the waveguide 900 μm long, the ratio was about 200. The photocurrent ratio at 1550 nm was about 200 (~23 dB) irrespective of waveguide length. This is because light at this wavelength has small propagation loss through waveguide and a small fraction of the light was absorbed at PD₁. Thus it can be said that the fabricated device can demultiplex both 1480 and 1550 nm wavelength.

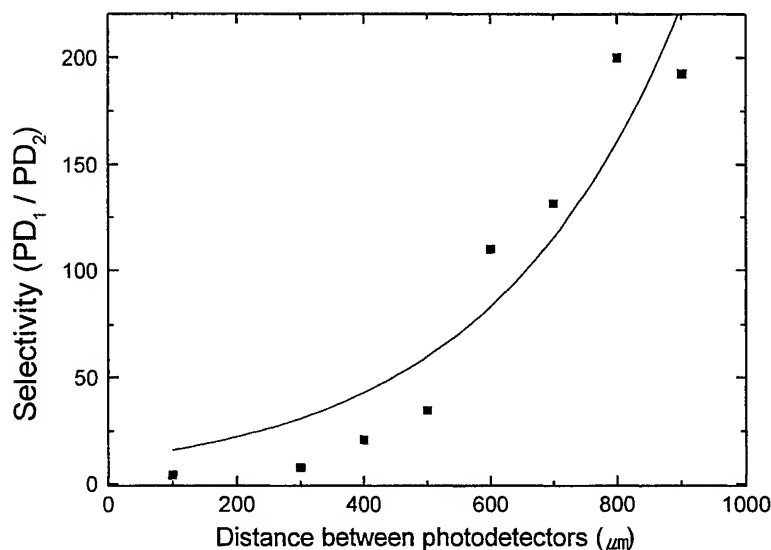


Fig. 7. Current ratio of PD₁ and PD₂ when the wavelength of coupled light was 1477 nm. Solid line shows exponential fitting curve.

4. CONCLUSION

A simple and effective fabrication method for producing two wavelengths demultiplexing p-i-n waveguide type photodetector was demonstrated. Selective area intermixing of InGaAs/InGaAsP MQW structure by SiO₂ dielectric cap annealing was used in the fabrication process. Large bandgap difference was seen in the wafer with and without by SiO₂ dielectric cap annealing. Spectral response of integrated photodetectors was measured for the wavelength range of 1480 to 1625 nm. Photodetectors of large bandgap shows blue shift in photocurrent spectrum for the TE and TM mode with respect to that of small bandgap. It was shown that integrated photodetectors could demultiplex 1480 and 1550 nm wavelength. Photocurrent ratio was greatly enhanced by increasing the length of dummy waveguide between two photodetectors. For sufficiently long dummy waveguide, photocurrent ratio of 200 was seen at a wavelength of 1480 and 1550 nm. This area selective quantum well intermixing can be further applied to implementation of monolithic integration of optical devices on a chip.

5. REFERENCES

1. N. Uchida et al., "Low-cost high-performance hybrid WDM module integrated on a PLC platform for fiber-to-the-home", 22nd European Conference on Optical Communication, pp. 107-114, 1996
2. H. Nakajima, A. Leroy, and J. Charil, "Full-Duplex Performance Assessment of In-Line Transceivers Emitting at 1.3 μm and Receiving at 1.55 μm ", IEEE Photon. Technol. Lett., Vol. 8, pp. 1561-1563, 1996
3. Yasuhiro Suzuki, Ryuzo Iga, Takeshi Yamada, Hideo Sugiura, and Mitsuru Naganuma, "Crosstalk Characteristics of a 1.3- μm /1.5- μm Wavelength Demultiplexing Photodetectors Using Laser-Assisted MOMBE Growth", Journal of Lightwave Technol., Vol. 17, pp. 483-489, 1999
4. D. Moss, F. Ye, D. Landheer, P. E. Jessop, J. G. Simmons, H. G. Champion, I. Templeton, and F. Chatenoud, "Ridge Waveguide Quantum-Well Wavelength Division Demultiplexing Detector with Four Channels", IEEE Photon. Technol. Lett., Vol. 4, pp. 756-759, 1992
5. A. N. M. Masum Choudhury, P. Melman, A. Siletti, Emil. S. Koteles, B. Foley, and B. Elman, "Metal-Semiconductor-Metal Demultiplexing Waveguide Photodetectors in InGaAs/GaAs Quantum Well Structures by Selective Bandgap Tuning", IEEE Photon. Technol. Lett., Vol. 3, pp. 817-820, 1991
6. Sang Ki Si, Deok Ho Yeo, Kyung Hun Yoon and Sung June Kim, "Area Selectivity of InGaAs-InP Multiquantum Well Intermixing by Impurity-Free Vacancy Diffusion" IEEE J. Sel. Top. Quantum Electron. Vol. 4, pp. 619-623, 1998
7. Deok Ho Yeo, Kyung Hun Yoon and Sung June Kim, "Characteristics of intermixed InGaAs/InGaAsP Multi-Quantum Well structure", Jpn J. Appl. Phys. Vol. 39, pp. 1032-1034, 2000
8. Xiucheng Wu, Paul E. Jessop, Doug M. Bruce, Brad J. Robinson, and David A. Thompson, "Inline Quantum-Well Waveguide Photodetectors for the Measurement of Wavelength Shifts", J. Lightwave Technol., Vol. 15, pp. 2278-2283, 1997

Concentration Effect of Spectroscopic Properties of Yb³⁺-doped Borate Glasses^{*}

Chun Jiang^a Qingji Zeng^a Fuxi Gan^b

^aCenter for Broadband Optical Networking Technology, College of Electronics & Information,
Shanghai Jiaotong University, Shanghai 200030, P.R.China

^bShanghai Institute of Optics and Fine Mechanics, the Chinese Academy of Sciences, Shanghai 201800,
P.R.China

ABSTRACT

The concentration effect of the spectroscopic properties of Yb³⁺-doped borate glasses have been determined from absorption and emission measurements at room temperature. The systematic variations of the spectroscopic properties and laser performance parameters with activator concentration can be used to optimize the doping concentration.

Key words Yb³⁺, borate glasses, spectroscopic property, concentration effect.

1. INTRODUCTION

The emission cross-section and fluorescence lifetime are fundamental spectroscopic properties of laser glasses. These properties can be calculated using intensity parameters Ω_t ($t=2,4,6$) based on the Judd-Ofelt theory^[1,2]. The optical and spectroscopic properties of rare-earth ion-doped glasses have been discussed in the terms of the variation of Ω_t parameters with composition^[3~5]. Since there is only the $^2F_{7/2}$ - $^2F_{5/2}$ transition for Yb³⁺, it is impossible to directly calculate three Ω_t parameters for Yb³⁺, and thus the compositional dependence of optical and spectroscopic properties of Yb³⁺-doped glasses are not well established. Up to now, there is only a few papers involving with the effect of composition on the stimulated emission cross section of Yb³⁺ in simple system such as borate, phosphate and silicate glasses^[6~9]. It is shown that integrated absorption cross section is mainly determined by the site asymmetry of Yb³⁺ ion and covalency of Yb-O bond or polarizability of O²⁻ ion. Meanwhile, the addition of La₂O₃ to borate or Nb₂O₅ to phosphate glass can enhance the asymmetry and polarizability, thus the emission cross section increase. In these glasses the largest emission cross section is less than 1.35 pm². Recently, we reported the borate glass composition 50B₂O₃-40ZnO-10La₂O₃ with emission cross

^{*} Correspondence: Email:cjiang@online.sh.cn; Fax:0086-021-62820892.

section of more than 1.70pm^2 [10]. In this paper, spectroscopic properties of the borate glasses doped by different concentration of Yb_2O_3 are measured and calculated, and compared to optimize the doping concentration.

2. EXPERIMENT

2.1 Sample preparation

B_2O_3 was introduced in the form of reagents H_3BO_3 , other materials are 99.99% purity oxides or carbonates. The glass melts were poured into stainless steel plate. Each glass was annealed for 2 hour near the transition temperature.

2.2 Measurements of refractive index and spectroscopic properties

Glass samples 2~3 mm thick with two polished faces were used for refractive index, absorption, emission and fluorescence lifetime measurements. The absorption spectra were measured by HITACHI330 spectrophotometer in the range 800~1100 nm at room temperature. The emission spectra were obtained by exciting the samples with LD970 nm as pumping laser (excited at 970 nm). The light from the light source was chopped at 80 Hz and focused to the front surface of sample. The position of 1 mm from the edge was excited to minimize the re-absorption of emission. The emission from the sample was focused to a monochromator and detected by a Ge detector in the range 800~1100 nm. The fluorescence lifetimes were measured by exciting the samples with the same LD970 nm and detected by a photomultiplier tube and the Ge detector. The fluorescence decay curves were recorded and averaged with a computer controlled transient digitizer.

2.3 Sample evaluation

2.3.1 Spectroscopic properties

The integrated absorption cross section (Σ_{abs}), the spontaneous emission probability (A_R), the emission cross section (σ_{em}) and effective fluorescence linewidth ($\Delta\lambda_{\text{eff}}$) of Yb^{3+} were calculated by fackbauer-landenburger equations [11,12].

$$\sigma_{\text{em } p} = \frac{\lambda_{\text{em}}^4 A_R}{8\pi c n^2 \Delta\lambda_{\text{eff}}} \quad (1)$$

Where

$$\Delta\lambda_{\text{eff}} = \frac{\int I(\lambda) d\lambda}{I_{\text{max}}} \quad (2)$$

$$A_R = 8\pi n^2 c \lambda_p^4 \frac{g_j}{g_i} \int \sigma_{\text{abs}}(\lambda) d\lambda \quad (3)$$

$$\sigma_{abs}(\lambda_p) = \frac{2.303 \log \frac{I_0}{I}}{NL} \quad (4)$$

where $\Delta \lambda_{eff}$ is fluorescence effective linewidth, A_R spontaneous transition probability, $I_{(\lambda)}$, I_{max} is fluorescence intensity at wavelength λ and peak intensity; g_i, g_j is degeneracy at upper level and terminal level, λ_p is absorption peak wavelength; $\sigma_{abs}(\lambda)$ is absorption cross section at wavelength λ ; $\log(I_0/I)$, N, L , n and c is absorption intensity, Yb^{3+} doping concentration, sample thickness, refractive intensity and light velocity, $\sigma_{emp}, \sigma_{ems}$ is peak emission cross section and secondary peak emission cross section. The ${}^2F_{7/2}$ - ${}^2F_{5/2}$ transition of Yb^{3+} includes not only the electronic dipole transition but also the magnetic dipole transition. Since the magnetic dipole transition contributes are less than 10% of the oscillator strength in the ${}^2F_{5/2}$ - ${}^2F_{7/2}$ transition, the contribution of the magnetic dipole transition was disregarded..

2.3.2 Laser performance parameters

(1) Minimum fraction of excited state ion which is defined as the minimum fraction of Yb^{3+} ions that must be excited to balance the gain exactly with the ground state absorption at laser wavelength.

$$\beta = \frac{\sigma_{abs}(\lambda_{em})}{\sigma_{em}(\lambda_{em}) + \sigma_{abs}(\lambda_{em})} = \left\{ 1 + \frac{Z_l}{Z_u} \exp\left[\frac{(E_{zl} - hc\lambda_{em}^{-1})}{kT}\right] \right\}^{-1} \quad (5)$$

(2) Saturation Pump intensity is the easy with which the ground state depletion may be accomplished depends on the absorption cross section and fluorescence lifetime.

$$I_{sat} = \frac{hc}{[\lambda_p \sigma_{abs}(\lambda_p) \tau_m]} \quad (6)$$

(3) Minimum pump intensity which is the figure of merits of Yb^{3+} laser material and is defined as a measure of the ease of pumping the laser material and is given by the following equation

$$I_{min} = \beta \cdot I_{sat} \quad (7)$$

$$I_{min} = \frac{hc}{[\lambda_p \sigma_{abs}(\lambda_p) \tau_m]} \left\{ 1 + \frac{Z_l}{Z_u} \exp\left[\frac{(E_{zl} - hc\lambda_{em}^{-1})}{kT}\right] \right\}^{-1} \quad (8)$$

Obviously, β , I_{sat} and I_{min} rely on absorption and emission properties of Yb^{3+} laser materials, for laser performance, smaller β , I_{sat} and I_{min} give better materials.

In addition to β , I_{sat} and I_{min} , stored energy parameter which is defined as the product ($\alpha \tau_m$) of absorption coefficient and fluorescence lifetime is used to characterize the measure of stored energy of the material. And gain parameter which is defined as the product of absorption coefficient and emission cross section and fluorescence lifetime is used to characterize the measure of amplification ability of the material as gain medium.

3. RESULTS

3.1 Effect of Yb^{3+} ion concentration on the spectroscopic properties of Yb^{3+} glasses

The relative fluorescence intensity (I) and fluorescence lifetime (τ_m) of $50\text{B}_2\text{O}_3\text{-}10\text{La}_2\text{O}_3\text{-}40\text{ZnO}$ glass with different concentration of Yb^{3+} ion are shown in Table 1. It is obvious that there is quenching effect of Yb^{3+} ion in this glass. The largest fluorescence intensity occurs at about 7.5×10^{20} ion/cm³, while the lifetime shortens gradually. Quenching mechanism of Yb^{3+} ion in this glass will be discussed in another paper.

Table 1 Concentration effect of spectroscopic properties of Yb^{3+} ion in $50\text{B}_2\text{O}_3\text{-}10\text{La}_2\text{O}_3\text{-}40\text{ZnO}$

Concentration (10^{20} ion/cm ³)	λ_p (nm)	σ_p (pm ²)	λ_{em} (nm)	σ_{em} (pm ²)	α (cm ⁻¹)	I (arb.unit)	τ_m (ms)
1.5	973.2	1.50	1016.0	1.73	2.25	60	1.15
4.5	973.2	1.49	1016.0	1.71	6.71	70	1.10
7.5	973.2	1.47	1016.5	1.70	11.03	100	0.76
10.5	973.2	1.45	1018.0	1.68	15.23	80	0.60
13.5	973.2	1.44	1020.0	1.65	19.44	60	0.39
16.5	973.2	1.41	1021.0	1.63	23.27	50	0.20

3.2 Effect of Yb^{3+} ion concentration on the laser performance parameters of Yb^{3+} glasses

The minimum pump intensity and saturation pump intensity and minimum fraction of excited ion in $50\text{B}_2\text{O}_3\text{-}10\text{La}_2\text{O}_3\text{-}40\text{ZnO}$ glass with different concentration of Yb^{3+} ion are shown in Table 2.

Table 2 Concentration effect of laser performance parameters of Yb^{3+} ion in $50\text{B}_2\text{O}_3\text{-}10\text{La}_2\text{O}_3\text{-}40\text{ZnO}$

Concentration (10^{20} ion/cm ³)	$\alpha \tau_m$ (cm ⁻¹ .ms)	$\alpha \sigma_{em} \tau_m$ (10^{-20} cm .ms)	β (100%)	I_{sat} (kw/cm ²)	I_{min} (kw/cm ²)
1.5	2.59	4.48	0.0413	34.85	1.44
4.5	7.38	12.62	0.0417	12.23	0.51
7.5	8.38	14.25	0.0418	10.77	0.45
10.5	9.14	15.35	0.0426	9.87	0.42
13.5	7.58	12.51	0.0428	11.91	0.51
16.5	4.66	7.59	0.0438	19.37	0.85

4. DISCUSSION

Figure 1 shows that the variation of stored energy parameters and saturation pump intensity as Yb^{3+} ion concentration. It is shown that with variation of doping concentration from 1.5×10^{20} ion/cm³ to 16.5×10^{20} ion/cm³, the stored energy parameters first increase and reaches maximum (9.14 cm⁻¹.ms) near concentration of 10.5×10^{20} ion/cm³, then decreases. The saturation pump intensity first decrease and reaches minimum (9.87 cm⁻¹.ms) near concentration of 10.5×10^{20} ion/cm³, then increases.

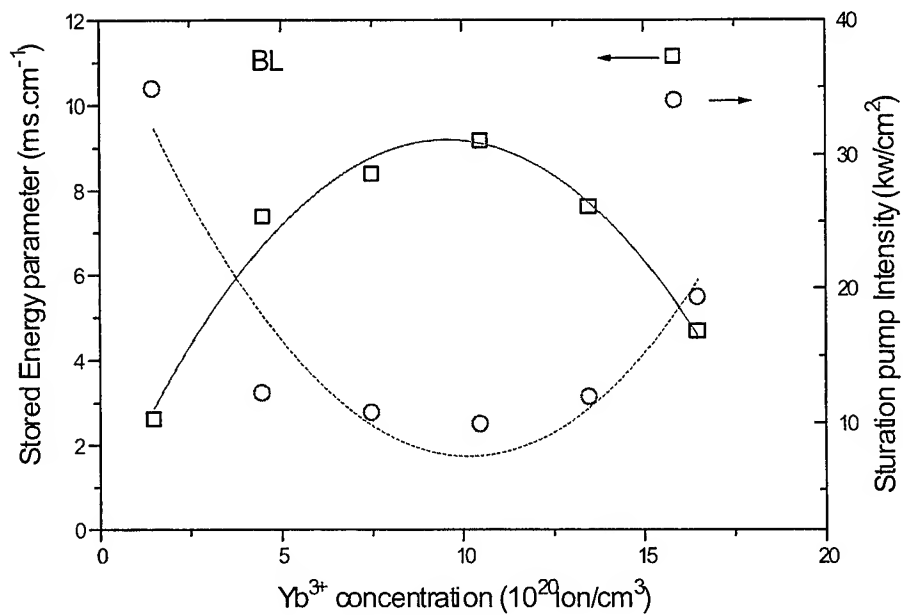


Figure 1 Variation of stored energy parameters and saturation pump intensity as Yb³⁺ ion concentration.

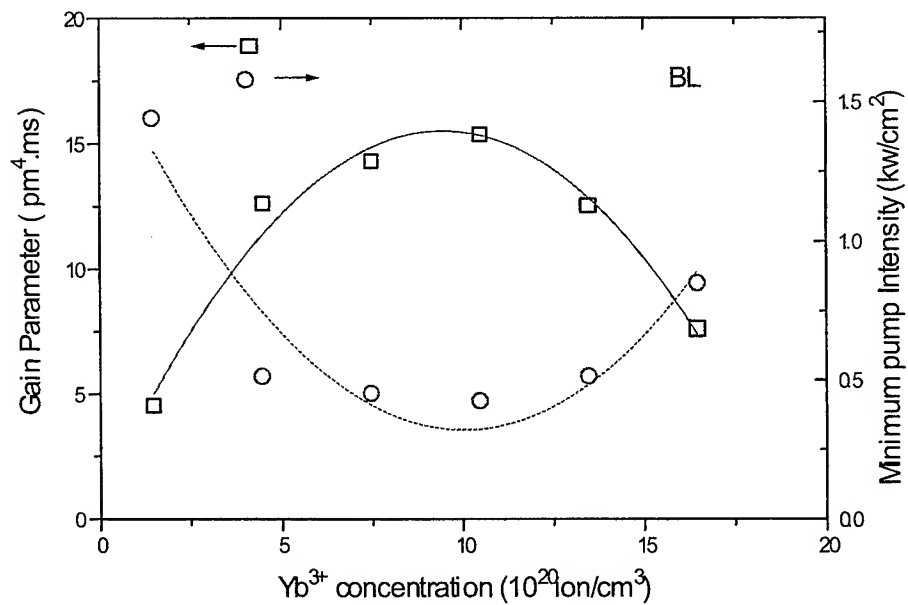


Figure 2 Variation of gain parameters and minimum pump intensity as Yb³⁺ ion concentration.

Figure 2 shows that the variation of gain parameters and minimum pump intensity as Yb^{3+} ion concentration. It is shown that with variation of doping concentration from $1.5 \times 10^{20} \text{ ion/cm}^3$ to $16.5 \times 10^{20} \text{ ion/cm}^3$, the gain parameters first increase and reaches maximum ($15.35 \times 10^{-20} \text{ cm} \cdot \text{ms}$) near concentration of $10.5 \times 10^{20} \text{ ion/cm}^3$, then decreases. The minimum pump intensity first decrease and reaches minimum (0.42 kw/cm^2) near concentration of $10.5 \times 10^{20} \text{ ion/cm}^3$, then increase. It is shown from table 2 that the minimum fraction of excited ion increase as doping concentration.

As results and discussion mentioned above, for borate glass, when Yb^{3+} ion concentration is $10.5 \times 10^{20} \text{ ion/cm}^3$, the stored energy and gain parameters reaches maximum value, and saturation pump intensity and minimum pump intensity reaches minimum value, therefore, the optimal concentration of Yb^{3+} ion is $10.5 \times 10^{20} \text{ ion/cm}^3$.

5. CONCLUSION

The concentration effect of the spectroscopic properties of Yb^{3+} -doped borate glasses have been determined from absorption and emission measurements at room temperature. The systematic variations of the spectroscopic properties and laser performance parameters with activator concentration can be used to optimize the doping concentration. It is shown that for borate glass, when Yb^{3+} ion concentration is $10.5 \times 10^{20} \text{ ion/cm}^3$, the stored energy and gain parameters reaches maximum value, and saturation pump intensity and minimum pump intensity reaches minimum value, therefore, the optimal concentration of Yb^{3+} ion is $10.5 \times 10^{20} \text{ ion/cm}^3$.

ACKNOWLEDGMENTS

This work is funded by National Natural Science Foundation of China under project of 56978026.

REFERENCES

- 1 B. R. Judd. Optical Absorption Intensities of Rare-earth ions. *Phys. Rev.*, 1962, 127(3):756~761
- 2 G. S. Ofelt. Intensities of Crystal Spectra of Rare-Earth ions. *J. Chem. Phys.*, 1962, 37(3):511~520
- 3 Y. Nageno, H. Takebe, K. Morinaga et al.. Effect of modifier on fluorescence and absorption of Eu^{3+} in Alkali and Alkaline earth silicate glasses. *J. Non-Crystalline Solids*, 1994, 169(3):288~294
- 4 H. Takebe, Y. Nageno, K. Morinaga. Effect of network modifier on spontaneous emission probabilities of Er^{3+} in oxide glasses. *J. Am. Ceram. Soc.*, 1994, 77(8):2132~2136
- 5 H. Takebe, K. Morinaga, T. Izumitani. Correlation between radiative transition probabilities of rare-earth ions and composition in oxide glasses. *J. Non-Crystalline Solids*, 1994, 178(3):58~63
- 6 Xuelu Zou, Hisayoshi Toratani. Evaluation of spectroscopic properties of Yb^{3+} -doped glasses. *Phys. Rev. B*, 1995, 52(22):15889~15897
- 7 H. Takebe, T. Murata, K. Morinaga. Compositional dependence of Absorption and fluorescence of Yb^{3+} in oxide glasses. *J. Am. Ceram. Soc.*, 1996, 79(3):681~687
- 8 M. J. Weber, J. E. Lynch, D. H. Blackburn et al.. Dependence of the stimulated emission cross section of Yb^{3+} on host glass composition. *IEEE J. Quantum Electron.*, 1983, QE-19(10):1600~1608
- 9 B. Peng, Teturo IZUMITANI. Next Generation Laser for Nuclear Fusion. *The Review of Laser Engineering*, 1993, 21(12):1234~1244

- 10 W. F. Kruppe. Dependence of the Induced-Emission Cross Section in neodymium laser glasses. IEEE J. Quantum Electron., 1974, QE-10(4):450~457
- 11 M. J. Weber. Radiative and Multiphonon Relaxation of Rare-Earth Ions in Y_2O_3 . Phys. Rev., 1967, 171:283~291

SESSION 11

Poster Session

Theoretical study on coupling effects of modulation depth between two photorefractive phase gratings with an external applied field

Baohong Yuan*, Zhongxiang Zhou, Chunfeng Hou, Xiudong Sun
Department of Applied Physics, Harbin Institute of Technology, Harbin 150001,
People's Republic of China

ABSTRACT

In this paper, we have applied a perturbative expanding method to the hopping model, and studied the coupling effects of modulation depth between two pieces of photorefractive phase gratings stored in one point with an external applied dc field. The coupling equations of modulation depth and their steady solution have been derived. It has been found that the spatial charge-field of one of the two gratings is seriously affected by the modulation depth of the other grating.

Key words: photorefraction, hopping model, modulation depth

1. INTRODUCTION

With big capacity and high readout speed, multiple holographic storage is a good kind of data storage method. By angle-multiplexing, wave length-multiplexing, phase code, space-multiplexing, we can store a large number of datum at a point of storage medium¹⁻³. But the storage capacity and quality are greatly limited by the cross-talk among different images. People have done much work about the cross-talk of multiple holographic storage⁴⁻⁶. But these studies are based on the Bragg diffraction theory and consider that the different gratings are independent each another, so the resultant scattered intensity from the off-Bragg gratings constitutes the cross-talk noise. In fact, different phase gratings stored at one point in the photorefractive material by angle-multiplying are not independent. The coupling of different order harmonics of space-charge field (SCF) in single grating⁷⁻⁸ and the coupling among different gratings must exist because of the non-linear response of photorefractive materials. Zhou *et al.*⁷⁻⁸ applied a perturbative expansion to the hopping model of Feinberg⁹ for single grating. They find that in single grating the fundamental harmonic(FH) is coupled with the second-order harmonic(SH) and the SH is coupled with the FH and the third-order harmonic. The third-order harmonic is coupled with the SH. We apply a perturbative expansion to the hopping model of Feinberg⁹ for the two gratings and discuss coupling effects of modulation depths between the two gratings, that is $m \neq m'$ with an external applied dc field.

2. THEORY

The charge hopping equation is firstly given by Feinberg⁹

$$\frac{dW_n^0}{dt} = -\sum_m D_{mn} [W_n^0 I_n^0 \exp(\beta \Phi_{n,m}^0) - W_m^0 I_m^0 \exp(\beta \Phi_{m,n}^0)] \quad (1)$$

where W_n^0 is the probability that a migrant charge occupies the n th site that is at position z_n . I_n^0 is optical intensity at this site. The sum is over neighbouring sites m and $D_{mn} \exp(\beta \Phi_{mn}^0)$ is the tendency toward light-induced hopping from site m to site n . Here $\beta = q/2k_B T$, where q is the charge, k_B is Boltzmann's constant, and T is the lattice temperature.

*Correspondence: Email: optics@hope.hit.edu.cn; Telephone: 0451 641 4129; Fax: 0451 622 1408

$\Phi_{nm}^0 = \Phi_n^0 - \Phi_m^0$ where $\Phi_n^0 = \Phi^0(z_n)$ and $\Phi^0(z_n)$ is the quasi-static potential existing in the crystal because of internal charge migration, externally applied fields and intrinsic chemical potentials. For photovoltaic material such as LiNbO_3 , the photovoltaic potential is also included in the quasi-static potential $\Phi^0(z_n)$. Further, it is assumed that any uniform electric field and k are parallel (or antiparallel) to the optical c axis in a uniaxial crystal and we take $kl \ll 1$, where l is the distance of neighbouring sites, and in this case the hopping rate D_{mn} is zero except between nearest-neighbour sites, when it has the value D . So the hopping equation (1) includes four terms as follows:

$$\begin{aligned} \frac{dW_n^0}{dt} = & -DW_n^0 I_n^0 \exp(\beta\Phi_{n,n-1}^0) - DW_n^0 I_n^0 \exp(\beta\Phi_{n,n+1}^0) \\ & + DW_{n-1}^0 I_{n-1}^0 \exp(\beta\Phi_{n-1,n}^0) + DW_{n+1}^0 I_{n+1}^0 \exp(\beta\Phi_{n+1,n}^0) \end{aligned} \quad (2)$$

For simplicity it is generally assumed that the incident intensity takes form of a simple one dimensional sinusoid generated by the interference of two plan waves:

$$I_n(z_n) = I_0 \left[1 + \frac{m}{2} \exp(ikz_n) + \frac{m}{2} \exp(-ikz_n) \right] \quad (3a)$$

$$I'_n(z_n) = I'_0 \left[1 + \frac{m'}{2} \exp(ik'z_n) + \frac{m'}{2} \exp(-ik'z_n) \right] \quad (3b)$$

where $I_n(z_n), I'_n(z_n)$ are two different pieces of intensity distribution pattern. They are stored in one space point of photorefractive material by using angle-multiplexing. So the total intensity distribution at position z_n is

$$I_n^0(z_n) = I_n(z_n) + I'_n(z_n) \quad (3c)$$

In equations 3(a)–3(b) I_0, I'_0 is respectively the total incident intensity of the two pieces of intensity distribution pattern, and m, m' is their modulation. k, k' is their spatial vector. We take into account only the fundamental and second-order harmonics. So it is appropriate to try approximate solutions for W_n and Φ_n of the following forms:

$$W_n(z_n) = W_0 + \text{Re}[W_1 \exp(ikz_n)] + \text{Re}[W_2 \exp(i2kz_n)] \quad (4a)$$

$$W'_n(z_n) = W'_0 + \text{Re}[W'_1 \exp(ik'z_n)] + \text{Re}[W'_2 \exp(i2k'z_n)] \quad (4b)$$

$$\Phi_n(z_n) = \Phi_{n0} + \text{Re}[\Phi_1 \exp(ikz_n)] + \text{Re}[\Phi_2 \exp(i2kz_n)] \quad (5a)$$

$$\Phi'_n(z_n) = \Phi'_{n0} + \text{Re}[\Phi'_1 \exp(ik'z_n)] + \text{Re}[\Phi'_2 \exp(i2k'z_n)] \quad (5b)$$

So the total charge occupying probability $W_n^0(z_n)$ and total quasi-static potential $\Phi_n^0(z_n)$ at position z_n is respectively

$$W_n^0(z_n) = W_n(z_n) + W'_n(z_n) \quad (4c)$$

$$\Phi_n^0(z_n) = \Phi_n(z_n) + \Phi'_n(z_n) \quad (5c)$$

The higher-order harmonics of the potential Φ_r and the charge distribution amplitude W_r must be related by $\Phi_r = W_r N q / r^2 \varepsilon k^2$ $r = 1, 2$ [13]. If we consider, $I_0 = I'_0$, $k = k'$, $W_0 = W'_0$, $\Phi_{n0} - \Phi_{(n\pm 1)0} = \Phi'_{n0} - \Phi'_{(n\pm 1)0}$, $m \neq m'$ and use the foregoing approximations and ignore the square terms, with substitution of Eqs.(3)(4)(5) into Eqs.(2), we obtain Eqs.(6) by equating coefficients of $\exp(irkZ_n)$ ($r = 1, 2$):

$$\frac{d\omega_1}{dt} = -\Gamma \left[(\omega_1 + m + (\frac{m}{4} + \frac{m'}{8})\omega_2 + (\frac{1}{8})m\omega'_2)(a^2 + i2af) + 2\omega_1 + (\frac{m}{4} + \frac{m'}{8})\omega_2 + (\frac{1}{8})m\omega'_2 \right] \quad (6a)$$

$$\frac{d\omega_2}{dt} = -\Gamma \left[(\frac{m}{2} + \frac{m'}{4})\omega_1 + 2\omega_2 + (\frac{1}{4})m\omega'_1 \right] (2a^2 + i2af) + (m + \frac{m'}{2})\omega_1 + 2\omega_2 + (\frac{1}{2})m\omega'_1 \quad (6b)$$

$$\frac{d\omega'_1}{dt} = -\Gamma \left[(\omega'_1 + m' + (\frac{m'}{4} + \frac{m}{8})\omega'_2 + (\frac{1}{8})m'\omega_2)(a^2 + i2af) + 2\omega'_1 + (\frac{m'}{4} + \frac{m}{8})\omega'_2 + (\frac{1}{8})m'\omega_2 \right] \quad (6c)$$

$$\frac{d\omega'_2}{dt} = -\Gamma \left[(\frac{m'}{2} + \frac{m}{4})\omega'_1 + 2\omega'_2 + (\frac{1}{4})m'\omega_1 \right] (2a^2 + i2af) + (m' + \frac{m}{2})\omega'_1 + 2\omega'_2 + (\frac{1}{2})m'\omega_1 \quad (6d)$$

Here $\Gamma = DI_0 k_0^2 l^2$ is a characteristic hopping rate; $\omega_r = \frac{W_r}{2W_0}$, $\omega'_r = \frac{W'_r}{2W_0}$ ($r = 1, 2$) is the charge wave amplitude

normalised by $2W_0$; $a = k/k_0$ is the grating wave vector normalised by k_0 ; $k_0 = \sqrt{2NW_0 q^2 / \varepsilon k_B T}$ is the characteristic

wave vector. $f = -\frac{\Phi_{n0} - \Phi_{(n-1)0}}{lf_0} = -\frac{\Phi_{(n+1)0} - \Phi_{n0}}{lf_0}$ is the uniform electric field normalised by a characteristic field

$$f_0 = (k_0 k_B T) / q.$$

Equations 6(a)–6(d) are the coupling differential equations of modulation depth relative to the two photorefractive phase gratings. By solving the Eq. 6(a)–6(d), we can get the coupling characteristics of modulation depths of the two photorefractive phase gratings. At the same time, it is indicated from Eq. 6(a)–6(d) that the coupling effect between the two pieces of photorefractive phase gratings is symmetric. In the following we will only discuss the effect of the second piece of grating on the first piece of grating.

We now only consider the steady solution, that is $\frac{d\omega_r}{dt} = \frac{d\omega'_r}{dt} = 0$ ($r = 1, 2$), and the photovoltaic field can be neglected.

So the solution for the differential equations 6(a)–6(d) are obtained:

$$\omega_1 = -\frac{U_1 m - V_1 (1 + \beta)^2 m^3}{U_0 - V_0 (1 + \beta)^2 m^2 + Q_0 f(\beta) m^4} \quad (7a)$$

$$\omega_2 = \frac{U_2 (1 + \beta) m^2 - V_2 (1 + \beta)^3 m^4}{U_0 - V_0 (1 + \beta)^2 m^2 + Q_0 f(\beta) m^4} \quad (7b)$$

where

$$U_0 = 4(a^2 + i2af + 2)^2 (2a^2 + i2af + 1)^2$$

$$\begin{aligned}
U_0 &= 4(a^2 + i2af + 2)^2(2a^2 + i2af + 1)^2 \\
V_0 &= \frac{5}{8}(a^2 + i2af + 1)(a^2 + iaf + 1)(a^2 + i2af + 2)(2a^2 + i2af + 1) \\
Q_0 &= \frac{1}{64}(a^2 + i2af + 1)^2(a^2 + iaf + 1)^2 \\
f(\beta) &= 1 + 4\beta + 6\beta^2 + 4\beta^3 + \beta^4, \quad \beta = m'/m \\
U_1 &= 4(a^2 + i2af)(2a^2 + i2af + 1)^2(a^2 + i2af + 2) \\
V_1 &= \frac{1}{8}(a^2 + i2af)(a^2 + i2af + 1)(a^2 + iaf + 1)(2a^2 + i2af + 1) \\
U_2 &= 2(a^2 + i2af)(a^2 + iaf + 1)(a^2 + i2af + 2)(2a^2 + i2af + 1) \\
V_2 &= \frac{1}{16}(a^2 + i2af)(a^2 + iaf + 1)^2(a^2 + i2af + 1)
\end{aligned}$$

According to poisson's equation, the higher-order harmonics of the space-charge field E_r and W_r must be related⁹

$$E_r = \frac{qN}{ir\epsilon k} W_r \quad (r = 1, 2)$$

The expressions for the first two order harmonics of the space-charge field of one of the two gratings are given as

$$e_1^{sat} = i \frac{\alpha_1 m - \beta_1 (1 + \beta)^2 m^3}{\alpha_0 - \beta_0 (1 + \beta)^2 m^2 + \gamma_0 f(\beta) m^4} \quad (8a)$$

$$e_2^{sat} = -i \frac{\alpha_2 (1 + \beta) m^2 - \beta_2 (1 + \beta)^3 m^4}{\alpha_0 - \beta_0 (1 + \beta)^2 m^2 + \gamma_0 f(\beta) m^4} \quad (8b)$$

where

$$\begin{aligned}
\alpha_0 &= 4(e_D + i2e_0 + 2)^2(2e_D + i2e_0 + 1)^2 \\
\beta_0 &= \frac{5}{8}(e_D + i2e_0 + 1)(e_D + ie_0 + 1)(e_D + i2e_0 + 2)(2e_D + i2e_0 + 1) \\
\gamma_0 &= \frac{1}{64}(e_D + i2e_0 + 1)^2(e_D + ie_0 + 1)^2 \\
f(\beta) &= 1 + 4\beta + 6\beta^2 + 4\beta^3 + \beta^4, \quad \beta = m'/m \\
\alpha_1 &= 4(e_D + i2e_0)(2e_D + i2e_0 + 1)^2(e_D + i2e_0 + 2) \\
\beta_1 &= \frac{1}{8}(e_D + i2e_0)(e_D + i2e_0 + 1)(e_D + ie_0 + 1)(2e_D + i2e_0 + 1) \\
\alpha_2 &= 2(e_D + i2e_0)(e_D + ie_0 + 1)(e_D + i2e_0 + 2)(2e_D + i2e_0 + 1) \\
\beta_2 &= \frac{1}{16}(e_D + i2e_0)(e_D + ie_0 + 1)^2(e_D + i2e_0 + 1)
\end{aligned}$$

where $e_r^{sat} = \frac{E_r}{E_q}$, $e_D = \frac{E_D}{E_q}$, $e_0 = \frac{E_0}{E_q}$ are the normalised space-charge field, diffusive field, and external applied dc field respectively. Here $E_D = \frac{k_B T}{q} k$, $E_q = \frac{2qNW_0}{\epsilon k}$. Because of the symmetry between the two pieces of gratings, e_1^{sat} can be got by the exchanging of m' and m in the e_r^{sat} .

3. DISCUSSION

There are two main differences between Eqs.(6) and equations given by Zhou⁷⁻⁸ for single grating. One is that in Eqs.(6) the SH of the second grating couple in the FH of the first grating and the FH of the second grating couple in the SH of the first grating, but there are not this kinds of coupling in the case of storing single grating. This kinds of coupling have been discussed in our previous paper¹¹. The other difference is that the modulation depth of the second grating couple in the equations of the first grating and that of the first grating same couple in the equations of the second grating. In our previous paper¹², we have discussed the coupling effects of modulation depth between two photorefractive phase gratings without external applied field. In this paper, we will discuss the coupling effects with an external applied dc field.

In Fig.1 we plot the real and imaginary parts of the saturation spatial harmonics e_r^{sat} as a function of the normalized applied dc field e_0 at $m = 1$ and $e_D = 2$: Fig.1(a) is for the real parts and Fig.1(b) for the imaginary parts. From Fig.1, firstly it can be seen that there are peak values for the real parts and no peak values for the imaginary parts with increasing external fields e_0 . Then it is shown that no matter real and imaginary parts or the fundamental and the second harmonics, they are all affected by m' (the modulation depth of the second grating), that is to say that m' can properly adjust the position of the curves in some range. Adjustability ranges (AR) of the fundamental harmonics (FH) of real and imaginary parts, which result from m' , become larger and larger with increasing of normalized electric field e_0 , but that of the second harmonics (SH) of real and imaginary parts aren't so. The maximal AR of real part of the SH appears at the position of peak value of the curves and with increasing of normalized electric field e_0 AR of real part of the SH tends to zero, but AR of imaginary part of the SH tends to a constant with increasing of normalized electric field e_0 . In addition, we can also notice that AR of the SH is always larger than that of the FH, no matter real or imaginary parts. This conclusion is in agreement with the result presented by our previous paper [15]. Lastly, when $e_0 = 0$, the real parts are zero but the imaginary parts are nonzero constants which are directly related with m' (in Fig.1(b)), e_D (in Fig.2(b)) and m (in Fig.3(b)).

Fig.1 (a), (b)

In Fig.2 we present the result with the small diffusive field $e_D = 0.01$, $m = 1$. Comparing Fig.2(a) with Fig1(a), we can found that not only the peak values are larger at the small diffusive field than that at large diffusive field, but also the position of the peak value shifts toward the origin for both the two harmonics. In addition, AR of both FH and SH which result from m' get the maximum at the position peak values and they are larger than that of larger diffusive field. In Fig.1(b), 2(b), one of the differences is

the various nonzero constant when $e_0 = 0$, though the nonzero constants are very small in Fig2(b). The reason is when $e_0 = 0$, the spatial charge field is mainly formed by the diffusive field. Comparing Fig2(b) with Fig1(b), we can also discover that AR of both FH and SH of small diffusive field e_D are almost equal with that of large e_D except at the small e_0 . That is to say that AR of both FH and SH of imaginary part aren't affected by e_D , but that of real part isn't so.

Fig.2 (a)(b)

In order to know the relation between AR of both FH and SH and m (the modulation depth of the first grating), we plot the Fig.3 where $m = 0.5, e_D = 2$ and Fig.4 where $m = 0.5, e_D = 0.01$. Comparing Fig.3 with Fig.1, and Fig.4 with Fig.2 we can draw the conclusion: AR of FH and SH both real and imaginary parts are all become small with the decreasing of m .

Fig.3 (a)(b)

Fig.4 (a)(b)

In Fig.5, we give the relation curves between the normalized electric field e_0 and the amplitude of the first-two order harmonics of normalized spatial charge field. When external applied field is small, the increasing rates of amplitudes of both FH and SH for small diffusive field are larger than that for large diffusive field. When external applied field is large, the amplitudes of both small and large diffusive field get to the same saturation value. No matter for small diffusive field or for large diffusive field, AR of both FH and SH increase with the increasing of e_0 and finally attain to a stable value. In addition, AR of amplitude of SH are larger than that of FH.

Fig.5 (a)(b)

In Fig.6, the relation between normalized electric field e_0 and phase of e_r^{sat} is given. When $e_0 = 0$, the phases of e_r^{sat} are $\pi/2$, and with the increasing of e_0 , the phases of e_r^{sat} quickly decrease and get to a minimum. But after this point it begin to increase with the increasing of e_0 , and finally when e_0 is enough high, the phase of e_r^{sat} can get to $\pi/2$ once again. It can also be easily noticed that the FH and the SH are in phase when e_0 is very low and out of phase when e_0 is slight high. The positions of minimum for small diffusive field shift toward the origin. In addition, m' almost don't affect the phase except e_1^{sat} at $e_D = 2$ and with high e_0 .

Fig.6 (a)(b)

In Fig.7(a), Fig.7(b), we plot the normalized grating vector (k/k_0) as a function of the normalized spatial charge field: Fig7(a) is for $e_0 = 1, m = 1$, and Fig7(b) for $e_0 = 0.1, m = 1$. AR of FH and SH for the cases of $e_0 = 1$ and $e_0 = 0.1$ are clearly shown out.

Fig.7 (a)(b)

4. CONCLUSIONS

In summary, for two pieces of phase gratings stored in one point of photorefractive material with the external applied dc field, the coupling equations of modulation depth and steady solution of spatial-charge-field are presented by using "the hopping model" of Feinberg. The results indicate that spatial-charge-field of the first grating are mainly decided by m (the modulation depth of the first grating) and at same time also can be adjusted by m' (the modulation depth of the second grating). No matter real parts, imaginary parts or amplitudes of spatial-charge-field, adjustability range of the second-order harmonic is always larger than that of the fundamental harmonic. For real parts and amplitudes of spatial-charge-field, AR of both FH and SH are larger at the small diffusive field e_D than that at the large one. But AR of imaginary parts of both FH and SH haven't relation with diffusive field e_D . Adjustability range of both the harmonics is smaller and smaller with the decreasing of their modulation depth. In addition, we also found that m' almost hasn't the effect on the phase of spatial-charge-field.

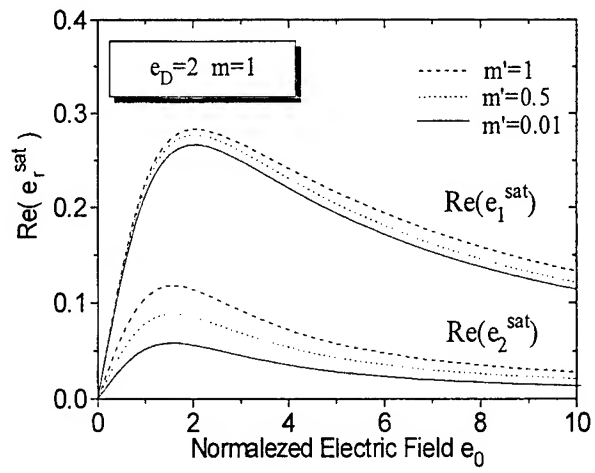
ACKNOWLEDGEMENT

This research was supported by the Nature Science Foundation of Nation and the Science Foundation of Harbin Institute of Technology.

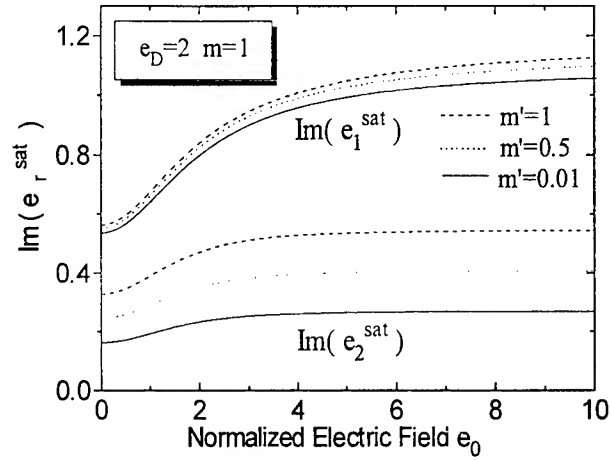
REFERENCES

1. F. H. Mok, M. C. Tackitt, and H. M. Stoll, "Storage of 500 high-resolution holograms in a LiNbO₃ crystal," *Opt. Lett.* 16, pp. 605-607, 1991.
2. F. H. Mok, "Angle-multiplexed storage of 5000 holograms in lithium niobate," *Opt. Lett.* 18, pp. 915-917, 1993.
3. G. W. Burr, F. H. Mok, and D. Psaltis, "Angle and space multiplexed holographic storage using the 90° geometry," *Optics Communications*, 117, pp. 49-55, 1995.
4. F. T. S. Yu, F. Zhao, H. Zhou, and S. Yiu, "Cross-talk noise in a wavelength multiplexed reflection-type photorefractive fiber hologram," *Optic Letters*, 18, pp. 1849-1851, 1993.
5. W. J. Burke, and P. sheng, "Cross talk noise from multiple thick-phase holograms", *J. Appl. Phys.* 48, pp. 681-685, 1977.
6. C. Gu, J. Hong, and I. Mcmichacl, "Cross-talk-limited storage capacity of volume holographic memory," *J. Opt. Soc. Am. A.* pp. 1978-1983, 1992.
7. Z. Zhou, X. Sun, Y. Li, Y. Jiang, H. Zhao, and K. Xu, "Kinetics of the higher-order response of photorefractive materials," *J. Opt. Soc. Am. B* 13, pp. 2580-2586, 1996.
8. Z. zhou, Y. Li, X. Sun, Y. Jiang, H. zhao, and K. Xu, "Perturbative analytical solution of tow-wave coupling in photorefractive materials at large modulation depth," *J. Appl. Phys.* 80, pp. 4268-4273, 1996.
9. J. Feinberg, D. Heiman, A. R. Tanguay, and R. W. Hellwarth, "Photorefractive Effects and Light-induced Charge Migration in Barium Titanate," *J. Appl. phys.*, 51, pp. 1297-1305, 1980.
10. E. Serrano, M. Carrascosa, and F. Agullo-López, "Nonperturbative analytical solution for steady-state photorefractive recording," *Opt. Lett.* 20, pp. 1910-1912, 1995.

11. Baohong Yuan , Zhongxiang Zhou , Chunfeng Hou , Xiudong Sun . Perturbative analysis of cross talk between two phase gratings stored in photorefractive material by angle-multiplexing (unpublished)
12. Baohong Yuan , Zhongxiang Zhou , Chunfeng Hou , Xiudong Sun. Theoretical study on coupling effects of modulation depth between two photorefractive phase gratings . Opt. Commu. 175 (2000) 233



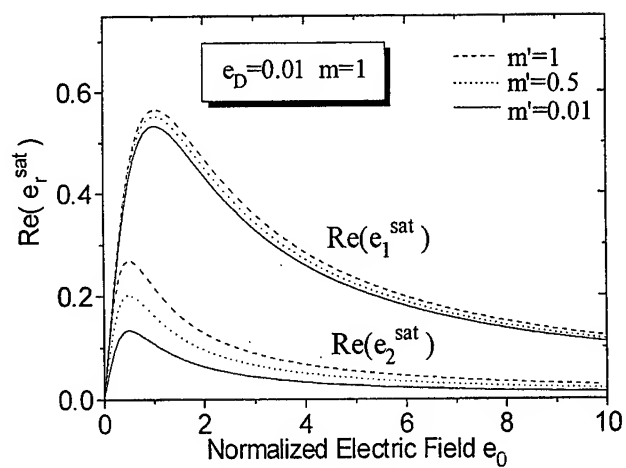
(a)



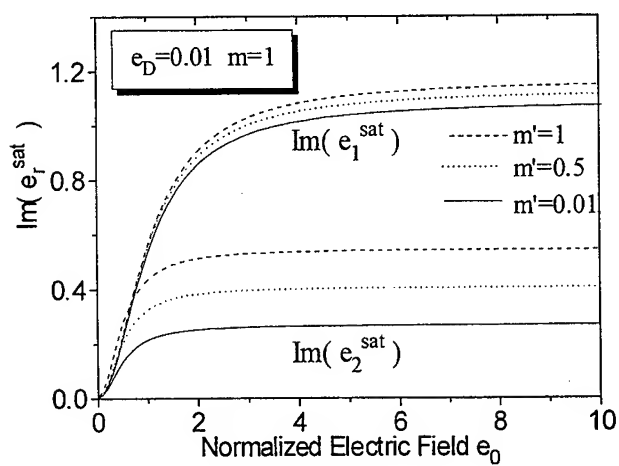
(b)

Fig. 1 The (a) real, (b) imaginary parts of the saturation spatial fields

as a function of the normalized applied dc field e_0 with $e_D = 2$ $m = 1$

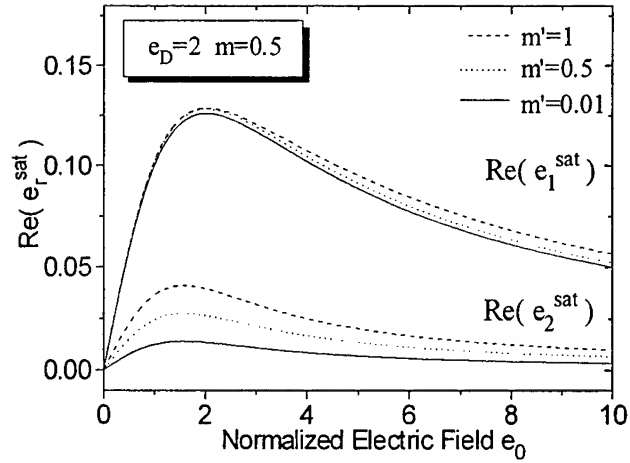


(a)

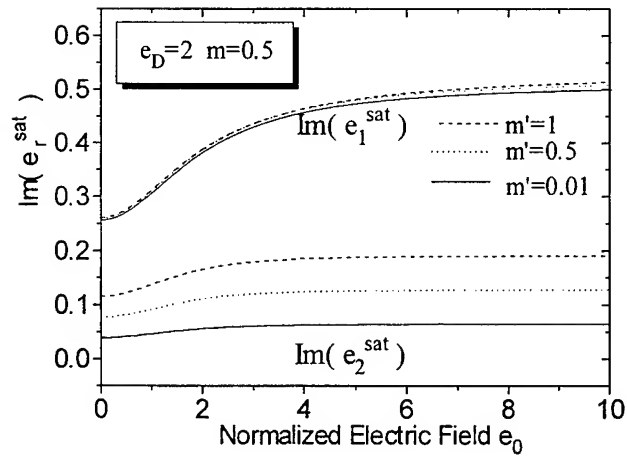


(b)

Fig. 2 The (a) real, (b) imaginary parts of the saturation spatial fields as a function of the normalized applied dc field e_0 with $e_D = 0.01$ $m = 1$

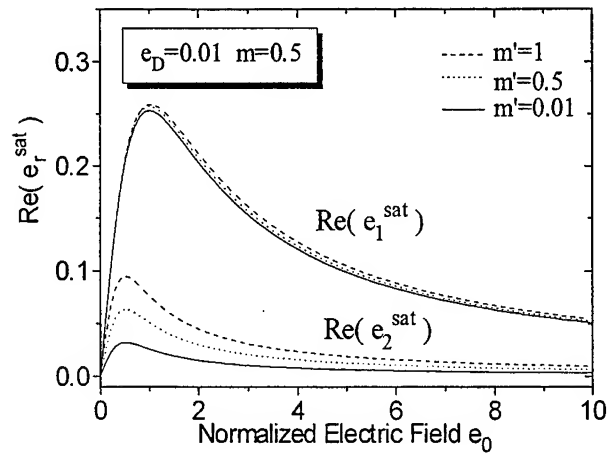


(a)

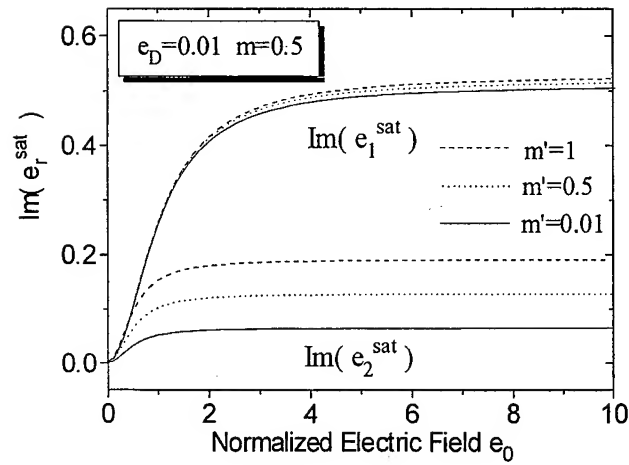


(b)

Fig. 3 The (a) real, (b) imaginary parts of the saturation spatial fields as a function of the normalized applied dc field e_0 with $e_D = 2$ $m = 0.5$

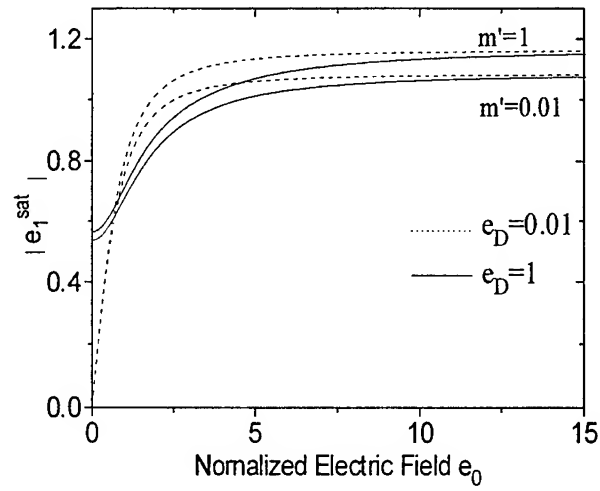


(a)

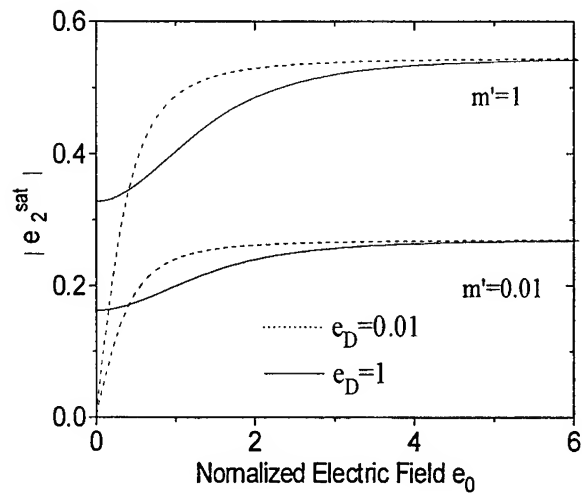


(b)

Fig. 4 The (a) real, (b) imaginary parts of the saturation spatial fields as a function of the normalized applied dc field e_0 with $e_D = 0.01$ $m = 0.5$



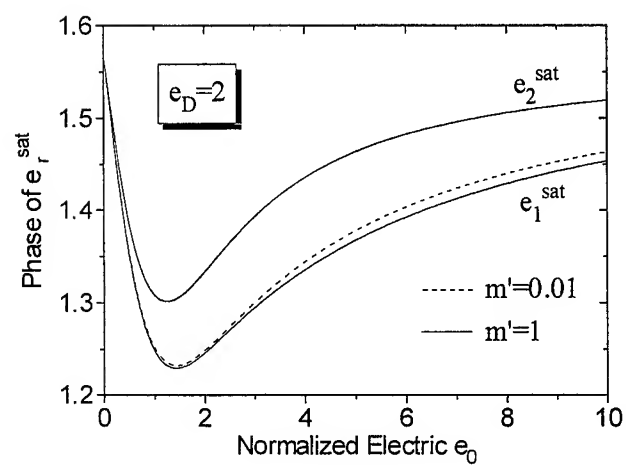
(a)



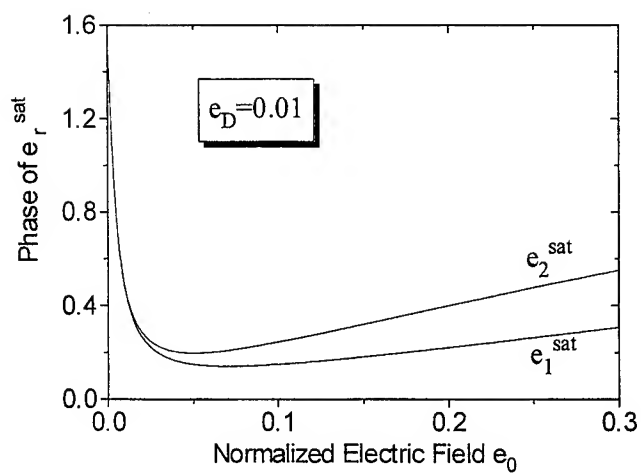
(b)

Fig. 5 The amplitude of saturation spatial fields as a function of the normalized applied dc field e_0

(a) the fundamental harmonic (b) the second harmonic



(a)

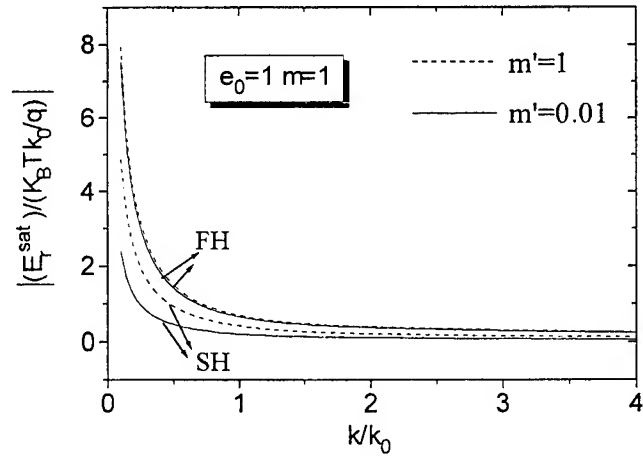


(b)

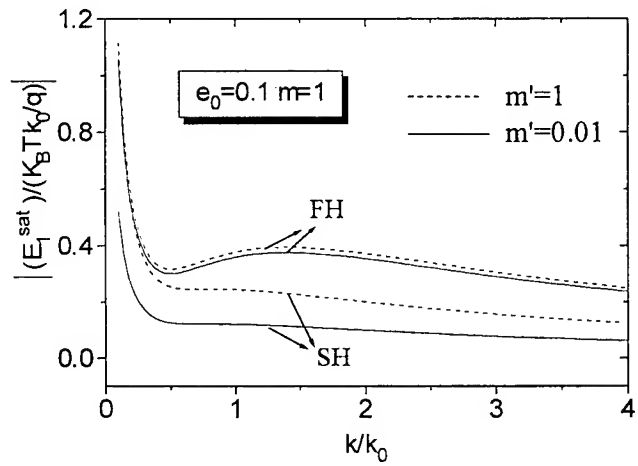
Fig. 6 The phase of saturation spatial fields as a function of the normalized applied dc field e_0

(a) $e_D = 2$

(b) $e_D = 0.01$



(a)



(b)

Fig. 7 The amplitude of saturation spatial fields as a function of k / k_0

(a) $e_0 = 1$ (b) $e_D = 0.1$

Performance improvement in XGM wavelength conversion exploiting SLAOLM

Zhang Xinliang^{*a}, Huang Dexiu^a, Sun Junqiang^a, Liu Deming^a, Yi Heqing^b

^aDept. of Optoelectronic Engineering, Huazhong Univ. of Sci. and Tech., Wuhan, 430074, China

^bWuhan Research Institute of Posts and Telecommunications, Wuhan, 430074, China

ABSTRACT

In this paper, a simple wavelength conversion scheme based on SLAOLM is proposed out for the first time, and its extinction ratio performance and noise characteristics can be improved simultaneously. Theoretical study shows that the conversion mechanism is still based on gain saturation effect, but the phase modulation effect existing in SLAOLM is helpful for extinction ratio improvement. Furthermore, the weak signal will be compressed and the strong signal will be amplified in the SLAOLM, then the Signal-Noise Ratio (SNR) can be also improved. Experiment results shows that, after exploiting this scheme, the output extinction ratio has been improved to be 10dB from 6dB, and the SNR has also been improved to be 13dB from 5dB.

Keywords: Wavelength conversion, SLAOLM, Extinction Ratio, Noise, Gain saturation, Phase modulation

1. INTRODUCTION

All-optical wavelength converters are expected to become key components in the future broad-band optical networks based on wavelength division multiplexed architecture. It allows data transfer from one wavelength to another without entering the electrical domain. Wavelength conversion based on cross-gain modulation in semiconductor laser amplifier has been studied widely for its simple implementation, high conversion efficiency and large wavelength conversion span^[1]. As we know, wavelength converters exploited in communication systems should operate without degrading the extinction ratio over a large dynamic range and a large wavelength window. However, due to the gain saturation mechanism and inverse process of the band-filling effect, the output extinction ratio performance in this scheme is not so good, especially in wavelength up conversion. High input pump power and low probe power are helpful for extinction ratio improvement, and schemes based on double-stage amplifiers^[2], and integrated SOA/DFB Laser^[3], are also demonstrated to improve extinction ratio performance. At the same time, semiconductor optical amplifiers with long active region are widely exploited to achieve good extinction ratio performance and high conversion bitrates, Whereas, Amplified Spontaneous Emission (ASE) noise would become more serious.

The SLAOLM (Semiconductor Laser Amplifier in a Loop Mirror) is an essential device^[4-6] which can be used as demultiplexer for data rates up to 100Gbit/s, as nonlinear gain element providing shaping and contrast enhancement of

* Correspondence: Email: fiber@mail.hust.edu.cn, zhangxl71@263.net; Telephone: 86-27-87543355; Fax: 86-27-87545438.

optical pulses, as optical correlator providing retiming of optical data signals and header decoding in optical packet switching, as wavelength converter^[7]. A simpler wavelength conversion scheme based on SLAOLM, in which only one wavelength division multiplexer and one directional coupler are exploited, is proposed out firstly. Experimental results show that the extinction ratio performance and noise characteristics have been improved simultaneously. Experimental setup is depicted in section 2, theoretical model for SLAOLM is presented in section 3, and experimental results and theoretical analysis are discussed in section 3.

2. EXPERIMENTAL SETUP

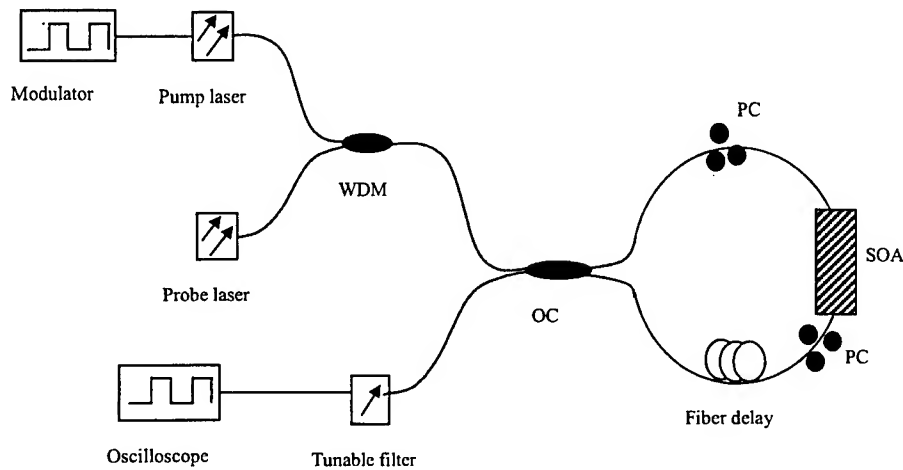


Figure 1 Experimental setup diagram for wavelength conversion based on SLAOLM

Experimental setup for wavelength conversion scheme based on SLAOLM is depicted in Fig.1. The 1562.6nm pump DFB laser is provided by the transmitter of Error and Jitter Test Set, and its modulation format can be tunable. The 1549.8nm, CW probe optical signal and the pump signal are multiplexed by a wavelength division multiplexing (WDM) element. The input port and the output port of the SLA are connected with the two output ports of the 3dB directional coupler, then a nonlinear loop mirror based on SLA can be constructed simply. The mixed optical signals will be divided into two parts, which travel in clockwise (cw) and counter-clockwise (ccw) direction through the loop, respectively. The two polarization controllers are set to control the polarization states of the input signal. The fiber delay can control the phase difference between clockwise and counter-clockwise signals. The converted signal can be selected out by a 1nm tunable bandpass filter.

The SOA is fabricated with mixed strained multi-quantum-well structure. Its active material, which is grown with MOCVD epitaxy equipment in Wuhan Research Institute of Posts and Telecommunications (WRI), is consisted of the matched quantum wells and tensile strained quantum barriers based on quaternary material $\text{In}_{1-x}\text{Ga}_x\text{As}_{1-y}\text{P}_y$. The length, width and height of the active cavity are 500 μm , 2.0 μm and 0.09 μm , respectively. The facets of the SOA are coated with 10^{-4} order AR film.

3. THEORETICAL MODEL

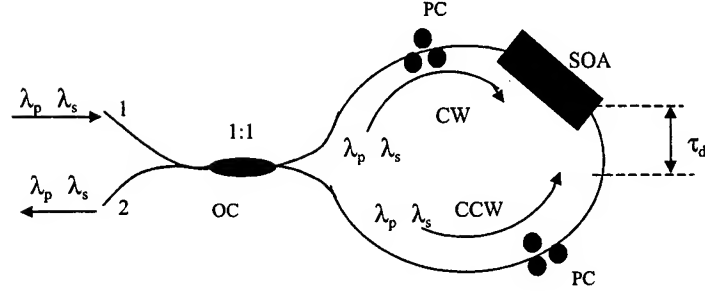


Figure 2 Schematic diagram for wavelength conversion based on SLAOLM

Schematic diagram for wavelength conversion based on SLAOLM is shown in Figure 2. Assuming an ideal 50:50 coupler and a spatially concentrated SLA, the output powers in the output port 2 of the directional coupler can be derived from the following equations:

$$P_{p,out}(t) = G_{p,cw}(t - t_d) \cdot P_{p,in}(t - t_d) \cdot \left[\frac{1}{4} + \frac{1}{4} \cdot \frac{G_{p,ccw}}{G_{p,cw}} - \frac{1}{2} \cdot \sqrt{\frac{G_{p,ccw}}{G_{p,cw}}} \cdot \cos(\phi_{p,cw} - \phi_{p,ccw}) \right] \quad (1)$$

$$P_{s,out}(t) = G_{s,cw}(t - t_d) \cdot P_{s,in}(t - t_d) \cdot \left[\frac{1}{4} + \frac{1}{4} \cdot \frac{G_{s,ccw}}{G_{s,cw}} - \frac{1}{2} \cdot \sqrt{\frac{G_{s,ccw}}{G_{s,cw}}} \cdot \cos(\phi_{s,cw} - \phi_{s,ccw}) \right] \quad (2)$$

Where $i = p, s$ means pump wave and probe wave, respectively; $G_{i,cw}$ and $G_{i,ccw}$ represent the gain of the clockwise traveling signal and the counter-clockwise traveling signal, respectively; $\phi_{i,cw}$ and $\phi_{i,ccw}$ represent the phase change of the clockwise traveling signal and the counter-clockwise traveling signal, respectively; t_d is the signal round trip time in the loop; τ_d is the time delay of the counter-clockwise traveling signal. At time t , $G_{i,cw}$, $G_{i,ccw}$, $\phi_{i,cw}$ and $\phi_{i,ccw}$ can be obtained from

$$\begin{aligned} G_{i,cw}(t) &= G(t + \frac{t_d}{2} - \tau_d) & \phi_{i,cw}(t) &= \phi(t + \frac{t_d}{2} - \tau_d) \\ G_{i,ccw}(t) &= G(t + \frac{t_d}{2} + \tau_d) & \phi_{i,ccw}(t) &= \phi(t + \frac{t_d}{2} + \tau_d) \end{aligned}$$

Where $G(t)$ is the gain of the input signal after traveling through the SLA, and $\phi(t)$ is the phase change of the input signal after traveling through the SLA. It can be seen from the equation (1) and (2), that the output power mainly depends

on the gain ratio $\Delta G_i = (G_{i,ccw} / G_{i,cw})$ and the phase difference $\Delta \phi_i = \phi_{i,cw} - \phi_{i,ccw}$.

For the SLA, there are four input signals at time t . Therefore the carrier density $N(z, t)$ at a specific longitudinal coordinate in the SLA, at time t , will be determined by the rate equation

$$\begin{aligned} \frac{\partial N(z, t)}{\partial t} = & \frac{I}{eV} - \frac{N(z, t)}{\tau_s} - \frac{P_{p,cw}(z, t) \Gamma g_p [N(z, t) - N_T]}{h\nu_p A} \\ & - \frac{P_{p,ccw}(z, t) \Gamma g_p [N(z, t) - N_T]}{h\nu_p A} \\ & - \frac{P_{s,cw}(z, t) \Gamma g_s [N(z, t) - N_T]}{h\nu_s A} \\ & - \frac{P_{s,ccw}(z, t) \Gamma g_s [N(z, t) - N_T]}{h\nu_s A} \end{aligned} \quad (3)$$

Where I is the effective injection current; e is the electron charge; V is the volume of the active region of the SLA; τ_s is the carrier lifetime; Γ is the mode confinement factor; g_i is the differential gain coefficient ($i=p$ corresponds to the pump signal while $i=s$ corresponds to the probe signal); N_T is the transparency carrier density; $h\nu_i$ is the photon energy; A is the cross-section area of the active region. The first term on the right hand side of equation (3) describes carrier injection, the second term represents carrier consumption due to radiative and nonradiative recombination, while the following terms accounts for carrier consumption due to stimulated emission, i.e. amplification of the input signals.

At the same time, the optical power propagating in the SLA can be derived from the following traveling-wave equations:

$$\begin{aligned} \frac{\partial P_{p,cw}(z, t)}{\partial z} &= [\Gamma g_p (N(z, t) - N_T) - \alpha_{in}] \cdot P_{p,cw}(z, t) \\ \frac{\partial P_{p,ccw}(z, t)}{\partial z} &= [\Gamma g_p (N(z, t) - N_T) - \alpha_{in}] \cdot P_{p,ccw}(z, t) \\ \frac{\partial P_{s,cw}(z, t)}{\partial z} &= [\Gamma g_s (N(z, t) - N_T) - \alpha_{in}] \cdot P_{s,cw}(z, t) \\ \frac{\partial P_{s,ccw}(z, t)}{\partial z} &= [\Gamma g_s (N(z, t) - N_T) - \alpha_{in}] \cdot P_{s,ccw}(z, t) \end{aligned} \quad (4)$$

Where α_{in} is the internal loss coefficient of the active region. It should be noted that the differences of the internal loss, the mode confinement factor and the transparency carrier density for two different input channels have been neglected. For simplicity, we introduce an average carrier density $N_{av}(t)$ at time t , which is independent of z , and it can be derived from

$$N_{av}(t) = \frac{1}{L} \int_0^L N(t, z) dz$$

On the other hand, the phase change can be determined by the refractive index change induced by carrier density variation^[8], and it can be expressed as

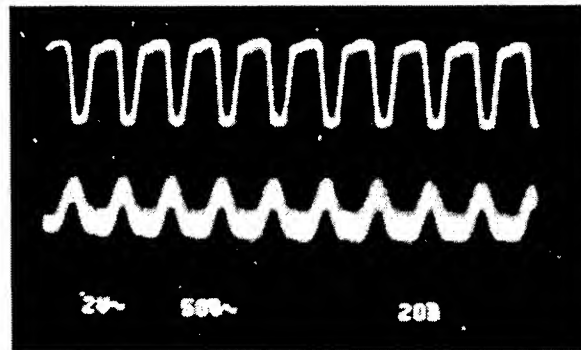
$$\begin{aligned}\phi_p(t) &= \frac{2\pi L}{\lambda_p} (n_g + \Gamma N_p \frac{dn}{dN}) + \frac{2\pi L}{\lambda_p} \Gamma [N_{av}(t) - N_T] \frac{dn}{dN} \\ \phi_s(t) &= \frac{2\pi L}{\lambda_s} (n_g + \Gamma N_p \frac{dn}{dN}) + \frac{2\pi L}{\lambda_s} \Gamma [N_{av}(t) - N_T] \frac{dn}{dN}\end{aligned}\quad (5)$$

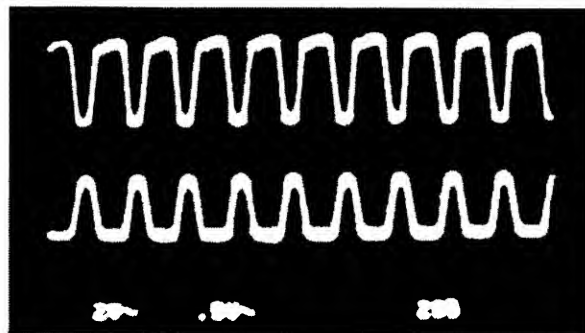
Where n_g is the effective refractive index corresponding to transparency, N_p is the transparency carrier density corresponding to gain peak wavelength, dn/dN is the variation rate of the refractive index due to the variation of the carrier density. Having determined the average carrier density $N_{av}(t)$ by equation (3) and (4), the gain ratio and the phase difference at time t can be derived

$$\begin{aligned}\Delta G_i(t) &= \frac{G_{i,ccw}(t + \frac{t_d}{2} + \tau_d)}{G_{i,cw}(t + \frac{t_d}{2} - \tau_d)} \\ \Delta \phi_i(t) &= \phi_{i,cw}(t + \frac{t_d}{2} - \tau_d) - \phi_{i,ccw}(t + \frac{t_d}{2} + \tau_d)\end{aligned}\quad (6)$$

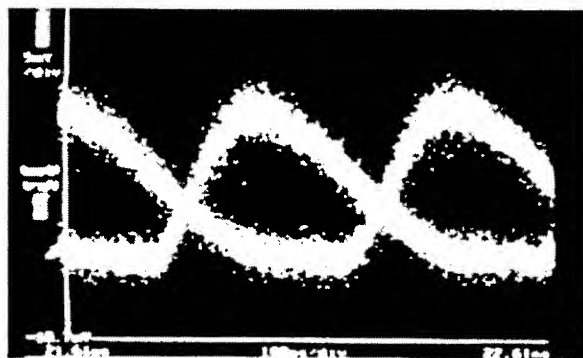
Therefore, exploiting equation (1), (2) and (6), the output power in the port 2 of the directional coupler can be determined. As discussed above, we can conclude that there exists gain saturation effect and phase modulation effect simultaneously in the wavelength conversion scheme.

4. RESULTS AND DISCUSSIONS

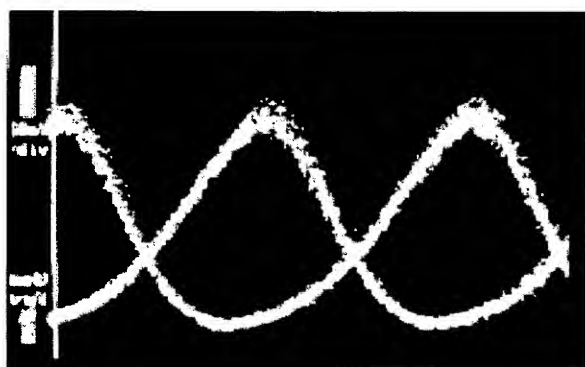




3.2



3.3



3.4

Figure 3 Comparison of the conversion results for different conditions: 3.1, wavelength conversion based on conventional scheme with 140Mbit/s “110110” bit sequence; 3.2, wavelength conversion based on SLAOLM with 140Mbit/s “110110” bit sequence; 3.3, wavelength conversion based on conventional scheme with 2.5Gbit/s “101010” bit sequence; 3.4 wavelength conversion based on SLAOLM with 2.5Gbit/s “101010” bit sequence.

Comparison of the conversion results for different conditions is presented in Figure 3. Figure 3.1 and 3.3 are corresponding to the conventional XGM conversion scheme^[9] in which the SLA has not been constructed into a loop mirror, while 3.2 and 3.4 are corresponding to the novel conversion scheme based on SLAOLM. Figure 3.1 and 3.2 are the conversion results for 140Mbit/s "110110" bit sequence, while Figure 3.3 and 3.4 are the conversion results for 2.5Gbit/s "101010" bit sequence. In Figure 3.1 and 3.2, the upper waveform represents the electrical modulated signal that has the same phase with the pump signal, while the lower waveform represents the converted signal, which has been transferred into electrical signal. It is shown that the phase of the converted signal is inverted to the pump signal. In Figure 3.3 and 3.4, the waveform represents the converted signal. The conversion results show that 10dB output extinction ratio and 13dB SNR can be achieved in wavelength conversion scheme based on SLAOLM, whereas only 6dB extinction ratio and 5dB SNR were achieved in conventional wavelength conversion scheme. Therefore it can be concluded that the extinction ratio performance as well as the noise characteristics in the novel scheme has been improved greatly, comparing with that in the conventional schemes, whether in 140Mbit/s or in 2.5Gbit/s wavelength conversion.

Based on the theoretical model presented in section 3, we can conclude that the phase modulation effect is the main reason for performance improvement. The clockwise traveling signal and the counter-clockwise traveling signal will obtain different phase change while traveling through the loop mirror, and the SLAOLM operates actually as a Mach-Zehnder Interferometer. To some extent, the SLAOLM can be regarded as a "filter" in which the weak signal will be compressed and the strong signal will be amplified, then the signal-noise ratio and the extinction ratio of the converted signal can be improved.

5. CONCLUSIONS

A simple wavelength conversion scheme based on SLAOLM is proposed out firstly. Theoretical model for this novel scheme is also presented. Experimental results for 140Mbit/s and 2.5Gbit/s wavelength conversion show that the extinction ratio performance and noise characteristics have been improved greatly, comparing with that in conventional schemes. Gain saturation effect and phase modulation effect exists simultaneously in the SLAOLM, and the phase modulation effect is found to be the main reason for performance improvement. It should be noted that only elementary analysis is provided in this paper, more detail analysis on mechanism for performance improvement and theoretical calculation for different input format are necessary for more reasonable explanation.

ACKNOWLEDGMENTS

The author would like to thank Dr. Zhang Zheming, Dr. Huang Gefan, Dr. Duan Zigang for their help on fabricating the SOA. The work related to this paper is sponsored by High Technology Developing Project of China(863-307-16-03).

REFERENCES

1. T. Durhuus, B. Mikkelsen, C. Joergensen, S. L. Danielsen, and K.E. Stubkjaer. "All-optical wavelength conversion by Semiconductor Optical Amplifiers." *J. of Lightwave Technology*. 14, pp942-956, 1996.

2. S.Chelles, F.Devaux, D.Meichenin, D.Sigogne, and A.Carenco, "Extinction ratio of cross-gain modulated multistage wavelength converters:Model and experiments," *IEEE Photonics Technology letters*. 8, pp.533-535,1996.
3. M.F.C.Stephens, R.V. Penty, and I.H. White. "All-optical Regeneration and Wavelength Conversion in An Integrated Semiconductor Optical Amplifier /Distributed-Feedback laser." *IEEE Photonics Technology letters*.11, pp.979-981, 1999.
4. M.Eiselt, W.Pieper, G.Grobkopf, R.Ludwig, and H.G.Weber. "One million pulse circulations in a fiber ring usng a SLAOLM for pulse shaping ad noise reduction." *IEEE Photonics Technology letters*. 4, pp.422-424,1993.
5. M.Eiselt, W.Pieper, and H.G.Weber. "A decision gate for all-optical data retiming using a semiconductor laser amplifier in a loop mirror configuration." *Electronics Letters*. 29, pp107-109, 1993.
6. M.Eiselt, W.Pieper, and H.G.Weber. "SLAOLM: Semiconductor Laser amplifier in a loop mirror." *J. of Lightwave Technology*. 13, pp2099-2111, 1995.
7. D.A.O. Davis, A.D.Ellis and G.Sherlock. "Regenerative 20Gbit/s wavelength conversion and demultiplexing using a semiconductor laser amplifier nonlinear loop mirror." *Electronics Letters*. 31, pp1000-1001, 1995.
8. Mehdi Asghari, Ian H. White, and Richard V. Penty. "Wavelength Conversion Using Semiconductor Optical Amplifiers." *J. of Lightwave Technology*. 15, pp1181-1190, 1997.
9. Zhang Xinliang, Sun Junqiang, Huang Dexiu, and Yi Heqing. "Experimental Study on Performances of Wavelength Converters Based on XGM in SOAs." *Journal of Huazhong University of Science and Technology*. 27(10), pp15-17, 1999.

SPICE circuit models for semiconductor lasers with effects of carrier and lattice heating

Chin-Yi Tsai^a, Chih-Hsiung Chen^a, Tien-Li Sung^a, Chin-Yao Tsai^b, and C. C. Yang^c

^aDepartment of Electronic and Electrical Engineering, De Montfort University, Leicester LE1 9BH, United Kingdom

^bDepartment of Electrical Engineering, National Cheng Kung University, Tainan, Taiwan

^cDepartment of Electrical Engineering and Graduate Institute of Electro-Optical Engineering, National Taiwan University, Taipei, Taiwan

ABSTRACT

A SPICE circuit model for semiconductor lasers is developed to simultaneously incorporate the effects of the carrier and lattice heating. Numerical simulations for the dc, ac and transient responses of this circuit model are demonstrated. The circuit model is transformed from the rate equations that govern the dynamics of carrier density, photon density, electron temperature, hole temperature and lattice temperature in the active region of semiconductor lasers. SPICE codes are developed exactly according to this circuit model. The results from this work demonstrate the capacities and versatilities of the SPICE circuits in simulating the complicated carrier and lattice heating processes for semiconductor lasers. The possibility of simulating optoelectronic systems in conjunction with electronic circuits and devices all by SPICE circuit models is also discussed.

Keywords: SPICE, circuit models, semiconductor lasers, carrier heating, lattice heating

1. INTRODUCTION

Developing circuit models for semiconductor lasers certainly has many advantages if they can then be used alongside other circuit models for design purposes. Computer-aided design (CAD) tools are gradually becoming indispensable for designing electronic processes, devices, circuits and systems, and in achieving the goal of electronic design automation (EDA) [1]. With thousands or even millions of transistors in a single chip, it is almost impossible to design electronic circuits or electronic systems using analytical methods without the help of CAD simulations. In a comparative manner, it is thus predictable that CAD tools for optoelectronic devices and systems will become critically important in the future. Through numerous efforts over more than three decades, CAD tools for electronics processes, devices, circuits and systems have been well developed. Several simulation packages have been commercialised, for example, SUPREM for processes, MEDICI and ATLAS for devices. Some of the simulation languages have become industrial standards, such as SPICE for analogue circuits [2], and VHDL or Verilog for digital circuits. Despite such success, it is surprising to find that the development of CAD tools for optoelectronic devices or systems is still not fully explored and as yet, no standard associated with them has emerged.

Generally, compared to their electronic counterparts, developing CAD tools for optoelectronic devices and systems is still in its infancy and currently lacks a commonly accepted standard. As a result, the approach to develop any simulation tool is either by establishing a new one or accommodating the well-established ones. For optoelectronic devices, especially optical transmitters, receivers converting electronic and optical signals, used in conjunction with other electronic devices, the latter seems a viable choice. Especially, for semiconductor lasers used in fibre optic communication systems as electronic driving circuits provide their electronic signals. As SPICE circuit simulation is widely used to design the driving circuits of semiconductor lasers, it is logical to develop SPICE circuit models for these devices. This has the advantage of using established software tools in an integrated systems approach. Unlike electronic devices that are usually characterised by current and voltage, while optoelectronic devices are normally characterised by light intensity and current. Since light

intensity cannot be represented by any physical circuit quantities, modelling optoelectronic devices by SPICE circuit model is certainly not physically transparent and should be implemented with caution. Nevertheless, if the circuit model is well constructed to take account of the realistic physical models and sufficiently represents the physical properties of the optoelectronic device, it will certainly bring great benefit for designing the optoelectronic module working within an electronic system such as optical transmitter and receiver. This approach avoids modelling optoelectronic devices by stand-alone tools or languages. This provides the motivation for undertaking the work.

The importance of the theoretical models for the development of any semiconductor device is definitely beyond doubt. In fact, theoretical models for semiconductor devices have been well developed; and several popular commercial packages, such as MEDICI, ATLAS and DESSIS, have been widely used by industrial and academic institutions. Basically, any theoretical models for electronic devices should be able to describe the behaviour of electrons inside the devices. Theoretical models used for simulating the electronic devices can be categorised into three different methods based on the assumed nature of the carrier transport in the devices: the Monte Carlo analysis, partial differential equation (PDE) or balance equation, and ordinary differential equation (ODE) or rate equation. For each carrier, electron or hole, in a device, three parameters are needed to fully characterise its movement inside the device: time (t), space (r) and momentum (k). The Boltzmann equation is used to describe the motions of all of the carriers inside the devices. Since it is almost impossible to analytically solve the Boltzmann equation even for a very simple and artificially defined case, a numerical method, such as the Monte Carlo method, is commonly implemented to solve the distribution of carriers in the (t, r, k) domain. Although, this method includes all the details of device physics, its simulation is rather complicated and time-consuming. In most cases, it does not provide a transparent explanation for the physical properties of the device. Alternatively, if the dynamics in the k -coordinate can be calculated by first principles or represented by average quantities (such as density, momentum and energy relaxation times), then the Boltzmann equations can be established by partial differential equations or balance equations. These balance equations can describe the carrier distribution (for example, density and temperature) in the temporal (t) and spatial (r) domains. Since the numerical methods for solving PDE equations are highly developed, simulating the devices' properties by solving such balance equations are certainly tractable. This is the reason why such PDE balance equations are implemented in all the major simulation packages for electronic devices. However, since the measurable physical quantities such as current and voltage are only functions of time, this implies that all the spatial effects, such as carrier density and temperature distributions in the spatial domain, that affect the output current or voltage can be further simplified if they can be represented by some average quantities. They can totally be neglected if such spatial effects are insignificant. Averaging or neglecting the physical quantities in the spatial domain can further simplify the original PDE balance equations into the ODE rate equations. This dramatically simplifies the theoretical models and numerical procedures for device simulations. However, it should be noted that the approach is only valid if the spatial effect of carrier distribution can really be treated as an average or totally neglected.

Since carrier transport in semiconductor lasers is rather similar to other electronic devices, therefore all the theoretical models discussed for electronic devices are applicable to semiconductor lasers. In fact, the physical processes occurring in the active region, where electrons and holes recombine and generate photons, almost determining all the physical properties of semiconductor lasers. As a result, the spatial effects can usually be ignored (except, for example, the spatial-hole-burning effect in DFB lasers) and rate equations employed. This explains why rate equations are widely implemented for simulating the physical properties of semiconductor lasers. Although many commercial simulation packages use PDE balance equations, for example, PISC3D, the method of rate equations is the most popular theoretical approach indeed for modelling semiconductor lasers. Basically, all the major physical properties such as L - I relationship, linewidth, modulation response, chirp and noise can successfully be characterised by rate equations. Therefore, the rate-equation approach is used in this work. The SPICE circuit model proposed in this work is exactly achieved from the rate equations.

As discussed, it can be anticipated that developing SPICE models is invaluable for realising the EDA of optoelectronic devices, which are used in conjunction with electronic devices or systems. Following such a strong anticipation of future need, several SPICE models for semiconductor lasers have been proposed [3]-[14]. The circuit models for bulk semiconductor lasers, that is, heterostructure, derived from the carrier-photon rate equations were first proposed by Tucker [3][4]. Based on this model, Lu et al. developed a SPICE circuit model for quantum-well lasers by incorporating additional effects of carrier transport [5][6]. In contrast, instead of concentrating on the carrier transport effects which only became important in the high-speed modulation mode, the Xu group proposed SPICE circuit models for quantum well lasers particularly emphasising on the heating effects [7][8]. This is based on the fact that the nonlinearity in the L - I relationship of any semiconductor laser can satisfactorily be explained by considering the heating effect. Tsou et al. also proposed a SPICE circuit model for quantum-well lasers including the carrier-transport effect [9]. In addition, the effect of the coulomb enhancement on the gain coefficient and thus the properties of the high-speed modulation were investigated using their

SPICE model [10]. A more evolved SPICE model including the carrier-transport effect was proposed by Rossi et al. [11]. They used their SPICE model to analyse and design 1.55 μm quantum-well lasers for improving the high-speed performance. Madhan et al. proposed a SPICE circuit model for the multimode lasers and investigated the bistable behaviour of the devices [12]. Czotscher et al. produced an approach in which they combined their circuit model with the physical models of optical fibres and photodetectors to simulate the intensity modulation and chirp in a fibre optic communication system [13]. Recognising that heating has a paramount effect on the properties of vertical-cavity surface-emitting lasers (VCSELs), Mena et al. proposed a SPICE circuit model with heating effects for VCSELs [14]. Mena et al. used their model to fit experimental data and thereby extracted the related physical parameters of the device. However, it should be noted that heating effects in their model and in the model of the Xu group are only referred to the lattice heating. Carrier heating effects are neither included nor discussed in their models.

From the foregoing it is seen that the temperature-dependent performance characteristics of devices are well established in SPICE circuit models. Consequently, physical quantities such as resistance and capacitance are assigned to a function of temperature ($TEMP$) in the SPICE codes. Therefore, it is widely accepted that SPICE circuit models for semiconductor lasers should represent this temperature-dependent feature in order to further integrate their implementation into electronic circuits and increase their accuracy in predicting performance. In fact, the heating problem is well recognised as one of the most important factors influencing both the static and dynamic performance of semiconductor lasers. However, all the published SPICE models, which include heating effects in semiconductor lasers, solely refer to the lattice heating while the direct effect of the carrier heating has totally been neglected. It should be noted that the injection current supplies energy to carriers, which then release their energy to lattice via phonon emission. Since the injection current supplies energy directly to electrons and holes, not directly to lattice in a semiconductor laser, any issue regarding the lattice heating in semiconductor lasers will inevitably involve the issue of the carrier heating. Consequently, theoretical models used for predicting the heating effects on the performance of semiconductor lasers are thus anticipated to be able to simultaneously accommodate the physical mechanisms of the carrier and lattice heating. This certainly implies that any attempt to establish the temperature-dependent feature for SPICE circuit models of semiconductor lasers should be able to incorporate the features of the carrier and lattice heating in the same model, not just the lattice heating alone.

2. RATE EQUATIONS

It has been well recognised that the conventional carrier-photon rate equations can successfully describe many static and dynamic properties of semiconductor lasers. Therefore, any theoretical model that is proposed for further refinement should be able to accommodate these rate equations. Theoretical models for semiconductor lasers based on such a rate-equation approach certainly implies that the spatial effects of physical quantities will be either averaged or neglected. For example, the optical confinement factor is an average quantity characterising the overlap of the optical field with the carriers in the active region. The injection efficiency is an average quantity describing the percentage of current goes into the active region. The behaviours of the carrier and lattice heating outside the active region were neglected.

In order to incorporate the effects of the carrier and lattice heating, additional rate equations are needed to supplement the conventional carrier-photon rate equations. In this work, rate equations governing the carrier density n , photon density s , electron temperature T_e , hole temperature T_h and lattice temperature T_L will be used, that is, the five rate equations are used to describe the time variation of the carrier density n , photon density s , electron temperature T_e , hole temperature T_h

$$\frac{dn}{dt} = \frac{\eta_{inj} I_{inj} - I_{leak}}{eV} - R_{SRH} - R_{spont} - R_{Aug} - \nu_g Gs \quad (1)$$

$$\frac{ds}{dt} = \Gamma \nu_g Gs - \frac{s}{\tau_s} + \Gamma \beta R_{spont} \quad (2)$$

$$\begin{aligned} \frac{dT_e}{dt} = & \left(\frac{\partial u_e}{\partial T_e} \right)^{-1} \left[\left\langle \Delta E_{inj}^e \right\rangle \frac{\eta_{inj} I_{inj} - I_{leak}}{eV} + \left\langle \Delta E_{stim}^e \right\rangle \nu_g Gs + \left\langle \Delta E_{Aug}^e \right\rangle R_{Aug} \right. \\ & \left. + \left\langle \Delta E_{fca}^e \right\rangle \nu_g \alpha_{fca}^e s - \frac{u_e(T_e) - u_e(T_L)}{\tau_{e-L}} - \frac{u_e(T_e) - u_e(T_h)}{\tau_{e-h}} \right] \end{aligned} \quad (3)$$

$$\frac{dT_h}{dt} = \left(\frac{\partial u_h}{\partial T_h} \right)^{-1} \left[\left\langle \Delta E_{inj}^h \right\rangle \frac{\eta_{inj} I_{inj} - I_{leak}}{eV} + \left\langle \Delta E_{stim}^h \right\rangle \nu_g Gs + \left\langle \Delta E_{Aug}^h \right\rangle R_{Aug}^h + \left\langle \Delta E_{fca}^h \right\rangle \nu_g \alpha_{fca}^h s - \frac{u_h(T_h) - u_h(T_L)}{\tau_{h-L}} + \frac{u_h(T_h) - u_h(T_e)}{\tau_{h-e}} \right] \quad (4)$$

$$\frac{dT_L}{dt} = -\frac{T_L - T_{HS}}{\tau_k} + \frac{1}{c_L \rho_L} \left[\frac{u_e(T_e) - u_e(T_L)}{\tau_{e-L}} + \frac{u_h(T_h) - u_h(T_L)}{\tau_{h-L}} + (E_{Fe} - E_{Fh}) R_{SRH} \right] \quad (5)$$

where n only denotes the carrier density in the active region, e is the unit of electron charge, V is the volume of the active region, I_{inj} represents the external injection current, η_{inj} represents the percentage of the injection current that reaches the active region, I_{leak} is the leakage current, R_{SRH} , R_{spont} , R_{Auger} and $\nu_g Gs$ represent the carrier recombination rates (i.e., loss rates) due to the Shockley-Read-Hall (SRH) recombination, spontaneous-emission recombination, Auger recombination and stimulated-emission recombination, s is the photon density of the lasing light inside the cavity, Γ , ν_g , G and τ_s are confinement factor, group velocity, gain coefficient and photon lifetime, respectively, β is the percentage of photons emitted by spontaneous emission coupling into the stimulated emission, $u_c(T)$, $c = e$ or h , is the carrier energy density at temperature T , α_{fca}^c is the coefficient of the free-carrier absorption, $\langle \Delta E_{process}^c \rangle$, $process = inj, stim, Aug$ and fca is the average energy change per carrier due to the processes of the injection, stimulated-recombination, Auger recombination and free-carrier-absorption heating, T_{HS} is the temperature of the heat sink, c_L is the specific heat capacity of the lattice, and ρ_L is the material density of the lattice. In these rate equations, there are four time constants: τ_k is the thermal conduction time, τ_{e-L} is the electron-lattice energy relaxation time, τ_{h-L} is the hole-lattice energy relaxation time and τ_{e-h} is the electron-hole energy relaxation time. These time constants govern the overall energy exchange rates between electrons, holes and lattice.

Apparently, (1) describes that the injection current supplies carriers into the active region, while the leakage, SRH, spontaneous emission, Auger and stimulated emission processes annihilate carriers in the active region. Similarly, (2) manifests that the stimulated emission and the coupling of the spontaneous emission supply the lasing photons, while the losses due to the internal loss and the mirror loss deplete the photons inside the cavity. From (3), it can be seen that the electron temperature will increase due to the injection heating, stimulated-recombination heating, Auger-recombination heating and free-carrier-absorption heating; and it will decrease due to the electrons releasing their energy to lattice and holes as they relax. In the same manner, as described in (4), the hole temperature will increase due to the same heating mechanisms and the receiving of electron energy. Similarly, it will decrease due to the holes releasing their energy to lattice. The lattice temperature will increase as it obtains energy from the electrons and holes via the intraband energy relaxation and the interband SRH process with multiple-phonon emission, as described in (5).

3. SPICE CIRCUIT MODELS

In order to implement the rate equations into the circuit models, the physical quantities described by the equations require to be transformed into circuit quantities which model each physical process as, for example, currents, voltages and passive elements. Perhaps the most challenging aspect in such a transformation is to adequately represent the carrier density by a circuit quantity or element.

The rate equation for carrier density (1) can be rewritten in a 'current form' as:

$$eV \frac{dn}{dt} = \eta_{inj} I_{inj} - I_{leak} - eVR_{SRH} - eVR_{spont} - eVR_{Aug} - eV\nu_g Gs \quad (6)$$

$$\equiv \eta_{inj} I_{inj} - I_{leak} - I_{SRH} - I_{spont} - I_{Aug} - I_{stim}$$

where $I_{SRH} = eVR_{SRH}$, $I_{spont} = eVR_{spont}$, $I_{Aug} = eVR_{Aug}$, and $I_{stim} = eV\nu_g Gs$ represent the recombination currents due to the SRH, spontaneous emission, Auger and stimulated emission, respectively. The task in transforming this rate equation is to choose a proper circuit element to represent the term $eV(dn/dt)$. The most obvious one is by using a capacitor as: $eV(dn/dt) \rightarrow C_n(dV_n/dt) \propto I$. Since the value of the carrier density n above the threshold is within the range of 10^{24} m^{-3} , it is unreasonable to directly represent n by any circuit element or value. To circumvent this problem, it is necessary to

transform the carrier density n into another physical quantity. Fortunately, the voltage drop V_n in the active region of a semiconductor laser actually corresponds to the separation of the quasi-Fermi energies between electrons and holes, that is, $eV_n = E_{Fe} - E_{Fh}$. Therefore, since the carrier density is determined by its quasi-Fermi energy (i.e., $n(E_{Fe})$ and $n(E_{Fh})$), it is a function of V_n as well; i.e., $n(V_n)$. As a result, if the change rate of the carrier density is implemented by a capacitor, then

$$eV \frac{dn}{dt} = eV \frac{\partial n}{\partial V_n} \frac{dV_n}{dt} \equiv C_n \frac{dV_n}{dt} \quad (7)$$

where the capacitor is defined by $C_n(V_n) = eV(\partial n / \partial V_n)$. It should be noted that the value of this capacitor strongly depends on V_n . In fact, it resembles the exponential relationship. In the SPICE syntax, the nonlinear element of a capacitor can only be represented by a second-order polynomial form as given in [1]. That is: $C(V) = C_0(1 + a_1V + a_2V^2)$. Since the carrier density is exponentially dependent on the Fermi energy, it is almost impossible to represent $C_n(V_n)$ by such a second-order polynomial form with reasonable accuracy. However, such an approach has been used by the Xu group [7][8], Rossi et al. [11] and Mena et al. [14]. Unfortunately, no justification is given for representing the rate equation by $C_n(V_n)$ in their work, nor is the method by which the relationship is implemented the $C_n(V_n)$ in SPICE codes given. As a consequence of this discussion, it was decided not to use this approach in this work.

An alternative approach is to transform the change rate of the carrier density as: $eV(dn/dt) \rightarrow \tau_n(dI_n/dt) \propto I$. Such a transformation links the value of the carrier density to the value of the current. This can be achieved if the carrier density n is transformed into a current I_n by the definition: $I_n \equiv eVn/\tau_n$, where τ_n is arbitrary time constant. The reason for the choice is that since the value of n is a function of V_n ; the current I_n should be a function of V_n . As a result, a circuit element must be found to represent the relationship between I_n and V_n . Since the value of the carrier density n is exponentially dependent on the value of the quasi-Fermi energy E_{Fe} , and thus V_n , it can be expected that I_n will also be exponentially dependent on V_n . Coincidentally, the current in a diode exponentially depends on the voltage; therefore, $I_n(V_n)$ can be well represented by a diode. In SPICE, the I - V relationship of a diode is described by

$$I_n(V_n) \approx I_s \left[\exp\left(\frac{V_n - I_n R_s}{\eta_d V_T}\right) - 1 \right] \quad (8)$$

where $V_T = k_B T/q$, I_s is the saturation current, R_s is the series resistor of the diode, and η_d is the parameter to distinguish the different contribution between the diffusion current ($\eta_d \approx 1$) and the recombination generation current ($\eta_d \approx 2$). The parameters I_s , R_s and η_d are chosen to represent the real $I_n(V_n)$ as close as possible. In this model, $\eta_d = 2$ is chosen to characterise the recombination feature in the active region. Note that at $V_n = 0$ and $I_n = I_s$, the carrier density is the intrinsic carrier density for the intrinsic active region, i.e., $n = n_i$. Therefore, $I_s = eVn_i/\tau_n$ is used in this work. Representing $I_n = eVn(V_n)/\tau_n$ by a diode, (6) can be rewritten as

$$\eta_{inj} I_{inj} = I_{leak} + I_{SRH} + I_{spont} + I_{Aug} + I_{stim} + \tau_n \frac{dI_n}{dt} \quad (9)$$

Following this transformation, the physical meaning of the original rate equation is more transparent. For the dc case, that is, $\tau_n \cdot dI_n/dt = 0$ in (9), the injection current is channelled into the leakage current, SRH recombination, spontaneous-emission recombination, Auger recombination or stimulated-emission recombination. Of course, the leakage, SRH and Auger process do not produce any light, so they are nonradiative recombinations. In contrast, the spontaneous-emission and stimulated-emission recombinations are radiative processes because they generate light: incoherent light by spontaneous emission and coherent light by stimulated emission.

After settling this controversial issue (representing the dn/dt term), it appears almost impossible to directly represent $\tau_n \cdot dI_n/dt$ by a SPICE circuit. To circumvent this problem, a 'derivative circuit' with an *artificial* capacitor and a current-controlled voltage source $C_n(dV_{I_n}/dt)$ can be used to represent $\tau_n(dI_n/dt)$ utilising the following transformations: $\tau_n \rightarrow C_n$ and $I_n \rightarrow V_{I_n}$. Note that in the discussion, the arrow symbol is used to indicate the transformation of variables, although such a transformation may not preserve the physical unit of the original variables. For example, in this case, if τ_n

= 10 ns is assumed, then its correspondent capacitance will be $C_n = 10$ nF. This part of circuit should be detached from the main circuits for carrier density. If it is connected to the main circuits for carrier density, then there will be a conflict between the voltage on the diode V_n and the 'dummy' voltage V_{I_n} . However, because V_n represents the quasi-Fermi energy separation in the active region, a physical quantity in which is interested, the diode is kept in the main circuit for carrier density and the circuit representing $C_n(dV_{I_n}/dt)$ is detached from the main circuit for carrier density. For this reason, $C_n(dV_{I_n}/dt)$ is termed a derivative circuit, because the main function of $C_n(dV_{I_n}/dt)$ is to represent $\tau_n(dI_n/dt)$ in the circuits.

The next step taken is to transform the photon rate equation into a circuit equation bearing in mind that $I_{spon} = eVR_{spon}$ and $I_{stim} = eV\psi_g G_s$ in the device are to represent the real spontaneous and stimulated recombination currents in the circuit model. Multiplying (2) on both sides by eV/Γ , this gives

$$I_{stim} + \beta I_{spon} = \frac{eV}{\Gamma} \cdot \frac{s}{\tau_s} + \frac{eV}{\Gamma} \cdot \frac{ds}{dt} \quad (10)$$

Since the unit on the right-hand side of (10) is current, and only the circuit element of a capacitor has the characteristics that the time derivative of its voltage equals its current, that is, $C_s(dV_s/dt) = I_s$; there is no choice but to relate the photon density to the voltage, that is, $s \propto V_s$. In addition, if the photon density is chosen to be related to the current, $s \propto I_s$, then $(eV/\Gamma) \cdot (ds/dt)$ will be in the form of $\tau_s(dI_s/dt)$. The drawback of this latter choice is that another additional "derivative circuit" becomes involved, which is more complicated than incorporating a simple capacitor. Therefore, a voltage in this work will represent the photon density. However, it can be proved to be very impractical if the photon density s is directly transformed into voltage, since usually $s \approx 10^{20} \sim 10^{22} \text{ m}^{-3}$ when the device is biased above the threshold. In addition, the SPICE compiler will not accept such a range of voltage values. Fortunately, the optical power P , which directly relates to the photon density s , emitted by a laser diode is usually within the mW range. This suggests that the emitted optical power turns out to be a suitable variable for transforming photon density s into the voltage unit having a mV range. It is well known that the total output power from *two mirror facets* is related to the photon density s by:

$$P = \frac{\hbar\omega_l \psi_g \alpha_{mirr} V}{\Gamma} s \quad (11)$$

Defining the 'optical voltage' by $P[\text{W}] \rightarrow V_s[\text{V}]$, the final circuit equation for the photon rate equation becomes:

$$I_{stim} + \beta I_{spon} = \frac{V_s}{R_s} + C_s \frac{dV_s}{dt} \quad (12)$$

where the resistor R_s and the capacitor C_s are defined by $\hbar\omega_l \tau_s / e\tau_m \rightarrow R_s$ and $e\tau_m / \hbar\omega_l \rightarrow C_s$, respectively, and the mirror lifetime of a photon $\tau_m \equiv 1/\psi_g \alpha_{mirr}$ is used in the equations.

Transforming the rate equation for the electron temperature into a circuit model follows a similar pattern. First, some coefficients are defined as the following:

$$\begin{aligned} \gamma_{inj}^e &\equiv \frac{\tau_{e-L}}{eV} \left(\frac{\partial u_e}{\partial T_e} \right)^{-1} \langle \Delta E_{inj}^e \rangle, \quad \gamma_{stim}^e \equiv \frac{\tau_{e-L}}{eV} \left(\frac{\partial u_e}{\partial T_e} \right)^{-1} \langle \Delta E_{stim}^e \rangle, \\ \gamma_{Aug}^e &\equiv \frac{\tau_{e-L}}{eV} \left(\frac{\partial u_e}{\partial T_e} \right)^{-1} \langle \Delta E_{Aug}^e \rangle, \quad \gamma_{fca}^e \equiv \frac{\tau_{e-L}}{eV} \left(\frac{\partial u_e}{\partial T_e} \right)^{-1} \langle \Delta E_{fca}^e \rangle, \end{aligned} \quad (13)$$

and the free-carrier-absorption current is represented by $I_{fca}^e \equiv eV\psi_g \alpha_{fca}^e s$. Note that $u(T_e) \equiv (\partial u_e / \partial T_e) T_e$ can be used and also it can be assumed that $(\partial u_e / \partial T_e) \approx (\partial u_h / \partial T_h)$. Since $u_e \approx 3n_e k_B T_e / 2$, $u_h \approx 3n_h k_B T_h / 2$ and $n_e = n_h$ are also assumed in this work, this assumption implies that $T_e \approx T_h$. As long as the electron temperature is not significantly different from the hole temperature, this assumption seems to be reasonable. Implementing the assumption, (3) becomes

$$\gamma_{inj}^e (I_{inj} I_{inj} - I_{leak}) + \gamma_{stim}^e I_{stim} + \gamma_{Aug}^e I_{Aug}^e + \gamma_{fca}^e I_{fca}^e = (T_e - T_L) + \frac{\tau_{e-L}}{\tau_{e-h}} (T_e - T_h) + \tau_{e-L} \frac{dT_e}{dt} \quad (14)$$

Since the physical quantities on the left-hand side of (13) are currents, the same unit on the right-hand side of (14) should be kept as well. Therefore, either $C_e(dV_e/dt)$ or $\tau_e(dI_e/dt)$ can be used to represent the $\tau_{e-L}(dT_e/dt)$ term on the right-hand side of (14) to match the unit of current. However, since $C_e(dV_e/dt)$ only involves a single capacitor, while $\tau_e(dI_e/dt)$ needs an additional 'derivative circuit'. $C_e(dV_e/dt)$ is chosen rather than $\tau_e(dI_e/dt)$ to represent $\tau_{e-L}(dT_e/dt)$. Now since the temperatures T_e , T_h and T_L in the device are usually of the order of 300 K, it is sensible directly to represent them by voltages: $T_e[\text{K}] \rightarrow V_e[\text{V}]$, $T_h[\text{K}] \rightarrow V_h[\text{V}]$, $T_L[\text{K}] \rightarrow V_L[\text{V}]$, and the capacitor by $\tau_{e-L}[\text{s}] \rightarrow C_e[\text{F}]$. It should be noted that the values of voltage, resistance and capacitance defined in this part of the circuits do not really represent the physical units of volts, ohms and farads. They represent the values of the original variables instead. For example, the voltage V_L in volt actually represents the lattice temperature T_L in Kelvin. The original physical unit of γ is K/A while it is dimensionless in (14).

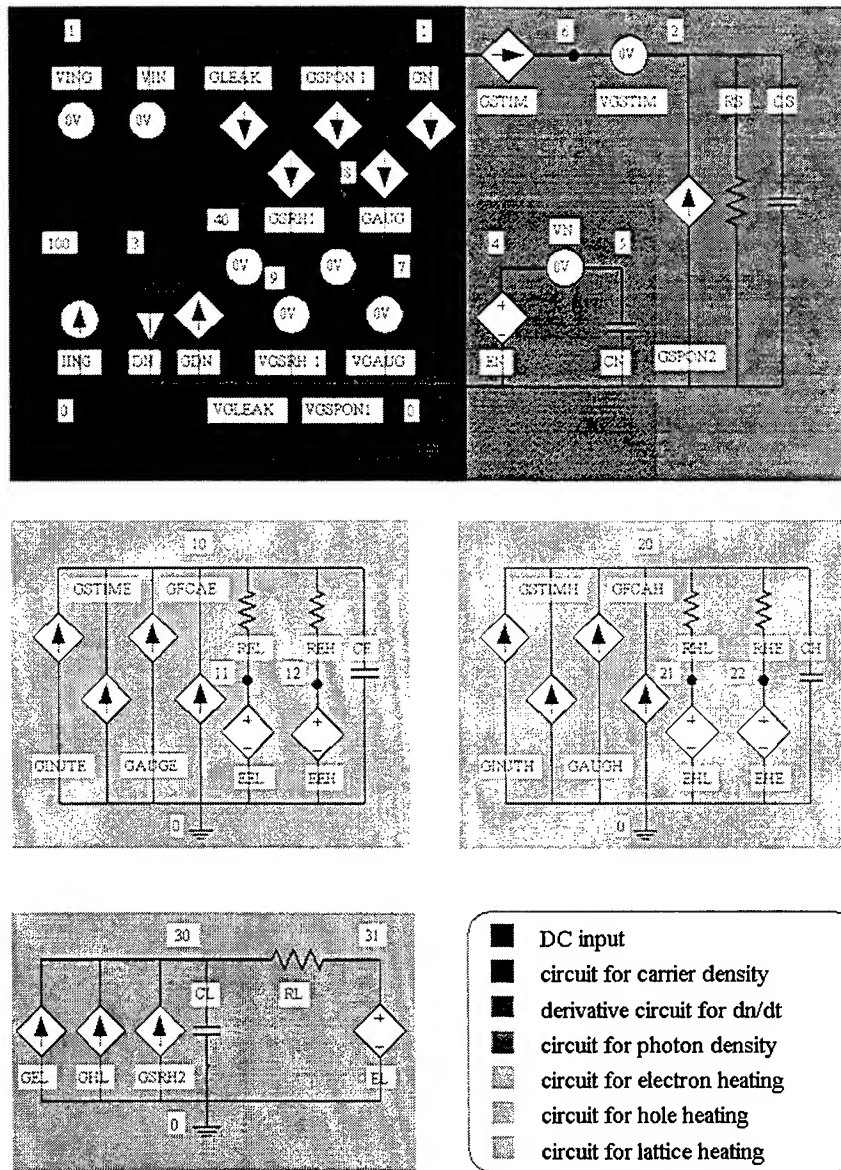


Fig. 1. SPICE circuit model with carrier and lattice heating.

The choice of representing the electron temperature T_e by a voltage V_e certainly causes difficulties for the first and second term on the right-hand side of (14) because of the disagreement among their units with others. To circumvent this problem, two 'dummy' resistors are used $1\Omega \rightarrow R_{eL}$ and $\tau_{e-h}/\tau_{e-L} [] \rightarrow R_{eh}[\Omega]$ adding to the first and second terms in (14), respectively. As a result, the units of all the terms in (14) are currents. Finally, the rate equation of the electron temperature becomes

$$\gamma_{inj}^e (\eta_{inj} I_{inj} - I_{leak}) + \gamma_{stim}^e I_{stim} + \gamma_{Aug}^e I_{Aug}^e + \gamma_{fca}^e I_{fca}^e = \frac{V_e - V_L}{R_{eL}} + \frac{V_e - V_h}{R_{eh}} + C_e \frac{dV_e}{dt} \quad (15)$$

which can be implemented into SPICE codes. By a similar derivation, transforming the rate equation for the hole temperature into a circuit model can be achieved by setting the hole temperature T_h to a voltage V_h and T_L to a voltage V_L . The circuit model based on the results of (9), (11), and (14) is shown in Fig. 1.

4. RESULTS AND DISCUSSION

Once the circuit models are given, it will be rather straightforward to write a SPICE code according to the circuit models. Though, attentions should be paid to the numerical limitations of the SPICE compiler itself. SPICE provides three basic features to probe and characterise a circuit system: dc, ac and transient responses. Generally, these three features are also used to characterise the properties of a semiconductor laser. Of course, the ac response and the transient response characterise the same temporal behaviour of the device. The ac response represents the system properties in the frequency domain while the transient response directly characterises the system behaviour in the time domain. For semiconductor lasers, the ac response is generally used to characterise the bandwidth of the devices. In addition, the transient response is usually employed to describe the turn-on behaviour of the devices. These built-in features in simulating the dc, ac and transient responses unquestionably give SPICE circuit models an unambiguous merit over their counterpart, the rate equations. For example, in order to simulate the ac response, a small-signal analysis on the rate equations must be provided. Such an analysis can be rather involved (sometimes unnecessarily complicated) especially in the case when dealing with the issues of the carrier and lattice heating. In addition, different numerical procedures must be implemented separately for the ac and transient responses when using the rate-equation approach. This certainly adds more numerical complexity onto the theoretical models themselves, even to the models representing the same device. Apparently, the simplicity and consistency in simulating the dc, ac and transient responses by using the SPICE circuit model provides a definite merit to allow the extraction of the physical parameters from the measurement data of the device. It should be kept in mind that, the purpose of the simulations presented in this work is not to exhaustively evaluate the effect of each parameter on the performance of the device, or to extract the values of these parameters by fitting the simulation results with the measurement data. The simulation presented in the following is for the purpose of demonstrating the capabilities especially with respect to the influences or performance of the heating effects and versatilities of the SPICE circuit models for semiconductor lasers.

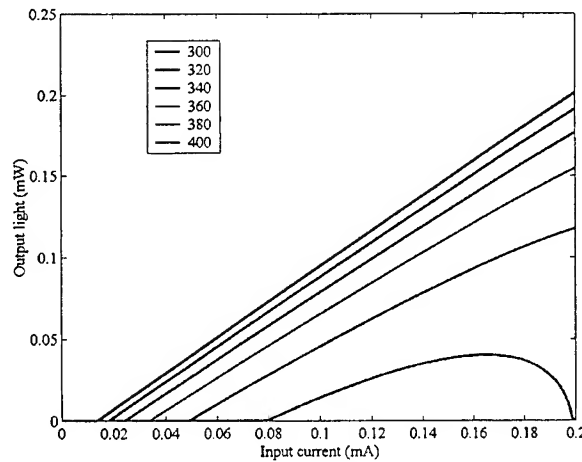


Fig. 2. L-I relationship of a semiconductor laser simulated with the temperature-dependent feature of the leakage current and Auger process for different heat-sink temperatures T_{HS} (in the unit of Kelvin).

In practice, the heating effects are usually investigated by changing the heat-sink temperature. This is because the changes of the carrier or lattice temperature within the device due to the injection current is almost impossible to directly measure by experimental means, and can only be estimated by theoretical tests. Of course, this work is useful in assessing the carrier and lattice temperatures in the active region of the devices but is carried out following device fabrication. However the circuit models developed can be used to simulate realistic experimental situations by changing the heat-sink temperatures T_{HS} in the SPICE codes. The simulation results of the L-I relationship for different heat-sink temperatures T_{HS} are shown in Fig. 2. Apparently, increasing the heat-sink temperature increases the threshold current and L-I nonlinearity. In this simulation, if the heat-sink temperature changes from 300K to 400K, the threshold current will change from 10 mA to 80 mA. This certainly validates that the threshold current is almost exponentially dependent on the heat-sink temperature: $I_{th} \propto \exp(T_{HS}/T_0)$, where the characteristic temperature $T_0 \approx 50$ K is extracted from the simulation.

The L-I nonlinearity is usually attributed to the lattice heating if the heat-sink temperature is kept at a constant value. However, the results in the simulation shown in Fig. 2 demonstrate that the L-I nonlinearity can be influenced by the electron energy relaxation time τ_{e-L} . Of course, attributing all heating effects just to the lattice heating is not only physically unrealistic but also numerically questionable. Incorporating the carrier heating into the heating model, which appears necessary and indispensable if realistic physical models are to be established.

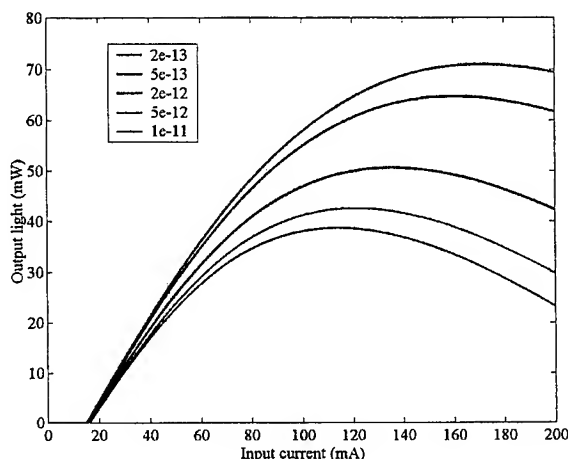


Fig. 3. L-I relationship for different electron-lattice energy relaxation times τ_{e-L} (in the unit of second).

The transient responses simulated by SPICE for the output power and electron temperature with different electron-lattice energy relaxation time τ_{e-L} are shown in Fig. 4 and 5, respectively.

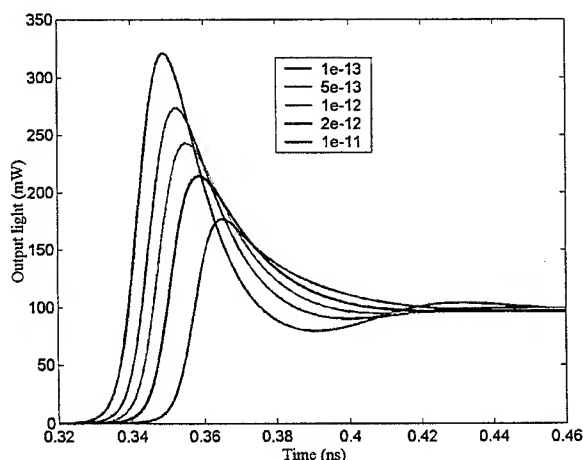


Fig. 4. Transient response of the output light for different electron-lattice energy relaxation times τ_{e-L} (in the unit of second).

Unambiguously, the results in Fig. 4 show that increasing τ_{e-L} will increase the damping rate γ in the transient response case. That is, the carrier heating will result in a damping in the dynamic properties of a semiconductor laser. The electron and hole temperatures will rapidly increase as the injection current switches on at $t = 0$ sec. Initially, only a small number of carriers exist in the active region, and the sudden supply of the injection heating will be distributed among them. As a result, each carrier will gain a huge amount of energy and thus the carrier temperature will suddenly rise to a dramatic level. As the heated carriers start to release their energy and the carrier density gradually increases as well, the carrier temperature will then progressively cool down. As the laser light starts to build up inside the cavity and then emitted by the mirrors, the stimulated recombination and free-carrier-absorption heating effects will heat carriers. Consequently, the carrier temperature will raise again, the increase of the carrier temperature being proportional to the photon density. After the initial transient variation the photon density settles down to its dc value, that is, the steady-state, and the carrier temperature will correspondingly settle down to its dc value. It should be noted that the small increase of the electron temperature between 0.1 ns and 0.2 ns in Fig. 5 is resulted from the Auger heating that will becomes effective when the carrier density in the active region reaches a certain value.

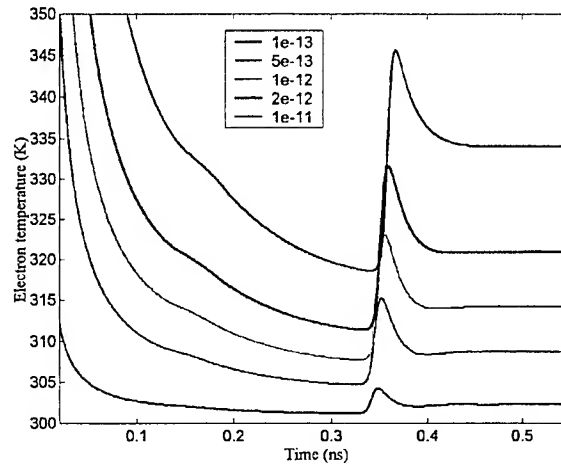


Fig. 5. Transient response of the electron temperature for different electron-lattice energy relaxation times τ_{e-L} (in the unit of second).

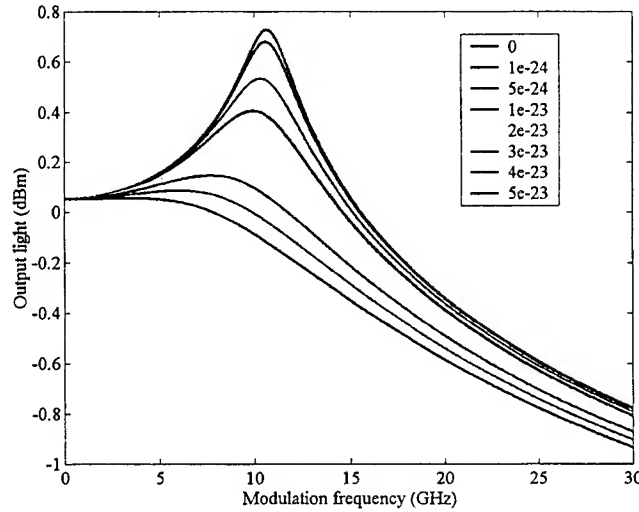


Fig. 6. AC response of a semiconductor laser with different nonlinear gain coefficients \mathcal{E}_{shb} (in the unit of m^3).

The damping caused by the carrier heating coincidentally has similar features to the damping due to the spectral-hole burning. As a result, the effects of the carrier heating are conventionally included into the nonlinear gain coefficient ε_{shb} as the effect of spectral-hole burning. The value of the nonlinear gain coefficient ε_{shb} only affects the damping rate and does not significantly affect the value of the resonant frequency. This is also clearly verified by the simulation results shown in Fig. 6.

5. CONCLUSION

In this thesis, a new proposed SPICE circuit model for semiconductor lasers incorporating the effects of the carrier and lattice heating, which has been developed, implemented and realised. The circuit is achieved from the rate equations that govern the dynamics of carrier density, photon density, electron temperature, hole temperature and lattice temperature in the active region of semiconductor lasers. The set of the rate equations used provide a solid, sound and physically based theory for quantitatively describing the carrier and lattice heating in semiconductor lasers without unnecessary non-physical arguments (such as $I \cdot V - P$ in the previous work) to justify the heating effects. Based on this physical model, the rate equations have been transformed into a circuit model by tactically choosing suitable circuit elements and quantities to represent the physical quantities in the rate equations. All the physical quantities that depend on the carrier temperature (such as gain, the Auger process and leakage current) are explicitly included in the circuit model by representing them as voltage-controlled current source, the carrier temperatures then being represented by voltages. SPICE codes have been developed exactly according to this circuit model. It has been shown and demonstrated that this single SPICE circuit model alone can simulate the dc, ac (i.e., small signal in the frequency domain), and transient (i.e., large signal in the time domain) responses of semiconductor lasers. The new proposed SPICE circuit thus fully meets the initial objectives set, i.e. it is universal, physically based, flexible and expandable.

Without doubt, the role of Electronic Design Automation (EDA) in the modern electronic industries cannot be over emphasised. SPICE circuit simulation is almost indispensable in designing analogue electronic circuits. The needs of the SPICE circuit models for semiconductor lasers used in conjunction with other electronic circuits and systems (for example, the transmitter modules of fibre optic communication systems) are thus foreseeable. One of the major merits of using SPICE circuit models for devices is its flexibility in modifying the developed SPICE codes to accommodate more physical properties associated with devices. In other words, any physical properties that can be transformed into the models of resistances, capacitances, inductance, voltage and current sources can be incorporated into the original circuits without too many elaborate efforts. This suggests that further work can be under taken in order to improve the new SPICE circuit models presented in this work, for example:

- 1) In this work, the new SPICE circuit model only simulated the physical processes in the active region. In other words, the physical processes outside the active region were either neglected (for example, the heating mechanism outside the active region) or averaged (such as the injection efficiency). It should be noted that, in vertical-cavity surface-emitting lasers (VCSELs), the heating processes in the distributed Bragg reflection (DBR) mirrors could be as significant as in the active region. Under such a circumstance, additional circuits are needed to correctly model the overall heating behaviour within the devices. To incorporate these physical processes into the circuit model is certainly feasible; but attentions should be paid to the numerical complexity or numerical stability for SPICE codes with too many circuit elements.
- 2) In this work, only the intrinsic physical properties were considered for semiconductor lasers. In other words, their extrinsic properties, such as parasitic resistances and capacitances associated with the devices themselves or the external wire bonding, were not considered. In practice, the parasitic properties might be an important factor affecting the properties of semiconductor lasers, especially in their high-speed performance. Including parasitic resistances and capacitances into the SPICE circuit model will be reasonably straightforward. However, their values usually cannot directly be assessed by either experimental measurements or theoretical calculations. But, if the parasitic resistances and capacitances are included into the circuit model presented in this work, their values can be estimated by measured ac data. This feature demonstrates another merit of using an extensive SPICE circuit model in characterising the properties of semiconductor lasers.
- 3) Only bulk semiconductor lasers are used as the numerical examples in this work, while quantum-well (QW) lasers are not particularly discussed. However, the physical models presented in this work are general and can be applied to QW lasers if the correspondent parameters are given. The carrier and lattice heating processes in QW lasers should be rather similar to those in bulk lasers. It has been shown that the carrier energy relaxation time for QW lasers calculated by first principles do not present any considerable difference from those for bulk lasers. On the other hand, the differential gain of QW lasers is substantially higher than that of bulk lasers. In addition, it should be noted that, other physical processes, such as the carrier transport, capture and escape, are not presented in bulk lasers but unique to QW lasers. In

some cases, for example, if the separate confinement heterostructure (SCH) is very large, their effects may become crucial. Under such a circumstance, additional rate equations are needed to characterise their effects. Accordingly, extra circuits should be incorporated to describe the carrier transport, capture and escape processes.

- 4) The SPICE circuit model provides an indisputable advantage for designing semiconductor lasers used in conjunction with other electronic circuits or systems, especially in designing the transmitter modules for fibre optic communication systems. The transmitter modules, receiver modules and the optical fibres are the three major components in a fibre optic communication system. It is thus perceivable that, if SPICE circuit models can be further implemented for the receiver modules and optical fibres, they can be used to simulate a whole fibre optic communication system. This surely defines one of the ultimate goals for using SPICE circuit models in simulating the optoelectronic devices and systems.

In conclusion, the SPICE circuit models presented in this work demonstrate the capability and versatility of SPICE in simulating the complicated carrier and lattice heating processes in semiconductor lasers and represent a state of the art modelling tool using leading edge understanding of physical processes. Further enhancement to this work can provide a step towards simulating the optoelectronic devices and systems for fibre optic communication systems.

REFERENCES

- [1] G. F. Carey, W. B. Richardson, C. S. Reed, B. J. Mulvaney, *Circuit, Device, and Process Simulation: Mathematical and Numerical Aspects*, New York: John Wiley & Sons, 1996.
- [2] P. W. Tuinenga, *SPICE: A Guide to Circuit Simulation & Analysis Using PSpice*, 3rd ed., New Jersey: Prentice-Hall, 1995.
- [3] R. S. Tucker, "Circuit model of double-heterojunction laser below threshold," *IEE Proc. -Optoelectron.*, vol. 128, pp. 101-106, 1981.
- [4] R. S. Tucker, "Large-signal circuit model for simulation of injection-laser modulation dynamics," *IEE Proc. -Optoelectron.*, vol. 128, pp. 180-184, 1981.
- [5] M. F. Lu, C. Juang, M. J. Jou, B. J. Lee, "Study of carrier transport effects on quantum well lasers using a SPICE simulator," *IEE Proc. -Optoelectron.*, vol. 142, pp. 237-240, 1995.
- [6] M. F. Lu, J. S. Deng, C. Juang, M. J. Jou, and B. J. Lee, "Equivalent circuit model of quantum-well lasers," *IEEE J. Quantum Electron.*, vol. 31, pp. 1418-1422, 1995.
- [7] N. Bewra, D. A. Suda, G. L. Tan, F. Chatenoud, and J. M. Xu, "Modeling of quantum-well lasers with electro-opto-thermal interaction," *IEEE J. Quantum Electron.*, vol. 1, pp. 331-340, 1995.
- [8] D. S. Ellis and J. M. Xu, "Electro-opto-thermal modeling of threshold current dependence on temperature," *IEEE J. Quantum Electron.*, vol. 3, pp. 640-648, 1997.
- [9] Benjamin P. C. Tsou and David L. Pulfrey, "A versatile SPICE model for quantum-well lasers," *IEEE J. Quantum Electron.*, vol. 33, pp. 246-254, 1997.
- [10] Benjamin P. C. Tsou and David L. Pulfrey, "The influence of coulomb enhancement on modulation properties of quantum-well lasers," *IEEE J. Quantum Electron.*, vol. 34, pp. 318-324, 1998.
- [11] Giammarco Rossi, Roberto Paoletti and Marina Meliga, "SPICE stimulation for analysis and design of fast 1.55 μm MQW laser diodes," *IEEE J. Lightwave Technol.*, vol. 16, pp. 1509-1516, 1998.
- [12] M. Ganesh Madhan, P. R. Vaya, and N. Gunasekaran, "Circuit Modeling of multimode bistable laser diodes," *IEEE Photon. Technol. Lett.*, vol. 11, pp. 27-29, 1999.
- [13] K. Czotscher, S. Weisser, A. Leven and J. Rosenzweig, "Intensity modulation and chirp of 1.55- μm multiple-quantum-well laser diodes: modeling and experimental verification," *IEEE J. Quantum Electron.*, vol. 5, pp. 606-612, 1999.
- [14] P. V. Mena, J. J. Morikuni, S. M. Kang, A. V. Harton, and K. W. Wyatt, "A simple rate-equation-based thermal VCSEL model," *IEEE J. Lightwave Technol.*, vol. 17, pp. 865-872, 1999.
- [15] C. Y. Tsai, C. H. Chen, T. L. Sung, C. Y. Tsai, and J. M. Rorison, "Theoretical modeling of carrier and lattice heating effects for frequency chirping in semiconductor lasers," *Appl. Phys. Lett.*, vol. 74, pp. 917-919, 1999.
- [16] C. Y. Tsai, C. H. Chen, T. L. Sung, C. Y. Tsai, and J. M. Rorison, "Theoretical modeling of the small-signal modulation response of carrier and lattice temperatures with the dynamics of nonequilibrium optical phonons in semiconductor lasers," *IEEE J. Select. Topics Quantum Electron.*, vol. 5, pp. 596-605, 1999.

HF signal measurement device for DVD disc

Shuh-Tai Lu King-Yin Wang Kuang-Yang Chuang
Ching-Ping Kuei Der-Ray Huang

Opto-Electronics & System Laboratories
Industrial Technology Research Institute
Chutung, Hsinchu 310, Taiwan, R.O.C.

ABSTRACT

A DVD disc signal measurement device is introduced in this paper. The device is fed high frequency signal and EFM+ signal from a DVD disc driver. By using EFM+ signal as input reference, the device is capable of recording all the peak (or bottom) values of a specified xT signal in an user defined duration. To improve the accuracy of the measurement device, the ac and dc components of high frequency signal are proceeded individually and then combined to give the corrected peak (or bottom) values. The corrected peak value is given by adding the dc component and the peak of the AC component. The corrected bottom value is given by subtracting the peak of inverse AC component from the dc component.

Keywords: DVD disc, HF signal, Peak hold

1. INTRODUCTION

In recent years, the technology of information storage, especially that based on optical recording media, has been rapidly developed and accepted [1-10]. Optical storage techniques are adequate for audio as well as video data recording. Moreover, they are especially suitable for the storage of information such as pictures, computer softwares, and papers. In general, optical storage technique is one of the most advanced techniques to be adopted in the information storage. Many advantages have been found in this technique, including

- (i) noncontact recording
- (ii) moistureproof
- (iii) long data saving time
- (iv) compact and solid.

Usually, the shape and position of pits on a disc are important items in optical storage research. They keep close relation with two indices, peak values and bottom values of high frequency (HF) signal [11-14], which can be used to evaluate the quality of pits on the disc. Therefore, this paper proposes a HF signal measurement device to record the peak (or bottom) values of the xT HF signal in an user defined duration ΔT . After all peak values and bottom values are collected and processed, the quality of pits can then be evaluated. In addition, with a standard disc, the quality of disc driver can be verified.

2. BASIC PRINCIPLE

Fig. 1 is the flow chart of signal processing of the device. The device has two inputs, HF signal and EFM+ signal, that come from a DVD disc driver. The device will pick up every peak (or bottom) value of the HF signal, no matter what the period of the EFM+ is. Before the next peak (or bottom) of HF signal coming, the period of current EFM+ has been decided by the device. If the period of current EFM+ is equal to xT , then the picked up peak (or bottom) value is saved in static random access memory (SRAM), otherwise it is abandoned. The notation T means the period of system clock and the x , which can be specified by the user, is an integer between 3 and 14. The user can also specify a data collection time ΔT . When the collection time is up, the computer will down load data from the SRAMs. After the down load procedure is completed, all the collected xT peak (or bottom) values of HF signal can be analyzed and the quality of pits can then be decided.

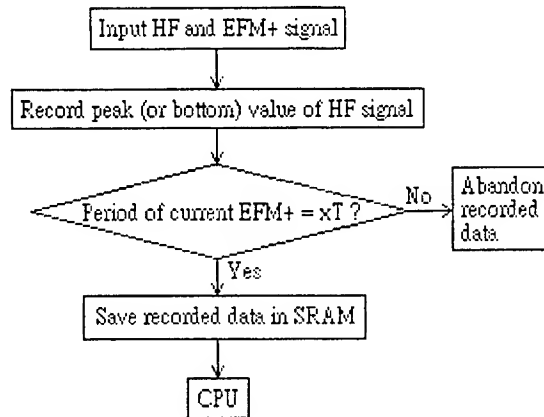


Fig. 1 Flow chart of signal processing

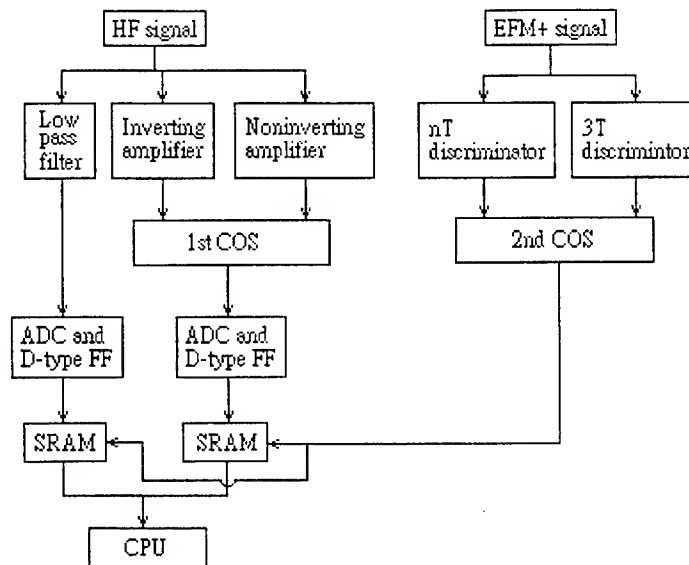


Fig. 2 Block diagram of HF signal measurement device

Fig. 2 is the block diagram of HF signal measurement device. The HF signal is fed to a low pass filter, an inverting amplifier, and a non-inverting amplifier. The output of the low pass filter is dc component of the HF signal. The inverting amplifier provides signal inversion with respect to the ac component of the HF signal. That means the original bottom value can be determined from

$$V_{\text{bottom}} = V_{\text{avg}} - (V_{\text{npeak}} - V_{\text{avg}}) / A_n \quad (1)$$

where V_{bottom} = original bottom value of the HF signal
 V_{avg} = dc component of the HF signal
 V_{npeak} = peak value of the inverting amplifier output
 A_n = gain of the inverting amplifier.

The non-inverting amplifier provides signal amplification with respect to the ac component of the HF signal. Thus, the original peak value of the HF signal can be described by

$$V_{\text{peak}} = V_{\text{avg}} + (V_{\text{ppeak}} - V_{\text{avg}}) / A_p \quad (2)$$

where V_{peak} = the original peak value of the HF signal
 V_{ppeak} = the peak value of the non-inverting amplifier output.
 A_p = gain of the non-inverting amplifier.

Also from Fig. 2 the output of low pass filter is fed to an analog to digital converter (ADC) and the converted data is then latched by the D-type Flip-Flop (FF). At the same time, the output of inverting amplifier and the output of non-inverting amplifier are also fed to the first change over switch (COS). If the bottom values are measured, the input of the 1st COS should be switched to the output of the inverting amplifier before the device working. On the other hand, if the peak values are measured, the input of the 1st COS should be switched to the output of the non-inverting amplifier before the device working. The output of the 1st COS is fed to the other ADC and the converted data is then latched by the other D-type FF.

The SRAM receives data from the relative D-type FF. But it does not hold the data in its memory unless the 2nd COS outputs a trigger signal. If the trigger signal doesn't present till the next EFM+ cycle coming, the latched data in the D-type FF will be abandoned and the data is not stored in the SRAM either. When the input of the 2nd COS is switched to the output of 3T discriminator, it means x is equal to 3 and the 3T discriminator is selected. In this case, a trigger signal will show up at the time when the EFM+ cycle is just discriminated to be 3T. On the other hand, if nT HF signal will be analyzed, the input of the 2nd COS should be switched to the output of the nT discriminator. Table 1 lists the COSs setting with respect to different HF signal analyzing requirement.

Table 1 The COSs setting with respect to different HF signal analyzing requirement

	3T HF peak values	3T HF bottom values	nT HF peak values	nT HF bottom values
The input of the 1st COS is switched to	the output of the non-inverting amplifier	the output of the inverting amplifier	the output of the non-inverting amplifier	the output of the inverting amplifier
The input of the 2nd COS is switched to	the output of the 3T discriminator	the output of the 3T discriminator	the output of the nT discriminator	the output of the nT discriminator

3. CONFIGURATION OF THE DEVICE

A detail configuration of the device is shown in Fig. 3. Some qualitative waveforms are shown in Fig. 4 for reference. The EFM+ signal shown in Fig. 4 has about 170nS to 190nS delay with respect to the HF signal V_{HF} . The dc component of V_{HF} (V_{avg}) can be fetched through the low pass filter shown in Fig. 3. The V_{avg} is acted as a reference voltage for the non-inverting amplifier, the inverting amplifier, and also the comparator. The output of the non-inverting amplifier (V_{ppeak}) combines V_{avg} and an amplified ac component of V_{HF} . Due to the slew rate limit of the non-inverting amplifier, V_{ppeak} also has a little bit time delay with respect to the HF signal V_{HF} . The output of the comparator (ENC) changes its state from LOW to HIGH at t_1 when the signal V_{ppeak} is lower than level a. At t_4 when the voltage level of V_{ppeak} is grater than level b, the ENC change back to LOW again. The peak holder keeps peak value of V_{ppeak} till the coming of a discharge signal (DISC) which is generated by the delay pulse generator Δt_1 later after t_1 . Within the duration Δt_1 the A/D converters get enough time to complete data conversion. An A/D converter converts analog signal V_{avg} into 8-bit digital data XAVG and another A/D converter converts analog signal V_{peak} into 8-bit digital data XPKD. Both digital data are locked into D-type flip-flop at the falling edge of DISC and received by SRAMs through the bus buffers. At $t_5 + \Delta t$ the 3T discriminator completes discrimination function and outputs a pulse signal (WR3T). If 3T is the selected specified period, the SRAMs will save the digital data coming from D-type flip-flops at the rising edge of WR3T. The counter will be increased at the falling edge of WR3T, which means the address of SRAMs is increased. And, the SRAMs are ready to receive the next XAVG and XPKD. If nT is the selected specified period, the nT discriminator should be used, and a pulse signal (WRnT) will be generated by the nT discriminator Δt later with respect to an nT period EFM+ signal transition from HIGH to LOW state. Now, the peak value of a specified nT HF signal (PEAK) can be calculated in digital form as

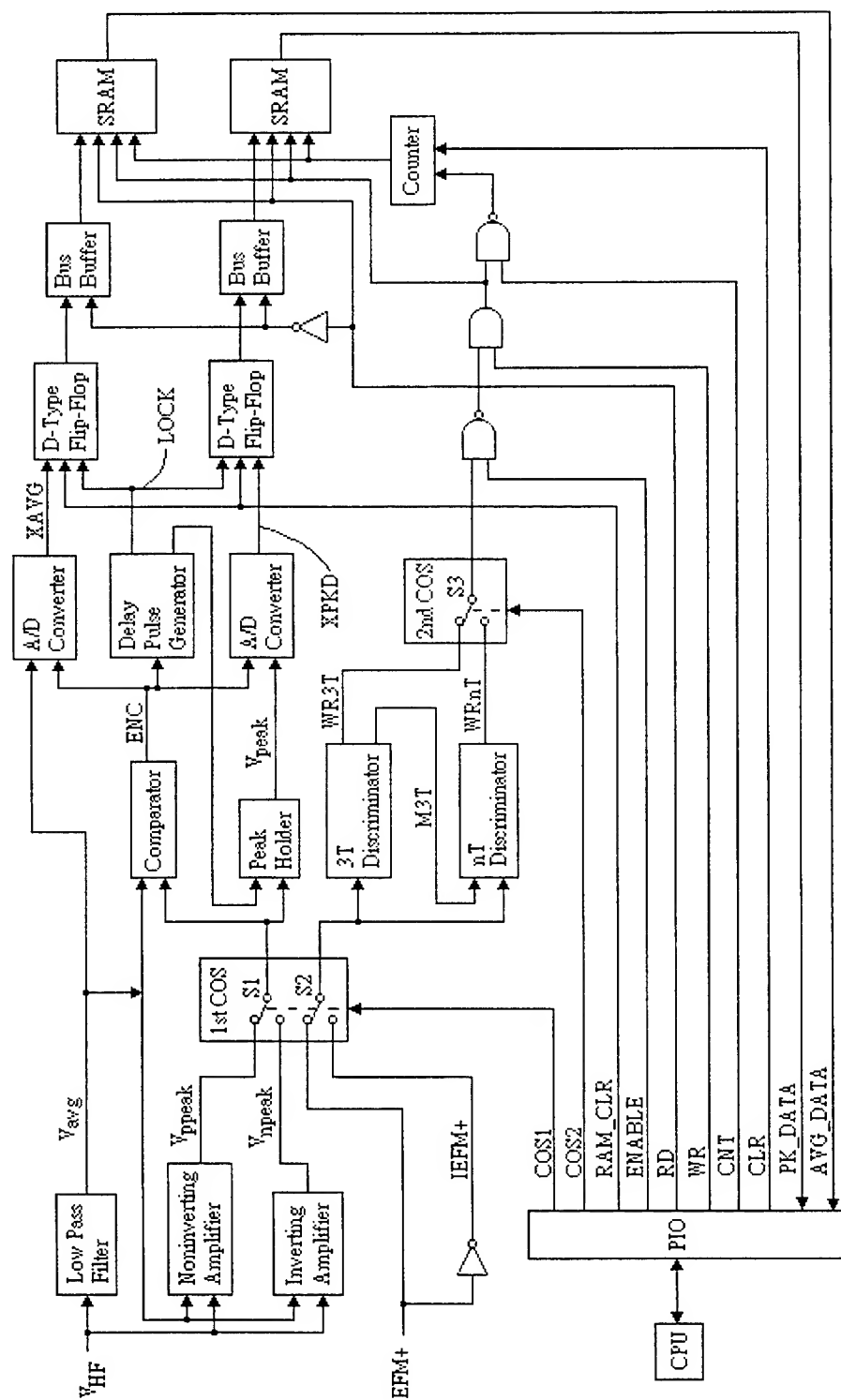


Fig. 3 Configuration of the device

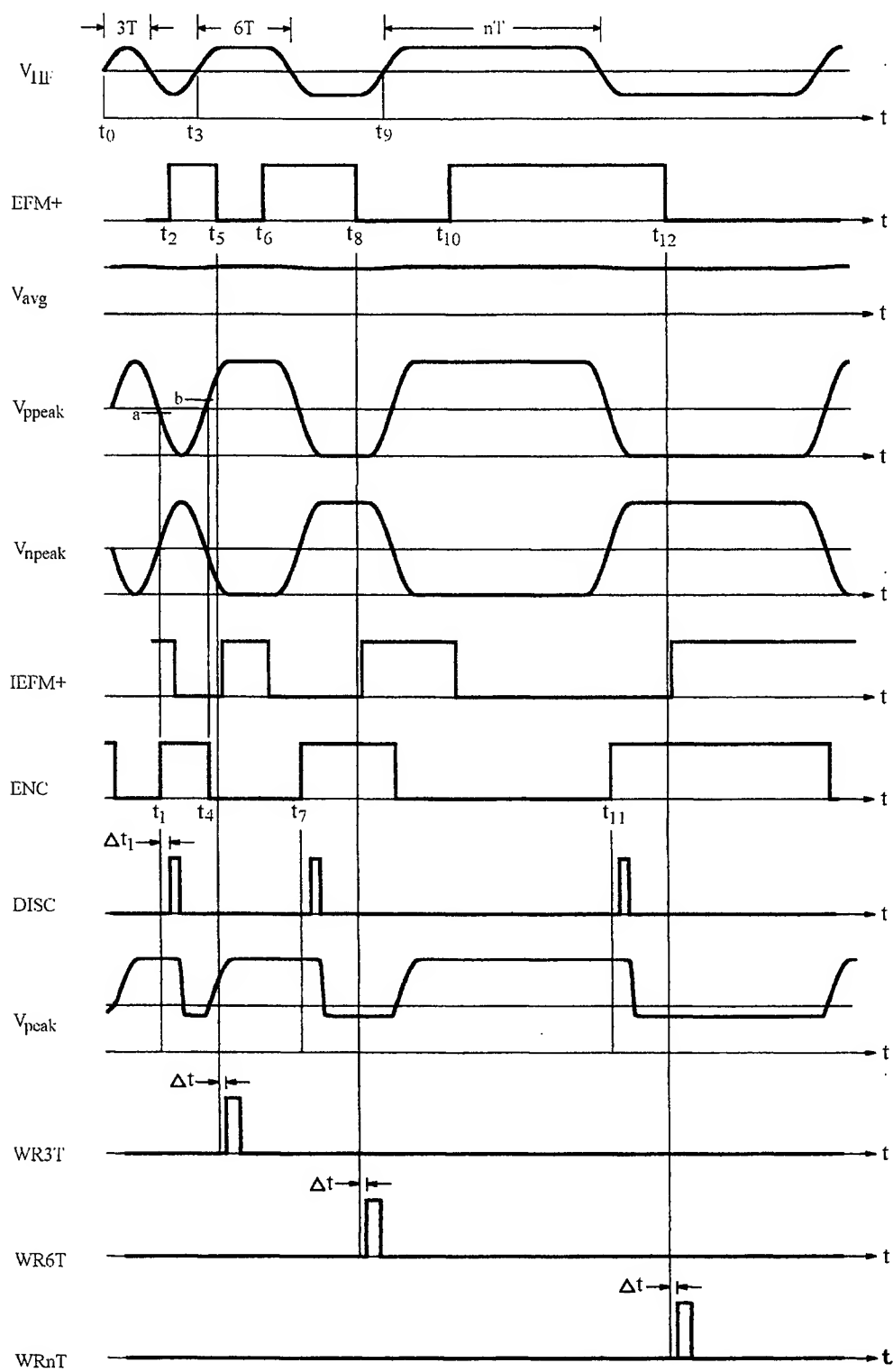


Fig. 4 Waveforms for HF measurement device

$$PEAK = K_1 \times (XAVG + (XPKD - XAVG) / A_p) \quad (3)$$

K_1 is a scaling factor which is defined as the ratio of $PEAK_{true}$ and $PEAK_{measured}$.

Also from Fig. 4 comparing the waveforms V_{ppeak} to V_{npeak} and EFM+ to IEFM+, we find the relation between V_{ppeak} and EFM+ is just like the relation between V_{npeak} and IEFM+. So the peak data recording technique can also be used in bottom data recording. Now, the bottom value of a specified nT HF signal (BOTTOM) can be calculated in digital form as

$$BOTTOM = K_2 \times (XAVG - (XPKD - XAVG) / A_n) \quad (4)$$

K_2 is a scaling factor which is defined as the ratio of $BOTTOM_{true}$ and $BOTTOM_{measured}$.

In Fig. 3 the PIO has 24 I/O pins. Sixteen pins are used as data input, where PK_DATA uses 8 pins for down load XPKD and AVG_DATA uses the remaining 8 pins for down load XAVG. Eight pins are used as control signal output where COS1 is for peak value or bottom value measurement selection. COS2 is for 3T or nT HF signal selection. ENABLE is for measurement duration setting. CLR is for resetting the counter. RD, WR, RAM_CLR, and CNT are for SRAMs clearing. RD and CNT are for down load control.

The SRAMs should be cleared before HF signal measuring. First, CLR is switched to LOW and then HIGH which clears the output of counter to 0. The RAM_CLR is set to LOW and RD is set to HIGH, which will force the input of SRAMs equal to 0. Then ENABLE and WR are set to LOW and CNT is toggled till all the memories of SRAMs are cleared.

If the HF signal measurement is going to process, RD, WR, RAM_CLR and CNT are set to HIGH. The specified nT XAVGs and XPKDs data will be saved in SRAMs in sequence from starting address 0 when ENABLE is switched to HIGH in a short specified duration. After data collection completed, the data in SRAMs will be down load to computer. At that time WR is set to HIGH, CLR is switched from LOW to HIGH to clear the counter, RD is set to LOW to isolate the D-type FFs and the SRAMs, ENABLE is set to LOW, and CNT is toggled till all the memories of SRAMs are down load into the computer memory.

Next we introduce the operation of 3T and nT discriminators illustrated in Fig. 3. Fig. 5 depicts their functional block diagram and waveforms. For illustration convenience, n uses 14 in the figure (n can be represented by any integer ranged from 4 to 14, of course). The pulse width of EFM+ could be any n times T where n is between 3 to 14. The quasi-stable interval of each monostable multivibrator is shown in Table 2.

Table 2 Quasi-stable interval setting of monostable multivibrator

monostable multivibrator	1st	2nd	3rd	4th
quasi-stable interval	2.6T	0.8T	13.6T	0.8T

The 3T discriminator operates as follows: At $t=0$, the positive-going edge of EFM+ triggers the 1st monostable multivibrator. 2.6T later, the falling edge of M3T triggers the 2nd monostable multivibrator to switch to HIGH for 0.8T (M3TP). The 1st JK FF can only outputs a pulse (WR3T) if the EFM+ has a negative transition exactly within the duration 0.8T. NOT gates exist for automatically resetting the JK FFs and make the output pulse of JK FFs about 8nS.

The 14T discriminator operates the way a little bit different from the 3T discriminator. The 3rd and the 4th monostable multivibrator will be resetted at the instant when the falling edge of EFM+ signal isn't 14T. The resetting function is accomplished by using an XOR gate and the 2nd JK FF. This avoiding wrong WR14T signals result from $(i+j)T$ EFM+ signal where $i+j$ is equal to 14.

Now consider the nT case where n isn't equal to 14. The device still can function well just only to change the quasi-stable interval of the 3rd monostable multivibrator to $(n-0.4)T$.

4. CONCLUSION

This paper introduces a DVD disc signal measurement device which can be used as a HF signal analyzing equipment to evaluate discs quality and pick up heads quality with a standard pick up head and a standard disc, respectively. The device evaluates a specified period HF signal for its peak or bottom values once at a time. Therefore, only one peak holder is

needed in the device. If different periods, peak or bottom values are going to be fetched at the same time, devices with different COSs setting are needed.

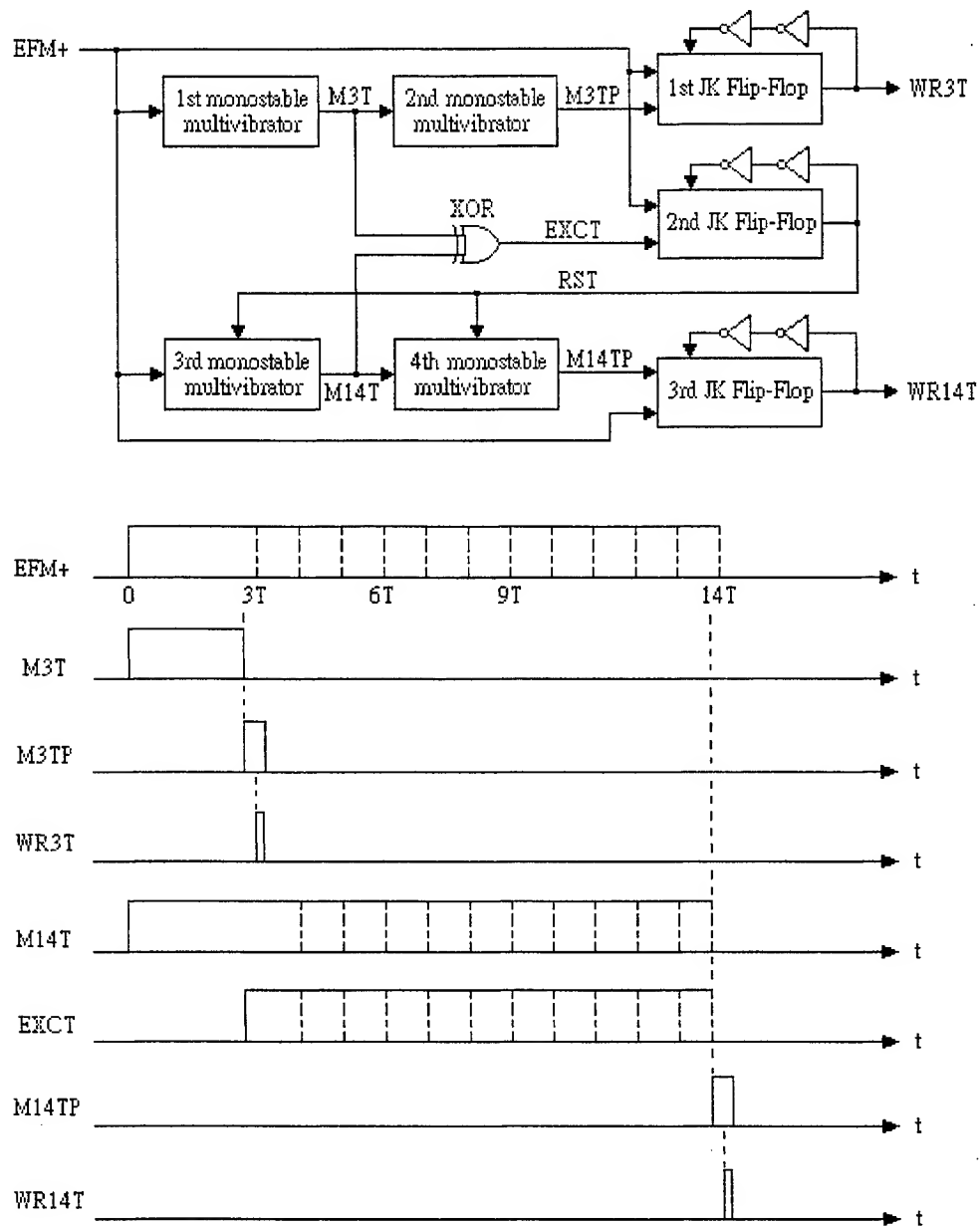


Fig. 5 Block diagram and waveforms of discriminators

5. REFERENCE

1. Nomura Shigeru, Kadoya Tetsuo, and Kinoshita Takeo, 'Process for preparing a substrate for optical recording media'. US Patent 04743409, 1988
2. Bearden Alan J. and O'Neill Michael P., 'Laser-amplified motion detector and method'. US Patent 05029023, 1991

3. Lindmayer Joseph, 'Optical disk drive system utilizing electron trapping media for data storage'. US Patent 05007037, 1991
4. Kato Yoshiaki and Fukumoto Atsushi, 'Optical pick-up device for a multi-layer recording medium with a photodetector arrangement for focusing and tracking control'. US Patent 05923632, 1999
5. Raczynski Walter, 'Digital optical disc with writeable regions and optical disc player for reading the writeable regions'. US Patent 05870364, 1999
6. Furukawa Takahiro, 'Writing system for a recordable compact disc storing information of a writing operation'. US Patent 05831950, 1998
7. Dodds David R. and Stahl K. John, 'Optical disc cartridge with a flexible storage medium'. US Patent 05077726, 1991
8. Miki Tadashi and Kozuka Masayuki, 'Write once read many optical disc storage system having directory for storing virtual address and corresponding up-to-date sector address'. US Patent 05040110, 1991
9. Kawamura Takayuki, 'Recording format for optical recording medium'. US Patent 04982077, 1991
10. Wilkinson Richard L. and Winslow John S., 'Direct read after write optical storage medium and information storage system'. US Patent 04963901, 1990
11. Kurihara Shinji, 'Track detection circuit for optical disc playback apparatus'. US Patent 05854781, 1998
12. C.M. Zhao, C.P. Liao, S.J. Wang, M.D. Wu, D.R. Huang, T.F. Ying, E.G. Lean, H.C. Wang, A. Hong, C.C. Huang, and Y.R. Hong, 'Spindle motor for optical disc drives'. US Patent 05923110, 1999
13. Ohta Shinji, and Ito Hiroyuki, 'Asymmetry detector for use in an optical recording and reproducing device'. US Patent 05490127, 1996
14. Koishi Kenji, Kubota Shinji, and Ishibashi Kenzo, 'Semiconductor laser control circuit'. US Patent 04845720, 1989

Design of Two-Dimensional 1×16 and 1×32 Array Waveguide Optical Power Splitters

Shyh-Lin Tsao* and Peng-Chun Peng
Department of Electrical Engineering
Yuan Ze University
Chung-Li, Taiwan, R.O.C

ABSTRACT

Silicon will play a practical role in the future optoelectronics devices. Silicon microelectronics fabrication techniques can be largely exploited to fabricate low-loss and high volume optical devices. In this paper, we report the concept and realization of new two-dimensional 1×16 and 1×32 array waveguide optical power splitters that offer the possibility of a free choice of the output power ratio in silicon-on-insulator (SOI). The power splitters compose one dimensional multimode interference (MMI) optical power splitter and multi-layers coupler at wavelength $1.55 \mu\text{m}$. According to the design, we can reduce the size of SOI power splitters waveguide without increasing propagation loss, efficiently. The results achieved show a remarkable improvement with respect to those of classical MMI power splitters.

Keywords: Silicon on insulator (SOI), multimode interference (MMI), optical coupler, integrated optics

1. INTRODUCTION

Optical power splitters are one of the basic integrated optical devices for application in fiber communication networks. Such a device is a key component of passive optical distribution networks, as well as of advanced active optical components such as interferometers, switches, etc. In the recent years, various components have been developed to realize optical power splitter including directional couplers¹, Y-junction power splitters², star-coupler³, and MMI couplers⁴. In the last few years, there has been a growing interest in the application of MMI effects in integrated opticals⁵⁻⁶. Moreover, MMI power splitters have compact, tolerant to the fabrication parameters, low optical loss, wide bandwidth, inherent balance and polarization-independent when strongly guided structures are used⁷.

SOI is an excellent substructure material for future electronic high-speed integrated circuits. In the recent years, SOI wafer used for designing CMOS (Complementary Metal-Oxide Semiconductor) electronics circuits exhibited the future technology for low-power and high-speed systems potential⁸⁻⁹. The SOI structure also has strong guiding optical properties owing to the large refractive index different between silicon and SiO_2 . Therefore, SOI optical waveguide have recently

*Correspondence: E-mail:jimmy@saturn.yzu.edu.tw, Telephone: 886-3-4638800-424, Fax: 886-3-4639355

emerged as an attractive class of optical waveguide elements¹⁰⁻¹³. For SOI single mode waveguide with low propagation loss have been demonstrated at $\lambda=1.55\mu\text{m}$ ¹⁴. Several studies have been reported where the silicon film of SOI substrates is used as a waveguide¹⁵⁻¹⁷. Excellent SOI properties as well as true compatibility with silicon CMOS integrated circuits technology is highly promising for future low-cost photonic integrated circuits. In this paper, we present the basic concept and new designs of some 1×16 and 1×32 multimode interference (MMI) optical power splitters that offer the possibilities of implementation of the optical power splitting functions on SOI wafers. These MMI devices are designed with a new multi-layers waveguide coupling idea. The multi-layer coupler can reduce device size, control power ratio, and achieved with submicron gap vertical coupling, easily. The coupler can be applied in optical switches, modulators, tunable filters etc. The optical power splitting characteristics are analyzed by three dimensional beam propagation method (3D-BPM) in this paper. According to the numerical results, we can reduce the size compared with the other one-dimensional SOI MMI waveguide power splitters without increasing propagation loss, efficiently.

2. DESIGN AND SIMULATION OF SOI POWER SPLITTER

2.1 One dimensional 1×8 and 1×16 MMI power splitter

In this section, we will describe the design of a one dimensional $1\times N$ MMI power splitter. The schematic diagram of the SOI single mode rib waveguide is shown in Fig. 1. The rib waveguide height is $0.55\mu\text{m}$ and the total thickness of Si layer is $1.5\mu\text{m}$. The SiO_2 layer has thickness $0.4\mu\text{m}$ below Si waveguide. We use 3D-BPM simulation and analyze the rib waveguide and use fundamental mode as our initial mode. The output waveguide mode pattern is shown in Fig.2 by 3D-BPM simulation. The loss of single mode SOI rib waveguide is below 0.1dB/cm . Fig.3 shows structure of the one-dimensional $1\times N$ MMI power splitter on SOI wafer. It consists of a rectangular section of width W and length L , for multimode interference (MMI). The rectangular region supports a large number of modes that propagate with different phase velocities leading to periodic self-imaging. The output waveguides are designed at the positions of the constructive interference peaks. Self-images of equal intensities appear in an rectangular section, whose length L is given by¹⁸

$$L \cong \frac{n * W^2}{N * \lambda} \quad (1)$$

where N is the number of images and the output ports. The effective refractive index of the rectangular section of the one dimensional $1\times N$ MMI power splitter is represented by n . In this paper, taken $N=8$ and 16 as our device output port numbers as examples, we use 3D-BPM to simulate the field propagation through the one dimensional 1×8 and 1×16 MMI power splitter structures at first. The one dimensional 1×8 MMI power splitter is designed with using $W=72\mu\text{m}$ and $L=1475\mu\text{m}$. Fig.4 (a) shows the simulated light propagation through our designed 1×8 MMI power splitter. The output optical fields intensity is shown in Fig.4 (b). The total insertion loss of one dimensional 1×8 MMI optical power splitter in SOI devices is 0.506 dB .

The one dimensional 1×16 MMI power splitter dimensions are designed with $W=144\mu\text{m}$ and $L=2525\mu\text{m}$. Fig.5(a)

shows the simulated light intensity patterns propagation in one dimensional 1×16 MMI power splitter. The output optical fields distribution is shown in Fig.5 (b). The insertion loss of one dimensional 1×16 MMI optical power splitter device we designed can be controlled as low as 0.632 dB.

2.2 Design of an optical two-layers SOI vertical waveguide coupler

In this section, we designed and simulated an optical two-layers SOI waveguide coupler by 3D-BPM. The schematic diagram of the optical two-layers SOI waveguide coupler is shown in Fig.6. The wafer structure consisting of two $1.5 \mu\text{m}$ thick silicon layers and two $0.4 \mu\text{m}$ buried-oxide layers. We took fundamental mode as initial field to simulate the propagation condition along the optical two-layers SOI waveguide coupler. We observed the coupling effect between two rib SOI waveguide with various varied gap distances and coupling lengths at wavelength $1.55 \mu\text{m}$. Fig.7(a-e) shows the output mode pattern at different cross sections of two-layers' SOI vertical waveguide directional coupler with the gap distance $0.1 \mu\text{m}$. Fig.8 shows the relation between normalized coupling coefficient k and coupling length L with various gap distances. The normalized coupling coefficient k increases as reducing the gap distance. The minimum completely power coupling length of our designed two-layers SOI vertical waveguide coupler is $201 \mu\text{m}$ with gap distance $0.1 \mu\text{m}$ at wavelength $1.55 \mu\text{m}$. A useful function of coupling coefficient k functioned of the coupling length L with gap distance $0.1 \mu\text{m}$ is fitted as the following equation

$$k = \sin^2(0.00785 \cdot L) \quad (2)$$

In general, designed two identical coupler waveguides are placed as closed as a few micrometers for acquiring coupling effect. But a long gap distance is difficult to implemented in integrated circuit (IC) process when gap distance is below $0.18 \mu\text{m}$ in horizontal parallel waveguide coupler. The two-layers' SOI vertical waveguide coupler can be achieved with submicron gap vertical coupling, easily. According to the result, we can design any two dimensional waveguide by multi-layer vertical coupler.

2.3 Design of two 1×16 and 1×32 two dimensional array waveguide optical power splitters

This technology can reduce the size of multiport optical couplers. We compose two dimensional $1 \times N$ MMI optical coupler with two-layers' vertical coupling techniques. We design an one dimensional $1 \times (N/2)$ SOI MMI optical coupler at first. Then, at each output of the $N/2$ output port in first layer, we design the second layer optical $N/2$ SOI vertical waveguide coupler. The output of the cross-section of two dimensional $1 \times N$ power splitter shown in Fig.9. In this section, taken 16 and 32 output as two examples, we use 3D-BPM to simulate the field propagation through two-dimensional 1×16 and 1×32 array waveguide optical power splitters. Fig.10(a)and(b) shows the simulation results of the outputs mode of our designed two dimensional 1×16 and 1×32 array waveguide optical power splitters, respectively. According to our analysis, we can reduce the size of optical multiple output couplers without increasing propagation loss, efficiently.

3. CONCLUSION

We have designed a two dimensional 1×16 MMI optical power splitters, a two dimensional 1×32 MMI optical power splitters in this paper. The multi-layers waveguide coupler and two dimensional array waveguide optical power splitters show great potential for using in fiber-optical communication systems at the wavelength $1.55 \mu\text{m}$. These devices are key components for wavelength multiplexer/demultiplexers based on phased-array waveguide grating and also useful for optical clock distribution in multi-layer silicon ULSI chips. This work demonstrates the potential of SOI technology for the fabrication of low-cost monolithic optical power splitter photonic circuits.

ACKNOWLEDGMENT

This work was supported in part by National Science Council under Grant No. NSC 89-2215-E-155-003 and NSC 89-2815-C-115-003-E. The authors would like to thank Mr. Sheen-Je Lee for valuable discussions and simulation supports.

REFERENCE

1. Trinh, P. D., Yegnanarayanan, S., and Jalali, B. "Integrated optical directional coupler is silicon-on-insulator." *Electron Lett*, **31**, pp. 2097-2098, 1995.
2. Adar, R., Henry, C.H., Kazarinow, R.E., Kistler, R. C., and Weber, G. R. "Adiabatic 3-db couplers, filters, and multiplexers made with silica waveguides on silicon." *J. Lightwave Technol*, **10**, pp. 46-50, 1992.
3. Okamoto, K.; Takahashi, H.; Yasu, M.; Hibino, Y., "Fabrication of wavelength-insensitive 8×8 star coupler" *IEEE Photonics Technology Letters*, **4**, pp. 61 -63, 1992.
4. L. Soldano, F. Veerman, M. Smit, B. Verbeek, A. Dubost, E. Pennings, "Planar monomode optical couplers based on multimode interference effects" *J. Lightwave Technol.*, **10**, pp. 1843-1849, 1992.
5. J. M. Heaton, R. M. Jenkins, D. R. Wight, J. T. Parker, J. C. H. Birbeck, and K. P. Hilton, "Novel 1-to-N way integrated optical beam splitters using symmetric mode mixing in GaAs/AlGaAs multimode waveguides" *Appl. Phys. Lett.*, **61**, pp. 1754-1756, 1992.
6. L. Soldano and E. Pennings, "Optical multi-mode interference devices bases on self-imaging: Principles and applications" *J. Lightwave Technol.*, **13**, pp. 615-627, 1995.
7. P. A. Besse, M. Bachmann, H. Melchior, L. B. Soldano, and M. K. Smit, "Optical bandwidth and fabrication tolerances of multimode interference coupler" *J. Lightwave Technol*, **12**, pp. 3905-3911, 1994.
8. H. Shimano, N. Sakashita, F. Okuda, T. Oashi, Y. Yamaguchi, T. Eimori, M. Inuishi, K. Arimoto, S. Maegawa, Y. Inoue, S. Konwri, K. Kyuma, "1V 46ns 16MB SOI-DRAM with body control technique", *IEEE Journal of Solid- State Cirauits*, **33**, pp. 1712-1720, 1997.
9. Y.-H. Koh, Pq.-R. Oh, J.-W. Lee, J.-W. Yang, W.-C. Lee, C.-K. Park, J.-B. Park, Y.-C. Heo, K.-M. Rho, B.-C. Lee, M.-J. Chung, M. Huh, H.S. Kim, K.-S. Choi, W.-L. Lee, "1 giga bit SOI DRAM with fully bulk compatible process and body contacted SOI MOSFET structure" *Proceedings of the 1997 International Electron Device Meeting*, pp. 579-582, 1997.
- 10 .P. D. Trinch, S. Yegnanarayanan, and B. Jalai, "Guided-wave optics in silicon-on-insulator technology", *IEE Proc. J.*

Optoelectron, **143**, pp. 307-311, 1996.

- 11 .E. K. Lin, G. Z. Li, Y. Gao, C. S. Guo, "Zero-gap directional coupler switch integration into a silicon-insulator for 1.3 μ m operation", *Optical Letters*, **21**, pp.1664-1666, 1996.
12. A. Layadi, A. Vonsovical, R. Orobitchouk, D. Pascal, A. Koster, "Low loss optical waveguide on standard SOI/SIMOX substrate", *Optical Communication*, **146**, pp. 31-33, 1998.
13. Takato. N., Kominato. T., Sugita. A., Jinguri K., Toba. H., and Kawachi M., "Silica-based integrated optic Mach-Zehnder multi/demultiplexer family with channel spacing of 0.01 250nm", *IEEE J. Set. Areas Commum*, **8**, pp. 1120-1127, 1990.
14. Soref, R. A., Schmidtchen. J., and Petermann. K., "Large single-mode rib waveguides in GeSi-Si and Si-on-SiO₂", *IEEE J. Quantum Electron*, **27**, pp.1971-1974, 1986.
15. P. D. Trinh, F. Coppinger and B. Jalali, "Compact silicon-based integrated optical time delays", *IEEE Photonics Technology Letters*, **9**, pp.634-635, 1997.
- 16 .A. Cutolo, M. Iodice, A. Irace, P. Spirito and L. Zeni, "Electrically controlled Bragg reflector integrated in a rib silicon on sulator waveguide", *Applied Physics Letts*. **71**, no. 2, pp.199-201, 1997.
17. A Cutolo, M Iodice, P. Spirito and L. Zeni, "Silicon electro-optic modulator based on a three terminal device integrated in a low-loss single-mode SOI waveguide", *J. of Lightwave Technol.*, **15**, pp.505-518, 1997.
18. R. Ulrich and G. Ankele, "Self-imaging in homogeneous planar optical waveguides," *Appl. Phys. Lett.*, **27**, pp. 337-339, 1975.

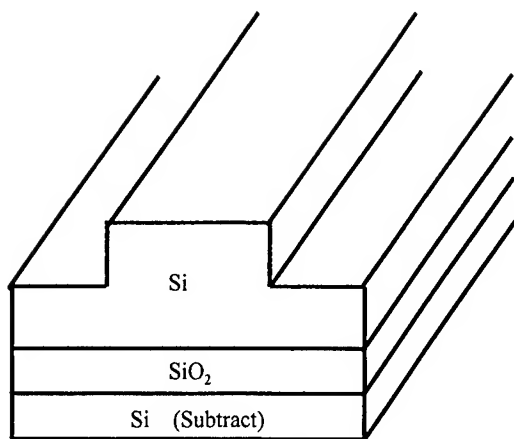


Fig.1 The structure of single mode waveguide in silicon-on-insulator

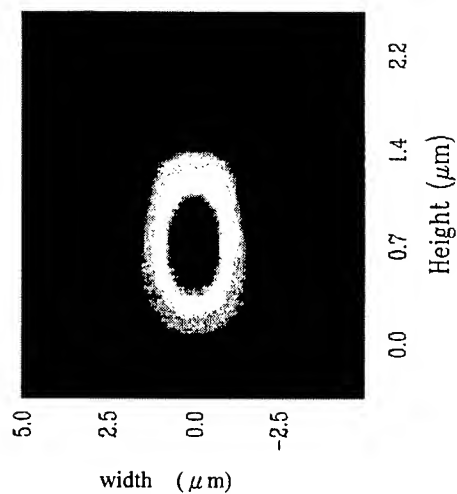


Fig.2 Output mode pattern of single mode SOI waveguide at $w=3\ \mu\text{m}$

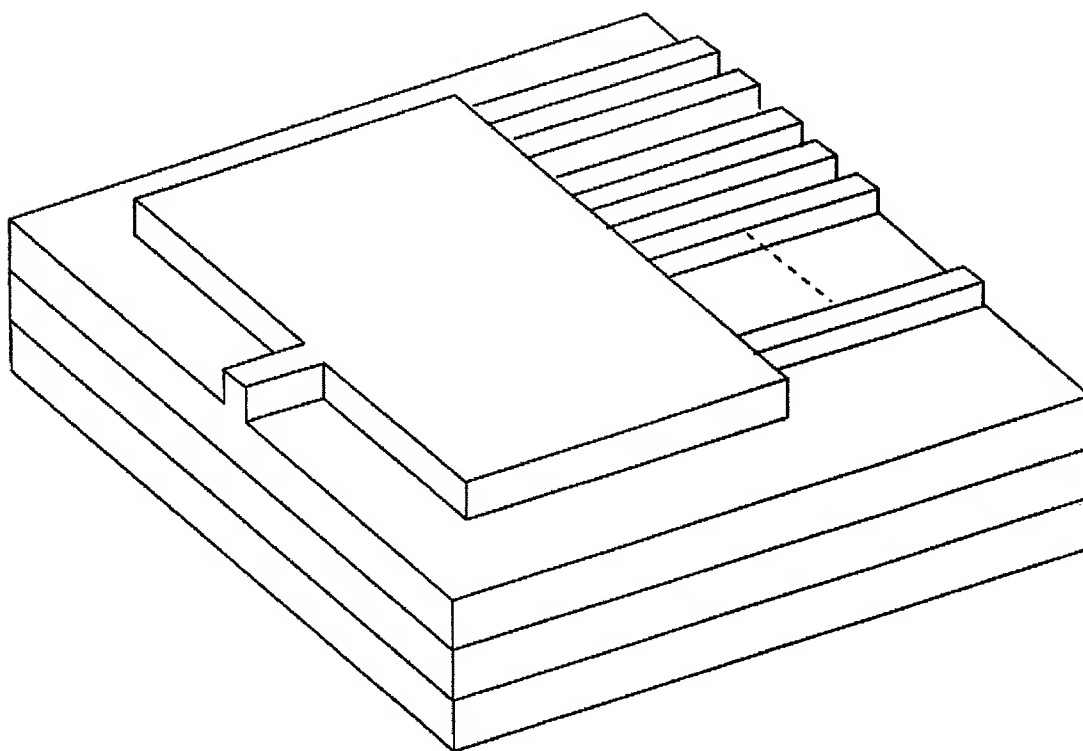
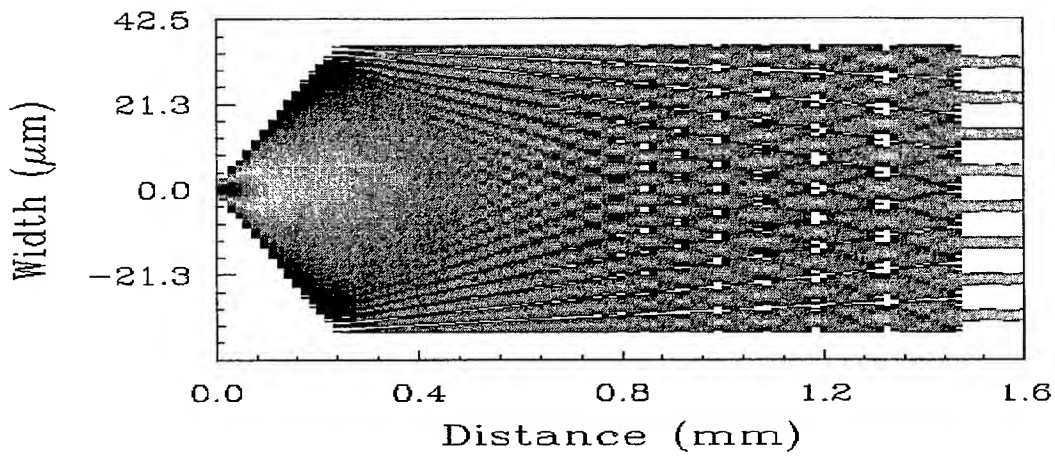


Fig.3 The structure of one dimensional $1 \times N$ MMI power splitter



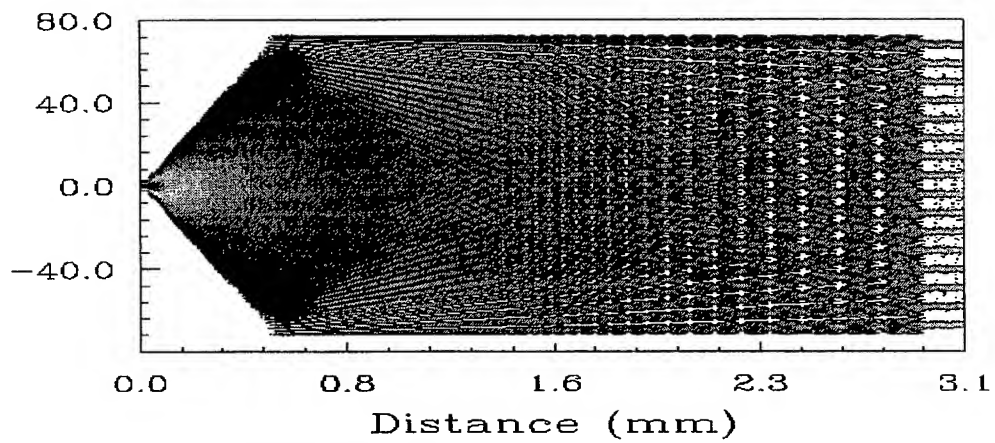
(a)



(b)

Fig.4 (a) Top view of optical light propagation through the one dimensional 1× 8 MMI optical power splitter

(b) Output optical field intensities of our designed one dimensional 1× 8 MMI optical power splitter



(a)



(b)

Fig.5 (a) Simulation of optical light propagating through our designed one dimensional 1× 16 MMI optical power splitter

(b) Output optical fields distribution of our designed one dimensional 1× 16 MMI optical power splitter

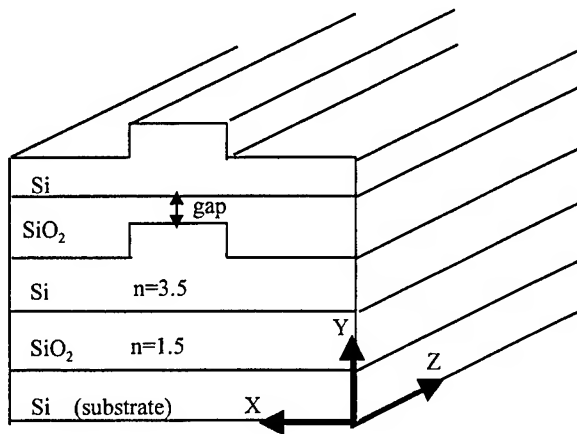


Fig.6 optical multi-layers SOI waveguide coupler structure

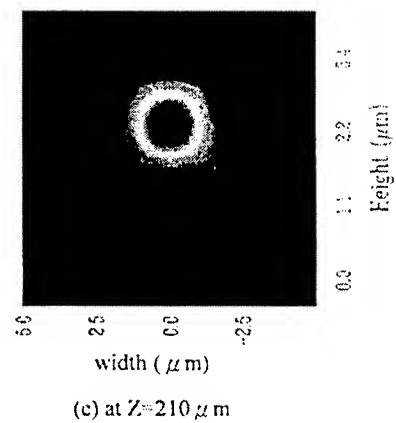
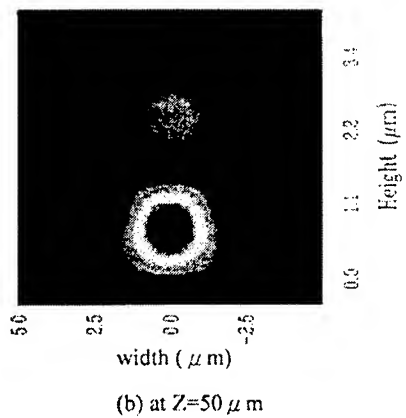
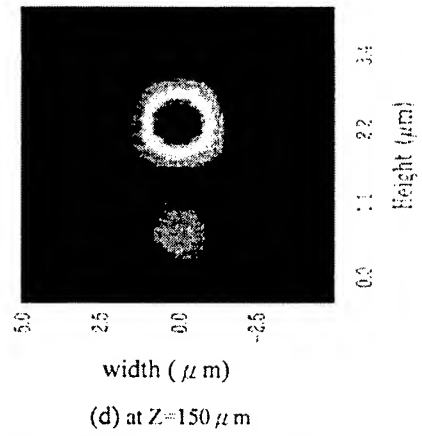
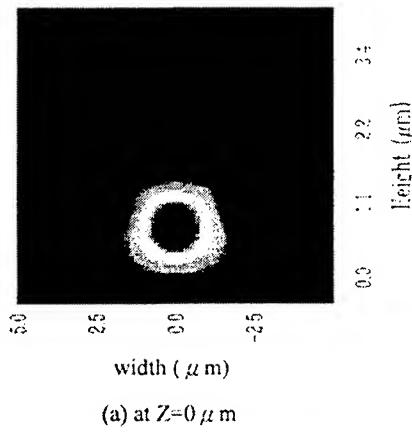
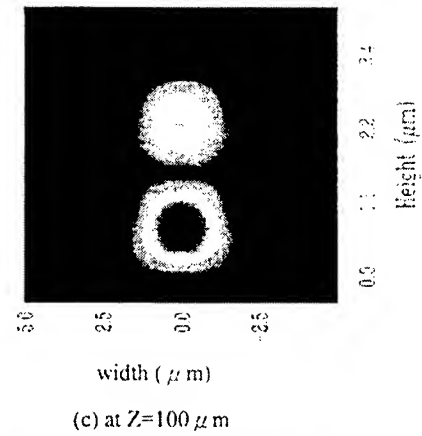


Fig.7(a-e). Optical output fields representing the vertical coupler of optical two SOI waveguide layers at $Z=0, 50, 100, 150, 210 \mu m$ for Fig. 7(a), (b), (c), (d), (e)

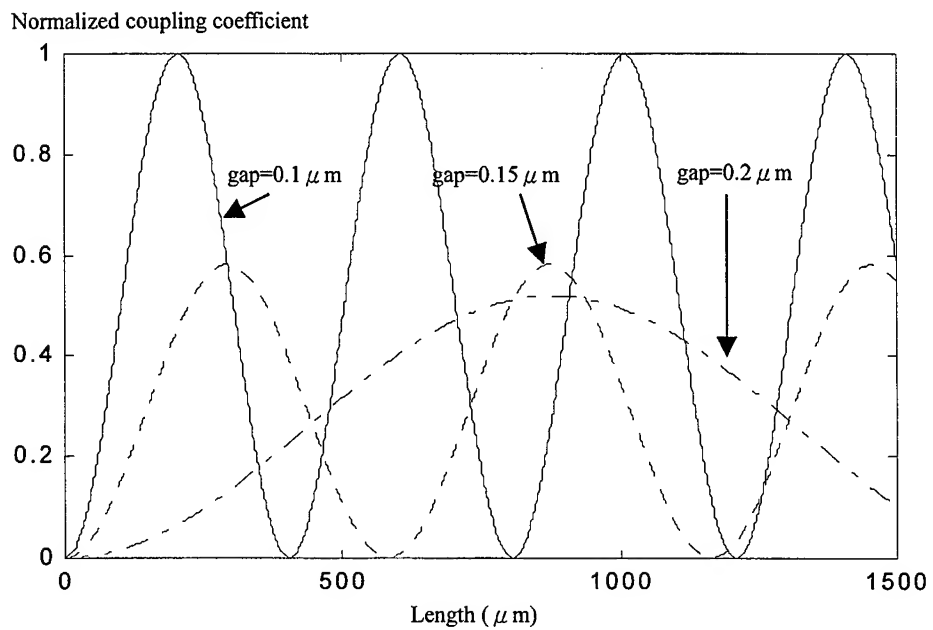


Fig.8 The relation between the coupling length and coupling coefficient

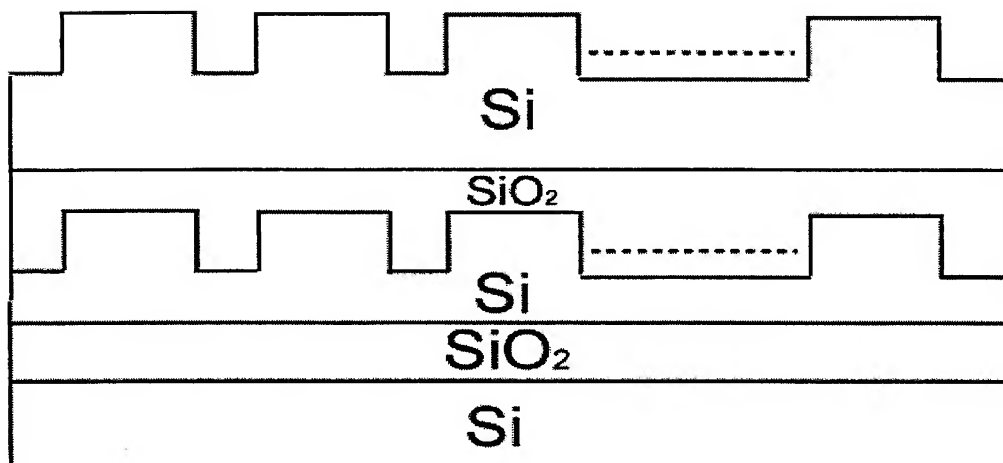


Fig.9 The output of the cross-section of two dimensional 1x N power splitter

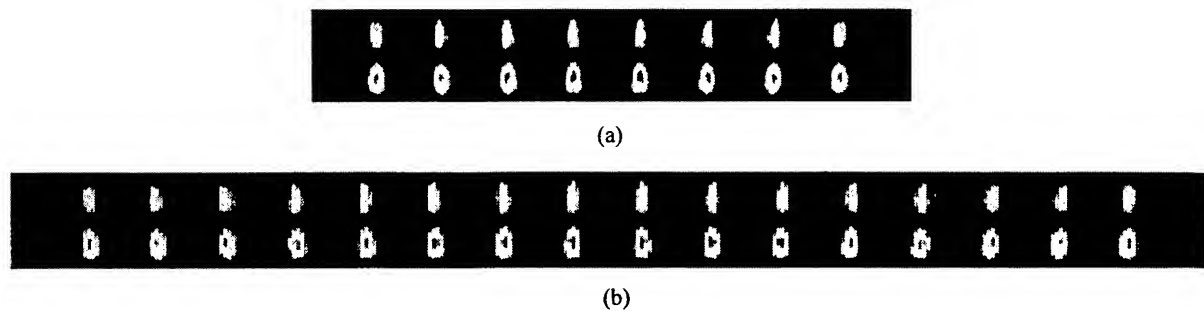


Fig.10 (a) Output mode field of the two dimensional 1× 16 array waveguide power splitter

(b) Output mode field of the two dimensional 1× 32 array waveguide power splitter

Shrinkage of spacing in fabricating sol-gel optical elements

Lin Pang*, Deer Yi, Yingbai Yan, Guofan Jin, Minxian WU

State Key Laboratory of Precision Measurement Technology and Instruments, Department of Precision Instruments, Tsinghua University, Beijing, 100084, P.R.China

ABSTRACT

Real-time effect was investigated with the binary masks and contact copy method in the processing of sol-gel hybrid material. The height of the real time relief increases slowly with the increase of exposure dose, but is no relation with the variation of the spatial frequency of the mask. Moreover, the height of the real-time relief is dependent on the thickness of the film deposited on substrate. Compared with the mask, the spacing of the exposed areas in sol-gel film shrinks, and the shrinkage rate is about 10-20%. The possible reason causing the real-time effect is discussed.

Keywords: sol-gel, optical element, polymerization, shrinkage

1. INTRODUCTION

The hybrid sol-gel method has been widely used in the fabrication of microstructural optical components for various applications. Because of its low optical loss, simple processing, and the properties of tailored at the molecular lever for a particular application, the method has attracted the attention of those material scientists and photonics device engineers who seek to take advantage of the appealing optical properties.^{1,2,3} In the processing, photo-induced polymerization was employed to form the pattern in the branch of the chain in the hybrid sol-gel material, the shrinkage cause by the polymerization must affect the fidelity of the pattern during the transfer of the mask. The exposure causes the enhancement of molecular weigh in exposed areas and the molecular shift between the exposed areas and unexposed ones, which results in the real-time relief. This effect would exert impact on the deepening of the relief and expanse of the transition region during the development. The study about the effect on real-time relief and the shrinkage of the spacing is significant to fabricate optical element with accuracy feature.

In the paper we report our present experimental results on the real-time relief and the shrinkage of spacing in fabricating optical element in the hybrid sol-gel glass. After sol-gel coating deposited on the substrate, with a binary mask and a contact copy, real-time relief and its shrinkage of spacing compared with the mask were investigated. The process of composing the hybrid sol-gel material was presented in section 2. In section 3, the characteristic of real-time relief was given, followed by the investigation of the shrinkage of the spacing in section 4. Finally, the mechanism of those effects was discussed.

2. INORGANIC-ORGANIC SOL-GEL MATERIAL

A silicon oxide matrix was synthesized by hydrolysis and polycondensation actions. The silicon oxide network was formed from tetraethoxyorthosilicate (TEOS) and 3-methacryloxypropyl trimethoxy silane (MAPTMS) with a molar ratio of 10:1, which were dissolved in adequate volume of alcohol, and then hydrolyzed by 0.1M hydrochloric acid solution. The procedure was given in Fig.1.

The addition of MMA can both intensify the network and adjust the property of material. The quantity of MMA would directly influence the transmittance of the hybrid material in the UV wavelength range.

After the solution was prepared, it was aged at room temperature for one week. The prepared composite was made photosensitive by a photoinitiator. The photoinitiator forms free radicals during UV exposure, which leads to free-radical

* Correspondence: Email: pangl@pim.tsinghua.edu.cn; Telephone: 8610 62781187; Fax: 8610 62784691

cross-linking polymerization of unsaturated bonds and thus makes the material act as a negative tone photoresist. The photoinitiator, benzoin, was added to the hybrid sol-gel material solution in a molar ratio of 1:100. Films derived from sol were dip-coated on borosilicate glass substrate. Because organically modified silicate glasses tolerate stress relaxation more effectively than do glasses derived from traditional silica sources, like tetraethoxyorthosilicate, film could be deposited in one step in thickness ranging from 2 to 15 μm . Film thickness varies linearly with dip-coating speed in some speed range.⁴ After precision dip-coating, film were immediately heated (prebaked) in air at 100°C for 2 min to remove the solvent and improve the adhesion of the sol-gel material to the substrate.

The films were illuminated by a 100W mercury UV lamp with a diffuser, placed at 20 cm for some time through a contact mask. After exposure the films were investigated by an interference microscope.

3. REAL-TIME RELIEF

Illumination with UV radiation induces free radical polymerization of the vinyl substituent on both MAPTMS and MMA. The polymerization takes place not only in them, but also between them, which promote additional condensation and densification of the radiation. In other words, difference between the exposed areas and unexposed ones is caused by the exposure.

3.1. Effect of exposure on height of real-time relief

With 100 lines/mm binary mask, Fig.2 and Fig.3 give the results of real-time relief, which were taken by an interference microscope, exposure time of 40 min and 96 min, respectively. It can be seen that the height of the real-time relief is strong dependent on the exposure dose, and the height of relief increases with the exposure dose enhanced. In order to quantitatively show the dependence of height on exposure dose, detailed experiments were designed and performed. In the experiments, a binary mask with transparent of 8.4 μm and dark width of 21.9 μm , was used to investigate the relation between the height of real-time relief and exposure doses. The thickness of the film used in the present work was $\sim 2.1 \mu\text{m}$. Films were exposed to UV light in a range from 13 min to 148 min.

Fig.4 depicts the dependence of the height of real-time relief on exposure time. In the initial period of exposure, from 13 min to 30 min, the height of relief increases promptly, from 0.09 μm to 0.26 μm , its average rate of increase is ~ 9.5 nm/min. During the exposure time from 40 min to 70 min, the rate slows down, ~ 2.2 nm/min. With further increase in exposure time, the rate is very slow, only ~ 0.3 nm/min. The dependence of height of relief with exposure time is related to the process of free radical polymerization.

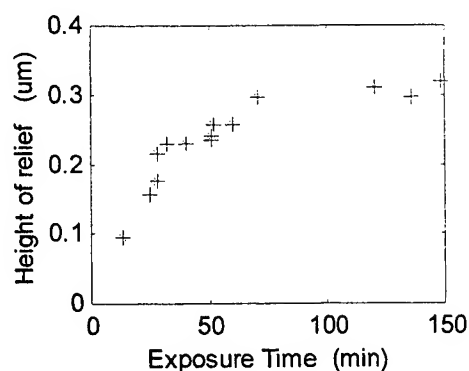


Fig.4. The height of real-time relief as a function of exposure time.

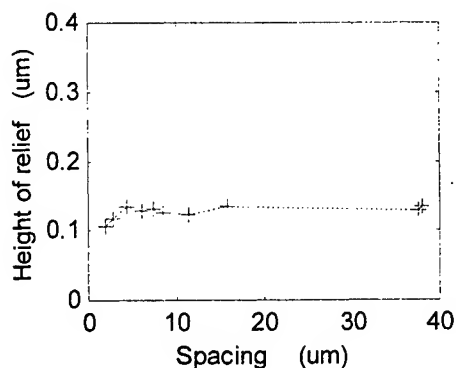


Fig.5. The height of real-time relief as a function of spacing.

3.2. Effect of spacing on height of real-time relief

When we observed the different parts of a Fresnel array of lens made by contact copy with thickness of $3.5\mu\text{m}$, we found that the height was different at different parts, different spacing, as shown in Fig.6 and Fig.7. Fig.6 shows that the height is about $0.08\mu\text{m}$ at low spacing. Fig.7 shows that the height is about $0.14\mu\text{m}$ at high spacing. It can be seen that the height of real-time relief is probably dependent on the spacing.

Fresnel Binary mask with various spatial frequencies was used to investigate the relation of height of real-time relief with spacing of exposed areas. In these experiments, $2\mu\text{m}$ thick films were exposed to UV-light for 20 min. Fig.5 shows the variation in height of relief as a function of the spacing of exposed areas. From Fig.5, it can be seen that the height of relief is basically independent of the spacing, with an exception of the areas with smaller spacing than $3\mu\text{m}$.

3.3. Effect of thickness of film on height of real-time relief

Binary grating mask with $30\mu\text{m}$ in spacing was used to investigate the relation of height of real-time relief with the thickness of the films. To avoid the errors arising from different batches, films with various thicknesses, were deposited on a substrate by varying the withdrawal speeds. The thickness obtained was measured in the opposite areas on the substrate, corresponding to the patterned ones. In the experiments, oversaturated exposure dose was employed to avoid the effect of the exposure on the experimental results. Fig.8 shows the variation in height of real-time relief as a function of the thickness of films, in which the exposure time is 5 h.

It can be seen that, as for the films thinner than $4.0\mu\text{m}$, the height of real-time relief strongly depends on the thickness of the films, and there is an approximately linear relation between the height of relief and thickness of the films. As the thickness is more than $4.0\mu\text{m}$, the variation of the height is not manifest as the thickness increases.

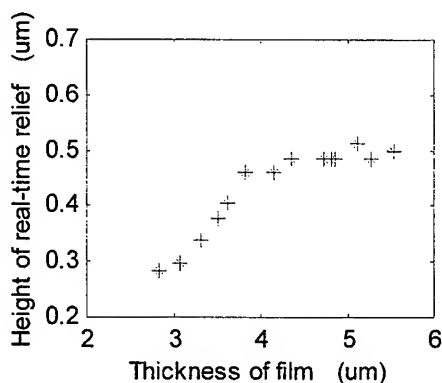


Fig.8. Height of real-time relief as a function of the thickness of film.

The above relation directly corresponds to the variation of the amount of the monomer in the coatings in the polymerization induced by the exposure to UV-light.

3.4. Relation between spacing and the thickness of film.

From Fig.5, compared with relief at higher spacing, the real-time height is lower at narrower one. Fig.8, in addition, shows that height of relief is of some relation with the thickness of the film. The thickness of film in Fig.6 and Fig.7 is $3.5\mu\text{m}$, and the exposure time is 173 min. From Fig.6 and Fig.7, the height at high spacial frequency, spacing of $\sim 2\mu\text{m}$, is about $0.08\mu\text{m}$, which is much lower than that at low frequency, height of $\sim 0.2\mu\text{m}$. The thickness of film in Fig.9 and Fig.10 is $4.3\mu\text{m}$, and exposure time is 60 min. It can be seen from these figures that the difference of height between high frequency, height of $\sim 0.10\mu\text{m}$, and low frequency, height of $\sim 0.13\mu\text{m}$, is indistinctive. Therefore, the thickness of sol-gel film should

be more than 4 μ m for fabrication of optical elements with different spacial frequencies, especially frequency higher 200 line/mm.

4. SHRINKAGE OF THE SPACING

A binary mask, with transparent of 8.4 μ m and dark width of 21.9 μ m, was used to investigate the shrinkage of spacing. Fig.11 gave the profile of a real-time relief. From Fig.11, it can be seen that the sidewall of the relief is not vertical as expected, but trapeziform in the crosssection. The upper side of the trapeziform is regarded as the width of the real-time relief, on which the developed width of the relief depends. The slope side of the trapeziform is known as transition region, which corresponds to the quality of the elements. In the experiments, the films with thickness of 2.0 μ m and binary mask was used to investigate the shrinkage. Experimental data are shown in Table 1.

Table 1. The relation between shrinkage percentage and exposure time

	1	2	3	4	5
Exposure Time (min)	15	37	40	45	136
Shrinking Percentage	17.5	17.5	21.1	16.9	16.6

The shrinking percentage was obtained as the ratio of the width of difference between the width of exposed areas and that of the upper side of real-time relief, and exposed width. There was some errors arising from distinguish of the boundary between the upper side and the transition region. Table 1 shows that the shrinkage is independent on he exposure dose. The shrinkage can be formed during the initial exposure.

5. DISCUSSION

The formation of the real-time relief rises from two aspects: one is the polymerization of the monomer in the exposed areas, the other is the shift of monomer from the unexposed areas during the exposure. Before exposure to UV-light, the surfaces between exposed areas and unexposed ones are in the same level. If there is no shift of monomer, due to the shrinkage induced by polymerization during the exposure, the surface of the exposed induced must be lower than that of unexposed ones, which is not inconsistent with the experimental results. The process of exposure exerts no impact on the unexposed areas without the consideration of scattering of UV-light, so the drop of its surface level must be owed to the shift of the monomer caused by the vast difference of the concentration of monomer between these two areas.

Compared to other negative optical materials, such as DCG, the hybrid sol-gel material is of a very strong characteristic of forming real-time relief. The reason for this is incompact structure in sol-gel material besides its free radical polymerization, which is of more shrinkage than the cross-linking in DCG during exposure. The degree of polymerization in the sol-gel material is low, which cause the molecules to move easily. Irregularly accumulated molecules cause a large lap between the molecules.

ACKNOWLEDGEMENTS

Authors acknowledge support from a grand from China Postdoctoral Science Foundation as well as a grant for fundamental research from school of machine and engineering of Tsinghua University.

REFERENCES

1. J.T.Rantala, P.Ayras, R.Levy, S.Honkanen, M.R.Descour, N.Peyhambarian, "Binary-phase zone-plate arrays based on hybrid solgel glass", Opt.Lett. 23, (1998),1939-1941
2. S.I.Najafi, T.Touam, R.Sara, M.P.Andrews, M.A.Fardad, "Sol-gel glass waveguide and grating on silicon", J.Lightwav Tech. 16, (1998),1640-1646.

3. P.Muller, B.Braune, C.Becker, H.Krug, H.Schmidt, "Fabrication of monolithic refractive optical lenes with organic-inorganic nona-composites: Relations between composition and mechanical and optical properties", SPIE, 3136, (1997),462-469.
4. Lin Pang, Hui Wei, Bo Chen, Lurong Guo," Fabrication of sol-gel optical element with dichromated gelatin as photoresist", SPIE,Vol.3557, (1998),5-7.

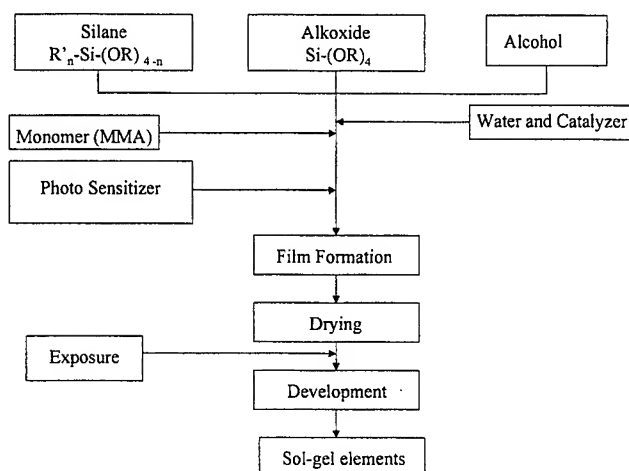


Fig.1. Schematic process for the preparation of sol-gel material and fabrication of optical elements

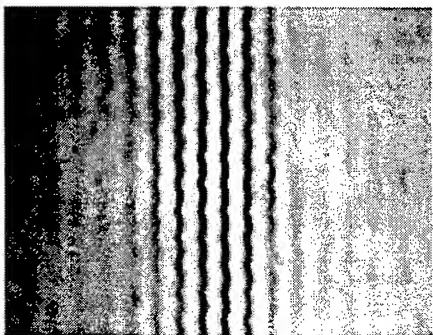


Fig.2. Real-time relief of exposure time of 40 min.

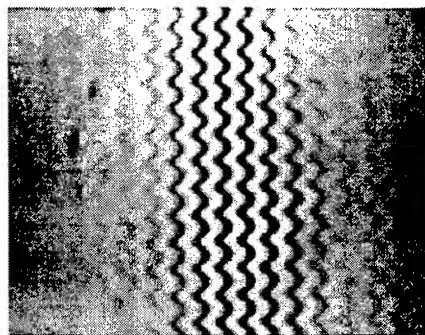


Fig.3. Real-time relief of exposure time of 96 min.

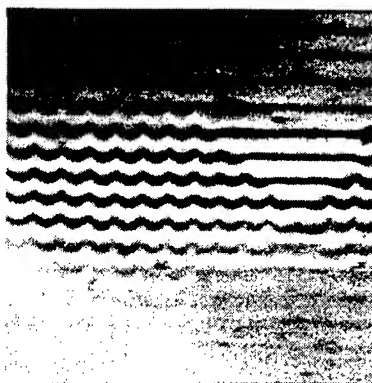


Fig.6. Interferogram of an array of lens at low spacing with thickness of $3.5\mu\text{m}$ and exposure time of 173 min.

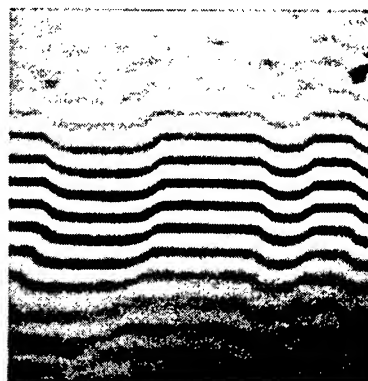


Fig.7. Interferogram of an array of lens at wide spacing.

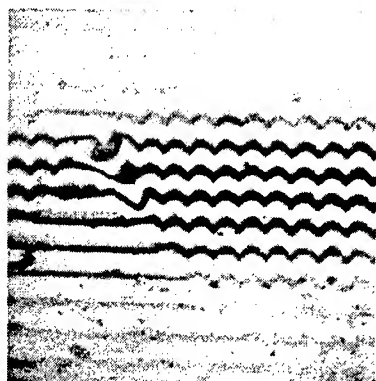


Fig.9. Interferogram of an array of lens at low spacing with thickness of $4.3\mu\text{m}$ and exposure time of 60 min.

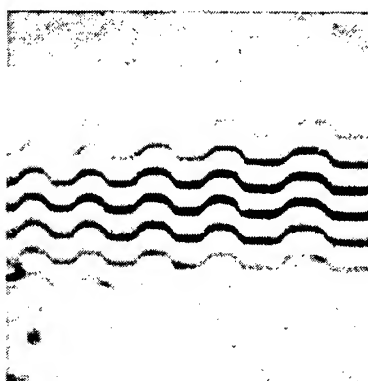


Fig.10. Interferogram of an array of lens at wide spacing.

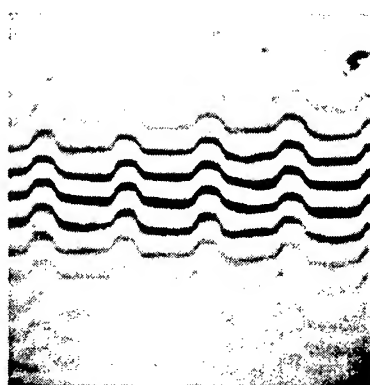


Fig.11. Profile of the real-time relief.

The Design of Wavelength Selective Directional Coupler made of W-index Waveguide for WDM

Jung-Hyun Yun^a, Kyoung Tae Ra^a, Phil-Jung Kim^a, Sang-Duk Kim^b, Jae-Gyu Lee^a, Jong-Bin Kim^{*a}

^aDept. of Electronic Engineering, Chosun University, Korea

^bDept. of Information & Communication Engineering, DongA-InJae College

ABSTRACT

An optical waveguides spectral filter constructed with a W-index waveguide, supporting a dominant mode with nonzero cutoff frequency, and a Step-index waveguide is proposed and analyzed. The proposed filter offers a spectral width on the order of one nanometer, considerably narrower than that provided by a filter made of two Step-index waveguides having the same transmission wavelength. The narrow spectral width is achieved by exploiting a relatively large slope difference between the dispersion characteristics of the W-index and Step-index waveguides constituting the filter.

For an example case, transmission characteristic of the proposed filter with peak transmission at $1.55\mu\text{m}$ is calculated and compared with that of a corresponding filter made of two Step-index waveguides.

1. INTRODUCTION

Wavelength division multiplexing(WDM) is now established as an effective technique to increase the information capacity of optical communication systems using the intensity modulation-direct detection scheme¹, several techniques have been proposed for multiplexing and demultiplexing of the light signals with different wavelengths. Among them are those based on grating reflections, dichroic filters and parallel-guide couplers²⁻⁶. In grating reflectors and dichroic filters, multiplexing/demultiplexing occurs outside the fiber. This process is usually associated with high insertion losses, back reflections, and critical alignments.

Waveguide spectral filters, on the other hand, provide considerably lower losses and back reflections, do not critical alignments.

Wavelength selective couplers may be made using two identical or dissimilar waveguides. The transfer of power between

* Correspondence : Email: jbkim@mail.chosun.ac.kr; Telephone:082-62-230-7062; Fax:082-62-232-3369

the cores of the two waveguides is strongly influenced by the propagation constants of the dominant modes of the waveguides. If the two waveguides are identical, their dominant modes are phase-matched at all frequencies and a complete transfer of power is possible at any frequency but over different coupling lengths. On the other hand, for couplers made of dissimilar waveguides, the propagation constants of dominant modes may be equal at discrete frequencies only. These frequencies correspond to the intersection points of the dispersion characteristics of the modes. At intersection frequencies, the modes are phase matched and a maximum transfer of power decreases. This decrease depends on the difference between the slopes of dispersion curves at intersection frequencies. Dissimilar waveguide couplers are thus much more wavelength selective than identical fiber couplers and may be utilized as narrow-band spectral filters.

Most dissimilar wavelength selective couplers reported in the literature consist of two single-clad fibers which differ in their core radii or core indexes⁷⁻¹⁰. In this article, a wavelength selective coupler constructed with a W-index waveguide and a step-index waveguide is proposed. Both waveguides are selected such that its dominant mode exhibits a nonzero cutoff frequency¹¹. As a result, a relatively large difference between the slopes of the dispersion characteristics for the modes of these two waveguides is obtained which is exploited to make a narrow-band waveguide spectral filter.

Spectral widths on the order of one nanometer are achieved. Using a coupled-mode theory, the transfer of power between the W-index and the step-index waveguide is analyzed. In doing so, the entire structure is viewed as a dual-core waveguide with a common cladding region. A section of the dual-core waveguide functions as a spectral filter.

As an example case, the transmission characteristic of the proposed filter with a transmission wavelength at $1.55\mu\text{m}$ is calculated and compared with a corresponding filter made of two single clad waveguides. It is shown that the proposed filter provides much narrower spectral width and lower side lobe levels.

2. ANALYSIS

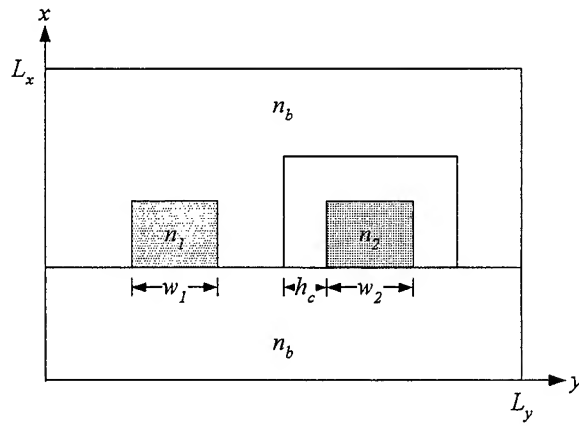
Let us consider an optical waveguide consisting of two core regions with Step and W-shape index profiles and a common cladding region with a constant refractive index n_b .

Fig. 1(a) and (b) illustrates the cross-sectional geometry and the index profile of the composite waveguide. The two core regions are assumed to be parallel with their axes separated by a distance S . The refractive indexes of different regions are expressed in terms of Step-index region and W-index region.

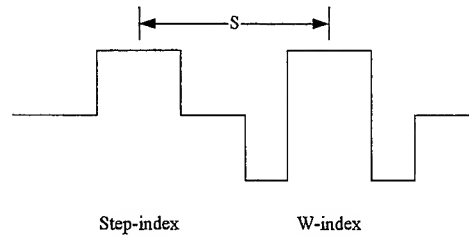
Each waveguide in isolation is assumed to be single-mode and weakly guiding so that the scalar-wave analysis can be applied. Assuming that each waveguide in isolation is supporting the dominant mode and the guides interact weakly with each other, the scalar field of the composite waveguide is expressed as

$$\psi = A(z)\psi_1(x, y)e^{-j\beta_1 z} + B(z)\psi_2(x, y)e^{-j\beta_2 z} \quad (1)$$

in the region of Step-index guide and in the region of W-index guide. In (1), β_1 and β_2 are propagation constants, ψ_1 and ψ_2 are fields referred to the axes of Step-index and W-index waveguides, respectively, A and B are z -dependent amplitude coefficients which account for the transfer of power between the two guides.



(a)



(b)

Fig. 1. Geometry and coordinates for a composite waveguide with Step-index and W-index core region.

Employing the theory of weakly coupled parallel waveguides, it can be shown that A and B are governed by the following set of coupled differential equations.¹²

$$\frac{dA}{dz} = -jC_{11}A(z) - jC_{12}B(z)e^{j\Delta\beta z} \quad (2)$$

$$\frac{dB}{dz} = -jC_{22}B(z) - jC_{21}A(z)e^{j\Delta\beta z} \quad (3)$$

where

$$\Delta\beta = \beta_1 - \beta_2 \quad (4)$$

$$C_{ij} = \frac{k_0^2}{2\beta_i} \int_s \psi_i^* (n - n)^2 \psi_j ds \quad i, j=1,2 \quad (5)$$

In (5), n refers to the reflective index of the composite waveguide structure, while n_i refers to the index of the single-clad guide for $i=1$ and that of W-index guide for $i=2$. k_0 is free-space propagation constant. s is the cross-section of the composite waveguides. Assuming that at $z=0$ the entire power is in the step-index guide; i.e., $B(0)=0$, the solutions for (2) and (3) are expressed as

$$P_1(z) = \frac{P_0}{k^2} \left[\frac{1}{4} (\Delta\beta + C_{11} - C_{22})^2 \sin^2 kz + k^2 \cos kz \right] \quad (6)$$

$$P_2(z) = \frac{P_0 C_{21}^2}{k^2} \sin^2 kz \quad (7)$$

where k is given by

$$k = \sqrt{\frac{1}{4} (\Delta\beta + C_{11} - C_{22})^2 + C_{12} C_{21}} \quad (8)$$

Equation (6) and (7) describe the transfer of power between the Step-index and W-index waveguides. It is noted that maximum transfer of power occurs at a particular wavelength for which $\Delta\beta = 0$ and $k_z = \pi/2$ (or more generally $k_z = \pi/2 + m\pi$, m being an integer). The coupling coefficients C_{11} and C_{22} are much smaller than C_{12} and C_{21} and do not influence k strongly. If at $\lambda = \lambda_0$, $z = L = \pi/2k$ is chosen, maximum transfer of power from the Step-index waveguide to the W-index waveguide occurs.

At wavelengths away from λ_0 , $\Delta\beta \neq 0$ and $L \neq \pi/2k$, indicating that much less power is transferred. Consequently, a section of the coupled waveguide structure functions as a spectral filter with peak transmission at wavelength λ_0 .

3. NUMERICAL RESULTS

To evaluate transmission properties of the proposed filter and compare its performance against the filter made of dissimilar Step-index waveguides, an example case corresponding to transmission at $\lambda=1.55\mu\text{m}$ is considered. First, in order to illustrate that the provided by a filter made of two Step-index waveguides, a set of parameters for the proposed filter is chosen such that peak transmission occurs at $\lambda=1.55\mu\text{m}$.

These parameters are: $n_1=1.452$, for the step-index waveguide, and $n_2=1.455$, $n_3=1.429$ for the W-index waveguide. And then, $n_6=1.444$, for the common cladding layer.

This process, however, changes the transmission wavelength slightly. Minor adjustments are finally made on the parameters to make the peak transmission occur again at $\lambda=1.55\mu\text{m}$. There core separation for both waveguide is $16\mu\text{m}$.

To obtain the transmission characteristics, propagation constants of constituent waveguides for each filter are calculated. Fig.2 illustrates mode index versus core width in step-step index filters. Fig. 3 illustrates mode index versus core width in step-W index filters.

The point of intersection for both sets of curves corresponds to $\lambda_0=1.55\mu\text{m}$. It is evident that the slope difference between the curves of W-Step index waveguide is markedly larger than that between the curves of Step-Step index waveguide,

indicating that the spectral width of the filter which includes the W-index waveguide is narrower than that of the filter made of two Step-index waveguides.

The transmission characteristic of each filter is calculated using the power transfer function $F(\lambda)$ defined as

$$F(\lambda) = \frac{P_2(L)}{P_1(L)} = \frac{C_{12}^2}{\kappa^2} \sin^2(\kappa(\lambda)L) \quad (9)$$

where L , the coupling length, is obtained from

$$L = \frac{\pi}{\left[\frac{1}{4}(C_{11} - C_{22})^2 + C_{12}C_{21} \right]^{1/2}}, \quad \lambda = \lambda_0 \quad (10)$$

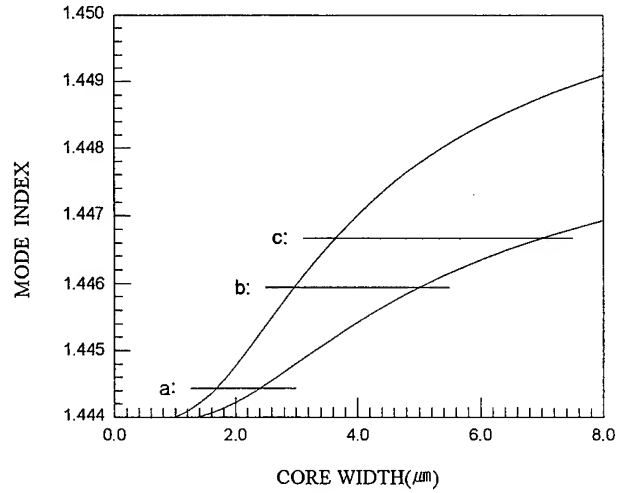


Fig. 2. Mode index versus core width in step-step index filters.

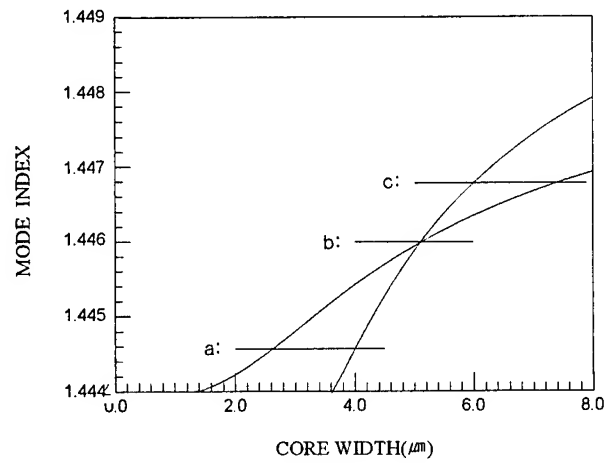


Fig. 3. Mode index versus core width in step-W index filters.

Fig. 4 illustrates transmission characteristics of Step-Step index filters and Fig. 5 illustrates transmission characteristics of W-Step index filters.

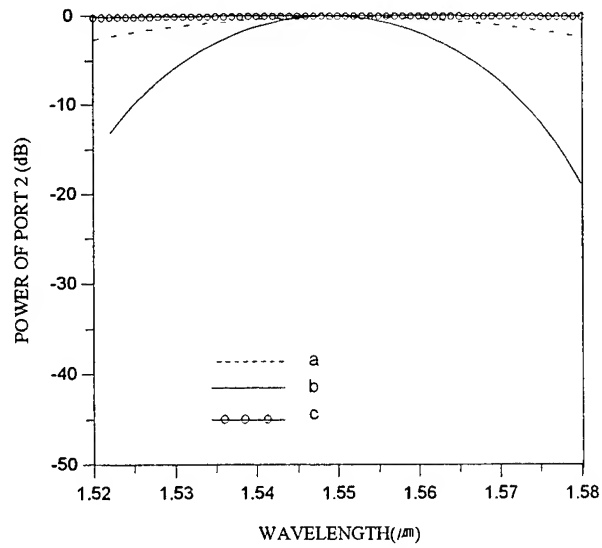


Fig. 4. Transmission characteristics of step-step index filters.

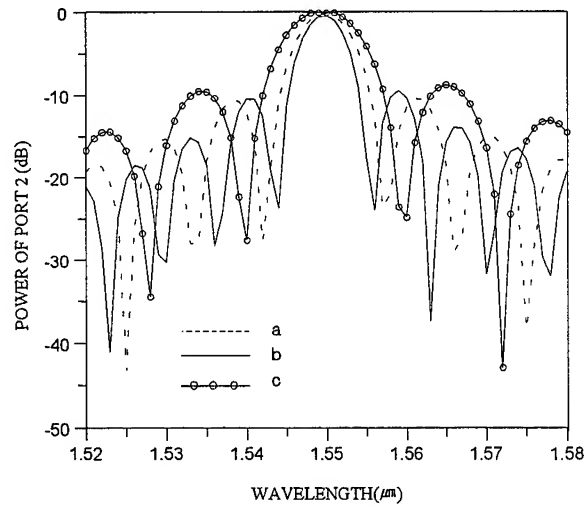


Fig. 5. Transmission characteristics of step-W index filters.

The coupling length L is determined such that $k(\lambda_0)L = \pi/2$. It is also noted that at $\lambda = \lambda_0$, $\Delta\beta = 0$. The 3-dB spectral width of the Step-Step filters is 8nm, while that of the W-Step filter is 1.5nm. This reduction in the spectral width is clearly due to the influence of the inner cladding of the W-index waveguide. It is further noted that the W-Step filter offers lower side lobe levels than the Step-Step filter hence better cross-talk rejection performance. This is more pronounced at wavelength. The insertion losses of both filters are expected to be very small.

Filter characteristics with peak transmission at 1.55μm and characteristics for different core separation at both 1.31μm and 1.55μm wavelength were also obtained.

Comparison of characteristics for W-Step and Step-Step filters at 1.55μm resulted in conclusions similar to those obtained for the characteristics at 1.31μm discussed above. The core separation d has a pronounced effect on the spectral width, but very little effect on side-lobe level was observed. For both filters, larger core separations resulted in narrower spectral widths.

4. CONCLUSION

A narrow-band spectral filter constructed with W-index and Step-index waveguides has been proposed and analyzed. Transmission properties of the proposed filter have been compared against those of a corresponding filter made of two Step-index waveguides. It has been shown that the proposed filter provides much narrower spectral width and lower side-lobe levels.

REFERENCE

- [1] H.Ishio, J.Minowa, and K.Nosu, "Review and status of wavelength division multiplexing technology and its applications," *J. Lightwave Technol.*, **2**, pp. 448-463, 1984.
- [2] G.Winzer, "Wavelength division multiplexing components-a review of single-mode devices and their applications," *J. Lightwave Technol.*, **2**, pp. 369-378, 1984.
- [3] M.Seki et al., "20-channel micro-optic grating demultiplexer for 1.1-1.6 μ m band using a small focusing parameter graded-index rod lens," *Electron Lett.*, **18**, pp. 257-258, 1982.
- [4] T.Suhara, Y. Handa, H. Nishihara, and J. Koyoma, "Monolithic integrated microgratings and photodiodes for wavelength demultiplexing," *Appl. Phys. Lett.*, **40**, pp. 120-122, 1982.
- [5] R. Watanabe, Y. Fujii, K. Nosu, and J-L. Minowa, "Optical multi/demultiplexers for single-mode fiber transmission," *IEEE J. quantum Electron.*, **QE-17**, pp. 974-981, 1981.
- [6] G. Winzer, H. F. Mahlein, and R. Reichelt, "Single-mode and multimode all-fiber directional couplers for WDM," *Appl. Opt.*, **20**, pp. 3128-3135, 1981.
- [7] K. Kitayama and Y. Ishida, "Wavelength selective coupling of two-core optical fiber: Application and design," *J. Opt. Soc. Amer. A.*, **2**, pp. 90-94, 1985.
- [8] R. Zengerle and O. G. Leminger, "Wavelength selective directional coupler made of non-identical single-mode fibers," *J. Lightwave Technol.*, **4**, pp. 823-827, 1986.
- [9] R. Zengerle and O. G. Leminger, "Narrow-band wavelength selective directional couplers made of dissimilar single-mode fibers," *J. Lightwave Technol.*, **5**, pp. 1196-1198, 1987.
- [10] K. Morishita, "Wavelength selective optical fiber directional couplers using dispersive materials," *Opt. Lett.*, **13**, pp. 158-160, 1988.
- [11] C. J. Chung, A. Safaai-Jazi, "Narrow-band spectral filter made of W-index and step-index fibers," *J. Lightwave Technol.*, **10**, no. 1, pp. 42-45, 1992.
- [12] A. Safaai-Jazi and G. L. Yip, "Cutoff conditions in three-layer cylindrical dielectric waveguides," *IEEE Trans. Microwave Theory Technol.*, **26**, no. 11, pp. 898-903, 1978.

Analysis of MMI Characteristics with Periodic Air Pads on SOI

Waveguide-Based Optical Interconnects

Shyh-Lin Tsao* and Huang-Chen Guo

Department of Electrical Engineering

Yuan Ze University

Chung-Li, Taiwan, R.O.C

ABSTRACT

In this paper, a new 1x4 multimode interference (MMI) SOI optical interconnects based on waveguide technology is presented. The MMI couplers including 2-D periodic air pads are analyzed. Especially the output powers adjustment of MMI SOI optical interconnects with considering the positions of those 2-D periodic air pads is studied. The SOI waveguide MMI interconnects is designed at wavelength 1.55 μ m region. We use beam propagation method to analyze the mode patterns. The mode patterns give the information of the power distributions of the output plane induced by guided wave propagating through those air pads. We analyze two cases of layout 40 pads and 70 pads for comparison.

Key words: Optical interconnect, Multimode Interference, Silicon on insulator, Optical waveguide

1. INTRODUCTION

High-capacity, small-size waveguide optical interconnects has attracted a lot of attention nowadays¹. One promising technology is using silicon-on-insulator(SOI) waveguide for light interconnection². Multiport-interconnections with multimode interference(MMI) waveguide couplers attract a lot attention recently³⁻⁴. Such a MMI device can reduce the coupler size and increase the fan out. Very recently, the two-dimensional photonic-bandgap lattices show the potential for guided light control⁵. The output power can be adjusted by the two-dimensional dielectric lattices.

The integration of integrated optical devices has become the future trend as the tremendous promising developments of integrated electrical circuits. In recent years, some researches related to optical waveguides using Si₃N₄, SiC layer on Si were reported⁶⁻⁹. Moreover, silicon-on-insulator (SOI) technology of MMI structure shows good ability of light splitting on the waveguide¹⁰⁻¹². Therefore, developments of optical and optoelectronic devices on SOI offer a path toward achieving low-cost, small size, monolithic high speed optoelectronic interconnection circuits. However, power adjustment of SOI MMI optical interconnects structure is not fully studied. In this paper, we pay our attention to study the propagation

* Correspondence: E-mail:jimmy@saturn.yzu.edu.tw, Telephone: 886-3-4638800-424, Fax: 886-3-4639355

characteristics of integrated optical interconnects on silicon-on-insulator wafers with air pads for power adjustment. The light propagation of SOI interconnects with 40 and 70 air pads are simulated with various refractive indices.

The simulation method we used is beam-propagation-method (BPM)¹³⁻¹⁵ which can simulate the light propagation by performing a step-by-step numerical calculation along the propagation direction. The procedure begins with a known electromagnetic field, that is the “initial” field. We optimize the “initial” field by using Alternating Direction Implicit Method (ADIM)¹⁶. Both of the light propagations and modal fields of 1x4 SOI MMI coupler are calculated in three dimensions with solving the semivectorial Helmholtz equation by BPM. The optical mode pattern, power transferring phenomenon and field on air pads are disclosed and analyzed. Those description and analysis are described in the following sections.

2. DESCRIPTION AND SIMULATION OF SOI WAVEGUIDES WITH AIR PADS

SOI MMI waveguide devices with constructive interference for optical interconnects have been demonstrated at wavelength $\lambda = 1.3 \mu\text{m}$ and $1.55 \mu\text{m}$, respectively¹⁷⁻¹⁸. In this section, we describe a 1x4 SOI coupler with air pads for optical interconnects. Fig.1 shows the cross-section diagram of our designed 1x4 MMI waveguide with air pads. The thickness of SiO_2 is $0.4 \mu\text{m}$, the depth of planar silicon waveguide is $0.95 \mu\text{m}$. The light input port width is $4 \mu\text{m}$, the depth of the rib waveguide is $0.55 \mu\text{m}$.

2.1 . Light propagating pattern though the SOI optical interconnect with 40 pads and 70 pads

As shown in Fig.2, we design the size of MMI region with width $W=40 \mu\text{m}$ and length $L=800 \mu\text{m}$. The width of all the pads is $1 \mu\text{m}$, the length of all the pads is $10 \mu\text{m}$ and the period of these air pads is fixed as $50 \mu\text{m}$. After the light go through the MMI region with air pads, four ports (1~4) are designed at the output of the waveguide. To analyze the effect of those pads, the light propagation in MMI region and the output field distribution are investigated at wavelength $1.55 \mu\text{m}$ by BPM. The top view of the light propagation through the MMI region with 40 air pads on the waveguide is shown in Fig.3. We can find that the light propagation direction can be controlled by periodic air pads. For comparison, the pads is filled with material whose index is 3, we show the simulation results in Fig.4. We find that the light interference will be changed by the variation of refractive index. Obviously, the constructive interference will increase with changing the refractive index from $n=1$ to $n=3$. The distance of the two positive interference pads becomes smaller with comparing Fig.3 and Fig.4. Increasing the pads number and fixed the pads periods, we analyze the 1x4 MMI SOI interconnects with 70 pads. The extra 30 air pads are added around the 40 air pads as analyzed in Fig.3. The top view of the light propagation though the 70 pads is shown in Fig.5. We can find that the lightwave propagation has two main directions of constructive interference at first, then thought these periodic pads, two destructive interference region is shown obviously at the middle of the waist of MMI region. For comparison, the SOI is filled with a material whose refraction of index $n=3$, the top view of the light propagation is shown in Fig.6. We can find the destructive interference waist appeared at the MMI region become weak. The lattice period and numbers can be adjusted to control the lightwave propagation direction and the locations of constructive interference. We can find that constructive interference waist in MMI region become wider with n increases. In

general, the MMI region with 70 pads has better constructive interference than 40 pads in MMI region with our design. The direction of constructive interference of light wave is shown obviously that can be controlled by the design of air pads.

2.2 . Simulation of output field patterns

The output field patterns of our designed 1x4 MMI SOI interconnect waveguides are simulated in this subsection. The output light field distribution of the MMI region with 40 square pads is shown in Fig.7. We can find the field pattern have symmetric output field pattern. For comparison, the pads filled with material whose index is 3, we show the field pattern in Fig.8. We can find the field pattern of 40 pads changes. The output power of 1 and 4 power is larger than output 2 and 3. This result shows the power variation controlled by the refractive index change. The output light field distribution of the MMI region with 70 square pads is shown in Fig.9. The output powers is approximately equal to the case of MMI with 40 pads ($n=1$). For comparing with $n=3$, the 70 pads are filled with material whose index is 3, we show the field pattern in Fig.10. The output powers of port 1 and port 4 become larger. The MMI optical interconnect with 70 pads ($n=3$) is better than MMI optical interconnect with 40 pads. Thus, we demonstrate the number and refractive index of these pads can be used to control the output optical powers for optical interconnection.

3. CONCLUSION

We have designed and simulated the structure of air pads on the MMI waveguide at wavelength $1.55\ \mu\text{m}$. We can find the MMI region with 70 pads can have better output than 40 pads. The refractive index raising is also affect the output power distribution. This waveguide can also be designed as power divider with arbitrary air pads for various power splitting optical interconnects with more than 4 outputs. The output direction of lightwave propagation constructive interference path can be designed with pads number control. We can also find the direction of lightwave propagation can be designed with changing the refractive index of periodic pads. In this paper, some preliminary results shows the power control can be achieved by various pads number design. The width and length of MMI region are also important parameters for designing such a device. We believe this work will be helpful for size reduction of optical interconnection devices.

ACKNOWLEDGMENT

This work was supported in part by National Science Council of Republic of China under contract no. NSC 89-2215-E-155-003.

REFERENCE

1. T. T. H. Eng, J. Y. L. Ho, P. W. L. Chan, S. C. Kan and G. K. L. Wong, "Large core($\sim 60\mu\text{m}$) SOI multimode waveguide for optical interconnect", IEEE photonic Technology Letter, **8**, pp. 1196-1198, 1996.
2. B. Jalali, P. D. Trinh, S. Yeguanarayanan, F. Coppinger, "Guided-wave optics in silicon-on insulator technology", IEE Proc. Optoelectron, **143**, pp. 307-311, 1996.
3. Q. Lai, M. Dachmann, W. Hunziker, P. A. Besse, H. Mechior, "Arbitrary ratio power splitters using angled silica on

- silicon multimode interference coupler”, *Electronics Letters*, vol. 32, pp. 1576-1577, 1998.
4. P. D. Trinh, S. Yeguanarayanan, and B. Jalali, “5x9 integrated optical star coupler in silicon-on-insulator technology”, *IEEE photonics Technology Letters*, **8**, pp. 794-796, 1996.
 5. D. Labilloy, H. Benisty, C. Weisbuch, T. F. Krauss, D. Cassagne, C. Jouanin, R. Houdre, U. Oesterle, and V. Bardinal, “Diffraction efficiency and guided light control by two-dimensional photonic-bandgap lattices”, *IEEE Journal of Quantum Electronics*, **35**, pp. 1045-1052, 1999.
 6. F. Navamar and R. A. Soref, “Optical waveguide in $\text{GeSi}_{1-x}/\text{Si}$ strained layer heterostructures”, *J. Appl. Phys.*, **70**, pp. 3370-3372, 1991.
 7. A. Splett, J. Schmidtchen, Schu ¨, B. Peter, K. Petermann, E. Kasper, and H. Kibbel, “Low loss optical ridge waveguides in silicon strained GeSi epitaxial layer grown on silicon”, *Electron. Lett.*, **26**, pp. 1035-1036, 1990.
 8. J. Schmidtchen, Schu ¨, B. Peter, A. Splett, and K. Petermann, “Germanium-diffused waveguides in silicon for $\lambda = 1.3 \mu\text{m}$ and $\lambda = 1.55 \mu\text{m}$ with losses below 0.5dB/cm”, *IEEE Photonics Technol. Lett.*, **4**, pp. 875-877, 1992.
 9. Y. M. Liu, and P. R. Prucnal, “Low-loss silicon carbide optical waveguides for silicon-based optoelectronic devices”, *IEEE Photonics Technol. Lett.*, **4**, pp. 704-707, 1993.
 10. L. Soldano, F. Veerman, M. Smit, B. Verbeek, A. Dubost, E. Pennings, “Planar monomode optical couplers based on multimode interference effects” *J. Lightwave Technol.*, **10**, pp. 1843-1849, 1992
 11. J. M. Heaton, R. M. Jenkins, D. R. Wight, J. T. Parker, J. C. H. Birbeck, and K. P. Hilton, “Novel 1-to-N way integrated optical beam splitters using symmetric mode mixing in GaAs/AlGaAs multimode waveguides” *Appl. Phys. Lett.*, **61**, pp. 1754-1756, 1992.
 12. L. Soldano and E. Pennings, “Optical multi-mode interference devices bases on self-imaging: Principles and applications” *J. Lightwave Technol.*, **13**, pp. 615-627, 1995.
 13. J. V. Roey, J. V. D. Donk., and D. Lagasse, “Beam propagation: analysis and assessment”, *Journal of the Optical Society of America*, **71**, pp. 803-810, 1981.
 14. Yu-Chiu Chao. “Optics measurement resolution and BPM errors ” *Particle Accelerator Conference, 1997. Proceedings of the 1997*, **12**, pp. 2125 -2127, 1998.
 15. Kawano, K.; Kitoh, T.; Kohtoku, M.; Takeshita, T.; Hasumi, Y. “3-D semivectorial analysis to calculate facet reflectivities of semiconductor optical waveguides based on the bi-directional method of line BPM (MoL-BPM) ” *IEEE Photonics Technology Letters*. **101** , pp. 108 -110, 1998.
 16. C. Chen, and S. Jungling, “Computation of higher-order waveguide modes by imaginary-distance beam propagation method”, *Optical and Quantum Electronics*, **26**, pp. 199-205, 1994.
 17. Huang, J.Z.; Scarmozzino, R.; Osgood, R.M., Jr. “A new design approach to large input/output-number multimode interference (MMI) couplers and its WDM applications ”, *Lasers and Electro-Optics Society Annual Meeting, 1998. LEOS '98. IEEE*, **1**, pp. 332 -333 vol.1, 1998.
 18. Pennings, E.C.M.; van Roijen, R.; van Stralen, M.J.N.; de Waard, P.J.; Koumans, R.G.M.P.; Verbeek, B.H. “Reflection properties of multimode interference devices ”, *IEEE Photonics Technology Letters*, **66**, pp. 715 -718, June 1994.

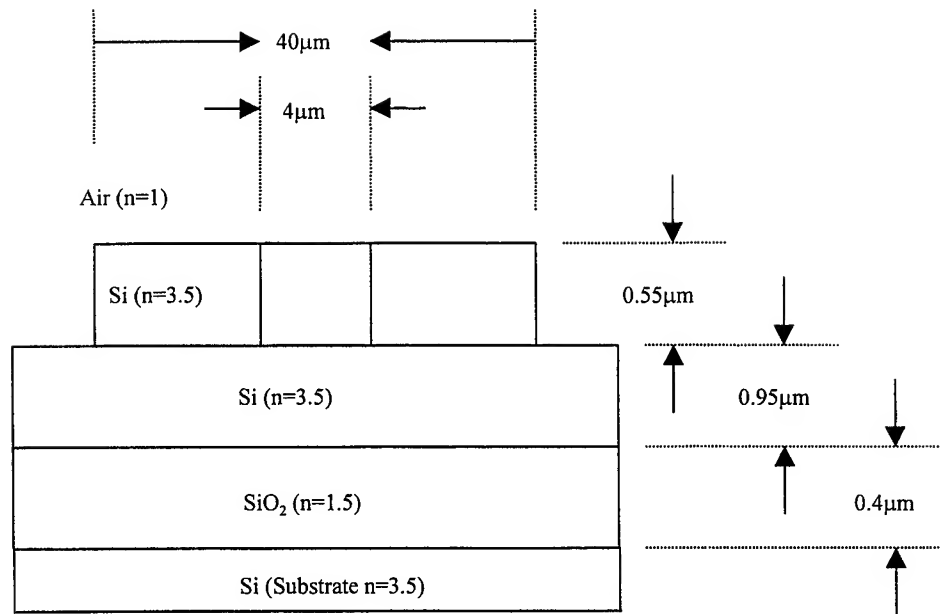


Fig.1 The cross-section diagram of 1x4 MMI waveguide

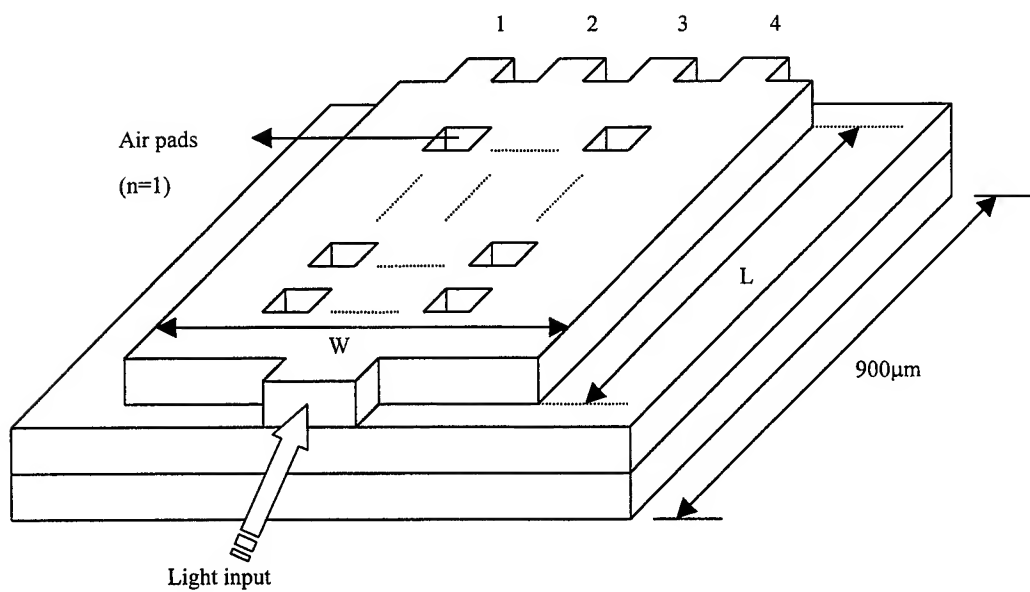


Fig.2 The structure diagram of 1x4 MMI waveguide with air pads

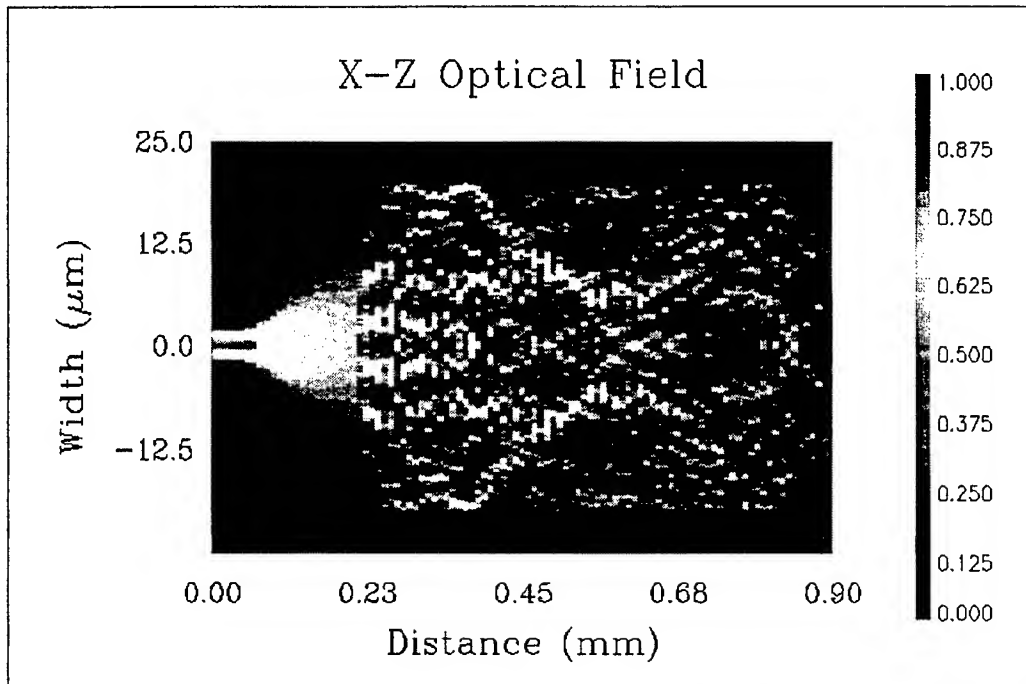


Fig.3 Top view of the light propagating through the MMI region with 40 square pads
(square pad $n=1$)

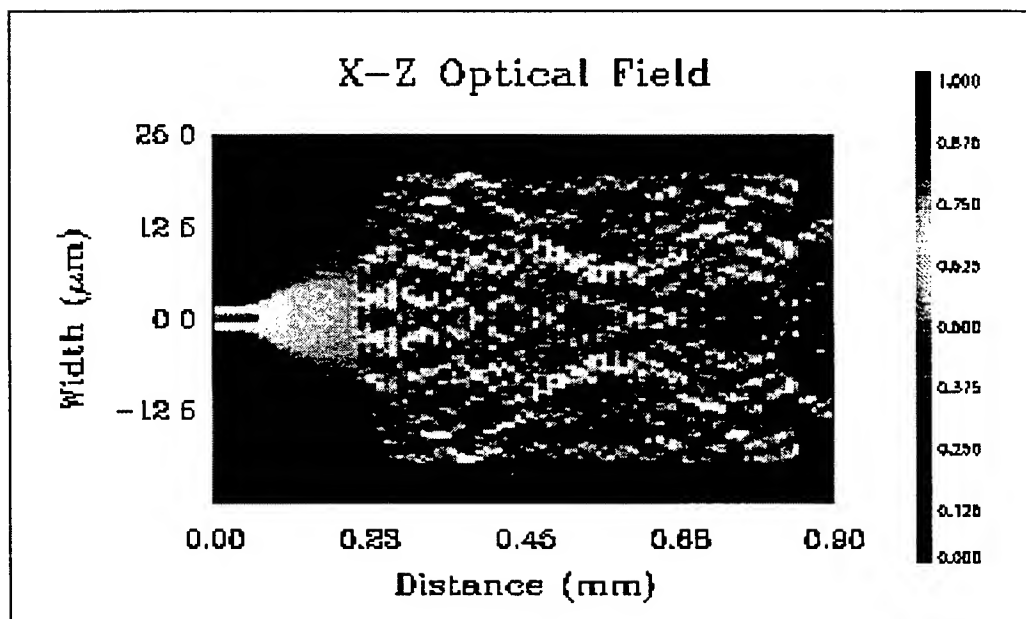


Fig.4 Top view of the light propagating through the MMI region with 40 square pads
(square pad $n=3$)

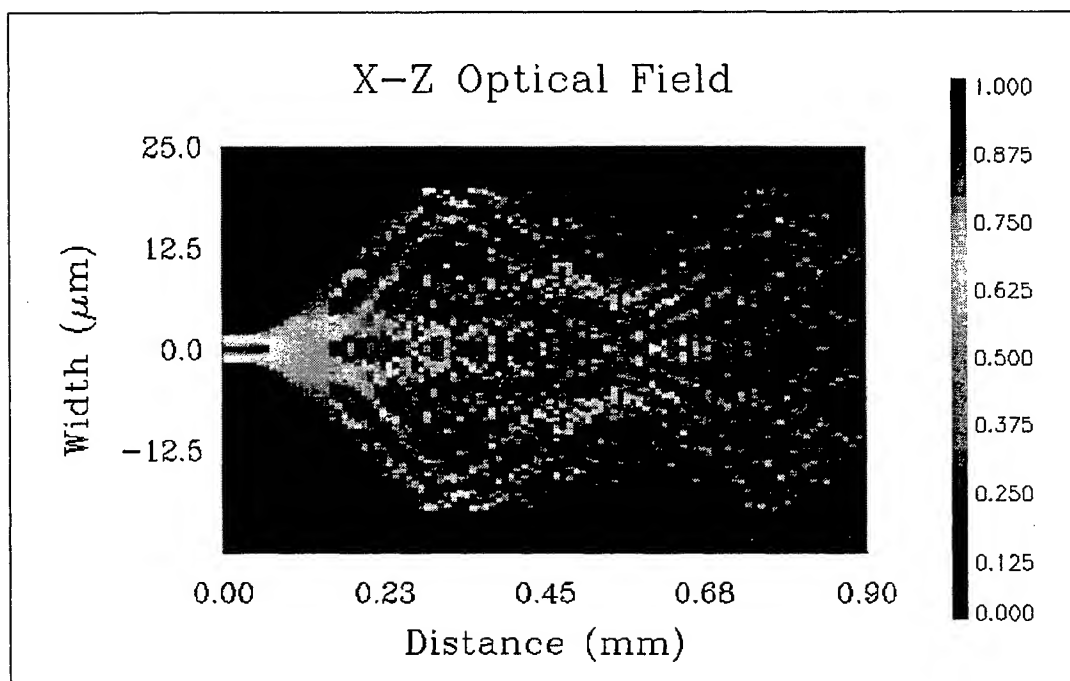


Fig.5 Top view of the light propagating through the MMI region with 70 square pads
(square pad $n=1$)

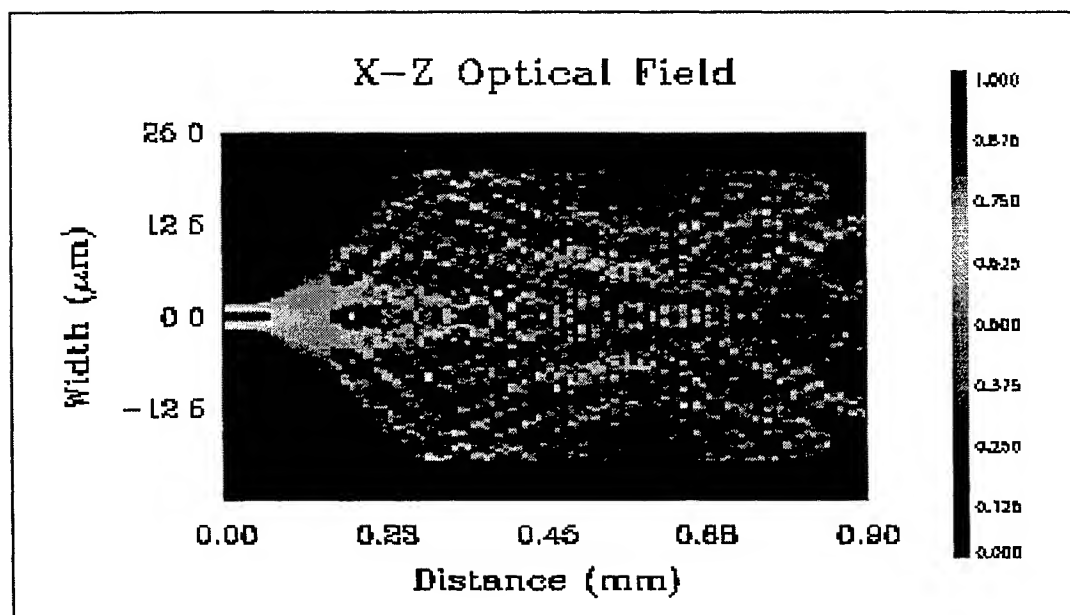


Fig.6 Top view of the light propagating through the MMI region with 70 square pads
(square pad $n=3$)

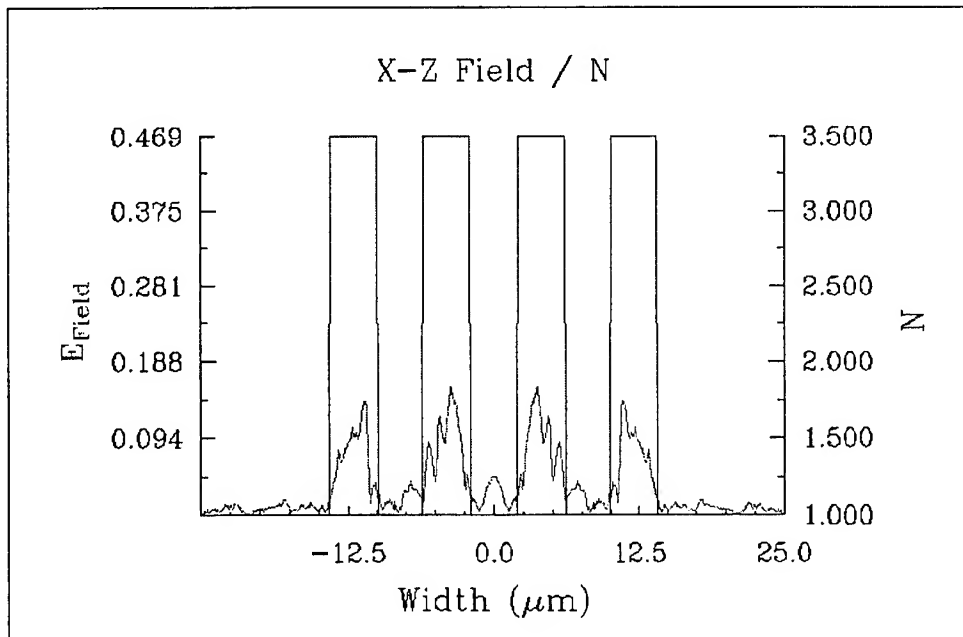


Fig.7 Output light field distribution of the MMI region with 40 square pads
(square pad n=1)

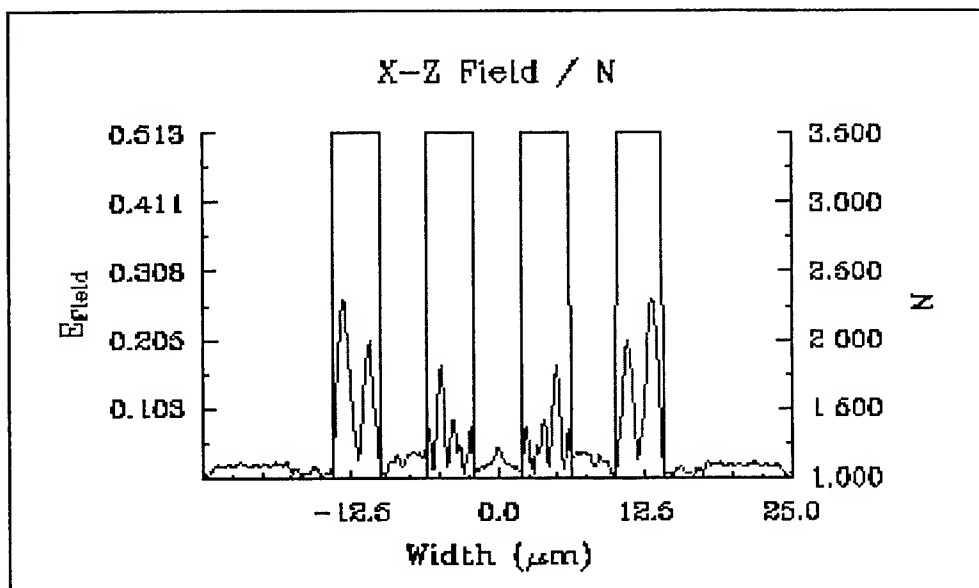


Fig.8 Output light field distribution of the MMI region with 40 square pads
(square pad n=3)

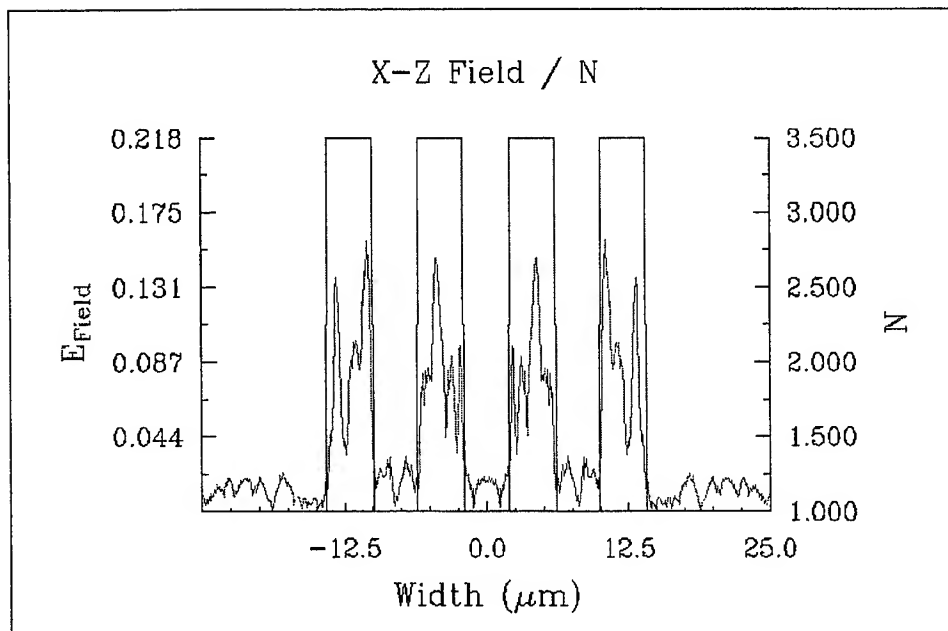


Fig.9 Output light field distribution of the MMI region with 70 square pads
(square pad $n=1$)

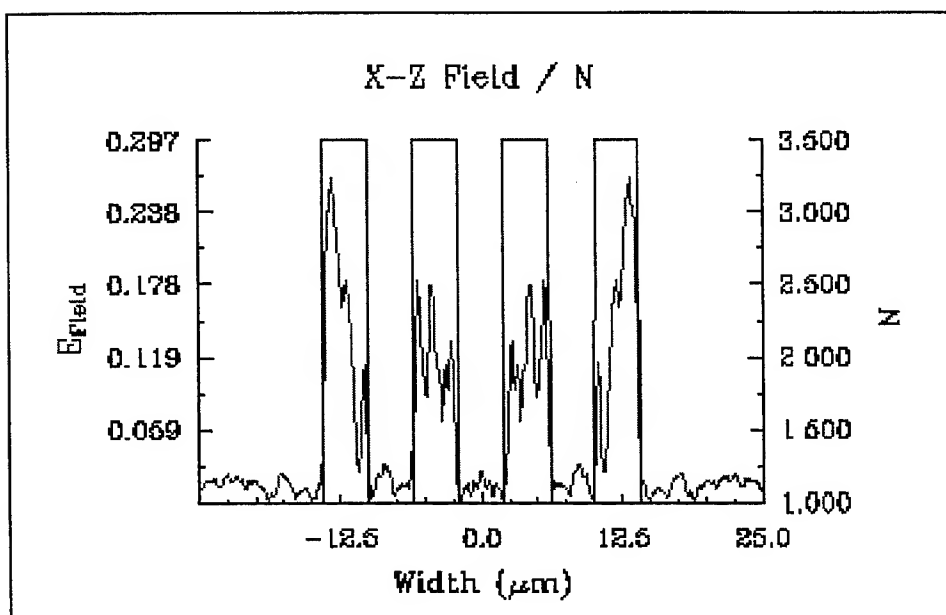


Fig.10 Output light field distribution of the MMI region with 70 square pads
(square pad $n=3$)

Analysis of the Optimal Light Launching Position of SOI Tapered

Waveguides

Shyh-Lin Tsao* and Ming-Chun Chen

Department of Electrical Engineering

Yuan Ze University

Chung-Li, Taiwan, R.O.C

ABSTRACT

In this paper, we design two tapered waveguides on the silicon-on-insulator (SOI) wafers. The shape of designed SOI waveguides are linearly and exponentially tapering varied along the propagation direction. The width of our designed SOI waveguide at starting point is $6\mu\text{m}$, the end width is $20\mu\text{m}$. We find out the optimal light launching position for maximum power output with single mode pattern. The linearly and exponentially tapered waveguides are compared. Finally, we add a polymer layer as a cladding layer, the differences between the exponentially tapered waveguide and the linearly tapered waveguide with the polymer cladding are analyzed. The best design of the tapered SOI waveguide with polymer cladding is obtained.

Key words: Tapered waveguide, integrated optics, polymer cladding, silicon on insulator

1. INTRODUCTION

In recent years, the silicon photonic integrated circuit (PIC's) attracts a lot of attention. Research on silicon-based photonic component can be utilized in the future optical devices. Some optical devices attract a lot of attention based on silicon¹⁻⁵. However, the rib optical waveguides formed from SOI materials have been designed⁶⁻⁷ in the wavelength range 1.3 μm to 1.55 μm . The SOI single-mode of rib waveguide compared with the optical fiber had been reported⁷. Therefore, the SOI technology developed for achieving low cost and monolithic high-speed PICs becomes an important issue.

Developments of OEIC optoelectronic devices based on waveguide technology are important for future optical communications⁸. The optical devices can achieve high functionality and low cost on silicon⁹. The passive integrated optical mode expander will reduce the coupling loss between the standard fiber and tightly confined waveguides. Recently, tapered waveguides are vastly studied for fiber coupling¹⁰⁻¹¹.

Correspondence: E-mail:jimmy@saturn.yzu.edu.tw, Telephone: 886-3-4638800-424, Fax: 886-3-4639355

With relaxed alignment requirements, the tapered waveguide can increase coupling power. Many tapered waveguides have been designed on III-V and II-VI compound material wafers¹²⁻¹³. The single mode optical fibers integrated with PICs using tapered waveguides are demonstrated for coupling efficiency improvement¹⁵⁻¹⁸. However, on SOI wafer, little tapered waveguide researches are reported and extended. The benefits of achieving tapered waveguide on SOI wafers are high yields, low cost and maturity of the silicon manufacture supporting technologies.

In this paper, we design a tapered rib waveguide with SOI structure we adopt the beam-propagation-method (BPM)¹⁴ which can simulate the light propagation in waveguide by step-by-step numerical calculation along the propagated direction. A fundamental Gaussian field with wavelength 1.55 μm is considered as a starting field. We analyze the input spot-size and launch position at the center along the Y-axis at first, then a polymer cover is considered to put on waveguide for protection.

2. TAPERED WAVEGUIDE

2.1 The Structure of the Tapered waveguide

In this section, we design the exponential tapered waveguide on UNIBOND wafer. At first, we design the rib waveguide. The thickness of substrate is 0.4 μm and the top silicon film thickness is 1.5 μm . The schematic diagram of our designed exponentially tapered waveguide is shown in Fig.1. The start width of the tapered waveguide is 20 μm and the end width is 6 μm .

We divided the tapered waveguide into three sections for analysis. As shown in Fig.2 the first section length is 500 μm , the second length is 500 μm and the third section is 3000 μm . the second section is the tapered region. The exponentially tapered waveguide has exponentially varied tapering shape along light propagation direction. The shape of the linearly tapered waveguide has a linear connection between 6 μm and 20 μm .

2.2 The power loss versus the input spot size

A Gaussian field is considered as an input field. The transmittances versus the spot-size of W_y Y-axis for linearly and exponentially tapered waveguide can be represented as the following two equations.

$$T_{\text{linear}} = -0.0098W_y^2 + 0.1742W_y + 0.1606 \quad (1)$$

$$T_{\text{exponentially}} = -0.0097W_y^2 + 0.18W_y + 0.0967 \quad (2)$$

We use BPM CAD to find out the optimal input laser spot size. The found input field is shown in Fig.3. Tuning the laser spot size in Y-axis direction from 0.75 μm to 15 μm , the power loss (dB) versus the spot size is shown in Fig.4. We compare two different structures of linearly and exponentially tapered waveguides with the same input spot size. According to the simulation result, the input spot size of 7 μm is the optimal cases for designing the tapered waveguide. Because the light input through the coupling lens with various spot sizes can be adjusted and launched into the waveguide. We can find the input power loss is low with using linearly tapered waveguide when the input light spot size is smaller than 8 μm . With the input spot size larger than 8 μm , the exponentially tapered waveguide has lower loss compared with linearly tapered waveguide.

2.3 Change input position

We simulate the input light spot locating at the center of X-axis, and regulating along the Y-axis position. We find the optimal light launching position is located at $0.8 \mu\text{m}$ height from the center of coordinate shown Fig.2. The exponentially tapered waveguide power transmittance versus launching position along Y-axis is shown in Fig.5. Similarly, the linearly tapered waveguide power transmittance versus launching position along Y-axis is shown in Fig.6. Obviously, the two cases exponentially and linearly tapered waveguide with optimal light input position in Fig.5 and Fig.6, the power losses can be designed less than 1dB. Most of the light can be confined in the SOI waveguide at optimal input position $0.8 \mu\text{m}$ at Y-axis. The light go through the exponentially and linearly tapered waveguide is single mode pattern during the simulation. The exponentially tapered waveguide power transmittance can reach 90.9% and the linearly tapered waveguide power transmittance can reach 92% of the input light power. We also consider the cases of covering the polymer film on SOI tapered waveguide. The refractive indices of polymer are typically in the range from 1.6 to 1.9. We chose the 1.49 and 1.51 as the refractive indices of polymer for simulation in Fig.5 and Fig.6. Comparing the three cases in Fig.5, we find that simulation results of air covered exponentially tapered waveguide have larger power losses, such as the light launching positions are located at $0.9 \mu\text{m}$ and $1 \mu\text{m}$ on Y-axis. Comparing Fig.6 with Fig.5, the linearly tapered waveguide show almost overlapping curves of the three cases in Fig.6. The optimal light input position is located at $0.8 \mu\text{m}$ located from the center of Y-axis. According to our simulation, the output mode pattern also is a single mode pattern. The transmittance versus the Y-axis position of the linearly tapered waveguide covered with polymer 1.51 can be represented as the following equation.

$$T = -0.7322y^2 + 1.0862y + 0.39515 \quad (3)$$

The output mode pattern of the best design of linear tapered waveguide covered with polymer 1.51 is shown in Fig.7.

3.CONCLUSION

In this paper, we analyze the power losses of two tapered waveguides by BPM. We find the better designed tapered waveguide is linearly tapered waveguide for comparing with exponentially tapered waveguide. The light going through the tapered waveguide is designed as a single mode lightwave for connection the light between two waveguides of $6 \mu\text{m}$ and $20 \mu\text{m}$. The optimal input light position is found to be $0.8 \mu\text{m}$ on the Y-axis. Obviously, the light input position and spot size will heavily affect the output power. This work is helpful for fiber coupling and laser launching position alignment.

ACKNOWLEDGMENT

This work was supported in part by National Science Council under Grant No. NSC 89-2215-E-155-003. The authors would like to thank Mr. Sheen-Je Lee and Peng-Chun Peng for valuable discussions and simulation supports.

REFERENCE

1. P. D. Trinh, F. Coppinger and B. Jalali, "Compact silicon-based integrated optical time delays", *IEEE Photonics Technology Letters*, 9, 5, pp. 634-635, 1997.

2. A. Cutolo, M. Iodice, A. Irace, P. Spirito and L. Zeni, "Electrically controlled Bragg reflector integrated in a rib silicon on insulator waveguide", *Applied Physics Letts.*, **71**, 2, pp. 199-201, 1997.
3. A. Cutolo, M. Iodice, P. Spirito and L. Zeni, "Silicon electro-optic modulator based on a three terminal device integrated in a low-loss single-mode SOI waveguide", *J. of Lightwave Technol.*, **15**, 3, pp. 505-518, 1997.
4. A. G. Rickman and G. T. Reed, "Silicon-on-insulator optical rib waveguide: loss, mode characteristics, bends and y-junctions", *Proc. Inst. Elev. Eng.-Optoelectron.*, **141**, pp. 391-393, 1944.
5. C. K. Tang and G. T. Reed, "Highly efficient optical phase modulator in SOI waveguides", *J. Lightwave Technol.*, **31**, pp. 451-452, 1995.
6. A. Rickman, G. T. Reed, B. L. Weiss, and F. Namavar, "Low-loss planar optical waveguides fabricated in SIMOX material", *IEEE Photon. Technol. Lett.*, **4**, 6, pp. 633-635, 1992.
7. J. Schmdtchen et al., "Low-loss single-mode optical waveguides with large cross section in silicon-on-insulator", *Electron. Lett.*, **27**, pp. 1486-1487, 1991.
8. L.D. Garrett, S. Chandrasehhar, J. L. Zyskind, J. W. Sculhoff, A. G. Dentai, C. A. Burrus, L. M. hunardi and R. M. Derosier, "Performance of 8-channal OEIC receiver array in 8×2 5Gbps WDM transmission experiment", *IEEE photonic Technology Letters*, **9**, 2, pp. 235-237, 1997.
9. M. Asghari, "Photonics integration on Silicon", *Proc. of SPIE*, **3795**, pp. 586-595, 1999.
10. R. E. Smith, C. T. Sullivan, G. A. Vawter, G. R. Hadley, J. R. Wendt, M. B. Snipes, and J. F. Klem, "Reduced coupling loss using a tapered-rib adiabatic-following fiber coupler", *IEEE Photon. Technol. Lett.*, **8**, pp. 1052-1054, 1996.
11. G. A. Vawter, R. E. Smith, H. Hou, and J. R. Wendt, "Semiconductor laser with tapered-rib adiabatic-following fiber coupler for expanded output-mode diameter", *IEEE Photon. Technol. Lett.*, **9**, pp. 425-427, 1997.
12. Muller, B. Stegmuller, H. Westermiere and G. Wenger, "Tapered InP/InGaAsP waveguide structure for efficient fiber-chip coupling", *Electron. Lett.*, **27**, pp. 1836-1838, 1991.
13. T. Brenner and H. Melchior, "Integrated optical mode shape adapters in InGaAsP/InP for efficient fiber-to-waveguide coupling", *IEEE Photon. Technol. Lett.*, vol. 5, pp. 1053-1056, 1993.
14. J. Van Roey, J. V. D. Donk., and Lagasse, "Beam propagation: analysis and assessment", *Journal of the Optical Society of America*, **71**, pp. 803-810, 1981.
15. I. Moerman, P. P. Van Daele, and P. M. Demeester, "A review on fabrication technologies for the monolithic integration of tapers with III-V semiconductor devices", *IEEE J. Select. Topics Quantum Electron.*, **3**, pp. 1308-1320, 1997.
16. J. Buus, W. J. Stewart, J. Haes, J. Willems, and R. G. Baets, "Spot size expansion for laser-to-fiber coupling using an integrated multimode coupler", *J. Lightwave Technol.*, **11**, pp. 582-588, 1993.
17. V. Vusirikala, S. S. Saini, R. E. Batolo, S. Agarwala, R. D. Whaley, F. G. Johnson, D. R. Stone, and M. Dagenais, "1.55μm InGaAsP-InP laser arrays with integrated-mode expanders fabricated using a single epitaxial growth", *IEEE J. Select. Topics Quantum Electron.*, **3**, pp. 1332-1343, 1997.
18. G. A. Vawter, C. T. Sullivan, J. R. Wendt, R. E. Smith, H. Q. Hou, J. F. Klem, "Tapered rib adiabatic following fiber couplers in etched GaAs materials for monolithic spot-size transformation", *IEEE J. Select. Topics Quantum Electron.*, **3**, pp. 1361-1371, 1997.

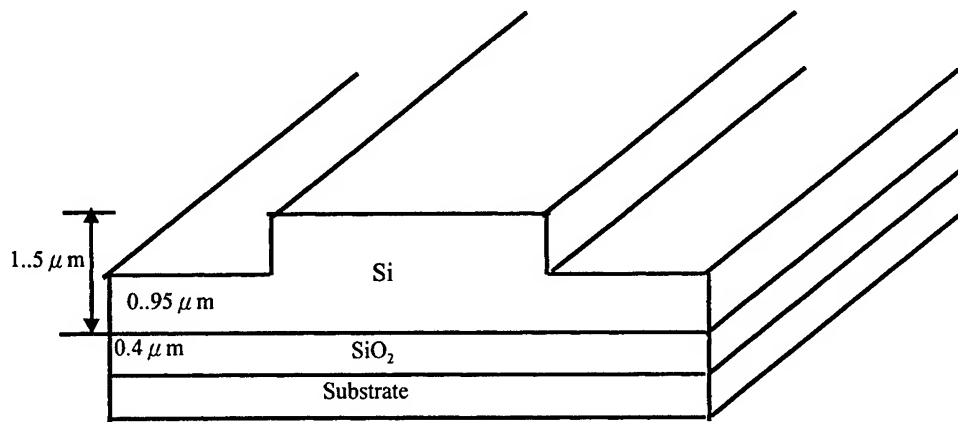


Fig.1 The structure of UNIBOND silicon-on-insulator rib waveguide

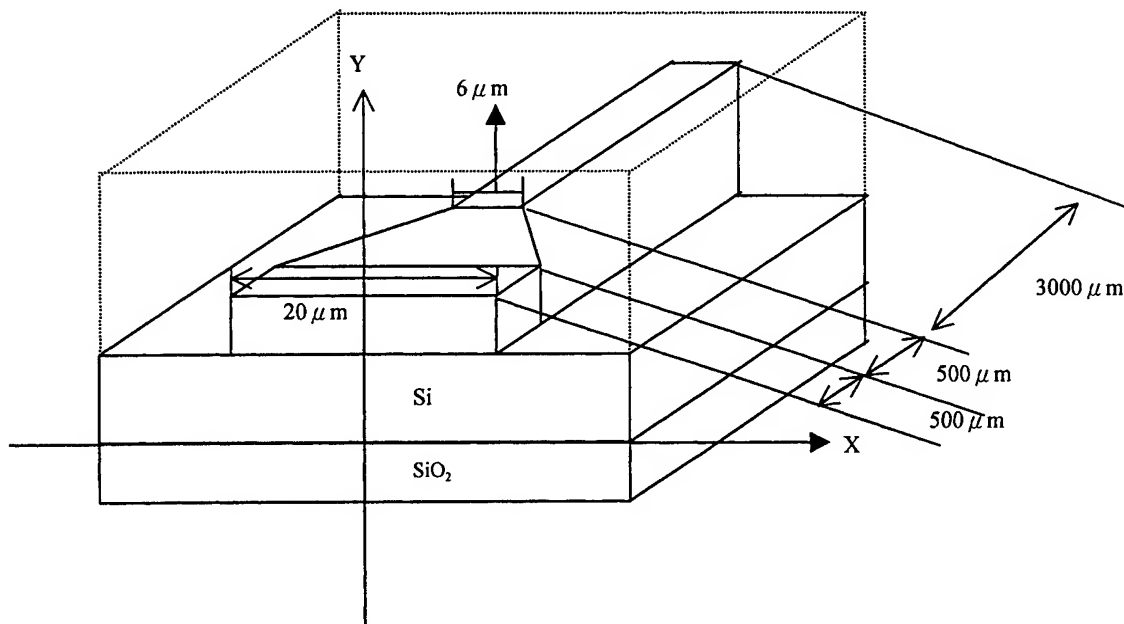


Fig.2. The schematic diagram of our designed exponentially tapered waveguide

X-Y Optical Field

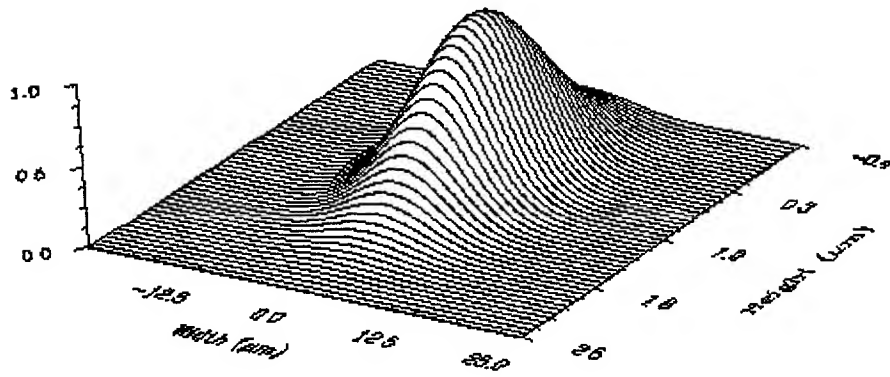


Fig.3 The Gaussian input starting field

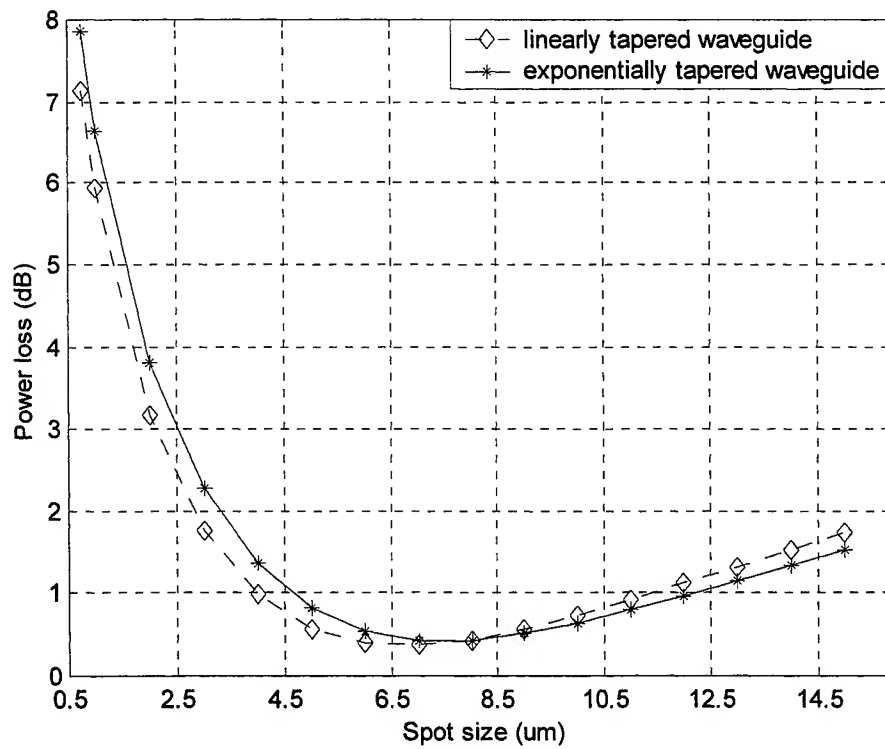


Fig.4 The power loss versus spot size at input location (0,0.75)

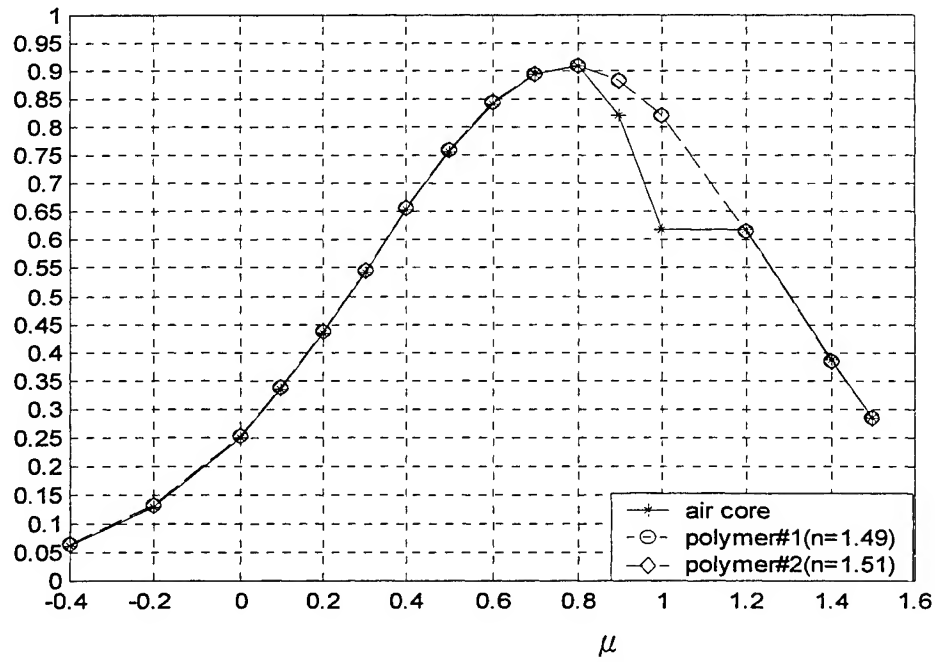


Fig.5 The power loss versus light launching position for exponentially tapered waveguide

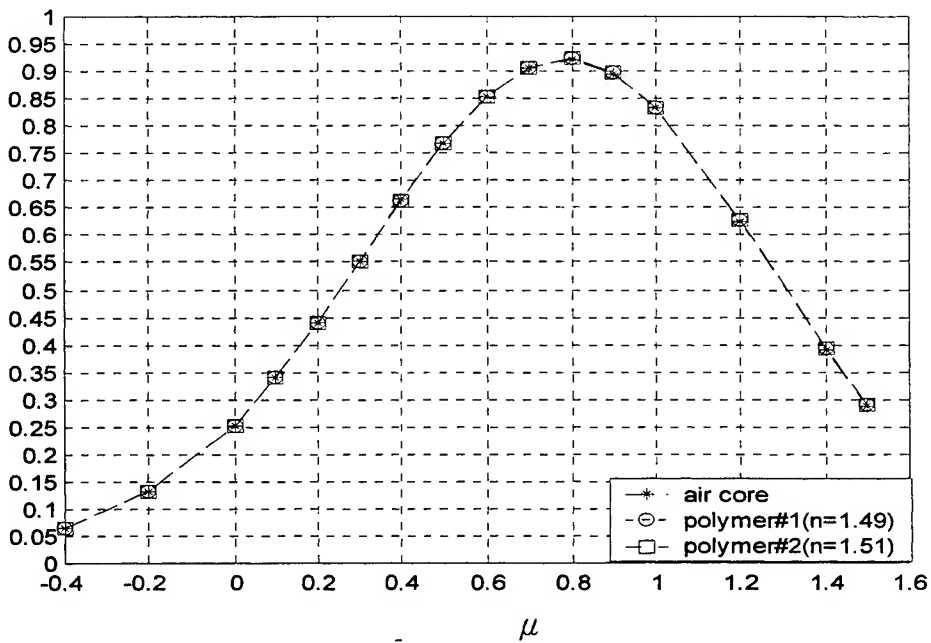


Fig.6 The power loss versus light launching position for linearly tapered waveguide

X-Y Optical Field

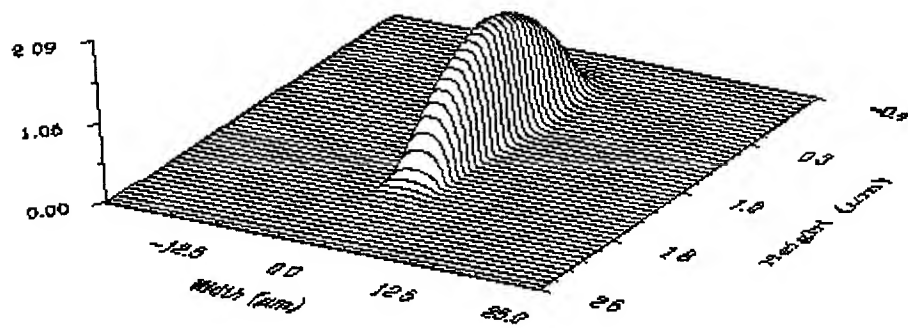


Fig.7 The output mode pattern of linearly tapered waveguide

Experimental Study of The Temperature Effect on The Polarization State of MQW Semiconductor Optical Amplifier

Shyh-Lin Tsao* and Yu-Long Shen
Department of Electrical Engineering
Yuan Ze University
Chung-Li, Taiwan, R.O.C

ABSTRACT

In this paper, we analyze the polarization variation of semiconductor optical amplifier (SOA) induced by temperature variation. This work is motivated by the requirement of high-speed optical signal transmission in fiber communication networks with using SOAs. Experimental polarization Stokes parameters are measured. The degree of polarization shows monotonically decreasing with temperature increasing. The temperature variation of SOA is monitored between 14°C to 33 °C. Our work is helpful for measuring the temperature effect on polarization of SOAs for application in optical communication systems.

Key words: Semiconductor optical amplifier, Polarization, Temperature effect, Stokes parameters, Fiber communication

1. INTRODUCTION

In optical fiber transmission systems, the SOA is an important device¹. SOAs can provide the function of optical signal amplification in fiber links. Recently, it is also considered for application in dynamic routing photonic integrated devices for Tbps SD/WD optical switches². Such applications need a lot of SOAs. Therefore, the characteristics measurement and analysis of SOAs should be researched before systems implementation³. Especially, reducing the polarization effect of the SOAs' light output attract a lot of attentions⁴. As we know, the polarization effect measurements of fiber components are important but little results have been reported. Very recently, distributed PMD measurement technique with a polarization OTDR shows a promising technique for fiber remote monitoring⁵. Accompany with such a method, one may measure the SOAs' characteristics in remote control center. In this paper, we study the polarization variation following the temperature variation of SOA. The Stokes parameters are measured in 14°C to 33 °C range. The following sections show some parameters definitions and experimental results.

* Correspondence: E-mail:jimmy@saturn.yzu.edu.tw, Telephone: 886-3-4638800-424, Fax: 886-3-4639355

2. Polarization Parameters Definitions

In this section, we define some polarization parameters⁶⁻¹¹ at first. Usually we use the following expressions to represent the x-component and y-component electric fields of the light to be examined.

$$E_x = \Re \left\{ A(t) e^{j[\omega t + P_x(t)]} \right\} \dots\dots\dots(1)$$

$$E_y = \Re \left\{ B(t) e^{j[\omega t + P_y(t)]} \right\} \dots\dots\dots(2)$$

where A and B represent the amplitudes of the electric fields in the x and y directions, respectively. P_x and P_y are the instantaneous phases, \Re means real part and ω means angular frequency. We define the phase difference as Delta shown in equation (3) for combining the equation (1) and (2) as the equation (4) as following :

$$D \stackrel{def}{=} P_y - P_x \dots\dots\dots(3)$$

$$\vec{E} = E_x \vec{x} + E_y \vec{y} = \Re \left\{ \left[A \vec{x} + B e^{jD} \vec{y} \right] e^{j[\omega t + P_x(t)]} \right\} \dots\dots\dots(4)$$

Adopting the widely used definitions, we define the Stokes Parameters as following :

$$S_0 \stackrel{def}{=} A^2 + B^2 \dots\dots\dots(5)$$

$$S_1 \stackrel{def}{=} A^2 - B^2 \dots\dots\dots(6)$$

$$S_2 \stackrel{def}{=} 2AB \cos D \dots\dots\dots(7)$$

$$S_3 \stackrel{def}{=} 2AB \sin D \dots\dots\dots(8)$$

and

$$D = \tan^{-1} \left(\frac{S_3}{S_2} \right) \dots\dots\dots(9)$$

Normalize the Stokes parameters by the total optical power (including polarized and unpolarized light), we can write

$$\varsigma_1 = \frac{S_1}{S_0}, \quad \varsigma_2 = \frac{S_2}{S_0}, \quad \varsigma_3 = \frac{S_3}{S_0} \dots\dots\dots(10)$$

The range of the normalized Stokes parameters is -1 to +1 which can be shown on a Poincar'e sphere.

3. Experimental Setup and Measuremental results

3. 1. Experimental Setup

Fig.1 shows a schematic diagram of experimental setup of polarization of SOA. The temperature range in the multiple quantum well semiconductor optical amplifier (MQW-SOA) can be controlled by a temperature controller from 14°C to 33 °C in a stabilized operation scheme. The basic components of the MQW-SOA is divided into three parts including a semiconductor optical amplifier, a current driver and a temperature controller. The current and temperature of the multiple quantum well semiconductor optical amplifier can be controlled by a temperature controller and a current driver. The power of the MQW-SOA can be adjusted by the current controller and the temperature of MQW-SOA can be adjusted by the temperature controller. A polarimeter is used for analyzing the output lightwave polarization states of MQW-SOA. Through the measurement of the polarimeter, the input lightwave can be divided into three Stokes parameters S_1 , S_2 , S_3 , etc. We can take the Stokes parameters, phase difference D and degree of the polarization on the screen.

The degree of polarization is represented as

$$DOP = \frac{P_{polarized}}{P_{polarized} + P_{unpolarized}} \dots\dots\dots(11)$$

where $P_{polarized}$ means fully polarized light and $P_{unpolarized}$ means completely unpolarized light.

3.2 . Experimental Results

Using the experimental setup shown in Fig. 1, we can measure the variation of polarization state versus the temperature variation on the Poincar'e sphere shown in Fig. 2. When we inject input current $I=0.027A$ to MQW-SOA, we can take the data the Stokes parameters (including S_1 , S_2 , S_3), phase difference D , and degree of polarization versus the temperature at same time. The results are shown in Fig. 3 ~ Fig. 7, respectively. In those figures, temperature effect on the polarization state versus Stoke's Parameters are analyzed.

The following are the semi-emperical equations we fitted :

$$S_1=0.0007T - 0.0558 \dots\dots\dots(12)$$

$$S_2=0.0009T - 0.0966 \dots\dots\dots(13)$$

$$S_3=0.000075T+ 0.99445 \dots\dots\dots(14)$$

$$\Delta=-0.1T + 95.5 \dots\dots\dots(15)$$

$$DOP=-0.1T + 11.15 \dots\dots\dots(16)$$

We find that the S_1 , S_2 , S_3 are almost linearly increasing as the temperature raising. However, the phase difference Delta and DOP are linearly decreasing as the temperature raising.

3. CONCLUSION

In summary, we found some linear relationships between the Stokes parameters and temperature. Among those results, the S_2 is the most sensitive parameter with respect to temperature. That is to say, we may measure the micro-variation of temperature by detecting the polarization parameters of SOAs in a optical fiber communication system. The further experiments for finding the remote sensing method will be reported in the near future.

ACKNOWLEDGMENT

This work was supported in part by National Science Council of Republic of China under contract no. NSC 89-2215-E-155-003

REFERENCE

- 1.C. Tai, S.-L. Tzeng, H.-C. Chang, and W. I. Way, "Reduction of nonlinear distortion in MQW semiconductor optical amplifier using light injection and its application in multi-channel M-QAM signal transmission systems", *IEEE photonic Technology Letter*, **10**, pp.609-611,1998.
- 2.K. Emura and Minoru Shikada, "High capacity optical networking technologies ",*proceeding of CLEO/pacific Rim '99*, **1**,pp.116-117,1999.
- 3.A. Sharaha, "Distortion analysis of the photodetection and gain spectral response of a semiconductor optical amplifier" *IEEE photonic Technology Letter*, **10**, pp.1031-1033, 1998.
- 4.A. D. Carlo, A. Reale, L. Tocca and P. Lugli, "Polarization-independent δ -strained semiconductor optical amplifiers: a tight-binding study", *IEEE Journal of Quantum Electronics*, **34**, pp.1730-1739, 1998.
- 5.B. Huttner, B.Gisin and N.Gisin, "Distributed PMD measurement with a polarization-OTDR in optical fibers", *IEEE Journal of Lightwave Technology*, **17**, pp.1843-1848, 1999.
- 6.Grogory D. Van Wiggeren, Rajarshi Roy. " High-speed fiber-optical polarization analyzer: measurement of the polarization dynamics of an erbium-doped fiber ring laser", *Optics Communications*, **164**, pp.107-120, 1999.
- 7.J. S. Wang, J. R. Costelloe, and R. H. Stolen. "Reduction of the Degree of Polarization of a Laser Diode with a Fiber Lyot Depolarizer"*IEEE Photonic Technology Letters*, **11**, pp.1449-1451, 1999.
- 8.Nigel G. Walker, and Graham G. Walker, "Polarization Control for Coherent Communications" *Journal of Lightwave Technology*, **8**, pp.438-458, 1990.
- 9.Ralph P. Tatam, David C. Hill, Julian D. C. Jones, and David A. Jackson, "All-Fiber-Optical Polarization State Azimuth Control: Application to Faraday Rotation" *Journal of Lightwave Technology*, **6**, pp.1171-1176, 1988
- 10.Peijuan Gao, Paola Bassi, Maurizio Zoboli, "Tunable Birefringent Optical Single-mode Fiber Filter" *Journal of Optical Communications*, **14**, pp.128-133, 1993.
11. Q. D. Liu, J. T. Chen, Q. Z. Wang, P. P. Ho, and R. R. Alfano, Senior Member, IEEE, "Polarization Stability of Circularly Polarized Laser Pulses Propagating in Non-Birefringent Single-Mode Optical Fibers" *IEEE Photonics Technology Letters*, **7**, pp.517-519, 1995.

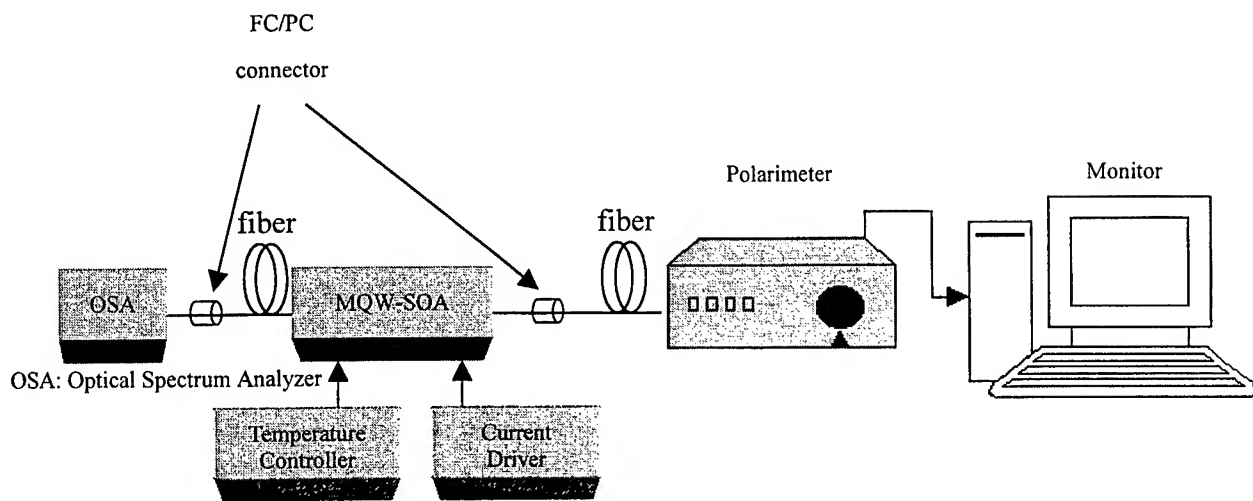


Fig. 1 Schematic diagram of the polarization measurement setup

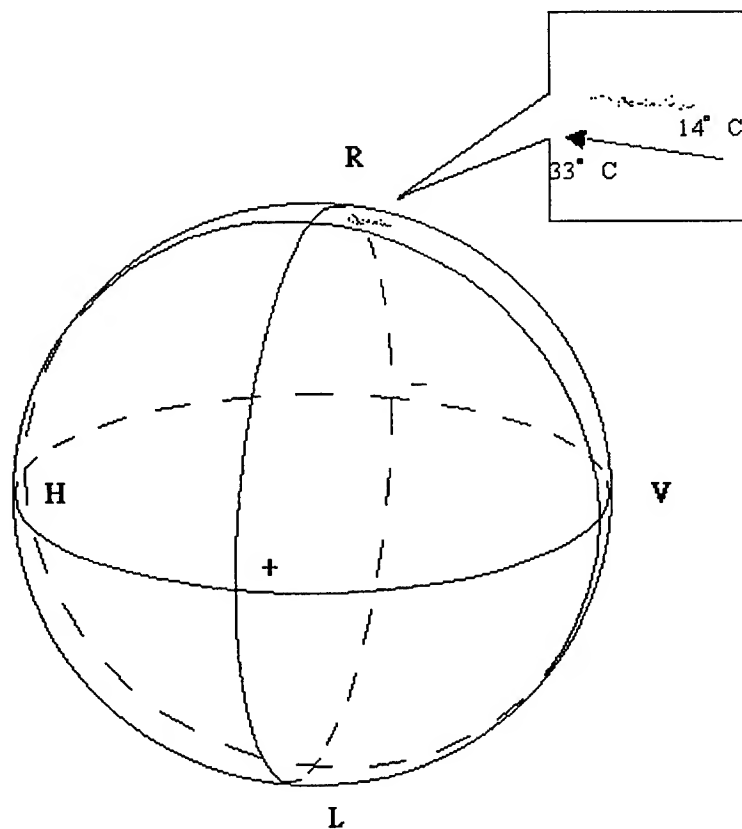


Fig. 2 The polarization state variation corresponding to the of temperature variation from 14°C to 33°C on Poincaré Sphere

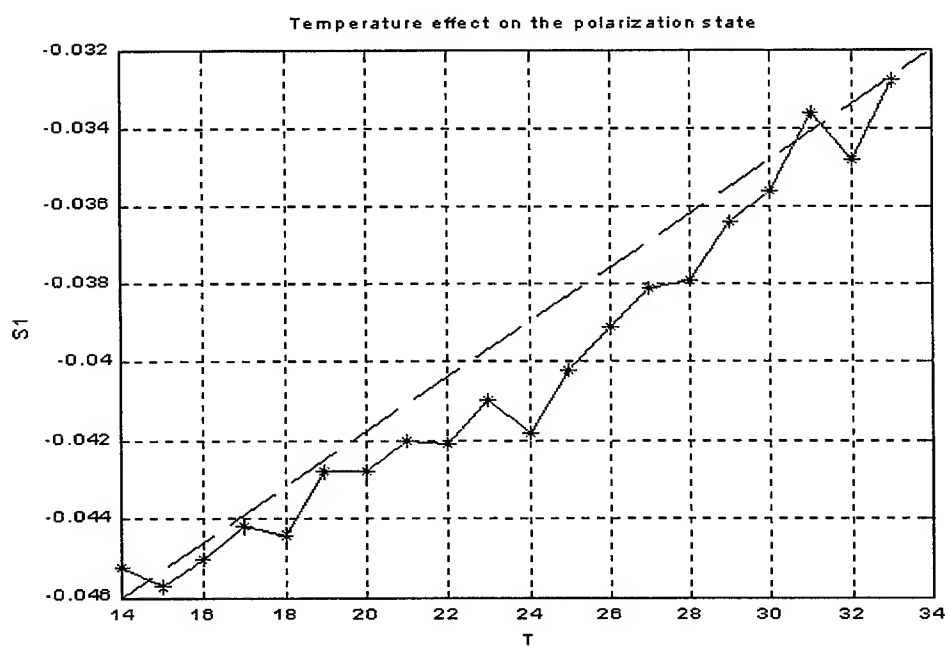


Fig. 3 Temperature effect on the polarization state versus Stoke's Parameter S_1
when the output current of the current controller is $I=0.027A$

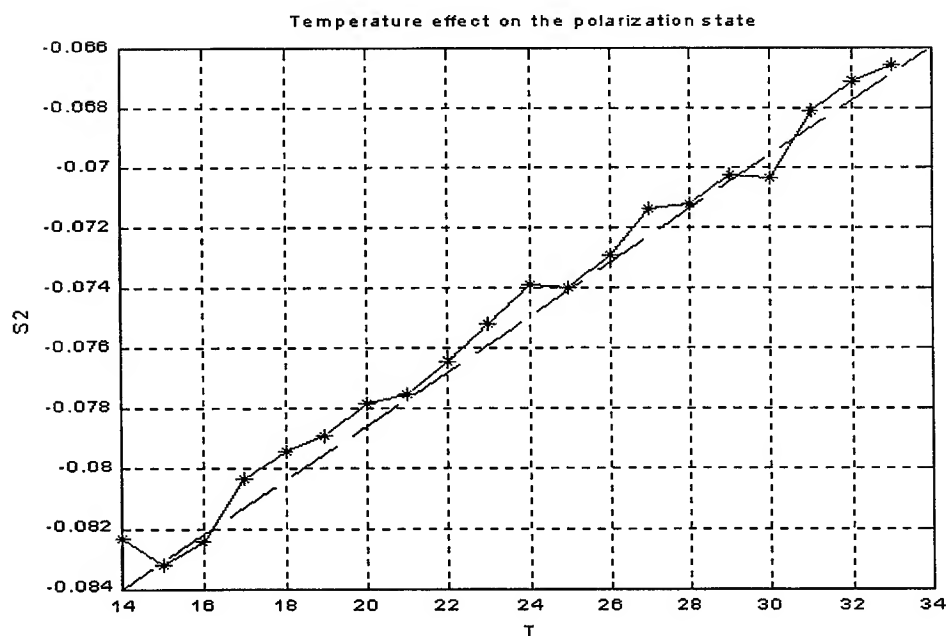


Fig. 4 Temperature effect on the polarization state versus Stoke's Parameter S_2
when the output current of the current controller is $I=0.027A$

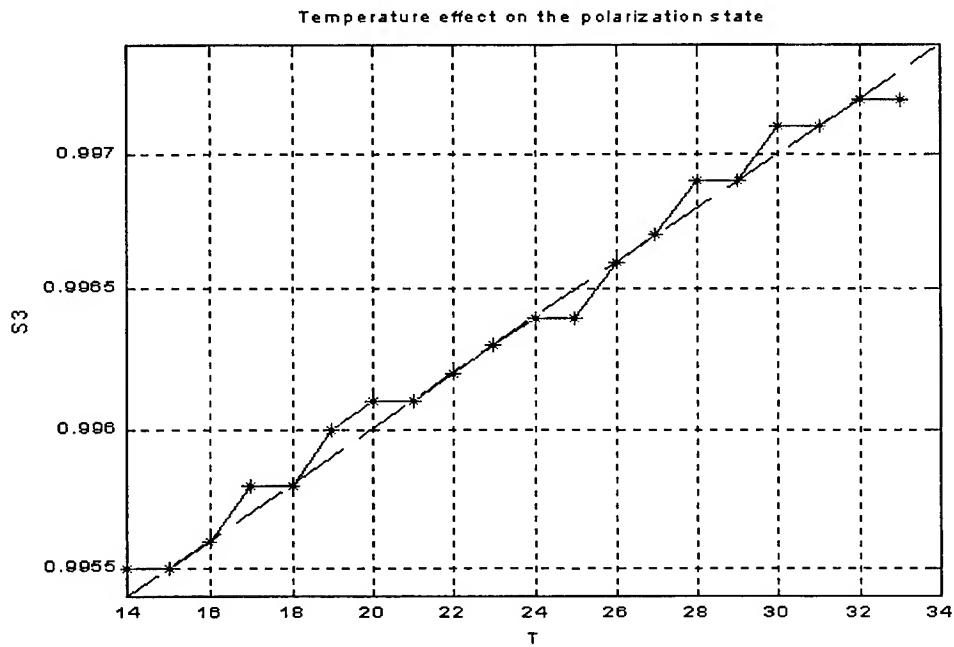


Fig. 5 Temperature effect on the polarization state versus Stoke's Parameter S_3
when the output current of the current controller is $I=0.027A$

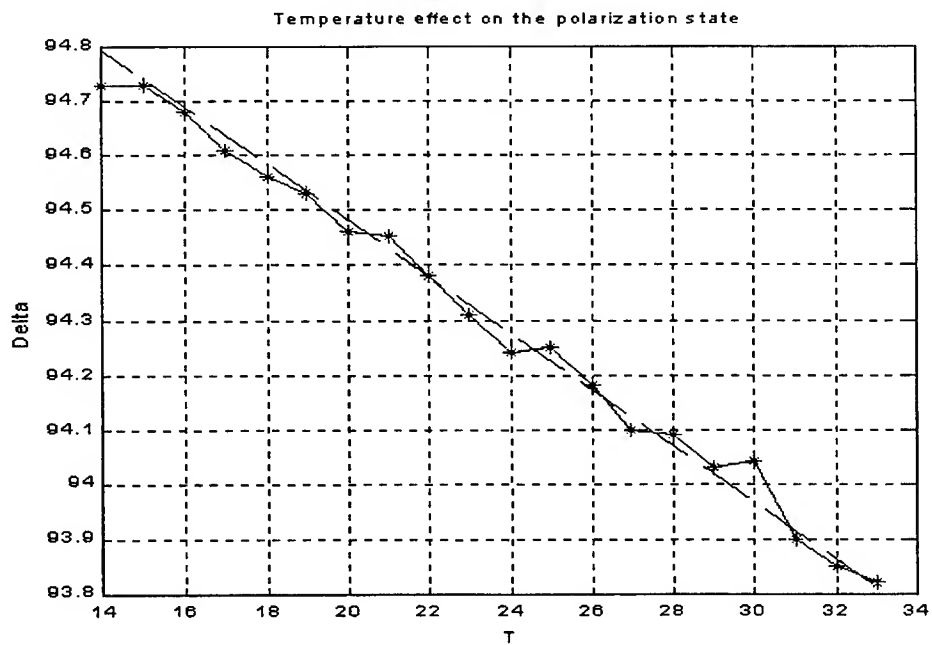


Fig. 6 Temperature effect on the polarization state versus Δ when the output current of the current controller is $I=0.027A$

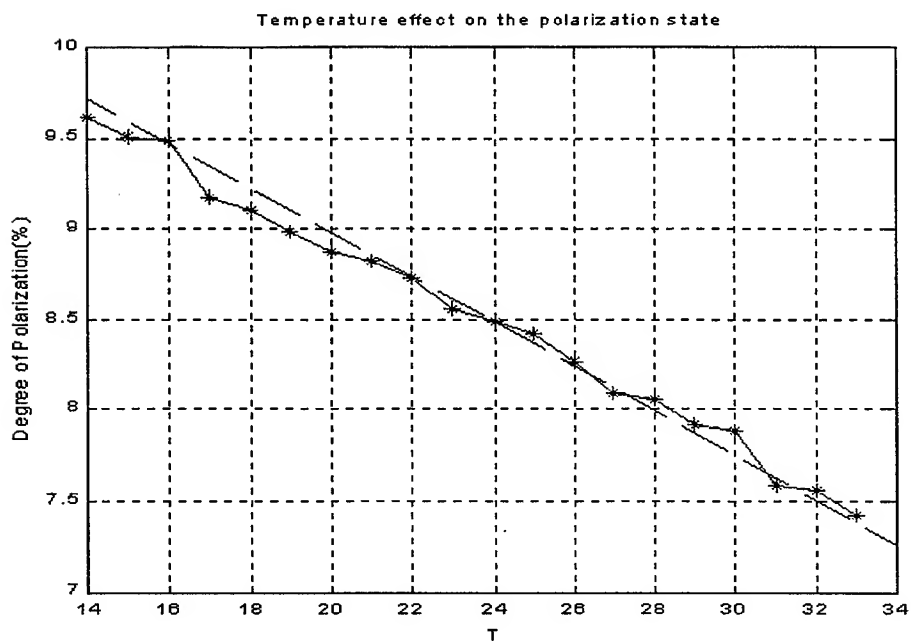


Fig. 7 Temperature effect on the polarization state versus Degree of Polarization
when the output current of the current controller is $I=0.027A$

Fermi level pinning of GaAs at room temperature directly determined by the amplitude of photoreflectance spectra

Yau Huei Chen^{*a} and Ruy Ming Chen^b

^aDept. of Physics, National Taipei Univ. of Technology, Taipei 10764, Taiwan, Republic of China

^bInstitute of Opto-electronic Technology, National Taipei Univ. of Technology, Taipei 10764, Taiwan, Republic of China

ABSTRACT

Photoreflectance (PR) measurements on an n-GaAs epitaxial layer as a function of the intensity of pumping light are reported. Based on the thermionic emission theory and current-transport theory, the pinning position of surface Fermi level can be determined from the dependence of the PR signal on the pumping light intensity. Experiments demonstrated that the PR amplitude depends upon the optical excitation intensity I as $\ln(\gamma I)$, which is normally the case experimentally and theoretically. From the analysis of the dependence of the amplitude of PR on optical excitation intensity, the surface Fermi level of GaAs at room temperature about 0.72 ± 0.02 eV below conduction band was evaluated easily and directly. This result is consistent with those accurately reported results using PR to characterize samples with specially designed complex surface-intrinsic-doped structures for obtaining a uniform Franz-Keldysh oscillations and derived the built-in electric fields then evaluated the Fermi level pinning position indirectly.

Keywords: Fermi-level pinning, Photoreflectance, Photoeffect, Modulation intensity.

1. INTRODUCTION

GaAs and related materials such as AlGaAs possess potential for optoelectronic and high speed electronic device applications. Because GaAs is a direct band gap semiconductor, it is an efficient photonic material. The GaAs/AlGaAs heterostructure is a promising material system due to its large conduction band discontinuity, which can result in a two-dimensional electron gas concentration. Besides, this system's small effective mass ensures high mobilities and larger electron saturation velocities for high-speed device operation. For device design and application, information pertaining to the surface Schottky barrier and surface Fermi level pinning are of paramount importance. Due to its influence of device applications, surface Fermi level pinning positions have attracted many interests of study.¹⁻⁴

^{*}Correspondence: Email: yhchen@ntut.edu.tw; Telephone: (02)27712171-3102; Fax: (02)27317180

In characterizing semiconductors, photoreflectance (PR) spectroscopy has become one of the most popular among the modulated spectroscopy methods because no electrical contacts are required and it is a nondestructive technique. This modulation technique is very attractive owing to its simplicity and room temperature performance. Besides, PR has the additional advantage in that it has better sensitivity than other optical measurements.⁵ In addition to optical transition energies, recently there has been growing interest in the use of Franz-Keldysh oscillations (FKOs) that are observed on the high-energy side of the band gap energy from the PR spectrum to determine the surface or interface electric field.⁶⁻⁸ Therefore, PR experiments may be used to study the temperature, doping-level, and structure variations of the internal electric fields in the semiconductor materials. The method can determine the surface electric field optically, and has been used to determine the position of the Fermi level (qV_F) on the surface of GaAs, AlGaAs, and InAlAs, etc..^{9,10} Because of the fast damping of FKOs being due to the broadening effect and/or nonuniform electric field in the space charge region, it does not allow for an accurate determination of the electric field deduced from the period of FKOs. Van Hoof et al.¹¹ have designed a GaAs structure with a combination of uniform electric field and small broadening parameter makes it possible to observe a large number of FKOs, and hence, to use PR as an effective probe of built-in electric fields. These structures are made by fabricating an undoped layer on a buried heavily doped n^+ or p^+ buffer layer, i.e., surface-intrinsic-doped (SIN or SIP) structures.^{12,13} Theoretically, it has been found that the period of FKOs from the space charge region in a doped sample is determined mainly by the maximum surface field.¹⁴ The derived values of the built-in electric field from the theoretical interpretation of FKOs are lower than the field values derived from the electrostatic calculations.^{11,15} Because PR is an optical characterization method in which electromodulation is produced internally by photoexcited electron-hole pairs (free carriers) generated by a secondary light pump source, the effect of the photovoltage on the electric field cannot be ignored as the sample is illuminated with photons with an energy larger than the band gap.¹⁶⁻¹⁹ To eliminate the photovoltage effect, the SIN or SIP samples were characterized at elevated temperature up to 500 °C. With the assumption that the temperature dependence of qV_F is assumed to be the same as that of the band gap which is described by the Varshni expression, then the qV_F at room temperature can be evaluated indirectly.²⁰⁻²² However, there are few reports about the quantitative analysis for PR signal amplitude.

In this letter, we use PR to determine the surface Fermi level of a low doped film of n-GaAs by fitting the amplitude of PR spectra as a function of pump beam intensity in a contactless manner. Because the amplitude of PR spectra (A) is proportional to the intensity of pumping light (P),^{23,24} the surface Fermi level of GaAs at room temperature can be deduced directly without the variation of a large scale temperature range, a hypothesis of the temperature dependence of surface Fermi level, and specially designed structures. The directly derived surface Fermi level energy of GaAs at room temperature by the relationship of A and P is 0.72 ± 0.02 eV below conduction band edge.

2. EXPERIMENTAL DETAIL

Samples were prepared by molecular beam epitaxy (MBE) with elementary solid source. An n-type GaAs epitaxial layer of about 10 μm thickness was grown on the substrate of undoped (100) GaAs. The n-type dopant is Si. The growth was under arsenic stabilized condition and the growth rate was about 2 $\mu\text{m/hr}$. Room temperature Hall measurements were utilized to determine the free-carrier concentration. The free-carrier concentration is $2.5 \times 10^{14} \text{ cm}^{-3}$. The PR apparatus was

similar to that described in the literature.²⁵ Light from a 150 W tungsten-halogen lamp passed through a 0.3 m McPherson monochromator with a 1200 grooves/mm grating blazed at 500 nm to produce a quasi-monochromatic light. Typical resolution is 6 Å with 100 μm × 4 mm slits. The exit light was focused onto the sample by a lens. The reflected probe light from the sample was focused onto an EG&G HUV 4000B silicon photodiode biased in photoconductive mode with high gain preamplifier. Modulation was achieved with the 633 nm line of a 5 mW air-cooling He-Ne laser chopped at 200 Hz and attenuated to the desired power by a neutral density filter. The spot size of pumping laser on the sample is about 3 mm in diameter. The pumping power density ranged from 0.6 μW/cm² to 8.06 mW/cm². Both light beams were nearly normal incident (<10°) on the sample spot. A long-pass filter was placed before the photodiode to eliminate the scattered light from reaching the detector. The modulated reflected signal (ΔR) was detected by a lock-in amplifier, and the reflected signal (R) was measured through a dc voltmeter. The dc signal from the photodetector was used as a feedback to the servo motor that varied the variable neutral density filter and hence the intensity of the light impinging on the sample hoops as a constant. With this type of renormalization procedure, PR signal is directly obtained from lock-in amplifier fed with the ac signal that contains information about the material under periodical perturbation. All the signals, ΔR, R, and the wavelength of incident beam were controlled by a personal computer.

3. RESULTS AND DISCUSSIONS

Based on current-transport theory, the photovoltage V_p can be approximated as²¹

$$V_p = \frac{kT}{q} \ln \left[\frac{J_p}{r J_0(T)} + 1 \right] \approx \frac{kT}{q} \ln \left[\frac{J_p}{J_0(T)} \right] \quad (1)$$

where r , as introduced first by Yin et al,²¹ is the geometrical factor that equals the fraction of the surface that has surface states, J_p is the induced photocurrent density in the depletion and buffer (diffusion) regions, and $J_0(T)$ is the saturation dark current density that depends on the dominant current flow mechanism. For a sample without special treatment, the geometrical factor (r) nearly equals to one. As the Fermi level is pinning nearly at the mid-gap ($\approx 0.5E_g$) of GaAs which will make the first term of bracket much larger than 1 and ensures the approximation been valued. For the sample configuration used in this study, diffusion and thermionic emission are the main contributions to $J_0(T)$ so that we can write²⁰

$$J_0(T) = \frac{A^* T^2}{1 + BT^{3/2}} \exp \left(-\frac{qV_F}{kT} \right) \quad (2)$$

where A^* is the modified Richardson constant with $A^*=8.0 \text{ A/cm}^2\text{K}^2$ and B is a constant related to the saturation velocity with $B=3.3 \times 10^{-4} \text{ K}^{-3/2}$. J_p can be written as²¹

$$J_p = \frac{qP \eta (1 - R)}{\hbar \omega} \left(1 - e^{-\alpha W} + \frac{\alpha L_d}{1 + \alpha L_d} e^{-\alpha W} \right) \quad (3)$$

where η is the quantum efficiency (≈ 1), R is the reflectivity of the light at the sample surface (≈ 0.34), $\hbar \omega$ is the photon energy of the pumping light, α is the absorption coefficient ($\approx 10^4 \text{ cm}^{-1}$), W is the depletion width, and L_d is the diffusion length of the minority carrier ($\approx 3.3 \text{ μm}$). As the diffusion length is much longer than the light penetration depth, $\alpha L_d \gg 1$, and $\alpha W \gg 1$, eq.(3) becomes

$$J_p \approx \frac{qP(1-R)}{\hbar\omega} = qf \quad (4)$$

where f is the flux of pumping photons. In this situation, eq.(4) is equivalent to the simplest approximation that effectively all the charge carriers generated by the pumping light contribute to J_p .

Since the signal of modulation is proportional to the amplitude of the effective perturbed dielectric function, PR signal is proportional to V_p to first order approximation. Assume the proportional constant between the amplitude of signal, A , and V_p is C , i.e., $A=CV_p$. Therefore, we can express A in terms of J_0 and J_p as

$$A = \frac{CkT}{q} \ln\left(\frac{J_p}{J_0}\right) = \frac{CkT}{q} [\ln(f) + \ln\left(\frac{q}{J_0}\right)] = C_1 \ln(f) + C_2 \quad (5)$$

From the eqs. listed above, qV_F can be evaluated in C_1 and C_2 as

$$qV_F = kT \left\{ \ln\left[\frac{A^2 T^2}{q(1 + BT^{3/2})} \right] + \frac{C_2}{C_1} \right\} \quad (6)$$

Fig.1 shows the amplitude of PR signal as a function of the photon flux of pumping light. The amplitude of PR spectra were derived using the well-known third derivative functional form.²⁶ When the pumping laser impinges on sample surface and creates electron-hole pairs, the created holes and electrons in depletion region are swept to surface states and bulk, respectively, to screen the electric field. This will effectively lower the band bending by an amount of V_p . Also taking place is the competing process of capturing the electrons provided by thermionic emission current from the undepleted region. This will limit the lowering amount of V_p to a certain value as a function of flux of photons. Since the signal of modulation is

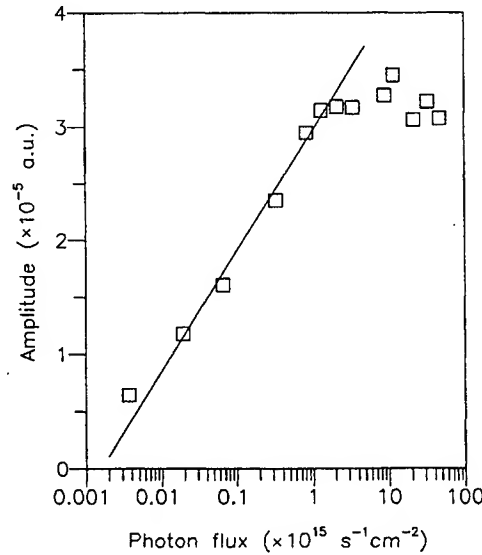


FIG.1 The amplitudes of PR spectra pumped by He-Ne laser versus the flux of photons. The straight line is linearly fitted to those data with $f \leq 2 \times 10^{15} \text{ s}^{-1} \text{ cm}^{-2}$.

proportional to $(F_{dc})^{1/3}(F_{ac})$, where F_{dc} is the surface dc electric field and F_{ac} is the surface ac electric field caused by the chopped laser, PR signal is proportional to V_p to the first order approximation. And saturation occurs when photo-induced current reaches its maximum. By fitting the linear part of data ($f \leq 2 \times 10^{15} \text{ s}^{-1} \text{ cm}^{-2}$) with the straight line in Fig.1, C_2/C_1 can be determined as -28.1 . Thus, using eq.(6), the surface Fermi level pinning of GaAs, qV_F , can be directly determined to be $0.72 \pm 0.02 \text{ eV}$. This result is quantitatively the same as those data published by measuring the built-in electric field through FKOs at different temperature. Although this approach gets a good agreement with those obtained from FKOs procedures, there still some cautions must be noted. First, the approximation of $\alpha W \gg 1$ is valued only for low doping concentration. The samples with high doping concentration could not use this approach. Second, the geometrical factor $r \approx 1$ is valued for usual samples. With specially treated samples such as H_2S plasma-passivated GaAs surface, this approach will not be valued.²⁷

4. CONCLUSIONS

In conclusion, we have investigated the effects of V_p on a simple (100) GaAs epitaxial layer grown by MBE with A as a function of f in the range of $3.7 \times 10^{12} \text{ s}^{-1} \text{ cm}^{-2} \leq f \leq 4.73 \times 10^{16} \text{ s}^{-1} \text{ cm}^{-2}$. We have demonstrated that without special structure (SIN or SIP) and a large variety of temperature range, the surface Fermi level energy of GaAs at room temperature can be evaluated directly from the linear dependence of A on $\ln(f)$ yielding the value of $qV_F = 0.72 \pm 0.02 \text{ eV}$ below conduction band edge. Because the variation of the intensity of pumping light can be achieved just by a neutral density filter, it is a simple and efficient method to approach the Fermi level of semiconductor surfaces. Using this approach, the deduced surface Fermi level value of GaAs is in good agreement with those obtained from FKOs procedures, which provides further support of this validity.

ACKNOWLEDGEMENTS

The author appreciates Professor G. J. Jan and H. H. Lin at the department of electrical engineering of National Taiwan University for the valuable suggestions and sample preparation, and H. P. Chen for several useful discussions. The authors also acknowledge the support of the National Science Council Contract No. NSC 89-2112-M-027-001-.

REFERENCES

1. G. S. Chang, W. C. Hwang, Y. C. Wang, Z. P. Yang, and J. S. Hwang, "Determination of surface state density for GaAs and InAlAs by room temperature photorefectance," *J. Appl. Phys.* **86**, pp. 1765-1767, 1999.
2. Y. M. Xiong, P. G. Synder, and J. A. Woollam, "Photoellipsometry of surface Fermi level in GaAs (100)," *J. Vac. Sci. Technol.* **A11**, pp. 1075-1082, 1993.
3. J. S. Hwang, S. L. Tyan, W. Y. Chou, M. L. Lee, David Weyburne, Z. Hang, H. H. Lin, and T. L. Lee, "Photorefectance study of surface Fermi level in molecular beam epitaxial grown InAlAs heterostructures," *Appl. Phys. Lett.* **64**, pp. 3314-3316, 1994.
4. H. Shen, F. C. Rong, R. Lux, J. Pamulapati, M. Taysing-Lara, M. Dutta, L. Calderon, and Y. Lu, "Fermi level pinning

in low-temperature molecular beam epitaxial GaAs," *Appl. Phys. Lett.* **61**, pp. 1585-1587, 1992.

5. D. E. Aspnes, *Handbook on Semiconductors*, edited by T. S. Moss (North-Holland, New York, 1980), Vol. 2, p.109 and references cited therein.
6. W. Y. Chou, G. S. Chang, W. C. Hwang, and J. S. Hwang, "Analysis of Fermi level pinning and surface state distribution in InAlAs heterostructures," *J. Appl. Phys.* **83**, pp. 3690-3695, 1998.
7. W. C. Lee, T. M. Hsu, S. C. Wang, M. N. Chang, and J. -I. Chyi, "The Fermi level of annealed low-temperature GaAs on Si- δ -doped GaAs grown by molecular beam epitaxy," *J. Appl. Phys.* **83**, pp. 486-490, 1998.
8. V. M. Airaksinen and H. K. Lipsenan, "Photorefectance study of photovoltage effects in GaAs diode structures," *Appl. Phys. Lett.* **60**, pp. 2110-2112, 1992.
9. H. Shen, M. Dutta, L. Fotiadis, P. G. Newman, R. P. Moerkirk, W. H. Chan, and R. N. Sacks, "Photorefectance study of surface Fermi level in GaAs and GaAlAs," *Appl. Phys. Lett.* **57**, pp. 2118-2120, 1990.
10. J. S. Hwang, W. Y. Chou, S. L. Tyan, H. H. Lin, and T. L. Lee, "Study of surface Fermi level and surface state distribution in InAlAs surface-intrinsic- n^+ structure by photorefectance," *Appl. Phys. Lett.* **67**, pp. 2350-2352, 1995.
11. C. Van Hook, K. Deneffe, J. De Boeck, D. J. Arent, and G. Borghs, "Franz-Keldysh oscillations originating on a well-controlled electric field in the GaAs depletion region," *Appl. Phys. Lett.* **54**, pp. 608-610, 1989.
12. D. P. Wang, K. M. Huang, T. L. Shen, K. F. Huang, and T. C. Huang, "Electroreflectance of surface-intrinsic- n^+ -type doped GaAs," *J. Appl. Phys.* **82**, pp. 3089-3091, 1997.
13. X. Yin, H-M. Chen, F. H. Pollak, Y. Cao, P. A. Montano, P. D. Kirchner, G. D. Pettit, and J. M. Woodall, "In situ study of the effects sputter/annealing on the Fermi level at (001) n - and p -type GaAs surfaces," *J. Vac. Sci. Technol.* **B 9**, pp. 2114-2117, 1991.
14. H. Shen and F. H. Pollak, "Generalized Franz-Keldysh theory of electromodulation," *Phys. Rev.* **B 42**, pp. 7097-7102, 1990.
15. M. Sydor, J. R. Engholm, M. O. Manasreh, C. E. Stutz, L. Liou, and K. R. Evans, "Photorefectance and the electric fields in a GaAs depletion region," *Appl. Phys. Lett.* **56**, pp. 1769-1771, 1990.
16. M. H. Hecht, "Role of photocurrent in low-temperature photoemission studies of Schottky-barrier formation," *Phys. Rev.* **B 41**, pp. 7918-7921, 1990.
17. M. Sydor, J. R. Engholm, D. A. Date, and T. J. Fergestad, "Surface and bulk modulation in photorefectance from undoped GaAs," *Phys. Rev.* **B 49**, pp. 7306-7312, 1994.
18. X. Yin, H-M. Chen, F. H. Pollak, Y. Chan, P. A. Montano, P. D. Kirchner, G. D. Pettit, and J. M. Woodall, "Photorefectance study of surface photovoltage effects at (100)GaAs surfaces/interfaces," *Appl. Phys. Lett.* **58**, pp. 260-262, 1991.
19. D. P. Wang, C. C. Chen, T. L. Shen, T. M. Hsy, and W. C. Lee, "Pumping-beam-induced photovoltaic effect on the photorefectance of a δ -doped GaAs film," *J. Appl. Phys.* **80**, pp. 6980-6983, 1996.
20. F. H. Pollak, "Contactless electromodulation investigations of surface/interface electric fields in semiconductor microstructures," *J. Vac. Sci. Technol.* **B 11**, pp. 1710-1716, 1993.
21. X. Yin, H-M. Chen, F. H. Pollak, Y. Chan, P. A. Montano, P. D. Kirchner, G. D. Pettit, and J. M. Woodall,

- "Photoreflectance study of the surface Fermi level at (100) n- and p-type GaAs surfaces," *J. Vac. Sci. Technol. A* **10**, pp. 131-136, 1992.
22. D. Yan, E. Look, X. Yin, F. H. Pollak, and J. M. Woodall, "Air stabilized (001) p-type GaAs fabricated by molecular beam epitaxy with reduced surface state density," *Appl. Phys. Lett.* **65**, pp. 186-188, 1994.
23. T. Kanata, M. Matsunaga, H. Takakura, Y. Hamakawa, and T. Nishino, "Photoreflectance characterization of surface Fermi level in as-grown GaAs(100)," *J. Appl. Phys.* **68**, pp. 5309-5313, 1990.
24. R. E. Wagner and A. Mandelis, "Intensity dependence of the photoreflectance amplitude in semiconductors," *Phys. Rev. B* **50**, pp. 14228-14236, 1994.
25. H. Shen, P. Parayanthal, Y. F. Liu, and F. H. Pollak, "New normalization procedure for modulation spectroscopy," *Rev. Sci. Instrum.* **58**, pp. 1429-1432, 1987.
26. D. E. Aspnes, "Third-derivative modulation spectroscopy with low-field electromodulation," *Surf. Sci.* **37**, pp. 418-442, 1973.
27. H. Shen, W. Zhou, J. Pamulapati, and F. Ren, "Photoreflectance study of H₂S plasma-passivated GaAs surface," *Appl. Phys. Lett.* **74**, pp. 1430-1432, 1999.

Analysis of a Novel Polarization Analyzer

Ruey-Ching Twu and Way-Seen Wang*

Department of Electrical Engineering and Graduate Institute of Electro-Optical Engineering,
National Taiwan University, Taipei 10617, Taiwan, ROC

ABSTRACT

In this paper, a novel polarization analyzer for measuring the state of polarization of light is proposed. The analyzer consists of a TE-TM mode splitter, a passive TE-TM mode converter, and three polarizers. Comparing with the previously reported methods, without using mechanically movable and actively modulated components for polarization control, the time response of measurement is less limited and the signal process for the determination of polarization parameters is easier. Where, the polarization parameters are obtained via three received optical signals based on the proposed methods. Moreover, the concept can be realized by waveguide or fiber devices, which are more compact. The dependence of measurement performance on the characteristics of composed elements is theoretically investigated and the results show that the measurement resolutions are determined mainly by the characteristic of individual elements.

Keywords: Polarization analyzer, state of polarization, mode splitter, mode converter, waveguide polarizer

1. INTRODUCTION

Analysis of the state of polarization (SOP) of light plays a major role in optical communication system and ellipsometric studies of dispersive materials.¹⁻³ The polarization states of a propagating light can be obtained by using a rotating polarizer or a rotating compensator/fixed analyzer scheme.⁴ The rotation speed and mechanical control of optical components in a bulk-optic apparatus limit the measurement time-response and resolution, respectively. To avoid above difficulties, an acousto-optical (A-O) or electro-optical (E-O) mode converter can replace the rotating waveplate used for polarization rotating. Therefore, a more compact and faster time response polarimetric analyzer has been successfully demonstrated^{1,5} However, the limitations of the measurement response are still existed due to the active modulation of the A-O and E-O converters.

In this paper, a novel method for measuring the SOP of light is proposed and theoretically investigated based on LiNbO₃ integrated waveguide devices. The present polarization analyzer consists of a TE-TM mode splitter, a time-independent TE-TM mode converter, and three waveguide polarizers. Without using mechanically movable components and actively modulating devices for polarization control, the measuring time response therefore will be less limited. The polarization parameters can be determined at once from only the three received signals. In general, the time response of the polarization analyzer is determined mainly by the time response of photodetectors. Moreover, the proposed polarization analyzer involves more integration and the signal processing is simpler than in those reported.^{1,5} Theoretical analysis of the measurement performance will also be discussed mainly by considering the operating properties of the elements in this device, such as the transfer ratio of the TE-polarized power in the mode splitter, the conversion efficiency of the mode converter, and the polarization-dependent propagation loss.

2. MEASUREMENT PRINCIPLE

The basic measurement scheme is illustrated in Fig. 1. An incident light \vec{E} and its electric field vector E_{ix} and E_{iy} in the x and y directions can be written as

$$\vec{E} = \begin{bmatrix} E_{ix} \\ E_{iy} \end{bmatrix} = E_{io} \begin{bmatrix} \cos(\theta)e^{+j\phi/2} \\ \sin(\theta)e^{-j\phi/2} \end{bmatrix} \quad (1)$$

where, E_{io} is the magnitude of electric field, the magnitude of the relative TE/TM amplitudes is specified by $\tan\theta$, while ϕ is the phase difference between the two states. Note that the two mentioned parameters θ and ϕ are time varying. In an ideal case (using perfect mode splitter and converter, without polarization-dependent propagation loss along the optical path), an incident light injecting into the device is spatially divided into TE and TM components by the mode splitter. Most of the TM wave in the through waveguide is converted into the TE one after passing through the mode converter while the TE one in the cross one is still kept in the same polarization. Then, the half of the two components was extracted via 3dB couplers from port 1 and 3, respectively, to monitor the amplitude of the TE and TM polarizations. The other half of the two components was fed into the Y-coupler and the interference intensity was observed at port 2. The power intensities of three output ports are received by the three photo-detectors at the same time and can be represented as follows

$$P_1 = \frac{1}{4}[E_{ix}][E_{ix}]^* = \frac{1}{4}E_{io}^2 \cos^2(\theta) \quad (2)$$

$$P_2 = \frac{1}{4}E_{io}^2 (1 + \sin(2\theta) \cos(\phi)) \quad (3)$$

$$P_3 = \frac{1}{4}[E_{iy}][E_{iy}]^* = \frac{1}{4}E_{io}^2 \sin^2(\theta) \quad (4)$$

$$\theta = \cot^{-1}(\sqrt{P_3/P_1}) \quad (5)$$

$$\phi = \cos^{-1}[(P_2 - (P_1 + P_3))/(2\sqrt{P_1 P_3})] \quad (6)$$

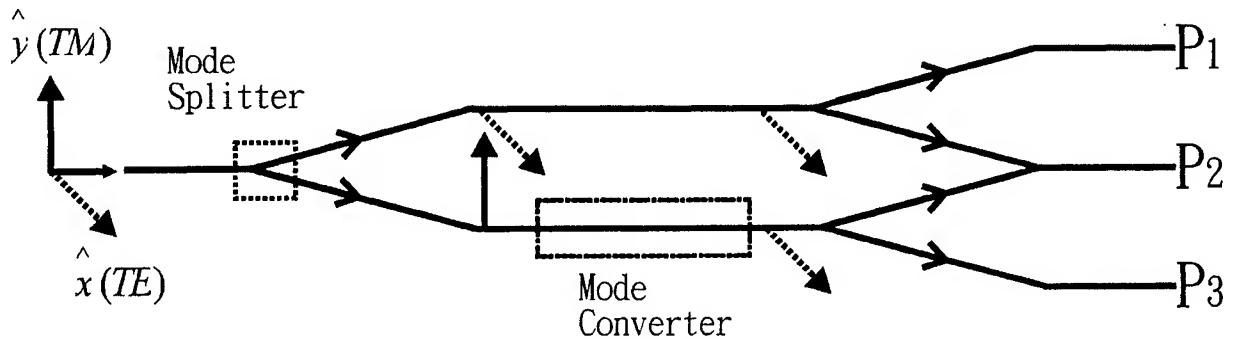


Figure 1. Schematic configuration of polarization analyzer.

Therefore, the parameters θ and ϕ can be retrieved by the three received signals with formulas (4) and (5). Actually, in real cases, the calculated θ' and ϕ' based on (4) and (5) are not identical to the θ and ϕ near the input port due to the imperfect optic-components used in the measurements. The measured errors are dependent on the properties of each component and defined as $\Delta\theta = \theta' - \theta$ and $\Delta\phi = \phi' - \phi$, respectively.

In the past, the functional devices such as mode splitter,⁶ mode converter,⁷ and waveguide polarizer⁸ have been successfully fabricated on LiNbO₃ substrate by Ti-indiffusion techniques. Here, an integrated polarization analyzer on a x-cut z-propagating LiNbO₃ substrate is schematically shown in Fig. 2. This analyzer consists of a mode splitter, a mode converter, and three waveguide polarizers.

In a metal-cladding waveguide, the TM wave is seriously absorbed and the TE one is slightly affected due to the different boundary conditions for them. Therefore, it can be used as a TE-pass waveguide polarizer.⁸ The coupling type mode splitter fabricated with metal-cladding structure is used for spatial separation of the TE and TM waves, where only the TE mode can be transferred to the cross waveguide and the most TM one is still left in the through waveguide due to large and slight difference of propagation constant between the two waveguides for the TM and TE polarization ($\Delta\beta_{TE}$ and $\Delta\beta_{TM}$), respectively. The transferred ratio of the TE polarization is dependent on the interaction length and the $\Delta\beta_{TE}$.

Moreover, the converted efficiency of the mode converter is dependent on the effective index difference between the TE and TM modes in the straight waveguide.⁷ The three electrodes is used to offer the needed coupling coefficient and to compensate the birefringence of the two modes that the efficiency can be improved. The advantages of these modulators are on the one hand their capability over a broad spectral range, and the other their resistance to optical damage since the ordinary refractive index n_o of LiNbO₃ is only used.

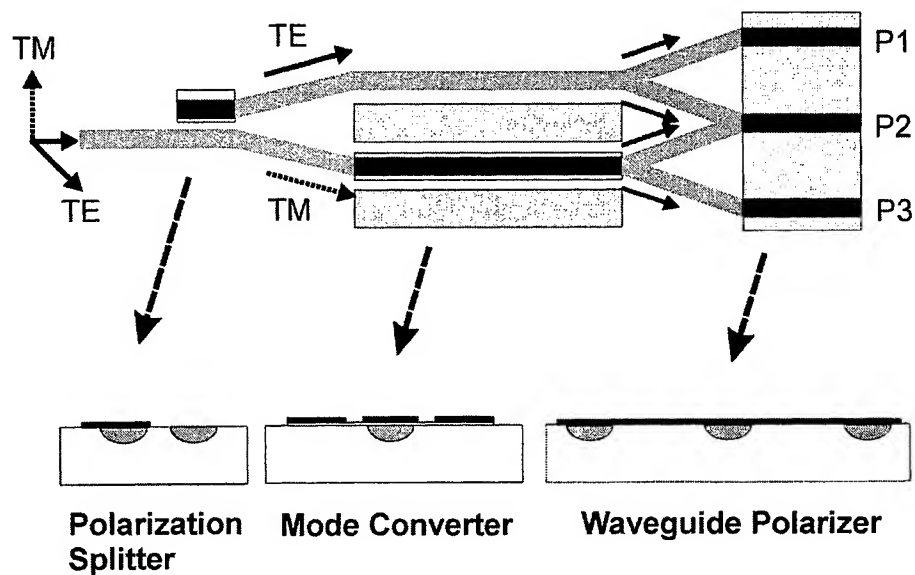


Figure 2. The configuration of the polarization analyzer integrated on lithium niobate substrate.

3. ANALYSIS AND DISCUSSION

In this section, we further discuss the dependence of the measurement resolutions of the polarization analyzer on the characteristics of the composed elements. Table. 1 lists the device parameters for simulation.

Table 1. Device parameters for simulation.

Channel waveguide loss for TM wave	$L_m=0.1\text{dB/cm}\sim 0.25\text{dB/cm}$
Channel waveguide loss for TE wave	$L_e=0.1\text{dB/cm}$
Metal-cladding waveguide loss for TM wave	$L_{tm}=30\text{dB/cm}$
Metal-cladding waveguide loss for TE wave	$L_{te}=0.8\text{dB/cm}$
Transfer efficiency of mode splitter	$S_e=0.99, 0.999$
Conversion efficiency of mode converter	$C_e=0.99, 0.999$
Polarization extinction ratio of polarizer	$P_{er}=3\text{dB/cm}, >10\text{dB/cm}$
Input channel waveguide length	0.3cm
Branch waveguide length	0.15cm
Mode converter length	0.2cm
Waveguide polarizer length	1cm
Polarization splitter length	0.5cm

Usually, the propagation loss of the TM mode (L_m) is higher than that of the TE mode (L_e) because of its higher sensitivity to the surface condition.⁹ Moreover, the loss difference between the two modes is dependent on the fabrication parameters. The transfer efficiency S_e of TE mode and the conversion efficiency C_e between TE and TM modes are used to specify the characteristics of the mode splitter and the mode converter, respectively, which are defined as follows

$$S_e = P_{TE}^{\times} / (P_{TE}^{\times} + P_{TE}^{\sim}) \quad (7)$$

$$C_e = P_{TM}^{TE} / P_{TM} \quad (8)$$

where P_{TE}^{\times} is the transferred TE-polarized power in the cross waveguide and P_{TE}^{\sim} is the TE-polarized power in the through waveguide; P_{TM}^{TE} is the TE-polarized power converted from the input TM wave and P_{TM} is the input TM-polarized power. Typically, the values of S_e and C_e are larger than 0.99 at the suitable process parameters.

In the idea case, the polarization parameters of θ and ϕ are independent. Actually, the cross talk resulting from the imperfectly composed elements is dependent on their performance. The measuring errors $\Delta\theta$ versus θ were shown in Fig. 3(a) and 3(b) for $P_{er}=3\text{dB/cm}$ and $P_{er}>10\text{dB/cm}$ at different ϕ , respectively. Here, the waveguide polarizers are 0.5cm long. The calculated results show that the measuring errors will be saturated, when the P_{er} is larger than 10dB/cm. Consider in a typical metal-cladding polarizer, the values of P_{er} are larger than 30dB/cm.⁸ Therefore, the polarizer length can be reduced to about 0.17cm without decreasing the measuring resolutions. Fig. 4 (a) and 4(b) give the measured errors $\Delta\phi$ versus ϕ for $P_{er}=3\text{dB/cm}$ and $P_{er}>10\text{dB/cm}$ at different θ , respectively. Also, the measuring resolutions can be increased by using larger values of P_{er} . In our analysis, we found that using the effective waveguide polarizer to filter the undesired signals will reduce the measured errors.

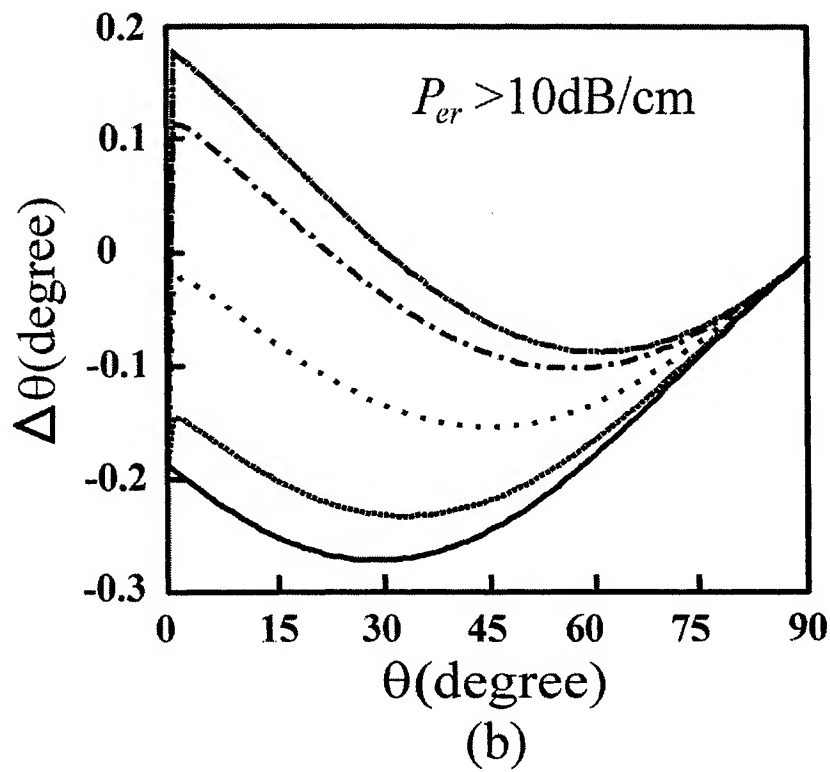
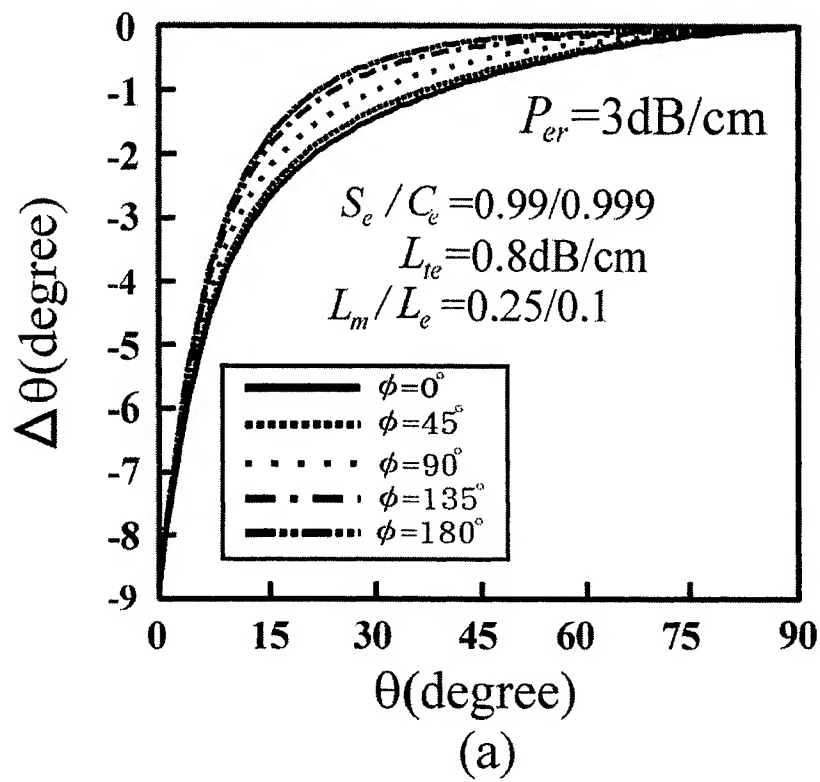


Figure 3. Measurement error $\Delta \theta$ versus θ for (a) $P_{er} = 3 \text{ dB/cm}$ and (b) $P_{er} > 10 \text{ dB/cm}$.

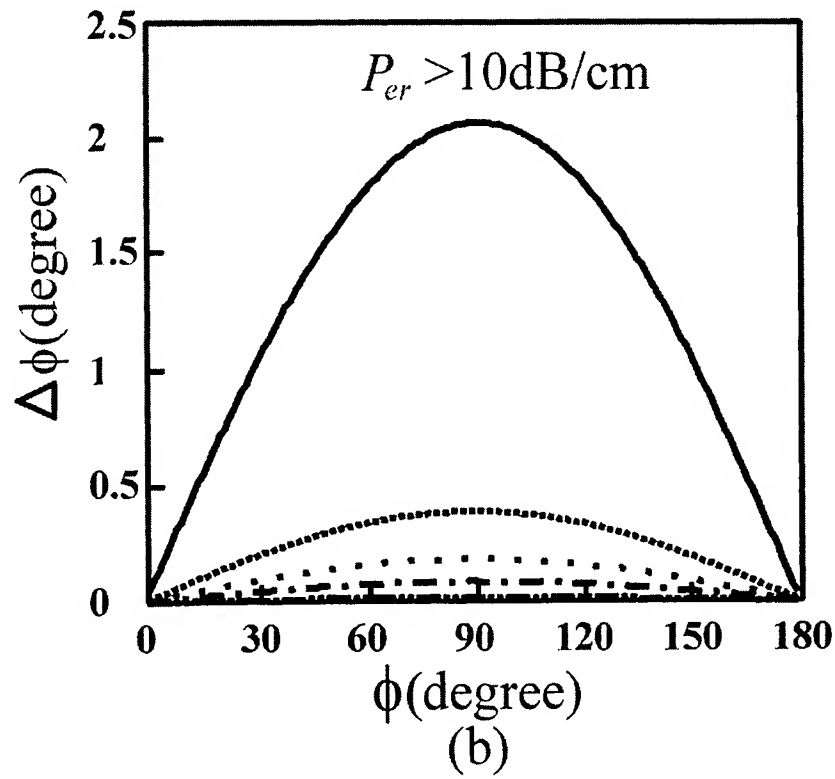
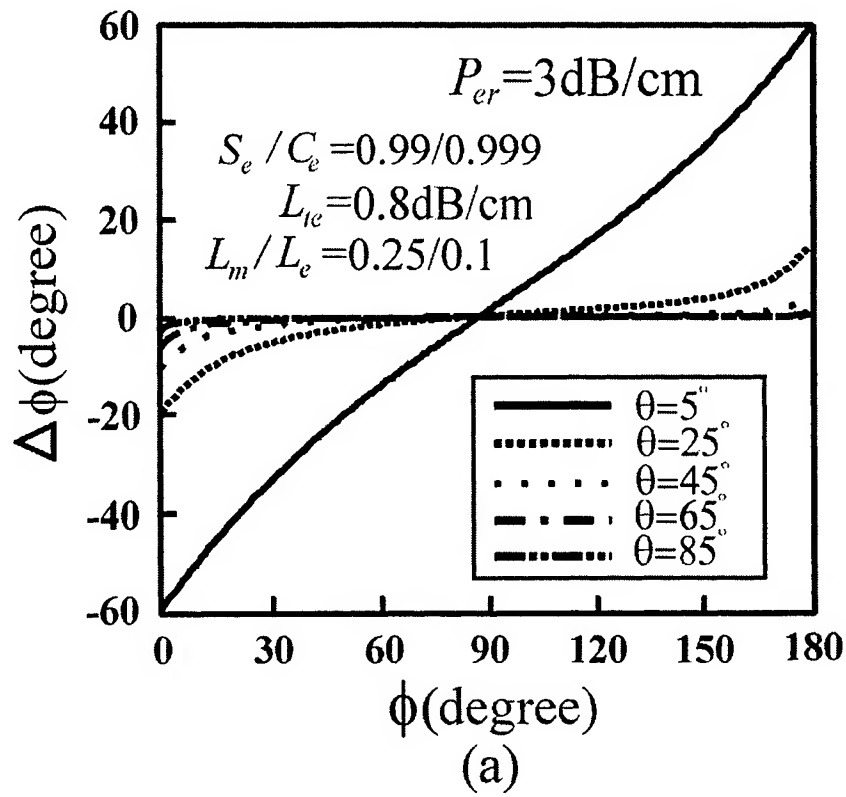


Figure 4. Measurement error $\Delta\phi$ versus ϕ for (a) $P_{er} = 3 \text{ dB/cm}$ and (b) $P_{er} > 10 \text{ dB/cm}$.

Fig. 5 gives the maximum $\Delta\phi$ ($\Delta\phi_{max}$) versus θ for different values of L_m/L_e and S_e/C_e . The results show that $\Delta\phi_{max}$ is greatly affected by the values of S_e/C_e when the values of θ are smaller than 5° . $\Delta\phi_{max}$ is smaller than 1° , when the S_e and C_e are 0.999 for $\theta > 5^\circ$. Fig. 6 gives the dependence of $\Delta\phi_{max}$ on ϕ for different values of L_m/L_e and S_e/C_e . Here, with the increase of L_m/L_e , $\Delta\phi_{max}$ is decreased. $\Delta\phi_{max}$ is smaller than 1° for $L_m/L_e=0.25/0.1$, which is insensitive to the variation of ϕ .

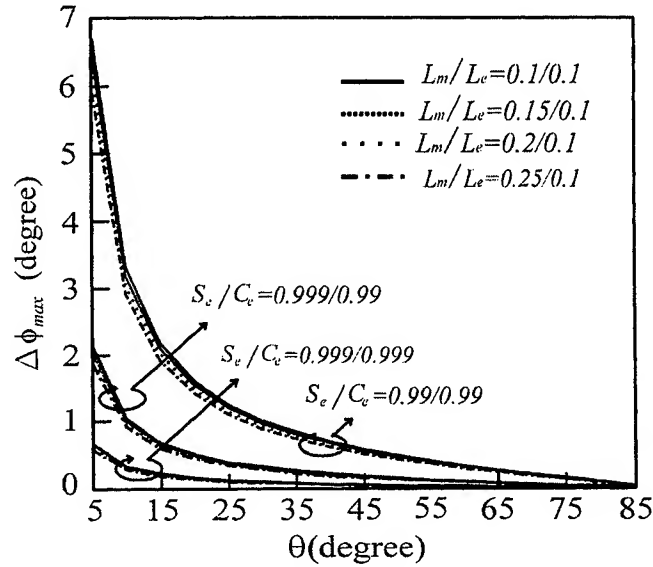


Figure 5. $\Delta\phi_{max}$ versus θ for different values of L_m/L_e and S_e/C_e .

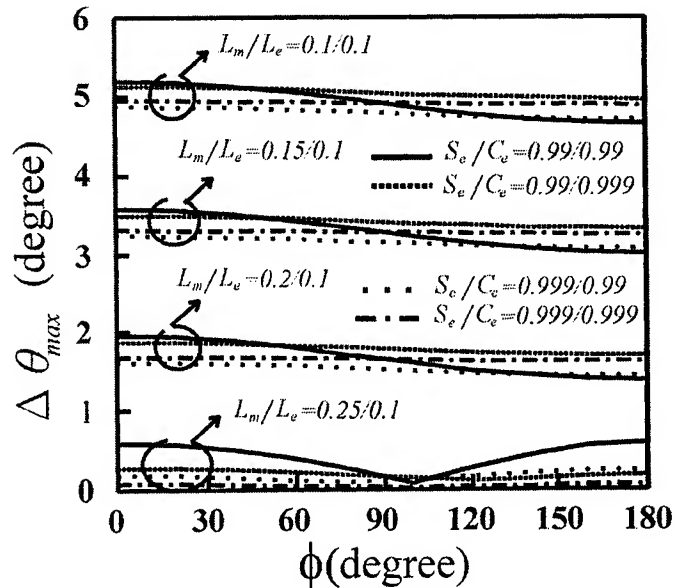


Figure 6. $\Delta\phi_{max}$ versus ϕ for different values of L_m/L_e and S_e/C_e .

4. CONCLUSION

In this work, an integrated polarization analyzer on an x-cut LiNbO₃ substrate has been proposed and theoretically investigated. Simple analytical formulas are used to calculate the polarization parameters based on three received signals. It has the advantages of compact integration, less limitations on the measurement time-response, and simple signal processing. The dependence of the measurement resolutions on the performance of the integrated components has been discussed. The simulation results show that $\Delta\phi$ is significant for $\theta < 5^\circ$, but the $\Delta\theta$ is insensitive to the variation of ϕ . The values of $\Delta\phi$ ($5^\circ < \theta$) and $\Delta\theta$ can be reduced to below 1 degree for $L_m/L_c = 0.25/0.1$ and $S_e/C_e = 0.999/0.999$. The measurement scheme not only can be realized on the LiNbO₃ substrate, but also can be demonstrated on fiber or silica waveguide devices.

ACKNOWLEDGMENT

This work was supported by the National Science Council, Taipei, Republic of China under contract No. NSC 89-2215-E-002-009.

REFERENCES

- 1 Y. Namihiro and H. Wakabayashi, "Real-time measurements of polarization fluctuations in an optical fiber submarine cable in a deep-sea trial using electrooptic LiNbO₃ device," *J. Lightwave Technol.* **7**, pp. 1201-1206, 1989.
- 2 F. Heismann, A. F. Ambrose, T. O. Murphy, and M. S. Whalen, "Polarization-independent photonic switching system using fast automatic polarization controllers," *IEEE Photon. Technol. Lett.* **5**, pp. 1341-1343, 1993.
- 3 V. Lapras, P. Mottier, and C. Chabrol, "Integrated optical detection circuit for magneto-optical drives," *IEEE Transactions on Consumer Electronics*, **41**, pp. 1039-1049, 1995.
- 4 P. S. Hauge, "Survey of methods for the complete determination of a state of polarization," *Proc. SPIE Int. Soc. Opt. Eng.*, (Polarized light), **88**, pp. 3-10, 1976.
- 5 M. Rehange and R. Noe, "Wavelength-selective polarization analyser with integrated Ti:LiNbO₃ acousto-optical TE-TM converter," *Electron. Lett.* **30**, pp. 1130-1131, 1994.
- 6 O. Mikami, "LiNbO₃ coupled-waveguide TE/TM mode splitter," *Appl. Phys. Lett.* **36**, pp. 491-493, 1980.
- 7 T. Kawazoe, K. Satoh, I. Hayashi, and H. Mori, "Fabrication of integrated-optic polarization controller using z-propagating Ti-LiNbO₃ waveguides," *J. Lightwave Technol.* **10**, pp. 51-56, 1992.
- 8 L. Sun and G. L. Yip, "Analysis of metal-clad optical waveguide polarizers by the vector beam propagation method," *Appl. Opt.* **33**, pp. 1047-1050, 1994.
- 9 T. Fujiwara, A. Watanabe, and H. Mori, "Polarization dependent loss in a Ti:LiNbO₃ polarization scrambler/controller," *IEEE Photon. Technol. Lett.* **8**, pp. 542-544, 1996.

*Correspondence: Email: wswang@cc.ee.ntu.edu.tw; Telephone: +886-2-23635251; Fax: +886-2-2321950

Characterizations of Zn-Diffused Lithium Niobate Directional Coupler by Post Thermal-Treatment

Ruey-Ching Twu and Way-Seen Wang*

Department of Electrical Engineering and Graduate Institute of Electro-Optical Engineering,
National Taiwan University, Taipei 10617, Taiwan, ROC

ABSTRACT

A study of fine adjustment of the coupling coefficient of Zn-diffused directional couplers on Z-cut lithium niobate substrate by a series of post thermal-treatment is presented for the first time. Optical mode profiles and propagation losses before and after the treatments are measured for the $1.32\ \mu\text{m}$ wavelength. Experimental results show that the post thermal-treatment is quite efficient for fine adjustment of the cross coupling power ratio of the directional coupler.

Keywords: Coupling coefficient, Zn-diffused, directional coupler, lithium niobate, thermal-treatment

1. INTRODUCTION

Integrated optical directional couplers are important components in optical communication and optical sensor systems. Power divider, optical switch or modulator, wavelength filter, and polarization splitter have been successfully demonstrated based on different design concepts of directional coupler.^{1,2} For the applications of these devices, the determination of coupling coefficient of the directional coupler is essential, which in turn depends on the fabrication process parameters. Unfortunately, process defects usually cause the specifications of the finished device out of the original optimum design. Post-adjustable technique, which can relax the fabrication tolerance, is then favor for restoring the device performance back to its optimum. There are two techniques can be used to change the coupling coefficients once the device is made. One is the modification of boundary conditions in the coupling region such as cladding with layers of different indices and thickness over ridge-coupled structures³ or etched grooves in the middle of the interaction region.⁴ The other approach is the redistribution of the index profile by post thermal-treatment such as using proton-exchange and then followed by thermal annealing.⁵

Recently, Zn indiffusion (ZI) waveguide has been studied extensively to make optical devices in LiNbO_3 substrate due to less susceptibility to photorefractive damage in comparison with Ti indiffusion (TI) waveguide.⁶ In this paper, the post thermal-treatment method is successfully used to modify the performance of ZI waveguide couplers. The diffusion temperature T and time t of a ZI waveguide are $800\text{--}950^\circ\text{C}$ and $30\text{--}180\text{min}$, respectively, which are lower and shorter than those of the conventional TI ones. Therefore, Zn indiffusion needs no additional out-diffusion suppression and saves the diffusion time. That provides more flexibility for the fabrication of optical waveguides.

The experimental results show that the use of the post thermal-treatment can efficiently adjust cross coupling power ratio of a directional coupler. The variation of mode profiles and propagation losses in a channel waveguide are also measured at the $1.32\ \mu\text{m}$ wavelength. A compromise between the adjustment of coupling coefficient and the optical propagation loss with the post thermal-treatment is discussed. The coupling coefficients can be adjusted in the range of $0.47\text{--}0.63\ \text{rad/mm}$ for waveguides of width $8\ \mu\text{m}$ and gap $6\ \mu\text{m}$, while the propagation losses are kept below $1.5\ \text{dB/cm}$. From these experimental results, precise fabrication of 3dB power divider and high-extinction-ratio uniform- $\Delta\beta$ optical switch become more possible.

2. EXPERIMENTS

A schematic diagram of a symmetrical directional coupler is shown in Fig. 1. Two sets of samples are prepared on the Z-cut LiNbO_3 substrate. One is with a gap G of $6\mu\text{m}$ between two adjacent waveguides but with a parallel coupled lengths L varying from 0.5 mm to 10.5 mm , the other is with $G=8\mu\text{m}$ and L varying from 1 mm to 10 mm . The waveguide width W is $8\mu\text{m}$ and the bending angle θ is 1° . The center-to-center distance D between two output waveguides is $100\mu\text{m}$.

In our experiment, a single TM-polarization waveguide can be easily demonstrated by Zn-indiffusion in the Z-cut LiNbO_3 . A Zn thin film of 400 \AA thickness is deposited over the substrate by thermal evaporation. As Zn atoms are difficult to leech on the surface of LiNbO_3 substrate in the initial period of evaporation, a metallic Ni film of thickness 50 \AA is predeposited onto the substrate in order to increase the adhesion of Zn atoms to the substrate. The diffusion temperature and time for only TM-polarization guiding are 850°C and 90 min , respectively. After the diffusion, the substrate end faces are cut and polished to allow butt coupling. A laser light source of wavelength $1.32\mu\text{m}$ is used for the measurement. Using lenses for light coupling to and out of the end faces of the waveguide, both output beams can be simultaneously detected by a CCD camera. Two-dimensional intensity distribution profiles are stored in a 120×120 data matrix. Integrating each optical spot by adding the relative elements of the data matrix gives rise to the output intensity. Then, a post thermal-treatment using $T=850^\circ\text{C}$ and $t=10\text{ min}$, is performed many times and the output power intensities are measured each time. Moreover, the cut-back method⁷ is used to measure the waveguide loss to ensure the loss is not significantly increased.

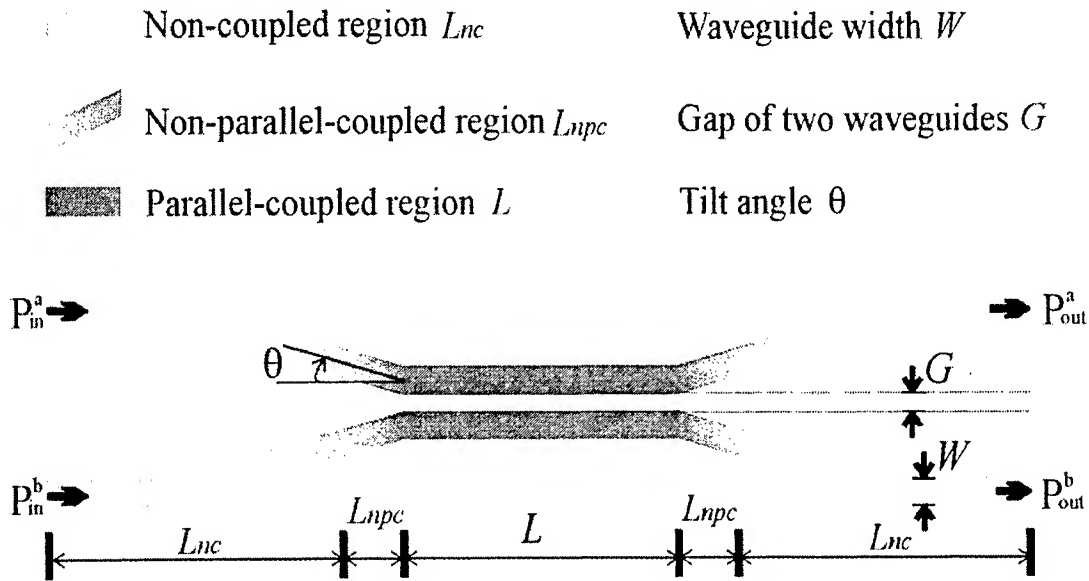


Figure 1. A schematic diagram of the symmetrical directional coupler.

3. RESULTS AND DISCUSSION

Propagation loss in channel waveguide includes intrinsic material absorption and guiding loss. Post thermal annealing is used to reduce the absorption of material and redistribute the diffused atoms. Fig. 2 shows the measured optical mode profiles after the thermal diffusion and a series of post thermal-treatment N . Obviously, the optical mode profile broadens as N increases due to the decrease of effective index of waveguide modes in the same time. Fig. 3 shows the optical propagation loss after the thermal diffusion and a series of post thermal-treatment. When $N > 4$, the propagation loss increases vastly because of the waveguiding is much weaker. Between the thermal diffusion and the fourth post thermal-treatment ($0 \leq N \leq 4$), the propagation loss is kept below 1.5 dB/cm.

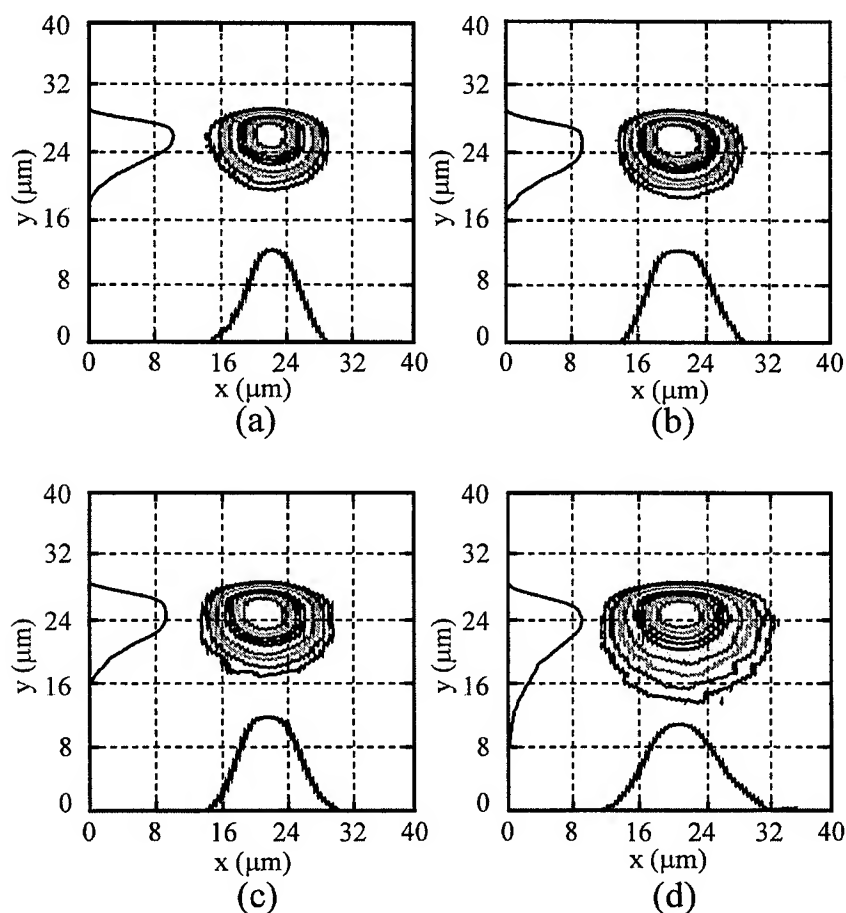


Figure 2. Optical mode profiles after (a) The thermal diffusion, (b) The second post thermal-treatment, (c) The fourth post thermal-treatment, (d) The sixth post thermal-treatment.

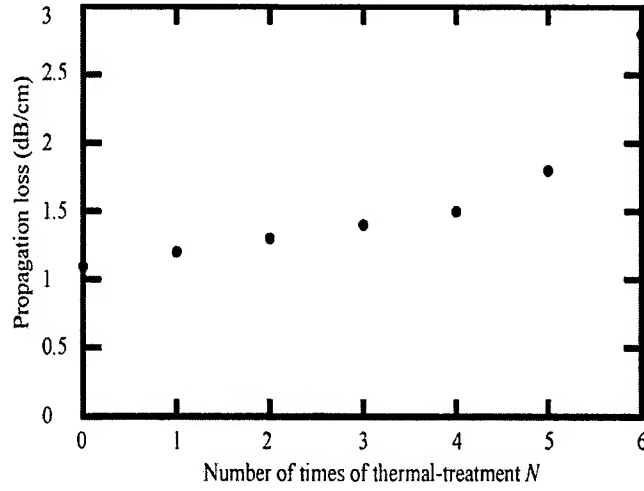


Figure 3. Optical propagation loss versus a series of post thermal-treatment ($N=0,1, 2, \dots, 6$).

The above experimental results show that the post thermal-treatment will affect both the mode size and propagation loss of a single channel waveguide. Then, the effect of post thermal-treatment on the performance of a directional coupler will be discussed.

Analysis of a directional coupler is based on the coupled mode equations. A laser light is launched into one of the input waveguides of the directional coupler. After propagating a distance L in the parallel-coupled region, the optical power in the bar state p_{out}^a and in the cross state p_{out}^b can be expressed as⁸

$$p_{out}^a = \cos^2(\kappa L + \theta_{np}) \quad (1)$$

$$p_{out}^b = \sin^2(\kappa L + \theta_{np}) \quad (2)$$

$$\eta = \frac{p_{out}^b}{p_{out}^a + p_{out}^b} \quad (3)$$

where κ is the coupling coefficient in the parallel-coupled region of the coupler, θ_{np} is the phase factor introduced from the non-parallel-coupled region, and η is the coupling power ratio.

The coupling coefficient is primarily determined by the difference between the symmetric and asymmetric propagation constants of the coupled waveguides, which in turn is dependent on the index profile of individual channel waveguide and the gap between two adjacent waveguides. Input optical power transfer between the two adjacent waveguides is due to the interference of symmetric and asymmetric modes of the coupled waveguides. Solving (1), (2), and (3) for $(\kappa L + \theta_{np})$ gives

$$\kappa L + \theta_{np} = n\pi \pm \left| \sin^{-1} \sqrt{\eta} \right| \quad n = 0, 1, 2, \dots \quad (4)$$

For constant κ and θ_{np} , η is a sinusoidal function of L . The choice of the plus or minus sign and n are determined by the number of the cycles of power transfer between the two waveguides for different L 's. For examples, when L lies within the first maximum and the second minimum of power transfer curve, then the proper choice of n is 1 and sign is minus. If L lies within the second minimum and the second maximum of power transfer curve, then the proper choice of n is 1 and sign is plus. The slope of the curve fitted by formula (4) is defined as the coupling coefficient κ of the directional coupler and the intercept at $L=0$ is defined as the non-parallel-coupled phase factor θ_{np} .

Fig. 4 gives the measured results of the total phase factor versus parallel-coupled length after the thermal diffusion and a series of post thermal-treatment for $G=6\mu\text{m}$. The slope and intercept at $L=0$ of such fitted curves represent the coupling coefficients and non-parallel-coupled coefficients, respectively.

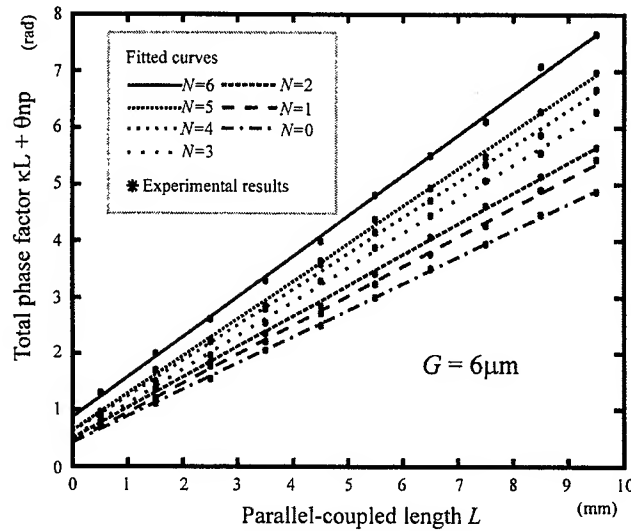
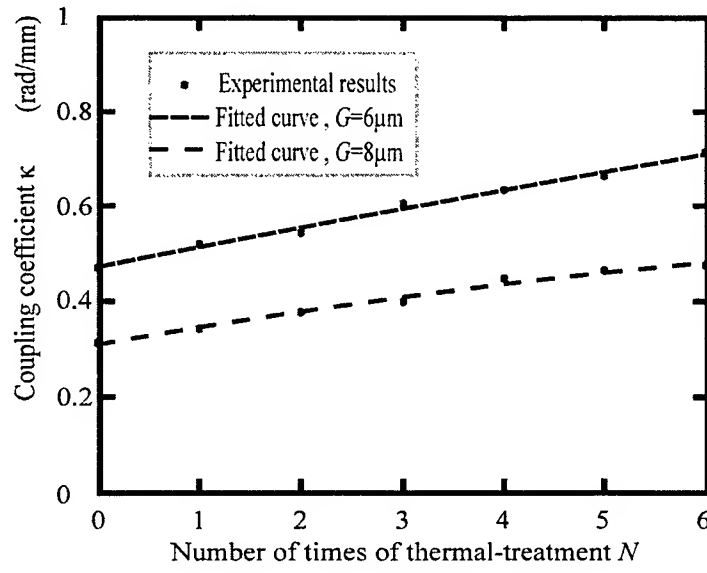


Figure 4. Total phase factor versus parallel-coupled length after the thermal diffusion and a series of post thermal-treatment.

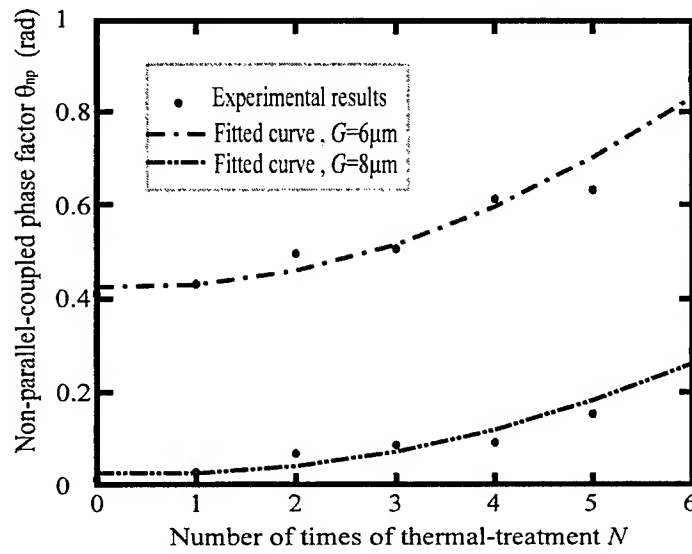
Fig. 5(a) and 5(b) show κ and θ_{np} versus a series of post thermal-treatment for $G=6\mu\text{m}$ and $8\mu\text{m}$, respectively. It is found that κ and θ_{np} are increased with the increase of diffusion time or the number of times of thermal-treatment. The change of κ and θ_{np} is more noticeable when the G is smaller.

As the output cross power ratio of a directional coupler is dependent on $\kappa L + \theta_{np}$, for a constant length L , the ratio can be adjusted by changing the value of κ . Fig. 6(a) and 6(b), show the cross coupling power ratio versus parallel-coupled length after different numbers of times of post thermal-treatment for $G=6\mu\text{m}$ and $G=8\mu\text{m}$, respectively. As the number of times of post thermal-treatment increases, the cross power ratio changes significantly. The change is more noticeable when the L is longer.

For the uniform- $\Delta\beta$ optical switch, its switching extinction ratio is dependent on the cross coupling power ratio at zero applied voltage. To achieve cross state with less than -25dB crosstalk, κL must be controlled within $\pm 3.5\%$, which, in general, is difficult to be reproduced¹. At the same time, optimized electrode lengths for an optical power switch are between 6mm and 10mm when operating at $1.32\mu\text{m}$ wavelength. Thus, an odd number of coupling length L_c , is required to fall in the range. The results shown in Fig. 6(a) and 6(b) certainly benefit for fabricating such optical switches in the near future.

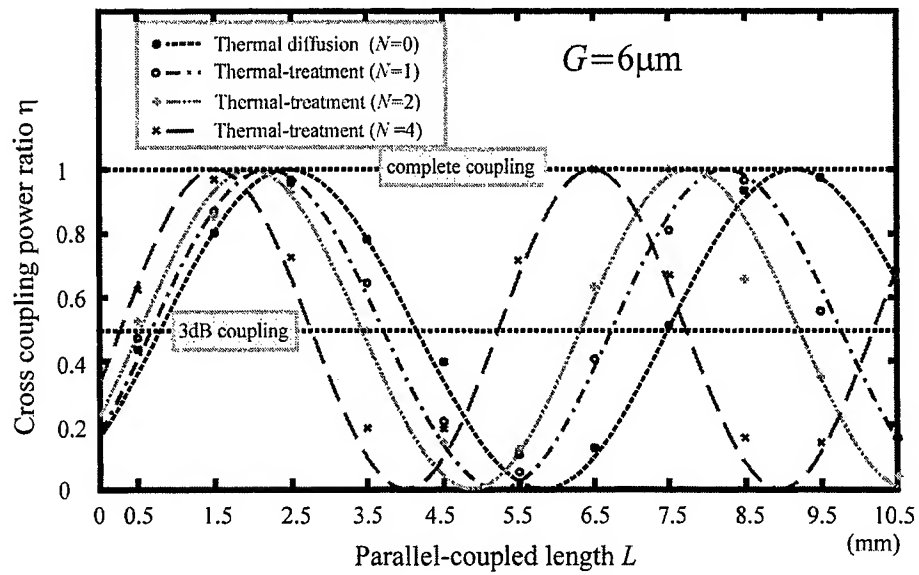


(a)

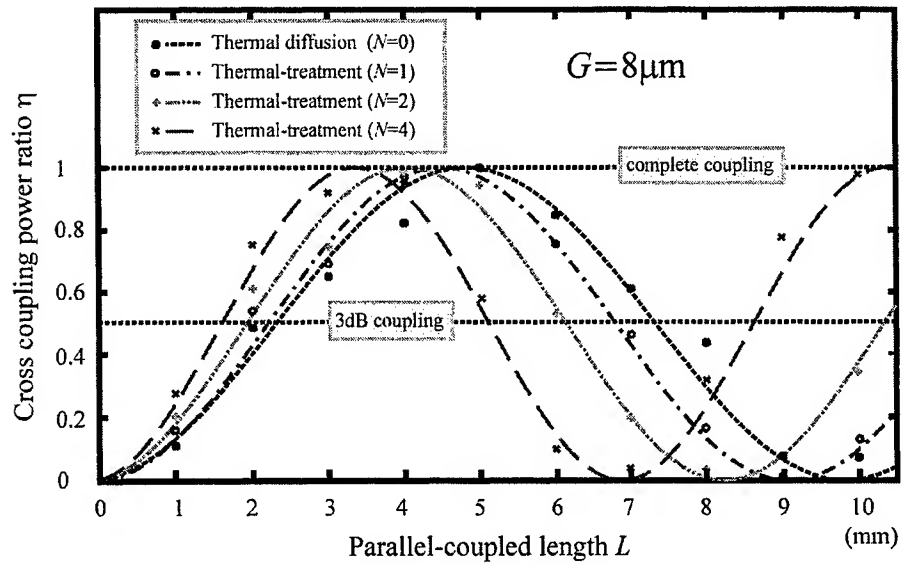


(b)

Figure 5. (a) and (b) show κ and θ_{np} versus a series of post thermal-treatment for $G=6\mu\text{m}$ and $8\mu\text{m}$, respectively.



(a)



(b)

Figure 6. Cross coupling power ratio versus parallel-coupled length after different numbers of times of post thermal-treatment, (a) $G=6\mu\text{m}$, (b) $G=8\mu\text{m}$.

4. CONCLUSION

Optical mode profiles and propagation losses before and after a series of post thermal-treatment are measured for the ZI waveguides in Z-cut LiNbO₃ substrates. Characterizations of directional couplers are also discussed based on coupled mode equations. The experimental results show that the use of the post thermal-treatment stage is a very useful way for the fine adjustment of the cross coupling power ratio. However, the coupling coefficient and propagation loss adjusted by the post thermal-treatment must be compromised. In this work, the coupling coefficient that can be adjusted is in the range of 0.47-0.63 rad/mm for $G=6\mu\text{m}$, while the propagation loss of the channel waveguides is still kept below 1.5 dB/cm. The adjustment range of κ can be increased when the G is decreased. Details of the application of the fine adjustment technique will be of great interest in the future.

ACKNOWLEDGMENT

This work was supported by the National Science Council, Taipei, Republic of China under contract No. NSC 89-2215-E-002-007.

REFERENCES

1. R. C. Alfiness, "Guided-wave devices for optical communication," *J. Quantum Electron.* **17**, pp. 946-959, 1981.
2. H. Maruyama, M. Haruna, and H. Nishihara, "TE-TM mode splitter using directional coupling between heterogeneous waveguide in LiNbO₃," *J. Lightwave Technol.* **13**, pp. 1550-1554, 1995.
3. D. Bosc and C. Durovary, "A new experimental method to improve parameter determination of integrated optical components," *IEEE Photon. Technol. Lett.* **9**, pp. 648-650, 1997.
4. S. J. Al-Bader, "Applications of etched grooves in integrated-optics channel isolation," *IEEE Photon. Technol. Lett.* **8**, pp. 1044-1046, 1996.
5. W. Charczenko, I. Januar, and A. R. Mickelson, "Modeling of proton-exchanged and annealed channel waveguides and directional couplers," *J. Appl. Phys.* **73**, pp. 3139-3148, 1993.
6. W. M. Young, M. M. Fejer, M. J. F. Digonment, A. F. Marshall, and R. S. Feigelson, "Fabrication, characterization, and index profile modeling of high-damage resistance Zn-diffused waveguides in congruent and MgO:lithium niobate," *J. Lightwave Technol.* **10**, pp. 1238-1246, 1992.
7. I. P. Kaminow and L. W. Stulz, "Loss in cleaved Ti-diffused LiNbO₃ waveguides," *Appl. Phys. Lett.* **33**, pp. 62-64, 1978.
8. H. C. Cheng and R. V. Ramaswamy, "Determination of the coupling length in directional coupler from spectral response," *IEEE Photon. Technol. Lett.* **2**, pp. 823-825, 1990.

*Correspondence: Email: wswang@cc.ee.ntu.edu.tw; Telephone: +886-2-23635251; Fax: +886-2-2321950

Improved interferometric method for the determination of the mechanical properties of metal oxide films

Chuen-Lin Tien^{*a,b}, Cheng-Chung Lee^b and Kie-Pin Chuang^b

^a Aeronautical Research Laboratory, Chung-Shan Institute of Science and Technology
Taichung 407, Taiwan, R.O.C.

^b Institute of Optical Sciences, National Central University, Chung-Li 302, Taiwan, R.O.C.

ABSTRACT

Most microelectronic devices and sensors are fabricated by using thin film deposition. Understanding metal oxide films is important in the electronic applications. We report an improved interferometric method based on a phase shifting technique to determine the mechanical properties of metal oxide films. Thin films were prepared by ion-beam sputter deposition at low substrate temperature. Quantitative determination of the mechanical properties such as the internal stress, the biaxial elastic modulus and the thermal expansion coefficient were investigated. A phase shifting Twyman-Green interferometer with the phase reduction algorithm was set up to measure the stress in thin films. Two types of circular glass plates, with known Young's moduli, Poisson's ratios and thermal expansion coefficients, were used as coating substrates. The temperature-dependent stress behavior of the metal oxide films was obtained by heating samples in the range from room temperature to 70 degree C. The stresses of thin films deposited on two different substrates were plotted against the stress measurement temperature, showing a linear dependence. From the slopes of the two lines in the stress versus temperature plot, the intrinsic stress, the biaxial elastic modulus and the thermal expansion coefficient of metal oxide films are then determined.

Keywords: Thin films, Stress, Ion-beam sputter deposition, Phase shifting interferometry, Biaxial elastic modulus, Thermal expansion.

1. INTRODUCTION

The stress and thermal expansion coefficient of thin films are very important mechanical properties in the field of thin film device processing. The quantification of stress and strain in thin films has been a significant matter in all application of optical coatings. Stress in thin films is mainly composed of a thermal stress and an intrinsic stress¹. The thermal stress is due to the difference in the thermal expansion coefficients of the coating and substrate materials. The intrinsic stress is induced during the film-growth process, but the mechanisms are complex, and not yet fully understood. Thin films stress causes many undesirable phenomena, for example, cracking or peeling the film and bending the substrate. In addition, thermal effects provide important contributions to film stress. Films prepared at an elevated temperature and cooled to room temperature will be thermally strained. It is well known that a material's physical thin film properties are very different from its bulk properties. Hence, a knowledge of the coefficient of thermal expansion (CTE) of a thin film

* Correspondence : Email: cltien@ios706.ios.ncu.edu.tw; Telephone:+886-3-4227151 ext. 5273 ; Fax:+886-3-4263918

can be very useful in understanding how this property will affect the study of the bulk material in the form of thin film. Owing to most microelectronic devices and sensors are fabricated by using thin film deposition. In thin film devices, the CTE data for the coating materials will be off the added value.

Many experimental techniques have been developed to measure the amount of stress and strain in thin films. The two general classes of commonly used techniques include deflection techniques based on measuring the curvature or deflection of the substrate²⁻¹³, and strain measurement techniques base on the direct measurements of interplanar spacing in the film using X-ray diffraction^{14,15}. The substrate curvature techniques include optical interferometry²⁻⁴, cantilevered bending beam⁵⁻⁷, optical levered laser scanning⁸⁻¹³ etc. The direct X-ray techniques are based on diffraction, they are limited to crystalline films; they cannot be used to find the stresses in noncrystalline materials, such as amorphous oxides. For this limitation, most approaches are based on the curvature or deflection measurement of a uniformly coated wafer. But these methods are somewhat elaborate and need a special thin substrate or cantilever strip.

In the traditional interferometry method²⁻⁴ have been used to estimate both the thermal expansion coefficient α_f and the biaxial elastic modulus $E_f/(1-\nu_f)$ of thin film, but processing the interference fringes may lead to significant errors. Hence, we propose a more reliable and convenient method associated with a phase shifting interferometry (PSI) technique to improve the accuracy. In this study, by using stress-temperature measurements on films deposited on two different substrate materials with known thermal expansion coefficients, Young's moduli and Poission's ratios, we have been able to determine simultaneously, both the thermal expansion coefficient and the biaxial elastic modulus of metal oxide films prepared by ion beam sputter deposition.

2. METHOD

2.1 Measurement technique

A phase shifting Twyman-Green interferometer, combing the phase reduction algorithm, was set up to measure the substrate deformation, as shown in Figure 1. A He-Ne laser through a micro-objective and a pinhole, as a spatial filter, form a point source and then propagate through a collimating lens to form a plane wavefront. The wavefront is divided in amplitude by a beam splitter. The reflected and transmitted beams travel to a reference plate and a test plate (BK-7 or Pyrex substrate with 25.4 mm in diameter, 1.5 mm in thickness). The flatness of the reference plate is within a tenth of the wavelength of the laser beam. The substrate is mounted on a sample holder and acts as a test plate. After reflection from both reference plate and test plate, the beams recombine at the beam splitter and travel toward the detector (CCD). The interference pattern can be seen on the monitor through the CCD camera. We use the phase shifting Twyman-Green interferometer to measure the deformation of fringes of a coated substrate. The principle of phase shifting measurement follows Hariharan's algorithm¹⁶ and is used to detect the phase of the fringes. We set up a PC-based stress measurement system to evaluate the film stress. The phase shifting fringe patterns are obtained by moving the reference plate to five positions equally spaced of 79.1 nm with a computer-controlled piezoelectric transducer (PZT) translation device. A programmable power supply controlled by a computer provides the PZT voltage.

For image acquisition and processing, the Hariharan algorithm requires that five separate interferograms of the part under test are recorded and digitized. A 90° phase shift is introduced into the reference beam between each of the sequential interferograms recorded by a PC-based frame grabber board. In practice, there are five interferograms with constant phase

difference, 90°, between frames are used to generate the phase map of the fringe patterns. The phase of the fringe is calculated from the digitized intensities at each point in the interferograms using the following equation ¹⁶

$$\Phi(x, y) = \tan^{-1} \left[\frac{2(I_2 - I_4)}{2I_3 - I_5 - I_1} \right] \quad (1)$$

where $\Phi(x, y)$ is a phase function, I_1 to I_5 represent the digitized intensity at a particular point of the five interferograms. The above equation is evaluated at each measurement point to obtain a phase map of the measured wavefront. This wavefront is related to the surface deformation of the test plate or the optical path difference (OPD). The deformation, h , between the reference and test plates can be found from the phase by the following expression

$$h(x, y) = \frac{\lambda}{4\pi} \Phi(x, y) \quad (2)$$

where x and y are the spatial coordinates and λ is wavelength of the He-Ne laser beam. Thin films deposited on a substrate will bend the substrate because of the stress. By measuring the difference in deflection between the substrate before and after thin film deposition, and assuming that the stress is isotropic, the stress in a thin film deposited on a substrate results in substrate deformation proportional to the film stress. Let $\delta = \sum \Delta h_i / N$, where Δh_i is the relative deflection at any position i at distance r from the center, and N is the number of sampling points. The film stress σ can then be related to the deflection change of the substrate before and after film deposition, by using the modified Stoney's formula ^{17,18}

$$\sigma = \frac{E_s \cdot t_s^2 \cdot \Delta \delta}{3(1 - \nu_s) t_f \cdot r^2} \quad (3)$$

where σ is the stress in the thin film, $\Delta \delta$ is the net deflection between the coated substrate and bare substrate, and r is the measured radius on the substrate. E_s and ν_s are the Young's modulus and Poisson's ratio of the substrate ($E_s=81$ GPa and $\nu_s=0.208$ for BK-7 glass), respectively. d_s and d_f are the thickness of the substrate and the film, respectively.

Equation (3) is only valid when $t_f \ll t_s$. This treatment assumes isotropic and homogeneous stress distribution in the coating in which deformations of the substrate are small compared to substrate thickness. If the film was thicker, the deformation would depend on the biaxial elastic modulus of both the substrate and the film. By convention, σ is negative for compressive stress and positive for tensile stress. The optical constants, including refractive index, extinction coefficient, and film thickness, are calculated from the transmittance spectra by the envelope method ¹⁹, which is based on an analysis of the transmittance spectrum of weakly absorbing film deposited on an absorbing-free substrate. The internal stresses, σ , included both the intrinsic stress (σ_i) produced during film deposition and the thermal stress (σ_{th}) due to thermal expansion mismatch between the film and the substrate. The internal stress can be written as

$$\sigma = \sigma_i + (\alpha_s - \alpha_f) \frac{E_f}{1 - \nu_f} (T_1 - T_2) \quad (4)$$

where

α_f, α_s = thermal expansion coefficients of the film and the substrate, respectively.

E_f, ν_f = Young's modulus and Poisson's ratio for the film, respectively.

$E_f/(1 - \nu_f)$ = biaxial elastic modulus of the film

T_1 = stress measurement temperature

T_2 = deposition temperature

From equation (4), it can be readily shown that the slope of the measured stress-temperature curve is equal to

$$\frac{d\sigma}{dT} = (\alpha_s - \alpha_f) \frac{E_f}{1 - \nu_f} \quad (5)$$

assuming that the values of α_s , α_f , E_f and ν_f are independent of the temperature. In the absence of any information about either α_f or $E_f/(1-\nu_f)$, both values can be obtained by simply determining $d\sigma/dT$ on each of two substrates, with known values of α_s , and solving two equations of the form of equation (5), for α_f and $E_f/(1-\nu_f)$ simultaneously. The material constants of the substrates used in calculations of the biaxial elastic modulus and the thermal expansion coefficient of the films are given in table 1. We assume that these material constants are in the temperature independent range from 25 to 70 °C.

2.2 Zernike polynomial fitting

The orthogonality of the Zernike polynomials is a very useful property to describe a wavefront within a circular pupil and simplifies the task of fitting polynomials to the measured data points. Usually, the Zernike polynomial is used in the polynomial fit of circular interferograms. The interferogram is digitized by a frame grabber and the phase value at each point is obtained in units of fringe order number. Each fringe corresponds to an optical path difference (OPD) of an integer number of waves. The distribution of digitized points depends on the fringe pattern and the data read point by point into the computer. The aberrations from piston, tilt and defocus should be removed by fitting the Zernike polynomials, since these terms are induced by the measurement process. The procedure for fitting measured wavefront is described in more detail as shown in references²⁰.

2.3 Software

The image processing software for phase-shifting fringe analysis was developed by using the Microsoft C language. The function of the software includes to grab five interferograms and digitize each frame, to calculate phase reduction and to generate phase map from the phase shifting fringe patterns. The deflection is calculated by the deformations at a distance $r=10$ mm from the center of a circular substrate before and after film deposited. Finally, the film stress can be derived from the resulting deflection of the substrate by the equation (3).

3. EXPERIMENTS

3.1 Substrates

Some researchers have shown that silicon wafers may be used for the measurement of stress in thin films using a laser scanning instrument¹¹⁻¹². In the present study, BK-7 and Pyrex glass (Corning Inc.) substrates, with known thermal expansion coefficients and Young's moduli were used. Two pieces of glass were polished on one side to a flatness of one wavelength and ground on the other side. The stresses were measured for films deposited on the polished face of the two glass substrates (25.4 mm in diameter, 1.5 mm in thickness). The glass substrates used in the experiments were first carefully cleaned with detergent. A final cleaning was made with acetone using an ultrasonic cleaner.

3.2 Thin Film Preparation

Metal oxide films of SiO_2 , Al_2O_3 , Ta_2O_5 and Nb_2O_5 were deposited on unheated BK-7 and Pyrex substrates in a

cryo-pumped vacuum chamber by the ion beam sputter deposition (IBSD). The deposition apparatus was contained in a previous publication²¹. The diameter of substrate was one inch and polished to a flatness of one wavelength. Before each deposition the vacuum chamber was pumped down to a base pressure of less than 3.0×10^{-7} Torr. During the deposition process, oxygen gas was fed near the substrate regulated by a needle valve. The oxygen partial pressure was 8.0×10^{-5} Torr for Al_2O_3 , 1.0×10^{-5} Torr for SiO_2 , 4.0×10^{-5} Torr for Ta_2O_5 and 8.0×10^{-5} Torr for Nb_2O_5 , respectively. The background pressure during the deposition was kept at approximately 1.0×10^{-4} Torr. The ion-beam voltage was 950 to 1000V and ion-beam current was 30 mA. The system was equipped with a quartz crystal and an optical monitor for deposition rate and film thickness control. During the deposition of thin films the temperature of glass substrates were cooled to an ambient temperature. Two substrates were deposited at the same time to avoid any differences in the deposition conditions. The optical constants of thin films were determined by the envelope method¹⁹ of optical transmission measurement. The optical constants of four oxide films prepared by IBSD are given in table 2.

3.3 Stress Measurement

The PSI method used for the measurement of stresses in films has been described in a previous section. The thermal stress was obtained by measuring the deflection of substrates during thermal treatment. The change in deflection with temperature is directly related to the thermal stress component. The experiments allowed for the measurement of intrinsic stress separate from thermal stress. The temperature in all the experiments was determined to a tenth of a degree Celsius. Temperature was measured by means of a thermometer whose sensor was in contact with a substrate adjacent to the films. The glass substrates were placed on a hot stage linked with an electric temperature controller. A k-type thermocouple sensed any temperature variations in the film surface. Interference fringes of reflected light between the reference plate and the substrate were detected with a CCD camera. The interferograms were recorded by a frame-grabber board. The temperature of the sample was controlled in the range from room temperature to 70 °C. The change in the deformation of the substrates after deposition indicated strain in thin films, which in turn is a measurement of stress in the films.

4. RESULTS and DISCUSSION

By using phase shift interferometry (PSI), interference fringe patterns after the metal oxide films were deposited on the BK-7 and the Pyrex glass substrates, varied from a uniform circular to distorted concentric rings, with temperature increases from room temperature to 70 °C. The phase in the interferograms was calculated using Hariharam's algorithm. This algorithm required five interferograms of digitized intensity with a constant phase difference of 90°. After the phase map data were fitted by means of the Zernike polynomials, a deformation plot of the bare substrate and the coated substrate was obtained, respectively. Subtracting the deformation of the coated substrate from the bare substrate, the deflection of the thin films may be obtained. The average deflection is calculated by the deformations at a distance of $r=10\text{mm}$ from the center of a circular substrate. The film stress can be derived from the average deflection by using equation (3). Figure 2 shows the processing procedure of the PSI method. Table 3 summarizes the results for the four oxides film stresses measured by the PSI method. The measuring error is less than 2 %.

In equation (5) the values of α_f and $E_f/(1-\nu_f)$ are unknown. As the intrinsic stress does not depend on the measurement temperature, the intrinsic stress, σ_i , can be calculated from the temperature dependence of the internal stress σ , assuming that E_f , ν_f , α_f , E_s , ν_s and α_s are temperature independent. The thermal expansion coefficient and the biaxial elastic modulus $E_f/(1-\nu_f)$ of thin film can be derived from the slope of the stress-temperature plot using at least two sorts of substrates, with

known thermal expansion coefficients and Young's moduli. We choose a Ta_2O_5 film as an example to demonstrate the PSI method of film stress-temperature measurement. In figure 3, the deflections of the Ta_2O_5 films deposited on two different substrates are plotted against the stress measurement temperature. This demonstrates a linear dependence on the temperature and shows that the assumption of the temperature independence of E_f , ν_f , α_f , E_s , ν_s and α_s is valid in this temperature range. The stress-temperature curves for the films on the two different substrates have different slopes, as shown in figure 4. This is mainly because of a thermal mismatch between films on the two different substrates. The thermal mismatch is caused by the different thermal expansion coefficients of the films and the substrates. The slope of the line for the difference data is determined by least squares fitting. From the difference in the slopes of the two lines in figure 4, the average intrinsic stress, α_f and $E_f/(1-\nu_f)$, are calculated being -0.405 GPa , $2.45 \times 10^{-6} \text{ }^\circ\text{C}^{-1}$ and 1549.4 GPa , respectively. The measurement of the stress, thermal expansion coefficient and biaxial elastic modulus of SiO_2 , Al_2O_3 and Nb_2O_5 follow the same way. The measurement results are summarized in table 3.

5. CONCLUSION

An improved interferometric method based on phase shifting interferometry for the measurement of the mechanical properties of metal oxide films has been presented. The application of the PSI technique for measuring thin films stress allows the phase distribution to be determined automatically and without need of human interpretation of the fringe pattern. It has the advantage that inherently high sensitivity, accuracy, easy operation and reproducible performance. In another application, by using stress-temperature measurements on films deposited on two different substrate materials with known thermal expansion coefficients, Young's moduli and Poisson's ratios, both the thermal expansion coefficient α_f and the biaxial elastic modulus $E_f/(1-\nu_f)$ of thin film could be obtained simultaneously. In addition, Zernike polynomial fitting algorithm can generate the 3-D contour plot of film deformation to present tensile stress or compressive stress. This method provides a visual means for observing stress distribution not apparent in individual average stress scans. The proposed method can facilitate the development of processes that produce more uniform films.

ACKNOWLEDGMENTS

The authors gratefully appreciate the support of the National Science Council of Taiwan, the Republic of China, under project number NSC 89-2215-E-097-001.

REFERENCES

1. R.W. Hoffman, *Physics of Nonmetallic Tin Films*, edited by C. H. S. Dupuy and A. Cachard, Ch.12, Plenum Press, New York, 1974.
2. H. Sunami, Y. Itoh, and K. Sato, "Stress and thermal-expansion coefficient of chemical-vapor-deposited glass films," *J. Appl. Phys.*, **41**, pp.5115-5117, 1970.
3. K. Roll and H. Hoffmann, "Michelson interferometer for deformation measurements in an UHV system at elevated temperatures," *Rev. Sci. Instrum.*, **47**, pp.1183-1185, 1976.
4. M. Miyagi and N. Funakoshi, "Internal stress and thermal expansion coefficient of Gd-Si films," *Jpn. J. Appl. Phys.*, **20**, pp. 289-290, 1981.
5. E. Klokholm, "An apparatus for measuring stress in thin films," *Rev. Sci. Instrum.*, **40**, pp.1054-1058, 1969.

6. S. N. Sahu, J. Scarminio, and F. Decker, "A laser beam deflection system for measuring stress variations in thin film electrodes," *J. Electrochem. Soc.*, **137**, pp.1150-1154,1990.
7. D. Sader, A. Enders and J. Kirschner, " A simple technique to measure stress in ultra thin films during growth, " *Rev. Sci. Instrum.*, **66**, pp.4734-4735,1995.
8. A. K. Sinha, H. J. Levinstein, and T. E. Smith, "Thermal stresses and cracking resistance of dielectric films on Si substrates," *J. Appl. Phys.*,**49**,pp.2423-2426,1978.
9. T. Aoki, Y. Nishikawa and S. Kato, " An improved Optical lever technique for measuring film stress, " *Jpn. J. Appl. Phys.*,**28**, pp.299-300,1989.
10. L .M. Mack, A. Reisman and P.K. Bhattacharya, "Stress measurements of thermally grown thin oxides on (100) Si substrates," *J. Electrochem. Soc.*, **136**, pp.3433-3437,1989.
11. D. S. Gardner and P.A. Flinn, "Mechanical stress as a function of temperature for aluminum alloy films," *J. Appl. Phys.* , **67**, pp.1831-1843,1990.
12. P. A. Flinn, D. S. Gardner, and W. D. Nix, " Measurement and interpretation of stress in Aluminum-based metallization as a function of thermal history," *IEEE Transaction on Electron Devices*, **34**, pp.689-698,1987.
13. E. Kobeda and E.A. Irene, "A measurement of intrinsic SiO₂ film stress resulting from low temperature thermal oxidation of Si," *J. Vac. Sci. Technol.*, **B4**,pp.720-722,1986.
14. D. S. Cambell, Mechanical properties of thin films, in *Handbook of Thin Film Technology*, edited by L.I. Massel and R.Glang, McGraw-Hill, New York ,1970.
15. A. Segmuller, J. Angilelo and S.J. Laplaca "Automatic X-ray diffraction measurement of the lattice curvature of substrate wafers for the determination of linear strain pattern," *J. App. Phys.*,**51**, pp.6224-6230,1980.
16. P. Hariharan, B.F. Oreb, and T. Eiju, "Digital phase-shifting interferometry: a simple error-compensating phase calculation algorithm," *Appl. Opt.*, **26**, pp.2504-2506,1987.
17. G. G. Stoney, "The tension of metallic films deposited by electrolysis, " *Proc. Royal Society, London*, **A 82**, pp.172 -175,1909.
18. A. Brenner and S. Senderoff, "Calculation of stress in electrodeposits from the curvature of a plated strip," *J. Research of the Nat'l Bureau of Standards*, **42**, pp.105-123,1949.
19. R. Swanepoel, "Determination of the thickness and optical constants of amorphous silicon," *J. Phys. E*, **16**, pp.1214-1222,1983.
20. D. Malacara and S. L. DeVore, Interferogram evaluation and wavefront fitting, in *Optical Shop Testing*, edited by D. Malacara, Ch. 13, John Wiley & Sons, New York, 1992.
21. C. C. Lee, J. C. Hsu, D. T. Wei ,and J. H. Lin, " Morphology of dual beam ion sputtered films investigated by atomic force microscopy," *Thin Solid Films*, **308-309**, pp.74-78,1997.

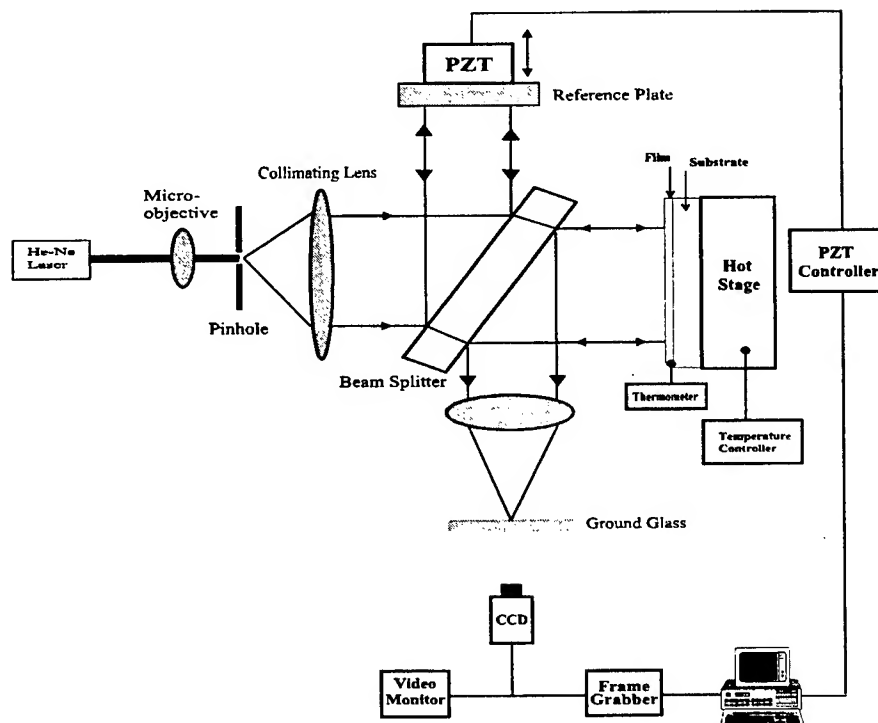


Figure 1 The schematic drawing of the stress measuring apparatus

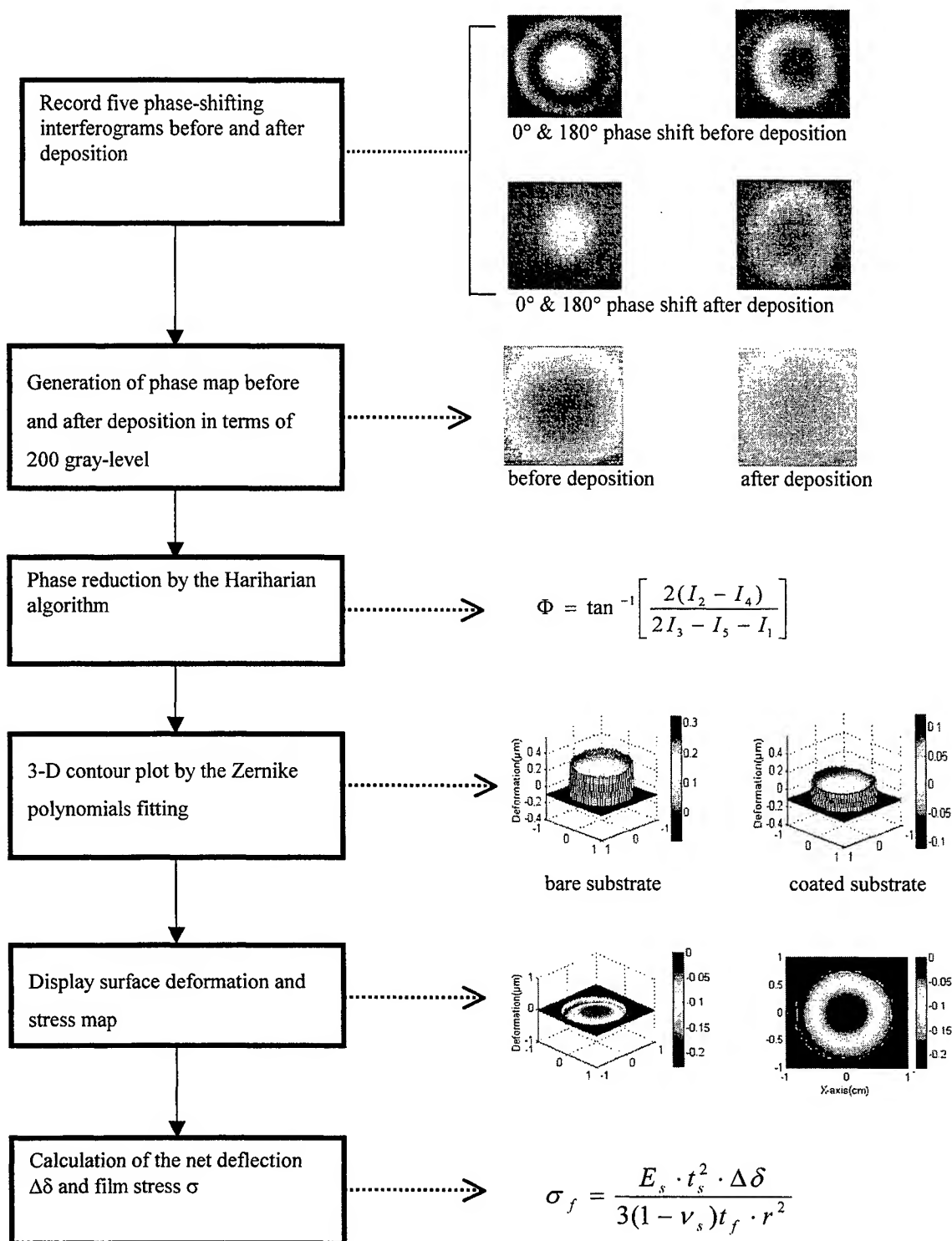


Figure 2 The processing procedure of the PSI method

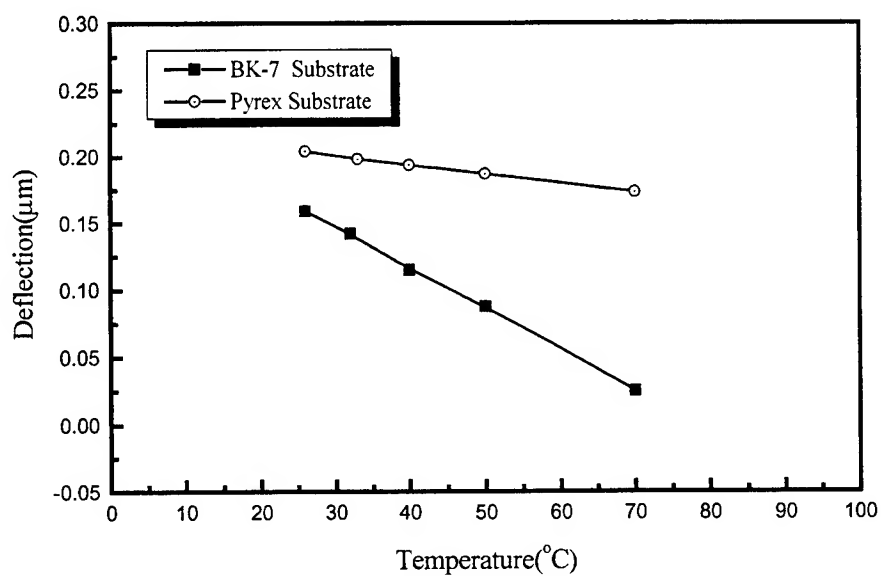


Figure 3 The deflection versus temperature for Ta_2O_5 films deposited on two different substrates

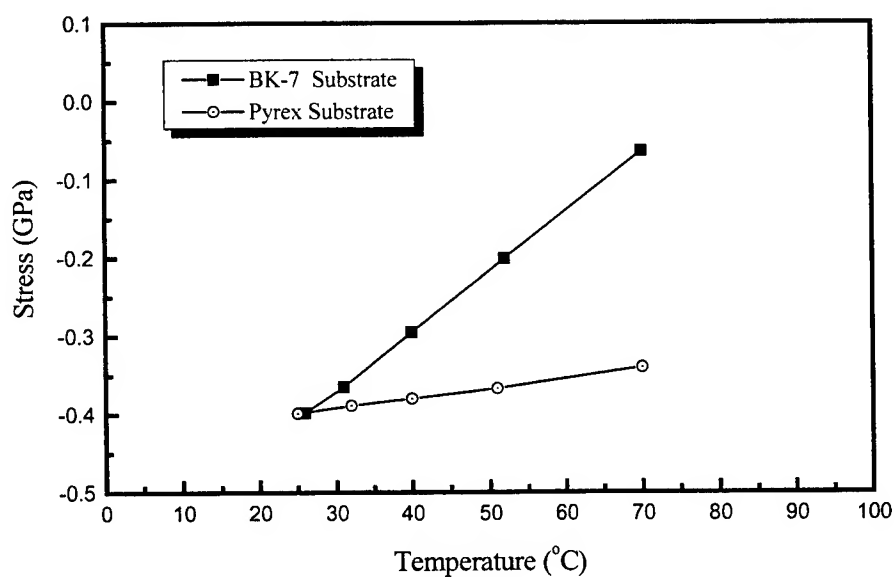


Figure 4 The variation of stress respect to measurement temperature in Ta_2O_5 films deposited on two different substrates

Table 1 The material constants of glass substrates for the calculation of film stress

Substrates	Young's modulus(GPa)	Poisson's ratio	Thermal expansion coefficient (°C ⁻¹)
BK-7	81.0	0.208	7.40×10^{-6}
Pyrex	62.7	0.200	3.25×10^{-6}

Table 2 The optical constant of metal oxide films prepared by IBSD

Thin films	Film thickness (nm)	Refractive index (at 633 nm)	Extinction coefficient (at 633 nm)
SiO ₂	264.4	1.47	7×10^{-4}
Al ₂ O ₃	308.4	1.66	9×10^{-4}
Ta ₂ O ₅	298.5	2.16	1×10^{-3}
Nb ₂ O ₅	291.2	2.29	4×10^{-3}

Table 3 Stress and thermal expansion coefficient of metal oxide films

Thin films	Stress (GPa) on BK-7 substrate	Stress (GPa) on Pyrex substrate	Thermal expansion coefficient (°C ⁻¹)	Biaxial elastic modulus (GPa)
SiO ₂	- 0.380	- 0.386	0.38×10^{-6}	3257
Al ₂ O ₃	- 0.493	- 0.390	2.04×10^{-6}	3852
Ta ₂ O ₅	- 0.407	- 0.402	2.45×10^{-6}	1549
Nb ₂ O ₅	- 0.396	- 0.356	1.52×10^{-6}	3820

Fabrications and characterizations of micromachined Fabry-Perot interferometers

Ran-Jin Lin

Microsystems Laboratory, Industrial Technology Research Institute, Chutung Hsinchu 310,
Taiwan, R.O.C.

ABSTRACT

Miniature micromachined Fabry-Perot interferometers (FPI) are composed of the corrugated silicon diaphragm and glass substrate. The flatness of the silicon diaphragms with a dimension of 4.2 mm in diameter can be controlled within 0.12 μm . The optimal deposition condition to grow thin Au films, as a reflector of FPI, can be established by studying the optical properties of Au-photoresist-Au etalons. The interference spectra of micro-machined gap-tunable FPI with a structure of Si-Cr-Au-air-Au-Cr-glass have been observed in the near infrared regions. The transmittance and FWHM bandwidth of the as-bonded FPI is 5.6 % and 3.84 nm at a peak wavelength of 1578.4 nm, respectively.

Keywords : Fabry-Perot, interferometer, micromachined, corrugated, silicon diaphragm, FPI

1. INTRODUCTION

A Fabry-Perot interferometer (FPI) is composed of two partially reflecting, parallel mirrors separated by a gap which is changeable by electrostatic, piezoelectric or magnetic force. The resonance wavelengths, λ_{res} , of the transmission spectra for these devices can be described by $\lambda_{\text{res}} = \frac{2L_{\text{eff}}}{q}$, where L_{eff} is the effective length of the cavity and q is an integer. The L_{eff} depends on the separation of the mirrors ($L_{\text{mirror separation}}$), the phase change on reflection of light from the mirrors ($L_{\text{phase change}}$) and the refractive indices (n) of the materials inside the cavity¹:

$$L_{\text{eff}} = n \cdot L_{\text{mirror separation}} + L_{\text{phase change}}$$

The micromachined FPI devices have been considered in wide applications, such as tunable laser sources², tunable light emitting diodes³, wavelength division multiplexers (WDM)⁴, portable spectrometers⁵, gas sensors⁶, pressure sensors⁷, chemical sensors⁸, and strain sensors⁹, etc..

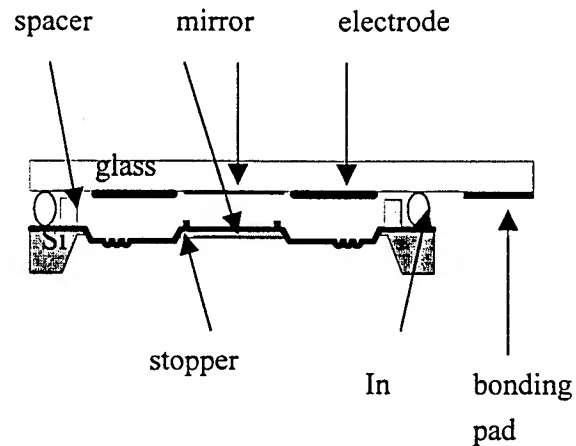


Fig. 1 Schematic structure of Si-Cr-Au-air-Au-Cr-glass FPI.

1 Etching Si ring: patterning PR;

dry etching Si (10-50 um);



2. Etching Si grooves: patterning

PR; dry etching Si (6-15um);



3. Boron diffusion: thermal SiO₂ deposition;

patterning PR ; wet etching SiO₂; removing PR;

boron diffusion; removing SiO₂



4. Backside etching: thermal SiO₂ deposition;

LPCVD SiN_x deposition;back side patterning PR

backside dry etching SiN_x; removing PR; KOH

etching Si; removing SiN_x



5. Gold deposition: sputtering Cr plus sputtering Au



6. Spacer: polyimide coating (6-20um), Al deposition ;

patterning PR; wet etching Al; dry etching Polyimide



7. Reflector: patterning PR; sputtering Cr +sputtering Au

patterning metal layer by -lift-off; removing PR



8. Bonding pad & electrode : patterning PR,

Al deposition, patterning al by lift-off.



Fig. 2 Schematic fabrication sequence of the FPI with a structure of Si-Cr-Au-air-Au-Cr-glass.

The application goals of our FPI are set in development of portable micro-spectrometer with a spectral range of 0.9 μm to 2 μm . Schematic structure of the Si-Cr-Au-air-Au-Cr-glass FPI is shown in Fig.1. In order to operate the FPI in this wide spectral range, we use thin gold films as reflecting mirrors. To obtain the gap-tunable FPI, the movable plate is the corrugated Si diaphragm. The characteristics of this diaphragm are to reduce the effect of the initial residual stress¹⁰, to extend the linear portion of the load-deflection behavior and to provide larger deflection than flat diaphragms for equivalent loads¹¹.

In this paper, the fabrication of flat large-diameter (4.2 mm) corrugated Si diaphragms, characterization of mechanical stiffness of diaphragms, optical characterization of fixed-gap Au-photoresist-Au etalons and gap-tunable FPI will be described.

2. EXPERIMENTS

The schematic fabrication sequence of the micromachined gap-tunable FPI with a structure of Si-Cr-Au-air-Au-Cr-glass is shown in Fig. 2. First, it was to fabricate the corrugated Si diaphragms (4.2 mm in diameter) with a center boss of 3.2 mm in diameter. The process started with a 4-inch n-type (100) silicon wafer. The thickness and resistivity of the wafer were 300 μm and 1-10 ohm-cm, respectively. Both sides of the wafers were polished. In order to attain the diaphragm with rigid center (center boss), the grooves of corrugations were fabricated below the front surface of the wafer using the reactive ion etching (RIE) method, as shown in Fig. 2(1),(2). Then, the thermal SiO_2 layer with a thickness of 400 nm was grown at 1100 $^\circ\text{C}$ in atmosphere of flowing wet-oxygen. The oxide layer, used as a mask of boron-diffusion, on front surface was patterned by buffered oxide etch (BOE; 6:1). The boron diffusion was performed using solid boron sources (boron source wafers, GS-245, made by Owens-Illinois, Inc.) at 1075 $^\circ\text{C}$ for 3 hr. Then, the silicon nitride (Si_3N_4) films with a thickness 160 nm, as a mask of etching Si, were deposited by low pressure chemical vapor deposition (LPCVD) at 750 $^\circ\text{C}$ with a $\text{SiH}_2\text{Cl}_2:\text{NH}_3$ gas flow ratio of 5:1 and gas pressure of 0.4 Torr. The nitride films on backside surface of the wafer were patterned using double-side aligner (Karsuss MA6) and RIE method. Then, the wafers were immersed in $\text{KOH-H}_2\text{O}$ solution for releasing the diaphragms by back-side etching of Si. The thin (30 nm) gold films were deposited on the surface of silicon after removing the etch mask.

Secondly, it was to fabricate the polyimide spacer films, Au reflectors and Al electrostatic electrodes on pyrex 7740 glass. The spun polyimide films were first soft-baked at 90 $^\circ\text{C}$, then cured at 350-400 $^\circ\text{C}$ for 1 hour. The Au films were deposited by a DC magnetron sputter at room temperature. The deposition of Al films was made using an electron-beam evaporator. Finally, it was to constitute the FPI by bonding the corrugated Si chip and glass chip together at 150-200 $^\circ\text{C}$ using indium (In) solders.

The surface profile and load-deflection behavior of the corrugated Si diaphragms were examined using a non-contact optical profilometer, made by WYKO. The optical properties of the Fabry-Perot etalons or interferometers were characterized by the optical spectrometers.

3. RESULTS AND DISCUSSION

3.1. Fabrication of corrugated Si diaphragms

The detailed geometry, cross-section profiles and surface profiles of our corrugated Si diaphragms were shown in previous paper¹². The surface profiles of corrugated Si diaphragms under zero applied pressure strongly related to the level of residual stress in the films and geometrical effect of the corrugated diaphragms. The residual stress of the films used in fabrication of the diaphragm at room temperature was tensile stress of 50-100 MPa for heavy boron-doped Si¹³, compressive stress of 500 MPa for thermal SiO₂, and tensile stress of 1100-1300 MPa for LPCVD-Si₃N₄. The residual stress of the films at room temperature is the summation of intrinsic stress of the films at deposition temperature and thermal stress from deposition temperature to room temperature. Since the coefficient of thermal expansion of Si₃N₄ is smaller than that of Si¹⁴, the compressive stress will be generated in Si₃N₄ films during cooling from deposition temperature of 750 °C. The intrinsic stress of the Si₃N₄ films must be tensile stress and its value is larger than the values of residual stress 1100-1300 MPa. Pearson et. al.¹⁵ showed that the yield stress of silicon crystal at 750 °C is about 6×10^9 dyn/cm². It is reasonable to predict the existence of plastic deformation in the interface between Si₃N₄ film and Si substrate. This results in the bow of center boss of the corrugated Si diaphragms even if the diaphragms are annealed at high temperature for long time¹². Therefore, it is necessary to lower the residual stress of the films for flat corrugated Si diaphragms. .

The simple way to reduce the residual stress of the films, grown by standard semiconductor processes, is to use the composite layers of compressive films and tensile films¹⁶. The residual stress, S , of the composite layers can be estimated by

$$S = \frac{t_1\sigma_1 + t_2\sigma_2}{t_1 + t_2},$$

where t_1 and t_2 are the thickness of the films, and σ_1 and σ_2 are the residual stress of the films. The residual stress of the composite layers can be adjusted from tensile value to compressive value. In the following experiments, the composite layers, as a etch mask of etching Si by KOH solution, is composed of thermal SiO₂ film (0.4 μ m) and Si₃N₄ film (0.16 μ m). The value of estimated residual stress in the composite layers is in the range of -42.9 to -14.3 MPa.

Typical effect of corrugation depth on the surface profile of the corrugated Si diaphragms with center-boss thickness of 10 μ m and 30 μ m is shown in Fig. 3 and Fig. 4, respectively. The corrugations and center boss of the diaphragms are bowed down to the backside of the wafer, irrespective of whether the composite layers is removed or not. Before removing the composite layers on the diaphragms with center-boss thickness of 10 μ m, the deflection of center boss varies from 2 μ m to 3 μ m with change of the corrugation depth from 6 μ m, 9 μ m, 12 μ m to 15 μ m. Additionally, the center boss moved down 10 μ m to 5 μ m below the front side surface of the wafer with increasing the depth of corrugation depth, as shown in Fig.3. The similar results are obtained for the diaphragms with thickness of center boss

With SiO₂/Si₃N₄ layers

Without i SiO₂/Si₃N₄ layers

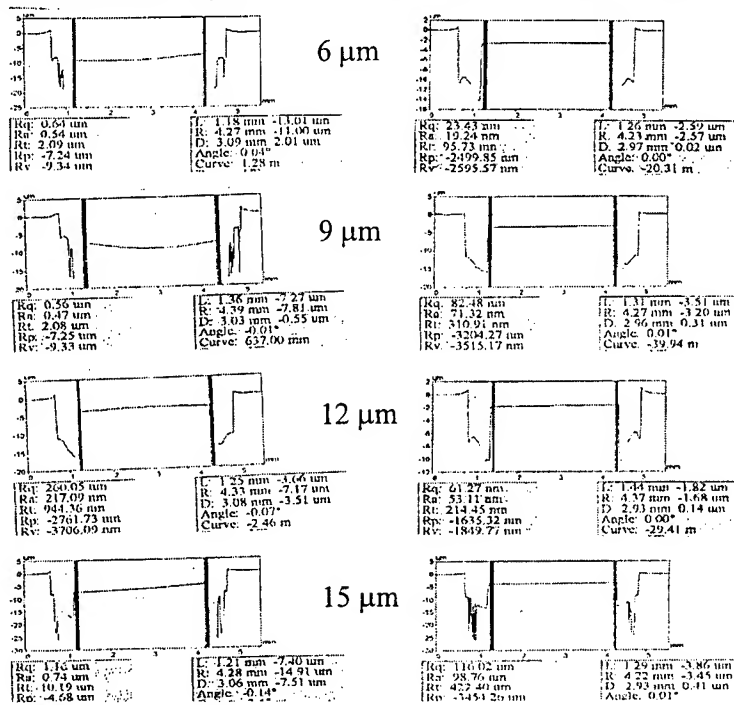


Fig. 3 Effect of corrugation depth on the surface profiles of corrugated Si diaphragms with center-boss thickness of 10 μm .

With SiO₂/Si₃N₄ layers

Without i SiO₂/Si₃N₄ layers

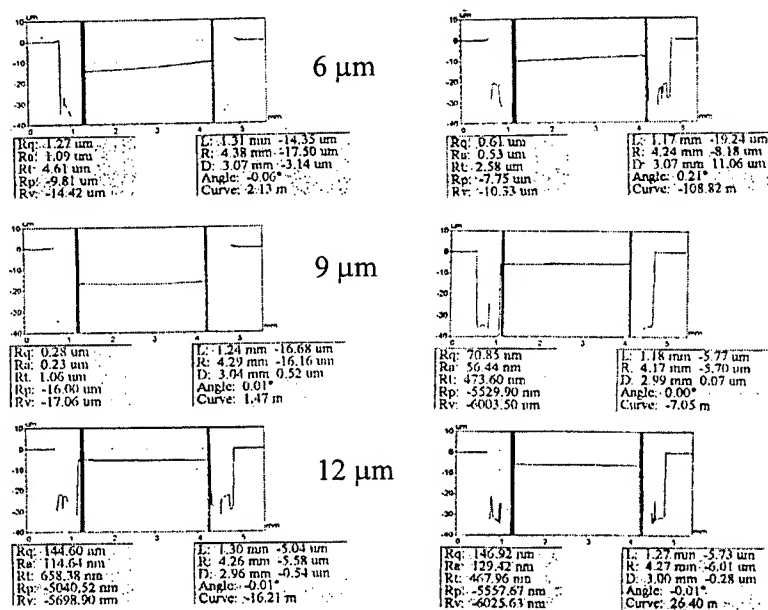


Fig. 4 Effect of corrugation depth on the surface profiles of corrugated Si diaphragms with center-boss thickness of 30 μm .

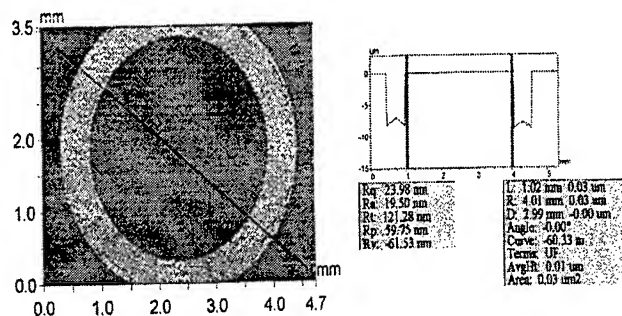


Fig. 5 Typical surface profile of the annealed Si diaphragm

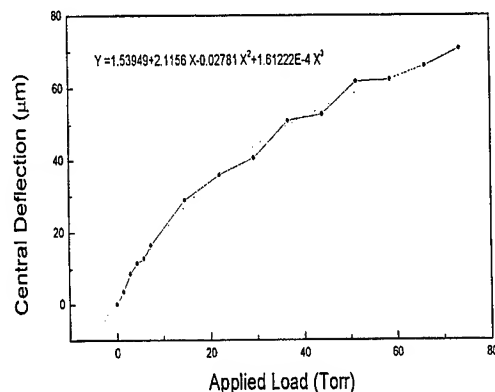


Fig. 6 Load-deflection relationship of the corrugated Si diaphragm.

30 μm , as shown in Fig. 4. After removing the composite layers, the deflection of the center boss is reduced to about 0.4 μm for all diaphragms. Simultaneously, the distance that the center boss moved down is reduced to 3 to 6 μm . After the corrugated Si diaphragms were annealed at 1050 $^{\circ}\text{C}$ for 60-120 min in atmosphere of flowing N_2 , the deflection of center boss was further reduced and the surface of center boss were almost moved up to the surface of the wafers. The typical surface profile of the annealed Si diaphragms is shown in fig. 5. The deflection of the center boss can be reduced to 0.12 μm within the area of 3.2 mm in diameter.

From the above-mentioned results, the surface profile of the corrugated Si diaphragms can be traced to deflection of corrugation, deflection of center boss and geometrical interaction of the diaphragm. The deflection of corrugation is caused by the residual tensile stress and stress gradient in Si due to heavy boron doping and existence of composition gradient. This deflection can almost be recovered by high temperature annealing treatment. The deflection of the center boss was mainly caused by the intrinsic stress and thermal stress of the films during fabrication and can be reduced by lowering residual stress in the films. By now, we do not understand the effect of geometrical interaction yet. More detailed analysis of mechanics is required.

3.2. Characterization of Mechanical Stiffness of the Corrugated Si Diaphragms

The relationship between deflection of corrugated diaphragm and applied gas (air) pressure was measured by gradually increasing the applied pressure. The measured deflection is the maximum deflection of the diaphragm, located at the center of the diaphragm. Fig.6 shows the load-deflection relationship of the typical corrugated Si diaphragm. The thickness and depth of corrugation were 2 μm and 6.4 μm , respectively. The thickness of the center boss was 10 μm . The diaphragm is easily deformed. The center deflection can be achieved to 76 μm under low applied pressure of 75 Torr.

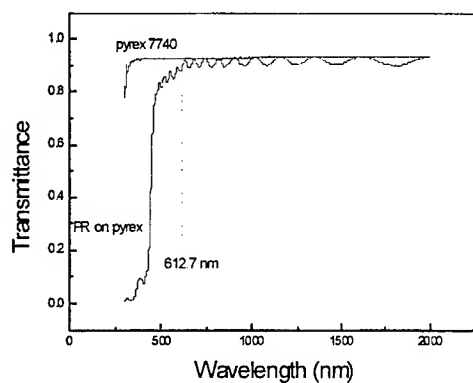


Fig. 7 Transmission spectrum of a photoresist film on glass.

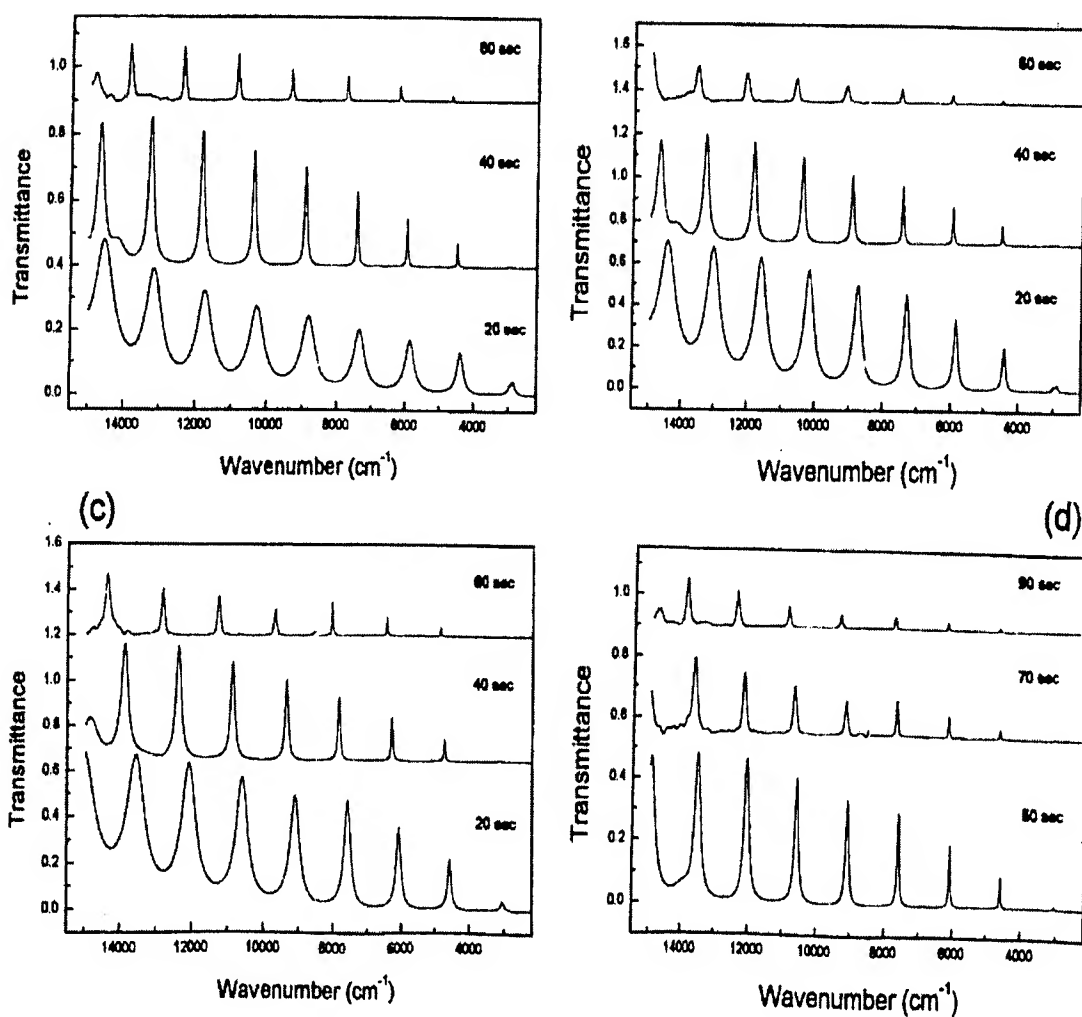


Fig. 8 Effect of sputtering parameters of the Au films on the transmission spectra of Au-photoresist-Au etalons on pyrex 7740 glass.

3.3. Au-photoresist-Au etalons on glass

Performance of Fabry-Perot interferometers (such as transmittance, finesse and chromatic resolving power) strongly relates to the optical properties of metal mirrors, such as reflectance, transmittance, absorption and scattering loss. These optical properties of metal mirrors depend on the thickness of metal films, methods of preparation and deposition parameters. The conventional photoresist (PR) films are transparent in the visible to near infrared (IR) regions, as shown in Fig. 7. Uniform PR film is also easily fabricated by spinning process. Therefore, we try to use a simple Au-photoresist-Au etalon to establish the suitable deposition condition of Au films, as mirrors of the gap-tunable FPI.

Fig. 8 shows the effect of sputtering parameters of the Au films on the transmittance and peak-bandwidth of Au-photoresist-Au etalons on pyrex 7740 glass. The transmittance of etalons is little affected by sputtering gas pressure from 2 mTorr to 20 mTorr under a rf power of 150 W. However, the transmittance and bandwidth of resonance peaks are strongly affected by deposition time (thickness of films). This is mainly caused that the reflectance of Au films increases and approaches its bulk value with increase of film thickness¹⁷. Another phenomenon is that the resonance peaks shift to the region of higher wave number (i.e. shorter wavelength). This is due to the existence of phase change on reflection from a Au mirror. Its value varies with wavelength and mirror thickness¹⁷. Therefore, the suitable deposition condition of Au mirrors for FPI is deposition time of 40 sec under a rf power of 150 W. The thickness of the Au films is about 30 nm and reflectance of the Au films is about 0.85 in the spectral range of 0.9 to 2 μm .

3.4. Gap-tunable interferometers of Si-Cr-Au-air-Au-Cr-glass

The schematic structure of the gap-tunable Fabry-Perot interferometers of Si-Cr-Au-air-Au-Cr-glass structure is shown in Fig. 1. Transmittance spectra of typical as-bonded FPI are shown in Fig. 9. The resonance peaks of interference can be clearly observed. The variations of the peak-numbers in the spectral ranges of 0.9 μm to 2.0 μm can be controlled to within one peak for the FPI devices fabricated by same conditions. This means that the gap of the interferometers can be reproducibly controlled using the present spacer-fabrication and Si-glass bonding technologies. As we know that the performance of FPI strongly depends on the measuring methods and systems. Therefore, the optical channel analyzer for characterizing DWDM transmission system was used to obtain the accurate data of transmittance and full width at half-maximum (FWHM) of FPI peaks. Simultaneously, the light source with high coherence, bandwidth of 40 nm, was used. Typical transmission peak of as-bonded Si-Cr-Au-air-Au-Cr-glass interferometers with gap about 17.4 μm is shown in Fig. 10. Excluding the resonance peak of the cavity, there are many small resonance peaks, which are generated by the interference in glass substrate with a thickness of 0.6 mm due to the highly coherent light source. By now, the maximum transmittance of the peak at a wavelength of 1578.4 nm is 5.6 %. This value can be further improved by coating the anti-reflection layer on Si surface. However, the FWHM bandwidth is 3.84 nm, which is far smaller than the value of 24.6 nm, measured by the conventional spectrometer, as shown in Fig. 9. This value is very close to the

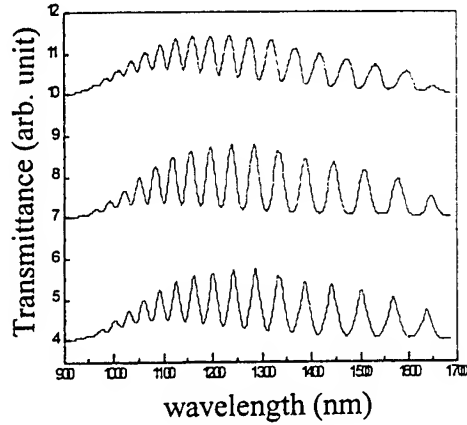


Fig. 9 Transmission spectra of as-bonded Si-Cr-Au-air-Au-Cr-glass FPI.

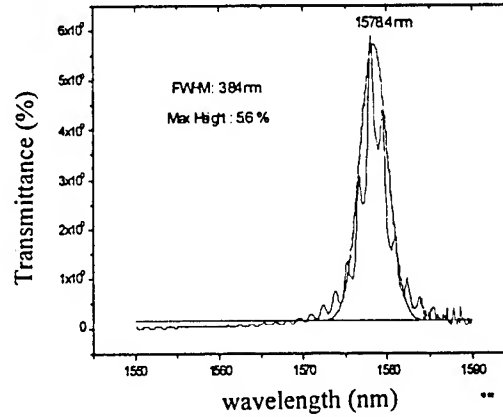


Fig. 10 Transmission spectra of as-bonded Si-Cr-Au-air-Au-Cr-glass FPI, measured by the optical channel analyzer.

theoretical value of 3.7 nm, predicted from formula $FWHM = \frac{\lambda(1-R)}{m\pi\sqrt{R}}$, where λ is resonance wavelength, R the mirror reflectance (0.86 for Au film), n the order of the interference. This means that there is good parallelism between mirrors in FPI. The scanning spectra of the FPI by varying the separation between two mirrors have also been achieved by controlling the gas pressure inside the cavity, as shown in Fig.11. The interference peaks can still be observed after changing the gap from 17.4 μm to 8 μm .

4. CONCLUSIONS

A new structure of corrugated silicon diaphragms with a diameter of 4.2 mm has been fabricated using (100) silicon wafers. The center boss with thickness of several μm to 50 μm can be easily fabricated using the structure that the grooves of corrugations were located below the front surface of the Si wafers. The deflection of the corrugated diaphragms under zero applied pressure strongly relates to the level of residual stress in the films during fabrication and geometrical interaction of the corrugated diaphragm. The flatness of the corrugated Si diaphragms can be controlled within 0.12 μm through lowering the residual stress in the films. The large displacement, 76 μm , of the corrugated Si diaphragms can be obtained under low applied pressure of 75Torr. The optimal deposition condition of thin Au films can be established by studying the optical properties of Au-photoresist-Au etalons. The interference spectra of micro-machined gap-tunable Si-Cr-Au-air-Au-Cr-glass FPI have been observed in the near infrared region. The transmittance and FWHM bandwidth of the as-bonded Si-Cr-Au-air-Au-Cr-glass FPI is 5.6 % and 3.84 nm at a peak wavelength of 1578.4 nm, respectively. The improving performance of FPI and scanning FPI by electrostatic force are in progress.

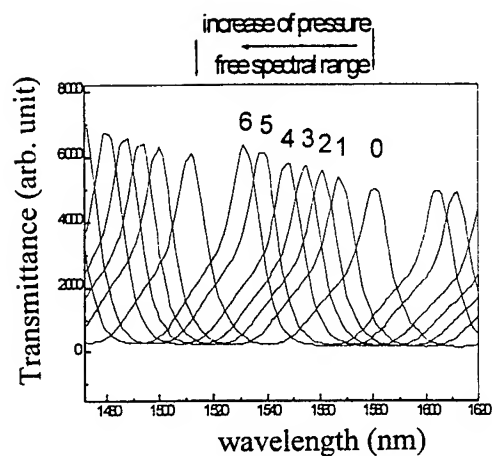


Fig. 11 Transmission spectra of gap-tunable Si-Cr-Au-air-Au-Cr-glass interferometer*.

* corresponding gap of FPI

0 : as-bonded gap 17.38 μm

1 : 17.24 μm 4 : 16.99 μm

2 : 17.15 μm 5 : 16.9 μm

3 : 17.06 μm 6 : 16.78 μm

ACKNOWLEDGEMENTS

The authors are grateful to Dr. S.P. Lee and Dr. K.K. Liu of ITRI, Professors R.S. Huang, W. Fang and H. S. Yie of Tsing-Hua university for their helpful discussion in design and processes. The work was supported by the Ministry of Economic Affairs, Republic of China, under contract No. 3KX1110 to the Industrial Technology Research Institute.

REFERENCES

1. H. Becker, R.H. Friend and T.D. Wilkinson, "Light emission from wavelength-tunable microcavities," *Appl. Phys. Lett.* 72, pp. 1266-8, 1998.
2. K. Bacher, B. Pezeshki, S.M. Lord and J.S. Harris, Jr., "Molecular beam epitaxy growth of vertical cavity optical devices with in situ corrections," *Appl. Phys. Lett.* 61, pp. 1387-9, 1992.
3. M.C. Larson and J.S. Harris, Jr., "Broadly tunable resonant-cavity light emission," *Appl. Phys. Lett.* 67, pp. 590-2, 1995.
4. H. Toshiyoshi, M. Kobayashi, D. Miyauchi, H. Fujita, J. Podlecki and Y. Arakawa, "Design and analysis of micromechanical tunable interferometers for WDM free-space optical interconnection," *J. Lightwave Technology* 17, pp. 19-25, 1999.
5. J. Noto, R.B. Kerr, K. Ng, R.S. Lancaster and M. Dorin, "Boston University's high-resolution near-infrared Fabry-Perot spectrometer," *Opt. Eng.* 33, pp. 451-6, 1994.
6. J.P. silveira and F. Grasdepot, "New signal processing for absorption-based gas sensing," *Sensors and Actuators B*

29, pp. 363-7, 1995.

7. J. Han and D.P. Neikirk, "Deflection behaviour of Fabry-Perot pressure sensors having planar and corrugated membrane," SPIE's Micromachining and Microfabrication '96 Symposium: Micromachined devices and Components II, edited by R. Roop and K. Chau, proc. SPIE 2882, pp. 79-90, 1996.
8. T. Eklov, H. Sundgren and I. Lundstrom, "Distributed chemical sensing," Sensors and Actuators B 45, pp. 71-7, 1997.
9. A. A. Chtcherbakov, P.L. Swart, S.J. Spammer and P.V. Bulkin, "Long dual-cavity fiber optic Fabry-Perot strain sensor with rugate mirrors," Opt. Eng. 35, pp. 1059-63, 1996.
10. Q. Zou, Z. Wang, R. Lin, S. Yi, H. Gong, M. Lim, Z. Li and L. Liu, "A study on corrugated diaphragms for high-sensitivity structures," J. Micromech. Microeng. 7, pp. 310-5, 1997.
11. J.H. Jerman, "The fabrication and use of micromachined corrugated silicon diaphragms," Sensors and Actuators, A21-A23, pp. 988-92, 1990.
12. R.J. Lin, S.P. Lee, K.K. Liu, H.H. Chen, C.A. Hung and R.S. Hung, "Fabrication and characterization of corrugated silicon diaphragms," Proc. 2nd Nano Engineering and Micro System Technology Workshop, ITRI-Taiwan, pp. 3-175-182, 1998.
13. X. Ding, "Behavior and application of silicon diaphragms with a boss and corrugations," Dig. IEEE Solid-State Sensor and Actuator Workshop, Hilton Head, SC, pp. 166-9, 1992.
14. A.K. Sinha, H.J. Levinstein and T.E. Smith, "Thermal stresses and cracking resistance of dielectric films (SiN , $\text{Si}/\text{sub } 3/\text{N}/\text{sub } 4/$, and $\text{SiO}/\text{sub } 2/$) on Si substrates," J. Appl. Phys. 49, pp. 2423-6, 1978.
15. G.L. Pearson, W.T. Read and W.L. Feldmann, Acta. Meta. 5, pp. 181, 1957.
16. C. Thielemann and G. Hess, "Inorganic electret membrane for a silicon microphone," Sensors and Actuators A 61, pp. 352-5, 1997.
17. H. Becker, S.E. Burns, N. Tessler and R.H. Friend, "Role of optical properties of metallic mirrors in microcavity structures," J. Appl. Phys. 81, pp. 2825-9, 1997.

256x256 InSb Focal Plane Arrays

Yau-Tang Gau, Li-Kuo Dai, Shue-Ping Yang, Ping-Kuo Weng, Kaung-Shin Huang, Yion-Ni Liu,
Cheng-Der Chiang, Far-Wen Jih, Ya-Tung Cherng* and Horng Chang

Materials & Electro-Optics Division

Chung Shang Institute of Science and Technology

P.O.Box 90008-8-7, Lung Tan, Taoyuan 325, Taiwan

ABSTRACT

A 256x256 backside illuminated photovoltaic indium antimonide (InSb) focal plane arrays having spectral response in the medium wavelength infrared (3 to 5 μm) was designed and developed at Chung Shang Institute of Science and Technology for use in a variety of military and commercial applications. Operating at 77°K, the arrays had a mean laboratory detectivity of $3.12 \times 10^{11} \text{ cmHz}^{1/2}/\text{W}$ with f/3 optics. The responsivity non-uniformity was 3%, and the operable yield exceeded 99%. The FPA achieves an Noise Equivalent Temperature Difference (NETD) is less than 0.025°K at 300°K background with f/3 optics.

Keywords : InSb, Focal Plane Array, Readout Integrated Circuit (ROIC) , Indium bump, Hybridization

1. INTRODUCTION

Infrared imaging utilize the thermal infrared radiation emitted by all objects to provide temperature information. Large staring infrared focal plane arrays are being developed for a wide variety of military and commercial applications. Military applications include advanced tactical systems such as FLIRs, missile seekers, threat warning sensors, and thermal weapon sights. Rapidly growing commercial applications include use by firefighters in reduced visibility; use by law enforcement agencies; and expanded security applications.

Indium antimonide (InSb) is an well established material for infrared focal plane array (IRFPA's) operating in the medium wavelength (3 to 5 μm) region.¹⁻⁴ A hybrid focal plane array consists of a two-dimensional array of InSb junction photodiodes in contact with a readout silicon multiplexer. The arrays are bump bonded, and cooled down to a cryogenic temperature for high sensitivity. In the backside illuminated configuration, the substrate is thinned to less than the minority carrier diffusion length with improved quantum efficiency.⁵

This paper presents the 256x256 backside illuminated photovoltaic indium antimonide (InSb) focal plane arrays which was designed and developed at Chung Shang Institute of Science and Technology. The InSb detector arrays that have the best responsivity was described in section 2. In section 3, the development of our readout integrated circuit (ROIC) that has a well capacity of 1.1×10^7 electrons and 60 or 120 frames per second using 2 or 4 outputs was reported. In section 4, the hybridization technique between detector array and readout integrated circuit was described. In section 5, we give the FPA

* Correspondence : Email : ytch@tpts5.seed.net.tw : Telephone : 886-3-4712201ext.357090 : Fax : 886-3-4711024

performance data. Finally, conclusion is drawn in section 6.

2. DETECTOR ARRAYS

Fabrication techniques for InSb detector arrays use thermal diffusion and a subsequent surface etch results in a p-type mesa on n-type substrate. To approach the minimum surface leakage current, insulating layers were evaporated as passivation. Then the metals were evaporated as ohmic contact and bonding pad.

Each focal plane array consists 256× 256 element p⁺/n diodes. The active areas are 25 microns square on 30 micron pitches. IR radiation is absorbed in the thinning substrate with the charge collected by the pn junction and inject into the input stage via the indium bump which connect each pixel of the CMOS CKTs.

The I-V characteristics of dark current verse bias voltage were measured by HP4145B parameter analyzer while the focal plane arrays were kept at 77°K. As shown in Fig. 1, the arrays have an $R_{oA} = 2.5 \times 10^4 \Omega \text{ cm}^2$, and a leakage current of 166pA at a reverse bias of 250mV.

3. READOUT INTEGRATED CIRCUITS (ROIC)

CMOS circuit has the advantages of low power and low noise while providing sophisticated multiplexing and control logic for an infrared FPA readout. A high performance CMOS switched FET readout multiplexer was developed using standard foundry compatible processing. Fig. 2 is the schematic diagram of the 256× 256 readout circuit used in our hybrid FPA. Each unit cell in the readout has a direct injection input circuit, a source follower amplifier, a reset MOSFET, and a cell access MOSFET. The input circuit is a common gate amplifier that performs the functions of interfacing to the detectors, integrating the photocurrent and converting this current to a voltage. The gate bias labeled IG in Fig. 2 is adjustable externally to maintain the operating point of the detector. Internal timing generator generates most of the control clocks so that only three clocks are required. Two rows (512 inputs) are sampled simultaneously by peripheral sample and hold amplifiers. The readout also incorporates logic that can be programmed to select 2 or 4-output mode. Multiple outputs will enhance the readout data speed. Since each output can multiplex data at least a 2 MHz rate, the FPA can be operated up to 60 or 120 frames per second using the 2 or 4 outputs respectively. The detail specifications of the readout integrated circuit are listed in Table 1.

4. HYBRIZATION

Indium bump technology was utilized to electrical and mechanical interconnection between the InSb detector array and the silicon readout integrated circuit (ROIC). The identical indium bumps are grown on arrays and readout chips. A flip chip bonding technology was used to hybridize the 256× 256 indium antimonide detector array and silicon readout multiplexer. After alignment, these bumps are joined together by M9 flip chip bonder (Research Devices, U.S.A.) . The machine gives simultaneous viewing of the detector and ROIC by an IR illuminator. A built-in contact force indicator permits continuous monitoring of bump force during bonding.

The major concern in this process is that all the detector arrays should be connected electrically and mechanically to the readout silicon multiplexer with the minimum degradation in the signal-to-noise ratio. The percentage of functionally

operability of the FPA depends on the yield of indium bump hybridization process assuming that the InSb detector arrays and Si readout multiplexer chosen were such that all of those were fully functional prior to hybridization.

After hybridization, the device was thinned from the detector backside to optimize the quantum efficiency. A mechanically lapped to about 50 μ m thickness, followed by a mechanically polished to about 20 μ m thickness. A chemical etching technique was developed in order to achieve good thickness uniformity and to avoid mechanical lapping and polishing defects on the InSb surfaces. Then, backside was passivated with a carefully chosen insulator and a well controlled passivation process to ensure optimum performance.

5. FPA PERFORMANCE

Referring to Fig. 3, the FPA test scheme is organized as follows: The 256x 256 InSb FPA was bonded in a 68-pin leadless ceramic chip carrier. The DUT (Detector Unit Test) is mounted on the test dewar which is evacuated to a pressure of $10^{-4} \sim 10^{-5}$ torr and kept the FPA at their operating temperature of 77°K. A cavity-type blackbody source (CI SR-20) at a high temperature (700° K to 1000° K) was placed a distance away from the test dewar to provide a uniform illumination on FPA through the CaF₂ optical window and cold spectral filter. The optical window transmission is > 95 % over the 3-5 μ m range. The spectral filter is mounted in the F/3 cold shield assembly to limit the spectral content and thus the photon noise. The filter in the test dewar is a 3-5 μ m bandpass filter.

The electrical output of the FPA is fed into the sensor buffer board which provides the function of driving the ROIC and signal conditioning the output current of ROIC to match the input range of A/D converter. The sensor buffer board receives the power and clock from the test system and produced bias voltage, driving clock for the operation of ROIC. The current output of FPA is signal conditioned by a two-stage amplifier to convert the current to voltage. Due to the current output nature, the sensor buffer board is mounted directly on the test dewar as near as possible to avoid noise picking. The two-stage amplifier also provides gain and offset adjustable function to optimize the A/D converter dynamic range.

The two-stage amplifier circuit is depicted in Fig. 4, the first stage amplifier provides the current-to-voltage converter (TIA) function and bias the operation point of ROIC to 5V. A constant 12V bias is applied to the first stage amplifier to balance the effect of bias voltage for the operation point of ROIC and this can avoid the output saturation of first stage amplifier. The offset port provides an adjustable current range of ± 6 mA to make the output voltage of the sensor buffer board bipolar.

The second stage amplifier provides the buffer and adjustable gain function. The sensor buffer board has four gain setting which are selectable through the control of a analog multiplex and was not depicted in the figure. The scalable gain setting was used to properly adjust the rail-to-rail output of sensor buffer board to match the input range of A/D converter, thus to optimize the A/D dynamic range. A compensated capacitor is added in the pin 5 of AD 846 to limit the bandwidth of the amplifier circuit to 10M Hz. With properly choice of the feedback resistor and compensated capacitor, an optimized R/C combination can be obtained and this can avoid the gain peaking of the TIA amplifier. In addition to the compensation effect, pin 5 can provide the output clamp capability to limit the rail-to rail output. The adjustable clamp range is ± 10 V depended on the external applied bias voltage (V20,V21).

The rail-to-rail output range of sensor buffer board is limited to ± 4 V, the noise produced by the sensor buffer board

and test system is about 1.2 mV which is less than a count in the 12 bits A/D counts.

The FPA test system is composed of four main units, The A/D converter unit, Data processing and control unit, the programmable pattern generator and power supply unit. The sensor buffer board acquires four clock signals and three bias power supplies from the test system, and produces the necessary bias and clock signal to drive the FPA. The FPA operated in its two-output mode at a pixel rate up to 2MHz per channel. The sensor buffer board buffered the two output of FPA and the analog data are digitized by the 12 bits A/D converter unit. Digitized data is sent to the cache of Data processing unit for post processing and download to the test computer for analysis. The Data processing unit also received command from the test computer and instructed the test system to operate the data acquisition.

For testing, the FPA views controlled radiometric configurations. The signal from each elements is measured at the output of sensor buffer board. The voltages are digitized and processed using the data acquisition of the test system. The digitized data is analyzed and data reduction in the test computer. The reported voltage is all referred to the integration capacitor. For each measurement, the FPA are reversed biased about 30 ~ 40 mV to minimized the DC non-uniformity. Thirty consecutive frames were taken for the DC uniformity and noise measurement, then transferred to the test computer for analysis and display. The integration time and frame rate were chosen to make the integration capacitor at 50% full.

The mean of DC response of the FPA as a functions of integration time at different illumination of flux is showing in Fig.5. The mean output voltage approximately linearly with the integration time over a range of 5V. The statistical deviation of linearity from measured mean output to linear curve is $< \pm 1\%$. The pixel to pixel variation in the non-linearity has not been measured but the DC non-uniformity of the FPA $< 6\%$. The measured noise voltage is expressed as the voltage referred to the integration capacitor, which is 0.64 mV only (typical $< 1\text{mV}$ for other FPA). The dynamic range of the FPA, measure as the full signal response to the no light level noise is excess of 72 dB.

Fig 6 shows the histogram distribution of RA product for the FPA, the measurement of RA product is at the hybrid level by measuring the data of each pixel in the FPA at two different bias. The FPA bias is chosen at a reversed bias larger than 50mV to make the DC response of FPA more uniform. The mean RA value of FPA is $\sim 2.7 \times 10^4 \Omega \text{cm}^2$.

The quantum efficiency of the non-AR coated FPA has been measured at the hybrid level by measuring the output signal swing at different photon flux input. Fig. 7-a is a quantum efficiency map of a 256×256 FPA operated at 1.41×10^{14} photons/cm²/sec. The wavelength chosen for this measurement is 3 ~ 5 μm .. The mean quantum efficiency is 0.61. Fig. 7-b show the histogram distribution of the 256x256 FPA, the RMS variation is 2.88% of the mean value, the value represents an extremely uniformity process. In the test results, the inoperative pixel due to the failure of QE is typically $< 0.6\%$.

The mean D* values measured for the FPA in the f/3 test dewar are shown in Fig. 8. The detectivity for a typical array are measured under conditions of 1.41×10^{14} photons/cm²/sec, at 80° K, and in the 3 ~ 5 μm band. The mean D* is $3.12 \times 10^{11} \text{ cmHz}^{1/2}/\text{W}$. NEAT has been measured using f/3 optics to be 0.025° K. Fig.8-a show the D* map of the FPA, white pixel is marked as inoperative pixel, the inoperative pixel in D* measurement is usually $< .5\%$. The histogram distribution of D* is show in Fig. 8-b.

Typically, the FPA tested has an operable yield exceeded 99%. The pixels in the FPA that are marked as inoperative pixels satisfy the criterion. The pixels with QE which is less than 0.5 x array mean of QE, or QE which is larger than 1.33 x array mean of QE are marked as inoperative pixels. The pixels with D* which is less than $1 \times 10^{+11} \text{ cmHz}^{1/2}/\text{W}$. or D* which

is larger than $1 \times 10^{-12} \text{ cm}^2/\text{Hz/W}$ are marked as inoperative pixel also. The pixels with noise larger than 4mV are marked as inoperative pixels also. (for a 12 bits ADC, the full voltage of integration capacitor is 4.5 ~ 5.4V, 4mV means 4 counts). The test data of FPA reported here has a yield of 99.3%, the total inoperative pixel # is 440, which are represented as white pixels in Fig. 7-a, 8-a.

The FPA was used for imaging. Due to the gain and offset non-uniformity, a two-point calibration process is applied on the FPA data at two different temperature and the bad pixel in the FPA is replaced by the neighborhood good pixels. The final imaging of the FPA is shown in Fig. 9-a with a pseudo-color image (256 color) and in Fig. 9-b with a 256 gray-level image. The two images are taken at 45 frame rate and integration time 2.08 ms.

6. CONCLUSION

The high performance 256×256 InSb IRFPA has been successfully developed at CSIST. The 256×256 InSb sensor and focal plane array hybridized technology were developed successfully in our facility. This was the first time we designed Si-CMOS readout chip which was operated at 77°K. Initial goals of the development program have been met or exceeded. The arrays have high operability and good uniformity; the quantum efficiency is close to theoretical; the readout noise and detector dark current are low. 512×512 formats of focal plane arrays will be developed in the future.

REFERENCES

1. I. Bloom and Y. Nemirovsky, "Bulk Lifetime Determination of Etch-Thinned InSb Wafers for Two-Dimensional Infrared Focal Plane Array", *IEEE Trans. Electron Devices*, **39**, pp. 809-812, 1992.
2. W.J. Parrish, J.D. Blackwell, G.T. Kincaid and R.C. Paulson, "Low-Cost High Performance InSb 256×256 Infrared Camera", *SPIE* **1540**, pp. 274-284, 1991.
3. C.A. Niblack, H.A. Timlin, C.J. Martin, R.C. Fischer, C. Walmsley and C. Steele, "Initial characterization of a new 64×64 multiplexer InSb FPA", *SPIE* **1157**, pp.124-132, 1989.
4. A. Hoffman and D. Randall, "High-performance 256×256 InSb FPA for astronomy", *SPIE* **1540**, pp. 297-302, 1991.
5. I. Bloom and Y. Nemirovsky, "Quantum Efficiency and Crosstalk of an Improved Backside-Illuminated Indium Antimonide Focal-Plane Array", *IEEE Trans. Electron Devices*, **38**, pp. 1792-1796, 1991.

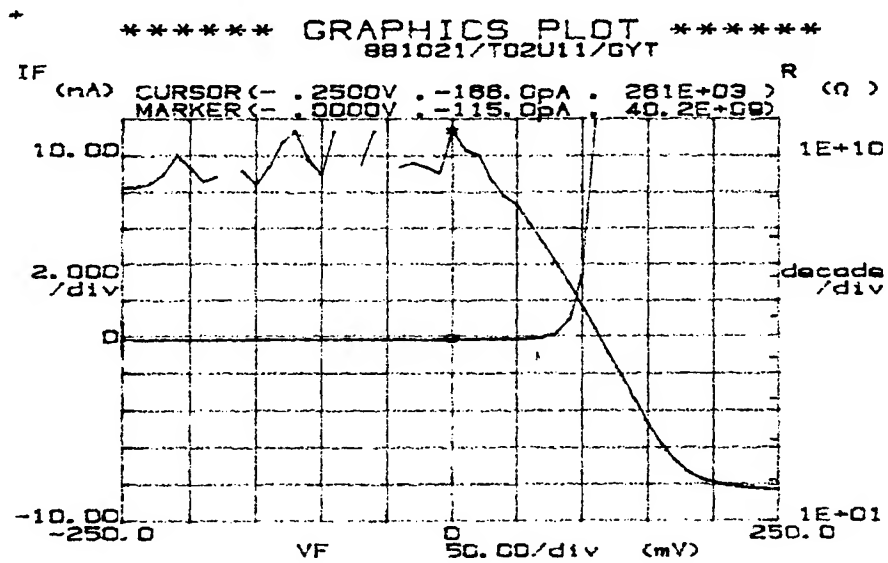


Fig. 1. The I-V characteristics of dark current vs. bias voltage.

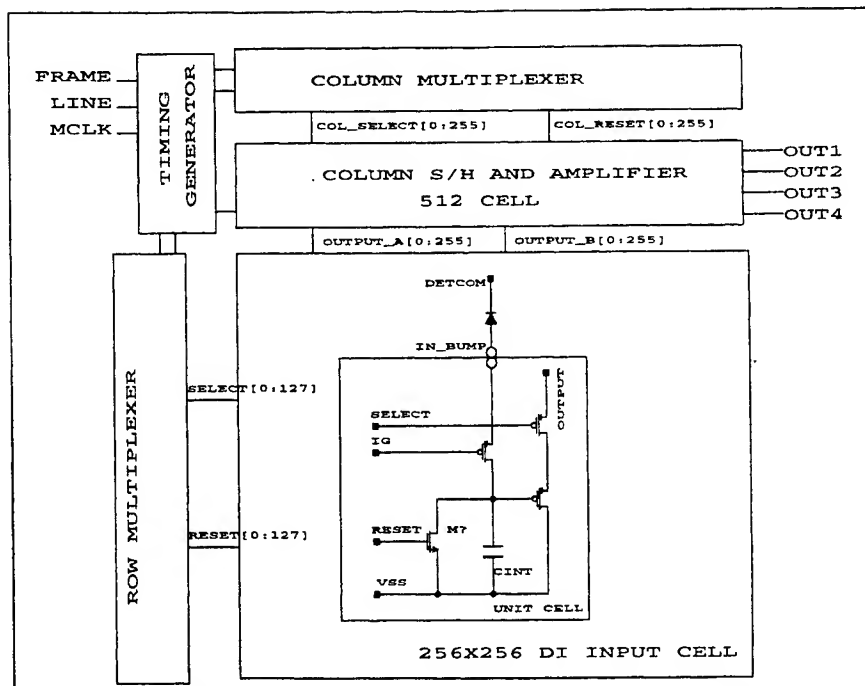


Fig. 2. Schematic of the 256x 256 direct-injection readout circuit.

Table 1. 256x 256 InSb FPA Readout Specifications

Parameters	Specifications
Detector	InSb 256x 256
Pixel Size	30 μ m x 30 μ m
Die size	8.7mm x 8.9mm
Process	DPDM 0.5 μ m CMOS
Frame rate	60Hz (2 output)
Well Capacity	$>1.1 \times 10^7$ e-
Output Mode	Current
Outputs	Selectable 2 or 4
Integration Mode	Rolling
Integration Time	1/128 to 127/128 of frame time
Clocks	3
Power supply	5V
Power dissipation	<25mW

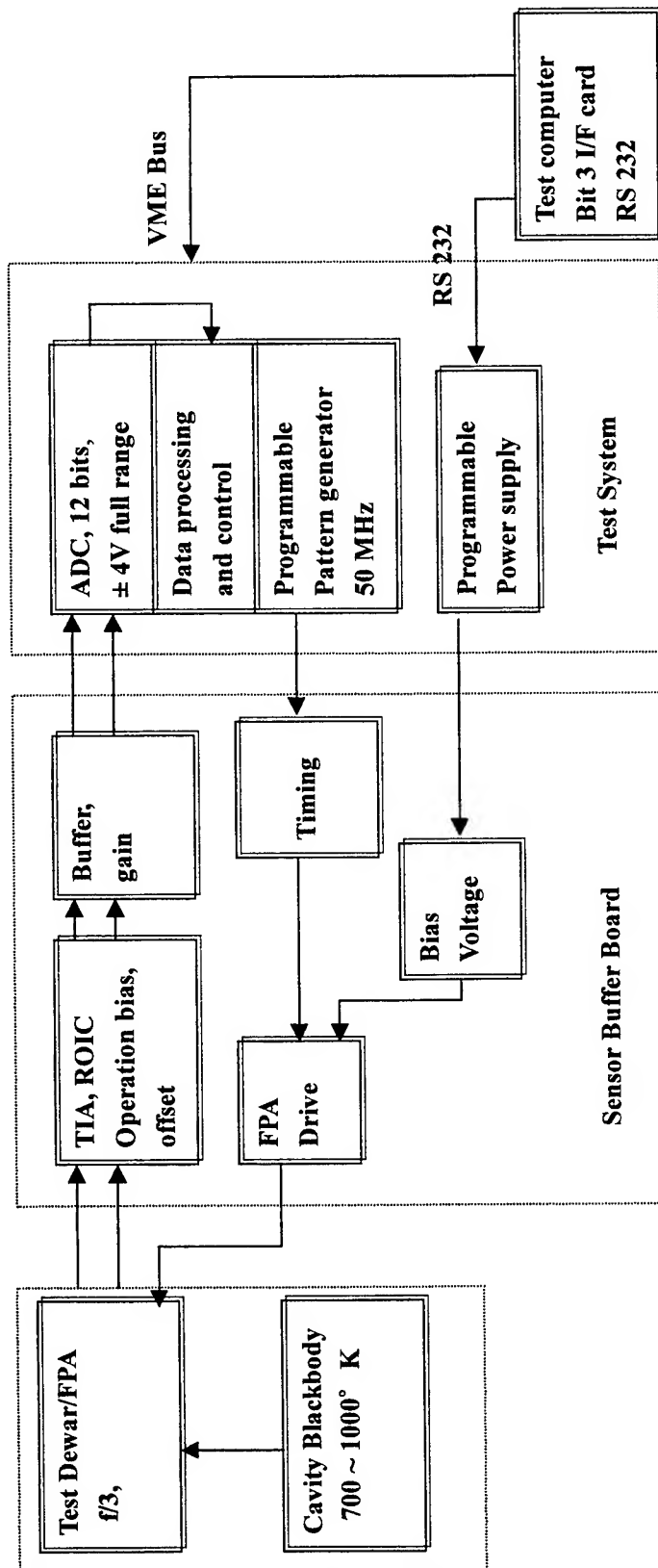


Fig. 3 The Block diagram of test scheme

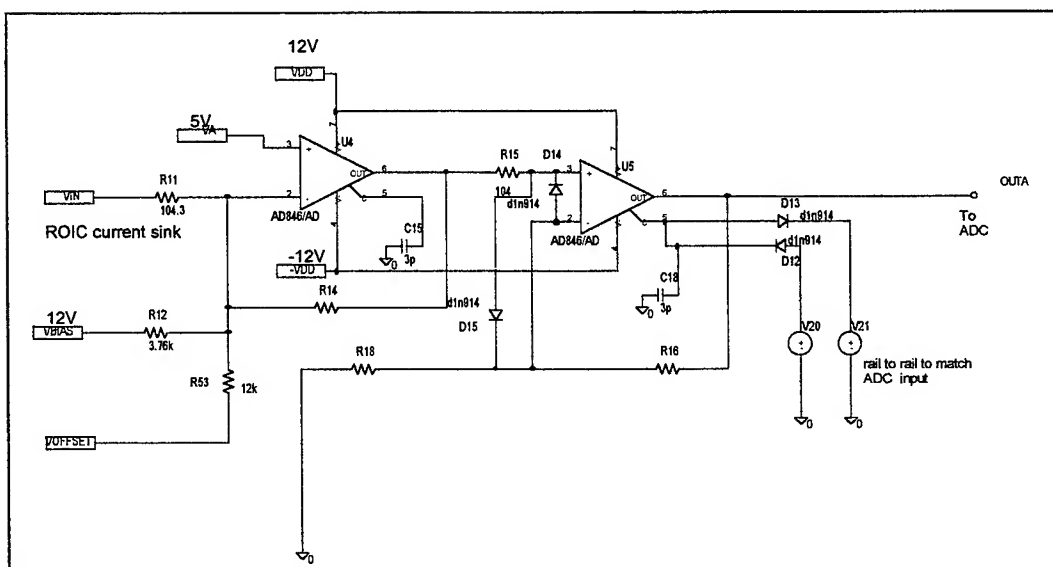


Fig. 4 The two-stage amplifier circuit in the sensor buffer board

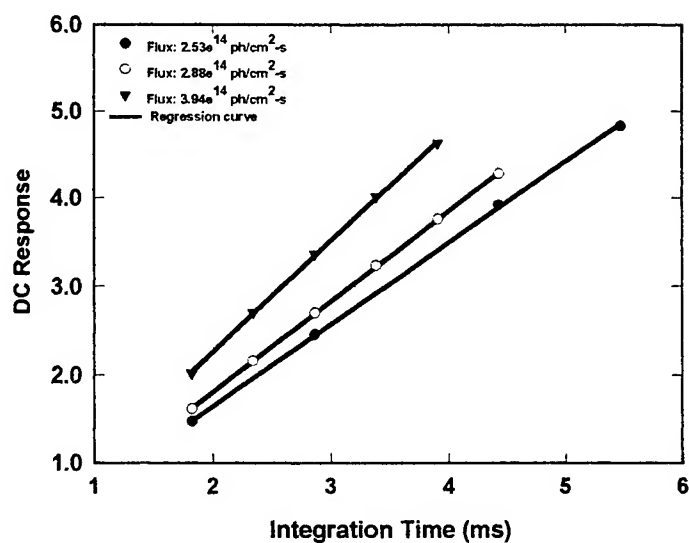


Fig.5 FPA DC response via integration time

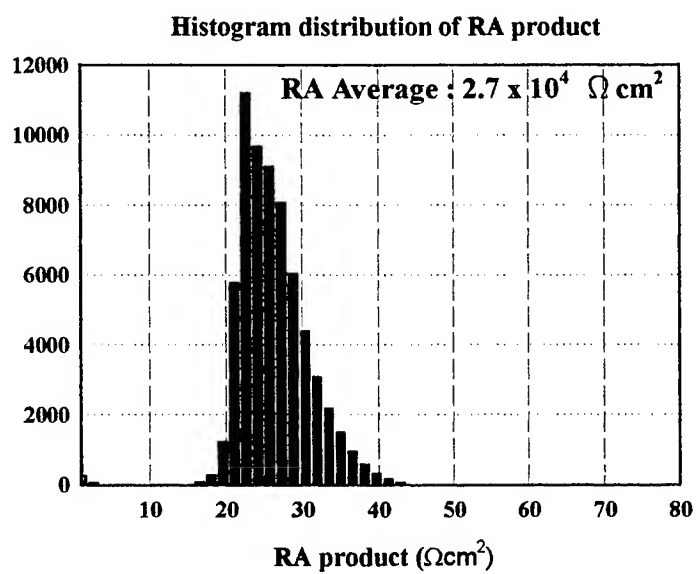


Fig.6 The Histogram distribution of RA

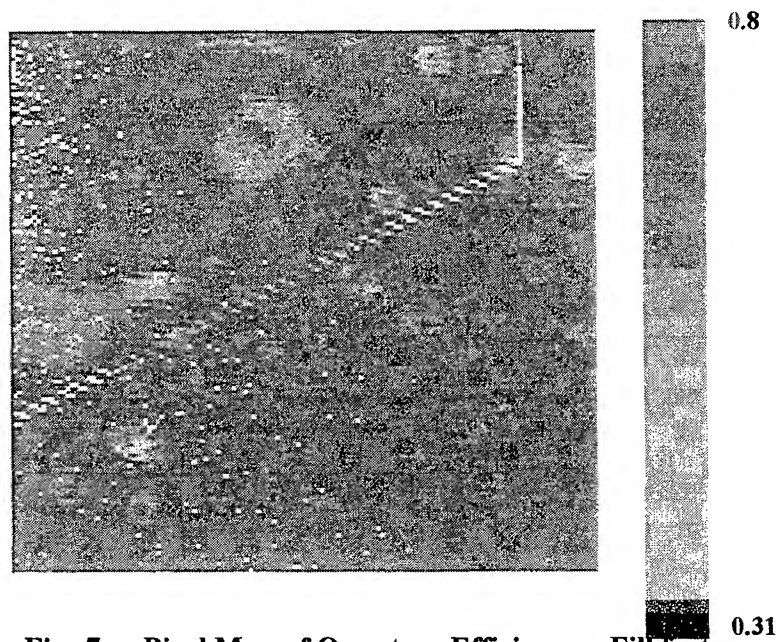


Fig: 7-a. Pixel Map of Quantum Efficiency x Fill factor

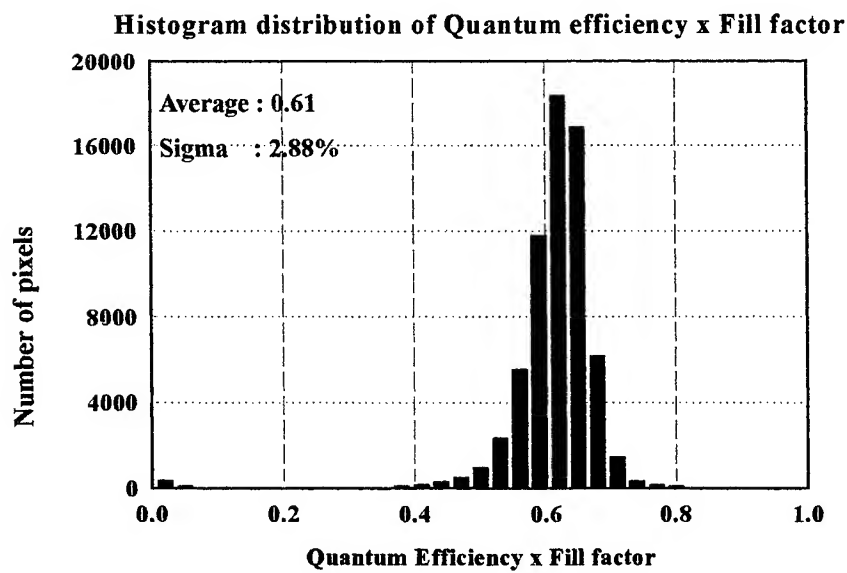


Fig: 7-b. Histogram distribution of Quantum Efficiency x Fill factor

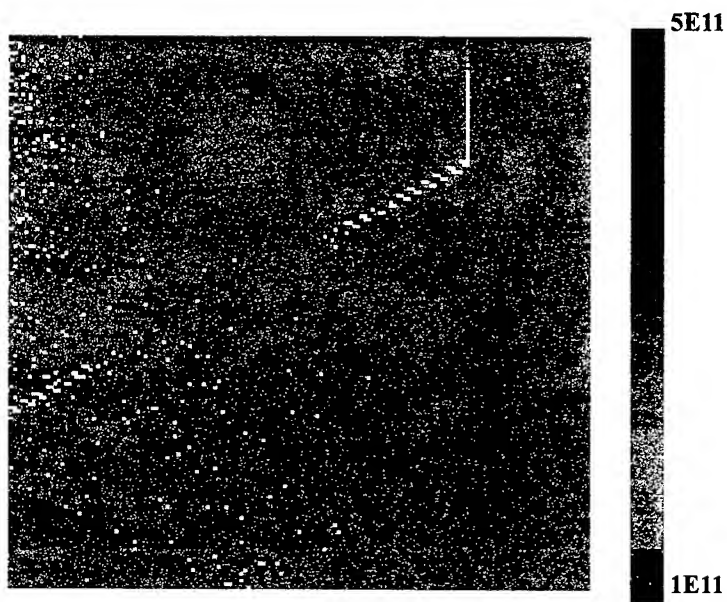


Fig: 8-a. Pixel Map of Detectivity

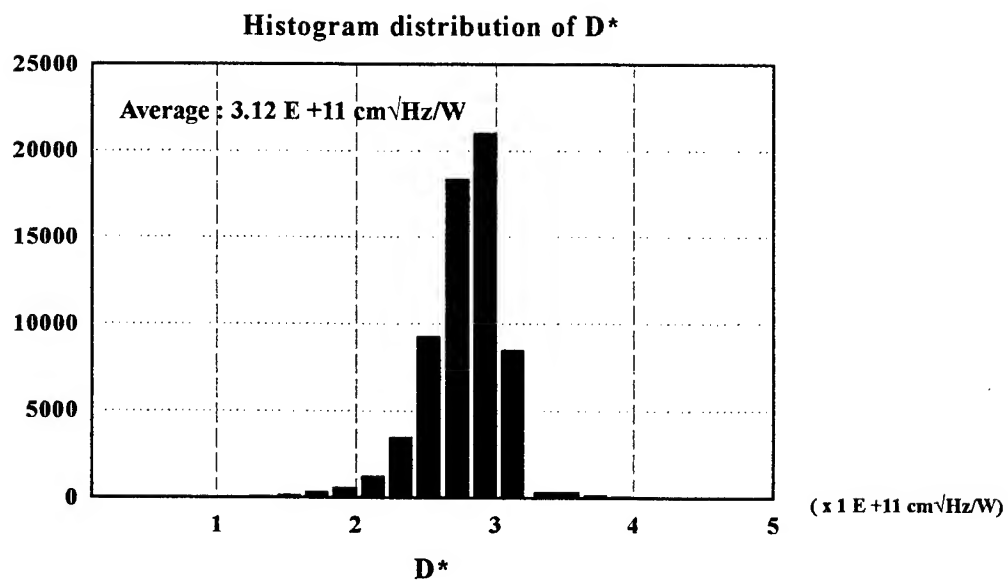


Fig: 8-b. Histogram distribution of Detectivity

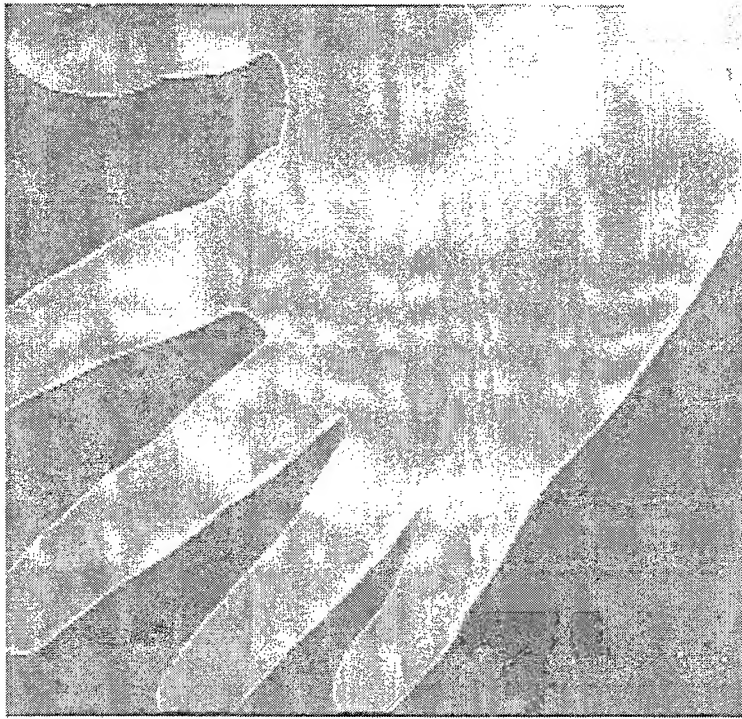


Fig. 9-a The 8 bits pseudo-color image for the 256x256 FPA imaging

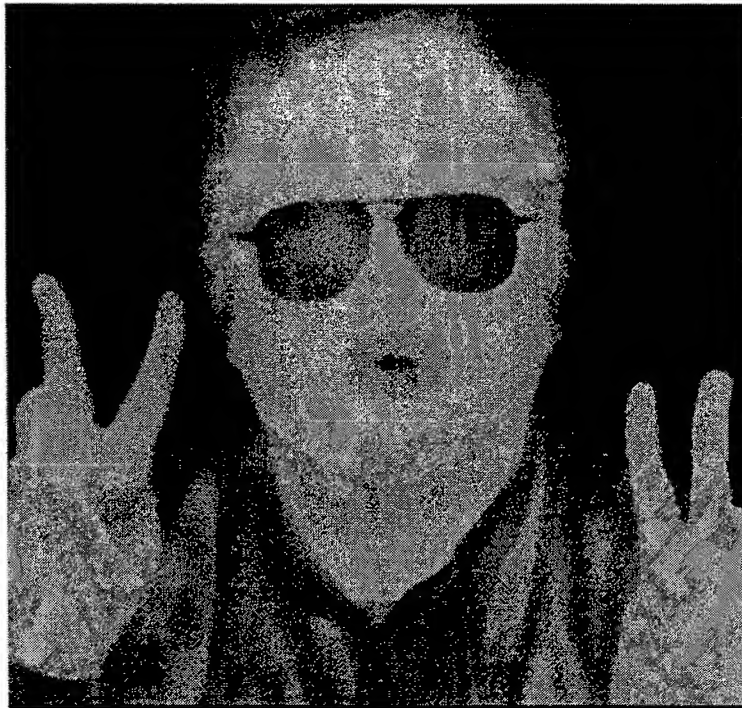


Fig. 9-b The 8 bits grey-level image for the 256x256 FPA imaging

Cosputtering Effect in Titanium Oxides by Ion-Beam Sputtering Deposition

Jin-Cherng Hsu^{*a}, Cheng-Chung Lee^a, Luu-Gen Hwa^b

^aInstitute of Optical Sciences, National Central University, Chung-Li (320), Taiwan

^bPhysics Department, Fu Jen Catholic University, Taipei, Taiwan

ABSTRACT

Cosputtering of titanium oxide films with aluminum (Al), fuse silicon (SiO₂) and silicon (Si) is investigated. Their optical properties, surface morphology and structure show better than pure titanium oxide. In general, the extinction coefficient and surface roughness of the cosputtered films are smaller than the pure TiO₂ film. Also, the microstructure of the cosputtered films are improved to an amorphous structure even though post-baked up to 450°C.

Key words: Cosputtering effect, ion-beam sputtering deposition, titanium oxide, amorphous structure.

1. INTRODUCTION

The fabrication of high quality optical coatings with low scattering and low absorption losses has recently become significant. Among those coatings, titanium dioxide (TiO₂) has been studied extensively, since it has a high refractive index and transparent range in the visible and near infrared. It is mechanical hard, environmentally stable. It can be produced by many kinds of deposition methods. However, the best method to produce the TiO₂ film with ultralow loss is ion beam sputtering deposition (IBSD). The optical properties of the TiO₂ film are influenced by oxygen partial pressure (P_{O2}) during deposition and the post-baking temperature in air¹. The film deposited by IBSD at low temperature (<150°C) are completely amorphous. In general, the surface morphology of the as-deposited film has small grain structures in the surface. When the film is post-baked at an optimum temperature, 275°C, the surface roughness and the extinction coefficient (*k*) values decreased to the minimums². If the films is post-baked at higher temperature, such as 450°C, there is amorphous-crystalline transformation which causes the *k* values increase³ and the film re-crystallizes to the anatase and rutile grain⁴. The TiO₂ film also changes easily to oxygen deficient⁵. Fig. 1 shows the morphology as measured by atomic force microscope. The pure TiO₂ film which is produced by IBSD and post-baked at 450°C for 6 hours. It is a mildew-like polycrystalline structure and so irregular that some areas draw the surface down obviously¹. This might be due to the thermal instability of titanium oxide, since titanium has positive ions Ti⁺², Ti⁺³ and

* Correspondence: E-mail: jchsu@ios706.ios.ncu.edu.tw; Tel: 886-3-4227151 ext.5292; Fax: 886-3-4263918

Ti⁴⁺. The effective ionic radii of the ions are 100, 81, and 65 pm respectively⁶. The reduction of the ionic radii with increasing the positive charge value for titanium is more obvious than other metallic ion. The thermal energy from the higher baking temperature stimulates the titanium ion to the high positive charge, Ti⁴⁺, which becomes smaller radius in the film. Then, the surface of the film is drawn down. Its microstructure becomes so irregular that the loss increases largely. This phenomenon can be improved by cosputtering deposition with some other materials². We will extend out the studies in this article to explore how the cosputtered materials affect the titanium oxide films.

It is difficulty to determine the structure of the post-baked IBSD film with an x-ray diffractometer, since the measurement of the diffraction signal of the crystalline grain works well only for a thick film⁷. Thus, Raman spectroscopy is necessarily applied to characterize the films molecular structures. It is a simple and effective tool for dynamical study of such a phase transformation³. Moreover, atomic force microscope (AFM) is an auxiliary instrument to profile the morphologies of the samples. The deposited films are also examined though the patterns of binding energy revealed by x-ray photoelectron spectroscopy (XPS) for stoichiometry analysis.

2. EXPERIMENTS

Fig. 2 is the schematic diagram of sputtering system. I₁ and I₂ are main ion source and pre-clear ion source respectively. Both are made by Ion Tech Inc. with 3-cm grids. The target, mounted on a water-cooled polygon turret, is a pure titanium metal (99.995%) disk 100 mm in diameter. Before each deposition the vacuum chamber is cryogenically pumped down to a base pressure of less than 7×10^{-7} Torr. Oxygen is fed near the substrate and regulated at 2×10^{-5} Torr by a needle valve. The background pressure is about 1×10^{-4} Torr during the deposition. The substrate is Corning glass 7059, 2.5 cm×2.5 cm in size.

The beam voltage (V_b) and beam current (I_b) of the main ion source are 1100 V and 30 mA respectively, during the deposition process. The ion current density is about 1 mA/cm². The films are deposited with an optical thickness about 0.5λ (at $\lambda = 650$ nm) as monitored by an optical monitor. Meanwhile, a quartz crystal thickness monitor measured the deposition rate.

The materials, selected for cosputtering simultaneously with the titanium target by IBSD, are aluminum (Al), fused silica (SiO₂) and silicon (Si) slices. The slices in various sizes are placed on the surface of the Ti target. Portions of the coatings are baked in an oven in air at 275°C and 450°C for 6 hours with a heating rate about 5°C/min. All the samples are examined by a spectrophotometer (Hitachi U-3501) with an error less than 0.1% in transmission spectral range from 240 nm to 1840 nm. The optical parameters, refractive index n and extinction coefficient k , are calculated from the transmittance spectra by the envelope method⁸. A Digital Instruments Nanoscope II atomic force microscope instrument is used to scan surface terrain of the samples in a typical area of $1 \mu\text{m} \times 1 \mu\text{m}$ (256×256 pixels) on a vibrating-free platform. The RMS, surface roughness value, is obtained with the software that comes with the instrument. The film structures are invergated by a Raman spectroscopy within the spectra ranges from 100 cm⁻¹ to 1000 cm⁻¹ wavenumbers. On the other hand, the XPS spectra are measured on a full binding energy scale and several expanded binding energy scales. Then, a superposition curve fitting process is utilized to analysis the XPS spectra.

3. RESULTS and DISCUSSIONS

3.1. Optical constants

Let M - R be the co-sputtering films, where M is the selected material: Al, SiO₂, or Si; and R is the area ratio of M to titanium target in size. Fig. 3 shows the refractive index (n) and the extinction coefficient (k) of the films vs. post-baking temperature. The sample labeled by 'Ti' is deposited by ion-beam sputtering of pure Ti target. Comparing all the cosputtered samples with the 'Ti' film, the extinction coefficient and the refractive index of all the films are reduced. Specially, the index of the sample labeled by Si-1/10 is less than 2.1 due to the larger R -value for the Si cosputtered material.

3.2. Surface morphology

Fig. 4 shows the RMS values of the cosputtered films as comparing with that of the 'Ti' film. The surface roughness of some cosputtered films, such as Al-1/10, SiO₂-1/5 and all Si- R , are improved even though post-baking at 450°C. Regarding the sample labeled Al-1/10, the k value is higher than those of the other cosputtered samples due to the optical absorption, shown in Fig. 3.

Fig. 5 shows the morphology of the co-sputtered film baked at 450°C. The mildew-like area decreases when the size of Al, the co-sputtered material increases. For the SiO₂-1/20 and SiO₂-1/10 samples, the mildew-like area becomes small holes due to aggregation of the atoms of the film. When the size of SiO₂ increases as sample SiO₂-1/5, the holes disappear and become a flat surface. For all the samples of the Si- R , the surfaces are smooth and the RMS values are less than 0.15 nm.

3.3. Raman spectrum

The films baked at 450°C and measured by Raman spectroscopy is shown in Fig. 6. The Al-1/10, Si-1/20 and SiO₂-1/5 curves are recognized as the amorphous structures, because their Raman spectra respectively have an indicative low-frequency scattering shoulder near 480-cm⁻¹ and 790-cm⁻¹ that are similar to the features of the substrate spectra³.

The two curves labeled by 'E-B' and 'Ti' are spectra of TiO₂ film respectively fabricated by electron-beam deposition at 250°C temperature and by IBSD of pure Ti metallic target at an oxygen particular pressure of 2×10^{-5} Torr. Both films are made of the pure TiO₂ material and post-baked at 450°C. They have the Raman signals of anatase lines at ~550-cm⁻¹ higher than that of the low-frequency scattering shoulder of the substrate spectrum near 480-cm⁻¹. Both features of the anatase signals agree approximately with that of the peak signal reported by Pawlewicz *et al*⁹.

Al-1/20 is not an amorphous type because that the Raman spectra rise at 200-cm⁻¹ and 580-cm⁻¹ and are relatively higher than the background signal of the substrate near 480-cm⁻¹. Oppositely, the Al-1/10 sample is an amorphous film since no anatase signal appears except the signal of the substrate in the Raman spectrum. So, the more cosputtered material, Al, makes the film the more amorphous-like. Then, Al-1/40 sample is neither an amorphous type since the amount of Al co-sputtered material in the film is less than that in Al-1/20 sample.

The cosputtered film, Si-1/20, is amorphous types from above discussion. Si-1/10 and Si-1/15 are also amorphous types due to the more amount of the Si material cosputtered into the films. For the SiO₂ cosputtered material, the film needs

the more amount of SiO₂ material cosputtered into the film to become an amorphous type due to the larger *R*-value of SiO₂-1/5.

3.4. XPS spectrum

When the cosputtered films are measured with X-ray photoelectron spectroscopy (XPS), different binding energies of the atoms in the cosputtered films exhibit at the spectra as shown in Fig. 7 on an expanded energy scale. The Ti_{2p} lines of all films are doublets where the larger peaks theoretically are the Ti_{2p_{3/2}} lines and the smaller are Ti_{2p_{1/2}} lines. The larger Ti_{2p_{3/2}} peaks broaden strongly at ~460 eV because that the majority of Ti atom in the films is bonded by two oxygen atoms and a few cosputtered atoms. And, the broadened peaks can be separated into two sub-peaks with computer simulation software as the dotted lines are shown in Fig. 7. Furthermore, the right sub-peak areas relatively increase and the lefts decrease with the *R*-values, for the same cosputtered material (such as: SiO₂-1/40, SiO₂-1/20 and SiO₂-1/10). The energy of the right sub-peak basically is lower than that of the left as the scale shown in spectrum, which means that the binding energy of titanium atoms decreases due to the cosputtering effect.

Moreover, the oxygen atoms in the films are bonded by titanium atoms and a few cosputtered atoms. The O_{1s} peaks of the oxygen atoms can also separate two sub-peaks just like the Ti_{2p_{3/2}} peaks of the titanium atoms. But, the left sub-peak areas relatively increase and the rights decrease with the *R*-values (such as: SiO₂-1/40, SiO₂-1/20 and SiO₂-1/10). The energy of the left sub-peak is higher than that of the right. So, the cosputtering effect increases the binding energy of the oxygen atoms.

The cosputtering effect shifts and broadens their binding energy in the Ti_{2p_{3/2}} and O_{1s} regions. The binding energy of the oxygen atom increases but that of the titanium atom decreases. The oxygen atoms would absorb the cosputtered atom that replaces the titanium atom and deliver some binding energy between the titanium and oxygen atoms. So, the bond length between the titanium and oxygen atoms in the cosputtered film becomes larger than that in the pure TiO₂ film. Thus, the decrease of the binding energy between the titanium and oxygen atoms in the film may release the drawing force on the film surface², which make the surface morphology smoother if the amount of the selected material in the film is sufficient.

At the same time, the XPS signals of Al_{2p} of the aluminum atom and Si_{2p} of the silicon atoms arise obviously at ~74.5 eV and ~103.4eV, respectively. However, the Al_{2p} signal only appears at the spectrum of Al-1/10 sample and the Si_{2p} signals appear at the spectra of SiO₂-1/5 and all Si-*R* samples. These samples are completely consistent with their smoother surface morphologies shown in Fig. 5. They are also confirmed to be the amorphous structure from the observation of the Raman spectrum illustrated in Fig. 6.

Comparing the three-selected material at the same *R*-value condition, the right Ti_{2p_{3/2}} and the left O_{1s} sub-peak areas of the films cosputtered by Si material are apparently larger than that of the other materials (such as: Al-1/10, SiO₂-1/10 and Si-1/10). Thus, we can declare that Si material has the best cosputtering effect among the three materials.

4. CONCLUSIONS

On the whole, cosputtering with Al, SiO₂ or Si is beneficial to the titanium oxide film in IBSD process. The thermal

stability and microstructure of the cosputtered films are obviously improved as baking at 450°C. Specially, Si is the best material for the cosputtering effect since that the cosputtered film is low surface roughness, low optical absorption and amorphous type. Otherwise, the size of the cosputtered Si slice is the smallest than that of the other cosputtered materials when the cosputtered film begin to an amorphous type; thus, the refractive index of the Si cosputtered film approaches to that of pure TiO₂ film as shown in Fig.3. The SiO₂ cosputtered material is also a good choice, but the size of the SiO₂ slice must be larger, then the refractive index of the cosputtered film becomes lower. Otherwise, Al is not recommendable cosputtered material due to the higher optical absorption film, although the surface roughness is improved.

ACKNOWLEDGMENT

This research was sponsored by the National Science Council, Taiwan under contract NSC89-2215-E-008-002.

REFERENCES

1. C. C. Lee, D. T. Wei, J. C. Hsu and C. H. Shen, "Influence of Oxygen on Some Oxide Films Prepared by Ion Beam Sputter Deposition," *Thin Solid Films*, **290-291**, pp. 88-93, 1996.
2. J. C. Hsu and C. C. Lee, "Single and Dual Ion Beam Sputter Deposition of Titanium Oxide Films," *Appl. Opt.* **37**, pp. 1171-1176, 1998.
3. L. S. Hsu, R. Rujkorakarn, J. R. Sites, and C. Y. She, "Thermally Induced Crystallization of Amorphous-Titanium Films," *J. Appl. Phys.* **59 (10)**, pp. 3475-3480, 1986.
4. P. Löbl, M. Huppertz, D. Mergel, "Nucleation and growth in TiO₂ films prepared by sputtering and evaporation," *Thin Solid Film* **251**, pp. 72-79, 1994.
5. P. Kofstad, "Thermogravimetric Study of the Defect Structure of Rutile (TiO₂)," *J. Phys. Chem. Solids* **23**, pp. 1579-1586, 1962.
6. R. D. Shannon, *Acta Crystallogr.* **A32**, page 751, 1976.
7. L. M. Williams and D. W. Hess, *J. Sci. Technol.* **A1**, page 1810, 1983.
8. R. S. Swanepoel, "Determination of the Thickness and Optical Constants of Amorphous Silicon," *J. Phys. E: Sci. Inst.* **16**, pp. 1214-1221, 1983.
9. W. T. Pawlewicz, G. J. Exarhos, and W. E. Conaway, "Structural Characterization of TiO₂ Optical Coating by Raman Spectroscopy," *Appl. Opt.* **22**, pp. 1837-1840, 1983.

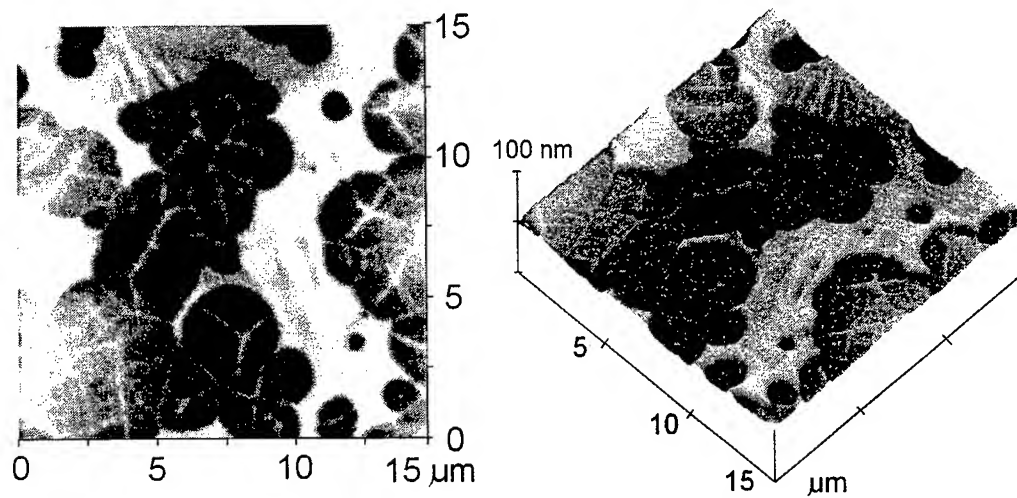


Fig. 1 Morphology of TiO_2 film deposited at $P_{\text{O}_2} = 2 \times 10^{-5}$ Torr and baked at 450°C , $\text{RMS} = 1.7\text{nm}$.

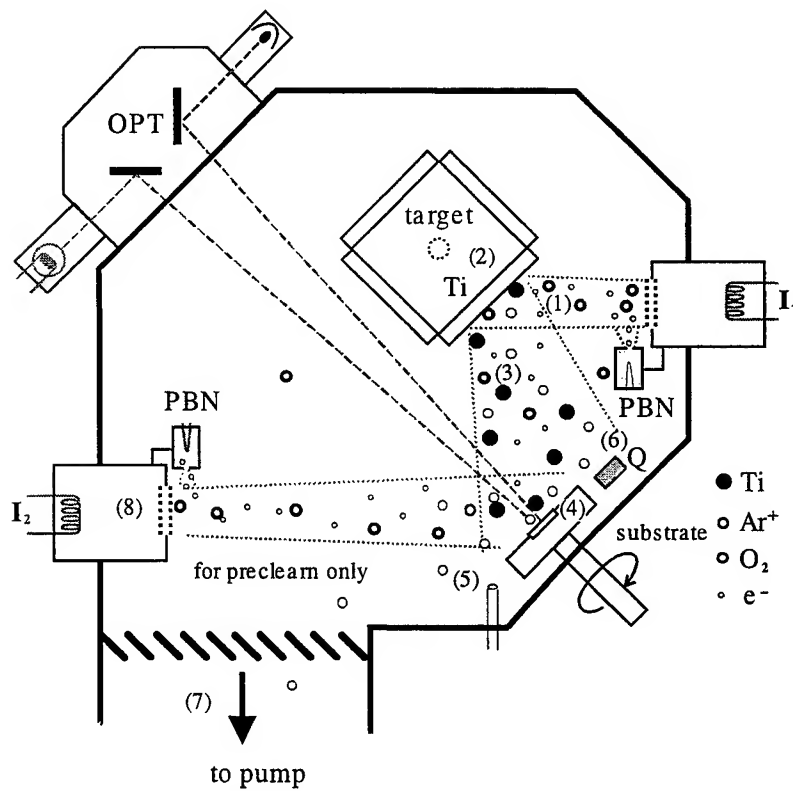


Fig.2 Schematic drawing of the ion beam sputtering system.

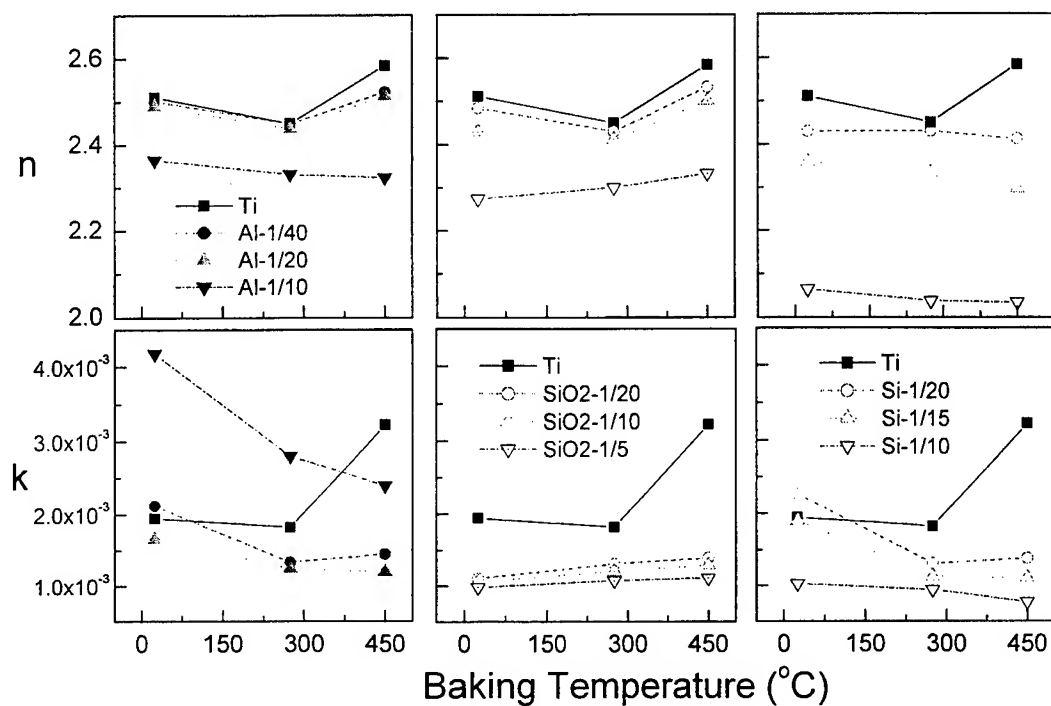


Fig.3 The refractive index (n) and the extinction coefficient (k) of cosputtered films vs. baking temperature.

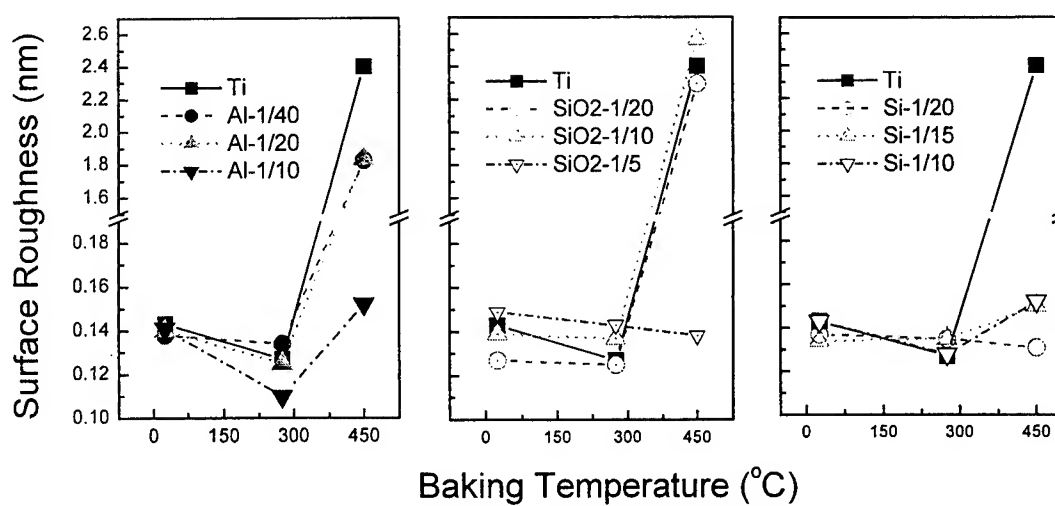


Fig. 4 The RMS surface roughness vs. baking temperature of co-sputtered deposited by IBSD.

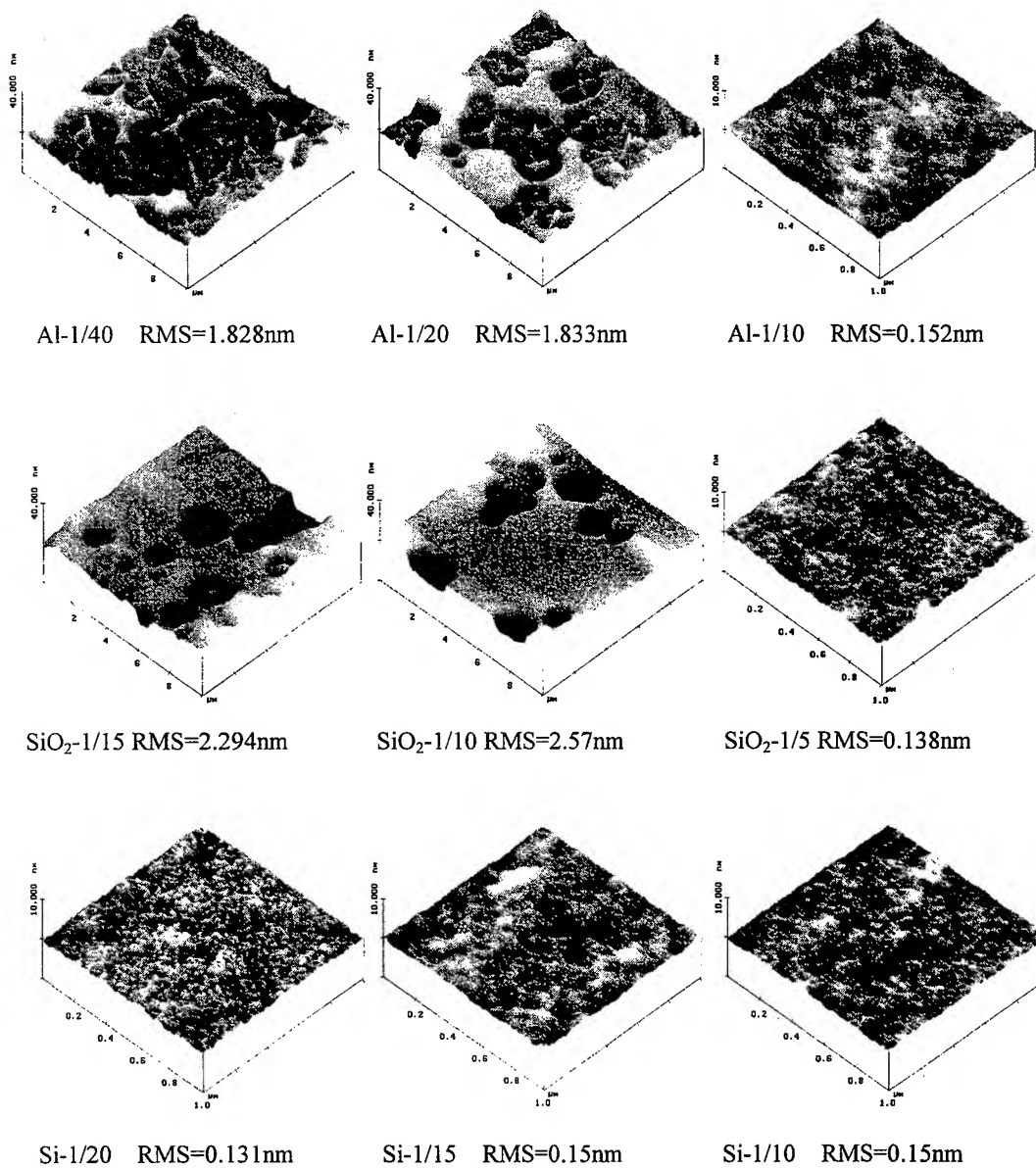


Fig.5 The surface morphology and the roughness of the IBSD films baked at 450°C.

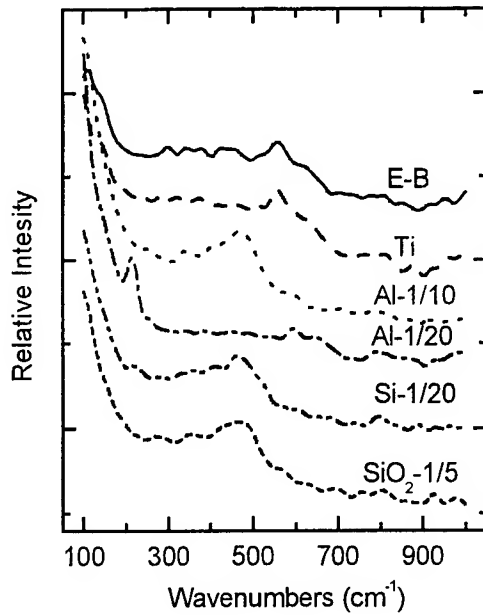


Fig. 6 Raman spectra of titanium oxide films on 7059 substrates:

E-B: Pure TiO_2 deposited by E-beam;

Ti: Pure TiO_2 deposited by IBSD.

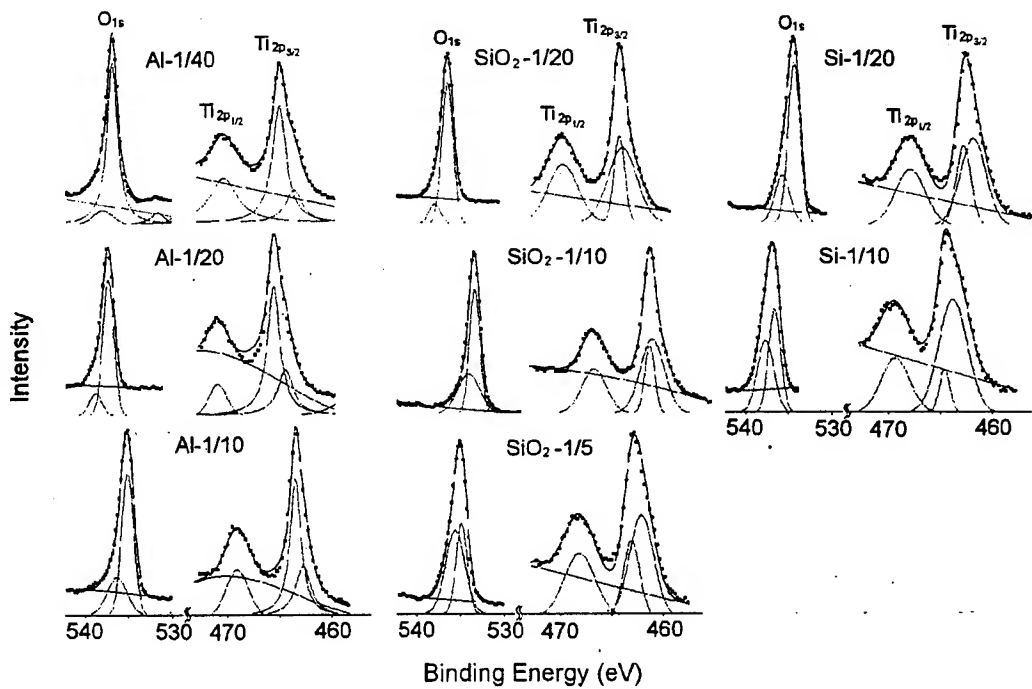


Fig. 7 XPS spectra of the cosputtered films at O_{1s} and Ti_{2p} energy regions. The square points are measurement data. Solid and dotted lines are the fitted curves of the measurement data and their sub-peaks respectively.

Raman and Hot Electron-Neutral Acceptor Luminescence Studies of Electron-Optical Phonon Interactions in GaAs/Al_xGa_{1-x}As Quantum Wells

Chih.Ming. Wang^a, Horng. Yu. Chang^a, Kien.Wen. Sun^a,
Shyang.Yeu. Wang^b, Chien.Ping. Lee^b

^aDepartment of Electronic Engineering, Feng Chia University, Taichung, Taiwan, R.O.C.

^bDepartment of Electronics Engineering and Institute of Electronics, National Chiao Tung University,
Hsin Chu, Taiwan, R.O.C.

ABSTRACT

Using two optical techniques, we have measured the Fröhlich interactions between electrons and optical phonons on a number of different Be-doped GaAs/Al_xGa_{1-x}As multiple quantum well structures. Raman scattering measurements at 15 K are presented for GaAs/Al_xGa_{1-x}As quantum wells with Al compositions of $x=0.3, 0.5, 0.7$ and 1.0 . And also for GaAs/AlAs, GaAs/Al_{0.7}Ga_{0.3}As with fixed well width of 50 \AA and barrier with between 5 to 120 \AA . The GaAs-like and AlAs-like phonon frequencies of the first-order modes are measured as a function of Al composition and barrier widths.

We have also performed hot electron – neutral acceptor luminescence in order to determine average optical phonon energies emitted by the photoexcited electrons in quantum wells with the acceptor levels of the GaAs wells. It is shown that the relaxation of hot electrons in the GaAs/Al_xGa_{1-x}As quantum wells is dominated by the GaAs LO phonon emission for small x , but by AlAs-like LO phonons for larger Al compositions. For the quantum wells with largest barrier width investigated, the average energy of the emitted LO phonon is close to the AlAs LO phonon mode. At a barrier width of 5 \AA , the energy of emitted LO phonon decreases to a value close to the GaAs LO phonons, nevertheless, there is still a significant contribution from the emission of AlAs-like modes.

Keywords: LO phonon, Raman scattering, Hot electron luminescence, quantum wells

1. INTRODUCTION

Semiconductor quantum well structures such as GaAs/AlGaAs systems not only have important device applications, but also provide a challenge to our understanding of the physics of hot carrier dynamics in semiconductors. Techniques such as molecular beam epitaxy have stimulated much research on semiconductor heterostructures. Of the semiconductor multiple quantum wells, those from GaAs/AlGaAs have been the most studied. In order to learn about the characteristic properties of such thin crystalline films, many different methods are employed. Optical methods like reflection, transmission, and luminescence experiments are employed to characterize single and multiple quantum layers, to learn about recombination mechanisms and the role of interfaces on these mechanisms. There has been a great number of experimental and theoretical studies focused on optical phonons in quantum wells and their interactions with electrons. Raman scattering has been proven as a versatile and efficient tool for probing long-wavelength and short-wavelength lattice dynamics of ternary alloys¹⁻⁵. The electron-phonon interactions in semiconductor alloys have also been studied by using time-resolved Raman spectroscopy⁷⁻⁹. It is well known that the Al_xGa_{1-x}As barrier in the quantum wells is a two-mode alloy, in that two longitudinal-optical (LO) phonon modes of lattice vibration exist, even though the material is assumed to be a smooth alloy with average Al/Ga concentration on a single sublattice. More recently, Kash et al.⁸ were able to evaluate the relative interaction strength of these two LO modes, with the electrons, using picosecond Raman spectroscopy.

In addition to Raman scattering techniques, it is well known that the radiative recombination of photoexcited carriers with the neutral acceptors can be used to study the hot carrier relaxation processes. The relaxation of hot electrons through optical phonon emission in bulk GaAs¹⁰⁻¹² and heterostructures¹³⁻¹⁵ has been extensively studied using above techniques. Sapega¹⁶ has demonstrated that, for GaAs/AlAs quantum wells with large barrier widths, the energy relaxation mechanism for hot electrons is dominated by the AlAs phonons. For smaller barriers, emission via GaAs phonon is more important. By using conventional hot electron luminescence techniques, E. Ozturk et al.¹⁷ have demonstrated that in GaAs/AlAs the dominant electron relaxation mechanism is via the interaction with the AlAs interface mode for a device having a well width of 80 \AA . But for a similar GaAs/Al_{0.24}Ga_{0.76}As structure, the GaAs phonons provide the energy relaxation. Recently, Mirlin et al.¹⁸ have studied electron relaxation in GaAs/AlAs quantum wells with fixed barrier width of 10 nm and well

width varying from 4 to 13 nm. It was shown that, for larger wells, the electron relaxation is dominated by GaAs LO phonons. But in the smallest well width sample, it is dominated by AlAs optical phonons.

In this work, we first use Raman spectroscopy to determine the optical phonon energies in GaAs/ $\text{Al}_x\text{Ga}_{1-x}\text{As}$ quantum wells samples with Al composition of $x=0.3, 0.5, 0.7$ and 1.0 , and GaAs/ $\text{Al}_{0.7}\text{Ga}_{0.3}\text{As}$, GaAs/AlAs quantum well samples with different barrier widths. With the measurements of the energy separation of peaks in the hot electron-neutral acceptor luminescence spectra and the LO phonon energies retrieved via Raman experiments, we then analyze the type of optical phonon emitted during hot electrons relaxation processes in the quantum wells.

2. EXPERIMENTAL TECHNIQUES

The samples investigated were grown by molecular-beam epitaxy on (100)-oriented undoped semi-insulating GaAs substrate. One type of the MQW samples studied here were 5 nm GaAs wells, with $x=0.3, 0.5, 0.7$ and 1.0 $\text{Al}_x\text{Ga}_{1-x}\text{As}$ barrier of 12 nm thickness. The other were 50 Å GaAs wells, with $\text{Al}_{0.7}\text{Ga}_{0.3}\text{As}$ or AlAs barrier of 5, 25, 50, 120 Å in thickness, respectively. The central regions of 1 nm of the GaAs layer were doped with Be to 10^{18} cm^{-3} . An Ar^+ laser was used on 514.5 nm exciting line for the Raman experiments. About 150 mW of the laser power was directed on the samples which were kept in a closed-cycled refrigerator at 15 K. Raman spectra were obtained in back scattering geometry and the scattered light was collected by a camera lens and passed through a notch filter before entering the spectrometer. The spectra were recorded with a combination of a SPEX 0.6 m triplemate spectrometer equipped with a liquid nitrogen cooled CCD detector. For the excitation of hot electron-neutral acceptor luminescence, a dye laser (DCM) pumped by an Ar^+ laser was used. The dye laser was operated at 1.893 eV with output power of about 30 mW. The hot electron luminescence was analyzed with the same spectrometer and detector in the Raman experiments.

3. RESULTS AND DISCUSSION

3.1 Dependence of electron-LO phonon interactions on Al composition

In this experiment, the Stokes Raman spectrum measured in back scattering geometry $z(x'x')\bar{z}$ [where z and \bar{z} are the directions of propagation of the incident and scattered laser beams, respectively, normal to the layers, and x' is the corresponding polarization vector along (110) in the plane of the layers] detects the LO phonon modes of the samples. Figure 1 shows the Raman spectra for the (50/120) Å quantum wells of four different Al compositions excited with Ar^+ laser. On the bottom of the spectra we have placed the Raman spectrum of the bulk GaAs sample for comparison. The GaAs LO phonon mode is at 36.7 meV and, for the $\text{Al}_x\text{Ga}_{1-x}\text{As}$ layers, the optical phonons display a two-mode behavior: the GaAs-like (whose energy is below the GaAs LO phonon energy) and AlAs-like modes (whose energy is below the AlAs LO phonon energy). Our detection system is not capable of resolving the splitting of the GaAs LO phonon into confined modes and there is also no evidence of scattering from interface phonons⁹. Please note the broadening and asymmetry nature of the peaks which is due to the alloy potential fluctuations¹⁹.

In figure 2 we have plotted the AlAs-like and GaAs-like phonon frequencies as a function of Al composition at two excitation wavelengths. The AlAs-like phonon frequencies approach those of the phonons in AlAs as x approach 1. On the other hand, the GaAs-like phonons have frequencies approach those of the phonons in GaAs as x approach zero. We found no dependence of the phonon frequencies with the excitation wavelength. We have also measured the anti-Stokes Raman spectrum, but find no evidence related to the phonon absorption by photons. We attribute this to the vanishingly small thermal occupation of the LO phonon modes at very low temperature.

In figure 3 we have shown the hot electron-neutral acceptor luminescence spectra of four samples. The principles of this technique are shown in the inset of figure 3⁶. The peak labeled "unrelaxed" in each spectrum corresponds to recombination of electrons, from the state at which they were created, with a neutral acceptor. The peak labeled "1" represents electrons recombining with neutral acceptors after emitting one LO phonon. The width of the peaks is determined by the electron energy distribution at the point of generation, which is related to heavy hole subband warping, as well as the energy distribution of acceptors, the final state of recombination for the hot luminescence process. The power density of the laser used for the excitation was low enough so the main mechanism of energy relaxation in the sample studied is the emission of optical phonons and the phonon-plasmon coupling can be ignored. In order to demonstrate the change of the luminescence spectra with different Al compositions, we have centered the first unrelaxed peaks in the spectra for four samples. The separation of the "unrelaxed" and "1" peaks in the spectra should allow one to determine the energy of the phonons emitted by hot electrons during the relaxation processes. In order to determine the energy separation more accurately, we first subtract the background (which was originated from the band-to-band luminescence) from the spectra and the energy spectra of the two remaining peaks were then fitted by Gaussian distributions. The energy difference between the two peaks

is plotted for all the four samples as a function of Al mole fraction as shown in figure 4. For the samples with larger x , the energy separation in the spectrum approaches 400 cm^{-1} , a value in the AIAs phonon regime.

In according to Ref. [16], the emission strength of a particular phonon mode is proportional to the square of the overlap integral of the phonon scalar potential with the initial and final electron states in the GaAs layer. The different relaxation paths were weighted by $(\varphi_{\text{Ga}}/\varphi_{\text{Al}})^2$, where φ_{Ga} is the sum for the scalar potentials for all the calculated GaAs modes and φ_{Al} is the sum of the AIAs modes at particular barrier width. In their works, for samples with smaller barrier widths, relaxation through the emission of GaAs modes is more important. But, for the 8 nm barrier widths, the energy relaxation was dominated by the AIAs phonons.

However, in our experiments the barrier widths are fixed at 12 nm and we have changed the Al composition in the barriers instead. The monotonic increase of the energy separation between the peaks (the phonon energies emitted by hot electrons) in the hot electron luminescence spectra suggests that the coupling strength between hot electrons and AIAs-like phonon is becoming stronger as the Al composition is increased. Therefore, we can estimate the emission strength of AIAs-like LO phonons relative to the GaAs LO phonons by taking into account the optical phonon energies measured in the Raman experiments and the energy separations in the hot electron luminescence spectra. In figure 5 we have plotted the fraction emission strength of AIAs-like optical phonon to the GaAs LO phonon emitted by electrons as a function of Al composition. In the case for $x=0.3$, the energy separation of the peaks is about 29 cm^{-1} larger than the energy of the GaAs LO phonons. This indicates that although interaction with the GaAs LO phonon is strong, there is still a significant contribution from the AIAs-like LO phonon. However, for $x=1.0$, the spectra are dominated by AIAs-like LO phonons and the energy separation are very close to the AIAs LO phonon mode.

Investigations of the GaAs/AIAs multiple-quantum wells by Ozturk et al.¹⁷ have also demonstrated the substantial influence of the AIAs-like LO phonon modes in the hot electron relaxation processes. On the contrary, the GaAs phonons provide the energy relaxation in a similar GaAs/ $\text{Al}_{0.24}\text{Ga}_{0.76}\text{As}$ structure. The predominance of the AIAs-like phonon modes is attributed to the stronger scattering strength and to their shorter lifetime compared to the GaAs modes. Our results have also indicated that, for quantum wells whose barriers have large Al molar fractions, the hot electrons relax mostly via the AIAs-like optical phonon emission.

3.2 Dependence of electron-LO phonon interactions on barrier width

In the second experiment, the Stokes Raman spectrum also measured in back scattering geometry to detect the LO phonon modes of the samples. Figure 6 and 7 shows the Raman spectra for GaAs/ $\text{Al}_{0.7}\text{Ga}_{0.3}\text{As}$ and GaAs/AIAs quantum wells samples with different barrier widths excited with Ar^+ laser. At the bottom of each figure we have placed the Raman spectrum of the bulk GaAs sample for comparison. In figure 6, the GaAs LO phonon mode is at 36.7 meV and, for the $\text{Al}_{0.7}\text{Ga}_{0.3}\text{As}$ layers, the optical phonons display a two-mode behavior: the GaAs-like and AIAs-like modes. However, in figure 7, due to different compositions of the barriers only the AIAs-like and GaAs phonon mode were observed. In figure 8 and 9, we have plotted the AIAs-like and/or GaAs-like phonon frequencies as a function of barrier width at two different excitation wavelengths. In figure 8, we found that both the GaAs-like and AIAs-like phonon frequencies kept relatively constant throughout the whole range of the barrier width. However, for samples with AIAs barrier, the AIAs-like phonon frequencies approach those of the phonons in AIAs with increasing barrier widths as shown in figure 9. No dependence of the phonon frequencies was found with the two different excitation wavelength. We have also measured the anti-Stokes Raman spectrum, but found no evidence related to the phonon absorption by photons.

In figure 10 and 11, we have shown the hot electron-neutral acceptor luminescence spectra from GaAs/AIAs and GaAs/ $\text{Al}_{0.7}\text{Ga}_{0.3}\text{As}$ quantum well samples.

In order to demonstrate the change of the luminescence spectra with different barrier widths and compositions, we have centered the first unrelaxed peaks in the spectra for all four samples. The energy difference between the two peaks is determined by following the same procedure used in the previous experiment and is plotted for all the four samples as a function of barrier width as shown in figure 12. For samples with the largest barrier, the phonon energies emitted by the electrons in the GaAs/ $\text{Al}_{0.7}\text{Ga}_{0.3}\text{As}$ and the GaAs/AIAs quantum wells approach 360 cm^{-1} and 380 cm^{-1} , respectively. In the cases with smallest barriers, the emitted phonon energies measured from both samples approach 300 cm^{-1} that is still higher than the GaAs LO phonon energy — 293 cm^{-1} .

In our experiments, the monotonic increase of the energy separation between the peaks in the hot electron luminescence spectra suggests that the coupling strength between hot electrons and AIAs-like phonon is becoming stronger as the barrier width is increased. Therefore, we can estimate the emission strength of AIAs-like LO phonons relative to the GaAs LO phonons by taking into account the optical phonon energies measured in the Raman experiments and the energy separations in the hot electron luminescence spectra. In figure 13 we have plotted the fractional emission strength of the AIAs-like optical phonon relative to the GaAs LO phonon as a function of barrier width for both samples by assuming that the emitted

phonon energy was partitioned by AlAs-like and GaAs LO phonon. In the case for the smallest barrier width, the energy separation of the peaks is about 13 cm^{-1} larger than the energy of the GaAs LO phonons. This indicates that although interaction with the GaAs LO phonon is strong, there is still a significant contribution from the AlAs-like LO phonon. However, for the larger barrier, the spectra are dominated by AlAs-like LO phonons and the energy separation are very close to the AlAs LO phonon mode. We have also found that the fraction of the AlAs-like mode increases more rapidly in samples with AlAs barriers as the barrier width is increased in comparing to the GaAs/ $\text{Al}_{0.7}\text{Ga}_{0.3}\text{As}$ quantum wells. Our results have also indicated that, for quantum wells with AlAs barriers, the hot electrons relax mostly via the AlAs-like optical phonon emission with barrier width larger than 25 \AA . However, for samples with $\text{Al}_{0.7}\text{Ga}_{0.3}\text{As}$ barriers, the AlAs-like mode emission dominates the relaxation processes only when the barrier width is larger than 100 \AA .

4. CONCLUSION

In conclusion, we have observed phonons in the present Raman scattering and hot electron-neutral acceptor luminescence investigation of the GaAs/ $\text{Al}_x\text{Ga}_{1-x}\text{As}$, GaAs/ $\text{Al}_{0.7}\text{Ga}_{0.3}\text{As}$ and GaAs/AlAs multiple quantum wells. In the Raman scattering experiments, the dependence of the mode frequency on the Al composition is the important factor in distinguishing the phonon modes from the bulk optical phonons. Also in the Raman scattering experiments, we have observed two-mode behavior from $\text{Al}_{0.7}\text{Ga}_{0.3}\text{As}$ barrier, but only one LO phonon mode is observed from AlAs barrier. The AlAs-like and GaAs-like phonon frequencies were measured as a function of barrier width. We have also demonstrated that, for smaller x in the barrier, the emission of the GaAs optical phonon mode is stronger. But for the largest x investigated, the energy relaxation of hot electrons is dominated by the AlAs-like phonon. We have also demonstrated that, for smaller barrier, the emission of the GaAs optical phonon mode is stronger. But for the largest barrier, the energy relaxation of hot electrons is dominated by the AlAs-like phonon.

5. ACKNOWLEDGEMENTS

This work was supported by the National Science Council of Republic of China under contract Grant No. NSC87-2112-M-035-004 and NSC88-2112-M-035-001.

6. REFERENCES

1. A.K. Sood, J. Menendez, M. Cardona, and K. Ploog, *Phys. Rev. Lett.* **54**, 2111 (1985).
2. A.K. Arora, A.K. Ramdas, M.R. Melloch, and N. Otuka, *Phys. Rev.* **B36**, 1021 (1987).
3. P. Parayanthal and Fred H. Pollak, *Phys. Rev. Lett.* **52**, 1822 (1984).
4. A.J. Shields, M.P. Chamberlain, M. Cardona, and K. Eberl, *Phys. Rev.* **B51**, 17728 (1995).
5. G. Abstreiter, E. Bauser, A. Fischer, and K. Ploog, *Appl. Phys.* **16**, 345 (1978).
6. G. Fasol, W. Hackenberg, H.P. Hughes, K. Ploog, E. Bauser, and H. Kano, *Phys. Rev.* **B41**, 1461 (1990).
7. K.T. Tsen, D.K. Ferry, A. Salvador, and H. Morkoc, *Phys. Rev. Lett.* **80**, 4807 (1998).
8. J.A. Kash, S.S. Jha, and J.C. Tsang, *Phys. Rev. Lett.* **58**, 1869 (1987).
9. M.C. Tatham and J.F. Ryan, *Phys. Rev. Lett.* **63**, 1637 (1989).
10. B.P. Zakharchenya, V.D. Dymnikov, I.Ya. Karlik, and I.I. Reshina, *J. Phys. Soc. Jpn.* **49**, 573 (1980).
11. B.P. Zakharchenya, D.N. Mirlin, V.I. Perel, and I.I. Reshina, *Sov. Phys. Usp.* **25**, 143 (1982).
12. B.P. Zakharchenya, P.S. Kop'ev, D.N. Mirlin, D.G. Polakov, I.I. Reshina, V.F. Sapega, and A.A. Sirenko, *Solid State Communications* **69**, 203 (1989).
13. G. Fasol, K. Ploog, and E. Bauser, *Solid State Commun.* **54**, 383 (1985).
14. J.A. Kash, *Phys. Rev.* **B48**, 18336 (1993).
15. K.W. Sun, T.S. Song, C.-K. Sun, J.C. Wang, S.Y. Wang, and C.P. Lee, to be published in *Physica B*.
16. V.F. Sapega, M.P. Chamberlain, T. Ruf, M. Cardona, D.N. Mirlin, K. Totemeyer, A. Fischer, and K. Eberl, *Phys. Rev.* **B52** (1995) 14144.
17. E. Ozturk, N.C. Constantinou, A. Straw, N. Balkant, B.K. Ridley, D.A. Richie, E.H. Linfield, A.C. Churchill, and G.A.C. Jones, *Semicond. Sci. Technol.* **9**, 782 (1994).
18. D.N. Mirlin, P.S. Kop'ev, I.I. Reshina, A.V. Rodina, V.F. Sapega, A.A. Sirenko, and V.M. Ustinov, in proceedings of the 22nd International Conference on the Physics of Semiconductors, edited by D.J. Lockwood (World Scientific, Singapore), pp. 1288 (1995).
19. P. Parayanthal, and F.H. Pollak, *Phys. Rev. Lett.* **52**, 1822 (1984).

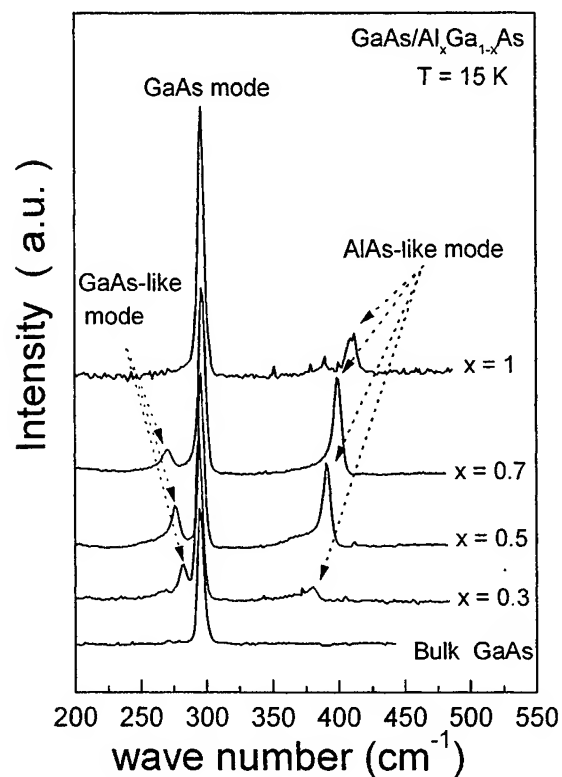


Figure 1 Raman spectra of four GaAs/Al_xGa_{1-x}As multiple quantum wells and bulk GaAs samples at 15 K in the back scattering geometry for incident wavelength of 514.5 nm. The peak labeled GaAs mode is the LO phonon arising from the GaAs wells. The order two peaks labeled GaAs-like and AlAs-like mode are related to the Al_xGa_{1-x}As barrier layers.

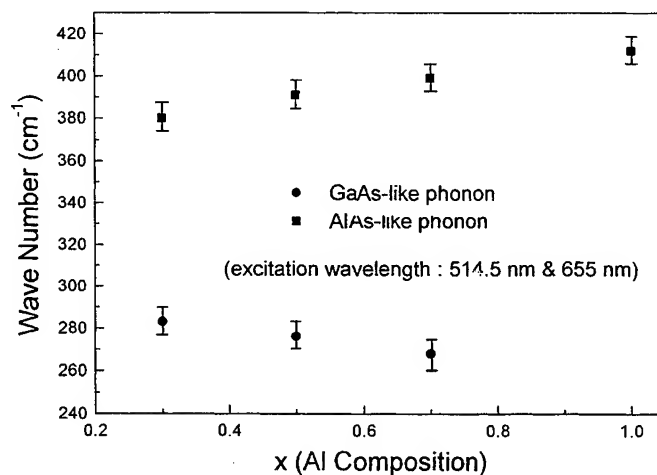


Figure 2 The AlAs-like LO phonon frequency (square) and GaAs-like LO phonon frequency (circle) as a function of the Al composition for $0 < x \leq 1$ at incident wavelengths of 514.5 and 655 nm.

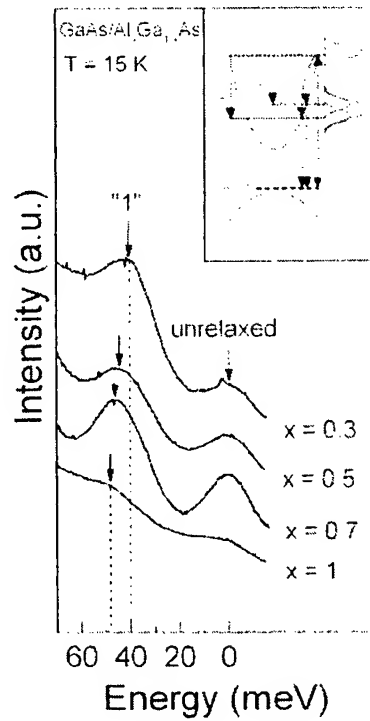


Figure 3 Hot electron luminescence spectra for four GaAs/Al_xGa_{1-x}As multiple quantum wells samples plotted as a function of the electron energy above the ground state of the quantum wells. The vertical line labeled "unrelaxed" is the energy peak corresponding to recombination at the energy of creation. The peak labeled "1" represents the electron distribution after the emission of one LO phonon. The inset shows schematically the principles of the hot electron-neutral acceptor luminescence technique.

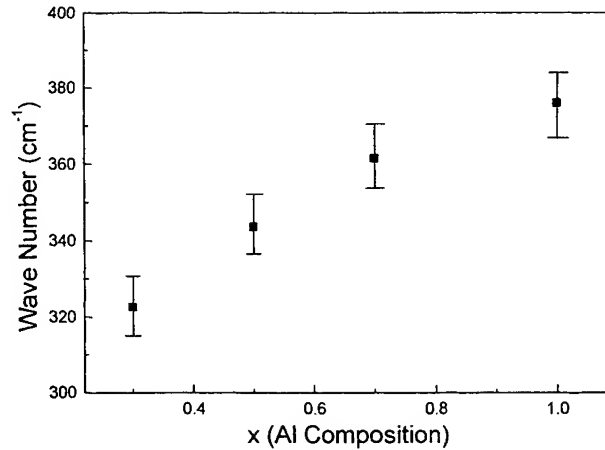


Figure 4 Measured energy separation between the "unrelaxed" and "1" phonon peaks in the hot electron luminescence spectra as a function of Al composition.

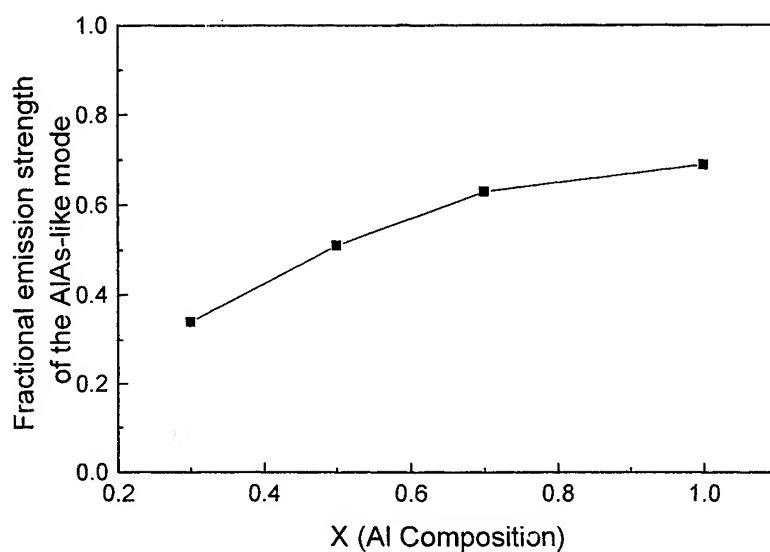


Figure 5 The estimate relative emission strength of AlAs-like LO phonon mode with electrons as a function of the Al composition.

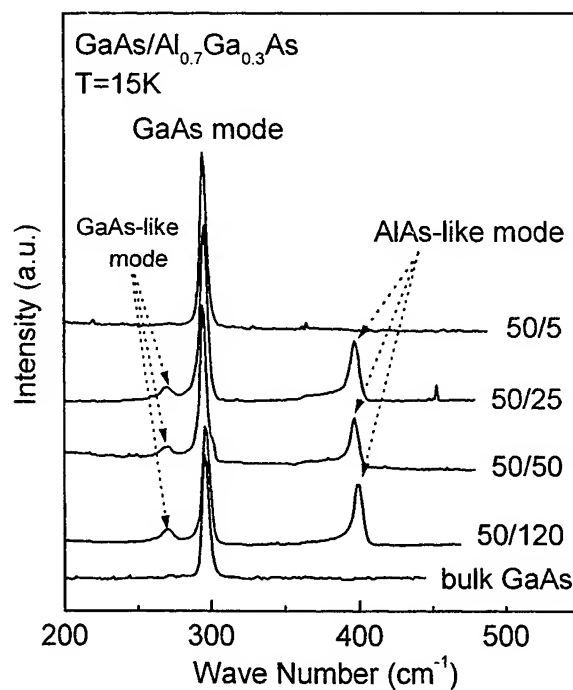


Figure 6 Raman spectra of GaAs/Al_{0.7}Ga_{0.3}As multiple-quantum wells and bulk GaAs samples at 15 K in the back scattering geometry for incident wavelength of 514.5 nm. The peak labeled GaAs mode is the LO phonon arising from the GaAs wells. The other two peaks labeled GaAs-like and AlAs-like modes are related to the Al_{0.7}Ga_{0.3}As barrier layers.

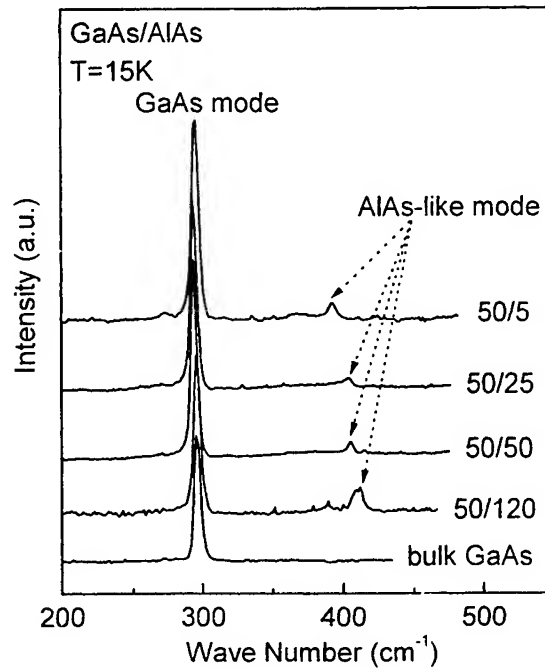


Figure 7 Raman spectra of GaAs/AlAs multiple quantum wells and bulk GaAs samples at 15 K in the back scattering geometry for incident wavelength of 514.5 nm. Only the AlAs-like LO phonon mode was observed from the barriers.

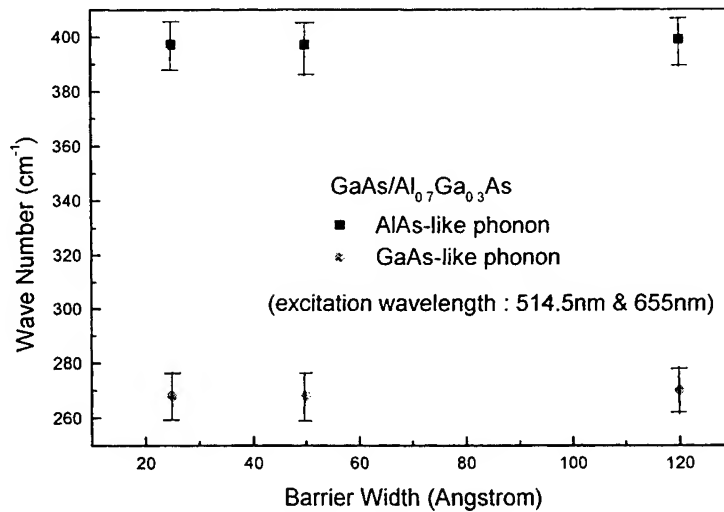


Figure 8 The AlAs-like LO phonon frequencies (square) and GaAs-like LO phonon frequencies (circle) from the GaAs/Al_{0.7}Ga_{0.3}As multiple quantum wells were plotted as a function of barrier width at incident wavelengths of 514.5 and 655 nm.

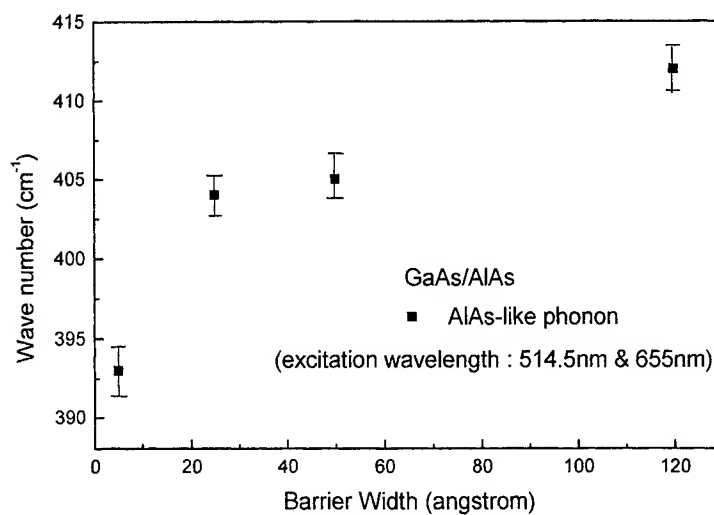


Figure 9 The AlAs-like LO phonon frequencies (square) from the GaAs/AlAs multiple quantum wells were plotted as a function of barrier width at incident wavelengths of 514.5 and 655 nm.

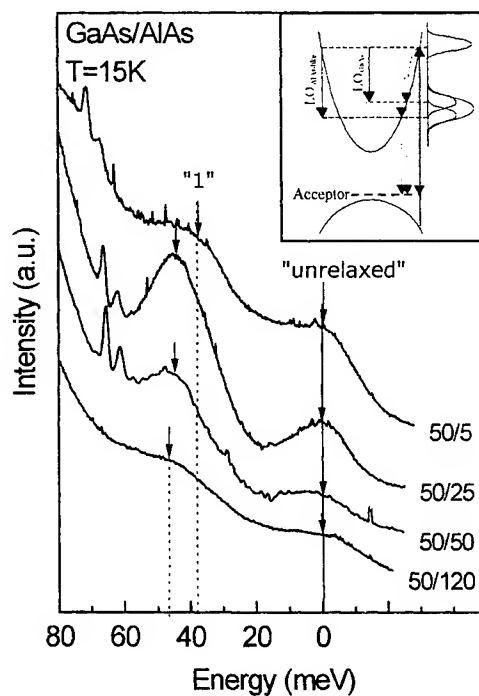


Figure 10 Hot electron luminescence spectra of GaAs/AlAs multiple quantum wells samples plotted as a function of the electron energy above the ground state of the quantum wells. The vertical line labeled "unrelaxed" is the energy peak corresponding to recombination at the energy of creation. The peak labeled "1" represents the electron distribution after the emission of one LO phonon. The inset shows schematically the principles of the hot electron-neutral acceptor luminescence technique.

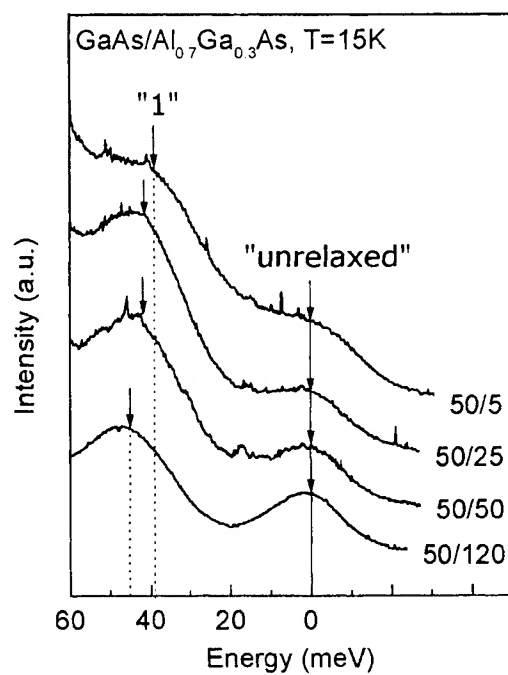


Figure 11 Hot electron luminescence spectra of GaAs/Al_{0.7}Ga_{0.3}As multiple quantum wells samples plotted as a function of the electron energy above the ground state of the quantum wells.

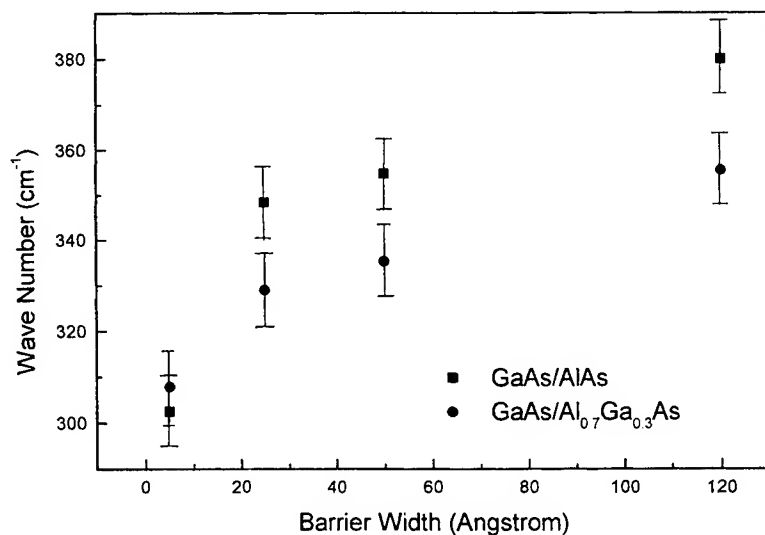


Figure 12 Measured energy separations between the "unrelaxed" and "1" phonon peaks in the hot electron luminescence spectra from GaAs/Al_{0.7}Ga_{0.3}As (square) and GaAs/AlAs (circle) quantum wells as a function of barrier width.

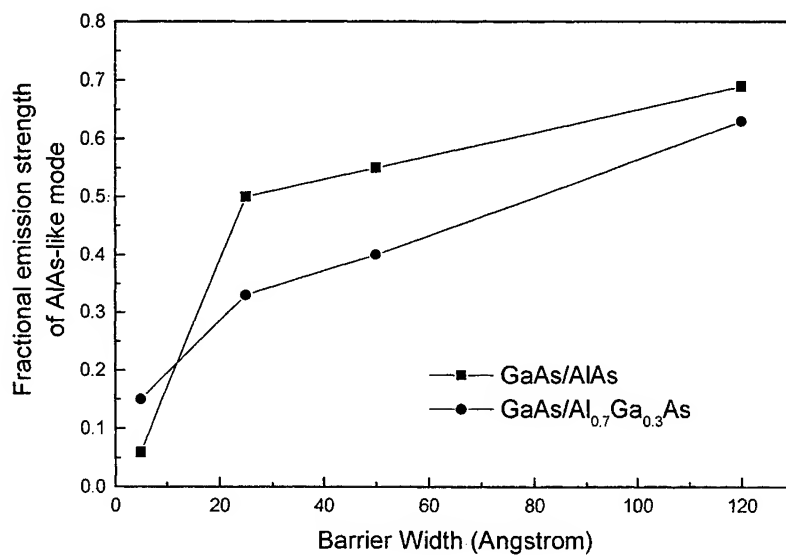


Figure 13 The estimate emission strength of the AlAs-like LO phonon mode relative to the GaAs LO phonon as a function of the barrier width from both samples.

High growth rate epitaxy of InN film by a novel-designed MOCVD

Fuh-Hsiang Yang^a, Ying-Jay Yang^a, Jih-Hsien Hwang^b,

Chung-Han Lee^b, Kuei-Hsien Chen^b, Ching-Yen Lin^c

^aInstitute of Electrical Engineering, National Taiwan University, Taipei, Taiwan

^bInstitute of Atomic and Molecular Sciences Academia Sinica, Taipei, Taiwan

^cAdvanced Instrumentation Center, National Taiwan University, Taipei, Taiwan

ABSTRACT

Indium nitride (InN) film was successfully grown on the Si(111) substrate. The growth rate of InN film can be enhanced about four times by a novel-designed MOCVD system with a NH₃ pre-cracking device, in which the NH₃ gas was fed through a quartz tube passing over a high temperature (650-850 °C) graphite. A maximum growth rate of about 6 μm/hr in our system was achieved due to high cracking efficiency of NH₃. The growth temperature of substrate widely ranged from 350 to 600 °C provides more flexible conditions to improve the film quality. The X-ray diffraction peaks of 31.7° and 65.5° were obtained from the (0002) and (0004) InN respectively, indicating (0001)-oriented hexagonal InN was epitaxially grown on the silicon(111) substrate.

Keywords: Indium nitride, InN, MOCVD, pre-cracking

1.INTRODUCTION

Indium nitride (InN), which is a III-V compound semiconductor with a stable wurtzite crystal structure and a direct band gap of about 1.9 eV,¹ is promising for visible optoelectronics and high efficiency solar cells. It is predicted that a tandem solar cell with a Si solar cell on the bottom and a solar cell with a bandgap 1.85eV on the top, a maximum efficiency of 32.1% (AM1.5 global) can be achieved,² which indicates that InN has the potential to be a non-toxic, high efficiency solar cell. Many studies have been done on the epitaxial growth of InN on sapphire, GaN and GaAs,³⁻⁷ but only a few works done on the Si substrate.⁸⁻⁹ Different methods have been used including metalorganic chemical vapor deposition (MOCVD)³⁻⁷, sputtering¹⁰, molecular beam epitaxy (MBE)¹¹, and halogen-transport vapor phase epitaxy (VPE)¹². However, high quality InN hasn't been achieved yet mainly due to the lack of a lattice-matching substrate, and restricted growth conditions which are limited by the low dissociation temperature of InN and required high equilibrium vapor pressure of N₂.¹³ Usually the growth temperature of InN should be kept relatively low (~500°C) to prevent the dissociation of InN, however the cracking efficiency of N₂ or NH₃ at such low temperature is poor, resulting in a low growth rate. In the case of MOCVD using plasma-cracked N₂, a low growth rate of ~0.3 μm/h was

reported,⁴ which is not suitable for solar cell applications. In this paper, we report that a high growth rate of 6 $\mu\text{m/h}$ epitaxy of InN on Si(111) was achieved by a novel-designed MOCVD system with a NH_3 precracking device.

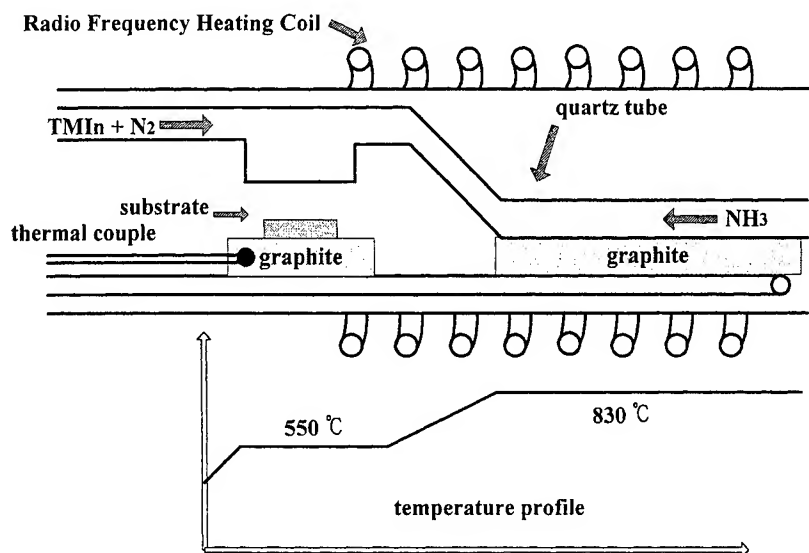


Fig. 1. Configuration of the novel-designed MOCVD reactor.

2. EXPERIMENTAL PROCEDURE

A schematic diagram of the MOCVD apparatus for the InN growth is shown in Fig.1. Trimethylindium (TMIn : $(\text{CH}_3)_3\text{In}$) kept at 10°C and high-purity NH_3 were used as the precursors. TMIn vapor was carried by 40~80 sccm high-purity N_2 gas and then another 200 sccm N_2 gas was added to increase the gas velocity of group-III line. NH_3 flow rate varied from 800 to 1600 sccm, which corresponds to a V/III ratio about several hundred. To prevent pre-reaction between TMIn and NH_3 , they were fed into chamber separately through quartz tube. The tube delivering NH_3 passed over a high temperature graphite (temperature range 600~900 °C) for NH_3 cracking. The precracked NH_3 gas was mixed with TMIn and carrier gas just above the substrate and jetted vertically onto a sapphire substrate. The growth temperature at substrate varied at the temperature range of 400~600 °C. The typical horizontal temperature profile of the reactor was shown in the lower part of Fig.1. The Si(111) substrate was prepared by solvent degreasing with acetone, followed by a HF dipping to strip the native oxide. After loading into the growth chamber, high purity N_2 flashed during temperature rising to the set point. TMIn is introduced to the chamber before NH_3 to prevent the Si surface from the formation of amorphous SiN_x . It was reported that amorphous SiN_x on the Si surface severely degrades the epitaxial quality⁸. InN films were characterized by XRD using a Rigaku D/MAX C diffractometer. The surface morphology and cross-section were studied using a Hitachi S800 scanning electron microscope. Raman spectra were obtained through a Renishaw system 2000 micro-Raman spectrometer with a Ar^+ laser as the light source.

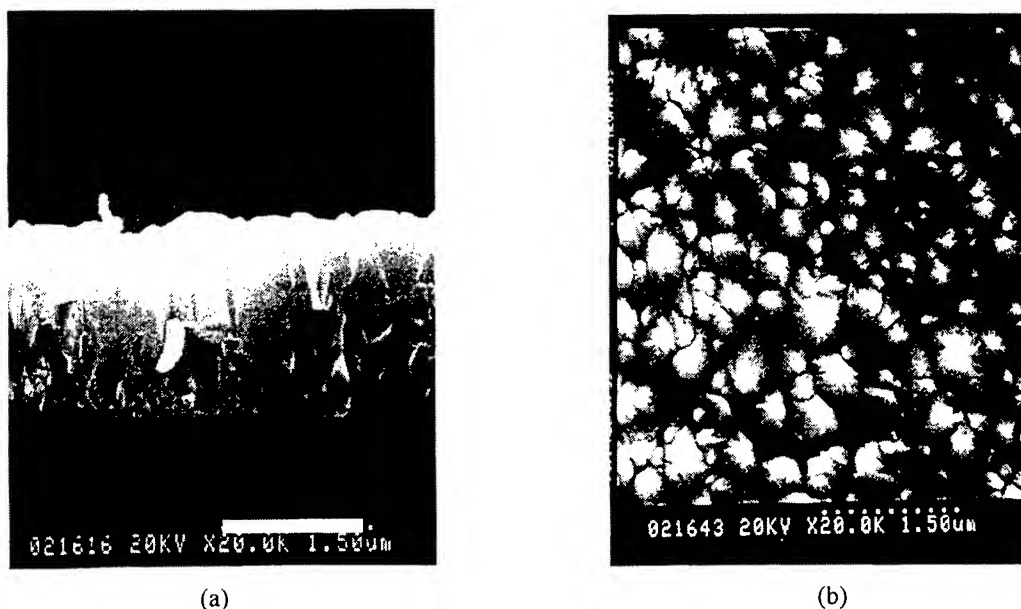


Fig.2. SEM photographs of InN grown on Si(111). The substrate temperature is 450°C and the preheating temperature is 650°C. The white mark represents 1.5 μ m corresponding to a growth rate of 2 μ m/hr.

3. RESULTS AND DISCUSSION

Fig. 2 shows the SEM photographs of InN film. The cross-section (Fig. 2 (a)) shows columnar structure which may be due to large lattice-mismatch (about 8%) between Si(111) and InN. The top view (Fig. 2 (b)) reveals small island structures with hexagonal pyramids. Using a thin buffer layer to improve the crystal quality is underway and the results will be published elsewhere.

As shown in Fig. 3, typical θ -2 θ XRD scan shows InN (0002), InN (0004) and Si(111) at 31.3°, 65.3° and 28.4° respectively, indicating the (0001) hexagonal InN is grown on the Si(111) substrates. The lattice constant obtained from Fig.3 is about 5.73 Å. There are small peaks also shown, corresponding to InN (1011), (1012), (1013) indicating few polycrystalline is formed. The reason is attributed to the native oxide or amorphous nitride formed on the Si surface before or during the growth of InN film.

Fig. 4 shows the Raman spectrum of a typical InN film grown on Si(111). The h-InN related peak at 487 cm^{-1} (E_2 mode) could be clearly identified. The $A_1(\text{LO})$ modes shifted toward lower wavenumber at 583 cm^{-1} . Both peaks broaden with respect to other work¹⁴ indicating there are strain and many defects in the film.

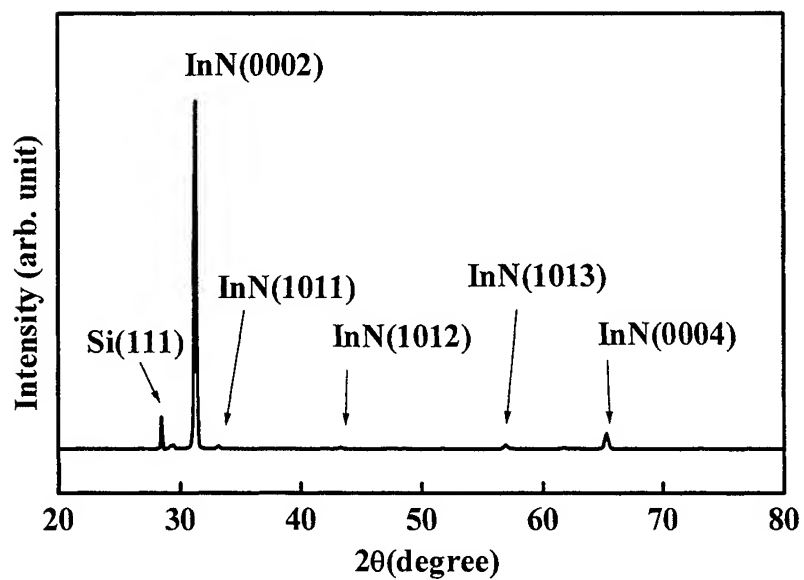


Fig.3. XRD θ - 2θ scan of the InN / Si(111) film

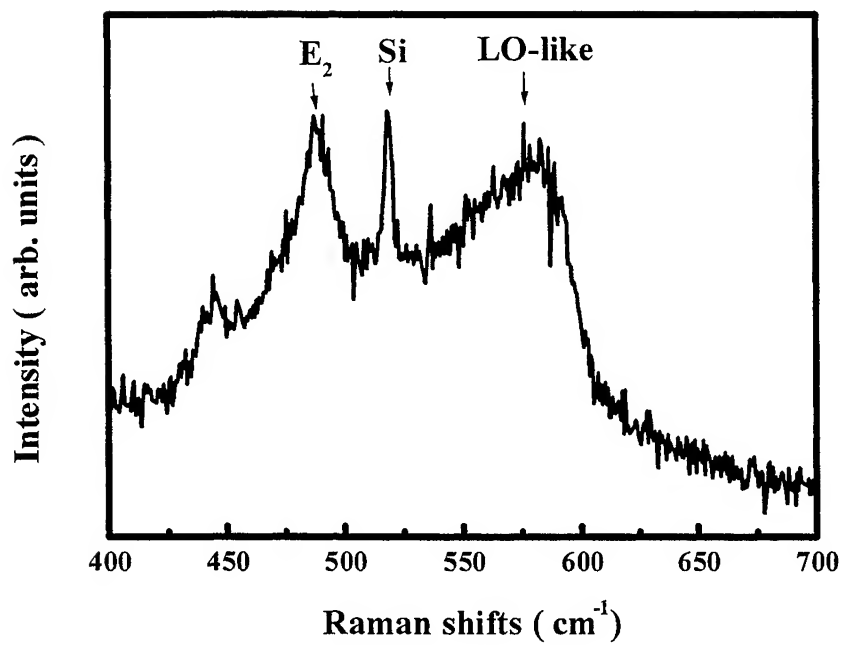


Fig.4. Raman spectra of the InN/Si(111) film.

Fig. 5 shows both the InN growth rate as a function of substrate temperature without NH_3 preheating and the InN growth rate as a function of preheating graphite temperature respectively. All the works are done with the same chamber configuration except the preheating graphite to exclude the dependence of the chamber configuration on the growth rate. Fig. 5 (a) shows that the growth rate increases with substrate temperature first, then it starts to decrease when the substrate temperature is over 500°C . A maximum growth rate of about $1.5\ \mu\text{m/h}$ at 500°C is obtained, which is relatively high compared to the other published works.⁴ Fig. 5 (b) shows the InN growth rate as a function of the preheating graphite temperature with substrate temperature at 500°C . The maximum growth rate as high as $6\ \mu\text{m/h}$ is obtained when the preheating graphite is set at 750°C , which is enhanced four times compared to that without NH_3 preheating. The enhancement of the InN growth rate is attributed to the much efficient NH_3 cracking with the preheating process. It should be mentioned that the temperature of NH_3 with a large flow rate after passing through the preheating region is somewhat lower than that of the preheating graphite, since the thermal equilibrium of the gasses can't be reached with such NH_3 flow. High flow rate of NH_3 reduces the reaction time between NH_3 and TMIn and allow the gasses reach the substrate without pre-reaction occurred. The InN growth rate increases with the preheating temperature first, then decreases when the graphite temperature is larger than 750°C . It is suggested that preheated NH_3

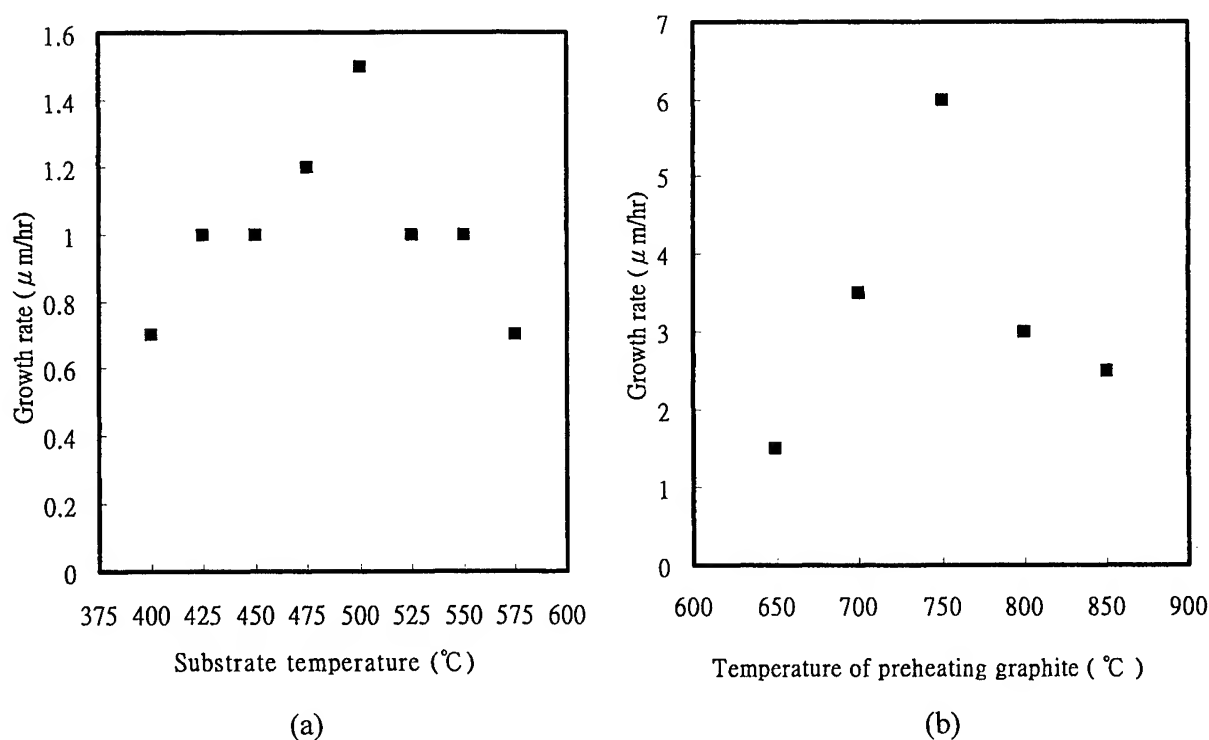


Fig. 5. (a) InN growth rate as a function of substrate temperature without NH_3 preheating. (b) InN growth rate as a function of preheating graphite temperature with the substrate temperature at 500°C .

can heat up the surface of substrate, resulting in a higher dissociation rate and a lower growth rate of InN. Although the V/III ratio of our growth condition is much lower than that of other work^{3,4}, but no indium droplets were observed on the surface, indicating sufficient supply of nitrogen atoms is obtained from the efficient NH₃ cracking by the preheating device.

CONCLUSION

Epitaxial growth of InN film on Si(111) substrate is achieved by a novel-designed MOCVD with a NH₃ preheating device. The growth rate of InN with NH₃ preheating can be enhanced by four times up to 6 μ m/h compared to that without NH₃ preheating in our system, which is in general much higher than other works reported. XRD scan indicates that (0001) oriented hexagonal InN is grown on Si(111) substrate and the InN peak is at 31.3° with a corresponding lattice constant of 5.73 Å. Raman spectrum with E₂ mode peak at 487 cm⁻¹ and A₁ (LO) mode peak around 583 cm⁻¹ also confirm the hexagonal InN growth. SEM shows the morphology with island structure with hexagonal pyramids. The crystal quality is expected to be improved using a thin buffer layer for the InN growth.

ACKNOWLEDGEMENTS

The authors are grateful to the Financial support from the Institute of Atomic and Molecular Sciences, Academia Sinica.

REFERENCES

1. T.L. Transley and C.P. Foley, "Optical band gap of indium nitride", J. Appl. Phys. **59**, pp.3241-3244, 1986.
2. E. N. Matthias and B. M. Allen, "The spectral p-n junction model for tandem solar-cell design", IEEE Transactions on electron devices, **ED-34**, pp.257-265, 1987.
3. A. Wakahara, T. Tsuchiya and A. Yoshida, "Epitaxial growth of indium nitride", J. Crystal Growth **99**, pp.385-389, 1990.
4. M. Sato, "Epitaxial growth of InN by plasma-assisted metalorganic chemical vapor deposition", Jpn. J. Appl. Phys. **36**, pp. L595-L597, 1997.
5. Q. Guo, M. Nishio, H. Ogawa and A. Yoshida, "Low-temperature growth of InN films on (111)GaAs substrates", Jpn. J. Appl. Phys. **38**, pp. L490-L491, 1999.
6. A. Yamamoto, Y. Yamauchi, M. Ohkubo, A. Hashimoto, "A comparative study of OMVPE-grown InN heteroepitaxial layers on GaAs(111)B and α -Al₂O₃(0001) substrates", J. Crystal Growth **174**, pp.641-646, 1997.
7. S. Yamaguchi, M. Kariya, S. Nitta, T. Takeuchi, C. Wetzel, H. Amano and I. Akasaki, "Structural properties of InN on GaN grown by metalorganic vapor-phase epitaxy", J. Appl. Phys. **85**, pp.7682-7688, 1999.
8. A. Yamamoto, M. Tsujino, M. Ohkubo and A. Hashimoto, "Nitridation effects of substrate surface on the metalorganic chemical vapor deposition growth of InN on Si and α -Al₂O₃ substrates", J. Crystal Growth **137**, pp.415-420, 1994.

9. S. E. Aleksandrov, V. A. Zykov, T. A. Gavrikova and D. M. Krasovitskii, "Electric and photoelectric properties of $n\text{-Ga}_x\text{In}_{1-x}\text{N/p-Si}$ anisotropic heterojunctions", *Semiconductors* **32**, pp.412-416, 1998.
10. T. J. Kistenmacher, S. A. Ecellberger, and W. A. Bryden, "Structural and electrical properties of reactively sputtered InN thin films on AlN-buttered (0001) sapphire substrates: Dependence on buffer and film growth temperatures and thickness ", *J. Appl. Phys.* **74**, pp.1684-1691, 1993.
11. C. R. Abernathy, S. J. Pearton, F. Ren, and P. W. Wisk, "Growth of InN for ohmic contact formation by electron cyclotron resonance metalorganic molecular-beam epitaxy", *J. Vac. Sci. Technol. B* **11**, pp.179-182, 1993.
12. O. Igaracshi, "Epitaxial growth of InN by halogen transport method", *Jpn. J. Appl. Phys.* **31**, pp.2665-2668, 1992.
13. O. Ambacher et.al. " Thermal stability and desorption of Group III nitrides pre-pared by metal organic chemical vapor deposition" *J. Vac. Sci. Technol. B* **14**(6), 3532(1996).
14. M. C. Lee, H. C. Lin, Y. C. Pan, C. K. Shu, J. Ou, W. H. Chen and W. K. Chen, "Raman and x-ray studies of InN films grown by metalorganic vapor phase epitaxy", *Appl. Phys. Letters* **73**, pp.2606-2608, 1998.

Performance and reliability of wafer-bonded AlGaInP /mirror/Si light-emitting diodes

R. H. Horng^{a,*}, D. S. Wu^b, W. C. Peng^b, M. F. Huang^c, P. H. Liu^c, C. H. Seieh^c, and K. C. Lin^c

^aInstitute of Precision Engineering, National Chung Hsing University, Taichung 402, Taiwan

^bInstitute of Electrical Engineering, Da-Yeh University, Chang-Hwa 515, Taiwan

^cVisual Photonics Epitaxy Company, Lung-Tan, Taoyuan 325, Taiwan

ABSTRACT

AlGaInP light emitting diode (LED) with a mirror substrate has been successfully fabricated by wafer bonding. The bonding technique using a metallic interlayer has been developed to eliminate handling the fragile, free-standing epilayers. Various structures of the mirror substrate have been studied, and a suitable structure of Au/AuBe/SiO₂/Si is proposed. From the observation of the chip fabrication process, it was found that the SiO₂ layer could isolate the stress causing from the Si substrate. The device performance of bonded LED is obviously far superior to that of the standard absorb-substrate LED. It exhibits normal p-n diode behavior with a low series resistance. Moreover, the emission wavelength of the bonded LED was independent of the injection current. The low forward series resistance and a good heat sink provided by Si substrate solve the joule heating inhering in conventional LED problem. Furthermore, the bonded LED with high reliability has been demonstrated.

Keywords: Wafer bonding, light emitting diode, mirror substrate, absorb substrate, joule heating, reliability

1. INTRODUCTION

High-efficiency light-emitting diodes (LEDs) operating in the wavelength region from red to green light have been recently realized employing the AlGaInP alloy system grown on a lattice-matched GaAs substrate. The lattice-matched growth ensures that crystalline defects leading to poor internal efficiency and poor reliability are minimized in the structure. After the almost 20 years effort, the good quality AlGaInP double heterostructures presenting the high internal quantum yields, well over 90 % efficient, can be obtained. However, in LEDs the external quantum efficiency is rather poor, generally only a few percent. Since the large difference in optical refractive index between the LED semiconductor material and the emission ambient (typically epoxy), causes the majority of photons emitted from the active layer to be reflected back into the semiconductor the majority of which are absorbed by the absorbing GaAs substrate. The absorbing GaAs substrate significantly limits the performance of the device. This problem can be minimized by growing a distributed Bragg reflector (DBR) between the LED epitaxial layers and the absorbing substrate^{1,2} or alternatively by replacing the GaAs substrate with a GaP transparent substrate via wafer bonding after epitaxial growth, as performed by Hewlett-Packard in high volume manufacturing.³⁻⁵ An increase in luminous efficiency can be achieved by the first method, since the DBR will reflect light that is emitted or internally reflected in the direction of the absorbing substrate. However, the improvement is limited, because the DBR only reflects light that is of near normal incidence. On the other hand, the AlGaInP LEDs with wafer-bonded GaP substrates have been demonstrated with highly reliable and performance.^{6,7} Because the substrate removal precedes wafer bonding, it is necessary to handle the thin epitaxial layers. The thin epilayers are difficult to handle without breaking, rendering fabrication more difficult. It is worthy to mention that the AlGaInP/GaP bonding process needs high temperature (>600°C) and long thermal-anneal duration (≥1h). This might result in additional disadvantage of redistributing the doping profile. Moreover, an important step in this wafer bonding process is the matching of the

* Corresponding author: Ray-Hua Horng, e-mail address: huahorng@dragon.nchu.edu.tw

crystallographic orientations of the bonded wafers. This crystallographic alignment makes the LED operate at low voltage and high efficiency.⁸

In our previous study, we have demonstrated that the performance of LEDs can be improved by bonding the LED to a metal mirror at low bonding temperature ($\sim 300^\circ\text{C}$) and short duration time (~ 20 min).^{9,10} The metal mirror has a higher effective reflectivity than a multi-layers DBR. The performance of mirror-substrate (MS) LED is superiors than that of LED with DBR structure. The reflective mirror can directly be fused onto the device structure before selective removal of the GaAs substrate. The problem of handling thin epitaxial layers is also avoided. On the other hand, due to the fact that LED is fused to metal, the alignment of the crystallographic axes of the bonded wafers occurring in the wafer fusion of LED to GaP substrate does not be required. In this work, the requirements of mirror structures will be discussed. The reliability of the MS LED will also be demonstrated.

2. EXPERIMENTAL

There are many techniques to bond the semiconductor wafers. In our study, the LED was bonded to the Si substrate by inserting the intermediate metal layer. The LED structure employed in this work is p+-AlGaInP/undoped AlGaInP active layer/n-AlGaInP/n+-GaAs/n+-AlGaAs/n+-GaAs substrate and is grown by metalorganic chemical vapor deposition. The thickness of n+GaAs is very thin (~ 5 nm) and used for an n-metal contact layer. The n+-AlGaAs layer is used for the etching stop layer. The LED structure described in this work is shown in Fig. 1. The wafer bonding process has been detail described at the previous reported.¹⁰ The Au/AuBe/(SiO₂)/Si is bonded to the LED structure at elevated temperature (300°C for 20 min) and under applied uniaxial pressure to form robust chemical bonds. Notably, it is not necessary to care the crystallographic alignment between the bonded wafers. Following the fused process, the GaAs substrate was removed by chemical etching. Because wafer bonding precedes substrate removal, there is no need to handle thin epitaxial layers. The removal process is a first check of the fusion quality and uniformity. The fused epilayer was mesa-etched into isolated devices with $300 \times 300 \mu\text{m}^2$ area until the Au/AuBe metal surface exposed (for p-side contact). The patterned Au/AuGeNi with diameter of $100 \mu\text{m}$ was deposited onto the n-side (n+-GaAs contact layer) and then alloyed for ohmic contact processing. For comparison, the absorbing substrate LEDs fabricated from the same as AlGaInP/GaAs epitaxial material were also prepared and as standard LEDs. The LED samples with mirror and absorbing substrates described here were diced into chips but not encapsulated before electrical and optical measurements.

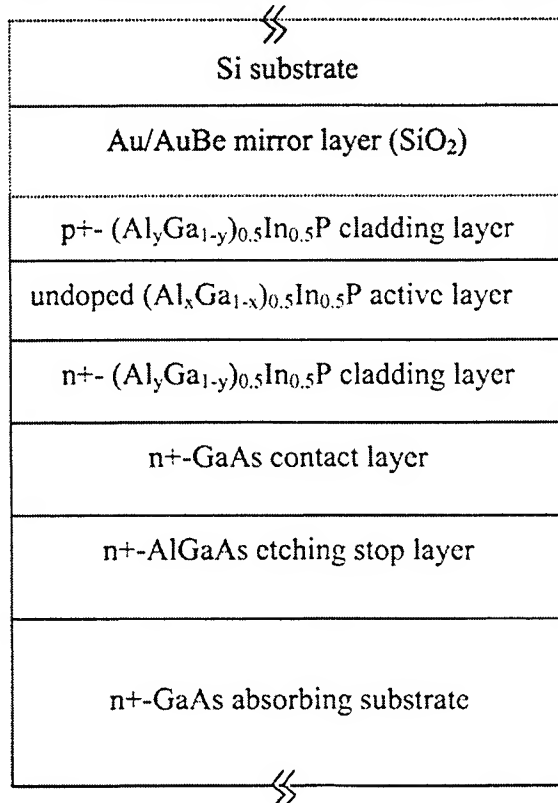


Fig. 1 Schematic structure of the AlGaInP LEDs. The shadowed regions are the structure of mirror substrate.

3. RESULTS AND DISCUSSION

A key requirement for the application of intermediate-layer wafer bonding to the fabrication of MS LEDs is the realization of high reflectivity at the mirror. Furthermore, successful implementation of this technique requires that the perfect bonding epilayer can endure wafer and die fabrication, packaging, and environmental stress that occurs over the operating life of the LED. Generally, AuBe is used in AlGaInP LEDs to make ohmic contacts to p-type material. Thus AuBe was used as an adhesive layer and mirror in the wafer-fused MS LED structure. The Si substrate supporting the metal improves the LED performance at high currents because the high thermal conductivity of Si facilitates heat removal. A successful sample of AlGaInP LED wafer bonded on an Au/AuBe/Si substrate can be obtained as shown in Fig. 2(a), and no visible artifacts are present in the mirror-like surface. Instead, only a uniform dark red color is observed. Figure 2(b) shows the optical microscope view of the chip LED epilayers after p-contact region of bonded LED epilayers was chemically removed and n-side ohmic contact process was made. Obviously, the bonded LED/Au/AuBe/Si substrate chips cannot withstand the ohmic contact process. There exist voids in the chips area after the metallization-alloyed process. Because of the temperature (450 °C) of ohmic contact process is higher than the bonded temperature (300 °C). The thermal stress induced by the metallization-alloyed process should be considered. The thermal expansion coefficients of Si, metal and LED are ~ 2.6 , 14 and $\sim 4.5 \times 10^{-6}/\text{K}$, respectively. As the temperature from 450 °C down to room temperature, Si substrate provides the tensile stress to the LED epilayers through the metal. Due to the high freedom for the LED chips ($300 \mu\text{m} \times 300 \mu\text{m}$), the tensile stress would be released by inducing the voids in the LED chip area. These will make the LED performance degrade.

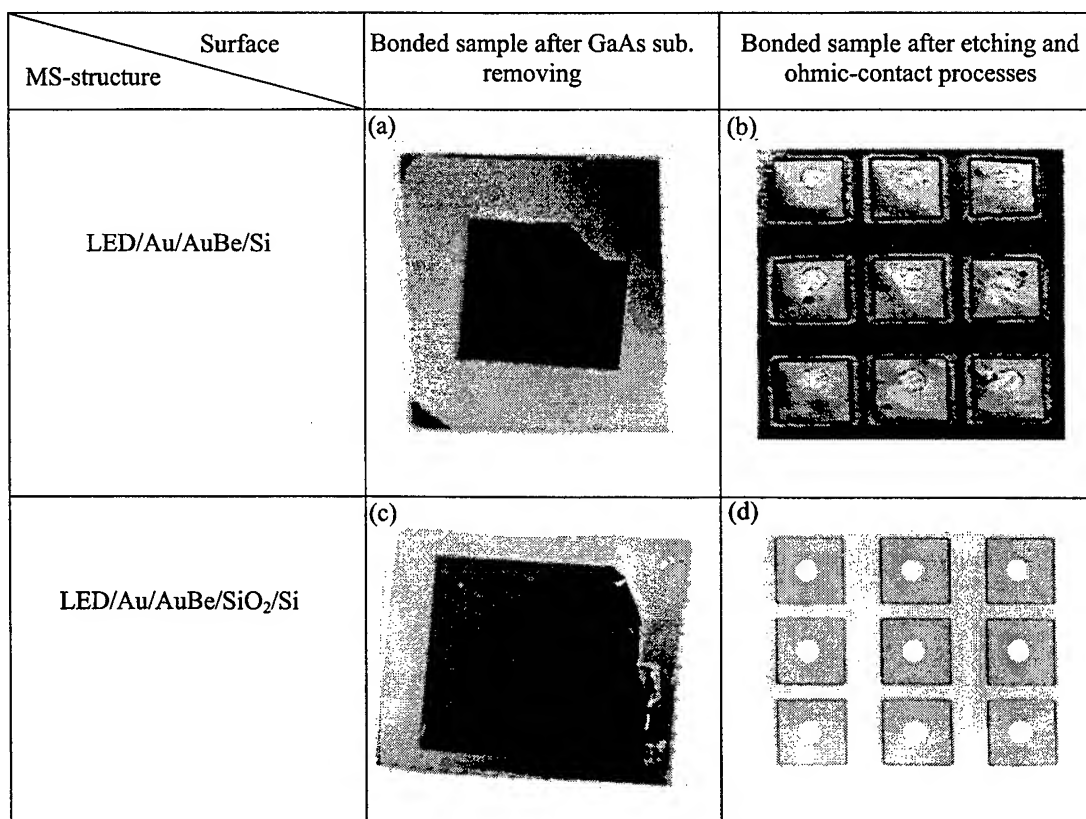


Fig. 2 Top-view photograph of a successfully wafer-bonded sample and optical microscope view of processed chip epilayers for LED/Au/AuBe/Si sample as compared with those for LED/Au/AuBe/SiO₂/Si sample.

In order to reduce the thermal stress existing in the LED/Au/AuBe/Si substrate, it is necessary to introduce a layer with very small thermal expansion coefficient. The suitable material is SiO₂, and its thermal expansion coefficient is about $0.35 \times 10^{-6}/K$. As the SiO₂ is inserted in the interface between AuBe and Si, the tensile stress induced by Si substrate could be isolated by the SiO₂ layer. In addition, the mirror metals are thin and can deform plastically like an elastic body. Thus the chips still present very high fusion quality after the ohmic process for the LED/Au/AuBe/SiO₂/Si substrate. Figure 2(c) show a successful sample of AlGaInP LED wafer bonded on an Au/AuBe/SiO₂/Si substrate. Figure 2(d) presents the corresponding optical microscope view of the chip LED/Au/AuBe/SiO₂/Si substrate after p-contact region of bonded LED epilayers was chemically removed and n-side ohmic contact process was made. Clearly, the voids induced by ohmic process occurring in the LED/AuBe/Au/Si sample do not be observed. On the other hand, the bottom metal (p-contact region) still presents mirror surface. This point can be confirmed by the reflectivity measurement after removing the bonded LED epilayers. The reflectivity of the processed mirror is over 90% as the incident wavelength variation from 600 to 900 nm. It suggests that the metal still is a high reflective mirror for the LED emission wavelength.

As concerning the stress coming from Si substrate isolated by SiO₂ layer, it can be confirmed by the emission-wavelength measurement. Figure 3 shows the room temperature electroluminescence (EL) spectra at 10 mA forward currents injection for the MS (with SiO₂) LED and compared with that for the standard LED. The peak wavelength of the LED bonded on the Au/AuBe/SiO₂/Si substrate is the same as that of the standard LED. This suggests the LED samples dose not be under the stress of Au/AuBe/SiO₂/Si substrate after the chip process. It is worthy to note that the full width at half maximum (61.4 meV) of EL spectrum for the LED/Au/AuBe/SiO₂/Si is smaller than that (77 meV) of the EL spectrum for the standard sample.

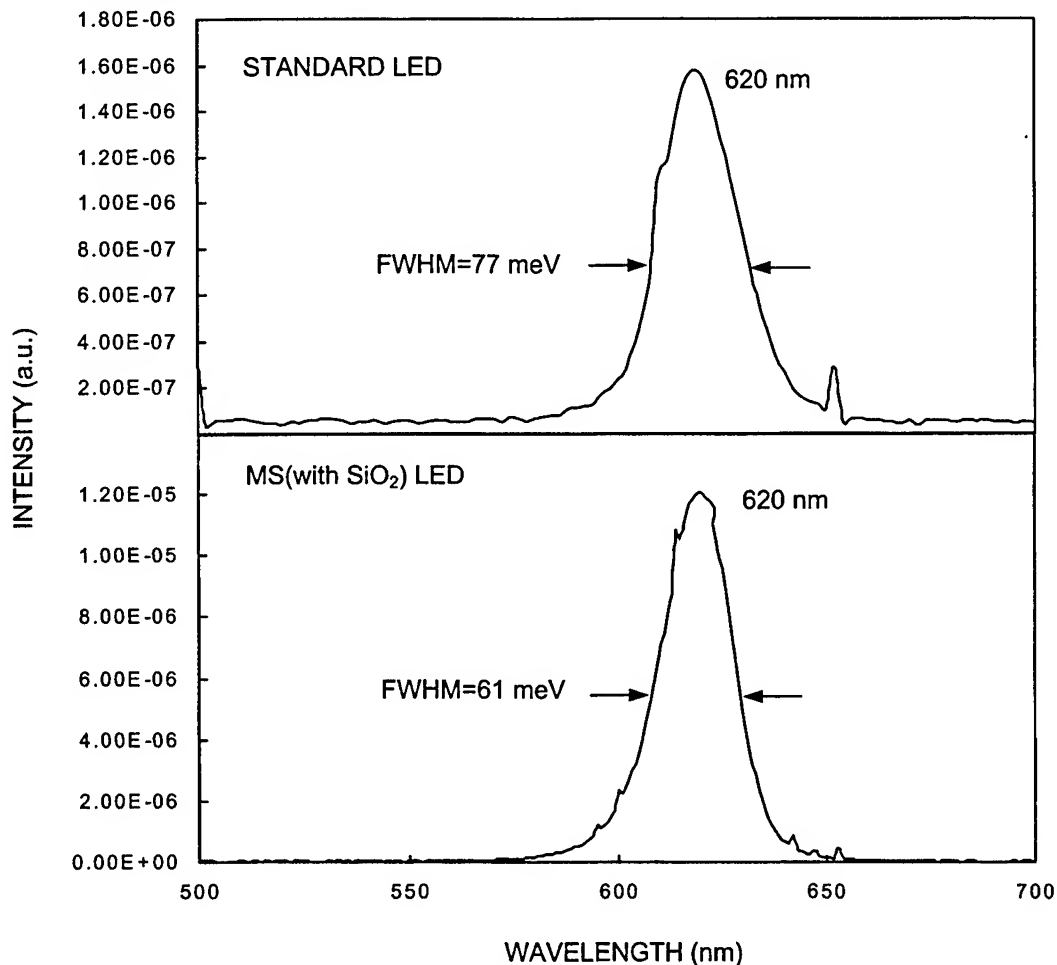


Fig. 3 Room temperature electroluminescence (EL) spectra at 10 mA forward currents injection for the MS (with SiO₂) LED and compared with that for the standard LED.

The current vs voltage (I-V) curves of a standard and bonded MS (with SiO₂) LEDs are shown in Fig. 4. Similar I-V characteristics were obtained for both devices. The diode ideality factors in the radiative region (1.5~2 V) and the non-radiative (<1.5) regions are 1.4 and 2.1, respectively. This result indicates that the wafer bonding technique does not adversely affect the I-V characteristic of the LED device. It is worthy to note that the standard LED has a higher series resistance of 7Ω than MS (SiO₂) LED does (1~3 Ω). A small series resistance is most important for decreasing the Joule heating effect and thus increasing the quantum efficiency of the LEDs. In the bonded LED structure, the forward current can be directly injected into the LED through the Au/AuBe metals without through the bonded Si substrate. On the other hand, the resistances of bulk GaAs substrate have been removed for the bonded LED. These results in smaller series resistance existing in the bonded mirror-substrate LED as compared with that in the absorbed-substrate LED.

Fig. 5 shows the room-temperature EL spectra at different forward currents for this MS (with SiO₂) LED. All the EL emission peak wavelengths are located at around 620 nm. For the LED bonded to metal/SiO₂/Si substrate, the emission peak wavelength is almost the same. The phenomenon of emission peak wavelength shift with increasing injection current caused by joule heating, which occurs in standard LED, dose not be observed in the bonded MS (with SiO₂) LED. Note that, the Si substrate has 3.2 times higher thermal conductivity than the GaAs substrate. The high thermal conductivity substrate of the bonded LED provides a good heat sink. The small series resistance (as shown in Fig. 4) and good heat sink substrate are important factors for alleviated the joule heating effect and thus increasing the quantum efficiency of the bonded LEDs.

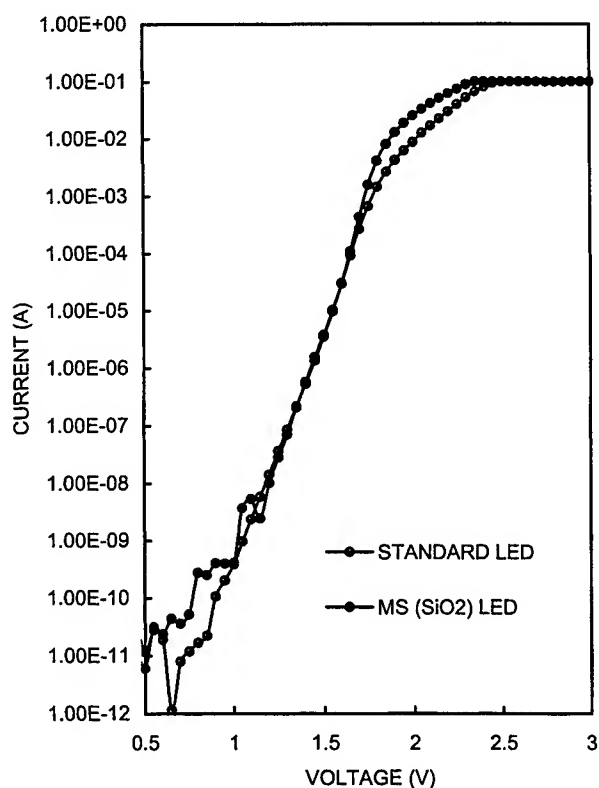


Fig. 4 Current vs voltage curves of a standard and bonded MS (with SiO₂) LEDs

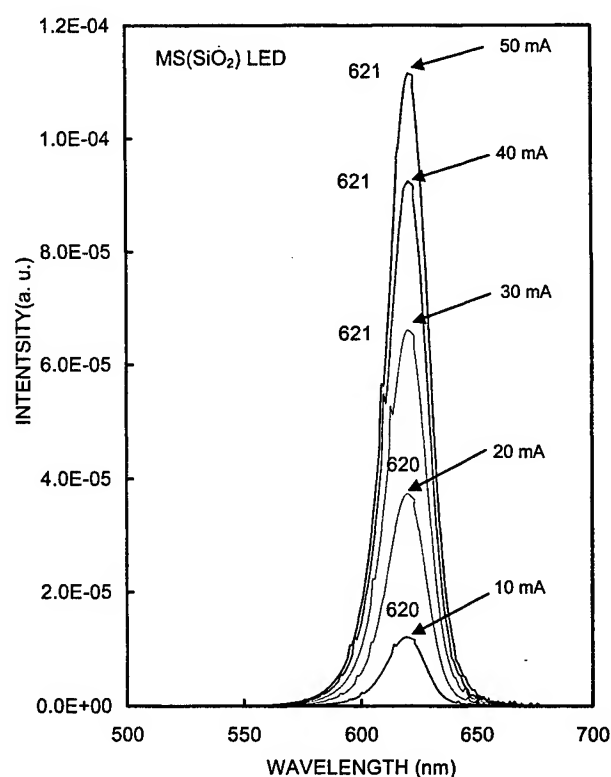


Fig. 5 Room-temperature EL spectra at different forward currents for this MS LED

Fig. 6 shows long-term reliability behavior of twenty MS AlGaInP LED chips stressed at 50 mA, 80°C ambient temperature. After 300 h stress, the performance of wafer-bonded LED do not degrade. They exhibit an average improvement of 3% of their initial light output. This increase in brightness may be the result of recombination-enhanced annealing of defects or other nonradiative recombination centers in the active layers of these device. On the other hand, the lack of increase in forward voltage in these devices is indicative of the high integrity of the wafer-bonded interface. These results demonstrate that the MS (with SiO₂) LEDs present excellent reliability characteristics of these solid-state emitters.

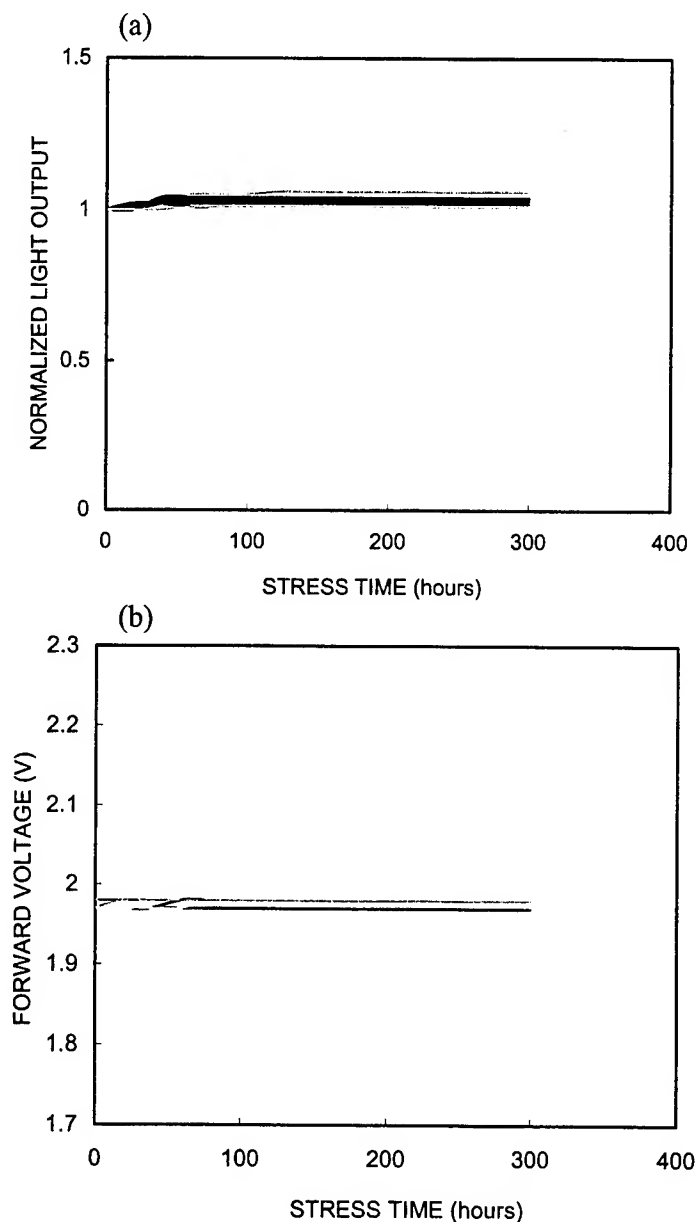


Fig. 6 (a) Normalized light output and (b) forward voltage against stress time for MS (with SiO₂) AlGaInP LEDs operated at 80°C ambient temperature and 50 mA.

4. SUMMARY

High-brightness mirror-substrate AlGaInP LEDs have been fabricated by wafer bonding technique at low-temperature and short duration time. The structures of mirror substrate have been investigated. Suitable SiO₂ layer inserting in the MS structure (i.e. Au/AuBe/SiO₂/Si) can prevent LED chip from thermal stress. Measurements of the device performance of the mirror-substrate AlGaInP LED are superiors to that of the conventional LED. The metals not only act as adhesion layers, but also act as mirror. On the other hand, the bonded LED structure provides a small series resistance and the Si substrate provides a good heat sink. These suggest that the joule heating inhering in conventional LED problem can be solved. Data have been presented demonstrating the high-reliability operation of wafer-bonded MS AlGaInP LEDs. These indicate that the MS LED and their corresponding wafer-bonding technique are viable for application requiring high-reliability.

REFERENCES

1. H. Sugawara, K. Itaya and G. Hatakoshi, *Jpn. J. Appl. Phys.* **33**, 6195, 1994.
2. H. Sugawara, K. Itaya and G. Hatakoshi, *J. Appl. Phys.* **74**, 3189, 1993.
3. F. A. Kish, F. M. Steranka, D. C. DeFever, D. A. Vanderwater, K. G. Park, C. P. Kuo, T. D. Osentowski, M. J. Peanasky, J. G. Yu, R. M. Fletcher, D. A. Steigerwald, M. G. Craford, and V. M. Robbins, *Appl. Phys. Lett.* **64**, 2839, 1994.
4. G. E. Hofer, D. A. Vanderwater, D. C. DeFever, F. A. Kish, M. D. Camras, F. M. Steranka, and I. -H. Tan, *Appl. Phys. Lett.* **69**, 803, 1996.
5. I. H. Tan, D. A. Vanderwater, J. -W. Huang, G. E. Hofler, F. A. Kish, E. I. Chen and T. D. Ostentowski, *J. Electron. Mater.* **29**, 188, 2000.
6. F. A. Kish, D. A. Vanderwater, D. C. DeFever, D. A. Steigerwald, G. E. Hofler, K. G. Park, and F. M. Steranka, *Electron. Lett.* **32**, 132, 1996.
7. F. A. Kish, D. A. DeFever, D. A. Vanderwater, G. R. Trott, R. J. Weiss, and J. S. Major. Jr., *Electron. Lett.* **30**, 1791, 1994.
8. F. A. Kish, D. A. Vanderwater, and M. J. Peanasky, M. J. Ludowise, S. G. Hummel, and S. J. Rosner, *Appl. Phys. Lett.* **67**, 2060, 1995.
9. R. H. Horng, D. S. Wu, S. C. Wei, M. F. Huang, K. H. Chang, P. H. Liu, and K. C. Lin, *Appl. Phys. Lett.* **75**, pp.154-156, 1999.
10. R. H. Horng, D. S. Wu, C. Y. Tseng, M. F. Huang, K. H. Chang, P. H. Liu, and K. C. Lin, *Appl. Phys. Lett.* **75**, pp. 3054-3056, 1999.

Build in electric field investigation on InAs and InGaAs nanostructures by photoreflectance

Chih-Ming Lai, Jung-Hao Huang, and Gwo-Jen Jan
Department of Electrical Engineering,
and
Graduate Institute of Electro-optical Engineering
National Taiwan University,
Taipei 10617, Taiwan

ABSTRACT

The photoreflectance has been measured on InGaAs/GaAs multiple strained quantum wells structures at room temperature. The Franz-Keldysh Oscillation (FKOs) features are clearly observed on photoreflectance spectra. Based on FKOs features above the energy band gap, the built-in electric field was studied by conventional FKOs calculation and Fast Fourier Transform, and Airy function fit techniques. The built-in electric fields were evaluated and discussed. The results show that Fast Fourier Transform could provide an accurate and fast method to calculate the built-in electric field.

Keywords: Photoreflectance, Franz-Keldysh Oscillations, Built-in electric field, InGaAs/GaAs nanostructures.

1. INTRODUCTION

Photoreflectance (PR) is an important and useful tool to investigate and qualify the optical properties of materials in epitaxial structures^{1,2}, because of its derivative like nature and sharp spectral features. PR is equivalent to a noncontact form of electroreflectance (ER), and uses a chopped laser pumping beam to modulate the electric field, dielectric function, and thus reflectance R , and records the differential reflectance ΔR . It has commonly been used with much success to determine the energies of critical point (CP) and confined-quantum-well (QW) transitions in the presence of small built-in fields³. For a medium field strength, the PR spectra exhibit Franz-Keldysh oscillations (FKOs) above the band-gap energy. The feature of the Franz-Keldysh oscillations (FKOs) on photoreflectance spectrum can be used to determine the built-in electric field from surface, interface and buried layers on the specimens^{4,5}. It is also used to study the bend-banding and Fermi-level pinning as well as photovoltaic effect by doping and temperature-dependent.

As well known, the FKO periods are related to the electric field F and the reduced mass μ in the direction of electric field. Due to the different reduced mass μ for HH and LH, the FKO demonstrates two different periods. Recently, Alperovich *et al.*⁶ and Wang *et al.*⁷ proposed that sharp HH and LH transition peaks would be observed after taking the fast Fourier transformation (FFT) to the FKO line shapes. However, in addition to HH and LH, the modulation field δF also affects the FKO line shape periods. Shen and Pollak *et al.*⁸, Bhat-tacharya *et al.*⁹ suggested that the spectra should be treated as the difference between the flat-band modulated FKO with an electric field $F-\delta F$ and $F+\delta F$ for ER, or F and $F-\delta F$ for PR. Therefore the FKO will generally contain four frequencies. If the modulated electric field is not much smaller than built-in electric field, the interference beats are then not only due to the HH and LH, but also influenced by the modulated electric field. It would be interesting to know how the modulation field qualitatively distorts the FKO beats and how it quantitatively affects the line shape analysis.

2. THEORY

In the case of a flat band condition under an electric field F , $\Delta\epsilon$ is defined as¹⁰

$$\Delta\epsilon = \epsilon(E, F) - \epsilon(E, 0) \quad (1)$$

where E is the photon energy. If the effects of excitons and electric field nonuniformities are negligible, then the change of dielectric function $\Delta\epsilon$ including the effects of broadening can be expressed as

Correspondence: Email: gjian@cc.ee.ntu.edu.tw, Telephone: 886-2-23635251 ext. 421
Fax: 886-2-23671910

$$\Delta\varepsilon(E, F) = \frac{B}{(E - i\Gamma)^2} (\hbar\theta)^{\frac{1}{2}} H(\eta) \quad (2)$$

where B is related to optical transition matrix elements. The parameters $\hbar\theta$ and η are

$$(\hbar\theta)^3 = e^2 \hbar^2 F^2 / 2\mu \quad (3)$$

$$\eta = \frac{Eg - E + i\Gamma}{\hbar\theta} \quad (4)$$

where μ is the reduced mass in the direction of F and Eg is the energy gap. And the electro-optic function $H(\eta)$ is given by

$$H(\eta) = 2\pi \left\{ e^{-i(\pi/3)} \cdot Ai'(\eta) \cdot Ai'(\eta e^{-i(2\pi/3)}) + \eta \cdot e^{-i(2\pi/3)} \cdot Ai(\eta) \cdot Ai(\eta e^{-i(2\pi/3)}) \right\} + i\sqrt{\eta} \quad (5)$$

The line shape of photoreflectance spectra is a response of the field-induced change of reflectivity, which is written as

$$\frac{\Delta R}{R} = \alpha(\varepsilon_1, \varepsilon_2) \delta\varepsilon_1 + \beta(\varepsilon_1, \varepsilon_2) \delta\varepsilon_2 \quad (6)$$

in which α and β are the Seraphin coefficients, and $\delta\varepsilon_1$ and $\delta\varepsilon_2$ are the modulation-induced changes in the real and imaginary parts, respectively, of the complex dielectric function. In the case of a uniform built-in electric field F and a modulation field δF , it was proposed that

$$\delta\varepsilon(E, F) = \Delta\varepsilon(E, F) - \Delta\varepsilon(E, F - \delta F) \quad (7)$$

The conventional method for determining F from FKOs is to use asymptotic expressions of the electro-optic function in Eq. (5).

$$H(\eta) \approx \frac{1}{4\eta} \exp\left(\frac{4}{3}\eta^{\frac{3}{2}}\right) - i\frac{1}{32}\eta^{\frac{5}{2}} \quad (8)$$

The extrema of FKOs are given by

$$n\pi = \phi + \frac{4}{3} \left(\frac{E_n - Eg}{\hbar\theta} \right)^{\frac{3}{2}} \quad (9)$$

where n , ϕ , E_n are the index of the n th extrema, arbitrary phase factor, the photon energy of the n th oscillation, respectively.

An alternative way to obtain electric fields is to apply the FFT to the PR spectra. This approach has the advantage of determining F without the ambiguity of choosing reduced mass. The frequency f_i evaluated from the fast Fourier transform is related to F by

$$f_i = \frac{2}{3\pi} (2\mu_i)^{\frac{1}{2}} \left(\frac{1}{e\hbar F} \right) \quad (10)$$

where $i=hh$ or lh , stand for heavy- and light-hole, respectively.

3. EXPERIMENTAL SETUP

The experimental setup for photoreflectance are carried out at room temperature using 632.8 nm line of 3 mW He-Ne laser as modulated and chopped at 199 Hz as the pumping beam. The probe light from a 150 W quartz tungsten halogen lamp was passed through a 0.3 m scanning monochromator and then focus onto the sample by lens. The reflected light from the sample was detected by a Si photodiode detector.

The sample S0 is in $i-n^+-i-p^+$ structure. 1 μm p^+ doped Si with the concentration $1 \times 10^{19} \text{ cm}^{-3}$ GaAs buffer layer was first grown on the p^+ substrate, followed by a 500 Å undoped intrinsic layer, then 600 Å Be doped with the concentration $5 \times 10^{18} \text{ cm}^{-3}$ n^+ GaAs layer. Then deposit 1000 Å undoped GaAs cap layer on it. The sample S1, S2, S3, and S4 are grown with different number of quantum wells on (111)B GaAs semi-insulating substrate. The structures of samples consisted of a 0.8 μm n^+ GaAs ($1 \times 10^{18} \text{ cm}^{-3}$), followed by an intrinsic region consisting of m periods ($m=0, 1, 3, 5$) InGaAs/GaAs (6.0 nm/8.0 nm) quantum wells clad on both sides by (96.0-7.0 nm) nm of undoped GaAs, to keep a total intrinsic thickness of 0.2 μm . Finally, a 0.3 μm p^+ GaAs ($9.65 \times 10^{16} \text{ cm}^{-3}$) was grown.

The sample S5 was grown by gas source molecular beam epitaxy on heavily n -type doped GaAs(001) mis-oriented 7° toward (110) substrate. Upon reaching the growth temperature, 720°C , we started with the deposited of 200 nm GaAs buffer

and 2ML InAs quantum dots layer. Then, we continued to grow 10 nm GaAs on quantum dots layer at 490°C, to avoid InAs migration. Finally, deposit 20 nm GaAs cladding layer at 720°C.

4. RESULTS AND DISCUSS

The photoreflectance spectra of the S1, S2, S3, and S4 are displayed in Fig. 1(a). The detail results of the transition in quantum wells are published in Ref. 11. Here, we paid work on the feature above the GaAs bandgap energy. The GaAs (barrier) bandgap for S1 to S4 are indicated by arrows in the figure. Spin-orbital transition is observed in PR spectra, it represents good quality of sample. The damped oscillations, between 1.45 eV and 1.75 eV, correspond to the FKOs above the fundamental absorption edge of the i-GaAs layers. And the beat is observed clearly. Fig. 1(b) shows the PR spectra of sample S0, S1, and S5 also exhibit oscillations above GaAs bandgap energy. But, the behavior is more complex. Especially, for sample S5, the oscillations are very slow damped and the periods increase as photon energy increases. In Ref 12, the electric field in barrier of quantum dot structure is determined by photoreflectance, using conventional method. Here, we tried to identify it by FFT and FKO airy function fitting methods.

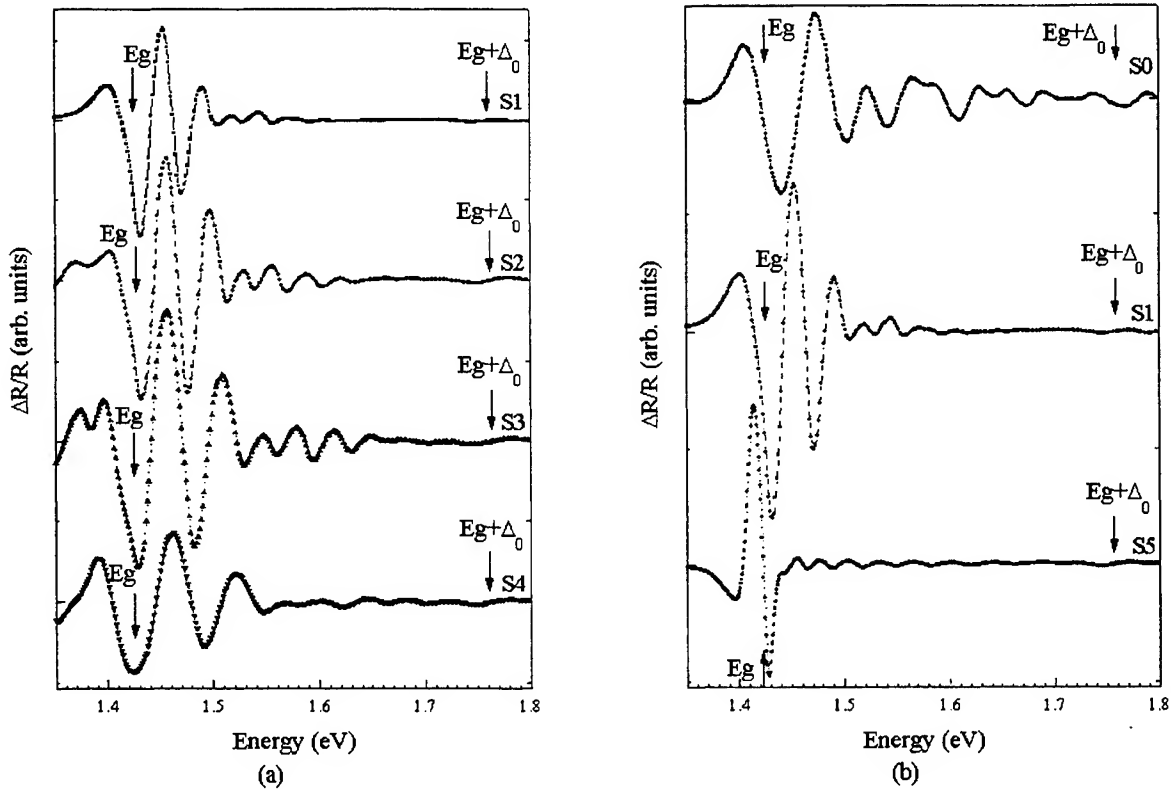


Fig.1 Room temperature PR spectra. (a) samples S1, S2, S3 and S4. (b) sample S0, S1 and S5.

A plot of $\frac{4}{3\pi}(E_n - E_g)^{\frac{3}{2}}$ as a function of index n , for all samples are shown in Fig. 2(a) and (b). Fig. 2(a) shows that t extreme value of the oscillations and linear fit of $\frac{4}{3\pi}(E_n - E_g)^{\frac{3}{2}}$ with n . The results indicate that the electric field is rather uniform in the p - i - n structures and allow to evaluate the electric field accurately. The electron and heavy-hole effective mass (in unit of free electron mass) are 0.066 and 0.930 along (111) direction¹³, respectively. Hence, the electric fields are obtained by Eq. (9). The results are listed in Table I. Fig. 2(b) displays that the plot curves are not straight line obviously

and can not be fitted linearly. The curve displays the slope changed at index number 8. It's reasonable that there are two origination of electric field for i-n⁺-i-p⁺ structure. Therefore, the electric fields are determined by dual straight lines fitting. One is 45.7 kV/cm for index n is less than 8. And the other is 100.3 kV/cm for the rest points. The curve of sample S5 in Fig. 2(b) is like a parabolic line and the slope can not be fitted linearly.

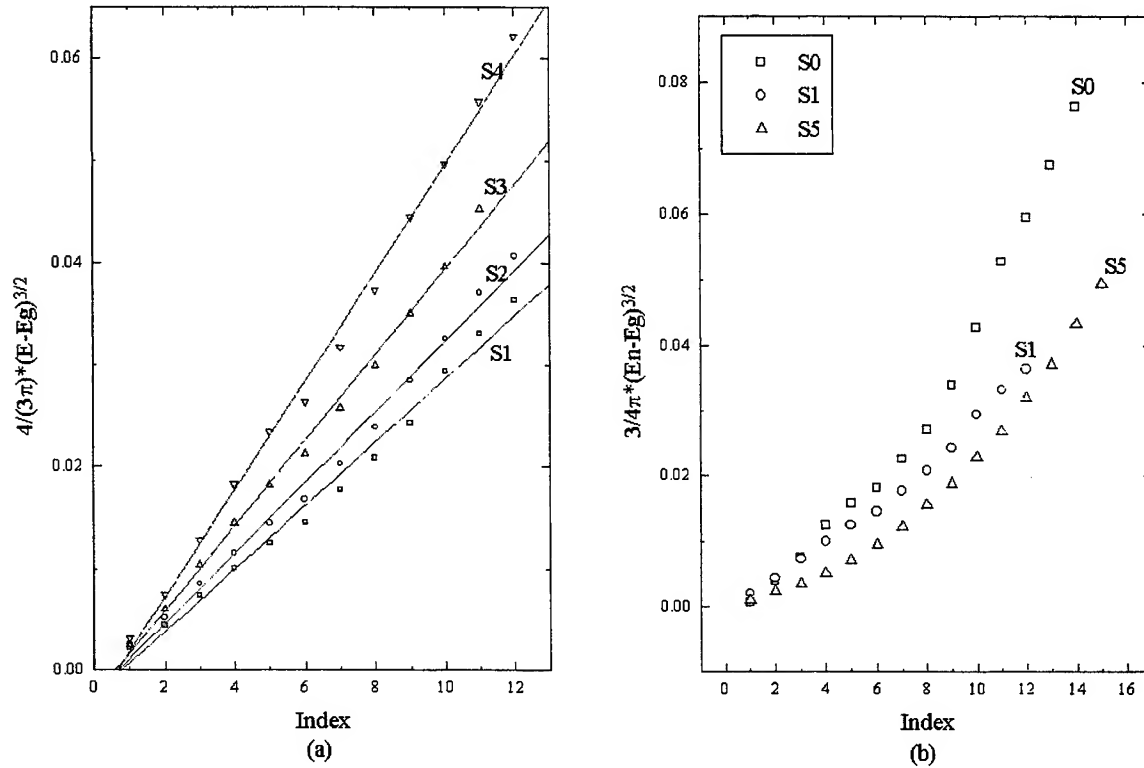


Fig. 2 Extreme values of FKO energy feature on PR spectra versus peak index number

Table I Electric field from conventional method and fast Fourier transform method and the frequency ratio of FFT results.

Sample	Bandgap energy (eV)	Conventional Method	FFT Method	
		Electric Field (kV/cm)	Peak frequency (LH, HH)	Frequency ratio
S0	1.425	45.7, 100.3	(18.0, 24.4) (37.8, 47.5)	1.36 1.26
S1	1.4264	39.1	(51.5, 82.1)	1.59
S2	1.4252	43.0	(45.9, 69.3)	1.51
S3	1.4308	53.7	(36.9, 51.6)	1.40
S4	1.4270	70.7	(29.5, 41.6)	1.41

In order to evaluate the electric field, an alternative way to determine the electric field is to adopt the fast Fourier transform method. The FFT spectra from PR spectra are shown in Fig. 3. The peak frequencies are listed in Table I. The advantages of FFT method are described. Reduced mass is unambiguous in the determination of F . And if there are more than one field existing in the signals, they can be resolved in the transformed spectra. The ratio between peak frequencies for light-hole and heavy-hole in same electric field strength is expressed by

$$\frac{f_{HH}}{f_{LH}} = \sqrt{\frac{\mu_{HH}}{\mu_{LH}}} \quad (12)$$

The ratio of peak frequencies range between 1.31 and 1.39. The values are larger than that as electric field along (001) direction. It is comparable with sample S3 and S4. However, for sample S1 and S2, the ratio is too large. The reason is that the FFT spectra of S1 and S2 are broadening, the peak frequencies can not be determined precisely. The effect of broaden may be due to the modulation electric field strength δF . The variation of the dielectric constant is proportional to $\Delta\epsilon(E, F) - \Delta\epsilon(E, F - \delta F)$. When δF is comparable with the built-in electric field, F is almost cancelled by δF . Due to high resolution of FFT spectra for low electric field, the difference between peak frequencies correspond to F and $F - \delta F$ become distinguishable. It is clearly shown in Fig. 3(a). The more field strength of the built-in electric is, the less bandwidth of the broadening phenomena to be shown in FFT spectra. Two peak frequencies are displayed in this figure. The calculated field strengths of the built-in in this sample are 590.6 and 82.3 kV/cm.

Theoretically, there are two electric field strengths in sample S0 because of the $i-n^- - i-p^+$ structure. And Fig. 3(b) display apparently four well resolved peak with frequency 17.99, 24.38, 37.81 and 47.46. And the electric field strengths are calculated as 116.6, 108.0, 53.1, and 55.5, respectively. Again, for sample S5, the FFT spectrum has different feature from other samples.

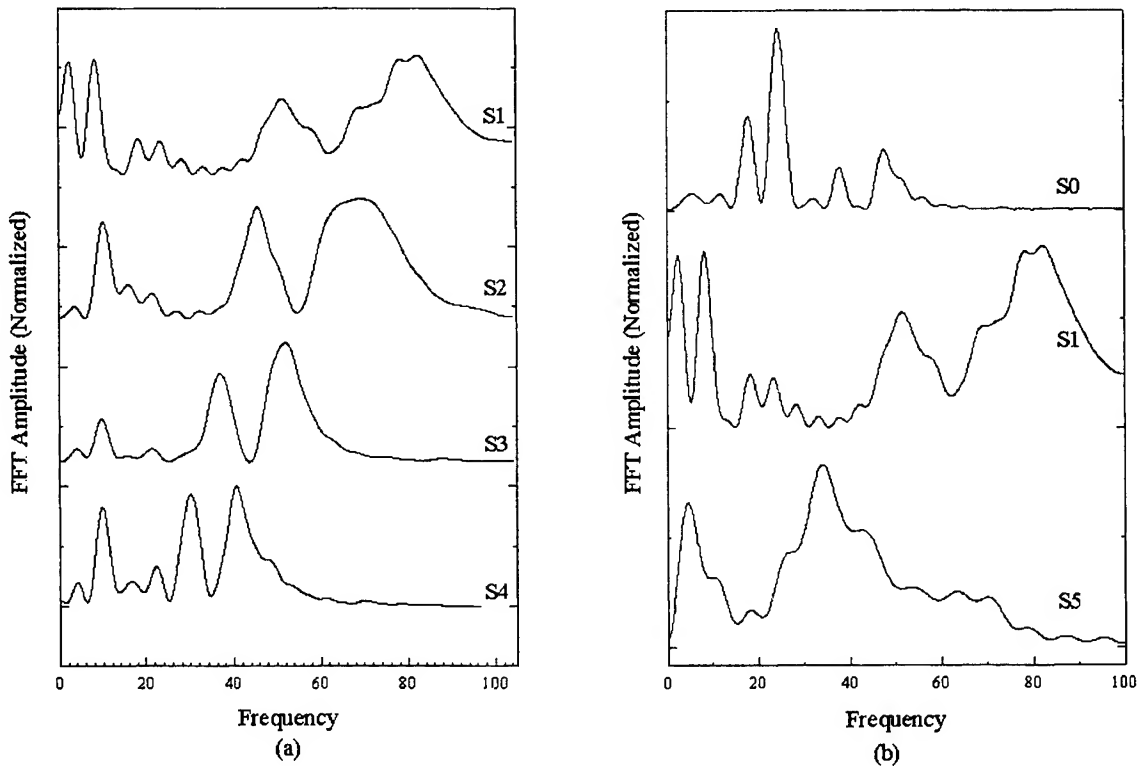


Fig. 3 FFT spectra are transferred from PR spectra for all samples.

Using lineshape function fitting method, the electric fields can be obtained. The reduced masses of light- and heavy-hole are 0.034 and 0.0585 for sample S0, and 0.0625 and 0.0322 for sample S1 to S4. The spectra are fitted by first derivative Gaussian function and two FKO airy functions for all samples. Theoretically, samples S1 to S4, there is only one electric field in $p-i-n$ structure. However, the error is large, if only use one FDGF and one FKO airy function to fit the PR spectra. The fitted spectra are displayed in Fig. 4. In the figure, the solid lines are fitting curves. The parameters obtained by

fitting PR spectra are listed in Table II. For sample S1 to S4, the electric fields F_1 are consistent with the results of conventional and FFT methods. But, the origination of the electric fields F_2 are still unknown.

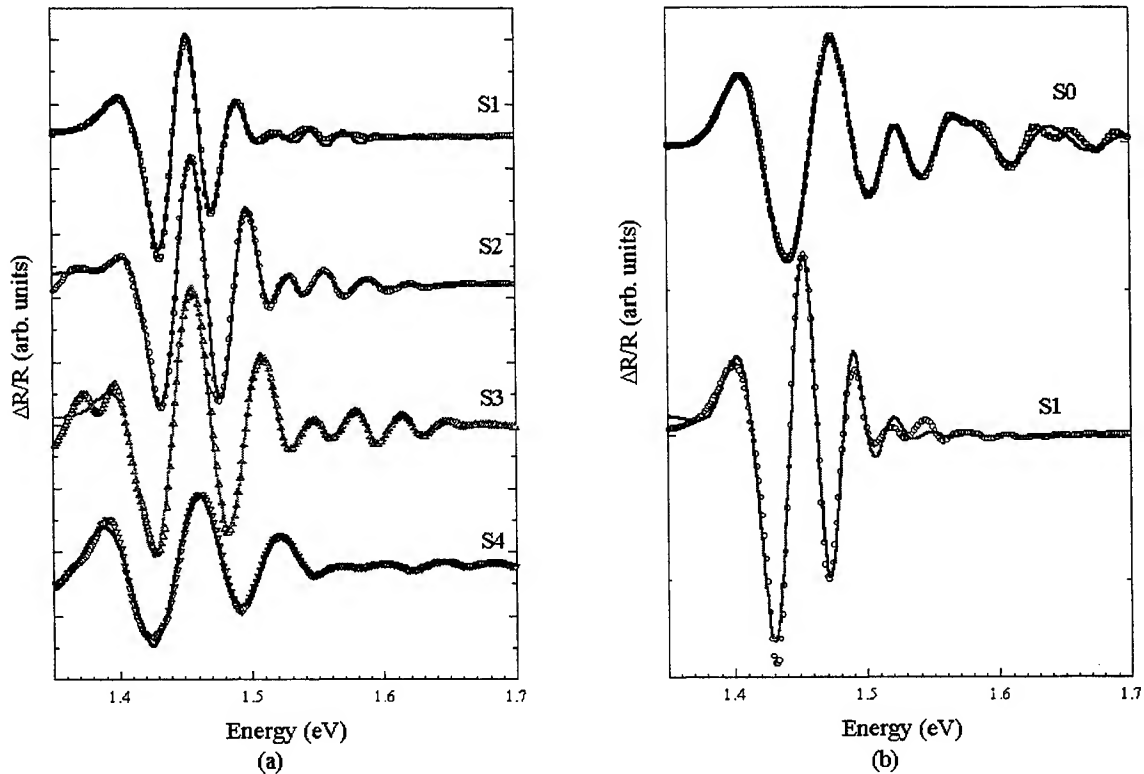


Fig. 4 Lineshape function fit of FKO from PR spectra. The solid lines are fitting curves.

Table II The electric field strength (kV/cm units) obtained by conventional, FFT and FKO airy function fitting methods.

Samples	FKO Airy function fit		Conventional method	FFT method	
	F_1	F_2	F	$F(LH)$	$F(HH)$
S0	93.5	41.4	45.7 100.3	53.1 108.0	55.5 111.6
S1	34.7	18.1	39.1	37.9	33.1
S2	41.6	23.9	43.0	42.6	39.3
S3	55.0	35.7	53.7	52.9	52.7
S4	69.1	45.6	70.7	66.2	65.4
S5	---	---	---	424.0 59.1	590.6 82.3

5. SUMMARY

Photoreflectance has been measured on InGaAs/GaAs multiple strained quantum wells, $i-n^- - i-p^+$ homostructure as well as InAs/GaAs quantum dots samples at room temperature. Based on FKOs features above the energy band gap, the built-in electric field was studied by conventional FKOs calculation, Fast Fourier Transform (FFT) and FKOs line-shape fit techniques. The results of InGaAs/GaAs multiple quantum wells and $i-n^- - i-p^+$ structure are in agreement by these three methods. However, the oscillations in quantum dots structure can not be identified by FKO theory, the origination is not clear and should be studied in future.

ACKNOWLEDGE

This research work was sponsored by the grants NSC89-2115-E-002-022 from National Science Council, the Republic of China.

REFERENCES

1. X. Yin, H. M. Chen, F. H. Pollak, Y. Chan, P. A. Montano, P. D. Kirchner, G. D. Pettit and J. M. Woodall, "photoreflectance study of surface Fermi level at (001) n- and p-type GaAs surfaces ", *J. Vac. Sci. Technol.* **A10**, 131, 1992.
2. H. Shen, M. Dutta, L. Fotiadis, P. G. Newman, R. P. Moerkirk, W. H. Chang and R. N. Sacks, "Photoreflectance study of surface Fermi level in GaAs and GaAlAs ", *Appl. Phys. Lett.* **57**, 2118, 1990.
3. T. J. C. Hosea, D. Lancefield and N. S. Garawal, "Detailed analysis of room-temperature photoreflectance of strained $\text{In}_x\text{Ga}_{1-x}\text{As}/\text{Al}_y\text{Ga}_{1-y}\text{As}$ undoped single quantum wells", *J. Appl. Phys.* **79**, 4338, 1996
4. X. Yin, H. M. Chen, F. H. Pollak, Y. Chan, P. A. Montano, P. D. Kirchner, G. D. Pettit and J. M. Woodall, "Photoreflectance study of surface photovoltage effect at (100) GaAs surfaces/interfaces", *Appl. Phys. Lett.* **58**, 260, 1991.
5. V. M. Airaksinen and H. K. Lipsanen, "Photoreflectance study of photovoltage effects in GaAs diode structures ", *Appl. Phys. Lett.* **60**, 2110, 1992
6. V. L. Alperovich, A. S. Jaroshevich, H. E. Scheibler, and A. S. Terekhov, "Determination of built-in electric fields in delta-doped GaAs structures by phase-sensitive photoreflectance.", *Solid-State Electron.* **37**, 657, 1994.
7. D. P. Wang and C. T. Chen, "Fast fourier transform of photoreflectance spectroscopy of δ -doped GaAs", *Appl. Phys. Lett.* **67**, 2069, 1995.
8. H. Shen and F. H. Pollak, "Generalized Franz-Keldysh theory of eletromodulation", *Phys. Rev.* **B42**, 7097, 1990.
9. R. N. Bhattacharya, H. Shen, P. Parayanthal, F. H. Pollak, T. Coutts, and H. Aharoni, "Electroreflectance and photoreflectance study of the space-charge region in semiconductors: (In-Sn-O)/InP as a model system", *Phys. Rev.* **B37**, 4044, 1988.
10. D. J. Hall, T. J. C. Hosea, and D. Lancefield, "Airy fuction analysis of Franz-Keldysh oscillations in the photoreflectance spectra of $\text{In}_{1-x}\text{Ga}_x\text{As}_y\text{P}_{1-y}$ layers", *J. Appl. Phys.* **82**, 3092, 1997.
11. C. H. Chan, M. C. Chen, H. H. Lin, Y. F. Chen, and G. J. Jan, "Characterization of piezoelectric (111)B InGaAs/GaAs p-i-n quantum well structures using photoreflectance spectroscopy", *Appl. Phys. Lett.* **72**, 1208, 1998.
12. V. Davydov, I. Ignatiev, H.-W. Ren, S. Sugou, and Y. Masumoto, "Observeation of built-in electric field in InP self-assembled quantum dot systems", *Appl. Phys. Lett.* **74**, 3002, 1999.
13. P. Pfeffer and W. Zawadzki, "Five level k dot p model for the conduction and valence bands of GaAs and InP", *Phys. Rev.* **B53**, 12813, 1995.

Metastable photoluminescence in heavily Mg-doped GaN grown by metalorganic chemical vapor phase epitaxy

C. K. Shu, W. H. Lee, Y. C. Pan, H. Y. Huang, H. H. Chen, W. H. Chen, W. K. Chen, and M. C. Lee

Department of Electrophysics, National Chiao Tung University, Hsinchu, 300, Taiwan, R. O. C.

ABSTRACT

The long-term transient spectra of heavily Mg-doped GaN have been investigated. As the excitation power density increased, the broad Mg-induced emission band showed blue-shift revealing characteristic of donor-acceptor pair (DAP) recombination. We also observed an unusually slow intensity decay. The characteristic time constants range from several tenths to a few hundred seconds for emission between 360 and 460 nm. Our results are interpreted in terms of metastability due to compounded effects of differential DAP population and recombination rates and uneven acceptor distribution.

Keywords: Metastable, Mg-doped GaN, Photoluminescence

1. INTRODUCTION

Since the breakthrough of p-type doping in GaN-based materials, high brightness blue/green light emitting devices have been commercially available.^{1,4} However, it is difficult to avoid defects and impurities during material growth. To identify and even eliminate the defects are thus very needed. In recent years, some interesting phenomena related to various defects have been reported.⁵⁻⁹ For instance, the persistent photo-conductivity is one that can be attributed with meta-stability of energy levels within band gap.^{5,6,9} The photoluminescence (PL) blue shift with the increasing excitation power is another.^{7,10} In this paper, we report an unusually slow PL intensity reduction of donor-acceptor pair (DAP) recombination in a heavily Mg-doped GaN (GaN:Mg) film. The characteristic time constants range from several tenths to a few hundreds seconds between 360 and 460 nm. Our results are interpreted in terms of meta-stability due to combined effects of differential DAP population and recombination rates, and non-uniform acceptor distribution that is believed to consist of broad sub-bands by overlapping shallow Mg acceptor levels with deep impurity band.

2. EXPERIMENTAL

The GaN:Mg film was grown on the (0001) sapphire substrate at 1075 °C by metalorganic chemical vapor phase epitaxy.¹¹ A 375 Å GaN buffer layer was prepared at 520 °C before the epilayer growth. The Ga and N precursors were trimethyl-gallium (TMGa) and ammonia using the flow rates of 10.3 μ mol/min and 0.7 standard liter per minute, respectively. For Mg doping, bis(cyclopentadienyl)-magnesium (Cp₂Mg) diluted with hydrogen was used at a flow rate of 0.16 μ mol/min that is equivalent to a Cp₂Mg/TMGa mixing ratio of 0.0154. The Mg concentration was determined to be about 4.5×10^{19} cm⁻³ by secondary ion mass spectrometry calibrated with a Mg ion-implanted standard. For the PL measurements, we utilized a He-Cd laser (Kimmon IK 5552R-F) operating at 325 nm for above-band-gap excitation, and a monochromator (ARC PRO-500) and a photomultiplier tube (Hamamatsu R-955) for detection.¹² The samples were held in a closed-cycle refrigerator (APD Cryogenics HC-2) for different temperature measurements between 10 and 350 K. The incident probe power density was varied from 2.5 to 950 W/cm² by optical glass filters neglecting reflection, transmission and scattering parts. The evolution of luminescence intensity at a range from 2.84 to 3.16 eV was also monitored by a fast data acquisition system.

3. RESULT AND DISCUSSION

Fig. 1 shows the PL spectra of GaN:Mg at 21 K with the probe power density increased from 2.5 to 925 W/cm². Only a broad violet-blue emission is observed and its intensity is seen to grow more than 1500 times (see circles in Fig. 2) and not saturated yet. This broad band shows a tail extended beyond 500 nm that represents the overlapping of many unresolved structures. It can be attributed to either free electron- or donor-to-deep Mg-related acceptor (e,dMg⁰ or D⁰, dMg⁰) transitions,¹³ because unintentional donor states are likely present in a heavily doped sample. The Mg-related sub-band has been

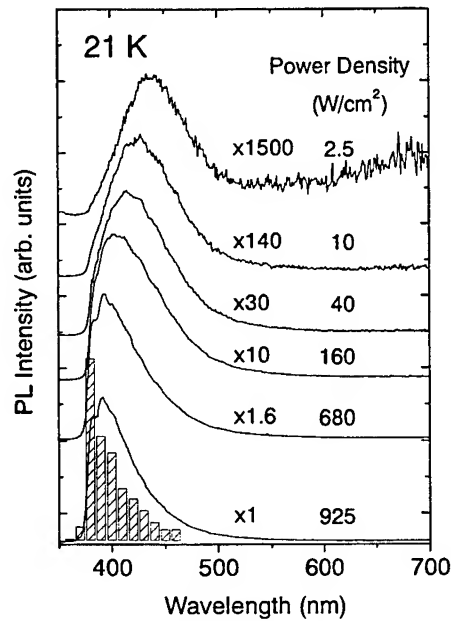


Figure 1. PL spectra of Mg-doped GaN obtained at 21 K ($\lambda=325$ nm) with various probe powers.

reported as deep as 650 meV from the valence band and yet may overlap with the shallow Mg acceptor (Mg^0) levels. It is due to randomly dispersed deep acceptors,¹⁴ defects and impurities (such as V_{Ga} , V_{N} , Mg_{Ga} , O_{N} and Mg-complexes).^{7,8,15-17} As the probe power increases, the emission profile appears less symmetric and skews towards shorter wavelength with a narrower line width. Such an excitation induced blue-shift from 2.82 to 3.16 eV (see squares in Fig. 2) reveals the DAP characteristics,¹⁸ that is opposite to the temperature induced red-shift from band gap renormalization.¹⁹

The small peak around 392 nm on top of the broad band (in high power spectra) is assigned to the DAP one-phonon rep-

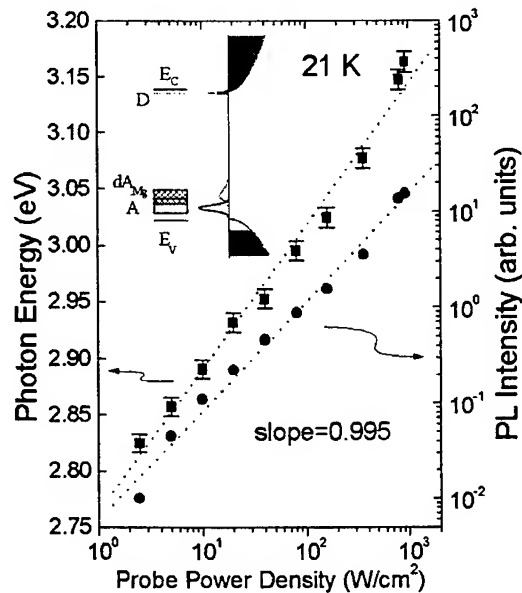


Figure 2. PL peak positions (linear) and intensities (logarithmic) vs. excitation powers in logarithmic scale. The inset shows schematically picture of the energy levels involved in the transition on the left and the corresponding distribution of states on the right.

lica,^{10,20,21} since the barely resolved shoulder at 382 nm is commonly referred to the DAP zero-phonon line.^{22,23} They involve the shallow (Mg^0) levels about 220 meV from valence band edge. To interpret the excitation induced blue shift and intensity variation, we propose in the inset of Fig. 2, a schematic energy diagram on the left with the corresponding density of states on the right. Both shallow and deep sub-bands in this diagram play important roles in the spectral distribution of the violet-blue emission. Under low probe powers, the DAPs are scarce with large separation ($>30 \text{ \AA}$, considering the Coulomb interaction, $E_{DA}=E_g-E_D-E_A+e/4\pi\epsilon r_{DA}$) so that recombination is weak and in the long wavelength range as if the deep sub-band dominates the transitions. On the other hand, more localized ($<15 \text{ \AA}$) DAPs are excited under high probe powers to give off strong emission at short wavelength as if the shallow sub-band becomes dominant.

Besides, we observed the intensity reduction of the broad violet-blue emission on a time scale of several tenths to a few hundreds seconds, and found that the schematic diagram mentioned above is helpful to elucidate this behavior. The intensity evolution was monitored every 10-nm across this band under the fixed excitation of 925 W/cm^2 of which only six lines are shown in Fig. 3. Through constant pumping, photo-excited electrons will either undergo free-to-bound, or relax to the shallow donor levels first and then recombine with holes in both shallow and deep sub-bands. Because of local minimum energy,²⁴ electrons trapped in the deep sub-band usually relax slowly to the shallow sub-band and valence band. However, they may be re-excited by the continuous pumping and thus the overall recombination rate varies with time. This meta-stable behavior can be modeled by a simple two-intermediate-band system (using coupled rate equations) in which electron transition rate is approximately given by,

$$I = A_0 + A_1(1 - e^{-t/\tau_1}) + A_2e^{-t/\tau_2} + A_3e^{-t/\tau_3}, \quad (1)$$

where τ_1 is the rising time constant, τ_2 and τ_3 are the decay time constants, respectively.

As an illustration, we have simulated the upper part of the intensity evolution at 400 nm in Fig. 3. The circles are the experimental data and the solid line represents the least-square fit by adopting a tri-exponential function that looks extremely good. The temporal behavior can be divided into two parts, in the first 10 seconds the PL intensity increases rapidly with a time constant of $\tau_1 = 1/k_1 = 1$ second, and afterwards it decreases slowly with two decay constants of $\tau_2 = 1/k_2 = 39$

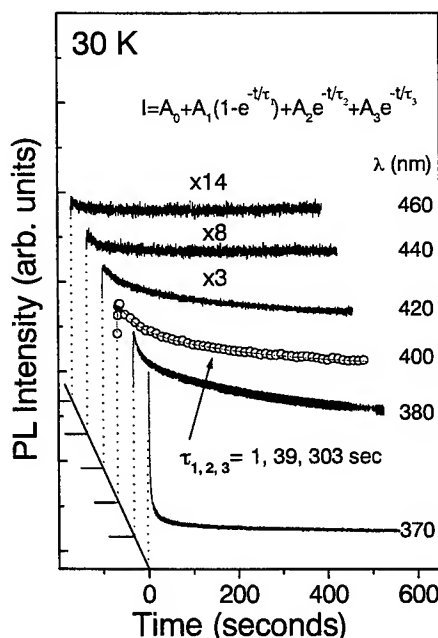


Figure 3. PL intensity reduction at different spectral positions. The solid curve at 400 nm is a fitting with equation

$$I = A_0 + A_1(1 - e^{-t/\tau_1}) + A_2e^{-t/\tau_2} + A_3e^{-t/\tau_3}.$$

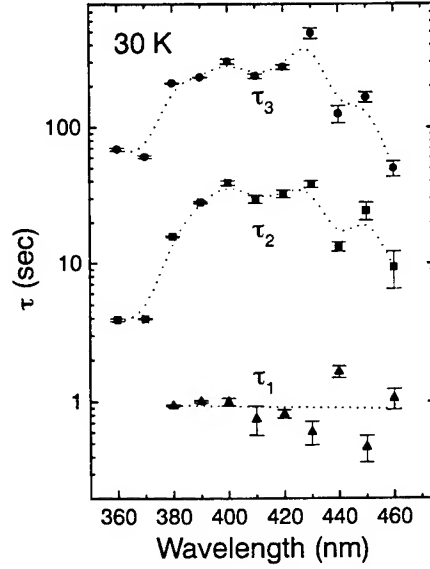


Figure 4. Three characteristic time constants for emission lines between 360 and 460 nm.

and $\tau_3 = 1/k_3 = 303$ seconds. The fittings for other wavelengths are also very good and their characteristic time constants are summarized in Fig. 4, in which three time constants (τ_1 to τ_3) between 390 and 430 nm are in the same order range as those at 400 nm except that at 360, 370 and 460 nm. For emission below 380 nm, the rising portion disappears and its decay time constants (τ_2 and τ_3) are almost one order of magnitude shorter than those above 390 nm. Thus, the recombination mechanisms for shallow sub-band are different from deep one. From Eq. (1) the products $A_1\tau_1$, $A_2\tau_2$ and $A_3\tau_3$ represent the time integrated intensities. Fig. 5 shows the emission energy dependence of the three components ($A_1\tau_1$, $A_2\tau_2$, $A_3\tau_3$) extracted from a series of decay curves. The profile of the rising component $A_1\tau_1$ looks like an exponential function versus wavelength. However, we cannot detect the $A_1\tau_1$ at the 360 and 370 nm, because the short decay time τ_2 (~4 sec) overshadows the rising time τ_1 at the same wavelength. The $A_2\tau_2$ profile resembles closely to the $A_3\tau_3$ profile and indicates that the decay components τ_2 and τ_3 represent the similar recombination deep traps. The asymmetric profile of $A_2\tau_2$ or $A_3\tau_3$ also reflects in the highest excitation spectrum of Fig. 1 about 390 nm.

On the other hand, different time constants would cause serious distortion in the spectral line shape, especially when one uses a scanning spectrometer combined with a single channel detector (photo-multiplier tube, PMT). Since it may take 5 to 15 minutes to acquire a typical PL spectrum, the final spectral distribution will be dominated by the emissions having long time constants. We show such an effect as the crosshatched area in Fig. 1, where the histograms of the integrated PL intensity over a 10-second period in the interval from 50 to 150 seconds are drawn from the emissions displayed in Fig. 3. Evidently, the main portion of luminescence is from emissions having long time constants. In order to correct the aforementioned spectral distortion, it is preferable to use a multi-channel detector that is able to record signals simultaneously over a wide spectral range. Besides, a proper integration time is very crucial for a true spectrum without significant distortion. If the multiple exposure method were used, one could even obtain the temporal evolution of the entire spectral distortion.

Regarding the time constant variation, there are at least two factors involved in the DAP recombination rate. First, the sub-band distribution is not necessarily flat, but likely bulging at roughly the sub-band minimum (see the inset of Fig. 2). This means that more DAPs available for the transition to occur at higher energy than lower energy. Under the same pumping power, it will take longer time for the intensity to reduce that is actually reflected by the longer time constants between 430

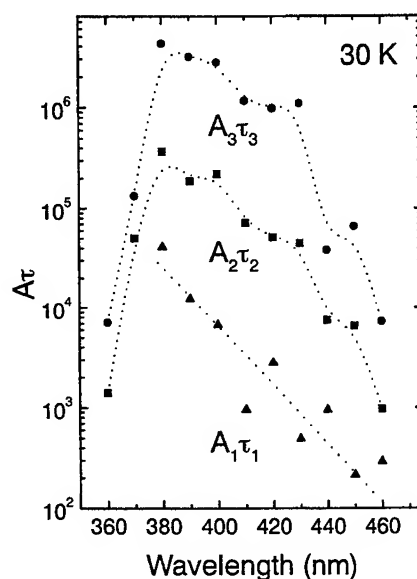


Figure 5. The time integrated intensities $A_1\tau_1$, $A_2\tau_2$ and $A_3\tau_3$ for emission lines between 360 and 460 nm.

and 390 nm. Secondly, the recombination rate for the high energy DAPs is greater than that for the low energy pairs because of smaller separation. Greater transition rate causes faster intensity reduction and hence shorter time constant as shown by $\tau_2 = 16$ seconds at 380 nm.

The long decay times indicate that electrons or holes are likely trapped into metastable states. We believe that the slow PL intensity reduction at 30 K is due to finite unoccupied acceptors in the sub-band. Once the pumping starts DAP recombination, the population of unoccupied acceptors begins to deplete and hence reduces the number of DAPs for transitions. This gradually quenches the recombination process and diminishes the luminescence intensity. At room temperature, the intensity reduction is insignificant, instead it is observed to rise at the commencement of pumping. As the time goes by, it rises further and eventually reaches the plateau of steady state. We have measured a very long characteristic time of 650 seconds at 450 nm and noticed that the emission color changes gradually from violet to blue (observable with naked eye). It can be attributed to thermal quenching of unoccupied acceptors in the sub-bands which limits the DAP recombination rate and forces an equilibrium state of pumping and de-excitation to prevail.

4. SUMMARY

In conclusion, we have observed the power dependent blue-shift and intensity variation in Mg-doped GaN film that suggest DAP transition characteristics. Luminescence intensity decay was studied at 30 K with the time constants varying from a few to several hundreds seconds for emission between 360 to 460 nm. The transition mechanism and influencing factors involved in the violet-blue emission were discussed in terms of metastability due to compounded effects of uneven acceptor distribution and differential DAP population and recombination rate.

ACKNOWLEDGMENTS

The authors wish to acknowledge the support by the National Science Council of Republic of China under contract numbers NSC88-2112-M009-021, 022 and 031.

REFERENCE

1. Proceedings of The Second International Conference on Nitride Semiconductors, ICNS'97, Tokushima, Japan, Oct. 27-31, 1997.
2. M. Kneissl, D. P. Bour, N. M. Johnson, L. T. Romano, B. S. Krusor, R. Donaldson, J. Walker, and C. Dunnrowicz, "Characterization of AlGaInN diode lasers with mirrors from chemically assisted ion beam etching," *Appl. Phys. Lett.* **72**, 1539, 1998.
3. Proceedings of The Second International Symposium on Blue Laser and Light Emitting Diodes, 2nd ISBLLED, Kisarazu, Chiba, Japan, p 371, Sep. 29 - Oct. 2, 1998.
4. S. Nakamura, M. Senoh, N. Iwasa, S. Nagahama, T. Yamada, and T. Mukai, *Jpn. J. Appl. Phys. Part 2* **34**, L1332, 1995.
5. M. T. Hirsch, J. A. Wolk, W. Walukiewicz, and E. E. Haller, "Persistent photoconductivity in n-type GaN," *Appl. Phys. Lett.* **71**, 1098, 1997.
6. C. Johnson, J. Y. Lin, H. X. Jiang, M. Asif Khan, and C. J. Sun, "Metastability and persistent photoconductivity in Mg-doped p-type GaN," *Appl. Phys. Lett.* **68**, 1808, 1996.
7. U. Kaufmann, M. Kunzer, M. Maier, H. Obloh, A. Ramakrishnan, B. Santic, and P. Schlotter, "Nature of the 2.8 eV photoluminescence band in Mg doped GaN," *Appl. Phys. Lett.* **72**, 1326, 1998.
8. E. Oh, H. Park, and Y. Park, "Excitation density dependence of photoluminescence in GaN:Mg," *Appl. Phys. Lett.* **72**, 70, 1998.
9. J. Z. Li, J. Y. Lin, H. X. Jiang, A. Salvador, A. Botchkarev, and H. Morkoc, "Nature of Mg impurities in GaN," *Appl. Phys. Lett.* **69**, 1474, 1996.
10. L. Eckey, U. von Gfug, J. Holst, A. Hoffmann, A. Kaschner, H. Siegle, C. Thomsen, B. Schineller, K. Heime, M. Heuken, O. Schön, and Beccard, "Photoluminescence and Raman study of compensation effects in Mg-doped GaN epilayers," *J. Appl. Phys.* **84**, 5828, 1998.
11. H. C. Lin, C. K. Shu, J. Ou, Y. C. Pan, W. K. Chen, and M. C. Lee, "Growth temperature effects on $\text{In}_x\text{Ga}_{1-x}\text{N}$ films studied by X-ray and photoluminescence," *J. Cryst. Growth*, **189-190**, 57, 1998.
12. C. K. Shu, J. Ou, H. C. Lin, W. K. Chen, and M. C. Lee, "Isoelectronic In-doping effect in GaN films grown by metalorganic chemical vapor deposition," *Appl. Phys. Lett.* **73**, 641, 1998.
13. D. J. As, T. Simonsmeier, B. Schöttker, T. Frey, D. Schikora, W. Kriegseis, W. Burkhardt, and B. K. Meyer, "Incorporation and optical properties of magnesium in cubic GaN epilayers grown by molecular beam epitaxy," *Appl. Phys. Lett.* **73**, 1835, 1998.
14. H. C. Casey, Jr., J. Muth, S. Krishnakutty, and J. M. Zavada, "Dominance of tunneling current and band filling in In-GaN/AlGaIn double heterostructure blue light-emitting diodes," *Appl. Phys. Lett.* **68**, 2867, 1996.
15. J. Neugebauer and C. G. Van de Walle, "Atomic geometry and electronic structure of native defects in GaN," *Phys. Rev. B* **50**, 8067, 1994.
16. M. Smith, G. D. Chen, J. Y. Lin, H. X. Jiang, A. Salvador, B. N. Sverdlov, A. Botchkarev, H. Morkoc, and B. Goldenberg, "Mechanisms of band-edge emission in Mg-doped p-type GaN," *Appl. Phys. Lett.* **68**, 1883, 1996.
17. P. Boguslawski, E. L. Briggs, and J. Bernholc, "Native defects in gallium nitride," *Phys. Rev. B* **51**, 8067, 1995.
18. P. Y. Yu, M. Cardona, *Fundamentals of Semiconductors - Physics and Materials*, Springer-Verlag Berlin Heidelberg, New York, p. 344-349, 1996.
19. J. M. Myoung, K. H. Shim, C. Kim, O. Gluschenkov, K. Kim, S. Kim, D. A. Tumbull, and S. G. Bishop, "Optical characteristics of p-type GaN films grown by plasma-assisted molecular beam epitaxy," *Appl. Phys. Lett.* **69**, 2722, 1996.
20. G. Popovici, G. Y. Xu, A. Botchkarev, W. Kim, H. Tang, A. Salvador, H. Morkoc, R. Strange, and J. O. White, "Raman scattering and photoluminescence of Mg-doped GaN films grown by molecular beam epitaxy," *J. Appl. Phys.* **82**, 4020, 1997.
21. S. Fischer, C. Wetzel, E. E. Haller, and B. K. Meyer, "On p-type doping in GaN-acceptor binding energies," *Appl. Phys. Lett.* **67**, 1298, 1995.
22. M. Leroux, B. Beaumont, N. Grandjean, P. Lorenzini, S. Haffouz, P. Vennéguès, J. Massies, P. Gibart, "Luminescence and reflectivity studies of undoped, n- and p-doped GaN on (0001) sapphire," *Mater. Sci. Eng.* **B50**, 97, 1997.
23. G. P. Yablonskii, A. L. Gurskii, E. V. Lutsenko, I. P. Marko, B. Schineller, A. Guttzeit, O. Schön, M. Heuken, K. Heime, R. Beccard, D. Schmitz, and H. Juergensen, "Optical properties and recombination mechanisms in GaN and GaN:Mg grown by metalorganic vapor phase epitaxy," *J. Elec. Mater.* **27**, 222, 1998.
24. P. Bäume, J. Gutowski, D. Wiesmann, R. Heitz, A. Hoffmann, E. Kurtz, D. Hommel, and G. Landwehr, "Intensity-dependent energy and line shape variation of donor-acceptor-pair bands in ZnSe:N at different compensation levels," *Appl. Phys. Lett.* **67**, 1914, 1995.
25. A. A. Istratov, and O. F. Vyvenko, "Exponential analysis in physical phenomena," *Rev. Sci. Instr.* **70**, 1233, 1999.

ZnSe/Si growth by liquid phase deposition

Min Yen Yeh, Hung Ming Yen
Department of Electronic Engineering
Yung-Ta Institute of Technology & Commerce
Ping-Tung, 90902, Taiwan

ABSTRACT

ZnSe is an important semiconductor material with a large bandgap (2.68 eV), which has the potential to be used for photoluminescent and electroluminescent devices and for window layer of solar cells. In this work, a low-cost and large-area growth method for ZnSe layer on Si substrate was studied by liquid phase deposition (LPD). The micrograph of the surface shows specular, but a roughness surface texture is obtained. The island texture could be improved by raising growth temperatures. The crystallinity could be improved by the growth temperature considerations. High resistivity and specular layers were obtained as grown at room temperature. The abrupt interface resulted from less interdiffusion between ZnSe layers and substrates was reasonable under the growth condition at room temperatures.

Keywords: Liquid phase deposition, ZnSe, Si substrate

1. INTRODUCTION

ZnSe with a direct band gap of 2.68 eV at room temperature has received considerable attention for light emitting devices such as blue LEDs and short wavelength lasers. ZnSe has been prepared on various closely lattice-matched substrates, such as GaAs and ZnSe. However, the Ga atom diffusion into the ZnSe epilayer from the GaAs substrate is an unintentional impurity source which leads to a broad band in photoluminescence spectra.¹ A high-quality and large-area ZnSe wafer for homodeposition is still not available. Presently, device-quality and large-area silicon wafers are readily available. Silicon as a substrate inherently possesses good mechanical strength and thermal conductivity in comparison with GaAs and ZnSe substrates. Besides, silicon-related semiconductor technology has been highly developed. Therefore, ZnSe based on a Si substrate system which combines optical devices with VLSI-Si devices into optoelectronic integrated circuits (OEICs) has attracted much interest. High quality ZnSe has been successfully obtained by organometallic chemical vapor deposition (OMCVD),^{2,3} and molecular beam epitaxy (MBE).^{4,5} Recently, a much attractive method with the possibility of large area deposition at low cost for producing ZnSe thin films is the liquid phase deposition.⁶⁻¹¹ A solution composition $\text{NH}_3/\text{NH}_2\text{-NH}_2/\text{SeC}(\text{NH}_2)_2/\text{Na}_2\text{SO}_3/\text{ZnSO}_4$ is used for ZnSe thin films deposition by LPD. The mechanism of the deposition process is briefly illustrated as followed. The characterization of the as deposited ZnSe thin films on Si substrate including electrical, optical, crystallinity, and compositional studies is presented.

2. EXPERIMENTAL

In this work, (100) 25-45 Ω -cm p-type Si substrates were used. Prior to growth, the Si substrate was chemically cleaned by degreasing in solvents followed by repeated chemical oxidation and etching in acidic solutions. Finally, the substrate was dipped in a 10% HF solution for 2 min. The solution chemistry-ZnSe thin films can be prepared by decomposition of selenourea in an alkaline solution containing a zinc salt and a suitable complexing agent. The deposition of ZnSe occurs when the ionic product of Zn^{2+} and Se^{2-} exceeds the solubility product, K_{sp} of the ZnSe. Selenourea is very unstable in aqueous solutions where it tends to oxidize. To avoid this problem, Na_2SO_3 was used as an antioxidant agent and was present in every case. The solutions were prepared using analytical-grade reagents (commercial ZnSO_4 , selenourea, 25% ammonia, and 80% hydrazine hydrate). The Si substrates were placed vertically in a closed beaker where the zinc salt solution was added first to the solution under stirring, and the selenourea solution was added to the reaction vessel only when an appropriate temperature was reached and maintained by means of a temperature-controlled water bath. The growth temperature is kept below 60 $^{\circ}\text{C}$. The depositions occurred with NH_3 concentrations in the range of 0.28 to 3.2 M. The films were grown about 5 to 60 min. The film thickness and surface structure were measured using a scanning electron microscopy (SEM). The crystallinity of these films was examined by conventional and grazing-angle x-ray diffraction (XRD). The film composition was determined by energy dispersive spectroscopy (EDS). From Auger in-depth profile, the interface distributions of ZnSe and Si substrate component can be obtained. The electrical conductivity measurements were made at room temperature using two coplanar evaporated indium electrodes. These electrodes made ohmic contact with the ZnSe thin film.

3. RESULTS AND DISCUSSION

Figure 1(a) shows the SEM surface morphology of the ZnSe/Si(100) grown at room temperature. The micrograph of the surface shows specula, but a roughness texture is observed on the surface. The migration energy of ZnSe clusters seems to be not enough for nucleation on proper Si surface site. The coalesce of ZnSe island clusters is not well completed. The island texture could be improved by raising growth temperature, and this would be further studied in future.

Figure 1(b) indicates the cleaved cross section of ZnSe/Si(100). The interface between the ZnSe layer and Si substrate is abrupt, and the thickness of the overall epilayer is uniform. The deposition of ZnSe films by liquid phase deposition was carried out at the temperatures far below that by OMCVD or MBE. The good interface quality could be observed from the cleavage of ZnSe on Si substrate.

The deposition thickness of ZnSe on Si substrates has been studied for different temperatures (Fig. 2). It can be seen that the deposition process clearly shows a quasilinear and a saturation phase. This saturation phase appears earlier at higher temperatures. This is probably due to the two competitive processes of the film formation and the homogeneous precipitation. It is not necessary to reach an expected thickness of ZnSe films early at a higher growth temperature.

In figure 3 is presented the growth rate dependences on ZnSO_4 and $\text{SeC}(\text{NH}_2)_2$ concentrations. There is an increase of the

growth rate with the increase in quantity of either ZnSO_4 or $\text{SeC}(\text{NH}_2)_2$. However, increase is restricted to the very low concentration and appears to saturate. The suitable species of Zn^{2+} and Se^{2-} doesn't increase with higher concentration of ZnSO_4 and $\text{SeC}(\text{NH}_2)_2$. The growth rate is determined by not only the concentration of ZnSO_4 and $\text{SeC}(\text{NH}_2)_2$, but also that of NH_3 and $\text{NH}_2\text{-NH}_2$.

Figure 4 shows the influences of the NH_3 and the $\text{NH}_2\text{-NH}_2$ concentrations on the growth rates. The dependence of NH_3 is linear. However, as we see that there is an optimum value for the hydrazine concentration to obtain the maximum growth rate. The presence of NH_3 gives the formation of complex $\text{Zn}(\text{NH}_3)_4^{2+}$. The specie is soluble in this medium, preventing the precipitation of $\text{Zn}(\text{OH})_2$. With the presence of $\text{NH}_2\text{-NH}_2$ there will also appear the $\text{Zn}(\text{NH}_2\text{-NH}_2)_3^{2+}$ complex. The $\text{Zn}(\text{NH}_2\text{-NH}_2)_3^{2+}$ complex is in a very low concentration due to its lower equilibrium constant with respect to the $\text{Zn}(\text{NH}_3)_4^{2+}$ equilibrium constant.¹²

The crystallinity of the ZnSe layer was examine by x-ray diffraction method. The x-ray diffraction pattern of ZnSe on Si(100) grown at room temperature is shown in Fig. 5. The results of the x-ray diffraction pattern shows that the polycrystal of ZnSe is obtained by liquid phase deposition grown at room temperature. A further experiment is worth to do to improve the crystallinity of the ZnSe. The parameter of growth temperature could be the major considerations.

An Auger depth profile of a 0.5-um-thick ZnSe on (100)Si substrate prepared at room temperature is shown in Fig. 6. The composition of the as-grown ZnSe layer is uniform. The small transition region shows a sharp interface between ZnSe and Si, which coincides with the observation of SEM cross-section cleavage. The abrupt interface resulted from less interdiffusion between ZnSe layers and substrates was reasonable under the growth condition of room temperature.

4. CONCLUSION

We have obtained the uniform and specular ZnSe thin films on Si by LPD. The poly-crystal of ZnSe is obtained by liquid phase deposition at room temperature. The use of $\text{NH}_2\text{-NH}_2$ as a complementary complexing agent for the classically used NH_3 reaction baths improves the adherence, homogeneity, and the growth rate of the films. The ZnSe thin films obtained by this method seem to come from processes of aggregation of colloidal ZnSe particles formed in the solution.

These characteristics make the LPD a very attractive and inexpensive method for obtaining ZnSe thin films for various applications.

ACKNOWLEDGMENTS

We would like to thank the National Science Council of the Republic of China for the support of this project. (Project No. NSC 88-2215-E-132-001)

REFERENCES

1. T. Yao, M. Ogura, S. Matsuoko, and T. Morishita, *Jpn. J. Appl. Phys.*, **22**, L44(1983).
2. S. Sritharan and K. A. Jones, *J. Cryst. Growth* **68**, 656(1984).
3. N. Shibata, A. Ohki, and S. Zembutsu, *Jpn. J. Appl. Phys.* **26**, 1305(1978).
4. T. Yao, *J. Cryst. Growth* **72**, 31(1985).
5. K. Yoneda, Y. Hishida, T. Tocl, H. Ishii, and T. Niina, *Appl. Phys. Lett.* **45**, 300(1984).
6. G. A. Kitaev and T. P. Sokolova, *Russ. J. Inorg. Chem.*, **15**, 167(1970).
7. G. A. Kitaev, A. A. Uriskaya, and S. G. Mokrushin, *ibid.*, **39**, 1101(1965).
8. I. Kaur, D. K. Pandya, and K. L. Chopra, *J. Electrochem. Soc.*, **127**, 943(1980).
9. D. Lincot and J. Vedel., *10th European Photovoltaic Solar Energy Conf. Lisbon*, P. 931(1991).
10. J. M. Dona and J. Herrero, *J. Electrochem. Soc.*, **139**, 2810(1992).
11. J. M. Dona and J. Herrero, *ibid.*, **141**, 205(1994).
12. R. A. Zingaro, F. C. Bennett, Jr., and G. W. Hammar, *J. Org. Chem.*, **18**, 292(1953).

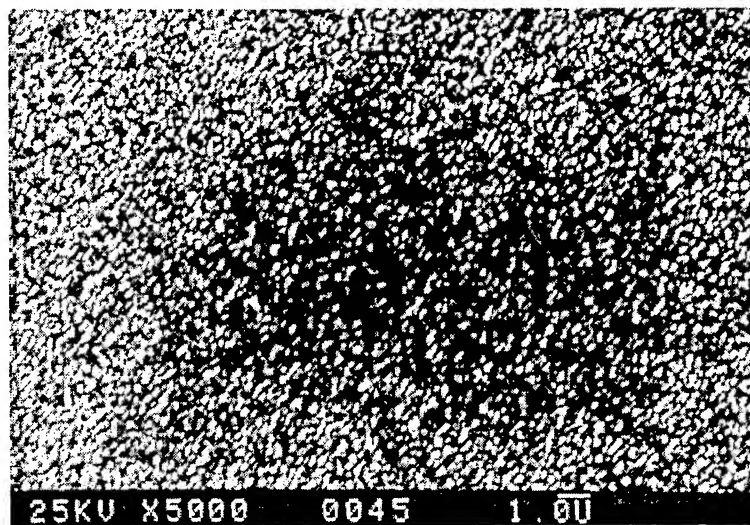


Fig. 1(a) SEM micrograph of ZnSe/Si(100)

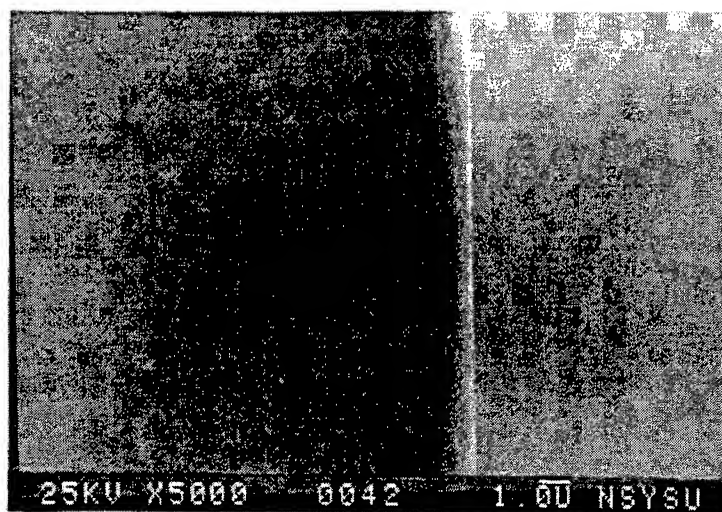


Fig. 1(b) SEM micrograph of ZnSe/Si(100) cleaved cross-section.

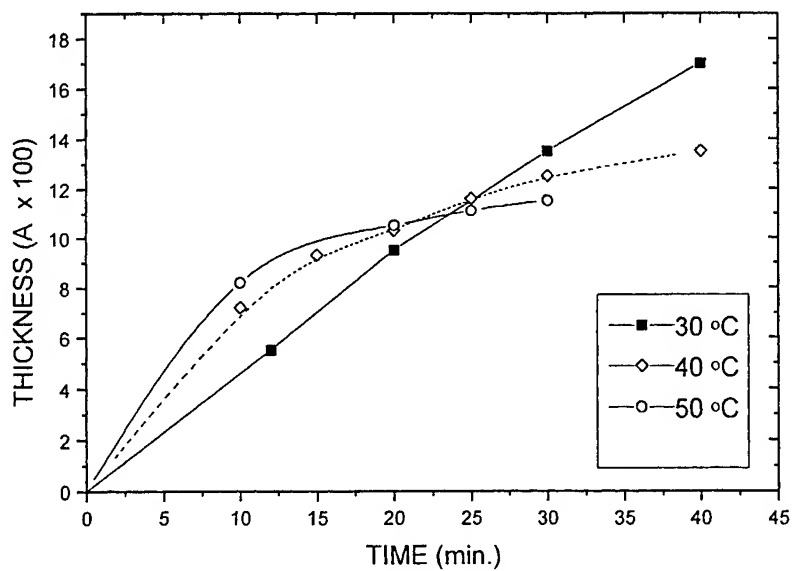


Fig. 2 Thickness variation with time as a function of growth temperatures.

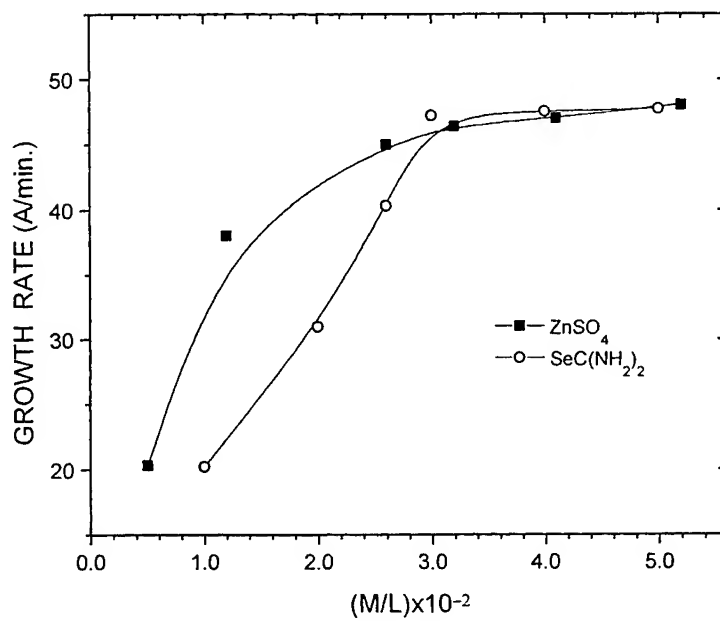


Fig. 3 Growth rate dependences on ZnSO_4 and $\text{SeC}(\text{NH}_2)_2$ concentrations.

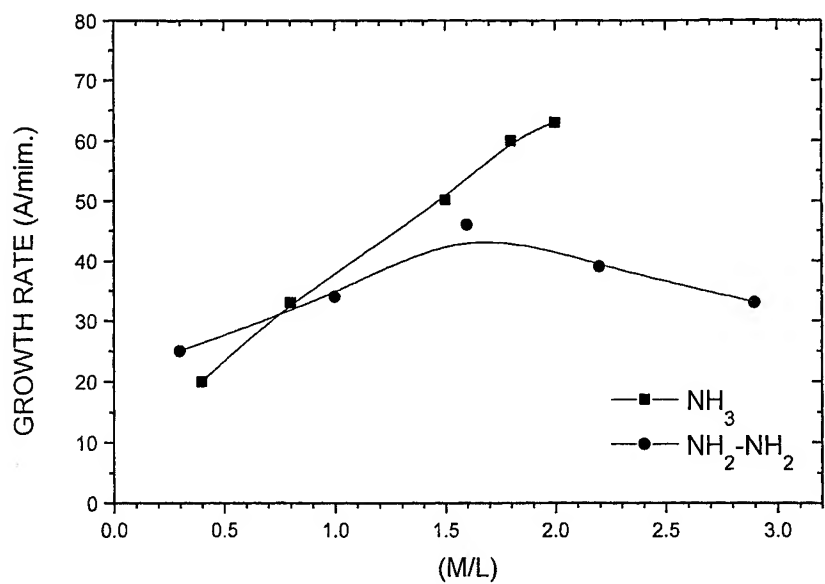


Fig. 4 The influences of the NH_3 and the $\text{NH}_2\text{-NH}_2$ concentrations on the growth rates.

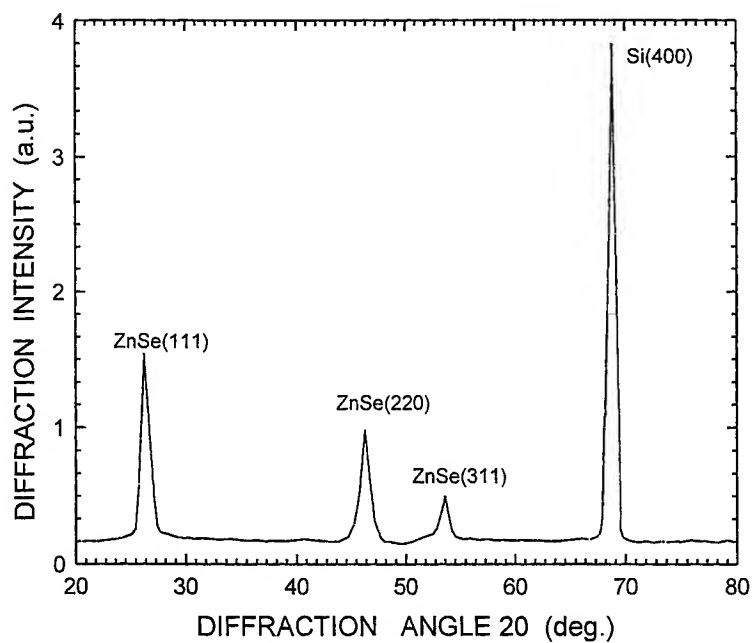


Fig. 5 X-ray diffraction pattern of ZnSe/ Si(100)

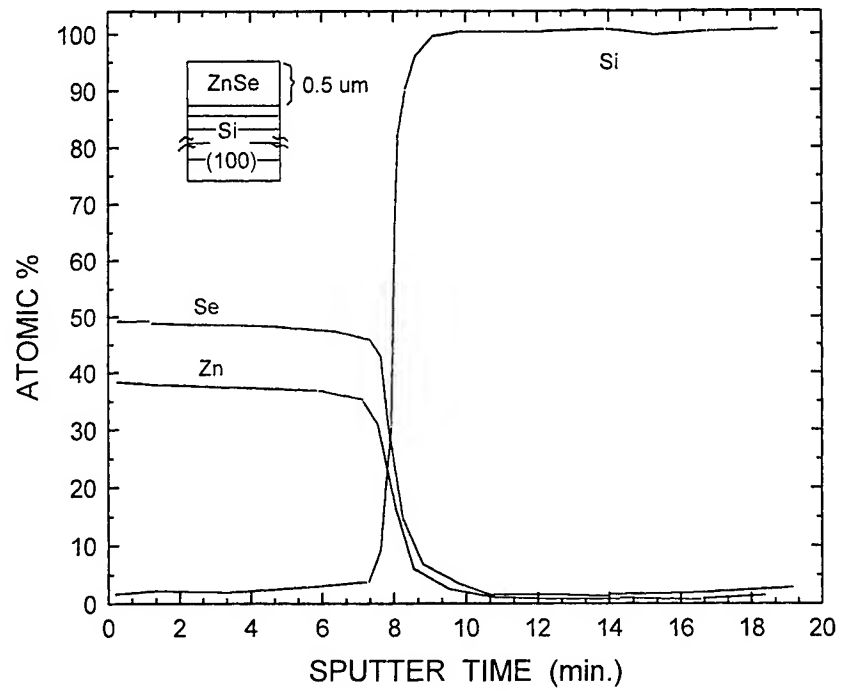


Fig. 6 Auger depth profile of ZnSe/Si(100)

Gallium K-Edge EXAFS Study of GaN:Mg Films

Yung-Chung Pan^a, Shu-Fang Wang^a, Wen-Hsiung Lee^a, Wei-Cherng Lin^a, Chen-Ke Shu^a,
Chung-I Chiang^b, Chin-Hwa Lin^b, Horng Chang^b, Jyh-Fu Lee^c, Ling-Yun Jang^c, Deng-Sung Lin^d,
Ming-Chih Lee^a, Wen-Hsiung Chen^a, and Wei-Kuo Chen^a

^aDepartment of Electrophysics, National Chiao-Tung University, Hsin-Chu, Taiwan, 300, R.O.C

^bChung-Shan Institute of Science & Technology, Tao-Yuan, Taiwan, 325, R.O.C.

^cSynchrotron Radiation Research Center, Hsin-Chu, Taiwan, 300, R.O.C.

^dInstitute of Physics, National Chiao-Tung University, Hsin-Chu, Taiwan, 300, R.O.C.

Abstract

Ga K-edge extended X-ray absorption fine structure (EXAFS) measurement was employed to investigate the local structure of GaN:Mg films grown by metalorganic vapor phase epitaxy (MOVPE) with various Cp_2Mg dopant flow rates using both in-plane and out-of-plane polarization modes of X-ray. The near edge absorption spectra were found to depend on X-ray polarization strongly for undoped GaN sample and weakly to minutely for heavily Mg-doped and amorphous films. The results indicate Mg incorporation modifies the local structure around the absorber Ga atom and, hence, alters the molecular orbital electron transition of GaN sample. EXAFS analysis showed both vacancy and Mg-interstitial defects contribute to the reduction of coordination numbers along the hexagonal *c*-axis of GaN:Mg film.

Keyword : EXAFS, GaN:Mg, MOVPE, polarization, structure, vacancy, interstitial

*Correspondence : E-mail : u8321810@cc.nctu.edu.tw ; Telephone : 886-3-5712121 ext 24426 ; Fax : 886-3-5725230

1. INTRODUCTION

With wide direct band gap and thermal stability, group III-nitride have continuously found applications in short-wavelength light-emitting and detecting, as well as high-temperature and high-power electronic devices.^[1-2] The development of GaN-based devices, such as the brightness blue and green LEDs^[3] and CW blue LDs^[4], have achieved significant breakthrough. However, there still remains many problems for manufacturing high-quality GaN materials. The activation mechanism is one of the important issues for *p*-GaN. Mg dopant can be activated electrically to *p*-type performance by additional thermal process, such as low energy electron beam irradiation (LEEBI)^[5] and thermal annealing (TA)^[6]. However, it is still hard to obtain hole density higher than 10^{18} cm^{-3} in commercial *p*-type epilayer. It is important for Mg impurity to occupy right site to enhance *p*-type conductivity. Owing to about 10%-radius difference between Mg and Ga^[7], a strong local lattice distortion can be expected once a Ga atom is replaced by Mg. Recent study of Si-doped GaN has shown that Si is not randomly distributed in the epilayer using polarized extended X-ray absorption fine structure (EXAFS).^[8] In order to investigate problems of Mg-doped *p*-GaN, we also examined our samples with EXAFS measurement. Analyzing and simulation towards the understanding of the effect of Mg doping on the native defect population and the local microstructure around the Ga atom in epitaxial GaN were then followed.

2. EXPERIMENTAL

All Mg-doped GaN samples (thickness $\sim 0.5\text{-}1 \mu\text{m}$) used in the experiment were grown on (0001) Al_2O_3 substrate by metalorganic vapor phase epitaxy (MOVPE) in atmospheric pressure. Trimethylgallium (TMGa), ammonia (NH_3), and bis(cyclopentadienyl)magnesium (Cp_2Mg) were used as the Ga, N, and Mg sources, respectively. The carrier gas was purified nitrogen. Prior to the epilayer growth, the substrate was preheated for 10 minutes at $1,100^\circ\text{C}$, nitridated for 2 minutes at $1,050^\circ\text{C}$ and then cooled down to 520°C under about 1 slm ammonia flow for the deposition of GaN nucleation layer of about 400\AA -thickness. The GaN:Mg epitaxial layer was grown at $1,075^\circ\text{C}$ using V/III ratio = 3,000 with Cp_2Mg flow rate varying from 0 to $0.79 \mu\text{mol/min}$.

In EXAFS experiment, the samples were oriented to have the hexagonal GaN *c*-axis either perpendicular or parallel to the electric field vector of the incident X-ray, corresponding respectively to in-plane (*i.e.* *E* field in *ab*-plane, or $E \perp c$) and out-of-plane (*i.e.* *E* field along *c*-axis, or $E \parallel c$) cases. Gallium K-edge EXAFS spectra were recorded at the wiggler beamline BL17C at Synchrotron Radiation Research Center (SRRC). The intensity of the incidence beam was measured by a N_2 -filled ionization chamber as reference signal I_0 and the fluorescence emitted from the sample following the absorption of x-ray was measured by a Stern-Heald-Lytle detector with argon gas as the sampling signal I_F . The absorption coefficient μ is proportional to (I_F/I_0) . A Si(111) double-crystal monochromator with a 0.5 mm entrance slit was used for energy scanning. In order to record the spectra for Ga K-edge, a Zn-filter with thickness of 6 absorption length was placed between the sample and the window of the detector. Such an arrangement can efficiently lower the noise level resulting from the scattering of X-rays by the sample or the air.

3. RESULTS AND DISCUSSIONS

The intensity response of near edge X-ray absorption fine structure (NEXAFS) spectrum is very sensitive to the crystal group symmetry and the local structural around the central absorbing atom. The X-ray absorption cross section in an electric dipole approximation is given by

$$I \propto |\langle f | \mathbf{e} \cdot \mathbf{p} | i \rangle|^2 \propto (1/|\mathbf{E}|^2) |\langle f | \mathbf{E} \cdot \mathbf{p} | i \rangle|^2,$$

where \mathbf{e} is a unit vector of the electric field vector \mathbf{E} , \mathbf{p} is the electric dipole operator, $|i\rangle$ is the $1s$ initial core level state and $|f\rangle$ is $2p$ final conduction band states of the transition. For in-plane polarized synchrotron radiation ($\mathbf{E} \perp c$), the X-ray absorption spectrum shows the ab -plane crystalline information. On the other hand, for out-of-plane case ($\mathbf{E} \parallel c$), the spectrum reveals more about the structural information along the crystal c -axis. Samples used in this report includes undoped (u-GaN), various content Mg-doped (GaN:Mg), and amorphous GaN (a-GaN).

Figures 1(a) and 1(b) show the Ga K-edge NEXAFS spectra of the three different GaN samples using respectively the $\mathbf{E} \perp c$ - and the $\mathbf{E} \parallel c$ -axis polarizations. It is found that the NEXAFS profiles of a-GaN are similar in both polarization modes because of their amorphous characteristic. On the other hand, dissimilarities of u-GaN and GaN:Mg NEXAFS spectra are seen in the two polarization modes. The anisotropic distribution of p -partial density of states (p -DOS) (final wave function, $|f\rangle$) in the conduction band between in ab -plane and along out-of- ab -plane (c -axis direction) is expected to consistent in a hexagonal crystal. It is further seen, the NEXAFS oscillation damped in the GaN:Mg case, in particularly, in $\mathbf{E} \parallel c$ -axis polarization direction. This suggests that the influence of Mg impurity along c -axis direction is more serious than in ab -plane. Since our X-ray photon energy covers from 10200 to 11300 eV, it is sufficient to have EXAFS spectra analyzed. The routine pre-edge and atomic absorption subtraction followed by normalization to unit atom scale were performed with AUTOBK program for all samples. A typical Ga K-edge EXAFS spectrum from u-GaN in $\mathbf{E} \parallel c$ -axis polarization, its corresponding k -space oscillation $\chi(k)$ (3.3-14 \AA^{-1}), and Fourier Transform (F.T.) profile of GaN sample are showed in Fig. 2(a), 2(b), and 2(c), respectively. The processed experimental data were plotted in solid line and the fitting curves using FEFF program in dashes. They matched fairly well as can be seen from Figs. 2(b) and 2(c). From Fig. 2(c), the first and second strong features at ~ 1.6 and ~ 2.8 \AA in the F.T. magnitude versus radial distance plots belong to the first-shell (Ga-N) and second-shell (Ga-Ga) contributions from a central Ga absorber, respectively. The FEFFIT fitting procedure was used to extract shell distances (R) and coordination numbers (N) for the nearest-neighbor shells adjacent to Ga atom for all GaN:Mg samples. The fitting results of $R_{\text{Ga-N}}$, $R_{\text{Ga-Ga}}$, $N_{\text{Ga-N}}$, and $N_{\text{Ga-Ga}}$ versus Cp_2Mg flow rate from 0 to 0.79 $\mu\text{mol/min}$. are plotted in Figs 3(a), 3(b), 3(c), and 3(d), respectively. The amplitude reduction factor was fixed at 0.98 for all of the samples and calculated Debye-Waller factors always showing less than $7 \times 10^{-3} \text{\AA}^2$.

In Figs. 3(a) and 3(b), the first-shell distance $R_{\text{Ga-N}}$ decreases only slightly and the second-shell $R_{\text{Ga-Ga}}$ increases also slightly as a function of Mg concentration around the values of ~ 1.95 and ~ 3.19 \AA in both polarization modes, respectively. This trend agrees well with the results of N K-edge NEXAFS spectra, where the positions of the shape-resonance peaks shift in opposite directions as Mg concentration increases.^[9] From the small variation of bond distances of the two shells, it can be deduced that crystalline structure remained in good quality even down to the heavy Mg-doped sample. In Figs. 3(c) and 3(d), however, show more noticeable change in coordination numbers for both polarization modes. These $\sim 30\%$ and $\sim 8\%$

decreases respectively for the first-shell nitrogen and the second-shell gallium coordination numbers in *ab*-plane reflect a large amount of N- and Ga-vacancy defects were created during the Mg incorporation and the vacancy population was to vary with the flow rate. In addition to H passivation during the GaN epi-growth using NH₃ source, these vacancies may also passivate acceptors of as-grown *p*-GaN causing electrical property change and reducing carrier mobility. Neugebauer *et al.* argued both nitrogen and gallium vacancies, V_N and V_{Ga}, are apt to be formed during the sample preparation due to their low formation energy.^[10] It is known V_{Ga} and V_N act as shallow acceptors and donors, which, then, cause severe self-compensation effect and result in high resistivity in *p*-GaN. In addition to associating with Mg acceptors to lower the free hole carrier concentration, V_N donors could also passivate V_{Ga} acceptors to form scattering centers that increase impedance intensively. Therefore, the suppression of formation of these vacancy defects may be of essential and constitutes a key factor for good characteristic performance of *p*-type GaN.

It is also seen from Figs. 3(c) and 3(d), the first-shell N_{Ga-N} appears to decrease less than the second-shell N_{Ga-Ga} noticeably from 2.0 to ~0.75 and 6.0 to ~2.1 along the *c*-axis direction, respectively. Such a near by 65%-decrease of both coordination numbers definitely would damage the crystalline structure of hexagonal GaN epilayer and degrade the film properties. However, this speculation is not consistent with the results of good crystalline characteristics for GaN:Mg sample from the tendency of shell distances change as a function of Mg concentration. Consequently, these great decreases of first- and second-shell coordination numbers along the *c*-axis can not be explained solely by the formation of vacancy defects. Reboredo and Pantelides have suggested that, in addition to substitutional Mg (Mg_{Ga}) in Mg_{Ga}-N-H form, interstitial Mg (Mg_i) plays also a significant role for self-compensation of *p*-materials.^[11] Therefore, in addition to Mg_{Ga} there must be Mg_i situated to provide acceptors and reduce the F.T. magnitude. These interstitial defects could also contribute crucially to the reduction of coordination numbers. As we have no direct data to confirm this, we simulated some possible cases for comparing to our data using both in-plane and out-of-plane polarizations. Figs. 4(a) and 4(b) show respectively the $k^3\chi(k)$ variation in *k*-space and the simulated F.T. magnitude in *R*-space of u-GaN (solid curve) and GaN:Mg with interstitial defect Mg_i (dotted curve). Fig. 4(a) shows a phase shift of nearly π between the simulated curves of the two samples near the low *k* region and in Fig. 4(b) the F.T. magnitude of the doped model decreases when interstitial Mg_i are present in GaN film. Both indicate that interstitial defects would induce the cancellation of the amplitude of the corresponding F.T. oscillation and, hence, reduce the coordination numbers. The coordination number reduction was also reported in ZnSe:Cu II-XI compound sample, whose Cu⁺² occupy either at the zinc substitutional site (Cu_{Zn}) or at the interstitial site (Cu_i).^[12] Therefore, we conclude that both Mg interstitial defects as well as N and Ga vacancies all favor to occur along the *c*-axis direction of the hexagonal GaN crystal and they collectively contribute to the reduction of coordination numbers along that direction.

4. CONCLUSION

The doping effect of GaN:Mg samples were investigated with Ga K-edge X-ray absorption spectroscopy. The data showed that NEXAFS profiles and the corresponding structural parameters have a strong anisotropic aspect between in *ab*-plane and along out-of-*ab*-plane (*c*-axis direction). Moreover, the neighboring shell distances and coordination numbers around Ga atom are very sensitive to the Mg concentration. The N- and Ga-vacancies were induced simultaneously during the

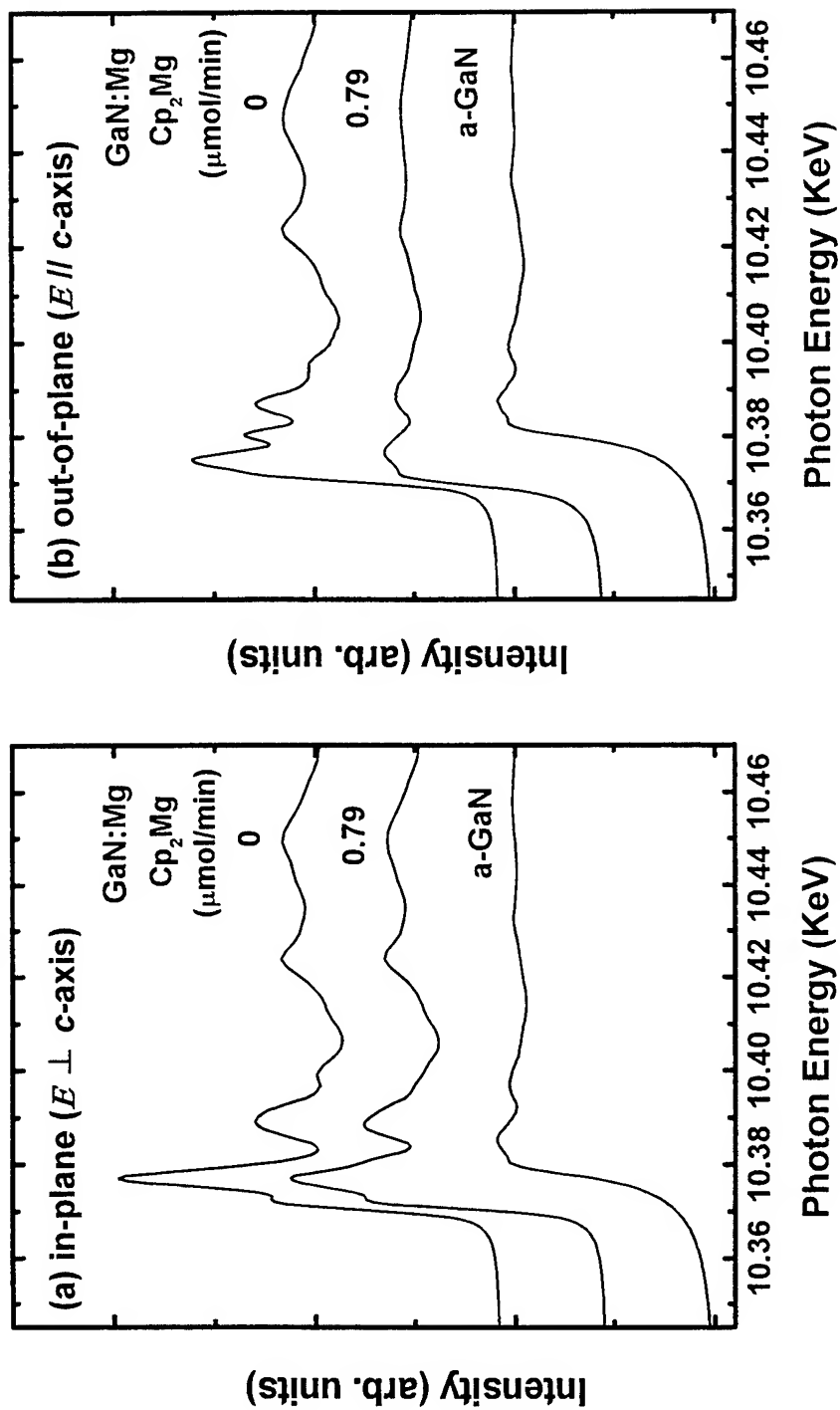
incorporation of Mg impurity, which caused coordination number reduction. However, a 65% decrease of coordination numbers along the *c*-axis direction was considered too large to be explained solely by vacancy formation. In addition to the substitutional Mg_{Ga} , simulation results based on interstitial Mg_i model did show its contribution to the coordination number reduction. Those multiple induced defects were formed to appear along the *c*-axis direction favorably when examined with polarized EXAFS measurements.

ACKNOWLEDGMENTS

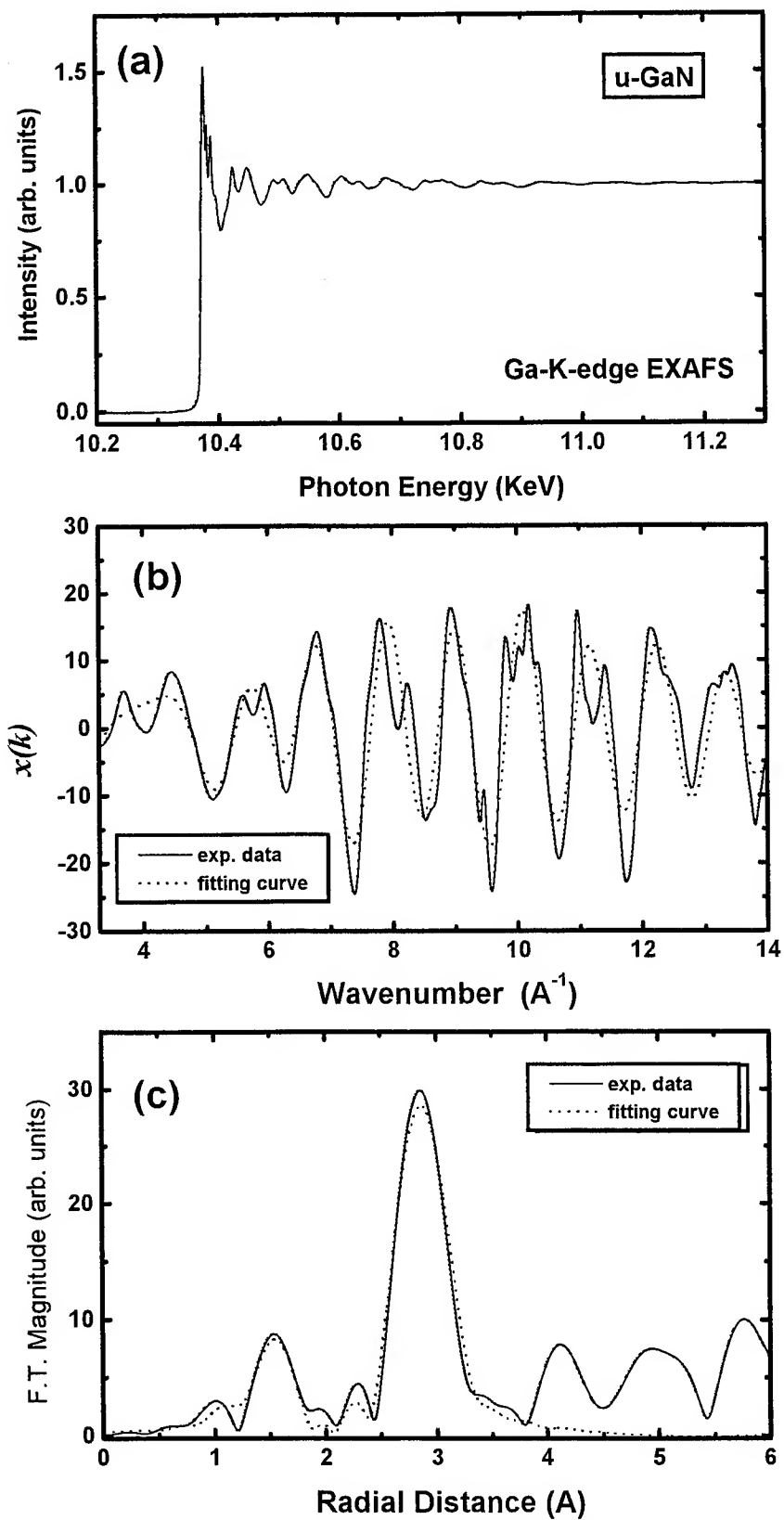
The authors would like to thank the National Science of the Republic of China for the financial support of this research under contract numbers NSC88-2112-M-009-021, -022, and -031.

REFERENCES

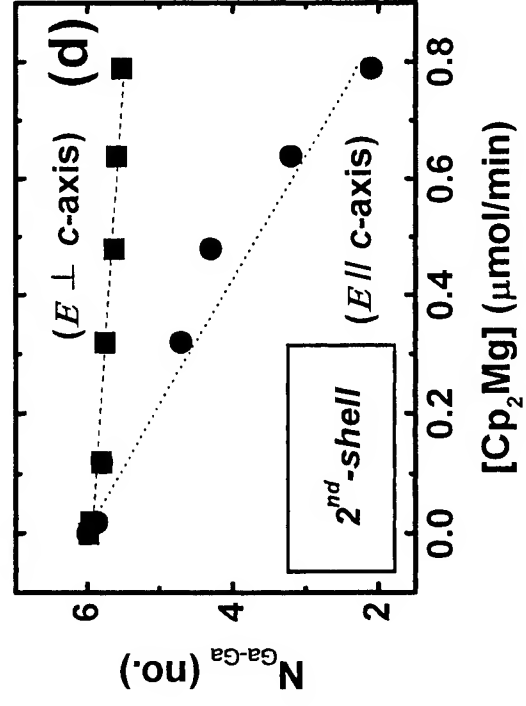
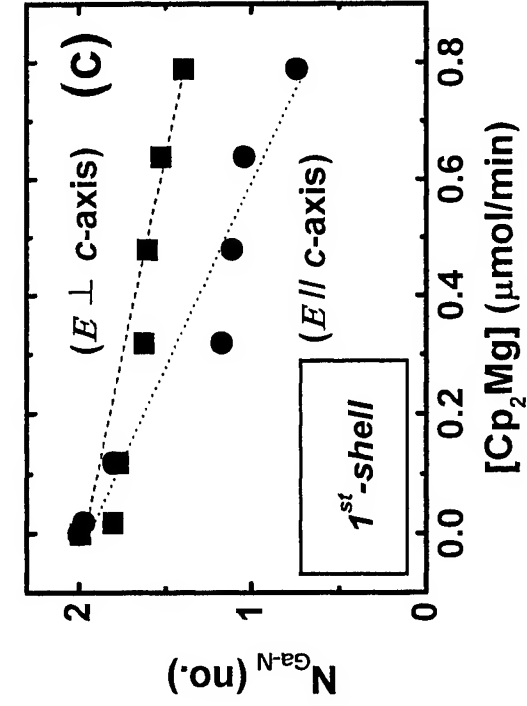
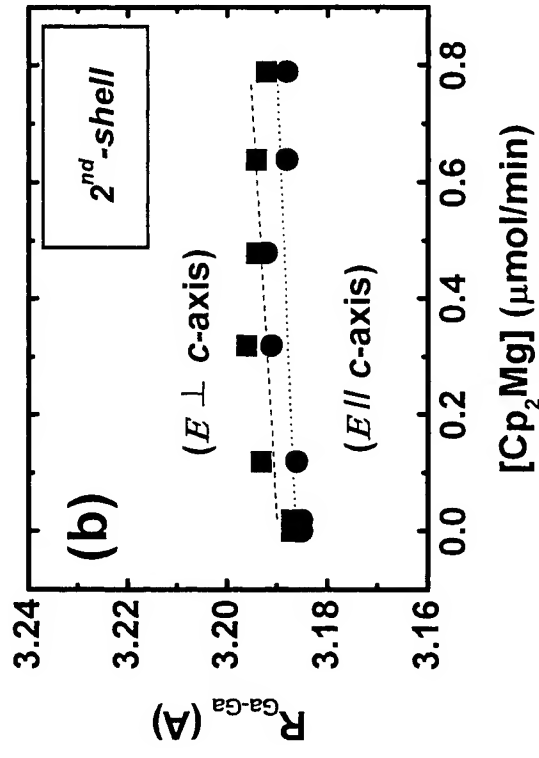
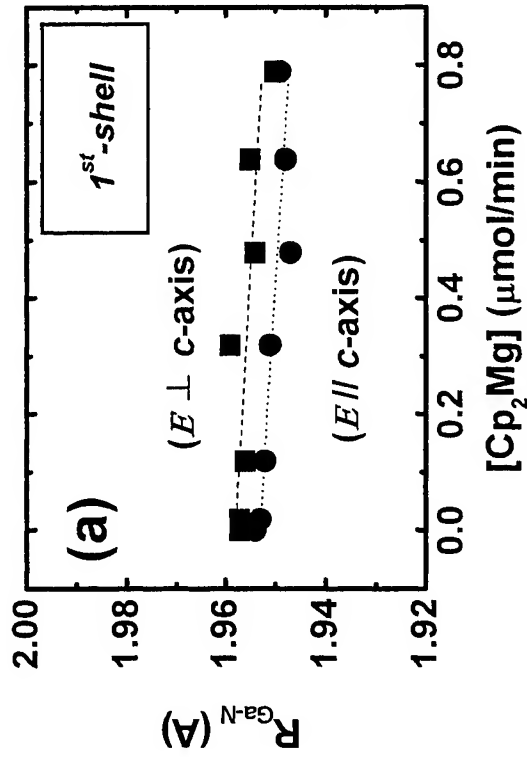
1. S. Strite and H. Morkoç, "GaN, AlN, and InN: A review," *J.V.S.T.* **B 10**, pp. 1237-1266, 1992.
2. H. Morkoc, S. Strite, G. B. Gao, M. E. Lin, B. Sverdlov, and M. Burns, "Large-band-gap SiC, III-V nitride, and II-VI ZnSe-based semiconductor device technologies," *J. Appl. Phys.* **76**, pp. 1363-1398, 1994.
3. S. Nakamura, M. Senoh, N. Iwasa, and S. Nagahama, "High-Brightness InGaN Blue, Green and Yellow Light-Emitting Diodes with Quantum Well Structures," *Jpn. J. Appl. Phys.* **34**, pp. L797-L799, 1995.
4. S. Nakamura, M. Senoh, S. Nagahama, N. Iwasa, T. Yamada, T. Matsushita, H. Kiyoku, Y. Sugimoto, T. Kozaki, H. Umemoto, M. Sano, and K. Chocho, "High-power, long-lifetime InGaN/GaN/AlGaN-based laser diodes grown on pure GaN substrates," *Jpn. J. Appl. Phys.* **37**, pp. L309-L312, 1998.
5. H. Amano, M. Kitoh, K. Hiramatsu and I. Akasai, "P-Type Conduction in Mg-Doped GaN Treated with Low-Energy Electron Beam Irradiation (LEEPI)," *Jpn. J. Appl. Phys.* **28**, pp. L2112-L2114, 1989.
6. S. Nakamura, N. Iwasa, M. Senoh, and T. Mukai, "Hole Compensation Mechanism of P-Type GaN Films," *Jpn. J. Appl. Phys.* **31**, pp. 1258-1266, 1992.
7. S.-G. Lee and K. J. Chang, "Atomic model for blue luminescences in Mg-doped GaN," *Semicond. Sci. Technol.* **14**, pp. 138-142, 1999.
8. Z. H. Lu, T. Tyliczszak, P. Broderson, A. P. Hitchcock, J. B. Webb, H. Tang, and J. Bardwell, "Local microstructure of Si in GaN studied by x-ray absorption spectroscopy," *Appl. Phys. Lett.* **75**, pp. 534-536, 1999.
9. Y.C. Pan, S. F. Wang, W. C. Lin, W. H. Lee, C. I. Chiang, H. Chang, H. H. Hsieh, J. M. Chen, D. S. Lin, M. C. Lee, W. K. Chen, and W. H. Chen, "Structure Study of GaN:Mg Films by Near Edge Absorption Fine Structure Spectroscopy and X-Ray Diffraction," to be published in *Jpn. J. Appl. Phys.*
10. J. Neugebauer and C. G. Van de Walle, "Atomic geometry and electronic structure of native defects in GaN," *Phys. Rev.* **B 50**, pp. 8067-8070, 1994.
11. F. A. Reboredo and S. T. Pantelides, "Novel Defect Complexes and Their Role in the *p*-Type Doping of GaN," *Phys. Rev. Lett.* **82**, pp. 1887-1890, 1999.
12. A. I. Goldman, E. Canova, Y. H. Kao, B. J. Fitzpatrick, R. N. Bhargava, and J. C. Philips, "Extended x-ray absorption fine structure studies of diffused copper impurities in ZnSe," *Appl. Phys. Lett.* **43**, pp. 836-838, 1983.



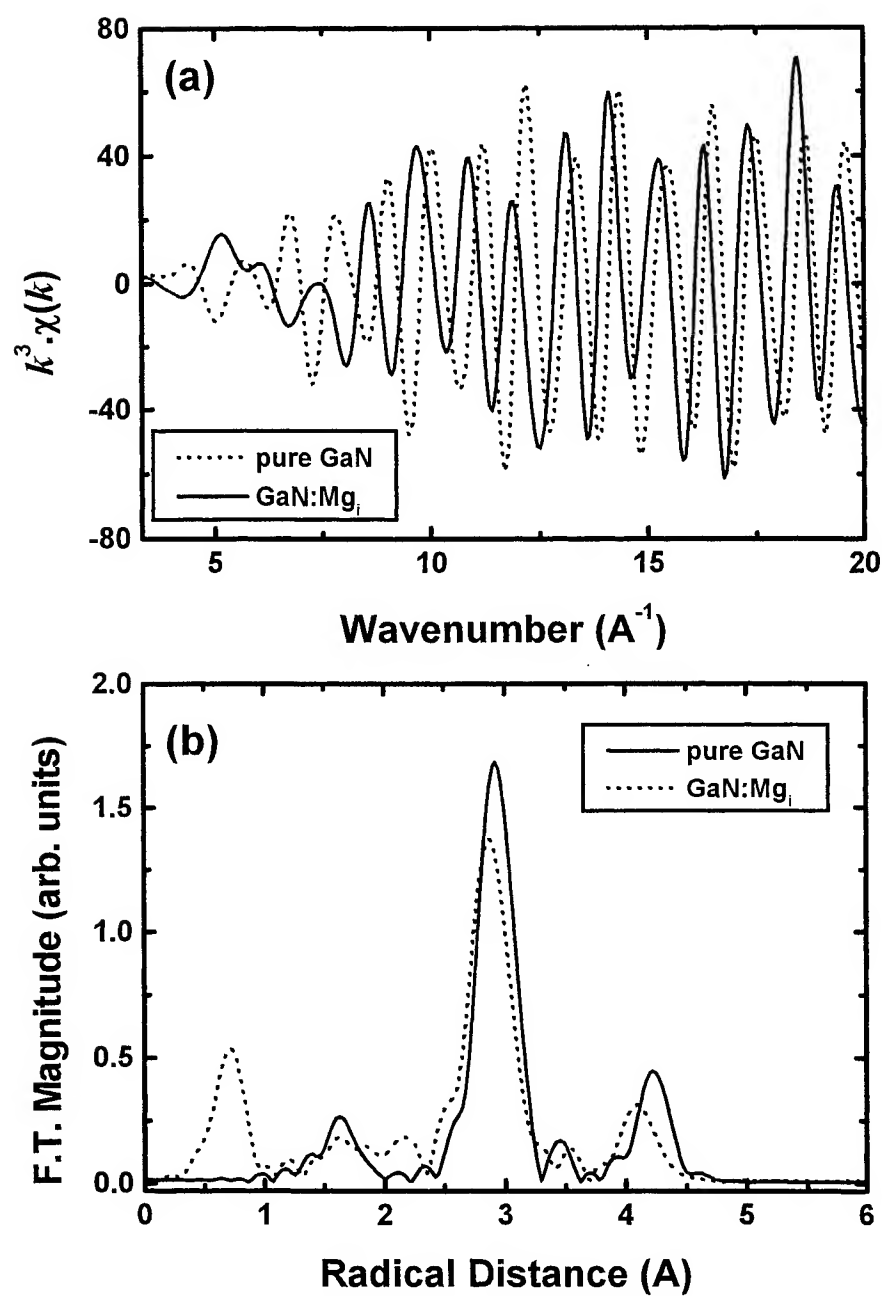
1. Ga K-edge NEXAFS spectra from undoped, Mg-doped, and amorphous GaN films for (a) in-plane ($E \perp c$) and (b) out-of-plane ($E \parallel c$) polarization modes.



2. (a) Ga K-edge EXAFS spectrum, (b) corresponding k -space oscillation $\chi(k)$, and (c) Fourier Transform (F.T.) profile of u-GaN in E // c -axis polarization.



3. (a) The shell distances ($R_{\text{Ga-i}}$) and (b) the corresponding coordination numbers ($N_{\text{Ga-i}}$) of the first- ($i=\text{N}$) and the second- ($i=\text{Ga}$) shells for various Mg-doped GaN samples in both polarization modes.



4. The simulated (a) k -space oscillation and (b) R -space F.T. profiles of undoped (solid curve) and Mg-doped (dotted curve) hexagonal GaN.

A New Methodology to Predict Energy Bandgaps in $\text{Ga}_x\text{In}_{1-x}\text{As}_y\text{P}_{1-y}$ Compounds by ANFIS Theories

Shen-Li Chen and Der-Ann Fann

Dept. of Electrical Engineering, Da-Yeh Univ., Chang-Hwa 515, Taiwan

Tel : (886) 4-852-8469 ext. 2170, Fax : (886) 4-852-1904

E-mail : jackchen@aries.dyu.edu.tw

ABSTRACT

In this paper, a novel, fast, and accurate method to predict the energy bandgap E_g in $\text{Ga}_x\text{In}_{1-x}\text{As}_y\text{P}_{1-y}$ quaternary compounds by using fuzzy theory and neural network is proposed. It has been developed to analyze the energy bandgap due to the adjustable ratios x and y of quaternary compounds. The prediction results are compared with experimental data obtained from actual devices. A good agreement (error < 0.75%) has been obtained on the energy bandgap versus the adjustable ratios x and y of quaternary compounds.

I. Introduction

III-V compound semiconductors have acted an important role in the semiconductor industry, which are due to utilize in many electronic and photonic areas such as HBTs, LEDs, and lasers. There are two factors being necessary in developing efficient heterojunction devices: a single-crystal substrate available, and a semiconductor system that provides an energy bandgap range at constant lattice parameter. The relationship between lattice constant and bandgap in III-V alloys can be relaxed by incorporating a fourth component, thus adding an extra degree of freedom so that both bandgap and lattice constant can be adjusted independently[1-5]. The binary compounds are represented by points, ternary compounds are represented by lines, and quaternary compounds by areas bounded by ternary alloy lines. The $\text{Ga}_x\text{In}_{1-x}\text{As}_y\text{P}_{1-y}$ quaternary system shown is bounded by the InAsP, GaInAs, and GaAsP ternaries. The key advantage of this system is that two commercially available substrates, GaAs and InP, can be employed for the epitaxial growth of lattice-matched quaternary layers.

While further progress is expected, the future of the $\text{Ga}_x\text{In}_{1-x}\text{As}_y\text{P}_{1-y}$ technology is assured with clearly recognized applications in fiber-optic communications and potential improvements in microwave and integrated-circuit technologies. Therefore, we have a motivation to investigate the energy bandgap prediction in very smart $\text{Ga}_x\text{In}_{1-x}\text{As}_y\text{P}_{1-y}$ quaternary compound materials.

II. Extracting E_g of $\text{Ga}_x\text{In}_{1-x}\text{As}_y\text{P}_{1-y}$ alloys

As for arbitrary values of x and y in Fig. 1[6], we can extract the energy

bandgap of $\text{Ga}_x\text{In}_{1-x}\text{As}_y\text{P}_{1-y}$ quaternary compound to regard as experimental data. For example, it can be set $x=0$ and adjusted y in group 1, then we get the $\text{InAs}_y\text{P}_{1-y}$ energy bandgaps due to the adjustable ratio of compounds. It can be set $x=1$ and adjusted y in group 2, then we get the $\text{GaAs}_y\text{P}_{1-y}$ energy bandgaps due to the adjustable ratio of compounds. Similarly, it can be set $y=0$ and adjusted x in group 3, then we get the $\text{Ga}_x\text{In}_{1-x}\text{P}$ energy bandgaps due to the adjustable ratio of compounds. Finally, it can be set $y=1$ and adjusted x in group 4, therefore, we get the $\text{Ga}_x\text{In}_{1-x}\text{As}$ energy bandgap due to the adjustable ratio of compounds.

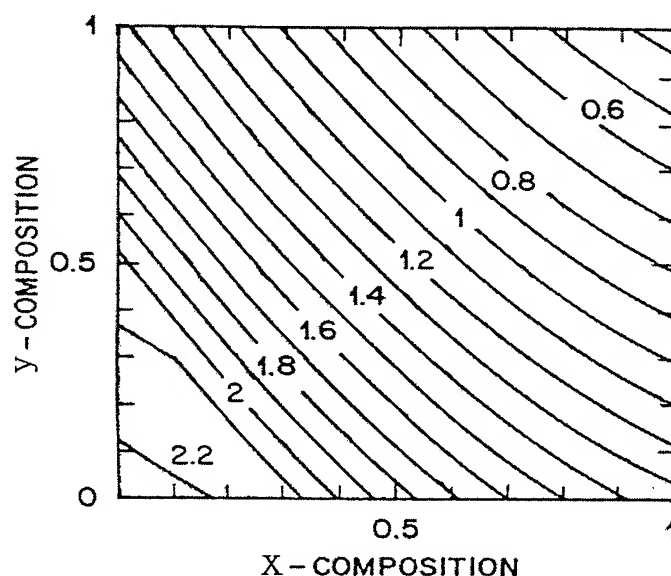


Fig. 1 The energy bandgap relationship with ratios x and y of $\text{Ga}_{1-x}\text{In}_x\text{As}_y\text{P}_{1-y}$ quaternary compound

III. Neuro-Fuzzy Theory Learning

It is known that the E_g relationship between ratio x and ratio y is very complicated, such that it is difficult by using an exact formula to express the involvement. Therefore, in this paper, we will bring up an idea with fuzzy theory[7-10] to predict the energy bandgap of $\text{Ga}_x\text{In}_{1-x}\text{As}_y\text{P}_{1-y}$ alloys. Fortunately, this method doesn't need any assumed parameters. If the predicted values are not near the training experiment quantities, it is necessary an neural network iterative learning procedure.

The predict procedure is described in the neuro-fuzzy training flow chart of Fig. 2. At the first, make the values of x and y in groups 1, 2, 3, and 4 acted as input data. Afterwards fuzzifier, Fuzzy Inference System (FIS) and then

defuzzifier, we will obtain the predict value of energy bandgap.

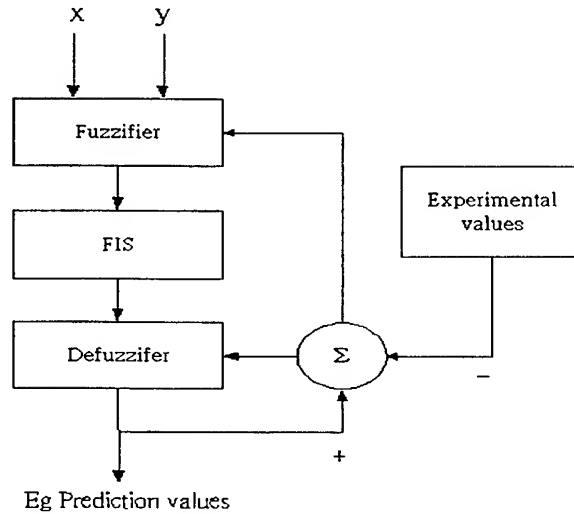


Fig. 2 Neuro-Fuzzy training flow chart

IV. Results and Discussion

In this paper, we have adopted the bell membership function(MF), therefore, which before carrying out and after training process, the membership functions are shown in Figs 3 and 4. All the experimental data of groups 1, 2, 3, and 4 can be treated as the training data, after iterative learning until the error percentages converged, see Fig. 5, the predict value of energy bandgap can be obtained. A 3-D like energy bandgap prediction surface versus x & y is shown in Fig. 6. A good agreement has been obtained, see Figs 7 and 8, as comparing the prediction results and the experimental data of the $\text{Ga}_x\text{In}_{1-x}\text{As}_{0.5}\text{P}_{0.5}$ and $\text{Ga}_{0.5}\text{In}_{0.5}\text{As}_y\text{P}_{1-y}$ materials.

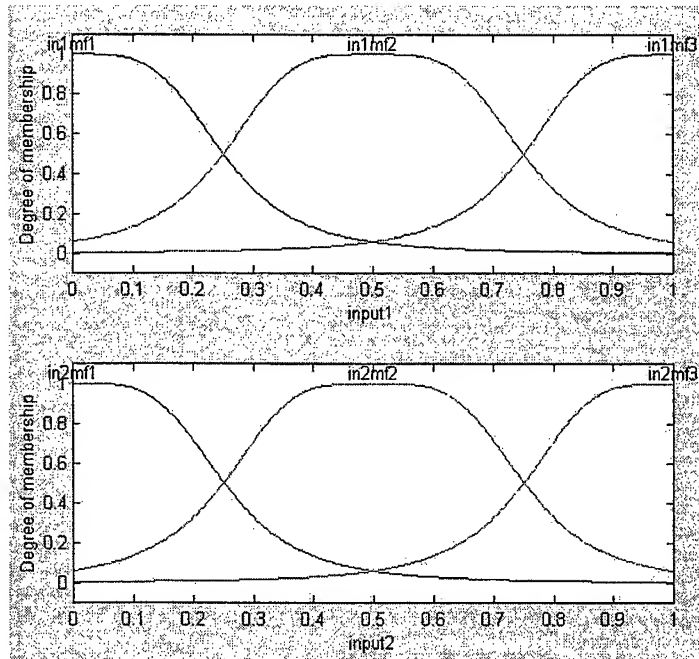


Fig. 3 Membership function before training process

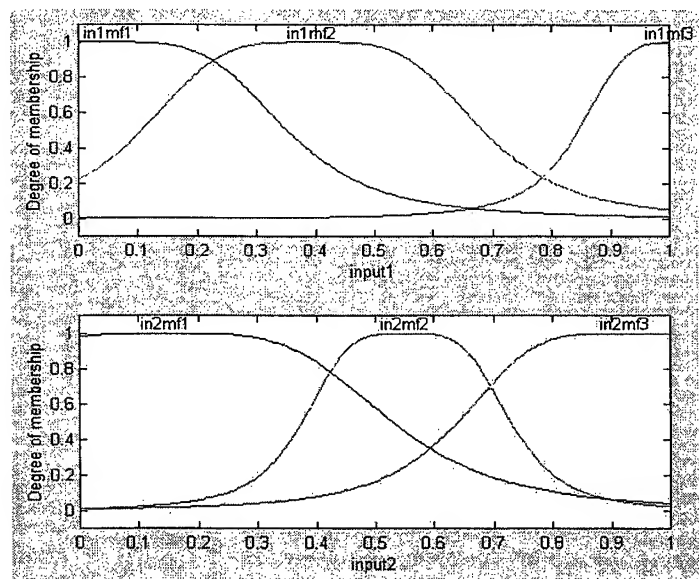


Fig. 4 Membership function after training process

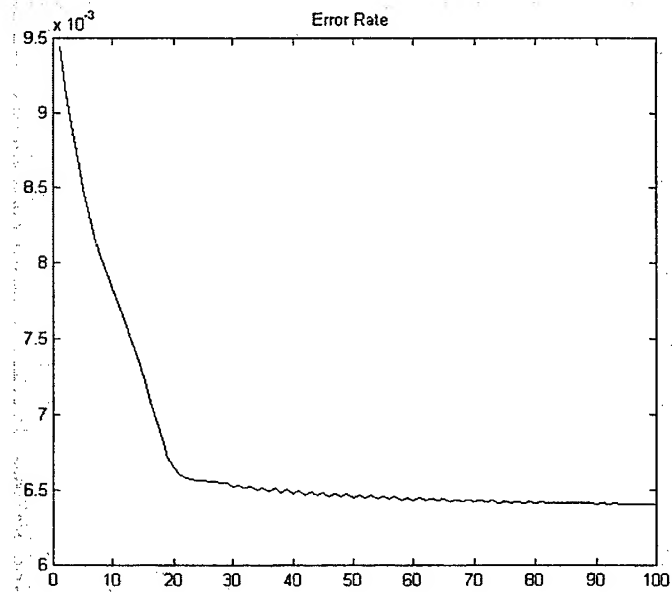


Fig. 5 The root-mean-square error versus training-process epoch

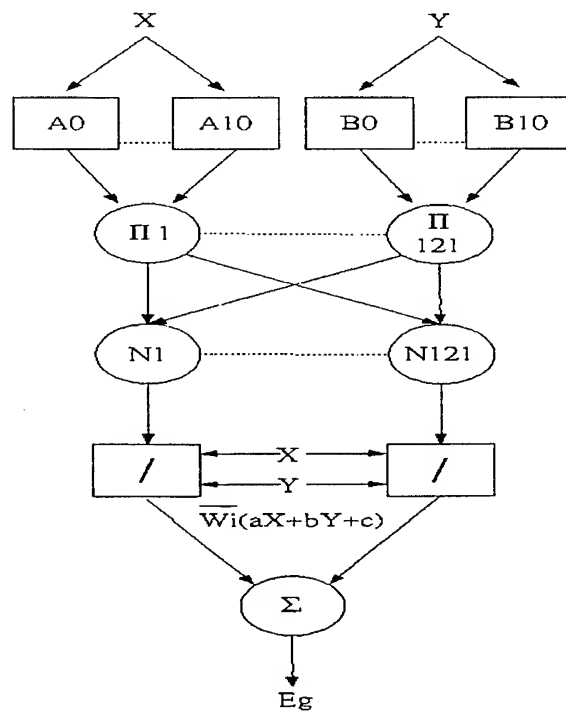


Fig. 6 Neuro-Fuzzy network flow chart of E_g prediction

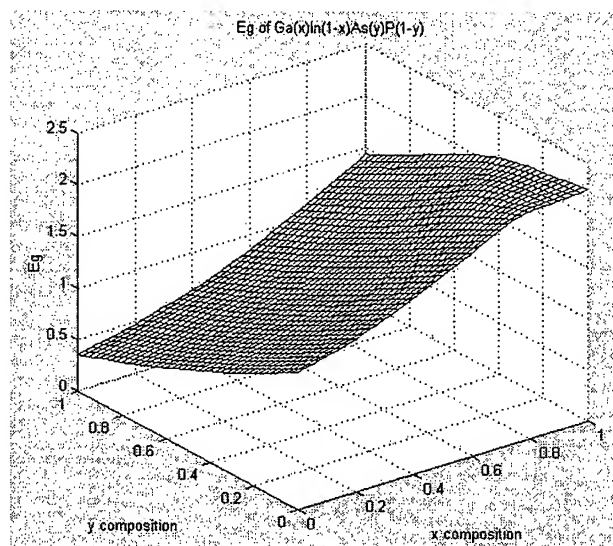


Fig. 7 A 3-D like energy bandgap prediction surface of $\text{Ga}_x\text{In}_{1-x}\text{As}_y\text{P}_{1-y}$.

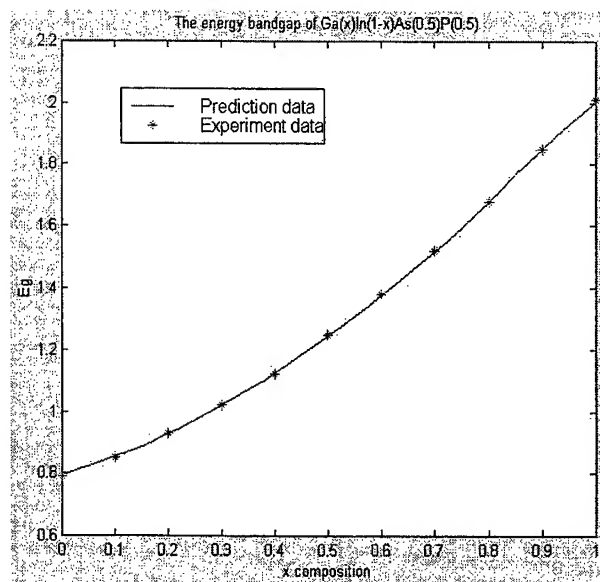


Fig. 8 The energy bandgap of $\text{Ga}_x\text{In}_{1-x}\text{As}_{0.5}\text{P}_{0.5}$

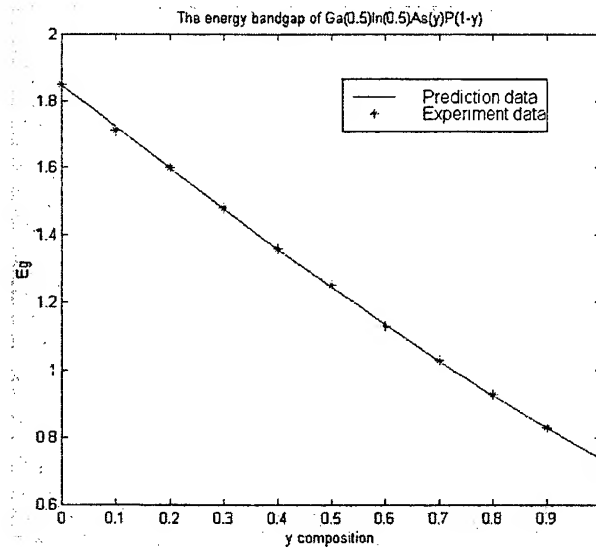


Fig. 9 The energy bandgap of $\text{Ga}_{0.5}\text{In}_{0.5}\text{As}_y\text{P}_{1-y}$

V. Conclusion

This study is provided a new method to predict the energy bandgaps of $\text{Ga}_x\text{In}_{1-x}\text{As}_y\text{P}_{1-y}$ quaternary compounds by using fuzzy theory and neural network. A good agreement has been obtained as comparing the prediction results and the experimental data of the $\text{Ga}_x\text{In}_{1-x}\text{As}_{0.5}\text{P}_{0.5}$ and $\text{Ga}_{0.5}\text{In}_{0.5}\text{As}_y\text{P}_{1-y}$ materials.

References

- [1] G. A. Antypas, R. L. Moon, L. W. James, J. Edgecumbe, and R. L. Bell. "III-V quaternary alloys", *Gallium Arsenide and Related Compounds*, 1972, Conf. Ser. no.17, Institute of Physics, London. P. 48, 1973.
- [2] A. P. Bogatov, L. M. Dolginov, L. V. Druzhinina, P. G. Eliseev, B. N. Sverdlov, and E. G. Shevchenko. "Heterojunction lasers made of GaInAsP and AlGaSbAs solid solutions", *Sov. J. Quantum Electron.*, 4, 1281, 1975.
- [3] J. J. Hsieh, "Room-temperature operation of GaInAsP/InP double-heterostructure diode laser emitting at $1.1 \mu\text{m}$ ", *Appl. Phys. Lett.*, 28, 283, 1976.
- [4] E. Kuphal, *J. Cryst. Growth* 67:441, 1984.
- [5] T.P. Pearsall, *GaInAsP Alloy Semiconductors*, John Wiley & Sons, 1982.
- [6] V. Swaminathan and A. T. Macrander, "Materials Aspects of GaAs and InP Based Structures", Prentice-Hall, Inc., 1991.
- [7] "Neuro-Fuzzy and Soft Computing" by J. S. R. JANG, C. T. SUN, E. MIZUTANI.
- [9] Fuzzy Logic Toolbox for use with MATLAB, The Math Works, Inc., 1995.
- [10] Neural Network Toolbox for use with MATLAB, The Math Works, Inc., 1994.

GaAs-based long-wavelength traveling-wave photodetector

Jin-Wei Shi^a, Chi-Kuang Sun^{*a}, Ying-Jay Yang^b, Yi-Jen Chiu^c, and John E. Bowers^c

^aGraduate Institute of Electro-Optical Engineering, National Taiwan University, Taipei 10617,
TAIWAN, R.O.C.

^bDepartment of Electrical Engineering, National Taiwan University, Taipei 10617, TAIWAN, R.O.C.

^cDepartment of Electrical and Computer Engineering, University of California, Santa Barbara, CA
93106, USA

ABSTRACT

GaAs-based high-speed photodetectors attract lots of attention in the past twenty years due to their maturity in material growth and processing. However their wide bandgap characteristic (830nm) restricts their applications in fiber communication wavelength (1.3 μ m~1.55 μ m). Recently some research groups had demonstrated GaAs-based n-i-n, p-i-n waveguide type photodetectors operating at 1.55 μ m by taking advantage of the mid-gap defect absorption of low-temperature grown GaAs (LTG-GaAs). In this paper we propose and analyze different bandwidth-limiting factors for LTG-GaAs based metal-semiconductor-metal traveling wave photodetector (MSM TWPd) for both long and short wavelength cases. According to our calculation results, MSM TWPds release the bandwidth limitation bottleneck in previous n-i-n and p-i-n TWPd structures, especially in the long wavelength case. Our analysis indicates that LT-GaAs based traveling-wave photodetectors can offer excellent bandwidth as well as high saturation power performances in fiber communication wavelength, which corresponds to long absorption length regime.

Keywords: Traveling-wave photodetector, metal-semiconductor-metal photodetector, high-speed photodetector

1. INTRODUCTION

Ultra-high speed photodetectors have been studied extensively in the past ten years due to their extensive applications^{1,2} such as in high bit rate fiber communication channels, in the measurement systems for electrical and optical signal linking, or in optoelectronic generation of high-power microwaves/millimeter waves³. There are two major trends in the development of these high-speed photodetectors. One is to obtain high bandwidth-efficiency product and the other is to improve the saturation output current under intense light illumination². Several photodetector technologies based on edge-coupled structures have been demonstrated to enhance the bandwidth-efficiency product and saturation power, such as waveguide photodetectors (WGPd)^{4,5,6}, traveling-wave photodetectors (TWPd)^{7,8,9}, and periodic traveling-wave photodetectors (P-TWPd)¹⁰. By utilizing optical wave and microwave guiding structure in a TWPd, first proposed by Taylor *et al.*¹¹ and pursued independently by several research groups^{7,8,9}, the traditional R-C bandwidth limitation was released and replaced by velocity mismatch between optical and electrical waves¹². Higher bandwidth-efficiency product can thus be achieved. A bandwidth-efficiency product of 76GHz at near infrared (IR) wavelength (830nm) was demonstrated by Kirk *et al.* with GaAs based p-i-n structure¹³. Recently Chiu *et al.* achieved a record bandwidth of 560GHz at the same wavelength regime by using low-temperature-grown (LTG) GaAs as the photo-absorption intrinsic layer¹⁴, utilizing the sub-picosecond carrier trapping time of the LTG-GaAs at the expense of internal quantum efficiency. There is also a trend to use LTG-GaAs in the active region of the TWPd for the telecommunication wavelength (1.3-1.55 μ m) applications^{15,16,17}, taking advantage of its short carrier lifetime and low optical absorption constant which originates from mid-gap defect state to conduction band transitions in the telecommunication wavelength to increase both the output saturation current and device bandwidth^{16,17}. However, when we compare these telecommunication devices' bandwidth performances with those of the p-i-n TWPds in short wavelength, serious bandwidth degradation was observed (560GHz vs. 17GHz). This observation is caused by the low absorption constant, which indicates long device absorption length, in communication wavelength that will result in serious velocity-mismatch and microwave loss bandwidth limitations.

In this paper we propose and analyze the bandwidth limitation factors in MSM TWPds for both long and short optical wavelength applications. Instead of traveling at a slow-wave mode as in p-i-n TWPds, the electrical wave will propagate at quasi-TEM mode in our proposed MSM TWPd structure¹⁷. We consider all bandwidth limitation factors including

carrier drift/trapping time, microwave loss dispersion, microwave velocity dispersion, and velocity mismatch, in our simulation model. Some of these limitation factors are not critical for short-absorption-length TWPDS but are crucial for long-absorption-length TWPDS. According to our simulation results, MSM TWPDS structure has a better bandwidth performance than p-i-n TWPDS especially in the long absorption length regime (long wavelength case) owing to its low microwave loss and high microwave velocity that is the nature of a quasi-TEM mode. The simulation results in this paper indicate that LTG-GaAs based MSM TWPDS can not only offer bandwidth performance superior to that of p-i-n TWPDS for both short wavelength (~ 800 nm) and fiber communication long wavelength (1.3-1.55 μm).

2. DEVICE STRUCTURE

The MSM TWPDS structures for short wavelength and long wavelength applications are shown in Figure 1(a) and (b). The simulation values of all parameters are given in Table 1.

	MSM short wavelength (830nm)	MSM long wavelength (1.55 μm)
Center strip width (w_c)	5 μm	9 μm
LT GaAs thickness	500 nm	500 nm
CPW air gap (w_g)	0.25 μm	5.5 μm
Undoped AlGaAs thickness	1 μm	1 μm
Metal (Ti/Au) thickness (t)	0.15 μm	1 μm
Ground plane width (w_s)	30 μm	30 μm
Optical modal absorption constant ($\Gamma\alpha$)	6000 cm^{-1}	44 cm^{-1}
Device absorption length (l)	5 μm	350 μm
Carrier trapping time (t_{life})	200 fs	200 fs
Ridge Height (h)	0.25 μm	0.25 μm

Table 1 Simulation parameters. Values of 9 μm and 5 μm for w_c are used for long and short wavelength bandwidth calculation respectively. Different size of waveguide width is chosen to maintain good coupling efficiency for both long and short wavelengths.

In both figures, there is a co-planar waveguide (CPW) structure, which consists of multiple undoped epi-layers with semi-insulating (S.I.) substrate below three metal strips. The top layer is made by LTG-GaAs, which acts as photoabsorption layer. The photo-excited carriers in this layer can be collected directly by three CPW metal strips. By utilizing the optical index difference between these epi-layers, optical wave can be guided along y-direction of both structures. The x-direction guiding is achieved with a ridge waveguide structure, which has a depth of h in the region below the center strip metal with a width of w_c ¹⁸. With respect to microwave property in this structure, undoped AlGaAs and LTG-GaAs epi-layers, which both have high resistivity, will ensure that the propagation microwave mode is a “quasi-TEM mode” instead of a “slow wave mode” as in the p-i-n TWPDS structure. With this quasi-TEM mode higher microwave velocity and lower microwave loss can be achieved¹⁹. The main difference between Figure 1 (a) and Figure 1 (b) is the width of CPW air gap w_g . In the case of short wavelength application, both electrons and holes will be generated and contribute to the output photocurrent. In order to get good quantum efficiency, the distance between center strip and

ground plane must be as close as possible to collect photo-excited carriers. This can be achieved by a "self-aligned" structure as shown in Figure 1 (a). Compared with the standard e-beam lithography method, self-alignment can obtain sub-micron width and distance between metal fingers more easily. The value of w_g is taken as 250nm and is given in Table 1 due to that the depth h of optical ridge waveguide structure is 250nm. On the other hand for the long wavelength case, single type of carrier (electron) will be generated²⁰ and collected. A small width of CPW air gap w_g is thus not necessary. A wider w_g can reduce microwave loss significantly and this is especially important for the bandwidth performance of long absorption length TWPd as discussed below.

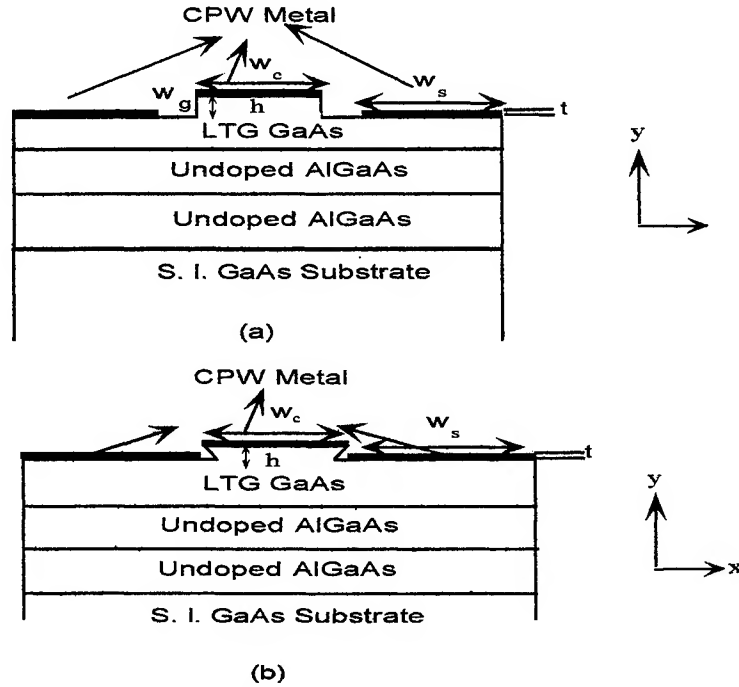


Figure 1 Cross-sectional diagrams of (a) MSM-TWPD for long wavelength application and (b) MSM-TWPD for short wavelength application.

3.ELECTRICAL TRANSMISSION LINE MODEL AND CALCULATION

TWPD is mainly composed by an electrical transmission line and an optical waveguide. The characteristics of the transmission line (such as microwave loss, velocity..etc) and the optical waveguide underneath directly determine the device bandwidth performance and the input optical field coupling efficiency. We model the MSM TWPD transmission line by semi-empirical formulas, which are well developed for CPW on a S.I. substrate due to the fact that all materials in our modeled MSM TWPD structures are undoped with high resistivity. Because that the CPW line is usually fabricated on a multi-layer structure for optical wave-guiding purposes, the electrical effective dielectric constant is slightly different from the case with GaAs substrate only. Its analytic formula is given by²¹

$$\epsilon_{re} = q_1 \epsilon_1 + q_2 \epsilon_2 + \dots + q_n \epsilon_n, \quad (1)$$

with

$$q_1 + q_2 + \dots + q_n = 1, \quad (2)$$

$$q_i = \frac{C_s^a}{C^a}, C_{si}^a = 2\epsilon_0 \frac{K(k_i)}{K'(k_i)}, C_a = 4\epsilon_0 \frac{K(k)}{K'(k)}, k = \frac{a}{b}, \quad (3)$$

and

$$k_i = \begin{cases} a/b & \text{for the half plane with infinite layer thickness} \\ \frac{\sinh(\pi a/2d)}{\sinh(\pi b/2d)} & \text{for a dielectric layer of thickness } d \\ \frac{\tanh(\pi a/2d)}{\tanh(\pi b/2d)} & \text{for a dielectric layer backed by a conductor with thickness } d. \end{cases} \quad (4)$$

K and K' are the complete elliptic integrals of the first kind and its complement. a is one-half the center strip width of the CPW signal line ($w_c/2$) and b is one-half the total width of air gaps and signal line ($1/2w_c + w_g$). q_b , ϵ_i are the filling factor and the relative dielectric constant for each layer respectively. ϵ_{re} is the total relative effective dielectric constant. With the knowledge of ϵ_{re} we can further calculate microwave loss. Microwave loss is calculated by summing the dielectric loss, conductor loss, and radiation loss using semi-empirical formulas. Conductor loss is described by²²

$$\alpha_c^{CPW} = \frac{R_s \sqrt{\epsilon_{re}}}{480\pi K(k)K'(k)(1-k^2)} \left\{ \frac{1}{a} \left[\pi + \ln \left(\frac{8\pi a(1-k)}{t(1+k)} \right) \right] + \frac{1}{b} \left[\pi + \ln \left(\frac{8\pi b(1-k)}{t(1+k)} \right) \right] \right\}, \quad (5)$$

where t is the metal thickness (in meter). R_s is the surface resistance with

$$R_s = 8.24 \times 10^{-3} \sqrt{\frac{f_g \mu_r \rho_{metal}}{\rho_{Cu}}}, \quad \Omega \quad (6)$$

where ρ_{Cu} and ρ_{metal} are the resistivities for copper and strip metal respectively and are in $\Omega \cdot \text{cm}$. f_g is the operation frequency in GHz. μ_r is the relative permeability of the metal that equals to 1 for gold and copper in our specific case. Dielectric loss is described by²³

$$\alpha_d^{CPW} = \frac{\pi f \sqrt{\epsilon_{re}(0)}}{c} \left[\frac{1 - 1/\epsilon_{re}(0)}{1 - 1/\epsilon_r} \right] \tan \delta_\epsilon, \quad \text{nepers/m} \quad (7)$$

where δ_ϵ is the loss angle for the S. I. GaAs neglecting the effect of different epi-layers with $\tan \delta_\epsilon = 0.006$. c is the speed of light in free space. Radiation loss is described by²⁴

$$\alpha_r^{CPW} = \left(\frac{\pi}{2} \right)^5 2 \left[\frac{\left(1 - \frac{\epsilon_{re}(f)}{\epsilon_r} \right)^2}{\sqrt{\frac{\epsilon_{re}(f)}{\epsilon_r}}} \right] \frac{(2b)^2 \epsilon_r^{3/2}}{c^3 K'(k)K(k)} f^3. \quad \text{nepers/m} \quad (8)$$

$\epsilon_{re}(f)$ is the total effective relative dielectric constant that considers the dispersion effect with²⁴

$$\sqrt{\epsilon_{re}(f)} = \sqrt{\epsilon_{re}(0)} + \frac{\sqrt{\epsilon_r} - \sqrt{\epsilon_{re}(0)}}{1 + G(f/f_{TE})^{-1.8}}, \quad (9)$$

where

$$G = e^{u \ln(2a/(b-a)) + v}$$

$$u = 0.54 - 0.64p + 0.015p^2$$

$$v = 0.43 - 0.86p + 0.54p^2$$

$$p = \ln(2a/h)$$

f_{TE} is the cutoff frequency for the TE_0 surface wave mode of the substrate and its value is given by

$$f_{TE} = \frac{c}{4h\sqrt{\epsilon_r - 1}} \quad (11)$$

The total effective relative dielectric constant $\epsilon_{re}(0)$ equals to ϵ_{re} in equation (1) and ϵ_r , h are the relative dielectric constant and thickness of GaAs substrate respectively.

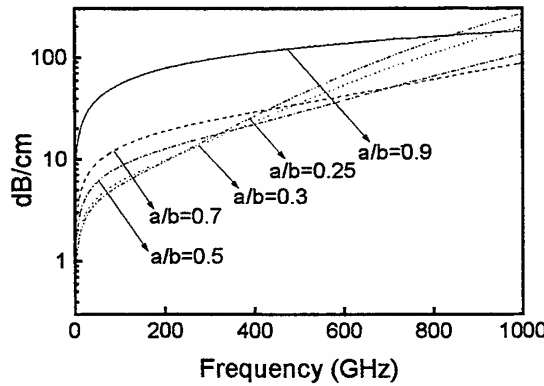


Figure 2. Microwave loss versus frequency for different CPW geometric size ratio (a/b).

Calculated microwave loss as a function of frequency with different geometric size ratio (a/b) with a fixed metal thickness of 500nm is shown in Figure 2. We can clearly see a frequency dependent loss for different geometry sizes, which acts like a low pass filter and will limit device high-speed performance. Besides, in the frequency between DC to several hundreds GHz (below 400GHz), lower a/b ratio is desired for low microwave loss. However, in the high frequency regime (above 400GHz), lower a/b ratio will have a higher microwave loss. This result is caused by two dominant loss mechanisms, including conductor loss for low microwave frequency and radiation loss for high microwave frequency respectively²⁴. With respect to microwave velocity, it can be expressed as follows

$$\begin{cases} V_e = \frac{c}{\sqrt{\epsilon_{re}}} \\ V_e(f) = \frac{c}{\sqrt{\epsilon_{re}(f)}} \end{cases} \quad (12)$$

where ϵ_{re} and $\epsilon_{re}(f)$ are in equation (1) and (9), which corresponds to the velocity with or without dispersion effect.

4. BANDWIDTH CALCULATIONS AND MODELING

Bandwidth calculation is based on a photo-distribute current model²⁵. This model can include various bandwidth degradation factors such as microwave loss, velocity mismatch, carrier drift/trapping time, and boundary reflection effect. The output photo-current can be expressed as follows in frequency domain,

$$I_f(\omega) = \frac{\exp(-\gamma_m l)}{1 + j\omega t_{lfe}} \left(\frac{1 - \exp(-(\gamma_o - \gamma_m)l)}{\gamma_o - \gamma_m} + \frac{1 - \exp(-(\gamma_o + \gamma_m)l)}{\gamma_o + \gamma_m} \right), \quad (13)$$

where $I_f(\omega)$ is the output photocurrent at the load end, which is a function of microwave angular frequency ω . l is the device absorption length. γ_m is the microwave propagation constant that includes microwave loss and velocity dispersion with

$$\gamma_m = \alpha_e + j \frac{\omega}{V_e(f)} \quad (14)$$

where α_e is the total microwave loss that equals to the sum of α_c , α_r , and α_d . $V_e(f)$ is given by equation (12). γ_o is the propagation constant of photo-induced charge with

$$\gamma_o = \Gamma \alpha_o + j \frac{\omega}{V_o} \quad (15)$$

where V_o is the optical group velocity and Γ and α_o are the confinement factor and absorption constant of photo-absorption layer respectively. Optical absorption coefficient of LTG-GaAs at telecommunication wavelength (1.3~1.55 μm) and short wavelength (830nm) are about $\alpha_o=110\text{cm}^{-1}$ ¹⁷ and $\alpha_o=1.5 \times 10^4\text{cm}^{-1}$ ²⁶. The reasonable values for confinement factor Γ of photo-absorption layer and optical group velocity V_o in GaAs/AlGaAs optical waveguide are 0.4 and 8.9×10^7 m/sec respectively. The corresponding optical modal absorption coefficient $\Gamma \alpha$ is thus 44cm^{-1} and 6000cm^{-1} for long and short wavelength respectively. The large difference in the modal absorption constant cause different device length for completely absorption (350 μm vs. 5 μm). t_{life} is the carrier trapping time for LTG-GaAs, which is assumed to be 200fs with a single exponential-like decay^{27, 28, 29}.

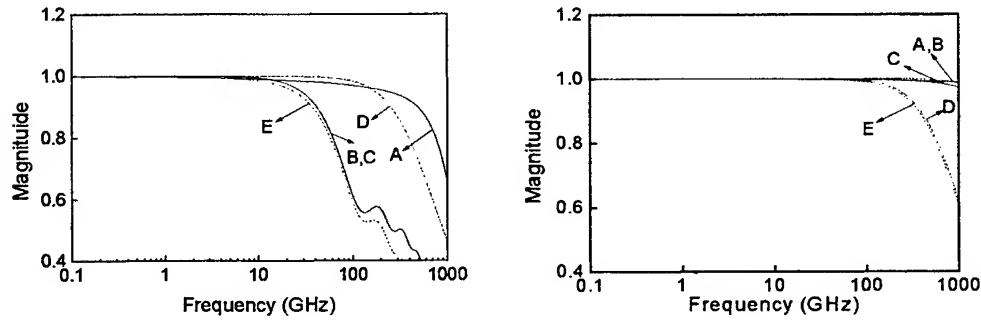


Figure 3. Frequency response due to different bandwidth-limiting factors for (a) long wavelength MSM TWPD and (b) short wavelength MSM TWPD structures. Trace A: microwave loss. Trace B: velocity mismatch without microwave velocity dispersion. Trace C: velocity mismatch with microwave velocity dispersion. Trace D: carrier trapping time. Trace E: net frequency response.

5. CALCULATION RESULT AND DISCUSSION

The frequency responses of each bandwidth limitation factor for long and short wavelength devices are shown in Figure 3 (a) and Figure 3 (b) respectively. By utilizing the data shown in Figure 2, we duplicate our results for the normalized microwave loss dispersion curves of the 350 μm and 5 μm long device structures in Figure 3 (a) and (b) as the solid lines "A". Strong frequency response degradation can be observed in the high frequency region, which is ~1 THz for the MSM TWPD in long device-length/wavelength case, and far above 1 THz for short device-length/wavelength regime. Large microwave loss in short wavelength MSM TWPD is induced by narrow CPW gap as shown in figure 2. However with short device length, serious bandwidth degradation will not happen. In order to observe the effect of velocity mismatch on bandwidth performance, we modified equations (13) and (14) and let t_{life} , α_e equals to zero. We calculated the frequency response of the velocity mismatch effect as traces "B" without microwave velocity dispersion and as traces "C" with microwave velocity dispersion effect. For both cases, microwave velocity was given by equation (12). From traces "B" and "C" we can find that the dispersion effect is not a serious bandwidth degradation factor for both structures and it can be completely neglected in bandwidth calculation. The tremendous difference between traces "C" of figure 3(a) and figure 3(b) (100GHz and above 1THz) is because that for long absorption length devices, a large walk-off distance between photo-excited electrical pulse and optical pulse will happen. The electrical pulse will thus suffer serious distortion and broadening in

time domain so that the transformed bandwidth is reduced.

The corresponding frequency responses of carrier trapping time t_{tr} are shown as dash-dot lines marked "D" in both figures 3(a) and 3(b). The net frequency responses for both structures can be calculated from equation (13). The calculated traces are shown as short-dash lines marked "E". These results include microwave loss, velocity dispersion, velocity-mismatch, and carrier trapping time effects. We can see that the major bandwidth-limiting factors are different for these two cases. For short absorption length case, the net bandwidth is limited by carrier-trapping effect. The result implies that the device bandwidth is no-longer limited by traditional R-C or velocity-mismatch as in WGPLDs and p-i-n TWPDLs and is replaced by the intrinsic carrier dynamics in LTG-GaAs. By utilizing the ultra-wide electrical bandwidth and the dge coupled structure, this device can be applied in high power ultrafast photoconductive switches³⁰, THz photomixers³¹, and E-O conversion probes³² for high-speed device characterization. Regarding with long device-length case, device bandwidth is still limited by velocity-mismatch as shown in figure 3(b). However, compared with previous works in LTG-GaAs-based long-wavelength photodetectors (p-i-n and n-i-n structure), the velocity-mismatch and microwave loss bandwidth limitations are greatly released in MSM TWPDL structures due to the low loss high velocity nature of "quasi-TEM mode" compared with that of "slow wave mode". On the other hand, the carrier trapping time is not the device major bandwidth limitation. In order to achieve the optimum bandwidth-efficiency product, a suitable carrier-trapping-time/absorption-constant combination will be desired which can be engineered through temperature control of the LTG-GaAs post-growth annealing³³.

6.CONCLUSION

We calculate and analyze all the bandwidth-limiting factors for LTG-GaAs based MSM TWPDLs in both long and short wavelength case with a photo-distribute current model. According to our calculation results, carrier trapping time and velocity mismatch are the major bandwidth limiting factors for MSM TWPDLs in short and long wavelength applications respectively. This new device structure can support superior bandwidth performance than traditional LTG-based p-i-n structured TWPDL due to the nature of the electrical "quasi-TEM mode" especially in long-wavelength application. LTG-GaAs MSM TWPDLs can be monolithic integrated with mature GaAs high speed IC technology. Low cost GaAs based photo-receiver units, which operate at both long /short wavelengths (for long haul and short haul fiber communication), can thus be expected.

REFERENCE

1. J. E. Bowers and C. A. Burrus, Jr., "Ultrawide-Band Long-Wavelength p-i-n Photodetectors," *J. Lightwave Technol.*, **5**, pp. 1339-1350, 1987.
2. K. Kato, "Ultrawide-Band/High-Frequency Photodetectors," *IEEE Trans. Microwave Theory Tech.*, **47**, pp. 1265-1281, 1999.
3. M. Alles, T. Braasch, and D. Jager, "Traveling wave photodetector for optical generation of microwave signals," in *Int. Conf. Indium Phosphide Related Materials*, 1996.
4. J. E. Bowers, and C. A. Burrus, "High-speed zero-bias waveguide photodetectors," *Electron. Lett.*, **22**, pp. 905-906, 1986.
5. K. Kato, S. Hata, A. Kozen, J. Yoshida, and K. Kawano, "Highly efficient 40 GHz waveguide InGaAs p-i-n photodiode employing multimode waveguide structure," *IEEE Photon. Technol. Lett.*, **3**, pp. 820-822, 1991.
6. K. Kato, A. Kozen, Y. Muramoto, Y. Itaya, T. Nagatsuma, and M. Yaita, "110-GHz, 50% efficiency mushroom-mesa waveguide p-i-n photodiode for a 1.55 μ m wavelength," *IEEE Photon. Technol. Lett.*, **6**, pp. 719-721, 1994.
7. D. Jager and R. Kremer, "Traveling-wave optoelectronic devices for microwave application," in *Proc. Int. 1994 IEEE MTT-S Topical Meet. Optical Microwave Interactions*, Nov. 21-23, 1994, pp. 11-14.
8. G. A. Vawter and V. M. Hietala, "Unlimited-bandwidth distributed optical phase modulators and detectors: Design and fabrication issue," in *Proc. Int. 1994 IEEE MTT-S Topical Meet. Optical Microwave Interactions*, Nov. 21-23, 1994, pp.3-6.
9. C. L. Goldsmith, G. A. Magel, B. M. Kanack, and R. J. Baca, "Coherent combing of RF signals in a traveling-wave photodetector array," *IEEE Photon. Technol. Lett.*, **9**, pp.998-990, 1997.
10. L. Y. Lin, M. C. Wu, T. Itoh, T. A. Vang, R. E. Muller, D. L. Sivco, and A. Y. Cho, "Velocity-matched distributed photodetectors with high saturation power and large bandwidth," *IEEE Photon. Technol. Lett.*, **8**, pp.1376-1378, 1996.
11. H. F. Taylor, O. Eknayan, C. S. Park, K. N. Choi, and K. Chang, "Traveling wave photodetectors," *Optoelectron. Signal*

Processing Phased-Array Antennas II, pp. 59-63, 1990

12. K. S. Giboney, M. J. W. Rodwell, and J. E. Bowers, "Traveling-wave photodetector theory," *IEEE Trans. Microwave Theory Tech.*, **45**, pp. 1310-1319, 1997.
13. K. S. Giboney, R. Nagarajan, T. Reynolds, S. Allen, R. Mirin, M. Rodwell, and J. Bowers, "Traveling-wave photodetectors with 172-GHz and 76-GHz bandwidth-efficiency product," *IEEE Photon. Technol. Lett.*, **7**, pp. 412-414, 1995.
14. Y. J. Chiu, S. B. Fleischer, and J. E. Bowers, "High-Speed Low-Temperature-Grown GaAs p-i-n Traveling-Wave Photodetector," *IEEE Photon. Technol. Lett.*, **10**, pp. 1012-1014, 1998.
15. A. C. Warren, J. H. Burroughes, J. M. Woodall, D. T. McInturff, R. T. Hodgson, and M. R. Melloch, "1.3 μ m p-i-n photodetector using GaAs with As precipitates (GaAs: As)," *IEEE Electron Device Lett.*, **12**, pp. 572-579, 1991.
16. Y. J. Chiu, V. Kamam, S. Z. Zhang, J. E. Bowers and U. K. Mishra, "A novel 1.54 μ m n-i-n photodetectors based on low-temperature grown GaAs," in *Proceeding of IEEE Lasers and Electro-Optics Society 1998 Annual Meeting*, pp. 155-156, Dec. 1998.
17. Y. J. Chiu, S. Z. Zhang, S. B. Fleischer, J. E. Bowers and U. K. Mishra, "GaAs-based, 1.55 μ m high speed, high saturation power, low-temperature grown GaAs pin photodetector," *Electronics Letters*, **34**, pp. 1253-1254, 1998.
18. J. W. Shi, C.-K. Sun, and Y. J. Yang, "Metal-semiconductor-metal traveling-wave-photodetectors," in *Conference on Lasers and Electro-Optics*, OSA Technical Digest (Optical Society of America, Washington DC, 1999), pp. 256-257, 1999.
19. H. Hasegawa, M. Furukawa, and H. Yanai, "Properties of Microstrip Line on Si-SiO₂ System," *IEEE Trans. Microwave Theory Tech.*, **19**, pp. 869-881, 1971.
20. C.-K. Sun, J.-C. Wang, T.-M. Liu, Y.-J. Chiu, and J. E. Bowers, "Electron capture time versus annealing temperature in low temperature grown GaAs," in *Conference Proceeding of IEEE Lasers and Electro-Optics Society 12th Annual Meeting*, paper WCC0003, 1999.
21. S. S. Bedair, and I. Wolff, "Fast, Accurate and Simple Approximate Analytic Formulas for Calculating the Parameters of Supported Coplanar Waveguides for (M)MIC's," *IEEE Trans. Microwave Theory Tech.*, **40**, pp. 41-48, 1992.
22. G. Ghione, "A CAD-Oriented Analytical Model for the losses of general Asymmetric Coplanar Lines in Hybrid and Monolithic MICs," *IEEE Trans. Microwave Theory Tech.*, **41**, pp. 1499-1510, 1993.
23. S. Ramo, J. R. Whinnery, T. Van. Duzer, *Fields And Waves In Communication Electronics*, John Wiley & Sons, New York, 1984.
24. M. Y. Frankel, S. Gupta, J. A. Valdmanis, and G. A. Mourou, "Terahertz Attenuation and Dispersion Characteristics of Coplanar Transmission Lines," *IEEE Trans. Microwave Theory Tech.*, **39**, pp. 910-916, 1991.
25. Y. J. Chiu, Ph. D. Thesis, University of California at Santa Barbara, 1999.
26. J. I. Pankove, *Optical Processes In Semiconductors*, Dover, New York, 1971.
27. S. S. Prabhu, S. E. Ralph, M. R. Melloch, and E. S. Harmon, "Carrier dynamics of low-temperature-grown GaAs observed via THz spectroscopy," *Appl. Phys. Lett.*, **70**, pp. 2419-2421, 1997.
28. W. H. Knox, G. E. Dorn, M. Asom, G. Livescu, R. Leibenguth, and S. N. G. Chu, "Low-temperature-grown GaAs quantum wells: Femtosecond nonlinear optical and parallel-field transport studies," *Appl. Phys. Lett.*, **59**, pp. 1491-1493, 1991.
29. Shantanu Gupta, J. F. Whitaker, and G. A. Mourou, "Ultrafast carrier dynamics in III-V semiconductors grown by molecular-beam epitaxy at very low substrate temperatures," *IEEE Journal of Quantum Electronics*, **28**, pp. 2464-2472, 1992.
30. D. H. Auston, "Picosecond optoelectronic switching and gating in silicon," *Appl. Phys. Lett.*, **26**, pp. 101-103, 1975.
31. Shuji Matsuura, and Geoffrey A. Blake, "A traveling-wave THz photomixer based on angle-tuned phase matching," *Appl. Phys. Lett.*, **74**, pp. 2872-2874, 1999.
32. Taiichi Otsuji, Nabil Sahri, Naofumi Shimizu, Tadao Nagatsuma, and Tadao Ishibashi, "A 105-GHz Bandwidth Optical-to-Electrical Conversion Stimulus Probe Head Employing a Unitraveling-Carrier Photodiode," *IEEE Photon. Technol. Lett.*, **11**, pp. 1033-1035, 1999.
33. J. P. Ibbetson, Ph. D. Thesis, University of California

*Correspondence: Email: sun@ee.ntu.edu.tw; Telephone: 886-2-23635251 ext 319; Fax: 886-2-23677467

A novel electrically tunable FBG laser

Lei Ding*, Yanjun Xu, Dejun Feng, Guiyun Kai, Xiaoyi Dong
Institute of Modern Optics, Nankai Univ., Tianjin 300071, China

ABSTRACT

A novel electrically tunable fiber Bragg grating (FBG) laser is reported. The FBG can be coupled to the fiber efficiently. The FBG is pasted on the surface of a magnetostrictive rod. The magnetostrictive rod is placed in a solenoid and it stretches under the magnetic field. Then the FBG is tuned, and the laser's wavelength alters. The tuning range is 1.6nm, the line-width is narrower than 0.3nm.

Keywords: EDFL, FBG, magnetostrictive rod, magnetic field

1. INTRODUCTION

In the optical communication system with high speed and large capacity, tunable laser with narrow line-width is needed to act as light source to diminish the influence induced by the fiber distribution and the temperature drift. A distributed feedback temperature sensing system also needs a wavelength-scanning light source which is satisfied by a tunable laser. A tunable laser is of important purport and wide foreground of application.

A semiconductor laser diode (LD) can be tuned through several ways. However, every method has its unconquered shortcomings. Compared with an LD, a fiber laser has quite a few advantages, such as low threshold and high efficiency. Among the many kinds of rare earth doped fiber lasers, the Er-doped fiber laser's (EDFL) wavelength is in 1500nm waveband, which is the 3rd window of the optical communication. What is more, because the Er-doped fiber has a wide gain band and the techniques of tuning are fairly simple, much attention is paid on the tunable EDFL. The research on the tunable fiber lasers has been developing rapidly during these years.

2. PRINCIPLE

Many methods can be used to tune fiber lasers, such as rotating grating, acoustic-optical modulator, electrically tunable LC etalon, *et al.* The tuning ranges of these methods are always up to tens of nanometers, but they suffer from a common malpractice: low coupling efficiency between the no fiber device and the fiber. The low coupling efficiency induces insertion losses which result in the low slope efficiency and the high threshold of the laser. A fiber Bragg grating (FBG) is a kind of fiber device, so it can conquer this malpractice.

In a ring-cavity EDFL, the FBG serves as a feedback device (shown in Fig. 1). Once the Bragg wavelength of the FBG is

* Correspondence: Email: dinglei@tjmail.com; ding_l@263.net; Telephone: (8622) 23509849

changed, the wavelength of the output laser is tuned. It is well known that the grating's Bragg condition is

$$\lambda_B = 2\Lambda n_{\text{eff}} \quad (1)$$

where λ_B is the FBG's central wavelength, Λ is the grating's period and n_{eff} is its effective refractive index. In order to change λ_B , Λ or n_{eff} must be changed. When the FBG is applied an axial stress, Λ is changed, then λ_B is tuned by the stress. The relationship between λ_B and the stress can be expressed as

$$\Delta\lambda_B = (1 - p_e)\epsilon_f \lambda_B \quad (2)$$

where $\Delta\lambda_B$ is the shift of λ_B , ϵ_f is the grating's strain, and p_e is the effective photoelastic coefficient which can be expressed as

$$p_e = \frac{n_{\text{core}}^2}{2} [p_{12} - \nu(p_{11} + p_{12})] \quad (3)$$

where p_{11} and p_{12} are the photoelastic coefficients of the strain tensor, ν is the Poisson ratio and n_{core} is the fiber core's refractive index. According to equation (2), the Bragg wavelength can shift under an axial stress.

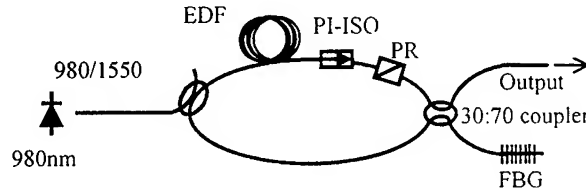


Fig.1 Schematic of the electrically tunable FBG laser

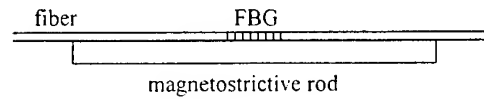


Fig. 2 FBG tuning device

Many methods can be used to supply an axial force on the FBG^{1,2}. The magnetostrictive material is a special kind of metal which can stretch under the magnetic field. Thus it can apply stress on the FBG³. In this paper, we use a magnetostrictive rod is used tune the EDFL. The FBG of the EDFL is pasted on the surface of a magnetostrictive rod, as Fig. 2 shows. The magnetostrictive rod is placed in a solenoid. Input a certain current into the solenoid, the magnetostrictive rod will elongate under the magnetic field. Thus the FBG also elongates and its Bragg wavelength shifts. Finally the output laser of the EDFL is tuned.

3. EXPERIMENT AND RESULT

The schematic of the tunable EDFL is shown in Fig. 1. A 980nm LD pumps a ring cavity. The ring cavity is composed of a 980/1550nm WDM, a piece of EDF, a polarization-independent isolator (PI-ISO), a fiber polarizer (PR) and a 30:70 coupler whose 70% port output the laser and 30% port is connected to the FBG. The FBG of the EDFL is pasted on the surface of a magnetostrictive rod. The magnetostrictive rod is made of TbDy(FeM)₂ system material. The rod is 10cm long, and its diameter is 5mm. The solenoid has about 2000 circles.

The primary wavelength is 1548.9nm, and its line-width is 0.277nm (shown in Fig.3). We input a certain current into the solenoid, and observe the shift of the laser's wavelength. The relationship between the current and the wavelength is shown in Fig. 4. In order to protect the solenoid and prevent the heat effect from affecting the fiber, the maximum current is decided to be 1.8A. Then the maximum shift of the wavelength is 1.6nm. The relationship curve's goodness-of-fit is 0.9982 and its slope is 0.8533. This indicates that the wavelength is linearly related to the current within a certain limit. Fig. 5

shows the relationship between the output power and the wavelength. The maximum power is $662\mu\text{W}$, the minimum is $637\mu\text{W}$, the average is $649.8\mu\text{W}$, and the variance is 0.00006. The output power is fairly stable in the tuning process.

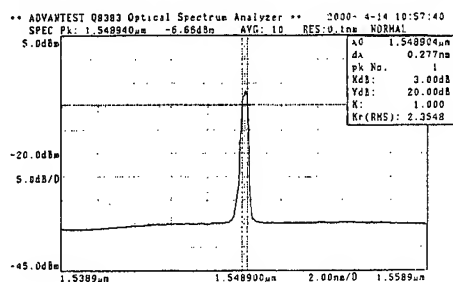


Fig. 3 Spectrum of the laser

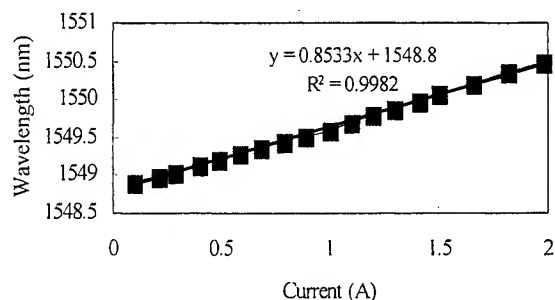


Fig. 4 Function of the wavelength vs the current

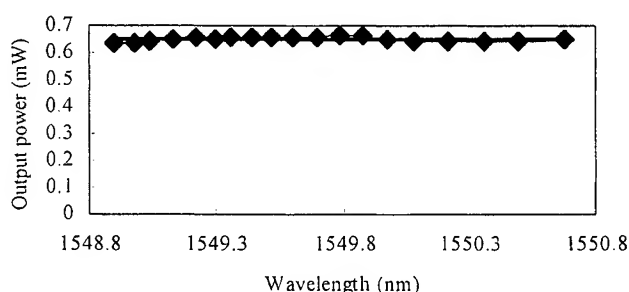


Fig. 5 Function of the output power vs the wavelength

4. CONCLUSION

We tune the ring-cavity fiber EDFL electrically with a magnetostrictive rod to realize the shifts of the output wavelength. Through this method, the laser's wavelength can be tuned in about 1.6nm range linearly. The electrically tunable EDFL laser can be utilized in the optical communication system and the sensing system. It can be developed to be a computer-controlled programmable EDFL.

ACKNOWLEDGEMENT

This work is supported by Chinese Natural Science Fund and Chinese National "863 Project" Fund

REFERENCES

1. G. A. Ball, W. W. Morey, "Continuously tunable single-mode erbium fiber laser", *Opt. Lett.*, **17** (6), pp.420-421, 1992
2. G. A. Ball, W. W. Morey, "Compression-tuned single-frequency Bragg grating fiber laser", *Opt. Lett.*, **19** (23), pp.1979-1980, 1994
3. J. L. Cruz, A. Diez, M. V. Andres, A. Segura, B. Ortega and L. Dong, "Fiber Bragg gratings tuned and chirped using magnetic fields", *Electron. Lett.*, **33** (3), pp.235-236, 1997

The Rapid Thermal Annealing Effects on Radio-Frequency Magnetron Sputtered P-Type GaN Thin Films and Al/P-type GaN Schottky Diodes

Ching-Wu Wang, Bo-Shao Soong, Jing-Yu Chen,
Chung-Tung Tseng, and Chih-Liang Chen
Dert. of Electronic, I-Shou University
Ta-Hsu Hsiang, Kaohsiung County,
Taiwan, ROC.

ABSTRACT

In this article, we report the effects of RTA on Mg-diffused GaN thin films and Al/Mg-diffused GaN Schottky diodes. After Mg-diffusion process, the samples were exposed to RTA treatment in the temperature from 800 to 900°C. The samples were studied by variable temperature Hall effect measurements, and PL spectroscopy. The reduced resistivity by higher RTA temperature is due to the increased activated acceptor. Evidence, showed that both near-band-edge emission and deep level luminescent in PL spectrum could be all enhanced by raising the RTA temperature. Considering the Al/Mg-diffused GaN Schottky diodes, the higher RTA temperature resulting in the superior forward conduction characteristics are suggested to be due to the more concentrations of hole and lower resistivity of the GaN thin film. However, the greater reverse leakage current and lower breakdown voltage were deduced to be the creation formation of Ga-Al compounds at the metal-semiconductor interface.

Keywords: RTA, Mg-diffused GaN, Schottky diodes, Hall effect, PL, resistivity, acceptor, p-type conductivity, reverse leakage, Ga-Al compounds

1. INTRODUCTION

Wide band-gap semiconducting GaN is a promising material for the blue light-emitting diodes (LEDs)¹ and laser diodes (LDs)². The problem to be solved in order to realize these emitting devices is how to obtain a higher hole concentrations of *p*-type GaN film. As is well known, present *p*-type GaN doping is achieved more readily with Mg impurities.³ Moreover, Mg doping renders the as-grown GaN by metalorganic chemical vapor deposition (MOCVD) highly resistive. Nowadays, most case to activate the acceptor dopant are either by a low energy electron beam irradiation (LEBBI)⁴ or a post-growth thermal annealing in a nitrogen ambient. Activating the Mg dopants in order to obtain a *p*-type conduction is possible due to the dissociation of H-Mg complexes.⁵⁻⁶ Quite recently, as-deposited *p*-type doping GaN has been achieved by molecular beam epitaxy (MBE) without post-growth treatment,⁷⁻⁹ which has been tentatively attributed to the absence of H in MBE growth. Despite of the progress in the in-situ Mg doping process, the conventional post-growth doping techniques, such as the diffusion process to achieve higher hole concentration for better device operation, has not been successfully demonstrated yet. In addition, a reliable rapid thermal annealing (RTA) process and therefore its influence on the properties of *p*-type GaN thin film still remains uncertain. The aim of this work is to ascertain the RTA effects on radio-frequency (RF) magnetron sputtered *p*-type GaN thin films and Al/*p*-type GaN Schottky diodes. Data from Hall effect measurement reveal that higher temperature of RTA treatment can effectively increase the concentration of activated acceptor leading an evidently reduced resistivity of *p*-type GaN thin film as well as a superior rectifier characteristic of Al/*p*-type GaN Schottky diodes. A relationship between photoluminescence (PL) spectra and RTA-treated *p*-type GaN sample is also discussed.

2. EXPERIMENT

The experiment in detail is described as in the following: GaN thin films were prepared by a two-stage-growth¹⁰ of RF magnetron sputtering method. The source material, made by Superconductive Components, Inc. (USA), was GaN target (3 inch diam.) with 99.999 % purity. Prior to loading the *p*⁺-Si (111) substrates into the sputter chamber, the wafers were rinsed in 10:1 HF acid to remove the native oxide layer and blown dry. During the growth process, the RF power was

* Correspondence: E-mail: cwwang@isu.edu.tw; Telephone: 886-7-6577711 ext. 6668; Fax: 886-7-6577056

controlled at 50W and a mixed sputtering gas of N_2 and Ar was utilized to keep the sputtered pressure at 5×10^{-3} Torr. For the first stage, a thin GaN buffer layer ($\approx 500 \text{ \AA}$) was deposited on Si substrate at 400°C . Subsequently, the substrate temperature was elevated to 500°C for annealing the GaN buffer under a purified N_2 atmosphere for 30 min. Next, a 4500 \AA thickness of GaN epilayer was grown on top of GaN buffer at 700°C . Then, we deposited a Mg/Ag film on top of GaN/p⁺-Si sample by thermal evaporator. For Mg diffusion, the samples were sealed in a vacuumed quartz ampoule and were put into the furnace at 950°C for 24 hours. After Mg diffusion, the sample was removed from the ampoule and the Mg/Ag was etched off by a solution of $\text{HCl} : \text{H}_2\text{O} = 1 : 1$. Finally, various temperatures of RTA treatment ($800 \sim 900^\circ\text{C}$) on the Mg-diffused GaN samples were carried out in a 0.5 Torr of purified N_2 ambient for 1 min.

SIMS analysis were performed using Cameca IMS-4f instrument with a Cs^+ primary ion source. The impact energy is 1.5 keV, and the sputter rate is about 0.2-0.3 nm/s. The SIMS profiles were taken by MCs^+ secondary ions to minimize matrix effects¹¹ (where M is the element to be analyzed). The Mg concentration is quantified using relative sensitivity factors derived from the analysis of GaN standards with known doses of Mg implants.

The Hall effect measurements were conducted in the temperature range from 80 to 500 K. The magnetic field was 18 K Gauss. For the Hall-effect measurements, samples of $5 \times 5 \text{ mm}^2$ size were cut from the wafers and indium metal dots were evaporated in the four corners of the samples to obtain electrical contacts in the Van der Pauw geometry. The indium contacts were annealed at 400°C for 1 min in the vacuum and exhibited an Ohmic characteristic over the entire temperature range of the measurement.

For the PL measurement, the 325 nm He-Cd laser was used as the excitation source at room temperature. For I-V measurement, Schottky diodes were made by evaporating aluminium (Al) and gold (Au) on top of GaN thin film, respectively, which provide Schottky contact at Al/GaN and Ohmic contact at Au/GaN junctions.

3. RESULTS AND DISCUSSION

Fig. 1 shows the SIMS depth profile of Mg dopant which diffused into GaN thin film at 950°C for 24 hours. The profile with double fronts agrees with the previous results of Mg-diffused in $\text{Al}_x\text{Ga}_{1-x}\text{As}$,¹² which can be well explained by the kick-out mechanism.¹³ Furthermore, the profile reveals a Mg concentration of $\sim 2 \times 10^{19} \text{ cm}^{-3}$ underneath the GaN surface with a slowly varying monotonic decrease to a value of $\sim 7 \times 10^{17} \text{ cm}^{-3}$ at a depth of $0.5 \mu\text{m}$. Under the interface of GaN/p⁺-Si, the Mg concentration is rapidly decrease. It means that the Mg atoms are difficult to enter the p-Si substrates by high temperature diffusion.

Hole concentrations were measured as functions of reciprocal temperature for Mg-diffused p-type GaN after RTA treatment at 800, 850, and 900°C , which are shown in Fig. 2. The solid lines were calculated from the charge neutrality condition. The hole concentrations, p , were obtained from the experimental Hall constants, R_H , with $p = r_H / qR_H$ (q = electron charge, r_H is Hall scattering factor). The Hall measurement data obtained above 200 K for the samples annealed at 800°C shows an activation energy ($E_A = 182 \text{ meV}$) of a shallow acceptor. In addition, higher temperature, 850°C and 900°C , of RTA-treated samples reveal that more shallow acceptor with thermal activation energies of $E_A = 176 \text{ meV}$ and 165 meV , can be obtained, respectively. Such a result coincide with the measurement that hole concentration could be increased by raising the RTA temperature.

The resistivity was measured as a function of temperature from RTA-treated GaN samples, which is illustrated in Fig. 3. For the as-diffused specimens, reliable resistivity measurements could only be obtained at temperatures more than 400 K, with the resistivity as high as $10^{11} \Omega\text{cm}$ at 400 K. Evidence should that if only high temperature ($\geq 800^\circ\text{C}$) of RTA was applied, the resistivity can be significantly decreased. Moreover, the higher RTA temperature the less resistivity can be measured.

Fig. 4 illustrates the photoluminescence (PL) spectra which were taken from as-diffused and different temperature of RTA treated Mg-diffused GaN samples. These spectra show near-band-edge emission and the deep luminescence at 2.7 eV were evidently enhanced by raising the RTA temperature. The relationship between the intensity of commonly observed "yellow" emission and RTA temperature was not significantly detected.

In recent years, substantial effort has been focused on the investigation of electrical characteristics [current-voltage (I-V)] of Schottky contact of Ti/Au, Pt, Ni, Au, Ti on MOCVD and MBE-made p-GaN¹⁴⁻¹⁶. In this work, we observe the consistence that RTA temperature has a significant effect on the Mg-diffused Al/sputtered p-GaN Schottky diodes. In Fig. 5, it is clear that for samples treated with higher RTA temperature superior forward conducting characteristics could be resulted, i.e., smaller turn-on voltage and bigger forward conduction current despite the reverse leakage current is a little bit larger. It is our assertion that such a phenomenon is due to higher the fact that temperature of RTA-treated samples possesses more concentrations of hole and lower resistivity. Nevertheless, in the reverse-biased condition, the large leakage current and the smaller breakdown voltage were deduced by the presence of Ga-Al compounds at the metal-semiconductor interface. Such a formation of Ga-Al compounds has been identified in the x-ray diffraction measurements and been

demonstrated to reduce the Schottky barrier height, yielding the larger reverse leakage current and smaller breakdown voltage.

4. CONCLUSIONS

We have investigated the RTA effects on the performance of Mg-diffused GaN thin films and Al/Mg-diffused Schottky diodes. Evidence shows that the higher RTA temperature not only increases the hole concentrations of Mg-diffused GaN thin films but also significantly enhances the near-band-edge emission and deep level luminescence of Mg-diffused GaN thin films in the PL spectrum. The higher RTA temperature leading a superior forward conduction characteristic was suggested to be due to the more concentrations of hole and lower resistivity. However, the greater reverse leakage current and lower breakdown voltage due to higher RTA temperature were deduced to be the creation of Ga-Al compounds at the metal-semiconductor interface. Further work in this direction is necessary.

ACKNOWLEDGMENTS

One of the authors (Ching-Wu Wang) gratefully acknowledges the financial support from the National Science Council (NSC) in Taiwan under contract number : NSC89-2215-E-214-004.

REFERENCES

1. H. Shen, J. Pamulapati, M. Taysing, M. C. Wood, R. T. Lareau, M. H. Ervin, J. D. Mackenzie, C. R. Abernathy, S. J. Pearton, F. Ren, and J. M. Zavada, *Solid-State Electronics* **43**, p.1231 (1999).
2. Shuji Nakamura, Masayuki Senoh, Shin-ichi Nagahama, Toshio Matsushita, Hiroyuki Kiyoku, Yasunobu Sugimoto, Tokuya Kozaki, Hitoshi Umemoto, Masahiko Sano and Takashi Mukai, *Jpn. J. Appl. Phys. Part 2*, **38**, p. L226 (1999).
3. H. Morkoc, S. Strite, G. B. Gao, M. E. Lin, B. Sverdlov, and M. Burns, *J. Appl. Phys.* **76**, p. 1363 (1994).
4. H. Amano, M. Hiramatsu, and I. Akasaki, *Jpn. J. Appl. Phys.* **28**, p. L2112 (1989).
5. S. Nakamura, N. Iwasa, M. Senoh, and T. Mukai, *Jpn. J. Appl. Phys.* **31**, p. 1258 (1992).
6. S. Nakamura, M. Senoh, and T. Mukai, *ibid.* **32**, L8 (1993).
7. M. S. Brandt, N. M. Johnson, R. J. Molnar, R. Singh, and T. D. Moustakas, *Appl. Phys. Lett.* **64**, p. 2264 (1994).
8. M. Rubin, M. Newman, J. S. Chan, T. C. Fu, and J. R. Ross, *Appl. Phys. Lett.* **64**, p. 64 (1994).
9. M. E. Lin, G. Xue, G. L. Zhou, J. E. Green, and H. Morkoc, *Appl. Phys. Lett.* **63**, p. 932 (1993).
10. T. Sasaki and T. Matsuoka, *J. Appl. Phys.* **77**, p. 192 (1995).
11. K. Wittmaack, in *Secondary Ion Mass Spectrometry SIMS VIII*, edited by A. Benninghoven, K. T. F. Janssen, J. Tumpner, and H. W. Werner (Wiley, Chichester, p. 91,(1992)).
12. S. Mukai, Y. Kaneko, T. Nukui, M. Mori, M. Watanabe, H. Itoh, and H. Yajima, *Jpn. J. Appl. Phys.* **28**, L1 (1989).
13. S. Yu, T. Y. Tan, and U. Gosele, *J. Appl. Phys.* **69**, p. 3547 (1991).
14. T. Mori, T. Kozawa, T. Ohwaki, Y. Taga, S. Nagai, S. Yamasaki, S. Asami, N. Shibata, and M. Koiki, *Appl. Phys. Lett.* **69**, p. 3537 (1996).
15. Hidenori Ishikawa, Setsuko Kobayashi, Y. Koide, S. Yamasaki, S. Nagai, J. Umezaki, M. Koike, and Masanori Murakami, *J. Appl. Phys.* **81**, p. 1315, (1997).
16. M. Asif Khan, J. N. Kuznia, D. T. Olson, M. Blasingame, and A. R. Bhattarai, *Appl. Phys. Lett.* **63**, p. 2455 (1993).

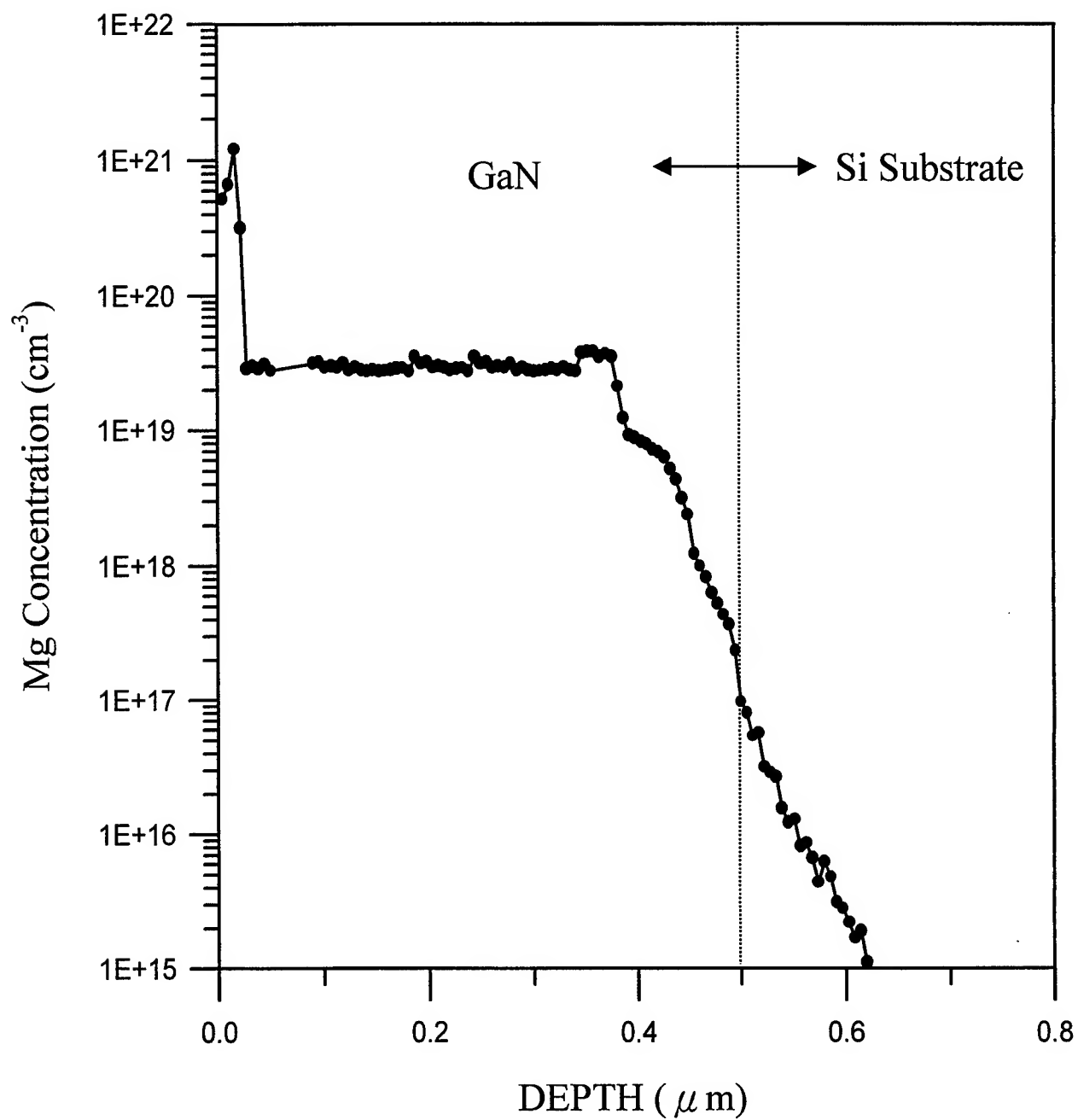


Fig. 1. SIMS profile for Mg diffusion in GaN at 950°C for 24 hours.

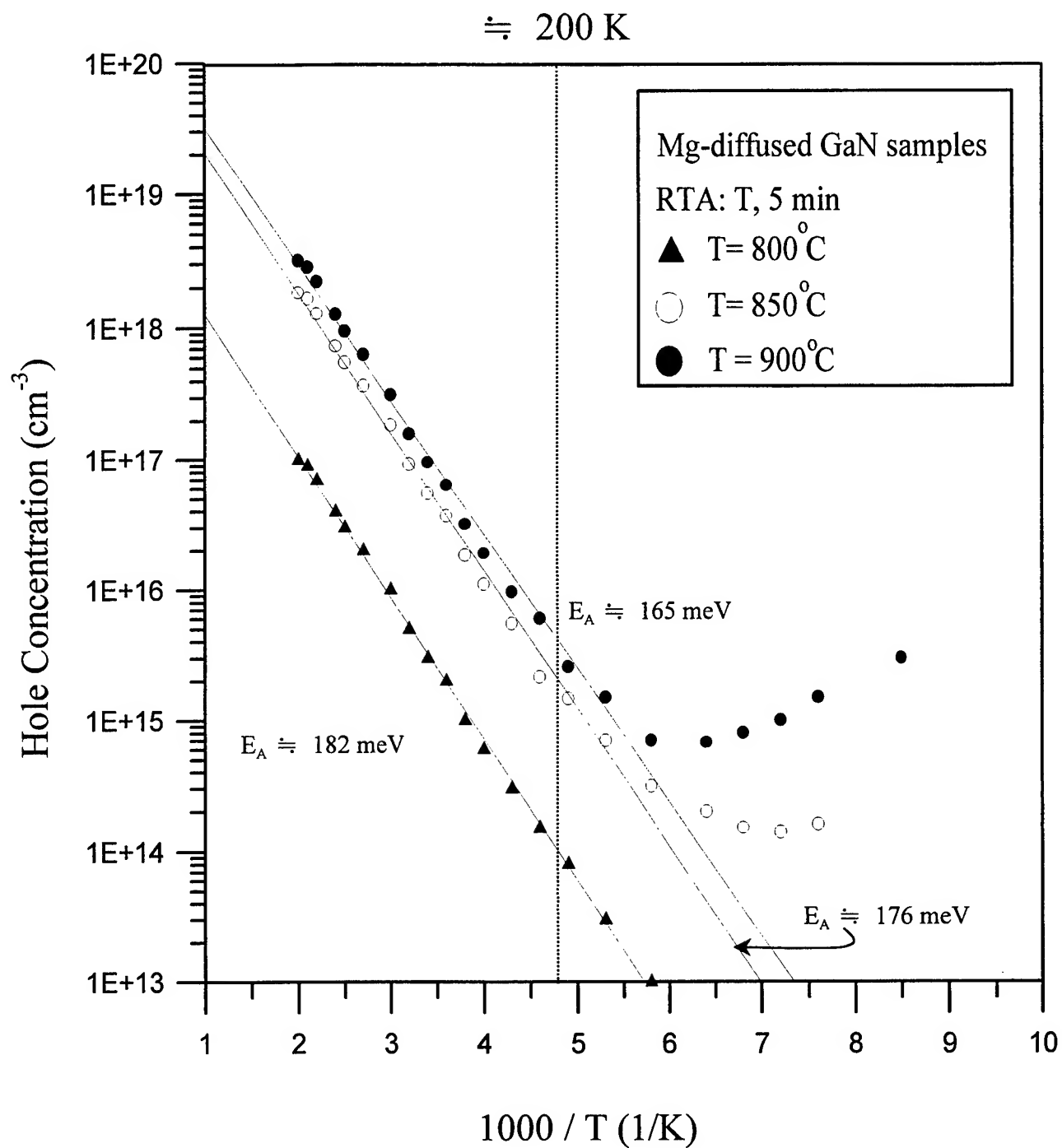


Fig. 2. Hole concentration vs. temperature (symbols) as determined from Hall effect measurements for a p-type, Mg-diffused GaN sample after acceptor activation at incremental temperatures T. The solid lines represent calculated hole concentrations.

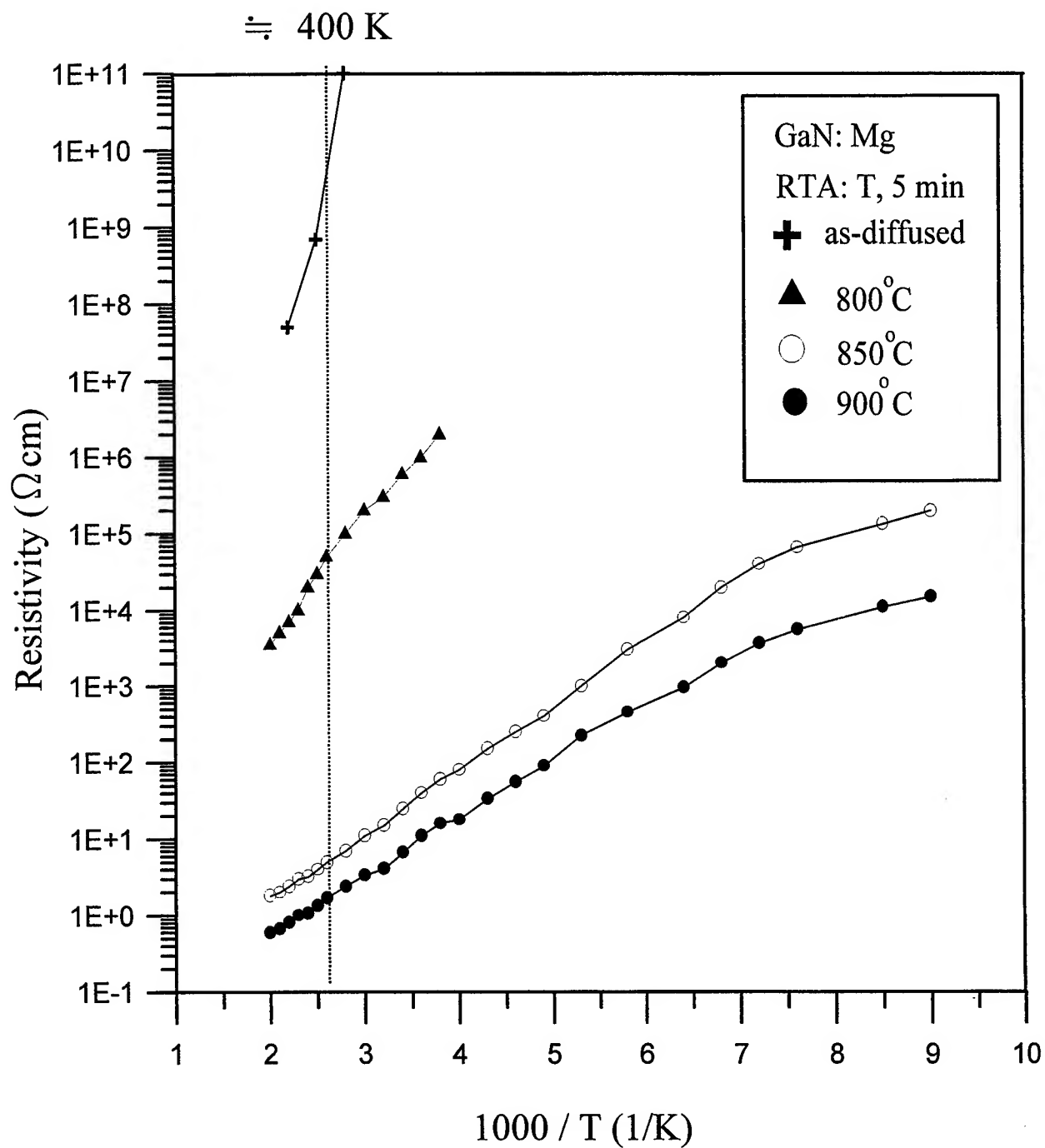


Fig. 3. Resistivity of a Mg-diffused GaN sample as a function of reciprocal temperature. Data are shown for as-diffused sample and after annealing for 5 min in a RTA system at incremental temperatures T.

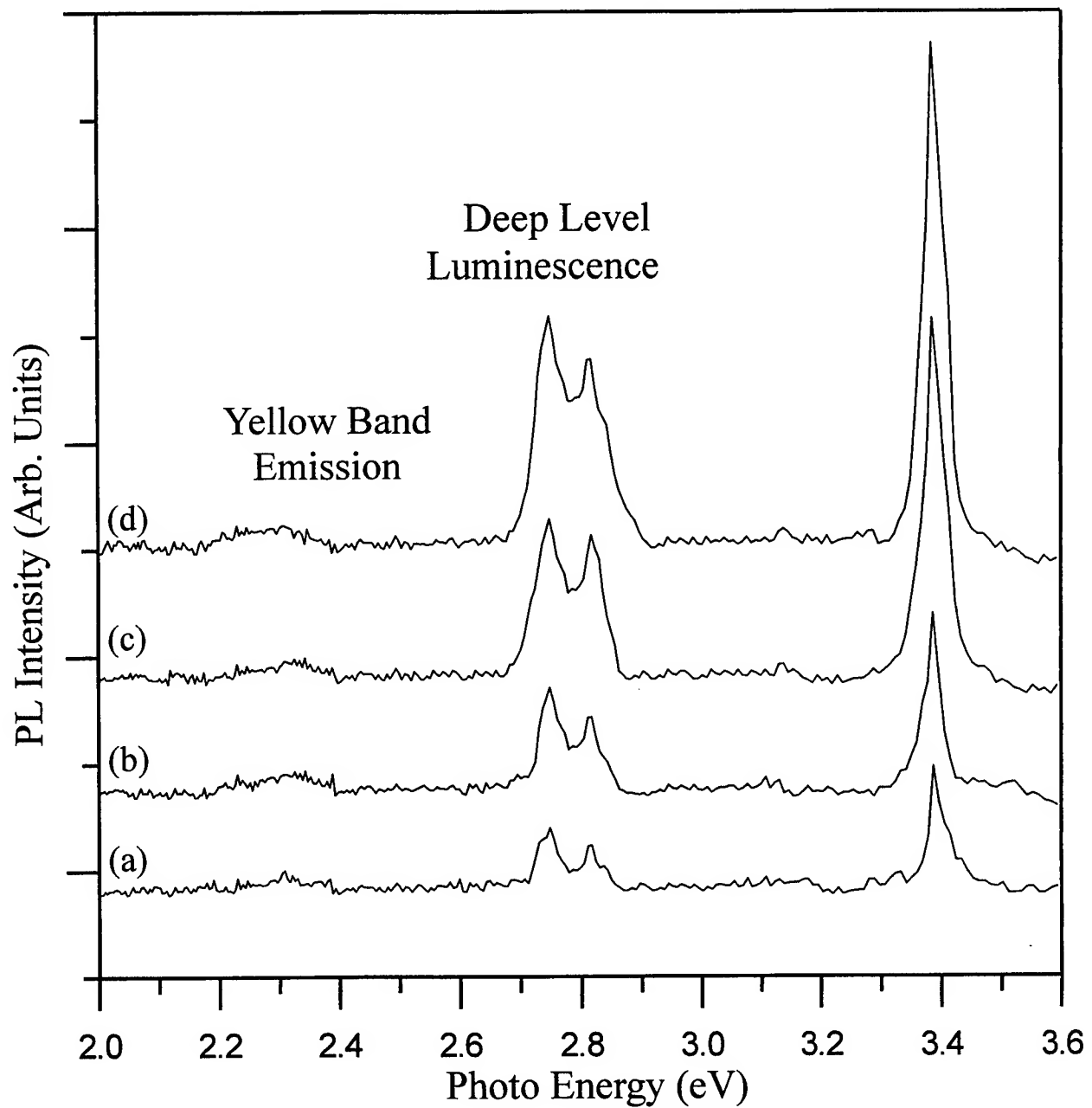


Fig. 4. Typical PL spectra of as-diffused and after RTA treatment GaN samples at room temperature.

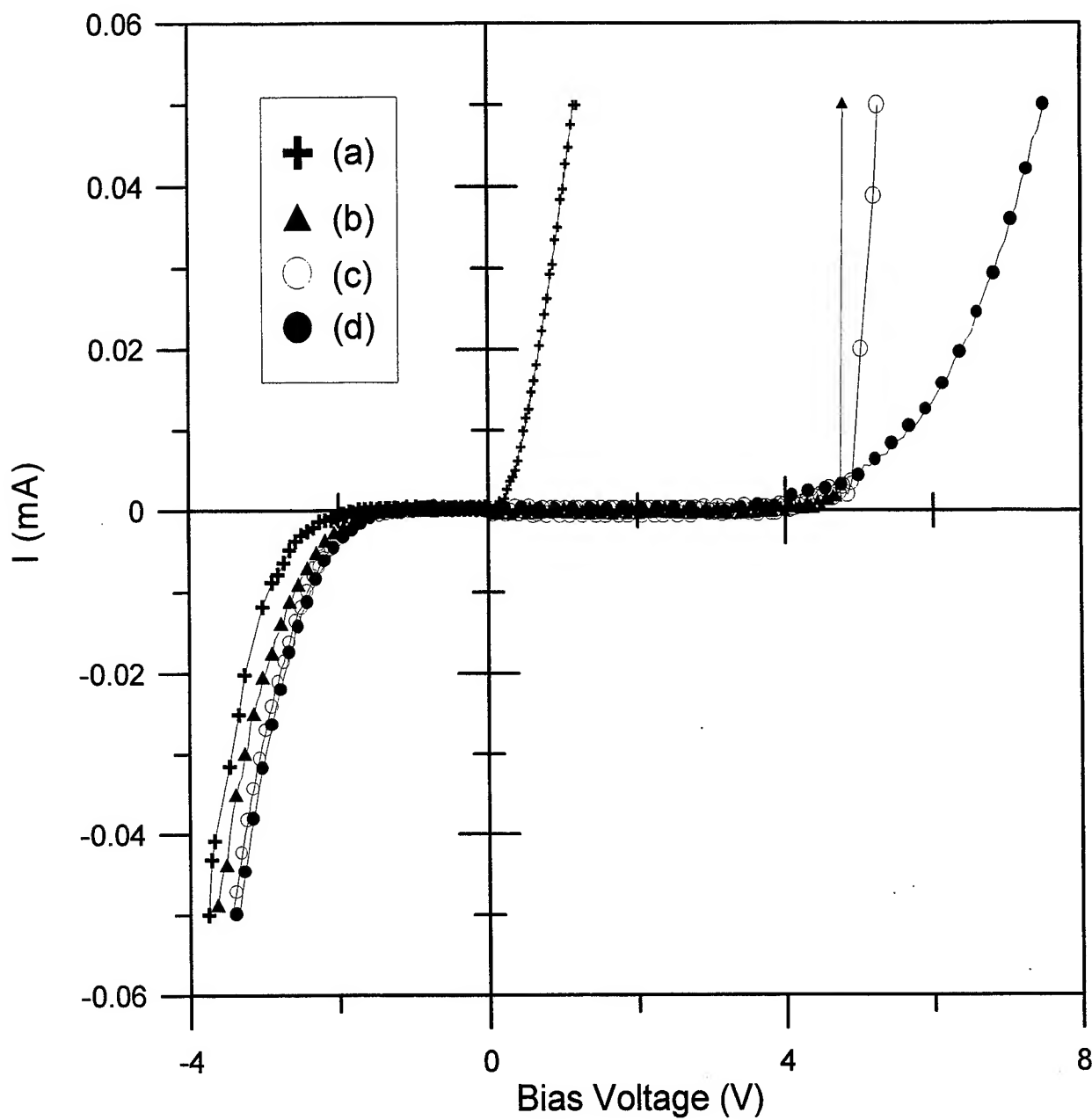


Fig. 5. Current-voltage characteristics of Al/p-GaN Schottky diodes. Curve (a), (b), and (c), represent the samples treated by RTA temperatures of 900, 850, 800°C for 5 min, respectively. Curve (d) represents the as-diffused sample.

II-VI Light Emitting Diode with Low Operation Voltage

Wen-How Lan, Y. T. Cheng, Alpha C. H. Lin, Y. T. Cheng and H. Chang
Chung Shan Institute of Science and Technology, Taoyuan, Taiwan, R.O.C.

Wen-Ray Chen, Yan-Kuin Su and Shoou-Jinn Chang
Department of Electrical Engineering, National Cheng Kung University
Tainan, 70101, Taiwan, R.O.C.

W. C. Chou and C. S. Yang
Department of Physics, Chung Yuan Christian University, Chungli, Taiwan,
R.O.C.

Keywords : II-VI, ZnSe, ZnCdSe, light emitting diode,

Abstract

In our previous work, we first propose the Au/AuBe is a good ohmic contact material to p-type ZnTe. After apply the material to II-VI light emitting diode, the operation voltage as low as 2.4 V can be observed. The II-VI blue light emitting diode (LED) were grown in a RIBER 32P system with Zn(6N), Se(6N), Te (6N), Cd(6N) on (001) GaAs n⁺ substrate. The structure consisted a GaAs:Si (n⁺) buffer layer, ZnSe:Cl (0.5um), ZnSe(200Å)/ZnCdSe (100Å) multiple quantum well, ZnSe(200Å), ZnSe:N(0.3um), ZnSe:N/ZnTe:N multilayer and ZnTe:N (300Å). Standard photolithography technology was done to fabricate the diode. The mesa etch was done by K₂Cr₂O₇ : H₂SO₄ : H₂O etching solution. The p-type ohmic was done by AuBe/Au metal. The emission wavelength was 530nm (room temperature) and 495 nm (30 K) with 2.4 V under CW operation. Since low operation voltage introduced less heat in the device, better thermal behavior can be expected with this low operation voltage.

I. Introduction

The ZnSe based semiconductor diode has led to a world-wide interest in blue/green light emitting devices. Since the first demonstration of ZnSe-based green laser¹, the lifetime of these structures has been increased. Until now, the lifetime of ZnSe based laser structure seems to be limited due to the degradation caused by lattice defect. The defect may act as a recombination center and were characterized as dark line defect². These dark line defects may enhance after the thermal process and cause the degradation of device. Thus, lower heat anticipate process such as lower specific contact resistance plays an important role in the fabrication of ZnSe based light emitting diode.

The development of ohmic contact to p-type II-VI semiconductor such as ZnTe³⁻⁵, ZnSe⁶⁻⁹ and ZnMgSSe¹⁰ have been widely studied. The use of Au/Pt/Ti/Ni as low as $1.1 \times 10^{-6} \Omega\text{-cm}^2$ to p-type ZnTe ($N_A - N_D = 3 \times 10^{19} \text{ cm}^{-3}$) can be achieved after 250C anneal⁵. In our previous study, we introduction of AuBe as a p-type contact metal to ZnTe:N epilayer³, the contact resistance as low as $3 \times 10^{-6} \Omega\text{-cm}^2$ can be achieved. In this work, we applied this technology to the formation of II-VI light emitting diode grown by molecular beam epitaxy (MBE).

II. Experimental details

The II-VI blue light emitting diode (LED) were grown in a dual chamber RIBER 32P system with Zn(6N), Se(6N), Te (6N), Cd(6N) on (001) GaAs n+ substrate. The n+ (100) GaAs was thermal cleaned in the III-V chamber and the GaAs buffer layer was deposited on the GaAs substrate. After that, the wafer was transferred to the II-VI chamber. After the temperature raised gradually to 280 C, the II-VI LED structure were deposited on the GaAs sequentially. As shown in figure 1, the structure consisted a GaAs:Si (n+) buffer layer, ZnSe:Cl (0.5 μm , $2.0 \times 10^{18} \text{ cm}^{-3}$), ZnSe(200Å)/Zn_{0.8}Cd_{0.2}Se (100Å) multiple quantum well, ZnSe(200Å), ZnSe:N(0.3 μm), ZnSe:N/ZnTe:N multilayer and ZnTe:N (300Å, $2.0 \times 10^{19} \text{ cm}^{-3}$). The multilayer of ZnSe:N / ZnTe:N consists six ZnSe:N barriers (16Å) and six ZnTe:N wells(4Å, 5Å, 6Å, 8Å, 11Å, 17 Å thick). These multiple quantum well were designed for reduction of the contact resistance.

The device mesa were etched to 3000Å proceed with $K_2Cr_2O_7 : H_2SO_4:H_2O$ solution. After the chemical cleaning with $HF:H_2O=1:20$ (volume ratio) , the normal lift-off process of AuBe/Au (1000/2000Å) metals were deposited on the p-type ZnTe surface by thermal deposition, followed by the metals AuGe/Au (1000Å/2000Å) were deposited on the backside (GaAs n+ substrate) as the n-type ohmic contact. The device were thermal annealed in hydrogen ambient with 150 C in 10 minute to achieve a good ohmic contact.³.

III. Results and discussions

Fig. 2 shows the voltage - current ($V - I$) and light intensity - current ($L - I$) relations of the II-VI diode before annealing. The threshold voltage from I-V curve is around 3.3 V. The light output can be observed as the applied voltage higher than 4.3 V. Thus, within the applied voltage from 3.3V to 4.3 V, some certain quantity of current were considered not to pass through the quantum well region and act as leakage current.

Fig. 3 shows the current - voltage ($I - V$) and light intensity - voltage ($L - V$) relations of the II-VI diode after annealing. An improved I-V curve can be observed clearly compared with Fig. 2. The threshold voltage was improved to around 2 V. The light output can be observed as the applied voltage higher than the threshold voltage (~ 2 V).

The total threshold voltage is a summation of effective resistance (3) , conduction and valance band offset (ΔE_c , ΔE_v). Since the interdiffusion of ZnSe/ZnCdSe can be observed only as high as 350 C¹¹ , we may assumed that no conduction and valance band offset change can be observed in the 150 C annealing process. The improvement of I-V characteristic may come from the reduction of contact resistance.

In the operation range from 2 to 2.8V shown in Fig, 3, the current and light output increases simultaneously. The electron – hole recombination happened in the quantum well region and generate the light output. The light output increase as the injection carrier increase.

In the operation range from around 2.8 V to 3.5 V shown in Fig. 3, the current increase while we increase the voltage. Yet, the light output seems not increase as the current increase. The electron may flow through the ZnSe/ZnCdSe multiple quantum well region in this voltage and may pass to p-ZnSe region. Similarly, the hole may pass through to the n-ZnSe region also and thus reduce the recombination probability in the ZnCdSe quantum well. Since there were no midgap luminescence under strong forward bias ¹², some certain defect may exist in the p-type and n-type ZnSe region. The electron-hole combination may caused by these defect and thus reduce the effective recombination current in the ZnCdSe quantum well region and reduce the light output

With the bias voltage higher than 3.5 V, a lot of electron and hole may inject into the ZnCdSe quantum well region. The light intensity increases almost linearly as the current increase.

IV. Summay

We have described the characteristics of ZnSe/ZnCdSe/ZnSe/ZnTe light emitting diode fabricated in our laboratory, and shown the AuBe is an effective p-metal to this structure. The threshold as low as ~2 V can be achieved in this structure. The light output with the applied voltage (~2.4V) lower than the band gap of ZnSe (~2.6eV) has been observed and thus led us to obtain the carrier overflow mechanism under different bias.

V. Acknowledgements

This work was supported by the National Science Council, R.O.C.

Reference

1. M.A.Haase, J.Qiu, J.M.deOuydt and H. Cheng
Appl. Phys. Lett.,59, pp1272 , 1991.
2. Degradation of II-VI based blue-green light emitters
S.Guha, J.M.DeOuydt, M.A.Haase, J.Qiu, H.Cheng
Appl. Phys. Lett, 63(23), pp3107, 1993
3. AuBe Ohmic contacts to p-type ZnTe.
W.H.Lan, W.J.Lin, Yi.Cheng.Cheng, K.Tai, C.M.Tasi, P.H.Wu, K.H.Cheng,
S.T.Chou, C.M.Yang, Yi.Chang.Cheng and K.F.Huang
Electronics Letters. 34(25), pp2434, 1998
4. Low resistance ohmic contacts for p-type ZnTe
M. Ozawa, F. Hiei, M. Takasu, A. Ishibashi, K. Akimoto
Appl. Phys. Lett. 64(9), pp1120, 1994.
5. Electrical properties and microstructures of Au/Pt/Ti/Ni ohmic contacts of
p-type ZnTe
K.Mochizuki, A.Terano, M.Momose, A.Taike,M.Kawata, J.Gotoh, S.I.
Nakatsuka.
Appl. Phys. Lett. 67(1), pp112, 1995
6. Improved ohmic contacts for p-type ZnSe and related p-on-n diode structure.
Y. Lansari, J. Ren, B.Sneed, K.A.Bowers, J.W.Cook, Jr. and J.F.Schetzina
Appl. Phys. Lett. 61(21), pp2554, 1992.
7. Cd and Te-Based Ohmic contact materials to p-type ZnSe.
K.Hashimoto, Y.Koide, O.Tadanaga T.Oku, N. Teraguchi, Y.Tomomura and A.
Suzuki, M. Murakami
J. of Electronic Materials, 24(12), pp1823, 1996
8. Au-Ag/Ni/Te metal multilayer contact to p-type ZnSe
S. Yoshii, T. Yokogawa, Y. Sasai
Jpn. J. Appl. Phys., 36(4A), pp. L386, 1997.

9. Electrical transport and trap properties in the nitrogen-doped p-type MBE-grown ZnSe layers on GaAs using different contact materials.
G.Prosch, R.Beyer, M. Behringer, M.Fehrer, H. Burghardt, E.Thomas, D.Hommel, D.R.T. Zahn.
Journal of Crystal Growth, 184, pp440, 1998
10. Ohmic contact to p-ZnSe and p-ZnMgSSe
S.J.Chang, W.R.Chen, Y.K.Su, R.C.Tu, W.H.Lan, H.Chang
Elec. Lett. 35(15), pp1280, 1999
11. Contactless electroreflectance study of strained ZnCdSe/ZnSe double quantum wells
R. C. Tu, Y.K Su, D.Y.Lin, C.F.Li, Y.S.Huang, W.H.Lan S.L.Tu, S.J.Chang, S.C.Chou, W.C. Chou
J. Appl. Phys, 83 (2), pp1043, 1 Jaunary 1998.
12. Comparison of electrical and optical properties of n-I-I and p-I-n ZnSSe heterostructure diodes
Y. Fujii, I.Suemune, M.Fujimoto
Jpn. J. Appl. Phys. 33(1B), pp840, 1994

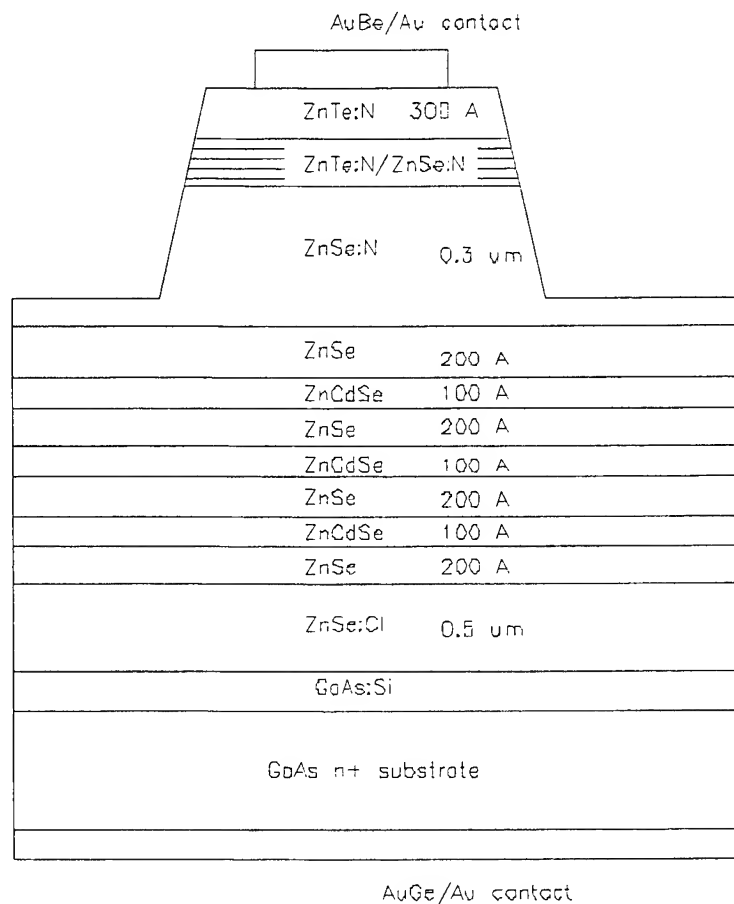


Figure 1 Schematic structure of the II-VI light emitting diode (LED) structure grown by molecular beam epitaxy (MBE)

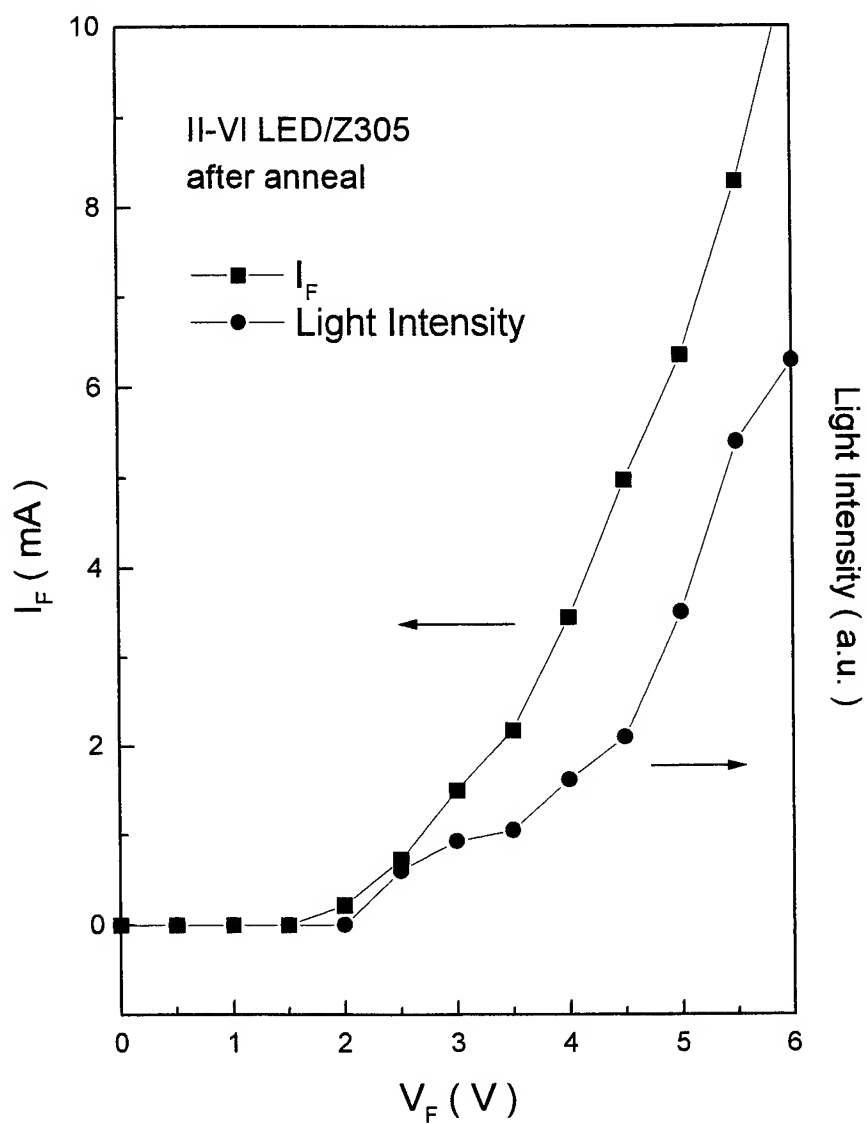


Figure 2 The the current - voltage (I - V) and light intensity - voltage (L - V) relations of the II-VI diode before annealing.

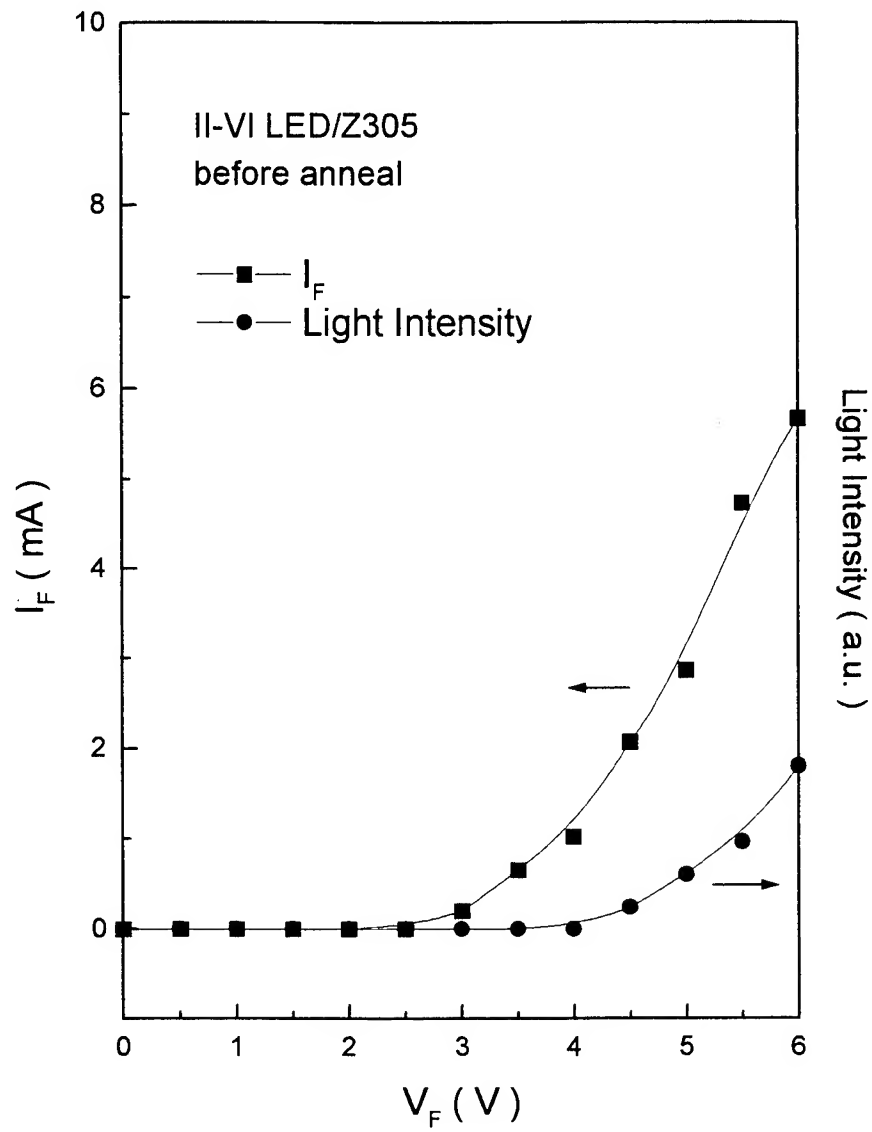


Figure 3 The the current - voltage (I - V) and light intensity - voltage (L - V) relations of the II-VI diode after annealing.

Temperature dependent optical properties of the InGaN semiconductor materials: experimental and numerical studies

Yen-Kuang Kuo*, Jih-Yuan Chang, Kuo-Kai Horng, Ya-Lien Huang,
Yuni Chang, Hsu-Ching Huang

Department of Physics, National Changhua University of Education,
Changhua 50058, Taiwan

ABSTRACT

The InGaN semiconductor materials have important applications in short-wavelength light emitting diodes and semiconductor lasers. In this work, we study the optical properties of a single quantum well and a multiple quantum well InGaN devices experimentally with a photoluminescence measurement system and numerically with a commercial *Lastip* simulation program. Important optical parameters such as the peak wavelength, the emission intensity, and the bandwidth of the photoluminescence spectra at various temperatures and pump power levels are characterized and compared to the results obtained from the *Lastip* numerical simulation. The effects of the indium concentration in quantum well, the well width, and the bowing parameter on the optical properties of the InGaN quantum well structures are also studied numerically with the *Lastip* simulation program. Good agreement between the experimental and numerical results is observed.

Keywords: InGaN, quantum well, photoluminescence, numerical simulation.

1. INTRODUCTION

Gallium nitride semiconductor materials have received great attention in the past few years due to their important applications in short wavelength (blue and green) light emitting diodes and semiconductor lasers.¹⁻⁵ Owing to the lack of lattice matched substrates, the crystal growth and the device fabrication for the III-N semiconductor materials are not as simple as the conventional semiconductor materials. In the mean time, the physics related to gallium nitride materials has not been well developed. Therefore, much effort is still required to learn more about this new material system.

Among the most important characterization and analysis methods, photoluminescence (PL) measurement is one of the most convenient and effective means to investigate the optical properties of the gallium nitride materials. In this paper, we investigate the temperature dependent optical properties of an InGaN single quantum well (SQW) and an InGaN multiple quantum well (MQW) structures experimentally with a photoluminescence measurement system. In addition, we utilize a commercial *Lastip* simulation program to study the optical properties of the InGaN devices numerically. If good agreement between the experimental and numerical results may be obtained, the *Lastip* simulation program can then be utilized to explore other physical properties of the InGaN materials, such as the effects of the indium concentration in quantum well, the well width, and the bowing parameter.

The bowing parameter is one of the most important parameters for the characterization of the InGaN optical properties. However, different bowing parameters are found in different publications.^{3,6,7} In this study we use different bowing parameters in our simulation program which make the simulation results best fit to the experimental results.

2. RESULTS OF EXPERIMENTS AND SIMULATIONS

Both of the InGaN quantum well structures under study are grown on c-face sapphire substrates. The structures of both wafers are shown in Fig. 1. For the SQW structure, the active layer is sandwiched between two n-type GaN layers. The active layer of the MQW structure contains five pairs of quantum wells where each well has a thickness of 3.5 nm and each barrier has a thickness of 9 nm. For the temperature dependent PL measurements, the 351.1-nm ultraviolet output of an

argon ion laser is used as the pump source and a UV-enhanced, liquid nitrogen cooled CCD array (1340×100 pixels) is used as the photo detector.

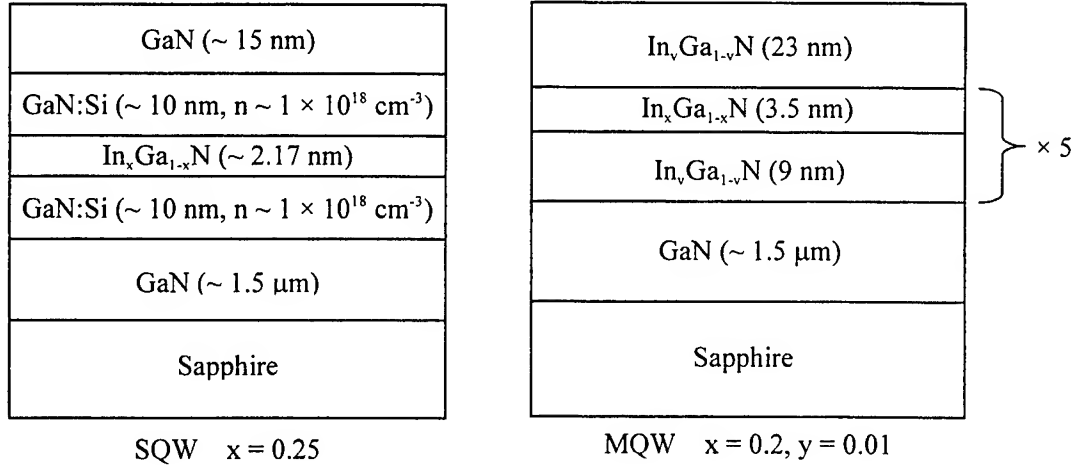


Fig. 1. Structures of the InGaN SQW and MQW devices.

Figure 2 shows the photoluminescence spectra of the SQW InGaN as functions of the temperature, ranging from 300 K to 19 K. Figure 2(b) is an expanded picture of Fig. 2(a) where the curves at high temperatures can be visualized. Since it is a quantum well structure, the quantum efficiency is high and blue luminescence can easily be observed even at room temperature. As shown in Fig. 2(b), the peak wavelength is near 453 nm and the spectral width (FWHM) is about 25 nm at 300 K. Full emission spectrum (400-700 nm) shows that no yellow luminescence⁸ is observed.

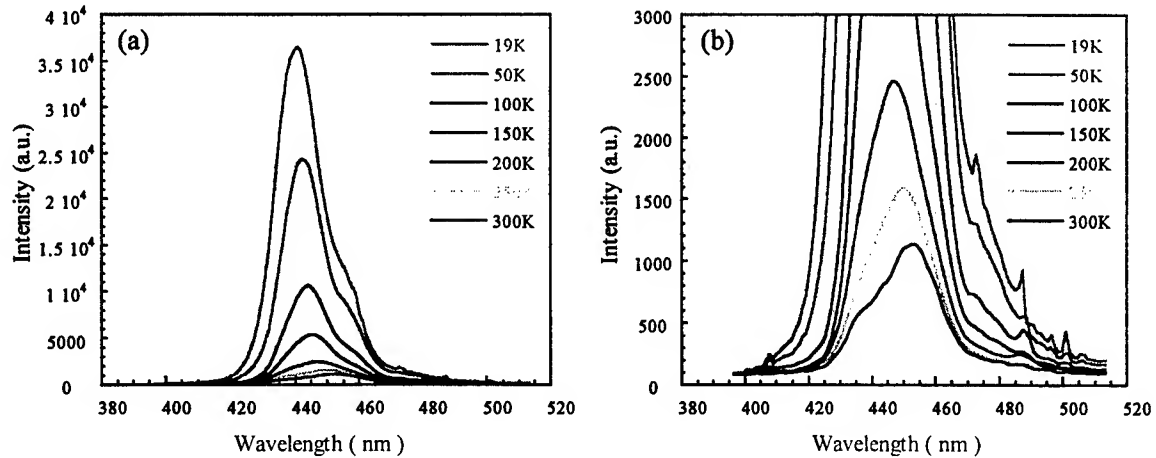


Fig. 2. Photoluminescence spectra of the SQW InGaN at various temperatures. Figure 2(b) is an expanded picture where the curves at high temperatures can be visualized.

The PL spectra of the MQW structure show strong interference effect, especially at high temperatures. Hence, it is difficult to determine the peak wavelength. We conduct a homogeneity measurement for the MQW wafer. We find that there are two peaks with a spectral difference of about 11 nm between them at room temperature. As position changes, the relative intensities at the two peaks change accordingly, which implies that the thickness of the active layer is a function of position. Figure 3 shows the peak wavelength of the SQW structure and the PL intensity, obtained by integrating the spectra over the

spectral range of interest, as functions of temperature for both the SQW and MQW structures. As shown in Fig. 3, the peak wavelength of the SQW structure decreases when temperature decreases and, the PL intensity of both SQW and MQW structures increase when temperature decreases, as expected from the theory.

The energy bandgap of the $\text{In}_x\text{Ga}_{1-x}\text{N}$ materials can be approximated by^{3,6}

$$E_g(x) = xE_{g,\text{InN}} + (1-x)E_{g,\text{GaN}} - bx(1-x), \quad (1)$$

where $E_g(x)$ is the energy bandgap of $\text{In}_x\text{Ga}_{1-x}\text{N}$, $E_{g,\text{InN}}$ (1.95 eV) is the energy bandgap of InN, $E_{g,\text{GaN}}$ (3.40 eV) is the energy bandgap of GaN, and b is the bowing parameter. Since bowing parameters are usually determined experimentally, in present study we will use the appropriate parameters that make the best fit of the experimental data to those obtained numerically by *Lastip* simulation program. Based on the experimental and numerical results we conclude that a bowing parameter of 2.6 eV has a better fit for the SQW structure and 1.0 eV for the MQW structure.

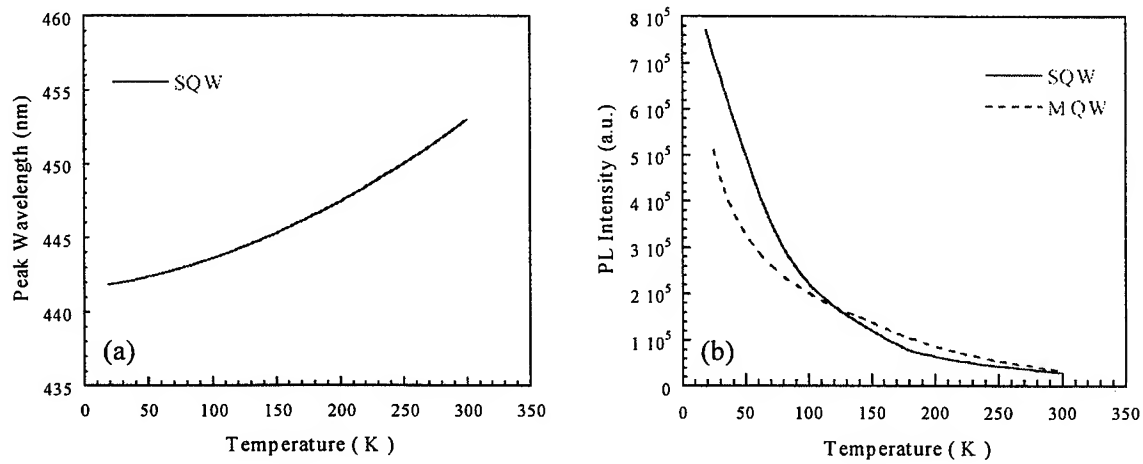


Fig. 3. (a) Peak wavelength of SQW InGaN as a function of temperature, (b) PL intensity of SQW and MQW InGaN as functions of temperature.

In order to simulate the photoluminescence we use the function of spontaneous emission rate versus carrier concentration in *Lastip* simulation program. In *Lastip*, we treat the energy bandgap of the $\text{In}_x\text{Ga}_{1-x}\text{N}$, and the effective masses of the carriers, as a linear combination of those of the InN and GaN. The relation between the energy bandgap of the III-N materials and the temperature may be approximated by the *Varshni formula*:^{7,9}

$$E_g(T) = E_g(0) - \frac{\gamma \cdot T^2}{T + \beta}, \quad (2)$$

where $E_g(0)$ is the energy bandgap at 0 K and $E_g(T)$ is the energy bandgap at temperature T . For InN material, the γ parameter has a value of 0.245×10^{-3} eV/K and the β parameter has a value of 624 K. On the other hand, for GaN material, the parameter γ has a value of 0.939×10^{-3} eV/K and the β parameter has a value of 772 K.⁷ The effective masses of the electrons and the holes in the $\text{In}_x\text{Ga}_{1-x}\text{N}$ material used in *Lastip* simulation are

$$m_{e,\text{In}_x\text{Ga}_{1-x}\text{N}} = m_{e,\text{GaN}} + x(m_{e,\text{InN}} - m_{e,\text{GaN}}), \quad (3)$$

$$m_{h,\text{In}_x\text{Ga}_{1-x}\text{N}} = 0.8 \times m_0, \quad (4)$$

where $m_{e,\text{InGa}}$ is the effective mass of the electrons in $\text{In}_x\text{Ga}_{1-x}\text{N}$, $m_{h,\text{InGa}}$ is the effective mass of the holes in $\text{In}_x\text{Ga}_{1-x}\text{N}$, $m_{e,\text{InN}}$ ($= 0.11 m_0$) is the effective mass of the electrons in InN, $m_{e,\text{GaN}}$ ($= 0.22 m_0$) is the effective mass of the electrons in GaN, and m_0 is the free-electron mass.

The results obtained from both the PL measurements and the *Lastip* simulations are shown in Fig. 4. Figures 4(a) and 4(b) show the peak wavelength and the peak emission intensity as functions of the temperature for the SQW structure, respectively. And, Figs. 4(c) and 4(d) show the peak wavelength and the total emission intensity as functions of the temperature for the MQW structure, respectively. From Fig. 4(a) we find that both experimental and simulation curves have the same tendency. Moreover, the peak wavelengths for both situations are almost the same at room temperature. When temperature decreases, the difference between the two curves becomes a little larger; however, it becomes smaller when the temperature is below 100 K. Similar results are found for the peak emission intensity. The results show that the intensity increases rapidly at low temperature range.

For the MQW structure, since it is difficult to determine the exact position of the peak wavelength, only the *Lastip* simulation results are shown in Fig. 4(c). Never the less, good agreement between experimental and simulation results is observed at low temperature range. For example, the peak wavelength obtained from PL measurement and *Lastip* simulation are close to each other at 25 K (417 nm vs. 415 nm). Similarly, it is difficult to compare the peak intensity between the experimental and simulation results for the MQW structure due to the interference effect. Instead, we compare the emission intensity by integrating the curves for the two situations. As shown in Fig. 4(d), adequate agreement between experiments and simulation is observed.

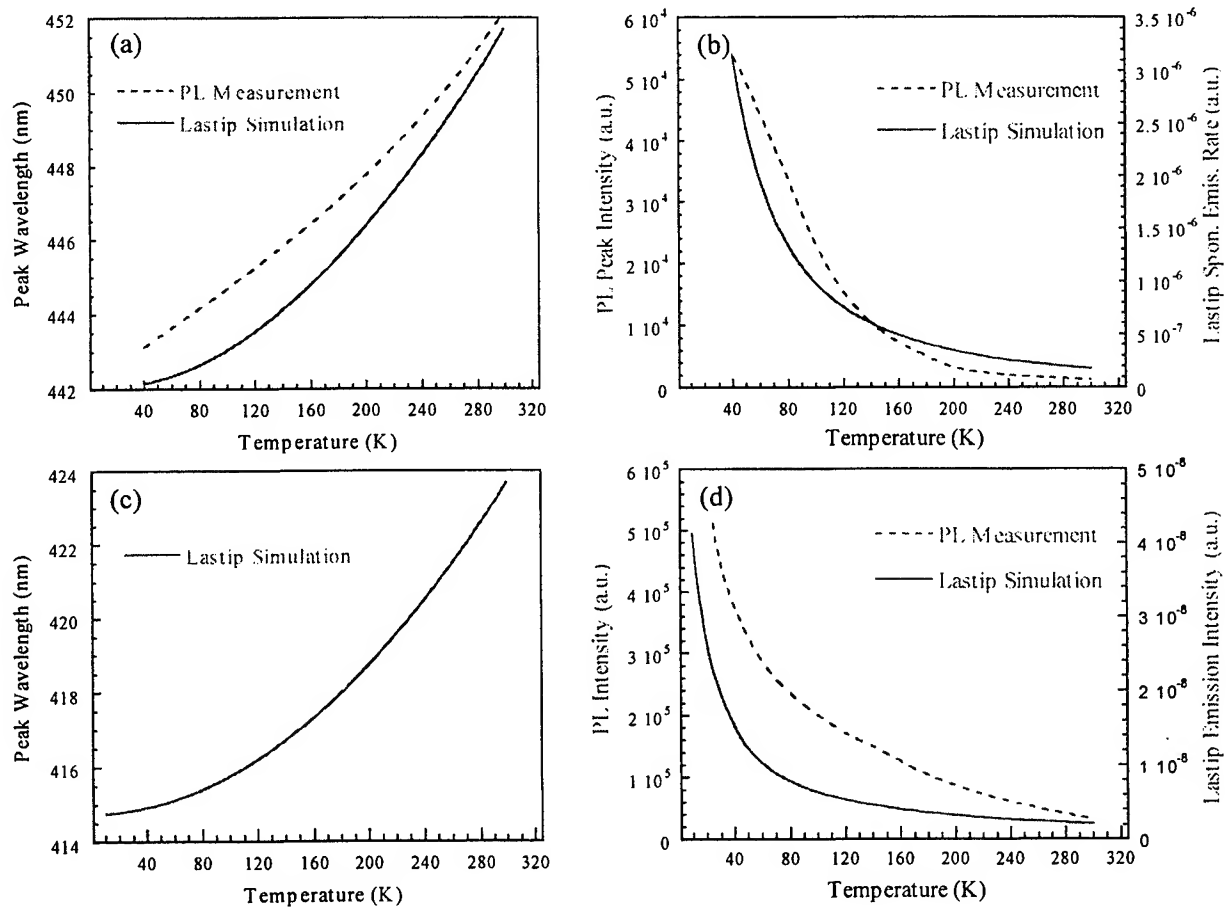


Fig. 4. Comparison between PL measurements and *Lastip* simulation: (a) Peak wavelength as a function of temperature for SQW. (b) Peak intensity as a function of temperature for SQW. (c) Peak wavelength of *Lastip* simulation as a function of temperature for MQW. (d) Total emission intensity as a function of temperature for MQW.

In addition to the temperature dependent study, we investigate the photoluminescence characteristics of the quantum well structures by varying the pump power level. As an example, Fig. 5 shows the PL spectra of the MQW structure as functions of the pump power when the temperature is maintained at 25 K. The PL spectrum of the MQW structure has a peak wavelength near 417 nm and a spectral width of about 7.5 nm at 25 K. When pump power increases the luminescence intensity increases accordingly as expected. Moreover, the peak wavelength of the emission spectrum has a slight blue shift when the pump power increases.

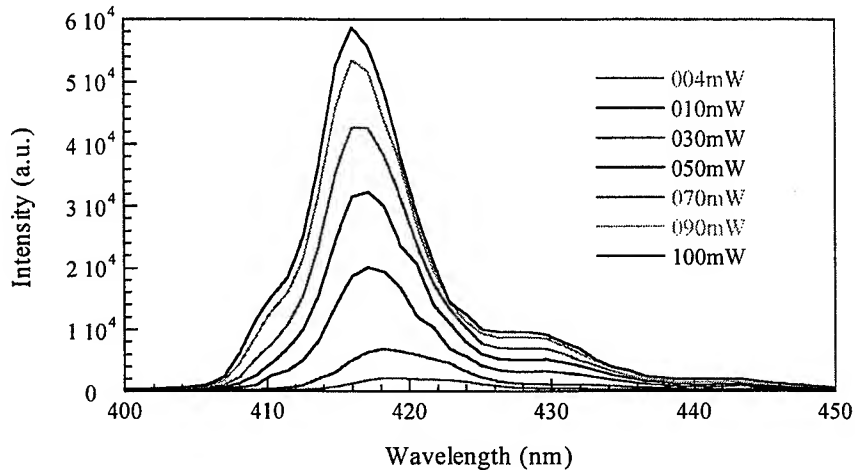


Fig. 5. PL spectra at different pump power levels for the MQW structure at 25 K.

In order to simulate the experimental results shown in Fig. 5, we obtain the spontaneous emission rate as a function of the carrier concentration in *Lastip* program. The results of the *Lastip* simulation are shown in Fig. 6. The inset shows the simulation results when the carrier concentration is low. As expected from theory, the spontaneous emission rate increases when the carrier concentration increases. Similar to the PL measurements, blue shift of the emission spectra at high carrier concentration due to band filling effect is observed. When the carrier concentration is high enough to fill the first quantum state, the carriers start to occupy the second quantum state and a second emission peak of a shorter peak wavelength is observed.

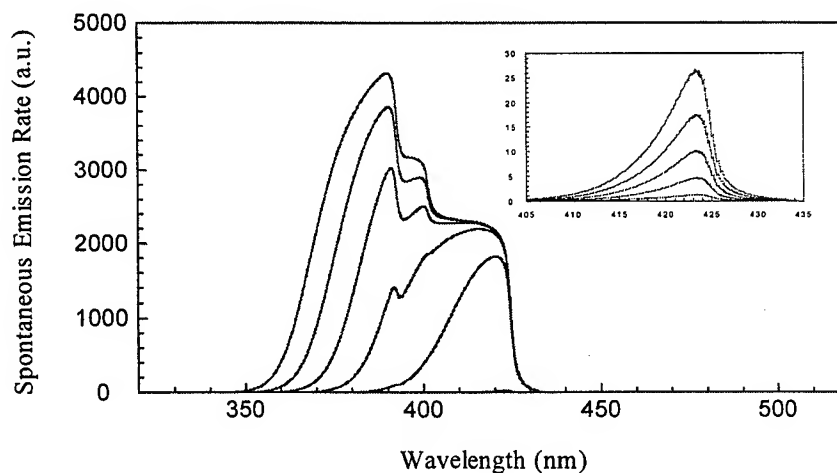


Fig. 6. Lastip spontaneous emission rate as a function of the carrier concentration. The inset shows the spontaneous emission rates at low carrier concentration levels.

Different emission wavelength (or, equivalently, different color) can be obtained from the $\text{In}_x\text{Ga}_{1-x}\text{N}$ materials by varying the indium composition. Figure 7 shows the peak wavelength and the peak intensity of the spontaneous emission rate as functions of the indium composition in $\text{In}_x\text{Ga}_{1-x}\text{N}$, obtained with the *Lastip* program. When indium composition increases the emission wavelength increases, as expected from Eq. (1). The peak intensity of the spontaneous emission rate as a function of the indium composition is also shown in Fig. 7. The simulation results show that the peak intensity increases when the indium composition increases, especially when the indium composition is below 20%.

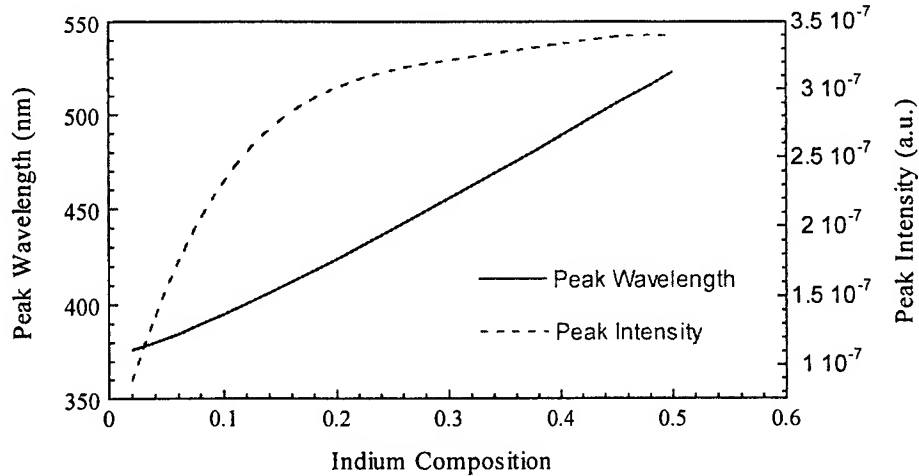


Fig. 7. Peak wavelength and peak intensity of the *Lastip* spontaneous emission rates as functions of the indium composition in $\text{In}_x\text{Ga}_{1-x}\text{N}$.

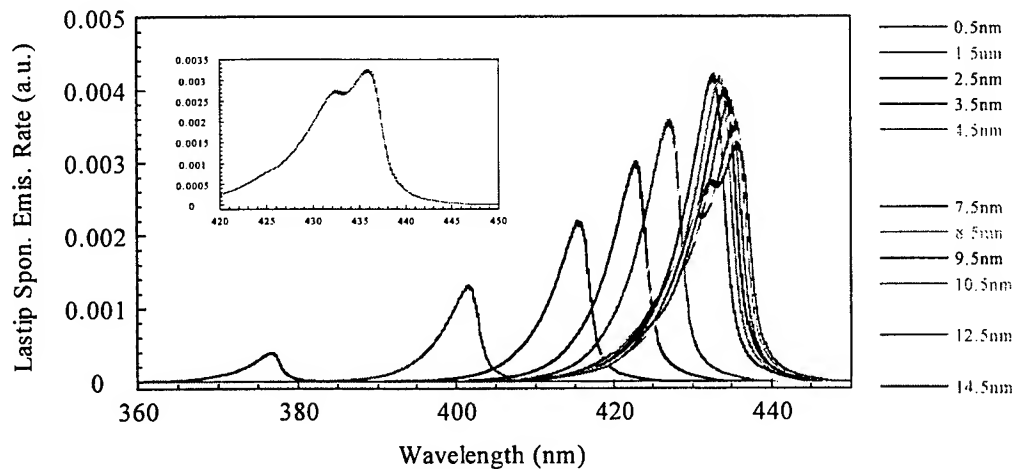


Fig. 8. Emission spectra for various well width of the MQW structure when the carrier concentration is equal to $1 \times 10^{22} \text{ m}^{-3}$. The inset is for well width equal to 14.5 nm.

Figure 8 shows the emission spectra for various well width of the MQW structure when the carrier concentration is equal to $1 \times 10^{22} \text{ m}^{-3}$, obtained with the *Lastip* program. As expected from the quantum theory, the emission wavelength increases when the well width increases. In addition, as shown in Fig. 8, the emission intensity increases when the well width increases. When the well width is greater than $\sim 8 \text{ nm}$, a second emission peak appears in the short wavelength side of the emission spectrum, which is due to the electronic transitions from the second quantum state in the quantum well. The inset of Fig. 8 is the emission spectrum for well width equal to 14.5 nm. Two emission peaks are observed in this spectrum.

Figure 9 shows the peak wavelength and the intensity of the *Lastip* spontaneous emission rate as functions of the well width of the MQW structure. As shown in Fig. 9(a), the peak wavelength increases rapidly with the well width when the well width is smaller than ~5 nm, which can be explained by the quantum effect. On the other hand, as shown in Fig 9(b), both of the peak intensity and the total emission intensity increase when the well width increases, when the well width is small. However, when the well width is greater than ~8 nm, the total emission intensity starts to saturate and the peak intensity starts to decrease.

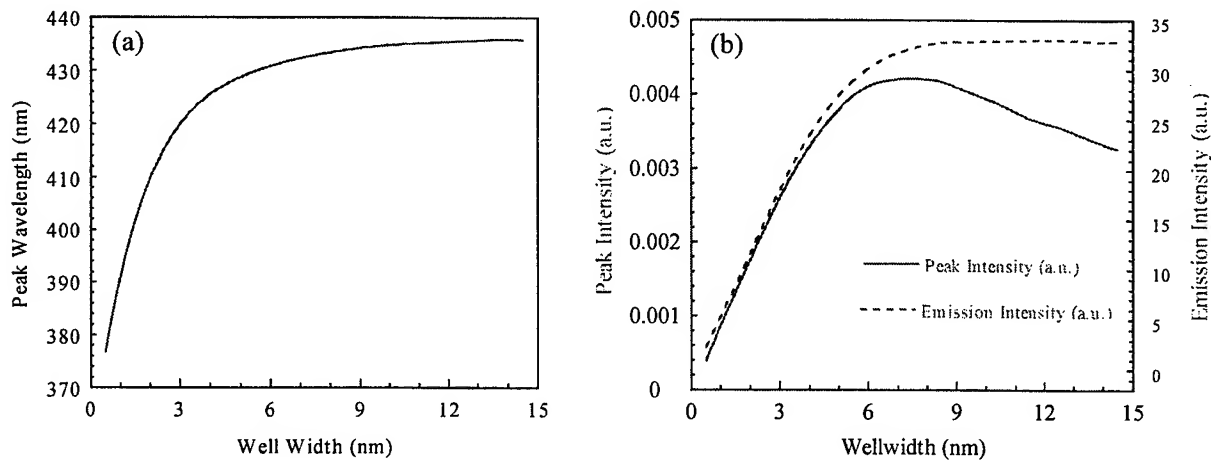


Fig. 9. Peak wavelength, peak intensity, and emission intensity of the *Lastip* spontaneous emission rates as functions of the well width.

3. CONCLUSION

Temperature dependent photoluminescence characteristics of a single quantum well InGaN wafer and a multiple quantum well InGaN wafer are investigated in this paper. The 351.1-nm ultraviolet output of an argon ion laser is used as the pump source and a UV-enhanced, liquid nitrogen cooled CCD array is used as the photo detector. The InGaN emission spectra show that the peak wavelength and the spectral width decrease, and, the peak intensity increases when the temperature decreases. On the other hand, the InGaN emission spectra at various pump power levels are also explored. The emission intensity increases, and, the peak wavelength decreases when the pump power increases due to the band filling effect.

The experimental results obtained from the photoluminescence measurements are compared to those derived by the commercial *Lastip* simulation program. Good agreement between the experimental and simulation results is observed. The simulation results show that at low carrier concentration the spontaneous emission rate increases and the peak wavelength decreases slightly when the carrier concentration increases, similar to the situation of the photoluminescence measurements. When the carrier concentration is high enough to fill the first quantum state, a second emission peak of a lower peak wavelength may appear in the emission spectrum.

The *Lastip* simulation program has also been utilized to investigate the optical properties of the InGaN quantum well structures for different indium compositions and well widths. The peak wavelength of the InGaN quantum well structure increases when the indium composition increases, as expected from the theory. On the other hand, the emission wavelength increases when the well width of the quantum well structure increases due to the quantum effect. Simulation results also show that the emission intensity increases when the well width increases.

ACKNOWLEDGMENTS

The authors are grateful to Professor Jen-Inn Chyi of the Department of Electrical Engineering, National Central University, Taiwan for the SQW and MQW InGaN semiconductor wafers used in this paper. We would also like to acknowledge Professor Jiann Lin of the Department of Physics, National Changhua University of Education, for the usage of the *Lastip* simulation program, and Gorden Yu of the Titan Electro-Optics Co., Ltd. for the sample mount used in experiments. This work is supported by the National Science Council (NSC) of the Republic of China under grant NSC-89-2112-M-018-003.

REFERENCES

1. S. Nakamura, M. Senoh, S. Nagahama, N. Iwasa, T. Matsushita, and T. Mukai, "InGaN/GaN/AlGaIn-Based LEDs and Laser Diodes," MRS Internet J. Nitride Semicond. Res. **4S1**, G1.1, 1999.
2. S. Nakamura and G. Fasol, *The Blue Laser Diode*, Springer-Verlag, Heidelberg, 1997.
3. G. B. Stringfellow and M. George Craford, *High Brightness Light Emitting Diodes - Semiconductors and Semimetals Volume 48*, Academic Press, San Diego, California, USA, 1997.
4. J. I. Pankove and T. D. Moustakas, *Gallium Nitride (GaN) I - Semiconductors and Semimetals Volume 50*, Academic Press, San Diego, California, USA, 1998.
5. J. I. Pankove and T. D. Moustakas, *Gallium Nitride (GaN) II - Semiconductors and Semimetals Volume 57*, Academic Press, San Diego, California, USA, 1999.
6. K. Osamura, S. Naka, and Y. Murakami, "Preparation and optical properties of $\text{Ga}_{1-x}\text{In}_x\text{N}$ thin films," J. Appl. Phys. **46**, 3432, 1975.
7. A. V. Dmitriyev and A. L. Oruzhenikov, "The Rate of Radiative Recombination in the Nitride Semiconductors and Alloys," MRS Internet J. Nitride Semicond. Res. **1**, 46, 1996.
8. N. Yoshimoto, T. Matsuoka, T. Sasaki, and Katsui, Appl. Phys. Lett. **59**, 2251, 1991.
9. Y. P. Varshni, Physica **34**, 149, 1967.

*Correspondence: Email: ykuo@cc.ncue.edu.tw; Telephone: 886-4-723-2105 Ext. 3341; Fax: 886-4-721-1153.

Broadband Cr:YSO solid-state saturable absorber for ruby, alexandrite, and Cr:LiCAF lasers: numerical study on passive Q-switching performance

Yen-Kuang Kuo*, Jih-Yuan Chang, Horng-Min Chen

Department of Physics, National Changhua University of Education,
Changhua 50058, Taiwan

ABSTRACT

The Cr:YSO solid-state crystal has broad absorption bands in visible and near infrared spectral region. Although Cr:YSO was originally developed for laser applications, our experiments and numerical simulations show that it can act as an effective saturable absorber Q switch for the ruby laser at 694.3 nm, for the tunable alexandrite laser from 700 to 818 nm, and for the tunable Cr:LiCAF laser from 725 to 840 nm. Since the Cr:YSO is a robust solid-state crystal, the durable Cr:YSO Q-switched solid-state laser systems may find various practical applications. In this paper, theory of passive Q-switching with solid-state saturable absorber is briefly reviewed. Details of the numerical simulation for the passively Q-switched solid-state laser systems are presented.

Keywords: Laser, Q switch, numerical simulation, ruby, alexandrite, Cr:LiCAF, Cr:YSO.

1. INTRODUCTION

The Cr:YSO ($\text{Cr:Y}_2\text{SiO}_5$) was originally developed for laser applications. Observation of laser action in this crystal was first reported in 1992.¹ In 1993 this crystal was demonstrated to be an effective saturable absorber Q switch for the ruby ($\text{Cr:Al}_2\text{O}_3$) laser at 694.3 nm by Chen *et al.*; unfortunately, the host of the saturable absorber was incorrectly identified as GSGG ($\text{Gd}_3\text{Sc}_2\text{Ga}_3\text{O}_{12}$) at the time of publication.^{2,3} In the same year, passive Q-switching of the tunable Cr:LiSAF (Cr:LiSrAlF_6) laser with the Cr:YSO was realized by Munin *et al.*⁴ Subsequently, the Cr:YSO crystal was used to effectively Q-switch the alexandrite ($\text{Cr:BeAl}_2\text{O}_4$) laser at 750 nm and the tunable Cr:LiCAF (Cr:LiCaAlF_6) laser near 780 nm by Kuo *et al.* in 1995.^{5,6}

However, passive Q-switching of the alexandrite laser, which is tunable from 700 to 818 nm, with the Cr:YSO was demonstrated only at 750 nm, i.e., the peak of the gain spectrum.⁵ Tunable passive Q-switching was not performed. On the other hand, for the Cr:LiCAF laser, which is tunable at least from 725 to 840 nm, passive Q-switching with the Cr:YSO was demonstrated only at a few different wavelengths near 780 nm.⁶ In this paper, we investigate the passive Q-switching performance of the Cr:YSO Q-switched ruby, alexandrite, and Cr:LiCAF laser systems over all their operational laser range by solving the laser rate equations with the Runge-Kutta-Fehlberg method.

2. CHARACTERISTICS OF THE Q-SWITCH

Unlike chromium doped YAG ($\text{Y}_3\text{Al}_5\text{O}_{12}$) and forsterite (Mg_2SiO_4), in which Cr^{3+} ions exist in the octahedral sites, Cr:YSO is a pure tetravalent chromium system. Some of the important material parameters of the Cr:YSO are listed in Table 1. The Cr:YSO is blue in color and is a biaxial solid-state crystal. It has a melting point of as high as 2070 °C and a fluorescence lifetime of 0.7 μs at room temperature. The emission spectrum of the Cr:YSO covers a spectral range from 1000 nm to 1500 nm with a peak near 1250 nm, which is the laser wavelength of the Cr:YSO when it is utilized as a laser crystal.

Figure 1 shows the absorption cross-section of the Cr:YSO when the polarization is along the n_z axis of the Cr:YSO crystal. As shown in Fig. 1, the Cr:YSO has four absorption bands peaked near 390 nm, 595 nm, 695 nm, and 750 nm. Obviously, the absorption spectrum of the Cr:YSO covers the visible and near infrared spectral region and, hence, can potentially be used as a saturable absorber Q switch for the ruby, alexandrite, Cr:LiCAF, and Cr:LiSAF lasers.

Table 1. Material properties of Cr:YSO

Chemical formula	$\text{Cr}^{4+}:\text{Y}_2\text{SiO}_5$
Color	Blue
Crystal system	monoclinic, biaxial
Lattice constants	$a = 10.41 \text{ \AA}$, $b = 6.72 \text{ \AA}$, $c = 12.49 \text{ \AA}$, $\beta = 102^\circ 39'$
Melting point	2070 °C
Cr atoms / mole%	$9.7 \times 10^{19} / \text{cm}^3$
Main absorption peaks	390 nm, 595 nm, 695 nm, and 750 nm
Emission spectrum	1000 nm to 1500 nm (peaked near 1250 nm)
Fluorescence lifetime at 25°C	$\sim 0.7 \mu\text{s}$
Density	4.6 g/cm ³
Refractive index	1.8

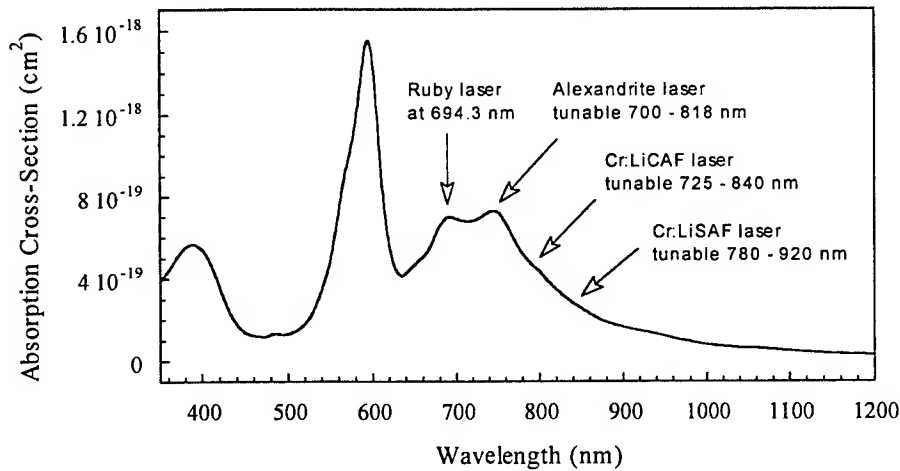


Fig. 1. Absorption cross-section of the Cr:YSO.

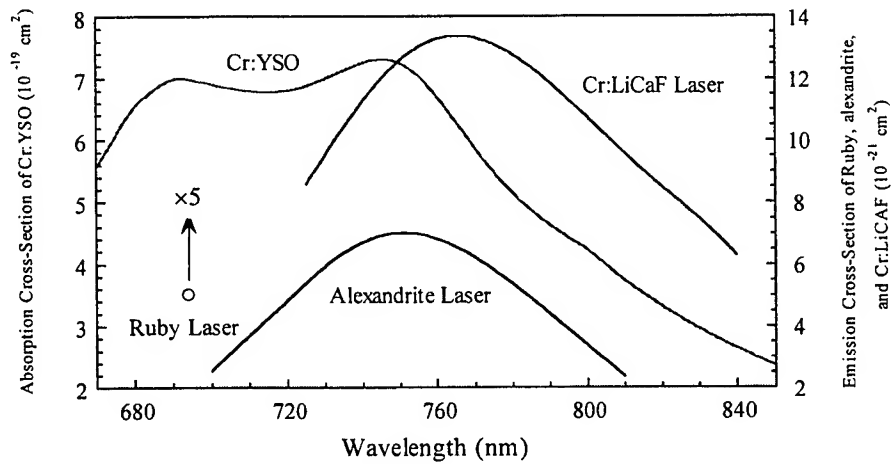


Fig. 2. Absorption cross-section of the Cr:YSO and emission cross-sections of the ruby, alexandrite, and Cr:LiCAF lasers.

Since the ruby laser, the alexandrite laser, and the Cr:LiCAF laser have long fluorescence lifetime (3 ms, 260 μ s, and 170 μ s, respectively) and the Cr:YSO has substantially higher absorption cross-sections than the emission cross-sections of the lasers over the whole range of their laser spectra, the Cr:YSO may be used as an efficient Q switch for these lasers according to the passive Q-switching theory.^{6,7} Figure 2 shows the absorption cross-section of the Cr:YSO in the spectral range from 670 nm to 850 nm and the emission cross-sections of the ruby laser, the alexandrite laser, and the Cr:LiCAF laser over the spectral range of interest. Note that the emission cross-section of the ruby laser (2.5×10^{-20} cm²) has been divided by a factor of five in order to be shown in Fig. 2 with another two lasers in the same scale.

According to the passive Q-switching theory, in a passively Q-switched laser system the absorption cross-section of the saturable absorber Q switch, σ_a , has to be greater than the emission cross-section of the laser, σ_g , in order to obtain the giant laser pulses. Figure 2 indicates that the Cr:YSO can be used to effectively Q-switch these three lasers over all their operational laser range. Table 2 shows the absorption cross-sections of the Cr:YSO and the emission cross-sections of the ruby, alexandrite, and Cr:LiCAF lasers at three characteristic wavelengths of the lasers. For the ruby laser at 694.3 nm, the ratio of σ_a to σ_g has a value of 28. For the alexandrite laser at 750 nm, the ratio of σ_a to σ_g has a value of 103. For the Cr:LiCAF laser at 780 nm, the ratio of σ_a to σ_g has a value of 40. At these three characteristic wavelengths, the absorption cross-sections of the saturable absorber Q switch are substantially greater than the emission cross-sections of the lasers. Therefore, we expect to achieve good laser performance for these passively Q-switched laser systems.

Table 2. Absorption cross-section of the Cr:YSO and emission cross-sections of the ruby, alexandrite, and Cr:LiCAF lasers at three characteristic wavelengths of the lasers.

	σ_g (cm ²)	σ_a (cm ²)	σ_a/σ_g
Ruby (at 694.3 nm)	2.5×10^{-20}	7.0×10^{-19}	28
Alexandrite (at 750 nm)	7.0×10^{-21}	7.2×10^{-19}	103
Cr:LiCAF (at 780 nm)	1.3×10^{-20}	5.2×10^{-19}	40

3. THEORY OF PASSIVE Q-SWITCHING

The schematic diagram for a solid-state laser with a saturable absorber Q switch is shown in Fig. 3. The laser resonator consists of a high-reflecting mirror, with a reflectivity of about 100%, and an output-coupling mirror. The saturable absorber Q switch can be placed either between the laser crystal and the high reflector or between the laser crystal and the output coupler. For the lasers under study, flashlamps are usually utilized as the pumping sources.

In our prior papers^{6,7} we have proposed three coupled rate equations which may be used to model a laser passively Q-switched by a solid-state saturable absorber:

$$\frac{dn}{dt} = [K_g N_g - K_a N_a - \beta K_a (N_{a0} - N_a) - \gamma_c] n, \quad (1)$$

$$\frac{dN_g}{dt} = R_p - \gamma_g N_g - \gamma K_g N_g n, \quad (2)$$

$$\frac{dN_a}{dt} = \gamma_a (N_{a0} - N_a) - K_a N_a n. \quad (3)$$

The factor γ equals to one for a four-level laser and two for a three-level laser. Other parameters are defined as following: n is the photon number in the laser cavity; N_g is the population inversion of the laser; N_a is the ground state population of the

saturable absorber; N_{a0} is the initial value of N_a ; γ_g is the effective decay rate of the upper laser level; γ_a is the effective relaxation rate of the saturable absorber; R_p is the pumping rate; γ_c is the cavity decay rate; K_g and K_a are coupling coefficients; and β is the ratio of the excited state absorption cross-section to the ground state absorption cross-section of the saturable absorber.

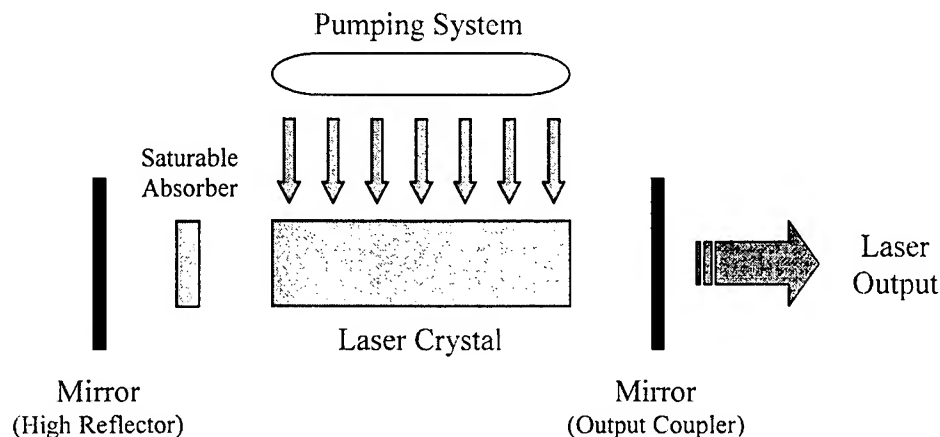


Fig. 3. Schematic diagram for a solid-state laser with a saturable absorber Q switch.

In order to compare the population inversion of the laser to the loss of the overall laser system when interpreting the numerical simulation results, it is convenient to define a normalized loss parameter, $Loss$, from Eq. (1) as

$$Loss \equiv \frac{K_a N_a + \beta K_a (N_{a0} - N_a) + \gamma_c}{K_g}. \quad (4)$$

It can be shown⁷ that the laser population inversion required for laser action, N_{g0} , the threshold population inversion after the saturation of the Q switch, N_{th} , and the final population inversion after the release of the giant laser pulse, N_f , can be approximated by the following equations:

$$N_{g0} \equiv \frac{K_a N_{a0} + \gamma_c}{K_g}, \quad (5)$$

$$N_{th} \equiv \frac{\beta K_a N_{a0} + \gamma_c}{K_g}, \quad (6)$$

$$N_{g0} - N_f - N_{th} \ln\left(\frac{N_{g0}}{N_f}\right) \equiv 0. \quad (7)$$

It can also be shown⁷ that the pulse width, τ_{pulse} , and the output energy, E_{out} , of the Q-switched giant laser pulses can be approximated by the following equations:

$$\tau_{pulse} \equiv \tau_c \frac{N_{g0} - N_f}{N_{g0} - N_{th} - N_{th} \ln\left(\frac{N_{g0}}{N_{th}}\right)}, \quad (8)$$

$$E_{out} \equiv \frac{N_{g0} - N_f}{\gamma} (h\nu) \eta_c, \quad (9)$$

where τ_c is the cavity lifetime, $h\nu$ is the photon energy, and η_c is the output coupling efficiency.

4. PERFORMANCE OF PASSIVE Q-SWITCHING

As discussed in section 2, the Cr:YSO may be used to Q-switch the ruby laser, the alexandrite laser, and the Cr:LiCAF laser. The alexandrite laser is highly efficient and has important application in medical surgery (dermatology), water-vapor and temperature differential absorption lidar, solid-state laser pumping, and generation of ultraviolet laser radiation. Passive Q-switching of the alexandrite laser with the Cr:YSO at 750 nm, i.e., the peak of the laser spectrum, has been numerically studied in Ref. 7. Tunable passive Q-switching of the alexandrite laser with the Cr:YSO over the alexandrite tuning range has also been numerically investigated in Ref. 8. Therefore, in this paper we will pay special attention to the passive Q-switching of the ruby and the Cr:LiCAF lasers with the Cr:YSO.

4.1. Passive Q-switching of the Ruby Laser with the Cr:YSO

The ruby laser was the first working laser which was introduced by Theodore H. Maiman in 1960. Although Nd:YAG laser has replaced ruby laser as general-purpose pulsed solid-state laser, ruby laser is still playing an important role in various applications. Ruby laser is capable of generating high-energy, visible red pulses which are powerful tools for removal of tattoos and disfiguring pigmented lesions from the skin. Ruby laser can also generate high-energy pulses from a compact package which makes the ruby laser a valuable tool for holographic nondestructive testing, double-pulse holography, and plasma diagnostics.

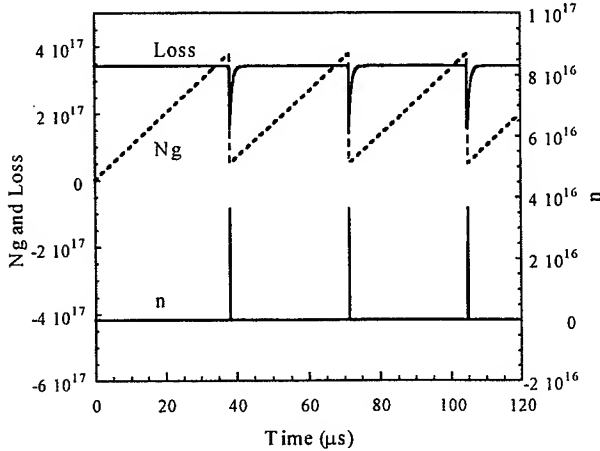


Fig. 4. Results of the numerical simulation for the ruby passive Q-switching with the Cr:YSO: N_g , Loss, and n as functions of time.

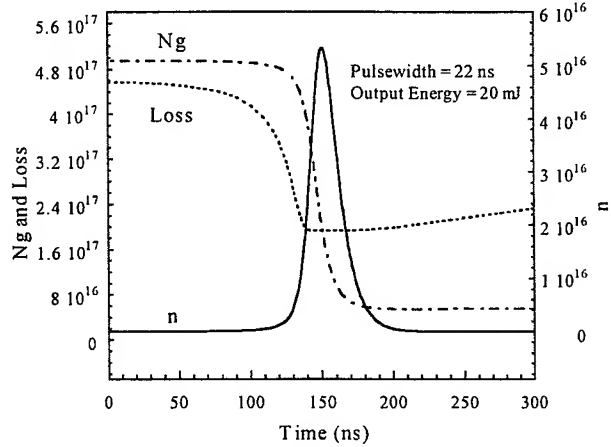


Fig. 5. Expanded picture of Fig. 4 near the occurrence of the first giant laser pulse.

The ruby laser is a three-level laser; that is, a photon is created at the expense of two inverted population in the laser crystal since the lower laser level is, in fact, the ground laser level. Hence, the population reduction factor γ equals to two, instead of one, unlike the regular four-level lasers. Figure 4 shows the results of the numerical simulation for the ruby passive Q-switching with the Cr:YSO, obtained by solving Eqs. (1) to (3) with the Runge-Kutta-Fehlberg method. The parameters used in this simulation are: $\gamma = 2$, laser wavelength = 694.3 nm, length of laser cavity = 30 cm, reflectivity of output coupler $R = 0.9$, effective laser beam diameter = 2 mm, ruby laser emission cross-section = $2.5 \times 10^{-20} \text{ cm}^2$, Cr:YSO ground-state absorption cross-section = $9.9 \times 10^{-19} \text{ cm}^2$, $K_g = 7.96 \times 10^{-10} \text{ sec}^{-1}$, $K_a = 3.15 \times 10^{-8} \text{ sec}^{-1}$, $\gamma_c = 5 \times 10^7 \text{ sec}^{-1}$, $\gamma_g = 3.33 \times 10^2 \text{ sec}^{-1}$, $\gamma_a = 1.43 \times 10^6 \text{ sec}^{-1}$, $\beta = 0.33$, $R_p = 1.0 \times 10^{22} \text{ sec}^{-1}$, and $N_{a0} = 1 \times 10^{16}$.

As shown in Fig. 4, the laser population inversion, N_g , increases with time due to optical pumping. It takes about 34.5 μs for the N_g to be equal to Loss, which is defined in Eq. (4). After this specific time the N_g is greater than Loss and, finally, a giant laser pulse is developed at a time of about 38.2 μs after the pumping starts. The N_g decreases to a lowest value of about 4.9×10^{16} . It then increases with time and another giant laser pulse is developed at a time of about 71.6 μs . When compared to the development of the first Q-switched laser pulse, it takes less time to develop the second and subsequent laser pulses because the laser population inversion, N_g , does not reach to zero after the release of each laser pulse.

Dynamic characteristics of the ruby passive Q-switching with the Cr:YSO can better be visualized in Fig. 5, which is an expanded picture of Fig. 4 near the occurrence of the first giant laser pulse. As indicated in Fig. 5, the photon number, n , reaches to its maximum value when N_g equals to L_{oss} . The pulsewidth of the giant laser pulse is 22 ns (full width at half maximum). The output energy of the Q-switched laser pulse is 20 mJ, obtained by integrating the curve of the photon number over a temporal range covering the entire laser pulse. Note that the pulsewidth and the output energy obtained from the numerical simulation are very close to those calculated with Eqs. (8) and (9). It is also worth to note here that the N_{g0} , N_{th} , and N_j obtained in Fig. 5 are in good agreement with those calculated by Eqs. (5) to (7). The simulation results thus justify the derivation and usefulness of the equations discussed in section 3.

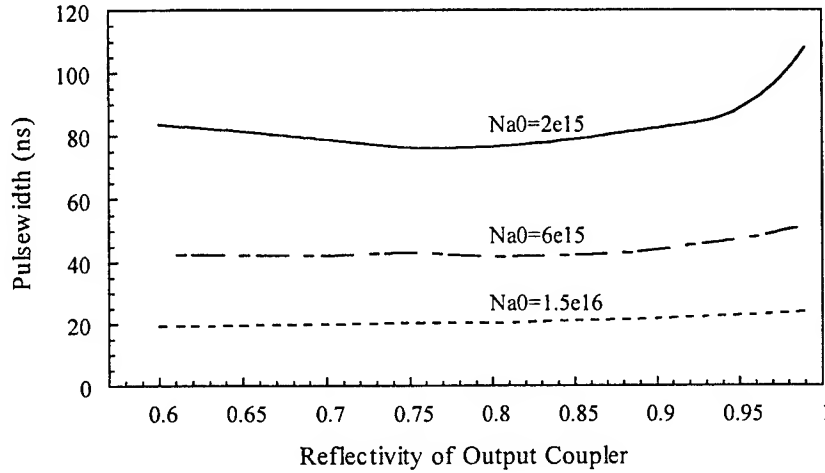


Fig. 6. Pulsewidth as a function of the reflectivity of output coupler for various N_{a0} .

Figure 6 shows the pulsewidth of the Q-switched laser pulse as a function of the reflectivity of output coupler for various N_{a0} . It is obvious from Fig. 6 that the pulsewidth becomes smaller when N_{a0} is higher; i.e., when a saturable absorber Q switch of a thicker length or a higher doping concentration is used. We would like to mention here that a higher pumping rate is required to obtain the laser action with a higher N_{a0} since it results in a higher system loss. Therefore, the system design is in fact a trade-off study. When N_{a0} is high, the pulsewidth does not change markedly when the reflectivity of the output coupler varies. When N_{a0} is low, an optimum reflectivity exists with which the shortest pulsewidth may be obtained.

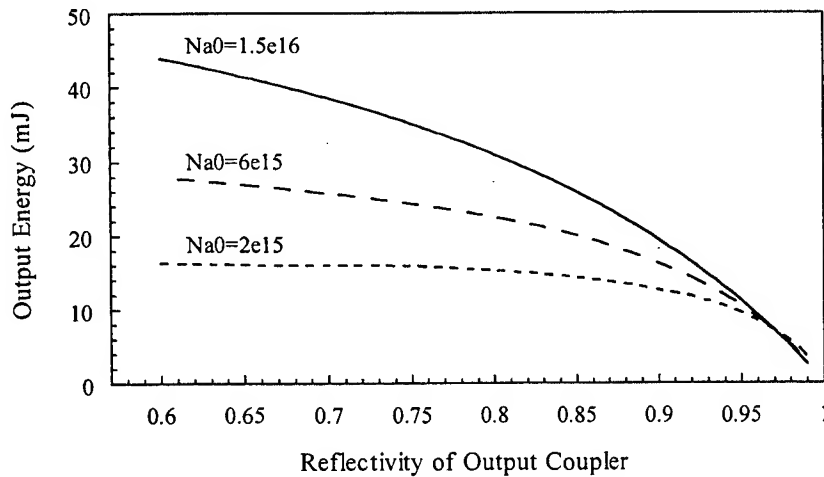


Fig. 7. Output energy as a function of the reflectivity of output coupler for various N_{a0} .

Figure 7 shows the output energy of the Q-switched laser pulse as a function of the reflectivity of output coupler for various N_{ao} . The output energy increases when N_{ao} increases. In the mean time, the output energy increases when the reflectivity of output coupler decreases, since the output energy relates directly to the amount of output coupling. Therefore, from Figs. 6 and 7 we conclude that better passive Q-switching performance may be obtained when N_{ao} is higher and, a higher output energy may be obtained with a lower reflectivity of the output coupler.

4.2. Passive Q-switching of the Tunable Cr:LiCAF Laser with the Cr:YSO

As a transition-metal vibronic laser Cr:LiCAF exhibits a broad emission spectrum, long lifetime of the upper laser level, low nonlinear refractive index, low thermal lensing, and low excited state absorption that make it a unique source for tunable or short pulse lasers. The two broad absorption bands near 425 nm and 625 nm permit efficient flashlamp pumping. Laser diode pumping of the Cr:LiCAF laser has also been demonstrated in 1991 and, hence, a compact Cr:YSO Q-switched Cr:LiCAF laser system is feasible. The fluorescence lifetime of the Cr:LiCAF is about 170 μ s at room temperature. The long metastable lifetime makes both flashlamp pumping and Q-switched operation of the Cr:LiCAF laser superior to that of the Ti:sapphire laser which is tunable over the same spectral range.

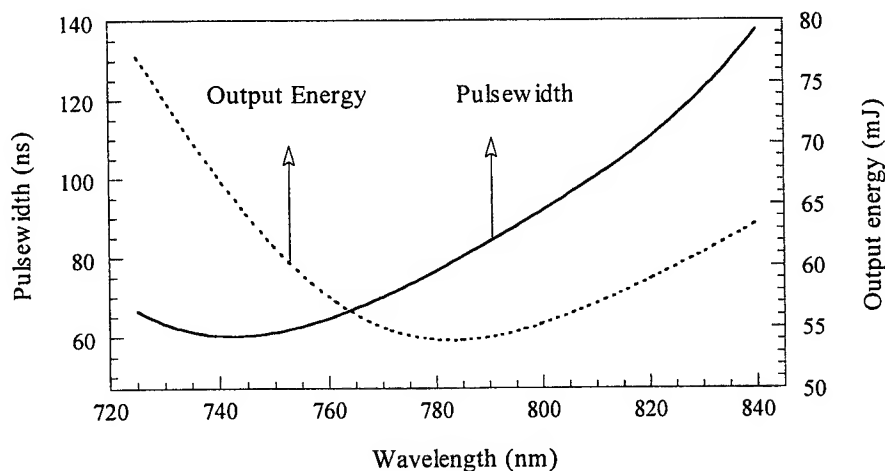


Fig. 8. Pulsewidth and output energy as functions of the wavelength.

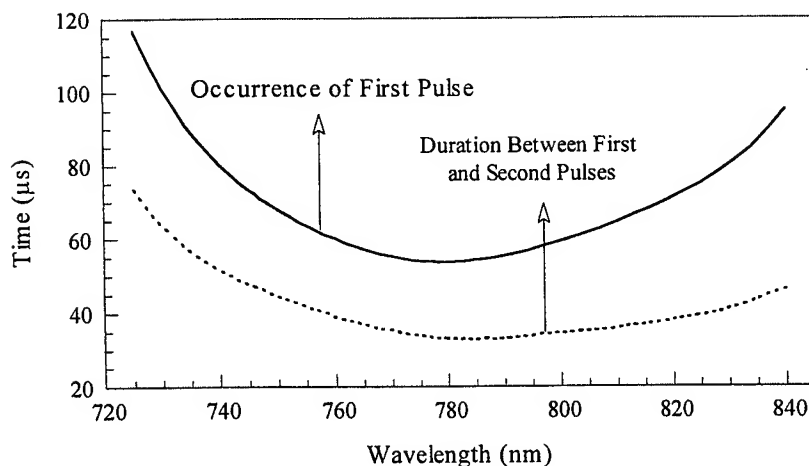


Fig. 9. Time required to develop the first and the second laser pulses.

Passive Q-switching of the tunable Cr:LiCAF laser with the Cr:YSO is also numerically investigated. Figure 8 shows the pulsewidth and the output energy as functions of the wavelength. The parameters used in this simulation are: $\gamma = 1$, length of laser cavity = 34 cm, reflectivity of output coupler $R = 0.8$, effective laser beam diameter = 2 mm, $K_g = 3.59 \times 10^{-10} \text{ sec}^{-1}$, $K_a = 1.44 \times 10^{-8} \text{ sec}^{-1}$, $\gamma_c = 9.1 \times 10^7 \text{ sec}^{-1}$, $\gamma_g = 5.88 \times 10^3 \text{ sec}^{-1}$, $\gamma_a = 1.43 \times 10^6 \text{ sec}^{-1}$, $\beta = 0.33$, $R_p = 1.0 \times 10^{22} \text{ sec}^{-1}$, and $N_{a0} = 4 \times 10^{15}$. The Cr:LiCAF laser emission cross-section and the Cr:YSO ground-state absorption cross-section are obtained from Fig. 2. From Fig. 8 we note that the pulsewidth has a minimum value of about 60 ns near 740 nm, and the output energy has a minimum value of about 54 mJ near 780 nm. We need to mention here that although the output energy is larger at both ends of the Cr:LiCAF tuning spectrum, the laser gain is small in this spectral range and more pumping is required to obtain the laser action. Figure 9 shows the time required to develop the first and the second laser pulses as functions of the wavelength. It is obvious that it takes less time to develop the laser pulses when the operating wavelength is near 780 nm, the peak of the Cr:LiCAF lasing spectrum.

5. CONCLUSION

We have reviewed the passive Q-switching theory related to the use of the slow-relaxing solid-state saturable absorbers. In the mean time, we have numerically shown that the Cr:YSO is an effective solid-state saturable absorber Q switch for the ruby laser at 694.3 nm, for the tunable alexandrite laser from 700 to 818 nm, and for the tunable Cr:LiCAF laser from 725 to 840 nm. These passively Q-switched laser systems are powerful, durable, and economical. They can be very useful when compactness is a primary concern.

ACKNOWLEDGMENTS

This work is supported in part by the National Science Council (NSC) of the Republic of China under grant NSC-89-2112-M-018-003.

REFERENCES

1. C. Deka, B. H. T. Chai, Y. Shimony, X. X. Zhang, E. Munin, and M. Bass, "Laser performance of $\text{Cr}^{4+}:\text{Y}_2\text{SiO}_5$," *Appl. Phys. Lett.* **61**, pp. 2141-2143, 1992.
2. W. Chen, K. Spariosu, R. Stultz, Y. K. Kuo, M. Birnbaum, and A. V. Shestakov, " $\text{Cr}^{4+}:\text{GSGG}$ saturable absorber Q-switch for the ruby laser," *Opt. Commun.* **104**, pp. 71-74, 1993.
3. W. Chen, K. Spariosu, R. Stultz, Y. K. Kuo, M. Birnbaum, and A. V. Shestakov, "Erratum, $\text{Cr}^{4+}:\text{GSGG}$ saturable absorber Q-switch for the ruby laser," *Opt. Commun.* **112**, p. 349, 1994.
4. E. Munin, A. B. Villaverde, X. X. Zhang, and M. Bass, "Broadband, intensity dependent absorption in tetravalent chromium-doped crystals," *Appl. Phys. Lett.* **63**, pp. 1739-1741, 1993.
5. Y. K. Kuo and M. Birnbaum, "Passive Q-switching of the alexandrite laser with a $\text{Cr}^{4+}:\text{Y}_2\text{SiO}_5$ solid-state saturable absorber," *Appl. Phys. Lett.* **67**, pp. 173-175, 1995.
6. Y. K. Kuo, M. F. Huang, and M. Birnbaum, "Tunable $\text{Cr}^{4+}:\text{YSO}$ Q-switched Cr:LiCAF laser," *IEEE J. Quantum Electron.* **31**, pp. 657-663, 1995.
7. Y. K. Kuo, H. M. Chen, and C. C. Lin, "A theoretical study of the Cr:BeAl₂O₄ laser passively Q-switched with Cr:YSO solid state saturable absorber," *Chinese J. Phys.* **38**, No. 3-I, June 2000.
8. Y. K. Kuo, J. Y. Chang, C. C. Lin, and H. M. Chen, "Tunable Cr:YSO Q-Switched Cr:BeAl₂O₄ laser: numerical study on laser performance along three principal axes of the Q switch," *Jpn. J. Appl. Phys.* **39**, No. 7A, July 2000.

*Correspondence: Email: ykuo@cc.ncue.edu.tw; Tel. 886-4-723-2105 Ext. 3341; Fax. 886-4-721-1153

Experimental and numerical study on the optical properties of yellow-green AlGaInP light emitting diodes

Man-Fang Huang^{*a}, Pin-Hui Liu^a, J. S. Liu^a, Yen-Kuang Kuo^{**b}, Ya-Lien Huang^b,
Yuni Chang^b, Hsu-Ching Huang^b, Kuo-Kai Horng^b, Jih-Yuan Chang^b

^aVisual Photonics Epitaxy Co., Ltd., Lung-Tan, Taoyuan 325, Taiwan

^bDepartment of Physics, National Changhua University of Education,
Changhua 50058, Taiwan

ABSTRACT

AlGaInP LEDs with emission wavelengths near 570 nm are important in liquid crystal display backlight application. However, high brightness in this spectral region is difficult to achieve due to the reduction of the radiation efficiency in the high-aluminum-containing active region and the smaller band offset between the active and the cladding region. In order to improve the performance of the 570-nm AlGaInP LEDs, we have grown several wafers with different structure designs and studied the optical properties as functions of the device temperature and the excitation power experimentally with a photoluminescence measurement system and numerically with a commercial *Lastip* simulation program. Specifically, important factors such as the barrier height in quantum wells, the tensile strain barrier cladding next to the MQW region, the compensated strain in MQW, and the distributed Bragg reflector are investigated. Good agreement between the experimental and numerical results is observed.

Keywords: AlGaInP, high brightness LED, yellow-green LED, photoluminescence, numerical simulation

1. INTRODUCTION

The AlGaInP semiconductor materials are capable of emitting light in the red, orange, and yellow spectral range.¹ The AlGaInP laser diodes have important applications in optical data storage (i.e., the digital versatile disk) systems, laser pointers, bar-code readers, etc. High brightness AlGaInP light emitting diodes (LEDs) are now commercially available and have important applications in automotive signal lighting, automotive interior lighting, traffic signal lights, large area display, and liquid crystal display backlighting. Specifically, for the liquid crystal display backlight application, the AlGaInP LEDs with emitting wavelengths near 570 nm, i.e., the yellowish green region, are favorable. However, high brightness of the AlGaInP LEDs near 570 nm is difficult to achieve due to the reduction of the radiation efficiency in the high-aluminum-containing active region and the smaller band offset between the active and the cladding region.

High-performance AlGaInP laser diodes and LEDs are usually fabricated by growing the $(Al_xGa_{1-x})_{0.5}In_{0.5}P$ alloy onto a lattice matched misoriented GaAs substrate.² The emission wavelength of the $(Al_xGa_{1-x})_{0.5}In_{0.5}P$ alloy is about 650 nm when the wells of the AlGaInP multiple quantum well (MQW) are without aluminum, i.e., when x equals to zero. The emission wavelength of the $(Al_xGa_{1-x})_{0.5}In_{0.5}P$ alloy becomes shorter when the aluminum composition is increased. It should be noted that the $(Al_xGa_{1-x})_{0.5}In_{0.5}P$ alloy is a direct bandgap semiconductor material when the aluminum composition, x , is smaller than 0.53, corresponding to an emitting wavelength of about 555 nm (or, a color of green). It becomes an indirect bandgap semiconductor material when the aluminum composition is greater than 0.53. As a matter of fact, the emission efficiency of the AlGaInP semiconductor material becomes poor when the emission wavelength is shorter than 570 nm.

In addition to increasing the aluminum composition in the $(Al_xGa_{1-x})_{0.5}In_{0.5}P$ alloy, short emission wavelength of the AlGaInP material may be obtained by using the quantum well structures or with the strain effect.³⁻⁶ In order to improve the performance of the 570-nm AlGaInP LEDs, we have grown several wafers with different structure designs and studied the optical properties as functions of the device temperature and the excitation power experimentally with a photoluminescence (PL) measurement system and numerically with a commercial *Lastip* simulation program. In this paper, important factors such as the barrier height in quantum wells, the tensile strain barrier cladding (TSBC) next to the MQW region, the compensated strain in MQW, and the distributed Bragg reflector (DBR) are investigated.

2. RESULTS OF EXPERIMENTS AND SIMULATIONS

The structure of the AlGaInP semiconductor devices is shown in Fig. 1. Since the GaAs substrate is absorptive in the spectral range of interest, an n-type DBR was grown on the GaAs substrate to reflect the light back to the upward direction. Then, an n-type AlGaInP cladding layer was grown on DBR, followed by the AlGaInP MQW active layer. A carrier block layer was then grown between the MQW active layer and the p-type AlGaInP cladding layer to help reduce the carrier overflow problem. On top of the p-type AlGaInP cladding layer a p-type GaAs cap layer was grown to complete the structure. Since the GaAs cap layer is absorptive in the spectral range of interest as mentioned above, it is chemically removed with the $\text{NH}_3\text{-H}_2\text{O}_2\text{-H}_2\text{O}$ solution before the photoluminescence measurements were executed.

Layer Number	Layer Structure
5	p-GaAs cap
4	p-AlGaInP cladding
4'	Carrier block layer
3	MQW active region
2	n-AlGaInP cladding
1	n-DBR
0	GaAs substrate

Fig. 1. Structure of the AlGaInP semiconductor devices.

Five AlGaInP semiconductor devices of different structures were fabricated to investigate the effect of the barrier height in quantum wells, the tensile strain barrier cladding next to the MQW region, the compensated strain in MQW, and the distributed Bragg reflector on the optical properties of the devices. For this specific study, device A was used as a reference device. The aluminum composition of each barrier in MQW of device B is 10% higher than that of device A. A tensile strain barrier cladding was grown next to the MQW region for device C. In device D the pair number of the DBR is half that of device A. And, finally, compensated strain in MQW is created in device E. Note that, in device E, the pair number of the DBR is also half that of device A.

Table 1. AlGaInP semiconductor devices with different structures

Device Number	LED Structure Description
A	Reference
B	Higher Al composition for each barrier in MQW
C	A tensile strain barrier cladding next to MQW region
D	Half DBR pair number
E	Compensated strain in MQW Half DBR pair number

Theoretically, short emission wavelength of the AlGaInP semiconductor devices near the green spectral region may be obtained by increasing the aluminum composition in wells of the MQW; however, as mentioned before, this is not favorable due to the reduction of the radiation efficiency in the high-aluminum-containing active region and the smaller band offset between the active and the cladding region. The effect of aluminum composition in wells of the AlGaInP MQW on the optical performance of the AlGaInP devices⁵ may be numerically studied with the *Lastip* simulation program.

For the *Lastip* simulation, following formula is used to relate the energy bandgap of the $(Al_xGa_{1-x})_{0.5}In_{0.5}P$ semiconductor material, $E_g(x)$, to the aluminum composition, x , at 300 K:

$$E_g(x) = 1.891 + 0.49x + 0.0025x^2 \text{ (eV)}. \quad (1)$$

In our simulation, the relation between the energy bandgap of the AlGaInP semiconductor material and the temperature is approximated by the *Varshni formula*:⁸

$$E_g(T) = E_g(0) - \frac{\gamma \cdot T^2}{T + \beta} \text{ (eV)}, \quad (2)$$

where $E_g(0)$, equal to 2.123 eV, is the energy bandgap at 0 K and $E_g(T)$ is the energy bandgap at temperature T . The γ parameter has a value of 4.1×10^{-4} eV/K and the β parameter has a value of 136 K. The effective masses of the electrons and the holes in the AlGaInP material used in our simulation were

$$m_e = (0.0124 + 0.0915x)m_0, \quad (3)$$

$$m_h = 0.56m_0, \quad (4)$$

where m_e is the effective mass of the electrons in AlGaInP, m_h is the effective mass of the holes in AlGaInP, and m_0 is the free-electron mass.

Figure 2 shows the results of the *Lastip* numerical simulation on the peak intensity and the PL intensity, obtained by integrating the spectra over the spectral range of interest, as functions of the aluminum composition. From the results we find that both the peak intensity and the PL intensity decrease monotonically when the aluminum composition is increased gradually from 0.12 to 0.24.

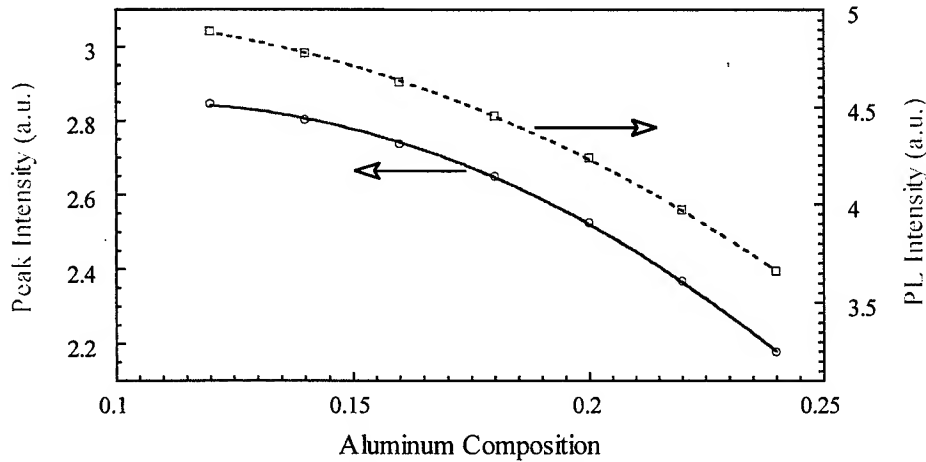


Fig. 2. Results of *Lastip* simulation on peak intensity and PL intensity as functions of the aluminum composition in the wells of the AlGaInP MQW.

2.1. Effect of Barrier Height in Quantum Wells

It is expected from the theory that a better optical performance should be obtained with a higher barrier height owing to less carrier overflow. Figure 3 shows the PL spectra and the *Lastip* spontaneous emission rate of devices A and B measured at room temperature. For PL spectra, as shown in Fig. 3a, device A has a peak wavelength near 575 nm and a peak intensity of about 395 counts relative to the system noise level while device B has a peak wavelength near 571 nm and a peak intensity of about 920 counts. It is obvious from the results that device B, which has a higher barrier height than device A, has a shorter emission peak wavelength and a higher emission efficiency when compared with device A. Similar results are found in the *Lastip* simulation, as shown in Fig. 3b. The second emission peak of a shorter wavelength present in each spectrum of Fig. 3b is owing to the electronic transitions from the second quantum state in MQW.

Figure 4 shows the peak wavelength of devices A and B as functions of the temperature for the PL measurements and the *Lastip* simulation. The peak wavelengths of both devices decrease when temperature decreases. The emission light of both devices has a peak wavelength near 552 nm at 23 K, corresponding to a color of green. Good agreement between the experiments and the simulation is observed.

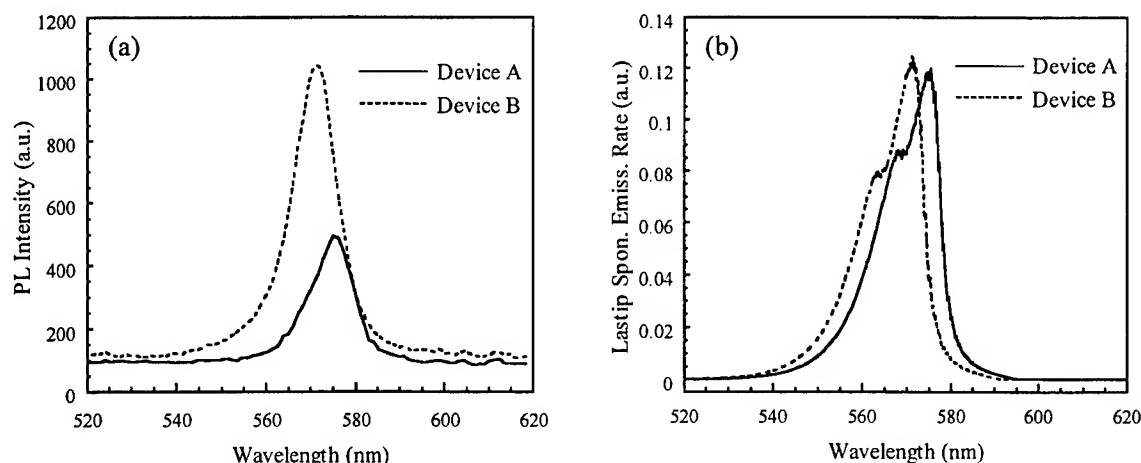


Fig. 3. Emission spectra of devices A and B at 300 K: (a) PL measurements, (b) Lastip simulation.

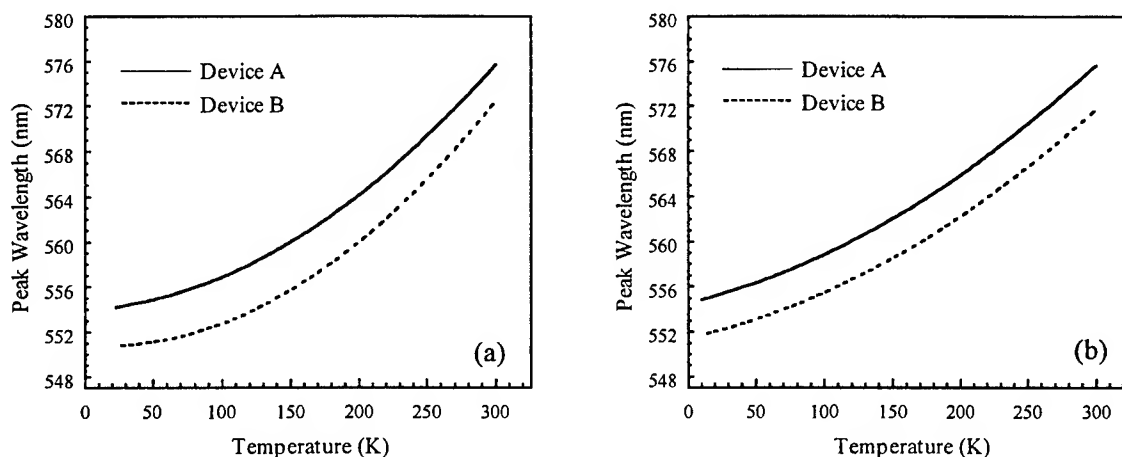


Fig. 4. Peak wavelength of devices A and B as functions of temperature: (a) PL measurements, (b) Lastip simulation.

It is expected from the theory⁷ that, for the AlGaInP semiconductor materials, the radiative recombination process tends to dominate at low temperature while the non-radiative recombination process may play important role at high temperature. Figure 5 shows the PL intensity, obtained by integrating the spectra over the spectral range of interest, of devices A and B as functions of the excitation power at 23 K and room temperature. Note that both x and y axes are plotted in log scales in Fig. 5. From the results we notice that the curves measured at room temperature have higher slopes when compared to those measured at 23 K, implying that the radiative recombination process tends to dominate at 23 K while the non-radiative recombination process plays important role at room temperature.⁷

From Fig. 5 we also notice that device A has a higher slope than device B at room temperature, which indicates that the non-radiative recombination is more severe for device A at room temperature since its barrier height of the quantum wells is lower than its counterpart in device B. On the other hand, as shown in Fig. 5, devices A and B have similar slopes at 23 K, indicating that barrier height has less influence on luminescence mechanism at low temperature for this specific situation.

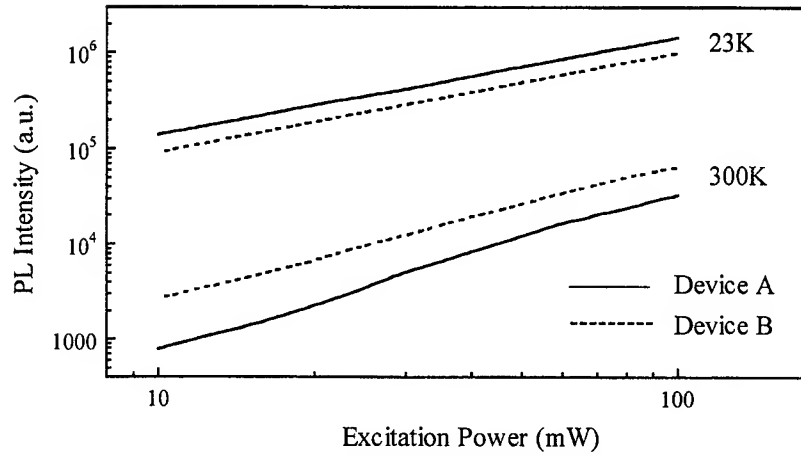


Fig. 5. PL intensity of devices A and B as functions of the excitation power at 23 K and room temperature.

2.2. Effect of Tensile Strain Barrier Cladding Next to MQW Region

Optical performance may be improved by growing a tensile strain barrier cladding (TSBC) next to the MQW region. As shown in Fig. 6, device A has a peak wavelength near 575 nm and a peak intensity of about 395 counts at 300 K. Device C has a peak wavelength near 572 nm and a peak intensity of about 1650 counts at 300 K. It is obvious from the results that device C, which has a tensile strain barrier cladding next to the MQW region, has a shorter emission peak wavelength and a higher emission efficiency when compared with device A. Figure 7 shows the peak intensity of the PL spectra of devices A and C as functions of the temperature. The results show that device C has much better optical performance, especially at low temperature, as compared to device A. It indicates that TSBC may play important role in improving the optical performance of the AlGaInP semiconductor materials in the yellow-green spectral region.

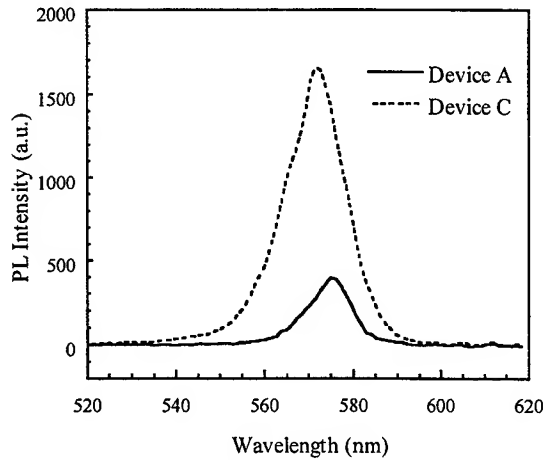


Fig. 6. PL spectra of devices A and B at 300 K.

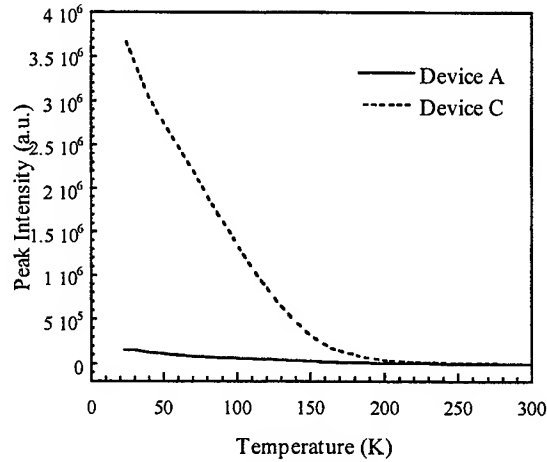


Fig. 7. PL intensity of devices A and B as functions of temperature.

2.3. Effect of Compensated Strain in MQW

In addition to TSBC, optical performance of the AlGaInP MQW structures may also be improved by introducing compensated strain to the MQW in the active region. Figure 8 shows the PL spectra of devices D and E, which contain the same structure of DBR, at room temperature. It is obvious from the results that, when compared to device D, device E has better optical performance since its MQW possesses compensated strain.

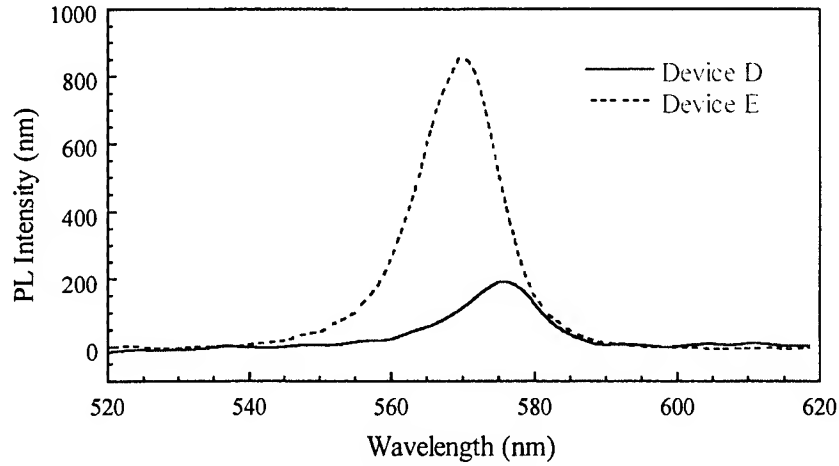


Fig. 8. PL spectra of devices D and E at room temperature.

2.4. Effect of Distributed Bragg Reflector

The emission light in the upward direction of the device may be increased with the use of a distributed Bragg reflector (DBR). Devices A and D have the same structure except that the DBR pair number of device D is half that of device A. Figure 9 shows the PL spectra of devices A and D at 300 K. As expected from theory, device A has a peak wavelength close to that of device D but has a higher peak intensity than device D.

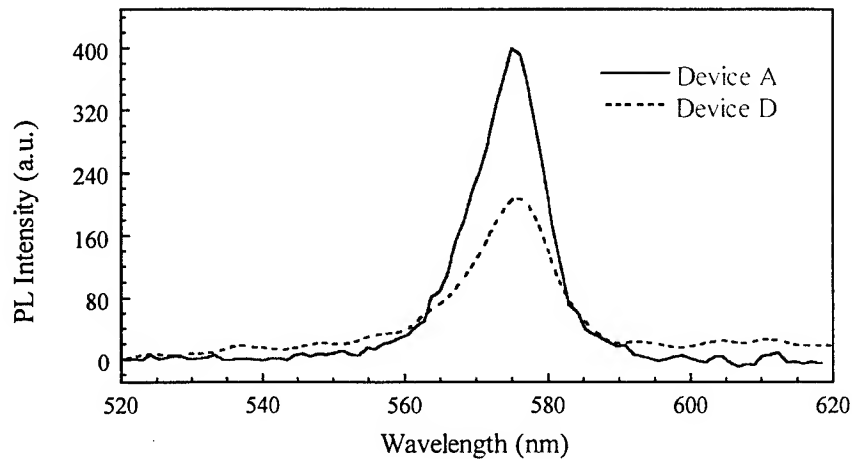


Fig. 9. PL spectra of devices A and D at 300 K.

Figure 10 shows the peak wavelength and the bandwidth (full width at half maximum) of devices A and D as functions of the temperature. It shows that both devices have almost the same peak wavelength for temperature ranging from 20 to 300 K. The bandwidths of both devices are close to each other at room temperature. When temperature decreases the bandwidth of device A becomes a little larger than that of device D. Peak intensity of devices A and D as functions of the temperature are shown in Fig. 11. In order to have better identifiable pictures near 300 K, the figure is split into two temperature ranges. As shown in Fig. 11, when the temperature is higher than 70 K, device A has higher peak intensity than device D; however, when the temperature is low the difference between the two figures becomes very small. Figure 12 shows the PL intensity, obtained by integrating the spectra over the spectral range of interest, of devices A and D as functions of the temperature. For all temperature range device A has higher PL intensity than device D. Although both devices A and D have almost the same peak intensity when the temperature is low, as shown in Fig. 11a, device A has a higher PL intensity than device D since the bandwidth of device A is higher than that of device D at low temperature, as shown in Fig 10b.

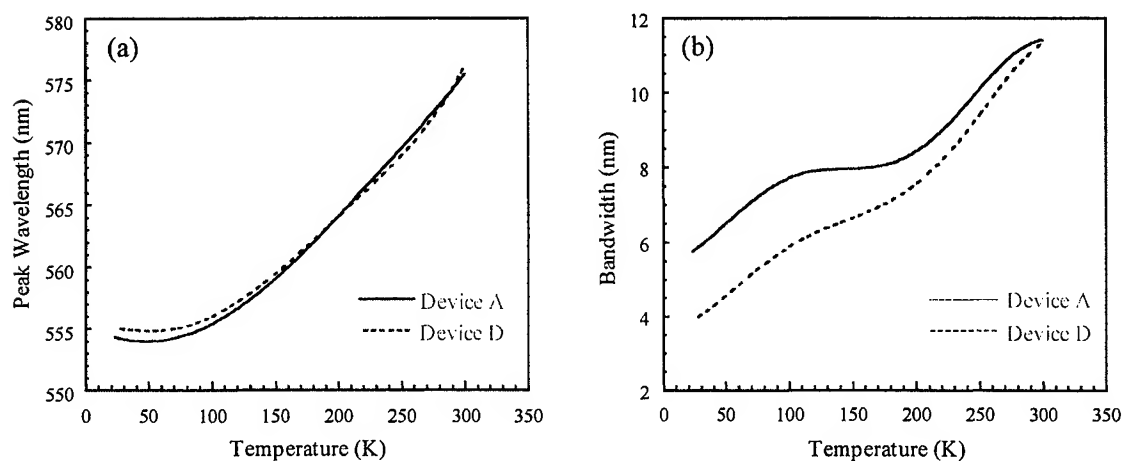


Fig. 10. (a) Peak wavelength and (b) bandwidth of devices A and D as functions of the temperature.

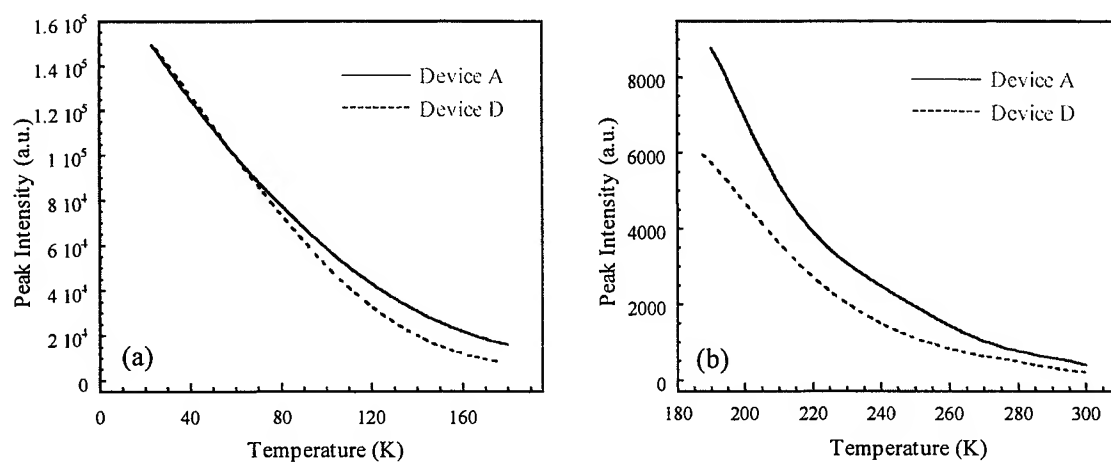


Fig. 11. Peak intensity of devices A and D for temperature range: (a) from 23 K to 180 K, and (b) from 180 K to 300 K.

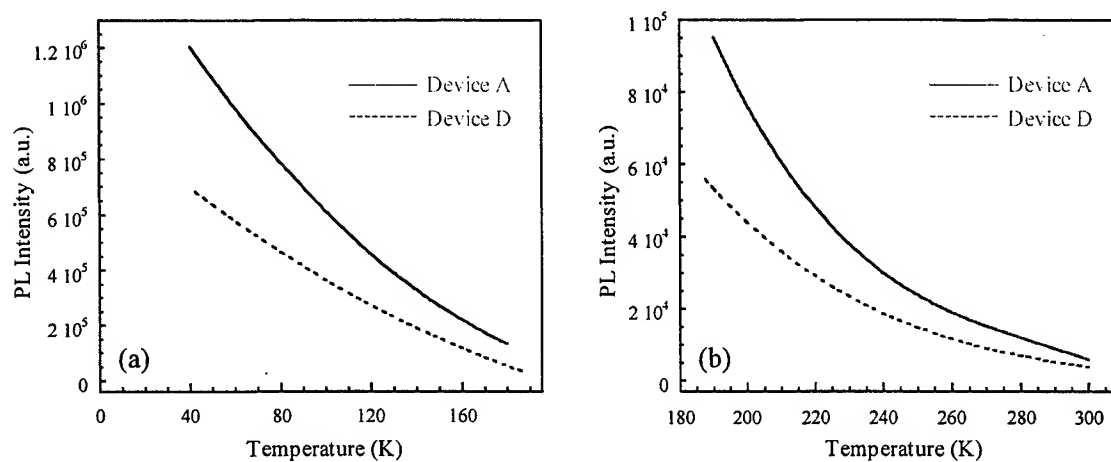


Fig. 12. PL intensity of devices A and D for temperature range: (a) from 23 K to 180 K, and (b) from 180 K to 300 K.

3. CONCLUSION

In order to improve the performance of the 570-nm AlGaInP semiconductor devices, we have grown five wafers with different structure designs and studied the optical properties as functions of the temperature and the excitation power experimentally with a photoluminescence measurement system and numerically with a commercial *Lastip* simulation program. The effect of aluminum composition in wells of the AlGaInP MQW is numerically studied with the *Lastip* simulation program. The results show that PL intensity decreases when the aluminum composition in wells increases. Effects of TSBC near the active region, compensated strain in the active region, and DBR on the optical properties of the AlGaInP devices are also investigated. Photoluminescence measurement results show that TSBC near the active region and compensated strain in the active region both lead to better optical performance. Experiments and simulations also show that DBR has important impact on the optical performance of the AlGaInP devices. Good agreement between the experimental and numerical results is observed.

ACKNOWLEDGMENTS

The authors are grateful to Professor Jiann Lin of the Department of Physics, National Changhua University of Education, Changhua, Taiwan for the use of the *Lastip* simulation program. This work is supported by the National Science Council (NSC) of the Republic of China under grant NSC-89-2112-M-018-003.

REFERENCES

1. G. B. Stringfellow and M. George Craford, *High Brightness Light Emitting Diodes - Semiconductors and Semimetals Volume 48*, Academic Press, San Diego, California, USA, 1997.
2. R. S. Kern, "Progress and status of visible light emitting diode technology," in *Light-Emitting Diodes: Research, Manufacturing, and Applications III*, E. Fred Schubert, Ian T. Ferguson, H. Walter Yao, Editors, Proceeding of SPIE Vol. 3621, pp. 16-27, 1999.
3. T. Fukunaga, M. Wada, and T. Hayakawa, "High-power 0.8 μm InGaAsP/InGaP/AlGaAs single quantum well lasers with tensile-strained InGaP barriers," *Jpn. J. Appl. Phys.* **38**, pp. L387-L389, 1999.
4. S. Kamiyama, T. Uenoyama, M. Mannoh, and K. Ohnaka, "Strain effect on 630 nm GaInP/AlGaInP multi-quantum well lasers," *Jpn. J. Appl. Phys.* **33**, pp. 2571-2578, 1994.
5. I. Nomura, K. Kishino, A. Kikuchi, and Y. Kaneko, "600-nm-range GaInP/AlInP strained quantum well lasers grown by gas source molecular beam epitaxy," *Jpn. J. Appl. Phys.* **33**, pp. 804-810, 1994.
6. H. Sugawara and M. Ishikawa, "Compensated-strain multiquantum-well active layer for InGaAlP-based visible light emitting diodes," *Jpn. J. Appl. Phys.* **34**, pp. L1458-L1460, 1995.
7. S. Naritsuka, Y. Nishikawa, H. Sugawara, M. Ishikawa, and Y. Kokubun, "Photoluminescence studies on InGaAlP layers grown by low-pressure metalorganic chemical vapor deposition," *J. Electron. Mater.* **20**, pp. 687-690, 1991.
8. Y. P. Varshni, *Physica* **34**, 149, 1967.

*Correspondence: Email: grace@vpec.com.tw; Telephone: 886-3-419-3333 Ext. 333; Fax: 886-3-419-2968.

**Correspondence: Email: ykuo@cc.ncue.edu.tw; Telephone: 886-4-723-2105 Ext. 3341; Fax: 886-4-721-1153.

Nearly Single-Mode, High-Density two-dimensional Vertical-Cavity Surface-Emitting Laser Arrays for Optical Communications

Hung-Pin D. Yang*, Mei-Li Wang, Wen-Chang Jiang, Yeung-Sy Su, and
Chia-Pin Sung

Division of Optoelectronic Materials and Devices
Opto-Electronics & Systems Laboratories
Industrial Technology Research Institute
Chutung 310, Hsinchu, Taiwan, R. O. C.

Phone : +886-3-5915126, Fax : +886-3-5915138, E-mail : hpyang@itri.org.tw

ABSTRACT

We have made AlGaAs/GaAs gain-guided two-dimensional (8×8 and 4×4) vertical-cavity surface-emitting laser array in the 850-nm range for optical communication applications. Higher optical power with nearly single transverse mode output can be achieved by using high-density two-dimensional VCSEL arrays with smaller emitting element windows ($\leq 5 \mu\text{m}$). The distributed Bragg reflectors (DBRs) of the VCSELs consist of $\text{Al}_{0.12}\text{Ga}_{0.88}\text{As}/\text{AlAs}$ quarter-wave stacks. The GRINSCH active region is consisted of an undoped three-quantum-well GaAs/ $\text{Al}_{0.3}\text{Ga}_{0.7}\text{As}$ and two undoped linearly graded $\text{Al}_x\text{Ga}_{1-x}\text{As}$ confinement layers. The emitting windows of the individual VCSEL elements are $5 \mu\text{m} \times 5 \mu\text{m}$. A high cw optical power of 15.3 mW was measured for a 8×8 array, with a maximum pulsed optical power of 28 mW at 160 mA. The spectrum of the VCSEL array showed single transverse mode characteristics. The near-field characteristics of the arrays were measured. Almost all the VCSEL elements emitted TEM_{00} mode. The modulation characteristics of the VCSEL arrays were also measured at different operating current.

Keywords: vertical-cavity, surface-emitting lasers, 2D VCSEL array, spectrum, modulation

1. INTRODUCTION

Vertical-cavity surface-emitting lasers (VCSELs) have attracted a lot of attention because of their applications for optical interconnects, [1] data communications, optical storage, CD-ROM (compact disc-read only memory), DVD (digital video disc) pickup head, [2] optical printing, and wavelength-division multiplexing (WDM). [3], [4] The emission wavelengths are 650 nm to $1.55 \mu\text{m}$. [1]-[10] The development of blue/green semiconductor lasers has led to the study of blue/green VCSELs. Recently, oxide-confined VCSELs were also vastly investigated because of their very low threshold current and their capability of generating single-mode output. [5-8] The basic structure of a VCSEL includes an active region, sandwiched between heavily-doped p-type and n-type DBRs, and conducting electrodes. The thickness of the active region is the multiple of the emitting wavelength. The p-type and n-type DBRs form the top and bottom reflecting mirrors of the laser cavity. Laser beam resonates between the n-type and p-type DBRs of the laser cavity. The advantages of the VCSELs include circular beam, lower threshold current, lower beam divergence, lower temperature sensitivity, one-dimensional and two-dimensional arrays, and on-wafer testability. The processing and on-wafer testing techniques are somewhat similar to those of the light-emitting diodes (LEDs). Compared to the edge-emitting lasers, the optical power density of VCSELs is higher due to smaller volume of the active region. The cavity-length of a VCSEL is often less than $1 \mu\text{m}$, which is much less than the cavity-length (several hundred μm) of an edge-emitting laser. Therefore, VCSELs emit laser beam with single longitudinal mode.

Also, high-packing-density VCSEL arrays are suitable for higher power applications. [9]-[11] P-type ohmic contact grid lines were used to subdivide rectangular broad-area VCSELs into small VCSEL array elements. [9], [11] These metal grid lines were used for current conduction, the emission characteristics of the subdivided VCSELs array elements were similar to

* Correspondence: Email: hpyang@itri.org.tw; Telephone: 886-3-5915126

those of the smaller aperture VCSELs. Higher optical power can be achieved for VCSEL arrays with more laser-emitting elements. The broad-area VCSELs, on the other hand, exhibit high-order modes emission characteristics. Here, we refer broad-area VCSELs as lasers with the aperture sizes of greater than $20\text{ }\mu\text{m}$. Higher optical power can be obtained for VCSELs with larger laser-emitting windows. The series resistance of the top DBR is higher for current flow in the direction parallel to the surface of the light-emitting window of the VCSEL. The current density is higher at the periphery than the current density in the central region, so that the laser beam intensity is lower in the central region.

For optical communication applications, single-mode lasers are often needed because of lower dispersion loss in the optical fibers. Single transverse-mode laser output can be obtained for VCSELs with their emitting aperture of less than $5\text{ }\mu\text{m}$. The maximum output power of these VCSELs are usually lower than 3 mW . In addition to long-wavelength semiconductor laser, near-infrared VCSEL arrays with higher output power can also be used for longer distance optical fiber transmission. In this work, higher optical power with nearly single transverse mode output can be achieved by using high-density two-dimensional VCSEL arrays with smaller emitting element windows ($\leq 5\text{ }\mu\text{m}$). We have made high-packing-density 4×4 and 8×8 VCSEL arrays optical fiber communications. The high-speed modulation characteristics of the VCSEL arrays were also studied.

2. DEVICE FABRICATION

The epitaxial wafer of the 850-nm AlGaAs/GaAs vertical-cavity surface-emitting lasers were grown in a MOCVD system on a (100) $\text{n}^+\text{-GaAs}$ substrate. The epitaxial structure is the following (from bottom to top): a $\text{n}^+\text{-GaAs}$ buffer, a n-DBR, an undoped AlGaAs/GaAs active region, a p-DBR, and a $\text{p}^+\text{-GaAs}$ contact layer. The graded-index separate-confinement heterostructure (GRINSCH) active region contained an undoped three-quantum-well $60\text{\AA}/80\text{\AA}$ GaAs/ $\text{Al}_{0.3}\text{Ga}_{0.7}\text{As}$, two undoped $\text{Al}_{0.3}\text{Ga}_{0.7}\text{As}$ confinement layers, a linearly graded undoped- $\text{Al}_x\text{Ga}_{1-x}\text{As}$ ($x = 0.6\rightarrow 0.3$) lower waveguide layer and an linearly graded undoped- $\text{Al}_x\text{Ga}_{1-x}\text{As}$ ($x = 0.30.6$) upper waveguide layer. The bottom mirror is a n-type distributed Bragg reflector (DBR) consisted of 30.5 periods of $\text{n}^+\text{-Al}_{0.12}\text{Ga}_{0.88}\text{As}/\text{n}^+\text{-AlAs}$ quarter-wave ($\lambda/4$) stacks. The top mirror is a p-DBR consisted of 20 periods of $\text{p}^+\text{-Al}_{0.12}\text{Ga}_{0.88}\text{As}/\text{p}^+\text{-AlAs}$ (C-doped) quarter-wave stacks. Carbon doping was used for the p-DBR in order to obtain higher carrier concentration in the p-DBR layers. Both the n-type and p-type $\text{Al}_{0.12}\text{Ga}_{0.88}\text{As}/\text{AlAs}$ interfaces of the DBRs are linearly graded mainly to reduce the energy barriers of the hetero-interface so as to reduce the series resistance of DBR layers. The doping level in the interface grading layers was same as those in the $\text{Al}_{0.12}\text{Ga}_{0.88}\text{As}$ and AlAs layers. The series resistance is much higher for the p-DBR layers than for the n-DBR layers because the hole mobilities are much lower in the $\text{p}^+\text{-Al}_{0.12}\text{Ga}_{0.88}\text{As}$ and $\text{p}^+\text{-AlAs}$ layers than the electron mobilities in the $\text{n}^+\text{-Al}_{0.12}\text{Ga}_{0.88}\text{As}$ and $\text{n}^+\text{-AlAs}$ layers. A 50-\AA $\text{p}^+\text{-GaAs}$ (Zn-doped at $1\times 10^{19}\text{ cm}^{-3}$) cap layer was grown on top of the p-DBR to facilitate p-ohmic contacts. Reflectance measurement showed that the absorption dip of the GaAs/ $\text{Al}_{0.3}\text{Ga}_{0.7}\text{As}$ quantum wells was about 840 to 850 nm.

The planarized gain-guided VCSEL array fabrication processes are described as follows. Firstly, current conducting aperture of the gain-guided top-emitting VCSEL array was defined by using proton (H^+) implantation. The proton implantation energy was 280 KeV, with a dosage of $6\times 10^{14}\text{ cm}^{-2}$. The separation between implantation boundary and outermost VCSEL element was $5\text{ }\mu\text{m}$. A very thick positive photoresist of $6\text{ }\mu\text{m}$ was used as an implantation mask for the current conduction region. The proton-implanted region of the VCSEL device become highly resistive so that the current was confined to the laser-emitting region. P-type ohmic contacts, which defined the laser-emitting windows, were formed by evaporating Ti/Au, lift-off, and annealing. The individual $5\text{ }\mu\text{m}\times 5\text{ }\mu\text{m}$ VCSEL elements of the array were separated by p-type metal grid contacts surrounding the laser-emitting windows. The width of the metal grid line was $2\text{ }\mu\text{m}$. A SiN_x film was deposited by PECVD to prevent current leakage. After that, pad metal of Ti/Au was evaporated on top of the SiN_x film to facilitate bonding. After forming the n-ohmic contacts at the backside of the wafer, the VCSEL wafer was then diced into laser array chips. The two-dimensional VCSEL arrays were made with 4×4 and 8×8 VCSEL elements. The dimension of the square VCSEL array element was $5\text{ }\mu\text{m}\times 5\text{ }\mu\text{m}$. These VCSEL array chips were packaged for further tests. The cross sectional device structure of the 8×8 VCSEL array is shown in Fig. 1.

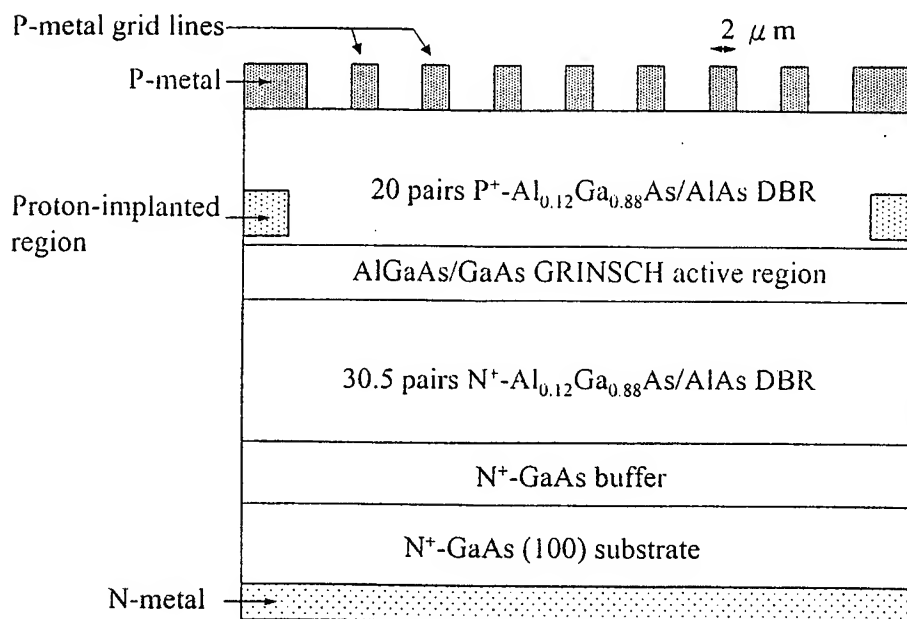


Fig. 1 Cross-sectional device structure of a 8×8 ($5 \mu\text{m} \times 5 \mu\text{m}$) AlGaAs/GaAs VCSEL array.

3. RESULTS AND DISCUSSION

The current-voltage (I-V) characteristics of the two-dimensional 8×8 ($5 \mu\text{m} \times 5 \mu\text{m}$) and 4×4 ($5 \mu\text{m} \times 5 \mu\text{m}$) VCSEL arrays were measured. The differential resistance, dV/dI , were 5.1Ω at 35 mA for a 8×8 array device. The differential resistance were 10Ω at 35 mA for a 4×4 array. The differential resistance is larger for smaller (4×4) VCSEL array. The threshold voltage was 1.65 V. The CW and pulsed optical power versus injection current (L-I) characteristics of the 8×8 AlGaAs/GaAs VCSEL array is shown in Fig. 1. The pulse duty cycle of the pulsed L-I measurements were 0.1%. The pulsed and CW curves both have the same threshold current of 22.8 mA. The threshold current density is 557 A/cm^2 . As the current increases beyond 32 mA, the pulsed optical power becomes higher than the CW optical power. This is due to the heating effect within the device at higher CW current levels. The series resistance of the device is mostly attributed to the series resistance of the p-DBR. A maximum CW optical power of 15.3 mW was measured at a current of 144 mA. This means that a thermal roll-over occurs at very high current level of 144 mA, and the CW optical power starts to decrease with increasing current. At very high current levels, joule heating effect become more evident because more injecting electrical power was converted into heat. As the temperature of the device started to increase, the optical power started to decrease. A pulsed optical power of 28 mW was measured for this device at 160 mA. The pulsed and CW L-I characteristics of a 4×4 VCSEL array is shown in Fig. 3. The pulsed and CW threshold current of the 4×4 VCSEL array were both 8.8 mA. The threshold current density is 681 A/cm^2 for this device. The threshold current is lower for smaller VCSEL array, while the threshold current density is higher for smaller device. A maximum CW optical power of 8.83 mW was measured for a 4×4 VCSEL array, with a maximum pulsed optical power of 13.8 mW. Thermal roll-over occurred at the maximum optical power and then the optical power decreased with increasing current. Thermal roll-over occurs for the CW L-I curve as the injection current increases beyond 27 mA. These pulsed L-I results are comparable to a previous report on the VCSEL array with similar device aperture dimensions. [9] The threshold current versus temperature plot of 8×8 and 4×4 VCSEL arrays are shown in Figs. 4 and 5, respectively. For this 8×8 VCSEL array, the threshold current increases monotonically with temperature from 26.2 mA at 20°C to 33 mA at 20°C . The optical power and slope efficiency decreases with increasing temperature. The characteristics temperature (T_0) of the 8×8 VCSEL array is estimated to be 157 K from 20 to 40°C , and is 101 K from 40 to 50°C . The temperature-dependent L-I characteristics of 8×8 and 4×4 VCSEL arrays are shown in Figs. 6 and 7, respectively.

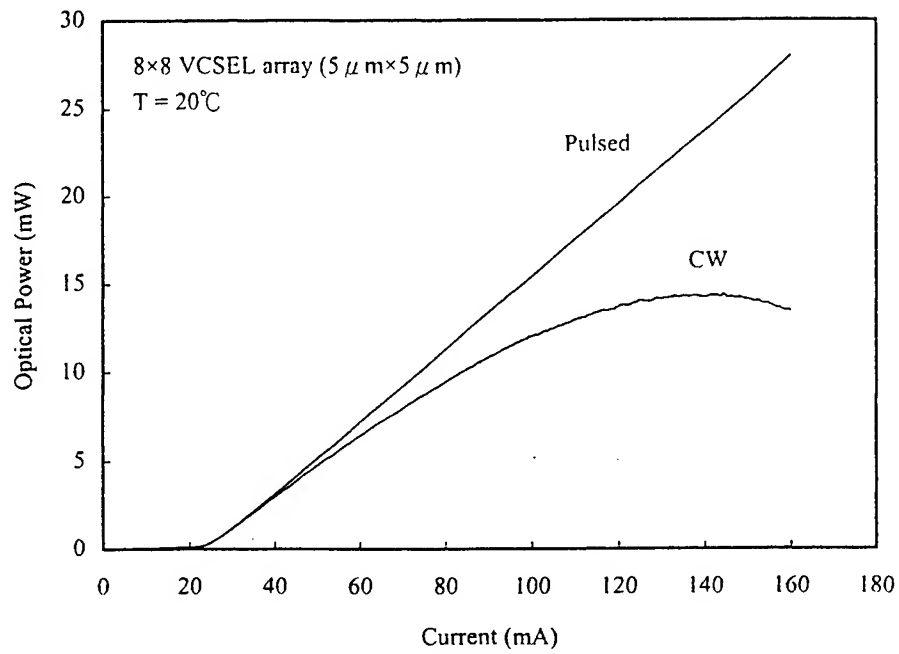


Fig. 2 Pulsed and CW L-I characteristics of a 8×8 ($5\ \mu\text{m} \times 5\ \mu\text{m}$) VCSEL array.

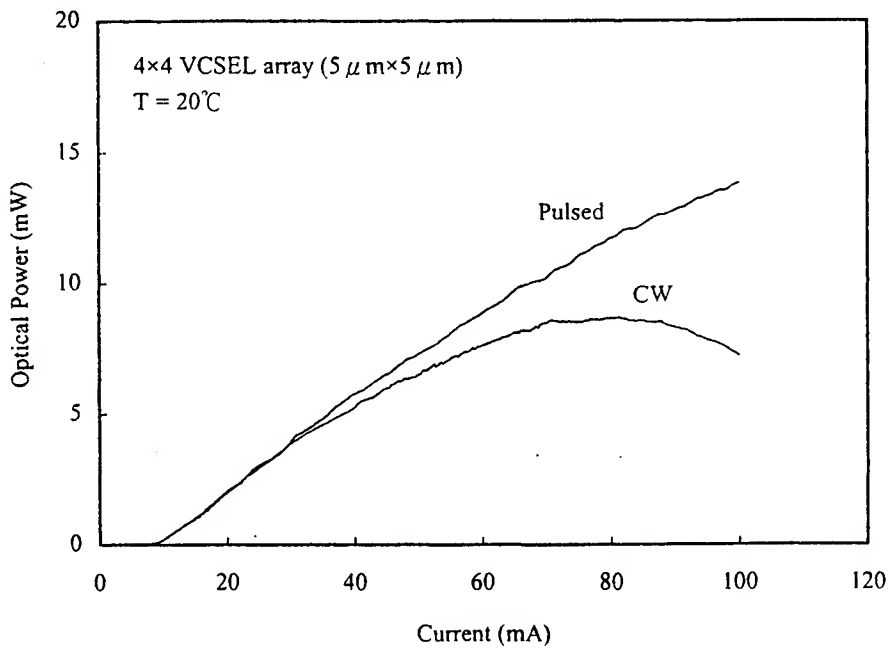


Fig. 3 Pulsed and CW L-I characteristics of a 4×4 ($5\ \mu\text{m} \times 5\ \mu\text{m}$) VCSEL array.

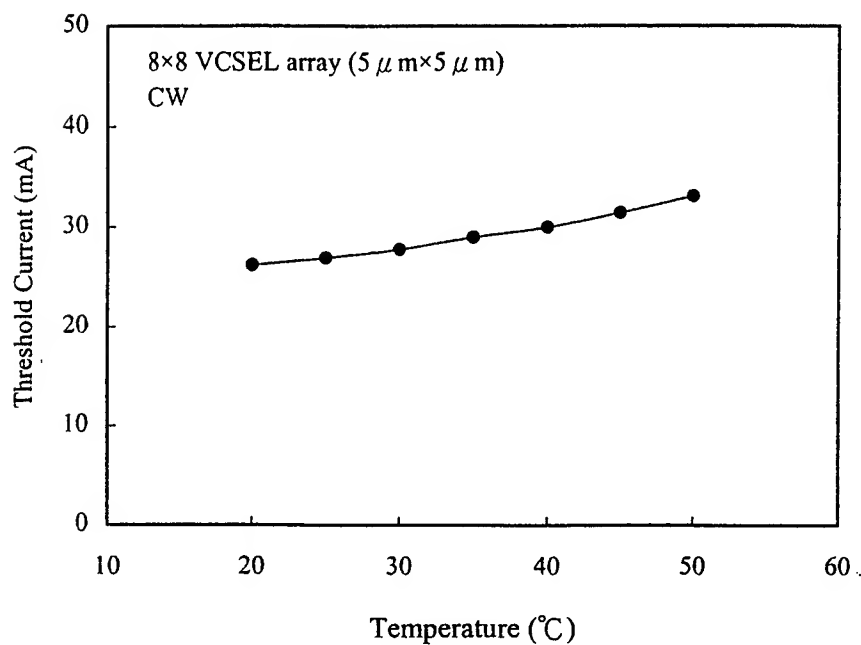


Fig. 4 Threshold current versus temperature plot of a 8×8 ($5\ \mu\text{m} \times 5\ \mu\text{m}$) VCSEL array.

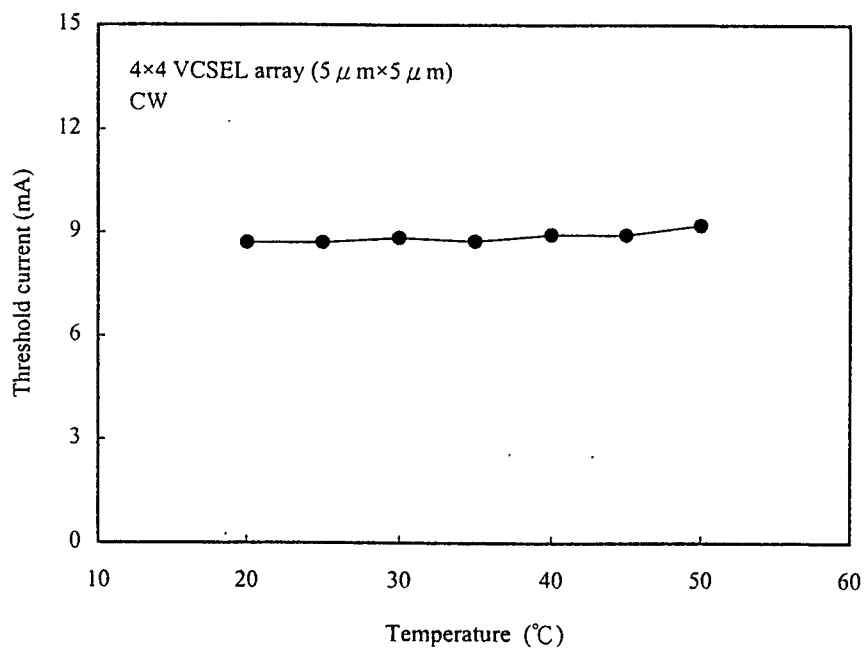


Fig. 5 Threshold current versus temperature plot of a 4×4 ($5\ \mu\text{m} \times 5\ \mu\text{m}$) VCSEL array.

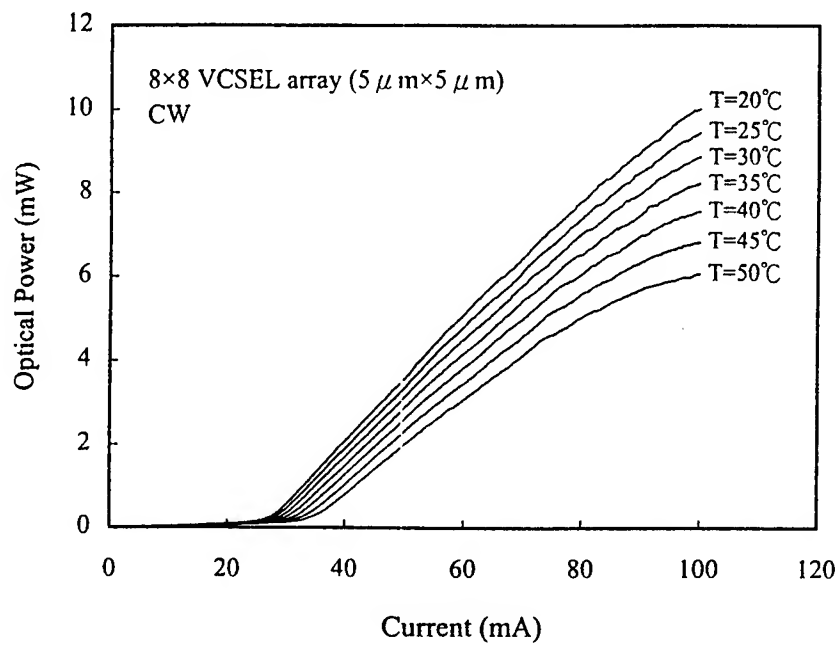


Fig. 6 Temperature-dependent L-I characteristics of the 8x8 ($5\ \mu\text{m} \times 5\ \mu\text{m}$) VCSEL array.

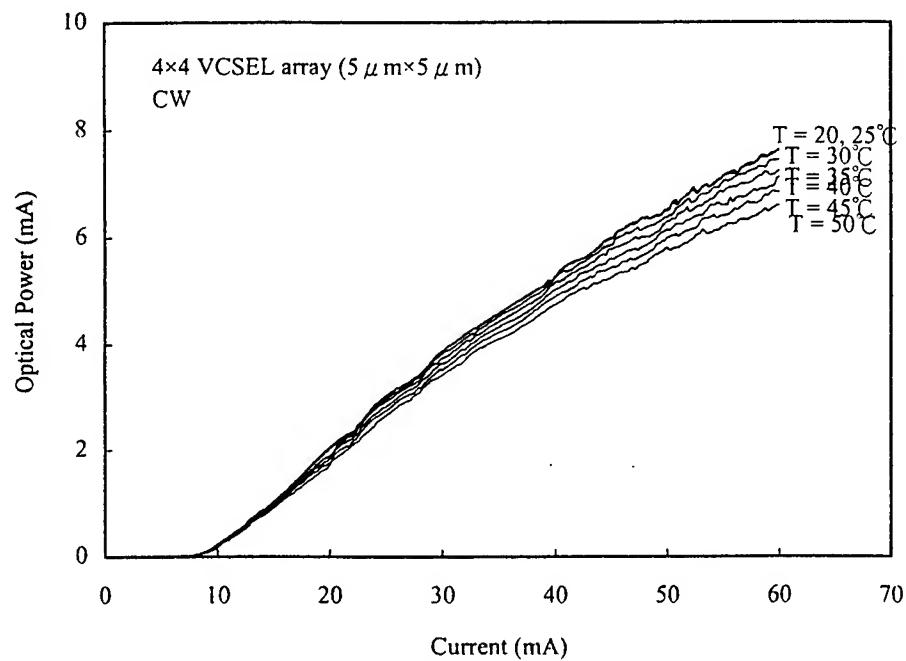


Fig. 7 Temperature-dependent L-I characteristics of the 4x4 ($5\ \mu\text{m} \times 5\ \mu\text{m}$) VCSEL array.

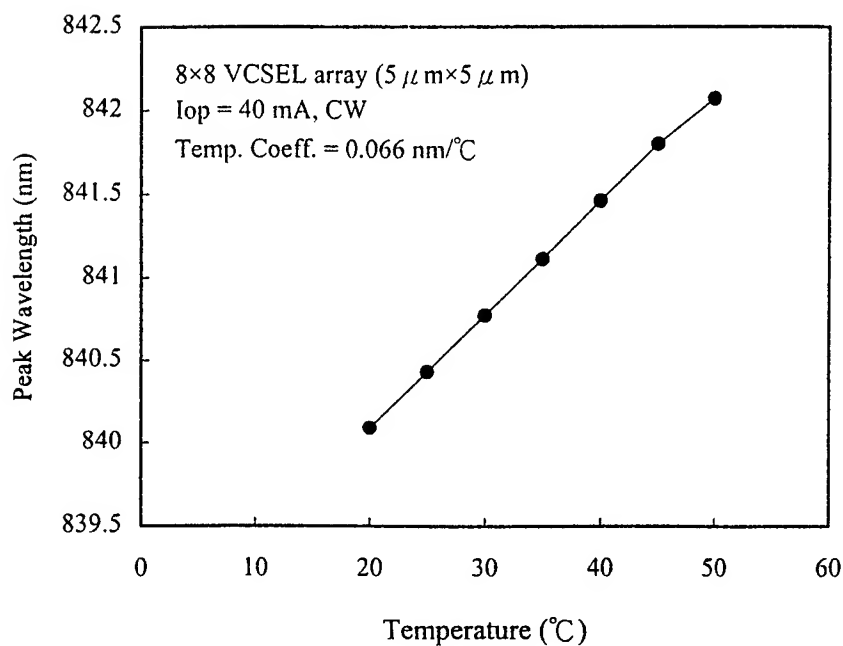


Fig. 8 Peak wavelength versus temperature plot of the 8x8 VCSEL array.

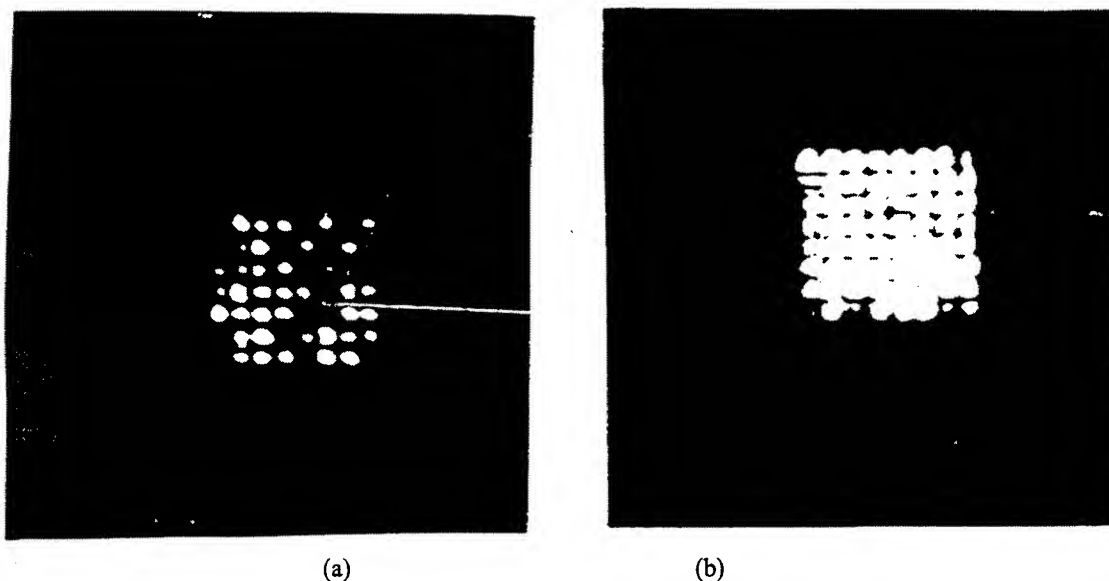


Fig. 9 Near-field pattern of the 8x8 VCSEL array at (a) 40 mA and (b) 75 mA.

The laser output power decreases with increasing temperature. These results suggest that heat sinks with high thermal conductivity are needed in order to achieve higher optical power.

The lasing spectrum of the 8x8 (5 μm x 5 μm) and 4x4 (5 μm x 5 μm) VCSEL arrays were measured. Nearly single-mode characteristics were obtained. The peak wavelength is 840 nm at 40 mA. Fig. 8 shows the peak wavelength versus

temperature plot of the 8×8 ($5 \mu\text{m} \times 5 \mu\text{m}$) VCSEL array. The peak wavelength temperature coefficient is low, $\sim 0.066 \text{ nm}/^\circ\text{C}$ at 40 mA. The CW near-field pattern of the 8×8 ($5 \mu\text{m}$) VCSEL array was also measured, as a function of injection current. Fig. 9(a) shows the photograph of the near-field pattern of the 8×8 array with a CW current of 40 mA. Only some of the lasers emit laser beam. This means that only some of the emitting lasers are contributing to the total output power (shown in Fig. 1) of the array with a total current level of 40 mA ($1.5 I_{th}$). We therefore conclude that the lasers in the array gradually reach their threshold and start to lase as the current increases. This can also be observed in the change of the near-field pattern of the array by continuously tuning up the injection current. Fig. 9(b) shows the near-field pattern of the 8×8 array with a CW current of 75 mA. All the 36 VCSEL elements lase. The VCSEL arrays emit laser beams with small-aperture characteristics, while the total differential resistance characteristics are similar to those of the broad-area VCSELs. These high-packing-density VCSELs are suitable for optical communication applications.

4. CONCLUSION

In conclusion, we have made a systematic study on the emission characteristics high-packing-density AlGaAs/GaAs VCSEL array in the 850-nm range for optical fiber communications. The L-I characteristics of the VCSELs show a high CW output power of 15.3 mW for a 8×8 ($5 \mu\text{m} \times 5 \mu\text{m}$) VCSEL array. The near-field patterns of the devices were also measured and analyzed.

ACKNOWLEDGEMENT

The authors would like to thank Drs. C. A. Chang and J. Chi for useful discussions.

REFERENCES

1. P. Schnitzer, M. Grabherr, R. Jager, F. Mederer, R. Michalzick, D. Wiedenmann, and K. J. Ebeling, "GaAs VCSEL's at $\lambda = 780$ and 835 nm for short-distance 2.5-Gb/s plastic optical fiber data links", *IEEE Photon. Technol. Lett.* vol. 11, no.7, pp. 767-769, 1999.
2. H. K. Shin, I. Kim, E. J. Kim, J. H. Kim, E. K. Lee, M. K. Lee, J. K. Mun, C. S. Park, and Y. S. Yi, *Jpn. J. Appl. Phys.* vol. 35, pp. 506, 1996.
3. W. Yuen, G. S. Li, C. Chang-Hasnain, "Multiple-wavelength vertical-cavity surface-emitting laser arrays with a record wavelength span", *IEEE Photonics Technol. Lett.*, vol. 8, pp. 4-6, 1996.
4. G. G. Ortiz, S. Q. Luong, S. Z. Sun, Julian Cheng, H. Q. Hou, G. A. Vawter, and B. E. Hammons, "Monolithic, multiple wavelength vertical-cavity, surface-emitting laser arrays by surface-controlled MOCVD growth rate enhancement and reduction", *IEEE Photon. Technol. Lett.* vol. 9, no. 8, pp. 1069-1071, 1997.
5. K. L. Lear, K. D. Choquette, R. P. Schneider, S. P. Kilcoyne, and K. M. Geib, "Selectively oxidized vertical cavity surface emitting lasers with 50% power conversion efficiency", *Electron. Lett.* vol. 31, pp. 208-209, 1995.
6. M. Grabherr, R. Jager, R. Michalzick, B. Weigl, G. Reiner, and K. J. Reiner, "Efficient single-mode oxide-confined GaAs VCSEL's emitting in the 850-nm wavelength regime", *IEEE Photon. Technol. Lett.* vol. 9, no. 10, pp. 1304-1306.
7. C. L. Chua, R. L. Thornton, D. W. Treat, and R. M. Donaldson, "Independently addressable VCSEL arrays on $3\text{-}\mu\text{m}$ pitch", *IEEE Photonics Technol. Lett.*, vol. 10, pp. 917-919, 1998.
8. G. Giarretta, M. Y. Li, G. S. Li, W. Yuen, and C. J. Chang-Hasnain, "A novel 4×8 single-mode independently addressable oxide isolated VCSEL array", *IEEE Photon. Technol. Lett.* vol. 9, no. 9, pp. 1196-1198.
9. R. A. Morgan, K. Kojima, T. Mullally, G. D. Guth, M. W. Focht, R. E. Leibenguth, and M. Asom, "High-power coherently coupled 8×8 vertical cavity surface emitting laser array", *Appl. Phys. Lett.* vol. 61, pp. 1160-1162, 1992.
10. R. Michalzick, M. Grabherr, R. Jager, M. Miller, and K. J. Ebeling, "Progress in high-power VCSELs and arrays," *Photonics-Taiwan, Taipei, Proc. SPIE-3419*, pp. 187-195, 1998.
11. J. P. VAN DER ZIEL, D. G. Deppe, N. Chand, G. J. Zyzdzik, and S. N. G. Chu, "Characteristics of single- and two-dimensional phase coupled arrays of vertical cavity surface emitting GaAs/AlGaAs lasers", *IEEE J. Quantum Electron.* vol. 26, pp. 1873-1882, 1990.

DC and AC Characteristics of 850 nm Broad-Area Vertical-Cavity Surface-Emitting Lasers

Hung-Pin D. Yang, Yeung-Sy Su, Wen-Chang Jiang, Mei-Li Wang, Sin-Jei Yu, and Chia-Pin Sung

Division of Optoelectronic Materials and Devices
Opto-Electronics & Systems Laboratories
Industrial Technology Research Institute
Chutung 310, Hsinchu, Taiwan, R. O. C.

ABSTRACT

In this work, we have made AlGaAs/GaAs gain-guided broad-area vertical-cavity surface-emitting lasers (VCSELs) in the 850-nm range. For higher power applications such as optical pumping and optical communications, broad-area VCSELs and VCSEL arrays are needed. The distributed Bragg reflectors (DBRs) of the VCSELs consist of $\text{Al}_{0.12}\text{Ga}_{0.88}\text{As}/\text{AlAs}$ quarter-wave stacks. The GRINSCH active region is consisted of an undoped three-quantum-well GaAs/ $\text{Al}_{0.3}\text{Ga}_{0.7}\text{As}$, two undoped $\text{Al}_{0.3}\text{Ga}_{0.7}\text{As}$ confinement layers, and two undoped linearly graded $\text{Al}_x\text{Ga}_{1-x}\text{As}$ layers. The current confinement of the VCSELs was made by proton implantation with an implantation energy of 280 KeV. The emitting window diameters are 30 to 50 μm . A very high cw optical power of 23.4 mW and a pulsed optical power of over 36 mW were measured for a 50- μm aperture device. These VCSELs are suitable for higher power applications. The VCSELs showed multiple transverse mode characteristics. The near-field characteristics and spectrum of the devices were measured and analyzed. The modulation characteristics of the VCSELs were also measured. A 3 dB bandwidth ($f_{3\text{dB}}$) of 5.6 GHz was measured for a 30- μm aperture device at 20 mA.

Keywords: vertical-cavity, surface-emitting lasers, broad-area VCSEL, spectrum, near-field

1. INTRODUCTION

Vertical-cavity surface-emitting lasers (VCSELs) have attracted a lot of attentions because of their applications in data communications, optical interconnects, printing, optical storage, CD-ROM (compact disc-read only memory), and DVD (digital video disc). [1]-[5] The emission wavelengths are 650 nm to 1.55 μm . [1]-[10] The development of blue/green edge-emitting semiconductor lasers has led to the development of blue/green VCSELs. Recently, oxide-confined VCSELs were vastly investigated because of their very low threshold current and capability of generating single-mode output. [6]-[8] The basic structure of a VCSEL consists an active region, sandwiched between heavily-doped p-type and n-type DBRs, and conducting electrodes. The thickness of the active region is the multiple of the emission wavelength. The p- and n-DBRs are the top and bottom mirrors of the laser cavity. Laser beam resonates between the p-type and n-type DBRs of the laser cavity. Single transverse-mode laser output can be obtained for VCSELs with their emitting aperture of less than 5 μm . The advantages of the VCSELs include circular beam, lower threshold current, lower beam divergence, lower temperature sensitivity, one-dimensional and two-dimensional arrays, and on-wafer testability. The processing and on-wafer testing techniques are somewhat similar to those of the light-emitting diodes (LEDs). Compared to the edge-emitting lasers, the optical power density of VCSELs is higher due to smaller volume of the active region. The cavity-length of a VCSEL is often less than 1 μm , which is much less than the cavity-length (several hundred μm) of an edge-emitting laser. Therefore, VCSELs emit laser beam with single longitudinal mode.

Moreover, for higher output power applications such as optical pumping, broad-area VCSELs [9], [10] and high-packing-density VCSEL arrays [10], [11] can be used. By increasing the area of the laser-emitting window of the VCSEL, higher laser output power can be achieved. The laser-emitting window can be circular, rectangular, or rhombus in shape. Here, we refer to broad-area VCSELs as lasers with the aperture diameter of greater than 20 μm . For optical fiber communication systems, higher power VCSELs can be used for longer distance transmission. It is therefore the motive of this work to study the DC and AC characteristics of the broad-area VCSELs for optical communications. The gain-guided,

circular, top-emitting broad-area AlGaAs/GaAs VCSELs are made with 30- to 50- μm aperture sizes. The pulsed and CW optical power-current characteristics were measured. A very high cw optical power of 23.4 mW and a pulsed optical power of over 36 mW were measured for a 50- μm aperture device. The emitting peak wavelength was about 844 nm. The emission characteristics of these VCSELs were measured and analyzed. The modulation characteristics of the broad-area VCSELs were measured as a function of operating current. A 3-dB bandwidth ($f_{3\text{dB}}$) of 5.6 GHz was measured at 20 mA for a 30- μm aperture device.

2. DEVICE FABRICATION

The epitaxial layers of the 850-nm AlGaAs/GaAs vertical-cavity surface-emitting lasers were grown in a MOCVD system on a (100) $\text{n}^+\text{-GaAs}$ substrate. The epitaxial structure is the following (from bottom to top): a $\text{n}^+\text{-GaAs}$ buffer, a n-DBR, an undoped AlGaAs/GaAs active region, a p-DBR, and a $\text{p}^+\text{-GaAs}$ contact layer. The GRINSCH (graded-index separate confinement) active region mainly consists of an undoped three-quantum-well $60\text{\AA}/80\text{\AA}$ GaAs/ $\text{Al}_{0.3}\text{Ga}_{0.7}\text{As}$, two undoped $\text{Al}_{0.3}\text{Ga}_{0.7}\text{As}$ confinement layers and two linearly graded undoped- $\text{Al}_x\text{Ga}_{1-x}\text{As}$ ($x = 0.6 \rightarrow 0.3$ and $x = 0.3 \rightarrow 0.6$) cladding layers grown on top and below the quantum wells. The total thickness of the active region was about 1λ . The n-DBR (Si-doped at $2 \times 10^{18} \text{ cm}^{-3}$) consists of 30.5 pairs of $\text{n}^+\text{-Al}_{0.12}\text{Ga}_{0.88}\text{As}/\text{n}^+\text{-AlAs}$ quarter-wave ($\lambda/4$) stacks. The p-DBR (C-doped at $3 \times 10^{18} \text{ cm}^{-3}$) consists of 20 pairs of $\text{p}^+\text{-Al}_{0.12}\text{Ga}_{0.88}\text{As}/\text{p}^+\text{-AlAs}$ quarter-wave stacks. Carbon doping was used for the p-DBR in order to obtain higher carrier concentration in the p-DBR layers. Both the n-type and p-type $\text{Al}_{0.12}\text{Ga}_{0.88}\text{As}/\text{AlAs}$ interfaces of the DBRs are linearly graded mainly to reduce the energy barriers of the hetero-interface so as to reduce the series resistance of DBR layers. The doping level in the interface grading layers was same as those in the $\text{Al}_{0.12}\text{Ga}_{0.88}\text{As}$ and AlAs layers. The series resistance is much higher for the p-DBR layers than for the n-DBR layers because the hole mobilities are much lower in the $\text{p}^+\text{-Al}_{0.12}\text{Ga}_{0.88}\text{As}$ and $\text{p}^+\text{-AlAs}$ layers than the electron mobilities in the $\text{n}^+\text{-Al}_{0.12}\text{Ga}_{0.88}\text{As}$ and $\text{n}^+\text{-AlAs}$ layers. Reflectance measurement showed that the absorption dip of the GaAs/ $\text{Al}_{0.3}\text{Ga}_{0.7}\text{As}$ quantum wells was about 840 to 850 nm.

The gain-guided top-emitting broad-area VCSEL fabrication processes are described as follows. Firstly, current confinement apertures were defined by using proton implantation. The implantation energy was 280 KeV, with a dosage of $8 \times 10^{14} \text{ cm}^{-2}$. A photoresist layer of 6 μm was used as an implantation mask for the current conducting area. The diameters of the current conducting region of the devices were 40- μm and 60- μm for the 30- μm and 50- μm devices, respectively. P-type ohmic contacts, which also defined the light-emitting window, were formed by evaporating Ti/Au, lift-off, and annealing. The aperture sizes of the laser-emitting windows were 30- and 50- μm . Pad metal of Ti/Au was evaporated to facilitate bonding. After forming the n-ohmic contacts at the backside of the wafer, the VCSEL wafer was diced into VCSEL chips. These chips were then packaged for further tests. The device structure of the broad-area VCSEL is shown in Fig. 1.

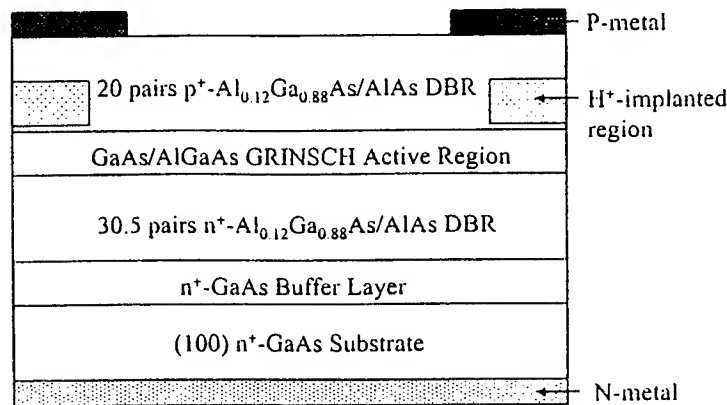


Fig. 1 Schematic of the 850-nm AlGaAs/GaAs broad-area VCSEL.

3. RESULTS AND DISCUSSION

The current-voltage (I-V) characteristics of the broad-area VCSELs were measured. The differential resistance, dV/dI , of the 50- μm aperture VCSELs were about $7\ \Omega$ at 35 mA, with a threshold voltage of 1.7 V. The differential resistance was about $11\ \Omega$ for the 30- μm aperture devices at 35 mA. The differential resistance is lower for the larger devices because of larger current conducting area. The CW and pulsed optical power versus operating current (L-I) characteristics of a AlGaAs/GaAs VCSEL with 50- μm aperture diameter is shown in Fig. 2. The pulse duty cycle of the pulsed L-I measurement was 0.1% so that there was no heating in the device. The pulsed and CW threshold currents were both 16 mA, which were converted to threshold current density of $566\ \text{A}/\text{cm}^2$. As the current increases beyond 40 mA, the pulsed optical power becomes higher than the CW optical power. This is due to the heating effect within the device at higher CW current levels. The series resistance of the device is mostly attributed to the series resistance of the p-DBR. A maximum CW optical power of 23.4 mW was measured at a current of 128 mA. This means that a thermal rollover occurs at very high current level of 128 mA, and the CW optical power starts to decrease with increasing current. At very high current levels, joule heating effect become more evident because more injecting electrical power was converted into heat. As the temperature of the device started to increase, the optical power started to decrease. A pulsed optical power of 28.5 mW was measured for this device at 150 mA. A maximum pulsed optical power of 30.1 mW was measured at 150 mA for the 50- μm aperture devices. The pulsed and CW L-I characteristics of a 30- μm aperture VCSEL is shown in Fig. 3. The pulsed and CW threshold current of the 30- μm aperture device were both 7 mA. The threshold current density is $990\ \text{A}/\text{cm}^2$ for this device. The threshold current is lower for smaller aperture device, while the threshold current density is higher for larger device. A maximum CW optical power of 17.9 mW was measured for a 30- μm aperture device, with a maximum pulsed optical power of 24.6 mW. Thermal roll-over occurred at the maximum optical power and then the optical power decreased with increasing current. There are no COD (catastrophic optical damage) for these 30- and 50- μm devices. These results show that the broad-area VCSELs in this work are suitable for high power applications. The maximum optical power achieved for the broad-area VCSELs are much higher than those of the smaller aperture devices. This is because that the thermal roll-over occur at much smaller current levels for smaller devices, the optical power does not increase monotonically with operating current.

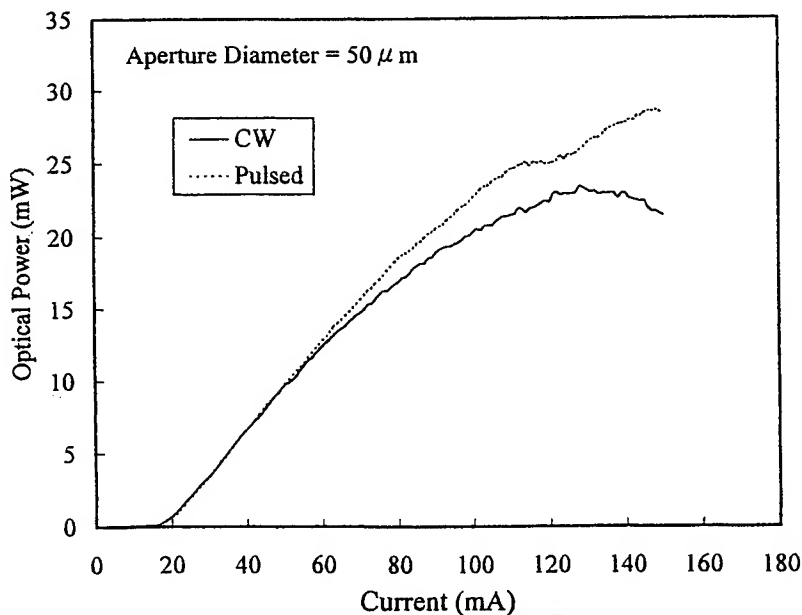


Fig. 2 Pulsed and CW L-I characteristics of a 50- μm aperture broad-area VCSEL.

The temperature-dependent L-I curves of the 30- and 50- μm devices are shown in Fig. 4 and Fig. 5, respectively. The optical power of the VCSELs decreases with increasing temperature. The threshold current increases with increasing temperature, at the measurement temperature range. Broad-area VCSEL chips need to be mounted on heat sinks with higher thermal conductivity for heat conduction in order to achieve higher CW optical power up to several hundred milli-Watt. [10]

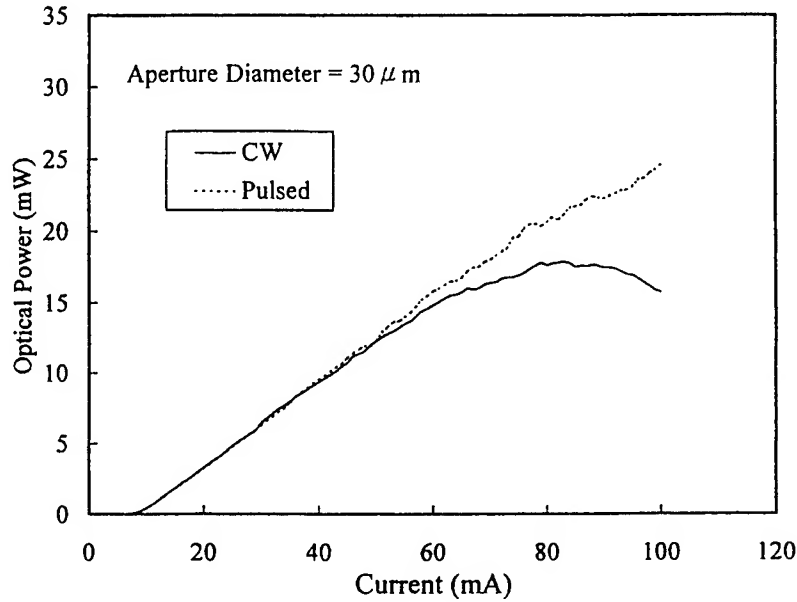


Fig. 3 Pulsed and CW L-I characteristics of a 30- μm aperture broad-area VCSEL.

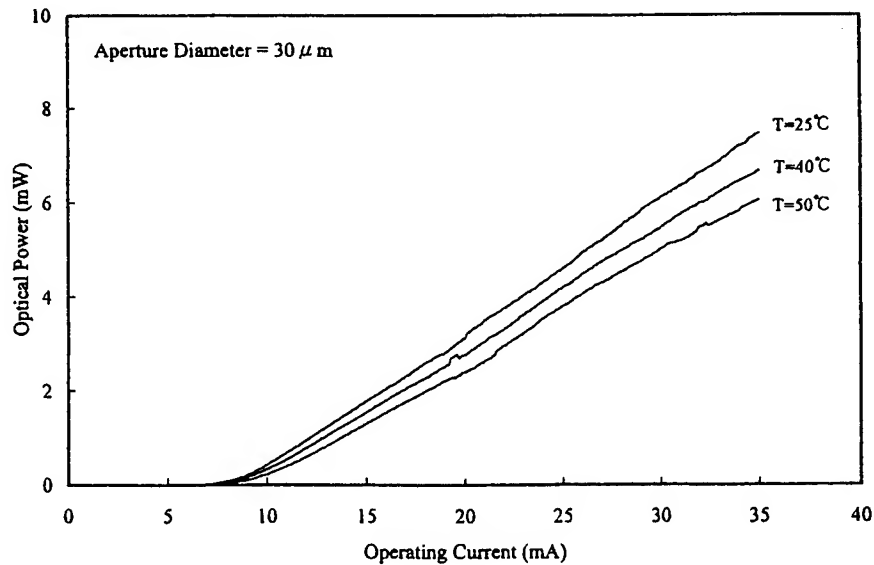


Fig. 4 Temperature-dependent CW L-I characteristics of a 30- μm aperture broad-area VCSEL.

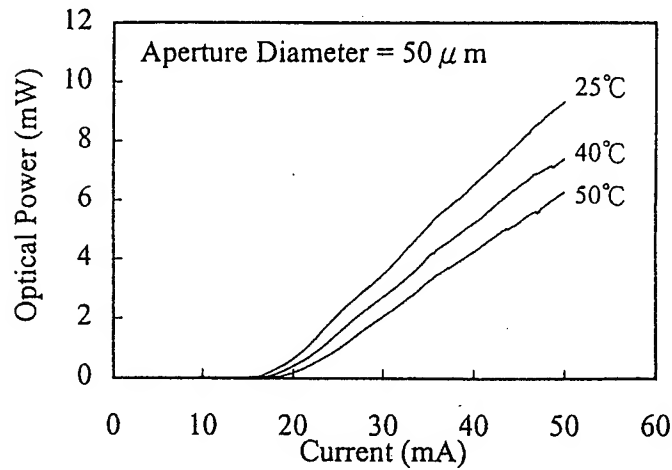


Fig. 5 Temperature-dependent CW L-I characteristics of a 50- μm aperture broad-area VCSEL.

The CW spectrum of the 30- μm aperture device is shown in Fig. 6. Multiple transverse mode characteristics were obtained. The peak wavelength is 844.4 nm, with an operating current of 10 mA. The mode spacing between neighboring emission peaks is about 6 nm. The width ($\Delta\lambda$) of the main emission peak is about 0.6 nm. The peak wavelength versus operating current plot of a 30- μm aperture device is shown in Fig. 8, measured from 25 to 50°C. The peak wavelength temperature coefficient is low for this 30- μm aperture device, $\sim 0.074 \text{ nm}/^\circ\text{C}$, at an operating current of 10 mA. The peak wavelength current coefficient is about $0.043 \text{ nm}/\text{mA}$ at 25°C. The spectrum of a 50- μm aperture device is shown in Fig. 7. The peak wavelength is 844.5 nm, measured with a current of 35 mA.

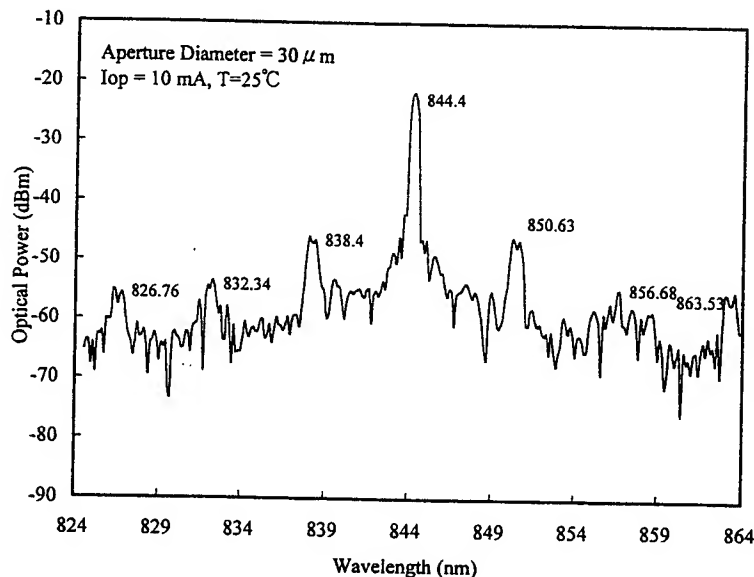


Fig. 6 Spectrum of a 30- μm aperture broad-area VCSEL at 10 mA.

The near-field patterns of the broad-area VCSELs were also measured, as a function of operating current. Fig. 9(a) and (b) show the near-field patterns of the 30- μm device at 10 and 20 mA, respectively. The CW operating current is 20 mA. The output beam, which is consisted of higher order transverse modes, is nearly circular at 20 mA. As the current were gradually increased, higher order modes appeared. At the current of 35 mA, the superimposed lasing modes distributed over the entire laser-emitting aperture. Fig. 10(a) and (b) show the near-field patterns of the 50- μm device at 35 mA and 100 mA, respectively. The output beam of the 50- μm device has lower intensity at the central region at 35 mA, which is similar to the near-field patterns of a previous report on the 980-nm broad-area VCSELs. [10] At 100 mA, the near-field pattern shows a much higher intensity at the periphery of the light-emitting aperture. The main reason for this laser output pattern is because of higher resistance for current flow in the direction parallel to the surface of the light-emitting window of the VCSEL. The current density is higher at the periphery than the current density in the central region, so that the laser beam intensity is higher in the periphery region.

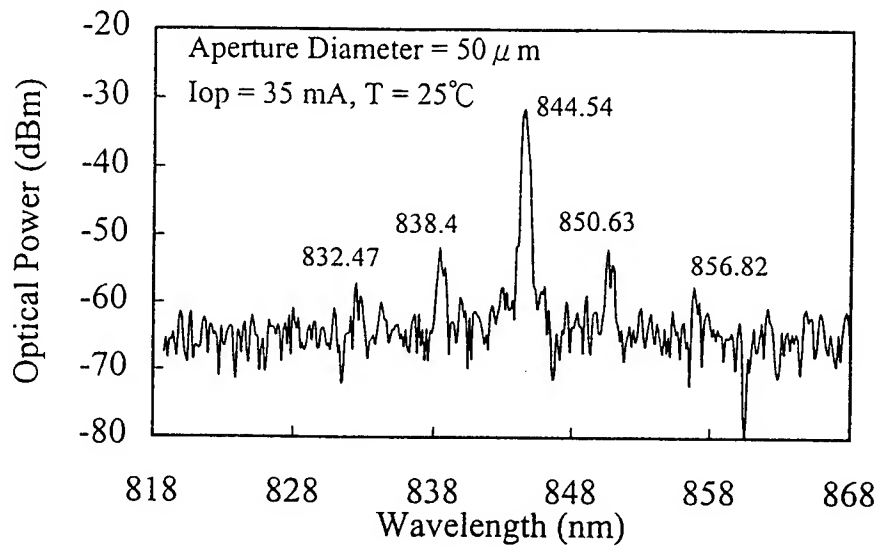


Fig. 7 Spectrum of a 50- μm aperture broad-area VCSEL at 35 mA.

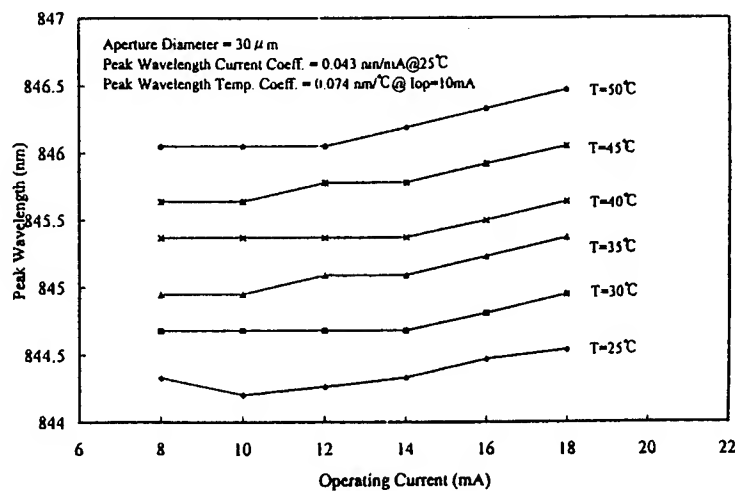


Fig. 8 Peak wavelength vs. temperature plot of a 30- μm aperture broad-area VCSEL.

The modulation characteristics of these broad-area VCSELs were also measured, as a function of operating current. Fig. 11 shows the modulation frequency response of a 30- μm aperture VCSEL. The 3-dB bandwidth ($f_{3\text{dB}}$) is 5.6 GHz at 20 mA. The $f_{3\text{dB}}$ is 1.7 GHz and 4.7 GHz at 10 mA and 15 mA, respectively. The 3-dB bandwidth increases with increasing current.

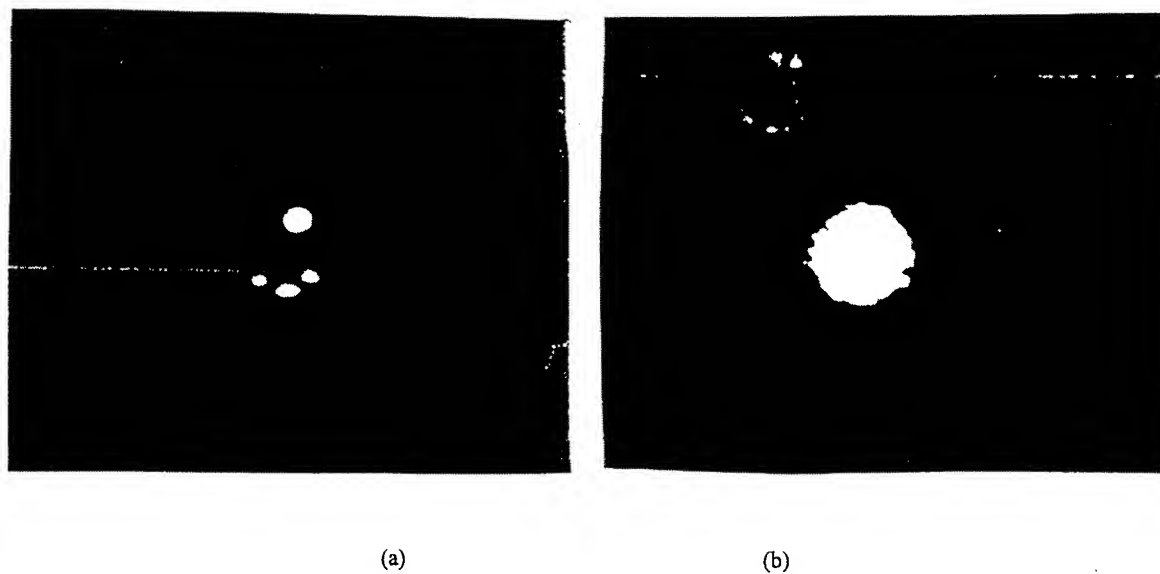


Fig. 9 Near-field pattern of the 30- μm aperture broad-area VCSEL at (a) 10 and (b) 20 mA.

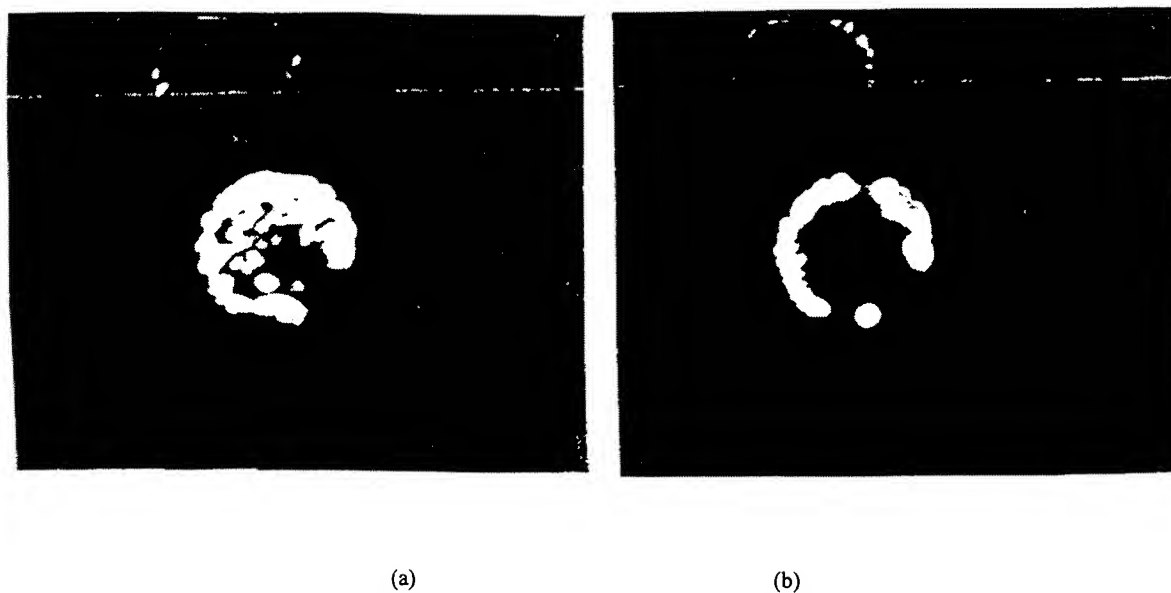


Fig. 10 Near-field pattern of the 50- μm aperture broad-area VCSEL at (a) 35 and (b) 100 mA.

The modulation frequency response of a 50- μm aperture device is shown in Fig. 12. At the operating current of 10 mA, the VCSEL is not lasing, the $f_{3\text{dB}}$ is very low. The threshold current of this 50- μm aperture device is about 14 mA. The $f_{3\text{dB}}$ are 3.6 GHz and 4.7 GHz at 15 mA and 20 mA, respectively. These broad-area VCSELs are suitable for high-speed applications.

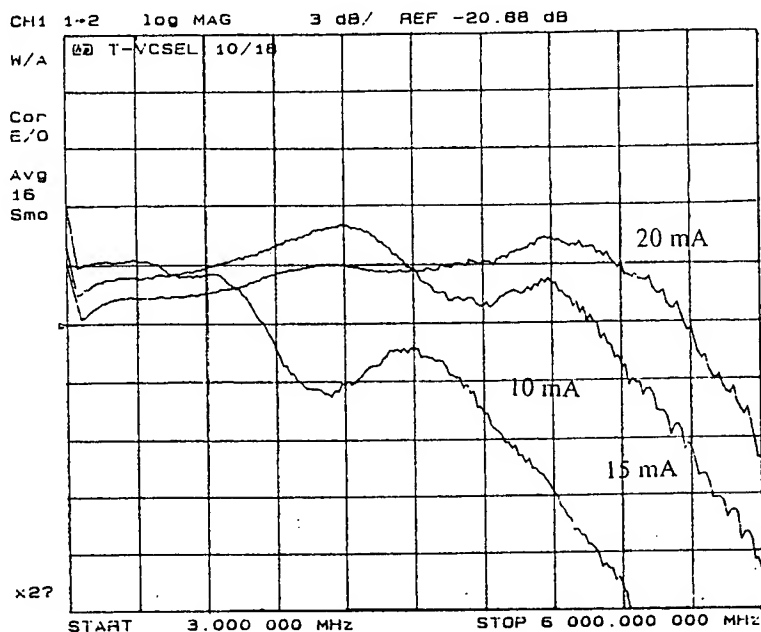


Fig. 11 Modulation frequency response of a 30- μm aperture broad-area VCSEL.

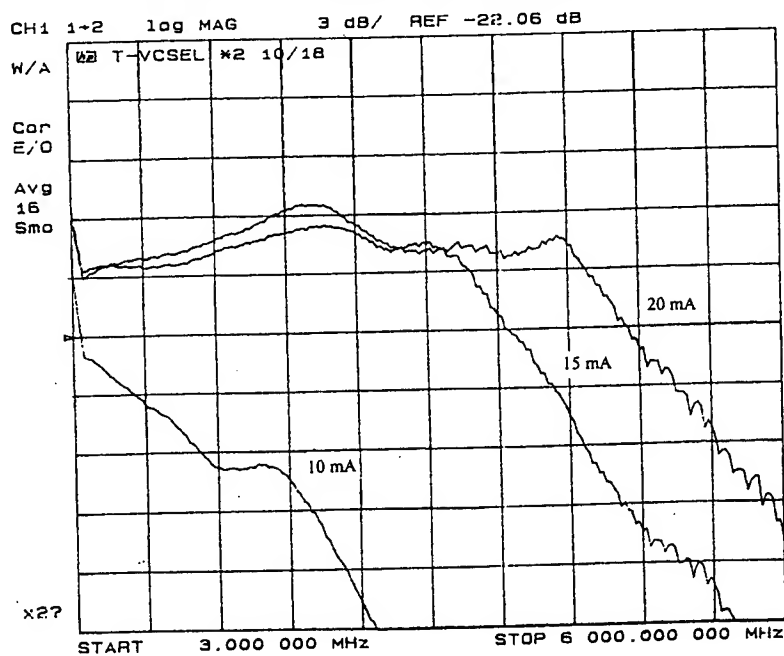


Fig. 12 Modulation frequency response of a 50- μm aperture broad-area VCSEL.

4. CONCLUSION

In conclusion, we have made a systematic study on the DC and AC characteristics broad-area AlGaAs/GaAs VCSELs in the 850-nm range. The L-I characteristics of the VCSELs show a very high CW output power of 23.4 mW for a 50- μ m device. The near-field patterns of the devices were also measured and analyzed. A 3-dB bandwidth of 5.6 GHz was measured at 20 mA for a 30- μ m VCSEL.

ACKNOWLEDGEMENT

The authors would like to thank Drs. C. A. Chang and J. Chi for useful discussions.

REFERENCES

1. F. Koyama and K. Iga, in Photonics-Taiwan, Taipei, "Surface-emitting lasers for parallel data transmission and data storage," Proc. SPIE-3419, pp. 178-186, 1998.
2. H. K. Shin, I. Kim, E. J. Kim, J. H. Kim, E. K. Lee, M. K. Lee, J. K. Mun, C. S. Park, and Y. S. Yi, Jpn. J. Appl. Phys. vol. 35, pp. 506, 1996.
3. G. Giaretta, M. Y. Li, G. S. Li, W. Yuen, and C. J. Chang-Hasnain, "A novel 4 \times 8 single-mode independently addressable oxide isolated VCSEL array," IEEE Photon. Technol. Lett. vol. No. pp. ,
4. S. Uchiyama, N. Yokouchi, and T. Ninomiya, "Continuous-wave operation up to 36°C of 1.3 μ m GaInAsP-InP vertical-cavity surface-emitting lasers," IEEE Photon. Technol. Lett. vol. 9, no. 2, pp. 141-143, 1997.
5. W. Yuen, G. S. Li, C. Chang-Hasnain, "Multiple-wavelength vertical-cavity surface-emitting laser arrays with a record wavelength span", IEEE Photonics Technol. Lett., vol. 8, no. 1, pp. 4-6, 1996.
6. K. D. Choquette, R. P. Schneider, Jr., K. L. Lear, and K. M. Geib, "Low threshold voltage vertical-cavity surface-emitting lasers fabricated by selective oxidation," Electron. Lett. vol. 30, no. 24, pp. 2043-2044, 1994.
7. M. H. MacDougall, P. D. Dapkus, V. Pudikov, H. Zhao, and G. M. Yang, "Ultralow threshold current vertical-cavity surface-emitting lasers with AlAs oxide-GaAs distributed Bragg reflectors," IEEE Photon. Technol. Lett. vol. 7, no. 3, pp. 229-231, 1995.
8. B. Weigl, M. Grabherr, R. Michalzik, G. Reiner, and K. J. Ebeling, "High power single-mode selectively oxidized Vertical-cavity surface-emitting lasers," IEEE Photon. Technol. Lett. vol. 8, no. 8, pp. 971-973, 1996.
9. M. Grabherr, B. Weigl, G. Reiner, R. Michalzik, M. Miller, and K. J. Ebeling, "High power top-surface emitting oxide confined vertical-cavity laser diodes," Electron. Lett. vol. 32, pp. 1723-1724, 1996.
10. R. Michalzik, M. Grabherr, R. Jager, M. Miller, and K. J. Ebeling, "Progress in high-power VCSELs and arrays," Photonics-Taiwan, Taipei, Proc. SPIE-3419, pp. 187-195, 1998.
11. R. A. Morgan, K. Kojima, T. Mullally, G. D. Guth, M. W. Focht, R. E. Leibenguth, and M. Asom, "High-power coherently coupled 8 \times 8 vertical cavity surface emitting laser array", Appl. Phys. Lett. vol. , pp. 1160-1162, 1992.

FABRICATION OF A MICROMACHINED OPTICAL MODULATOR USING THE CMOS PROCESS

Hunglin Chen, Kaihsiang Yen, Huiwen Huang, Jinhung Chio

Microsystems Laboratory, Industrial Technology Research Institute
Bldg. 52, 195, sec. 4, Chung Hsing Rd., Chutung, Hsinchu, Taiwan 310, R. O. C.

Chingliang Dai

Department of Mechanical Engineering, Oriental Institute of Technology
Pan Chiau, Taipei, 220, Taiwan, R. O. C.

Chienliu Chang, Peizen Chang

Dept. of Applied Mechanics, National Taiwan University,
Taipei, Taiwan 310, R. O. C.

ABSTRACT

This investigation presents a micromachined optical modulator with electrostatic actuation fabricated by the conventional CMOS process. The modulator is operated by interaction of fixed part, stationary gratings, and movable part, sliding gratings. The period of the gratings varies with the slide of the movable part, thereby allowing different diffraction patterns of the reflected light. In addition, 100% modulation in the first order can serve as an optical switch.

All procedures following the CMOS process merely require a simple post-process. With maskless etching, the micromachined optical modulator is developed to obtain a high-aspect-ratio structure and high efficiency of modulation. Compare to the commercially available acoustic ones, the micromachined optical modulator proposed herein is smaller and weighs less.

Keywords: micromachine, modulator, gratings, CMOS

1. INTRODUCTION

Advances in semiconductor fabrication technology have inspired a new generation of Micro-Electro-Mechanical Systems (MEMS)^{1,2} that is designed using microfabrication equipment and processing methods. Optical devices are one among the most important applications of MEMS because miniaturization of the system can be useful for small light spots, quick response, low power consumption, and specific work that can't be done by the traditional optical elements. Correspondingly, optical switches and modulators have received considerable attention.

A modulator, settled between the source and observed point, treats the physical variable. In optical system, the variable may be amplitude, frequency, phase, polarization, or intensity. Therefore, the optical modulator is useful for industrial application. For instance, the acoustic optical modulator could be used as optical switch, scanner, filter, or isolator³. Correspondingly, micromachined optical modulators have received considerable attention⁴. The light is modulated by the mechanical deformation involving into three types, vertical⁵, horizontal⁶, and rotatory modulators⁷⁻⁹. The modulator we proposed herein belongs to the horizontal type that operates in plane. Comparing to the last version of micromachined optical modulator reported in *Transducers '99*, the stationary part in the new design strongly fixes to the anchor, and the precision etching control is unnecessary. We present the configuration of the modulator and simulation of the optical modulation are also described.

2. DEVICE DESIGN

2.1 OPERATIONAL PRINCIPLES

A periodic-frame shape designed to achieve the different transmission or reflective light is called diffraction grating. Various patterns can be observed according to the wavelength, incident angle, depth, or the period of the gratings. The concept can be translated via the grating equation (1), which is developed by the path difference for the optical waves. For the light incident angle, θ_i , and related diffractive angle, θ_m , the relation can be expressed as

$$\sin \theta_m - \sin \theta_i = \frac{m\lambda}{a} \quad m = 0, \pm 1, \pm 2, \dots \quad (1)$$

where m is the order number, λ is the wavelength of the incident light, and a is the period of the gratings.

The intensity between the different orders is also relative to equation (1). Therefore, the micromachined optical modulator proposed herein simply alters the period of the gratings to modulate the incident light. According to Fig. 1, the condition of the gratings dramatically varies before and after movement. Consequently, the optical intensity redistributes to each order with the change of the period of the gratings. Furthermore, in some particular orders, light would fully turn on and off with the actuation and, thereby, it can also serve as an optical switch.

2.2 REQUIREMENTS AND CHARACTERISTICS

The micromachined optical modulator must satisfy several performance and structural requirements. First, it should modulate the optical intensity efficiently, which corresponds to the shape of the gratings. Correspondingly, computer software is used to assess the performances of light and, then, the design is modified to obtain a higher efficiency.

The second requirement is the stiffness. The structure must have a high z-directional stiffness to avert unwanted vibration and low in-plane stiffness, thereby producing a lower driving voltage. Thus, to satisfy this requirement, this work adopts a laminated high-aspect-ratio microstructure consisting of metal and oxide layers in the CMOS process^{10, 11}.

Another requirement is easy fabrication. A significant amount of time can be saved in developing related technologies since the CMOS process is already a mature technology and foundry services already exist. Besides, the post-process proposed herein merely needs maskless etching to release the structure, thereby making it relatively easy to actualize the full device.

Still yet another requirement is integration. Since the design corresponds with the CMOS process, micromachined devices can be feasibly integrated with operating circuits in monolithic chips since the proposed design corresponds to the CMOS process. This feature will not only reduce the noise between devices and circuits, but will also easily constructs the final package of chips without the need for wire bonding.

The final requirement is low cost. As mentioned earlier, a relatively short development time to effectively respond to fluctuating market demands, a monolithic chip to achieve a high performance, batch processing, and a lower manufacturing cost make mass production possible.

2.3 DIFFRACTION EFFICIENCY

The micromachined optical modulator, which is involved in sliding and stationary gratings, changes the period of the gratings with electrostatic actuation to modulate the incident light. Next, the different diffraction pattern of the reflected light is observed for the same incident light. The behavior simulated using the computer software, GSOLVER¹², which is derived from the rigorous coupled wave algorithm (RCWA). As shown in Fig. 2, the model before and after movement is built in GSOLVER on scale. Various input parameters, such as angle of incidence, wavelength, and the period, allow us to derive the corresponding solutions that contain diffraction efficiency, field magnitude and phase. Herein, the diffraction efficiency is calculated as follows.

Figures 3 illustrate the diffraction efficiency for the micromachined optical modulator. At the primary condition, the reflected light distributes to all the orders initially. After the movable part slides into the side of the fixed part, the highest intensity shifts from the 2nd order to the 0 order. Notably, the modulation in the 2nd order is obvious. This observation

suggests that 100 % modulation efficiency occurs at the odd orders, particularly at the 1st order. Therefore, the micromachined optical modulator can serve as an optical switch in a direction corresponding to the odd orders.

3. FABRICATION

3.1 POST-PROCESS

The design proposed herein adheres to the 0.6 μm SPTM (Single Poly and Triple Metals) CMOS process. According to the foundry service and design rules, the micromachined optical modulator is developed. All procedures of the post-process just need maskless dry etching and, thereby, the sticking problem is avoidable.

As shown in Fig. 4, following the CMOS foundry service, the all passivation nitride is already removed and the metal layer is exposed. Although this violates the design rules that regulate the top metal layer to exist when passivation nitride is absent, the process still works by the point of microfabrication and, in doing so, we could save etching time in the follow process. Two main steps are involved in the post-process for releasing the structure. First, all silicon dioxide is etched by anisotropic CF_4/O_2 RIE (reactive ion etching), and the structure is defined by the metal layer since it is a good etching mask for F-based plasma etch. For releasing the structure, silicon substrate is then anisotropically etched by SF_6 RIE. Finally, with electrostatic actuation, the suspended parts slides to the side of the fixed parts to modulate the light. In Fig. 5, a close-up view of the fabricated structure is shown.

3.2 DISCUSSIONS AND RESULTS

In the structure of the micromachined optical modulator, the stiffness proportional to the square of the aspect ratio is enhanced. A 5:1 aspect ratio laminated structure, which theoretically enables a 25:1 flexure stiffness ratio, is shown in Fig. 5(b). Levitation phenomenon caused by less z-directional stiffness could be eliminated by using the high-aspect-ratio laminated structure to construct the body.

The fixed gratings connect to big anchors and, in contrast, the free gratings connect small mass with etching holes. The design ensures not only that the movable part is fully released, but also the fixed part still is attached to the substrate. The bending effect in the micromachined optical modulator would propose a serious problem to the optical field, which requests the accuracy in the level of less than a half wavelength. Therefore, the levitation phenomena and stiffness may limit the working range. In addition, metal is deposited at a high temperature, implying the occurrence of residual stress at room temperature. After the sacrificial layer is removed, the structure bends vertically to the substrate. The active area of $500\text{ }\mu\text{m} \times 500\text{ }\mu\text{m}$ and $100\text{ }\mu\text{m} \times 100\text{ }\mu\text{m}$ modulators are tested, with the former and later having maximum levitation at about 5 μm and 1 μm , respectively. This phenomenon causes an additional voltage demand for the displacement in the vertical direction (z direction).

Next to the post-CMOS process, we apply the voltage to actuate the fully released structure. A simple actuator merely consisted of proof mass, supported beams and comb is tested prior to the proposed micromachined optical modulator. The actuator starts to move with 8 volts, and with 20 volts it would move 5 μm . Therefore, using the comb structure for the actuator is successful in our experiment. Furthermore, the same actuation mechanism is adopted in the micromachined optical modulator. The pitch of the gratings would vary with actuation.

4. CONCLUSIONS

This work has proposed a micromachined optical modulator with small volume, quick response, and full compatible with the CMOS process. The function of modulation with and without actuation is also simulated. Maskless dry etching completes all of the procedures in the post-process, and only a low voltage of 20 is necessary to drive the released structure. For getting high stiffness in the direction vertical to the substrate, a high-aspect-ratio microstructure is developed, and the beam widths can be as small as the minimum allowable metallization linewidth in the given CMOS foundry service.

ACKNOWLEDGEMENTS

This work is accomplished with much needed support and the authors wish to thank the following people: Jennyi Chen, Chiyuan Lee, Hunghsuan Lin, Fuyuan Xiao, Tsungwei Huang, Shihchen Chang, Chunyuan Chi of the Institute of Applied Mechanics, Nation Taiwan University, for their valuable advise and assistance in experiment.

REFERENCE

1. J., Bryzek, "Impact of MEMS Technology on Socility ," *Sensors and Actuators A* 56, pp. 1-9, 1996.
2. H. K., Wen, "The Future of Sensor and Actuator Systems ," *Sensors and Actuators A* 56, pp. 193-197, 1996.
3. B. E. A., Saleh, M. C., Teich, Fundament of Photonics, *John Wiley & Sons, Inc.*, pp815-825, 1991.
4. R. K., Bättig, O., Anthamatten, B., Valk, "A Reflective Modulator Based on Silicon Micromechanics," *Optical and Hybrid Access Networks, IEE Colloquium*, pp. 10/1-10/4, 1996.
5. F. S. A., Sandejas, R. B., Apte, W.C., Banyai, D. M., Bloom, "Surface Microfabrication of Deformable Grating Light Valves for High Resolution Displays," *The 7th International Conference on Solid-State Sensors and Actuators (Transducer '93)*, pp. 6-7, 1993.
6. D. E., Sene, J. W., Grantham, V. M., Bright, and J. H., Comtois, "Development and Characterization of Micro-Mechanical Gratings for Optical Modulation," *IEEE Transaction on Electron Devices*, Vol. ED-68, pp. 222-227, 1996.
7. D. A., Winick, W. M., Teague, P. D., Franzon, "A Micro-Machined Approach to Optical Interconnect," *IEEE*, pp. 780-785, 1995.
8. D. M., Burns, V. M., Bright, "Micromachined Thermally Based CMOS Microsensors," *Proceeding of the IEEE MEMS*, pp. 55-60, 1997.
9. J., Bryzek, "Development of Microelectromechanical Variable Blaze Gratings ," *Sensors and Actuators A* 64, pp. 7-15, 1998.
10. G. K., Fedder, S., Santhanam, M. L., Reed, S. C., Eagle, D. F.,Guillou, M. S. C., Lu, L. R.,Carley," Laminated High-Aspect-Ratio Microstructures in a Conventional CMOS Process," *J. MEMS*, pp 13-18, 1996.
11. G. K., Fedder, S., Santhanam, M. L., Reed, S. C., Eagle, D. F., Guillou, M.S.-C., Lu, L. R., Carley, "Laminated High-aspect-ratio Microstructures in a Conventional CMOS Process," *Sensors and Actuators A* 57, pp 103-110, 1996.
12. <http://www.gsolver.com/>

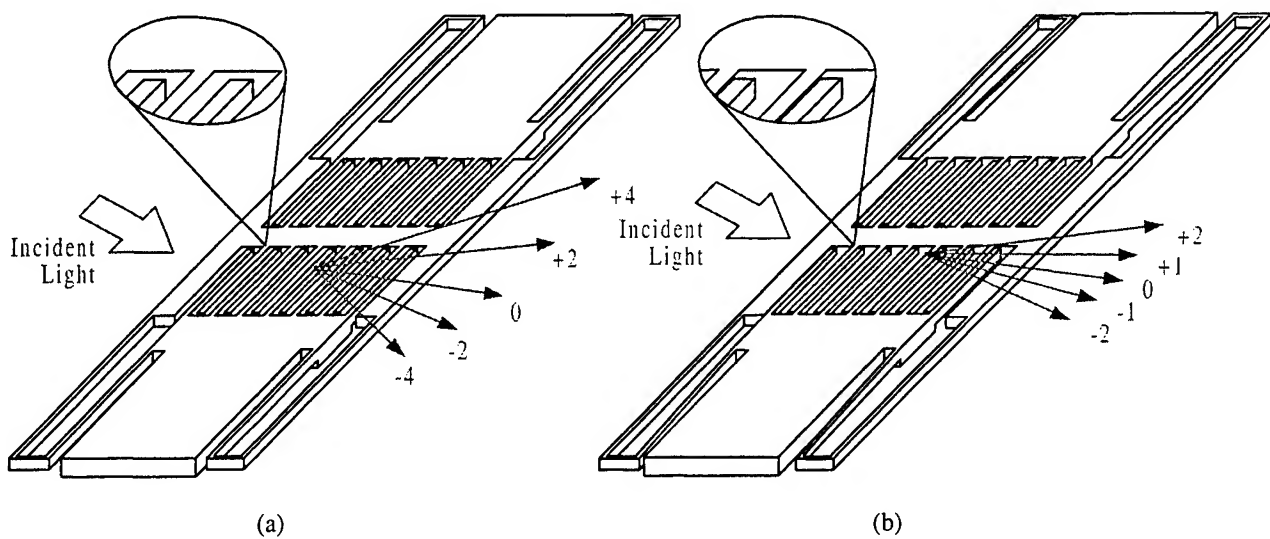


Figure 1 Micromachined optical modulator (a)without and (b)with actuation. The intensity of reflected light redistributes to different order with mechanical driving.

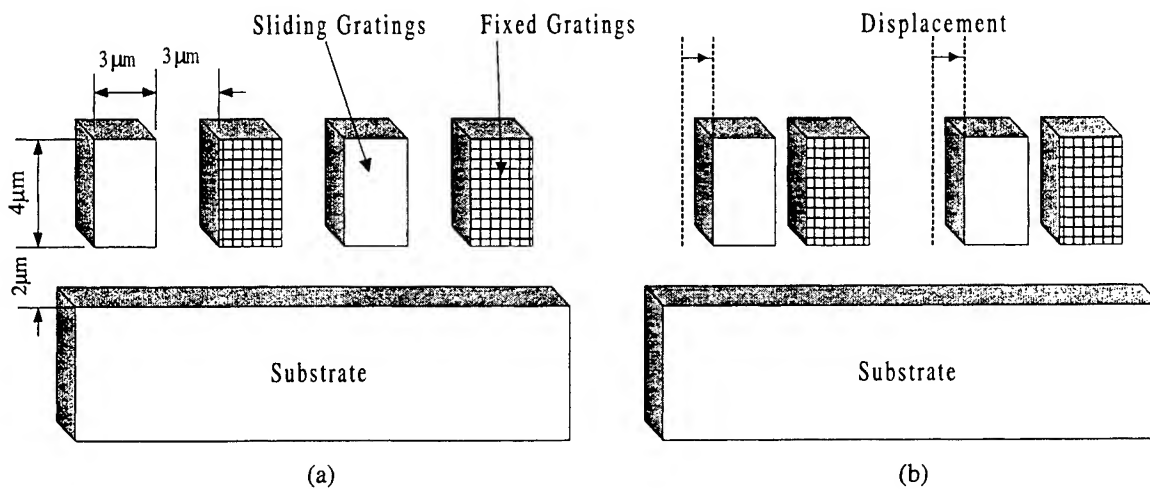


Figure 2 The model of the gratings (a)the initial position of each gratings (b)displacement for the movable part

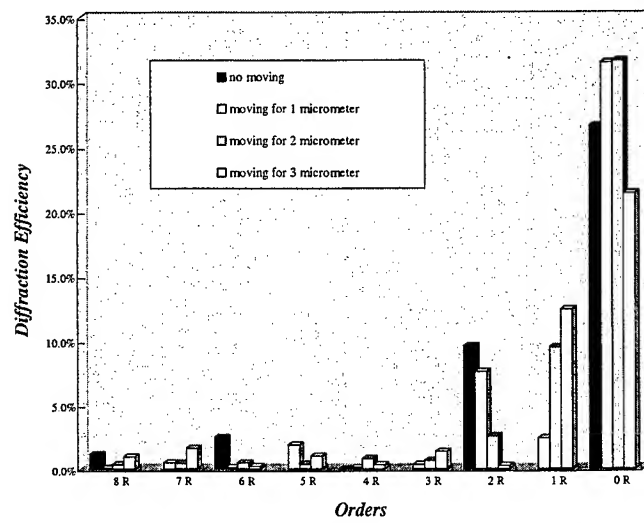


Figure 3 The mode graph of diffraction efficiency with different orders

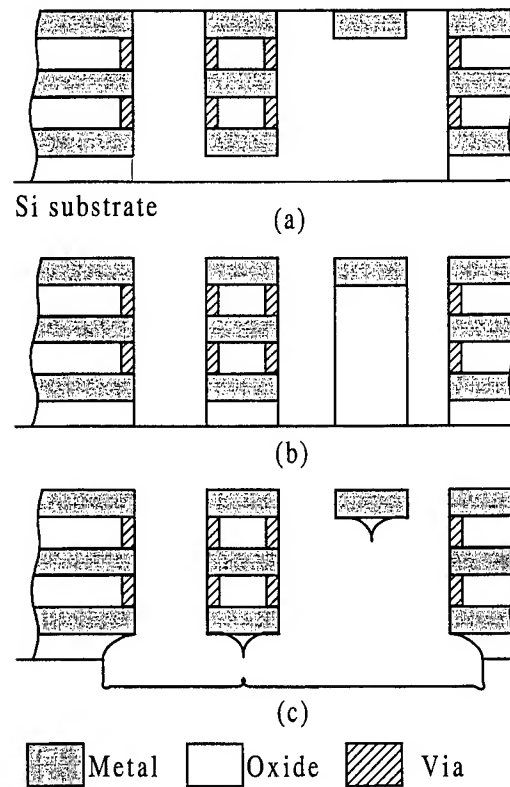
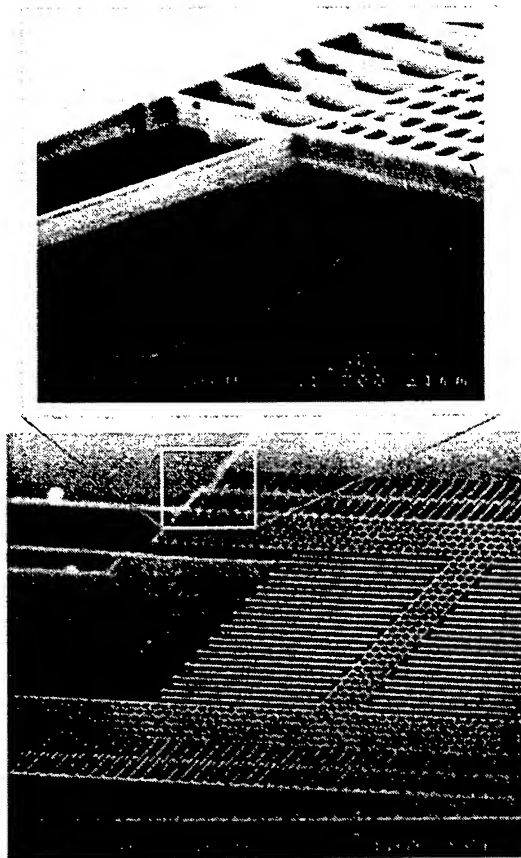
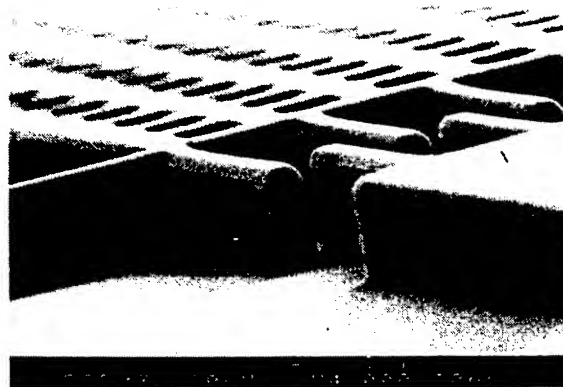


Figure 4 Fabrication sequence. (a) after the CMOS service, (b) anisotropic oxide etching, (c) isotropic silicon etching.



(a)



(b)

Figure 5 Scanning electron micrograph (a) the micromachined optical modulator (b) laminated high-aspect-ratio structure

FABRICATION OF DIFFRACTIVE OPTICAL ELEMENTS USING THE CMOS PROCESS

Hunglin Chen, Huiwen Huang, Kaihsiang Yen, Jinhung Chio

Microsystems Laboratory, Industrial Technology Research Institute
Bldg. 52, 195, sec. 4, Chung Hsing Rd., Chutung, Hsinchu, Taiwan 310, R. O. C.

Chingliang Dai

Department of Mechanical Engineering, Oriental Institute of Technology
Pan Chiau, Taipei, 220, Taiwan, R. O. C.

Chienliu Chang, Peizen Chang

Dept. of Applied Mechanics, National Taiwan University,
Taipei, Taiwan 106, R. O. C.

ABSTRACT

This investigation presents a novel type of DOEs fabricated by the conventional CMOS process. A simple post-CMOS process is applied to form the relief pattern, which can be used directly for its optical properties or serve as a mold for the subsequent replication. By using the CMOS process, in addition to reducing the depth, alignment, dimension, and shape errors of the pattern, the scale is minimized by the advancing microfabrication as well.

The performance of arbitrary DOEs can be directly related to the diffraction efficiency of the gratings. Therefore, in this investigation, the shape of the multi-level gratings is designed and the diffraction efficiency is calculated by the rigorous vector coupled-wave analysis. The largest constraint of the CMOS process for the multilevel gratings is that the depth of each layer is different and unchangeable. However, a suitable length for each level can be determined and, in doing so, the diffraction efficiency can reach 81%.

Keywords: grating, CMOS, DOEs, diffraction efficiency

1. INTRODUCTION

The rapid advances of diffractive optics technology have resulted in high performance and compact optical system. DOEs (Diffractive Optical Elements) can perceptibly minimize the optical system and satisfy some particular demands compared to the traditional optical elements. Hybrid lenses, thin lenses, wavefront correctors, wavefront generators, beam samplers, and lens arrays can be improved by DOEs¹. Many researches have been performed involved into the three categories, design², pattern generation³, and pattern replication⁴⁻⁷. First, the shape of the pattern should be designed to attain high diffractive efficiency. The pattern is then generated by various kinds of fabricative methods to satisfy the requirements. Finally, the replication technique is commonly used for low cost and high volume industrial production⁸ processes.

The design of DOEs must correspond to the theoretical constraints to determine the shape. The scalar theorem is usually used to predict the diffraction efficiency, however, it just provides an approximative solution that is overly optimistic. In contrast, the rigorous electromagnetic theorem is more precise but complicated. Therefore, the extended scalar theorem adds a degree of intuition in understanding how the solutions various, and the exact solutions are calculated by the commercial computer software that based on the rigorous electromagnetic theorem.

Table 1 Various fabrication methods of DOEs

Fabricative methods	Advantages	Process
Gray level mask	Continuous profile & Only one mask is need	Photolithography & dry etching
Half-tone mask	Only one mask is need	Photolithography
Bulk micromachining	Form a special blazed angle	Wet etching
Electron beam writing	Fine feature	Electron beam lithography
Laser beam writing	Fine feature Cheaper equipment	Laser beam lithography
LIGA	High numerical aperture	Thermal treatment

According to the design, the relief pattern can be carried out by various approaches, including gray level mask⁹, half-tone mask¹⁰, bulk micromachining¹¹, electron beam writing¹²⁻¹⁵, laser beam writing¹⁰, and LIGA¹⁶ process. The advantages and process are summarized in Table 1.

Until now, the technology for the replication of DOEs achieves high resolution and large area futures. Nanometer sized microstructures over areas of many centimeter square can be made by casting, embossing, and moulding¹⁷. In addition, the compact disks are also fabricated in this way. In the point of mass production, replicating DOEs is the most economical way to produce.

The novel type of DOEs we proposed herein adapted to the conventional CMOS process, and the scale is minimized following the microfabrication. A simple post-CMOS process with plasma etching is just needed to transfer the accurate relief pattern. The relief pattern can be used directly for its optical properties or served as a mold for the subsequent replication. Configuration of the component and the diffractive efficiency are also described.

2. DEVICE DESIGN

2.1 DIFFRACTION EFFICIENCY

The diffraction efficiency that can reasonably be expected is an important parameter for DOEs. Whether the DOEs will work for particular applications is ultimately determined by the obtainable diffraction efficiency. Moreover, the diffraction efficiency of arbitrary DOEs can be directly related to the diffraction efficiency of the gratings.

Assume that light can be treated as a scalar rather than vector field, electric and magnetic field components are uncoupled. In other words, the size of the diffracting components must be large compared to the incident wavelength, and the diffracted field must be observed far from the diffracting structure. Then the scalar theory is used to predict the diffraction efficiency. The first-order diffraction efficiency η of an optimized N-level element can be expressed as³

$$\eta = \left[\frac{\sin(\pi / N)}{\pi / N} \right]^2 \quad (1)$$

The relation between the diffraction efficiency and phase levels is solved, but the result is higher than the exact solution due to the assumptions differ from the practical condition to a degree.

Owing to minimizing of the optical system is great benefit for applications, we try to reduce a thick lens to a thin lens as shown in Fig. 1. However, the rigorous continuous profile is difficulty to make. According to (1), Fig. 1(f) is plot and shows that the diffraction efficiency is already 81 % for the four phase levels of gratings. Since the multilevel gratings

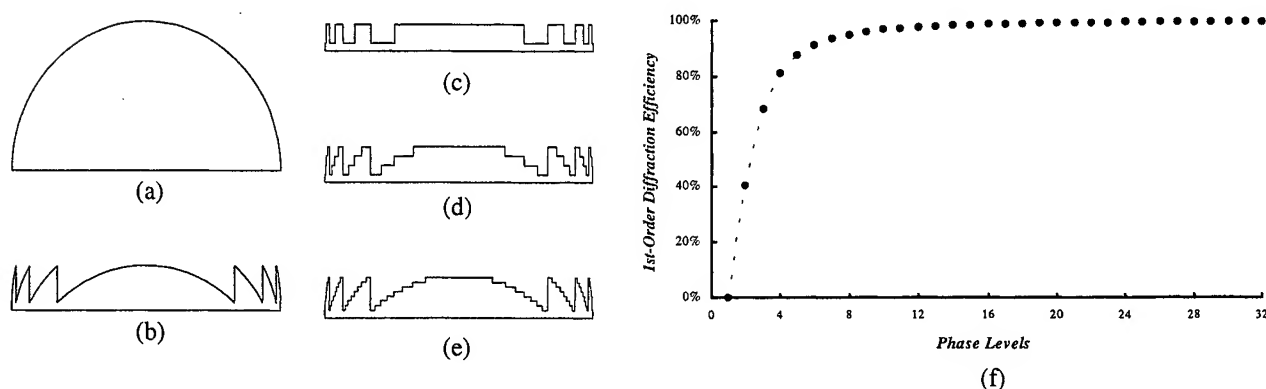


Figure 1 A thick lens reducing to a thin lens (a)thick lens (b)thin lens (c)2-phase levels (d) 4-phase levels (e) 8-phase levels (f)1st-order diffraction efficiency versus Phase levels calculated by scalar theory

instead of the rigorous continuous profile still can get high diffraction efficiency, we design four and eight phase levels gratings in this propose.

2.2 SIMULATION

In addition to fabricate the multilevel gratings by the CMOS process, the suitable size is designed to get high diffraction efficiency at 1st-order. The computer software, GSOLVER, based on the rigorous vector coupled-wave analysis is employed to calculate the various cases, and then the analytical equation derived from the extended scalar theory is used to check the computational result.

Although the layout can be made to adapt to the design, there are some restrictions, such as depth and property of each layer, in the CMOS process. Therefore, our design couldn't fully coincide with (1), which is an optima case. In the model as shown in Fig. 2, the eight-level grating built in GSOLVER assumes that the index and period equal to 1.5 and 12 μm , respectively. The dash line shows the original continuous gratings and the brazed angle is 35.7 degree. Due to the height of each layer is unchangeable and different from each other in the CMOS process, we modify the width to fit the dash line.

When the incident light is perpendicular to substrate, 1st-order diffraction efficiency is found with various wavelength of incident light as in Fig. 3. The most maximum diffraction efficiency is 81.4% with 2.531 μm wavelength. The efficiency seems to high enough to utilize, but the corresponding wavelength is big. Though we change of the incident angle, period and duty cycle of the model, the corresponding wavelength is beyond 2 μm . We find out the parameter that dominates the results as follow.

The depth of gratings greatly affects the corresponding wavelength to the maximum diffraction efficiency. Various depth and wavelength of gratings is computed as shown in Fig. 4. It expresses that depth corresponding to maximum diffraction efficiency becomes higher when the wavelength increases. Accordingly, for high diffraction efficiency in case of 5.005 μm depth, the corresponding wavelength beyond 2 μm is reasonable. A further result is shown in Fig. 5, more various data is shown but varies routinely.

By the extended scalar theory, the finite thickness of the grating is treated by combining the scalar theory (based on wave propagation) with a geometrical theory (based on ray tracing)³. The equation for optimum grating profile depth can be written as

$$d = \frac{\lambda}{n - \sqrt{1 - (\lambda / T)^2}} \quad (2)$$

where d is depth, λ is wavelength, n is index, T is period of the optimum grating profile. Let d and n be equal to 5.005 μm and 1.5, the various T corresponding to λ is plot in Fig. 6. The result is more precise for bigger period, because (2) is only valid for diffractive structures that have very large period-to-wavelength ratio. In the case of T and d equal to 12 and 5.005 μm , the derived optimum wavelength is 2.515 μm , which approximates to the result, 2.5 μm , computed by GSOLVER.

Summarized the result mentioned above, we prove the CMOS multilevel gratings really have high diffraction efficiency in both software computation and analytical equation.

3. FABRICATION

Expanding the CMOS process, we fabricate an optical component besides integrated circuit. The multilevel gratings are fabricated by the conventional CMOS process and simple post-CMOS process. Compare to the methods shown in Table 1, it follows the commercial technique and can be batch produced immediately.

Since aluminum layer is a good etching mask for F-based plasma etching, the SPTM CMOS service of tsmc (Taiwan Semiconductor Manufacturing Company) with three metal layers is adopt to fabricate the multilevel gratings. Fig. 7(a) illustrates the cross-section of the four-level gratings. The silicon dioxide above the metal layers must be full removed and expose the metal layers, so the passivation layer is pre-removed in the layout. Although it violates the design rules due to absent of metal 3 by removing pass, it is realizable in point of microfabrication. Fig. 8(a) shows the profile before post process, the metal 2 and metal 3 layers are already exposed. After silicon dioxide etching, the profile of metal 1 and substrate, as shown in Fig. 8(b), is formed and the work is completed. Fig. 9 shows the oblique view of multilevel gratings.

Although the four-level gratings have been gotten by standard CMOS process, the diffraction efficiency is not high enough (see Fig. 1(f)). We attempt to design eight-level gratings to get higher diffraction efficiency. As shown in Fig. 7(b), the three metal layers, poly, via and contact layers are included to form the eight levels. The via means etching a tunnel in silicon dioxide between two metal layers, so the upper metal layer would fill the via and drop down after deposited. However, the entire making for contact is tungsten deposited in the etching hole. The design of eight-level gratings does not correspond to the CMOS rules that requests the metal layer must be existed above the via or contact, but the design still can work because it is not IC but an optical element. Finally, the CMOS gratings can be used directly as reflected type DOEs, or treated as a mold for replication.

4. CONCLUSIONS

We have fabricated the multilevel gratings by the commercial CMOS process. The surface consisting of the metal layers could be formed merely with the silicon dioxide etching process. In addition, the eight-level gratings are designed with high diffraction efficiency. The criterion for the diffraction efficiency of multilevel gratings is also found out and, advance of the design to other standard CMOS process is possible.

Since the CMOS is a mature technology and batch process, the CMOS multilevel gratings saves the developing time and could be mass production immediately. Furthermore, the Depth, alignment, dimension, and shape errors could be reduced following the advance of the CMOS process.

ACKNOWLEDGEMENTS

This work is accomplished with much needed support and the authors wish to thank the following people: prof. C. K. Lee, Jennyi Chen, Chiyuan Lee, Hunghsuan Lin, Fuyuan Xiao, Tsungwei Huang, Shihchen Chang, Chunyuan Chi of the Institute of Applied Mechanics, Nation Taiwan University, for their valuable advise and assistance in experiment.

REFERENCE

1. C. K. Lee, *Diffraction Optical Elements*, Institute of Applied Mechanics, National Taiwan University, 1998.
2. T. K. Gaylord, and M. G., Moharam, "Analysis and Application of Optical Diffraction by Gratings," *Proc. IEEE*, pp 894-937, 1985.
3. G. J. Swanson, "Binary Optics Technology: Theoretical Limits on the Diffraction Efficiency of Multilevel Diffractive Optical Elements," *Technology Report, Lincoln Laboratory, Massachusetts Institute of Technology*, 1991.
4. M. F. Chang, and M. C., Wu, "Surfaced Micromachined Devices for Microwave and Photonic Application," *SPIE*, Vol. 3419, pp 214-268, 1998.
5. M. B. Stern, "Pattern Transfer for Diffractive and refractive Microoptics," *Microelectronic Engineering* 34, pp 299-319, 1997.
6. D. Macintyre, and S. Thoms, "The Fabrication of High Resolution Features by Mould Injection," *Microelectronic Engineering* 41/42, pp 211-214, 1998.
7. M. T. Gale, "Replication Technology for Diffractive Optical Elements," *Microelectronic Engineering* 34, pp 321-339, 1997.
8. MEMS optical Inc. (<http://www.memsoptical.com/diff.htm>)
9. W. Däschner, P. Long, M. Larsson, and S. H. Lee, "Fabrication of Diffractive Optical Elements Using a Singal Optical Exposure with a Gray Level Mask," *J. Vac. Technol. B* 13(6), pp 2729-2731, 1995.
10. H. Rothuizen, D. Prongué, F. Vasey, and P. Vettiger, "A Conic Primitive-Based Pattern generator for E-Beam Lithography of Diffractive Optical Elements," *Microelectronic Engineering* 34, pp 243-260, 1997.
11. E. B. Kley, "Continuous Profile Writing by Electron and Optical Lithography," *Microelectronic Engineering* 34, pp 261-298, 1997.
12. N. Rajkumar, and J. N. McMulin, "V-Groove Gratings on Silicon for Infrared beam splitting," *Applied Optics*, Vol. 34, No. 14, pp 2556-2559, 1995.
13. H. Rothuizen, D. Prongué, F. Vasey, and P. Vettiger, "A Conic Primitive-Based Pattern generator for E-Beam Lithography of Diffractive Optical Elements," *Microelectronic Engineering* 34, pp 243-260, 1997.
14. J. Fan, D. Zaleta, K. S. Urquhart, and S. H. Lee, "Efficiency Encording Algorithms for Computer-Aided Design of Diffractive Optical Elements by The Use of E-Beam Fabrication," *Applied Optics*, Vol. 34, No. 14, pp 2522-2533, 1995.
15. W. Däschner, M. Larsson, and S. H. Lee, "Fabrication of Monolithic Diffractive Optical Elements by The Use of E-Beam Direct Write on an Analog Resist and a Singal Chemically Assisted Ion-Beam-Etching Step," *Applied Optics*, Vol. 34, No. 14, pp 2534-2539, 1995.
16. N. Moldovan, N. Dumbravescu, M. Danlia, A. Vitriuc, P. Sindile, and J. Mohi, "LIGA and Alternative Techniques for Microoptical Components," *Proc. IEEE*, pp 149-152, 1997.
17. N. Moldovan, N. Dumbravescu, M. Danlia, A. Vitriuc, P. Sindile, and J. Mohi, "LIGA and Alternative Techniques for Microoptical Components," *Proc. IEEE*, pp 149-152, 1997.

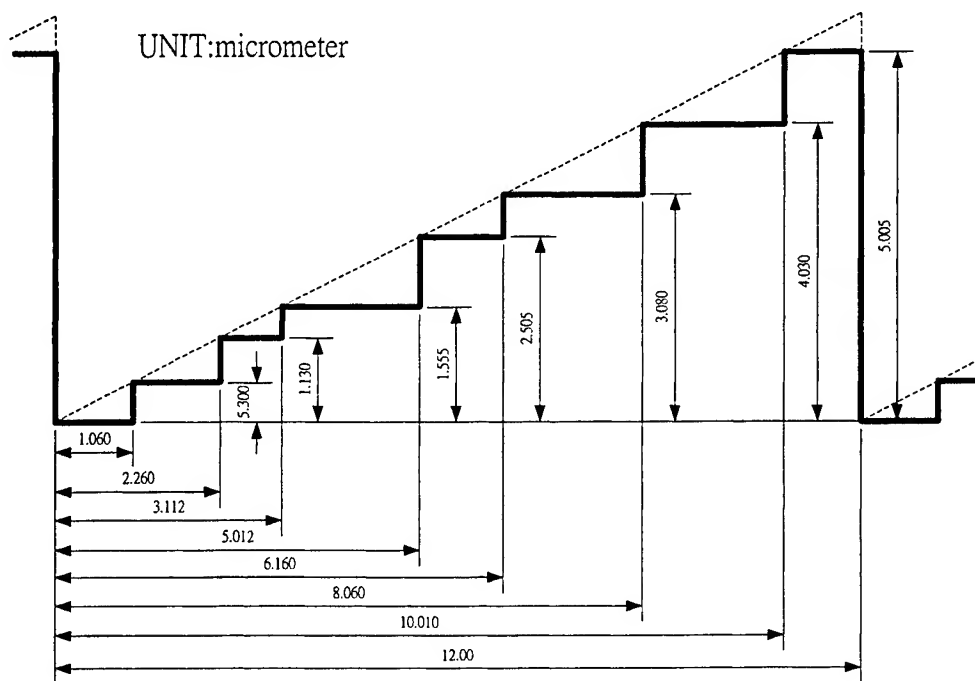


Figure 2 The shape and size of the model built in GSOLVER

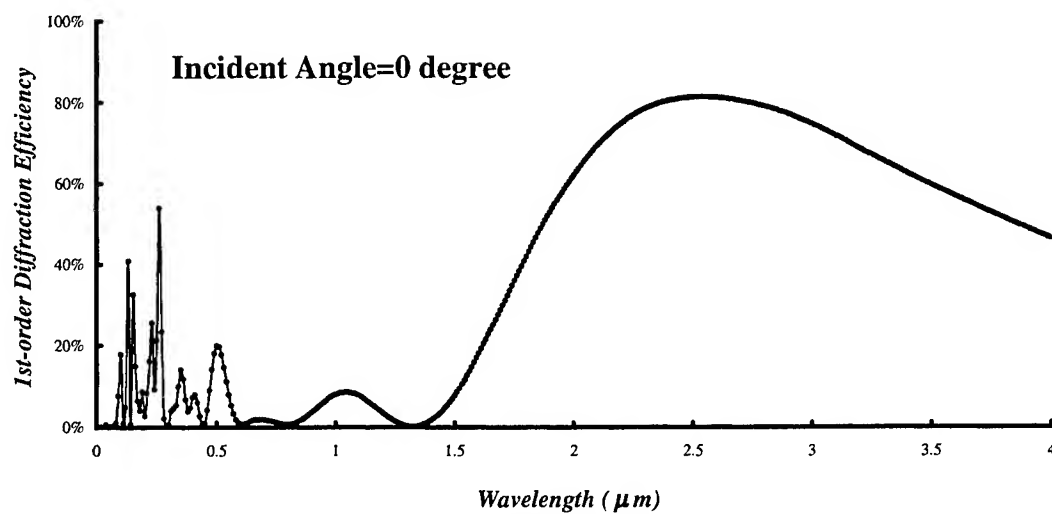


Figure 3 The 1st-order diffraction efficiency with various wavelength of incident light carried out by GSOLVER

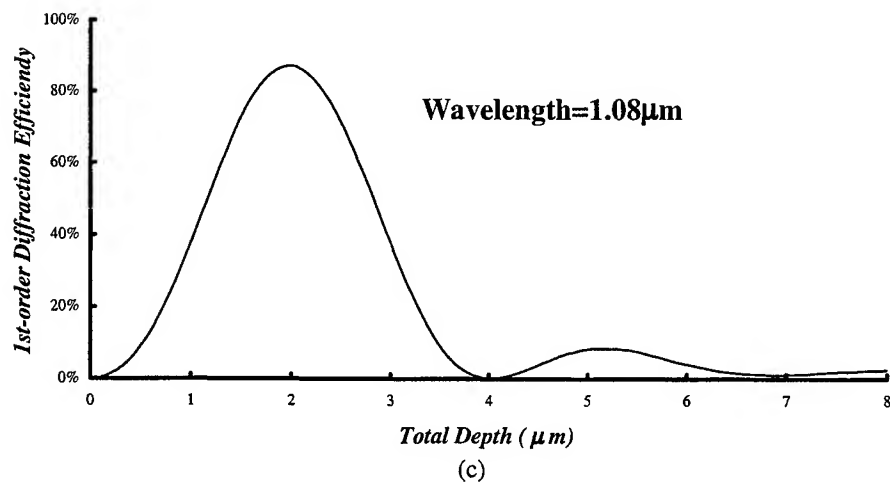
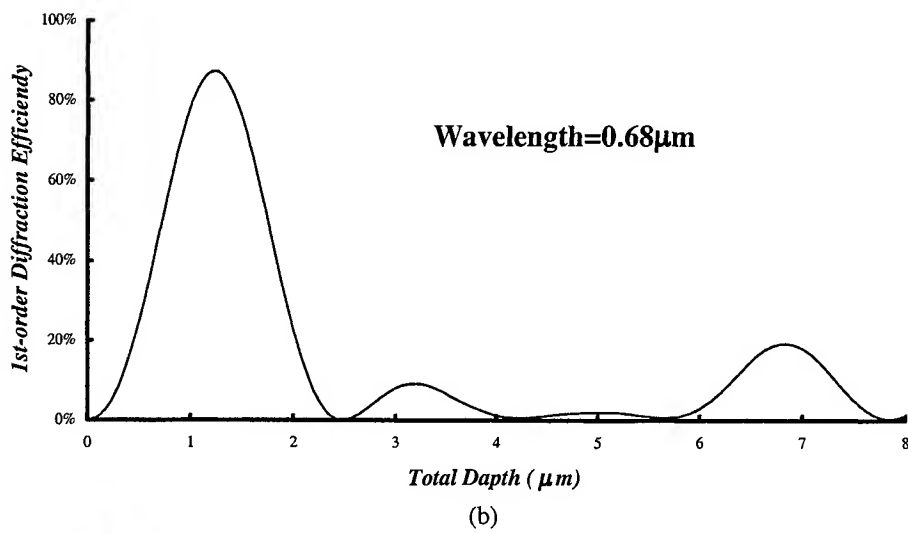
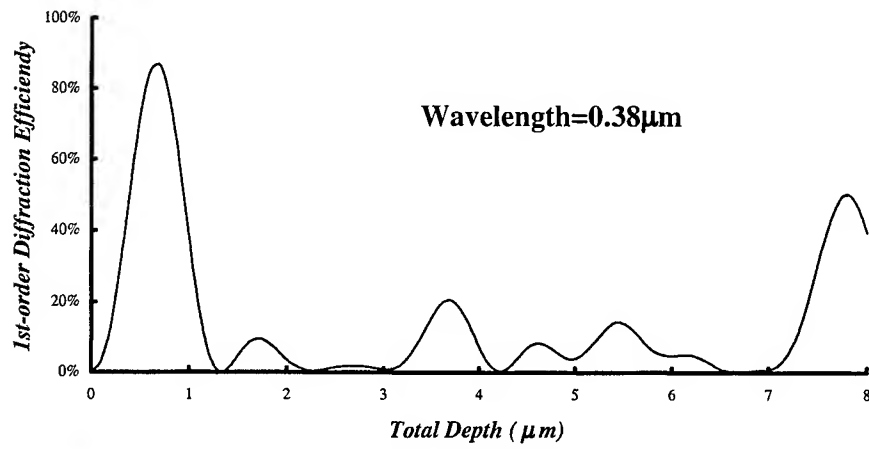


Figure 4 The 1st-order diffraction efficiency computed by GSOLVER with various total depth when wavelength is equal to (a)0.38(b)0.68 (c)1.08 μ m

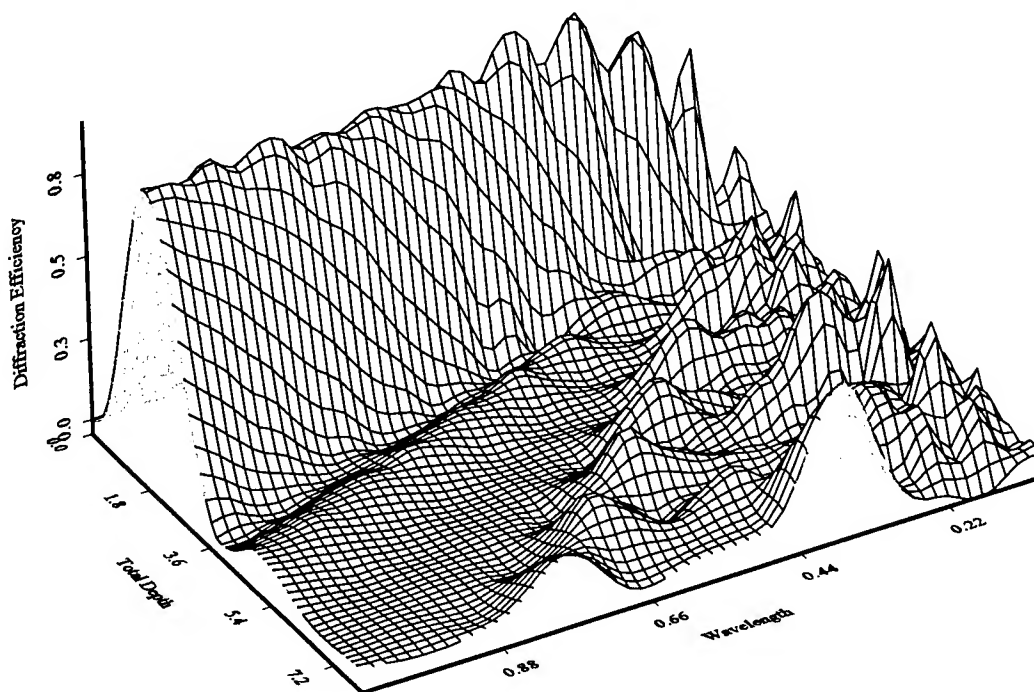


Figure 5 The 1st-order diffraction efficiency computed by GSOLVER with various depth and wavelength

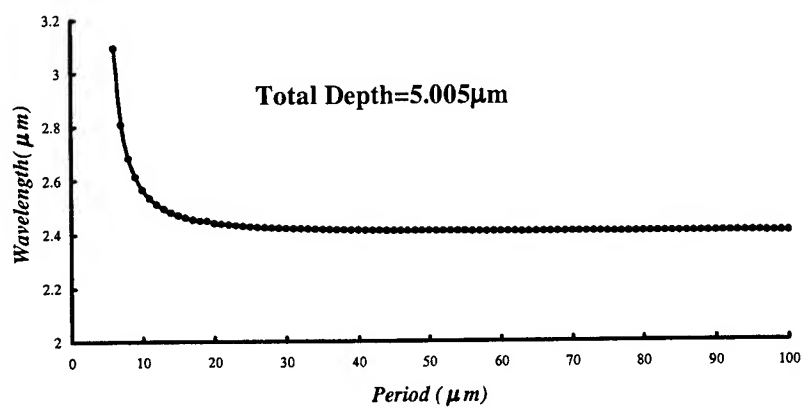


Figure 6 The Optimum wavelength for various period when the depth equal to 5.005 μm

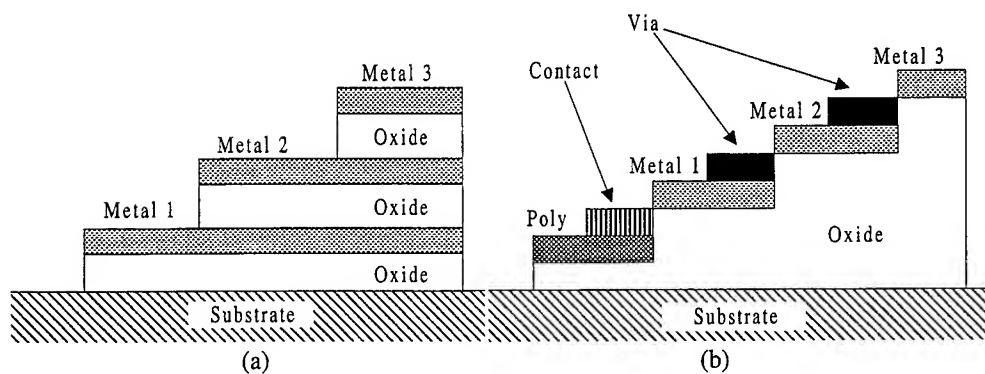


Figure 7 CMOS multilevel gratings (a)four levels (b)eight levels

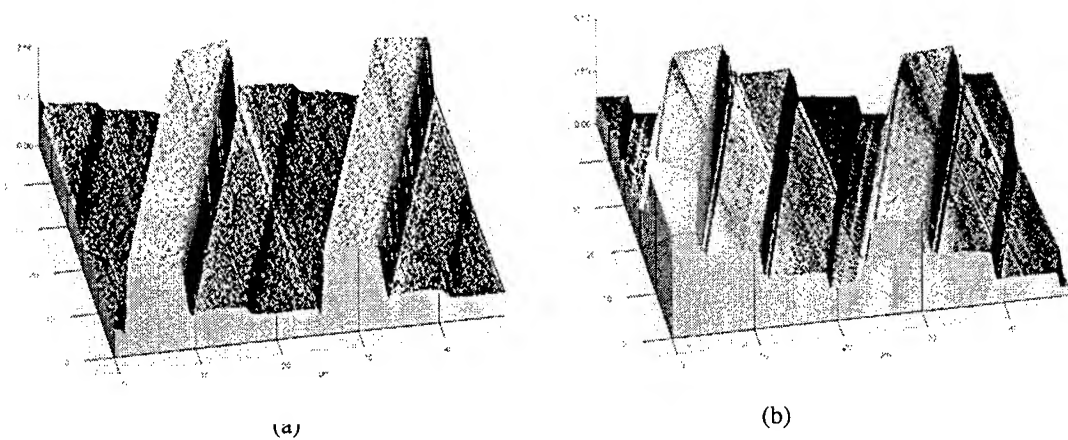
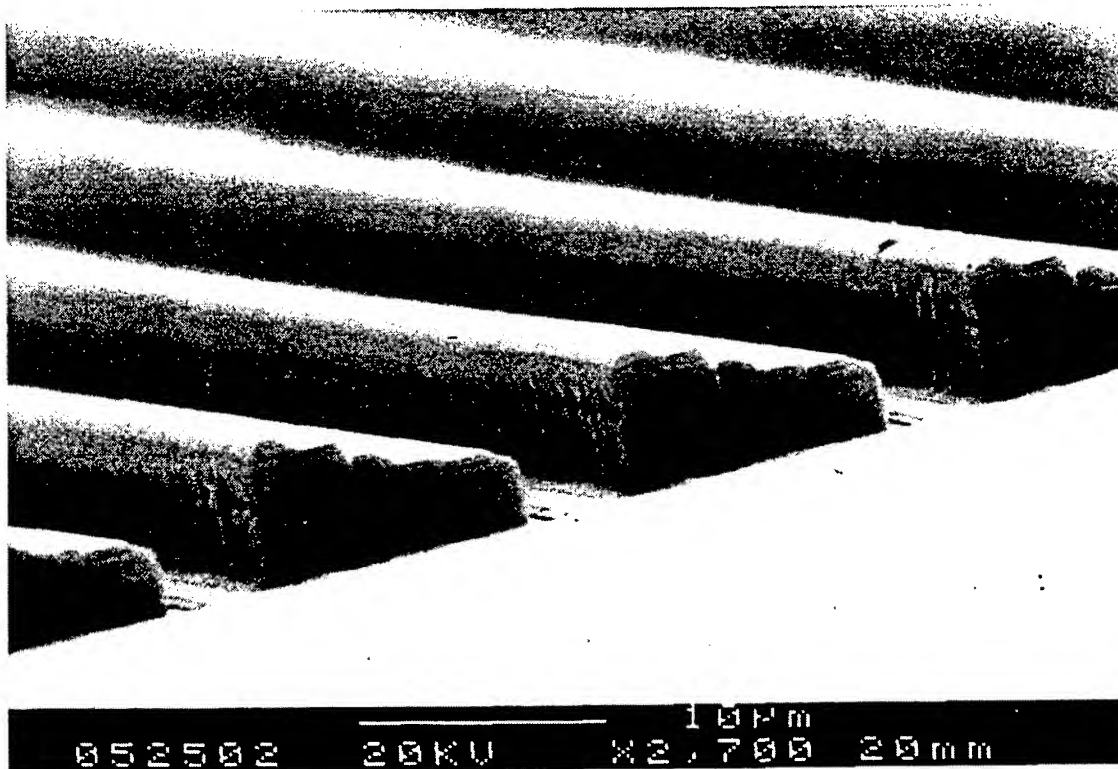


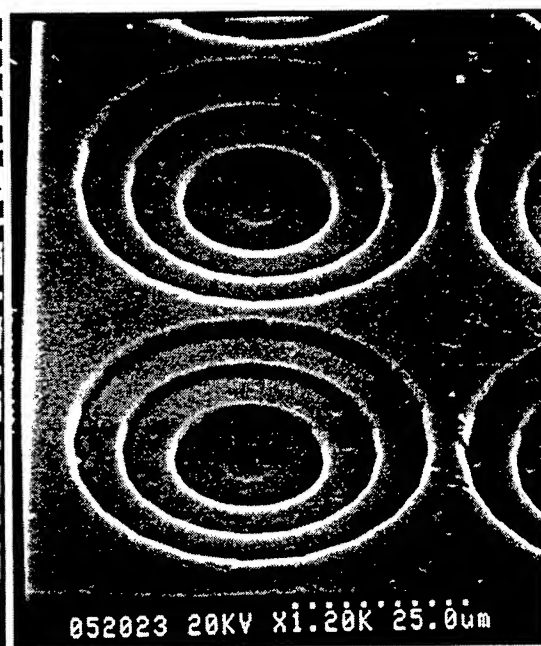
Figure 8 CMOS four-level gratings photography of AFM (a)before and (b)after silicon dioxide etching



(a)



(b)



(c)

Figure 9 Scanning electron micrograph of CMOS multilevel lens (a)multilevel gratings (b) convex and (c) concave multilevel micro lens

INTEGRATED EYEBALL-TRACKING DEVICE

Hunglin Chen, Kaihsiang Yen, Jinhung Chio, Huiwen Huang,

Microsystems Laboratory, Industrial Technology Research Institute
Bldg. 52, 195, sec. 4, Chung Hsing Rd., Chutung, Hsinchu, Taiwan 310, R. O. C.

Chingliang Dai

Department of Mechanical Engineering, Oriental Institute of Technology
Pan Chiau, Taipei, 220, Taiwan, R. O. C.

Chienliu Chang, Peizen Chang

Dept. of Applied Mechanics, National Taiwan University
Taipei, Taiwan 106, R. O. C.

ABSTRACT

This investigation presents a concept of integrated device, which tracks the movement of eyeball in real time. Integrated optical components are applied to perform infrared oculography to find the position of eyeball. First, the photodiodes emit infrared to human eyes via the output coupler, then the reflected light is collected by the input coupler and detected by the photodetectors. By analyzing the electrical signal, we could figure the position of eyeball out. The basic principle is based on the differential of reflected index between sclera and iris. The light source and detectors are settled on the side of goggles worn and, in doing so, the eyesight could be wide without obstacles. Therefore, the optical guiding interconnection is an essential issue for the eyeball-tracking device.

Since the fine line gratings are necessary for the optical coupler, the electron beam writing is used to meet the requirement. The gratings with 40 nm line width are achieved, and it is sufficient for optical coupling. On the other hand, the electrical signal related eyeball position is simulated. We could translate the electrical signal readout into the coordinate of the eyeball position. The whole eyeball-tracking device would be small volume, less weight, and portable.

Keywords: infrared oculography, eyeball tracking, gratings, coupler

1. INTRODUCTION

A man-machine interface is of great importance for the spinal-cord-injury patient disabled from muscle controlling, learning and communicating. Especially, the eyeball-controlling system would benefit the sufferers with paralysis of whole body. According to the movement of the eyeball and a wink, they could express their words via the tracking system. Therefore, many methods, including electro oculography (EOG), search coil (SC), infrared video system (IRVS), dual purkinje image (DPI), and infrared oculography (IROG), are developed to realize the eyeball-controlling system.

Potentially, the eyeball-controlling system could apply to the portable communication products, such as wearable computer and head-mounted display. For minimizing the volume of the device, integrating the integrated optical components to the whole system should be a promising approach. In light above developments, the research we proposed herein suggests an integrated component in the eyeball-tracking device with the mechanism of IROG. Configuration of the component and simulation of the eyeball-tracking operation are also described.

2. DEVICE DESIGN

2.1 GRATING COUPLER

Fine period structures, fabricated by electron beam lithography¹ or interferometric technology², is usefully used for integrated optical components, including input/output coupler^{3,4}, waveguide coupler^{5,6}, deflector, reflector⁷, mode converter⁸, wavelength filter, waveguide lens⁹⁻¹¹, focusing coupler^{12,13}, and butt-coupled reflection grating¹³. The grating assisted coupling input/output is the main topic we try to analysis and use herein. However, the period of gratings, Λ , is too small to easily fabricate. For instance, consider a grating coupler, as shown in Fig. 1, gives a radiation beam at an angle of $\theta = 15^\circ$ in air for the fundamental diffraction order ($q = -1$). From phase matching equation

$$n_{c/s}k \sin \theta_q^{c/s} = Nk + \frac{2\pi}{\Lambda}q \quad (1)$$

where $n_{c/s}$ is the index of cover/substrate, k is the propagation constant, q is the order of coupling, and N is the effective index. The grating period is determined to be $\Lambda = 0.51 \mu\text{m}$. Therefore, the gratings should be fine lines and, thereby, we adopt electron beam writer to satisfy the requirement. Next, we would introduce both the electron beam lithography and the purposed application.

2.2 OPERATIONAL PRINCIPLES

Originally, the waveguide input/output coupler is found out for particular application, eyeball tracking device¹⁴. As shown in Fig. 2, the light (IR source) safe for human eyes emits to eyes via waveguide coupler, and then the arrayed photodiode detect the reflected light to determine the position of eyeball^{15,16}. The principle is based on the differential of reflected index between sclera and iris. The light source and detector settled on the side of goggles worn and, in doing so, the eyesight could be wide without obstacles. Therefore, the optical guiding interconnection is a key issue for the eyeball-tracking device.

Several researchers have suggested that integrated optical devices integrated of waveguide coupler, laser diode, and detector in monolith¹⁷. In the light of recent developments, we propose an optical guiding interconnection device for eyeball tracking device. However, the alignment accuracy between the waveguide and diode is extreme rigorous, the tolerance only allowed in order of submicron.

The most important of the design is that the device should not be a shelter for eyesight. As shown in Fig. 3, the device consisting of glass and PMMA resist is fully transparency. For guiding the wave, the thickness of the 7059 glass, t_g , has minimum limitation. For instance, the wavelength of light source, λ_0 , the index of 7059 and 7740 glass equals to 0.6328 μm , 1.544 and 1.474, respectively. According to

$$t_g^2 > \frac{\lambda_0^2(2m+1)^2}{16(n_2 - n_3)(n_2 + n_3)} \quad (2)$$

The relation between the guiding modes, m , and t_g could be expressed as Fig. 4. The thickness of the guiding layer related to guiding modes is an important parameter. The light couldn't be guided in the layer with thickness below cut off and, in contrast, thick thickness would result in multi modes.

2.3 SIMULATION

For identifying the position of eyeball, the detection circuit is necessary. The eyes roughly categorize into iris, the dark part, and sclera, the white part. The light reflected from iris and sclera should be much difference and, therefore, arrayed photo detectors are used to detect the differential signal. According to the readout, we could reversely calculate the position of the eyeball. For example, the output signal would equal to zero if the eyeball stays in the center. As shown in Fig. 5(a), the part of the light would be strongly reflected from human eyes to the array photo detectors, then the signal output is generated from the differential amplifier. In addition, owing to the signal derived from photo detector is not voltage but

current, the current to voltage converter is required. With proper impedance, the signal could be detected in corresponding range.

We simulated the operation of the detection of eyeball tracking device. The lamp instead of reflected light lights up the arrayed photo detectors. LabVIEW, a graphical programming language, is then adopted to perform data acquisition with AT-MIO board. The signal generated by arrayed photo detectors inputs to the AT-MIO board via the current to voltage converter. The operation of differential amplifier is then achieved in LabVIEW. Owing to the resolution and sampling rates are up to 12 bits and 1.25 Mbytes per second, respectively, we could process the signal in real time.

As shown in Fig. 6, the lamp turns off with zero voltaic output, and the lamp turns on in middle, left, and right part with near zero, negative, and positive voltages, respectively. In addition, the noise with high frequency could be eliminated by the low pass filter as shown in Fig. 5(b)(c).

Although the installation is bigger than the useful one settled on the eyeball tracking device, the detection with high resolution and frequency response is achieved and could be a preceding survey.

3. FABRICATION

3.1 ELECTRON BEAM LITHOGRAPHY

Electron beam lithography (EBL), an ideal technology in terms of resolution and flexibility for writing structures in the medium to lower nanometer-scale range¹⁸, is used herein for the fine line gratings. Currently, EBL is used principally in support of the integrated circuit industry, where it has three niche markets, including mask-making, direct writing, and studies of quantum effects¹⁹. However, the throughput of EBL is too low for applications on a large industrial scale (forty 8 in. wafers per hour). Therefore, SCALPEL (scattering with angular limitation projection electron-beam lithography)²⁰ and multiple beam techniques²¹ are proposed to achieve a production-worthy tool that can be scaled to further generation.

There are two methods, raster and vector scanning, for pattern generation in EBL²². Raster scanning is the usual control method, where the reticle is printed as a number of adjacent strips. In a typical system, electron beam first passes through a pair of blanking plates that can deflect the beam into a beam stop. For each strip, the beam is scanned electronically only in the y-direction, while the stage moves as a constant velocity in the x-direction. Therefore, the pattern is transferred only by control of the blanking plates. The main problem with raster scanning is that it is necessary to access every pixel in the pattern, and this can be inefficient on some geometry. In contrast to raster scanning, the electron beam is controlled electronically to scan in both the x and y directions for vector scanning. Vector scanning endeavors only to access those pixels that need to be written, but at the cost of increased system complexity. The drawback of vector scanning is difficult to accurately control the relative position in two dimensions.

The resolution of EBL is not directly limited by the spot size or diffraction. Instead, the limiting factor with EBL is electron scattering by the interaction with medium. Scattering also causes a proximity effect that means two adjacent spots require less exposure than two separated spots, due to their mutual scattering. Beside, proper dose is also needed to compensate this effect²³.

The space charging effect is another problem in EBL. Electrons generated from emitter would mutually repel each other in the space, and in high current systems this can seriously degrade the resolution of the system. Classical space charge results from the average field of the electron cloud and causes a defocus that is correctable using a dynamic focus system.

3.2 FINE LINE GRATINGS

Since the gratings of output coupler usually are in order of sub micron, we use EBL to fabricate fine line gratings to meet the requirement. In EBL, The size of the feature, meaning the scanning area of the electron beam, also restricts to the performance. Due to the lower linearity of scanning coil for bigger range, the pattern size should be smaller than $500\text{ }\mu\text{m} \times 500\text{ }\mu\text{m}$. In addition, the acceleration voltage and resist must be determined. With higher acceleration voltage, the clearer image is attainable that benefits to write. However, high acceleration voltage may damage the sample. Until now, an optimum resist that has zero scattering and one hundred percent contrasts is never realized. Hence, we should reduce the unwanted interaction between electron and resist. For instance, the forward scattering is given empirically by the formula¹⁹:

$$d_f = 0.9 \left(\frac{R_t}{V_b} \right)^{1.5} \quad (3)$$

where d_f is the effective beam diameter, is the resist thickness in nanometers, and is the beam voltage in kilovolts. According to (3), forward scattering is minimized by using the thinnest possible resist and highest available accelerating voltage.

With proper dose and suitable operation, we write fine line gratings that line width 40 nm linewidth as shown in Fig. 7(a). The depth of resist is about 50 nanometers (see Fig. 7(c)) that could prevent forward scattering of the electron beam. For smaller period of the gratings (see Fig. 7(b)), the resist would collapse and connect each other after development. The phenomenon may cause by (i) the aspect ratio of the resist is not high enough to support the thin convex structure, or (ii) the electron would go on every hand nearby the pattern, and if two lines are very close, the interval would be exposed.

3.3 GLASS WAVEGUIDE

Since the eyeball-tracking device should be transparency for human eyes, glass waveguide is a suitable candidate for the system. The device includes three layers, 7740 glass substrate, 7059 glass guiding layer and PMMA resist. First, the 7059 glass is RF bias sputtered onto 7740 glass substrate in argon flow at a rate about 1000 Å/hour. Then the procedure roughly accords to the EBL mentioned above.

Owing to the substrate is an insulator, a very thin (~100 Å) Au conductive layer is deposited before EBL to avoid the charging up problem that results in accumulation of electrons and vague image. After EBL, the coating must be removed by etching before the development. Although the etchant (KI:I₂:H₂O=3g:1g:40ml) for Au is opaque, the etching stop is unnecessary by the high selectivity between Au and PMMA.

4. CONCLUSIONS

This work has proposed a concept of integrated eyeball-tracking device with small volume, less weight, and portable. The function is simulated and measured by the electrical signal, and fine line gratings sufficient for output coupler are produced by EBL. In addition, the configuration of the glass waveguide coupler has been determined, and the EBL process has achieved for the insulator. For advancing technology, the system integration and optical efficiency should be improvement to obtain appropriate performance.

ACKNOWLEDGEMENTS

This work is accomplished with much needed support and the authors wish to thank the following people: prof. C. T. Chen of ACADEMIA SINICA, prof. C. H. Chen of College of Electrical Engineering, Nation Taiwan University, Jennyi Chen, Chiyuan Lee, Hunghsuan Lin, Fuyuan Xiao, Tsungwei Huang, Shihchen Chang, Chunyuan Chi of the Institute of Applied Mechanics, Nation Taiwan University, for their valuable advise and assistance in experiment.

REFERENCE

1. H. Kotani, M. Kawabe, and S. Nambe, "Direct Writing of Grating by Electron Beam in Poly(metyl methacurylate) Optical Waveguide," *Japan Journal of Applied Physics*, Vol. 18, No. 2, pp. 279-283, 1979.
2. X. Mai, R. Moshrefzadeh, U. J. Gibson, G. I. Stegeman, and C. T. Seaton, "Simple versatile method for fabricating guided-wave gratings," *APPLIED OPTICS*, Vol. 24, No. 19, pp. 3155-3161, 1 October 1985.
3. K. E. Spaulding, and G. M. Morris, "Achromatic waveguide input/output coupler design," *APPLIED OPTICS*, Vol. 30, No. 9, pp. 1096-1112, 20 March 1991.
4. N. Eriksson, M. Hagberg, and A. Larsson, "Highly Directional Grating Outcouplers with Tailorable Radiation Characteristics," *IEEE JOURNAL OF QUANTUM ELECTRONICS*, Vol. 32, No. 6, pp. 1038-1047, JUNE 1996.
5. M. L. Dakss, L. Kuhn, P. F. Heidrich, and B. A. Scott, "Grating coupler for efficient excitation of optical guided waves in thin films," *APPLIED PHYSICS LETTERS*, Vol. 16, No. 12, pp. 523-525, 15 JUNE 1970.

6. S. Zhang, and T. Tamir, "Analysis and Design of Broadband Grating Couplers," *IEEE JOURNAL OF QUANTUM ELECTRONICS*, Vol. 29, No. 11, pp. 2813-2824, NOVEMBER 1993.
7. P. K. Tien, "Method of forming novel curved-line gratings and their use as reflectors and resonators in integrated optics," *OPTICS LETTERS*, Vol. 1, No. 2, pp. 64-66, August 1978.
8. H. Stoll, and A. Yariv, "Coupled -mode Analysis of Periodic Dielectric Waveguides," *APPLIED OPTICS*, Vol. 23, No. 11, pp. 1749-1753, 1 June 1984.
9. G. I. Hatakoshi, H. Fujima, and K. Goto, "Waveguide grating lenses for optical couplers," *Sensors and Actuators A* 57, pp 103-110, 1996.
10. L. Kocsanyi, R. Kosza, M. Barabas, G. Szarvas, and L. Jakab, "A Complex Design and Microfabrication System for Experimental Production of Planar Waveguide Lenses for Integrated Optical Circuits," *Microelectronic Engineering*, pp. 351-355, 1994.
11. C. Warren, S. Forouhar, W. S. C. Chang, and S. K. Yao, "Double ion exchanged chirp grating lens in lithium niobate waveguides," *Appl. Phys. Lett.*, Vol. 43, NO. 5, pp. 424-426, 1 September 1993.
12. T. Suhara, K. Okada, T. Saso, and H. Nishihara, "Focusing Grating Coupler in AlGaAs Optical Waveguide," *IEEE PHOTONICS TECHNOLOGY LETTERS*, Vol. 4, No. 8, pp. 903-905, 8 AUGUST 1992.
13. D. Heitmann, and C. Ortiz, "Calculation and Experimental Verification of Two-Dimensional Focusing Grating Couplers," *IEEE JOURNAL OF QUANTUM ELECTRONICS*, Vol. QE-17, No. 7, pp. 1257-1263, 7 JULY 1981.
14. J. G. Webster, *Encyclopedia of Medical Devices and Instrumentation*, Vol. 2, pp. 1259-1269, 1988
15. E. E. E. Frietman, "The Detection of Eye Ball Movements with the Eye-sistant" *Theoretical and Applied Aspects of Eye Movement Research*, 1984.
16. R. Jones, "Two dimensional eye movement recording using a photoelectric matrix method," *Vision Res.*, Vol. 13, pp. 425-431, 1973
17. S. Ura, T. Suhara, and G. Nishihara, "Integrated-Optic Interferometer Position Sensor," *JOURNAL OF LIGHTWAVE TECHNOLOGY*, Vol. 7, No. 2, pp. 270-273, FEBRUARY 1989.
18. W. Chen, and H. Ahmed, "Fabrication of 5-7nm wide etched lines in silicon using 100keV electron-beam lithography and polymethylmethacrylate resist," *Appl. Phys. Lett.*, Vol. 62, NO. 13, pp. 1499-1501, 29 March 1993.
19. P. R. Choudhury (Editor), *Handbook of Microlithography, Micromachining, and Microfabrication*, SPIE Optical Engineering Press, Ch2
20. L. R. Harriott, "Scattering with angular limitation projection electron beam lithography for suboptical lithography," *J. Vac. Sci. Technol. B*, 15(6), pp. 2130-2135, Nov/Dec 1997.
21. T. H. P. Chang, M. G. R. Thomson, E. Kratschmer, H. S. Kim, M. L. Yu, and K. Y. Lee, "Electron-beam microcolumns for lithography and related applications," *J. Vac. Sci. Technol. B*, 14(6), pp. 3774-3781, Nov/Dec 1996.
22. A. Hawryliw, "Pattern generation for the next millennium," *MICROELECTRONIC ENGINEERING*, pp. 501-507, 1997.
23. M. A. Mccord, "Electron beam lithography for 0.13um manufacturing," *J. Vac. Sci. Technol. B*, 15(6), pp. 2125-2129, Nov/Dec 1997

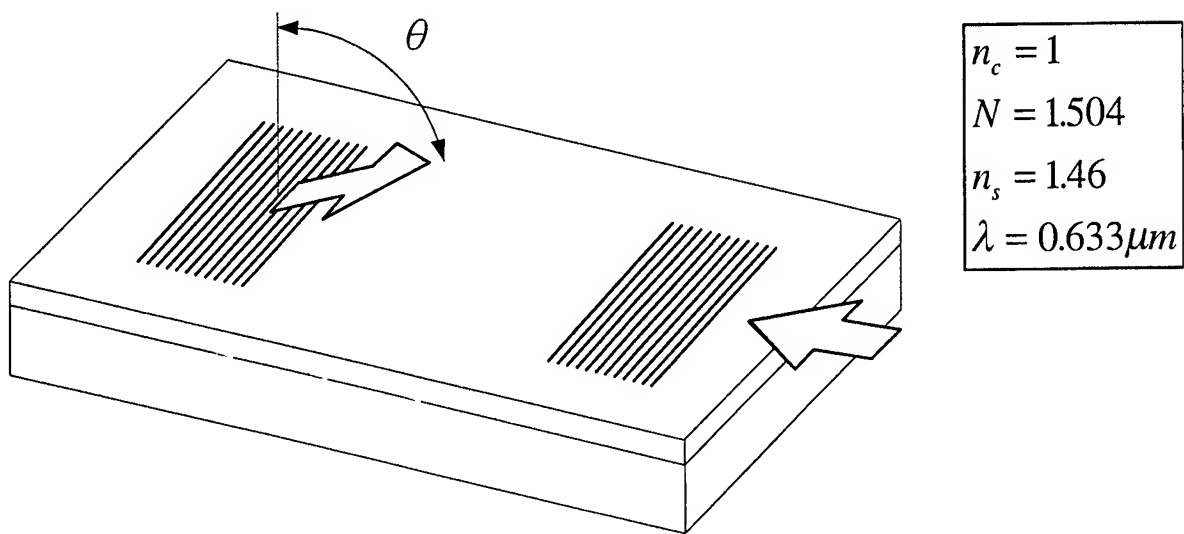


Figure 1 Input/output waveguide coupler

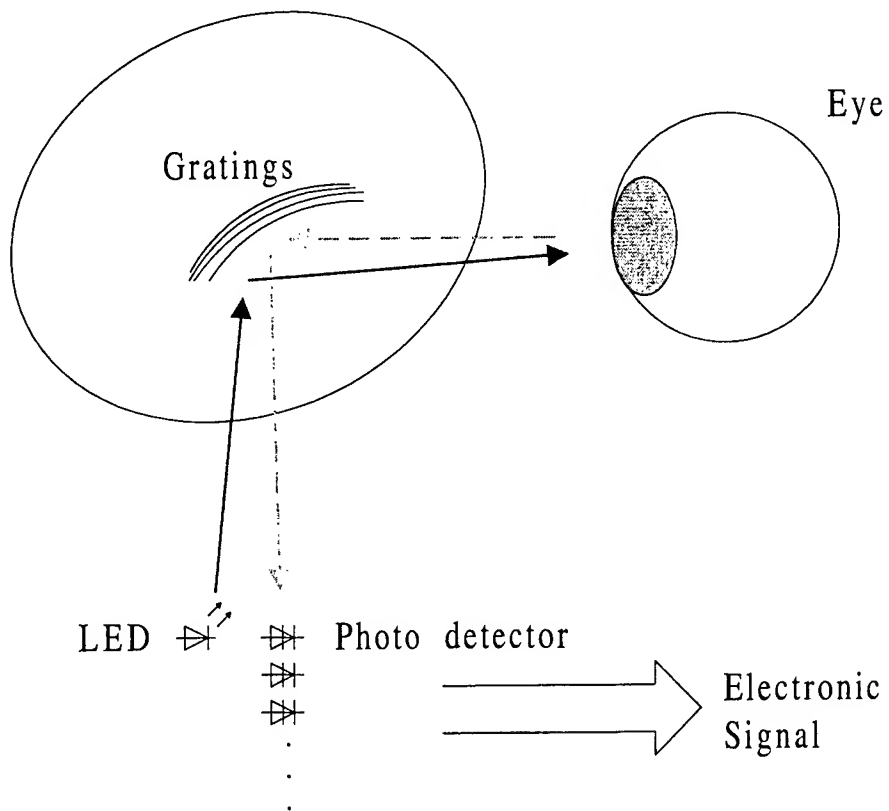


Figure 2 The eyeball tracking device

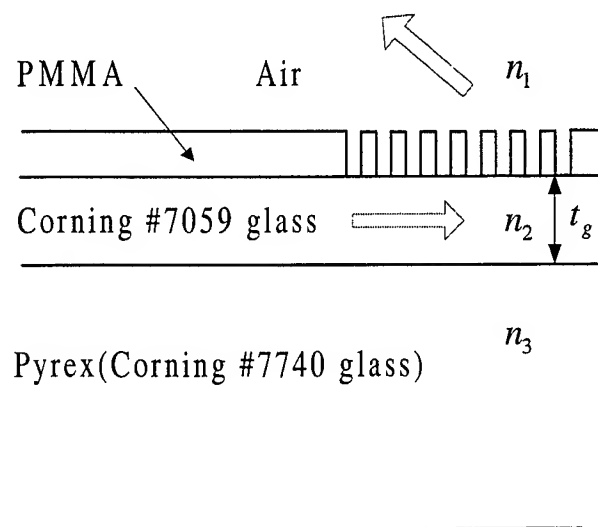


Figure 3 Schematic of the glass waveguide coupler

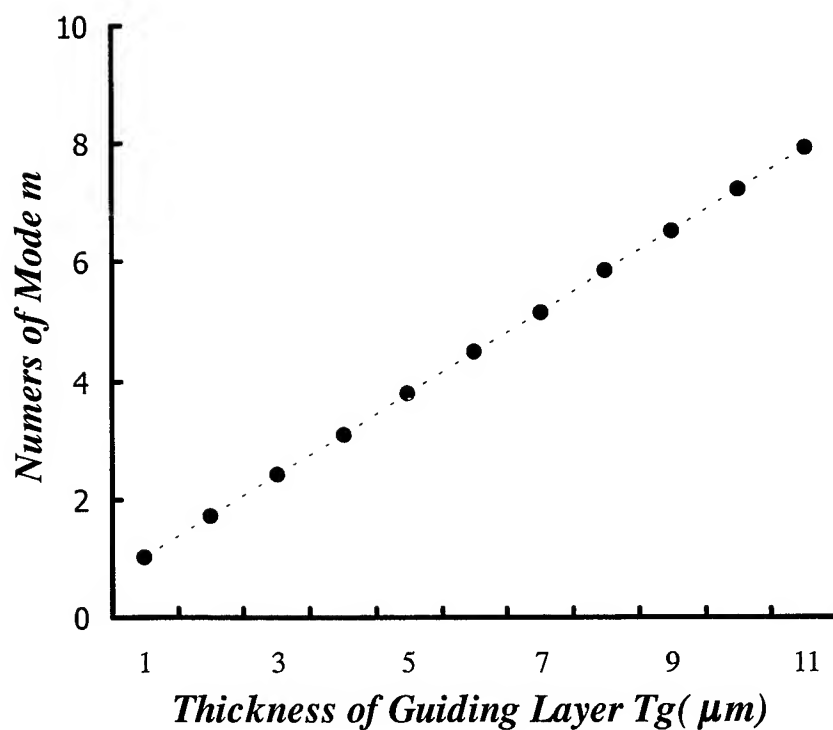


Figure 4 The relation between thickness of guiding layer and numbers of mode

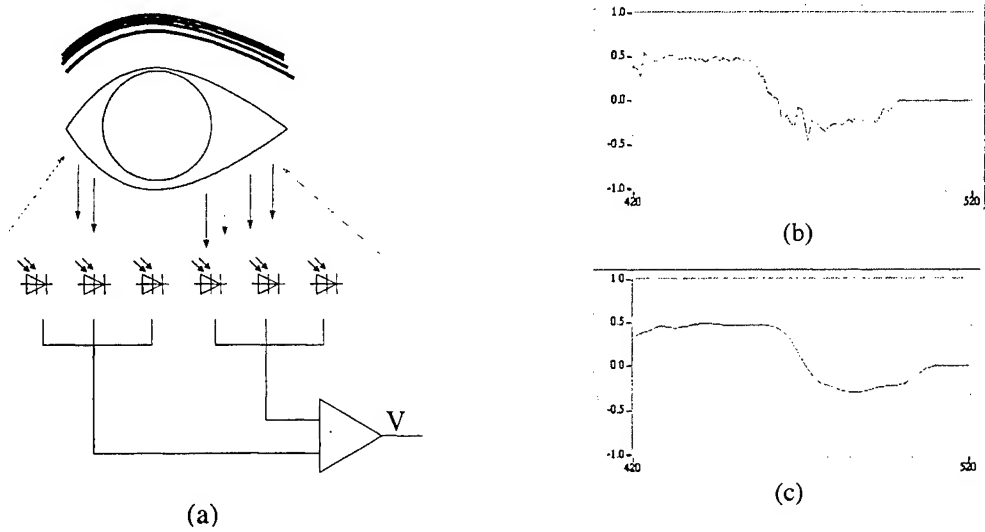


Figure 5 Schematic for the detection of eyeball tracking device (a)differential amplifier (b)without (c)with low pass filter

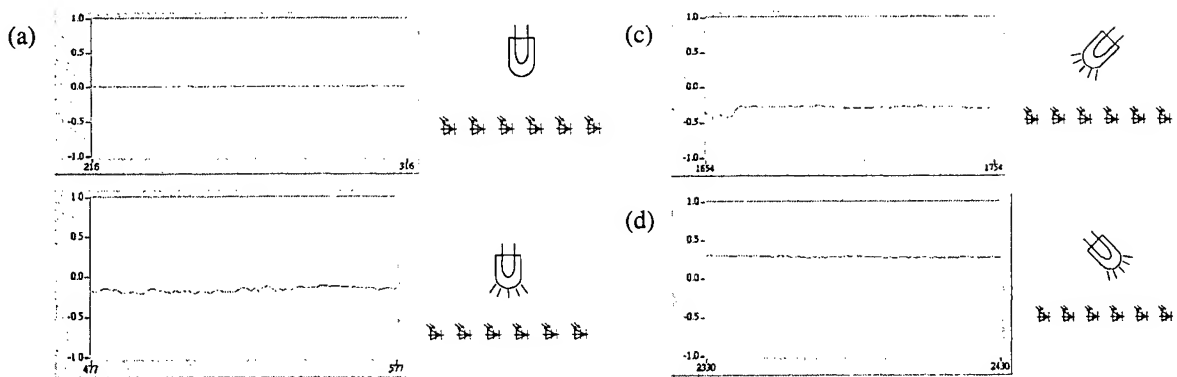


Figure 6 The output signal with the lamp turning (a)off and on in (b)middle (c)left (d)right part

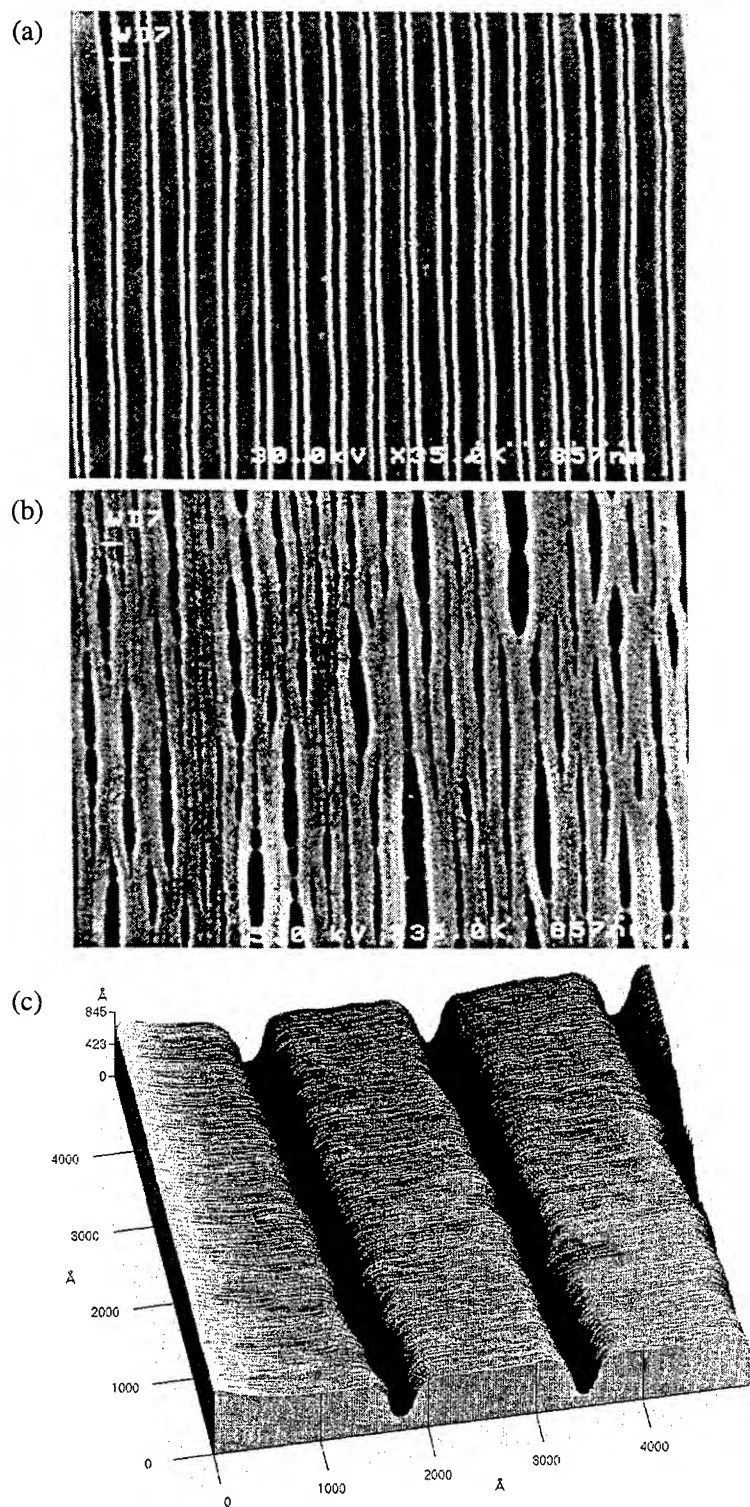


Figure 7 Fine line gratings (a)40 nm linewidth (b)wrong lines with smaller periods (c) surface profile of 3-dimension AFM graphy

Finite-Element Analysis of Solder Joint Strength in Laser Diode Packaging

Chi-Huang Chang[#], Maw-Tyan Sheen[#], Jao-Hwa Kuang[#]

Chi-Chen Chen^{*}, Gol-Lin Wang^{*}, and Wood-Hi Cheng^{*}

[#]Mechanical Engineering Department and ^{*}Institute of Electro-Optical Engineering,
National Sun Yat-sen University, Kaohsiung, Taiwan 804

Hung-Lun Chang, Szu-Chun Wang, Chungyung Wang, and Chih-Ming Wang
Chunghwa Telecom Laboratories, Yang-Mei, Taoyuan, Taiwan 326

ABSTRACT

The effect of PbSn solder joint strength on temperature tests in laser diode packaging has been studied experimentally and numerically. It was found that the solder joint strength increased as temperature cycle number increased. A finite-element method (FEM) analysis is performed on the calculation of joint strength of PbSn solder in temperature cycling tests for laser diode packaging. Numerical calculations were in good agreement with the experimental measurements that the solder joint strength increased as the temperature cycle increased. This may be due to the redistribution of the residual stresses within the solder during temperature cycling tests, and hence reducing the residual stresses and increasing the solder joint strength as the temperature cycle number increased. The result suggests that the FEM is an effective method for predicting the solder joint strength in laser diode packages.

Keywords: Solder joint strength, PbSn solder, temperature cycling, finite-element method

1. INTRODUCTION

For high performance laser-based transmitters in lightwave communication systems, box-type packages of the dual-in-line package (DIP) with fiber pigtails is widely used¹. A laser DIP consisted of a 1.3 μm laser diode, the Invar housing, and a single-mode fiber, as shown in Fig. 1 (a). Fig. 1 (b) shows the laser diode package that is a part of DIP. In Fig. 1 (b), the submount is bonded to substrate with AuSn solder to form submount-solder-Invar substrate assembly. The melting temperature of AuSn hard solder is 280°C. Then the laser diode chip is bonded to submount with PbSn solder to form laser-solder-submount assembly. The melting temperature of PbSn soft solder is 183°C. The purpose of the submounts is used to spread heat laterally from the active area of the laser, reduce the temperature rise at hotspots, and match the coefficient of thermal expansion (CTE)². To be used in system applications, the laser diode package is required for reliability test. One of the reliability test is the temperature cycling which is the most important tests for laser package reliability qualification.

Temperature cycling tests are commonly used in the semiconductor industry to characterize the thermal fatigue failure and to predict reliability of the solder joints in the microelectronics packaging technology³. Although other mechanisms, such as vibration, mechanical and thermal shocks, and humidity, may lead to solder joint failure, the primary mechanisms are caused by thermal and residual stresses during temperature cycling tests. In this work, we study the joint strength of PbSn solder in laser diode and submount assembly under temperature cycling tests. To simplify the study of the solder joints in laser diode assembly, the laser diode-solder-submount was substituted by the gold plated Al_2O_3 -solder-Invar plate, as shown in Fig. 1 (c). The dimension of Invar plate and Al_2O_3 were 12 x 6 x 1.5 and 3 x 3 x 0.75 mm³, respectively.

2. JOINT STRENGTH MEASUREMENTS

To examine the laser package solderability, the joint strength of the soldered sample was measured with a push test fixture of inhouse design. The test fixture consisted of a force gauge and a holder as shown in Fig. 2. Five samples of Al_2O_3 -solder-Invar assembly of PbSn solders were measured under push test. The joint force in kgf unit was obtained by measuring the amount required to break the soldered sample from the holder.

Fig. 3 shows the measured results of the average joint strength as a function of temperature cycle number. The solder joint strengths were measured and recorded for every 100 cycles. The joint strengths were 17 and 28 kgf at zero and 500 cycles, respectively. The joint strength increased as the cycle number increased to 500 cycles. In general, the stresses in optoelectronic packaging are often generated by soldering technique caused by coefficients of thermal expansion mismatch between different materials. Fig. 3 indicates that the redistribution of the residual stresses within the solder during temperature cycling tests may have an influence on joint strength in the soldering technique for laser diode packages.

3. FINITE-ELEMENT METHOD (FEM)

3.1 Finite-Element Model

Numerical simulations of the joint strengths in temperature cycling were performed using the commercial MARC⁴ and MENTAT⁵ finite element packages. A plane strain triangular element model with the temperature-varied material properties was employed in this work. Fig. 4 shows a representative FEM model of Al₂O₃ submount-solder-Invar plate. Table I lists the finite element parameters used in the simulation. Due to the geometry of the Al₂O₃ submount-solder-Invar plate as shown in Fig. 1, a cross section of the solder area was meshed for the FEM simulation. Meshes with triangle type elements were created with an automatic mesh generator.

3.2 Temperature Cycling Tests

The process of temperature cycling test was followed the Bellcore Reliability Assurance Practices of TA-TSY-000983⁶. During the temperature cycling test, the temperature was changed from - 40 to 85°C within a 3 hours cycle. The ramp rate was greater than 10°C/min and the dwell time was 30 min for a total of 500 cycles. The process of the temperature cycling test is shown in Fig. 5. The solder joint strengths were calculated for every 100 cycles.

3.3 Material Properties

The physical constants and material properties of Inver, PbSn solder, Au, and Al₂O₃ at room temperature used in the simulation are listed in Table II and III, respectively⁷. The values of the CTE, Young's modules, yield strength, Poisson's ratios, thermal conductivity, and specific heat are considered temperature dependent. Because of the limit of the experimental data available for the Inver, the temperature dependence of these material properties near the melting temperature region were assumed to have a tendency similar to that of stainless steel (SS) 304L. The material properties as a function of temperature for SS 304L were obtained from the Metals Handbook⁸.

4.4 FEM Simulation Results

The FEM simulations of the joint strength as a function of cycle number are shown in Fig. 3. The joint strength increased as the cycle number increased. Numerical calculations were in good agreement with the experimental measurements that the solder joint strength increased as the temperature cycle increased. This is may be due to the redistribution of the residual stresses within the solder during temperature cycling tests, and hence reducing the residual stresses and increasing the solder joint strength as the temperature cycle number increased. Fig. 3 clearly shows that FEM model can be used to predict the joint strength of solder joints in laser packaging.

5. CONCLUSION

In summary, we have presented both the experimental and the FEM numerical results of the PbSn solder joint strength in laser diode and submount assembly under temperature cycling tests. Numerical calculations were in good agreement with the experimental measurements that the solder joint strength increased as the temperature cycle increased. This is may be due to the redistribution of the residual stresses within the solder during temperature cycling tests. This suggests that the FEM is an effective method for predicting the solder joint strength in laser diode packages.

ACKNOWLEDGMENT

This work was partially supported by the National Science Council, Republic of China under contract NSC 89-2215-E-110-009.

REFERENCES

1. D.S. Alles, "Trends in laser packaging," in Proc. 40th ECTC, pp. 185-192, 1990.
2. A.R. Mickelson, N.R. Basavanahally, and Y.C. Lee, Optoelectronic packaging, John Wiley & Sons, ch. 5, 1997.
3. C. Basaran, and R. Chandaroy, "Finite element simulation of the temperature cycling tests," IEEE Trans. Comp., Hybrids and Manuf. Technol., 20, pp. 530-536, 1997.
4. MARC Analysis Research Corporation, MARC 6.3, User Guide, Palo Alto, CA, 1996.
5. MARC Analysis Research Corporation, MENTAL II, User Guide, Palo Alto, CA, 1996.
6. "Bellcore Reliability Assurance Practices for Optoelectronic Devices in Loop Applications," TA-TSY-000983, Issue 1, Jan. 1990.
7. J.H. Lau, and Y.H. Pao, Solder joint reliability of BGA, CSP, flip chips, and fine pitch SMT assemblies, McGraw-Hill, ch. 4, 1997.
8. Metals Handbook, 8th Ed. 3, pp. 2-73 and 2-200 (Metals Park, OH: ASM, 1973).

Table I.

The Parameters Used in Simulation of Fiber-Solder-Ferrule.

Nodes	1636
Elements	3045
Elements of Invar/thickness	1149/1.5mm
Elements of solder/thickness	1014/0.2mm
Elements of Al ₂ O ₃ /thickness	66/0.75mm
Elements of Au/thickness	816/0.01mm
Element type	Plan strain arbitrary triangle elements

Table II.

The Physical Constants of the Young's Modulus, Poission Ratio, and CTE.

Material	Invar	Pb(37)/Sn(63)	Al ₂ O ₃	Au
Young's modulus (GPa)	141	32	304.6	82.7
Poission ratio	0.3	0.4	0.3	0.43
Yield strength (Mpa)	275.6	34.43	234.4	207

Table III

The Material Properties of Thermal Expansion Coefficient,
Thermal Conductivity, Specific Heat, Mass Density, and Melting Temperature.

Material	Invar	Pb(37)/Sn(63)	Al ₂ O ₃	Au
Thermal expansion coefficient (ppm/°C)	1.393	24.7	4.88	14.1
Thermal conductivity (W/mK)	16.4	50.6	22.7	318
Specific heat (J/kg°C)	258.6	128	1050	128
Mass density (Kg/m ³)	8080	1080	3750	19700
Melting temperature (°C)	1450	183	1600	1063

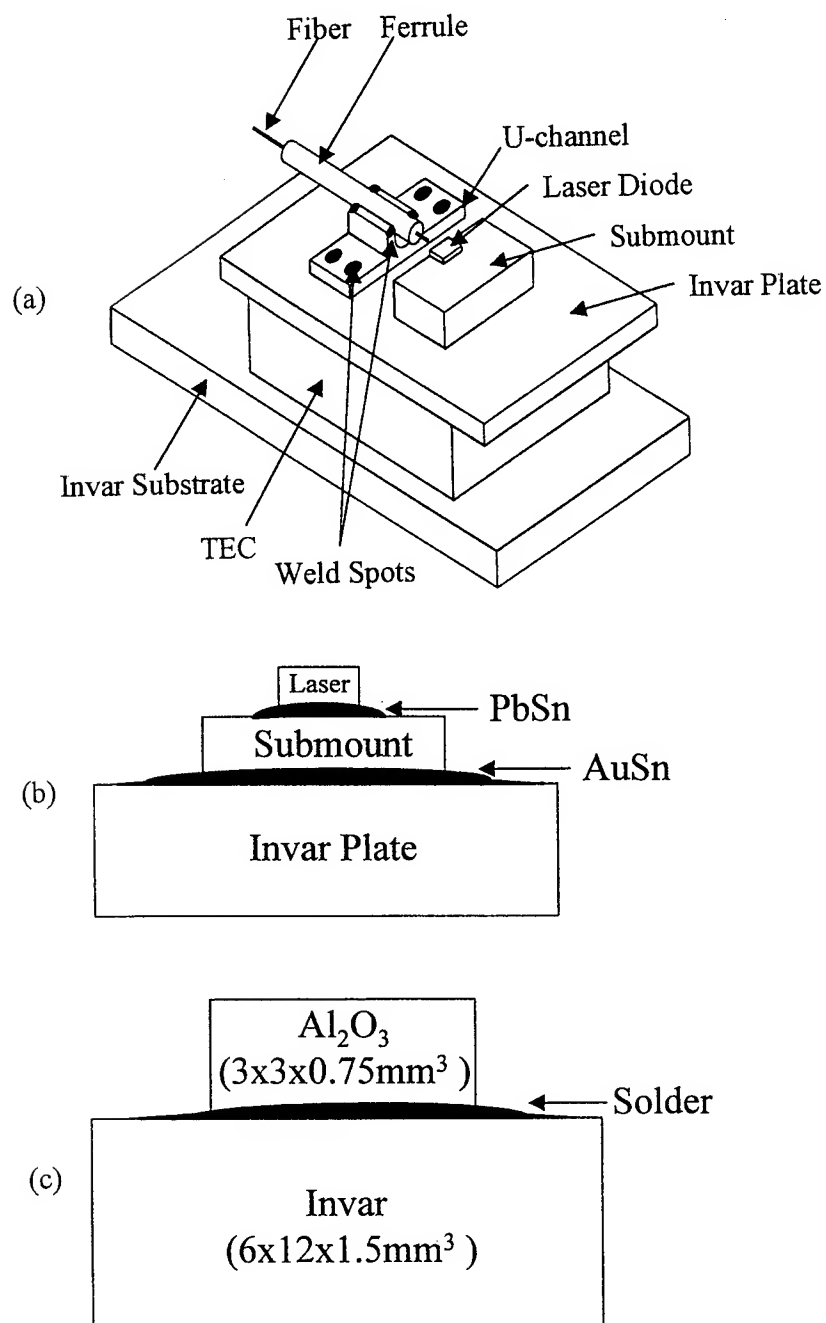


Fig. 1. (a) Schematic diagram of the top view of a DIP showing the pigtail fiber to laser connection, (b) a laser diode package, and (c) a submount-solder-substrate package.

Push Test

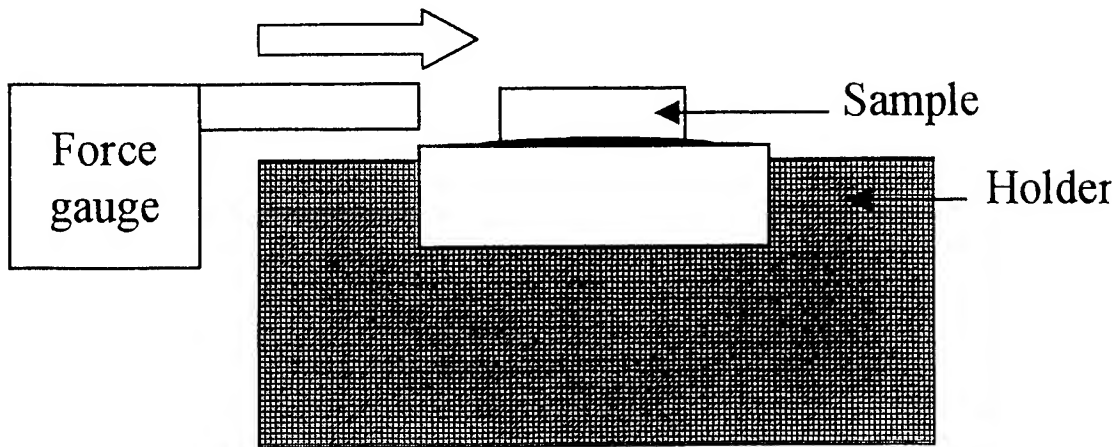


Fig. 2. A setup of push test fixture.

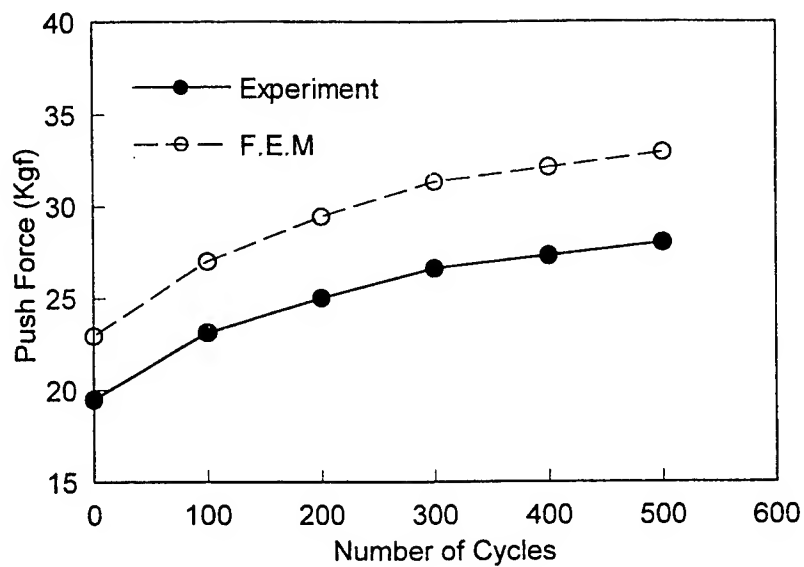


Fig. 3. The measurements and calculations of PbSn solder joint strength as a function of temperature cycle number.

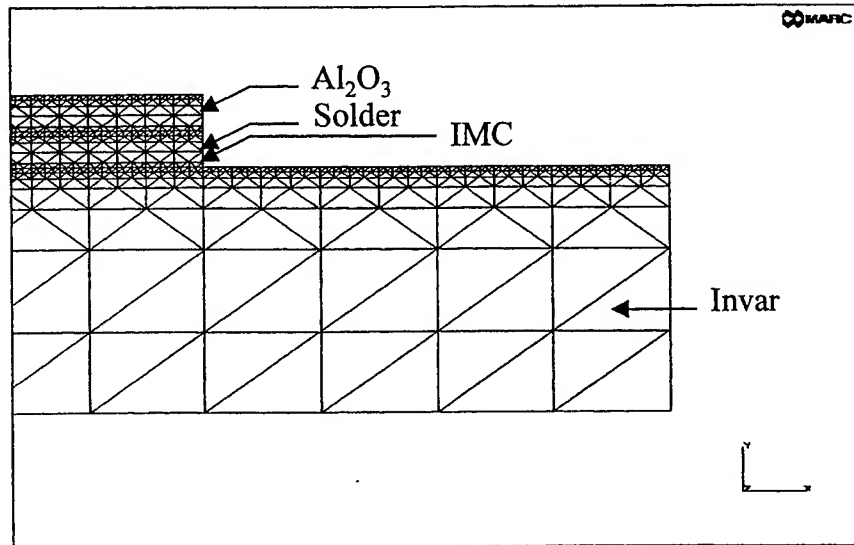


Fig. 4. A representative FEM model of a submount-solder-substrate.

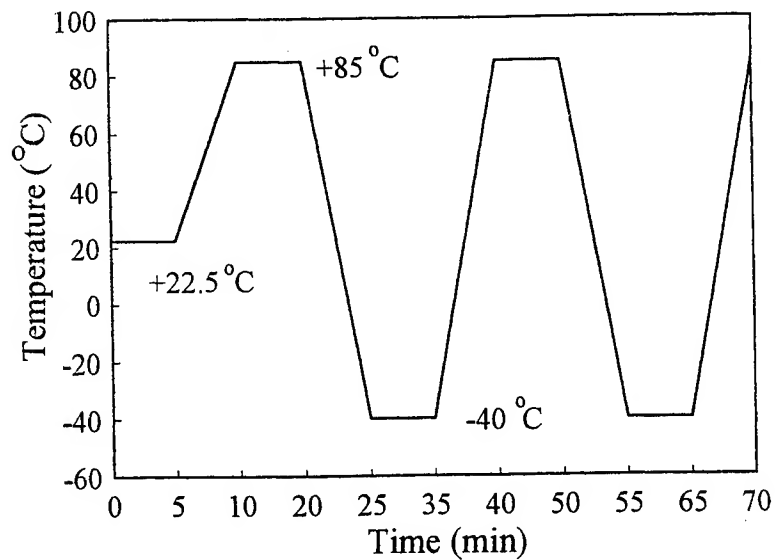


Fig. 5. A process of the temperature cycling test from -40°C to $+85^{\circ}\text{C}$.

Finite-Element Analysis of Fiber Shifts in Fiber-Solder-Ferrule Joints Using AuSn Solder

Maw-Tyan Sheen [#], Paul-Cheng Chen[#], Jao-Hwa Kuang [#], Gol-Lin Wang*, and Wood-Hi Cheng *

[#]Mechanical Engineering Department and *Institute of Electro-Optical Engineering,
National Sun Yat-sen University, Kaohsiung, Taiwan 804

Hung-Lun Chang, Szu-Chun Wang, Chungyung Wang, and Chih-Ming Wang
Chunghwa Telecom Laboratories, Yang-Mei, Taoyuan, Taiwan 326

ABSTRACT

The thermally induced fiber alignment shifts of fiber-solder-ferrule (FSF) joints in laser module packaging under temperature cycling tests have been studied numerically by a elastic-plastic finite-element method (FEM). The FSF joints were assembled by using both the Pb(37)/Sn(63) and Au(80)/Sn(20) solders. Comparison between calculated results shows that the Au/Sn solder in the FSF joint exhibits three times less fiber shift than Pb/Sn solder. This is due to the higher Young's modulus, yield strength, and melting temperature of AuSn hard solder than PbSn soft solder. This suggests that the hard solder of Au/Sn is more suitable use in FSF assembly than soft solder of Pb/Sn for laser module packaging to reduce the thermally induced fiber alignment shift. Numerical calculations show that the major cause of fiber shift in FSF joints may come from the plastic solder yielding introduced by the thermal stress variation and the redistribution of the residual stresses during temperature cycling.

Keywords: Fiber alignment shift, temperature cycling, laser packaging, finite-element method

1. INTRODUCTION

Temperature cycling tests are commonly used in the semiconductor industry to characterize the thermal fatigue failure and to predict reliability of the solder joints in the microelectronics packaging technology¹. Although other mechanisms, such as vibration, mechanical and thermal shocks, and humidity, may lead to solder joint failure, the primary mechanisms are caused by thermal and residual stresses during temperature cycling tests. For high performance laser-based transmitters in lightwave communication systems, box-type packages of the dual-in-line package (DIP) and butterfly package with fiber pigtailed are widely used²⁻³. Box-type packages allow enough room for an assembly thermoelectric cooler (TEC) component to keep laser operation at almost a constant temperature. The connected components of the DIP or butterfly package have different material properties and have different coefficients of thermal expansion (CTE), thermal conductivities, Poisson's ratios, and yield strengths. As a result of temperature cycles, the fluctuation of the thermal stress may introduce some thermal yielding locally and redistribute the residual stresses in the solder joints. An alignment shift of the fiber in the DIP or butterfly package may occur. Therefore, how to minimize the fiber alignment shift in the temperature cycling test is one of the key research topics for the study of yield and reliability in optoelectronic packaging applications.

There are so many components in the DIP or butterfly packages that it is difficulty to identify the specific components those should responsible for the fiber alignment shift under temperature cycling tests. In this work, we have studied the fiber alignment shift introduced in the key component, the fiber-solder-ferrule (FSF) assembly in the DIP.

2. LASER MODULE PACKAGE

2.1 Laser Package

A top view of a laser dual-in-line package (DIP) is shown in Fig. 1. The laser DIP consisted of a 1.3 μm laser, the Invar housing materials, a thermoelectric cooler (TEC), and a single-mode fiber. Fig. 2 shows a FSF packaging that is a part of DIP. The ends of metallized optical fibers are often sealed by soldering into ferrules prior to use in laser welding processes for joining between the ferrule and clip⁴⁻⁶. Obviously, the solder joint in an FSF assembly must be able to withstand higher thermal stress under temperature cycling and aging conditions. Various types of solder, such as Sn/Pb, In, Au, and Sn/Au, have been used for sealing between the metallized fiber and metal support ferrule⁴.

Both lead-tin, Pb(37)/Sn(63) ($T_m = 183^\circ\text{C}$), and gold-tin, Au(80)/Sn(20) ($T_m = 280^\circ\text{C}$) have been used in FSF assemblies to form the solder joints. Soft solders (low melting temperature) of Pb/Sn are often used to reduce both the stress caused by coefficients of thermal expansion (CTE) mismatch between the laser and submount and the operation temperature of the solder solidus. Soft solders exhibit low yield stress and are subject to the slow creep effect. Hard solders (high melting temperature) of Au/Sn exhibit higher yield strength and less creep effect. However, hard solders melting at higher temperatures and may cause a significant stress in the package⁷.

Due to the solidification shrinkage of the solder in the FSF assembly, the fiber is difficult to locate at the center of the ferrule tube. An undesired eccentric offset can be introduced. The fiber eccentric offset of an FSF assembly was specified by the center distance between the fiber and ferrule. In this work, we numerically studied the thermally induced fiber shifts of FSF joints with different fiber offsets in temperature cycling tests using both of the Au/Sn and Pb/Sn solders.

2.2 Temperature Cycling Test

The process of temperature cycling test was followed the Bellcore Reliability Assurance Practices of TA-TSY-000983⁸. During the temperature cycling test, the temperature was changed from -40 to 85°C within a 3 hours cycle. The ramp rate was greater than $10^\circ\text{C}/\text{min}$ and the dwell time was 30 min for a total of 500 cycles. The fiber shifts were measured and recorded for every 100 cycles.

3. FINITE-ELEMENT METHOD (FEM)

3.1 Finite-Element Model

Numerical calculations of the distribution of the residual stresses in the solidification, the fluctuation of the thermal stresses and fiber center shifts in the FSF joint during temperature cycling were performed by using the commercial MARC⁹ and MENTAT¹⁰ finite element packages. A plane strain triangular element model with the temperature-dependent material properties was employed in this work. The diameters of the ferrule, solder, and fiber were 0.9, 0.4, and 0.125 mm, respectively. Table I lists the finite element parameters used in the simulation. Fig. 3 shows a representative FEM model of an FSF joint with the fiber near the center. Due to the geometry of the FSF assembly as shown in Fig. 2, a cross section of the solder area was meshed for the FEM simulation. Meshes with triangle type elements were created with an automatic mesh generator.

3.2 Material Properties

The physical constants and material properties of Inver ferrule, Pb/Sn and Au/Sn solders, and fiber at room temperature used in the simulation are listed in Table II and III, respectively¹¹. The values of the CTE, Young's modules, yield strength, Poisson's ratios, thermal conductivity, and specific heat are considered temperature dependent. Because of the limit of the experimental data available for the Inver, the temperature dependence of these material properties near the melting temperature region were assumed to have a tendency similar to that of stainless steel (SS) 304L. The material properties as a function of temperature for SS 304L were obtained from the Metals Handbook¹².

3.3 Boundary and Initial Conditions

In this FEM model, the boundary nodes were considered free besides the most right and the most left edge points. The most right node is constrained and the most left edge node is considered only free horizontally. To calculate the residual stresses, the solder was assumed to be heated from the ambient temperature of 22.5°C to 195°C (Pb/Sn) or 295°C (Au/Sn) in 20 ms initially. Then the whole ferrule system was cooled down to ambient temperature with the assumption of free convection around the boundary. The calculated cooling time was about 180 ms in this study. The melting temperature of the Pb/Sn and Au/Sn solders in the melting area were 183°C and 280°C , respectively. The residual stresses caused from the CTE mismatch and the solidification shrinkage of the solder were calculated. In the simulation of the temperature cycling test, the surrounding temperature varied from -40 to 85°C within a 3 hours cycle⁸.

3. FEM SIMULATION RESULTS

Five FSF assemblies with different fiber eccentric offsets, e.g. 75, 80, 86, 95, and $103\ \mu\text{m}$, are used for fiber center shift simulations undergoing different temperature cycles. Figs 4 and 5 show the thermal stress variations of Pb/Sn and Au/Sn

solders at a node point which is near the fiber with an initial eccentric offset of 86 μm , respectively. Results indicate that the Au/Sn solder exhibits four times higher thermal stress peaks than Pb/Sn solder. This is due to the higher initial residual stresses within the Au/Sn solder introduced by the solidification process.

Fig. 6 shows the fiber displacement shifts of Au/Sn and Pb/Sn solders as the function of cycle number for different fiber offsets. Results in Fig. 6 indicate that the simulated fiber shifts depend upon the cycle number and the initial fiber eccentric offsets. Generally, the fiber shifts are increased as the cycle number increased. Up to a 1 and 0.3 μm fiber shifts were predicted after 500 temperature cycling tests for Pb/Sn and Au/Sn solders, respectively. Comparison between the calculated results shows that the Au/Sn solder in the FSF joints exhibits three times less fiber shift than Pb/Sn solder. This is due to the higher Young's modulus, yield strength, and melting temperature of Au/Sn hard solder than Pb/Sn soft solder. This suggests that the hard solder of Au/Sn is more suitable use in FSF assembly than soft solder of Pb/Sn for laser module packaging to reduce the thermally induced fiber alignment shift. Numerical calculations show that the major cause of fiber shift in FSF joints may come from the plastic solder yielding introduced by the thermal stress variation and the redistribution of the residual stresses during temperature cycling.

Fig 7 shows the fiber center shifts of Au/Sn and Pb/Sn solders are the function of cycle number and the initial fiber offsets at the early cycling tests. Results in Fig. 7 show that the Au/Sn solder in FSF joint always has a larger initial post-weld-shift introduced in the solder solidification process. However, this post-weld-shift of Au/Sn solders increase much slower than Pb/Sn solders as the temperature cycle undergoes, as shown in Fig. 6. This indicates that hard solder of Au/Sn has less sensitive to the temperature cycle loading.

4. CONCLUSION

In summary, we have presented the FEM numerical results of the thermally induced fiber alignment shifts of fiber-solder-ferrule (FSF) joints in semiconductor laser module packaging. Up to a 1 and 0.3 μm fiber shifts were predicted after 500 temperature cycling tests for Pb/Sn and Au/Sn solders, respectively. This suggests that the hard solder of Au/Sn is more suitable use in FSF assembly than soft solder of Pb/Sn for laser module packaging to reduce the thermally induced fiber alignment shift. These results can be used for design the high-performance laser module packages for use in lightwave communication system applications.

REFERENCES

1. C. Basaran, and R. Chandaroy, "Finite element simulation of the temperature cycling tests," *IEEE Trans. Comp., Hybrids and Manuf. Technol.*, **20**, pp. 530-536, 1997.
2. D.S. Alles, "Trends in laser packaging," in *Proc. 40th ECTC*, pp. 185-192, 1990.
3. J. H. Kuang, M.T. Sheen, S.C. Wang, C.H. Chen, and W.H. Cheng, "Crack formation mechanism in laser-welded Au-coated Invar materials for semiconductor laser packaging," *IEEE Trans. Comp., Hybrids and Manuf. Technol.*, **22**, pp. 94-100, 1999.
4. E. Suhir, "Thermally induced stresses in an optical glass fiber soldered into a ferrule," *J. Lightwave Technol.*, **12**, pp. 1766-1770, 1994.
5. W.H. Cheng, Y. D. Yang, S.C. Wang, S. Chi, M.T. Sheen, and J. H. Kuang, "Effect of Au thickness on laser beam penetration in semiconductor laser packages," *IEEE Trans. Comp., Hybrids and Manuf. Technol.*, **20**, pp. 396-402, 1997.
6. W.H. Cheng, M.T. Sheen, and J. H. Kuang, and C.H. Chen, "The principle cause of crack defects in optoelectronic materials with phosphorus-containing underlayer," *J. Electronic Materials*, **28**, pp.50-56, 1999.
7. A.R. Mickelson, N.R. Basavanahally, and Y.C. Lee, *Optoelectronic packaging*, John Wiley & Sons, ch. 5, 1997.
8. "Bellcore Reliability Assurance Practices for Optoelectronic Devices in Loop Applications," TA-TSY-000983, Issue 1, Jan. 1990.
9. MARC Analysis Research Corporation, MARC 6.3, User Guide, Palo Alto, CA, 1996.
10. MARC Analysis Research Corporation, MENTAL II, User Guide, Palo Alto, CA, 1996.
11. J.H. Lau, and Y.H. Pao, *Solder joint reliability of BGA, CSP, flip chips, and fine pitch SMT assemblies*, McGraw-Hill, ch. 4, 1997.
12. *Metals Handbook*, 8th Ed. **3**, pp. 2-73 and 2-200 (Metals Park, OH: ASM, 1973).

Table I.

The Parameters Used in Simulation of Fiber-Solder-Ferrule.

Nodes	685
Elements	1332
Elements of Invar	360
Elements of solder	432
Elements of Fiber	540
Diameter of Model	0.9mm
Element Type	Quadratic quadrilateral Elements

Table II.

The Physical Constants of the Young's Modulus, Poisson Ratio, and CTE.

Material	Invar	Pb(37)/Sn(63)	Au(80)/Sn(20)	Fiber
Young's modulus (GPa)	141	32	59	8
Poisson ratio	0.3	0.4	0.4	0.23
Yield strength (Mpa)	34.45	34.43	275	34.45

Table III

The Material Properties of Thermal Expansion Coefficient, Thermal Conductivity, Specific Heat, Mass Density, and Melting Temperature.

Material	Invar	Pb(37)/Sn(63)	Au(80)/Sn(20)	Fiber
Thermal expansion coefficient (ppm/ $^{\circ}$ C)	1.393	24.7	16	0.55
Thermal conductivity (W/mK)	16.4	50.6	251	165.43
Specific heat (J/kg $^{\circ}$ C)	258.6	128	128	840
Mass density (Kg/m 3)	8080	1080	1451	2800
Melting temperature ($^{\circ}$ C)	1450	183	280	500

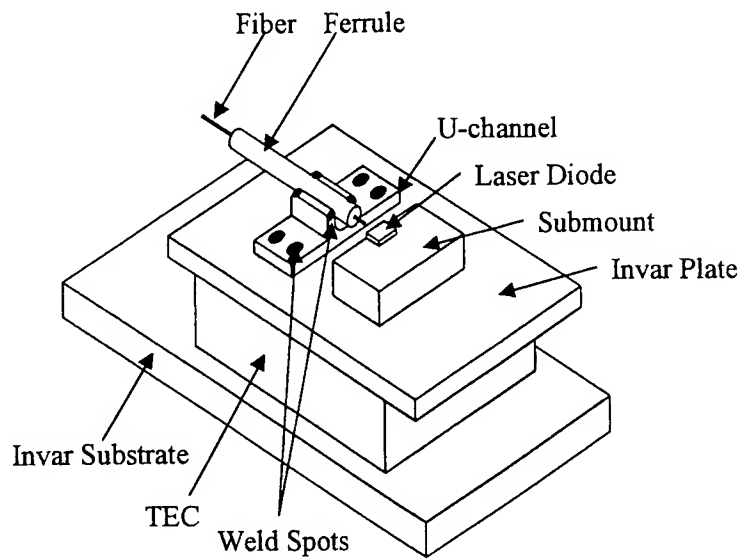


Fig. 1. Schematic diagram of the top view of a DIP showing the pigtail fiber to laser diode connection.

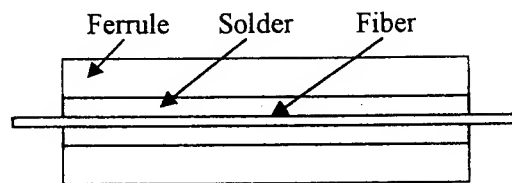


Fig. 2. A ferrule-solder-fiber (FSF) joint.

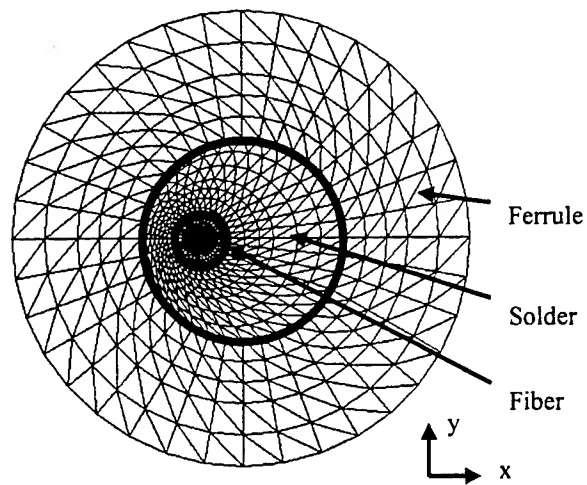


Fig. 3. A representative FEM model of an FSF joint with the fiber near the center.

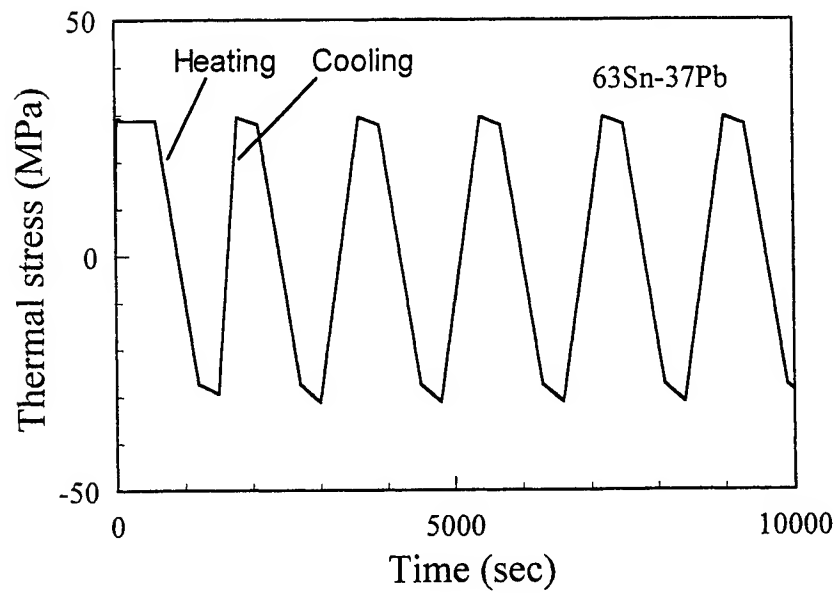


Fig. 4. The thermal stress of PbSn solder in FSF assembly as a function of time at node point of near fiber.

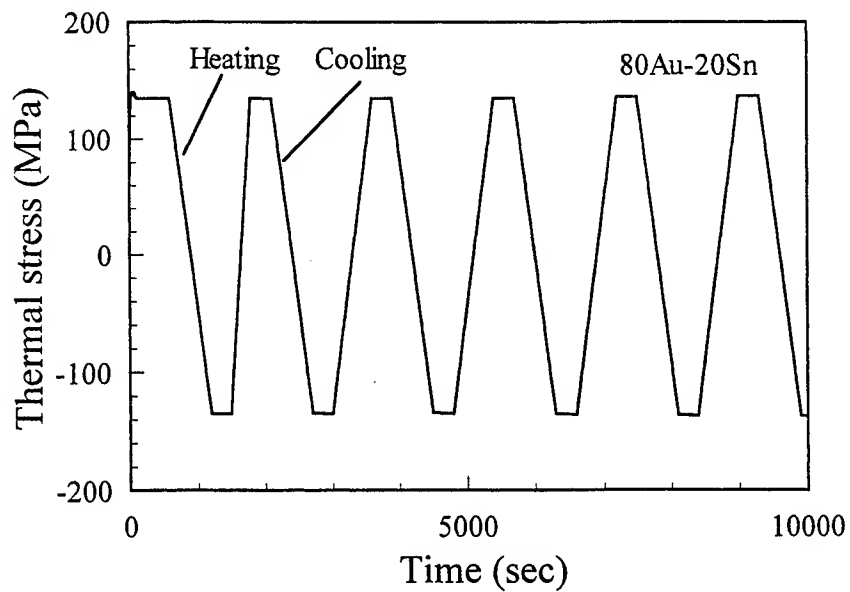


Fig. 5. The thermal stress of AuSn solder in FSF assembly as a function of time at node point of near fiber.

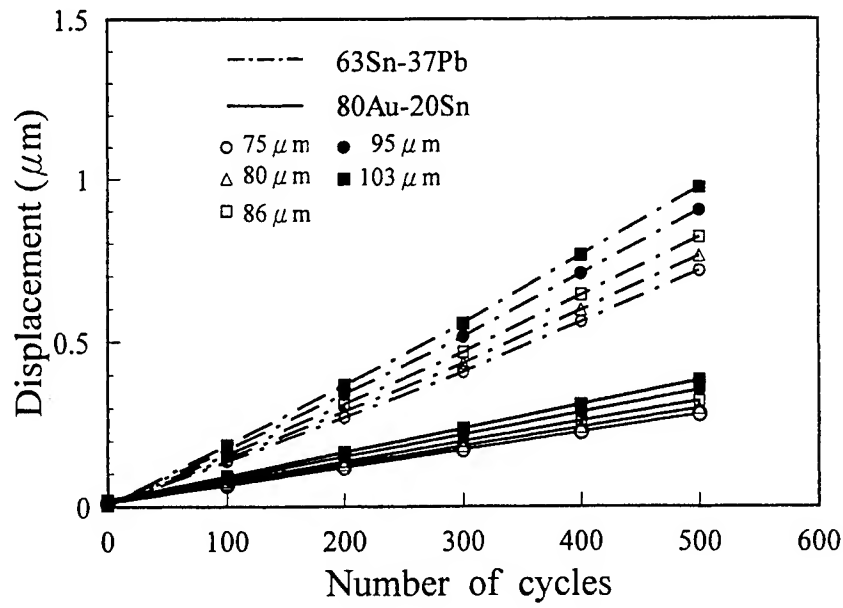


Fig. 6. The calculated fiber displacement shifts of FSF joint as a function of the cycle number for different fiber eccentric offsets.

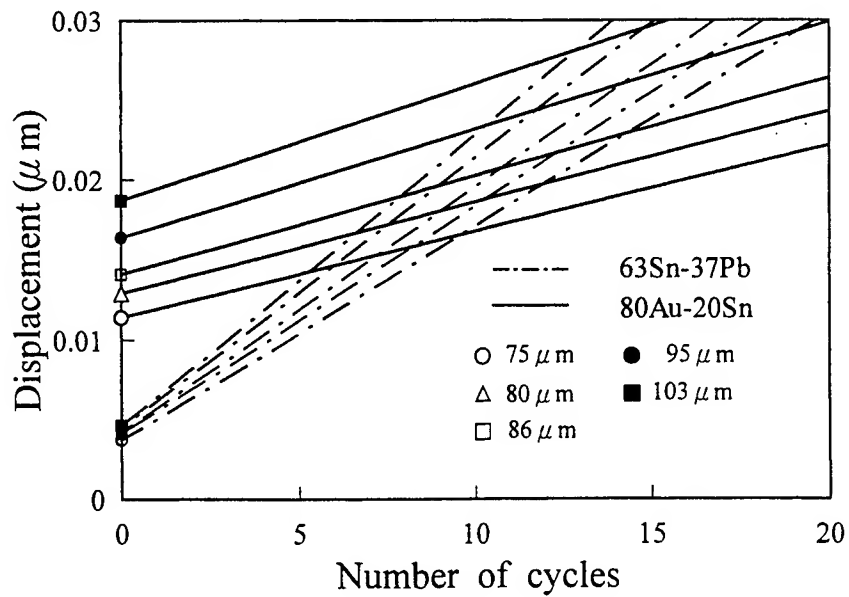


Fig. 7. The calculated fiber displacement shifts of FSF joint as a function of the cycle number for different fiber eccentric offsets at the initial temperature cycling tests.

Stress Distributions in Patterned-Substrate InGaAs/InP

Jacques Lefebvre, Geof C. Aers, Philip J. Poole and Robin L. Williams

^aInstitute for Microstructural Sciences, National Research Council Canada, Ottawa, Ont K1A 0R6, Canada

ABSTRACT

Under appropriate conditions, the growth of InGaAs/InP on patterned InP substrates leads to the development of atomically smooth triangular structures with [111]B sidewalls and embedded InGaAs quantum wells. Using finite element methods, we examine how the stress distribution arising from embedded compressive and tensile quantum well influences the subsequent growth of self-assembled InAs quantum dots on the sidewalls. By calculating the total strain energy of the structure we show that the InAs dots would locate preferentially along the sidewall near the location of a compressive quantum well and away from a tensile quantum well. We also show that the size distribution can be narrowed in a three-layer structure that consists of one compressive quantum well sandwiched between two tensile quantum wells.

Keywords: Quantum dots, stress, Stranski-Krastanov.

1. Introduction

The control of self-assembled dot (SAD) location and size distribution are two important issues that have to be addressed in order to challenge quantum wells as the basis of optical communications¹. On a fundamental point of view, mastering SAD location and size distribution would open up a wide range of new experiments on the interaction between small ensembles of similar SADs. However, the current Stranski-Krastanov growth mode that leads to the formation of SADs on crystalline substrates very often produces a rather broad size distribution and a quasi-random spatial distribution. The SAD formation results from an interplay between surface and strain energy, the latter building up as a consequence of an important difference in SAD and host lattice parameters. The broad size distribution is the consequence of a total energy, obtained from strain and surface energy, being a slowly varying function with a broad minimum as a function of SAD height/width. The quasi-random location is due to the spatial invariance of the underlying substrate, and to the weak interaction between SADs during growth. In this paper, we propose ways to steep the strain energy function and to break the translational symmetry. We report stress distribution and strain energy calculations based on a finite element method and find that InGaAs quantum wells imbedded in a re-grown InP mesa with [111]B facets produces a stress distribution that should affect both the location and size distribution of InAs SADs.

2. Finite element method

The effect of strain templating on InAs SADs can be described by a finite element model where the elastic deformation of quantum well and quantum dot materials is calculated within a lattice mismatched matrix. The calculation is two-dimensional as it assumes translational invariance along the length of a patterned mesa (plane strain approximation). A step-by-step description of the finite element method can be found in Ref. 2.

Since our model assumes translational invariance, it is rigorously valid only for wires, but we believe that the general conclusions should hold for SADs. In structures including SADs, we suppose the calculated energy per unit length is the same for the SAD as for the actual quantum wire structure. In practice, we expect the elastic energy for the dot to be slightly smaller due to strain relaxation at the additional dot edges introduced on segmenting the quantum wire, although we do not expect the difference to be important for dot dimensions greater than a few nanometers. In the following, InAs structure on the (111)B facet will be referred to as a SAD, keeping in mind the considerations just mentioned. In these calculations, the main effect that determines the equilibrium elastic configuration will be the lattice mismatch between the quantum well or dot and the InP matrix. Differences in the elastic coefficients, C_{ij} , between the semiconductor binaries InAs, GaAs and InP are considered small enough to be ignored.

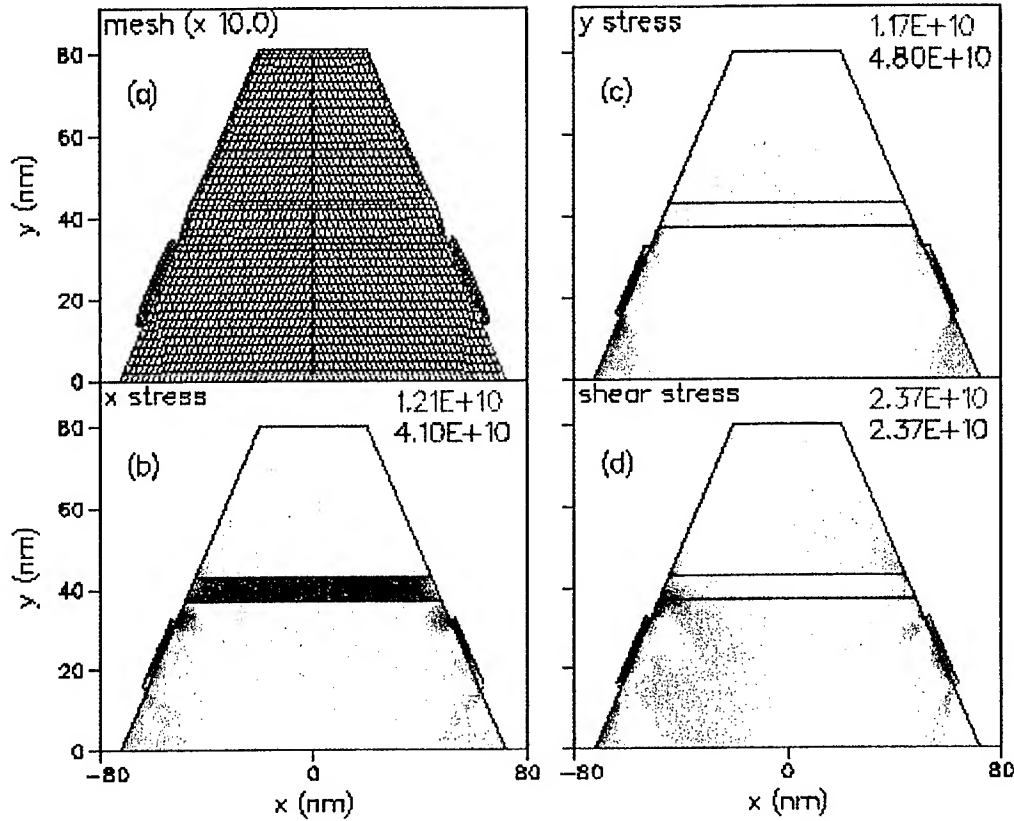


Fig. 1: Finite element calculations showing (a) the equilibrium mesh, (b) x-stress, (c) y-stress and (d) shear-stress distribution for a 2 nm thick, 20 nm wide InAs quantum dot on the (111)B sidewall of an InP patterned substrate template incorporating a 6 nm compressively strained $\text{In}_{0.7}\text{Ga}_{0.3}\text{As}$ quantum well. The maximum compressive, tensile and shear stresses are given in dynes/cm².

In Fig. 1(a) we show the equilibrium finite element mesh for a typical InP template in which we have incorporated a lattice mismatched InGaAs quantum well. $\text{In}_x\text{Ga}_{1-x}\text{As}$ quantum wells in InP can be either under compressive or tensile stress if $x > 0.53$ or $x < 0.53$ respectively. For these calculations, we have used eight-node isoparametric quadrilaterals and six-node isoparametric triangles. To help in visualizing the effects of strain, all displacements in these diagrams have been enhanced by a factor of 10. The mesh also includes an InAs quantum dot structure placed on the (111)B sidewall, just below the quantum well. For this example, we have chosen a 6 nm $\text{In}_{0.7}\text{Ga}_{0.3}\text{As}$ quantum well, so that the well is compressively strained in the bulk of the material. At the (111)B edge of the InP template, the free surface imposes a zero normal stress boundary condition, which allows the compressive quantum well to bow outwards from the surface. Such effects have recently been seen in cleaved edge InGaAs/InP material and the resulting surface displacements measured using STM techniques³. The InAs quantum dot structure placed on this surface is constrained by the InP lattice parallel to the surface but is free to expand in the perpendicular direction.

To quantify the details of elastic displacement, we extract the elastic stress distribution across the patterned InGaAs/InP structures. Calculated x-, y- and shear-stress maps are shown in Figs. 1(b), (c) and (d) respectively for the structure discussed above. These stress maps are color coded with blue representing compressive stress and red representing tensile stress or clockwise and counter clockwise respectively in the case of the shear-stress. The color representation is non-linear, so that low stress concentrations are accentuated. In the bulk of the template, the InGaAs quantum well shows a strong compressive x-stress as expected from the difference in lattice constant between the InGaAs well material and the InP cladding. In the region around the (111)B facet, the quantum well x-stress is considerably relaxed and is even slightly tensile. In this same region, the quantum well y-stress becomes highly tensile, in contrast to a value near zero in the bulk of the template. For wide enough InP mesa structures, the quantum well y-stress vanishes in the bulk in agreement with the infinite plane case. The x-

and y-stresses in the InAs quantum dot are seen from Fig. 4 to be highly compressive as expected, although these diminish considerably at the dot edges. Conversely, the InAs dot induces a slight tensile stress in the underlying region of the template, except near the dot edges where the template stress is again compressive. Finally, the shear-stress distribution for this structure is shown in Fig. 1(d). For the quantum well, shear stress concentrations are developed at the (111)B surface in comparison with much lower values at the mesa center. Shear stresses in the quantum dot appear mainly as a result of the dot placement at an angle to the normal x- and y-directions. The anti-symmetry of the shear-stress map reflects the symmetry of the twisting motion involved in the elastic displacement field.

3. Control of dot location

Using stress maps such as that shown in Fig. 1 and the corresponding strain fields, we calculate the elastic energy of the system for various positions of the InAs quantum dot. The energy as a function of dot position along the (111)B sidewall is shown in Fig. 2 for two different quantum dot thicknesses and for three different quantum dot widths. The energy displayed in these figures is $\Delta E/E_d = (E_w - E_t)/E_d$, where E_w is the energy of the complete structure including well and dot, E_t is the energy of the template alone and E_d is the energy of the dot on the (111)B facet in the absence of the quantum well. $(E_w - E_t)$ thus represents the additional energy due to the SAD and is simply equal to E_d when the SAD is far from the well. As a result, when the dot location is far from the well on either side, Fig. 2 displays energy values close to 1. Also, the normalizing factor E_d emphasizes the benefit of placing the SAD near the quantum well.

In Fig. 2(a), we see that placing the quantum dot in the vicinity of the compressive quantum well reduces the strain energy cost of creating the dot by approximately 30%. For these 20 nm wide quantum dots, the energy minimum is seen to occur somewhat above the position of the quantum well, i.e. nearer to the top of the InP template. Considering the stress distributions shown in Fig. 1, we believe this to be a result of the tensile y-stress induced in the structure above the quantum well, resulting in an expanded lattice constant more favourable to the InAs quantum dot. From Fig. 2(a), the position of the energy minimum is seen to be relatively insensitive to the quantum dot thickness. In Fig. 2(b), the position of the strain energy minimum is examined as a function of the quantum dot width for a fixed dot thickness of 2 nm. For a 10 nm wide dot, the energy minimum lies within the quantum well, whilst as the quantum dot width increases, the minimum position moves to positions slightly above the quantum well. The shift in the position of the energy minimum is also accompanied by a substantial broadening. These observations illustrate how the InAs quantum dot shifts position to avoid the more compressive stresses below the quantum well. The broadening of the energy minimum occurs when the dot width exceeds the extent of the underlying tensile stress induced by the quantum well, so that a convolution between the width of the quantum dot and the extent of the underlying tensile strain is observed.

Based on the results discussed to this point, one should be able to position self-organized InAs quantum dots on these strained templates within distances of approximately 10 nm. We have presented results for quantum dots placed on the (111)B surface in the absence of an InAs wetting layer. Using the finite element model we have verified that wetting layers of a few monolayers thickness have a negligible effect on the equilibrium location of InAs quantum dots positioned using the techniques described above.

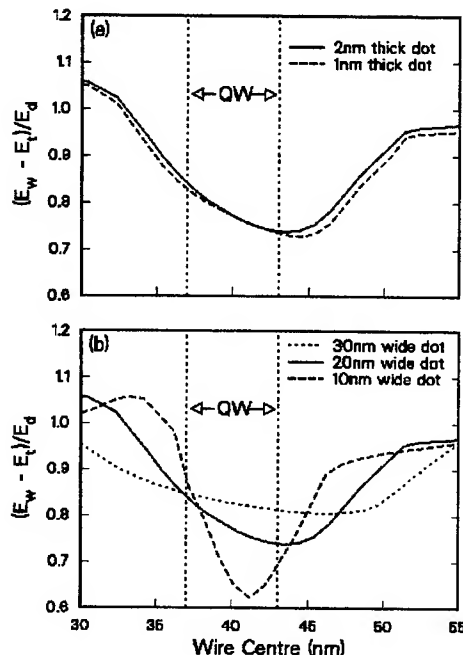


Fig. 2: Elastic strain energy as a function of dot position along the (111)B facet for (a) a 20 nm wide InAs quantum dot and (b) a 2 nm thick InAs quantum dot. The zero of position corresponds to the lower edge of the template in Fig. 1.

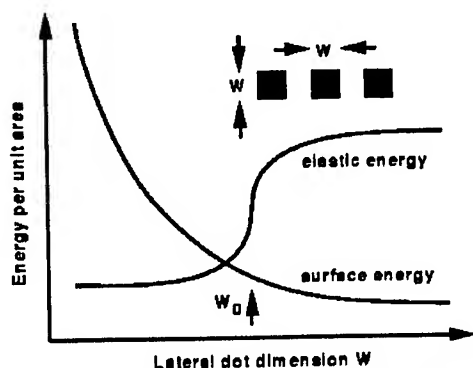


Fig. 3: Schematic diagram showing the contributions of elastic strain energy and surface energy to the total energy for an ensemble of dots located over a compressively strained quantum well. Each dot is assumed to be a square plate of side W .

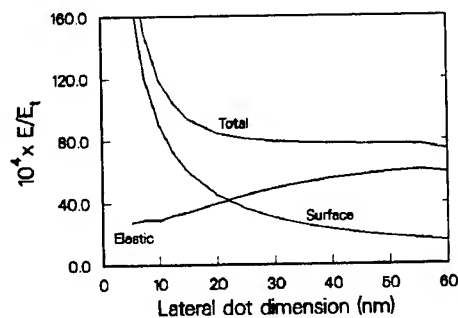


Fig. 4: Total energy per unit area of deposited InAs including elastic strain and surface energy contributions for an ensemble of dots as a function of lateral dot dimension W . The strain template corresponds to the single compressive quantum well structure of Fig. 1.

4. Control of dot lateral size.

Given that one can locate InAs quantum dots using strained quantum well stressors, the question arises as to whether one can also influence the lateral dimension of the dots. To investigate this question using our present elastic model, we make an assumption regarding the equilibrium shape of the quantum dots. For CBE grown InAs SADs on (001) InP material, we have shown recently that the dots are approximately square⁴, and we make the assumption that the dots remain square on the (111)B sidewalls. We also assume that the size of the quantum dot can be obtained as a balance between the surface energy and the elastic energy, so that we ignore any influence of the growth dynamics in determining the size. Under these approximations and assuming that the dots are positioned at the energy minimum discussed previously, the features determining the quantum dot lateral dimensions are shown schematically in Fig. 3.

In addition to the template energy E_t defined previously, an ensemble of dots will contribute both elastic and surface energy terms to the total energy of the system. We consider an area (A) of sidewall covered with a layer of InAs (thickness t), and for the sake of calculation, A is normalized per unit length of sidewall. The additional energy, $E(W, A) - E_t$ (per unit length), for cutting an area A into an ensemble of N dots ($N = A/W^2$, per unit length) of lateral dimension W and thickness t is given by

$$E(W, A) - E_t = NE_w W - NE_t W + 4NtE_s W \quad (1)$$

The first two terms represents the elastic contribution from the dot covered regions of the sidewall, and the last term is the surface energy contribution. Equation (1) can be written

$$E(W, A) = \frac{A}{W} (E_w - E_t) + \frac{A}{W} 4tE_s \quad (2)$$

A/W reflects the fraction of sidewall covered by dots. The surface energy contribution, as illustrated in Fig. 3, reflects the reduction in *ensemble* surface area as the lateral extent of individual dots increases at fixed A . For InAs, the surface energy per unit area E_s , is set to $42 \text{ meV}/\text{\AA}^2$, in agreement with recent data⁵.

Fig. 3 illustrates the expected behavior for the dot elastic energy as a function of dot size. At small values of W , the deposited InAs is strained to fit the quantum well lattice constant, whilst at large values of W , material being added at the wire edges is strained to fit the InP matrix. In both limits this results in a strain energy, E_w , that varies linearly with W , and therefore, the elastic contribution to the total energy of the dot *ensemble* is expected to become independent of W at both high and low W . The transition between these limiting values is expected at a width, W_0 , determined by the lateral extent of the quantum well strain field on the (111)B facet. In Fig. 4, we show the additional energy per unit area of deposited InAs, with surface and elastic contributions, calculated for the 6 nm compressive $\text{In}_{0.7}\text{Ga}_{0.3}\text{As}$ quantum well structure discussed previously. All

energies are normalized to the template energy, E_t . The surface and elastic strain contributions to the total energy have the general form discussed above, although the transition from the low to high W regimes is quite broad and not particularly well defined. In this case, the total energy decreases monotonically with increasing W , indicating that strain energy penalty arising from increased SADs lateral dimension is smaller than the decrease in surface energy. In order to obtain the desired size constraint, it is necessary to increase this energy penalty.

As mentioned above, at large values of W , the increasing strain energy arises from InAs accommodating the in-plane lattice constant of the InP matrix. At large W , we must therefore strain the InAs dot material to a lattice constant even less favorable than InP. This can be achieved if we incorporate tensile strained InGaAs quantum wells on either side of the original compressively strained quantum well. When the dot lateral dimensions are large enough to encompass the tensile quantum wells, we would expect a significant strain energy penalty. In Fig. 5, we show the total energy associated with the type of structure suggested above. In the case of Fig. 5(a), we have chosen a 10 nm $\text{In}_{0.7}\text{Ga}_{0.3}\text{As}$ quantum well bounded on one side by a 10 nm $\text{In}_{0.45}\text{Ga}_{0.55}\text{As}$ quantum well and on the other by a 5 nm $\text{In}_{0.36}\text{Ga}_{0.64}\text{As}$ quantum well. The structure is chosen to be strain neutral overall in the bulk, so that the compressive strain of the center well is compensated by the tensile strain of the wells on either side. Due to the presence of the tensile quantum wells, the total energy now has a minimum at a lateral dot dimension of approximately 30 nm, suggesting that such a structure should influence the quantum dot dimensions and hence the excited state spectrum of such dots. With this particular structure, which has not been optimized, the magnitude of the energy minimum is not particularly large, representing a reduction of approximately 15% in the asymptotic value at large dimensions. To enhance the dot size selectivity, a number of strategies are possible, including increasing the compressive stress of the center well and increasing the tensile stress of the bounding wells. In Fig. 5(b) we show the total energy variation with W for such a structure in which we have increased the composition of the top well to 82% gallium. The position of the energy minimum remains unchanged in this case, since it is determined primarily from the separation between the two tensile wells. However, the depth of the energy minimum has increased substantially, representing approximately 25% of the large W asymptotic value.

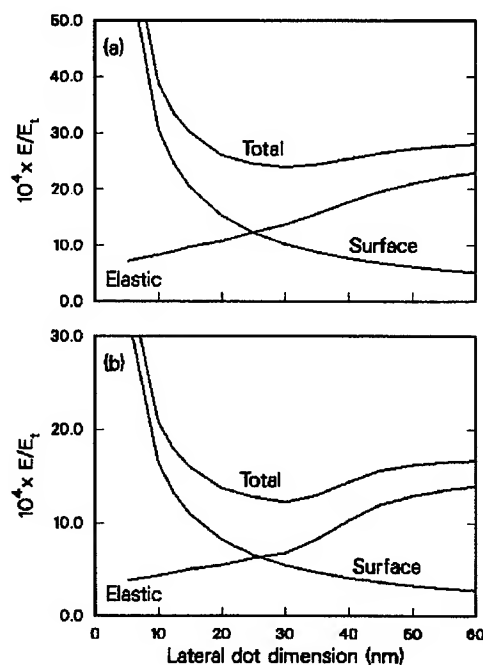


Fig. 5: Total energy per unit area of deposited InAs including elastic strain and surface energy contributions for an ensemble of dots as a function of lateral dot dimension W . Panels (a) and (b) correspond to the multi-well template structures discussed in the text.

5. References

1. J. Lefebvre, P. J. Poole, C. P. Lee, S. F. Hu, G. C. Aers, and R. L. Williams, "One-dimensional arrays of self-assembled InAs/InP quantum dots", this conference 4078-18.
2. Finite Element Analysis, From Concepts to Applications by Davis S. Burnett, (Addison-Wesley, 1987)
3. H. Chen, R. M. Feenstra, P. G. Piva, R. D. Goldberg, I. V. Mitchell, G. C. Aers, P. J. Poole, and S. Charbonneau, "Enhanced group-V intermixing in InGaAs/InP quantum wells studied by cross-sectional scanning tunneling microscopy", *Appl. Phys. Lett.* **75**, pp. 79-81 (1999).
4. P. J. Poole, R. L. Williams, J. Lefebvre, J. McCaffrey, C. Lacelle and G.C. Aers, submitted to *Appl. Phys. Lett.*
5. N. Moll, M. Scheffler, and E. Pehlke, "Influence of surface stress on the equilibrium shape of strained quantum dots", *Phys. Rev. B* **58** pp. 4566-4571 (1998)

OPTICAL AND TRANSPORT PROPERTIES OF MOCVD-GROWN InSb THIN FILMS

T. R. Yang^{*,a}, G. Kuri^a, M. R. Kim^a, Z. C. Feng^b, and S. J. Chua^b

^a Department of Physics, National Taiwan Normal University, Taipei – 116, Taiwan, ROC

^b Institute of Materials Research and Engineering, S7-L3, Kent Ridge, Singapore 119260

ABSTRACT

In this work we present optical investigations of metalorganic chemical vapor deposition (MOCVD) grown InSb thin films on GaAs(100) substrates and MeV ion implanted InSb(111) bulk crystals. Far-infrared (FIR) reflectance spectroscopy has been used to study the lattice vibration behavior of all the samples. For the MOCVD films the effects of III-V source ratios on the films crystalline quality have been reported. Two additional weak modes in the wavenumber regions of 210-240 cm⁻¹ are observed and they appeared more prominent at low temperatures. Interference fringe effects modify the FIR reflectance band of the GaAs substrate. They are related to the uniformity of film thickness and crystalline perfection. The relationship between these interference features and film quality as well as thickness uniformity was obtained from the measured spectra. The carrier concentration, mobility, effective mass as well as the dielectric constant of these films have been determined. For the bulk InSb crystals, high energy C⁺ ions have been implanted at MeV energies and, the optical as well as transport properties of the implanted layers have been presented and discussed.

Keywords: FIR reflectance, lattice vibration behavior

1. INTRODUCTION

Long-wavelength optical devices fabricated on InSb-based thin films are promising as infrared detectors.¹ Wavelengths greater than 12 μm can be detected with these compounds based photodiodes at 77K. For the preparation of InSb thin layers, it is required to have special technological conditions to ensure their growth quality with specified electrical as well as optical properties of the layers. There have been a number of studies on this material concerning the growth and optical characterization of InSb based compound semiconductors.^[2-4] However, the transport and lattice behaviors have mostly been studied by various growth technique on GaAs substrate, such as molecular beam epitaxy (MBE)^[5-10], liquid phase epitaxy (LPE)^[11], magnetron sputter epitaxy^[12], metalorganic vapor phase epitaxy (MOVPE) or metalorganic chemical deposition (MOCVD).^[13-15] For the time being, mass production, large size and multi-wafer growth of InSb on GaAs substrate by metal-organic chemical deposition (MOCVD) are increasing for industrial infrared applications. In this paper we report the far-infrared reflection experiment near the very long wavelength limit for temperature between 300K and 80K. The lattice vibration modes of all the samples were measured and characterized by the Fourier Transform

*Corresponding author: Email: yang@ftir.phy.ntnu.edu.tw, Fax: +886-2-29326408

Infrared Spectroscopy (FTIR) technique. The dielectric behavior, phonon modes, transport as well as optical parameters were calculated theoretically and using least square fit compared to the experimental results for all the spectrum of these samples. A part of the work is also devoted to optical and dielectric behavior of bulk InSb crystals implanted with MeV C⁺ ions. In recent years a special interest has arisen in the synthesis of ion implanted InSb crystals for materials modifications.¹⁶ MeV Ion implantation is one of the most promising method for creating a buried layer structure in semiconducting materials to achieve a selective area doping. C is a good choice as an acceptor dopant in InSb due to its low solubility and diffusivity in III-V compounds. To date, however, very little is known about the optical and transport properties of MeV ion implanted InSb compound.

2. EXPERIMENTAL

2.1. Epitaxial growth of the samples

These MOCVD InSb epitaxial films were grown on commercial GaAs(100) substrates of 1000 μm thickness. Sources used were Trimethylindium (TMIn) and Tris-dimethylamino-antimony (TDMASb) as In and Sb sources, respectively. The indium and antimony bubblers were operated at 429 and 323 Torr., respectively. Flows through the indium and antimony bubblers were varied from 130 sccm - 270 sccm and the carrier H₂ gas flow were in the range of 320 - 775 sccm, respectively. Growth rates investigated were between 0.65 $\mu\text{m/hr}$ - 1.2 $\mu\text{m/hr}$. Growth rates with an optimum growth rate of around 0.95 $\mu\text{m/hr}$. Growth temperature was monitored using a single wavelength low temperature pyrometer. Samples N01-08 were prepared at a III/V ratio of between 4.2 to 4.5. Runs at these III/V values typically showed indium droplets on the surface of the film after growth. A second set of growth runs starting with run sample N09 was done using a III/V ratio of 6.2. These growths have resulted in surfaces with excellent morphology that were typically free of indium droplets. For all epitaxial InSb samples, we have performed series of characterization measurements, including surface morphology, Hall measurements, RF Sheet resistivity, thickness measured by scanning electron microscopy (SEM), etc.

2.2. Ion implantation

Ion implantation was performed using a 3MV tandem Pelletron accelerator facility in our laboratory. The detail of our experimental set up has been described elsewhere.¹⁷ Commercially available, mirror polished and (111)-oriented InSb single crystal wafers were implanted at room temperature using 1.00 MeV C⁺ ions at fluences of 5×10^{14} atoms/cm². A rectangular mask was used in front of the samples to restrict the beam exposed area. Implantations were carried out at a tilted geometry of 7° from the surface normal to prevent any possibility of ion channeling during implantations.

2.3. Far-infrared reflectance measurements

The Far-infrared reflectance spectra at near normal incident in far-infrared range, 60 – 500 cm⁻¹, were measured by a BRUKER IFS 120HR Fourier transform spectrometer at different temperatures between 80K and 300K with resolution better than 1 cm⁻¹. Mercury-Arc lamp was used for infrared light source. A mirror like gold plate was mounted next to the samples on the cold finger of cryogenic. The absolute reflectivity value of samples was done by comparison with the gold mirror. An APD cryogenic system was employed to the temperature dependent measurements. The temperature of finger tip inside the cryogenic was controlled by Lake-Shore 331 temperature controller with a temperature stability of 0.5K or even better.

3. RESULT AND DISCUSSION

3.1. Experimental results for MOCVD films

III/V source ratio has an important influence on the resulting epitaxial InSb films. Behet et al.¹³ studied the dependence of InSb growth rate on III/V ratio in low-pressure (20 hPa) plasma MOVPE with triethylantimony (TESb) as Sb precursor. The Sample's III-V ratio, surface Normaski micro and thickness uniformity is shown in Table 1. Sample N01 -N08 were performed at a III-V ratio of between 4.2 - 4.5. Runs at these III-V values typically showed indium droplets on the surface of the films after growth. Sample N09 were done using a III/V ratio of 6.2. These growths have resulted in surfaces with excellent morphology that typically free of indium droplets. Hall measurements, Sheet resistivity, SEM, and Mid infrared spectrum measurement for thickness showed a high thickness uniformity distribution, high mobility of the films which are very good for fast speed electron device applications.

Table 1. III-V ratio, Surface morphology, Thickness uniformity of samples

Sample No	N01	N02	N03	N04	N05	N06	N07	N08	N09
III-V ratio	5.069	4.906	4.546 cal	cal	4.546 cal	4.106	4.528	4.448 scrap	
Surface morphology	In-rich / droplet	Sb rich / big lots	In-rich / droplet	Good / less drop	Good / no drop	In-rich / droplet	Good / no-drop	Sb rich / less drop	Good / no drop
Thickness uniformity	6.06%		7.81%	6%	6.88%		1.69%		

A series of mirror-like epitaxial InSb films on GaAs substrates were studied by FTIR method in the FIR region. The measured spectrum of these samples were shown in Fig. 1. The vibration modes of all these samples in these spectrum are shown around 180 cm^{-1} and between 270 - 300 cm^{-1} . We use dielectric function, ϵ_{∞} , including the contribution of inner shell dielectric value and a set of Lorentzian vibrators as well as carrier contribution and also the contribution of GaAs substrate to fit all these FIR spectrum. A multi-layers (InSb + GaAs two layers) fitting technique was applied in theses theoretical calculation. Some of the fitted datum were shown in Figs. 2 - 4. The modes of around 180 cm^{-1} by least square fit were assigned as InSb TO mode and the modes around 270 - 300 cm^{-1} were fitted with different InSb film thickness and assigned as GaAs TO mode in 270 cm^{-1} at 300K. The variation of temperature cause these modes have blue shift that were also fitted and studied. The detailed behavior of temperature dependent optical parameters will put in reports.

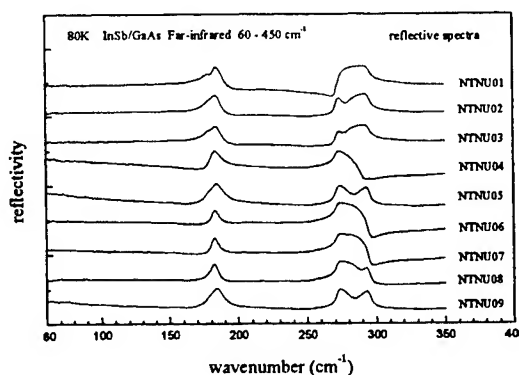


Fig 1 FIR reflectance spectrum of InSb/GaAs Samples at 80 K. From 500 cm^{-1} Mode 183 cm^{-1} is assigned for InSb TO phonon mode, Mode around 272 - 295 cm^{-1} is assigned for GaAs phonon mode from substrate.

3.1.1. The temperature dependent FIR spectrum

The temperature dependent FIR spectrum of all these samples has been measured and well fitted for all the measured spectrum. One of the datum were shown in Fig. 5. All of the phonon modes assignment of these samples were calculated and fitted by dielectric response model in the longwave limit^[18,19]. The fitted optical parameters of this films at 300K were shown in Table 2. The InSb TO modes has about 3 cm⁻¹ blue shift from temperature at 300K down to 80K. The GaAs modes from the substrate has about 1 - 2 cm⁻¹ blue shift mostly. The wavenumber of TO modes of InSb and GaAs of all these samples are correspondence to the value which were calculated by Kramers - Kronig (K-K) relation of the reflection spectrum.

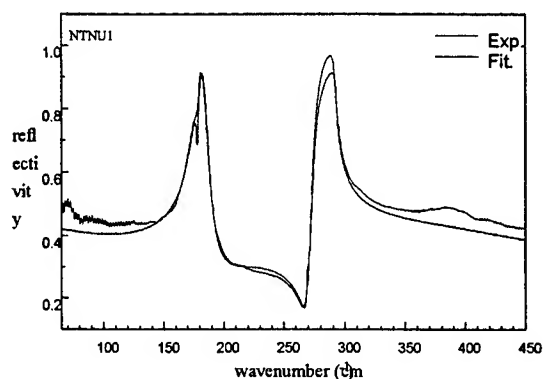


Fig 2. FIR reflectance spectrum of InSb/GaAs Samples N01 at 300 K From 50 – 500 cm⁻¹. Mode 180 cm⁻¹ is assigned for InSb TO phonon mode, Mode around 270 cm⁻¹ is assigned for GaAs TO phonon modes from substrate. The solid line is experimental value. The dotted line is fitted value.

Table 2. Samples optical parameters were fitted by dielectric response model in the longwave limit

Sample	III-V ratio	ϵ_{∞}	TO mode ω_{TO}	TO Strength (S)	damping Γ	Carrier concentration	Mobility	Effective mass	Thickness (micron)
N01	5.069	17.88	179.3	2.5	1.3	1.52 ¹⁶	6911	0.0129	1.98
N02	4.906	17.88	178.7	2.4	3.3	2.71 ¹⁶	10730	0.0170	1.43
N03	4.546	17.88	178.4	2.5	1.6	2.85 ¹⁶	11300	0.0173	1.55
N04		17.88	179.5	3.2	4.7	1.44 ¹⁷	20630	0.0152	1.09
N05	4.546	17.88	180.5	2.4	1.5	9.12 ¹⁶	14268	0.0186	1.57
N06	4.106	17.88	180.1	1.9	4.0	1.44 ¹⁷	40311	0.0176	0.66
N07	4.528	17.88	178.8	2.0	3.1	1.37 ¹⁷	35140	0.0177	0.61
N08	4.448	17.88	178.3	2.0	2.5	5.56 ¹⁶	10085	0.0135	0.91
N09		17.88	180.5	2.5	4.2	6.59 ¹⁶	18370	0.0166	1.41

3.1.2. Carrier concentration and mobility

Carrier concentration as well as sheet resistance are critical for device applications. The values of carrier concentration and mobility are sample growing dependence. The fitted values of carrier concentration are varies between 10^{16} - 10^{17} at 300K as shown in Table 2. These values are about the same order as Hall measurement with a very slight difference. The higher carrier concentration has higher absolute reflectance intensity in the longwave range as shown in Fig. 1. The higher reflection intensity in the long wave range is due to plasma effect and also InSb has very narrow band gap which enhance the plasma effect as long as the carrier concentration become higher.

3.1.3. Extra modes appear in FIR spectrum due to interface reaction

The large lattice mismatch (~14.5%) between InSb Films and GaAs²⁰ substrate is accompanied by a high density of dislocations and defects between the interface of the film that can deteriorate the thin film quality. Because of the longer penetration depth in the long wave range of FIR spectra, in Fig. 4, we can clearly see the third and fourth small vibration temperature dependent modes appear in around 218 cm⁻¹ and 228 cm⁻¹. This modes were due to the interface reaction of film and substrate. These vibration modes were assigned as InAs and GaSb TO modes.²¹ Also we see these modes have blue shift from 300K down to 80K from measured spectrum.

3.1.4. InSb films thickness and splitting of GaAs TO mode

The determination of InSb epitaxial film thickness and distribution over the entire layer is critical in the epilayer growth, especially in the large wafer diameter production. A SEM is usually employed to measure the InSb film thickness^[14,22]. But, it is destructive and not convenient for industrial production. The reflectance fringes do not appear in the ultraviolet and visible range from the InSb heterostructure. However, the reflectance fringes from InSb/GaAs can be observed in the mid-near infrared range and was reported.¹⁵ We have found that it is more easy to observe the interference fringes in far-infrared range of 60 -

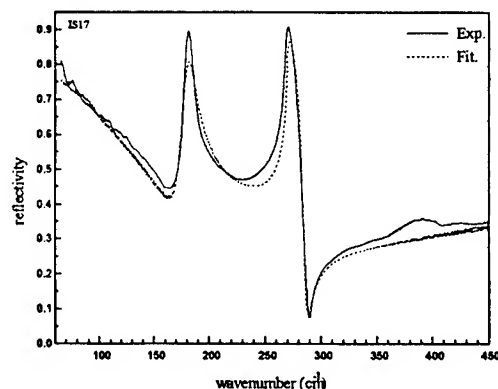


Fig. 3. FIR reflectance spectrum of InSb/GaAs Samples N04 at 300 K From 50 - 500 cm⁻¹. Mode 180 cm⁻¹ is assigned for InSb TO phonon mode, Mode around 270 - 290 cm⁻¹ is assigned for GaAs phonon mode from substrate.

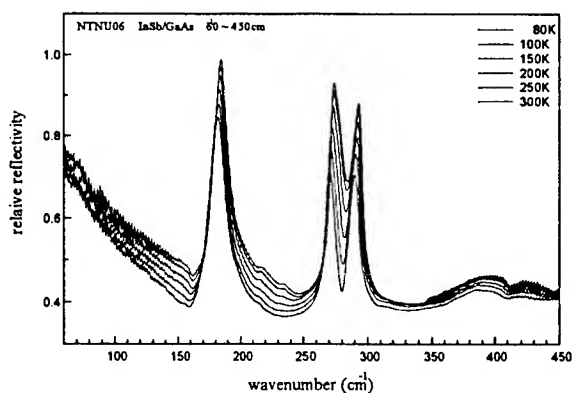


Fig. 4. FIR reflectance spectrum of InSb/GaAs Samples N06 at 80 - 300 K from 50 - 500 cm⁻¹. The InSb TO modes has about 3cm⁻¹ blue shift from temperature at 300 K down to 80 K. The GaAs modes from the substrate has about 1 -2 cm⁻¹ blue shift from temperature at 300 K down to 80 K.

500 cm⁻¹ or 160-20 symbol 109 Vf "Symbol" \s 12μm. In this study, we have the film thickness of InSb by experimental datum fitting. The contribution of InSb films absorption to it dielectric value in the longwave range limit of different film thickness were calculated and use these values to fit the experimental datum. The table of fitted film thickness was shown in Table 2. In Fig. 6, the TO mode in around 270 cm⁻¹ is well known as GaAs mode which is contributed from the film substrate. The splitting of this GaAs mode could clearly be seen in the FIR spectrum. We use the GaAs TO modes (~270 cm⁻¹, 300 K) instead of two modes and varing the thickness of InSb film's thickness to well fit all these FIR spectrum in this range as one of the data shown in Fig. 5. The GaAs mode splitting could be due to the contribution of InSb absorption of different layer thickness. The InSb film thickness in our dielectric response fitting is found to be exactly the factor contributed to this mode splitting as shown in Fig. 6.

3.2. Experimental results for ion-implanted InSb crystals

The results of our FTIR investigation at 300K on a pure (un-implanted) InSb(111) crystal and the C⁺-implanted specimen are shown in Fig. 7. In order to interpret these spectra, we fitted these spectra after considering various optical, electrical and transport parameters associated with the material. The fitting procedure was the same as in the cases of InSb thin films, described earlier. The simulated spectra obtained from these specimens are shown by the solid lines in Fig. 7. The pure InSb was considered as only one layer structure with a layer thickness of 377 μm , while the implanted specimen was approximated by three optically homogeneous layers. The pure InSb was considered as only one layer structure with a layer thickness of 377 micron. This thickness is basically the penetration depth of IR light in InSb. For the implanted specimens, a three layer (optically homogeneous) structure was considered: 1) a top layer of thickness 0.78 micron which is the less affected region by the implantation process containing no C atoms, 2) a second layer of 1.11micron containing the implanted C atoms and, 3) a third layer of thickness 375.1 micron upon the rest of the sample, which is basically the unaffected region of InSb. Infact, using the ion distribution profile and TRIM code, it is also possible to determine the thickness of the buried layer produced by C implantation in InSb. However, we do not present all those details here.

The results obtained this way for some of the optical dispersion parameters are shown in the Figure 7. One can notice a change in the dielectric function, ϵ_∞ , and damping constant, Γ , which is related to the implantation induced structural disorder in the material. It is also interesting to notice an enhancement in the free carrier concentration in the implanted specimen. Further descriptions are presented in some of our recent publications.^[23,24]

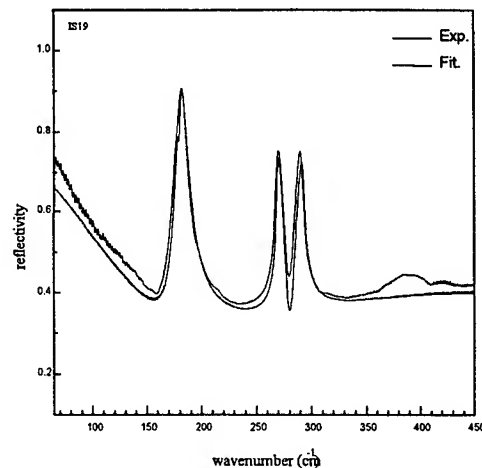


Fig. 5. FIR reflectance spectrum of InSb/GaAs Samples N06 at 300 K From 50 – 500 cm^{-1} . Mode 180 cm^{-1} is assigned for InSb TO phonon mode, Mode around 270 - 290 cm^{-1} is assigned for InSb phonon modes from substrate. The split of this GaAs mode is possibly due to the contribution of absorption of different InSb film thickness.

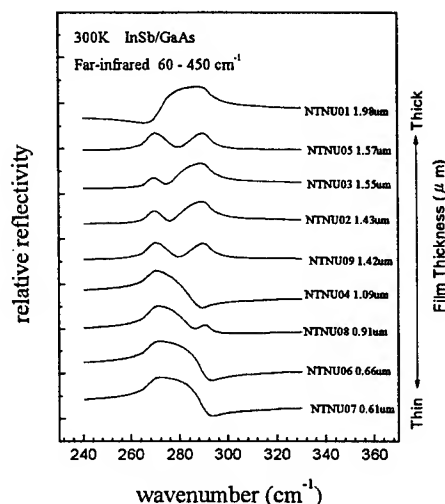


Fig 6. The TO mode in around 270 cm^{-1} is well known as GaAs mode which is contributed from the film substrate. The film thickness by fitted values is shown in the Figure. We use the GaAs TO modes ($\sim 270 \text{ cm}^{-1}$ 300 K) instead of two modes to well fit the splitting of this GaAs mode.

4. CONCLUSION

We had shown the optical characterization of FIR results. Various mode parameters, e.g., the TO mode frequency, carrier concentration, mobility, etc. of MOCVD InSb thin films grown on GaAs substrates and, bulk InSb single crystals implanted with MeV ion beams, were measured. All the specimens were characterized by a dielectric response model and also correspond to the value of K-K relation. For the thin films it was found that the extra modes appear in FIR spectrum due to the interface reaction of film and substrate. We also have used this dielectric response model to fit FIR reflectance spectrum to obtain the film thickness distribution and the relation of InSb film thickness with the splitting of GaAs mode. FIR spectroscopy was used successfully to study the effects of III/V source ratios and to optimize the growth parameters. The obtained distribution values of the InSb LO phonon mode frequency, full width at half maximum (FWHM), relative integrated intensity ratio between the

forbidden and defect-related TO phonon and the allowed LO mode are adopted as figures of merit for the quality of the InSb films. The results of FIR measurements show that MOCVD turbo disk technology is capable to produce high quality far infrared InSb epitaxial materials, and the FTIR method is a very useful tool for non-destructive characterization of large size wafers in industrial mass production. Concerning the ion implanted InSb, radiation damage destroys the crystalline perfection of the lattice and results in the formation of point defects and dislocation loops. However, the refractive index of the medium (which is related to the dielectric function) and the free carrier concentration are enhanced as a consequence of implantation process. Further investigations for the annealing characteristics of these specimens are underway.

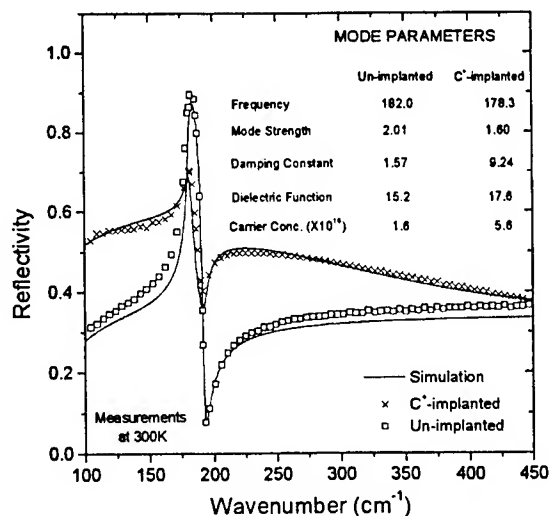


Fig. 7. Measured and calculated FIR spectra of the unimplanted and C⁺-implanted InSb(111).

REFERENCES

1. A. Cappy, B. Carnez, R. Fauquermegues, G. Salmer, E. Constant, IEEE Trans. Electron Devices **ED-27**, 2158, 1980.
2. J. R. Sendra, G. Armelles, T. Utzmeier, J. Anguita, F. Briones, J. Appl. Phys. **79**, 8853, 1996.
3. J. Wagner, J. Schmitz, Philosophical Magazine **B70**, 467, 1994.
4. R. Addinall, R. Murry, R. C. Newman, J. Wagner, S. D. Parker, R. L. Williams, R. Droopad, A. G. DeOliveira, I. Ferguson, R. A. Stradling, Semicond. Sci. Technol. **6**, 147, 1991.
5. G.M. Williams C.R. Whitehouse, C.F. McConville, A.G. Cullis, et al. Appl. Phys. Lett. **53**, 1189, 1988.
6. E. Michel G. Singh, S. Slivken, C. Besikci, P. Bove, et al, Appl. Phys. Lett. **65**, 3338, 1994.
7. R.M. Biefeld, J. Crystal Growth **75**, 255, 1986; **77**, 392, 1986.
8. P.K. Chiang and S.M. Bedair, J. Electrochem. Appl. Phys. Letters **46**, 383, 1985.
9. R.M. Biefeld and G.A. Hebner, Appl. Phys. Letters **57**, 1563, 1990.
10. J.-I. Chyi, S. Kalem, N.S. Kumar, C.W. Litton and H. Morkoc,, Appl. Phys. Letters **53**, 1092, 1988.
11. D. E. Holmes and G. S. Kamath, J. Electron. Mater. **9**, 95, 1980.
12. J. Webb and R. Rousina, in *Semiconductor Interfaces and Microstructures*, edited by Z. C. Feng, p-199, (World Scientific, Singapore, 1992).
13. M. Behet, B. Stoll, W. Brysch and K. Heime, J. Crystal Growth **124**, 377, 1992.
14. B.-S. Yoo, M. A. McKee, S.-G. Kim and E.-H. Lee, Solid State Commun. **88**, 447, 1993.
15. Z.C. Feng, et al., Mat. Res. Soc. Symp. Proc. materials Research Society. **450**, 61, 1997.

16. S. J. Pearton, S. Nakahara, A. R. Von Neida, K. T. Short, L. J. Oster, J. Appl. Phys. **66**, 1942, 1989.
17. G. Kuri, Appl. Phys. **A68**, 699, 1999.
18. N. Raj, et al., Solid State Comm. **55**, 373, 1985.
19. V. M. Agranovich et al., Solid State Comm. **55**, 85, 1985.
20. Z. C. Feng, S. Perkowitz, T. S. Rao and J. B. Webb, J. Appl. Phys. **68**, 5363, 1990; F. H. Pollak, in Analytical Raman Spectroscopy. edited by J. G. Grasselli and B. J. Bulkin, p-137, (Willey, New York, 1991).
21. C. Kittel, *Introduction to Solid State Physics 7th ed.*, John Wiley&Son, Inc. New York, p-292, 1996.
22. M.A. Mckee, B. -S. Yoo and R.A.Stall, J. of Crystal Growth **124**, 286, 1992.
23. T. R. Yang, G. Kuri, Physica B, 2000, [In Press].
24. G. Kuri, T. R. Yang, SPIE Conference Proceeding, Photonics Taiwan, [This Volume], 2000.

RADIATION DAMAGE AND SURFACE MODIFICATION OF InSb(111) BY MeV C⁺ AND C₂⁺ IONS

G. Kuri* and T. R. Yang

Department of Physics, National Taiwan Normal University, Taipei-116, Taiwan, ROC

ABSTRACT

The damage accumulation at the surface as well as deeper regions in InSb bombarded with MeV C⁺ and C₂⁺ ions have been studied. Mirror polished (111)-oriented InSb single crystal substrates were implanted with 1.00 MeV C⁺ and 2.00 MeV C₂⁺ ions to a total fluence of 5×10^{14} C-atoms/cm² at room temperature. The retained damage following implantation was analyzed by Rutherford backscattering/channeling technique and Raman scattering experiment. Fourier Transform Infrared Spectroscopy (FTIR) have been used to study the dielectric behavior, optical as well as transport properties of the implanted specimens. The FTIR spectra were analyzed within the framework of a dielectric response model. The surface structure of the implanted wafers has been measured by atomic force microscopy. The results show that the response of InSb crystal to C⁺ ion bombardment is widely different when compared to that of C₂⁺ implantation. A tentative explanation for the results have been presented.

Key-words: Ion implantation doping, InSb-crystal, Radiation damage, Surface morphology, Optical response.

1. INTRODUCTION

Fabrication of deep sub-micron microelectronic products with ultra-large scale integration architecture relies heavily on ion implantation to create *p*- and *n*-doped regions of modern devices.^[1,2] Often the implanted dopant influence is high enough that the surface of the implanted substrate crystal is damaged to an amorphous structure. In III-V compound semiconductors the influence of the implantation parameters on the defect structure resulting after ion implantation are much more pronounced than in the elementary semiconductors like Si or Ge. While a great deal of information has been already obtained for Si over the years, and therefore much is known about its behaviour and properties after implantation, this seems not to be the case for compound semiconductors like GaSb and InSb. Just because these materials are compounds with a very narrow stoichiometric solubility range, and their electrical properties strongly depend on stoichiometric composition, their behavior after implantation is much more delicate and complex than that of Si.

Some of the important aspects of ion implantation in III-V semiconductors have been studied extensively in the past. Annealing behavior and activation mechanisms for various elements in these materials have been investigated, but with not always consistent results.³ In GaAs, a remarkable decrease of the resulting defect concentration for implantation temperatures near room temperature as compared to implantation at low

*Corresponding author; Fax: +886-2-29326408; E-mail: kuri@mail.desy.de

temperature occurs. In other several III-V compounds defect annealing after heating up of low temperature implants to room temperature is observed. Also, the current density, ion mass and implant energy influence the nature and amount of damage produced.^[4,5]

In ion-implantation doping, in order to achieve the electrical activation of dopant atoms, the dopants have to occupy regular lattice sites. In addition, the implantation damage should be removed or at least minimized. In the cases of Si or any III-V semiconductors, this damage is regrown by solid-phase epitaxial growth, and dopants are activated by thermal annealing. However, there exist also reports that the dopants become electrically active right after ion implantation, for example, Li into InSb and the substitutional fraction of Li was measured to be 70%.⁶ Similar to Li, recently, Be atoms were found to occupy the In sites in an InSb crystal in the as-implanted state.⁷ Even annealing did not change impurity location in the sublattice and impurity removal from sublattice sites was not observed. The present study is a part of an ongoing investigation to gain some more insight into these aspects. In this work the incorporation of C in single crystals of InSb(111), by ion implantation at MeV energies, is studied. Although InSb is among the mostly studied semiconductors^[8,9], it has the highest electron mobility and narrowest band gap among III-V compound semiconductors. Therefore, it is attractive in the high speed electronic and optoelectronic devices in the infrared applications. C is expected to be a good choice as a dopant in this material since it has the lowest solubility and diffusivity in contrast to those of Be, Mg and Zn, which are more common acceptor dopants¹⁰ in III-Vs. We have further explored the possibility of implantations with molecular ions owing to their major advantages compared to implantations with mono-atomic ion beams.

2. EXPERIMENTAL

Substrates used for this study consisted of commercially available (111)-oriented InSb single crystals polished to a mirror-like finish. After rinsing in an ultrasonic cleaner the substrates were mounted on a sample stage in the implantation chamber. Implantations were performed at room temperature with a scanned beam of 1.00 MeV C⁺ and 2.00 MeV C₂⁺ ions to a dose of 5×10^{14} C-atoms/cm² in all the samples. The numerical TRIM¹¹ estimations with the computer program for 1.00 MeV C⁺ (which is expected to be equivalent to 2.00 MeV C₂⁺ as far as the ion distributions are concerned) show that the maximum C atomic concentration occurs at the projected range of 1.25 μ m from the surface with a full-width at half maximum (FWHM) of 675 nm, and a peak concentration of 7.4×10^{18} cm⁻³. The later is below the C solubility in InSb at 300K. The average beam current density was 10 nA/cm² for both the C⁺ and C₂⁺ ions. (It was our interest to get a direct comparison of irradiation effects between C⁺ and C₂⁺ implantations. Therefore, we have carried out the C⁺ and C₂⁺ implantations at the same energy/atom, dose rate and fluence). Before implantation, a part of each sample was masked to provide an un-implanted reference region. During implantation the samples were tilted 7° from normal incidence to prevent ion channeling and the pressure in the implantation chamber was about 3×10^{-7} mbar.

After the samples preparation, RBS/C analysis with a 2.50 MeV He⁺ ion beam at a scattering angle of 165° was used to investigate the damage distributions induced by C⁺ and C₂⁺ implantations in the as-implanted specimens. In order to reduce the beam induced effects the analyzing beam current was kept low (~ 8 nA). Furthermore, several fresh beam spots were chosen during channeling measurements. The surface morphology of the implanted specimens was examined using AFM (Atomic Force Microscopy) technique with a Si₃N₄ cantilever operated in the non-contact mode. The usual roughness parameter, peak/vally and root mean square (rms), were calculated by the microscope software. Further informations on the implantation damage, surface modifications, optical as well as dielectric properties of the implanted wafers were obtained by Fourier-transform Infrared spectroscopy (FTIR) and Raman scattering (RS) measurements. The infrared reflectivity at near-normal incidence were made at 83K on a Bruker model IFS-120-HR spectrometer in the far-infrared (FIR) range of 100 to 450 cm⁻¹ (0.0124 to 0.0557 eV) with a resolution of 1 cm⁻¹ (~ 10⁻⁴ eV). The unpolarised Raman spectra of implanted specimens at 90° scattering geometry were recorded on a Dilor X-Y Raman spectrometer. An argon ion laser, lasing at 514.5 nm with

20 mW power was used as the source. Further experimental details of our set-up have been described elsewhere.¹²

3. RESULTS and DISCUSSION

Fig. 1 shows typical [111] RBS/C spectra obtained for InSb samples implanted at 300K and fixed C^+ as well as C_2^+ flux and fluence. RBS spectra obtained for un-implanted material in channeling and random orientations are also shown for comparison purposes. Channel number 804 corresponds to the surface peak position for the InSb. From the figure one can notice that for C_2^+ implantation the backscattering yield under channeling condition has practically touched the random level at a depth of ~ 700 nm and reduced below the random level at a depth of around 1600 nm, indicating that this region (≈ 900 nm) is nearly amorphous. The minimum backscattering yield χ_{\min} rose from 4% in the unimplanted sample to about 53% in the C_2^+ implanted InSb. However, this is not the case for C^+ implantation where the implantation damage in InSb crystal is lower than that of C_2^+ implantation. Also the structure of the defective regions are not the same in two cases (of C^+ and C_2^+ implantations). The damage evolution is different at various depths of the samples, in particular, the surface and near-surface regions. These results indicate that an implantation of $5 \times 10^{14} C^+ / \text{cm}^2$ at 300K does not result in the formation of a continuous amorphous layer in InSb as one would also expect from the theoretical investigation of S. Furukawa.¹³ The threshold for amorphization of InSb crystals is expected to be $\sim 7 \times 10^{14} \text{ cm}^{-2}$ for C^+ implantation with an energy of 1.00 MeV at room temperature.¹³ The non-linear damage distribution between C^+ and C_2^+ implantations at the same energy/atom, flux-rate and total fluence can be understood by considering the collective effect of excessive damage due to coherent cluster atom passage and the overlap of individual ion cascade in the host medium. Recently, a similar result in the damage distributions in Si induced by molecular ions of 1.4 MeV N_2^+ at a dose of $1 \times 10^{15} \text{ N-atoms/cm}^2$, has been reported.¹⁴ The damage profiles were not equivalent to those of single-atomic ions (of 0.7 MeV N^+) and a considerable differences of up to 30% in the damage profile widths were found. We have also observed similar features in GaAs substrates implanted with C^+ and C_2^+ ions followed by Ga^{2+} co-implantation at MeV energies and at a comparable dose, reported recently.¹⁵ In fact, in a C^+ implantation, the impact events of two atoms impinging at the same spot are separated in general by comparatively long time intervals so that smaller target excitations and near-threshold displacements upon the first impact have ample time for annealing out before the second excitation of displacement takes place. On the other hand, for C_2^+ , or in a cluster ion impact, the cluster atoms fly initially coherently with each other within a small distance so that the total damage roughly adds up, thus giving rise to stronger collisional damaging effects with less recombination.. This might lead to defect clustering, dislocation loops, or even to local collapse of the crystal lattice, so that the structure of the damaged regions of cluster ions is different in nature to the structure of single ion damage. As the cluster ion penetrate more and more deeper, multiple small angle scattering and Coulomb repulsion lead to increase the inter-cluster atom distance, thus reducing the above collective effect of excessive damage due to coherent cluster atom passage. One may also note that, within the coherence range, the electronic energy transfer of the individual cluster atoms adds up non-linearly due to the collaborative effect of the molecular atoms in the regions near the surface. Therefore, even low energy cluster ion may result in very high electronic excitation, thus giving rise to effects which else are observed only after high energy ion impact. We will come back to this point later in this section.

RBS/C with MeV energy probing ions (e.g., H^+ or He^+) is not very ideal for characterizing the lattice disorder at the surface of an ion implanted specimen, due to the poor depth resolution ($\sim 8\text{-}10$ nm) of this method. Raman scattering is the technique ideally suited for probing the implantation induced lattice damage at the surface and near-surface regions of semiconductors, mainly because the thickness of the damage layer and the optical skin depth are essentially of the same order. Under special experimental conditions, for example the measurements at lower temperatures and thereby reducing the effects of thermally generated carriers and, at a grazing incidence of the incident laser light, the surface sensitivity of this technique can be further enhanced. Fig. 2 displays the normalized Raman spectra of InSb implanted

with C^+ and C_2^+ ions. The Raman spectrum from the un-implanted InSb is also included in the figure. One can notice that the TO (transverse optical) and LO (longitudinal optical) modes broaden and the intensity decreased as a result of implantation induced structural disorder. There are two reasons for the broadening and weakening of the TO and LO lines. First, the symmetry of the unimplanted sample will be destroyed by point defects and dislocations after implantation. Second, it may be due to inhomogeneity of strain which would effect the LO more than TO mode. It is also evident from the figure that a distinct new peak emerges for both the implanted specimens at 123 cm^{-1} which suggests the process of disorder induced Raman scattering.¹⁶ Another important feature in Fig. 2 is the enhancement of the Raman intensity in the spectral regions $90\text{--}160\text{ cm}^{-1}$ for both the implanted samples compared to un-implanted one. From these results, we can conclude that point defects and dislocations are formed in the implanted specimens. But a continuous amorphous layer is not formed in the near surface regions. In that case, depending on the extend of amorphization, both LO and TO modes will be asymmetrically broadened and possibly shifted in frequency which are not observed in our specimens. (It should be noted that in the present experimental conditions the probed zone in InSb crystal is about 35 nm top layer). The enhancement of the band intensity at low wavenumber regions (below 160 cm^{-1}) in the implanted samples can be partly attributed to the changes of surface roughnesses, leading to more diffusely scattered laser light. Let us discuss this aspect in more detail.

In Fig. 3, we have shown the AFM image of the surface morphology taken on the C_2^+ -implanted InSb(111) specimen. The measured surface roughness (rms value) of this sample was 4.51 nm. For the un-implanted and C^+ -implanted specimens of the same batch, the measured surface roughness (the AFM images were not shown here) was 1.82 and 4.26 nm, respectively. These results imply that the smooth surface of unimplanted InSb was affected by the ion bombardment. However, the little difference in the measured rms values between C^+ and C_2^+ implanted specimens may not be neglected. Since various mechanisms can contribute to the surface roughening or smoothing, the later can be rather complex, depending on the properties of the incident ion as well as the substrate. At high kinetic ion energy, the projectiles are deeply implanted into the bulk and neither the implanted species nor generated defects reach the surface. The amount of radiation damage imparted to the target by the impact of the ion results from the combination of local energy deposit which tends to impart damage, and the target temperature which tends to anneal it out. The energy deposit increase with the increase the nuclear energy loss (S_n) whereas electronic energy loss (S_e) induces a local heating which suppresses the formation of defects in the material. For the energy of C^+ ions used in our study, the dominant energy loss process in the surface and near-surface regions is the electronic energy loss. For 2.00 MeV C_2^+ ions, the effective electronic energy loss is more than that of 1.00 MeV C^+ ions, due to the collaborative effect of the two individual C atoms originating from the C_2 molecule, as already discussed earlier. Thus, we believe that the effective and total electronic excitation by C_2^+ has resulted a less surface roughness compared to that of C^+ irradiated specimen.

To identify the structural damage to the InSb lattice caused by ion implantation, FTIR spectra were also measured to determine the defect characteristics connected with the observed RBS/C results, AFM topography and Raman Spectra. Furthermore, FTIR spectroscopy together with a model calculation can provide a very detail information regarding the dielectric behaviour and optical as well as transport properties of an ion-implanted specimen. Fig. 4 shows the FTIR reflectance spectra of all the specimens measured at 83K. In the un-implanted InSb crystal, the vibrational band exists at 185.0 cm^{-1} (TO mode, FWHM 9.1 cm^{-1}) which corresponds to the vibration of In—Sb bond. After ion implantation, this mode shifts markedly toward low wavenumbers and its FWHM becomes broader. However, there is a distinct difference between the two cases of C^+ and C_2^+ implantations. The peak positions correspond to 183.8 and 182.6 cm^{-1} for C^+ and C_2^+ implanted samples, respectively, while the measured FWHM values are 13.0 and 14.9 cm^{-1} . These results indicate an implantation induced structural disorder and a higher lattice damage in the C_2^+ implanted specimen compared to C^+ implantation. This is also consistent with the Raman scattering results presented earlier. It may be pointed out in this context that RS results presented in Fig. 2 does not indicate any shift in the peak positions of TO (or LO) band for the implanted specimens. This is probably due to the fact that in FTIR spectra the penetration depth of incident light exceeds the total thickness of the implanted layer. Therefore, the contribution from the highly damaged (and possibly nearly amorphous) regions containing C atoms becomes dominating in the spectra whereas RS results are associated with only the surface and near-surface regions.

A further inspection of Fig. 4 reveals the structure due to free carrier response in the amplitude of the reflectivity spectra at about $100\text{--}150\text{ cm}^{-1}$, where the absolute values of reflectivity have increased in the implanted samples. This implies that some of the C atoms have occupied a substitutional lattice site in InSb and become electrically active although the close environment in the host matrix is still dominated by implantation damage. It is rather known that a higher carrier density exhibits a higher absolute reflectance intensity in the long-wave range.¹⁷ From the measured FTIR spectra presented in Fig. 4, we have also tried to derive various electrical and optical dispersion parameters associated with ion implanted InSb. The optical phonon behavior, conductivity, dielectric constant, and other optical parameters are analyzed by a dielectric response model based on classical approximations. The analysis is performed using the formalism reported by Agranovich and Kravtsov.¹⁸ The reliability of this model has been already established by a number of research work.^[19-22] In the present case, we have considered a three layer sample (layer 1 for the region near the surface, layer 2 for the next adjacent region of implanted C atoms and layer 3 for the unaffected InSb since the optical penetration depth of infrared light exceeds the thickness of implanted regions) for the implanted specimens. The results obtained this way for all the calculated values of the dispersion parameters have been already described in one of our recent publications.²⁰ It was indeed interesting to obtain a higher carrier concentration in the C_2^+ implanted specimen compared to C^+ one, which is also clear from the Fig. 4 presented here and measured even at a low temperature of 83K.

4. SUMMARY AND CONCLUSION

It has been recognized that high energy ion implantation is opening a new horizon for VLSI and ULSI device structure and fabrication processes. It is an attractive method that allows one to develop buried novel structures, and to alter or improve mechanical, physical, chemical, electrical and optical properties of semiconductors. In this work, we have studied the case of InSb(111) crystals implanted with MeV C^+ ions. We have also explored the possibility of implantation with molecular C_2^+ ions. Many problems of conventional ion implantation, such as space-charge effects, radiation-enhanced diffusion and channeling, can be overcome by cluster ion implantation. We have shown that there are significant differences in the response of InSb to ion bombardment of C^+ and C_2^+ ions under the conditions of the present study. The as-implanted damage was studied using RBS/channeling and Raman scattering measurements. In the mono-atomic and di-atomic comparison, both the total number of implanted atoms and energy per atom for both C^+ and C_2^+ irradiations were held constant, so that the total energy deposition per unit area, the cascade dimensions, the mean range and the straggling of the implanted atoms all remained constant. Under such conditions, the damage enhancement in the case of C_2^+ compared to C^+ in InSb suggests the occurrence of cascade-cascade interaction. In this case InSb was damaged more during the implantation as compared to that of C^+ . Using AFM technique, we have studied the surface morphology of the implanted specimens. Although implantation causes an overall increase of the surface roughness in the as-implanted specimens, the average surface roughness in the C_2^+ implanted sample is slightly lower compared to C^+ one. This is probably due to the higher electronic excitation effect induced by a molecular ion. Our FTIR investigation on these specimens indicates that, although the close environment is still dominated by the implantation damage, some of the implanted C atoms occupy a substitutional lattice sites in InSb and become electrically active and thereby contribute to the free carrier response in the Infrared absorption spectra. Experiments are now underway to study in detail the annealing behavior of C^+ - and C_2^+ -ion implanted InSb crystals concerning their radiation damage and optical as well as dielectric properties. It will be also of interest to examine consequences of using different ion species and higher atomic clusters for implantation which will alter the density of defects in the cascade.

Acknowledgement

We acknowledge the National Science Council, Taiwan, ROC, for providing financial assistance to carry out a part of this work.

REFERENCES

- 1 . O. H. Holland, Appl. Phys. Lett. **54**, 320, 1989.
- 2 . H. Dammak, A. Dunlop, D. Lesueur, A. Brunelle, S. Della-Negra, Y. LeBeyec, Phys. Rev. Lett. **74**, 1135, 1995.
- 3 . N. J. Barrett, J. D. Grange, B. J. Sealy, K. G. Stephens, J. Appl. Phys. **57**, 5470, 1985.
- 4 . J. E. Westmoreland, O. J. Marsh, R. G. Hunsperger, Radiat. Eff. **5**, 245, 1970.
- 5 . E. Wendler, W. Wesch, G. Gotz, Nucl. Instr. Meth. **B52**, 57, 1990.
- 6 . H. Hofsass, U. Wahl, M. Restle, C. Ronning, E. Recknagel, S. G. Jahn, Nucl. Instr. Meth. **B85**, 468, 1994.
- 7 . R. G. Wilson, F. A. Stevie, C. W. Magee, Secondary Ion Mass Spectrometry, Wiley, Chichester, 1989.
- 8 . S. J. Pearton, S. Nakahara, A. R. Von Neida, K. T. Short, L. J. Oster, J. Appl. Phys. **66**, 1942, 1989.
- 9 . S. Guha, A. Madhukar, K. C. Rajkumar, Appl. Phys. Lett. **57**, 2110, 1990.
- 10 . W. V. Schoenfeld, M. J. Antonell, C. R. Abernathy, Appl. Phys. Lett. **72**, 1235, 1998; and references therein.
- 11 . J. P. Biersack, L. G. Haggmark, Nucl. Instr. Meth. **174**, 257, 1980.
- 12 . G. Kuri, Appl. Phys. **A68**, 699, 1999.
- 13 . S. Furukawa, Jpn. J. Appl. Phys. **11**, 102, 1972.
- 14 . M. Muller, D. Fink, Appl. Phys. **A61**, 153, 1995.
- 15 . S. K. Ghose, G. Kuri, Amal K. Das, B. Rout, D. P. Mahapatra, B. N. Dev, Nucl. Instr. Meth. **B156**, 125, 1999.
- 16 . J. R. Sendra, G. Armelles, T. Utzmeier, J. Anguita, F. Briones, J. Appl. Phys. **79**, 8853, 1996.
- 17 . S. Perkowitz, Optical Characterization of Semiconductors, Academic Press, New York, 1993.
- 18 . V. M. Agranovich, V. E. Kravtsov, Solid State Commun. **55**, 85, 1985.
- 19 . L. Genzel, T. P. Martin, C. H. Perry, Phys. Stat. Sol. **B62**, 83, 1974.
- 20 . T. R. Yang, G. Kuri, Physica **B**, 2000 [In Press].
- 21 . T. R. Yang, C. C. Lu, W. C. Chou, Z. C. Feng, S. J. Chua, Phys. Rev. **B60**, 16058, 1999.
- 22 . H. L. Liu, M. A. Quijada, D. B. Tanner, H. Berger, G. Margaritondo, Eur. Phys. J. **B8**, 47, 1999.

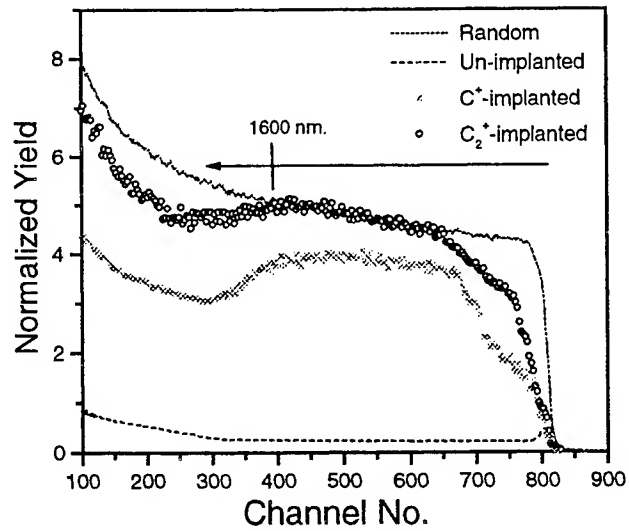


Fig. 1: Random and (111)-aligned backscattering spectra of 2.50 MeV He⁺ obtained on various InSb samples

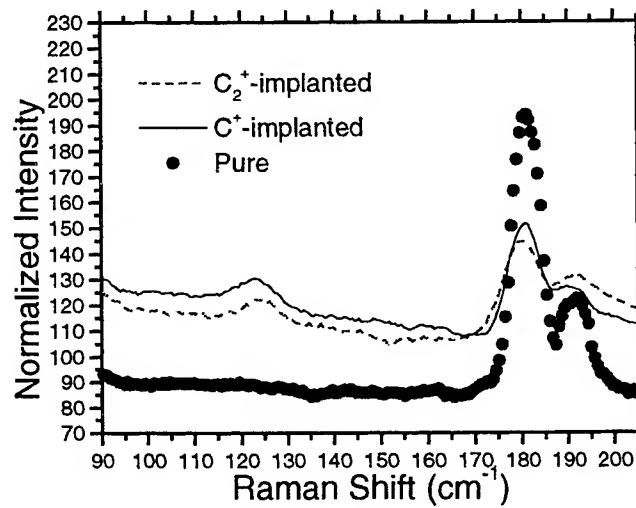


Fig. 2: Raman spectra taken on various samples. The samples were kept tilted by about 20° during the measurements

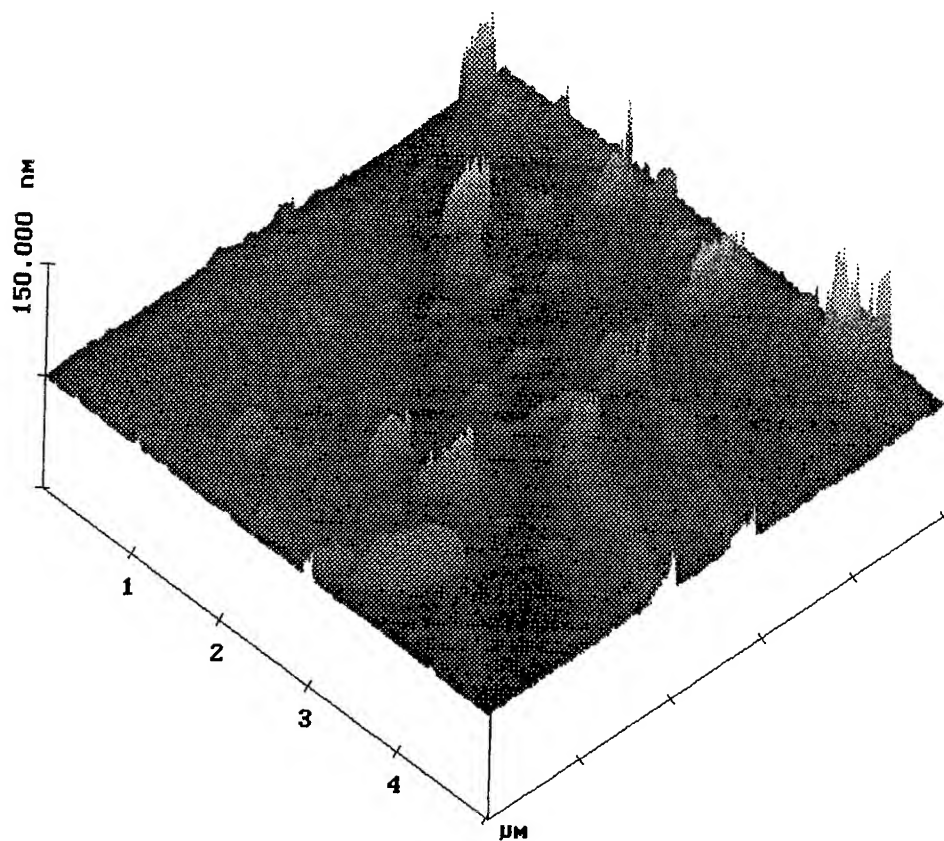


Fig. 3: A typical AFM image of the surface of an InSb(111) implanted with 2.00 MeV C_2^+ ions. See the text for details.

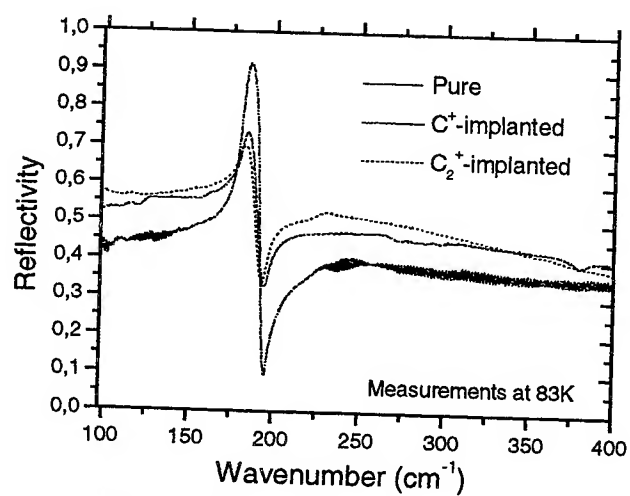


Fig. 4: Measured FIR reflectance spectra of the unimplanted and two implanted InSb(111) specimens.

The Conduction Mechanisms in Undoped Polycrystalline Diamond Films

Hsueh-Tao Chou*, Chia-Chang Lee, Chia-Hsin Sun

Institute of Electronics and Information Engineering, National Yunlin University of Science and Technology, Touliu, Taiwan 640, R. O. C.

ABSTRACT

The undoped polycrystalline diamond films are deposited on p-type silicon substrates by a microwave plasma chemical vapor deposition (MPCVD) system. The deposition conditions are $\text{CH}_4/\text{H}_2 = 0.5\%$, pressure = 45 torr, power = 2.2 kW, and substrate temperature = 885 °C. SEM was used to inspect the surface morphology, Raman Spectroscopy to determine the quality, and XPS to analyze the chemical composition. It is concluded that a cleaning procedure on diamond surfaces can eliminate the carbon phase but enhance the oxygenation on the films. The electrical characteristics were investigated by current-voltage-temperature measurements in a metal-insulator-semiconductor (MIS) structure with top metal contacts and back silicon substrates contacts. It can be found a transition electric field of 240 kV/cm, where Schottky emission (SE) mechanism is responsible for electric conduction below 240 kV/cm, and Poole-Frenkel transport (PF) mechanism dominates beyond 240 kV/cm. By the extrapolations, the Schottky barrier height of silver and diamond film is 2.4 eV, and the trap depth is 4.75 eV in the diamond film.

Keywords: CVD diamond, Schottky barrier height, electrical conductivity, Spectroscopy, trap

1. INTRODUCTION

Diamond has several particular properties, such as high mobility, high carrier saturation velocity, and wide energy gap. There has been a significant interest in studying diamond films on the applications for high power, high frequency, and high temperature electric devices¹⁻³ since the advances in synthesizing diamond films under low pressure and low temperature using the chemical vapor deposition system. The polycrystalline diamond films in this paper were deposited on silicon substrate by microwave plasma chemical vapor deposition (MPCVD) system in the gas mixtures of methane and hydrogen. As a result of the wide energy gap (5.5eV) and high resistivity, the undoped diamond films can be considered as insulators⁴. After sputtering metal contacts on the undoped polycrystalline diamond films, the metal-insulator-semiconductor (MIS) layered structures were analyzed by measuring voltage and current.

However, some studies⁵⁻⁸ have been carried out in detail to correlate the electrical conduction mechanism and the physical characteristics of undoped polycrystalline diamond films. The purpose of this research was to examine the possible conduction mechanisms of the MIS structure and calculate the Schottky barrier height between Ag and Diamond films, and the trap depth in the bulk diamond by means of conduction mechanism equation.

*Correspondence: E-mail: chouht@pine.yuntech.edu.tw; Telephone: (8865)5342601 Ext. 4323;

Fax:(8865)5312063

2. EXPERIMENTAL

The undoped polycrystalline diamond films were deposited using microwave plasma chemical vapor deposition system (MPCVD) on P-type and (100) orientation silicon substrates of 3 inches diameter. The MPCVD is Diamondtek® DMS-100 (Wavemat Inc.). The deposition conditions⁹ were shown as follows: $\text{CH}_4/\text{H}_2 = 0,5\%$, pressure = 45 torr, reactive power = 2.2 kW, substrate temperature = 885 °C, deposition time = 4 hrs, and thickness = 1 μm . The removal of the carbonaceous surface layer were achieved by the cleaning procedure as follows: the diamond films were placed in a saturated solution of CrO_3 in the H_2SO_4 at 180 °C for ten minutes, followed by a rinse in 1:1 boiling solution of H_2O_2 and NH_4OH for ten minutes as well, and then put in the ultrasonic cleaner with deionized water for about two minutes^{10,11}.

Scanning electron microscopy (SEM) was used to inspect the surface morphology of the diamond films. Raman spectroscopy was to identify the quality and properties of the polycrystalline diamond films. The Raman spectroscopy was performed using an Ar ion laser operated at a power of 30 mW and at a wavelength of 514.5 nm. X-ray photoelectron spectroscopy (XPS) was to analyze the chemical composition on the surface of the polycrystalline diamond films. The XPS system pressure was within approximately 10^{-9} torr, and the Mg K_α monochromatic source was operated typically at 12KV, 18mA.

Then, silver contacts on the polycrystalline diamond films were done by sputtering techniques through a shadow mask with circular dots of 150 μm diameter. The rear sides of silicon wafers were coated with silver paste in order to form ohmic contacts. The Current-voltage measurements were conducted on a microprobe station using Keithley Source Measuring Unit 236 system in the range of ± 110 V with different temperature varying from 30 to 150°C.

3. RESULTS AND DISCUSSION

SEM was to examine the surface morphology of the undoped polycrystalline diamond films after the cleaning procedure. As shown in Fig. 1, the observed morphology was crystallized and the orientation of the surface was (111) facet. As shown in fig. 2 was the Raman spectra with a characteristic peak of diamond at 1333cm^{-1} and a full-width at half maximum (FWHM) of 7.1cm^{-1} . As shown in Fig. 3, the spectra indicated the existence of oxygen (O) peak. The XPS results is consistent with other groups' study^{11,12} revealing oxygen can adsorb onto the surfaces of diamond films which were treated in the aforementioned cleaning procedure in order to remove the non-diamond components away from the surface of diamond film.



Fig. 1 SEM image of diamond film with (111) facet.

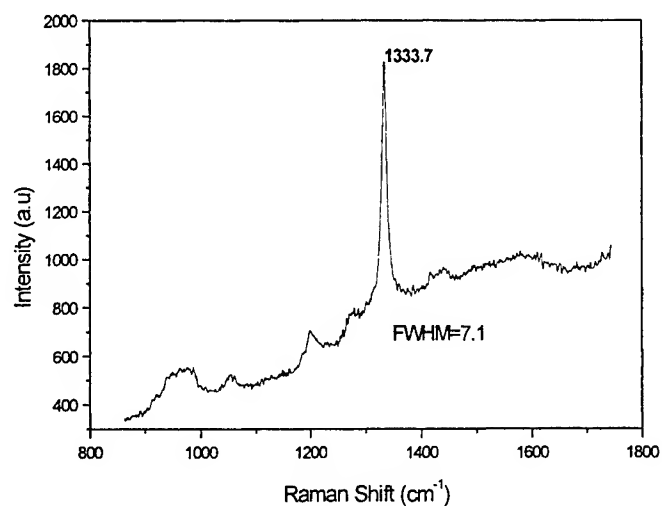


Fig. 2 Raman spectrum with diamond peak at 1333cm⁻¹

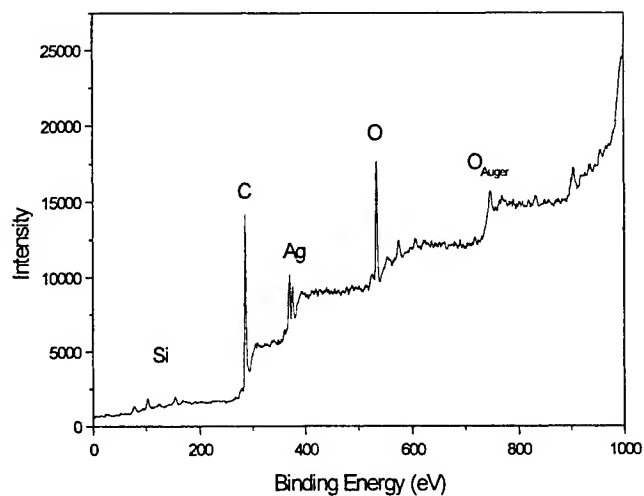


Fig. 3 XPS spectrum of diamond film with Ag contacts

The Arrhenius plot of $\ln(J)$ versus $1000/T$ under different electric fields, as shown in Fig. 4, indicated that the current density was a function of the measured temperatures. This suggests that the field-activated transport mechanism rather than the Fowler-Nordheim effect (or the tunnel effect) might control the conduction, because the tunnel effect is relatively independent of temperature.

The conduction mechanisms in the undoped diamond film can be attributed to either the Schottky emission (SE)¹³ or the Poole-Frenkel (PF)¹⁴. The current J_{SE} governed by SE transportation is expressed as¹⁵

$$J_{SE} = A^* T^2 \exp\left(-\frac{\phi_B - \beta_{SE} E^{\frac{1}{2}}}{kT}\right) \quad (1)$$

$$\beta_{SE} \equiv \left(\frac{q^3}{4\pi\epsilon\epsilon_0}\right)^{\frac{1}{2}} \quad (2)$$

, where A^* is a constant, ϕ_B is Schottky barrier height (SBH), ϵ_0 is the permittivity of free space, ϵ is the relative dielectric permittivity of diamond, q is the electric charge, k is Boltzmann's constant, T is the temperature, E is the external electric field, and β_{SE} is Schottky field-lowering coefficient caused by image force. The SE mode is on the analogy of PF conduction, which is governed by carriers thermally emitted from the trapped centers under a strong electric field. The PF current, J_{PF} , is expressed as¹⁶

$$J_{PF} = AE \exp\left(-\frac{\phi_t - \beta_{PF} E^{\frac{1}{2}}}{kT}\right) \quad (3)$$

$$\beta_{PF} \equiv \left(\frac{q^3}{\pi\epsilon\epsilon_0}\right)^{\frac{1}{2}} \quad (4)$$

, where A is a constant, ϕ_t is a depth of trapped level, and β_{PF} is Poole-frenkel constant.

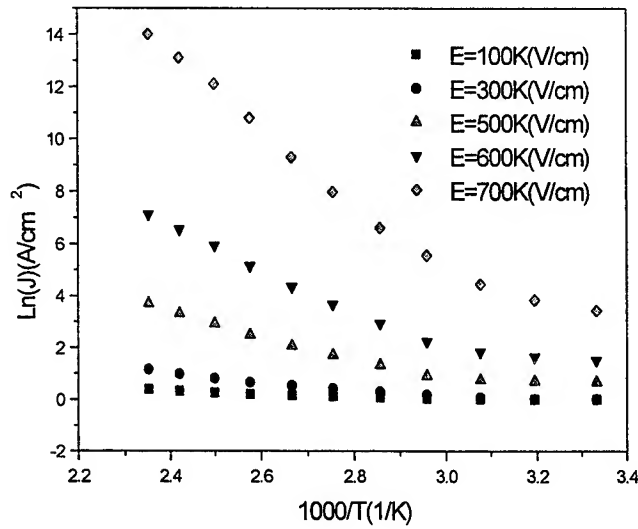


Fig. 4 The Arrhenius plot of $\ln(J)$ versus $1000/T$ under different electrical field for diamond MIS structure

On the basis of the $\ln(J)$ versus $E^{1/2}$ plot shown in Fig. 5, there are two slopes of linear regions and a turning electric field defined at 240 kV/cm, and the $\ln(J/E)$ versus $E^{1/2}$ plot shown in Fig. 6, there is also a turning electric field at 240 kV/cm. The two slope in Fig. 5 are 0.0066 and 0.013, β_{SE} and β_{PF} calculated from which are 1.63×10^{-4} , and 3×10^{-4} . The β_{SE} and β_{PF} are quite close to the values calculated directly from the equation (2) and (4) with $\epsilon = 5.5$. Hence, the conduction mechanism in the undoped polycrystalline diamond film was dominated by Schottky emission (SE) below the transition electric field of 240 kV/cm and was dominated by PF beyond 240 kV/cm.

The equation (1) is rewritten as

$$\ln\left(\frac{J_{SE}}{T^2}\right) = \ln(A^*) - \left(\frac{\phi_B + \beta_{SE} E^2}{kT}\right) \quad (5)$$

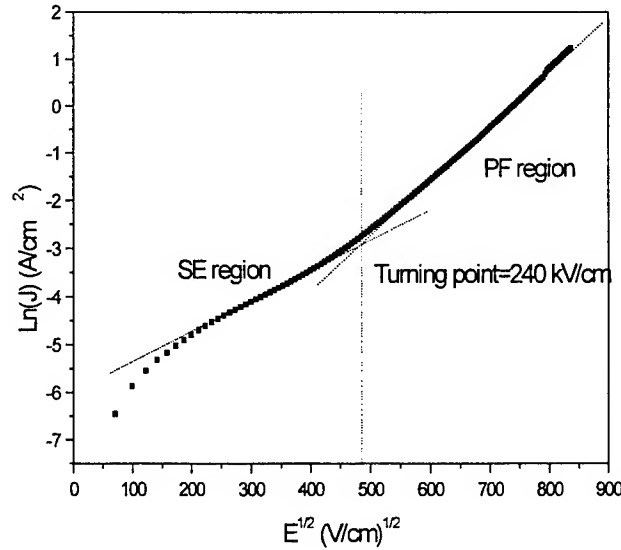


Fig. 5 $\ln(J)$ versus $E^{1/2}$ plot at the room temperature for diamond MIS structure.

The variations of $\ln(J/T^2)$ with $1000/T$ at different electric field from 50 kV/cm to 200 kV/cm plotted in Fig. 7. All of plots show good linearity with negative slopes. The activation energies at each electric field are calculated from the slopes of the graphs in Fig. 7 and are plotted in Fig. 8 as a function of $E^{1/2}$. The extrapolation of the line to $E^{1/2} = 0$ in Fig. 8 indicates the SBH of silver and diamond is 2.4 eV.

The equation (3) is rewritten as

$$\ln\left(\frac{J_{PF}}{E}\right) = \ln(A) - \left(\frac{\phi_t + \beta_{PF} E^2}{kT}\right) \quad (6)$$

The variations of $\ln(J/E)$ with $1000/T$ at electric field from 360 kV/cm to 700 kV/cm shown in Fig. 9. All the plots in Fig. 9 also have good linearity with negative slopes. The slopes of the graphs at each electric field in Fig. 9 are corresponding to the activation energies, which decrease in a linear fashion with $E^{1/2}$, plotted in Fig. 10. The extrapolation of the line to $E^{1/2} = 0$ in figure 10 suggests the trap depth in the bulk diamond is 4.75 eV.

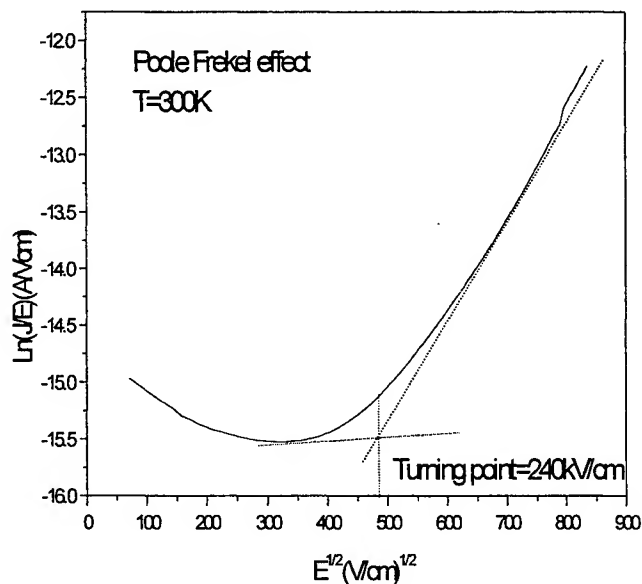


Fig. 6 $\ln(J/T^2)$ versus $E^{1/2}$ plot at room temperature for diamond MIS structure.

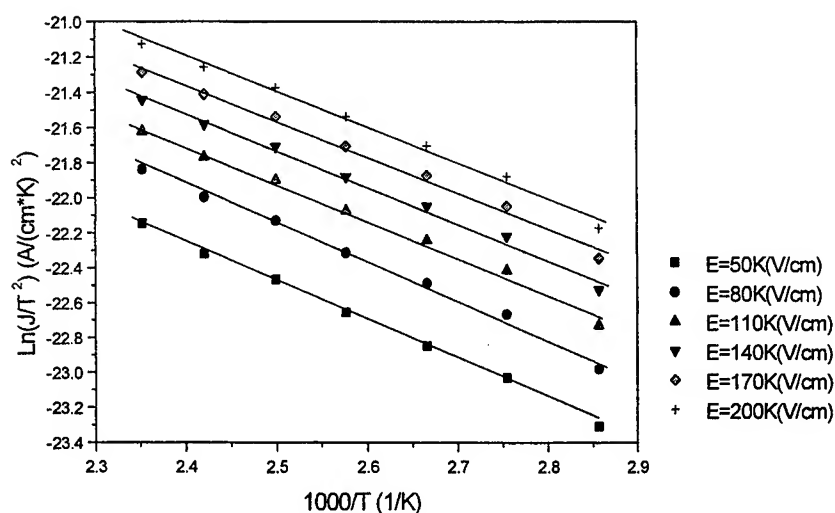


Fig. 7 The variations of $\ln(J/T^2)$ with $1000/T$ at electric field from 50kV/cm to 200kV/cm for diamond MIS structure.

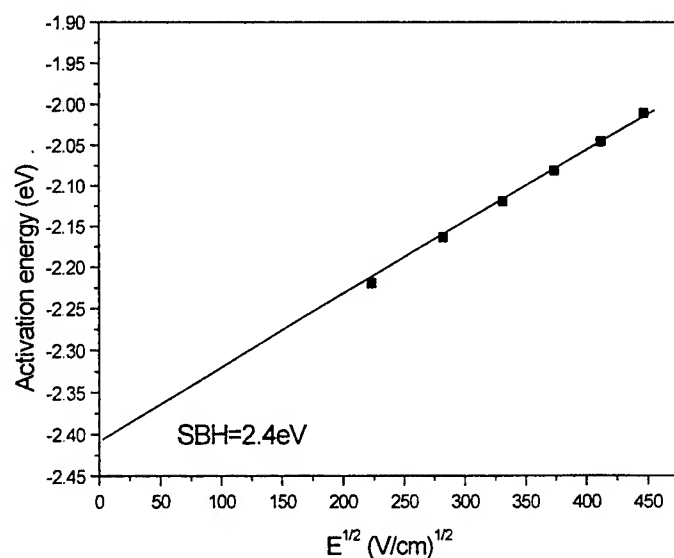


Fig. 8 The activation energies as a function of $E^{1/2}$. By extrapolation to $E^{1/2}=0$ indicating the SBH of silver and diamond is 2.4eV .

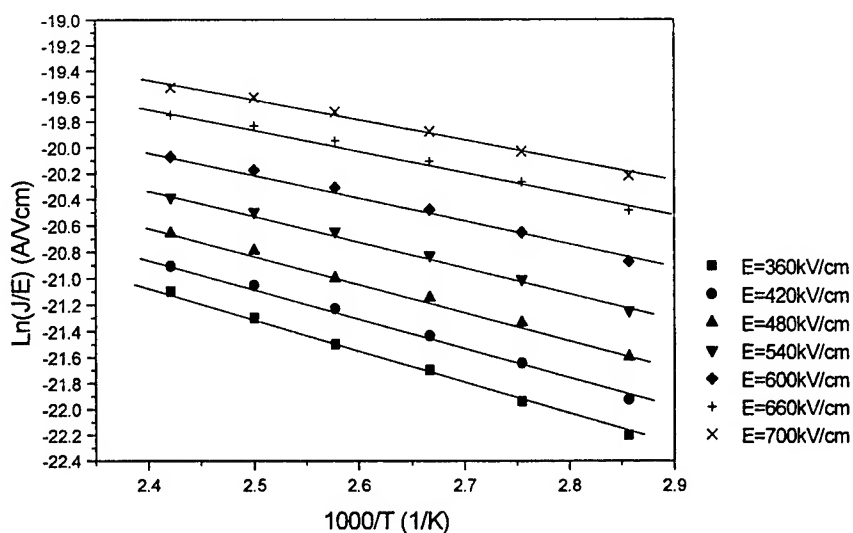


Fig. 9. The variations of $\text{Ln}(J/E)$ with $1000/T$ at electric field from 360kV/cm to 700kV/cm.

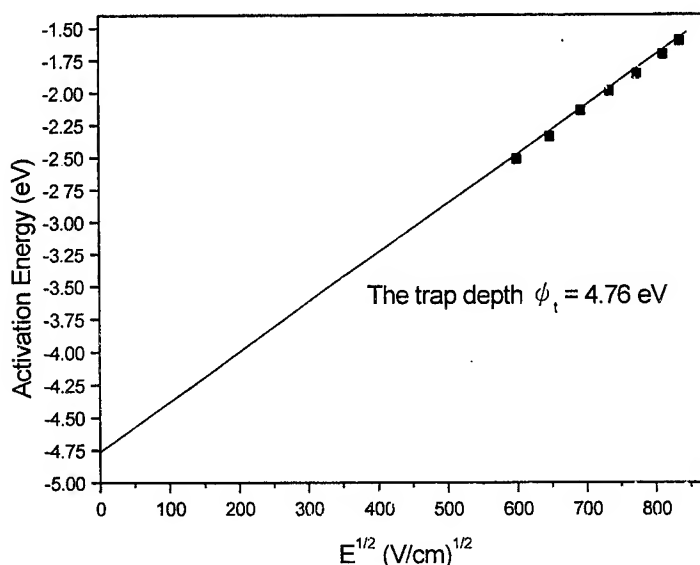


Fig. 10 The activation energies as a linear function of $E^{1/2}$, which suggests the trap depth in the bulk diamond is 4.75eV.

4. CONCLUSION

In this paper, the deposition parameters to grow undoped polycrystalline diamond films were $\text{CH}_4/\text{H}_2 = 0.5\%$, pressure = 45 torr, power = 2.2 kW, and substrate temperature = 885°C by using a MPCVD system. SEM shows the orientation of undoped diamond films was (111) facet. The Raman Spectra had a diamond characteristic peak at 1333cm^{-1} . By analyzing the XPS spectroscopy, we concluded that a cleaning procedure on diamond films can eliminate the carbon phase but enhance the oxidation on the films. The current-voltage-temperature measurements in a metal-insulator-semiconductor (MIS) structure of diamond films were performed to study its electrical characteristics. We found that, in electric conduction mechanism, Schottky emission (SE) transport dominate below an electric field of 240 kV/cm, and Poole-Frenkel (PF) effect dominates beyond 240 kV/cm. By the extrapolations, the Schottky barrier height of silver and diamond film is 2.4eV, and the trap depth is 4.75eV in the diamond film.

ACKNOWLEDGEMENTS

The authors would like to express gratitude to Mr. R. C. Lee at the Southern Instrument Center of National Cheng Kung University for XPS analysis, and to acknowledge C. H. Sun for providing some of the diamond samples. The National Science Council in Taiwan supported this research with grant No. NSC 87-2216-E224-003.

REFERENCES

1. I. M. Buckley-Golder and A. T. Collins, *Diamond and Relat. Mater.*, **1**, p.1083-1101, 1992.
2. K. Miyata, K. Kobashi, and D. L. Dreifus, *diamond and Relat. Mater.*, **2**, p.1107, 1993.

3. Gennady Sh. Gildenlat et al., , Proceedings of the IEEE. **79**, p.647-668, 1991
4. M. I. Landstrass and K. V. Ravi, Appl. Phys. Lett., **55**, 975, 1989.
5. G. De Cesare, S. Salvatori, R. Vincenzoni, P. Ascarelli, E. Cappelli, Diamond and Relat. Mater., **4**, p.628-631, 1995.
6. S. Ashok, K. Srikanth, A. Badzian, and R. Messier. Appl. Phys. Lett., **50**, p. 763-765, 1987.
7. T. Sugino, Yasuski Muto, and Junji Shirafuji, Diamond and Relat. Mater., **2**, p.797-802, 1993.
8. E. Boettger, X. Jiang, and C. P. Klages, Diamond and Relat. Mater., **3**, p.957-960, 1994.
9. C. H. Sun, National Yunlin university of science and technology, Mater Thesis, Touliu, Taiwan, 1998.
10. Y. Mori, H. Kwarada, and A. Hiraki, Appl. Phys. Lett., **58**, p.940, 1991.
11. G. Sh. Gildenbalt, A. R. Badzian, and T. Badzian, IEEE Electron Device Letter, **11**, p.371, 1990.
12. R. E. Thomas, and R. J. Markunas, J. Vac. Sci. Technol. A, **10**, p 2451, 1992.
13. A. K. Jonscher, Electronic properties of amorphous dielectric films, Thin Solid Films, **1**, p.213-234, 1967.
14. Robert M. Hill, Poole-Frenkel conduction in amorphous solids, Phil. Mag., **23**, p.59-86, 1971.
15. Bohr-ran Huang and W. Z. Ke, Mater. Chem. Phys., **60**, p.143, 1999.
16. M. S. Tsai and T. Y. Tseng, J. Electrochem. Soc., **145**, p.2853, 1998.

Sensing characteristics of ISFET based on AlN thin film

Jung-Lung Chiang^a, Shiun-Sheng Jan^a, Ying-Chung Chen^a, Jung-Chuan Chou^b

^aDepartment of Electrical Engineering, National Sun Yat-Sen University,
Kaohsiung, Taiwan 804, R.O.C.

^bInstitute of Electronic and Information Engineering, National Yunlin University
of Science and Technology, Touliu, Yunlin, Taiwan 640, R.O.C.

ABSTRACT

In the past years, the aluminum nitride (AlN) thin films were usually applied to the surface acoustic wave (SAW) devices, optical devices in the ultraviolet spectral region, acousto-optic devices and integrated circuit packaging. In this study, we first selected the AlN thin film as gate insulator for pH sensing ISFET in our laboratory. We have studied the relationship between pH sensitivity and surface potential for AlN gate ISFET in the different solutions. And we also have obtained the pH characteristics from the capacitance-voltage (C-V) and current-voltage (I-V) curves. Herein, we can obtain the shift of the linear region threshold voltage of the AlN/SiO₂ gate ISFET devices in the different buffer solutions. The AlN materials exhibited a high response, and the sensitivity was about 45~51 mV/pH. In addition, we have also compared with different sensing materials.

Keywords: ISFET, Aluminum Nitride (AlN), pH Sensitivity

1. INTRODUCTION

In the recent year, these materials (such as : a-WO₃¹⁻³, a-Si:H⁴, Ta₂O₅⁵, SnO₂^{6,7}, Si₃N₄⁸) were investigated and has been used as pH sensitive gate materials for the pH ISFET devices in our laboratory. We found that the pH sensitivity is one of the important characteristic parameters of ISFET devices and the response of ISFET is mainly determined with the type of the sensing membrane, therefore the sensing material plays a significant role.

In the past, the aluminum nitride (AlN) thin films were usually applied to the surface acoustic wave (SAW) devices⁹, optical devices in the ultraviolet spectral region, acousto-optic devices and integrated circuit packaging. Because of their energy gap is very large (about 5.9~6.2eV), the phase velocity is fairly high (~5280 m/s)⁹, high refractive index (1.9~2.1 for polycrystalline films), chemical and thermal stability, high density (3.3 g/cm³) and have large electrical resistivity (~10¹⁴ Ω-cm)¹⁰. In addition, the capacitance-voltage characteristics are similar to pure SiO₂, and a dielectric constant of 12.4.¹¹

According to the above mentional, AlN thin films have very large energy gap, chemical and thermal stability and C-V characteristics are similar to pure SiO₂. Therefore, in this study, we first selected the AlN thin film as gate insulator for pH sensing ISFET devices to measuring capacitance-voltage (C-V), current-voltage (I-V) curves and discussing pH sensitive characteristics in the different solutions.

2. EXPERIMENTALS

Generally, the aluminum nitride (AlN) thin films have been prepared by several methods: reactive rf sputtering⁹ or dc sputtering¹⁰ from a metallic aluminum target in an atmosphere of Ar-N₂ gas mixture. However, in our research, the aluminum nitride (AlN) thin films were deposited on substrates maintained at 150°C by rf sputtering from a 2 inch diameter, 1/4 inch thickness, and 99.9% purity of a compound target (aluminum nitride target). The experiment was achieving an ultimate pressure of 3-5 × 10⁻⁶ torr, and sputtering total operating pressure of 20 mtorr in Ar mixed N₂ gas for 2~4 hours. In addition, the rf power (Model : SKN-05P) was setting 65W, operating at 13.56 MHz and the fabrication conditions were shown in Table 1.

Further author information: (Send correspondence to Dr. Jung-Chuan Chou)

Jung-Lung Chiang: E-mail: d8631801@student.nsysu.edu.tw Tel: 886-75252000 ext.4127 Fax: 886-75254015

Shiun-Sheng Jan: E-mail: d8531801@student.nsysu.edu.tw

Ying-Chung Chen: E-mail: ycc@mail.nsysu.edu.tw

Jung-Chuan Chou: E-mail: Choujc@pine.yuntech.edu.tw Tel: 886-55342601 ext.2500 Fax: 886-5312029, 5312063

Table 1. Manufacturing conditions of AlN thin film

Parameters	Condition
Substrate temperature (°C)	150
Gas pressure (torr)	20×10^{-3}
Gas flow rate (sccm)	20
RF power (W)	65

2.1. EIS and MIS Structures

AlN thin films were deposited on the EIS structure (AlN/SiO₂/p-Si/Al) and MIS structure (Al/AlN/SiO₂/p-Si/Al). In this study, the EIS structure was made on a p-type Silicon wafer (8~12 Ω-cm). The thickness of the thermally grown silicon dioxide (SiO₂) is about 1000Å, and the AlN thin films were prepared by rf sputtering system, the thickness was between 800Å and 1200Å. Afterwards, the EIS samples were packaged with epoxy, and the C-V curves were measured in the different buffer solutions. The EIS structure was shown in Fig. 1.(a).

In addition, we used the thermal evaporation system to prepare metallic dot (aluminum, Al) on top of the EIS samples, and the MIS structure was finished. And then the MIS samples were bounded and tested at different frequencies. The MIS structure with AlN thin film was shown in Fig. 1.(b).

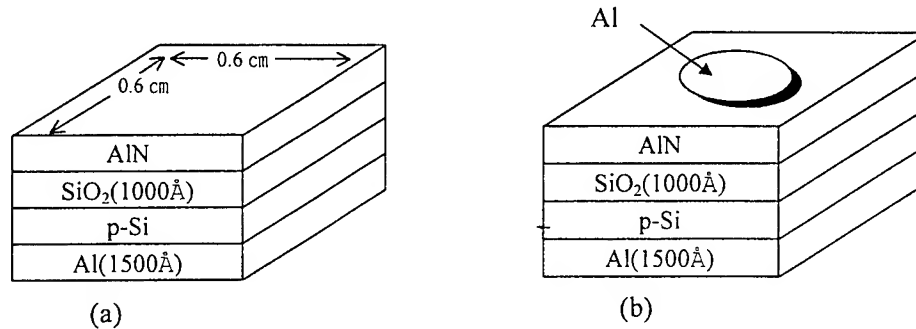


Figure 1. AlN thin films were prepared on different structures. (a) EIS structure and (b) MIS structure

2.2. ISFET Devices

In this study, the n-channel ISFETs were fabricated with four photo masks on p-type silicon wafers of 8~12 Ω-cm resistivity, (100)-oriented. The channel length and width were 50 μm and 1000 μm (i.e. W/L = 20), respectively. The thickness of the thermally grown SiO₂ layer was about 1000 Å. The fabrication processes were shown in Ref. 1, and without metal gate of MOSFET devices were finished. Afterwards, we used the rf sputtering system again to prepare the AlN thin films and the double layers of AlN/SiO₂ gate ISFET devices. Finally, we bounded wire and packaged to obtain the electrical characteristics in different buffer solutions. The structure of AlN/SiO₂ gate ISFET device was shown in Fig. 2.

2.3. Package Processes

For the measuring convenient and avoid the leakage current to be generated during testing, in our experiment, all samples were packaged with the resin epoxy. The several steps of package processes were listed as follows:

- (1). Clean samples;
- (2). N₂ gas to dry and baking in the oven (120°C, 5~10mins);
- (3). Bounding wire with Ag paste;

- (4). Baking Ag paste (120°C, 15mins), for connecting wire and contact;
- (5). Packaging with resin epoxy, and then baking 15~20mins at 120°C.
- (6). The devices were packaged completely.

2.4. C-V Measurement

The C-V curves of the EIS and MIS structures were obtained by the HP4284A LCR Parameter Analyzer. Furthermore, the measurement was operated at different frequencies, scanning voltage was between -8V and 8V. In addition, the C-V measurement needs to avoid thermal fluctuation and photoelectric effect during the measurement, therefore, all test instrumentation must be placed in the dark box, at constant temperature (25°C).

2.5. I-V Measurement

The I-V measurement (Keithley 236 semiconductor parameter analyzer) was used to measure the threshold voltage (V_{th}) of the AlN/SiO₂ gate ISFET devices in the pH=1,3,5,7 buffer solutions. In order to sure that the ISFET devices were under stable situation, the sensor head and the reference electrode were immersed in the buffer solution for 15~20 seconds before testing. In addition, to avoid the effect of light and temperature, all the measurements were carried out at room temperature (25°C) in air and were placed in the dark box. The I-V measurement system was the same as Ref. 1.

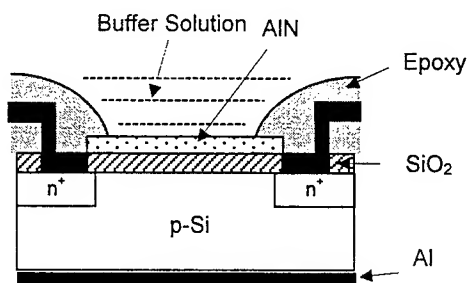


Figure 2. Structure of AlN/SiO₂ gate pH-ISFET

3. RESULTS AND DISCUSSION

3.1. C-V Characteristics of the MIS Structure

The capacitance varies as a function of the applied gate voltage and the measured capacitance-voltage (C-V) characteristic is of considerable practical importance. In our study, the C-V measurement (HP4284A) are performed with a computer in the dark box. The high frequency and low frequency C-V characteristics curves of the MIS structure are displayed in Fig. 3. The experimental results show that the C-V characteristics curves of the AlN MIS structure are operated at different frequencies (1KHz, 3KHz, 100KHz, 1MHz). When the d.c. bias is systematically changed, because of the charge inside an p-type MIS structure is dominated by applied a.c. signal, therefore, C-V curves can be changed from accumulation, through depletion, to inversion region. According to above mentioned, we found that the capacitance-voltage characteristics of AlN material are similar to pure SiO₂.

3.2. C-V Characteristics of the EIS Structure

The capacitance-voltage (C-V) method is often employed to study the double layer structure, electrokinetics, surface adsorption and material corrosion. However, the EIS equivalent circuit can be simplified by four capacitors connected in series.¹² In addition, the EIS C-V curves cover the region from accumulation, flat-band, depletion, weak inversion and strong inversion. Herein, at the accumulation and inversion regions, the space charge is dominated by the minority carrier, therefore, these regions will not be used for the study pH response of the EIS C-V measurement. However, at the flat band condition, the charge density is low and not dominating, therefore, the pH response of the EIS measurement in different H⁺ solutions can be shifted at this measurement region.¹³

As shown in Fig. 4, the C-V curves of the double layer (AlN/SiO_2) is obtained when EIS structure is immersed in the pH=1, 3, 5, 7 buffer solutions. These experimental results indicate linear shift at the flat band region (V_{FB}) of the C-V characteristic curves, and it is found that the pH sensitivity of the AlN thin film is about 48 mV/pH working at 3.3KHz. However, in the Ref 14, it found that the AlN thin films were dissolved in the very strong basic solution. For this reason, in this study, the samples were immersed in the acid solutions in the entire measured processes.

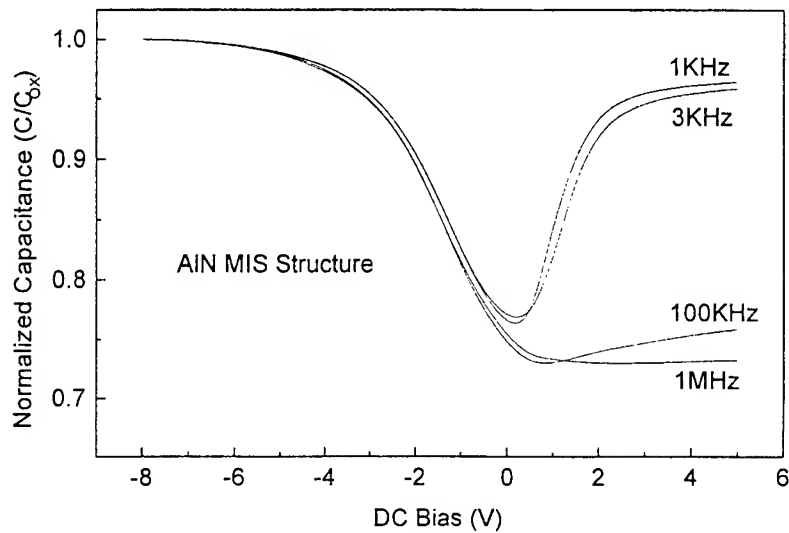


Figure 3. Capacitance versus voltage curves of the AlN MIS structure

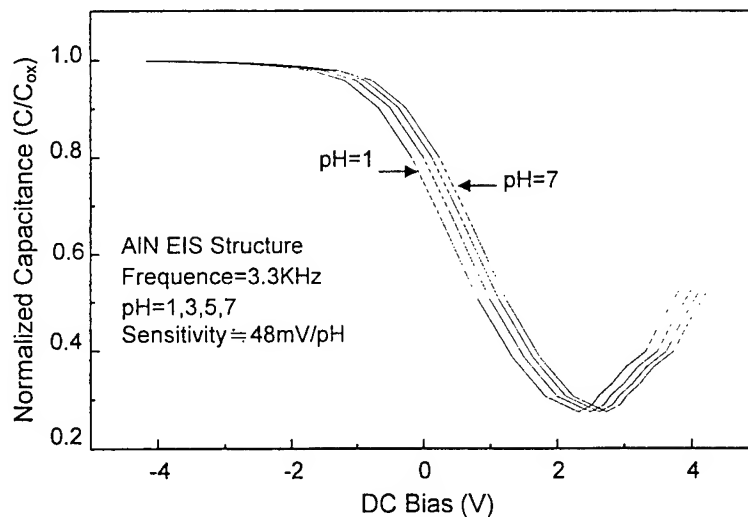


Figure 4. Capacitance versus voltage curves of the AlN EIS structure

3.3. I-V Characteristics of the ISFET

The operation of the ISFET is very similar to a conventional MOSFET, except that a metal gate is replaced by a reference electrode and electrolyte. The source and drain of ISFET devices were bounded wire and packaged with resin epoxy to avoid leakage current during the testing. When the AlN/SiO₂ gate ISFET and reference electrode (calomel electrode) were placed in the different buffer solutions, and V_{DS} is set 0.2V, namely, the ISFET device is operated at linear region. The relationship curves between drain current (I_{DS}) and reference electrode voltage (V_{GS}) were measured at the same temperature (25°C). Therein, the threshold voltage (V_{th}) of the ISFET device can be obtained in a family transconductance curves, and the measured result is shown in Fig. 5. The result shows that the AlN/SiO₂ gate ISFET has a linear pH sensitivity of approximately 51mV/pH in the pH=1, 3, 5, 7 buffer solutions, and the threshold voltage increases with increasing pH value.

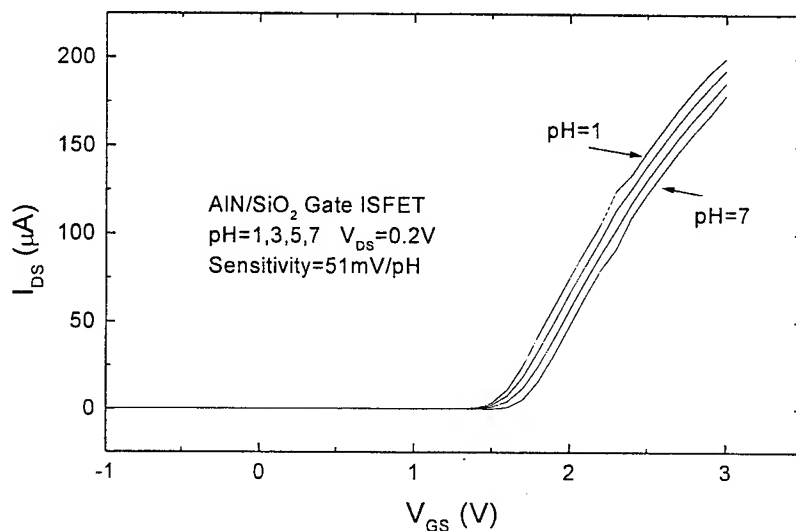


Figure 5. I_{DS} versus V_{GS} curves of the AlN/SiO₂ gate ISFET

In addition, in Fig. 6, a family of curves that the relationship between drain current (I_{DS}) and drain-source voltage (V_{DS}) can be obtained in pH=1, 3, 5, 7 buffer solutions. In the saturation region of curves, the result shows that the AlN/SiO₂ gate ISFET has a linear current variability during the constant reference electrode voltage (V_{GS}).

Moreover, we can also apply a series of step voltages at the reference electrode (V_{GS}) to measuring I_{DS} versus V_{DS} curves in the different concentrations between pH=1 and pH=7 buffer solutions. Afterwards, in the saturation region, the current-voltage's equation of MOSFET was utilized to calculating the saturation drain current that varies as the square of the reference electrode voltage (V_{GS}). The calculated result is shown in Fig. 7. According to the transform data, we can obtain another family curves of the $\sqrt{I_{DS}}$ versus V_{GS} characteristics, and we find that the threshold voltage also increases with increasing pH value.

3.4. Comparison

Additionally, for estimating the applicability and feasibility, the pH sensitivity of property for AlN gate ISFETs will be compared with some of a-WO₃¹⁻³, Ta₂O₅⁵, a-Si:H⁴, SiO₂¹⁵, Si₃N₄⁸, Al₂O₃¹⁵ and SnO₂⁶. The pH sensitivities of these ion-sensing membranes are listed in Table 2. The SiO₂ gate ISFET has low pH sensitivity, and the sensitivity is unstable because it is varied by pH value of electrolyte solutions. In contrast with Si₃N₄, Al₂O₃, SnO₂, a-Si:H, Ta₂O₅, a-WO₃ and AlN gate ISFETs indicate superior pH sensitivities.

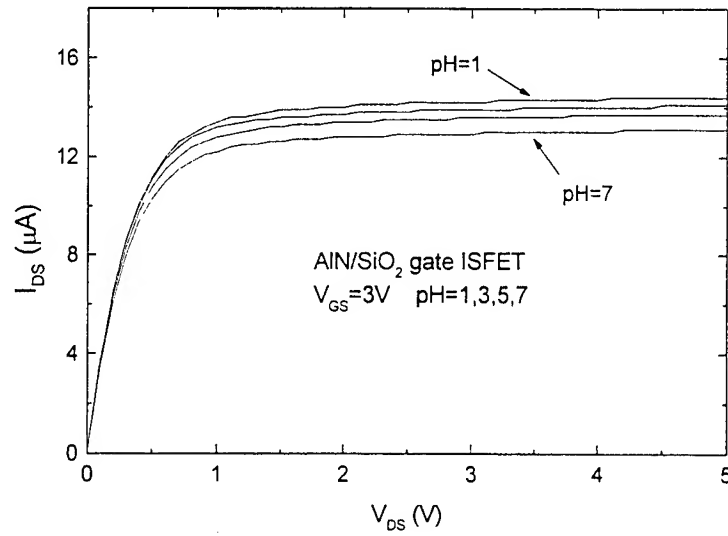


Figure 6. I_{DS} versus V_{DS} characteristic curves of AlN/SiO₂ gate ISFET device

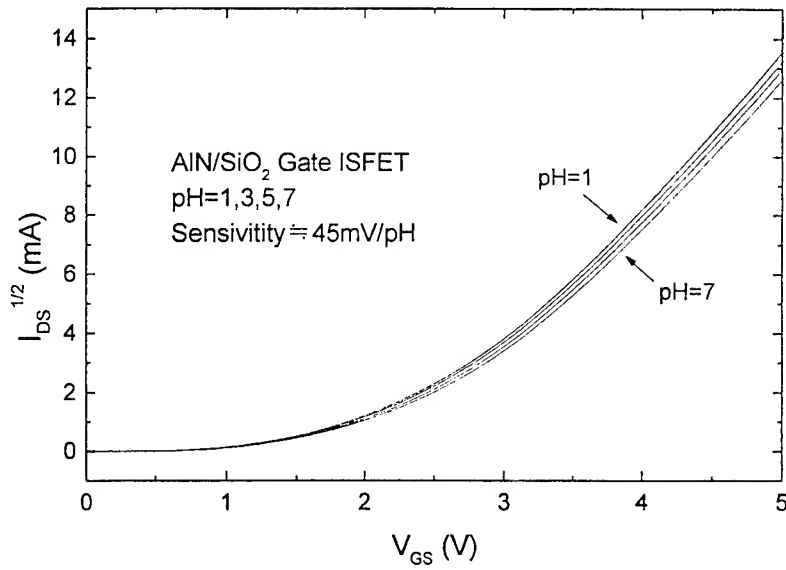


Figure 7. Current versus voltage characteristic curves of the AlN/SiO₂ gate ISFET

From the comparison results, the AlN thin film is selected as sensing membrane, which is shown the high response, namely, the pH sensitivity is approximately 50mV/pH. Thus, AlN thin film is also suitable apply for ion-sensing membranes of ISFET devices in the different testing environment.

Table 2. Comparison of pH sensitivity for different sensing membranes

Membrane	Test range	Sensitivity (mV/pH)
AlN	1 ~ 7	45~51
a-WO ₃ ¹⁻³	1 ~ 7	50.2~57.6
a-Si:H ⁴	2 ~ 7	51.3~56.5
SnO ₂ ^{6,13}	2 ~ 10	58
Ta ₂ O ₅ ⁵	2 ~ 12	57.1~58.3
Al ₂ O ₃ ¹⁵	1 ~ 13	53 ~ 57
Si ₃ N ₄ ^{8,15}	1 ~ 13	46 ~ 56
SiO ₂ ¹⁵	4 ~ 10	25 ~ 48

4. CONCLUSIONS

In this paper, we have measured the capacitance-voltage characteristics curves of AlN EIS structure and the current-voltage characteristics curves of AlN gate ISFET in the pH=1, 3, 5, 7 buffer solutions. And we can obtain the pH sensitivity is about 45~51mV/pH, and has near linear pH response in the C-V and I-V characteristics curves. From experimental results, it shows that the AlN thin film is suitable for pH sensing in the acid solutions.

ACKNOWLEDGMENTS

This study is supported by National Science Council, the Republic of China under the contracts NSC89-2216-E-110-022.

REFERENCES

1. J. C. Chou and J. L. Chiang, "Ion sensitive field effect transistor with amorphous tungsten trioxide gate for pH sensing", *Sensor and Actuators B*, **62**, No. 2, pp. 81-87, February 25, 2000.
2. J. L. Chiang, J.C. Chou and Y. C. Chen, "Study on the pH sensing property of amorphous tungsten trioxide thin films by rf sputtering", *Proceedings of 1998 International Electron Devices and Materials Symposia (IEDMS'98)*, National Cheng Kung University Tainan, Taiwan, R.O.C., Symposium B · C, CP-4, pp. 337-340, December 20-23, 1998.
3. J. C. Chou and J. L. Chiang, "Study on the amorphous tungsten trioxide ion sensitive field effect transistor", *Proceedings of Technical Digest of the 7th International Meeting on Chemical Sensors(IMCS7)*, Beijing International Convention Center, Beijing, China, pp. 535-537, July 27-30, 1998.
4. J. C. Chou and C. N. Hsiao, "Drift behavior of ISFET with a-Si:H-SiO₂ gate insulator", *Materials Chemistry and Physics*, **63**, pp. 270-273, 2000.
5. J. C. Chou, Y. S. Li and J. L. Chiang, "Simulation of Ta₂O₅-gate ISFET temperature characteristics", *Proceedings of 1998 Annual Symposium of the Biomedical Engineering Society (BMES'98)*, National Yang Ming University, Taiwan, R.O.C., pp. 471-474, December 18-19, 1998.
6. H. K. Liao, J. C. Chou, W. Y. Chung, T. P. Sun and S. K. Hsiung, "Study of amorphous tin oxide thin films for ISFET applications", *Sensors and Actuators B*, **50**, pp. 104-109, 1998.
7. H. K. Liao, L. L. Chi, J. C. Chou, W. Y. Chung, T. P. Sun and S. K. Hsiung, "Study on pH_{pzc} and surface potential of tin oxide gate ISFET", *Materials Chemistry and Physics*, **59**, pp. 6-11, 1999.
8. H. K. Liao, J. C. Chou, W. Y. Chung, T. P. Sun and S. K. Hsiung, "Study on the interface trap density of the Si₃N₄/SiO₂ gate ISFET", *Proc. 3rd East Asian Conference on Chem. Sensor*, Seoul, Korea, pp. 394-400, November 5-6, 1997.
9. Y. J. Yong and J. Y. Lee, "Characteristics of hydrogenated aluminum nitride films prepared by radio frequency reactive

- sputtering and their application to surface acoustic wave devices", *J. Vac. Sci. Technol. A* , **15**, No. 2, pp. 390-393, 1997.
10. D. Manova, V. Dimitrova, W. Fukarek and D. Karpuzov, "Investigation of d.c. reactive magnetron-sputtered AlN thin films by electron microprobe analysis, X-ray photoelectron spectroscopy and polarised infra-red reflection", *Surface and Coatings Technol.*, **106**, pp. 205-208, 1998.
 11. E. A. Chowdhury, J. Kolodzey, J. O. Olowolafe, G. Qiu, G. Katulka, D. Hits, M. Dashiell and D. van der Weide, "Thermal oxidized AlN thin films for device insulators", *Appl. Phys. Lett.*, **70**, No. 20, pp. 2732-2734, 1997.
 12. S. H. Wong, "Theoretical and experimental studies of CVD aluminum oxides as pH sensitive dielectric for the back contacts ISFET sensors", Ph. D. Dissertation, Department of Biomedical Engineering, Case Western Reserve University, May, 1985.
 13. H. K. Liao, "Study of tin oxide as a sensing film for ISFET applications", Ph. D. Dissertation, Department of Electronic Engineering, Chung-Yuan Christian University, September, 1998.
 14. N. W. Gao, Y. Q. Lu, Y. L. Qin, and Y. H. Wu, "Matallization of AlN substrates", *Electronic Components and Materials(China)*, **18**, No. 5, pp. 22-23, Oct. 1999.
 15. T. Matsuo and M. Esashi, "Method of ISFET fabrication", *Sensors and Actuators*, **1**, pp. 77-96, 1981.

Initial growth effects on the properties of GaN buffer layer and subsequent GaN overlayer by MOCVD

Dong-Sing Wu^{*a}, Wei-Hao Tseng^a, Wei-Tsung Lin^a, and Ray-Hua Horng^b

^aDepartment of Electrical Engineering, Da-Yeh University, Chang-Hwa 515, Taiwan ROC

^bInstitute of Precision Engineering, National Chung Hsing University, Taichung 402, Taiwan ROC

ABSTRACT

The role of temperature ramping rate during the two-step growth of GaN-on-sapphire by metalorganic chemical vapor deposition is explored. The surface morphology and crystalline properties of the GaN buffer layer annealed under various temperature ramping rates (20–60°C/min) were investigated by atomic force microscopy and x-ray measurements. For the lower ramping rates employed, a dramatic re-evaporation of the GaN buffer layer was observed. This makes the buffer layer thinner, yielding the GaN epilayer of hexagonal morphology. However, as the higher ramping rates applied, the surface becomes rougher and exhibits hexagonal three-dimensional islands. It could be due to the fact that the grains of the GaN buffer layer have no enough time to coarsen. Under a temperature ramping rate of 40°C/min, a smooth buffer-layer surface can be maintained and result in a subsequent high-quality over-layer deposition. The mirror GaN epilayer shows a near-band-edge peak (25 K) centered at 3.477 eV with a full width at half maximum as narrow as 13.1 meV. The observed temperature-ramping-rate effects can be interpreted by the coalescence mechanism of the GaN buffer layer involving Ostwald ripening, sintering and cluster migration.

Keywords: GaN epilayer, buffer layer, temperature ramping rate, MOCVD, AFM, XRD

1. INTRODUCTION

Nitride semiconductors are presently one of the most promising materials for optoelectronic devices operating in the visible-to-ultraviolet wavelength region ¹⁻³. Due to the chemical dissimilarity and large lattice mismatch between GaN and substrates (Si, GaAs, SiC, or sapphire, etc), mirror GaN epilayers grown by metalorganic chemical vapor deposition (MOCVD) often requires the two-step growth process. This method consists of a low-temperature (500–600°C) thin buffer-layer growth and a high-temperature ($\geq 1000^\circ\text{C}$) over-layer deposition. That is, the GaN epilayers were grown at high temperature on the buffer layer annealed, during the heating process, to beyond 1000°C . Various kinds of pretreatment for the sapphire substrate have been proposed. The natures of the nitridated layers formed on the (0001) sapphire substrate by heating at 1050°C in NH_3 and their influence on GaN nucleation have been demonstrated ⁴⁻⁶. An *in situ* thermal cleaning treatment of sapphire surface in H_2 ambient was confirmed to have a great benefit to the GaN film⁷. The effects of thickness, growth temperature and post thermal annealing time for the GaN buffer layer on the overall epilayer quality have been widely described ⁸⁻¹⁵. It was found that the GaN buffer layer exhibited significant recrystallization during the thermal annealing that occurred when the MOCVD reactor was ramped from the low buffer growth temperature to the higher temperature used for growth of the main epilayer^{16,17}. Up to now, most of the previous studies are based on a fixed temperature-ramping rate during the two-step growth process. The temperature-ramping-rate effects on the GaN buffer layer and subsequent main epilayer are not well understood. In this study, the surface morphology and the crystalline properties of the GaN buffer layers annealed under various temperature-ramping rates were analyzed. The mechanism of the GaN growth behavior based on the observed results is also presented.

2. EXPERIMENTAL

* Author to whom should be addressed. E-mail: dsw@aries.dyu.edu.tw; Fax: +886-4-8521904

In this work, the experiments were carried out in a dual-flow MOCVD reactor, as schematically shown in Fig. 1. The group V and group III sources were supplied separately into the chamber and mixed before the susceptor about 5 cm. This new dual-flow design can minimize the pre-reaction among the reactive gases, and the effects that NH_3 used for the V source was not mixed with the other sources into the reactor could be investigated in this study. Trimethylgallium (TMGa) and hydrogen were used for the column III source and the carrier gas, respectively. The (0001)-oriented sapphire wafer was used as the substrate. After the degreasing process, the substrate was etched in a H_2SO_4 : H_3PO_4 : H_2O_2 = 3: 1: 1 solution at 160°C for 10 min. Prior to the GaN growth, the substrate was thermal cleaning in the H_2 ambient at 1000°C for 10 min. Then the sapphire was nitridated at 1000°C in the NH_3/H_2 ambient. Following this treatment, a 25-nm-thick GaN buffer layer was deposited at 600°C under a V/III ratio of 3000. After the buffer-layer growth, the sample was ramped up to 1000°C with various ramping rates. Then the GaN buffer layer was annealed at 1000°C with 5 min and the GaN epilayer were grown on the GaN buffer layers annealed under various temperature-ramping rates at 1000°C under a V/III ratio of 6000. The parameters of GaN growth conditions are given in Table I. A timing chart of GaN growth process is shown in Fig. 2. The surface morphology and roughness of the GaN buffer layers annealed under various temperature-ramping rates were analyzed by atomic force microscopy (AFM, PSI AutoProbe). The crystalline properties of the GaN buffer layers annealed under various temperature-ramping rates were analyzed by X-ray diffraction (XRD, SIEMENS D5000) with Cu K α radiation. Scanning electron microscope (SEM, JEOL 6400) was used to examine the overall surface morphology of the GaN epilayer. The optical and electrical qualities of the GaN epilayer were characterized by photoluminescence excited by a 325-nm He-Cd laser and Hall measurement, respectively.

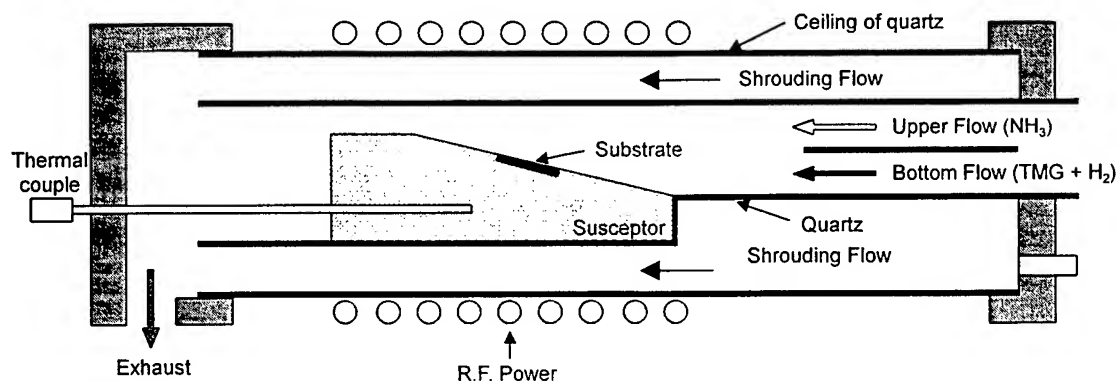


Fig. 1. Schematic diagram of a dual-flow MOCVD reactor used in this work.

Table I. Parameters of GaN growth condition.

Process	Temperature	Gas	Flow rate
(a) thermal cleaning	1000°C	H_2	2000cm ³ /min
(b) nitridation	1000°C	H_2	2000cm ³ /min
		NH_3	2000cm ³ /min
(c) GaN buffer layer	600°C	H_2	2000cm ³ /min
		NH_3	2000cm ³ /min
		TMGa	27.2 $\mu\text{mole/min}$
(d) temperature-ramping annealing		H_2	2000cm ³ /min
		NH_3	4000cm ³ /min
(e) thermal annealing	1000°C	H_2	2000cm ³ /min
		NH_3	4000cm ³ /min
(f) GaN overlayer	1000°C	H_2	2000cm ³ /min
		NH_3	4000cm ³ /min
		TMGa	54.4 $\mu\text{mole/min}$

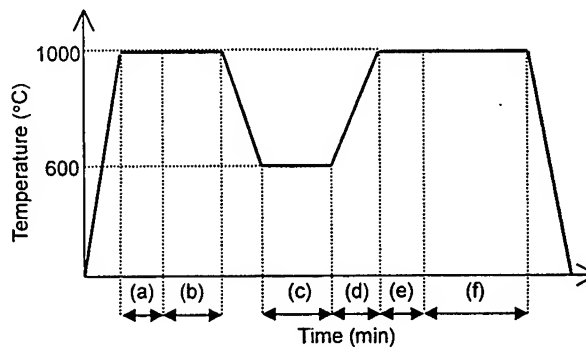


Fig. 2. A timing chart of GaN growth process.

3. RESULTS AND DISCUSSION

To explore the role of temperature ramping rate during the two-step growth of GaN-on-sapphire, a series of GaN buffer-layer samples were annealed under various temperature ramping rates. The corresponding AFM images of the as-deposited and annealed buffer layers are shown in Fig. 3. With decreasing the ramping rate from 60 to 20°C/min, the island size increased first and then decreased. It is noted that the coalescence mechanisms of the grains are involving Ostwald ripening, sintering and cluster migration¹⁸. Prior to coalescence there is a collection of the grains of varied size, and with time the larger grains grow or ripen at the expense of the smaller grains. Sintering is a coalescence mechanism involving grains in contact. The last mechanism for coalescence considered deals with migration of clusters on the substrate surface. For the higher ramping rate (>40°C/min) applied, the GaN buffer layer could not complete the coalescence mechanisms and only Ostwald ripening was finished. The higher ramping rate could shorten the annealing time so the islands of the buffer layer could have no enough time to coarsen. Under a ramping rate of 40°C/min, the appearance of large island size reveals that a more complete coalescence process can be achieved. The large islands would be grown at expense of the small island size through the process of clustering and recomposed GaN molecules^{18,19}. As the ramping rate decreased to 20°C/min, an evident reduction in island size was observed. The long annealing duration could contribute to dramatic re-evaporation of the GaN buffer layer and result in island size decreasing. The surface morphology of the GaN overlayer will be greatly affected if the buffer layer becomes thinner. Details about this point will be discussed latter (in Fig. 6). Moreover, the AFM results indicate that the surface roughness of the GaN buffer layer decreases from 7.8 to 2.5 nm as the ramping rate decreases from 60 to 20°C/min. This presents that a smooth buffer-layer surface could be maintained under a ramping rate of ≤40°C/min though the re-evaporation of GaN may occur.

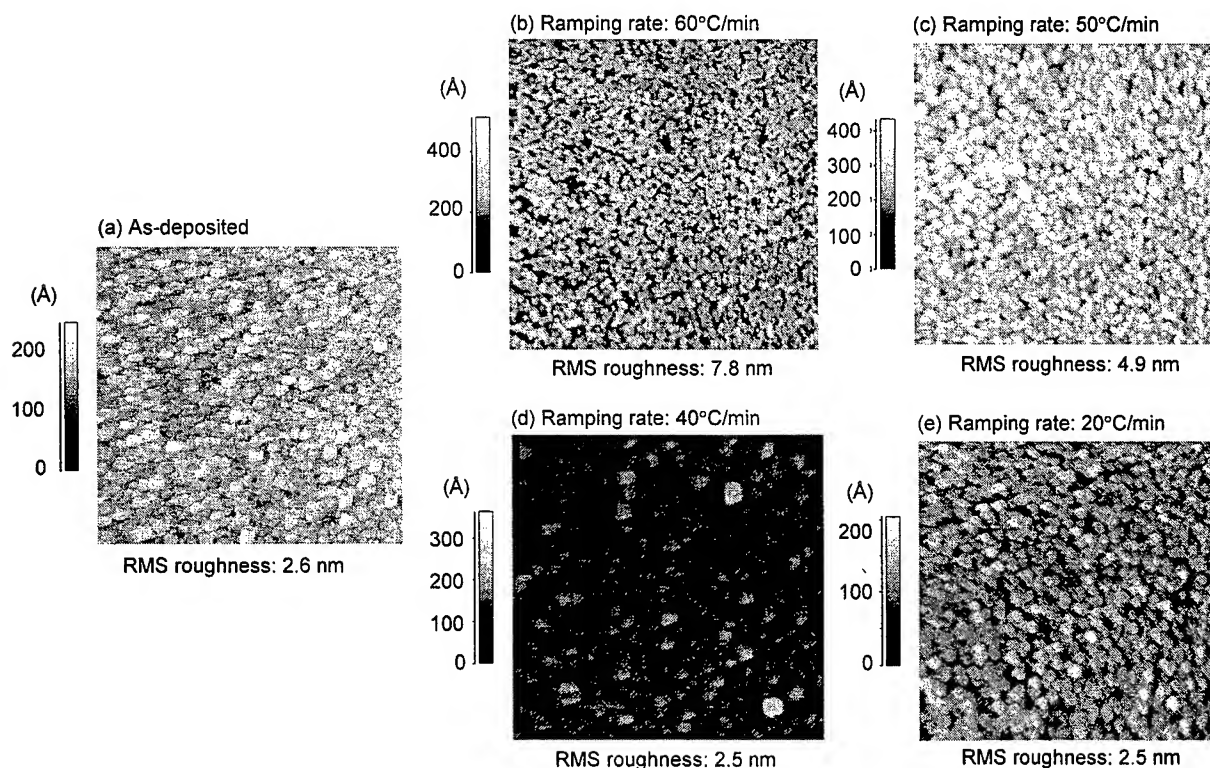


Fig. 3. AFM images for the GaN buffer layer annealed with various temperature ramping rates.

Fig. 4 shows x-ray diffraction rocking curve for [0002] plane of the GaN buffer-layer samples annealed under various temperature ramping rate. The average grain size (D) can be estimated from the full-width at half maximum (FWHM) of the hexagonal GaN (0002) peak by Scherrer's formula as

$$D = 0.9\lambda / (B \cos \theta), \quad (1)$$

where λ is the X-ray wavelength, B the FWHM of the XRD peak, and θ the diffraction angle. Fig. 5 depicts the corresponding FWHM value and the calculated grain size for these samples. It was found that the grain size decreased as the ramping rate decreased from 60 to 20°C/min. The XRD analyses agree well with the result obtained from the AFM measurements, except at the lower ramping rate (20°C/min). The discrepancy could be due to the fact that AFM only measures the surface island size, which will be changed once the re-evaporation of the GaN occurs at the lower ramping rate.

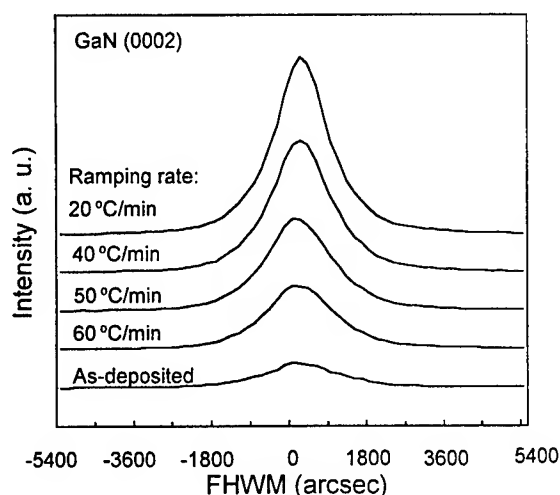


Fig. 4. XRD rocking curve for [0002] plane of the GaN buffer-layer samples annealed under various temperature ramping rate.

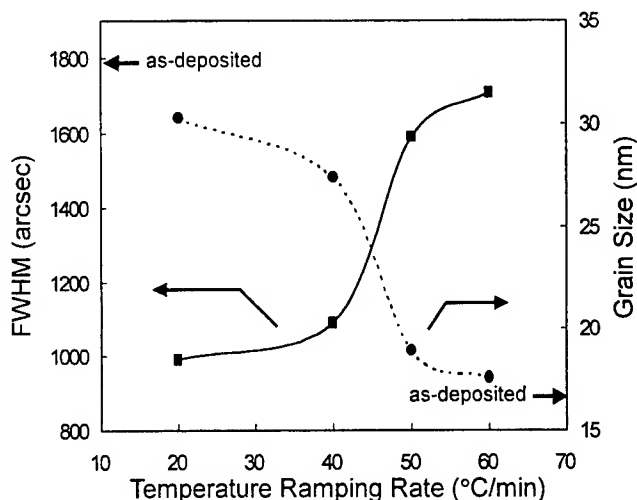


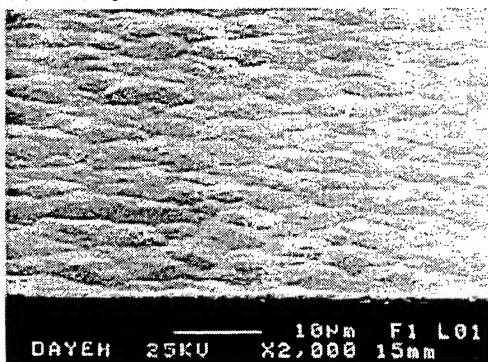
Fig. 5. The corresponding FWHM value and the calculated grain size.

Fig. 6 shows the surface morphology of the 2- μ m-thick GaN epilayer grown on the GaN buffer layer annealed under various temperature-ramping rates. For the higher ramping rate ($>40^\circ\text{C}/\text{min}$) applied, the GaN overlayer surface exhibited large hexagonal three-dimensional islands. According to the AFM result as described in Figs. 3 (b) and (c), the extent of roughness for the GaN buffer-layer surface after annealing can contribute the observed hexagonal hillocks in Fig. 6(a) and the hexagonal platforms in Fig. 6(b). A similar result was also reported by Hersee *et al* in their GaN-on-sapphire study that the hexagonal morphology was obtained with non-optimum buffer layer¹⁰. However, when the lower ramping rate ($20^\circ\text{C}/\text{min}$) was used, the GaN overlayer exhibits the hexagonal pyramid growth as shown in Fig. 6(d). Some previous studies^{8,9} have also described that the GaN-on-sapphire presents hexagonal pyramid growth as the GaN buffer-layer thickness is reduced. Maybe the lower ramping rate could induce the dramatic re-evaporation of the GaN buffer layer and yield the buffer-layer thickness thinner. Under a suitable ramping rate of $40^\circ\text{C}/\text{min}$, a smooth buffer-layer surface can be maintained and results in a subsequent mirror GaN epilayer as shown in Fig. 6 (c).

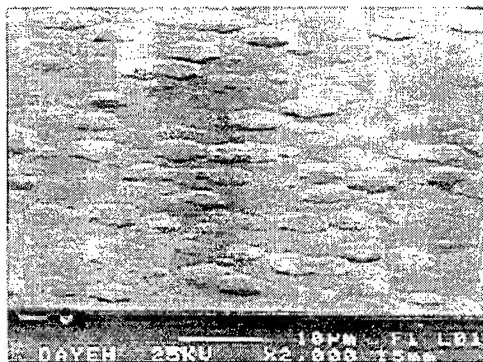
Based on the above results, a schematic diagram of the influences of temperature ramping rate on the GaN buffer layer and subsequent GaN overlayer is illustrated in Fig. 7. For the higher ramping rates applied, the annealing time is shortened and the coalescence mechanism of the buffer layer can not be completed yet. So the buffer-layer surface becomes rougher, yielding hexagonal three-dimensional islands. In addition, the lower ramping rates would induce re-evaporation of the GaN buffer layer due to the long duration of thermal treatment. This makes the buffer-layer thinner, resulting in the growth of the hexagonal GaN epilayer. With a suitable temperature-ramping rate, a smooth buffer-layer surface and the buffer-layer thickness can be maintained to obtain a subsequent high-quality GaN overlayer. From the 25-K PL measurement as depicted in Fig. 8, the mirror GaN epilayer shows a near-band-edge peak centered at 3.477 eV with a full width at half

maximum as narrow as 13.1 meV. A weak and broad emission was also detected at longer wavelengths peaking at 2.2 eV. The origin of this broad emission is most often believed to result from deep-level states in the band gap involving carbon impurities or native defects²⁰.

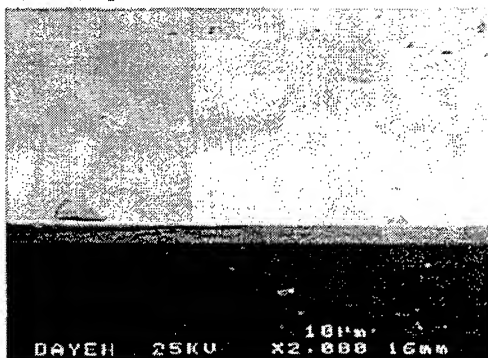
(a) Ramping rate: 60°C/min



(b) Ramping rate: 50°C/min



(c) Ramping rate: 40°C/min



(d) Ramping rate: 20°C/min

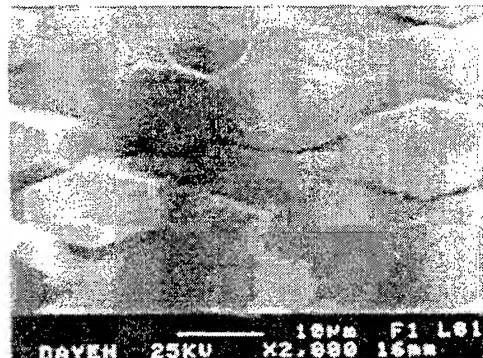


Fig. 6. SEM surface morphology of GaN epilayer changed by various temperature-ramping rates.

4. SUMMARY

The role of temperature ramping rate during the two-step growth of GaN-on-sapphire by MOCVD is investigated. It is confirmed that the temperature-ramping rate can greatly affect the surface morphology, roughness, thickness and crystalline properties of the GaN buffer layer and the subsequent GaN overlayer. The higher ramping rate (>40°C/min) can induce the rough buffer-layer surface and result in the growth of the hexagonal GaN epilayer. Besides, the lower ramping rate (20°C/min) will make the buffer-layer thinner due to the long thermal duration and yield the hexagonal pyramid growth. The behavior can be interpreted by the coalescence mechanism of the low-temperature GaN buffer layer involving Ostwald ripening, sintering and cluster migration. Under a suitable ramping rate of 40°C/min, the smooth buffer-layer surface and thickness can be maintained, resulting in a high-quality GaN overlayer.

ACKNOWLEDGEMENTS

The authors would like to express their thanks to Mrs. Lee of National Sun Yat-Sen University for x-ray diffracton measurements. The technical assistance of MOCVD system by Branchy Vacuum Technology Ltd. in Chung-Li, Taiwan is greatly acknowledged.

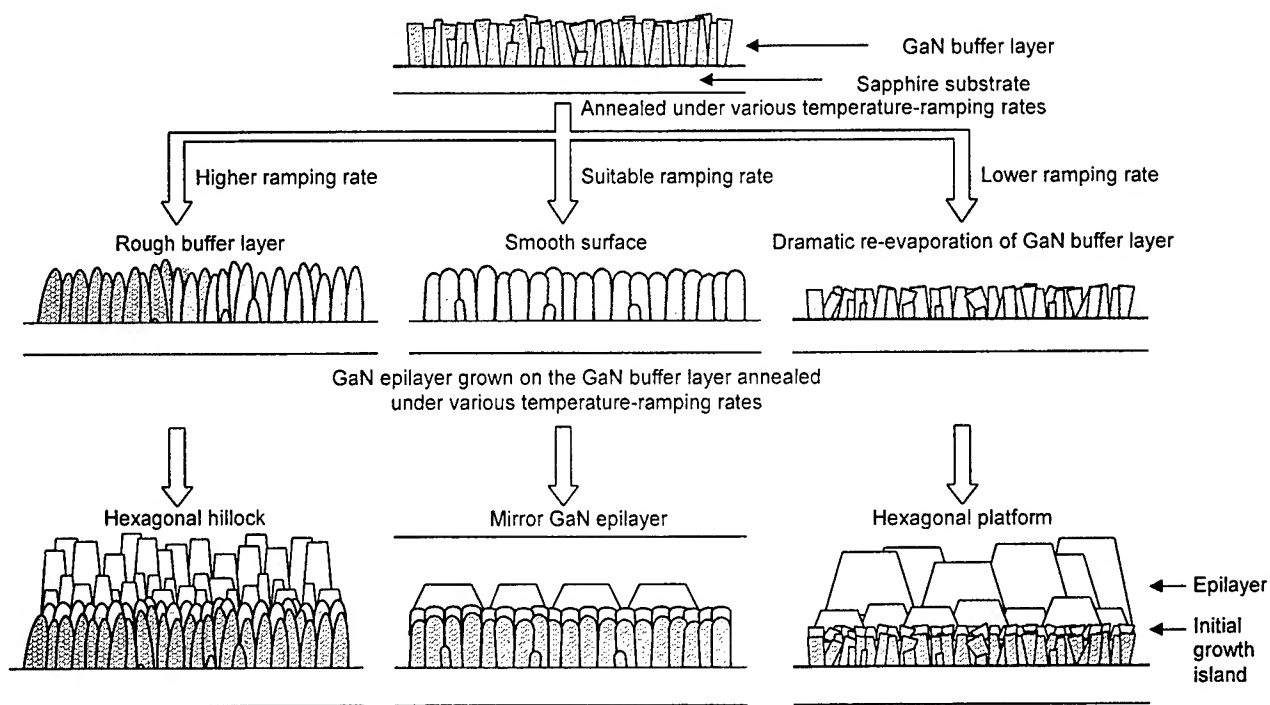


Fig. 7. A schematic diagram of the influences of temperature ramping rate on the GaN buffer layer and subsequent GaN overlayer.

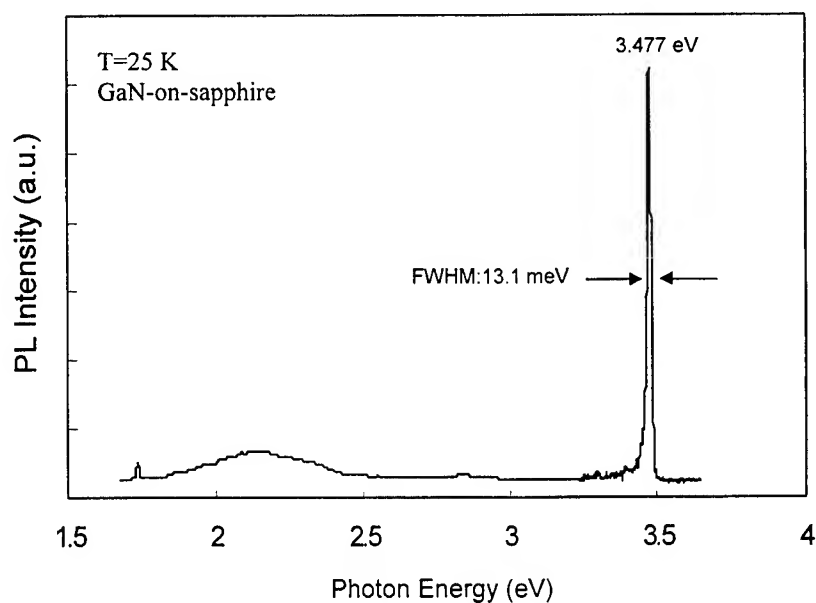


Fig. 8. PL spectrum for an undoped MOCVD-grown GaN epilayer at 25 K.

REFERENCES

1. S. Nakamura, M. Senoh, N. Iwasa, S. Nagahama, T. Yamada and T. Mukai, *Jpn. J. Appl. Phys.* **34**, 1332, 1995.
2. C. R. Lee, S. J. Son, I. H. Lee, J. Y. Lee and S. K. Noh, *J. Crystal Growth* **171**, 27, 1997.
3. S. Nakamura, M. Senoh, S. Nagahama, N. Iwasa, T. Yamada, T. Matsushita, H. Kiyoku, Y. Sugimoto, T. Kozaki, H. Umemoto, M. Sano and K. Chocho, *J. Crystal Growth* **189/190**, 820, 1998.
4. K. Uchida, A. Watanabe, F. Yano, M. Kouguchi, T. Tanaka, and S. Minagawa, *J. Appl. Phys.* **79**, 3487, 1996.
5. K. Uchida, A. Watanabe, F. Yano, M. Kouguchi, T. Tanaka, and S. Minagawa, *Solid-State Electronics*, **41**, 135, 1997.
6. S. Keller, B.P. Keller, Y.F. Wu, B. Heying, D. Kapolnek, J.S. Speck, U.K. Mishra and S.P. Denbaars, *Appl. Phys. Lett.* **68**, 1525, 1996.
7. J.H. Kim, S.C. Choi, J.Y. Choi, K.S. Kim, G.M. Yang, C.H. Hong, K.Y. Lim and H.J. Lee, *Jpn. J. Appl. Phys.* **38**, 2721, 1999.
8. S. Nakamura, *Jpn. J. Appl. Phys.* **30**, 1705, 1991.
9. O. Briot, J.P. Alexis, M. Tchoukueu, R.L. A. Ulombard, *Material Science & Engineering*, **B34**, 147, 1997.
10. S.D. Hersee, J. Ramer, K. Zheng, C. Kranenberg, K. Malloy, M. Banas and M. Goorsky, *J. Electronic Mater.* **24**, 1519, 1995.
11. X. Liu, L. Wang, D.C. Lu, D. Wang, X. Wang and L. Lin, *J. Crystal Growth* **189/190**, 287, 1998.
12. J.C. Zolper, M.H. Crawford, A.J. Howard, J. Ramer and S.D. Hersee, *Appl. Phys. Lett.* **68**, 200, 1996.
13. K. Uchida, K. Nishida, M. Kondo and H. Munekata, *J. Crystal Growth* **189/190**, 270, 1998.
14. K. Uchida, K. Nishida, M. Kondo and H. Munekata, *Jpn. J. Appl. Phys.* **37**, 3882, 1998.
15. J.C. Ramer, K. Zheng, C.F. Kranenberg, M. Banas, and S. D. Hersee, The 1st Int. Symp. on Gallium Nitride and Related Materials, Boston, Massachusetts, USA, p. 225, 1995.
16. A.E. Wickenden, D.K. Wickenden and T.J. Kistenmacher, *J. Appl. Phys.* **75**, 5367, 1994.
17. T. Ito, M. Sumiya, Y. Takano, K. Ohtsuka and S. Fuke, *Jpn. J. Appl. Phys.* **38**, 649, 1999.
18. K-N Tu, J. W. Mayer, L.C. Feldman, *Electronic Thin Film Science for Electrical Engineers and Materials Science*, (Macmillan Publishing Company, 1992), chapter 7.
19. M. Ohring, *The Materials Science of Thin Films*, (Academic Press, Inc., 1992), chapter 5.
20. R. Singh, R. J. Molnar, M. S. Unlu, and T. D. Moustakas, *Appl. Phys. Lett.* **64**, 336 1994.

Exchange interaction of 3d transition metal impurity with band electrons in diluted magnetic semiconductors

Tzuen-Rong Yang and Mi-Ra Kim *

*Department of Physics, National Taiwan Normal University, Taipei 116,
Taiwan, Republic of China*

Abstract

The effects of the exchange interaction between the localized d electrons of manganese ion and the delocalized host band electrons in $\text{II}_{1-x}\text{Mn}_x\text{VI}$ semiconductors are discussed based on the perturbation scheme and the $\mathbf{k} \cdot \mathbf{p}$ theory as a function of the manganese composition. We observe that the exchange interaction lead to the red shift of the energy gap and it is shown that the many-body interaction due to exchange play an important role in accurate depiction of the energy gap with variation of the manganese amounts in diluted magnetic semiconductors. In addition, we have compared the results with experimental data of IR spectroscopy.

Keywords: exchange interaction, diluted magnetic semiconductors

*Correspondence: Email: mirakim@ftir.phy.ntnu.edu.tw

1 INTRODUCTION

Since the existence of substitutional Mn^{2+} ions in II-VI semiconductors is responsible for a strong hybridization of the sp -electron states of the parent material with the d -electron states of the impurity Mn the coupling effects through the exchange interaction between the host material and Mn ions for a wide band-gap $\text{II}_{1-x}\text{Mn}_x\text{VI}$ diluted magnetic semiconductors (DMS) has been theoretically and experimentally appreciated [1, 2, 3, 4]. The magnetic ions, Mn^{2+} , are distributed at random on the available cation sites of the parent lattice leading to spectacular changes of optical and magnetic properties in the Mn included DMS such as Faraday rotation and Zeeman splitting.

In addition, the shift and anomaly [1] of the energy gap in DMS is related to the presence of the exchange interaction and this characteristic features considerably depend on the Mn mole fraction. Investigations on this matter with and without magnetic field have been carried out by some groups for various DMS materials such as $\text{Zn}_{1-x}\text{Mn}_x\text{Te}$, $\text{Zn}_{1-x}\text{Mn}_x\text{Se}$, and $\text{Cd}_{1-x}\text{Mn}_x\text{Te}$ as a function of the manganese mole fraction [1, 2, 3]. Accordingly, we have focused on $\text{Zn}_{1-x}\text{Mn}_x\text{Se}$ and evaluate the effects of the coupling on the energy gap through the exchange interaction between the Mn spins and the spins of other band electrons within the crystal. In this study, by employing the similar theoretical approach as [2], we have calculated the exchange interaction due to coupling between the II-VI semiconductors and the half-filled Mn $3d^5$ shells in zinc-blend $\text{Zn}_{1-x}\text{Mn}_x\text{Se}$ and evaluate the influence of the exchange to energy gap with variation of the Mn mole fraction. We have assumed that the conduction band is to be parabolic and the valence band is investigated by using the Luttinger-Kohn

Hamiltonian.

2 THEORETICAL MODEL

We have assumed the exchange interaction between the spin of delocalized host carriers and the localized manganese d electrons described by a Heisenberg-type Hamiltonian:

$$H_{sp-d} = \sum_i 2J(\mathbf{r} - \mathbf{R}_i) \mathbf{s} \cdot \mathbf{S}_i. \quad (1)$$

This Hamiltonian represents the interaction between the s or p like eigenstates of the conduction or valence bands and Mn^{2+} ions characterized by an exchange integral J , where \mathbf{r} and \mathbf{s} are the electron position and spin operator and \mathbf{R}_i and \mathbf{S}_i are the position and spin operators for the Mn^{2+} ions. Within this approximation, we can calculate the energy states and wave function of the conduction and valence electrons based on the $\mathbf{k} \cdot \mathbf{p}$ perturbation method [5, 6]. Here we have carried out the calculation of the second-order energy correction due to exchange by Eq.(1) using the perturbation method to obtain the contribution of the exchange effects on the energy gap.

The eigenvalue problem is solved within the $\mathbf{k} \cdot \mathbf{p}$ approach expanding the \mathbf{k} -dependent Bloch amplitudes in terms of \mathbf{k} -independent Luttinger-Kohn amplitudes taken at $\mathbf{k}=0$ and the spin-orbit coupling is not included. In order to estimate the energy gap for a given Mn mole fraction and temperature for $\text{Zn}_{1-x}\text{Mn}_x\text{Se}$ DMS the virtual crystal approximation are used assumig the energy gap bowing effect is rather small in $\text{Zn}_{1-x}\text{Mn}_x\text{Se}$ [3]:

$$E_g(x) = (1 - x)E_g(x = 0) + xE_g(x = 1). \quad (2)$$

The second-order exchange energy correction for the conduction and valence bands at $k=0$ is written by

$$E_g(x, T; k = 0) = E_g(x) - \frac{k_B T}{(2\pi\hbar g \mu_B)^2} \left[3m_c^*(\Omega\alpha)^2 + (0.67m_{lh}^* + m_{hh})(\Omega\beta^2) \right] \xi, \quad (3)$$

where m_c^* is the effective mass of the conduction band, and m_{lh}^* and m_{hh}^* are the heavy hole and light hole effective mass, respectively. Ω is the unit-cell volume, k_B the Boltzman constant, $g=2$ for Mn^{2+} ions, and μ_B the Bohr magneton. α and β are the exchange integrals for the conduction and valence bands which is given by in terms of the wave functions of the host band electrons and localized Mn ions, respectively. ξ represents the magnetic susceptibility, which is expressed by thermal average of S_z and S^\pm [2].

3 RESULTS AND DISCUSSION

In order to discuss the contribution of the exchange effects on the energy gap of $II_{1-x}Mn_xVI$ we have employed the $Zn_{1-x}Mn_xSe$ DMS on GaAs(001) substrates and carried out the calculations of the second-order energy correction due to exchange by using the perturbation approach for various Mn mole fractions. In our analysis, the energy gap for ZnMn and MnTe was taken as 2.82eV and 3.3eV at $T=6.5K$ and 2.80eV and 3.14eV at $T=80K$, respectively.

The energy correction due to exchange interaction as a function of the Mn mole fraction x at $T=6.5K$ and $T=80K$ is shown in Fig. 1. It is shown that the exchange interaction strongly depends on the x and temperature. The contribution of the exchange interaction to the rigid energy gap for various Mn mole fractions at $T=6.5K$ and $80K$ has similar dependence that the exchange interaction initially negatively increase and then decreases with increasing x .

This anomaly arises in smaller x with increasing temperature. Comparing with the energy correction due to exchange for $\text{Zn}_{1-x}\text{Mn}_x\text{Se}$ and $\text{Zn}_{1-x}\text{Mn}_x\text{Te}$ [1], the results in $\text{Zn}_{1-x}\text{Mn}_x\text{Se}$ is larger than the one for $\text{Zn}_{1-x}\text{Mn}_x\text{Te}$. This is mainly due to difference of the nearest neighbour distance between two materials. the nearest neighbour distance cause the change of the degree of hybridization and overlapping of the delocalized band electron and localized Mn wave functions. Our results for the exchange correction on the energy gap are qualitative agreement with the results of [2]. From Eq. (2) and the results of Fig. 1, in Fig. 2 we have presented the results of the calculated energy gap and the one which is obtained from the IR spectroscopy for $\text{Zn}_{1-x}\text{Mn}_x\text{Se}$ with various Mn mole fractions x at $T=80\text{K}$. We can see that the slope of the energy gap as a function of the Mn mole fraction is significantly changed when the exchange interaction is taken into account. We can also observe that the dip in the energy gap comes from the exchange interaction.

4 CONCLUSIONS

We have examined the contribution of the exchange interaction to the energy gap considering the direct exchange between the Mn^{2+} ions and the spins of the band electrons of the host material within the perturbation approach. The wave functions are obtained by solving the 4×4 Luttinger-Kohn Hamiltonian. We observe that the exchange interaction bring about the red shift and anomaly of the energy gap and it is play an important role in depiction of the energy gap of DMS.

References

- [1] H-C Mertins, H-E Gumlich, and Ch Jung Semicond. Sci. Technol. **8**, 1634 (1993).
- [2] R. B. Bylsma, W. M. Becker, J. Kossut, U. Debska, and U. Debska, Phys. Rev. B**33**, 8207 (1986).
- [3] J. K. Furdyna, J. Appl. Phys. **64**, 4 (1988).
- [4] G. Yang, J. K. Furdyna, and H. Luo, Phys. Rev. B**59**, 2768 (1999).
- [5] J. A. Gaj, J. Ginter, and R. R. Galazka, Phys. Stat. Sol. B**89**, 655 (1978).
- [6] J. Kossut, Phys. Stat. Sol B**78**, 537 (1976).

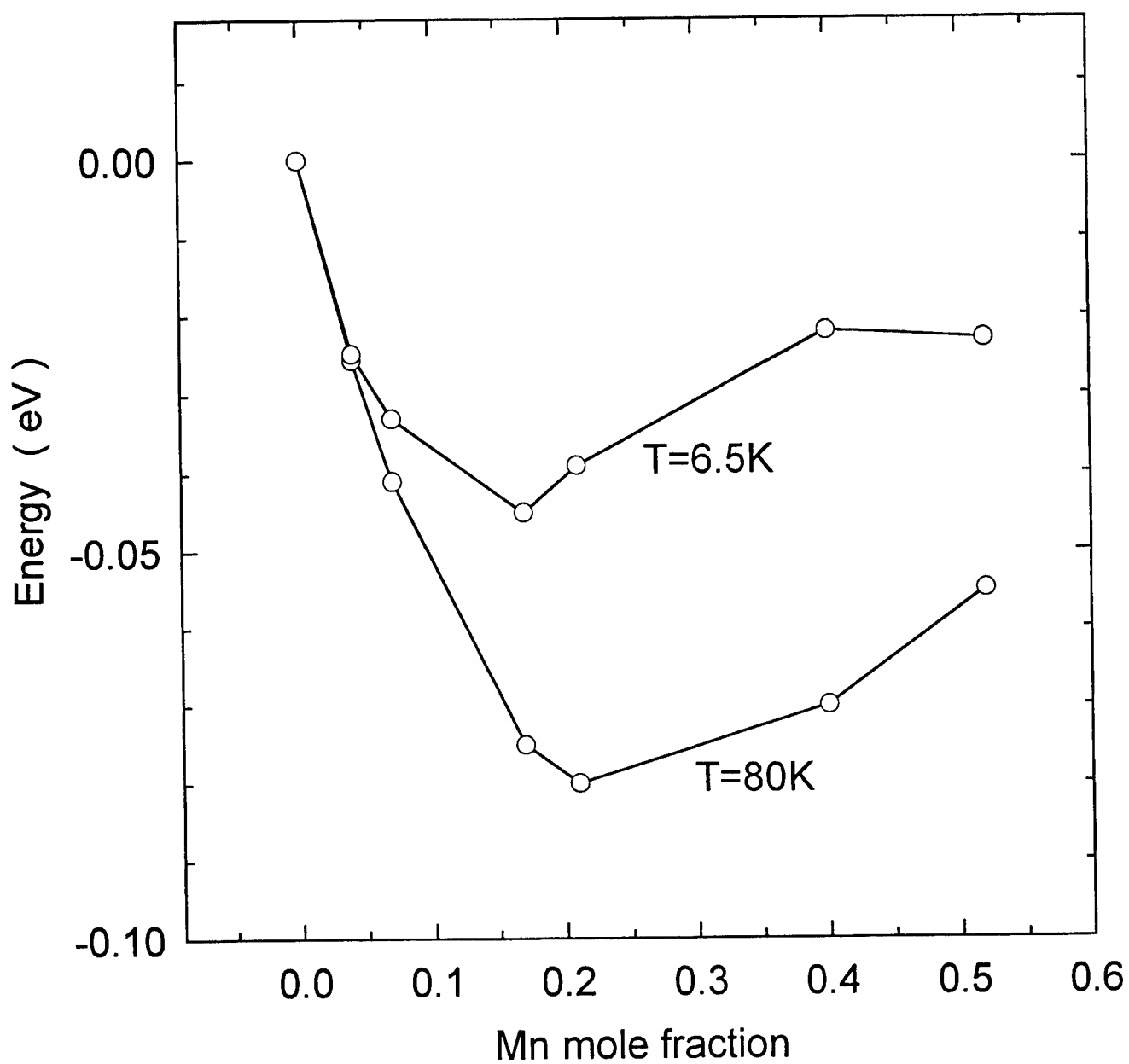


Figure 1: The energy correction due to exchange interaction for $\text{Zn}_{1-x}\text{Mn}_x\text{Se}$ as a function of the Mn mole fraction at $T=6.5\text{K}$ and $T=80\text{K}$. The lines are to guide the eye only.

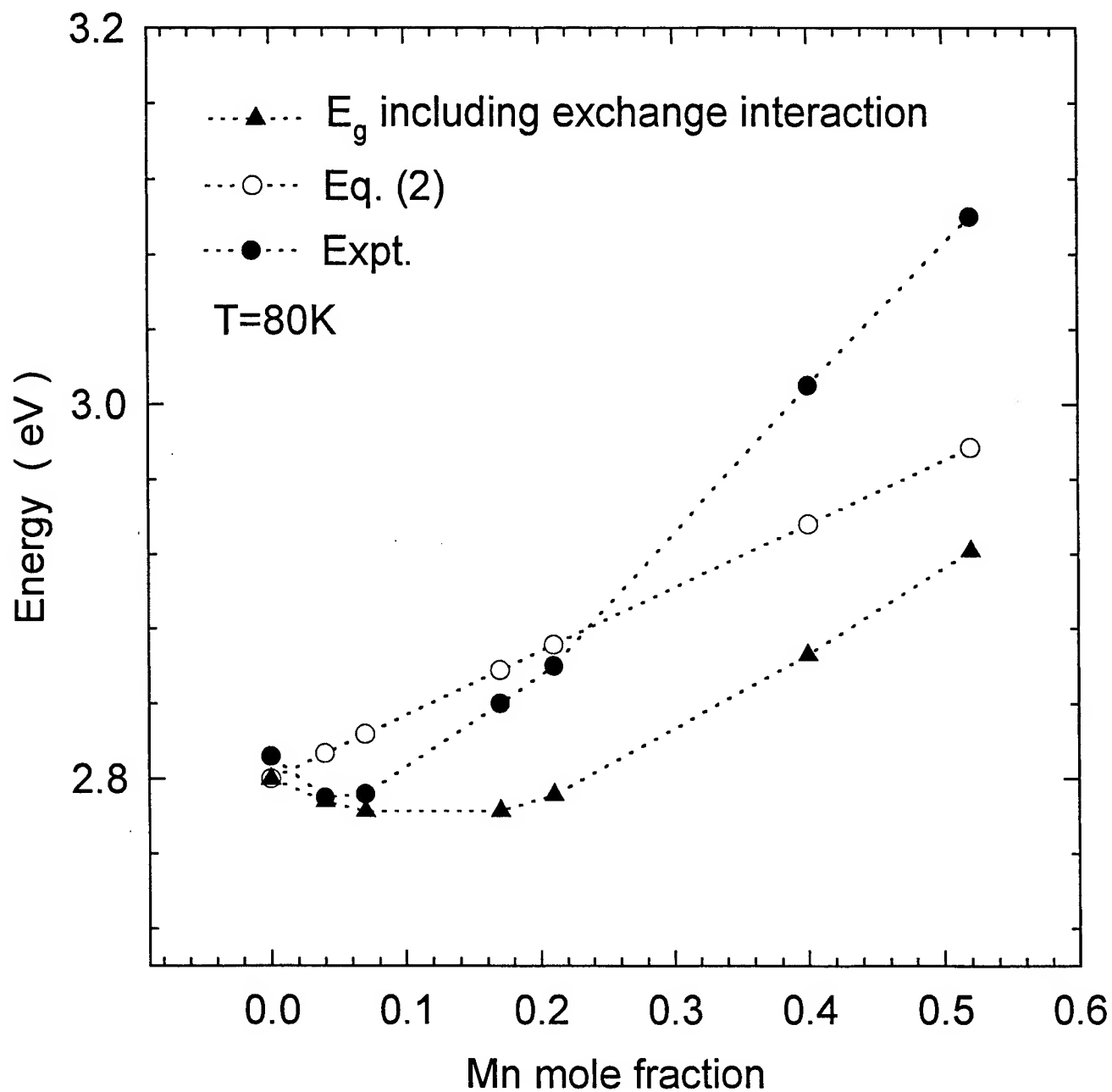


Figure 2: The experimentally determined energy gap (black circle) and the calculated energy gap with exchange interaction (black triangle) for $\text{Zn}_{1-x}\text{Mn}_x\text{Se}$ as a function of the Mn mole fraction at $T=80\text{K}$. The lines are to guide the eye only.

Optoelectronic frequency discriminated phase tuning technology and its applications

Gong-Ru Lin and Yung-Cheng Chang
Institute of Electro-Optic Engineering, Tatung University
No. 40 Chung Shan North Rd., Sect. 3, Taipei 10451, Taiwan, R. O. C.
E-mail: grlin180@ms15.hinet.net

ABSTRACT

By using a phase-tunable optoelectronic phase-locked loop, we are able to continuously change the phase as well as the delay-time of optically distributed microwave clock signals or optical pulse train. The advantages of the proposed technique include such as wide-band operation up to 20 GHz, wide-range tuning up to 640 degrees, high tuning resolution of $<6 \times 10^{-2}$ degree/mV, ultra-low short-term phase fluctuation and drift of 4.7×10^{-2} degree and 3.4×10^{-3} degree/min, good linearity with acceptable deviations, and frequency-independent transferred function with slope of nearly 90 degrees/volt, etc. The novel optoelectronic phase shifter is performed by using a DC-voltage controlled, optoelectronic-mixer-based, frequency-down-converted digital phase-locked-loop. The maximum delay-time is continuously tunable up to 3.9 ns for optical pulses repeated at 500 MHz from a gain-switched laser diode. This corresponds to a delay responsivity of about 0.54 ps/mV. The using of the OEPS as being an optoelectronic delay-time controller for optical pulses is demonstrated with temporal resolution of <0.2 ps. Electro-optic sampling of high-frequency microwave signals by using the in-situ delay-time-tunable pulsed laser as a novel optical probe is primarily reported.

Keywords: Optoelectronic, phase shifter, delay-time controller, pulsed laser, electro-optic sampling.

1. INTRODUCTION

Controlling the phase as well as the relative delay-time of microwave or optical signals has been comprehensively investigated for many decades due to its important applications in versatile communication and measurement systems. A phase shifter is such a two-port device with basic function of providing a change in the phase of the electronic signal with practically negligible attenuation. The typical applications of the phase shifters include such as electronic phase or delay-time scanning in array radars, phase-shifter-controlled variable power dividers, microwave frequency translators, etc. Most of the phase shifters are either mechanical, or electronic (inertialless), or all-optical typed. Prior to the advent of electronically variable phase shifters in the 1950s, almost all of the fixed and variable phase shifters were mechanical typed, such as the rotary vane adjustable waveguide phase changer primarily proposed by Fox in 1947 [1], and the helical line phase changer reported by Stark in 1957 [2]. The Mechanical typed phase shifters consist of either coaxial line or metallic waveguide structure which varies the phase by adjusting either the physical length of helical line or the rotation-displacement of dielectric slab in the waveguide. The merits of the mechanical phase shifters are easy to manufacture, and low insertion loss, etc. However, the operating frequency of such device is fixed since the phase shift is frequency-dependent. Moreover, the difficulties in remote control and volume-shrinkage further constrain the conventional phase shifters to compactly integrate with the antenna systems. Later on, a new era of electronic or ferrite phase shifter technology was initiated because of their superiorities in tuning flexibility and highly integratable geometry which meet the demands of most applications. In 1957, Reggia and Spencer [3] demonstrated the first electronically variable ferrite phase shifter that has been employed for scanning of phased array system. These phase shifters can be designed to operate in either analog or digital mode. In addition, the semiconductor diode [4-6] that utilizes semiconductor junctions to electronically control the phase variation was also emerged during the mid-1960s. The semiconductor phase shifters considered here are reciprocal in nature but can also be classified as digital or analog depending on whether the control element is used as an electronic switch or a continuously variable reactance. For example, the devices that can act as electronic switches are the *p-i-n* diodes, GaAs FET, and the Schottky diodes. For analog operation, the varactor diode is commonly utilized. Later on, particularly since the 1980s, several other types of electronic phase shifting devices have been developed. The GaAs metal semiconductor FET (MESFET), especially the dual-gate MESFET, is an active phase shifter that enables the dual function of signal amplification and phase-shifting. Alternatively, the true time-delay elements such as magneto-static wave (MSW) and the microwave acoustic delay lines have been receiving considerable attention since the late 1960s [7,8]. The former one offer time delays in the range 10 to 500 ns at instantaneous bandwidths and operating frequencies of up to 1 GHz and about 20 GHz[9], respectively. However, MSW devices are basically dispersive and

nonreciprocal. The latter one is based on the propagation of acoustic waves that is transduced from the launched electrical signal in single crystal material over a finite length. Although such devices give a non-dispersive insertion delay of fixed value and a linear phase-frequency response over a designed bandwidth, which become impractical due to increased propagation loss and fabricating problems for [10-11] operating frequency beyond 2 GHz. Yet another emerging development is in the area of optically controlled bulk semiconductor phase shifters particularly suited for millimeter-wave frequency range. Subsequently, the use of bulk semiconductor elements is reported as an alternative to implement the phase control at millimeter-wave frequencies [12,13] by dynamically varying the conductive properties of electron-hole plasma in a semiconductor material. The plasma can be created either through free carrier injection via contacts or optical illumination [14]. More recently, the traveling-wave tube (TWT) was developed as an excellent nonreciprocal phase shifter with approximately linear transferred characteristic (phase shift versus frequency). Notably, the TWT is available for large phase shift of up to 1700° at X-band with [15] practical limitations such as a high noise figure, interdependent phase and gain, bulky and heavy. Nowadays, the considerable emphasis has shifted either to implement the phase shifters in monolithic form [16,17] or to control the phase shifters via optoelectronic technologies. To date, there has been much interest in employing optical beam-forming networks for thinning microwave/millimeter-wave PAAs [18-21] recently. Several optical [22-24] and optoelectronic [25-27] phase-shifting schemes have been demonstrated at frequency up to tens GHz. For example, optical implementations of true-time-delay phase shifts by using fiber-optic delay [22] or a variable opto-mechanical delay line [24] have been demonstrated. Lately, optoelectronic phase shifting at 7 GHz has also been reported by controlling the dc bias-current of a RF-modulated laser diode [27]. The operation frequency the optically controlled phase-shifter can easily increase up to 60 GHz by using photonic techniques [24]. The compact and lightweight photonic phase-shifting modules have been considered as an alternative not only for reducing the volume and weight of PAAs [28], but also for their advantages of such as remote-controllable, wide-band frequency coverage, better immunity to electromagnetic interference, and compatibility to fiber-optic networks, etc.

In applications, the phase shifters have been extensively employed to microwave and millimeter-wave antennas for the long-haul wireless transmission, the satellite/mobile communications, and the military radar/radio astronomy works. In a phased-array antenna (PAAs) system that has been emerged since the beginning of the 1970's, individual variable phase shifters are connected to thousands of radiating antenna elements that acquires the basic capability of scanning the radiated beam in minimal time. This is usually implemented by changing the phase deviation between the adjacent phase shifters in PAAs. The PAA system is therefore the frequently used antenna that meets the demands of accurate control on field pattern, directivity, impedance, and bandwidth, etc. Previously, one of the drawbacks for practical implementations of PAAs by using conventional phase shifters is the large volume and weight of the RF electronic beam-forming network. This is due to that all of the power amplification components and the signal distribution networks for each of the elements must be crowded into the space between elements in conventional microwave PAAs. It is known that the spacing between elements of half the microwave wavelength ($\lambda/2$) is limited for the PAAs to steer over a large fraction of a hemisphere. As the frequency increases, less space becomes available to squeeze in all of the components. The phased array modules are usually built with components laid out behind the elements, which makes the antenna thick. Therefore, a thinner antenna by integrating the components on to the antenna plane is required to benefit from simple power distributing and cooling structures. Owing to these considerations, the evolution in printed antennas and GaAs integrated circuit technology thus opened up new challenges for developing fully monolithic PAA module. On the other hand, the continuously tunable phase shifters have also been considered to function as a delay-time controlling element in time-resolved measuring systems based on pump/probe or sampling techniques. In such systems, the sample or device is excited with a pump pulse, and is subsequently characterized after a variable delay-time by a probe pulse. [29] Typically, the relative delay-time between the pump and probe pulses from picosecond to nanosecond scale is usually adjusted by using an opto-mechanic true-time-delay line. However, The conventional delay-line requires precise alignment to prevent the measuring distortion from deviation in position of the probe beam spot during the delay-time tuning process. [30] To overcome the disadvantage, the tuning of delay-time in pump-probe systems has been implemented by phase-shifting the clock signals in active mode-locked lasers instead of using an the true-time-delay line. [31,32] However, the extension of this techniques to gain-switched or mode-locked semiconductor lasers at microwave frequencies were limited by the bandwidth of the electronic phase shifters. Furthermore, another requirement for the phase shifters to be employed in the aforementioned system is its phase-tuning range of at least larger than 2π (i.e., one period of signal). In addition to the delay-time control, the repetition rate of the optical probe pulses is required to track the clock of signal. This is essential for synchronous detecting the transient responses of the free-running high-speed devices. [33,34] Unfortunately, most of the present phase-tuning techniques are failed to reach the requirements of frequency independent, phase-synchronization and delay-time tuning simultaneously. Not long ago, an electronically phase-locked phase shifter [35] implemented by up-converting a microwave clock with a low-frequency phase-locked signal whose phase can be voltage-controlled was emerged.

Recently, we have successfully developed a laser-diode-based optoelectronic phase-locked loop (OEPLL) for phase-tracking of free-running microwave signals up to 20 GHz. [34] The phase-locked voltage-controlled oscillator (VCO) can

provide relatively pure and narrow-band microwave signal with ultra-low phase noise. The overall operating bandwidth of the OEPLL has shown to be greater than the 3-dB modulating bandwidth of laser diode. Later on, we further demonstrate a novel broadband optoelectronic microwave phase shifter by extending the OEPLL technology. Highly accurate phase shift was achieved by tuning the OEPLL-based phase shifter with a DC-voltage. Such an alternative optoelectronic technique was also designed for wide-range tuning of the phase of microwave signals up to nearly 4π . [36] In this work, The performances such as the maximum phase-shifting range, the linearity and responsivity, the tuning error and phase-switching accuracy, and the resolution of the OEPS are discussed. The effects of FM sensitivity of VCO, the gain/bandwidth of loop filter, the stability of the tuning voltage source on the maximum phase tuning range, the phase fluctuation, and the long-term phase drift of the OEPS were investigated. As an application, we extend the phase-shifting technique for phase-tracking the clock and continuous tuning of the relative delay-time of the optical pulses. Sampling of free-running microwave clock signals by using the optoelectronic delay-time controller are reported.

2. THEORETICAL AND EXPERIMENTAL

The basic principle of the optoelectronic phase shifter is based on a modified optoelectronic phase-tracking circuit. It consists of an optoelectronic harmonic mixer (OEHM) and a digital electronic phase lock loop. The OEHM is simulated by a microwave-biased photoconductor. It consists of a high-speed photoconductor incorporated into a transmission line. The microwave signal traveling down the transmission line can be gated by the photoconductive gap, where it mixes with the harmonic frequency components of the optoelectronic-converted electrical pulse train. That is, in a generic frequency-down-converted OEPLL, an unknown microwave clock, f_m , is input and heterodyned with either the fundamental or the high-order (for example, M^{th}) harmonic component of the optical local oscillator at repetition frequency of f_o . It can be shown that the IF photocurrent is

$$i_{\text{photon}} = \frac{R_{pc} I_o \tau \sqrt{\pi / \ln 2}}{2T} \sum_{n=1}^{\infty} \exp^{-(n\omega_o \tau)^2 / 16 \ln 2} \sin[n\omega_o - \omega_m], \quad (1)$$

where R_{pc} is the photoresistance of the photoconductor; I_o , τ , T , ω_o are respectively the peak intensity, pulse width, period, and angular frequency of the laser while ω_m is the angular frequency of the microwave signal. The conversion loss is given by

$$\frac{P_{in}}{P_{out}} = \frac{R_{pc}}{R_L}, \quad (2)$$

where P_{in} and P_{out} are microwave and IF power respectively, R_L is the load resistance at the IF port. In the short-noise limit, the signal-to-noise ratio of the OEHM is

$$\frac{S}{N} = \frac{V_m(R_{pc} + R_L)}{2\sqrt{2}qBR_{pc}^2}, \quad (3)$$

where V_m is the peak value (in volts) of the microwave signal biasing the photoconductor; q is the electronic charge; and B is the IF bandwidth. The output signal at the intermediate frequency (IF), $f_{IF} = Mf_o - f_m$, generated from the OEHM is then filtered, amplified, and fed to a phase/frequency detector (PFD). Subsequently, it is compared in phase with a reference signal from a signal source generated either by synchronizing to or by frequency-dividing from the microwave clock. The error signal output from a active loop filter is then sent back to the voltage-controlled-oscillator (VCO) in the OEPLL for tracking the microwave clock. In reality, the microwave signal might be free-running and originated from a MMIC, and the optical local oscillator is a gain-switched laser diode (GSLD). The GSLD can be driven by an amplified VCO signal for tracking the free-running oscillator (FRO) as the repetition frequency of GSLD is variable. By analyzing the phase noise model of the OEPLL, the phase noise at different nodes of the OEPLL circuit can be written as

$$\begin{aligned} \theta_e &= \theta_{IF} - [(\theta_{VCO} - \theta_{GSLD}) + \Phi_{OEHM} + \Phi_{Buf}] \\ \theta_{IF} &= \left[\frac{\Phi_{RF}}{N} + \Phi_{1/N} \right] \\ \theta_{GSLD} &= M\Phi_{RF} + M\Phi_{AMP} + \Phi_{Comb} + \Phi_{LD} \\ \theta_{VCO} &= [\theta_e K_d + N_s(\Phi_{PD}) - V_{REF}] F(s) K_o / s + \Phi_{VCO} \end{aligned} \quad (4)$$

where θ_e is phase error, $\Phi_{1/N}$, Φ_{AMP} , Φ_{Comb} , Φ_{LD} , Φ_{OEHM} , and Φ_{Buf} are component phases, $F(s)$ is active loop filter transfer function, K_o is FM sensitivity, and V_{REF} is controlled voltage. A DC reference voltage as the controlling signal, V_{REF} , which

was employed to offset the error signal, $V_d = V_{err} + V_{REF}$, was then feedback to the VCO through an active loop filter (LF). The phase noise of the VCO can therefore be described as

$$\begin{aligned}\theta_{VCO} &= \{[(M+1/N)\Phi_{RF} + \Phi_{SYSTEM}]K_d + N_S(\Phi_{PD}) - V_{REF}\} \frac{F(s)K_o/s}{1 + K_d F(s)K_o/s} + \frac{\Phi_{VCO}}{1 + K_d F(s)K_o/s} \\ &\approx [M\Phi_{RF} + \Phi_{SYSTEM} - \frac{V_{REF}}{K_d}] \frac{K_d F(s)K_o/s}{1 + K_d F(s)K_o/s} + \frac{\Phi_{VCO}}{1 + K_d F(s)K_o/s} \\ &\approx \Phi_{PLL} - V_{REF} \frac{F(s)K_o/s}{1 + K_d F(s)K_o/s} \\ &= \Phi_{PLL} - \Delta\theta_{VCO}\end{aligned}\quad (5)$$

where M is harmonic frequency number, N is frequency divider, and K_d is phase detector gain. That is, by adding a thermally stabilized high-precision voltage regulator with passive tuning circuit in FT-OEPLL system, the phase of the VCO as well as that of the optical pulse-train can be shifted.

Experimentally, the block diagram of the DC-voltage controlled optoelectronic phase shifter (OEPS) for optical microwave clock or pulse-train is shown in Fig. 1. It consists of a gain-switched laser diode (GSLD1, $\lambda=0.8 \mu\text{m}$) driven by a voltage-controlled oscillator (VCO, HP8640B, DC-FM mode), a digitally frequency-translated optoelectronic phase-locked loop (FT-OEPLL), and a thermally stabilized high-precision voltage regulator with passive tuning circuit. The optically distributed microwave signal was simulated by the optical pulse-train generated from a GSLD. The full-width-at-half-maximum (FWHM) and the repetition frequency of the optical pulse-train generated from GSLD are ~ 20 ps and ~ 500 MHz, respectively. A GaAs:Cr photoconductive switch with a $20\text{-}\mu\text{m}$ gap in microstrip line fabricated on a semi-insulating (S. I.) GaAs substrate functions as an optoelectronic harmonic mixer (OEHM) in the FT-OEPLL. The conversion loss and IF bandwidth of the OEHM is ≈ -39 dB and > 200 kHz. This GaAs photoconductive switch was employed to mix the fundamental frequency of optical pulse-train with an individual free-running oscillator (FRO, a microwave synthesizer HP8648A, $f_0=500$ MHz) for down-converted frequency in the OEPS. This facilitates handling of the microwave signals via mature intermediate frequency (IF) circuits and techniques. The down-converted intermediate frequency (IF) signal ($f_{IF} \approx 100$ KHz) was then preamplified, digitized (National Semiconductor, LM319, analog-to-digital voltage-compare converter) for phase comparison with a reference clock signal divided from microwave clock ($f_{REF}=f_0/5120$). The phase deviation between the digitized IF signal and the reference clock was transformed to an error voltage ($V_{err}=k_d\theta_e$) by a digital phase-frequency detector (PFD, Motorola MC4044). This error voltage was then feedback to the VCO. This architecture allows the stable phase tracking of optical pulse-train to the microwave clock. A typical single-side-band (SSB) phase noise of this OEPLL phase-locked to the microwave signal was < -80 dBc/Hz at 1 kHz offset from the carrier frequency. If the error signal (V_{err}) generated from the PFD was further offset by a controlling voltage (V_{REF}) via an active loop filter (LF) prior to the VCO, the phase shift as well as the delay-time of the optical pulse-train related to the clock of FRO can be continuously changed by varying the V_{REF} via a programmable digital-to-analog converter. The temporally delayed optical pulse-train was monitored by using high-speed sampling oscilloscope (HP 54750A) triggered with the FRO. The phase shift of the optical clock from OEVC and the transferred function of the ODT can be determined by using a lock-in amplifier (Stanford Research Systems, SRS830). The delay-time of phase-tracked optical pulse train with respect to the FRO can be monitored by using a high-speed sampling oscilloscope (HP54750A). The relative timing jitter of the optical pulses phase-locked to the FRO was calculated from single-sided-band (SSB) phase noise spectrum. The experimental apparatus for electro-optic measurement of the free-running microwave clock signal is slightly modified, which consists of two sub-systems: an optoelectronic phase locked loop (OEPLL) for phase-tracking and a reflection-mode electro-optic sampler (EOS). An OEPLL-PS is employed as a voltage-controlled ODT for optical pulse-train. Another GSLD (GSLD2, $\lambda=1.3 \mu\text{m}$) driven by the second VCO phase-locked to the FRO is employed as the optical source of the EOS. The pulsewidth and average power of the optical pulse-train generated from GSLD are ~ 20 ps and 0.5 mW, respectively. The DUT was simulated by connecting a free-running oscillator (FRO, HP8648A) with a microwave switch at frequency of 500 MHz. The reflection-mode electro-optic sampling scheme further takes the advantage of improved S/N (by a factor of 2) of the differential detection scheme. The laser beam from GSLD2 through a halfwave plate was focused and scanned along the edge of the planar waveguide. The reflected signal was intensity-modulated by the electric field of the standing waves along the transmission line. A pair of InGaAs photodiodes (PD1 and PD2), a polarizing beam splitter (PBS), and a quarter wave plate (QWP), completed the rest of the optical detection system. For signal processing, we employed a lock-in amplifier (LIA) with an external reference source at the intermediate frequency, f_{IF} , derived from the phase-locked VCO. This system allows measurement of both phase and amplitude of the standing wave pattern simultaneously and accurately.

3. RESULTS AND DISCUSSIONS

3.1 The performance of the optoelectronic phase shifter

The relative delay-time of the optical microwave signal after the OEPS that tuned at different controlling voltages (V_{REF}) was monitored. The upper trace in Fig. 2-4 is the original optical microwave signal from the OEVCO. Fig. 2 presents the signal at ~ 500 MHz output from the OEPS with $V_{REF}=0$. As the V_{REF} tuned from 0 to +1.35 volts, a phase shift of 90° was shown in Fig. 3. Alternatively, a phase shift of nearly -180° tuned by setting $V_{REF}=-2.38$ volts can be seen in Fig. 4. The resolvable minimum tuning step of the OEPS-based delay-time controller is about 20 ps as monitored by using the sampling oscilloscope under a system limit (see Fig. 5). The phase shift of the OEPS as a function of controlling voltages (V_{REF}) at 500 MHz is shown in Fig. 6. The maximum phase tuning range ($\Delta\theta_{max}$) of $\sim 340^\circ$ was measured by tuning V_{REF} from -1.4 volts to 3.8 volts. The phase-shift gain (defined as $K_d=V_{REF}/\Delta\theta_{max}$) of the OEPS is $64^\circ/\text{volt}$. This corresponds to a maximum delay-time and slope of ~ 1.9 ns and 0.36 ns/volt for the optical pulses at repetition rate of 500 MHz. The maximum phase-tuning range and the phase-shift gain were found to remain as constants as the operating frequency changes. However, the maximum delay-time of the optical pulse train can be tuned by the OEPS essentially decreases as the operating frequency increases. This is limited by the maximum tuning period of only about 2π by using current apparatus. The linearity of the transferred function for the OEPS was measured and shown in Fig. 7. It is found that the tuning error of the OEPS can be smaller than 5° at any desired V_{REF} . In addition, a periodically changed triangular function of controlling voltage was employed to realize the tracking performance of the OEPS under continuous voltage control. Fig. 8 shows that the continuously triangular phase-shift corresponding to the tuning V_{REF} with a period of 50 seconds. The switching accuracy of the OEPS was also measured via a phase-switching test at a period of about 20 seconds (see Fig. 9). The switching error of the OEPS controlled by a digital voltage signal is as small as 0.05° .

It is also observed that the phase-tracking ability and the maximum phase tuning range of the OEPS exhibit relatively high tolerance to the variation in loop parameters. For example, the effect of FM sensitivity on the phase tuning range ($\Delta\theta$) of the OEPS was characterized and shown in Fig. 10. As the K_o tuning from 5 kHz/volt to 1.28 MHz/volt, it is found that the $\Delta\theta_{max}$ almost remains as a constant. However, the $\Delta\theta_{max}$ and R_{OEPS} of $<320^\circ$ and $>71^\circ/\text{volt}$ were measured while the K_o increased to 2.56 MHz/volt or larger. This indicates that the OEPS with extremely large K_o can only lead to the decrease in $\Delta\theta_{max}$. In addition, a larger K_o of VCO benefits faster phase-tracking speed at cost of worse phase-tracking stability associated with increasing single-sided-band (SSB) phase noise of the OEPLL. A trade-off between the phase-shift responsivity (R_{OEPS}) of the OEPS and the phase noise of the out signal therefore has to be considered. Furthermore, the resistor in the LF was tuned to realize the effect of the gain constant (K_h) of the LF on the phase-tuning range of OEPS, as shown in Fig. 11. The OEPS is found to exhibit a stable phase-tuning range at smaller K_h . Nonetheless, the phase-shift gain of the OEPS can be greatly enhanced (up to $\sim 90^\circ/\text{volt}$) as K_h increases to be larger than 1 while $\Delta\theta_{max}$ decreased from 340° to $\sim 200^\circ$. We thus conclude that an OEPS with high-gain parameters can destroy the phase-tuning characteristic of the OEPS seriously. Furthermore, it is also found that a higher K_h also leads to a lower bandwidth of the LF. This seriously degrades the phase-tracking stability of the OEPS, although it is essential for inhibition of phase noise and timing jitter in phase-locked optical microwave signals. On the other hand, by tuning the capacitance (C) of LF during measurements, the $\Delta\theta_{max}$ was found to remain as a constant at C ranged from 0 μF to 11 μF . The $\Delta\theta_{max}$ was also found to remain as a constant at different C 's instead that a maximum phase tuning range associated with a minimum gain was obtained at $C=10.1$ μF . It is revealed again that the OEPS system exhibits relatively high stable performances. Furthermore, the minimum tuning step, i.e., the resolution of the OEPS is about 0.2° by setting an increment in V_{REF} of 3 mV. The long-term drift (>30 minutes) in phase of the OEPS controlled by using a thermal-stabilized high-precision voltage regulator is only 0.1° (slope $\approx 3.4 \times 10^{-3}^\circ/\text{min}$). It is found that the fluctuation in phase of the microwave from VCO controlled at a specified phase shift of 175.3° was less than 0.047° (in rms value). This corresponds to a temporal fluctuation (i.e. relative timing jitter) for the optical pulses generated from GSLD of $\Delta t \approx 0.26$ ps (in rms value). Since the voltage fluctuation ($\Delta V/V$) of the voltage-regulator can be as low as 1×10^{-4} , we conclude that the detected phase fluctuation should be dominated by the phase noise from the microwave clock, the GSLD, and the OEPLL itself.

3.2 Optoelectronic Delay-Time-Tunable pulsed Laser

Consequently, the delay-time of the optical pulses generated from GSLD can be tuned from sub-picosecond to nanosecond scale by using the ODTC. The optical pulse-train was detected by using GaAs:Cr photoconductor (switching response of ~ 100 ps) and sampling oscilloscope, as shown in Fig. 12. The upper trace in figure illustrates the original optical pulse-train repeated at 500 MHz from the GSLD without tuning V_{REF} of ODTC. As V_{REF} tuned from 0 to -3.19 volts, the pulse train was found to delay by 1.2 ns (see in Fig. 12). The minimum tuning step of the ODTC at $\Delta V_{REF}=0.07$ volt were primarily monitored by using sampling scope under a system limit ($\tau \approx 14$ ps), as seen in Fig. 13. Furthermore, the delay-time of the optical pulse train generated from the GSLD as a function of V_{REF} is shown in Fig. 14. By changing the

V_{REF} from -3.6 to 3.6 volts and carefully adjusting the gain and bandwidth of the active loop filter of the FT-OEPLL, the laser pulse-train repeated at 500 MHz was found to shift from -1.8 ns to 2.1 ns with respect to the FRO signal. This corresponds to two periods of the laser pulse train, i.e., a maximum phase-tuning range of up to 4π . In comparison, the maximum tuning range of a similar system reported previously was only one period (equivalent to a phase shift of 2π). [32] The relative delay-time of laser pulses with respect to microwave clock can be described as a monotonic transfer function of V_{REF} of the ODTC, that is

$$\Delta t = t_0 + R \cdot V_{REF} \quad (6)$$

, where Δt is the delay-time of the laser pulses, t_0 is an intrinsic delay-time between the optical pulse train and the FRO signal, R is the tuning responsivity of the ODTC in unit of ps/mV, and V_{REF} is the controlling voltage. The tuning responsivity and the intrinsic delay-time of the ODTC of 0.542 ps/mV and 0.14 ns were evaluated from the experimental data. It is worthy to mention that R is tunable from 0.36 to 0.55 ps/mV and t_0 can be tuned to zero by carefully adjust the propagation distances in practical implementation. In addition, the tuning linearity of the voltage-controlled ODTC is shown in the inset of Fig. 14. It is observed that the average tuning error can be less than 5 ps. Note that the anomalous increasing in tuning error of up to 15 ps at smaller delay-time regime is mainly due to the finite operating bandwidth of the PFD in the phase-tracking circuit. [36] This can be further improved by using a high-speed PFD with ultrashort rising time.

An accurate determination of the tuning resolution of the ODTC was demonstrated by using a lock-in amplifier. Figure 15 shows the measurement of the phase difference between the down-converted IF signal and the frequency-divided FRO clock by setting V_{REF} as a step function with increment of $\Delta V_{REF} = 0.001$ volt. The average tuning step of the ODTC is about 0.32 ps during the phase-holding test. The phase fluctuation of the optical pulses controlled by the ODTC at a specified delay-time was measured to be $<0.024^\circ$ in rms value. This corresponds to a timing fluctuation of $\Delta t \approx 0.13$ ps for the optical pulses. We thus conclude that the resolution of the ODTC is potentially smaller than 0.2 ps. To date, this is already short as compared to previous report ($\Delta t = 10$ ps). [32] In addition, the long-term drift of the optical pulses at a specified delay-time is less than 20 fs/min. For confirmation, the minimum tuning step of the ODTC was also resolved by using the sampling oscilloscope under a system limit. The measured resolution of the ODTC (with $R = 0.355$ ps/mV) is about 25 ps with $\Delta V_{REF} = 0.07$ volt, as shown in the inset of Fig. 15. The relative timing jitter between the phase-tracked GSLD and FRO clock was determined to be 5 - 10 ps. Note that these data were obtained by using a high-precision voltage-regulator ($\Delta V/V \leq 1 \times 10^{-4}$) with phase fluctuation of $<0.005^\circ$. The contributions of the SSB phase noise generated from OEPLL, microwave clock, and GSLD on the timing jitter of laser pulses are therefore more pronounced. Further improvement on reducing the relative timing is possible by using a VCO with lower SSB phase noise at offset frequencies out of phase-tracking bandwidth ($f_{3dB} = 50$ Hz in the present scheme). Nonetheless, this technique completely avoids the delay-time- or distant-dependent distortion of the measured signal caused by optical misalignment of variation in beam diameter and radius of curvature.

3.3 Electro-optic Sampling of Free-Running Microwave Clock Signals

Nowadays, the fast evolutions in high-speed electronics accelerate the ameliorations of new measurement techniques with picosecond or even subpicosecond time resolution. Optical time-domain measurement systems exhibit advantages of high temporal resolution, non-invasive (external) and in-situ probing, and broad-area spatial mapping of signals on circuits have been extensively investigated. Electro-optic sampling (EOS) is the state-of-the-art system which characterizes the temporal responses of devices with best temporal and spatial resolutions. The system's main application is the probing of electrical field distributions on free-running microwave circuits in the near and the far field, and time-resolves signal recovery of microwave signals with a time resolution of better than 1 ps. [37] Fourier spectra computed from these measurements resolve higher harmonics up to at least 150 GHz. [38] Previously, versatile pulsed optical sources such as the gain-switched, mode-locked, and Q-switched lasers (solid-state or semiconductor typed) have been used as an optical probe for the continuous- or impulse-mode EOS system. A pump-probe-like equivalent time detection scheme with an optical-path tunable apparatus allows absolute time scaling during the measurement. High stability of the signal frequency and the laser repetition frequency during the measurement time are required in this feedback-less concept, which limits the effective measurement time and making efficient signal averaging or mapping applications more complicated. In the future development of MMICs operating at hundreds GHz or THz frequency range, novel testing techniques should be able to probe continuous microwave signals on free-running circuits at any clock frequency of choice. A way to realize those measurements is to synchronize the fundamental or a higher harmonic of the laser pulse repetition frequency to the microwave signal. To sample the free-running microwave signals in the time domain by using continuous-mode EOS system, the repetition frequency of the pulsed laser is required to synchronize/phase-lock to the free-running microwave signal. This is usually implemented by electronically-controlled adjustment of either the frequency output from the signal generator in gain-switched and actively mode-locked lasers, or the cavity length in passively mode-locked lasers. In the

past, several locking concepts have been reported, all requiring an active control of both the laser repetition rate and the microwave signal locked to a common clock signal. Typically, a laser diode driven by a RF synthesizer and a microwave synthesizer have to be phase-locked to the same system clock to meet the demand of synchronization between clocks[38]. Such system has been proposed by using a photoconductive switch as a phase detector and a pump-probe scheme with a mechanical translation stage as optical delay line for absolute time scaling [39]. For example, the mapping of phase and amplitude of electrical fields up to 40 GHz has been demonstrated by employing an actively mode-locked Nd:YAG laser that synchronized to a RF synthesizer [40]. Optical measurements of a totally free-running oscillator (FRO) have been made by phase locking a laser diode driven by a RF synthesizer to the FRO [41]. In this approach, the laser control is not connected to and completely isolated from the clock driver of the FRO. The signal from the FRO is detected and fed into a control loop that locks the laser driver to the FRO signal.[34] Here, the signal at the intermediate frequency, defined by the offset between the microwave frequency and the respective higher harmonic of the laser repetition frequency, is processed by a fast data acquisition system triggered with the same signal. To overcome the problems of synchronization and delay-time scaling by using a single module that can be integrated with the laser source concurrently, we develop a novel picosecond laser source with inherently delay-time tunable capability for the EOS systems. No absolute time scaling is required to achieve the measurement with our concept.

In application, we primarily demonstrate the characterization of the waveform of free-running/phase-tracked microwave signals or the active microwave/millimeter-wave integrated circuits with inherent oscillators by using the OEPLL-PS-based electro-optic sampling system. In such system, the optical source is a picosecond GSLD in combination with an OTDC mentioned in the above section. This facilitates the system not only to recover the clock frequency of the unknown microwave signal, but also to continuously change the relative delay time between the signal-under-test and the local optical probe pulse train. For instance, a microwave signal fed through a power-amplifier (Mini-circuits ZHL-2-12) and a microwave switch (HP33190B+HP33144A) functions as the signal from device-under-test. The signal was sent to the microwave transmission line made on a S.I. GaAs substrate. A reflect-mode EOS regime was employed. As a result, the microwave signal generated from the phase-locked VCO was characterized by using a modified electro-optic sampling (EOS) system with our delay-time-tunable laser source, as shown in Fig. 16. A nearly perfect sinusoidal waveform of the microwave signal at 500 MHz associated with negligible fluctuations was probed by the OTDC-laser-based EOS system. The timing resolution was selected to be 5 ps. In spite of the region wherein the scanning time close to limitation of the tuning range, the sampled waveform was found to exhibits relatively low distortion as compared to that measured by using high-speed oscilloscope. By comparing the waveforms of the signal measured by using our system and a high-speed sampling oscilloscope, we determine that the measuring linearity of the modified EOS system is less than $\pm 5\%$. Note that there could be an inconceivable deviation between the measured and monitored waveforms at the scanning time, which corresponds to a change in magnitude of V_{REF} of larger than 3.1 volts. This is mainly attributed to the degradation in performance of the ODTC when operated at tuning limits. Nonetheless, the maximum tuning range of near- 4π for the optical pulse train from the GSLD has already exceeded one period of any signal to-be-test. We therefore conclude that the ODTC-based pulsed laser source is well compatible with the EOS sampling for continuous-mode characterization of the waveforms from the free-running or unknown circuits. Further study on impulse-mode EOS of high-speed signals by using the newly proposed laser source is straightforward.

4. SUMMARY

In conclusion, we demonstrate a novel optoelectronic phase shifter for frequency discriminated tracking and controlling the phase of the local optoelectronic oscillator with respect to an individually free-running microwave sources. This is implemented by using a frequency down-converted optoelectronic phase-locked loop in series connection with a DC voltage controller. The maximum phase tuning range can be up to $\sim 640^\circ$ under a change in controlling voltage (V_{REF}) of 6.6 volts. The transferred function of the phase shift versus controlled voltage for the OEPS is linear with a gain of about $64^\circ/\text{volt}$ at 500 MHz. The switching error of the OEPS controlled by a digital voltage signal is about 0.05° . The short-term fluctuation and long-term drift in phase of the OEPS by using a high-precision voltage reference were determined to be less than 0.05° and $0.0034^\circ/\text{min}$. The resolution of current apparatus is as small as 0.2° . Experiment results indicate that the OEPS exhibits relatively high tolerance to the variations of the parameters in OEPS. This indicates OEPS has potential for military and photonic applications, such as phased-array antennas (PAAs), and improved electro-optic sampling systems, etc. The OEPS module requires only one controlling unit for a single element of PAAs operating at different phase-shifts and frequencies as opposed to that in a switched network phase shifters, where a large amount of control lines are required to achieve the number of phase-switching bits. Monolithic integration of the OEPS module for optoelectronic control of the PAAs system is straightforward. By using the OEPS, we further propose a novel optoelectronic delay-time controller that enables the synchronization and continuous tuning of the relative delay-time of the optical pulse-train with respect to a free-running microwave clock. The delay-time of the optical pulse train generated from a pulsed lased diode can be tuned from -

1.8 ns to 2.1 ns, which corresponds to near two-period change of the laser pulse duration. The transfer function of the ODT is linearly proportional to the controlling voltage. The tuning responsivity of the ODT can be adjusted from 0.35 to 0.54 ps/mV. Programmable control of the delay-time is demonstrated with <0.2-ps resolution. The timing jitter between the GSLED and free-running microwave clock was determined to be less than 10 ps. The present scheme is completely free from the influence of laser misalignment and beam-expansion problems over this entire delay range. By using the picosecond delay-time-tunable laser diode as an optical source, we have successfully setup a modified electro-optic sampling system for characterizing of high-frequency signals with relative low distortion.

ACKNOWLEDGEMENT

This work was supported in part by the National Science Council (NSC) of the Republic of China and Tatung University, Taipei, Taiwan, R. O. C. under the grants NSC88-2215-E-036-002, NSC89-2215-E-036-002, and B88-2500-02, respectively.

REFERENCES

1. A. G. Fox, "An Adjustable Waveguide Phase Changer," *Proc. IRE*, Vol. 35, pp. 1489-1498, December 1947.
2. L. Stark, "A Helical Line Scanner for Beam Steering a Linear Array," *IRE Trans. on Antennas and Propagation*, Vol. AP-15, pp. 211-216, April 1957.
3. F. Reggia and E.G. Spencer, "A New Technique in Ferrite Phase Shifting for Beam Scanning of Microwave Antennas," *Proc. IRE*, Vol. 45, pp. 1510-1517, November 1957.
4. R.W. Bums and L. Stark, "In Diodes Advance High Power Phase Shifting," *Microwaves*, Vol. 4, pp. 38-48, November 1965.
5. J. F. White, "High Power p-i-n Diode Controlled, Microwave Transmission Phase Shifters," *IEEE Trans. on Microwave Theory and Tech.*, Vol. MTT-13, pp. 233-242, March 1965.
6. J. F. White, "Review of Semiconductor Microwave Phase Shifters," *Proc. IEEE* (Special Issue on Electronic Scanning), Vol. 56, pp. 1924-1931, November 1968.
7. J. H. Collins, "A Short History of Microwave Acoustics," *IEEE Trans. on Microwave Theory and Tech.*, Vol. MTT-32, pp. 1127-1140, September 1984.
8. W. S. Ishak, "Magnetostatic Wave Technology: A Review," *Proc. IEEE*, Vol. 76, pp. 171-187, February 1988.
9. J. P. Castera, "State of the Art in Design and Technology of MSW Devices," *J. Applied Physics*, Vol. 55, pp. 2506-2511, March 1984.
10. A. K. Ganguly and D. C. Webb, "Microstrip Excitation of Magnetostatic Surface Waves: Theory and Experiments," *IEEE Trans. on Microwave Theory and Tech.*, Vol. MTT-23, pp. 998-1006, December 1975.
11. L. R. Adkins, "Dispersion Control in Magnetostatic Wave Delay Lines," *Circuits Systems Signal Processing*, Vol. 4, No. 1-2, pp. 137-156, 1985.
12. H. Jacobs and M. M. Chrepta, "Electronic Phase Shifter for Millimeter Wave Semiconductor Dielectric Integrated Circuits," *IEEE Trans. on Microwave Theory and Tech.*, Vol. MTT-22, pp. 411-417, April 1974.
13. K. E. Mortenson *et al.*, "A Review of Bulk Semiconductor Microwave Control Components," *Proc. IEEE*, Vol. 59, pp. 1191-1200, August 1971.
14. A. M. Vaucher C. D. Striffler and C. H. Lee, "Theory of Optically Controlled Millimeter Wave Phase Shifters," *IEEE Trans. on Microwave Theory and Tech.*, Vol. MTT-31, pp. 209-216, February 1983.
15. R. C. Hansen (ad.), *Microwave Scanning Antennas*, Vol. 3, *Array Systems*, Academic Press, New York, 1966.
16. C. K. Pao *et al.*, "V-band Monolithic Phase Shifters," *10th Annual IEEE GaAs IC Symp. Digest*, pp. 269-272, 1988.
17. M. J. Schindler, "3 Bit 18 GHz to 40 GHz MMIC MESFET Phase Shifter," *IEEE Int. Monolithic Circuits Symp. Digest*, pp. 95-98, 1988.
18. J. Stulemeijer, F. E. van Vliet, K. W. Benoist, D. H. P. Maat, and M. K. Smit, "Compact photonic integrated phase and amplitude controller for phased-array antennas," *IEEE photo. Tech. Lett.*, 11, pp. 122-124.
19. H. Zmuda and E. N. Toughlian, "Photonic aspects of modern radar," 1st ed., Norwood, MA: Artech House, 1994.
20. A. J. Seeds, "Application of opto-electronic techniques in phased array antenna beamforming," in *Proc. Microwave photonics conf.*, pp. 15-20, 1997.
21. J. J. Lee, R. Y. Loo, S. Livingston, V. I. Jones, J. B. Lewis, H. W. Yen, G. L. Tangonan, and M. Wechsberg, "Photonic wideband array antennas," *IEEE Trans. Antennas Propagat.*, 43, pp. 966-982, 1995.
22. M. Y. Frankel and R. D. Esman, "True time-delay fiber-optic control of an ultrawide-band array transmitter/receiver with multibeam capability," *IEEE Trans. Microwave Theory Tech.*, 43, pp. 2387-2394, 1995.

23. J. F. Coward, T. K. Yee, C. H. Chafant, and P. H. Chang, "A photonic integrated-optic RF phase shifter for phased array antenna beam-forming applications," *J. Lightwave Technol.*, 11, pp. 2201-2205, 1993.
24. S.-L. L. Huang, C. H. Lee, and H.-L. A. Hung, "Optically controlled generation and true-time-delay phase-shifts of broad-band 60 GHz signals," *IEEE Microwave Guided Wave Lett.*, 3, pp. 42-44, 1993.
25. D. M. Krafcsik et al., "A dual-varactor analog phase shifter operating at 6-18 GHz," *IEEE Trans. Microwave Theory Tech.*, 36, pp. 1938-1941, 1988.
26. A. S. Rong and Z. L. Sun, "Phase shift and loss mechanism of optically excited E-plane electron-hole plasma," *IEEE Trans. Microwave Theory Tech.*, 42, pp. 1533-1539, 1994.
27. J. B. Georges and K. Y. Lau, "Broad-band microwave fiber-optic links with RF phase shifter control for phased-array antennas," *IEEE Photon. Technol. Lett.*, 5, pp. 1344-1346, 1993.
28. R. B. Wilds, "Try 1/8 stubs for fast fixed phase shift," *Microwaves*, 18, pp. 67-68, 1979.
29. G. R. Fleming, *Chemical Applications of Ultrafast Spectroscopy*, (Oxford University Press, New York, 1986), Chap. 4.
30. Ci-Ling Pan, Gong-Ru Lin, Jia-Min Shieh, Chia-Wen Tsai, S.-C. Wang, and Hsiao-Hua Wu, "Measurement of RF Standing Waves in a GaAs Microstrip Transmission Line Using a Laser-Diode-Based Optoelectronic Phase-Tracking System", *International Journal of High-speed Electronics and Systems*, Vol. 8, No. 4, pp. 145-158, December 1997.
31. J. M. Bostick, S. A. Mounter, and C. K. Johnson, *Opt. Comm.* 69, 54 (1988).
32. C. K. Johnson and J. Qian, "Picosecond laser timing by rf phase shifting," *Rev. Sci. Instrum.* 61 3, pp. 1158-1160, March 1990.
33. W. Kaiser, *Ultrashort Laser Pulses Generation and Applications*, 2nd ed., Chap. 4-6, pp. 113-274, Springer Verlag, New York, 1993.
34. Hsiao-Hua Wu, Gong-Ru Lin, and Ci-Ling Pan, "Optoelectronic Phase Tracking and Electrooptic Sampling of Free-Running Microwave Signals up to 20 GHz in a Laser-Diode-Based System", *IEEE Photonics Technology Letters*, Vol. 7, No. 6, pp. 670-672, June 1995.
35. A. W. Houghton and P. V. Brennan, "Phased array control using phased-locked-loop phase shifters," *IEE Proceedings H*, Vol. 139 1, pp. 31-37, Feb. 1992.
36. Gong-Ru Lin, T.-S. Hwang, Y.-H. Chuang, S.-C. Wang, and C.-L. Pan, "Broad-Band (≥ 20 GHz) Laser-Diode-Based Optoelectronic Microwave Phase Shifter", *IEEE Transactions on Microwave Theory and Techniques*, Vol. 46, No. 10, pp. 1419-1426, October 1998. G.-R. Lin, and C.-L. Pan, "Ultrafast Optical Characterization of Multi-dose Proton-bombarded GaAs", *Optical and Quantum Electronics, An International Journal*, Vol. 32, Issue 4/5, pp. 553-571, May 2000.
37. T. Pfeifer, H.-M. Heiliger, T. Löffler, C. Ohlhoff, C. Meyer, G. Lupke, H. G. Roskos, and H. Kurz, "Optoelectronic On-Chip Characterization of Ultrafast electric Devices: Measurement Techniques and Applications" *IEEE. J. Quantum Electron.* 2, 586, 1996.
38. G. Bauer, R. Hoffmann, G. Solkner, and H.-J. Pfeleiderer, "High Voltage Resolution with a Laser Diode based Electro-Optic Measurement System", *Microelectronic Engineering*, 24, 393-4080, 1994.
39. H.-H. Wu, C.-S. Chang, and C.-L. Pan, "Electro-Optical Sampling of Optoelectronically Phased-Locked 10.0 GHz Microwave Signals Using Laser Diodes", *Electron. Lett.*, 27, 1622-1623, 1991.
40. W. Mertin, A. Leyk, F. Novak, G. David, D. Jager, and E. Kubalek, "Characterization of a MMIC by direct and indirect electro optic sampling and by network analyzer measurements", *Microelectronic Engineering*, 24, 377-384, 1994.
41. G.-R. Lin, C.-L. Pan, and H.-H. Wu, "Optoelectronic Phase Tracking and Electro-Optic Sampling of Free-running Microwave Signals up to 20 GHz in a Laser-Diode-Based System", *Ultrafast Electronics and Optoelectronics*, Vol. 13, 1995 OSA.
42. K.S. Giboney, S.T. Allen, M.J.W. Rodwell, and J.E. Bowers, "Picosecond Measurements by Free-Running Electro-Optic Sampling" *IEEE Photon. Technol. Lett.*, 6, 1353-1355, 1994.

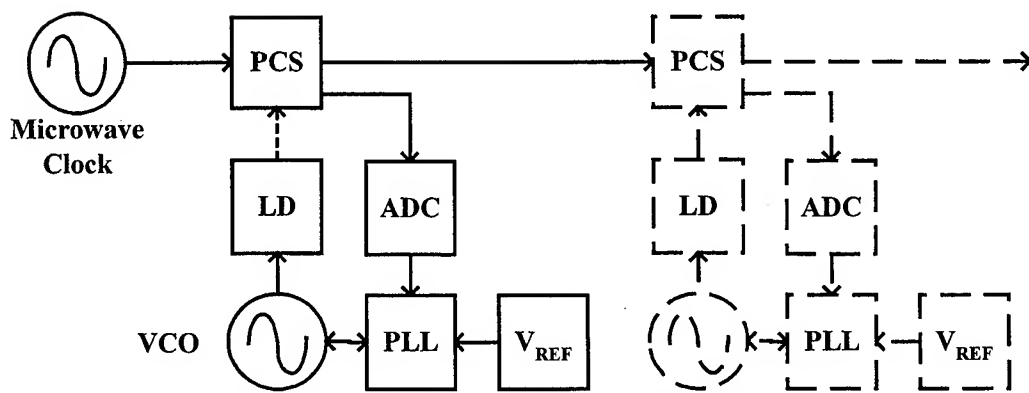


Fig. 1 Schematic diagram of OEPS.

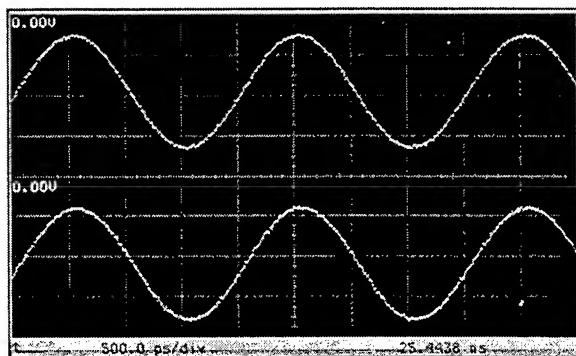


Fig. 2

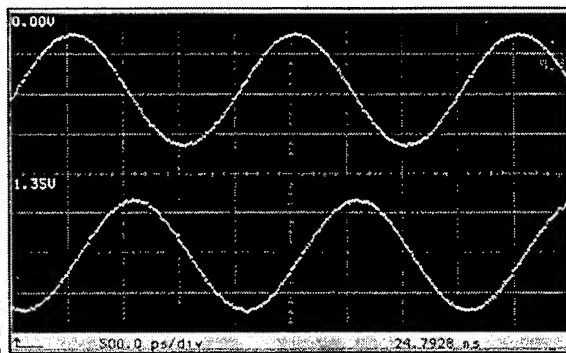


Fig. 3

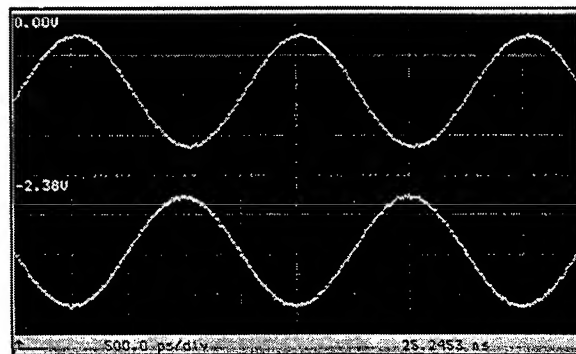


Fig. 4

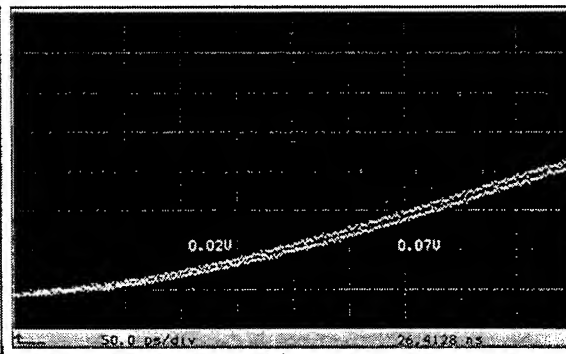


Fig. 5

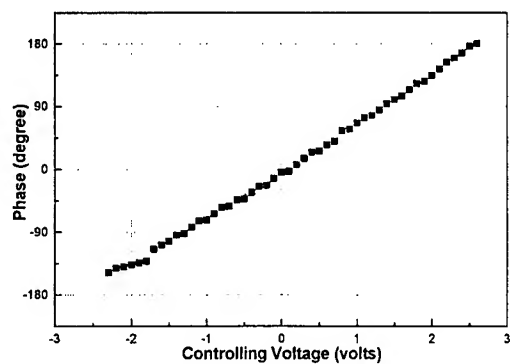


Fig. 6 Phase Shift of OEPS vs. controlling voltage.

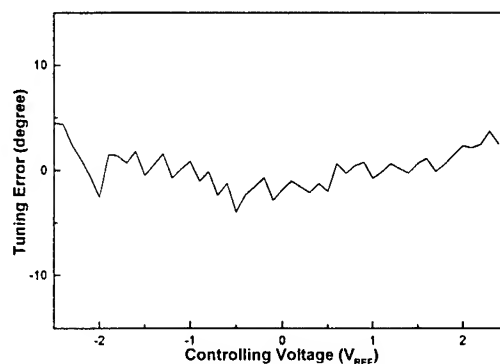


Fig. 7 Tuning error vs. controlling voltage.

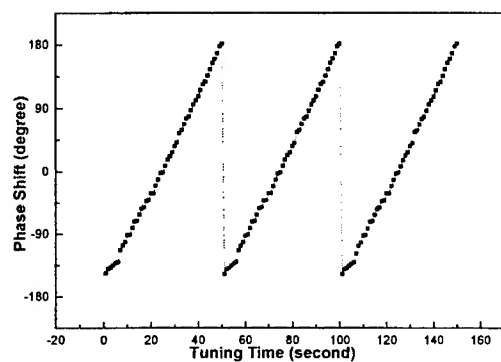


Fig. 8 The saw-tooth function test

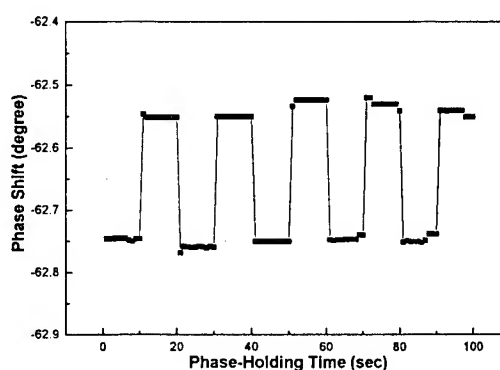


Fig. 9 The phase-switching test

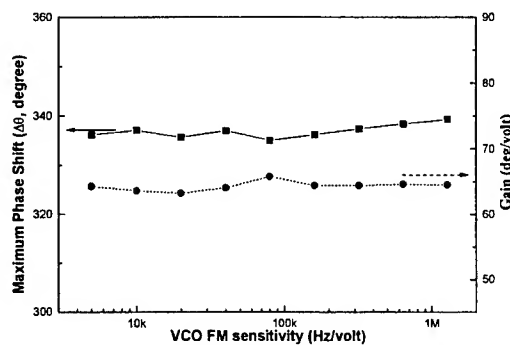


Fig. 10 The phase tuning range vs. VCO FM sensitivity.

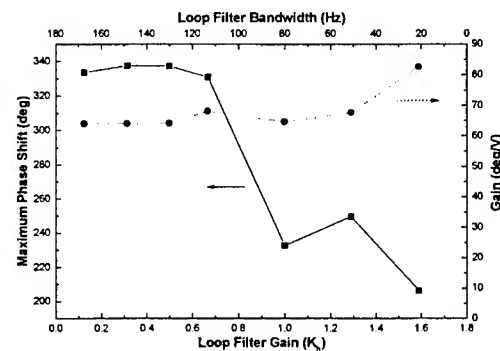


Fig. 11 The phase tuning range and Gain vs. K_h .

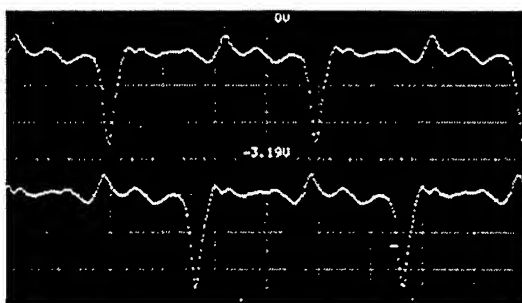


Fig. 12

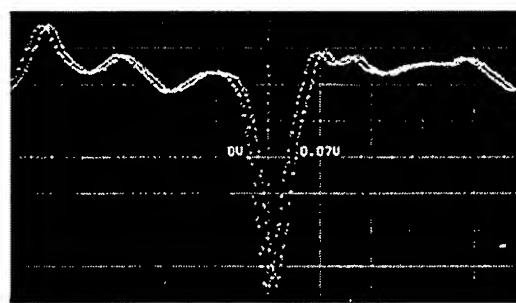


Fig. 13

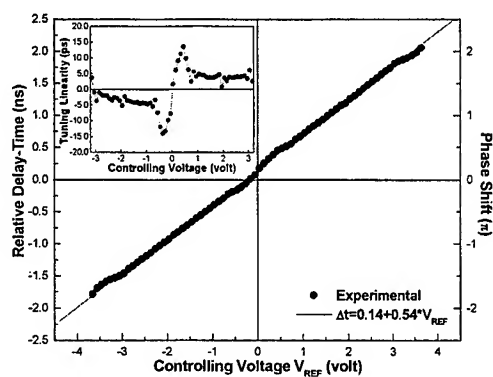


Fig. 14

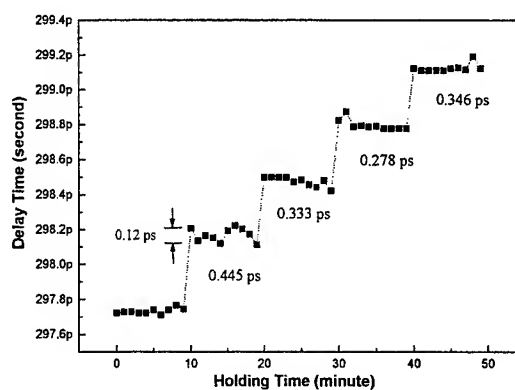


Fig. 15

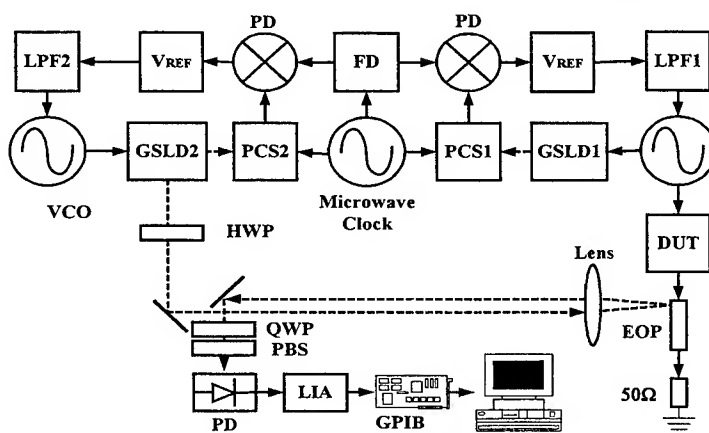


Fig. 16

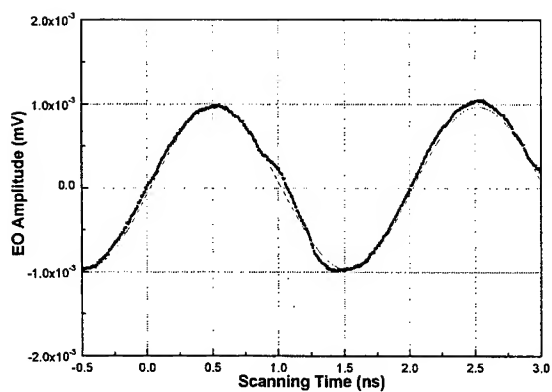


Fig. 17

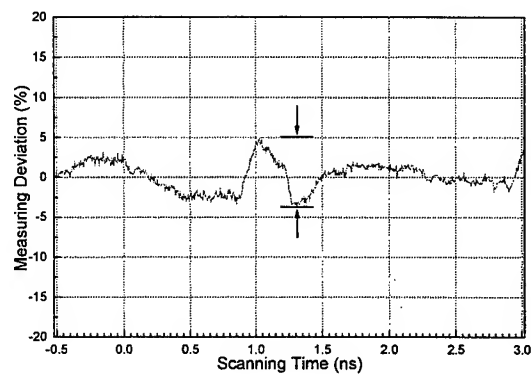


Fig. 18

High performances of InGaP/GaAs MSM photodetectors using Cu/Au Schottky contact

Chang-Da Tsai*, Yow-Jon Lin, Day-Shan Liu, and Ching-Ting Lee
Institute of Optical Sciences, National Central University
Chung-Li, Taiwan, Republic of China

ABSTRACT

We present the high performance of InGaP/GaAs metal-semiconductor-metal photodetectors (MSM-PDs) using copper as the interdigital Schottky electrodes. The devices exhibit ultra-low dark current (70 pA at bias of 10 V) and ultra-fast pulse response (over 9 GHz). The notable dark current characteristic and the absence of trap-induced gain are accredited to the superior properties of InGaP capping layer. The superior performances of InGaP/GaAs MSM-PDs make it promising for data communication.

Keywords: MSM-PDs; Copper, InGaP.

1. INTRODUCTION

To receive high density of optical information, it will be necessary to utilize ultrafast optical detectors. Interdigitated metal-semiconductor-metal (MSM) photodetectors have received considerable attention for this application because they are high-speed response, very low dark current, simple to fabricate and easily integrated with FET's. These superior performances make GaAs MSM photodetectors promising candidates for future optical link applications. However, it is commonly observed that low frequency internal gain is present in the GaAs MSM photodetectors¹. The responsivity of GaAs MSM photodetectors depends significantly on the bias voltage and the incident optical intensity due to high surface recombination velocity of GaAs and traps close to the contact metal. Burroughes reported that a wide bandgap AlGaAs capping layer can effectively passivate a GaAs surface to reduce the low frequency internal gain and improve the performance of its associated MSM photodetectors due to the absence of the trap-induced effect². However, the oxidation of AlGaAs, which is susceptible to the surface process history, will degrade the performance of the MSM photodetectors and deteriorate their long term reliability.

Recently, the ternary semiconductor $\text{In}_{0.49}\text{Ga}_{0.51}\text{P}$ (referred to as InGaP) lattice matched to GaAs has alternated for the AlGaAs as a promising wide bandgap material in the AlGaAs/GaAs system. The absence of deep level traps in InGaP layer³, good etching selectivity between InGaP and GaAs⁴, and relatively low surface recombination velocity⁵ are well-known advantages making this system superior to AlGaAs/GaAs in both electronic and optoelectronic devices application. These significant advantages make InGaP a promising alternative for AlGaAs as contact material.

Due to the excellent electrical and thermal conductivity and high electromigration resistance of Cu metal, high

performances of low dark current and high speed temporal response of GaAs MSM photodetectors with InGaP capping and buffer layer using interdigital Cu Schottky electrode were demonstrated.

2. EPITAXIAL GROWTH AND DEVICES FABRICATION

The novel InGaP/GaAs MSM-PDs sample were grown by a horizontal low-pressure organometallic vapor phase epitaxy (LP-OMVPE). The structure, as shown in fig. 1, consist of 0.3 μm InGaP buffer layer, a 1 μm GaAs absorption layer, and a thin InGaP capping layer (50 nm), grown on (100) GaAs substrate successively. The growth uses standard precursors including trimethylgallium (TMGa) and trimethylindium (TMIn) for Ga and In sources, and arsine (AsH_3) and phosphine (PH_3) for As and P sources, respectively. The growth conditions and processes were reported previously⁶. The unintentional concentration of GaAs and InGaP layer was measured as about $5 \times 10^{14} \text{ cm}^{-3}$ and $5 \times 10^{15} \text{ cm}^{-3}$, respectively.

After the epitaxial growth, an Si_3N_4 film with 150 nm thickness was deposited on the surface of the sample for the isolation of contact pads to semiconductor to reduce leakage current. The photosensitive region ($50 \times 50 \mu\text{m}^2$) was defined by standard photolithography technique. The Si_3N_4 layer without PR passivation was then etched using buffer oxide etchant (BOE). After etching with chemical solution of dilute HCl to remove the native oxidation of the capping layer InGaP surface, the interdigital Cu (300 nm) Schottky metals were formed by using lift-off process on the unpassivated photosensitive region. A thin gold protective film was deposited upon Cu Schottky metal subsequently to avoid oxidizing of Cu contact metal. The finger width and spacing of the interdigital electrodes are both 2 μm .

3. DEVICES PERFORMANCES

The measurement of current-voltage (I-V) characteristics was carried out using an HP 4145B semiconductor parameter analyzer. Under different bias voltages, the variation of the dark currents of InGaP/GaAs MSM-PDs are shown in fig. 2. The measured dark current is less than 70 pA at bias of 10 V because of the high performance of InGaP buffer and capping layers. To the best of our knowledge, these are the lowest reported dark currents (less than $3 \mu\text{A}/\text{cm}^2$) for MSM-PDs. The lower dark current is, the larger signal to noise ratio (SNR) is. Furthermore, the dark current is decreased, the minimum detectable optical power is decreased, resulting in a high performance optical data communication system.

Figure 3 show the photocurrent as a function of the bias voltage for the InGaP/GaAs MSM-PDs under different incident optical power at wavelength of 841 nm. The optical responsivity of 0.26 A/W was measured. It is worth noting that the photocurrent of the MSM-PDs is nearly independent on the bias voltage. The extremely low conductance of the MSM-PDs in the saturation region can be deduced that the trap-induced gain resulted from the surface states is very small.

The responsivities of the MSM-PDs as a function of the incident optical power with a wavelength of 841 nm at bias voltage of 10 V are shown in fig. 4. The wide linearity range of MSM photodetectors makes them more easy in circuit design.

To study high-frequency performance, the MSM photodetector were illuminated using a pulse laser with a wavelength of 827 nm and a full width at half maximum (FWHM) of 28.9 ps at 10V bias voltage. The associated temporal responses were measured using an HP 54120T oscilloscope. The temporal responses of InGaP/GaAs MSM-PDs with both 2 μm finger width and spacing and 50 μm square photosensitivity area was shown in fig. 5. The full width at half maximum (FWHM) of

the measured temporal responses is 29.8 ps and its corresponding 3 dB bandwidth is estimated by using Fourier transfer technique. Moreover, the measured FWHM of 29.8 ps is very close the pulse laser width of 28.9 ps. Because actually measured pulse width is a convolution of the optical pulse width, the photodetector impulse response width, all electrical equipment impulse response width⁷, we believe that the InGaP/GaAs MSM-PDs can be operated in higher frequency.

4. CONCLUSION

High performances of InGaP/GaAs MSM photodetectors with Cu metal was demonstrated. The devices show the ultralow dark current, high speed temporal response and insensitive responsivity with incident optical power as well as wide linearity range. The high performance of GaAs MSM-PDs with InGaP capping and buffer layer using Cu as Schottky contact electrode make them more suitable for the practical application in data communication.

ACKNOWLEDGMENTS

The authors wish to thank the financial support from the National Science Council of Republic of China, under contract number NSC 86-2215-E-008-017.

REFERENCES

1. M. Kingenstein, J. Kuhl, J. Rosenzweig, C. Mogl, A. Hulsman, J. Schneider, and K. Kohler, "Photocurrent gain mechanisms in metal-semiconductor-metal photodetector," *Solid-St. Electron.* **37**, pp. 333-340, 1994.
2. J.H. Burroughes, "H-MESFET compatible GaAs/AlGaAs MSM photodetector," *IEEE Photon. Technol. Lett.*, vol. 3, pp. 660-662, 1991.
3. H. Tanaka, Y. Kawamura, S. Nojima, K. Wakita, and H. Asahi, "InGaP/InGaAlP double-heterostructure and multiquantum-well laser-diodes grown by molecular-beam epitaxy," *J. Appl. Phys.*, vol. 61, pp. 1713-1719, 1987.
4. J.R. Lothian, J.M. Kuo, F. Ren, and S.J. Pearton, "Plasma and wet chemical etching of $\text{In}_{0.5}\text{Ga}_{0.5}\text{P}$," *J. Electron. Mater.* Vol. 21, pp. 441-445, 1992.
5. S.J. Pearton, F. Ren, W.S. Hobson, C.R. Abernathy, R.L. Masaitis, and U.K. Chakrabarti, "Surface recombination velocities on processed InGaP p-n junctions," *Appl. Phys. Lett.*, vol. 63, pp. 3610-3612, 1993.
6. C.D. Tsai, H.P. Shiao, C.T. Lee, and Y.K. Tu, "High performances and reliability of novel GaAs MSM photodetectors with InGaP buffer and capping layers," *IEEE Photon. Technol. Lett.* Vol. 9, pp. 660-662, 1997.
7. K.D. Li, Application Note 1, "Insights into high-speed detectors and high-frequency techniques," pp. 1-8, New Focus Inc.

*Correspondence : Email : cdtsai@ios.ncu.edu.tw

Fax : 886-3-4252897

undoped $\text{In}_{0.49}\text{Ga}_{0.51}\text{P}$ capping layer, 50 nm
undoped GaAs absorption layer, 1 μm
undoped $\text{In}_{0.49}\text{Ga}_{0.51}\text{P}$ buffer layer, 300 nm
S.I. GaAs substrate

Fig. 1 Schematic structure of MSM photodetector-grown epitaxial layers.

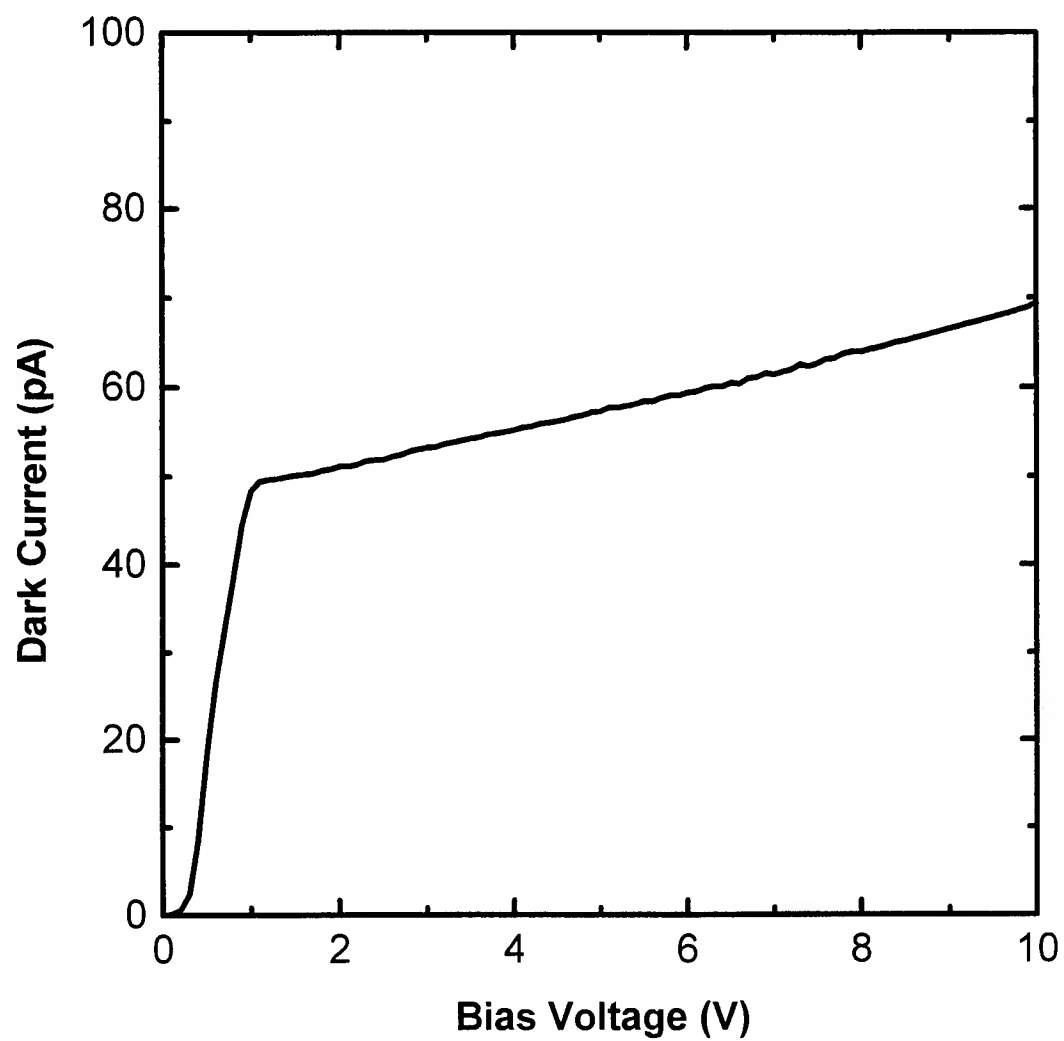


Fig. 2 Dark current as a function of bias voltage for Cu/InGaP/GaAs MSM photodetector with both 2 μm finger width and spacing.

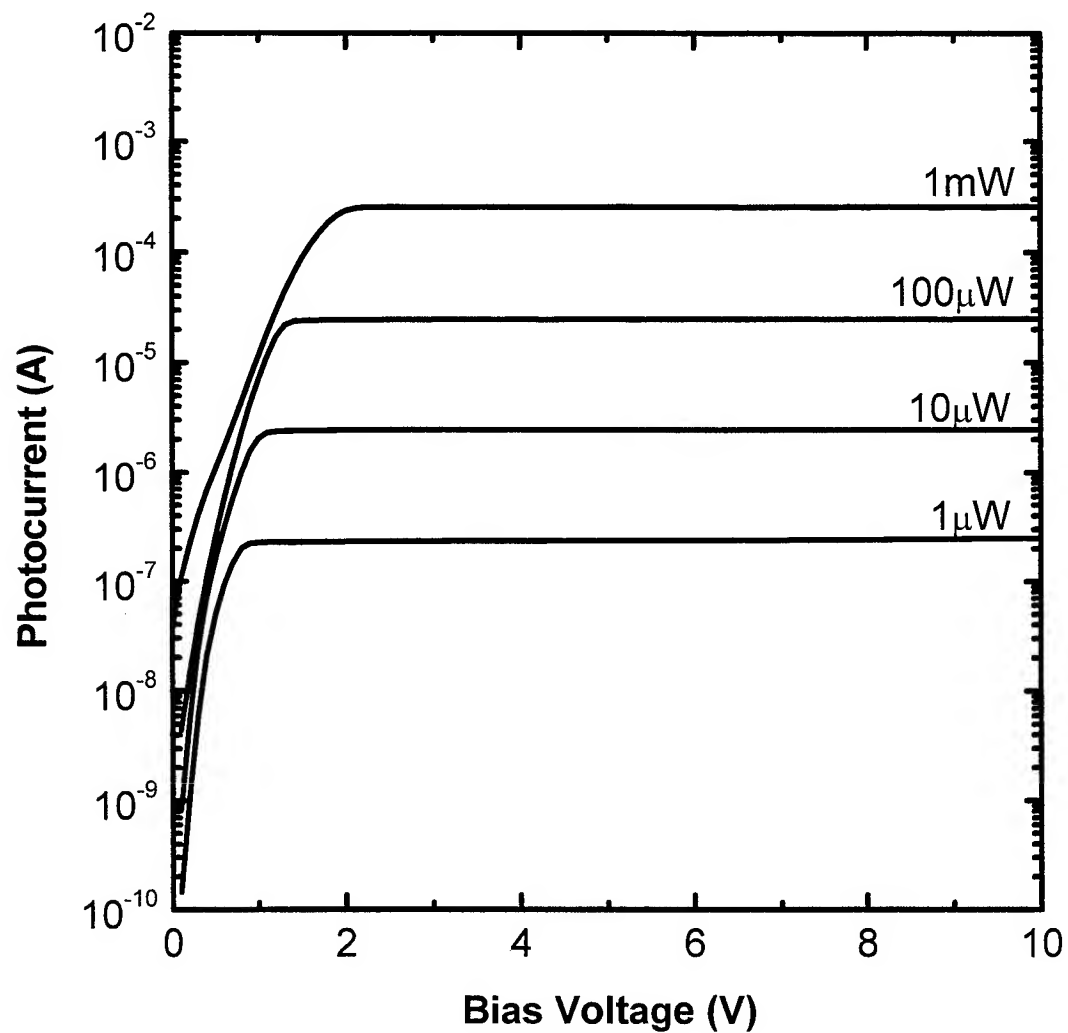


Fig. 3 Photocurrent as a function of bias voltage with various incident optical power at 841 nm wavelength and 50 μm square photosensitive area for Cu/InGaP/GaAs MSM photodetector with 2 μm finger width and 2 μm finger spacing.

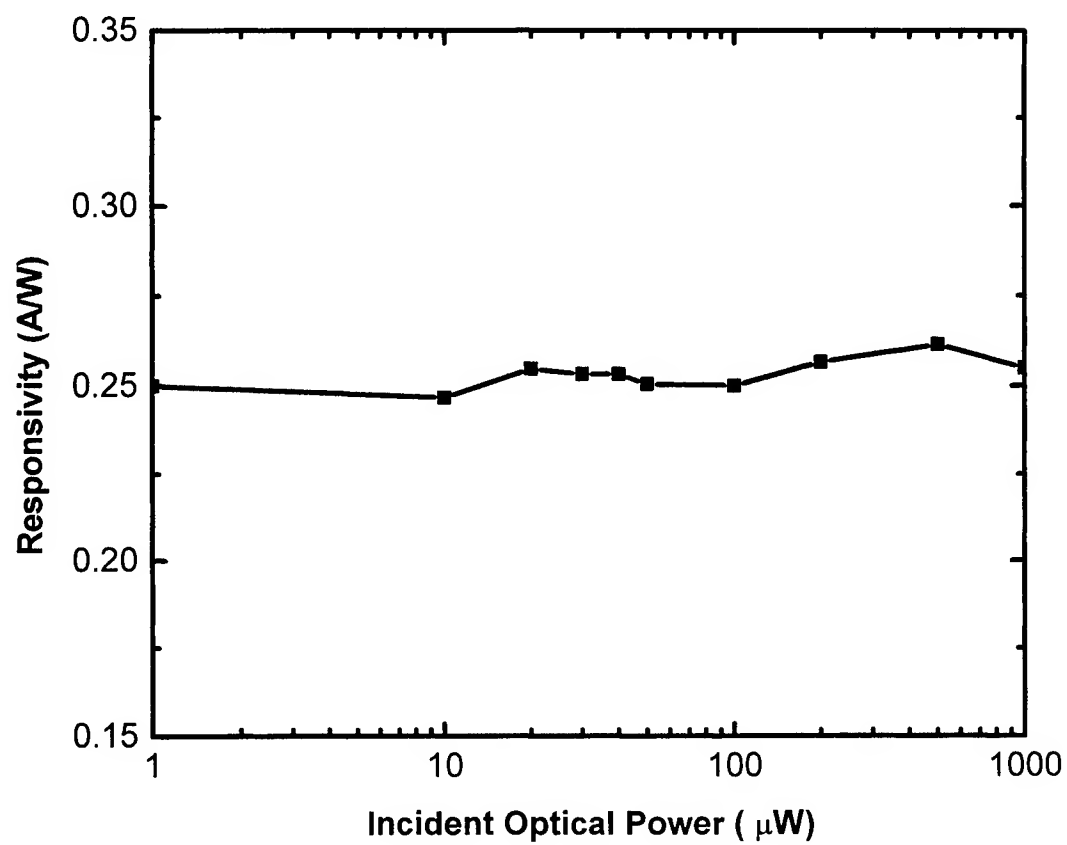


Fig. 4 Responsivity versus incident optical power for Cu/InGaP/GaAs MSM photodetector with 2 μm finger width and 2 μm finger spacing.

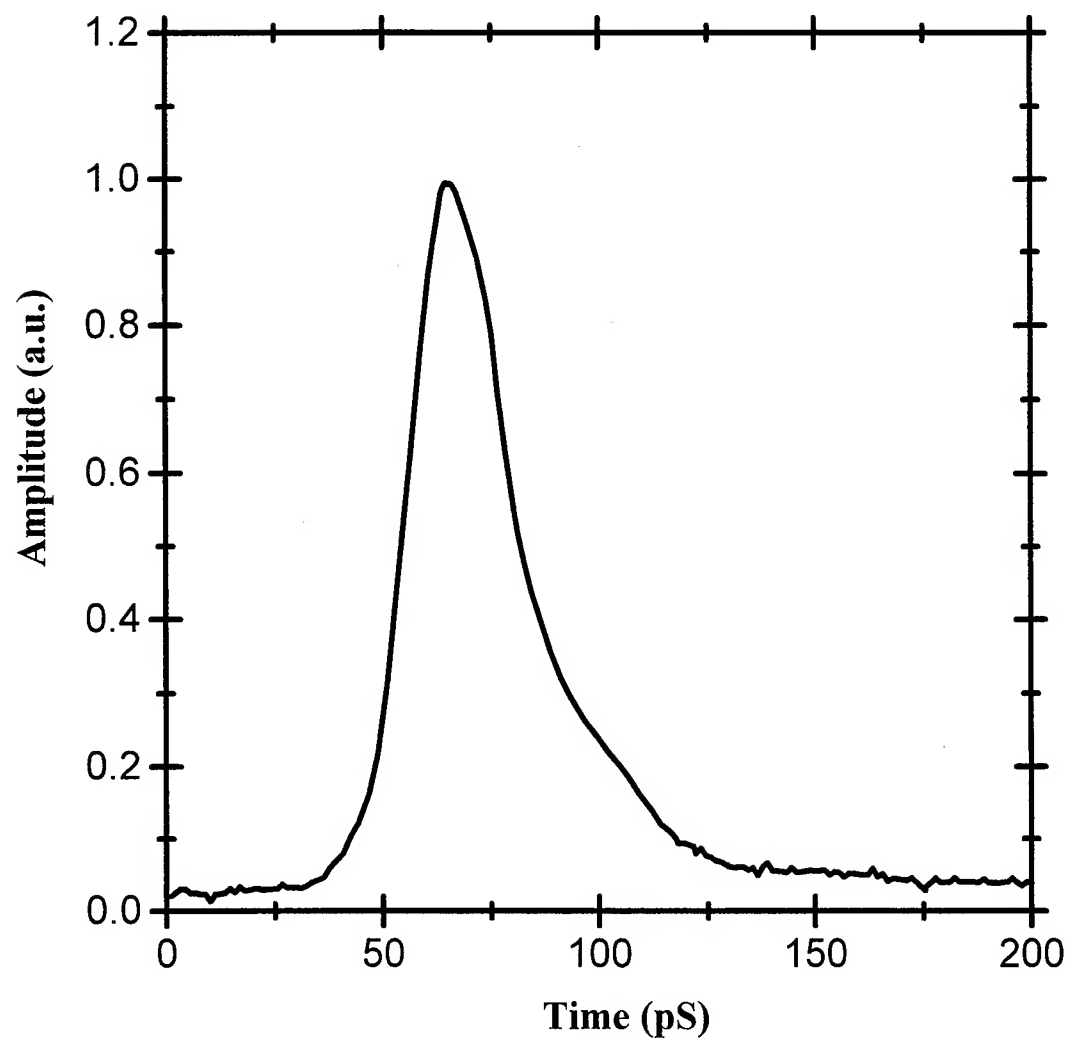


Fig. 5 The temporal responses of InGaP/GaAs MSM-PDs with both 2 μm finger width and spacing and 50 μm square photosensitivity area.

The ED-Litho Color Filter Process and its application

Chun-Hsiang Wen^{*a}, Shu-Huei Cheng^a, Yaw-Ting Wu^a,

Hong-Da Liu^b, Ching-Her Chao^b and Jun-Ichi Yasukawa^c

^aMRL, ^bERSO / ITRI ROC, ^cSumitomo Chemical Japan

ABSTRACT

The ED-Litho (Electrodeposition-Lithography) process is a unique method for making color filters, which combines electrodeposition of pigmented organic coating on ITO (Indium Tin Oxide) glass and a special photolithography technique based on a MDPR (MultiDeveloping PhotoResist). This process represents one of the potential methods to achieve low cost and high quality in the fabrication of color filter. This paper will report the related technologies and discuss the color performance used in TFT-LCD (Thin Film Transistor-Liquid Crystal Display) panel.

Keywords: Color filter, Electrodeposition, Lithography, Multideveloping, Photo Resist, TFT, LCD

1. INTRODUCTION

Liquid crystal displays are the most common type of flat panel displays (FPDs) and have been widely used since the early 1970's. Recently, the dramatic growth of LCD has been supported by strong demand for flat color display in NB (NoteBook) PCs. In order to broaden LCD's application to various products, the prime cost must be reduced continuously. Color filter plate is the major target in all the cost-down efforts. A color LCD panel has two glass plates, which are aligned to each other. One is color filter plate and other is driving plate. Liquid crystals are filled between the two plates, which are few microns apart. LCD consists of an array of picture element ("pixels") which can be individually addressed. Color filter plate is a key component for making color images. R, G, B, color elements and black matrix constitute color filter's pixel. The surfaces of color filter must be as smooth as possible for cell gap control and pixel size should be accurate for alignment.^{1,2}

We developed a method for color filter making. Which combines a special photo lithographic technique based on a self-developed MDPR and electrodeposition of pigmented organic coating on ITO glass, the so-called ED-Litho process represents one of potential methods to achieve low cost and high quality in the making of color filter.^{3,4}

1.1 ED Color Filter Process

The electrodeposition is a conventional color filter making process and a simple making method (Fig 1.). This method includes strip ITO patterning step and R, G, B electrodeposition process. The surface of the colored ED film is smoother than other color filter making method. The thickness of the color film is easily controlled by the electric current or applied voltage and time. The short tact time and low cost make it successful for commercial product in last decade. This method

has a patterning restriction, it is easy to make strip type pattern but triangle or mosaic is difficult to be patterned.^{5,6}

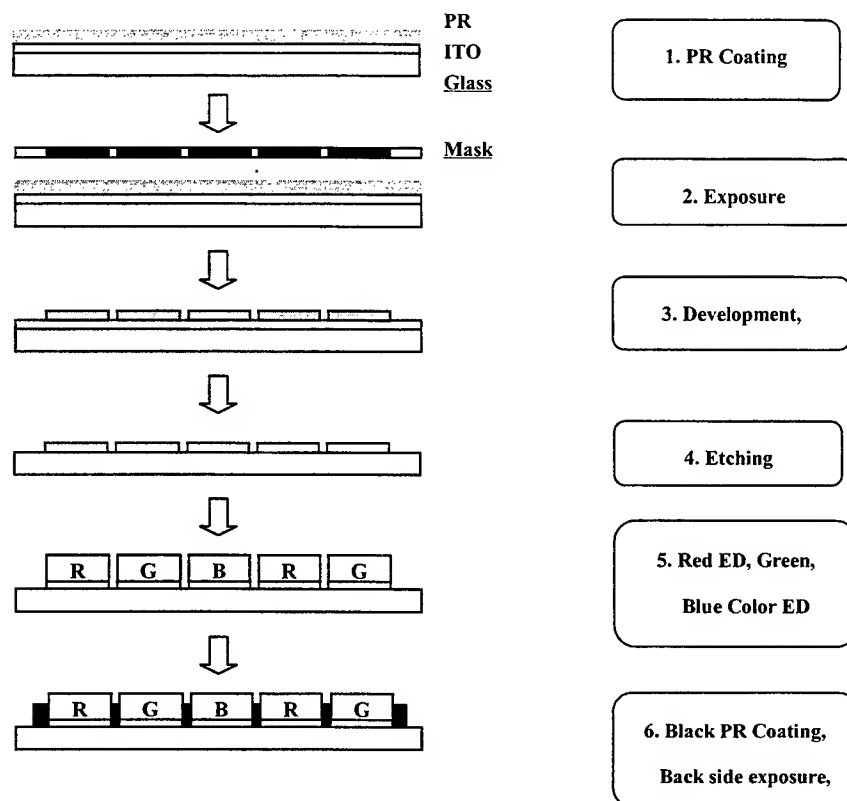


Fig 1. A typical ED-Litho Process Consists of multidevelopment and electrodeposition Process.

1.2. ED-Litho Color Filter Process

The key materials in the ED-Litho process is a positive MDPR coated on ITO glass, which upon exposure of UV light through a 3 or 4 step multidensity photomask, can then be removed to expose ITO layer sequentially according to the concentration of developer solution. Our goal is use a 4 step multidensity photomask to finish the process and Fig 2. is the 4-step ED-Litho color filter process.

In this application, a positive photosensitive coating MDPR film is formed on a transparent electrically conductive substrate. The photosensitive coating film is exposed to UV light through a mask having patterns of different degrees of light transmittances. Then a portion of the photosensitive coating film is developed and removed to register with one of the patterns of different degrees of light transmittances for exposing the transparent electrically conductive layer. Thereafter, a colored coating is electrodeposited on the exposed electrically conductive layer for forming a colored layer thereon. The

steps were repeated and the remaining colored layer were formed in sequence of different degrees of light transmittances.⁷

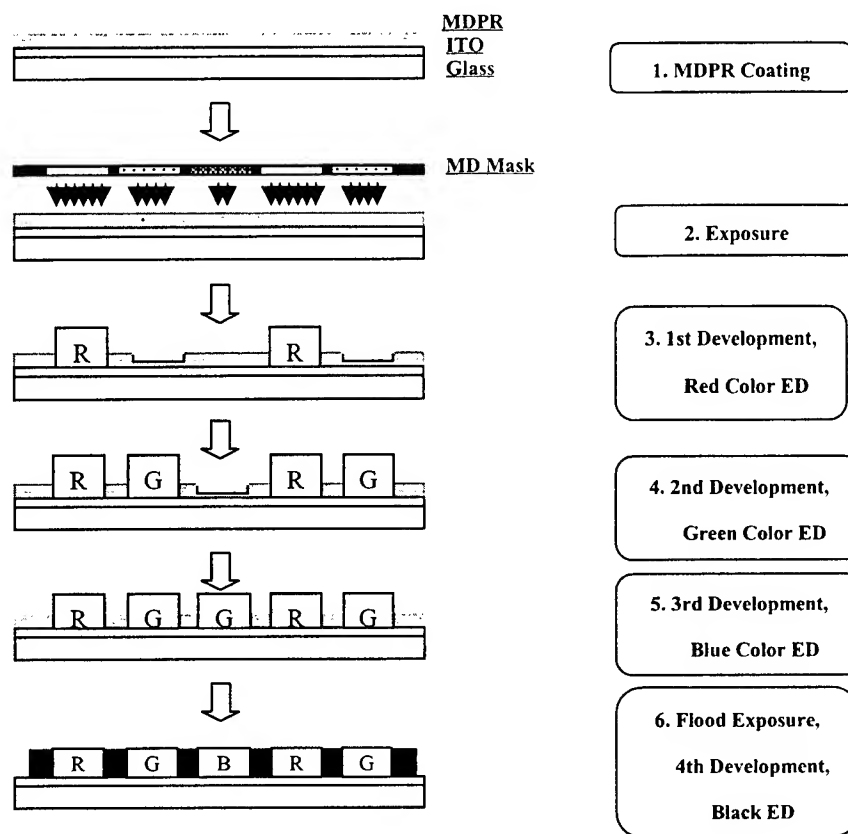


Fig 2. A typical 4-step ED-Litho Color Filter Process Consists of Multidevelopment and Electrodeposition Process.

2. Color Filter Making

The optical density of BM film of color filter for TFT LCD panel making should be equal or above 3.5 and the electrodeposited resin-BM is only near 3 per μm . So in this study, metal-BM is used in the color filter fabrication and the alternative ED-Litho Process is shown in (Fig 3.).

2.1 Black Matrix

The metal-BM-patterned glass was prepared firstly, and then the ITO film was deposited on the top of BM-patterned glass. The metal-BM film is composed with a three-layer structure of $\text{Cr}/\text{CrO}_x/\text{CrO}_x$. This structure can reduce light reflectivity and electric conductivity surface of BM film. The reasons are (1). High reflectivity of Cr film will reduce the contrast and color performance, (2). High reflectivity of Cr film will narrow down the exposure and development window. Besides, the developed pattern profile is not desired and (3). The topography and electric conductivity of Cr. BM will conduct a salient

with 1.2 μ m step in the electrodeposited color film step. (Fig 4.).

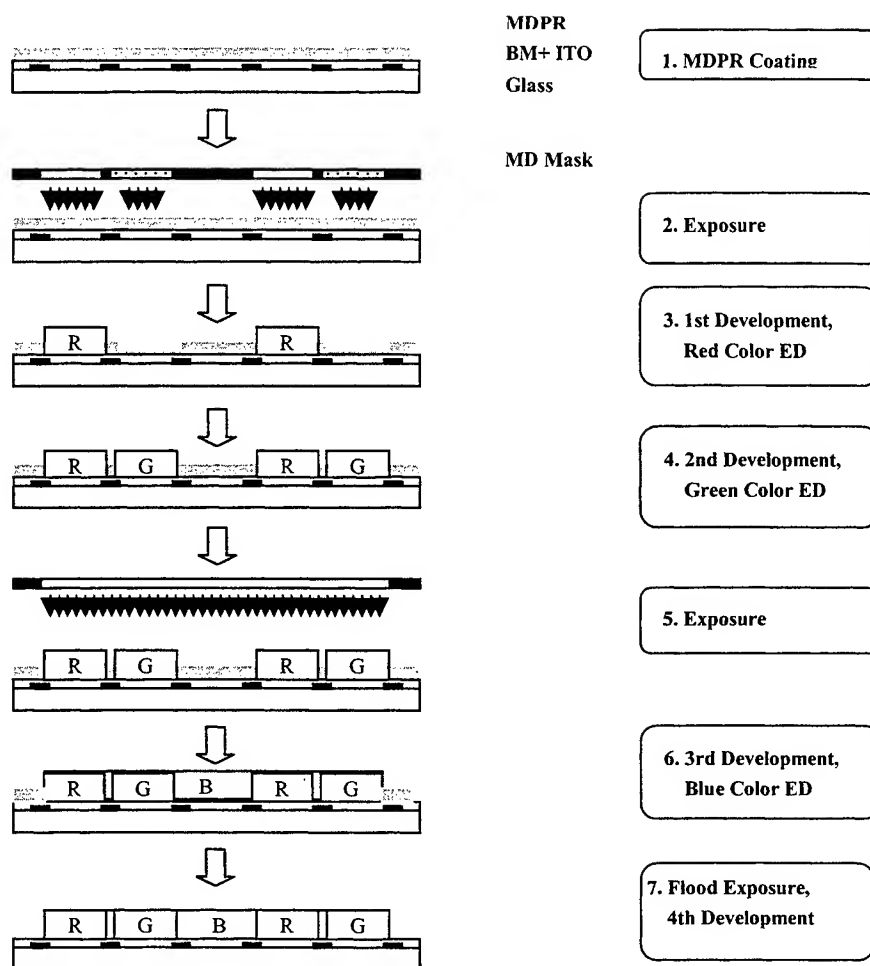


Fig 3. A typical ED-Litho Color Filter Process using metal-BM.

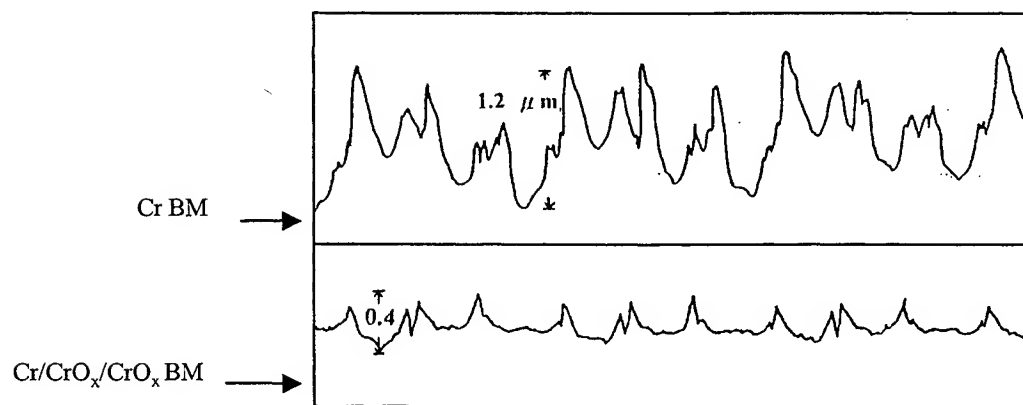


Fig 4. A roughness measurement of ED Color Film on metal-BM-patterned. Glass substrate.

2.2 ED-Litho Color Filter Fabrication

In this alternative ED-Litho Process, a positive photosensitive coating MDPR film is formed on a transparent electrically conductive substrate with metal-BM pattern. We used an alignment mask to instead the multidensity mask. An alignment mask was proximately contacted the photosensitivity MDPR film, and irradiated with UV rays of 200 mJ/cm² corresponding to red sub-pixel areas designed on panel pattern firstly. Then shifting the alignment mask to expose green sub-pixel areas designed on panel pattern with UV rays of 80 mJ/cm². Then a portion of the photosensitive coating film is developed and removed to register with one of the patterns of different degrees of light transmittances for exposing the transparent electrically conductive layer. Thereafter, a red-hued colored layer is electrodeposited on the exposed electrically conductive layer. The steps were repeated and the green-hued colored layer is formed in the portion of 80 mJ/cm². After finished the red-hued and green-hued color layer, a flood exposure of 200 mJ/cm² was carried out through open pixel area mask. After development all the remaining MDPR film in pixel area was selectively removed to expose the ITO layer. Thereafter, a blue-hued colored layer is electrodeposited on the exposed electrically conductive layer. After washing the glass substrate and drying at 110°C for 10 minutes, stripping the remaining MDPR, a post-baking was carried out at 260°C for 1 hour. The ITO was deposited on the previous prepared color filter substrate; following formed a PI alignment film, then finished panel assembly and module making.

3. RESULTS and DISCUSSION

We prepared color filter plate by ED-Litho Color Filter Process and successfully applied this color filter plate on the 6.4-inch 480 × 680 video graphic array (VGA) TFT module making.

This color filter plate without overcoat for that the flatness of the surface of the electrodeposition color film is well controlled within $\pm 0.2\mu\text{m}$ (see Fig 4.). The color pictures of pixels of color filter took by microscope in each step were shown in Fig 5. Table 1. show the chromaticity coordinate of each color of color filter plate and the TFT module. The chromaticity coordinates of each color of color filter slightly change after assembly with TFT plate and with backlight, the difference is mainly come from the backlight. Table 2. show the specifications of the 6.4-inch VGA TFT module. The response time and driving voltage are good and color performance is very sharp (see Fig 6.).

Table 1. The chromaticity coordinate for each color of color filter and TFT module.

Color	CIE Chromaticity					
	Color filter			TFT LCD		
	x	y	Y	x	y	L
Red	0.5586	0.3306	20.587	0.577	0.339	67.9
Green	0.305	0.5382	40.712	0.309	0.579	127
Blue	0.1408	0.1191	13.199	0.151	0.12	29.7



1st Development, Red Color ED 2nd Development, Green Color ED Exposure,
3rd Development, Blue Color ED

Fig 5. Color pictures of pixels of color filter in each step (ref Fig 3.)

Table 2. Specifications of the 6.4-inch VGA TFT module.

Display Area	6.4"	
Aspect Ratio	4 : 3	
Number of Pixels	640(H)×480(V)	
Pixel Size	67.5μm(H)×203μm(V)	
Cell Gap	4.75μm	
Response Time	30 ms	
Driving Voltage	5V	
White Balance CIE Cromaticity	x	0.319
	y	0.337
	L	237
Color Temperature	6124 °K	

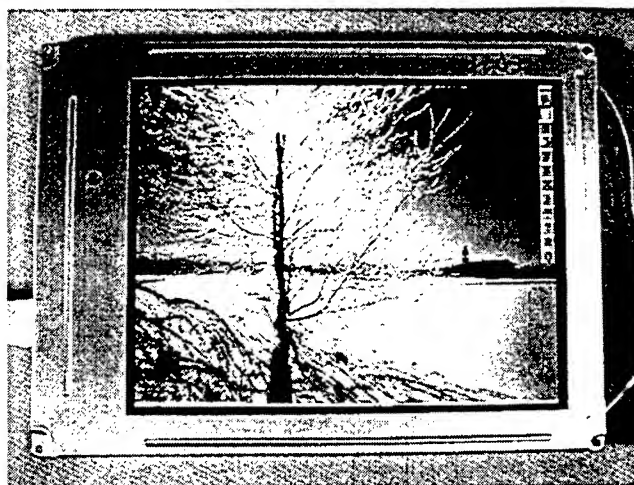


Fig 6. A Picture of 6.4-inch TFT LCD module

4. CONCLUSION

The ED-Litho (Electrodeposition-Lithography) process is a simple method for making color filters. The film thickness and uniformity are easily to be controlled. This process represents one of the potential methods to achieve low cost and high quality in the fabrication of color filter. Although the color filter plate prepared by this process having two layers of ITO film and it will reduce the transmittance. But the advantages of increasing picture size of LCD, using resin-BM and short tact time will make it more powerful.

5. ACKNOWLEDGEMENT

The Authors wish to express their thanks to MOEA/R.O.C. and Sumitomo Chemical/Japan for supporting this project and the PRIMVIEW Company for their help in the TFT plate offered and module making.

6. REFERENCES

1. Ram W. Sabnis, "Color filter technology for liquid crystal displays", *Displays* 20, pp119-129, 1999
2. Y. Hirai, H. Katoh, "Requirement on color filter for TFT-LCDs", Proceedings of the 2nd international display workshops, Vol. 2, pp49-52, *IDW'95*, Hamamatsu, Japan, 1995
3. Industrial Technology Research Institute, US Patent 5645970
4. J.M. Liu, C.H. Tzeng, H.C. Cheng, P.J. Hsieh, "Development of a Multideveloping Photoresist and Its Application to Make Color Filter" *Macromolecules*, 36th International Symposium, Seoul, Republic of Korea, 1996
5. Shinto Paint Corporation, US Patent 4873175
6. Shinto Paint Corporation, US Patent 5503952
7. Industrial Technology Research Institute, US Patent 5641595

*Correspondence: Email: 790756@itri.org.tw; Telephone: 886-3-5915292; Fax: 886-3-5820215

Low-dielectric constant photoresists for insulation on TFT array

Rong-Jer Lee, You-Cheng Wu*, Shih-Lieh Chen, Song-Shiang Lin, Hsien-Wen Chien

Materials Research Lab./ITRI, Bldg. 77, ITRI, Chutung, Taiwan, R.O.C.

ABSTRACT

This paper describes a low dielectric constant, high resolution and high brightness single layer positive photoresist on TFT array. A currently used positive photoresist comprising of low dielectric constant materials and a chemically amplified resist system is designed for the insulation layer on TFT array to enlarge pixel aperture ratio of TFT-LCD.

Keywords: positive photoresist, low-dielectric constant photoresist, PDCRs

1.INTRODUCTION

In recent years the important issues of LCDs are brightness, contrast and backlight power consumption. To improve aperture ratio can solve these problems. A new color filter being served as a passivation layer on a-Si TFT had been demonstrated¹. In this structure (figure 1) higher aperture ratio can be easily achieved and some photolithography steps can be eliminated along with the easiness of liquid crystal cell assembly alignment.

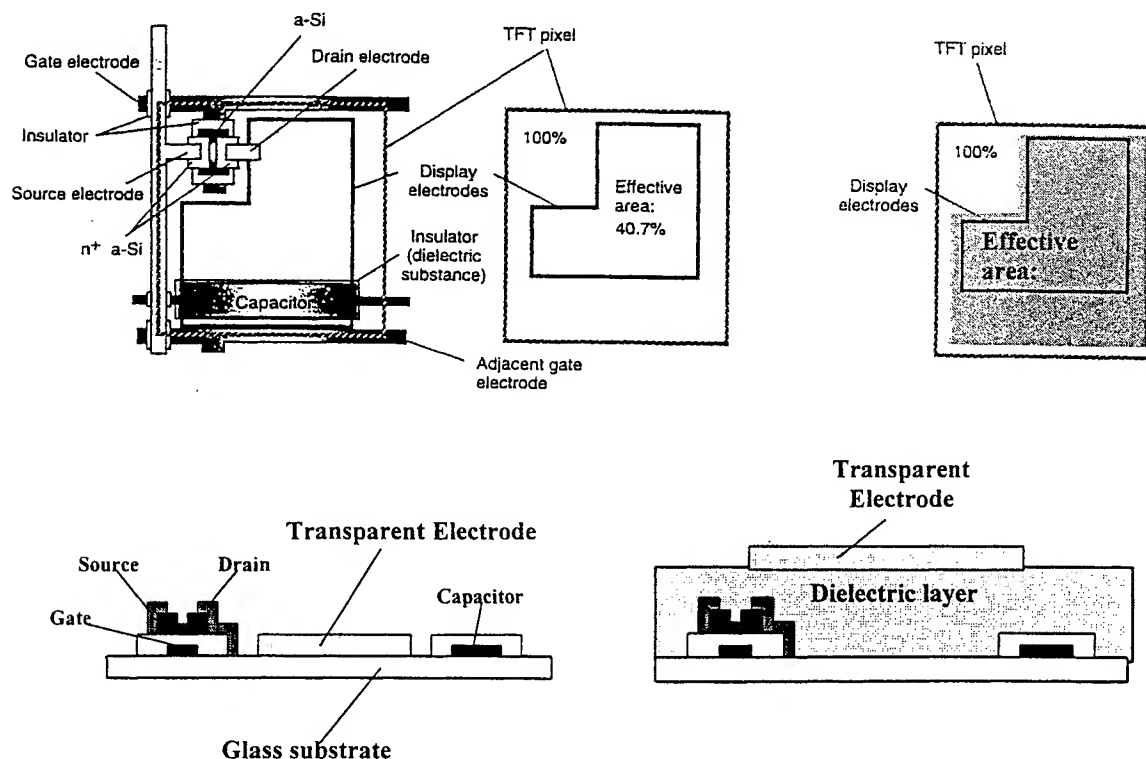


Figure 1 Comparison of the structure of conventional LCDs with color filter integrated on a-Si TFT

* Correspondence: Email: 880806@itri.org.tw; Telephone: 886-3-5912206

A low-dielectric constant photoresist plays an important role when it is integrated directly on TFT array. The requirements of the photoresist are low dielectric constant, high resolution and high transmittance of light. However, the negative photoresists have resolution limitation². It is hard to get finer patterns less than $10\ \mu\text{m}$ lines and spaces. Conventional positive photoresists using novolak resin system have a major drawback of their low thermal stability causing serious yellowing problem³.

In this paper, we will present a novel high performance pigment-dispersed color resist (PDCR), which gives low dielectric constant, high resolution and high brightness incorporating a chemically amplified system^{4,5}. This PDCR can be applied for color filter integrated on a-Si TFT array and other high-resolution CF fabrication.

2. COMPOSITION OF THE POSITIVE PDCR

In this invention, a positive PDCR system includes the organic pigments, an acrylic resin, a photoacid generator, a solvent and additives.

The standard pigments for a color filter are: Red 177 + Yellow 139 for Red, Green 36 + Yellow 139 for Green, and Blue 156 + Violet 23 for Blue. All pigments are broken down by a mechanical force into near the primary particle size before formulating with resin.

The acrylic resin is the most important part of the positive PDCR. It influences on coating flatness, developability and durability of PDCR. Higher molecular weight of acrylic resin can raise heat resistance, but lowering the light sensitivity due to the low dissolution rate of those resins in a diluted developer. Figure 2 shows the molecular weight of the acrylic resin used by us.

Mn = 14344 Mw = 30289
Mz = 57027 Mv = 26655
Mw/Mn = 2.11314

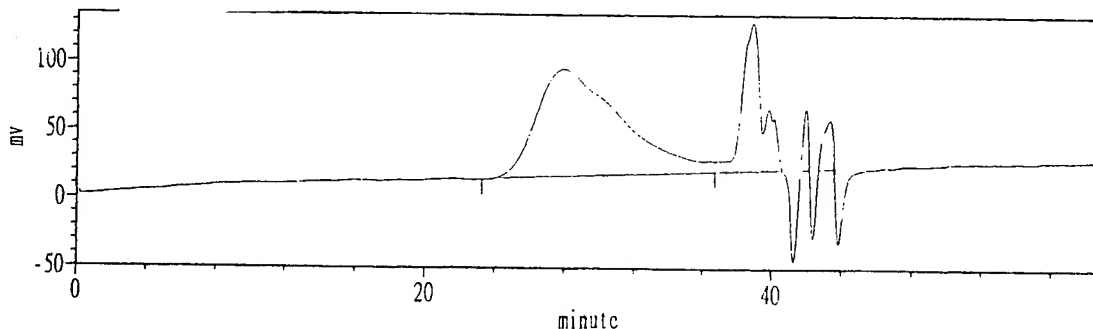


Figure 2 The molecule weight of acrylic resin

Figure 3 illustrates the dissolution rate diagram of a positive photoresist system⁶. R_n is the dissolution rate of the acrylic resin used in the positive photoresist. R_p is the dissolution rate of exposed parts and R_o is the dissolution rate of unexposed parts of the photoresist. The resolution capability depends on the ratio of R_p to R_o . The higher the R_p/R_o ratio leads to better resolution. The developer is a diluted alkali solution, so the acid value and the acid labile functional group control the R_n , R_p and R_o of the acrylic resin. From experiments, excellent results are obtained when the acid value of acrylic resin is in the range from 40 to 80 (mg KOH/g sample) and the acid labile functional group such as t-butyl carbonate is in an amount of 15% to 25% by weight.

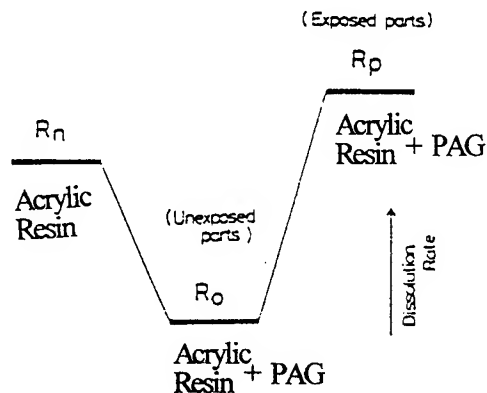


Figure 3 Dissolution rate diagram of a positive photoresist system

Diaryliodonium and triarylsulphonium salts are used as photoacid generators. Under UV light or thermal heating these PAGs are unique to produce the strong Lewis acid. These PAGs have maximum absorption in the short UV wavelength range (240 nm to 300 nm). They are generally used in combination with a sensitizer to extend the photosensitivity of formulations into the 350 nm to 400 nm range (the main emission lines of mercury lamps). The exposed parts of the photoresist generate strong protonic acid to unblock the acid labile functional group. The exposed and unexposed parts of the photoresist are readily distinguishable on the basis of their corresponding solubility and insolubility in a diluted alkaline developer.

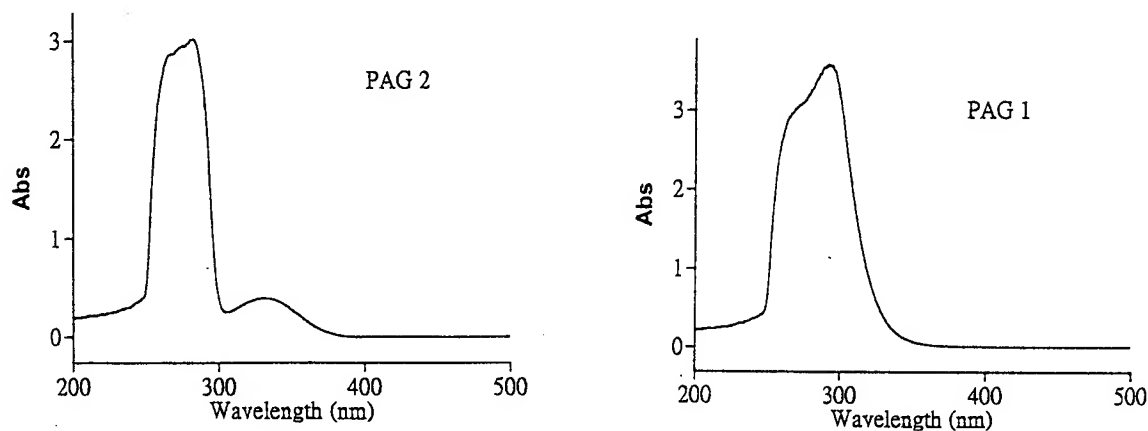


Figure 4 the UV absorption of PAGs

3. THE PROCESS FOR MAKING A COLOR FILTER SPECIMEN

The process for making a color filter specimen is as following:

- Clean the Corning 1737 glass with a detergent and rinse well (Substrate size 12x12 cm²)
- Spincoat the resist at a spin speed between 800 and 1000 (rpm)

- Prebake in an oven at 90 °C for 10 mins
- Expose with a dose of 200-300 mJ/cm²
- Post-Exposure-Bake(PEB) in an oven at 120°C for 10 mins
- Develop in a bath with 1% KOH + 1% surfactant solution
- Rinse and dry
- Post-bake in an oven at 200°C for 30 mins

4. RESULTS AND DISCUSSION

Figure 5 spectra of currently used PDCRs. The transmittance of blue and green color is over 80%, and is over 85% for red color at 460, 540 and 620nm. These color resists show high brightness and high transparency.

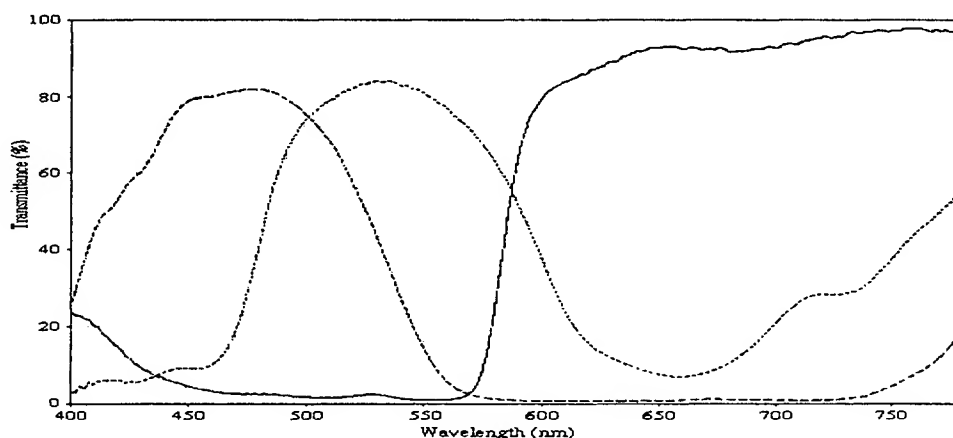


Figure 5. spectra of currently used PDCRs

The x, y and Y values of R.G.B photoresists are summarized in Table 1. They also show good chromaticity properties and high Y values (high brightness). We can adjust the x, y and Y values by varying the pigment /binder ratio. The higher P/B ratio is, the higher color purity is obtained. But the final x, y and Y values depend on the customers' requirements. We also examined the resolution and patterning properties of this series of PDCRs. As shown in Figure 6, the resolution of lines and spaces made by red color resist can be as narrow as 5 μ m.

Color	x	y	Y
Red	0.5918	0.3250	23
Green	0.3055	0.5265	63
Blue	0.1400	0.1967	23

Table 1. Chromaticity properties of PDCRs for 1.2 μ m film thickness

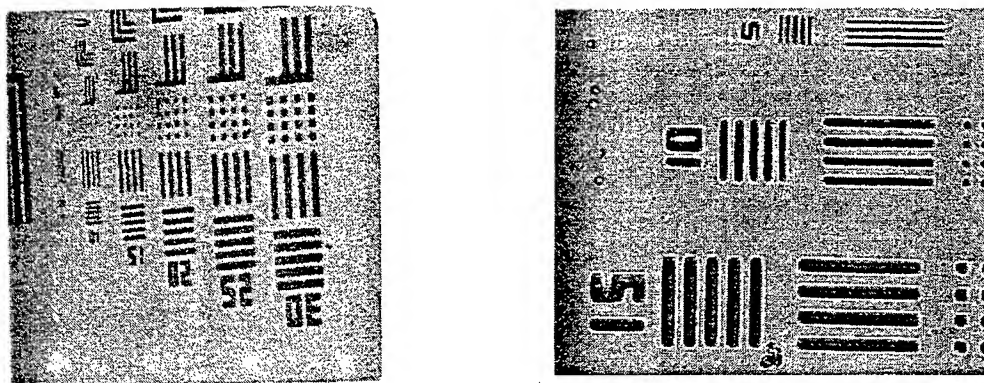


Figure 6 the resolution of lines and spaces made by red color resist

In this novel invention, a better resolution is obtained compared with conventional radical type color resist. Besides the high brightness and high resolution properties, there still exists further works to optimize the light sensitivity of the resists. The stability and reliability such as thermal and chemical resistance need to be further investigated and confirmed. We believe that much better resolution can be obtained after further modification of the formulation.

The photoresist which can be integrated on a-Si TFT must have a dielectric constant lower than 3. By using the fluorinated acrylic resin, the dielectric constant of our PDCR is 3.5. Further study is under way to get lower dielectric constant resists.

5. CONCLUSIONS

The currently used positive pigment-dispersed color resists based on a chemically amplified system give excellent resolution narrower than $5\ \mu\text{m}$ L/S, high transmittance of larger than 80%, high Y values of 23, 63, 23 for Red, Green, and Blue colors, and high color purity. They can offer advantages in high performance color filter manufacturing, compared with conventional pigmented resists.

The dielectric constant of our current PDCR is 3.5, but it must be further modified to obtain a value below 3 to be suitable for being integrated on a-Si TFT array.

We also synthesize an acrylic binder with acid labile and aromatic functional groups which have functions of acid catalyzed unblocking and good compatibility with pigments.

Further modification and examination are still in progress, the dielectric constant of these PDCRs will be further improved in the near future.

ACKNOWLEDGMENTS

The authors would like to acknowledge the support of many co-workers in Materials Research Lab./ITRI.

REFERENCES

1. D. B. Willem, Z.Z. John, and G. Tieer, "TFT structure including a photoimageable insulation layer for use with LCDs and image sensors", US patent 5780871.
2. I. Akihiko, N. Masato, P. Georg, and D. Ralph, "Negative photoresist compositions comprising a photosensitive compound, an alkoxymethylated melamine and novolak resin", US patent 5541036.

3. R. Dammel, *Diazonaphthoquinone-based resists*, SPIE tutorial texts series, volume TT 11, 1993.
4. B. J. Carpenter, J. G. McMaster, J. LaTorre, and L. L. Simpson, "Positive photoresist composition containing photoacid generator and use thereof", US patent 5498765.
5. E. Kobayashi, M. Murata, T. Ota, and A. Tsuji, "Chemically amplified resist composition", US patent 5629135.
6. M. Hnabata, Y. Uetani, and A. Furuta, "Design concept for a high-performance positive photoresist", *J. Vac. Sci. Technol.* **B7(4)**, 1989.

Novel Grating-frustrated Wavelength Division Multiplexer Using Polymer Waveguides with Inverted-Ridge Structure

Wei-Ching Chung^{*a}, Yun-Tai Hsueh^b, Wen-Chung Chang^b, Way-Seen Wang^c

^aDept. of Electro-optics Engineering, National Institute of Technology, Yunlin, Taiwan, R.O.C.

^bDept. of Electronics Engineering, Southern Taiwan University of Technology, Tainan, Taiwan, R.O.C.

^cDept. of Electrical Engineering, National Taiwan University, Taipei, Taiwan, R.O.C.

ABSTRACT

A set of grating-frustrated directional couplers is proposed here for wavelength division multiplexer(WDM). Instead of using optical fiber, integrated optical polymer waveguides with inverted-ridge structure was used in this design. This device is composed of two cascaded directional couplers. Each of the directional coupler is made up of two waveguides with the index of one of the waveguides being a periodic function of z which is the direction of propagation. The average index of the grating waveguide should be equal to that of the un-grated waveguide. According to the coupled wave theory, only the light with a specific wavelength will pass through the waveguide without grating while all other light will coupled to the grating waveguide when the mixed light is initially input at the un-grated waveguide. This phenomenon is called Bragg reflection and the specific wavelength is called Bragg wavelength. The Bragg wavelength is proportional to the period of the index grating. Therefore, this device is capable of selecting at least three different wavelengths. A detailed analysis of this design is also included in this paper.

Keywords: Wavelength division multiplexer(WDM), Integrated optical waveguide, Polymer waveguide, inverted-ridge, Bragg reflection, Bragg wavelength.

1. INTRODUCTION

Wavelength division multiplexer is an indispensable device in multiple-wavelength optical communication systems. For such a system, the communication channels can be expanded not only by modulation techniques but also by the wavelength of laser. Besides, WDM can be used to make a multiple-wavelength laser light source when a broadband laser light source is coupled to the WDM. Therefore, many WDM implementation schemes^{1,2,3,4} are developed and proposed to achieve aforementioned advantages. Among those techniques, fiber grating¹ and interference⁴ are most frequently used. J.-L. Archambault¹, etc., had demonstrated a grating-frustrated coupler for channel-dropping filter in single mode optical fiber. According to their report, the channel-dropping filter was operated at 1535nm with 0.7nm bandwidth, 13-dB isolation, and 70% peak transmission. Its coupling length was 3mm, and $\delta n = 6 \times 10^{-4}$ (index variation). It is believed that to make an all-fiber multiple-wavelength channel-dropping filter is difficult. The difficulty comes from two aspects: (1) making multiple index grating in one fiber, (2) making multiple fiber couplers using two fibers. On the other hand, integrated optics provides a feasible and easier way to fabricate a multiple-wavelength channel-dropping filter or equivalently a wavelength division multiplexer. Especially, the advent of sub-micron technology of integrated circuit makes the fabrication of fine grating easier. With sub-micron technology, half period of index grating can be made as small as $0.15 \mu\text{m}$. This dimension is good enough for making a WDM device with operating wavelength of 1530 ~ 1570 nm and waveguide effective index of 1.45 ~ 1.55. Therefore, we propose a WDM device using two cascaded grating-frustrated direction couplers with inverted-ridge polymer waveguides to separate three different wavelengths of laser light. We believe more wavelengths can be separated from a similar WDM device using more cascaded grating-frustrated directional couplers. The structure of this WDM device is shown in figure 1. The substrate of the device is quartz. The refractive index of the polymer is about 1.455, and its refractive index can be increased when the polymer is exposed under UV. The longer the polymer is exposed, the larger its refractive index becomes. The details of the structure will be described in section 3. The operation principle of grating frustrated direction coupler can be derived from coupled-wave theory⁵. And this will be analyzed in detail in section 2. Also, in section 2, a theoretical calculation of the structure is presented. The calculation includes transmission and reflection spectra, the

* Correspondence: Email: eocwc@sparc.nhit.edu.tw; Tel: 886-056329643 ext571

dependence of transmission and reflection on coupling length. From the calculation, the device parameters such as refractive index variation, coupling length, etc., will be proposed for fabrication.

2. THEORY AND CALCULATION

The fundamental operation principle of our proposed device is the same as that of grating-frustrated directional coupler. Although, two cascaded grating-frustrated directional couplers are used in the device. We can analyze only one of the grating-frustrated directional couplers and apply similar analysis and results to the other. The structure of grating-frustrated directional coupler is composed of two parallel waveguides with refractive index of one of the waveguides is a periodic function of distance in the light propagation direction. Figure 2 shows the structure of proposed device and illustrates the operation principle of grating-frustrated directional coupler. The average index of the grating waveguide is equal to that of the un-grated waveguide, and the index perturbation of the grating waveguide need not be large. The light propagates in the grating waveguide will experience reflection due to the refractive index discontinuity. According to couple-wave theory⁵, the reflected light will couple to the un-grated waveguide in both propagation direction and opposite propagation direction. Besides, the light propagates in the un-grated waveguide will couple to the grating waveguide in both directions, too. When the input light that is initially coupled to the un-grated waveguide meets the phase matching condition, it will emerge from the un-grated waveguide with only a little loss. This phenomenon is called Bragg reflection. The wavelength of the light that can emit from the un-grated waveguide is called Bragg wavelength. All light with wavelength other than Bragg wavelength will couple to the grating waveguide, and emits from the grating waveguide. The phase matching condition is given by

$$\lambda_B = 2n_{eff}\Lambda, \quad (1)$$

where λ_B is the Bragg wavelength, Λ the period of the refractive index grating, and n_{eff} the effective index of the waveguide. Since n_{eff} is dependent on the wavelength of input light, we know from eq.(1) Λ is not directly proportional to the Bragg wavelength. We will derive this condition later. Assume that the un-grated waveguide is denoted as waveguide 1, the grating waveguide is waveguide 2, the propagation direction is in +z-axis, the amplitude of light propagates in +z direction in waveguide 1, 2 is b_1, b_2 respectively, and the amplitude of light propagates in -z direction in waveguide 1, 2 is c_1, c_2 respectively. From couple-wave theory, the grating-frustrated directional coupler can be analyzed by the following differential equations.

$$\frac{db_1}{dz} = -j\beta_1 b_1 - jk_{12} b_2 + jk_{12}' c_2, \quad (2)$$

$$\frac{db_2}{dz} = -j\beta_2 b_2 - jk_{21} b_1 + jk_{21}' c_1 + jk_{22}' c_2, \quad (3)$$

$$\frac{dc_1}{dz} = j\beta_1 c_1 + jk_{12} c_2 - jk_{12}' b_2, \quad (4)$$

$$\frac{dc_2}{dz} = j\beta_2 c_2 + jk_{21} c_1 - jk_{21}' b_1 - jk_{22}' b_2, \quad (5)$$

where β_1, β_2 , are the propagation constants in waveguide 1,2 respectively, $k_{12}, k_{21}, k_{21}', k_{22}'$ are the coupling coefficients of forward propagation of waveguide 1 to forward propagation of waveguide 2, forward propagation of waveguide 2 to forward propagation of waveguide 1, backward propagation of waveguide 2 to forward propagation of waveguide 1, and forward propagation and backward propagation of waveguide. Due to the index grating, these coupling coefficients are periodic functions of z, too. Assume that the coupling length is L_C , then the boundary conditions to solve equations. (2), (3), (4), (5) are as follows.

$$b_1(0) = 1, b_2(0) = 0, c_1(L_C) = 0, c_2(L_C) = 0, \quad (6)$$

These boundary conditions are obtained by assuming the light is initially coupled to waveguide 1 and no reflection light or no backward propagation light at the output end that is away from the input end by L_C . This set of differential equations can be solved analytically^{2,3}. In this paper, we will solve this set of differential equations numerically. To solve the equations, we assume b_1, b_2, c_1, c_2 can be obtained from slow varying functions of z. Then they can be rewritten in the following forms.

$$b_1 = B_1 \exp(-j\beta_1 z), \quad (7)$$

$$b_2 = B_2 \exp(-j\beta_2 z) , \quad (8)$$

$$c_1 = C_1 \exp(j\beta_1 z) , \quad (9)$$

$$c_2 = C_2 \exp(j\beta_2 z) , \quad (10)$$

Substitute equations. (7), (8), (9), (10) into equations. (2), (3), (4), (5), we obtain another set of differential equations.

$$\frac{dB_1}{dz} = -jk_{12}B_2 \exp(j(\beta_1 - \beta_2)z) + jk'_{12}C_2 \exp(j(\beta_1 + \beta_2)z) , \quad (11)$$

$$\frac{dB_2}{dz} = -jk_{21}B_1 \exp(j(\beta_2 - \beta_1)z) + jk'_{21}C_1 \exp(j(\beta_1 + \beta_2)z) + jk'_{22}C_2 \exp(2j\beta_2 z) , \quad (12)$$

$$\frac{dC_1}{dz} = jk_{12}C_2 \exp(j(\beta_2 - \beta_1)z) - jk'_{12}B_2 \exp(-j(\beta_1 + \beta_2)z) , \quad (13)$$

$$\frac{dC_2}{dz} = jk_{21}C_1 \exp(j(\beta_1 - \beta_2)z) - jk'_{21}B_1 \exp(-j(\beta_1 + \beta_2)z) - jk'_{22}B_2 \exp(-2j\beta_2 z) , \quad (14)$$

If the grating waveguide are so designed that its width and average refractive index are equal to those of the un-grated waveguide, then we will obtain the following equations.

$$\beta_1 = \beta_2 = \beta , \quad (15)$$

$$k_{12} = k_{21} = k'_{12} = k'_{21} = k , \quad (16)$$

Since the refractive index grating is periodic, it can be represented by its Fourier cosine series. If higher order of variation (i.e., variation with period of 2Λ , 3Λ , ...) are ignored, then k can be expressed as the following equation.

$$k = k_0 + k_c \cos(2\pi z / \Lambda) , \quad (17)$$

where k_0 is the coupling coefficient of directional coupler without grating, and k_c is coupling coefficient of grating directional coupler. k_c can be approximated by the following equation¹.

$$k_c = \frac{\pi \delta n}{\lambda_0} , \quad (18)$$

where δn is the maximum index variation, and λ_0 is the wavelength in vacuum. By using Euler's formula, we can rewrite equation (17) as following equation.

$$k = k_0 + \frac{1}{2} k_c (\exp(2\pi z / \Lambda) + \exp(-2\pi z / \Lambda)) , \quad (19)$$

Substitute equations (15), (16), and (19) into equations (11), (12), (13), (14), and if we focus on the index variation term of equation (19), i.e. neglect k_0 in equation (19) (this is because the effect of k_0 can be calculated separately, and the result is nothing but as that of un-grating directional coupler), then we arrive at the following equations.

$$\frac{dB_1}{dz} = -jk_c B_2 \cos\left(\frac{2\pi z}{\Lambda}\right) + \frac{j}{2} k_c C_2 (\exp(j(2\beta - \frac{2\pi}{\Lambda})z) + \exp(j(2\beta + \frac{2\pi}{\Lambda})z)) , \quad (20)$$

$$\frac{dB_2}{dz} = -jk_c B_1 \cos\left(\frac{2\pi z}{\Lambda}\right) + \frac{j}{2} k_c (C_1 + C_2) (\exp(j(2\beta - \frac{2\pi}{\Lambda})z) + \exp(j(2\beta + \frac{2\pi}{\Lambda})z)) , \quad (21)$$

$$\frac{dC_1}{dz} = jk_c C_2 \cos\left(\frac{2\pi z}{\Lambda}\right) - \frac{j}{2} k_c B_2 (\exp(-j(2\beta - \frac{2\pi}{\Lambda})z) + \exp(-j(2\beta + \frac{2\pi}{\Lambda})z)) , \quad (22)$$

$$\frac{dC_2}{dz} = jk_c C_1 \cos\left(\frac{2\pi z}{\Lambda}\right) - \frac{j}{2} k_c (B_1 + B_2) (\exp(j(2\beta - \frac{2\pi}{\Lambda})z) + \exp(j(2\beta + \frac{2\pi}{\Lambda})z)) , \quad (23)$$

The phase matching condition is met when

$$2\beta - \frac{2\pi}{\Lambda} = 0 , \quad (24)$$

where

$$\beta = 2\pi m_{eff} / \lambda, \quad (25)$$

When the β in equation (24) is substituted by equation (25), the phase matching condition of equation (1) is obtained. Finite difference method is employed to solve equations (20), (21), (22), (23). According to these equations, we calculate the relationships between transmission/reflection and kL_C are shown in figure 3, and also the transmission and reflection of waveguide 1, 2 as a function of input wavelength is shown in figure 4. The results will be discussed in section 4.

3. PROPOSED STRUCTURE AND PROCESS

As mentioned before, the proposed structure is composed of two grating-frustrated directional couplers, and shown in figure 1. Each of the directional couplers is capable of selecting one specific wavelength. Therefore, at least two wavelengths of input light can be resolved by the proposed device. Because the phase matching condition of the grating-frustrated directional coupler requires the half period of the grating maybe as small as $0.2\mu\text{m}$, it is hard to fabricate the grating-frustrated directional coupler using integrated-optics process. The advent of sub-micron technology of integrated circuit makes fabrication of grating-frustrated directional coupler using integrated-optics waveguides feasible. The process of fabricating the proposed device is illustrated in figure 5. Here, the proposed device is fabricated on glass substrate. The waveguides are made by etching the glass using BOE (buffered oxide etchant), and dip-coated with polymer. The polymer can be prepared by sol-gel method⁶. This structure of waveguide is called inverted-ridge waveguide. The process of making waveguide is shown in figure 5 (a) to (e). Since the refractive index of polymer will be increased when the polymer is exposed under UV light⁶. The amount of index change is dependent on the intensity and the exposure time of UV. In general, the higher the UV intensity is or the longer the polymer is exposed, the larger the index becomes. To make the average index of the grating waveguide equals to that of un-grating, two steps of exposing the polymer waveguide are required. The grating waveguide is exposed using a grating mask, and the un-grating waveguide is also exposed in this step. Next, The grating waveguide is still exposed in this step, but the un-grating waveguide is not exposed in this step. If the exposure time of the two steps is the same, then the average index of the grating waveguide will equal to that of the un-grating waveguide. This process is shown in figure 5 (f), (g). Therefore, we can fabricate the proposed device through the process shown in figure 5.

4. CONCLUSIONS

The results of theoretical calculation of the proposed device are shown in figure 3, 4. Figure 3 shows the proposed device has good transmission efficiency(T_1) of selected input light, and good transmission extinction(T_2) of selected light to the grating waveguide. When the Bragg wavelength = $1.55\mu\text{m}$, the separation of the directional coupler is $1\mu\text{m}$, the width of the waveguide is $3\mu\text{m}$, the substrate refractive index = 1.45, the refractive index of the un-grating waveguide = 1.46, the maximum variation of the refractive index of the grating waveguide is 0.001, and $kL_C = 6$, we will find $T_1 \sim 0.8$ and $T_2 \sim 0.06$. Besides, the bandwidth of the device is about 5nm(as shown in figure 4). These features are very important and demanded for WDM device. The proposed device will satisfy the wanted features.

ACKNOWLEDGEMENT

The author^a would like to thank the national science council of Taiwan for financial support for this work under the contract no. NSC-89-2215-E-150-001.

REFERENCE

1. J.-L. Archambault, P. St. J. Russell, S. Barcelos, P. Hua, and L. Reekie, "Grating-frustrated coupler: a novel channel-dropping filter in single-mode optical fiber," *Optics Letters*, **19**, pp. 180-182, 1994.
2. R. R. A. Syms, "Optical directional coupler with a grating overlay," *Applied Optics*, **24**, No. 5, pp. 717-726, 1985.
3. B.-H. V. Borges and P. R. Herczfeld, "Coupled-Mode analysis of highly asymmetric directional couplers with periodic perturbation," *IEEE Trans. On Microwave Theory and Techniques*, **46**, No. 3, pp. 215-225, 1998.
4. M. A. Scobey and D. E. Spock, "Passive DWDM components using MicroPlasma optical interference filters," *OFC'96*, ThK1, San Jose, CA, Feb 1996.
5. D. Marcuse, *Theory of Dielectric Optical Waveguides*, Chapter 7, Academic Press, Inc., San Diego, 1991.
6. S. Iran Najafi, T. Touam, R. Sara, M. P. Andrews, and M. A. Fardad, "Sol-Gel glass waveguide and grating on silicon," *J. Lightwave Technology*, **16**, no. 9, pp. 1640-1646, 1998.

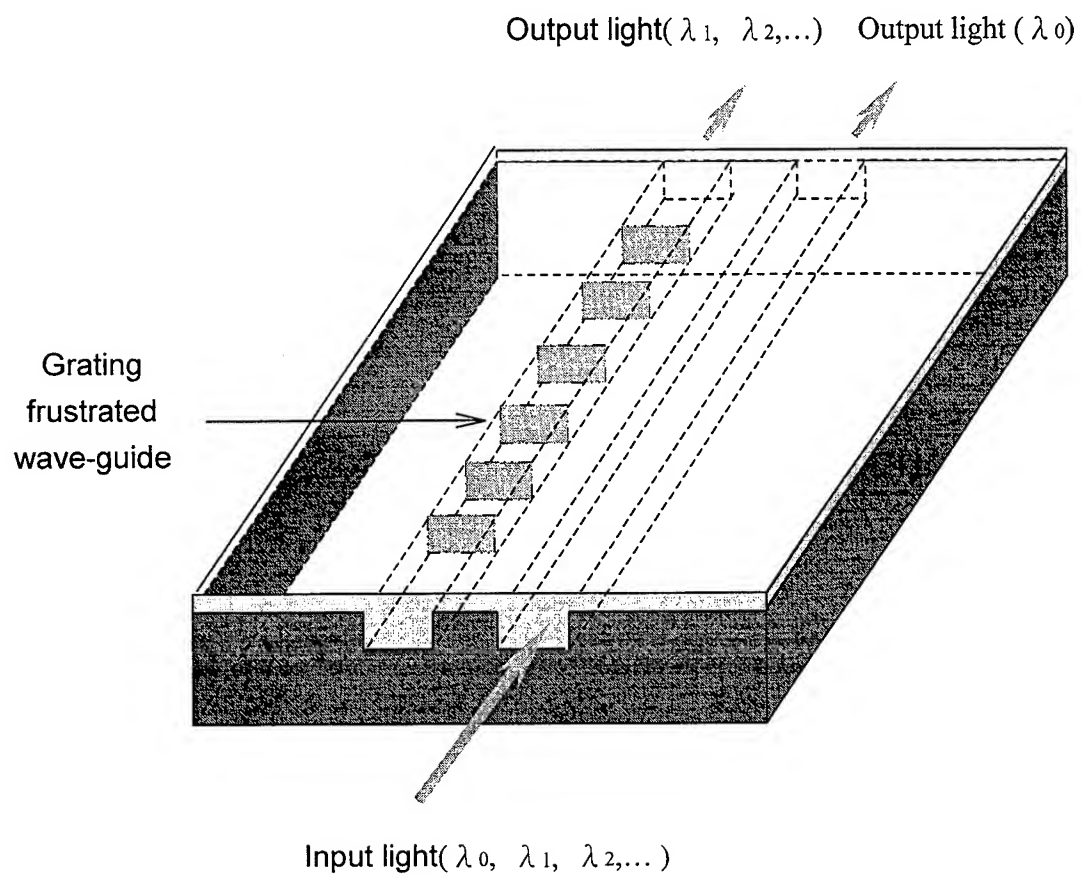


Figure 1. Schematic diagram of grating frustrated WDM using polymer wave-guide with inverted-ridge structure

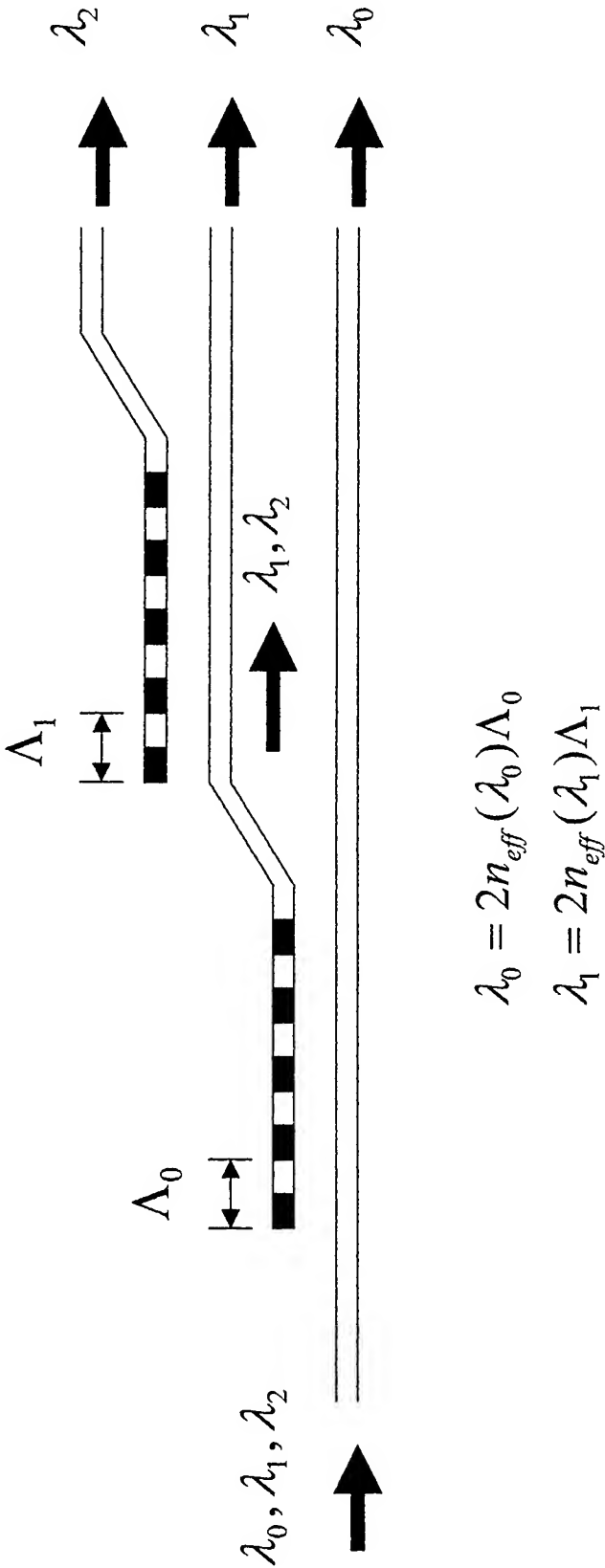


Figure 2. The proposed device and the conceptual scheme of operation principle

Figure 3. Dependence of transmission and reflection of the grating-frustrated directional coupler on kLc

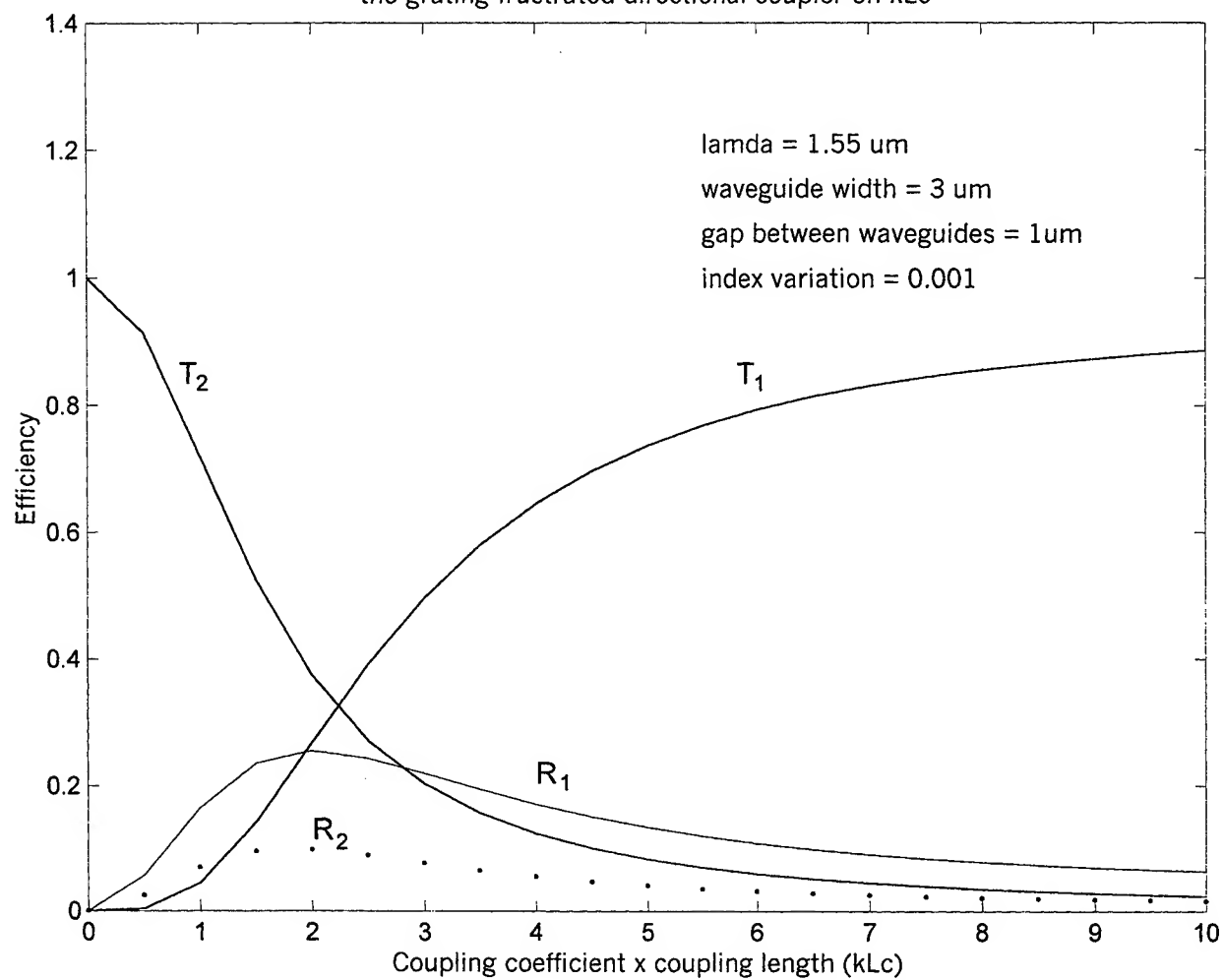
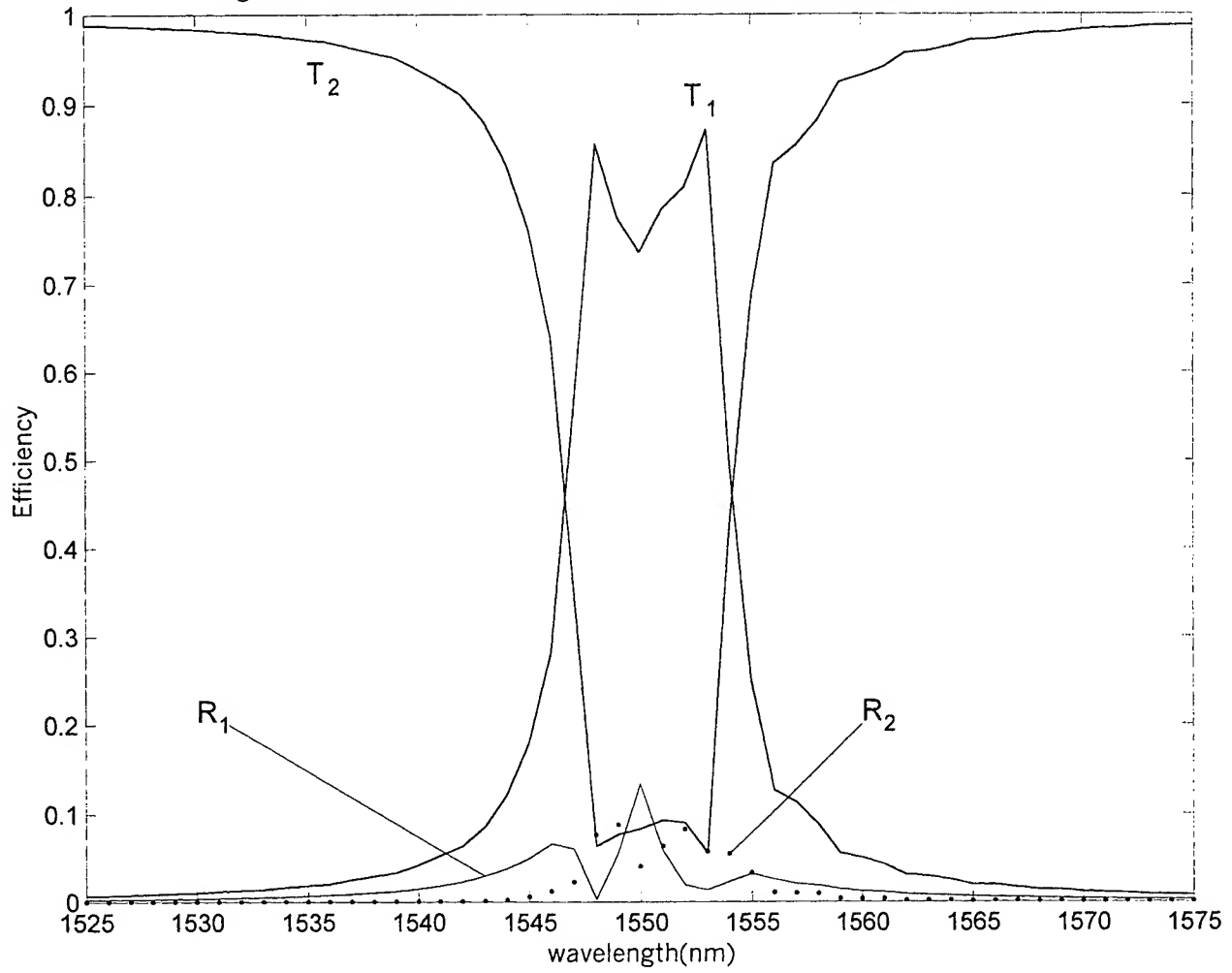


Figure 4. Calculated transmission and reflection spectra for $L_c=532\text{ }\mu\text{m}$



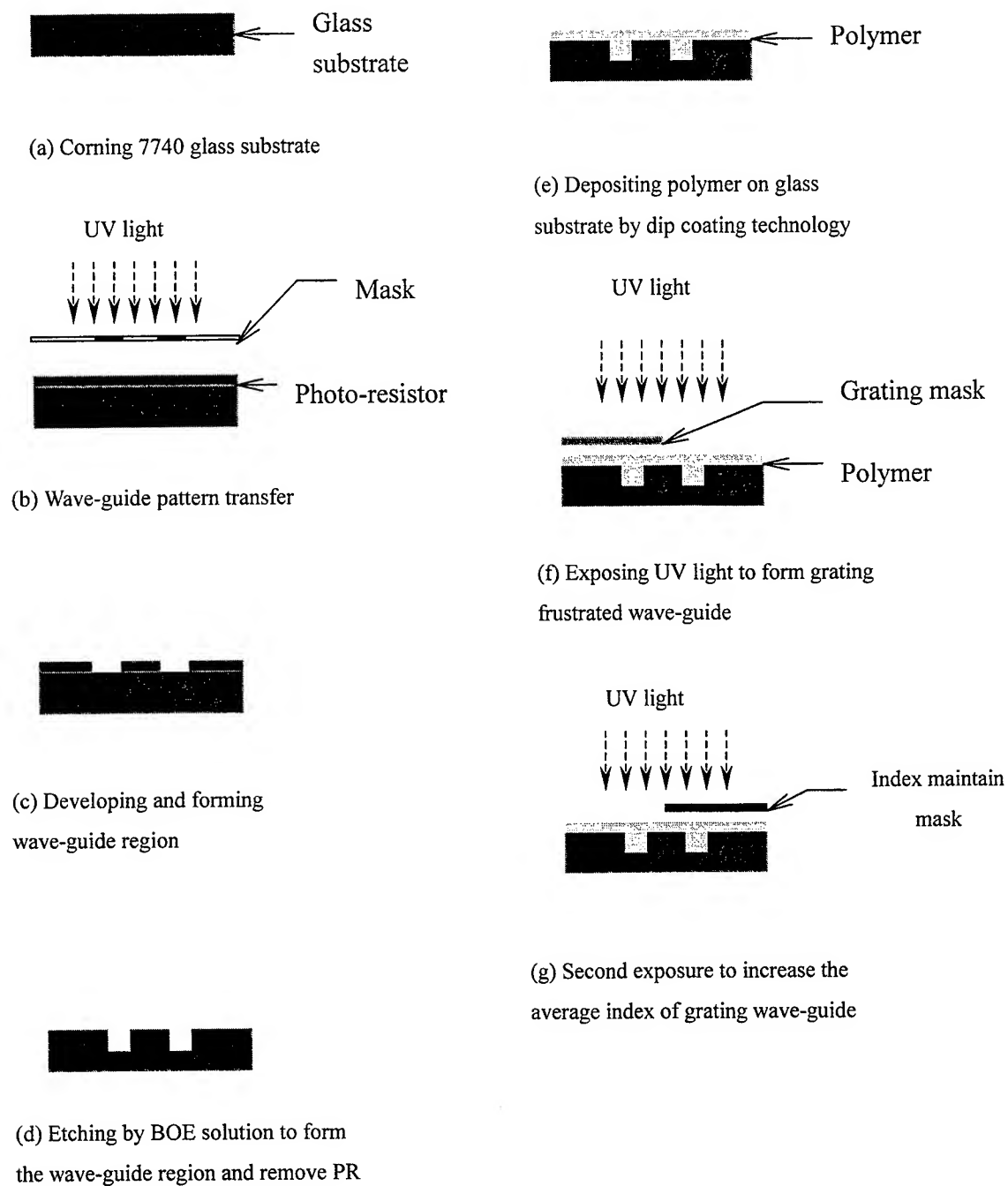


Figure 5. Fabrication process of grating-frustrated wavelength division multiplexer using polymer wave-guide with inverted ridge structure

Investigation of The Polymer Waveguide Polarizers Fabricated by Electric Poling

Shug-June Hwang¹ and Hsin Her Yu²

¹ Department of Electro-Optics Engineering, National Huwei-Institute of Technology.

² Department of Mechanical Materials Engineering, National Huwei-Institute of Technology.

ABSTRACT

A thin film waveguide of novel polymer Nylon 11 was fabricated and characterized. The active polymer waveguide film was formed by spin coating and poled by applying an electric field. The J-E and D-E curves with hysteresis characteristics of the Nylon11 film was measured during poling, as well as the absorption spectrum of this waveguide film was observed by the FTIR before and after completing the poling. In addition, we have investigated the influence of the waveguide position and electrode structure on the optic axis distribution in the poled polymer film. The numerical results are given to establish a useful guideline for designing the poled polymer waveguide devices.

KEYWORDS: Polymer waveguide polarizer, Electric poling, Birefringence, Optic axis, Spectroscopy, Dipole reorientation

1. INTRODUCTION

Recently, the investigation of optical polymers for integrated optic devices has been increasingly important in optical signal processing and optical communication systems[1-3]. Many polymer waveguide devices have been widely investigated due to their high electrooptic effects induced by electric field-poling process in the EO polymer films[4-6]. And these polymer materials allow waveguide devices to be made in layered structures and on a variety of substrates by simple manufacturing process. So the polymers for use in integrated electro-optical devices such as intensity modulator, directional or polarizer, have draw increasing attention[13-15]. In 1977, Litt *et al.* [7] pointed out that the structures of odd polyamides are also polar and the dipole direction can be switched, these polyamides would meet the requirement to be ferroelectric. Nylon 11 (Polyamide 11 or PA-11) was the first odd nylon to be examined because it was the only one commercially available. Nylon 11 is a representative choice for this new series since the unit cell can be prepared in a polar form, and uniaxial orientation followed by bulk electric field treatments align the unit cells in the field direction. Reorientation of the

Shug-June Hwang: Department of Electro-Optics Engineering, National Huwei-Institute of Technology, 64 Wunhua Road, Huwei, Yulin, Taiwan.

R.O.C.Tel:88656329643 ext571 and Fax:(05)6328863 E-mial:june@sunws.nhit.edu.tw. (paper numer 4078-121)

units cells in nylon 11 in response to electric fields has been proven by X-ray diffraction [8] with ex-situ studies while dipole reorientation has been shown by infrared techniques [9-10]. In this paper, we propose a novel polymer material, i.e., nylon 11, which exhibits the required properties in the optical communication applications, such as low attenuation and high E-O effect induced by the poling field, and furthermore we utilize this polymer material to fabricate the polarizers.

The properties of the slab Nylon 11 film waveguide are studied first. In this study, we present the absorption spectrum of the Nylon 11 film and demonstrate the electric field-induced dipole reorientation as well as the controllable birefringence in the Nylon 11 film. Based on the controllability of the poling-induced optic axis in EO polymer film, the various polarizers can be obtained by virtue of the special design of poling electrode pattern. To design the appropriate electrode structures and realize the required polarization components, the local poling field in the structure must be previously investigated. In our study, we use an efficient transform domain (DFT) method[16,17] to investigate the electric field distribution.

2. EXPERIMENT

2.1 Characterization of the polymer thin film

Previously, we already know that Nylon 11 is not only a piezoelectric functional polymer but also a ferroelectric functional polymer. In this study, we try to use nylon 11 as an Electro-optic (E-O) polymer. In order to obtain more information about the active polymer under the applied electric field, the J-E(Current density versus electric field) and D-E (electric displacement versus electric field) plots of the nylon 11 were measured by a hysteresis bridge [11] first. Figure 1 shows the J-E curve of the poling results. The strength of the coercive field (E_c), i.e., the electric field required to neutralized polarization, has a value between 70 and 80 MV/m. The E_c value can be read from the maximum band intensity versus electric field strength of the hysteresis loop in Fig. 1. This is consistent with the D-E curve measured in Figure 2, where E_c is found to be ca. 77 MV/m. the remanent polarization(P_r) and the coercive field (E_c) were determined from the Fig. 2 by the intercept of loop with the D- and E- axes, respectively, as $P_r = 75 \text{ mC/m}^2$ and $E_c = 77 \text{ MV/m}$.

Furthermore, FT-IR spectroscopy can be applied to characterize polymers in both a quantitative and qualitative way. The infrared spectrum is characteristic of the molecular vibrations. Quantized energy changes in the motion of the molecule are caused by absorption of infrared energy. The intensity of the absorption is a scalar product of the transition moment vectors and the cosine of the angle between the incident electric vector and transition moment vector. A Perkin-Elmer Fourier Transform Infrared spectrometer, model 2000, was employed. A Perkin-Elmer gold wire polarizer was used to collect the spectra. Since Nylon 11 film possesses a 3-D oriented nature, shown as Fig.3. , with hydrogen bonded sheet in the plane of the film, large C=O stretching mode is detected by using a polarized infrared light passing through the film, shown as Fig.4. Therefore, if the hydrogen bond breaks during poling and dipoles rotate toward the electric field direction, the absorption intensity of C=O stretching mode should decrease significantly after poling. A comparison of the spectra of before electric field poling films with that of poled samples demonstrated in Fig.5, shows that poling causes the C=O stretching peak intensity to decrease. When the direction of the transition moment of these modes with respect to the amide plane is considered, i.e., these changes establish that the average amide C=O peaks move towards the field direction (or electric field direction) of the film surface with poling treatments.

2.2 Waveguide Fabrication

The device structure of the polymer waveguide was fabricated in this study as shown in Fig.6(a). A thin film of Nylon 11 is formed by spin-coating onto a glass substrate, which is precoated with an approximation 250Å layer of indium tin oxide (ITO) that is a transparent conducting material. The polymer waveguide layer consists of a 4-μm-thick film of the active material and sandwiched between 2-μm-thick PTFE (Polytetrafluoroethylene) cladding layers above and below. After each spin-coating the polymer is cured sufficiently. Then a metal layer was evaporated on top. The active material was nylon 11, which was provided by the Rilsan Company (Glen Rock, NJ). However, the electrooptic polymer waveguide film is typically randomly orientation. So that the electric field poling is necessary procedure to obtain an electrooptic active polymeric thin film. In our laboratory, the polymer waveguide structure was poled by applying an electric field of 200 MV/m between the metal layers at room temperature.

3.THEORETICAL ANALYSIS

In this paper, the basic idea of the proposed Nylon11 waveguide polarizer is based on the controllability of the poling-induced optic axis and birefringence in EO polymer films[14]. It is well known that the optic axis is aligned parallel to the applied poling field and the magnitude of the poling-induced birefringence can be controlled by the magnitude of the poling electric field[12,13,15]. Hence the desired optic axis as well as the birefringence of the poled polymer waveguide can be obtained by virtue of the proper poling-electrode design. The schematic diagrams of the two basic polarizers are shown in Fig.6. To make a TM-pass polarizer, two vertically arranged electrodes may be used to pole the polymer waveguide. This poling arrangement makes the optic axis of the polymer waveguide be aligned in the vertical direction. So the TM mode can pass the guiding layer and the TE mode radiates. Another poling electrode configuration is the coplanar strip structure. The horizontal poling field makes the optic axis aligned horizontally in the active layer. Therefore the horizontally poled waveguide acts as a TE-pass polarizer. Owing to these properties of the electric field-induced dipole reorientation in Nylon 11 waveguide, the precise knowledge of the distribution of the poling-field created by electrodes in the waveguide structure must be investigated for the consideration of design.

In this paper, the electric field distribution of the horizontally poled polymer waveguide polarizer structure shown as in Fig.6(b) is performed. Two electrodes are deposited on the top of two-layer dielectric films. The upper layer is an isotropic buffer dielectric and lower is the anisotropic polymer Nylon 11 waveguide. The quasi-static approach is used to find the static electric field distribution \vec{E} in the structure which can be expressed as[16,17]

$$\vec{E}(x, y) = -\nabla \psi(x, y) \quad \text{-----} \quad (1)$$

Where ψ is the potential and satisfies the Laplace equation:

$$\nabla(\vec{E} \cdot \nabla \psi) = 0 \quad \text{-----} \quad (2)$$

Where ϵ is the dielectric constant of the dielectric in the structure and it can be represented as follows as

$$\begin{aligned} \frac{\partial^2 \psi_i}{\partial x^2} + \frac{\partial^2 \psi_i}{\partial y^2} &= 0 \quad \text{for } y \leq 0 \text{ and } y > d_1 \\ \epsilon_x \frac{\partial^2 \psi_2}{\partial x^2} + \epsilon_y \frac{\partial^2 \psi_2}{\partial y^2} &= 0 \quad \text{for } 0 < y \leq d_1 \end{aligned} \quad \text{----- (3)}$$

Where i is the label of subregion, $i=1,3,5$, shown in Fig.6. The potential Ψ is expanded in terms of the transform domain satisfying the Laplace equation(3)

$$\begin{aligned} \psi_1(x, y) &= \sum_k \varphi_1(k, y) e^{i \frac{2\pi k}{N} x} \cdot e^{-\frac{2\pi |k|}{N} (y-d_1)} \\ \psi_2(x, y) &= \sum_k \varphi_2(k, y) e^{i \frac{2\pi k}{N} x} = \sum_k \left[G_{1k} e^{-\frac{2\pi |k|}{N} \sqrt{\frac{\epsilon_x}{\epsilon_y}} y} + G_{2k} e^{\frac{2\pi |k|}{N} \sqrt{\frac{\epsilon_x}{\epsilon_y}} y} \right] e^{i \frac{2\pi k}{N} x} \\ \psi_3(x, y) &= \sum_k \varphi_3(k, y) e^{i \frac{2\pi k}{N} x} = \sum_k \left[A_{1k} e^{-\frac{2\pi |k|}{N} y} + A_{2k} e^{\frac{2\pi |k|}{N} y} \right] e^{i \frac{2\pi k}{N} x} \\ \psi_4(x, y) &= \sum_k \varphi_4(k, y) e^{i \frac{2\pi k}{N} x} \cdot e^{\frac{2\pi |k|}{N} y} \end{aligned} \quad \text{.....(4)}$$

The transform domain of potential can be solved by the boundary conditions: the continuity of the potential as well as the continuity of the displacement vector on the interface in the y direction. Once the transform domain potential is calculated by the numerical analysis, the local electric field can be obtained.

The local poling electric field components E_x and E_y for the symmetry and asymmetry coplanar electrodes are drawn in Fig.7 and Fig.8, respectively. In both cases, the left electrode width $W_1 = 10$ μm , electrode gap $G=5$ μm , electrode potentials of 10 and 0 V, and the buffer layer thickness d_2 is 0.5 μm . Fig.7 shows E_x and E_y field at different depths $y=0.8, 1.3, 1.8$ and 2.3 μm , respectively. It is obviously that the electric field distribution in the y direction is very small outside the electrode surface, and E_x is nearly null at the electrode surface. It is also seen that the electric field distribution between the two electrodes at the shallower depths is not significantly uniform and has stronger peaks at the edge of the electrodes for E_x and E_y components, respectively. Fig. 8 shows the effect of the different width of the two electrodes on the electric field distribution at depth $y=1.0$ μm . When the right-side electrode increases from $w_2/\text{gap} = 1$ to $w_2/\text{gap} = 5$, the electric field at

the edge of the right electrode becomes much weaker. Meanwhile, this increasing in the right electrode width enhances the electric field peaks near the left electrode side for E_x and E_y , respectively. And the E_y field between the two electrodes evidently increases as the width of the right electrode increases. So the field distribution in the guiding layer are no longer uniform. This non-homogenous poling field distribution would make the dipole reorientation of the polymer film be not uniform. Therefore, the optimized electrode configuration to obtain the uniform optic axis of the poling-induced polymer waveguide must be designed before manufacturing the poled polymer waveguide devices.

4. CONCLUSION

The Nylon 11 shows a significant birefringent activity if proper poling procedures and exhibits ferroelectric hysteresis behaviour. We made use of this novel material to manufacture the electro-optic devices. A novel polymer polarizer fabricated in electro-optic polymer Nylon11 was proposed and characterized. In addition, based on the numerical results, the poling electric field of the optical waveguide is presented as function of electrodes width and spacing. It is shown that the filed distribution of the guiding layer is not uniform especially for the asymmetry electrode structure. This property makes the birefringence of the polymer waveguide induced by the poling field become more non-uniform. We could establish a useful guideline for designing the specific waveguide polarizer by virtue of the numerical analysis.

ACKNOWLEDGMENTS

The authors gratefully thank Dr. Gen-Shin Lin for the assistance and the helpful suggestion for the numerical analysis.

5. REFERENCE

1. Emmanuel Van Tomme, Peter P. Van Daele , Roel G. Bates and Paul E. Lagasse, "Integrated Optic Devices Based on Nonlinear Optical Polymers", IEEE Journal of Quantum Electronics, vol.27(3), pp.778, 1991.
2. C.C.Teng, M.A.Mortazavi, and G.K.Boudoughian, "Origin of the Poling-Induced Optical Loss in a Nonlinear Optical Polymeric Waveguide", pp.667, 1995.
3. P.Kaczmariski, J.-P. Van de Capelle, P.E. Lagasse, R. Meynart, "Design of an Integrated Electro-Optic Switch in Organic Polymers", IEEE Proceedings, vol.136(3), pp.152, 1989. H.Kawai, Jpn. J. Appl. Phys., 8 (1969) 975 [1] H.Kawai, Jpn. J. Appl. Phys., 8 (1969) 975

4. H. Kawai, Jpn. Appl. Phys., 8 (1969) 975.
5. J.G. Bergman, J.H.McFee, and G. R. Crane, Appl. Phys. Lett. 18 (1971) 203
6. K. Nakamura, and Y. Wada, J. polym. Sci. A-29 (1971) 161
7. M.H. Litt, C.H.Hsu, and P. Basu, J. Appl. Phys.,48 (1977) 2208
8. J.W. Lee, J.I. Scheinbeim, B.A. Newman, Macromolecules, 25 (1992) 3729
9. H.H. Yu, L.J. Fina, Macromolecules 27 (1994) 6192;
10. H.H. Yu, L.J. Fina, J. Polym. Sci.: Polym. Phys. 34 , pp.78 ,1996
11. T. Mitsui, I. Tatsuzaki, E. Nakamura (1976) *Ferroelectricity and related phenomena*, (Gorden and Breach)
12. 12.Min-Cheol Oh, Sang-Yung Shin, Wol-Yon Hwang and Jang-Joo Kim, "Polin-Induced Waveguide Polarizers in Electrooptic Polymers", IEEE Phontonic Technology Lett., vol.8 (3), pp.375-377, 1996.
13. .9.J.W.Wu,"Birefringent and Electro-Optic Effects in Poled Polymer Films: Steady-State and Transient Properties",IEEE J.Opt.Soc.Am.B,vol.8(1),1991.
14. 10.Min-Cheol Oh and Sang-Yung Shin,Wol-Yon Hwang and Jang-Joo Kim,"Wavelength Insensitive Passive Polarization Converter Fabricated by Poled Polymer Waveguides",pp.1821,1995.
15. 11.S.Herminghaus,Barton A.Smith,and J.D.Swalen,"Electro-Optic Coefficients in Electric-Field-Poled Polymer Waveguides",IEEE Herminghaus,vol,8(11),pp.2311,1991.
16. 12.Jin-Shin Lin,The-Nan Chang ,Wei-Yu Lee,"Analysis of Asymmetric Coplanar Strip Electrodes with a Buffer Layer in Integrated-Optics Electrooptics Devices",IEEE J.Opt,pp.48,1995.
17. 13.O.G.Ramer,"Integrated Optic Electrooptic Modulator Electrode Analysis",IEEE Journal of Quantum Electronics,vol.QE-18(3),1982.

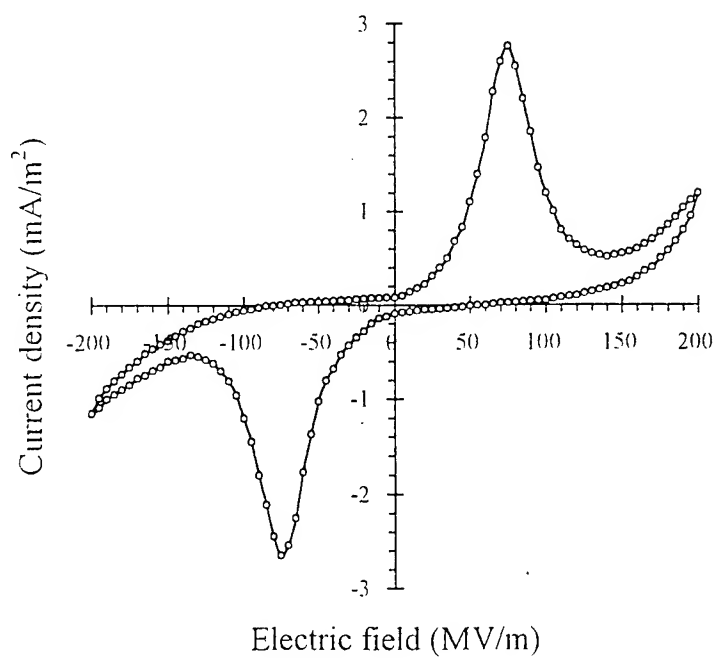


Fig. 1 Current density (J) versus electric field (E) for a poled nylon 11 film.

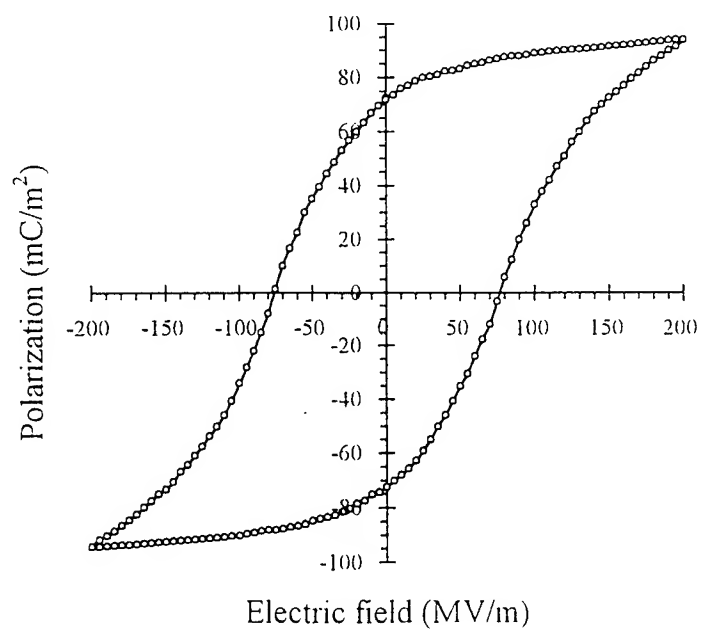


Fig. 2 Electric displacement (D) versus electric field (E) for a poled nylon 11 film.

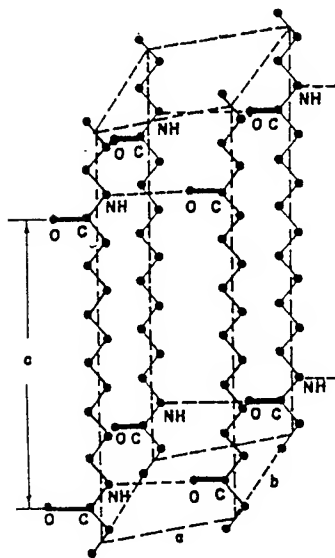


Fig.3 Nylon 11 structure

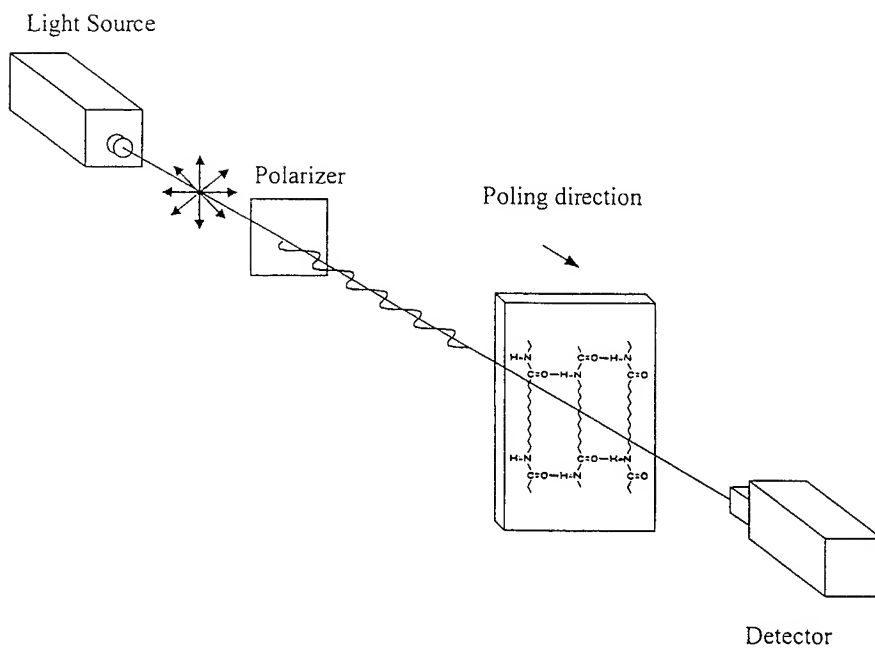


Fig. 4 FTIR set-up for measuring the dipole rotation phenomenon

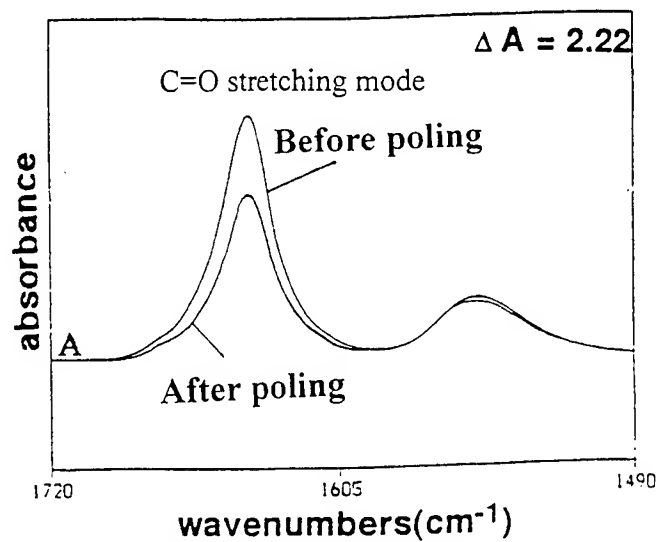


Fig. 5 Spectra change of the C=O stretching mode peaks following the application of a electric field.

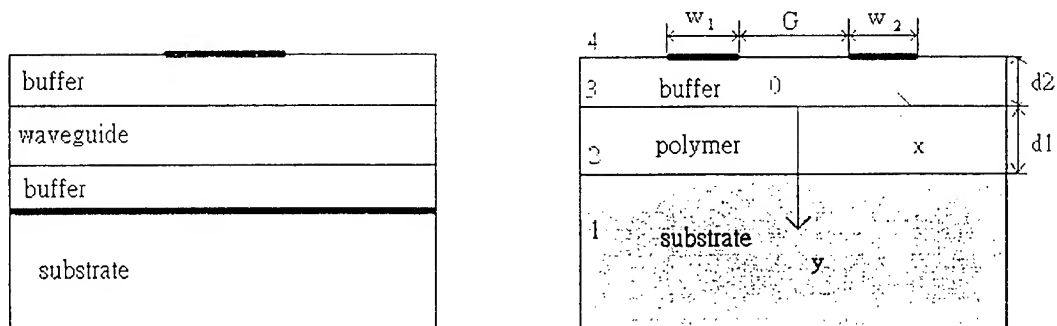


Fig. 6 The schematic diagram of the polymer waveguide polarizer.

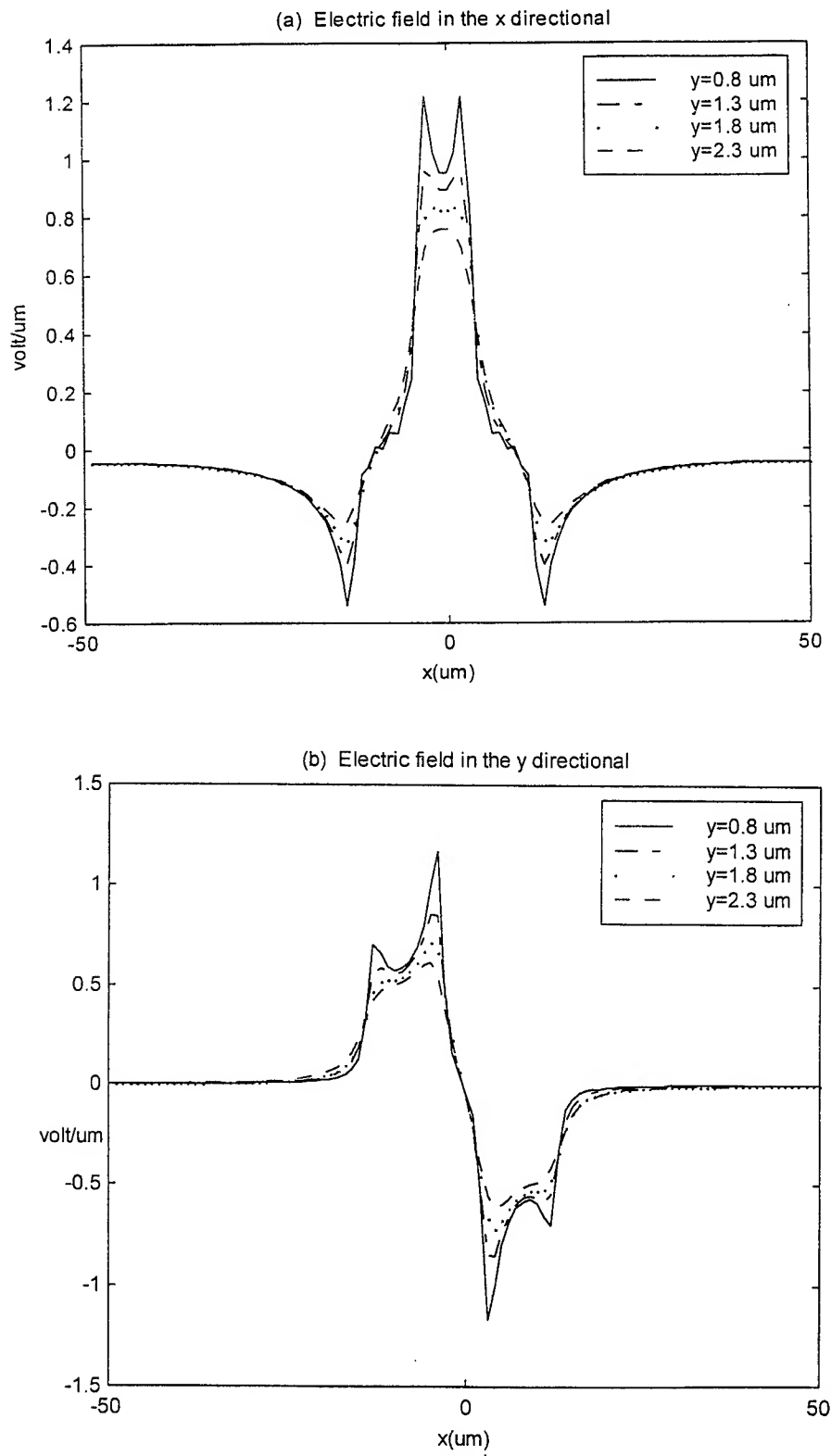


Fig. 7 The electric field distribution in the polymer waveguide layer along x-axis.

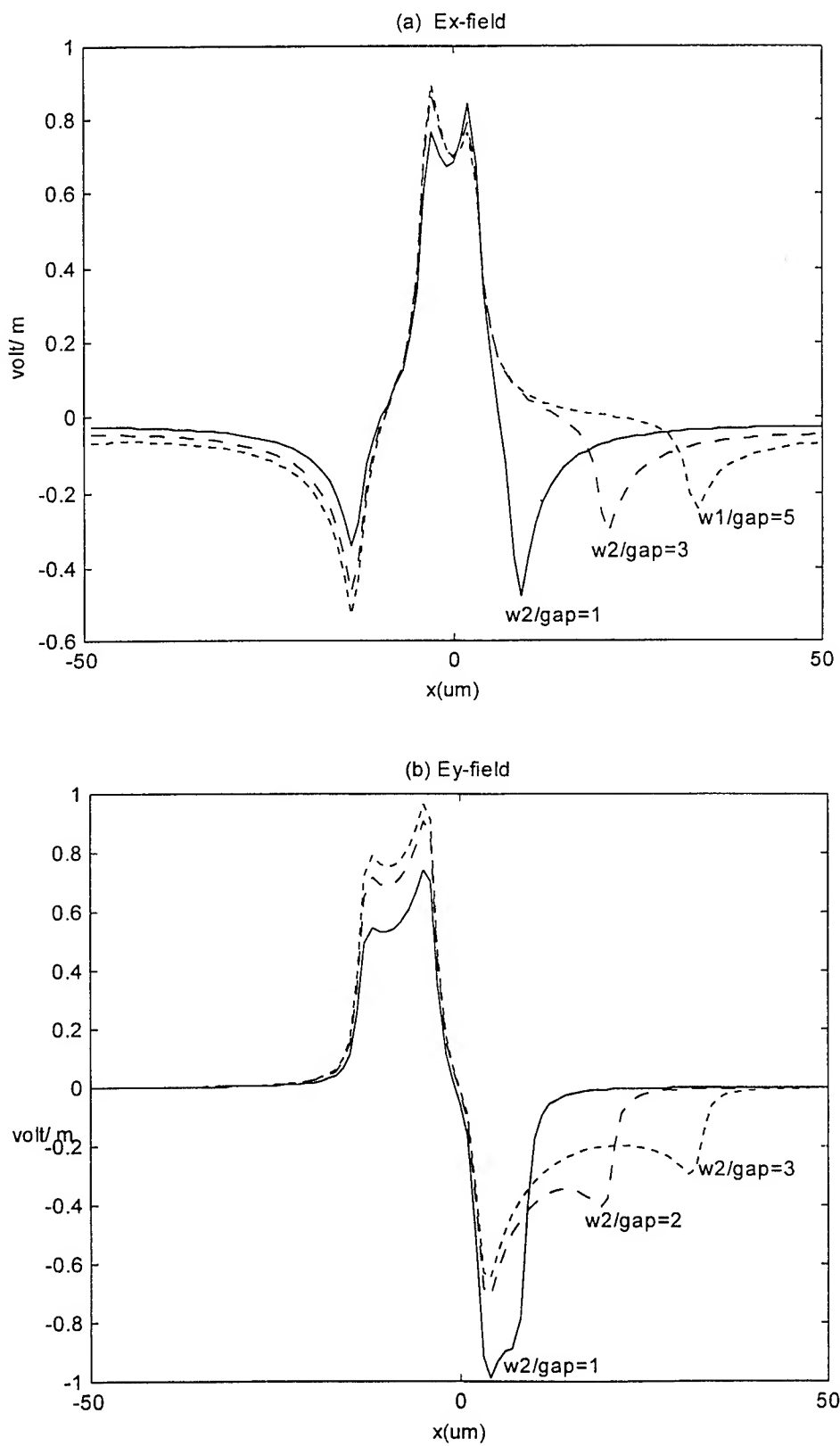


Fig. 8 The effect of the asymmetry electrode configuration on the filed distribution at the depth $y = 1 \text{ } \mu\text{m}$

Percolation and Ripening in $\text{Si}_{1-x}\text{Ge}_x/\text{Si}(001)$ Islands: Effect of Misfit Strain

R. Arief Budiman[†], Harry E. Ruda[†], D. D. Perović[§] and B. Bahierathan[§]

[†]Energenius Centre for Advanced Nanotechnology

[§]Department of Metallurgy and Materials Science

University of Toronto, Toronto, Ontario M5S 3E3, Canada

ABSTRACT

We study the island size distributions of $\text{Si}_{1-x}\text{Ge}_x/\text{Si}(001)$ ($x = 0.4 - 0.7$) islands of varying Ge fractions and thicknesses by ultrahigh vacuum chemical vapor deposition. The island size distributions of the percolating islands obey a dynamic scaling hypothesis admitting only one length scale governing the growth, in the limit of large island sizes. Although bimodal distributions are found in coherent islands at large misfit strain, due to the large stress concentration at island perimeters; faulted dislocation loops forming as islands grow remove this stress concentration. This re-establishes a unimodal distribution, reclaiming the scaling hypothesis. We show that the misfit strain is renormalized and, thus, is not essential in determining the size distribution. We also demonstrate evidence for Smoluchowski ripening mechanism occurring during growth. Finally, we discuss implications of these issues on achieving a uniform $\text{Si}_{1-x}\text{Ge}_x/\text{Si}(001)$ island distribution, which is crucial for technological applications.

Keywords: Smoluchowski Ripening, Size Distribution, Percolation, Quantum Dot, Silicon Germanium

1. INTRODUCTION

Growth and morphology of self-assembled epitaxially-grown islands have attracted considerable interest since these nanometer-scale islands can be dislocation-free.¹ Molecule-like optical properties due to strong electron confinement effects in these coherent islands have been exploited to fabricate a quantum dot laser.² However, optical emission from the islands suffers from inhomogeneous broadening due to the broad island size distribution. Efforts to control and enhance island size uniformity have been made, including alternative growth strategies, such as using vicinal substrates³ and selected-area epitaxy.⁴

Quantum dots are grown heteroepitaxially with relatively small misfit strain, originating in the lattice constant mismatch between substrate and film. Growth proceeds by establishing a macroscopically flat wetting layer of a few monolayers (ML) thick before the dots form. The thickness of the wetting layer is usually referred to as the (2D-3D) critical layer thickness h_c , which is significantly less than the critical thickness for dislocation formation in a lattice-mismatched system.⁵ Such a growth mode is called Stranski-Krastanov (SK) growth, representing an intermediate case between layer-by-layer (Frank-van der Merwe growth) in homoepitaxial or small lattice-mismatched systems, and direct islanding mode (Volmer-Weber growth) in highly lattice-mismatched systems.

To systematically study the island size distribution of these dots, a two-dimensional (2D) island size distribution function for submonolayer epitaxial growth has been proposed.⁶ It hinges on the assumption that the time variable t is represented by one length scale $L(t)$ that grows with time. This is the essence of dynamic scaling hypothesis. The size distributions at different growth times can then be rescaled as a function of this length scale. In other words, these distributions can be collapsed into one scaling function f_1 by rescaling them with a time-dependent $L(t)$. Under this assumption, the island size distribution for the submonolayer islands has the following form⁶:

$$N_s(\theta) = \frac{\theta}{\langle s \rangle^2} f_1(s/\langle s \rangle), \quad (1)$$

where θ is the amount of coverage (thickness), s is the island size, and $\langle s \rangle$ is the average island size (volume):

$$\langle s \rangle(\theta) = \frac{\sum_s s N_s(\theta)}{\sum_s N_s(\theta)}, \quad (2)$$

Corresponding author is at budiman@ecf.utoronto.ca

where the summation index runs from $s = s_c + 1$ up to the largest island s_m . The length scale L is then simply related to the island size s by the dimensionality of the system: $s \sim L^d$. The time dependence of $\langle s \rangle$ is given by the relation $\theta = Ft$, where F is the constant average growth rate. A typical value for the critical island size is $s_c = 1$, which means that monomers ($s = 1$) are free to diffuse on surface, while all island sizes larger than unity are stable.⁶

The form of the distribution function in Eq. (1) is actually derived from Eq. (2), implying that the sum rules in Eq. (2) are more fundamental. In fact, the sum rules are statements of two conservation laws. The first rule,

$$\theta = \sum_s s N_s(\theta), \quad (3)$$

conserves the number of deposited particles impinging on the surface per unit time for a constant F , while the second,

$$\sum_s N_s = Ft, \quad (4)$$

states that, when properly normalized with respect to θ , the total probability of finding all island sizes s is exactly unity.

Implicit in Eq. (3) is a condition for the submonolayer growth: $\theta < 1$. For this reason, Eq. (1) is strictly valid for submonolayer islands. The distribution function is found to be applicable for submonolayer islands grown in homoepitaxial Fe⁷ and heteroepitaxial InAs/GaAs⁸ thin films. In relation to the SK growth, this situation corresponds to the first monolayer deposited on the substrate, before the wetting layer forms. When the wetting layer already forms, such as for SK growth of quantum dots, the coverage must exceed unity: $\theta > 1$. It is very interesting, therefore, to note that the pre-coalescence (pre-percolation) distribution function (Eq. (1)) was demonstrated to fit the data very well for the multilayer InAs/GaAs islands, where $\theta \geq 1$.⁹ One important conclusion drawn from these studies is that the elastic strain, which is present in the heteroepitaxial growth, is not an essential factor in determining the island size distribution function.⁹

We extend these studies further into the ripening regime of the SK growth by analyzing the island size distributions for Si_{1-x}Ge_x/Si(001) islands of varying Ge fractions and thickness. Although for optoelectronic applications we do not want to grow the dots too large, their growth termination hinges on whether sufficient size uniformity is achieved. Thus, one motivation for such studies is to understand the underlying mechanisms that govern the size distribution. This in turn will provide us with a strategy to predict and control the uniformity of Si_{1-x}Ge_x islands.

We adopt the formalism of percolation theory to understand how the scaling function may change as the coverage θ exceeds unity. In addition, the percolation theory has allowed us to obtain an analogy between θ and site probability in a site percolation problem.¹⁰ We discuss this analogy in Sec. 2, which is then followed by our measurement results from Si_{1-x}Ge_x/Si(001) islands in Sec. 3. We find that an initially bimodal distribution for coherent islands can transform into a unimodal distribution after dislocations form at the island perimeter. The morphology of the islands strongly suggests a Smoluchowski ripening mechanism, in which islands collide (coalesce) with one another without having smaller islands being depleted by larger islands. This latter phenomenon is an indication of the presence of Ostwald ripening. In Sec. 3 we also discuss our results, which are summarized in Sec. 4.

2. ISLAND SIZE AND PERCOLATION

The definition for island size is self-evident in the submonolayer case as described above. In the multilayer case, however, we already have a percolating 2D cluster that underlies the 3D islands (dots). This percolating wetting layer connects all 3D islands; hence, we have to define an appropriate measure for the island size by excluding the percolating wetting layer.

To subtract the wetting layer, we use a co-moving coordinate provided by a mapping $\theta \mapsto \theta + Ft$. Thus, the height of each individual island is measured with respect to a global average height $h_o(t)$, which can be easily obtained from typical scanning probe measurements, such as from an atomic force microscope. To simplify the statistical analysis, we represent the island height, which is locally varying within an island, by its average value over each island, h_i . This individual-island averaging eliminates any possible bias toward a dominant aspect ratio that may emerge globally in the image. Thus, the co-moving island size is defined by

$$s \equiv A(h_i - h_o), \quad (5)$$

where A is the island base area and is therefore measured at h_0 . Such a definition was also used by Ebiko *et al.*⁹ by introducing an effective value of coverage, which was then subtracted from that of the wetting layer. The presence of a wetting layer actually invalidates Eq. (3) as explained above. The co-moving description suggests that the wetting layer can be considered as an infinite-size cluster. Hence, when we exclude the wetting layer in our co-moving definition, we basically limit the summation in Eq. (3) to a finite, but large s . This is an important assumption in our analysis, as we show in Sec. 3 that the distribution function N_s obtained produces a divergence for Eq. (3) if we allow $s \rightarrow \infty$.

The island geometry in the multilayer case does not break down since it has a well-defined boundary. The percolating wetting layer simply shifts the average height to a larger value during the growth. Numerical simulations of site percolation yield a typical value of about 0.6 ML for the percolation threshold coverage.¹⁰ When monomer diffusion is nonzero, the percolation threshold becomes a function of the ratio between the hop rate h per atom and the deposition rate r per site.¹¹ The former is approximately equal to the (collective) diffusion length, while the latter is approximated by the growth rate F . For a range of $h/r = 10 - 10^6$, the percolation threshold changes from $\theta_c \approx 0.55$ to 0.72 .¹¹ Thus, monomer diffusion slightly changes the percolation threshold.

To exclude the wetting layer, we need to modify the conservation law in Eq. (3) into:

$$\theta = \theta_c + \theta_w + \sum_s s N_s(\theta), \quad (6)$$

where θ_w is the wetting layer coverage. We obtain the form of Eq. (6) by a direct analogy with the percolation theory¹⁰ that regards θ_c as the normalized probability of any site belonging to an infinite cluster. In our case, we have to add θ_w , which is equal to the difference between the wetting layer thickness, h_c , and the percolation threshold θ_c : $h_c = \theta_c + \theta_w$. Hence, the sum rule for our co-moving island size definition is simply given by

$$\sum_{s < \infty} s N_s(\theta - h_c) = \theta - (\theta_c + \theta_w) = \theta - h_c. \quad (7)$$

We can further draw analogy with the percolation theory by postulating that the island size distribution for the multilayer case obeys a random percolation universality¹⁰:

$$N_s(\theta - h_c) = s^{-\tau} f_2((\theta - h_c) s^\sigma), \quad (8)$$

where $2 < \tau < 3$ and $\sigma > 0$ are 'critical' exponents to be obtained from either numerical or experimental results. As far as we know, there is no general expression for $f_2(x)$. The analogy we use for our analysis is motivated by the slight change of the percolation threshold for diffusing systems compared to that for the site percolation. Another compelling reason is the fact that in many cases wetting layer thickness h_c does not increase during island ripening; surprisingly, some materials systems actually exhibit a partial, local depletion of wetting layer. The wetting layer thickness is somehow pinned at some macroscopically uniform value across the substrate, even during the ripening. Bartelt and Evans¹¹ originally proposed Eq. (8) for $\theta \approx \theta_c$. In our work, we would like to determine whether this assumption works as well for $\theta > \theta_c$.

Experimentally, to determine the distribution function we measure the frequency of occurrence for each island size s . Thus, we obtain an island size histogram, from which we get N_s as a function of s . To obtain the scaling function $f_2(x)$, we transform Eq. (8) into an experimental definition for $f_2(x)$:

$$f_2(x; \sigma) \equiv s^\tau N_s(x; \sigma). \quad (9)$$

The dynamic scaling hypothesis is ascertained when all measurements for different samples yield an identical $f_2(x)$ by adjusting the values of τ and σ . The critical thickness h_c depends on the misfit strain ε with the following relationship¹²

$$h_c \propto \varepsilon^{-4}. \quad (10)$$

Hence, we can also determine whether the misfit strain changes the form of the scaling function $f_2(x)$.

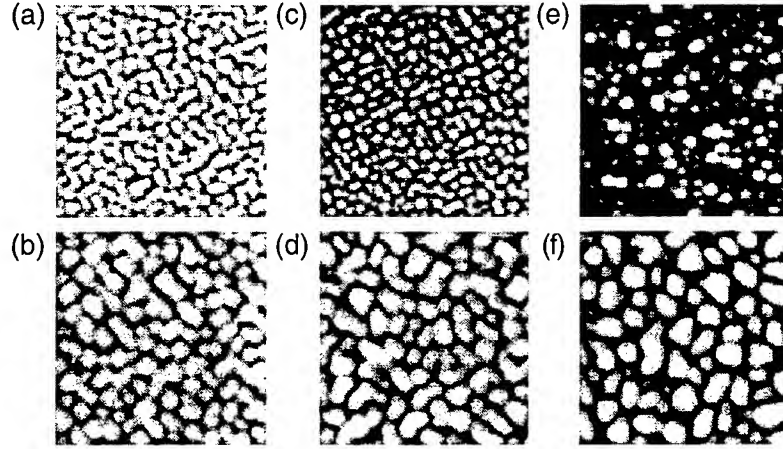


Figure 1. $1.25\mu\text{m} \times 1.25\mu\text{m}$ atomic force micrographs of $\text{Si}_{1-x}\text{Ge}_x/\text{Si}(001)$ samples with varying Ge fractions x and nominal thicknesses h_o . Sample group X: (a) X1: $x = 0.4, h_o = 5$ nm; (b) X2: $x = 0.4, h_o = 20$ nm. Sample group Y: (c) Y1: $x = 0.5, h_o = 5$ nm; (d) Y2: $x = 0.5, h_o = 20$ nm. Sample group Z: (e) Z1: $x = 0.7, h_o = 5$ nm; (f) Z2: $x = 0.7, h_o = 20$ nm.

3. RESULTS AND DISCUSSION

Six $\text{Si}_{1-x}\text{Ge}_x$ single layers were grown on a $\text{Si}(001)$ substrate by ultra-high vacuum chemical vapor deposition (UHV-CVD) at 525°C and with growth rate of 0.8 \AA/s as described in detail elsewhere.¹³ The samples have varying Ge fractions and thickness which are listed in the caption of Fig. 1. All samples were not post-annealed to preserve their surface morphologies and *ex situ* atomic force microscopy (AFM) Digital Instruments Nanoscope III was used to image the islands. Using a Si_3N_4 cantilever tip we obtained a few nanometer lateral resolution, which is due to the image convolution with the tip shape. It has been demonstrated that no significant island shape distortions result from such measurements in comparison with *in situ* measurements.¹⁴

Figure 1 shows images clipped from height-mode $5\mu\text{m} \times 5\mu\text{m}$ AFM images of our samples. At the lowest misfit strain ($x = 0.4$), flat square and rectangular islands co-exist and align themselves along elastically soft $[010]$ and $[100]$ directions [Fig. 1(a)]. (These directions are shown at an oblique angle—ranging from 30° to 45° —in Fig. 1.) This co-existence persists at 20 nm thickness [Fig. 1(b)] although they transform into hut-shaped islands with an average slope of 11.3° in agreement with $\{501\}$ -type facets.¹⁴ At increasing misfit strain ($x = 0.5$) the islands in Figs. 1(c)-(d) exhibit similar shape evolution although large domes appear at increasing thickness [Fig. 1(d)]. At the largest misfit strain ($x = 0.7$), however, we observe more isotropic (circular) flat islands of two different average sizes [Fig. 1(e)] which transform into large domes with increasing layer thickness [Fig. 1(f)]; we found no hut-shape islands at the highest misfit strain.

The time-dependent average height $h_o(t)$ was closely approximated by the median value of the height histogram so long as the histogram shows a unimodal distribution. For a bimodal distribution, which occurs in Fig. 1(e), we selected a minimum value between the two distribution peaks. This makes the “masking” procedure to define the island size consistent and visually unbiased since we can directly take the median value to be the global average height h_o . The island size histograms for all six images are shown in Fig. 2.

Floro *et al.*¹⁵ have shown that the sequence of shape evolution at low misfit strain ($x = 0.2$) is identical with that for pure Ge on $\text{Si}(001)$. The island shapes for $x = 0.4$ [Figs. 1(a)-(b)] and $x = 0.5$ [Figs. 1(c)-(d)] display such a trend. The average island size as defined by $\langle s \rangle(\theta) = \sum_s s N_s(\theta) / \sum_s N_s(\theta)$ [Eq. (2)] for these four samples increases monotonically for samples X1, Y1, X2, and Y2: $\langle s \rangle = 1.64 \times 10^6, 2.21 \times 10^6, 2.84 \times 10^6$, and $4.43 \times 10^6 \text{ nm}^3$, respectively. This strongly suggests that the snapshot sequence of Figs. 1(a)-(c)-(b)-(d) can represent the shape evolution for either $x = 0.4$ or $x = 0.5$. However, the islands at $x = 0.7$ do not evolve in the same way due to the bimodal histogram that occurs for sample Z1. The average island size for sample Z1 is $6.36 \times 10^5 \text{ nm}^3$, smaller than that of sample X1, while the average island size for sample Z2 is $15.65 \times 10^6 \text{ nm}^3$, far larger than that of sample Y2. This provides another indication that higher misfit strain accelerates the shape evolution in time, thus allowing for

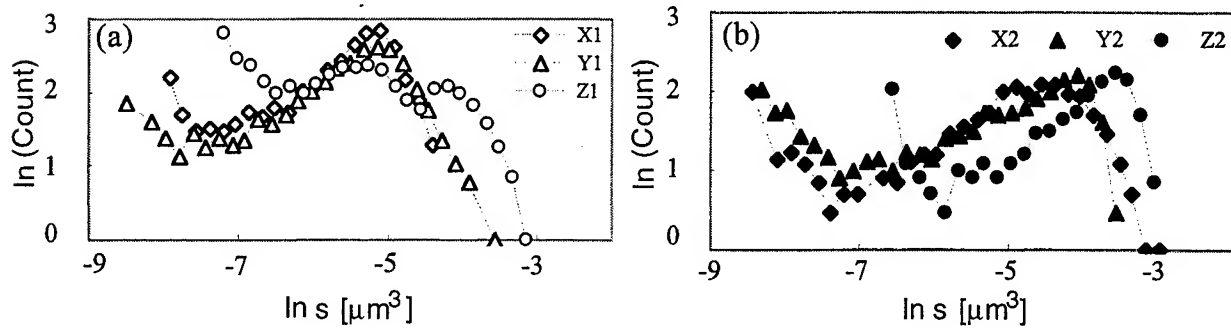


Figure 2. Island size histograms for sample groups X, Y and Z. (a) Thickness of 5 nm: X1, Y1 and Z1. (b) Thickness of 20 nm: X2, Y2 and Z2.

a faster evolution for a given constant time span. It is not yet clear as to how and why the bimodal histogram can arise from such a behavior. We suspect that the role of fluctuations may be increased with increasing misfit strain, thereby allowing some metastable state to appear.

Previously, Perović *et al.*¹² developed a continuum model that incorporates the activation energy for the sequential incorporation of adatoms at island step edges during nucleation. The model predicts kinetic (2D-3D) critical thickness ranging from $h_c = 4.0$ nm to 0.8 nm for coherent (dislocation-free) $\text{Si}_{1-x}\text{Ge}_x/\text{Si}(001)$ island formation from $x = 0.4$ to $x = 0.7$, respectively, at a growth rate of 0.8 Å/s at 525°C . Cross-sectional TEM investigation¹² confirmed these values and revealed that samples Y2 and Z2 developed faulted dislocation loops located below the island perimeters. Similar observations have been made in $\text{In}_x\text{Ga}_{1-x}\text{As}/\text{GaAs}$ islands.¹⁶

In light of the facts that for sample groups X and Y: (1) their respective critical thicknesses are 4.0 and 1.0 nm, respectively; (2) the average effective island length $L = \langle s \rangle^{1/d}$ ranges from 118.15 to 164.27 nm; and (3) their respective misfit strains are $\epsilon = 1.58\%$ and 1.98% , respectively, we conclude that their growth must have reached a ripening regime. This agrees as well with previous observations in $\text{Si}_{1-x}\text{Ge}_x/\text{Si}(001)$ system.^{15,17} This is also evident from the island geometries shown in Figs. 1(a)-(d). The critical thickness for sample group Z is 0.8 nm; thus we believe that at least sample Z2 has reached its ripening regime. Sample Z1, however, may not have entered a ripening regime as judged by its minimum average island size. In addition, sample Z1 produces a bimodal histogram as shown in Fig. 2(a). This may result from a significant stress concentration that develops along the perimeter of a larger island that prohibits earlier coalescence with smaller islands around it, thus creating a metastable island. This is visually indicated by depleted zones occupied by smaller islands around larger islands (see Fig. 1(e)). However, with increasing thickness in sample Z2 misfit dislocation injection will further relax the high stress concentration around the island perimeter and consequently remove the energy barrier associated with it. Islands can then coalesce (ripen) and a narrower unimodal histogram is produced for sample Z2 (see Fig. 2(b)).

To understand these results, we scale the histograms to determine the critical exponents τ and σ , which will help us determine the dominant mechanism during ripening. From percolation theory,¹⁰ we learn that

$$M_k = \sum_s s^k N_s \propto |\theta - h_c|^{(\tau-1-k)/\sigma}. \quad (11)$$

Eq. (11) can be used to obtain a dependence of the second moment of the distribution on the critical exponents:

$$\bar{s} = \frac{\sum_s s^2 N_s}{\sum_s s N_s} = \frac{M_2}{M_1} \propto |\theta - h_c|^{-1/\sigma}. \quad (12)$$

Thus, we can independently obtain σ from \bar{s} , allowing us to scale the histogram with just one parameter. We show the plot of \bar{s} v. $|\theta - h_c|^{-1}$ in Fig. 3(a), which gives $\sigma \approx 1.13$. To convert the histograms into the island size distribution functions, we normalize them so that $\sum_s N_s = 1$, where $s < \infty$. Using Eq. (8) to scale the distribution functions, we obtained $\tau \approx 3.0$, which is the allowable upper limit for the value of τ . The rescaled histograms are shown in Fig. 3(b), where we have used the layer thickness θ and the critical thickness h_c as well. The scaling function $f_2(x)$ in the log-log plot shows a breakdown of the scaling law for medium values of s , but it approaches its asymptotic scaling

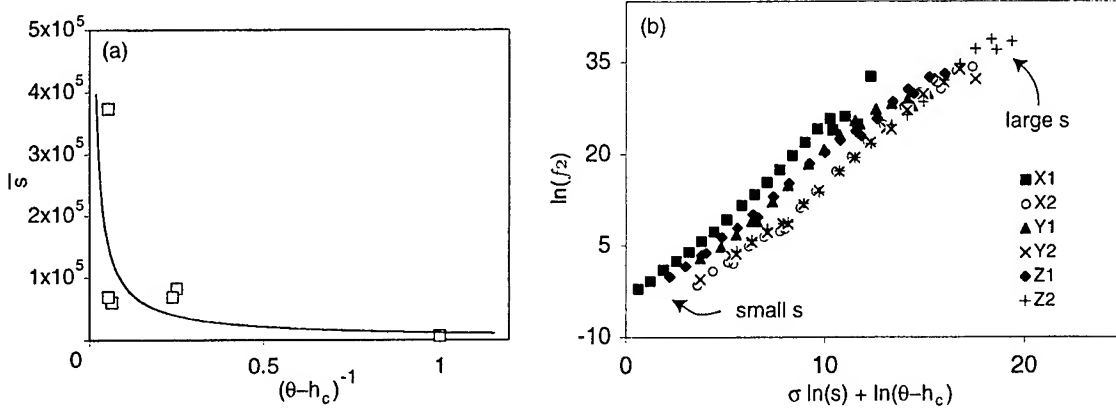


Figure 3. (a) The second moment of the island size distribution diverges as $\theta \rightarrow h_c$; this power-law relation gives $\sigma \approx 1.13$ as shown by the solid curve. (b) Scaling the histograms shown in Figs. 2(a)-(b) reveals the form of $f_2(x)$ and yield $\tau \approx 3.0$.

regimes as $s \rightarrow \infty$, and to some degree in the $s \rightarrow 0$ limit. Since the islands are already in the percolation regime, we need to consider only the $s \rightarrow \infty$ limit as indicated by the ‘large s ’ label in Fig. 3. In this region, the curve is linear, thus

$$\ln f_2 \propto \sigma \ln s + \ln(\theta - h_c),$$

which gives

$$f_2((\theta - h_c)s^\sigma) \propto (\theta - h_c)s^\sigma \quad \text{for } s \rightarrow \infty. \quad (13)$$

The functional form of $f_2(x)$ clearly disagrees with that for Ostwald ripening.¹⁸ In Ostwald ripening, smaller islands decompose as atoms residing in the smaller islands migrate and diffuse through surface, and eventually condense on larger islands. The island density, therefore, must decrease considerably during such a ripening process. It is also found in many instances that the size distribution function behaves self-similarly,¹⁹ i.e. f_2 has the form $f_2(s/L)$. In contrast, we only observe a scaling regime in $f_2(x)$ in the $s \rightarrow \infty$ limit. Hence, the island size distribution function has the following form:

$$\begin{aligned} N_s(\theta - h_c) &\propto s^{-3.0} \{(\theta - h_c)s^{1.13}\} \\ &\propto (\theta - h_c)s^{-1.9}. \end{aligned} \quad (14)$$

Thus, we show that misfit strain does not affect the form of the island size distribution function $f_2(x)$ in Eq. (8). The critical thickness h_c , which depends on the misfit strain ε , defines how far the growth condition is from the critical point (as can be seen from Fig. 3(a)), but this dependence is applied equally for all s . The exclusion of the wetting layer is built-in in Eq. (14) since the integral $\int s N_s ds \rightarrow \infty$ as $s \rightarrow \infty$.

Smoluchowski ripening provides another route for the islands to reach their late growth regime.²⁰ In this ripening process, the islands, small and large, coalesce via island diffusion. The island diffusion coefficient follows a power-law relationship: $D(s) \approx D_0 s^{-\alpha}$, where $\alpha > 0$ is some constant. A mean-field theory for the Smoluchowski ripening gives three possible values for α : (a) $\alpha = \frac{3}{2}$ for ‘perimeter diffusion’ that involves adatom hoppings along the island periphery, (b) $\alpha = 1$ for ‘terrace diffusion’ involving correlated detachment and re-attachment of adatoms from the island perimeter, and (c) $\alpha = \frac{1}{2}$ for random detachment and attachment of adatoms.²¹ The long-time solution for the Smoluchowski equation²² that assumes coalescence of islands only via two-body collisions is given by^{23,24}

$$N_{Sm}(t) \propto s^\alpha \exp(-bs) \quad (15)$$

by assuming that the collision process is time-independent and homogeneous. The term b carries the time dependence and is given by $b \propto t^{-(\alpha+1)}$. This time-dependence carries the dependence of the scaling function on the misfit strain through h_c . Here, we see that h_c may induce a nonlinear behavior in $N_{Sm}(t)$ for large s , since the Taylor expansion of $\exp(-bs)$, which is analytic for all s , contains increasing powers of b for higher powers of s .

The island size histograms in Fig. 2 suggest that neither Eq. (14) nor Eq. (15) alone provides a sufficient description for the ripening process for all island sizes $0 \leq s < \infty$ taking place in our $\text{Si}_{1-x}\text{Ge}_x/\text{Si}(001)$ samples. While Eq. (14) captures the ripening behavior in the $s \rightarrow \infty$ limit, and to some degree in the $s \rightarrow 0$ limit, the histogram peaks clearly favor the mathematical expression of Eq. (15). These indicate that both random percolation and two-island collision processes may occur concurrently during ripening. This is supported by a lack of scaling in the histograms from samples X1, Y1 and Z1 (see Fig. 3(b)). Granted that the random percolation process occur simultaneously with some ripening, the surface morphologies strongly indicate that the islands ripen via Smoluchowski ripening instead of Ostwald ripening. Although a precise form of Eq. (8) is often determined by either numerical simulations or experimental results, such as in our case, it has been proven that the scaling function $f_2(x)$ is analytic, implying that derivatives of $f_2(x)$ with respect to x are finite everywhere, even at $x = 0$.¹⁰ Obviously, the scaling functions in Eqs. (13) and (15) obey this postulate. We are currently investigating further the consequences of having both random percolation and Smoluchowski ripening governing the ripening of $\text{Si}_{1-x}\text{Ge}_x/\text{Si}(001)$ islands.

Qualitatively, we can observe their competing behavior in Fig. 3(b). The random percolation process governs the island ripening for small and large islands and clearly dominates as the layer thickness increases. The Smoluchowski ripening provides a size uniformity mechanism only in the medium-sized islands when the layer thickness is relatively near the critical thickness. From Fig. 3(b) we see that more uniform islands can be generated during their ripening regime when $\sigma \ln(s) + \ln(\theta - h_c) \approx 10$. This 'dimensionless' parameter may provide a practical measure on when the growth should be terminated.

4. SUMMARY

The scaling analysis of island size distributions of $\text{Si}_{1-x}\text{Ge}_x/\text{Si}(001)$ ripening islands suggests that random percolation and Smoluchowski ripening occur concurrently. They operate, however, on different length scales. While small and large islands are shown to follow the random percolation scaling function, we find a breakdown of the random percolation *ansatz* in middle-size islands. Surface morphologies of the islands do not conform with what is commonly observed in Ostwald-ripening islands, which suggest that Smoluchowski ripening takes place. For a two-island coalescence process, solution of the Smoluchowski equation that describes such a ripening allows for a size distribution with a single peak. Its fast exponential decay results in a vanishing influence at large islands. We also observe in our analysis that the random percolation *ansatz* regains its dominance in the limit $s \rightarrow \infty$. To control the uniformity of island sizes, the random percolation process is to be avoided as it allows the islands to grow indefinitely; thus, terminating the growth when the Smoluchowski ripening is still operative is suggested as a way to obtain relatively uniform large islands.

ACKNOWLEDGMENTS

It is a pleasure to thank B. G. Yacobi for valuable discussions and M. Paige for his help with the AFM. The authors gratefully acknowledge the financial support of the Natural Science and Engineering Research Council (NSERC), and the Mathematics of Information Technology and Complex Systems (MITACS). A. B. is also supported by the Open Fellowship and the International Student Award from the University of Toronto.

REFERENCES

1. D. J. Eaglesham and C. Cerullo, "Dislocation-free Stranski-Krastanow growth of Ge on Si(100)," *Phys. Rev. Lett.* **64**, 1943-6 (1990).
2. S. Fafard *et al.*, "Red-emitting semiconductor quantum dot lasers" *Science* **274**, 1350-3 (1996); M. Grundmann *et al.*, "Ultrasharp luminescence lines from single quantum dots," *Phys. Rev. Lett.* **74**, 4043-6 (1995).
3. R. Leon *et al.*, "Nucleation transitions for InGaAs islands on vicinal (100) GaAs," *Phys. Rev. Lett.* **78**, 4942-5 (1997).
4. T. I. Kamins and R. S. Williams, "Lithographic positioning of self-assembled Ge islands on Si(001)," *Appl. Phys. Lett.* **71**, 1201-3 (1997).
5. R. People and J. C. Bean, "Calculation of critical layer thickness versus lattice mismatch for $\text{Ge}_x\text{Si}_{1-x}/\text{Si}$ strained-layer heterostructures," *Appl. Phys. Lett.* **47**, 322-4 (1985).

6. J. G. Amar and F. Family, "Critical cluster size: island morphology and size distribution in submonolayer epitaxial growth," *Phys. Rev. Lett.* **74**, 2066-9 (1995); J. G. Amar *et al.*, "Dynamic scaling of the island-size distribution and percolation in a model of submonolayer molecular-beam epitaxy," *Phys. Rev. B* **50**, 8781-97 (1994).
7. J. A. Strosio and D. T. Pierce, "Scaling of diffusion-mediated island growth in iron-on-iron homoepitaxy" *Phys. Rev. B* **49**, 8522-5 (1994).
8. V. Bressler-Hill *et al.*, "Island scaling in strained heteroepitaxy: InAs/GaAs(001)" *Phys. Rev. Lett.* **74**, 3209-12 (1995).
9. Y. Ebiko *et al.*, "Island size scaling in InAs/GaAs self-assembled quantum dots," *Phys. Rev. Lett.* **80**, 2650-3 (1998).
10. D. Stauffer, *Introduction to Percolation Theory* (Taylor & Francis, London, 1985).
11. M. C. Bartelt and J. W. Evans, "Nucleation and growth of square islands during deposition: sizes, coalescence, separations and correlations," *Surf. Sci.* **298**, 421-31 (1993).
12. D. D. Perović *et al.*, "Strain relaxation at low misfits: dislocation injection vs. surface roughening," in *Materials Research Society Symposium Proceedings* **399**, 325-36 (1996).
13. H. Lafontaine *et al.*, "Characterization of Si_{1-x}Ge_x epilayers grown using a commercially available ultrahigh vacuum chemical vapor deposition reactor," *J. Vac. Sci. Technol.* **14**, 1675-81 (1996).
14. G. Medeiros-Ribeiro *et al.*, "Shape transition of germanium nanocrystals on a silicon(001) surface from pyramids to domes," *Science* **279**, 353 (1998).
15. J. A. Floro *et al.*, "Evolution of coherent islands in Si_{1-x}Ge_x/Si(001)," *Phys. Rev. B* **59**, 1990-8 (1999).
16. A. G. Cullis *et al.*, "Misfit dislocation sources at surface ripple troughs in continuous heteroepitaxial layers," *Phys. Rev. Lett.* **75**, 2368-71 (1995).
17. I. Goldfarb *et al.*, "Competing growth mechanisms of Ge/Si(001) coherent clusters," *Phys. Rev. B* **56**, 10459-68 (1997).
18. C. Sagui and R. C. Desai, "Ostwald ripening in systems with competing interactions," *Phys. Rev. Lett.* **74**, 1119-22 (1995).
19. G. R. Carlow and M. Zinke-Allmang, "Self-similar spatial ordering of clusters on surfaces during Ostwald ripening," *Phys. Rev. Lett.* **78**, 4601-4 (1997).
20. D. S. Sholl and R. T. Skodje, "Late-stage coarsening of adlayers by dynamic cluster coalescence," *Physica A* **231**, 631-47 (1996).
21. K. Binder and M. H. Kalos, "Critical clusters in a supersaturated vapor: theory and Monte Carlo simulation," *J. Stat. Phys.* **22**, 363-96 (1980).
22. S. Chandrasekhar, "Stochastic problems in physics and astronomy," *Rev. Mod. Phys.* **15**, 1-89 (1943).
23. M. Villarica *et al.*, "Application of fractals and kinetic equations to cluster formation," *J. Chem. Phys.* **98**, 4610-25 (1993).
24. R. Jullien, "The application of fractals to investigations of colloidal aggregation and random deposition," *New J. Chem.* **14**, 239-53 (1990).

A novel semiconductor/superlattice distributed Bragg reflector (DBR) grown by molecular beam epitaxy (MBE) and its characteristics

Changling Yan^a, Jingchang Zhong^{*b}, Yingjie Zhao^b, Ronghui Li^b

^aChangchun Institute of Optics, Fine Mechanics and Physics,
Chinese Academy of Sciences, Changchun, 130021, China

^bChangchun Institute of Optics and Fine Mechanics,
Changchun 130022, China

ABSTRACT

A novel semiconductor/superlattice AlAs/[GaAs/AlAs] DBR has been obtained through replacing the $\text{Al}_x\text{Ga}_{1-x}\text{As}$ in the AlAs/ $\text{Al}_x\text{Ga}_{1-x}\text{As}$ DBR with GaAs/AlAs superlattice. In experiment, a p-type of this kind of 19-period DBR has been grown by V80H MBE system. From the experimental reflection spectrum, the central wavelength of the DBR is about 850nm and the 19-period DBR has the reflectivity high up to as 99.5%. Moreover, by using twice self-designed tungsten filament mask and proton implantation method, the $10 \times 10 \mu\text{m}^2$ square current flowing area has been made to measure the series resistance of the p-type DBR. The method can solve the difficulty in controlling the depth of etching and prevent the occurrence of side etching in wet chemical etching usually used in experiments. From our experiment the series resistance of the DBR was just about 50 Ohms. Furthermore, the dependence of series resistance on temperature has also been studied. From the experimental results, it was found that the low series resistance of this kind of DBRs may be attributed to an increase in tunneling current on the semiconductor/superlattice minor structure that would lead to a decrease in the series resistance.

Keywords: Vertical-cavity surface-emitting laser (VCSEL), distributed Bragg reflector (DBR), superlattice, quantum well, reflection spectrum, series resistance, molecular beam epitaxy (MBE), proton implantation

1. INTRODUCTION

Recently the vertical cavity structures are available for two-dimensional (2D) array integration with their advantageous characteristics such as circular output beam with low divergence, high modulation speed, low threshold current, and ease of fabrication in 2D. The vertical-cavity surface-emitting lasers (VCSEL)¹, optical interconnections based on VCSEL expected to eliminate bottle necks in electronic connections^{2,3}, and VCSEL —based devices promised to play a key role in constructing large-bandwidth switching net works and massively parallel processors⁴ have been reported. Therefore, so much attention is being paid to DBRs, which form these vertical cavity structure devices, owing to their potentiality to realize optical microcavities^{5,6}. In some optoelectronic devices such as VCSEL, it is desirable to use semiconductor DBRs to allow current inject into the

*Correspondence: Email: zjc@public.cc.jl.cn; Telephone: 86 431 5381380;

structure via the mirrors. For example, for the short-wavelength VCSEL, it has been shown that the $\text{Al}_x\text{Ga}_{1-x}\text{As}/\text{AlAs}$ DBRs can be successfully used⁷. These DBRs made with semiconductor materials can simplify the fabrication process of the devices, but the semiconductor materials with large differences in reflective indices also have large band-gap differences. These band-gap differences would cause high electrical resistance and excess power consumption. In order to reduce the electrical resistance of semiconductor DBRs, various semiconductor DBRs with many kinds of graded layers structures placed in heterointerfaces have been designed^{8,9}. All these semiconductor DBRs consist of periods of two kinds of semiconductor materials, so we can name these DBRs as semiconductor/semiconductor DBRs.

In this paper, we introduced a novel semiconductor / superlattice DBR. By replacing the $\text{Al}_x\text{Ga}_{1-x}\text{As}$ with GaAs/AlAs superlattice, a p-type semiconductor/superlattice AlAs/[GaAs/AlAs] DBR has been grown by V80H MBE system in experiment. From the results of measurement, the central wavelength of the DBR reflection spectrum is about 850nm and the 19-period DBR has the reflectivity as high as 99.5%. Moreover, using twice self-designed tungsten filament mask and proton implantation method, we have made a $10 \times 10 \mu\text{m}^2$ square current flowing area to measure the series resistance of the DBR, and it was just about 50 Ohms. Furthermore, the dependence of the DBR series resistance on temperature has also been studied in the experiment.

2. DBR FABRICATION

By replacing $\text{Al}_x\text{Ga}_{1-x}\text{As}$ in AlAs/ $\text{Al}_x\text{Ga}_{1-x}\text{As}$ DBR with superlattice consisting of 18-period GaAs (3nm)/AlAs(0.7nm), the AlAs(73.3nm)/18[GaAs(3nm)/AlAs(0.7 nm)] DBR has been obtained. The schematic diagram of 1-period DPR structure was shown in Fig.1. According to the reflection data¹⁰ of $\text{Al}_x\text{Ga}_{1-x}\text{As}$ material, using the calculation method¹¹ of the reflectivity of DBRs, we calculated the reflectivity of the 19-period DBR for 805nm wavelength and found it was about 99.2%.

In experiment, a p-type AlAs(73.3nm)/18[GaAs(3nm)/AlAs(0.7nm)] DBR was grown by V80H MBE system on a (100) n-GaAs substrate and the layers were doped with Be. The structure of the epitaxial layers such as alloy composition, nominal layer thickness, number of pairs, doping levels and growing times were shown in Table 1.

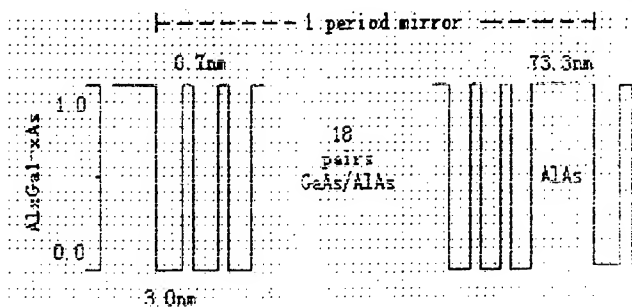


Fig 1. the schematic diagram of the DBR structure

A 0.4- μm -thick n-GaAs buffer layer, a 65-nm-thick p-GaAs buffer layer, a 19-period AlAs(73.3nm)/18[GaAs(3nm)/AlAs(0.7nm)] p type mirror, and p+-GaAs Ohmic contact layer were successively grown on n-GaAs substrate. An accurate determination of the growth rates had been carried out by high-resolution X-ray diffraction before the DBR growth. During the MBE growth, the RHEED was employed to observe the surface pattern of the epitaxial layer in order to avoid producing multiple crystalline. The substrate was rotated to make the epitaxial layers nominal.

Table 1. The structure of the epitaxial layers

layers	Thickness	Doping level	Growing time
Top P ⁺ -GaAs	50nm	Be:3x10 ¹⁹ cm ⁻³	10Min.
P-type19-period DBR (AlAs/18[GaAs/AlAs])	2.66 μ m	Be:3x10 ¹⁸ cm ⁻³	4Hr.And 30Min.26Sec.
Buff. P-GaAs	65nm	Be:2x10 ¹⁸ cm ⁻³	39Min.
Buff. N-GaAs	0.4 μ m	Si:2x10 ¹⁸ cm ⁻³	24Min.
Sub. N-GaAs		Si:1x10 ¹⁸ cm ⁻³	Total: 5Hr.43Min.26Sec.

After growing, the epitaxial chip was separated, dyed, and observed under the scanning electronic microscope (SEM). From the SEM microphotograph of the DBR, which is shown in Fig.2, it can be seen that the layers were straight, nominal, and the epitaxial structure was grown as good as it was designed.

The experimental reflectivity of the DBR was measured with a WDH3 type wide-wavelength scanning spectrometer. The experimental reflection spectrum of the DBR was shown in Fig.3. From the reflection spectrum, it can be found that the central wavelength of the reflection spectrum was about 847nm. The maximal reflectivity was as high as 99.5%. So, the high reflectivity can meet the requirement of optoelectronic devices, which needs high light feed back, such as VCSEL.

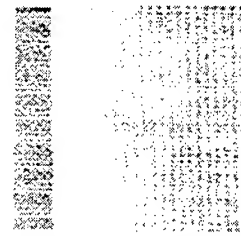


Fig.2 microphotograph of the DBR

3. MEASUREMENT OF SERIES RESISTANCE OF THE P TYPE DBR

In the measurement of the series resistance of DBRs, the wet chemical etching method is usually used to form the current flowing mesas¹². In our experiment, we found that there were some difficulties in controlling the depth of etching and that while etching down the sides of the mesas were also etched. In this way; the problem would make the measurement not accurate. In order to improve the measurement accuracy we self-designed the tungsten filament mask and proton implantation method to form a current flowing area to measure the series resistance.

In experiment, first, put the 10 μ m-diameter tungsten filament as a mask on the front face of the DBR, then implant protons, deposit Au-Zn on the surface; Second, put off the tungsten filament, turn 90 degrees and make the second mask. The process is completely the same as the first one. The depth of the implantation would be determined by the implantation energy. The dependence of the implantation depth on the proton energy was shown in Fig.4. Therefore, the depth was controlled easily by varying the proton energy. At the same time, this method can also prevent the occurrence of the side etching in wet chemical etching. The experimental data in implantation were shown in Table2. After separating,

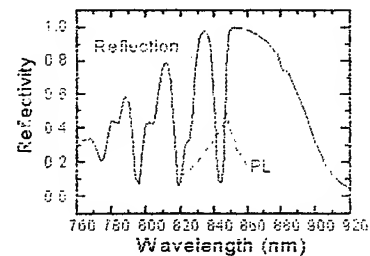


Fig.3 the experimental reflection spectrum of the DBR

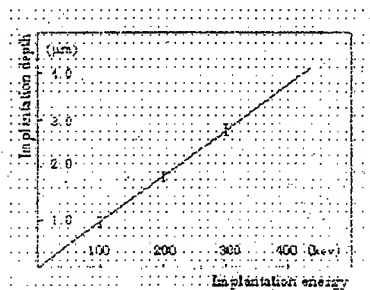


Fig.4 the dependence of the implantation energy on the depth of the implantation

Table 2. The experimental data in proton implantation

Ion	Depth	Energy	Dose	Implantation time	Thermal annealing temperature	Thermal annealing time
H ⁺	2.2 μ m	220 Kev	3x10 ¹⁵ cm ⁻²	1.5 Hours	400-420°C	1-2 Min.

displaying junction, and dying, it was found that the depth of the implantation agreed with the required one very well. Therefore, a 10x10 μ m² square current flowing area has been easily made. After that, the substrate backside was thinned to about 150 μ m to decrease the substrate contribution to electrical measurement. Then, Au-Ge-Ni alloyed contact was used for the n-GaAs substrate. The distribution of the experimental series resistance of 50 DBRs was shown in Fig. 5. From that, we can see that almost half of them were about 50 Ohms.

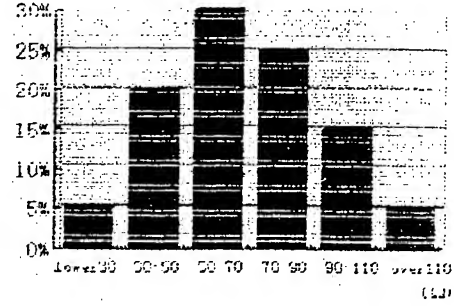


Fig.5 the distribution of series resistance

4. DEPENDENCE OF SERIES RESISTANCE ON TEMPERATURE

The dependence of series resistance of this kind of DBR on temperature has also been studied. While varying the temperature, the series resistance was measured and it was found that the series resistance varied with temperature slightly. Fig.6 is the dependence of the series resistance on temperature in experiment. The thermal current flow ing over a potential barrier is expressed as⁹.

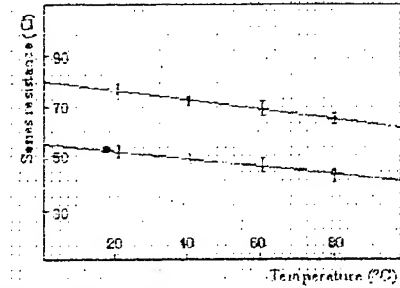


Fig 6 dependence of series resistance

$$J_{\text{thermal}} \propto T^2 \exp\left[-\frac{q}{kT} \phi \left(\frac{qV}{kT} - 1\right)\right] \quad (1)$$

Here, J_{thermal} is the thermal current, T is temperature, ϕ is the potential barrier height, k is the Boltzmann constant, q is the charge of electron and V is the applied voltage. The tunneling current flowing in a potential barrier is expressed as

$$J_{\text{tunnel}} \propto T_p \int_0^{\infty} \frac{1 + \exp[(E_f - E_s)/kT]}{1 + \exp[(E_f - E_s - qV)/kT]} dE_s \quad (2)$$

Here, J_{tunnel} is the tunneling current, T_p is the tunneling probability, E_f is the Fermi energy, and E_s is the energy of carrier.

From Eqs.(1) and (2), the thermal current depends more on temperature than the tunneling current. So the tunneling current accounts for the majority of the current flowing in this kind of DBR. From the dependence of the series resistance of the DBR with quasi-graded superlattice at the heterointerfaces on temperature⁹, it was found that an increase in the tunneling current can cause a reduction in the series resistance of the DBR. So, the mechanism of the low series resistance of the semiconductor/superlattice

DBRs may also cause that an increase in tunneling current on the semiconductor/superlattice mirror structure would lead to a decrease in the series resistance of this kind of DBRs.

5. CONCLUSION

We have shown a novel semiconductor/superlattice distributed Bragg reflector. In experiment, by replacing the $\text{Al}_x\text{Ga}_{1-x}\text{As}$ with GaAs/AlAs superlattice, a p-type 19-period semiconductor/superlattice DBR has been grown by MBE. From measurement, the central wavelength of the DBR reflection spectrum was about 850nm and the reflectivity was as high as 99.5%. Moreover, using twice self-designed tungsten filament mask and proton implantation method, we have made the $10 \times 10 \mu\text{m}^2$ square current flowing area to measure the series resistance of the DBR. The method could solve the difficulty in controlling the depth of etching and prevent the occurrence of side etching in wet chemical etching. From the results of the experiment, the series resistance was just about 50 Ohms. Therefore, the DBR has low series resistance while maintaining their high reflectivity. Furthermore, the dependence of series resistance on temperature was also studied and it was found that the tunneling current accounted for the majority of the current flowing in this kind of DBR with semiconductor/superlattice structure. We thought that might be the mechanism of lower series resistance of this kind of DBRs. Here we are now just on the threshold of the study of the semiconductor /superlattice DBR, initially, and the studying for their characteristics or their application into optoelectronic devices such as VCSEL would be required more deeply.

ACKNOWLEDGMENTS

The authors would like to thank Prof. J. M. Zhou, Prof. W. X. Wang and Dr. J. M. Sun in MBE Group of Beijing Institute of Physics, Chinese Academy of Sciences for their enthusiastic instruction in the growth of the DBR. At the same time, we also want to give our thanks to the professors in Ion Implantation Group in Beijing Institute of Semiconductors, Chinese Academy of Sciences for their supports in the proton implantation.

REFERENCES

1. Weng W. Chow, Kent D. Choquette, and Mary H. Crawford, "Design, fabrication, and performance of infrared and visible vertical-cavity surface-emitting lasers," IEEE Journal of Quantum Electronics, vol.33, no.10, pp.1810-1824, 1997
2. Hideo Kosaka, "Smart integration and packaging of 2D VCSEL's for high-speed parallel links," IEEE Journal of Selected Topics in Quantum Electronics, vol.5, no.2, pp.184-193, 1999
3. S.F. Yu, "Analysis and design of vertical-cavity surface-emitting lasers for self-sustained pulsation operation," IEEE Journal of Quantum Electronics, vol.34, no.3, pp.497-505, 1998
4. Thomas Maier, G. Strasser; and E. Gornik, "Monolithic integration of vertical-cavity laser diodes and resonant photodetectors with hybrid $\text{Si}_3\text{N}_4\text{-SiO}_2$ top Bragg mirrors," IEEE Photo. Technol. Lett., vol.12, no.2, pp.119-121, 2000
5. David W. Winson, and Russell E. Hayes, "Optoelectronic device simulation of Bragg reflectors and their

- influence on surface-emitting lasers characteristics," IEEE Journal of Quantum Electronics, vol.34, no.4, pp. 705-775, 1998
- 6.F.Delorme and G. Alibert, "Reliability study of 1.55. μ m distributed Bragg reflector lasers," Electronic Lett., vol.33, no.5, pp.394-396, 1997
 - 7.T. E. Sale, "Vertical Cavity Surface Emitting Lasers", New York: Wiley, Research Studies Press Ltd., 1995
 - 8.M.Hong and J. P. Mannaerts, "A simple way to reduce series resistance in p doped semiconductor distributed Bragg reflectors," Journal of Crystal Growth, vol.111, pp.1071-1075, 1991
 - 9.K.Kurihara, T.Numai and I.Ogura, "Reduction in the series resistance of the distributed Bragg reflector in vertical cavities by using quasi-graded superlattices of the heterointerfaces," J.Appl.Phys., vol.73, no.1, pp.21-27, 1992
 - 10.D. E. Aspnes, S. M. Kclso and R. A. Logan, "Optical properties of $\text{Al}_x\text{Ga}_{1-x}\text{As}$," J. Appl. Phys., vol.60, no.2, pp.754-767, 1986
 - 11.R. S. Geels, S.W. Corzine and L. A. Coldren, "InGaAs vertical-cavity surface-emitting lasers," IEEE J.Quantum Electron., vol.27, pp.1359-1367, 1991
 - 12.I.F.L.Dias, B.Nabet and A.Kohl, "Electrical and optical characteristics of n-type-doped distributed Bragg mirrors on InP," IEEE Photonics Technology Letters, vol. 10, no.6, pp.763-765, 1998

A basic element for integrated electro-optical devices based on Liquid Crystal waveguides

Pasquale Mormile ^a, Lucia Petti ^a, Giancarlo Righini ^b, Giancarlo Abbate ^c

^a IC-CNR, Dept. of Optics, via Toiano 6, I-80072 Arco Felice (Naples), Italy

^b IROE-CNR, Optoelectronics and Photonics Department, Via Panciatichi 64, 50127 Firenze, Italy

^c INFN Unità di Napoli e Dipartimento di Scienze Fisiche, Università di Napoli "Federico II",
Via Cintia M. S. Angelo, I-80126 Napoli, Italy

ABSTRACT

Integrated optical devices based on liquid crystal's (LC) features have been generally discarded for a long period mainly due to very high scattering losses. However, in the 90's this situation is rapidly changing. A better understanding of the physical phenomena underlying the observed effects, the use of new materials with improved performances, the discovery of new electro-optical and nonlinear optical effects make the applications of LC in integrated optics more and more attractive. We present here some recently obtained results in this field. In particular, we have designed and realized an integrated device in a three-stage planar waveguide, having as middle stage a nematic liquid crystal (NLC) film. We studied the device performance in different geometries using TE polarized light. By a proper choice of the material parameters we measured time responses in the microsecond range. Our experimental results confirm the possibility of employing such a device working as an optical switch and/or beam deflector.

Keywords: Liquid Crystals; Electro-optical switching; Beam deflector; Integrated waveguide.

1. INTRODUCTION

Many materials have been proposed for integrated optical devices as GaAs, LiNbO₃, poled polymers and MQW structures¹. The main problem with these materials is that they need very high applied field, optical or electrical, in order to induce significant changes of the refractive index. Liquid crystals (LC) have effective electro- and nonlinear optical coefficients that are orders of magnitude larger than other integrated optical materials². Ease of manufacturing process, low cost and possibility for integration with silicon circuit technology³ make the investigation of LC very attractive. Furthermore, in the last few years, studies of LC under strong confinement, such as in slab waveguide configuration, have shown that scattering losses in LC media can be strongly decreased. Losses of the order of few dB/cm (even less than 2dB/cm) have been measured in those systems⁴⁻⁶. An important drawback in using LC materials in practical devices is the slow optical response: the LC giant optical nonlinearity⁷ comes from a collective macroscopic reorientation process induced by an intensity dependent optical torque, which can take a time ranging from milliseconds to seconds. Thus, in most cases, LC devices are used either for fundamental studies or for those applications that do not require fast responses. In these cases, the advantage of using very low light power levels to reach the desired nonlinear effect is really unique with LC materials⁸.

Due to the effective large electro-optic coefficients exhibited by LC, their use for integrated optics modulators is also of interest⁹⁻¹². The limit of a slow optical response can be overcome using very thin LC films, of the order of 1 μm . For such a thin film, the losses decrease from 20 dB/cm (typical value for film thickness greater than 10 μm) to 2 dB/cm. Switching times also decrease as the inverse of thickness squared, in the limit of validity of the LC elastic theory.

We have designed and realized a particular waveguide structure working as both an optical switch and a beam deflector. In the present paper we report the experimental results of such an integrated electro-optical switch based on a NLC waveguide which exploits the electro-optical properties of NLC's, that is field induced realignment and dynamic scattering. Measurement of the response times and of the output signals as a function of the driving voltage are presented in the case of TE polarization of the incident light.

Email: ^a mormile@inter.cib.na.cnr.it; ^b righini@iroe.iroec.fi.cnr.it; ^c abbate@na.infn.it.

2. DESIGN AND REALIZATION OF A PLANAR WAVEGUIDE FOR ELECTRO-OPTICAL SWITCHING AND BEAM DEFLECTION

The manufacture of LC integrated optical devices requires the following steps: a) the choice of the most suitable waveguide fabrication method; b) the design of the guiding structure and of the LC cell which assure the most efficient interaction; c) the design and realisation of electrodes.

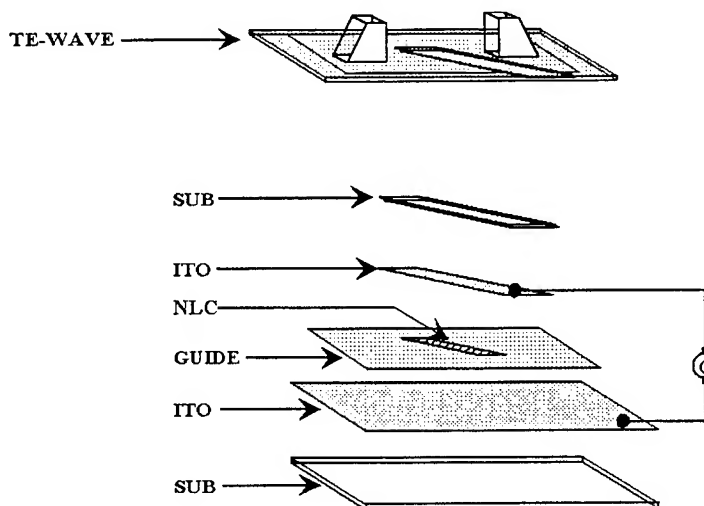


FIGURE 1: Schematic representation of the realised planar waveguide. SUB: substrate and cover; ITO: indium tin oxide; NLC: nematic liquid crystal; G: voltage generator.

In order to study light propagation in a waveguide filled with a NLC material, we designed and realised the guiding structure schematically shown in Fig. 1. The planar dielectric waveguide had been realised first, and then a rectangular cell with depth equal to the core thickness is etched in it with an angle of 21 degrees with respect to the direction of the incident light for the NLC inclusion (see figure 2). The cell is filled with LC and then covered with a glass plate having the same refractive index as the waveguide substrate. The cell's bottom and the top cover should be previously coated with proper surfactants in order to obtain alignment of the LC molecules. In this way one obtains a planar waveguide having LC as guiding medium in the central section. In order to apply the electric field we used a conducting film of ITO (Indium Tin Oxide) deposited both on the substrate and on the cover of the basin.

The waveguide was made by using the sol-gel deposition technique. The sol-gel method is an advantageous technique because of its versatility, which allows the production of glasses with largely different physico-chemical properties just by changing the starting solution composition¹³. In principle it allows a fine tuning of the refractive index of the produced film over a very large interval (e.g. using silica-titania binary glasses, refractive index may be varied approximately from 1.6 up to 2.3). This allows the design of the guiding structure to match the specific needs of the devices. In our case, sol-gel films have been prepared starting from an alcoholic solution (in ethanol) of tetraethoxysilane (TEOS) and titanium butylate with 70%/30% relative molar content as precursor of silica and titania, respectively. The films were deposited by dip-coating on silica substrate in a controlled temperature (30°C) and humidity (30% relative) environment. They were subsequently densified by annealing at 500°C. For the fabrication of the electro-optical devices we used soda-lime glass substrates coated with ITO films. The guiding film was deposited on the top of the ITO layer, and was then characterised first by using the usual dark-line arrangement (i.e. laser light coupling into the guide by an isosceles prism) and later on by loss measurements through the detection of out-of-plane scattered light¹⁴. Of course, the multilayer structure including ITO films is quite significantly affected by the properties of ITO itself: it can be ascribed mainly to its refractive index, which is high (effect on the waveguide modal structure) and may be complex (effect on the waveguide losses). Thus, when depositing waveguide layers we also used a reference substrate (without ITO coating) in order to compare the guiding properties of the two structures. Loss measurements indicated a sufficiently good quality of sol-gel waveguides onto uncoated substrates (with loss below 0.8 dB/cm), while higher losses (up to 2 dB/cm) are caused by the presence of the ITO layer, partly due to its intrinsic absorption, and partly due to its effect on the confinement of the guided optical field.

Finally, by an etching process we obtained the basin on the waveguide for the LC inclusion. In order to limit losses due to light scattering in the LC, the propagation length in the LC cell has been reduced to a minimum. The etching process

is particularly critical because one needs the cell walls to be of the lowest possible roughness, to avoid additional scattering of light at the boundaries between the glass waveguide and the LC one, as well as to obtain a very good alignment of LC molecules. We started using chemical etching, and good results have been obtained by using a fluoridric acid solution. It guarantees good etching rate and relatively low-roughness surfaces, with the further advantage that ITO is not attacked by this solution and therefore it can constitute an easy end-point of the process.

The liquid crystal chosen is thermotropic nematic material and is commercially available from Rolic under the trademark TN-3326: it is a mixture with nematic range from -20 to $+65$ °C, and its ordinary and extraordinary refractive indices at 514 nm are equal to 1.489 and 1.592, respectively. The LC molecules have been rigidly attached to the wall surface by *strong anchoring*¹⁵, by evaporating SiO_x at oblique incidence onto the cover and the substrate in order to obtain the desired planar alignment with the easy axis, which corresponds to the optical axis, perpendicular to the propagation direction.

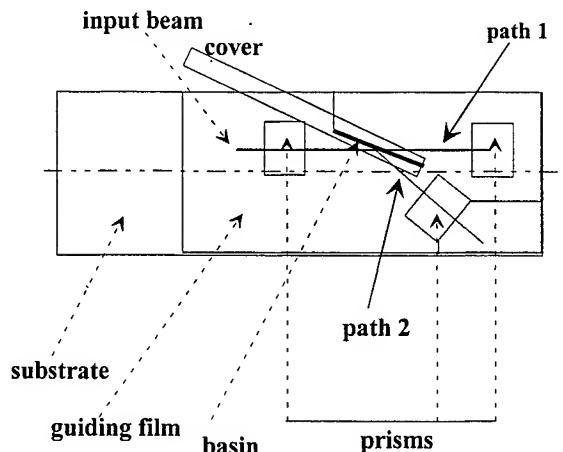


FIGURE 2: Schematic representation of the planar guiding structures showing the prisms for light coupling and decoupling of the transmitted and reflected beams.

Summarising, the final structure is constituted of a three-stage planar waveguide, having the LC cell as middle stage and the two glass waveguides as other stages. The resulting planar waveguide is a step-index bi-modal layer whose thickness is $0.8\text{ }\mu\text{m}$, the refractive index of the core in the glass sections is $n_g = 1.601$ at the wavelength of 514 nm. The cell to be filled with the LC has a length of $500\text{ }\mu\text{m}$ along the propagation direction and a depth equal to the thickness of the glass waveguide core.

3. INTEGRATED ELECTRO-OPTICAL SWITCH: RESULTS AND DISCUSSION

We have characterized our e-o switch using the set-up shown in Fig. 3. The light beam from a cw Ar^+ laser was focused and coupled by means of a high refractive index prism into the glass waveguide. A system of half wave retardation plates and polariser was used in order to select the TE component of the incident light beam. The coupled light can propagate in two ways: directly through the three stages (path 1 in figure 2) or totally deflected at the first boundary depending on the electric states of the applied film (path 2). In both cases the output light beam was finally decoupled by means of a prism and detected by a photodiode whose output was recorded or directly displayed on the oscilloscope.

For incident light polarisation parallel to the optical axis in the LC section, the guided wave feels the extraordinary index of the LC material, which is higher than the substrate one. The light is therefore guided through the whole device and the switch is in the ON state. An electric voltage was then applied to the ITO films used as transparent conductive electrodes. The applied electric field moves the average orientation of the LC molecules, hence moving the optical axis up to a direction normal to the polarisation direction. In this situation, the propagating light feels the ordinary refractive index of the LC materials, then we are in a total reflection condition: light is deflected at the first boundary in the LC stage, which thus acts as a shutter between the two glass stages. The switch is in the OFF state and the device is acting as a beam deflector.

In order to analyze the electro-optical behavior of our device, we changed the amplitude and frequency of the electric field. In all the tested configurations the field was driven by an applied square wave applied voltage.

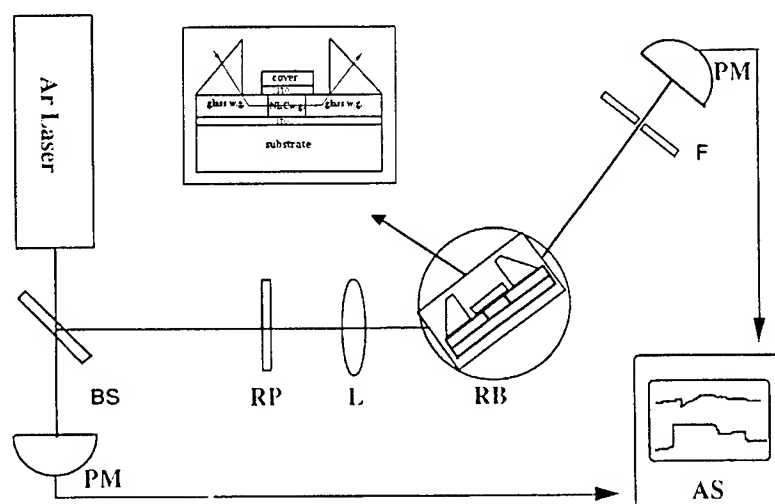


FIGURE 3: Experimental set up. BS = Beam splitter; RP = Polarizer; L = Lens; RB = rotating stage; F = Slit; PM = Power meter; AS = acquisition system.

In order to analyze the electro-optical behavior of our device, we changed the amplitude and frequency of the electric field. In all the tested configurations the field was driven by an applied square wave applied voltage. As a first step, TE-polarized light was used with a driving voltage up to $V_{pp} = 2V$ with a bias of 1V as a function of frequency. Over $\nu = 10Hz$ the optical signal was unable to follow the driving field. The results are summarized in Fig. 4.

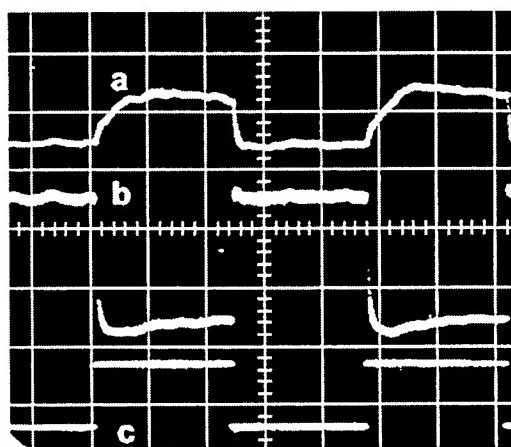


FIGURE 4: Optical response of our guiding device (a is the reflected signal and b is the transmitted one) for TE polarized light. In the lower trace (c) the driving voltage whose frequency is 10Hz is shown. The time scale is 20ms/div. The output transmitted voltage scale is 0.05 V/div, the output reflected voltage scale is 0.5V/div .

In such a situation, when the applied voltage is lower than a threshold value (approximately 1.5 V), no distortion is induced in the LC molecular director and the TE-mode, i.e. polarization parallel to the optical axis, sees a waveguide with an homogeneous refractive index equal to the extraordinary index of the NLC. Thus, the guiding condition is fulfilled and the optical output is ON.

When the voltage is increased above the threshold, the reorientation of NLC molecules occurs: due to the positive dielectric anisotropy of the considered LC, the molecules are forced to be aligned parallel to the applied electric field direction and the refractive index seen by the TE mode is n_o . In this case, the dominant condition is total reflection; this results in the beam deflection at the first glass-LC interface. As a consequence, the switch (the transmitted signal) is driven to the OFF state. The response times for the transmitted light were estimated to be $\tau_{ON} = 1.5$ ms and $\tau_{OFF} = 2$ ms.

An unexpected behavior of our device came out when we applied an additional bias voltage to the driving square wave: the optical signal response reversed as it is evident in Fig. 5. The applied driving voltage was of 4 V at 100 Hz with a constant bias of 3 V. The presence of such a bias should reorient almost completely the LC molecules and the additional square wave field should very little modify the reorientation. Following the previously given explanation, the device should stay ever in its OFF state exhibiting always switching. What is actually observed is quite different. While the modulated electric field is in the low state the device is OFF. But when the electric field is in the high state light transmitted is observed, so that the device is ON. The switching time was measured to be always faster than in the previous case and, depending on the driving field values up to peak performances of $\tau_{ON} = 500 \mu s$ and $\tau_{OFF} = 700 \mu s$ (see figure 5). These performances are certainly appealing.

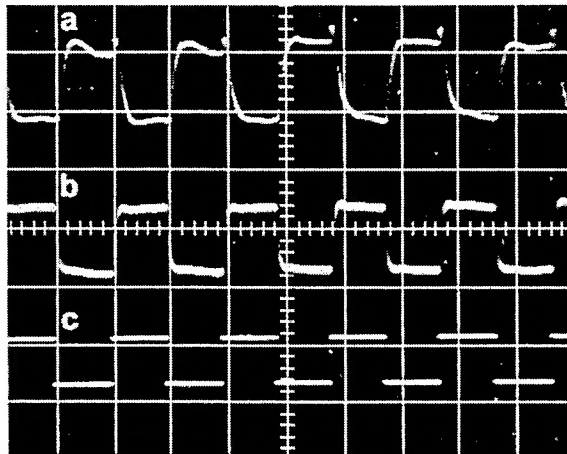


FIGURE 5: Optical response of our guiding device (a is the reflected signal and b is the transmitted one) for TE polarized light. In the lower trace (c) the driving voltage whose frequency is 100 Hz is shown. The time scale is 5 ms/div. The output transmitted voltage scale is 0.02 V/div, the output reflected voltage scale is 0.1 V/div .

In order to analyze this phenomenon we tried to avoid undesired charge effects induced by the positive driving voltage in the LC film using a waveform of the same amplitude as before but alternating positive and negative amplitude with a chosen period. The results are shown in Figs. 6-7: once again we had the expected optical response applying a driving field with an amplitude $|V_{PP}| = 3 \text{ V}$ and no bias (figure 6) and the reversed behavior at $|V_{PP}| = 3.5 \text{ V}$ with a constant bias of $|V_{OFS}| = 3 \text{ V}$ (figure 7).

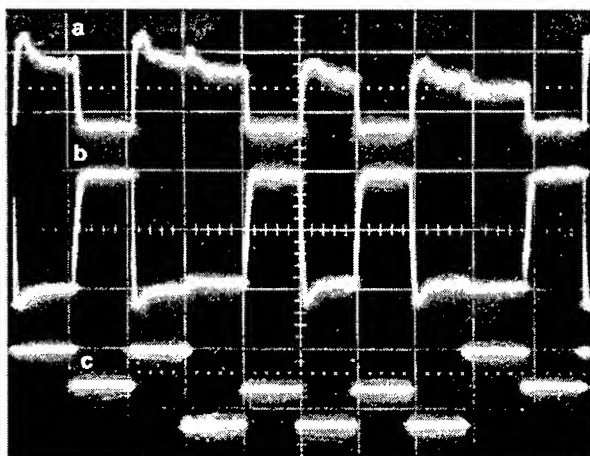


FIGURE 6: Optical response of our guiding device (a is the reflected signal and b is the transmitted one) for TE polarized light. In the lower trace (c) the driving voltage whose period is 500 ms, is shown. The time scale is 50 ms/div. The output transmitted voltage scale is 0.1 V/div, the output reflected voltage scale is 0.5 V/div .

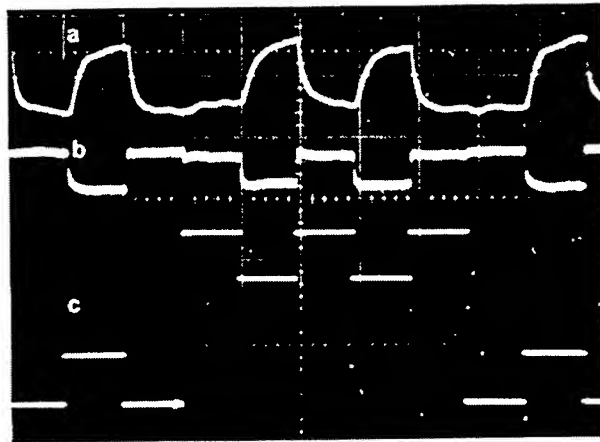


FIGURE 7: Optical response of our guiding device (a is the reflected signal and b is the transmitted one) for TE polarized light. In the lower trace (c) the driving voltage whose period is 50 ms, is shown. The time scale is 5 ms/div. The output transmitted voltage scale is 0.02 V/div, the output reflected voltage scale is 0.1 V/div .

Further analysis were carried out to get a deeper insight into the unexplained behavior of the device. First, we measured the amplitude of the output signals (both transmitted and reflected) as a function of the applied voltage at a frequency of 100 kHz. Such a frequency has been chosen in order to simulate a response to a dc field, avoiding undesired current effects. The experimental results are reported in figures 8 (A and B).

The data confirm both the switch and the beam deflection mechanism previously found and shown in the figures. In particular, we notice the existence of a minimum in the transmission and maximum in the reflection for $V_{pp} \approx 5V$, which clearly show the reason of the best performances of the device in terms of contrast ratio and response times for the chosen value of the bias. Again, the reason for the behavior shown in figure 8 is not clear to us and we can just make hypothesis on the occurrence of surface breaking mechanism. On the basis of simultaneous current measurements, we can further exclude dramatic change in the LC cell resistivity, due for example to dielectric breakdown, since our results give evidence of a linear increase of the current with the voltage, i.e. ohmic regime.

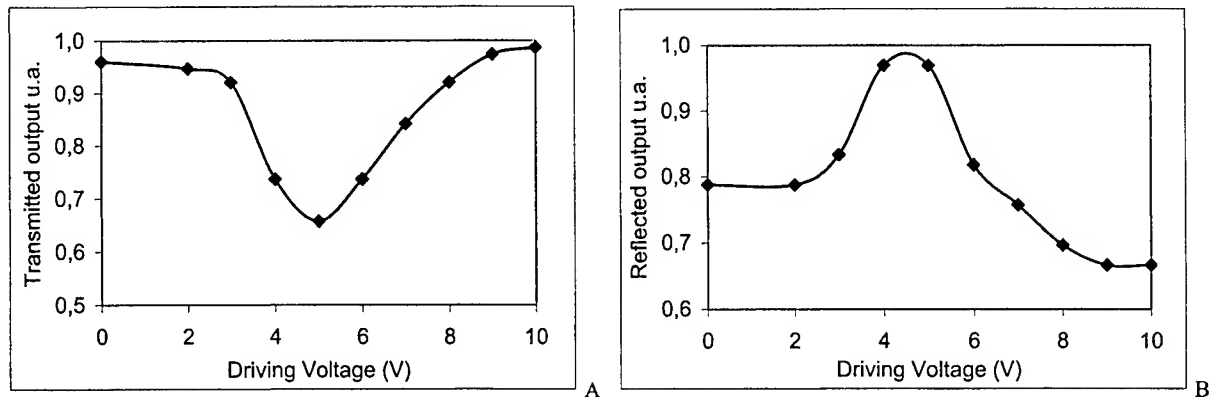


FIGURE 8: Transmitted optical response (A) and reflected optical response (B) of our guiding device for TE polarized light as a function of the driving voltage at a frequency of 100 kHz.

4. CONCLUSION

We have presented experimental results on the light propagation in a planar device constituted of a three-stages planar waveguide. This device exploits the well known electro-optical properties of nematic LC but also exhibits interesting behaviour related to not yet understood effects.

According to the expected behaviour, we obtained for both light polarizations, up to a critical value of the applied voltage, the light switch works as reported in the following scheme with the relative response times.

	Driving Voltage	Transmitted signal	Response times	Reflected signal
TE (10 Hz)	OFF	ON	$\tau_{ON} = 1.5 \text{ ms}$	OFF
	ON	OFF	$\tau_{OFF} = 2 \text{ ms}$	ON
TE (500 ms)	OFF	ON	$\tau_{ON} = 5 \text{ ms}$	OFF
	ON	OFF	$\tau_{OFF} = 3 \text{ ms}$	ON

Above the critical voltage, we noticed an anomalous response which contrasts with the phenomenological behaviour of such a LC switch device. Due to the employed voltages the switch regime of our device should be never reached, on the contrary unexpectedly the device still works as a switch with faster response time as reported in the following scheme.

	Driving Voltage	Transmitted signal	Response times	Reflected signal
TE (100 Hz)	OFF (bias)	OFF	$\tau_{ON} = 500 \mu\text{s}$	ON
	ON	ON	$\tau_{OFF} = 700 \mu\text{s}$	OFF
TE (50 ms)	OFF (bias)	OFF	$\tau_{ON} = 600 \mu\text{s}$	ON
	ON	ON	$\tau_{OFF} = 1 \text{ ms}$	OFF

Our experimental results demonstrate the validity of employing this waveguide structure to realize LC electro-optical switches and/or beam deflectors. Further investigations not only on this device but also on fundamental aspects of liquid crystal physics are suggested by this study.

ACKNOWLEDGEMENTS

This work was supported by a grant from Regione Campania - Assessorato alla Ricerca entitled «Programma Operativo Plurifondo, Azione 5.4.2».

REFERENCES

1. Donaldson, "Candidate materials and technologies for integrated optics: fast and efficient electro-optic modulation", *J. Phys. D* 24, pp 785-802, 1991.
2. M. Kobayashi, H. Terui, M. Kawachi, J. Noda, "2 x 2 optical waveguide matrix switch using nematic liquid crystal", *IEEE J. Quantum Electron. QE-18*, pp 1603-1609, 1989.
3. K.M. Johnson, D.J. McKnight, I. Underwood, "Smart spatial light modulators using liquid crystals on silicon", *IEEE J. Quantum Electron.* 29, pp 699-714, 1993.
4. M. Green, S.J. Madden, "Low loss nematic liquid crystal cored fiber waveguides", *Appl. Opt.* 28, pp 5202-5203, 1989.
5. S.K.Lo, L.M.Galarneau, D.J.Rogers, S.R.Flom, "Smectic liquid crystal waveguides with cylindrical geometry", *Mol. Cryst. Liq. Cryst.* 201, pp 137-145, 1991.
6. G.Abbate, L. De Stefano, P. Mormile, G. Pierattini, E. Santamato, M. Villiargio, "Electric field-induced mode splitting in a liquid crystal waveguide", *Opt. Comm.* 109, p 253, 1994.
7. D.Durbin, S.M.Arakelian, Y.R.Shen, *Phys. Rev. Lett.* 47, p 1411, 1981.
8. L. Petti, L. De Stefano, P. Mormile, G.C. Righini, L. Sirleto, G. Abbate: "Nonlinear Optical Propagation in dye-doped Liquid Crystal Waveguides". *JOPA: Pure and Applied Optics* 1, No3, p 390, 1999.
9. Okamura, K. Kitani, and S. Yamamoto, *J. Lightwave Technol. LT-4*, p 360, 1986.
10. Lin, P. Palffy-Muhoray, *Opt. Lett.* 17, p 722, 1992.
11. Khoo, H. Li, *Appl. Phys. B*, 59, p 573, 1994.
12. Abbate, L. De Stefano, E. Santamato, *J. Opt. Soc. Am. B*, 13, p 1536, 1996.
13. G.C. Righini, A. Verciani, S. Pelli, M. Guglielmi, A. Martucci, J. Fick, G. Vitrant, *Pure Applied Optics*, pp 655-666, 1996.
14. S. Pelli and G. C. Righini, in *Advances in Integrated Optics*, S. Martellucci, A. N. Chester and M. Bertolotti Eds., pp 1-20, Plenum Press, 1994.
15. H. L. Ong, *Phys. Rev. A* 28, p 2393, 1983.

An Estimation of Shallow Energy Level Location in BaTiO₃

Shang-Yeh Chiang, Ming-Tsung Chen, Yeong-Jenq Huang, Shoang C. Donn* and Jynq-Yang Chang[†]

*Institute of Applied Physics, Chung Yuan University

†Institute of Optical Sciences, National Central University

Keyword Shallow energy level, Barium titanate, Two-wave mixing, Low temperature

Abstract

Photorefractive crystals have emerged as ideal candidates for storing large amounts of optical image information. According to the Band Transport model, photorefractive results from absorption at various impurity levels inside the crystal. Thus an understanding of impurity levels within a photorefractive crystal will facilitate further understanding of photorefractive. The Band Transport model assumes that the electrons in the conduction band are excited via optical transitions. There are shallow energy levels, however, which may also contribute conducting electrons via thermal excitation. We report here a method for estimating the location of shallow energy levels in a barium titanate crystal (doped with 20ppm cobalt) by using two-wave mixing measurements at low temperatures. This method provides a lower limit of the location of the shallow energy level which is about 0.1 eV below the conduction band in this crystal.

1. Introduction

Photorefractive crystals have emerged as ideal candidates for storing large amounts of optical image information. According to the Band Transport model, photorefractive results from absorption at various impurity levels inside the crystal. Thus an understanding of impurity levels within a photorefractive crystal will facilitate further understanding of photorefractive. The Band Transport model¹ assumes that the electrons in the conduction band are excited via optical transitions. There are shallow energy levels, however, which may also contribute electrons via thermal excitation. We report here a method for estimating the location of shallow energy levels in a barium titanate crystal (doped with 20ppm cobalt) by using two-wave mixing measurements at low temperatures. As we will see later from the experimental results, the grating may not disappear after the pumping beam is turned off in two-wave mixing at low temperatures. In fact, it took some time for the grating to disappear. Assuming that the dominant mechanism for its disappearance is thermal excitation from the shallow energy level, we can estimate the lower limit of the location of the shallow energy level, which is about 0.1 eV below the conduction band in this crystal.

2. Experimental Measurement

In order to observe the time required for the grating to disappear (after the pumping is turned off in two-wave mixing), we have to conduct the experiment at low temperatures. Therefore we first describe the cooling arrangement. The sample was placed in the sample chamber in a model VPF-100 cryostat manufactured by Janis. A Lake Shore model 321 temperature controller was used to control the temperature of the cryostat. The temperature reduction rate is about 1 °K /min. The experimental set-up is shown in

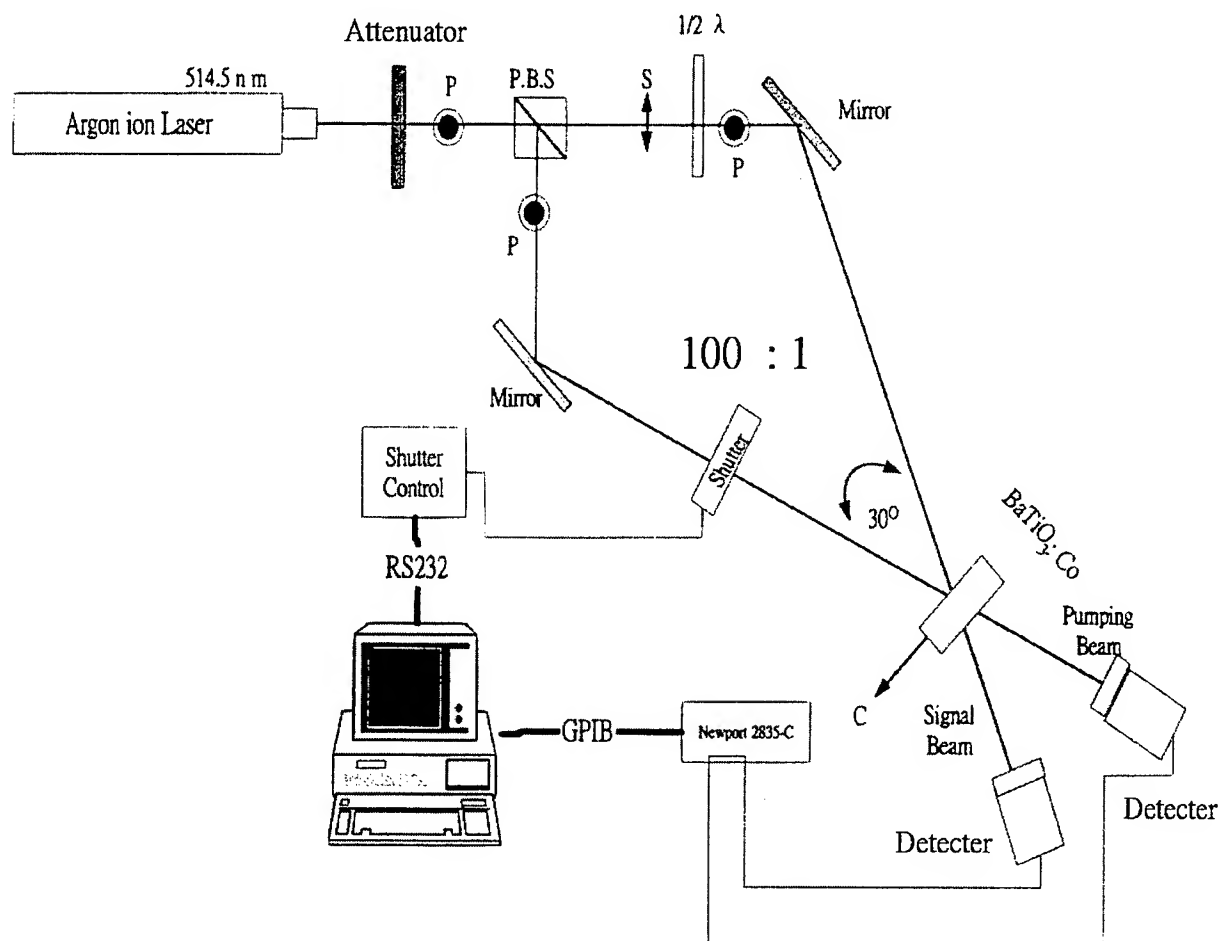


Fig.1 Experimental Set-up

Fig. 1. After the Argon laser is attenuated, the beam is split into two beams using a polarization beam splitter (PBS). The polarization of beam was chosen to be perpendicular to the C-axis of the crystal so we were using O-rays to establish the grating in order to avoid the adverse effect of beam-fanning. The pumping beam and the signal beam were read simultaneously using a Newport dual optical power meter (Model2835-C). The data was acquired by a Labview program which read the data at a rate of 5 samples /sec.

Before we proceed with the two-wave mixing experiment at low temperatures, we want to make sure that we can conduct the experiment inside the cryostat. So we performed the two-wave mixing experiment under the same condition inside and outside the cryostat. The results are shown in Fig. 2 and Fig.3. As one can observe from these two graphs, the signal gain for the one obtained inside the chamber is less than the one obtained outside the chamber (the signal is also noisier for the one inside). The reduction of signal is due to the reflection and scattering from the chamber windows. But in general, there is sufficient gain for the two-wave mixing experiment conducted inside the chamber. Thus, we can conclude

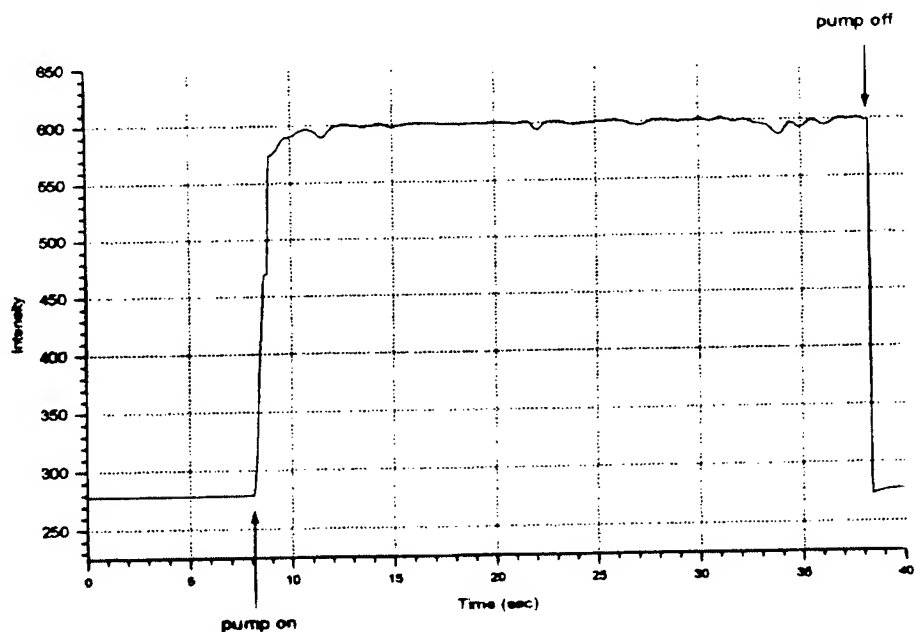


Fig. 2 Two-wave mixing performed outside the cryostat

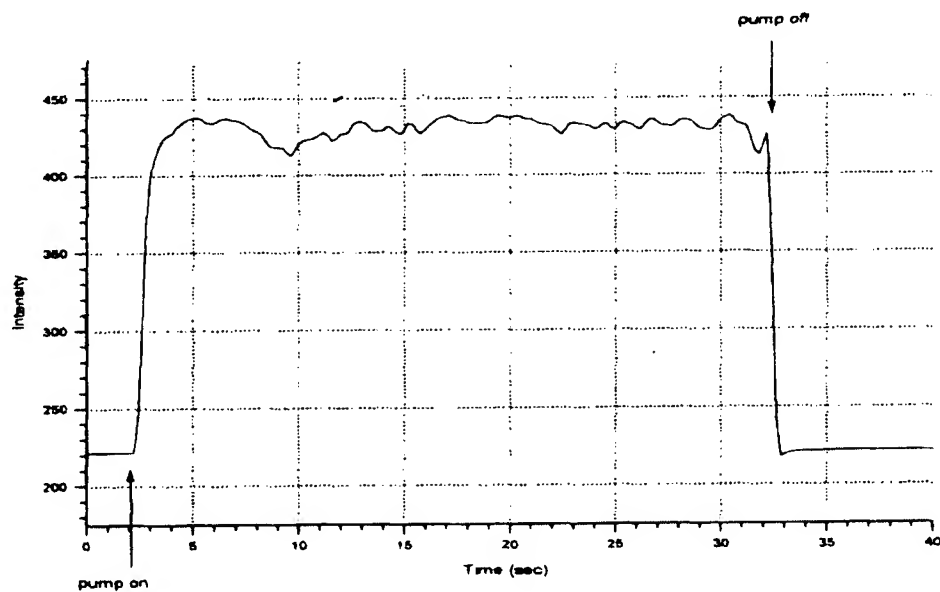


Fig. 3 Two-wave mixing performed inside the cryostat

that we can perform the two-wave mixing inside the cryostat.

Next, we performed a series of two-wave mixing experiments at various low temperatures using Argon laser as the light source. The pumping beam intensity was 100mW while the signal beam intensity was 1mW, and the two beams intersected at an angle of 30° outside the crystal. The results are shown from Fig. 4 to Fig. 8.

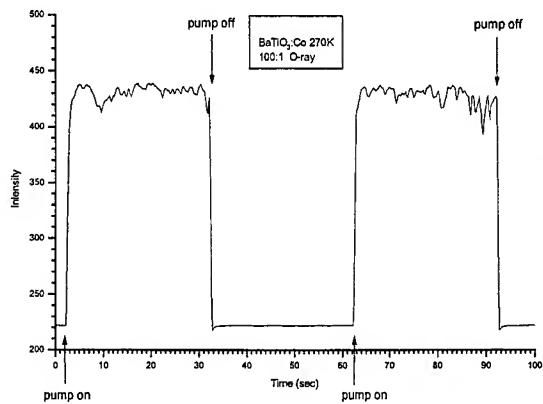


Fig. 4 Two-wave mixing at 270K

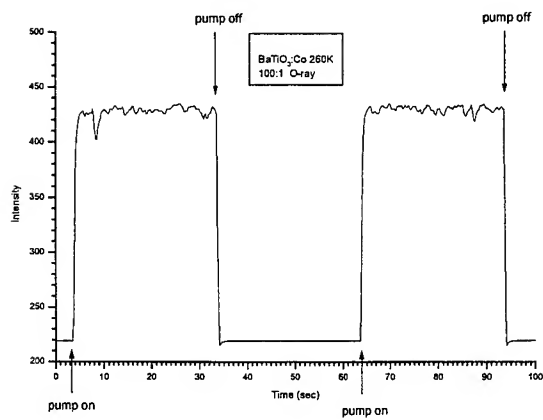


Fig. 5 Two-wave mixing at 260K

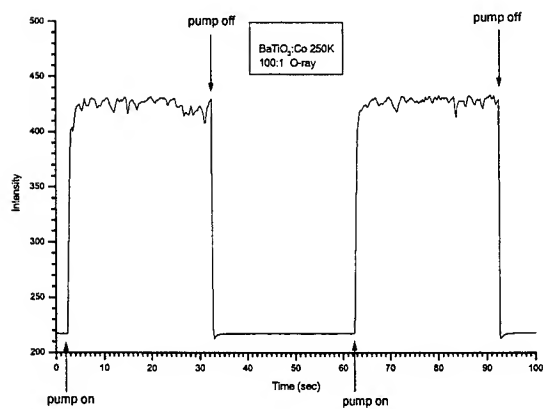


Fig. 6 Two-wave mixing at 250K

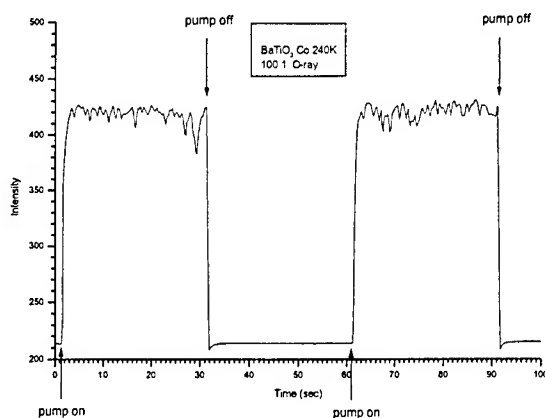


Fig. 7 Two-wave mixing at 240K

3. Data Analysis and Discussions

As the graphs show, as soon as the pumping beam was turned off the signal beam intensity dipped before it recovered to its original intensity. Fig. 8 shows the enlarged view of the dipped portion of the graphs. Fig. 9 is a further enlarged view of one of the signal beam intensity as a function of time after the pumping beam was turned off. It appears that electrons need more time to redistribute themselves (in order to clean up the grating) at low temperature than that at room temperature. There are three possible mechanisms for the electron redistribution: 1) diffusion, 2) excitation from deep impurity levels by the signal beam, 3) thermal excitation from shallow levels. In order to find out what's going on we will have to analyze the data. First, this set of data can be fitted into the following equation:

$$I = I_0 + Ce^{-t/\tau} \quad (1)$$

in which $1/\tau$ relates to the speed of recovery. The solid line in Fig. 10 is the fit from the above equation. Table 1 lists all the τ 's along with their corresponding temperatures. If diffusion is the only mechanism of electron redistribution, one would expect $1/\tau$ should be directly proportional to temperature. However, this is not the case. Furthermore, the signal beam intensity was 1mW which is unlikely to bring in any significant amount of optically-excited electrons from deep levels. A reasonable assumption therefore, is that the electrons generated via thermal excitation from a shallow level. Assuming the energy gap between the shallow level and the conduction band is Δ , the relation between the $1/\tau$ and the temperature T is given by the following equation²:

$$\tau^{-1} = \tau_0^{-1} + e^{-\Delta/T} \quad (2)$$

One can plot $\ln \tau^{-1}$ as a function of $1/T$ as shown in Fig. 11, which shows a good fit of a straight line. The slope of this graph will be Δ which turns out to be 1128 in temperature unit. It corresponds to 0.1 eV in energy unit. Since there are always contributions made by diffusion and excitation from deep impurity levels by the absorption of the signal beam, the above estimation represents the lower limit of the energy gap between the shallow level and the conduction band.

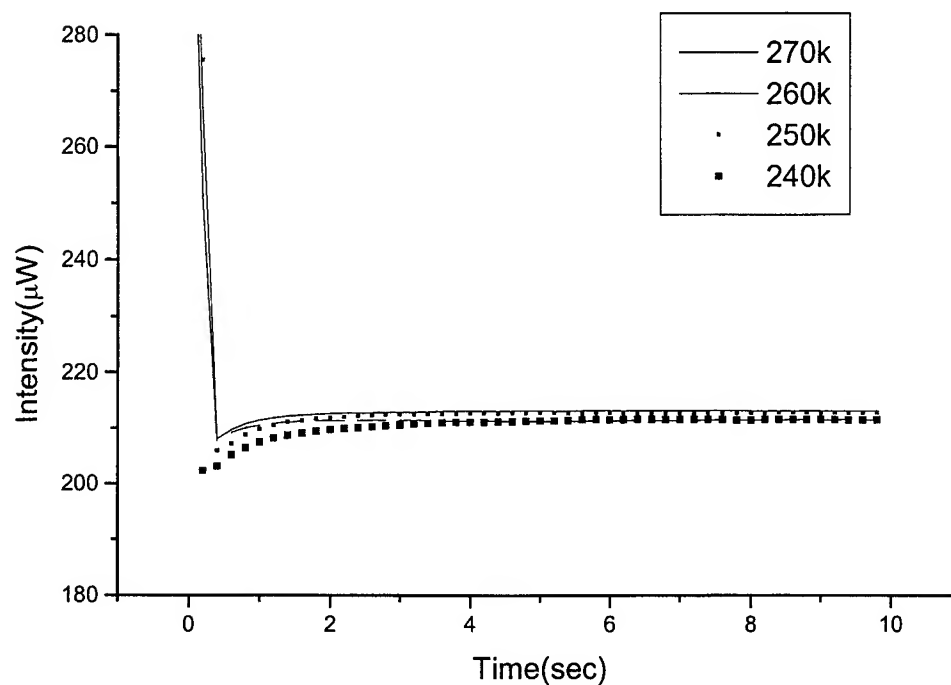


Fig. 8 Enlarged view of the dipped portion from Fig.4 through Fig.7

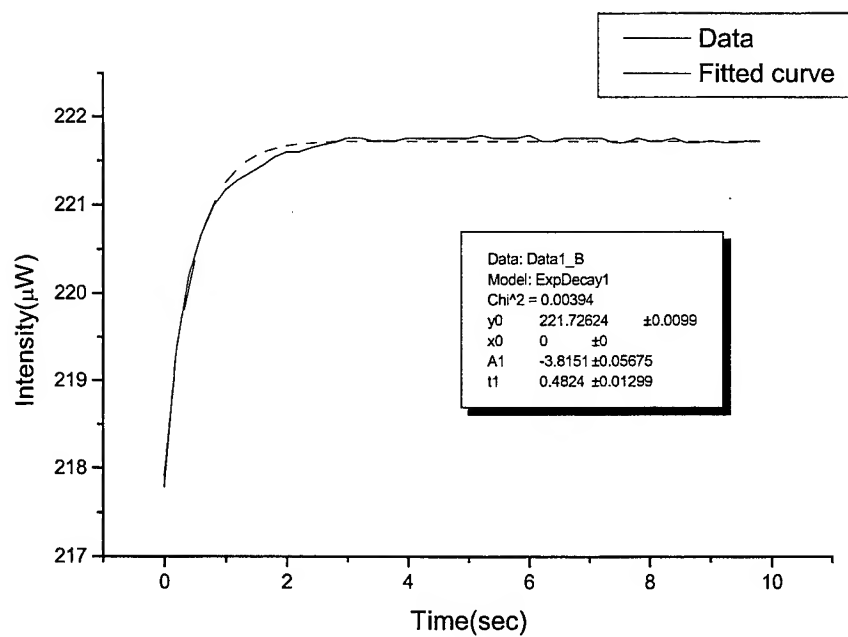


Fig.9 A typical exponential growth fit of one of the curve from Fig.8

T (°K)	ln(1/τ)	Error
270	0.659	0.04
260	0.469	0.03
250	0.294	0.015
240	0.134	0.035

Table.1 Time constant for various temperatures

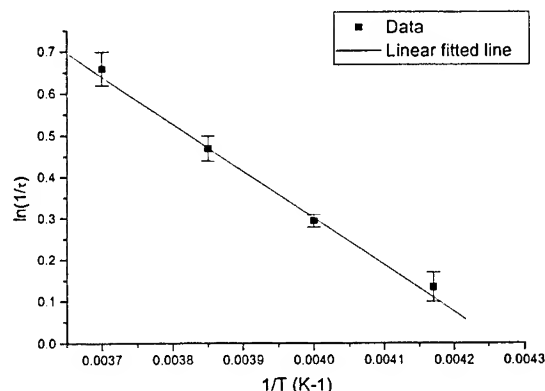


Fig 10 Linear line fit for the data listed in Table 1

4. Conclusions and Recommendations

From the above experimental results, we can make the following remarks:

- 1) We were able to estimate the lower limit of the location of the shallow energy level, which is about 0.1 eV in this crystal from the conduction band.
- 2) Our experiment did not tell whether we have performed the two-wave mixing in tetragonal phase or orthorhombic phase. We have to perform DSC experiments in order to answer this question. If we performed the experiment at tetragonal phase then the phase transition temperature reported in the literature (278 °K) was not observed in this experiment.

5. Acknowledgements

We are indebted to Prof. Ching-Chern Sun in the National Central University for his helpful discussions on this subject.

References:

- 1.P.Yeh " Introduction to photorefractive nonlinear optics ", John Wiley, New York (1993)
- 2.Hsiang T. Chen, ""Static and Dynamic Properties of Excitons in Tb(OH)₃", Master Thesis, University of Georgia, 1977

Study on the hysteresis effect of pH-ISFET based on Beckman Φ^{TM} 110 (Si_3N_4 gate pH-ISFET)

Jung-Chuan Chou*, Yu-Neng Tseng

Department of Electronic Engineering, National Yunlin University of Science and Technology, Touliu, Yunlin, Taiwan 640, R.O.C.

ABSTRACT

In this study, the commercial manufacture Beckman Φ^{TM} 110 (Si_3N_4 gate pH-ISFET) was acted as the sensitive membrane of pH-ISFET. The experimental results show that the Si_3N_4 material has a fairly high response, and the pH sensitivity was obtained 56.94 mV/pH in a concentration range between pH 1 and pH 11 at room temperature.

In our experiment, we use Keithley 236 Semiconductor Parameter Analyzer to measure the drain current (I_{DS}) versus gate voltage (V_G) curve of Si_3N_4 ISFET over a pH range from 1 to 11 at room temperature. The constant voltage-current circuit and time-voltage recorder were used to measure the hysteresis curve of Beckman Φ^{TM} 110 (Si_3N_4 gate pH-ISFET). The same procedure was also applied to a-Si:H gate pH-ISFET, which fabricated in our laboratory. From the I_{DS} versus V_G and hysteresis curve, we can obtain that the pH sensitivity was 56.94 mV/pH at constant temperature (25°C) and hysteresis widths of Beckman Φ^{TM} 110 (Si_3N_4 gate pH-ISFET) and a-Si:H gate pH-ISFET in the larger pH site are larger than in the smaller pH site, and the hysteresis width increased with the increasing loop time and measuring path.

Keywords: Beckman Φ^{TM} 110 (Si_3N_4 gate pH-ISFET), constant voltage-current circuit, hysteresis curve, hysteresis width.

1. INTRODUCTION

The ISFET was first reported by Bergveld in 1970,¹ which is an integrated device composed of a conventional ion selective electrode and a MOSFET. This device is similar to MOSFET except that the metal or polysilicon gate is replaced by sensing membrane and electrolyte solution in order to expose the sensing membrane to solution. The ISFETs have been widely applied in the field of the chemical and biomedical sensors due to the potential advantages over conventional ion-selective electrode in their rapid response, small size, low cost, high input impedance and low output impedance.²⁻⁵ However, they have been shown that the time dependent effects are major source of measurement error. These problems limited the progress of developing a commercial device. One of the time dependent effects, the hysteresis is a serious problem which results from slow response and drift.⁶⁻¹⁰

In this study, the commercial manufacture Beckman Φ^{TM} 110 (Si_3N_4 gate pH-ISFET) was selected as a pH sensitive material for the ISFET device, because it has high sensitivity for hydrogen ion. For the applications, the memory effect is one of the most important considerations. These memory effects can manifest themselves in various ways, such as hysteresis and drift⁷. In order to obtain the correct measuring for ISFET to pH sensitivity, the hysteresis of Si_3N_4 gate ISFET was measured in this paper. In addition, we can evaluate the pH sensitivity for Si_3N_4 gate ISFET by measuring the current versus voltage curve, another, the hysteresis effect, the ISFET device was operated in feedback mode of the constant voltage-current circuit to obtain the hysteresis curves.

2. EXPERIMENTALS

The device used in this work is the commercial manufacture Beckman Φ^{TM} 110 (Si_3N_4 gate pH-ISFET). We exposed the gate area (sensing membrane) to the standard pH solutions for measuring. In order to avoid the photoelectric and temperature effects, the device was placed in dark box at constant temperature (25°C) during the entire measuring processes.

Fig. 1 shows the I-V measuring system of Keithley 236 Semiconductor Parameter Analyzer, was used to measure the drain-source current (I_{DS}) versus gate voltage (V_G) curves of the commercial manufacture Beckman Φ^{TM} 110 (Si_3N_4 gate pH-ISFET). The pH sensitivity of the commercial manufacture Beckman Φ^{TM} 110 (Si_3N_4 gate pH-ISFET) was determined through the shift of the threshold voltage as shown in fig. 2. The operating drain to source current of pH-ISFET was fixed at $6 \mu A$, and then the sensitivity of 56.94 mV/pH at $25^\circ C$ was obtained indirectly as shown in fig. 3. Fig. 4 shows I_{DS} versus V_G curves of the commercial manufacture Beckman Φ^{TM} 110 (Si_3N_4 gate) ISFET at pH 7, I_{DS} was maintained at a constant value of $6 \mu A$. Then we can indirectly obtain the temperature coefficient at pH 7 which is shown in fig. 5. The data show that the Beckman Φ^{TM} 110 (Si_3N_4 gate) ISFET has linear values of approximately $-1.29 \text{ mV}^\circ C$ in a temperature range between $15^\circ C$ and $55^\circ C$. The above results show that the commercial manufacture Beckman Φ^{TM} 110 (Si_3N_4 gate pH-ISFET) has a linear pH sensitivity closed to the Nernstian response between pH 1 and pH 11. Next, the ISFET device was operated in the feedback mode which maintains a constant current ($I_{DS} = 17 \mu A$) as well as a constant voltage ($V_{DS} = 0.4V$). The response was reflected on the gate of ISFET, and the gate voltage was monitored and recorded by a V-T recorder (Data chart 3000 Voltage - Time recorder). Fig. 6 depicts the measurement setup, in order to obtain the output voltage of the ISFET, we choose one read out circuit shown in fig. 5.¹¹ From fig. 5,¹¹ we can see that one of two digital multi-meters was set at $I_{DS} = 17 \mu A$, and the other was set at $V_{DS} = 0.4V$, where the I_{DS} and V_{DS} are the current and voltage between the drain and source, respectively.

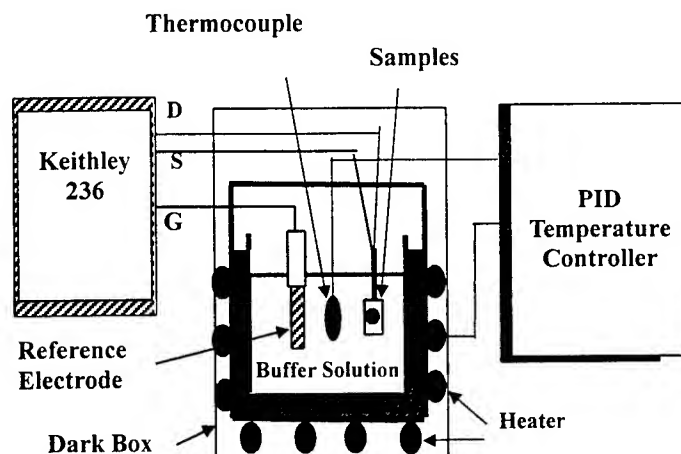


Fig. 1 I-V measuring system

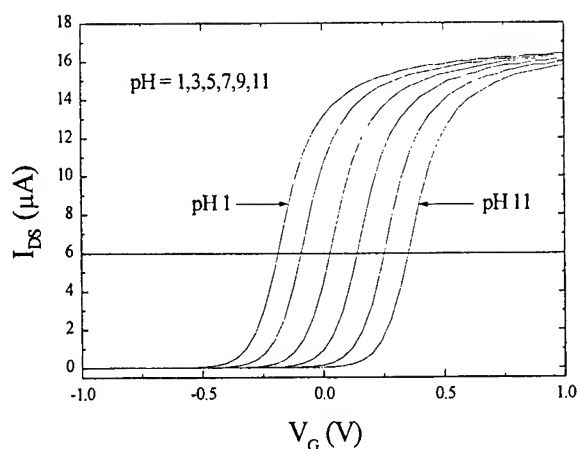


Fig. 2 I-V measurement of the commercial manufacture Beckman Φ^{TM} 110 (Si_3N_4 gate) pH-ISFET at $25^\circ C$

Clifford D. Fung *et al.*¹¹ recognized that the reference electrode was as the gate and connected to a measurement circuit with a digital voltage – time (V-T) recorder to provide output readings. The circuit shown in fig. 7 allows the drain voltage and current to be set by R1 and R2, respectively. The operational amplifier A2 provides a feedback so that the gate voltage V_G is varied during the hysteresis measurement. In this way, the drain current is maintained at a constant value set by the variable resistor R2.

The measuring system for the hysteresis is adopted with the following measurement conditions shown in table 1: $V_{DS} = 0.4V$; $I_{DS} = 17 \mu A$; pH loop = 7-3-7-11-7, 4-7-4 and 10-7-10; pH step = 1; loop time = 16min, 32min and 64min; temperature = 25 °C. For example, a pH loop was started, with the increment of one pH unit and extreme value of pH 3 and pH 11.⁷ The measured direction is acid first. We measured the hysteresis curve in different loop time such as 16min, 32min and 64min. The evolution of pH as a function of time was shown in fig. 8. Then the hysteresis widths were obtained in the pH 7-3-7-11-7, pH 4-7-4 and pH 10-7-10 loops. Finally, we have also compared the performance of different kinds of sensitive materials with the commercial Si_3N_4 gate for Beckman Φ^{TM} 110 pH-ISFET.

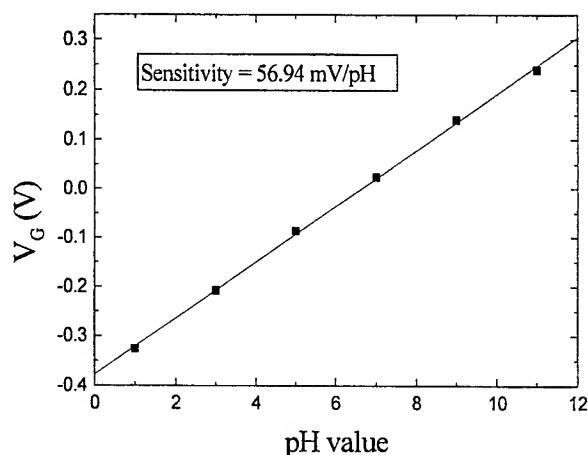


Fig. 3 Sensitivity of the commercial manufacture Beckman Φ^{TM} 110 (Si_3N_4 gate pH-ISFET) at 25°C

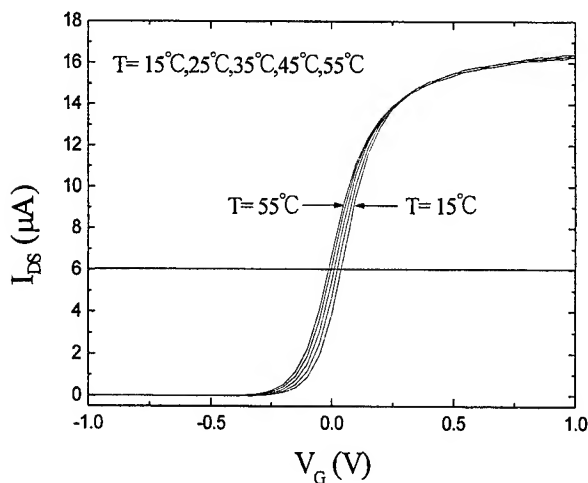


Fig. 4 I_{DS} versus V_G curves of the commercial manufacture Beckman Φ^{TM} 110 (Si_3N_4 gate) ISFET at pH 7

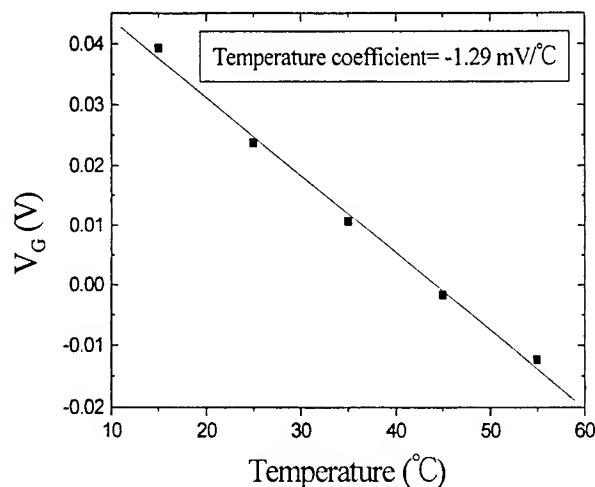


Fig. 5 V_G versus temperature characteristics of the commercial manufacture Beckman Φ^{TM} 110 (Si_3N_4 gate) ISFET at pH 7

3. RESULTS AND DISCUSSION

In the I-V measurement, the ISFET device and reference electrode were immersed in the different buffer solutions, a family of $I_{\text{DS}}-V_{\text{GS}}$ curves can be generated by applying a series of step voltage at the reference electrode. Then, the gate voltage of the commercial Si_3N_4 gate for Beckman Φ^{TM} 110 pH-ISFET was obtained, and the pH sensitivity of Si_3N_4 gate ISFET can be calculated from the gate voltage of device. According to the experimental results, the commercial Si_3N_4 gate for Beckman Φ^{TM} 110 pH-ISFET has a fairly high sensitivity in a concentration range between pH 1 and pH 11 at constant temperature (25°C), and it is found that the sensitivity is 56.94 mV/pH.

The hysteresis of the commercial Si_3N_4 gate for Beckman Φ^{TM} 110 pH-ISFET in a pH loop (pH 7→3→7→11→7), at various loop time with 16min, 32min and 64min are 2mV, 3mV and 4mV, respectively. Fig. 9 shows that the hysteresis curves at loop time of 32min. From fig. 9, we can't see the hysteresis width clearly, therefore we transfer fig. 9 to fig. 10. Fig. 10 shows that the residual plot of hysteresis curves at loop time of 32min. The data show the hysteresis width is 3 mV. Fig. 11 shows the residual plot of hysteresis curves at loop time of 16min, 32min and 64min. By the way, the hysteresis widths in the pH 4→7→4 and 10→7→10 at various loop time such as 16min, 32min and 64min are 1mV, 2mV, 3mV, 1mV, 3mV and 5mV, respectively.

According to the mentioned above, the acid-side hysteresis is smaller than the alkaline -side hysteresis, and the hysteresis width is increasing with loop time and measuring path. Due to the different size of H^+ and OH^- ions, the diffusion of H^+ ions to the buried site is faster than diffusion of OH^- ions, as described by T. Mikolajick *et al.*¹² This causes the asymmetric hysteresis of pH-ISFET. Additionally, the hysteresis of the commercial manufacture Beckman Φ^{TM} 110 (Si_3N_4 gate pH-ISFET) compared with Si_3N_4 ,⁶ Ta_2O_5 ,⁷ Al_2O_3 ⁸ and a-Si:H¹⁰ gate ISFET were shown in table 2. The data show that the Si_3N_4 gate pH-ISFET in the ref.6 have more hysteresis width than the commercial manufacture Beckman Φ^{TM} 110 (Si_3N_4 gate pH-ISFET), Ta_2O_5 ,⁷ Al_2O_3 ,⁸ and a-Si:H¹⁰ sensing membranes. The hysteresis of Ta_2O_5 is less than 2 mV, and according to the Luc Bousse *et al.*⁷ mentioned, the order of hysteresis magnitude is $\text{Si}_3\text{N}_4 > \text{Al}_2\text{O}_3 > \text{Ta}_2\text{O}_5$. Therefore, the hysteresis effect of the commercial manufacture Beckman Φ^{TM} 110 (Si_3N_4 gate pH-ISFET) is well.

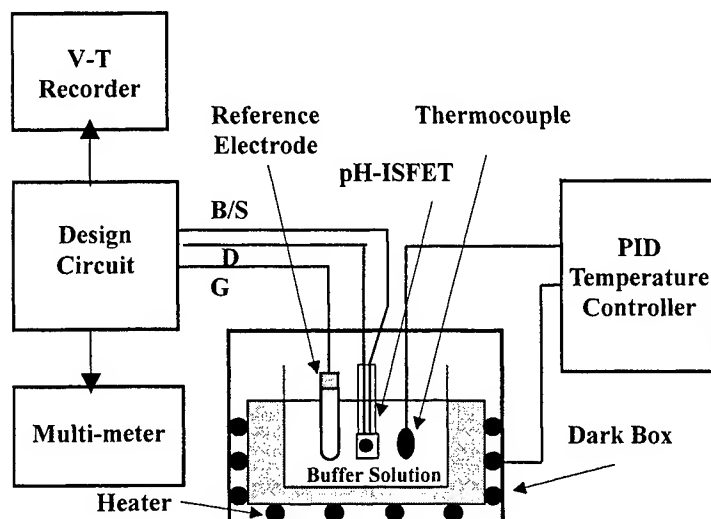


Fig. 6 Diagram of the measurement setup

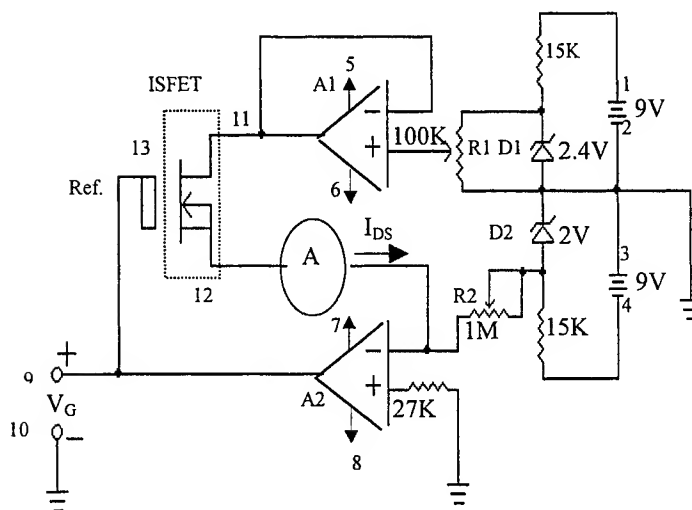


Fig. 7 Schematic diagram of the read out circuit¹¹.

Table 1 Conditions for measuring hysteresis

Parameters	Amount
V_{DS}	400mV
I_{DS}	17 μ A
pH loop	7-3-7-11-7, 4-7-4 and 10-7-10
pH step	1
Loop time	16min, 32min and 64min
Temperature	25°C

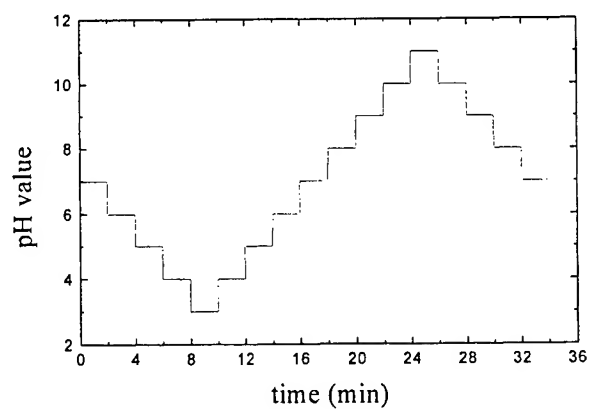


Fig. 8 Evolution of pH as a function of time during a example of the raw data for a measurement with a loop time 32min, 2min per step

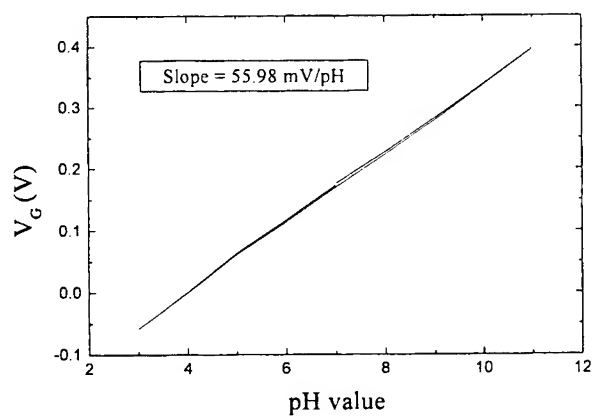


Fig. 9 Hysteresis curve for loop time of 32min

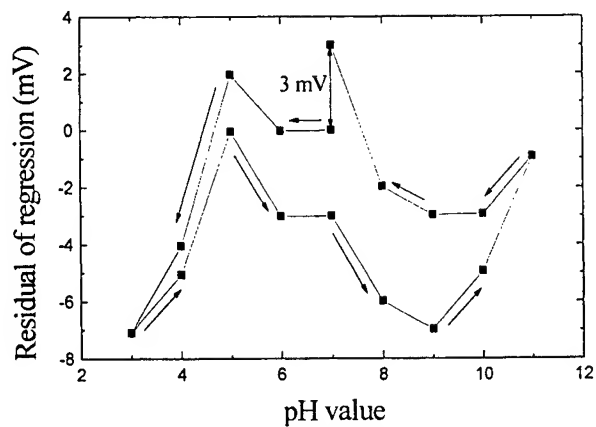


Fig. 10 Residual plot of hysteresis curve for loop time of 32min

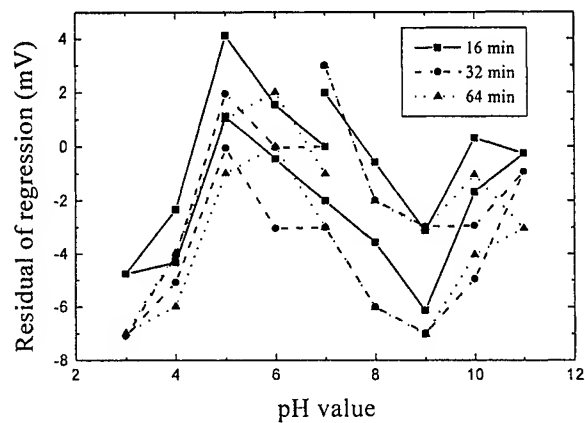


Fig. 11 Residual plot of hysteresis curves for various loop time

Table 2 Comparison results of the hysteresis for the different kinds of pH-ISFETs

Gate insulator	Hysteresis (mV)	Loop time (min)
Si ₃ N ₄ (measured) pH 7-3-7-11-7	2	16
Si ₃ N ₄ (measured) pH 7-3-7-11-7	3	32
Si ₃ N ₄ (measured) pH 7-3-7-11-7	4	64
Si ₃ N ₄ (measured) pH 4-7-4	1	16
Si ₃ N ₄ (measured) pH 4-7-4	2	32
Si ₃ N ₄ (measured) pH 4-7-4	3	64
Si ₃ N ₄ (measured) pH 10-7-10	1	16
Si ₃ N ₄ (measured) pH 10-7-10	3	32
Si ₃ N ₄ (measured) pH 10-7-10	5	64
Si ₃ N ₄ [6] pH 7-3-7-11-7	7.1	92
Al ₂ O ₃ [8] pH 8-3-8-11-8	4.2	155
Ta ₂ O ₅ [7] pH 7-3-7-11-7	4.0	160
a-Si:H[10] pH 4-2-4-6-4	3.1	144

4. CONCLUSIONS

Owing to the pH sensitivity is a decisive factor which affects the response of an ISFET device. In addition, the hysteresis is the non-ideal and unstable factor of ISFET devices for measuring. Hence, in this study, the pH sensitivity, temperature coefficient and hysteresis of the commercial manufacture Beckman Φ^{TM} 110 (Si_3N_4 gate pH-ISFET) are investigated. We could summary as follows:

1. In this study, the commercial manufacture Beckman Φ^{TM} 110 (Si_3N_4 gate pH-ISFET) which has a high pH sensitivity about 56.94 mV/pH in a concentration range between pH 1 and pH 11 at constant temperature (25°C) and temperature coefficients from pH 1 to 11 and pH = 7 are -1.29 mV/°C in a temperature range between 15°C and 55°C.
2. The hysteresis effect of the commercial Si_3N_4 gate for Beckman Φ^{TM} 110 pH-ISFET shows that the acid-side hysteresis is smaller than that of alkaline-side hysteresis, the hysteresis width increases with increasing loop time in the range of 16-64min during the pH 7→3→7→11→7, pH 4-7-4 and pH 10-7-10 cycles. They also find that the hysteresis width is dependent on measuring loop time and measuring path.
3. According to the compared results, the commercial manufacture Beckman Φ^{TM} 110 (Si_3N_4 gate pH-ISFET) has large sensitivity, linear response, and lower hysteresis effect etc., therefore it is attractive and suitable for ion-sensing membrane of ISFET device in the acid and alkaline environment.

ACKNOWLEDGMENTS

This work is supported by National Science Council, the Republic of China under the contracts NSC89-2815-C-224-021.

REFERENCES

1. P. Bergveld, "Development of an ion-sensitive solid-state device for neurophysiological measurements", IEEE Trans. Biomed. Eng., vol. BME-17, pp. 70-71, 1970.
2. A. Topkar and R. Lal, "Effect of electrolyte exposure on silicon dioxide in electrolyte-oxide-semiconductor structures", Thin Solid Films, 232, pp. 265-270, 1993.
3. B. D. Liu, Y. K. Su and S. C. Chen, "Ion-sensitive field-effect transistor with silicon nitride gate for pH sensing", Int. J. Electronics, vol. 67, pp. 59-63, 1989.
4. P. Bergveld, "Future applications of ISFETs", Sensors and Actuators B, 4, pp. 125-133, 1991.
5. Tadayuki Matso and Masayoshi Esashi, "Method of ISFET fabrication", Sensors and Actuators, 1, pp. 77-79, 1981.
6. Luc Bousse, Dean Hafeman and Nancy Tran, "Time-dependent of the chemical response of silicon nitride surfaces", Sensors and Actuator, B1, pp. 361-367, 1990.
7. Luc Bousse and Shahrar Mostarshed, "Comparison of the hysteresis of Ta_2O_5 and Si_3N_4 pH-sensing insulator", Sensors and Actuator B, 17, pp. 157-164, 1994.
8. Luc Bousse, H. H van der Vlekkert and N. F. de Rooij, "Hysteresis in Al_2O_3 -gate ISFETs", Sensors and Actuators B, 2, pp. 103-110, 1990.
9. P. Woias, L. Meixner, P. Frostl, "Slow pH response effects of silicon nitride ISFET sensors", Sensors and Actuator B, 48, pp. 501-504, 1998.
10. Jung Chuan Chou and Ching Nan Hsiao, "The hysteresis and drift effect of hydrogenated amorphous silicon for ISFET sensor", Proceedings of Technical Digest of the 7th International Meeting on Chemical Sensors, Beijing International Convention Center, Beijing, China, pp. 553-555, July 27-30, 1998.
11. Clifford D. Fung, Peter W. Cheung, and Wen H. Ko, "A generalized theory of an electrolyte-insulator-semiconductor field-effect transistor", IEEE Transactions on Electron Devices, vol. ED-33, No. 1, pp. 8-18, 1986.
12. T. Mikolajick, R. Kuhnhold, H Ryssel, "The ISFET-sensing properties of tantalum pentoxide films fabricated by metal organic low pressure chemical vapor deposition", Sensors and Actuators B, 17, pp. 262-267, 1994.

*Correspondence : E-mail: choujc@pine.yuntech.edu.tw; Telephone: (8865) 5342601 Ext. 2500, 4333
Fax: (8865) 5312029

Study on the sensitivity and hysteresis behaviour of the commercial Sentron 1090 Al_2O_3 gate pH-ISFET

Jung Chuan Chou^{*}, Chen Yu Weng

Department of Electronic Engineering, National Yunlin University of Science and Technology, Touliu, Yunlin, Taiwan 640, R.O.C.

Abstract

In this study, we utilize the commercial device, Sentron 1090 Al_2O_3 gate pH-ISFET to study the sensitivity and hysteresis behaviour. The experimental results show that the Al_2O_3 materials have a fairly high response, and the sensitivity was obtained from the pH response of Sentron 1090.

The hysteresis effect in a Sentron 1090 Al_2O_3 gate pH-ISFET was studied by exposing the device to two cycles of pH values. The hysteresis curves were measured in the sequence pH 8-3-8-11-8 and pH 7-3-7-11-7 at different loop time. According to experimental results, the hysteresis width is increasing with loop time and measuring path.

We also observed and compared the pH sensitivity and magnitude of the hysteresis width with others pH-sensing gate ISFETs studied in our laboratory and the related literatures.

Keywords: 1090 Al_2O_3 gate pH-ISFET, sensitivity, hysteresis, response

1. Introduction

The first ion-sensitive field effect transistor (ISFET) was fabricated by Bergveld[1]. The difference between ISFET and MOSFET is that there is no metal gate electrode in the former. Silicon dioxide (SiO_2) was first used as a pH-sensitive membrane for the ISFET. After this, Al_2O_3 [2,3], Si_3N_4 [4-6], Ta_2O_5 [7,8], SnO_2 [9,10] and a-Si:H[11] were used as pH-sensitive membranes because of the higher pH response. Although the ion-sensitive FETs (ISFETs) are attractive chemical sensors for many reasons, for instance, small size, low cost, high input impedance [12-14] and low output impedance, the progress in developing a commercially viable device has been quite slow.

When P. Bergveld first introduced ISFET[1], the device was operated without a reference electrode. However, later work by other investigators indicates that proper operation of ISFET requires a reference electrode to establish the electrolyte potential with respect to the semiconductor substrate[15]. The schematic representation of an ISFET device with reference electrode and sensing membrane is shown in Fig. 1. For applications, memory effect (i.e., slow response after a pH change) is one of the most important considerations, and hysteresis behavior is affected by slow response. This property limits the accuracy of ISFET. Up to now, there has been a research about the pH sensitivity and hysteresis behavior of a-Si:H[11] and a- Ta_2O_5 [18] in our laboratory. In this paper, we will continue to study the hysteresis phenomenon for the commercial Sentron 1090 Al_2O_3 gate pH-ISFET. We also compare the results with others pH sensing gate ISFETs studied in our laboratory and related literatures [4-6, 11, 18].

^{*}corresponding author: Dr. Jung Chuan Chou

Tel:(8865) 5342601 Ext.2500

Fax:(8865) 5312029

E-mail: choujc@pine.yuntech.edu.tw

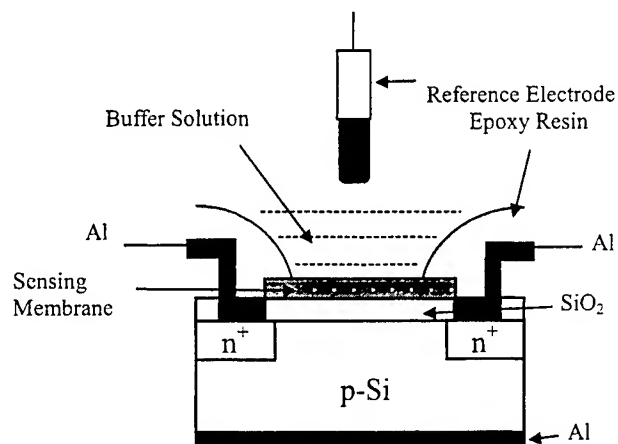


Fig.1 Schematic representation of an ISFET device

2. Experimental Methods

Measurement procedure of the hysteresis

Afterward we measured the I-V curves of device to investigate the relationship between pH values of solution and ISFET using the Keithley 236 semiconductor parameter analyzer.

Fig. 2 shows the diagram of the hysteresis measurement setup, and the hysteresis widths were obtained in the pH 7-3-7-11-7 and pH 8-3-8-11-8 loops. Finally, we have also compared the performance of different kinds of sensitive materials with the commercial Sentron 1090 Al_2O_3 gate thin film. Since the Sentron 1090 Al_2O_3 gate pH-ISFET is easily influenced by light illumination, especially gate region [16]. During measurement, the Sentron 1090 Al_2O_3 gate pH-ISFET was kept in the dark box.

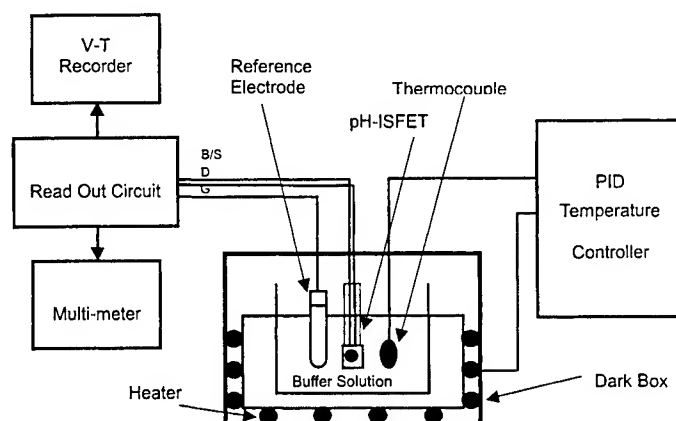


Fig. 2 Diagram of the measurement setup

The drain voltage was set at 0.2 V so that the ISFET device could be operated in the linear region. According to Zone Yule et al. [17], the surface response of ISFET would be stable after 5 h from pH variation. Therefore, we would calculate the shift of ISFET from 5 h to 12 h to gain the hysteresis of ISFET.

Clifford D. Fung *et al.* [15] recognized that the reference electrode was as the gate and connected to a measurement circuit with a digital V-T recorder to provide output readings. The circuit shown in Fig. 3 allows the drain voltage and current to be set by R_1 and R_2 , respectively. The operational amplifier A_2 provides a feed-back so that the gate voltage V_G is varied during the hysteresis measurement. In this way, the drain current is maintained at a constant value set by the variable resistor R_2 . The drain current was set from $100\mu\text{A}$ to 1mA . For the operating drain current from $100\mu\text{A}$ to 1mA , the response is found to be essentially independent of the operating current. The pH step of the pH loop is one pH unit and the extreme values are pH 3 and pH 11. The measured direction is lower pH in acid first. We measured the hysteresis curves in different loop time such as 960s, 1920s and 3840s. The evolution of pH as a function of time was shown in Fig. 4.

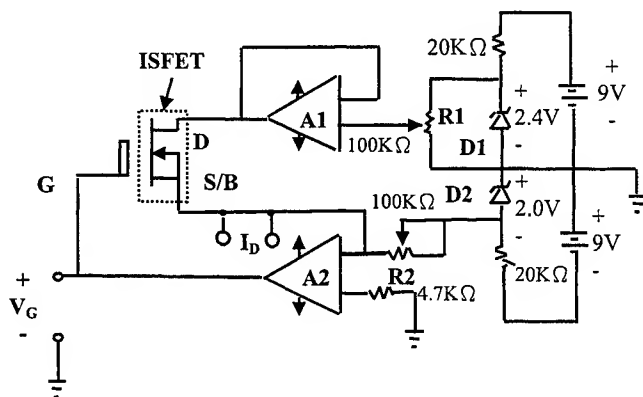


Fig. 3. Schematic diagram of the measurement circuit [15].

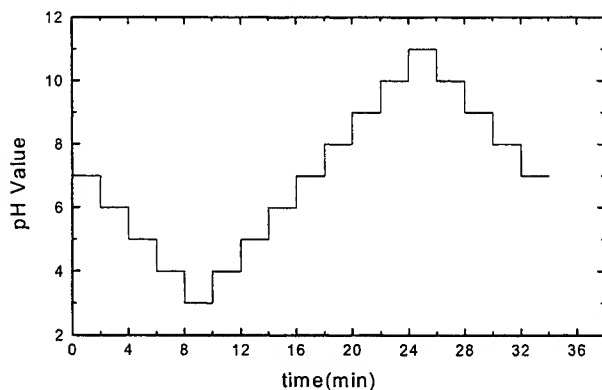


Fig. 4 Evolution of pH as a function of time during an example of the raw data for a measurement with a loop time 32 min (1920s), 2 min per step.

3. Results and Discussion

Comparison results of the sensitivity for the Sentron 1090 Al_2O_3 , a-Si:H and a-Ta₂O₅ gate pH-ISFETs

We can obtain the pH sensitivity of Sentron 1090 Al_2O_3 gate pH-ISFET at 25 °C, which is shown in Fig. 5. The pH sensitivity of Sentron 1090 Al_2O_3 gate pH-ISFET is 53.23 mV/pH at 25 °C. In our laboratory, we ever obtain the pH sensitivity of a-Si:H pH-ISFET at 25 °C, which is shown in Fig. 6[11]. The pH sensitivity of a-Si:H gate-pH ISFET at 25 °C is 50.62 mV/pH. And we ever obtain the pH sensitivity of a-Ta₂O₅ pH-ISFET at 25 °C, which is shown in Fig. 7[18]. The pH sensitivity of a-Ta₂O₅ gate-pH ISFET at 25 °C is 59.38 mV/pH. These pH sensitivities for different temperatures are shown in Table I, II and III.

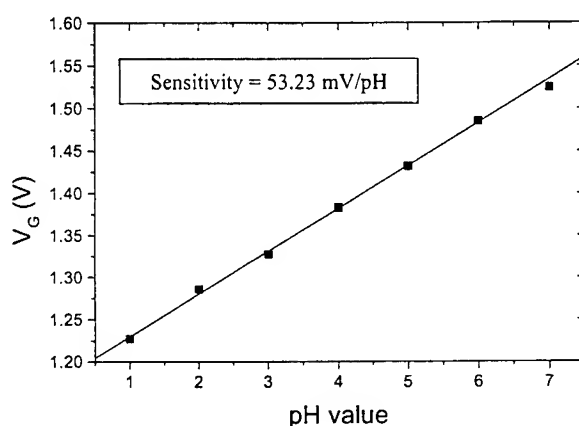


Fig. 5. V_G versus pH characteristics of Sentron 1090 Al_2O_3 gate pH-ISFET at 25 °C

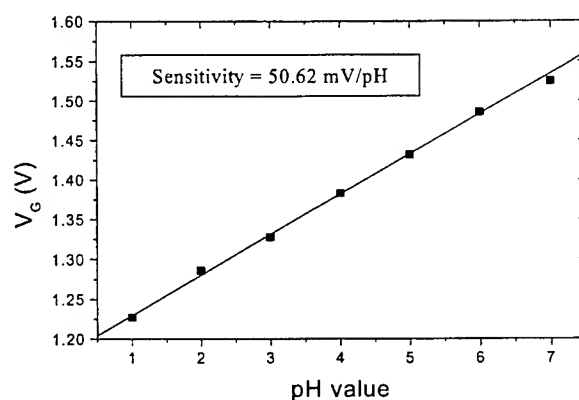


Fig. 6. V_G versus pH characteristics of a-Si:H gate pH-ISFET at 25 °C

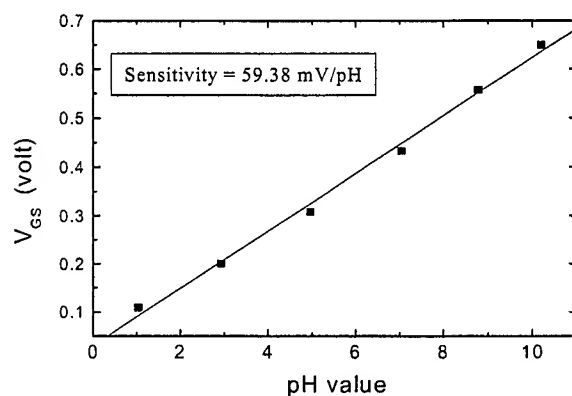


Fig. 7. V_G versus pH characteristics of a- Ta_2O_5 gate pH-ISFET at 25 °C

From Table I to Table III, we can observe that the pH sensitivity is increased with increasing temperature. The pH sensitivities of Sentron 1090 Al_2O_3 gate pH-ISFET for 25-55 °C (step 10 °C) are 53.23 mV/pH, 54.50 mV/pH, 59.99 mV/pH, and 61.92 mV/pH, respectively. The pH sensitivities of a-Si:H gate pH-ISFET for 25-55 °C (step 10 °C) are 50.62 mV/pH, 52.83 mV/pH, 54.21 mV/pH, and 58.36 mV/pH, respectively. The pH sensitivities of a- Ta_2O_5 gate pH-ISFET for 25-55 °C (step 10 °C) are 59.38 mV/pH, 62.87 mV/pH, 63.04 mV/pH, and 64.24 mV/pH, respectively. From the above results, we can obtain the sensitivities of all the Sentron 1090 Al_2O_3 , a-Si:H and a- Ta_2O_5 gate pH-ISFETs are higher than 50 mV/pH at different temperatures.

Table I pH sensitivities at different temperatures of Sentron 1090 Al_2O_3 gate pH-ISFET

Temperature(°C)	25	35	45	55
pH sensitivity (mV/pH)	53.23	54.50	59.99	61.92

Table II pH sensitivities at different temperatures of a-Si:H[11]

Temperature(°C)	25	35	45	55
pH sensitivity (mV/pH)	50.62	52.83	54.21	58.36

Table III pH sensitivities at different temperatures
of a-Ta₂O₅[18]

Temperature(°C)	25	35	45	55
pH sensitivity (mV/pH)	59.38	62.87	63.04	64.24

Hysteresis of Sentron 1090 Al₂O₃ gate pH-ISFET

The hysteresis curves of Sentron 1090 Al₂O₃ gate pH-ISFET in a pH loop pH 7-3-7-11-7 at various loop time with 960s is 4mV. Fig. 8 to Fig. 10 show that the hysteresis width is larger on the basic side than that of on the acid side. Due to the different size of H⁺ and OH⁻ ions, the diffusion of H⁺ ions to the buried site is faster than diffusion of OH⁻ ions.

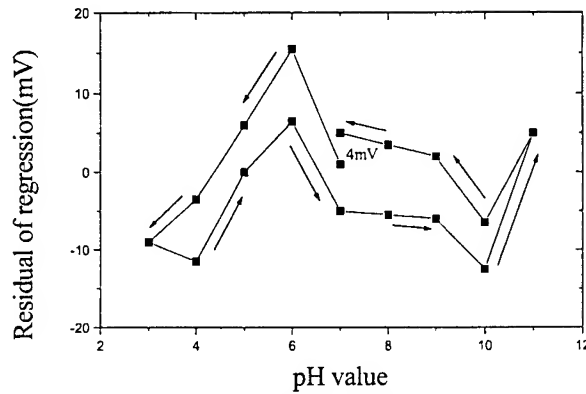


Fig. 8 Residual plot of hysteresis curves
for Sentron 1090 Al₂O₃ gate pH-
ISFET at loop time

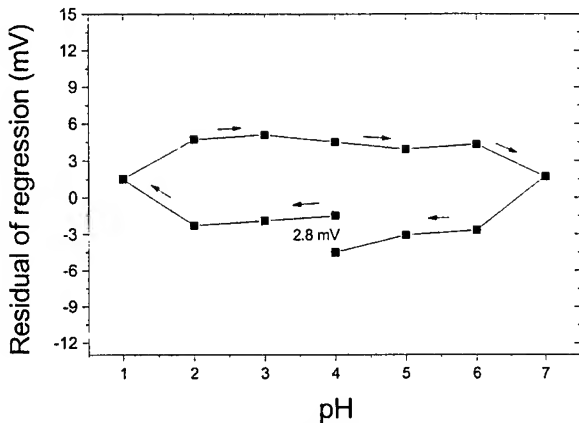


Fig. 9 Residual plot of hysteresis curves
for a-Si:H gate pH-ISFET at loop
time

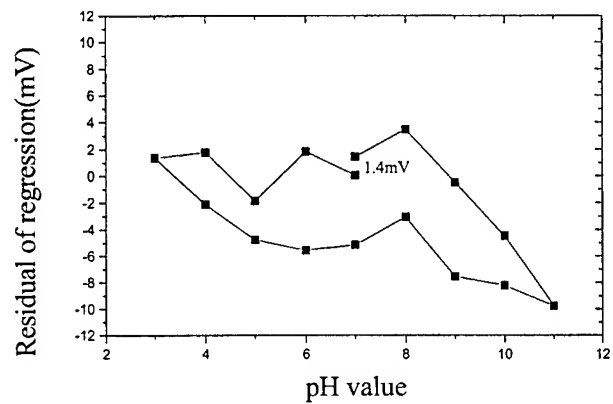


Fig. 10 Residual plot of hysteresis curves
for a-Ta₂O₅ gate pH-ISFET at
loop time

Comparison results of the hysteresis for Sentron 1090 Al_2O_3 , a-Si:H and a-Ta₂O₅ gate pH-ISFETs

Table IV compares the hysteresis of the four materials. Sentron 1090 Al_2O_3 gate pH-ISFET (pH7-3-7-11-7, loop time is 16 min), Sentron 1090 Al_2O_3 gate pH-ISFET (pH pH 8-3-8-11-8, loop time is 16 min), a-Si:H (pH 4-1-4-7-4, loop time is 16 min), Si_3N_4 (pH 7-3-7-11-7, loop time is 16 min), a-Ta₂O₅ (pH 7-3-7-11-7, loop time is 16 min), respectively. It can be evidenced by the comparison results of the Ching Nan Hsiao et al.[19] and experiment of this study. As the results of comparison above, the Sentron 1090 Al_2O_3 gate pH-ISFET is suitable for the insulator of pH-ISFET in the acid pH region (pH 3 – pH 11), the a-Si:H is suitable for the insulator of pH-ISFET in the acid pH region (pH 1 – pH 7)[11], and the a-Ta₂O₅ is suitable for the insulator of pH-ISFET in the acid pH region (pH 3 – pH 11)[18]. The hysteresis of pH sensing gate ISFETs is between 1.4 ~ 4 mV which is in the stable range.

Table IV Comparison results of the hysteresis of Sentron 1090 Al_2O_3 , a-Si:H, Si_3N_4 and Ta₂O₅ gate pH-ISFETs

Gate insulator	Hysteresis (mV)	Loop time (sec)
Sentron 1090 pH 7-3-7-11-7	4	960
Sentron 1090 pH 8-3-8-11-8	2	960
a-Si:H[11] pH 4-1-4-7-4	2.8	960
Si_3N_4 [4-6] pH 7-3-7-11-7	2	960
a-Ta ₂ O ₅ [18] pH 7-3-7-11-7	1.4	960

4. Conclusion

In this paper, we have investigated the non-ideal phenomena of the Sentron 1090 Al_2O_3 gate pH-ISFET. In summary, we can conclude and compare others gate materials.

1. The pH sensitivity of Sentron 1090 Al_2O_3 gate pH-ISFET is proportional to operating temperature. The pH sensitivities for 25-55 °C (step 10 °C) are 53.23 mV/pH, 54.5 mV/pH, 59.99 mV/pH, and 61.92 mV/pH, respectively. The sensitivities of both the a-Si:H and a-Ta₂O₅ gate pH-ISFETs are also higher than 50 mV/pH.
2. For the hysteresis phenomenon, the hysteresis of the Sentron 1090 Al_2O_3 gate pH-ISFET of 2 to 4 mV is obtained in the pH 8-3-8-11-8 and pH7-3-7-11-7 loops.

From the above information, the sensitivity of the Sentron 1090 Al_2O_3 gate pH-ISFET is higher than 50 mV/pH. Besides, its sensitive curve is linear, and has lower hysteresis effect. The hysteresis of pH sensing gate ISFETs is below 4 mV which can agree with the rule of stability so that the pH sensing gate ISFETs can be applied to the membrane of the pH-ISFET. To compare with Sentron 1090 Al_2O_3 gate pH-ISFET, both the a-Si:H and a-Ta₂O₅ designed by our laboratory can also be made as commercial devices.

Acknowledgments

The authors acknowledge the financial support of the National Science Council of Republic of China under grant NSC 89-2215-E-224 -003.

References

- [1]P. Bergveld, "Development of an Ion-Sensitive Solid-State Device for Neurophysiological Measurements", IEEE Trans. Biomed. Eng., vol BME-17 (1970) 70~71.
- [2]L. Bousse, H. H van der Vlekkert and N. F. de Rooij, "Hysteresis in Al_2O_3 -gate ISFETs", Sensors and Actuators B, 2 (1990) 103-110.
- [3]H. van den Vlekkert, L. Bousse and N. de Rooij, "The Temperature Dependence of the Surface Potential at the Al_2O_3 /Electrolyte Interface", Journal of Colloid and Interface Science, 122 (1988) 336-345.
- [4]L. Bousse, S. Mostarshed, B. van der Schoot and N. F. de Rooij, "Comparison of the Hysteresis of Ta_2O_5 and Si_3N_4 pH-Sensing Insulators", Sensors and Actuators B 17 (1994) 157-164.
- [5]D. L. Harame, L. J. Bousse, J. D. Shott and J. D. Meindl, "Ion-Sensing Devices with Silicon Nitride and Borosilicate Glass Insulators", IEEE Trans. Electron Devices, ED-34 (1987) 1700-1706.
- [6]M. N. Niu, X. F. Ding and Q. Y. Tong, "Effect of Two Types of Surface Sites on the Characteristics of Si_3N_4 -gate pH-ISFETs", Sensors and Actuators, B 37 (1996) 13-17.
- [7]A. S. Poghossian, "The Super-Nernstian pH Sensitivity of Ta_2O_5 -gate ISFETs", Sensors and Actuators B, 7 (1992) 367-370.
- [8]D. H. Kwon, B. W. Cho, C. S. Kim and B. K. Sohn, "Effect of Heat Treatment on Ta_2O_5 Sensing Membrane for Low Drift and High Sensitivity pH-ISFET", Sensors and Actuators B, 34 (1996) 441-445.
- [9]H. K. Liao, J. C. Chou, W. Y. Chung, T. P. Sun and S. K. Hsiung, "Study of Amorphous Tin Oxide Thin Films for ISFET Applications", Sensors and Actuators B, 50 (1998) 104-109.
- [10]H. K. Liao, J. C. Chou, W. Y. Chung, T. P. Sun and S. K. Hsiung, "Study of Amorphous Tin Oxide Thin Films for ISFET Applications", Sensors and Actuators B, 50 (1998) 104-109.
- [11]J. C. Chou, J. S. Lin, "pH Response of a-Si:H ISFET", Proceeding of SPIE Vol. 3897 – The International Symposium on Photonics and Applications (ISPA'99), Nanyang Technological University, Singapore. (1999) 758-766.
- [12]A. Topkar and R. Lal, "Effect of Electrolyte Exposure on Structures", Thin Solid Films, 232 (1993) 265-270.
- [13]B. D. Liu, Y. K. Su and S. C. Chen, "Ion-Sensitive Field Effect Transistor with Silicon Nitride Gate for pH Sensing", Int. J. Electronics, 1 (1989) 59-63.
- [14]Tadayuki Matso and Masayoshi Esashi, "Method of ISFET Fabrication", Sensors and Actuators, 1(1981) 77-79.
- [15]C.D. Fung, P. W. Cheung and W. H. Ko, "A Generalized Theory of an Electrolyte-Insulator -Semiconductor Field-Effect Transistor", IEEE Trans. Electron Devices, vol. ED-33 (1986) 8-18.
- [16]Pavel Neuzil, "ISFET Integrated Sensor Technology", Sensors and Actuators B", vol. 24-25 (1995) 232-235.
- [17]Z.Y. Zhao Shouan, and Lin Tao, "Drift Characteristics of pH-ISFET Output." Chinese Journal of Semiconductors, vol Dec., 838-834 (1994).
- [18]J.C Chou and K.Y Huang, "Study on the Drift and Hysteresis of pH-ISFETs with Amorphous Tantalum Pentoxide Gate Insulator", Conference on Chinese Medicine and Pharmacy, Engineering Technology and Applications to Chinese and Western Medicine, China Medical College, Taichung, Taiwan, R.O.C. (1999) 101-102.
- [19]J.C Chou and C.N Hsiao, "The Hysteresis and Drift Effect of Hydrogenated Amorphous Silicon for ISFET Sensor", Sensors and Actuator B, (accepted) (2000).

Study on the temperature dependence of the hysteresis for the a-Si:H gate pH-ISFET

Jung Chuan Chou*, Hsjian-Ming Tsai and Yii-Fang Wang

Institute of Electronic and Information Engineering, National Yunlin University
of Science and Technology, Touliu, Yunlin, Taiwan 640, R.O.C.

ABSTRACT

In application of the pH-ISFET, the hysteresis and temperature effects are two important influences of accuracy. There have been many studies about the above subjects, however, the hysteresis behaviour will change with the temperature and affect the reproducibility of the devices. Hence, we study the temperature dependence of the hysteresis behaviour for the pH-ISFET with a-Si:H gate insulator deposited by the PE-LPCVD system in this paper. The thickness of the a-Si:H was about 2000 Å. The temperature is controlled by the P.I.D. temperature controlled system and the hysteresis behaviour is measured by the constant voltage-constant current circuit and voltage-time recorder. The measurement is completed at 25 °C, 35°C, 45°C and 55°C and the time after the pH changed is 4 min. The experimental results also compared with other materials of the gate insulator for pH-ISFET at the room temperature.

Keywords: A-Si:H gate pH-ISFET, Hysteresis, Temperature effect.

1. INTRODUCTION

In 1969, it was proved that the a-Si:H membrane could use low RF power in SiH₄ by R. C. Chittick *et al.*[1]. The advantages of this method are low cost device-quality thin-film material, low power deposition, at low substrate temperatures and depositing on substrates of almost any shape, size, or composition. Thus, the a-Si:H is extensively used for photoelectric materials.

When the pH-ISFET (ion sensitive field effect transistor) was commercialized, making cheaper and better devices became a major study objective. The advantages of a-Si:H membranes deposited by RF power of the plasma-enhanced low pressure chemical vapor deposition (PE-LPCVD) are low cost and easy deposition. If the a-Si:H is used as the ion sensitive layer of a pH-ISFET, the cost of the ion sensors will decrease. However, a number of inherent drawbacks still exist in ISFET sensor measurements, which handicap wide application of ISFET sensors, such as temperature effect, drift and hysteresis, which influence the accuracy and reproducibility for the measurement.

According to Luc Bousse *et al.*[2], many surfaces (Si₃N₄, Al₂O₃ and Ta₂O₅, for instance) have a pH response that is close to Nernstian, which means that the amplitude of the pH response is not a decisive factor for the pH-ISFET. For our applications, the memory effect (i.e., slow response after a pH change) is one of the most important considerations. This memory effect can manifest itself in various ways, such as hysteresis or apparent drift, and constitute important limitations in many other applications.

Based on the surface site-binding theory [3], there are also models ascribing the hysteresis mechanism to the insulator bulk. Among them (1) model based on the pH dependent variation of the Si/SiO₂ surface state density is caused by a transport of hydrogen bearing species released at the SiO₂/electrolyte interface [4] and (2) models based on the assumption that the gel-like conducting layer is formed in the outer (near-surface) insulator bulk under the exposedness of the surface to solution [5, 6]. Summarizing, the hysteresis is mainly ascribed to the bulk mechanisms of the electrolyte/insulator interaction. The most frequently used explanation for the hysteresis phenomenon is presence of the buried sites.

There has been research on the pH sensitivity [6], temperature effects [8], drift behaviour [9] and hysteresis behaviour [10] of the hydrogenated amorphous silicon in our group. We will continue to study the temperature dependence of the hysteresis phenomenon for the a-Si:H gate pH-ISFET.

Correspondence: Dr. Jung Chuan Chou E-mail: Choujc@pine.yuntech.edu.tw Tel: 886-5-5342601 ext.2500
Fax: 886-5-5312029, 5312063

2. EXPERIMENTAL

2.1 Device fabrication and I-V measurement

The hydrogenated amorphous silicon (a-Si:H) which was fabricated using plasma-enhanced low-pressure chemical vapor deposition was used as a transistor pH-ISFET and the fabrication conditions are shown in Table 1. We chose RF power 30W and substrate temperature 210°C to fabricate the a-Si:H thin film. The structure of the a-Si:H gate pH-ISFET is shown in Fig. 1, where the thickness of the a-Si:H is 2000Å and SiO₂ is 1000Å, the channel is 50 μm long and 1000 μm wide. The power for the ion implantation in the drain and source region was 80 KeV, the dose density was 10¹⁵ cm⁻². The resistance for drain to source under no bias applied on gate is 7.5 × 10⁴ Ω. Because the a-Si:H film could easily be hydrolyzed in an alkali solution, all measurements were finished in an acid solution.

Table 1. Fabrication conditions of a-Si:H gate ISFET.

Fabrication Conditions	
Substrate Temperature(°C)	210
Gas Pressure(torr)	0.7
RF Power(W)	30
Silane Flow(SCCM)	108
Silane/H ₂ Ratio	1/9

2.2 Measurement setup

The hysteresis behaviours of a-Si:H gate pH-ISFETs were measured with a temperature controlled system, as shown in Fig. 2. The electrolyte solution was the standard buffer solution and the P.I.D. temperature controller controlled the temperature of the buffer solution. A glass reference electrode and one a-Si:H gate pH-ISFET were immersed in the buffer solution. In order to gain the output voltage of pH-ISFET, we chose one circuit design shown in Fig. 3 [11]. One of two digital multimeters was used to measure the I_{DS}, the other measured the V_{DS}, where the I_{DS} and V_{DS} are the current and voltage between the drain and source, respectively. The measuring parameters are shown in Table 2. The drain voltage was set at 0.2 V so that the pH-ISFET device could operate in the linear region.

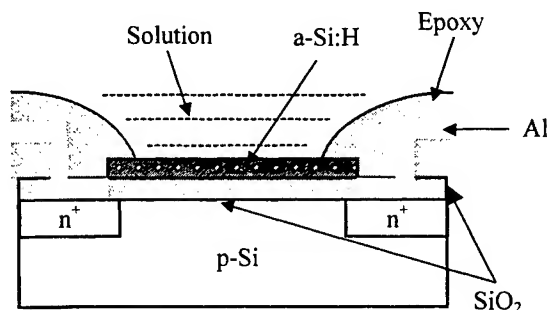


Fig. 1 Structure of a-Si:H gate pH-ISFET.

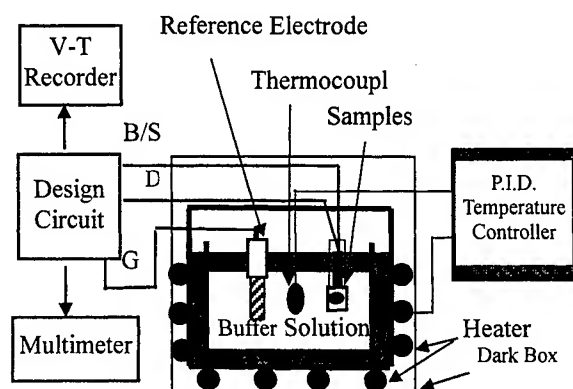


Fig.2 Diagram of the drift and hysteresis measurement set-up.

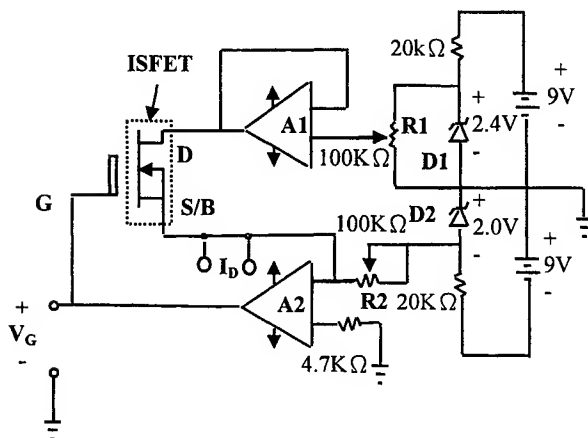


Fig.3 Schematic diagram of the measurement circuit.

Clifford D. Fung *et al.* [11] recognized that the reference electrode was as the gate and connected to a measurement circuit with a digital voltage – time (V-T) recorder to provide output readings. The circuit shown in Fig. 3 allows the drain voltage and current to be set by R1 and R2, respectively. The operational amplifier A2 provides a feedback so that the gate voltage V_G is varied during the drift measurement. In this way, the drain current is maintained at a constant value set by the variable resistor R2. The drain current was set from $30\mu\text{A}$ to $100\mu\text{A}$. For the operating drain current from $30\mu\text{A}$ to $100\mu\text{A}$, the response was found to be essentially independent of the operating current.

Table 2 Experimental conditions for response measurements.

Parameters	Amount
pH step	1
pH loop	pH 4→pH 1→pH 4→pH 7→pH 4
Loop time	3120s
I_D	$80\mu\text{A}$
V_D	200mV
Temperature	25°C , 35°C , 45°C , 55°C

2.3 Measurement procedure of hysteresis

In general cases, the hysteresis can be defined as: When the sequence of the measurement for the device is $pH_x \rightarrow pH_y \rightarrow pH_z \rightarrow pH_x$, the difference between the output of the first pH_x and final pH_x is the hysteresis value [2, 12, 13]. The measurement setup for hysteresis measurement is shown in Fig. 2. The pH step of the pH loop is one pH unit and the extreme values are pH 1 and pH 7. Using the P.I.D. temperature controller at 25°C, 35°C, 45°C and 55°C. The measured direction was lower pH in acid first and the loop time for the hysteresis measurement was 3120s. The pH evolution as a function of time is shown in Fig. 4.

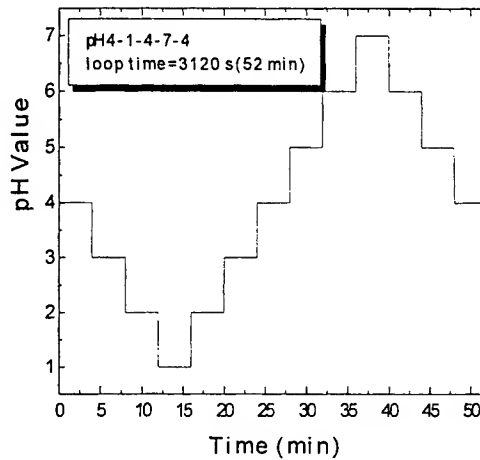


Fig. 4 Evolution of pH as a function of time during a example of the raw data for a measurement with a loop time 52 min (3120s), 4min per step.

3. RESULTS AND DISCUSSION

3.1 I-V characteristic of the a-Si:H gate pH-ISFET

Fig. 5 shows the I_{DS} versus V_G characteristic curves of the a-Si:H pH-ISFET ranging pH 1 to 7 at 25 °C. In Fig. 5, I_{DS} was maintained at a constant value of $80 \mu A$, in order to simulate the mechanism of constant current measuring circuit. Then we can obtain the relationship between V_G and pH value at 25 °C, which shown in Fig. 6. The slope of Fig. 6 is the pH sensitivity of a-Si:H pH-ISFET, which is 50.62 mV/pH. According to Fig. 5, we can observe that the gate voltage of a-Si:H pH-ISFET shift positively as pH value increases. These results imply that the surface potential (ϕ_0) decreases with increasing pH value.

3.1 Results of the hysteresis at different temperature

The hysteresis of a-Si:H gate pH-ISFET in a pH loop $pH 4 \rightarrow 1 \rightarrow 4 \rightarrow 7 \rightarrow 4$, at loop time with 3120s is 2.3mV for 25°C (Fig. 7), 4mV for 35°C (Fig. 8), 7mV for 45°C (Fig. 9) and 9mV for 55°C (Fig. 10). Fig. 11 is the temperature coefficient of the hysteresis (TCH) for a-Si:H gate pH-ISFET which is about 0.235 mV/°C. The results indicate that the hysteresis is

increase with the temperature, i.e. when the temperature of buffer solution being increased, the grade concentration of OH^- increased.

According to the Luc Bousse et al.[14], bulk diffusion mechanism was excluded due to divergence between pH fast response on a pH step and low diffusion coefficients for hydrogen ions even for pH which is not the best insulator. However, the immediate response is followed by the slow response. This fact was ascribed to penetration of water into the silica layer and formation SiOH groups near the surface. These groups are called buried sites. It was stated that in spite of the number of buried sites was small in comparison to the number of surface sites, but its increase after long time contact with water, might explain decrease of the pH sensitivity. Another observation based on experimental data was a convergence between low sensitivity and high hysteresis. It was finally concluded that the presence of buried sites might correlated with hysteresis. Hence, the SiOH groups near the a-Si:H is also existent, and it will increase with OH^- concentration and time for the device immersed in the solution. It can explain how the hysteresis behaviour was clearer at higher temperature, because the higher OH^- concentration will be appeared.

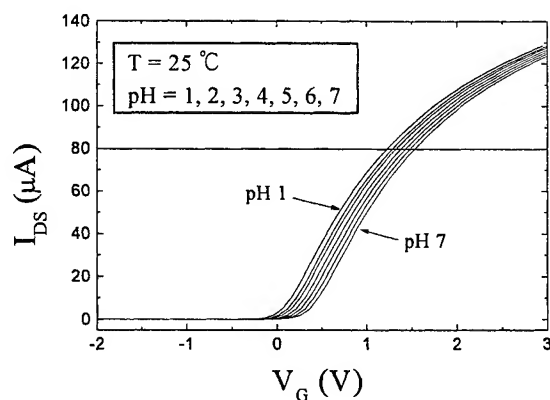


Fig. 5. I_{DS} versus V_G curves of the a-Si:H ISFET at 25 °C

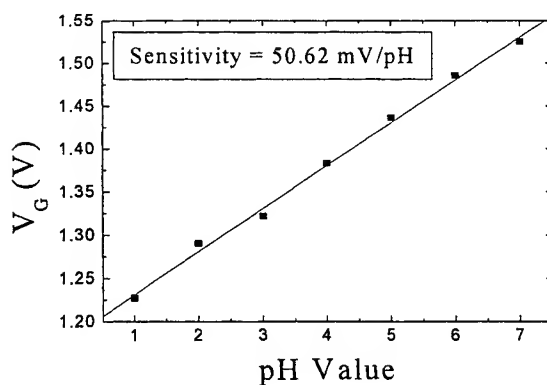


Fig. 6. V_G versus pH characteristics of the a-Si:H ISFET at 25 °C

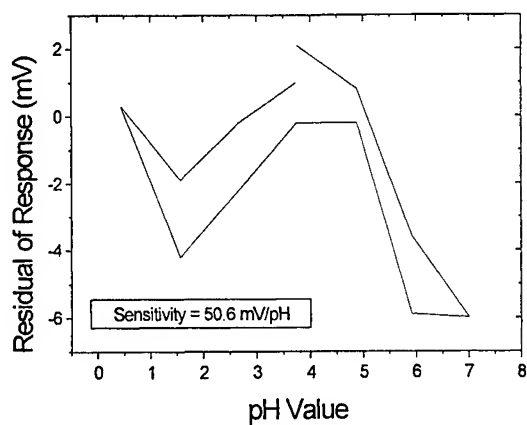


Fig. 7 Residual plot of hysteresis curves for a-Si:H gate pH-ISFET at loop time of 3120s (25°C).

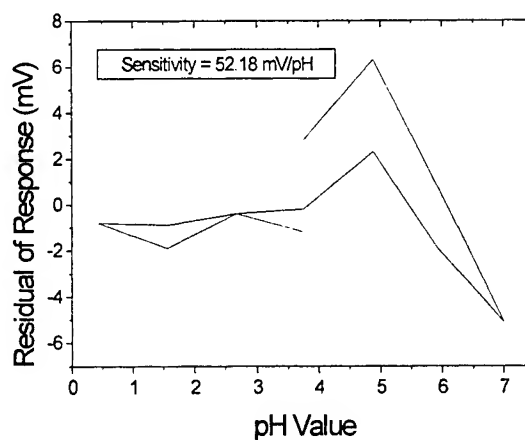


Fig. 8 Residual plot of hysteresis curves for a-Si:H gate pH-ISFET at loop time of 3120s (35°C).

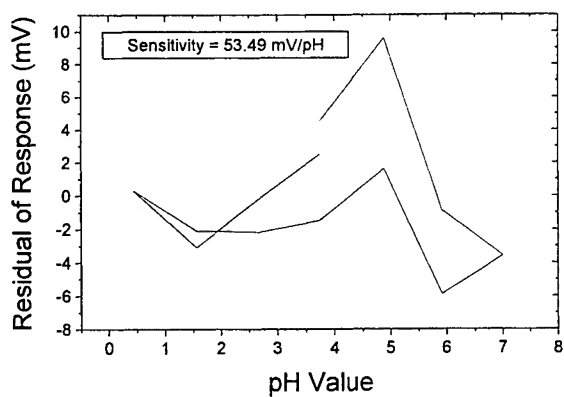


Fig. 9 Residual plot of hysteresis curves for a-Si:H gate pH-ISFET at loop time of 3120s (45°C).

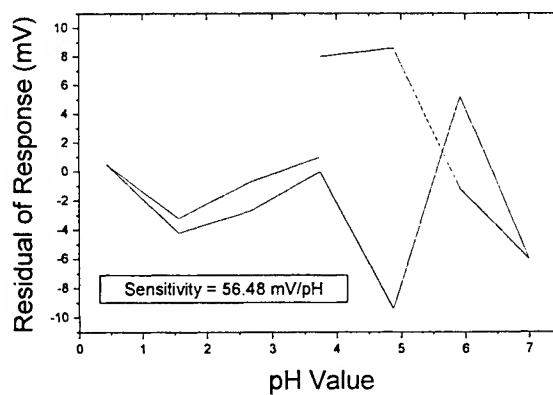


Fig. 10 Residual plot of hysteresis curves for a-Si:H gate pH-ISFET at loop time of 3120s (55°C).

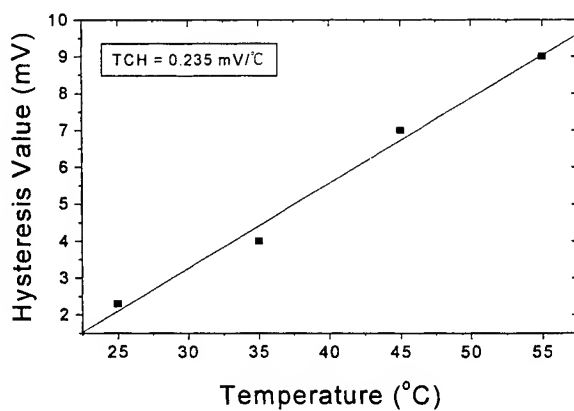


Fig. 11 Curves of sensitivity versus temperature for the a-Si:H pH-ISFET

It also can be shown that the hysteresis is more obvious in higher pH value range from Fig. 5 ~ Fig.8, which can be explained by different dominant potential-determining ions: H^+ and OH^- for two pH ranges, acidic and basic, respectively. In the case of buried sites, the reaction of proton exchange depends on diffusion of hydrogen ions and hydroxyl groups through the insulator, which tends to be slower for groups than for hydrogen ions.

3.2 Comparison results of the hysteresis with other materials

Table 5 compares the hysteresis of the four sensitive materials. The hysteresis magnitudes are 3 mV, 22.3 mV, 4.2mV, 4.0mV, 3.4 mV and 7.1 mV for a-Si:H(measured in this paper), a-Si:H[10] (pH 4 – 2 – 4 – 6 – 4, loop time is 144 min), a- Al_2O_3 [12] (pH 8 – 3 – 8 – 11 – 8, loop time is 155 min), a- Ta_2O_5 [2] (pH 7 – 3 – 7 – 11 – 7, loop time is 160 min), a- Ta_2O_5 [15] (pH 7 – 3 – 7 – 11 – 7, loop time is 64 min) and a- Si_3N_4 [2] (pH 7 – 3 – 7 – 11 – 7, loop time is 92 min), respectively. It can be seen that in this study that the hysteresis behaviour of the measured a-Si:H gate pH-ISFET is smaller than the others, which indicates that the reproducibility of the a-Si:H is good in that measurement. According to Luc Bousse *et al.*[2], the hysteresis would have larger magnitude at longer measuring time. It can be evidenced by the comparison results of Ching Nan Hsiao *et al.*[10] and the experiment in this study. Moreover, the cost of the a-Si:H is lower than the others. this indicates the a-Si:H is suitable for the gate material of pH-ISFET in the acid pH region (pH 1 – pH 7).

Table 3 Comparison results of the hysteresis of for the different sensitive gate materials in room temperature.

Gate insulator	Hysteresis (mV)	Loop time (min)
A-Si:H (measured in this paper) pH 4-1-4-7-4	2.2	52
A-Si:H [10] pH 4-2-4-6-4	22.3	144
Al_2O_3 [12] pH 8-3-8-11-8	4.2	155
Ta_2O_5 [2] pH 7-3-7-11-7	4.0	160
Ta_2O_5 [15] pH 7-3-7-11-7	3.4	64
Si_3N_4 [2] pH 7-3-7-11-7	7.1	92

4. CONCLUSION

In this study, the hysteresis of a-Si:H gate pH-ISFET in a pH loop pH 4→1→4→7→4, at loop time with 3120s is 2.3mV for 25°C, 4mV for 35°C, 7mV for 45°C and 9mV for 55°C. The temperature coefficient of the hysteresis (TCH) for a-Si:H gate pH-ISFET which is about 0.235 mV/°C. The results indicate that the hysteresis is increase with the temperature, i.e. when the temperature of buffer solution being increased, the grade concentration of OH^- increased. It also can be shown that the hysteresis is more obvious in higher pH value range. In the case of buried sites, the reaction of proton exchange depends on diffusion of hydrogen ions and hydroxyl groups through the insulator, which tends to be slower for groups than for hydrogen ions. In the comparison of the a-Si:H with other gate materials for the gate insulator of the pH-ISFET, The hysteresis would have a larger magnitude at longer measuring time and the reproducibility of the a-Si:H is well within the measurement that can be proved. This also indicates that the a-Si:H is suitable for the application of pH-ISFET in acid solution.

Acknowledgment

This work was supported by the National Science Council of The Republic of China under grant NSC 89-2215-E-224-003.

4. REFERENCES

- [1] R.C. Chittick, J.H. Alexander and H.F. Sterling. "The preparation and properties of amorphous silicon." J. Electrochem. Society Solid State Science, 116, 77-79 (1969).
- [2] Luc Bousse and Shahriar Mostarshed, "Comparison of the hysteresis of Ta₂O₅ and Si₃N₄ pH-sensing insulators", Sensors and Actuators B, vol. 17, 157-164. (1994).
- [3] D. E. Yates, S. Levine and T. W. healy, "Site-binding model of the electrical double layer at the oxide/water interface", J. Chem. Soc. Faraday Trans1, 70, 1807-1818 (1974).
- [4] N. F. de Rooji, P. Bergveld, "The influence of the pH on the surface state density at the SiO₂-Si interface", Proc. of Int. Topical Conf., (ed. S.T. Pantelides), Yorktown Heights, New York, March 22-24, 433 (1978).
- [5] I. R. Laukus, J. N. Zemel, "The si₂n₄/Si ion-sensitive semiconductor electrode, IEEE Trans. On El. Dev., ED-26, 12, 1979 (1959).
- [6] J. Lyklema, "The structure of the electrical double layer on porous surfaces", J. Electroanal. Chem., 18, 479 (1968).
- [7] Ching Nan Hsiao, Jung Chuan Chou, "Study the pH sensitivity of hydrogenated amorphous silicon", Proceedings of 1997 Annual Symposium of the Biomedical Engineering Society, Chung-Li, Chung Yuan Christian University, 58-59 (1997).
- [8] Jung Chuan Chou, Yii Fang Wang, Jin Sung Lin, "Temperature effect of a-Si:H pH-ISFET", Sensors and Actuators B, Vol. 62, 92-96 (2000).
- [9] Chou, J. C.; Hsjian Ming Tasi, Ching Nan Shiao, Jin Sung Lin, "Study and simulation of the drift behaviour of hydrogenated amorphous silicon gate pH-ISFET", Sensors and Actuators B, Vol. 62, 91-101 (2000)
- [10] Jung Chuan Chou, Ching Nan Hsiao, "The hysteresis and drift effect of hydrogenated amorphous silicon for ISFET sensor", Proceedings of Technical Digest of the 7th International Meeting on Chemical Sensors (IMCS-7), Beijing International Convention Center Beijing, China, July 27-30, 553-555 (1998).
- [11] Clifford D. Fung, Peter W. Cheung, and Wen H. Ko, "A generalized theory of an electrolyte-insulator- semiconductor field-effect transistor," IEEE Transactions on Electron Devices, vol. ED-33, No. 1, 8-18 (1986).
- [12] Luc Bousse, H. H. Van Den Vlekkert and N. F. De Rooij, "Hysteresis in Al₂O₃-gate ISFETs", Sensors and Actuators B, vol. 2, 103-110 (1990).
- [13] Aine Garde, John Alderman and Willian Lane, "Improving the drift and hysteresis of the Si₃N₄ pH response using RTP technique", Sensors and Materials, vol. 9, No. 1, 15-23 (1997).
- [14] Luc Bousse, P. Bergveld, "The role of buried OH sites in the response mechanism of inorganic-gate pH-sensitive ISFETs", Sensors and Actuators, 6, 65-78 (1984)
- [15] Jung Chuan Chou, Kai Ye Huang, "Simulation of time-dependent effects of pH-ISFETs", Sensors and Actuators B, 62, 88-91 (2000).

Compact laser sources for the photorefractive researches

Junewen Chen^{a,b}, Tzu-Chiang Chen^b, Hong-Chang Kung^b, Hon-Fai Yau^b,
Chao-Chia Cheng^b, Hung-Sheng Tsai^b and Hai-Pei Liu^b

^aE-O Section, Chung-Shan Institute of Science and Technology,
Lung-Tan, Taiwan 325, R. O. C.

^bInstitute of Optical Sciences, National Central University,
Chung-Li, Taiwan 320, R. O. C.

ABSTRACT

Phase conjugate phenomenon and mechanism with BaTiO₃ photorefractive crystals have been investigated using various cw sources and all the way down with ultrashort pulses of the femtosecond region. Our laser sources support all the various pulsewidths at a wide range of different spectral regions.

Key words: Phase conjugation, photorefractive effect, ultrashort pulse lasers,

1. INTRODUCTION

Phase conjugate waves have long been investigated because they are useful in many fields such as phase conjugated lasers, interferometry and optical signal processing. Conjugator made with photorefractive crystal especially has attract great interest of research due to the simplicity in the setup and the convenience in applications.

Conjugators making use of photorefractive crystals can be classified into two categories in terms of their mechanism for the generation of the conjugated waves. Degenerate four-wave mixing (DFWM) method to generate the conjugate waves is the first kind, and the stimulated photorefractive back scattering is the second kind.

The CAT conjugator developed by Feinberg⁽¹⁾ is the typical kind of DFWM. CAT type conjugators with nanosecond pulses have been reported by Monson et al.⁽²⁾ and Damzen et al.⁽³⁾. The pulse widths in these cases are on the order of meters, so that the pulses can be folded in the crystal several times. Accordingly, DFWM has been considered to be the mechanism underlying the phenomenon. Picosecond photorefractive phase conjugation has been first investigated by Cronin-Golomb et al.⁽⁴⁾. We have also reported phase conjugation with picosecond Ti:sapphire laser pulses in BaTiO₃⁽⁵⁾, self-pumped phase conjugation with femtosecond pulses by use of BaTiO₃⁽⁶⁾, and mechanism for ultrashort phase conjugate pulses with photorefractive crystals⁽⁷⁾ etc.. Yau et al. are the premier and the important research group that studies the photorefractive phase conjugation with CW sources⁽⁸⁾ and all the way down with ultrashort pulses to the femtosecond region. The laser center in the Institute of Optical Sciences, NCU, Taiwan, supports all the various pulsewidth laser sources as well as at different spectral regions.

2. LASER SOURCES FOR THE PHOTOREFRACTIVE RESEARCHES

Compact laser sources for the photorefractive researches include most of the solid state lasers, the liquid lasers and the gaseous lasers.

2.1 Solid state lasers

Nd:YAG solid state lasers both of cw output and pulsed output are used extensively. The output wavelength of the

frequency doubled cw Nd:YAG laser is 532 nm, which is near to the output wavelength of the Ar⁺ laser of 514 nm, and they are all in the visible region. Quadruple frequency at 266 nm is also obtainable from the Nd:YAG laser output. The pulsed Nd:YAG lasers of nanosecond Q-switched output(3 ns ~ 20 ns), of picosecond mode-locked pulses in the Q-switched envelope output(~180 ps)⁽⁹⁾, and dispersion compensated short picosecond pulses output(~10 ps) are the most typical and compact solid state laser sources. Fig. 1 shows the configuration of the dispersion compensated short picosecond Nd:YAG laser.

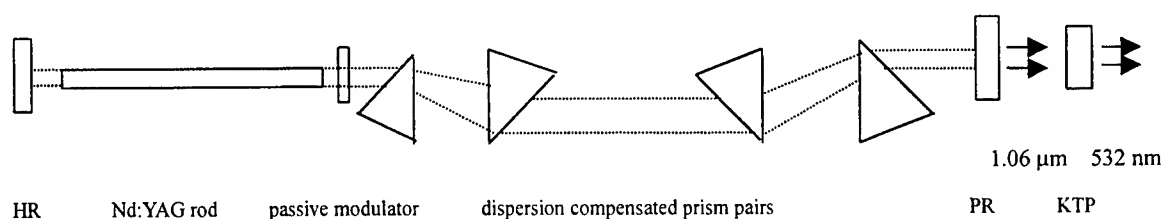


Fig. 1. The configuration of the dispersion compensated short picosecond Nd:YAG laser.

Diode pumped miniature Nd:YVO₄ lasers at output of 1.06 μm, are the advanced compact solid state lasers widely used nowadays. Ruby laser out bursts at 694.3 nm and with nanosecond pulsewidth is another available solid state laser. Tunable Alexandrite solid state laser(700 nm ~ 818 nm) is also a convenient and popular photorefractive research source. Er³⁺:glass laser that out burst at the eye-safe wavelength of 1.54 μm with nanosecond pulsewidth extended the spectral coverage of the solid state laser photorefractive researches from the visible wavelength to the near infrared region.

Moreover, the Ti:sapphire solid state laser is the most versatile laser that is tunable from 700 nm to over 1000 nm and the laser out bursts could be in the cw mode as well as in the pulsed mode with picosecond and ultrashort femtosecond pulsewidth(typically < 50 fs). Fig. 2 shows the configuration of a typical ultrashort pulse output of the Ti:sapphire laser. If we removed the prisms pair therefore the resonator oscillated with mirror M₁ in stead of M₁', and the mode-locking fold of M₅ · SA(saturable absorber) and M₄ as well, this Ti:sapphire laser is another typical cw output laser source. Our Ti:sapphire solid state lasers were pumped by a frequency doubled Nd:YAG solid state lasers we have in our laser center.

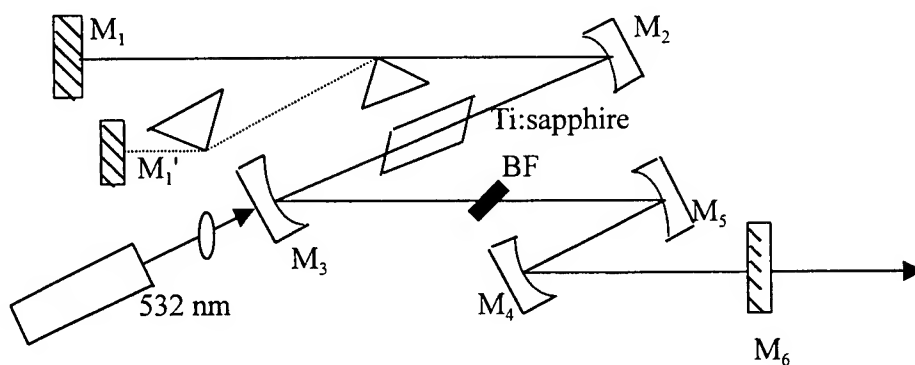


Fig. 2. The configuration of a typical ultrashort pulses output of the Ti:sapphire laser.

Fig. 3. Shows the multiple frequency up conversion of the Ti:sapphire solid state laser pumped by the frequency doubled Nd:YAG solid state laser. The output laser wavelengths of less than 200 nm could be obtained by using the OPG(optical parametric generation) technique. The solid state Nd:YAG lasers not only are useful photorefractive sources but can also be used as very effective pump source of the Ti:sapphire solid state laser.

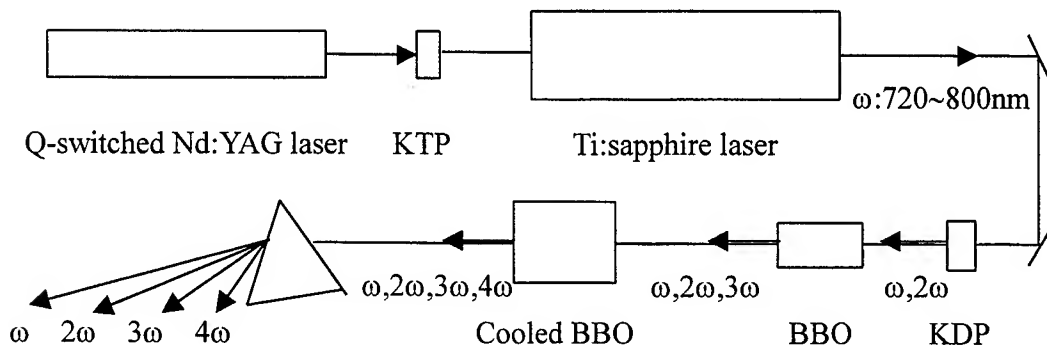


Fig. 3. 4ω generation of the Ti:sapphire laser pumped by the frequency doubled Nd:YAG solid state laser

Below in Fig. 4, shows the typical medium power output of the solid state lasers spectral coverage for the photorefractive researches with various pulsed laser outputs at different pulsewidth in two dimensions figure.

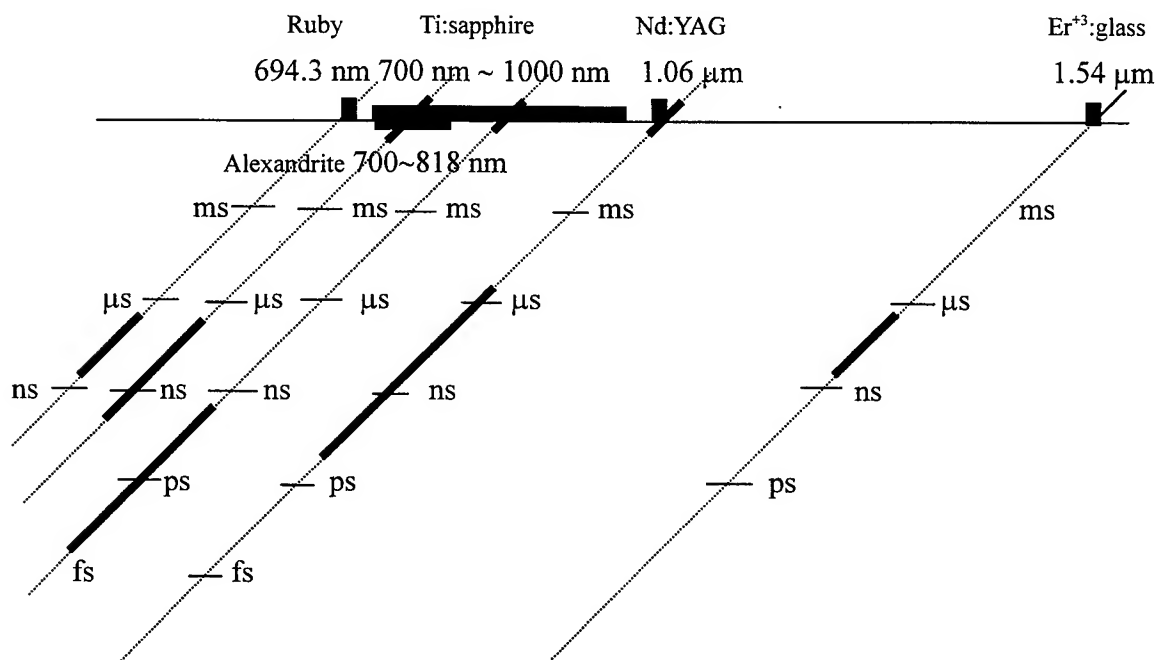


Fig. 4. The solid state lasers spectral coverage for the photorefractive researches with various laser outputs at different pulsewidth in two dimensions figure.

2.2 Liquid lasers

We have two dye lasers, C102/DOC1 and Rh 6G/DODCI dye lasers. The Coumarin 102 dye laser is a cw laser tunable between 493 nm and 502 nm. Fig. 5(a) shows a four mirrors cavity cw C102 liquid dye laser. If the passive dye jet of DOC1 saturable absorber together with two pairs of the dispersion compensated prisms were added to the resonator, constructs a CPM(colliding pulse mode-locking) ring laser resonator, as shown in Fig. 5(b), ultrashort laser pulse of 88 fs could be obtained⁽¹⁰⁾.

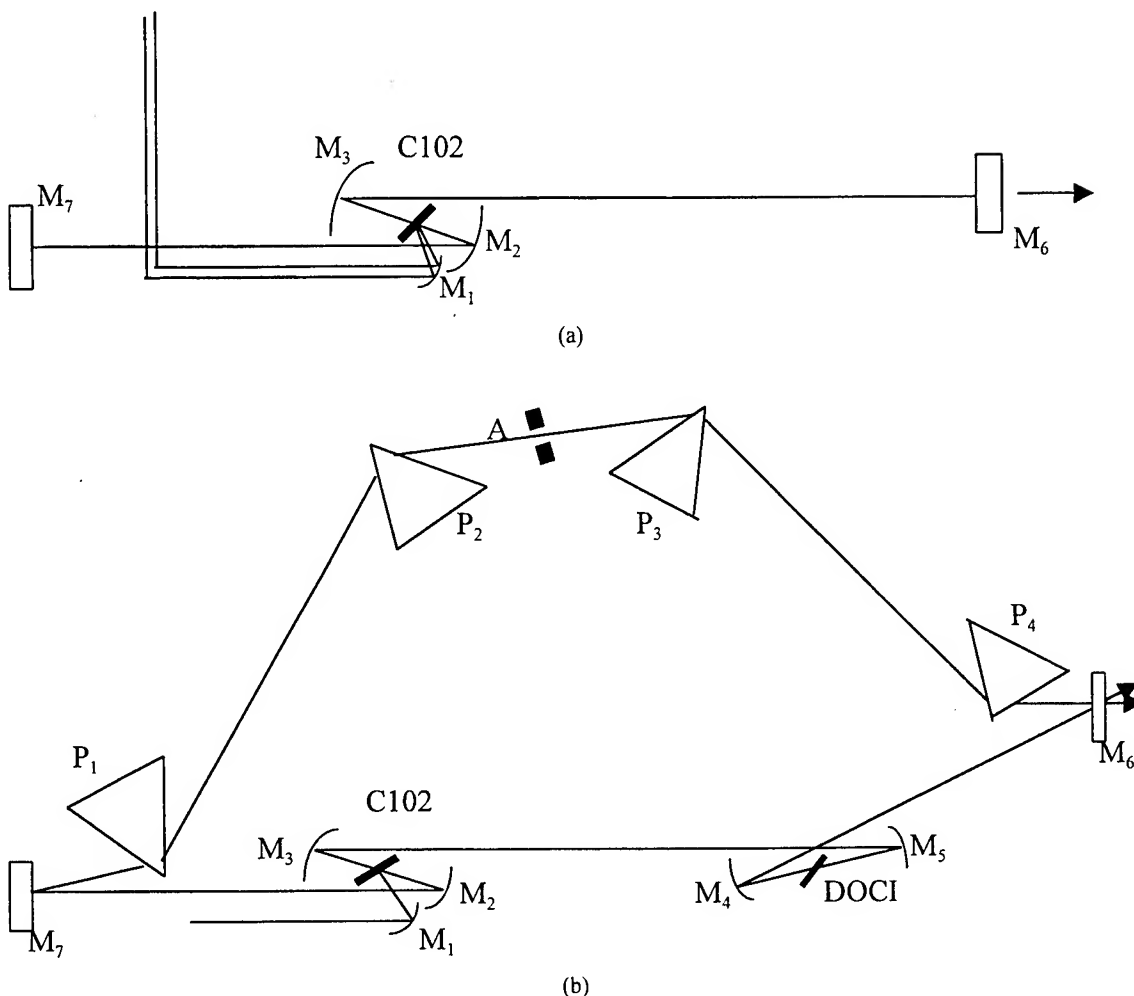


Fig. 5. Conventional C102 cw dye laser (a). and the ultrashort short pulse C102/DOCI dye laser (b).

The Rhodamine 6G dye laser is also one of the liquid laser frequently in use owing to its visible tuning ability between 590 nm and 640 nm. Rh 6G dye laser is a high gain laser, and could be efficiently modulated to generate ultrashort pulses. Ultrashort laser pulsewidth of less than 50 fs could be easily obtained and had been used⁽⁶⁾ to investigated the self-pumped phase conjugation using BaTiO₃ crystals. Fig. 6 shows the typical liquid dye lasers spectral coverage for the photorefractive searches with ultrashort pulsed laser outputs at different pulsewidth in the two dimensions figure.

The main reason to set up this dye laser is it can lase in the blue green region, and could be frequency doubled to the 248.6 nm and then amplified by the KrF excimer lasers to very high intensity. The configuration of this UV spectral, high intensity, ultrashort pulsewidth laser system shows in Fig. 8. With three stages four passes dye amplifiers of Coumarin 307, the pJ(pico-Joule) ultrashort laser pulses could be first amplified to the order of μ J(micro-Joule). Frequency doubled to the 248.6 nm and then amplified by a single stage KrF excimer amplifier to the output energy of mJ(milli-Joule). The laser pulsewidth could be optimized to less than 100 fs, and the laser output raw spot size is 2 mm in diameter. We could obtain focusing intensity of 10^{15} W/cm² easily. This laser output is very useful in the investigations of the above threshold ionization and the high order harmonic generation. One of the most outstanding feature of this high intensity ultrashort pulse UV laser system is that it can operated in a self-selected single amplified pulsed mode as well as quasi-cw mode with various repetition rates.

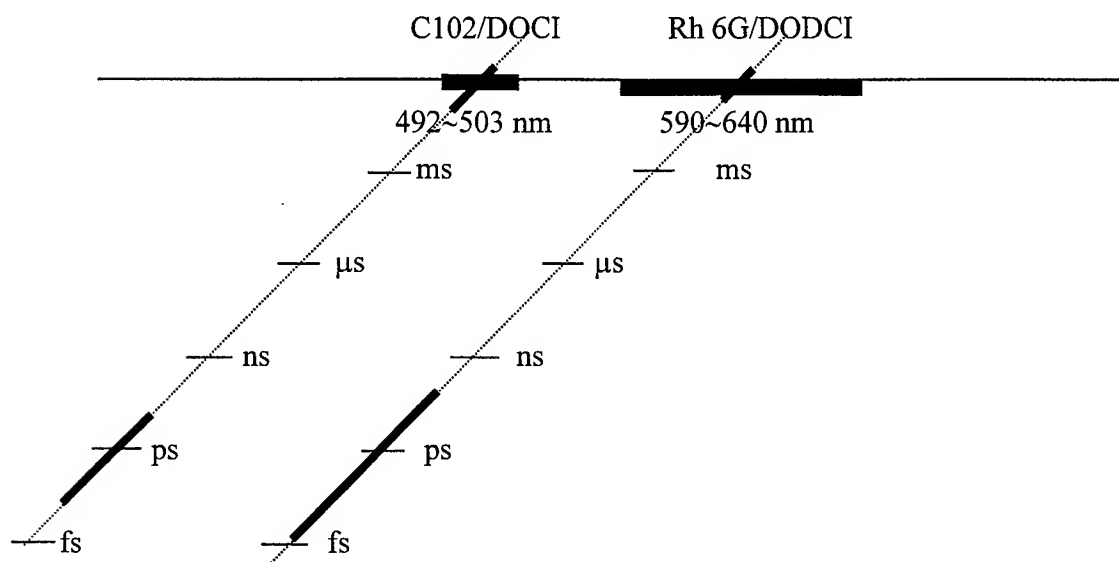


Fig. 6. Dye lasers spectral coverage for the photorefractive researches with laser outputs at various pulsewidth in two dimensions figure.

2.3 Gaseous lasers

For the gaseous lasers in photorefractive researches, Ar^+ laser in the visible wavelength of 514 nm and in the UV wavelength of 330 nm are the typical laser sources. We have several Ar^+ lasers with power output from 5 W, 7 W up 30 W in the visible range. We can also change the output mirrors of the Ar^+ laser to come out the maximum power of 5 W in the UV all lines of 330 nm to 360 nm. XeCl excimer laser of 308 nm and KrF excimer laser of 248 nm are also available. And the CO_2 lasers of 10.6 μm are available as well to be used for long wavelength mechanism explorations. Fig. 7 shows the typical gaseous lasers spectral coverage for the photorefractive searches with available pulsed laser outputs at nanosecond order pulsewidth in the two dimensions figure.

He-Ne gaseous laser typically operated in 632.8 nm. Yet it can as well operated at 3.39 μm . This spectral extension is very useful for the alignment of 3-5 μm optical systems. The collimated He-Ne laser output both at 632.8 nm and 3.39 μm are the standard set up in the laser center for multiple purpose applications.

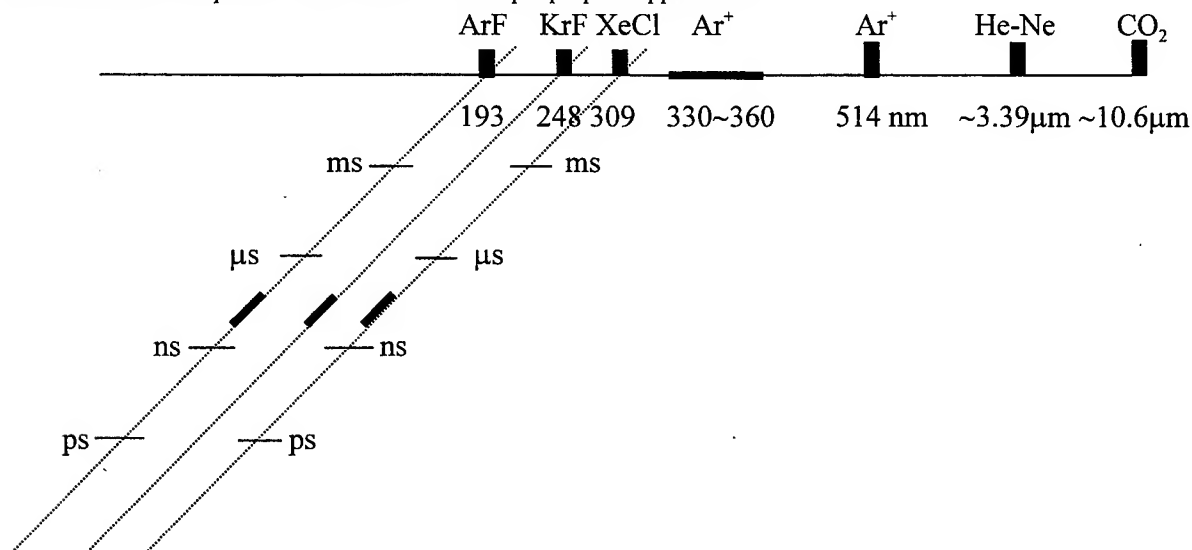


Fig. 7. The gaseous lasers spectral coverage for the photorefractive researches with laser outputs at different pulsewidth in two dimensions figure.

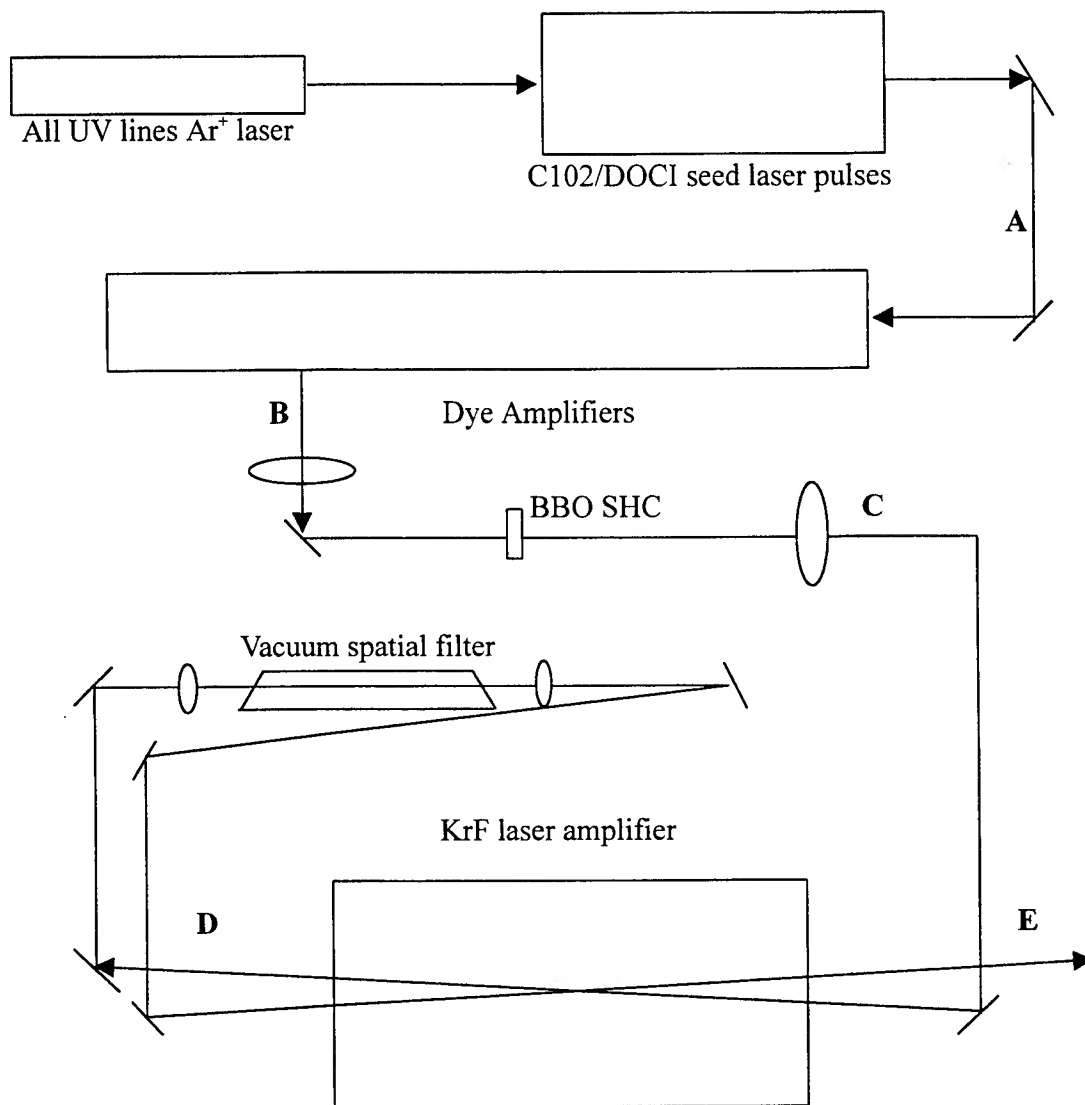


Fig. 8. High intensity ultrashort pulse UV laser system

3. CONCLUSION

Photorefractive researches especially the investigation of phase conjugators with BaTiO₃ crystals using laser sources of the continuous wave and the pulsed mode with laser pulsewidth of nanosecond, picosecond and femtosecond order. Our versatile laser sources provide various lasers with different laser pulsewidth as well as wide spectral coverage. It is very useful and important for the photorefractive, holography and nonlinear optics investigations.

REFERENCE

1. J. Feinberg, "Interferometer with a self-pumped phase-conjugating mirror" *Opt. Letts.*, 8, pp.569-571, 1983.
2. B. Monson and G. J. Salamo, "Self-pumped phaser conjugation with nanosecond pulses in strontium barium niobate" *Opt. Letts.*, 15, pp.12-14, 1990.
3. M. J. Damzen, N. P. Barry and M. Buttinger, "High-intensity effects in self-pumped photorefractive phase conjugation using nanosecond pulses" *J. Mod. Opt.*, 42, pp.2051-2057, 1995.
4. M. Cronin-Golomb, "Vibration resistance, short coherence length operation, and mock-locked pumping in passive phase conjugate mirrors" *Appl. Phys. Lett.*, 47, pp. 1131-1133, 1985.
5. H. F. Yau, E. Y. Pen, P. J. Wang and J. Chen, "Phase conjugation with picosecond pulses in BaTiO_3 " *Opt. Rev.*, 3, pp.312-314, 1996.
6. H. F. Yau, P. J. Wang, E. Y. Pen and J. Chen, "Self-pumped phase conjugation with femtosecond pulses by use of BaTiO_3 " *Opt.Letts.*, 21, pp.1168-1170, 1996.
7. H. F. Yau, E. Y. Pen, P. J. Wang, C. C. Chang, N. J. Cheng and J. Chen, "Mechanism for ultrashort phase conjugate pulse with photorefractive crystal" *Chinese J. of Phys.*, 36, pp.791-799, 1998
8. C. C. Chang, H. F. Yau, N. J. Chang and P. X. Ye, "Pentagon-shaped 0° -cut BaTiO_3 as an efficient self-pumped phase conjugator" *Appl. Opt.*, 38, pp.7206-7213, 1999.
9. J. Chen, H. F. Yau, H. P. Liu, T. C. Chen, F. M. Liu and C. C. Cheng, "Passive Q-switch and mode-locking modulators for Nd:hosted lasers" *Opt. and Laser Tech.*, Accepted, 28 February 2000.
10. J. Chen, Ph.D thesis, Imperial College, UK. 1991.

Author Index

- Abbate, Giancarlo, 779
 Aers, Geof C., 124, 304, 659
 Allen, C. Ni., 100
 Bahierathan, B., 765
 Benjamin, Seldon D., 211
 Bertsch, Nicholas, 148
 Bhat, Rajaram J., 137
 Bhattacharya, Pallab, 84
 Bowers, John E., 551
 Budiman, R. Arief, 765
 Chan, Michael C. Y., 289
 Chan, Yuen Chuen, 182, 191
 Chang, Chi-Hsiung, 646
 Chang, Chienliu, 620, 627, 637
 Chang, Horng, 467, 535, 570
 Chang, Horng Yu, 489
 Chang, Hung-Lun, 646, 652
 Chang, Jih-Yuan, 579, 587, 595
 Chang, Jynq-Yang, 786
 Chang, Peizen, 620, 627, 637
 Chang, Richard K., 254
 Chang, Shouu-Jinn, 570
 Chang, Wen-Chung, 745
 Chang, Wen Yi, 203
 Chang, Yung-Cheng, 712
 Chang, Yuni, 579, 595
 Chao, Ching-Her, 732
 Charbonneau, N. Sylvain, 298, 304
 Che, ChiMing, 292
 Chen, Chi-Chen, 646
 Chen, Chih-Hsiung, 353
 Chen, Chih-Liang, 66, 562
 Chen, Chii-Chang, 28
 Chen, Ching-An, 74
 Chen, Genmao, 211
 Chen, Horng-Min, 587
 Chen, Hsiao Hui, 521
 Chen, Hunglin, 620, 627, 637
 Chen, Jing-Yu, 66, 562
 Chen, Junewen, 817
 Chen, Kuei-Hsien, 500
 Chen, Ming-Tsung, 786
 Chen, Ming-Chun, 406
 Chen, Paul-Cheng, 652
 Chen, Ruy Ming, 422
 Chen, Shen-Li, 544
 Chen, ShihLieh, 739
 Chen, Tzu-Chiang, 817
 Chen, Wei-Kuo, 521, 535
 Chen, Wen-Ray, 570
 Chen, Wen-Hsiung, 521, 535
 Chen, Yau Huei, 422
 Chen, Ying-Chung, 689
 Cheng, C. C., 44
 Cheng, Chao-Chia, 817
 Cheng, Shu-Hway, 732
 Cheng, Wood-Hi, 646, 652
 Cheng, Y. T., 570
 Cheng, Y. T., 570
 Cherng, Ya-Tung, 115, 467
 Chi, Gou-Chung, 28
 Chiang, Cheng-Der, 467
 Chiang, Chung-I, 535
 Chiang, Jung-Lung, 689
 Chiang, Shang-Yeh, 786
 Chien, Hsien-Wen, 739
 Chio, Jinhung, 620, 627, 637
 Chiu, Yi-Jen, 551
 Chou, Hsueh-Tao, 680
 Chou, Jung-Chuan, 689, 793, 801, 809
 Chou, W. C., 570
 Chua, Soo Jin, 203, 664
 Chuang, Hui-Wen, 28
 Chuang, Kie-Pin, 445
 Chuang, Kuang-Yang, 365
 Chuang, Wei-Ching, 745
 Chuo, Chang-Cheng, 28
 Chyi, Jen-Inn, 28
 Coleridge, Peter T., 298
 Dai, Chingliang, 620, 627, 637
 Dai, Li-Kuo, 467
 Deppe, Dennis G., 90
 Ding, Lei, 559
 Djurišić, Aleksandra B., 35
 Dong, Xiaoyi, 559
 Donn, Shoang C., 786
 Du, Jinyu, 170
 Ebihara, Hiroyuki, 247
 Edirisinghe, Champika H., 211
 Fafard, Simon, 100
 Fann, Der-Ann, 544
 Feng, Dejun, 559
 Feng, Zhe Chuan, 203, 664
 Fong, W. K., 44
 Gan, Fu-Xi, 321
 Gao, Guo, 170
 Gao, M., 100
 Gau, Yau-Tang, 467
 Ge, Weikun, 279
 Goel, Aditya, 232
 Gould, C., 100
 Guo, Huang-Chen, 397
 Guo, Weiling, 289, 292
 Guo, WeiLing, 170

Guo, Xia, 170
 Hawrylak, Pawel, 100
 Haysom, Joan E., 304
 Hazell, John F., 148
 Hinzer, K., 100
 Hiruma, Teruo, 2
 Horng, Kuo-Kai, 579, 595
 Horng, Ray-Hua, 507, 697
 Hou, Chunfeng, 330
 Hsu, Jin-Cherng, 480
 Hsueh, YunTai, 745
 Hu, Shu-Fen, 124
 Huang, Der-Ray, 365
 Huang, Dexiu, 345
 Huang, Fujun, 247
 Huang, Hsu-Ching, 579, 595
 Huang, Huai Ying, 521
 Huang, Huiwen, 620, 627, 637
 Huang, Jung-Hao, 514
 Huang, Kaung-Shin, 467
 Huang, Man-Fang, 507, 595
 Huang, Ya-Lien, 579, 595
 Huang, Yeong-Jenq, 786
 Huang, Yuan Ming, 279
 Hwa, Luu-Gen, 480
 Hwang, Jih-Hsien, 500
 Hwang, Shug-June, 754
 Hwu, R. Jennifer, 130
 Ishibashi, Hiroki, 8
 Jan, Gwo-Jen, 514
 Jan, Shiun-Sheng, 689
 Jang, Ling-Yun, 535
 Jedral, Lech Z., 211
 Jeng, Guang-Kai, 74
 Jiang, Chun, 321
 Jiang, Wen-Chang, 162, 603, 611
 Jih, Far-Wen, 467
 Jin, Guofan, 383
 Juang, Fuh S., 272
 Kai, Guiyun, 559
 Kan, Steven L., 254
 Kim, Hang Ro, 313
 Kim, Jong-Bin, 389
 Kim, Mi-Ra, 664, 704
 Kim, Phil-Jung, 389
 Kim, Sang-Duk, 389
 Kim, Sung June, 313
 Klotzkin, David, 84
 Krishna, Sanjay, 84
 Kuang, Jao-Hwa, 646, 652
 Kubo, Shuichi, 58
 Kudo, Hiromitsu, 8
 Kuei, Ching-Ping, 365
 Kung, Hong-Chang, 817
 Kuo, Tsung-Nane, 74
 Kuo, Yen-Kuang, 579, 587, 595
 Kurai, Satoshi, 58
 Kuri, Goutam, 664, 672
 Lai, Chih-Ming, 514
 Lam, Jacky W. Y., 279
 Lam, Yee-Loy, 182, 191
 Lamontagne, Boris, 124
 Lan, Wen How, 570
 Landheer, Dolf, 298
 Lapointe, Jean M., 100
 Lee, Alex S. W., 148
 Lee, Cheng-Chung, 445, 480
 Lee, Chia-Chang, 680
 Lee, Chien-Ping, 124, 489
 Lee, Ching-Ting, 724
 Lee, Chung-Han, 500
 Lee, Hong-Ji, 74
 Lee, Jae-Gyu, 389
 Lee, Jyh-Fu, 535
 Lee, Ming-Chih, 521, 535
 Lee, Rong-Jer, 739
 Lee, Si-Chen, 115
 Lee, Wen-Hsiung, 521, 535
 Lefebvre, Jacques, 124, 659
 Letal, Gregory J., 148
 Leung, Benny H., 44
 Li, E. Herbert, 35, 289, 292
 Li, Ronghui, 773
 Liao, Yu-Cheng, 115
 Lin, Alpha C. H., 570
 Lin, Ching-Piao, 74
 Lin, ChingYen, 500
 Lin, Chin-Hwa, 535
 Lin, Deng-Sung, 535
 Lin, Gong-Ru, 712
 Lin, Jianyi, 203
 Lin, Kun Chuan, 507
 Lin, Ran-Jin, 456
 Lin, Shih-Yen, 115
 Lin, Song-Shiang, 739
 Lin, Wei-Cherng, 535
 Lin, Wei-Tsung, 697
 Lin, Yow-Jon, 724
 Liu, Day-Shan, 724
 Liu, Deming, 345
 Liu, Hai-Pei, 817
 Liu, Hong-Da, 732
 Liu, Hui C., 100
 Liu, J. S., 595
 Liu, Pin-Hui, 507, 595
 Liu, Qiang, 211
 Liu, ShiChuang, 289
 Liu, Shi Yong, 292
 Liu, Yion-Ni, 467
 Lu, Shuh-Tai, 365
 Luo, E. Z., 44
 Manabe, Shigeiki, 58
 Mao, Xiang-jun, 182, 191
 Marsh, John H., 220
 McCaffrey, John P., 100, 124
 McCann, Patrick J., 84

McMaster, Scott A., 18
 Mitchell, Ian V., 304
 Mitsuhashi, Manabu, 137
 Morita, Shinzo, 247
 Mormile, Pasquale, 779
 Nolan, Daniel A., 254
 Oe, Kunishige, 137
 Okazaki, Tomokazu, 58
 Pan, Yung-Chung, 521, 535
 Pang, Lin, 383
 Park, Gyoungwon, 90
 Peng, Peng-Chun, 373
 Peng, Wei Chi, 507
 Perović, D. D., 765
 Petti, Lucia, 779
 Phillips, Jamie D., 84
 Piva, Paul G., 304
 Poole, Philip J., 124, 304, 659
 Poon, Andrew W., 254
 Ra, Kyoung Tae, 389
 Ramanujachar, Kartik, 298
 Rana, J. L., 232
 Raymond, Sylvain, 100, 298, 304
 Righini, Giancarlo C., 779
 Robinson, Brad J., 18, 148
 Ruda, Harry E., 211, 765
 Sachrajda, A., 100
 Saha, Shymal K., 272
 Seieh, C. H., 507
 Shchekin, Oleg B., 90
 Sheen, Maw-Tyan, 646, 652
 Shen, Guangdi, 170
 Shen, Yu-Long, 414
 Shi, Jin-Wei, 551
 Shi, Yun-xi, 191
 Shu, Chen-Ke, 521, 535
 Simmons, John G., 148
 Simpson, Todd, 304
 Smith, Peter W. E., 211
 Soong, Bo-Shao, 66, 562
 Spanner, M., 100
 Streater, Richard W., 18
 Struby, C., 100
 Su, Yan-Kuin, 272, 570
 Su, Yeung-Sy, 603, 611
 Sun, Chia-Hsin, 680
 Sun, Chi-Kuang, 551
 Sun, Junqiang, 345
 Sun, Kien Wen, 489
 Sun, Xiudong, 330
 Sundaravel, B., 44
 Sung, Chia-Pin, 162, 603, 611
 Sung, Tien-Li, 353
 Surya, Charles, 44, 289
 Taguchi, Tsunemasa, 8, 58
 Tanabe, Tomoyuki, 8
 Tang, Ben Zhong, 279
 Tang, Shiang-Feng, 115
 Thompson, David A., 18, 148
 Tick, Paul A., 254
 Tien, Chuen-Lin, 445
 Tsai, Chang-Da, 724
 Tsai, Chen S., 239
 Tsai, Chin-Yi, 353
 Tsai, Chin-Yao, 353
 Tsai, Hsjian-Ming, 809
 Tsai, Hung-Sheng, 817
 Tsao, Shyh-Lin, 373, 397, 406, 414
 Tseng, Chung-Tung, 66, 562
 Tseng, Wei-Hao, 697
 Tseng, Yu-Neng, 793
 Twu, Ruey-Ching, 429, 437
 Ueki, Mineo, 137
 Wang, Chih-Ming, 646, 652
 Wang, Chih Ming, 489
 Wang, Ching-Wu, 66, 562
 Wang, Chungyung, 646, 652
 Wang, Gol-Lin, 646, 652
 Wang, Guohong, 170
 Wang, King-Yin, 365
 Wang, Mei-Li, 162, 603, 611
 Wang, QiuLai, 289
 Wang, Shu-Fang, 535
 Wang, Shyang Yeu, 489
 Wang, Szu-Chun, 646, 652
 Wang, Tahui, 298
 Wang, Tzyy-Jiann, 263
 Wang, Way-Seen, 263, 429, 437, 745
 Wang, Yii-Fang, 809
 Wasilewski, Z. R., 100
 Wen, Chun-Hsiang, 732
 Weng, Chen Yu, 801
 Weng, Ping-Kuo, 467
 Williams, Robin L., 124, 659
 Wilson, Ian H., 44
 Wu, Cheng-Zu, 162
 Wu, Minxian, 383
 Wu, Yaw-Ting, 732
 Wu, You-Cheng, 739
 Wu, Dong-Sing, 507, 697
 Xu, J. B., 44
 Xu, Yanjun, 559
 Yacobi, Ben G., 211
 Yamada, Yoichi, 8
 Yan, Changling, 773
 Yan, Yingbai, 383
 Yang, C. S., 570
 Yang, Cheng Chung, 353
 Yang, Fuh-Hsiang, 500
 Yang, Guo W., 130
 Yang, Hung-Pin D., 162, 603, 611
 Yang, Shue-Ping, 467
 Yang, Tzuen-Rong, 664, 672, 704
 Yang, Ying-Jay, 500, 551
 Yasukawa, Jun-Ichi, 732
 Yau, Hon-Fai, 817

Yeh, Jui-Hung, 74
Yeh, Min Yen, 527
Yen, Hung Ming, 527
Yen, Kaihsiang, 620, 627, 637
Yeo, Deok Ho, 313
Yi, Deer, 383
Yi, Heqing, 345
Yin, Tao, 148
Yoon, Kyung Hun, 313
Yu, Hsin Her, 754
Yu, Sin-Jei, 162, 611
Yuan, Baohong, 330
Yuan, Lixiang, 18
Yun, Jung-Hyun, 389
Zawadzki, P., 100
Zeng, Qingji, 321
Zhang, Xinliang, 345
Zhao, Yi, 292
Zhao, Yingjie, 773
Zheng, Ruisheng, 8
Zhong, Jingchang, 773
Zhou, Zhongxiang, 330
Zhu, C. F., 44
Zhu, Jing-yi, 182, 191
Zhu, Wenjun, 170
Zou, Deshu, 170